UNIVERSITAT POLITÈCNICA DE CATALUNYA

Escola Tècnica Superior d'Enginyers
de Camins, Canals i Ports

Departament d'Enginyeria Hidràulica, Marítima i Ambiental
Secciò d'Enginyeria Hidràulica i Hidrològica

TESI DOCTORAL

BEDLOAD TRANSPORT OF SAND-GRAVEL MIXTURES WITH ANTIDUNES

FLUME EXPERIMENTS

VOLUME I

Francisco Núñez-González

Director de Tesi:
Juan Pedro Martín Vide

Tesi presentada per obtenir el títol de doctor per la
Universitat Politècnica de Catalunya

Barcelona, Abril 2012

En memoria del
Profesor José Antonio Maza Álvarez

ABSTRACT

In this thesis, the interaction between flow and sediment in alluvial channels is studied from an empirical approach, for conditions close or pertaining to supercritical flow, and for four types of sediment: sand, gravel and two mixtures with sand and gravel in a relative proportion of 70-30 and 55-45, respectively. The objective is to obtain by means of laboratory experiments a data set with the characteristics of flow, sediment transport, bed configurations and sediment sorting patterns in sediment mixtures, for different conditions within upper- and transitional-regimes. From a practical perspective, the aim of this work is to reproduce similar conditions to those likely to occur in torrential ephemeral streams, common in the Mediterranean coast and known in Spain as "ramblas".

The experimental work consisted in searching for mobile-bed equilibrium states, for different water discharges and sediment-feed rates. The definitive data set comprises 22 runs, with durations up to 12 hours. Sediment-feed rates were constant during each run, and they were even higher than 1 kg/s. Dominant bed configurations included transitional bedforms and trains of antidunes, coexisting with alternate bars. Antidunes were mostly three-dimensional rather than two-dimensional, and in contrast to the most referred antidunes in literature, the antidunes herein reported moved in the downstream direction and were stable most of the time. Short-crested stationary waves on the water surface accompanied the antidunes.

Characterization of the experimental bedforms allowed identifying the range of Froude numbers in which transitional regime prevails for the studied sediment; also, this characterization allowed assessing the performance of theoretical and empirical diagrams for bedform stability phases. It is here demonstrated that for very coarse sand, fine gravel and mixtures of these two materials, plane bed does not occur in the transition from lower- to upper-regime, and if it would occur, it would be restricted to a very narrow range of Froude numbers. Regarding flow resistance related to bedforms in upper-regime, it has been here probed that for similar geometrical conditions, downstream-migrating antidunes produce less flow resistance than dunes, and more flow resistance than upstream-migrating antidunes.

An important concern in this work has been to investigate the effect of the relative sand content of sediment in bedforms, flow resistance and sediment transport. It is here demonstrated that bedforms in sand beds can be higher and they can produce much more drag than bedforms in gravel and sand-gravel mixtures. Regarding sediment transport, it is here shown that for the high sediment-feed rates tested in the experiments, certain ranges of sand content would affect sediment mobility. Besides sand content, it is shown that the ratio between sand and gravel grain sizes would also be relevant in the mobility of sediment in comparison to well-sorted material. A conceptual model is suggested for computation of sediment incipient motion, which model is based on the variation of bed porosity with sand content and on the relative size between particles.

Some supplementary themes considered in this work include the study of the required conditions for the formation of three-dimensional stationary waves over antidunes; the hydraulic analysis of flow over antidunes and the morphological consequences of such a flow for the three likely regimes of antidune direction of movement; sediment sorting patterns according to sand content, especially bed surface patches of homogeneous sediment; and finally, the analysis of the process by which fine sediment penetrates into a bed composed of particles of diverse sizes.

RESUMEN

En esta tesis se estudia de manera empírica la interacción entre el flujo y el sedimento en canales aluviales, para condiciones cercanas o pertenecientes al régimen rápido y para cuatro tipos de sedimento: arena, grava y dos mezclas con grava y arena, en una proporción relativa de 70-30 y 55-45, respectivamente. El objetivo es obtener de manera experimental en laboratorio un grupo de datos sobre las características del flujo, transporte de sedimento, configuraciones de fondo y patrones de clasificación en mezclas de sedimento, para diferentes condiciones dentro de los regímenes superior y de transición. De manera práctica, la intención de este trabajo es reproducir condiciones comparables a las que pueden ocurrir en ríos efímeros de carácter torrencial, comunes en la costa Mediterránea y conocidos en España como ramblas.

El trabajo experimental consistió en la búsqueda de condiciones de equilibrio dinámico en lecho móvil, para diferentes caudales líquidos y tasas de alimentación de sedimento. 22 ensayos, con duraciones de hasta 12 horas, conformaron el grupo de datos definitivo. Las tasas de alimentación fueron constantes durante cada ensayo, y alcanzaron valores de incluso más de 1 kg/s. Las configuraciones de fondo dominantes incluyeron formas de fondo de transición y trenes de antidunas, en coexistencia con barras alternadas. Predominaron las antidunas tridimensionales sobre las bidimensionales y, a diferencia de las antidunas más referidas en la literatura, las aquí descritas migraban hacia aguas abajo y eran bastante estables. En la superficie del agua acompañaban a las antidunas ondas estacionarias de cresta corta.

La caracterización de las formas de fondo experimentales permitió identificar el intervalo de números de Froude en el cual prevalece el régimen de transición en el sedimento estudiado y también evaluar diagramas teóricos y empíricos para las regiones de estabilidad de formas de fondo. Se demuestra que en arena muy gruesa, grava fina y mezclas de estos dos materiales, en la transición de régimen inferior a superior no ocurre el fondo plano, y si así fuese, estaría restringido a un intervalo muy estrecho de números de Froude. En cuanto a la resistencia al flujo producida por las formas de fondo en régimen superior, se ha probado que para condiciones geométricas similares las antidunas que migran hacia aguas abajo producen menos resistencia al flujo que las dunas y más resistencia que las antidunas que migran hacia aguas arriba.

De particular interés ha sido reconocer el efecto en las formas de fondo, la resistencia al flujo y el transporte de sedimento, del contenido relativo de arena en el sedimento. Se muestra que las formas de fondo desarrolladas en lechos compuestos sólo de arena pueden ser de mayor magnitud y producir mucha mayor resistencia de forma que las formas de fondo en grava y mezclas de grava-arena. En cuanto al transporte de sedimento, se muestra que para las altas tasas de transporte probadas ciertos intervalos de contenido de arena afectan la movilidad del sedimento. Además de la proporción de arena en la mezcla, el grado de afectación en la movilidad estaría relacionado con la relación entre tamaños de la arena y la grava. Se propone un modelo conceptual para el cálculo del inicio de movimiento de las partículas del fondo, el cual considera la variación de la porosidad en el lecho con el contenido de arena y la relación de tamaños de las partículas.

Algunos temas suplementarios abordados en este trabajo incluyen el estudio de las condiciones necesarias para la formación de ondas estacionarias tridimensionales sobre antidunas; el análisis hidráulico del flujo sobre antidunas y sus consecuencias morfológicas para sus tres posibles regímenes de propagación; el estudio de los patrones de clasificación del sedimento de acuerdo con el contenido de arena, en especial las manchas de material homogéneo sobre el lecho; y finalmente, el análisis del proceso de infiltración de sedimento fino en un lecho de partículas de tamaño diverso.

PREFACIO

[…] la movilidad heracliteana es una filosofía concreta, una filosofía total.
No nos bañamos dos veces en el mismo río, porque ya en su profundidad,
el ser humano tiene el destino del agua que corre.

Gastón Bachelard
El agua y los sueños.
Ensayo sobre la imaginación de la materia

Nuestra elección de una trayectoria profesional es a menudo deudora de una circunstancia, pero decantarse por el camino de la especialización doctoral es de común o de preferencia una decisión meditada, de convicción y gusto por profundizar en el conocimiento. Reconocer ese gusto, o en el mejor de los casos vocación, no es necesariamente inmediato y para muchos es tan solo una posibilidad latente capaz de despertar y desarrollarse si el entorno, la guía de un maestro o la admiración a un modelo referente la estimulan. La convergencia de estos tres aspectos convinieron en mi suerte para que optase por el derrotero de la tesis doctoral: mi tránsito como becario en el Instituto de Ingeniería, importante centro de investigación de la Universidad Nacional Autónoma de México (UNAM), me colocó en el entorno idóneo para descubrir mi gusto por la experimentación; distintos investigadores, con quienes trabajé en ese centro y en la Facultad de Ingeniería de la UNAM, fueron excelentes maestros que guiaron mi inquietud para seguir más adelante con mi formación académica; el modelo referente fue sin duda alguna el Profesor José Antonio Maza Álvarez, destacado precursor de la Ingeniería Fluvial en México y Latinoamérica. Su visión de la investigación y el mundo académico, pero sobre todo sus consejos, que revelaban una aguda sabiduría y calidad humana, marcaron en gran medida mi decisión de seguir con el doctorado y marcaron también el desarrollo mismo de mi investigación doctoral.

Tuve la fortuna de colaborar con el Profesor Maza Álvarez en el Instituto de Ingeniería y de que dirigiese mi tesis de maestría. Después de una primera experiencia académica en el extranjero favorecida por su intervención, al terminar la maestría le expresé mi interés por seguir el camino del doctorado en Ingeniería Fluvial fuera del país y le planteé las opciones que consideraba posibles. Él sugirió una más: la Universidad Politécnica de Cataluña y la tutela del Dr. Juan Pedro Martín Vide. En fechas recientes el Profesor Maza había impartido un curso en la Universidad de Castilla-La Mancha, donde había conocido el nuevo laboratorio de Hidráulica Fluvial que el Profesor Martín Vide había concebido. El Profesor Maza era un apasionado de la experimentación en modelos físicos y en repetidas ocasiones me había expresado su visión acerca de la superioridad de los experimentos en laboratorio sobre el modelado numérico; pensaba que los experimentos bien controlados, realizados con cuidado y bien documentados, eran siempre de suma valía. Supongo que le entusiasmó la idea de realizar experimentos en un laboratorio tan bueno como el de la Universidad de Castilla-La Mancha, así que me ofreció que, de ir a trabajar con el Profesor Martín Vide, él mismo podría colaborar con el seguimiento y la revisión de mi investigación. Si haber sido discípulo del Profesor Maza Álvarez durante la maestría había sido ya un gran privilegio, esta propuesta para contar con su consejo durante el doctorado merecía de inmediato dar por descartadas cualquiera de mis otras opciones de instituciones académicas.

Durante algunas charlas sabatinas en los meses previos a mi partida hacia Barcelona, el Profesor Maza me dio algunos consejos y recomendaciones de diversa índole.

Entre ellos, en el ámbito académico, me sugirió no precipitarme en la elección del tema para mi investigación doctoral. Me recomendó sopesar las opciones viables con detenimiento, y me indicó que era importante que el tema elegido fuese de particular interés para mi asesor, porque de esa manera me aseguraría de contar con su apoyo y acompañamiento a lo largo de la investigación, lo cual me permitiría tener mayor interacción con él y obtener mejor provecho de su experiencia. También me sugirió que lo mejor sería realizar experimentos en laboratorio, sin dejar de lado el aprendizaje de las herramientas y los métodos de modelación numérica, y que de preferencia me apartase del transporte de sedimentos, pues consideraba que era un tema complejo, en el que la innovación ya sólo podría venir del estudio profundo de la física del fenómeno, campo restringido a investigadores precoces y brillantes. Con este comentario era claro que el Profesor Maza conocía muy bien mis limitaciones, pero también que en él ligaba una más de sus recomendaciones: "Procura no tardarte demasiado en la realización de tu tesis", me indicó; entrar en un tema difícil implicaba un mayor esfuerzo y mucho tiempo para entenderlo y poder atacarlo.

De entre sus diversos comentarios y consejos, hubo uno que caló en mi moral profundamente: "No tienes opción al fracaso ─sentenció en lo que fue su primera reacción cuando le externé mi interés por hacer mi tesis doctoral fuera de México─; si haces tu doctorado en un país desarrollado y consigues tu objetivo con éxito, no habrá mayores aspavientos, tu logro pasará casi inadvertido, como uno más dentro de lo que debería esperarse; sin embargo, si fracasas, se juzgará ese desenlace como de antemano previsible por venir de donde vienes. Tu fracaso no será sólo tuyo, sino también de todos los mexicanos, y le cerrarás las puertas a los que en el futuro quisieran seguir por ese rumbo". Reconocí en esta advertencia el gran valor que el Profesor Maza daba al respeto por nuestros semejantes; a su vez, me hizo consciente del importante compromiso que yo asumía de manera implícita con mi decisión de salir del país a continuar con mis estudios.

Una vez en Barcelona, el Profesor Martín Vide me expuso una variedad de temas posibles para mi investigación doctoral y me proporcionó artículos e información diversa para considerar con detenimiento cada uno de ellos. También me expresó su interés por comenzar a trabajar con una instalación experimental en el laboratorio de la Universidad de Castilla-La Mancha, concebida para el estudio del transporte de sedimentos en ríos de grava y arena. Era evidente que entre todas las opciones este último tema le producía mayor entusiasmo en aquel momento. Después de algunas lecturas descubrí bastante atractiva el área de investigación del transporte de sedimentos en lechos de material heterogéneo, y al conocer la nueva instalación experimental en una posterior visita al laboratorio de la Universidad de Castilla-La Mancha, la motivación por abordar ese tema y participar en la puesta en marcha de esa nueva instalación me sedujo. Se me planteaba entonces una contradicción respecto de las recomendaciones del Profesor Maza, pues él me había sugerido, por un lado, apartarme del tema del transporte de sedimentos, y por otro, atender al tema de mayor interés para mi asesor, que en este caso conducía al área del transporte de sedimentos.

Aunque se trataba de una decisión personal, consideré que lo mejor sería pedir opinión al Profesor Maza; sin embargo, mientras barajaba las diferentes opciones, me fue notificada su muerte. No es que su desaparición me significase una especie de orfandad académica, sin embargo, me sentí afectado por la disolución de aquella expectativa de contar, más que con su apoyo y experiencia en el desarrollo de la investigación, con la posibilidad de estar próximo a su bonhomía y al goce vital que reflejaba en su curiosidad y en su gusto por el saber humano. Era una irremplazable pérdida para la Ingeniería Hidráulica en México y Latinoamérica.

Hice un profundo balance de las opciones. El tema del transporte de sedimentos en mezclas era muy atractivo, le interesaba a mi asesor y a mí también me motivaba, además

de que la nueva instalación experimental permitiría realizar ensayos en condiciones inusuales y por ello novedosas. Decidí abordarlo. Desatendería así una de las recomendaciones del Profesor Maza, pero me convencí de que a la sazón de las cosas él hubiese sugerido ese mismo camino. El contrapeso a los intríngulis de un tema tan escabroso como el transporte de sedimentos debería venir de una de las máximas del mismo Profesor José Antonio Maza, acerca de la enorme valía del conocimiento empírico aportado por la experimentación física hecha con rigor y documentada con sumo detalle. Lo excepcional de la instalación experimental abría las puertas a una aportación en el campo del transporte de sedimentos; en mis manos quedaría conferir calidad a los experimentos, a su registro y presentación.

Emprendí entonces el estudio del transporte de sedimentos en material no uniforme y su investigación experimental. El resultado es esta tesis ahora en manos del lector. El balance final ha dado la razón al Profesor Maza: acometer el tema ha sido arduo y prolongado. Pero si bien he incumplido con su llamamiento a la brevedad, ha sido en favor de atender a su más importante advertencia sobre la inviabilidad del descalabro. Considero que los resultados experimentales y la base de datos aquí presentados representan una modesta contribución al estudio del transporte de sedimentos.

La cita de Bachelard con que se inicia este prefacio no ha querido auspiciar pretensiones, sino apercibir de una significación diferente para el concepto heracliteano que es lugar ya común entre quienes nos ocupamos de cuestiones relacionadas con el flujo en los ríos. No nos bañamos dos veces en el mismo río: ni él ni nosotros somos inmutables, tenemos el mismo destino inestable del agua que corre (y del sedimento). Puedo intuir la verdad de la doctrina heraclítea del cambio a través del tránsito a la madurez de mis conocimientos en estos años; he querido con este trabajo rendir homenaje al Profesor Maza Álvarez y reconocerle de manera póstuma su labor en la enseñanza y su desinteresada guía que nos llevo, a mí y a diferentes generaciones de Ingenieros Hidráulicos en México, por el cauce adecuado para el fluir de este cambio, trascendente a nivel personal, pero, lo más importante, en beneficio de nuestro país.

Francisco Núñez González
Barcelona, junio de 2012

AGRADECIMIENTOS

La contribución de diferentes personas e instituciones fue fundamental para la realización de este trabajo. Estas personas e instituciones han contribuido de manera directa, a través de opiniones, sugerencias, discusiones, intercambio de ideas, lectura, revisiones, trabajo en laboratorio, guía e instrucción, y de manera indirecta, mediante patrocinio económico, confianza, aliento, condescendencia, paciencia, comprensión o la simple (pero no por ello menos valiosa) compañía emocional y solidaria, en la cercanía o en la distancia trasatlántica. A estas personas e instituciones deseo recordar con una modesta mención en este apartado, para reconocerles y agradecer así su aportación a la construcción de este volumen.

Los medios económicos que me permitieron plantear el inicio de mi trabajo doctoral en Europa y que me sustentaron durante más de la mitad del tiempo de desarrollo de mi investigación provinieron de una beca concedida por el programa Alβan "Becas de Alto Nivel para América Latina" de la Comisión Europea (becario E04D048796MX), y de una beca donada por el Consejo Nacional de Ciencia y Tecnología de México (CONACYT, becario 179047), que inicialmente fue un complemento y posteriormente se convirtió en una beca completa. Agradezco a ambas instituciones por sendos apoyos. A su vez, agradezco a la Universidad Politécnica de Cataluña por la ayuda económica para saldar algunos de los costes de viaje a dos congresos internacionales y por el pago de la revisión lingüística de buena parte de tres de los capítulos de esta tesis.

Agradezco a mi director de tesis, Dr. Juan Pedro Martín Vide, por su valioso apoyo, estímulo y guía; gracias a su entusiasmo por la investigación y gracias a la libertad que me brindó para explorar otras rutas o maneras de hacer -aunque en éstas a menudo discordásemos- la calidad de este trabajo y mi formación científica se vieron favorecidos. Le agradezco su proximidad y camaradería (no sus aprensiones ni intríngulis), que a lo largo de estos años han permitido consolidar una amistad afable; le agradezco también su paciencia para sortear mis arranques de mal humor y su aliento haciéndome valorar mi trabajo para seguir adelante en los momentos en que la motivación personal más mermaba.

De manera especial agradezco a mi gran amigo Carles Ferrer i Boix, quien desde el primer día que llegué a Barcelona para iniciar con la tesis ha sido un referente fundamental, no sólo en mi trabajo académico, sino también en mi entorno más familiar y en mi vida en esta ciudad y el conocimiento del idioma, la cultura, la historia y la política catalanes; bastante se ha beneficiado este trabajo y mi aprendizaje de las discusiones, consejos, críticas, ideas, sugerencias y ayuda de Carles. Ha sido una gran suerte andar así, hombro con hombro en la manufactura de la tesis y en el paso per Barna, amb aquest bon barceloní, merci per tot!

Durante la campaña experimental en la Universidad de Castilla-La Mancha, en Ciudad Real, la colaboración de Eduardo Díaz Poblete fue esencial y decisiva; le agradezco encarecidamente su entrega al trabajo bien hecho, su entusiasmo, amistad y simpatía durante ese año laborioso en aquel lugar de la Mancha. En esa misma etapa, la asistencia de la valdepeñera Juani Arias fue crucial para concluir el análisis de más de mil muestras granulométricas, a ella agradezco su ayuda y su empeño.

Most of Chapter 8 of this work benefited from commentaries, ideas and collaboration with Dr. Maarten G. Kleinhans of Utrecht University, thanks a lot for your time and interest in my work.

El texto de una porción del capítulo 3 y gran parte de los capítulos 4 y 5 fue revisado y corregido por Anne Murray, a quien agradezco su esmero y profesionalismo.

I thank Professor Gary Parker of Illinois University at Urbana-Champaign for providing me with a copy of Kennedy's original study on antidunes, that study was essential for my research and it opened my mind to tackle the interpretation of the

experimental observations. I also thank Professor Parker for his free books, lectures and sources in his web page, they have been a fundamental guide for my learning in river morphodynamics.

Agradezco a los revisores de esta tesis, el Profesor José Ángel Sainz Borda de la Universidad de Cantabria y el Profesor Antonio Heleno Cardoso del Instituto Superior Técnico de Lisboa, quienes hicieron el esfuerzo de realizar informes sobre este trabajo en un plazo breve a pesar de lo extenso del documento. Agradezco a su vez a los miembros del tribunal por acceder a participar en la defensa pública de este trabajo: Dr. Allen Bateman, Dr. Moisés Berezowsky, Dra. Astrid Blom y Dr. Benoît Camenen.

Agradezco a mi alma máter, la Universidad Nacional Autónoma de México (UNAM), epicentro de las ideas y surtidor de la mayoría de los profesionales que han construido y pretenden construir y guiar las mejores realidades de entre todas las que conviven, se subyugan y yuxtaponen en México; en muy diversos aspectos mucho de lo mejor que he obtenido se lo debo a esta insigne institución. Y dentro de la UNAM, quiero reconocer al Instituto de Ingeniería, donde gracias a sus investigadores en el área de Hidráulica, el trabajo con ellos y su impulso, y gracias a la convivencia con sus becarios, mi crecimiento profesional logró dar un salto fundamental al finalizar la carrera de ingeniería civil; mi paso por este centro fue decisivo en la construcción de la trayectoria que me condujo hasta el final de esta tesis. Del Instituto de Ingeniería agradezco con particular cariño al Maestro Víctor Franco por su continua presencia y seguimiento a mi trabajo a lo largo de estos años; su estímulo y confianza, su recomendación y el interceder a mi favor en diferentes circunstancias, en buena medida me encaminaron hacia esta senda académica, mientras que su amistad y el contacto sostenido durante este tiempo en la distancia no sólo ha sido un valioso vínculo con el Instituto de Ingeniería, sino un aliciente para dedicarme con pasión a este trabajo. También en la UNAM, agradezco al Dr. Gabriel Echávez Aldape, cuyas reflexiones y la formación que de él obtuve en el Posgrado de Ingeniería me han sido muy valiosas en diferentes aspectos de este trabajo, desde la experimentación hasta el tratamiento formal de diversos temas, así como en mi actitud hacia la investigación y la ciencia.

De mis compañeros en la Universidad Politécnica de Cataluña, quiero en especial agradecer a mis amigos chilenos Carlos Sepúlveda y su esposa Silvia, cuya cariñosa presencia fue desde el inicio un refugio de confianza, mimo y aliento; a mi querido amigo Gustavo Mazza de Almeida, con quien no solo aprendí a explorar Barcelona, sino también a reflexionar sobre mi trabajo desde otras perspectivas; a Marcelo Baldissone, sensible e impecable, amigo afable con quien descubrí otra cara de la gente de Argentina (y por supuesto, el acento coooordobés); a mi muy estimado camarada Tiago Olivera, con quien la amistad ha sido guiada por la música y las proximidades del talante portugués y el mexicano. Agradezco también a todos mis compañeros en el Departamento de Ingeniería Hidráulica quienes en diferentes etapas han permitido crear un ambiente de trabajo agradable, ignorando las fronteras (vergonzosas) invisibles entre puertas contiguas, y con quienes en muchos casos la convivencia ha traspasado las horas y los muros de la universidad en memorables convites: Guillaume Chevalier, Gonzalo Olivares, Francesco Bregoli, Anaïs Ramos, Albert Herrero, Andrés Díaz, Vicente Medina, mi compatriota y carnal de alma máter José Luis Aragón, Ana Mujal, Marta Roca, Raquel Plaza, i els més joves: en Sergi Capapé i en Gil Lladó, amb ells dos he après el que de debò significa el barcelonisme i l'ésser culé! A otros compañeros ingenieros de caminos a quienes agradezco su acompañamiento desde el centro de la península son Pedro Martín y su esposa Susana López.

La vida en Cataluña no hubiese sido igual de agradable, ni me hubiese aportado tantas satisfacciones en el trato humano y el conocimiento personal -esenciales para compensar el aturdimiento que a menudo provoca el trabajo mental-, de no haber sido por

los momentos compartidos con diferentes personas que se volvieron amigos irremplazables. En especial y con cariño agradezco a Elisabet Farrero (l'Eli), la meva germana petita catalana amb el seu peculiar accent de la Vall de Boí, quién me acompañó y toleró todos estos años, desde mis primeros días en Barna; las interminables charlas, discusiones, el entendimiento con Eli, sus reflexiones y sensibilidad me han aportado gran luminosidad estos años, moltes gràcies! Mi mejor descubrimiento de los países Catalanes lo debo a mi entrañable amigo Xavi Martín, compañero de cordada en las paredes de roca y de los caminos que pasan, marchan y vuelven a estas regiones, cruzando los Alpes y los Pirineos, gràcies per tan bons moments pinchi neeeng! Agradezco la más que buena convivencia de mis más apreciados flatmates en estos años, Agnés Vievard (Mme. Jaafar), Stephen Fox y Mercè Carreras, y la producción de alegrías gracias al encuentro con Eva Crego, Mireia Beneria, Riikka Laakso y Lina Tyroller.

En Barcelona y aún desde el otro extremo de la península ibérica, el acompañamiento fraternal y reflexivo de mi excelente amigo Juan José Cierto ha sido muy importante en estos años de tesis, ¡gracias carnal! También en la distancia, pero más extensa y que separa continentes, agradezco a aquellos que han estado presentes emocionalmente, como uno de los ganchos del ancla que me ha mantenido unido al Anáhuac. En especial agradezco a mi amigo, carnal, padrino Jorge Córdova, sustento de sabiduría y esperanza, refugio de ánimo y de alivio para apuntalar estos años en el extranjero; agradezco a mi queridísimo primo y amigo Raúl Eduardo González, quien me ha regalado magníficas treguas trayendo su música y poesía hasta Barcelona; y a todos mis grandes cuates chilangos: Carolina Arias, Rubén Lozano y Iaarah Montalvo, Gabriel Lozano y Guillermina Añorve, Daniel Escotto y Águeda Reséndiz, Octavio Arenas y Esther Ponce, René Caro y Adriana Sepúlveda, Carlos Sosa, Josué Mendoza, Iván Hernández y Alejandra, Lorena Sicilia y mi querida prima Gloria. Mi mayor vínculo con el devenir en México desde Cataluña ha sido a través del programa Sentido Contrario de radio-UNAM, del gran mexicano catalán Marcelino Perelló, a él agradezco esa presencia, aunque sea en el anonimato me considero como uno más de sus salmones.

Por último, quiero rendir gracias absolutas a mis más queridos y amados; de manera póstuma a mis abuelitos Porfiria Alvear y Teobaldo González, que aunque desaparecidos el mismo año en que inicié este trabajo, han estado conmigo presentes durante su hechura por su ternura, enseñanza y su modélica talla a la cual aspiro; a mis hermanas Karina y Karla, por sus inyecciones de optimismo, su apoyo incondicional e impagables muestras de cariño, su confianza en mí y su acompañamiento han sido fundamentales en este recorrido; a mis muy queridos sobrinos, Karla Paola y Rodrigo, quienes han crecido a la par con esta tesis, y que con los relatos e informaciones sobre sus progresos, sus hazañas y peripecias, me han dado muchas más satisfacciones que ésta y han sido así una gran motivación para esforzarme en encontrarle posibles pies y cabeza a este trabajo; a mis padres, Emir y Francisco, va mi gratitud y amor inconmensurables, su presencia constante aún en la distancia ha sido un soporte anímico esencial, que me ha dado fortaleza para marcar el rumbo en esta expedición doctoral, ellos son el fundamento de toda esta travesía vital, que se ha beneficiado de la confianza hecha de esa luz de hogar y grandeza moral que ellos mantienen. Y el agradecimiento que quisiera fuese el más elocuente es para mi querida Saskia, quien es ahora y ha sido durante el extenso esprint de este trabajo la más importante presencia a mi lado, le agradezco haber dado sentido a todos esos días con la razón vencida y protegerme del sectarismo físico-matemático, ¡gracias por estar aquí y ser tan especial!

A todos ellos, a quienes omito por lapsus inconsciente y a quien mueve los hilos invisibles de los sucesos aleatorios, gracias de todo corazón.

A la mar por ser honda se van los ríos,
y detrás de tus ojos se van los míos;
surcando los cañones y las cascadas,
a la mar por ser honda se van las aguas.

Inundan los aleros, luego las calles,
dejan su verde huella en cierras y valles;
cual miradas que vencen los desafíos,
a la mar por ser honda se van los ríos.

Raúl Eduardo González
"A la mar se parecen" (fragmento)

VII
En el rigor del vaso que la aclara,
el agua toma forma
-ciertamente.
Trae una sed de siglos en los belfos,
una sed fría, en punta, que ara cauces
en el sueño moroso de la tierra,
que perfora sus miembros florecidos,
como una sangre cáustica,
incendiándolos, ay, abriendo en ellos
desapacibles úlceras de insomnio.

José Gorostiza
"Muerte sin fin" (fragmento)

TABLE OF CONTENTS

VOLUME I

VOLUME II

NOTATION

Variable	Description
A	Flow area
A, B, A-B	Arbitrary denomination of two different well-sorted bed materials and a mixture of these two materials, respectively
A_b	Area of an obstacle exposed to the flow
A_b, A_w, A_e	Constants in linear functions fitted to the experimental bed, water and energy elevation profiles, respectively.
a	Constant and calibration constant for the sediment feeders
B	Channel width
B*	Sediment bimodality index
B_b, B_w, B_e	Constants for the bed slope in linear functions fitted to the experimental bed, water and energy elevation profiles, respectively.
B_{dif}	Parameter for evaluating the disparity between the slopes of bed and water experimental profiles
B_f	Width of the gate at the base of the feeder
b	Constant and calibration constant for the sediment feeders
$_b$	Subscript for bed
b_s	Width of intake opening of the sediment transport sampler
C	Chézy flow resistance coefficient
C'	Chézy coefficient related to grain roughness
C_D	Drag coefficient
C_f	Dimensionless bed resistance coefficient
C_f'	Dimensionless resistance coefficient due to skin friction
C_f''	Dimensionless resistance coefficient due to form drag
C_z	Dimensionless Chezy coefficient
c	Bed form celerity
c_w	Velocity of a water surface perturbation
D	Sediment grain size
D	Size of the bed material or coarse size fraction
D_*	Dimensionless particle parameter
D_c	Cutoff sediment size and grain size of the coarse mode in a sediment mixture
$D_{c,p}$, D_c	Bed material cut off size
D_f	Grain size of the fine mode in a sediment mixture
D_g	Representative size of gravel grain size fraction
D_i, D_i	Characteristic sediment grain size for the i-th grain size range
$D_{i(N)}$, $D_{i(N+1)}$	Fine and coarse class limits of the grain size D_i
D_m	Mean grain size
D_{max}	Maximum grain size in bed material
D_{mean}, D_m	Geometric mean grain size in bed material
D_{min}	Minimum grain size in bed material
D_r	Representative size for the sediment mixture
D_s	Representative size of sand grain size fraction
Dt_s	Sampling period of sediment transport

Variable	Description
D_x	Particle diameter for which x% of the particles in the sample are finer
D_{*x}	Particle diameter for which x% of the particles in the coarse fraction are finer
D_{50}	Median grain size
d	Size of the pore-filling sediment or fine fraction
d_m	Geometric mean diameter of infiltrating material
d_{max}	Maximum grain size of particles in the pore-filling sediment or fine fraction
d_x	particle diameter for which x% of the particles in the fine fraction are finer
E	Total energy at the channel section
$\overline{E}$	Elevation of the energy grade line computed with the best-fit line to the energy profile
e_z	Correction on the vertical displacement of the channel due to deformations
F	Froude number
F_a	Dimensionless number for the criteria of antidune migrating direction
F_c	Proportion of material in the coarse mode of a sediment mixture
F_D	Pressure drag
F_d	Froude number for the border between 2D and 3D antidunes (Kennedy 1963)
F_f	Proportion in the fine mode of a sediment mixture
F_i	Fractional content of the i-th size fraction in the bed material
F_p	Maximum Froude number for upstream-migrating antidunes to occur (Kennedy 1963)
F_{rp}	Particle Froude number
F_{SATi}	Maximum fractional content of the i-th size fraction of infilling sediment that can admit the bed
F_u	Minimum Froude number for upper-regime (Kennedy 1963)
f	Darcy-Weisbach flow resistance coefficient
f'	Darcy-Weisbach flow resistance coefficient due to skin friction
f''	Darcy-Weisbach flow resistance coefficient due to bedform drag
f_a	Functional relation
f_B	Fractional content of material B in a mixture composed of materials A and B
f_{bi}	Fractional content of the i-th size fraction in bed material
f_D	Proportion of large particles by volume in the bed
f_d	Proportion of small particles by volume in the bed
f_{di}	Fractional content of the i-th size fraction of sediment depositing on the bed surface
f_{dMAX}	Maximum fractional content by volume of small particles in the bed
f_i	Fractional content of the i-th size fraction in sediment discharge
f_{pi}	Fractional content of the i-th size fraction in the proportion of depositing sediment that is able to penetrate into the bed surface
f'_{pi}	Fractional content of the i-th size fraction of sediment depositing on the bed surface with a smaller size than the cutoff size
f_s	Sand content in a sediment mixture
$f_{sFEEDING}$	Sand content of the sediment mixture fed constantly into the channel
$f_{sSAMPLE}$	Sand content in a sample of bed material
$f_{S,i}^{k}$	Fractional content of the i-th size fraction in the aggregate of samples for the compartment k of the basket type sampler (k=1 and k=3 for the left and right compartments, respectively, and k=2 for the central compartment)
$f_{S,i}^{k_1-k_3}$	Arithmetic average of the fractional content of the i-th size fraction sampled in the lateral compartments of the basket type sampler
g	Gravitational acceleration
H	Mean water depth
$\overline{H}$	Average water depth for an intermidiate bed reach

Variable	Description
H_e	Water depth for computing the energy elevation at a channel cross-section
H_m	Reach average water-depth
H_s	Skin friction portion of the water depth for the shear stress partition method of Einsten
h	Pressure head on the bed surface
h_e	Expanssion loss
h_f	Openning of the sluice gate on the base of the sediment hopper
h_p	Pressure head due to centrifugal acceleration
i	i-th time step and constant for numbering the rulers for measuring bed and water surface elevations
j	j-th bed material and constant for numbering the intermidiate reaches used for the computation of hydraulic properties
K_n	Units conversion factor for the Maninng flow resistance formula, K_n=1 $m^{1/2}/s$ for V and R_h in SI units, 1.486 $ft^{1/3}m^{1/6}/s$ for English units.
k	Wave number $=2H\pi/\lambda$
k_e	Coefficient for expansion losses
ks	k-th bed material
k_s	Nikuradse's equivalent grain roughness
L_m	Wavelength of oblique standing wave for the m mode of vibration
l	Total number of grain size fractions
m	Total number of manual samples for sediment transport and mode of vibration of transverse cross-waves
m_s	Constant in the exponent of a power law approximation of Shields incipient motion criterion, and ranking of the i-th bed material sample ordered from higher to lower sand content
n	Manning flow resistance coefficient; n-th dimensionless reference sediment transport rate; constant for numbering the time intervals for measurements during a run; and total number of time steps
nc	Number of sediment size fractions in the bed that are lower than the cutoff size
nf	Total number of size fractions
nif	Number of size fractions with a diameter smaller than the cutoff size
n_p	Number of measured points in an intermidiate bed reach
n_{PE}	Number of bed and water profiles taken during the equilibrium state
n_R	Number of data for computing the correlation coefficient
n_s	Total number of bed material samples
P	Wetted perimeter
P_b	Bed porosity
Q_{IN}	Sediment discharge added to the hoppers
Q_{INg}	Sediment discharge added to the gravel hopper
Q_{INs}	Sediment discharge added to the sand hopper
Q_s	Total load sediment transport rate passing through the channel
Q_{SF}	Constant sediment feeding rate added to the channel
Q_{SFg}	Gravel feeding rate added to the channel
Q_{SFs}	Sand feeding rate added to the channel
Q_{sg}	Gravel load sediment transport rate passing through the channel
Q_{ss}	Sand load sediment transport rate passing through the channel
Q_w	Water discharge
q^*	Einstein number or unit dimensionless solid discharge
q_b	Total load sediment transport rate passing through the channel

Variable	Description
q_f	Coefficient for fluctuation of bedload transport rate
q_i	Unit load sediment transport rate of sediment in the i-th size fraction
q_i	Incoming sediment flux of the i-th size fraction through the bed per unit area
q_{Li}	Outgoing sediment flux of the i-th size fraction through the bed per unit area
q_o	Mean unit bedload transport rate
q_s	Unit bedload transport rate at a channel section
q_S	Unit total load sediment transport rate passing through the channel
q_{Sb}	Unit average bed load discharge
q_{SF}	Unit constant sediment feeding rate into the channel
q_{Sin}	Unit sediment transport rate passing through the channel for a finite time length
q_{Ss}	Unit total load discharge computed from sediment caught in the sediment transport sampler
q_{Su}	Unit average suspension load discharge for sediment caught by the sediment transport sampler
q_{TOT}	Total solid volume of sediment passing downwards through a finite bed volume per unit time and per unit area
q_w	Unit water discharge at a channel section
q_{0i}	Constant flux of sediment of the i-th size fraction downwards on the bed surface for the i-th size fraction
Re	Reynolds number
Re_p	Particle Reynolds number
R_{fs}	Ratio between the bed sample and the feeding material sand content
R_h	Hydraulic radius
R_{hb}	Hydraulic radius for the bed portion
R_{XY}	Correlation coefficient for X and Y variables
r	Radius of curvature
r	Size ratio between fine and coarse particles
r_{MAX}	Maximum likely size ratio between sand and gravel in a bed with natural sediment
r_s	Radius of the sampling area
S	Energy slope
$\overline{S}$	Average slope of the energy gradient for an intermidiate bed reach
S'	Energy slope due to skin friction
S"	Energy slope due to form resistance
S_c	Flume channel slope
S_d	Penetration depth of the adhesive for areal bed samples
S_o	Mean bed slope
S_s	Sediment relative density
S_w	Mean water surface slope
T_b	Period of a bedform unit, and dimensionless bed load transport function
T_l	Time lag
t	Time
t_m	Elapsed time during the run
T_w	Water temperature
$\%T_e$	Trapping efficiency of a bed load sampler
U_1	Mean velocity above the bedform crest
U_2	Smaller mean velocity downstream from the bedform crest

Variable	Description
u	Time-average flow velocity at a distance z above the bed
u*	Shear velocity
u'*	Shear velocity related to skin friction
V	Mean flow velocity
V_f	Velocity of the rotating band on the base of the sediment hopper
V_m	Reach average flow velocity
V_s	Flow velocity at the free surface
W	Mass weight in the hopper
W^*	Dimensionless sediment transport rate
W^*_i	Dimensionless sediment transport rate for the i-th size fraction
W^*_R	Reference dimensionless sediment transport rate
W_s	Dry mass of sediment caught by the sediment transport sampler
W_{sd}	Dry mass weight of the sample taken from the hopper
W_{sh}	Mass weight of the wet sample taken from the hopper
W_{ss}	Dry mass of sediment sampled arealy
$W^k_{Ss,i,j}$	Weight of the i-th size fraction for the j-th sample retained in the compartment k of the basket sampler
w	Subscript for wall
X	Variable
x	General direction of flow or horizontal direction
x_b	Horizontal coordinate at a given point on the bed surface
x_{bD}	Horizontal coordinate at a given point on the bed surface for measurements taken following the downstream direction
x_{bU}	Horizontal coordinate at a given point on the bed surface, for measurements taken following the upstream direction
x_{hi}	Distance between the i-th ruler and the origin of the coordinate system when the channel slope is zero
x_w	Horizontal coordinate at a given point on the water surface
x_{wD}	Horizontal coordinate at a given point on the water surface, for measurements taken following the downstream direction
x_{wU}	Horizontal coordinate at a given point on the water surface, for measurements taken following the upstream direction
Y	Variable
y	Trasversal direction to flow
z	Direction vertically perpendicular to x or vertical coordinate, and distance above the bed
$\tilde{z}$	Depth along the bed
z_b	Vertical coordinate at a given point on the bed surface
$\bar{z}_b$	Vertical coordinate of the bed surface computed with the best-fit line to the bed profile
z_{bD}	Vertical coordinate at a given point on the bed surface, for measurements taken following the dowsntream direction
z_{bU}	Vertical coordinate at a given point on the bed surface, for measurements taken following the upstream direction
$\langle z_b(x_{b,i})\rangle_E$	Average of bed elevation measurements at the i-th ruler in coordinate x_b during equilibrium state
z_{hi}	Measurement on the i-th ruler of the perpendicular distance from the bottom of the channel to the measurement point, corrected for errors in the rulers
$\tilde{z}_{max}$	Maximum depth of a sediment deposit
z_o	Bed roughness length, i.e. the distance above the bed where the flow velocity is equal to zero
z_s	Maximum depth of bed erosion
z_{sMAX}	Maximum transversal bed erosion
z_{sMEAN}	Mean transversal bed erosion

Variable	Description
z_w	Vertical coordinate at a given point on the water surface
z_{wD}	Vertical coordinate at a given point on the water surface, for measurements taken following the downstream direction
z_{wU}	Vertical coordinate at a given point on the water surface, for measurements taken following the upstream direction
$\bar{z}_w$	Vertical coordinate of the water surface computed with the best-fit line to the water profile
α	Angle between the horizontal and the channel bottom, and coefficient
α_{BR}	Bed roughness to grain diameter ratio (k_s/D_x) related to the bed load roughness layer
α_c	Coefficient for the Carnot's formula to estimate the expansion loss, and coriolis coefficient
α_{RL}	Bed roughness to grain diameter ratio (k_s/D_x) related to the grain roughness layer
α_S	Bed roughness to grain diameter ratio (k_s/D_x)
β	Angle between an oblique standing wave and the channel wall, and coefficient
β	Trap efficiency for infiltrating sediment, defined as the ratio between the portion of the incoming sediment retained in the bed and the total incoming sediment flux into a finite volume, when the material travels vertically a unit distance
γ	Exponent in the hiding-exposure function
Δ	Bedform height
Δ_b	Bar height
Δ_c	Distance from the mean bed-surface level to the bedform crest
Δf_d	Increments of fractional content of sediment depositing on the bed surface
$\Delta H''$	Expansion loss for a bedform
$\Delta_{s,max}$	Maximum sectional difference in height for the final experimental bed configuration
Δ_t	Distance from the mean bed-surface level to the bed form trough
Δt	Time interval
ΔV_{Ai}	Volume available for the i-th size fraction to penetrate to a bed finite volume
ΔV_{Ei}	Volume of sediment of the *i*–th size fraction entering into a bed finite volume
ΔV_{Li}	Volume of sediment of the i-th size fraction that goes out from a bed finite volume
ΔV_{Ri}	Volume of sediment of the i-th size fraction not able to penetrate deeper
ΔV_s	Volume of particles of a sediment mixture depositing on the bed surface
ΔV_{Ti}	Volume of sediment of the i-th size fraction trapped in a bed finite volume
Δ_w	Vertical distance from trough to crest of a water standing wave
$\Delta_{w,max}$	Maximum stationary wave height
$\Delta\tilde{\chi}$	Depth of a bed finite volume
δA	Cross-sectional area of a column of liquid
ε	Porosity of a sediment deposit
ε_D	Pure porosity of large particles
ε_d	Pure porosity of small particles
ε_{MIN}	Minimal fractional porosity in a bed mixture
η	Bed-surface level, and efficiency of the sediment transport sampler
η_b	Function for the bed elevation in the channel
η_o	Datum for the mean bed-surface level
η_w	Function for the water elevation in the channel
K_a	Antidune curvature
κ	von Karman's constant
λ	Bedform wavelength, and 3D waves wavelength
λ_e	Length scale
λ_m	Wavelength for the m mode of vibration of transverse cross waves
λ_t	Rooster tail wavelength transversal to the flow
ν	Kynematic viscosity of water
ν_m	Kinematic viscosity coefficient of fluid-sediment mixture for van Rijn partition method

Variable	Description
ρ	Water density
ρ_s	Sediment density
σ_b	Standard deviation of the bed surface elevation
$\overline{\sigma}_b$	Standard deviation of the measured bed elevations with respect to the line of best-fit of the bed profile
$\sigma_{bE}(x_{b,i})$	Standard deviation of bed surface elevation measurements at the i-th ruler in coordinate x_b during equilibrium state
σ_g	Geometric standard deviation of sediment
σ_g	Geometric standard deviation of bed material
σ_{gs}	Geometric standard deviation of sediment for a normal distribution of grain sizes
σ_s	Geometric standard deviation of infiltrating material
σ_{ss}	Standard deviation of sediment discharge
σ_w	Standard deviation of the water surface elevation
$\overline{\sigma}_w$	Standard deviation of the measured water elevations with respect to the line of best-fit of the water profile
$\sigma_{wE}(x_{w,i})$	Standard deviation of water surface elevation measurements at the i-th ruler in coordinate x_w during equilibrium state
σ_X	Standard deviation for variable X
σ_Y	Standard deviation for variable Y
τ	Mean boundary shear stress
τ'	Skin or grain friction
τ''	Form drag
τ^*	Dimensionless Shields parameter
τ'^*	Dimensionless Shields stress asociated to skin friction
τ'^*_c	Dimensionless critical Shields stress for initation of particle motion, asociated to skin friction
τ'^*_R	Dimensionless reference Shields stress value associated to skin friction
τ'^*_{Ru}	Dimensionless reference Shields stress value associated to skin friction for uniform material
τ_b	Bed shear stress
τ_b^*	Bed Shields stress
τ_b^*	Dimensionless bed shear stress
τ_{b50}^*	Dimensionless bed shear stress for the median grain size
τ_c	Critical shear stress
τ'_c	Critical stress for initation of particle motion, asociated to skin friction
τ_c^*	Critical Shields stress for initiation of motion of the bed material
$\tau_{c,i}^*$	Dimensionless critical shear stress for the i-th grain size range in a sediment mixture
$\tau_{c,m}^*$	Dimensionless critical shear stress for the mean grain size in a sediment mixture
τ'_R	Reference shear stress value associated to skin friction
τ'_{Ri}	Reference shear stress value associated to skin friction for the i-th grain size range
τ'_{Ru}	Reference shear stress value associated to skin friction for uniform material
τ_w	Sidewall shear stress
Ψ	Grain size on base-2 logarithmic psi scale
$\%\omega$	Water content
$\forall_{ret}$	Volume of sediment retained by the sediment transport sampler
$\forall_{tot}$	Total volume of sediment introduced through the intake opening of the sediment transport sampler

CHAPTER 1:

INTRODUCTION

1.1 OVERVIEW

Alluvial beds in rivers are deformed by the action of flowing water competent to mobilize sediment particles. In such a process, a sediment load is transported downstream and mesoscale bedforms are commonly developed which have a strong interaction with the fluid and sediment flow. These are the subjects of this work, the characteristics and interactions between water flow, sediment and bedforms in alluvial rivers; specifically, this work treats with flow conditions highly competent to mobilize the alluvial bed particles, and for these conditions beds composed of sediment grains with a narrow range of sizes are compared with beds composed of mixed-size particles.

The range of flows studied herein pertains to the transcritical and supercritical regimes. These flow regimes have received much less attention from research in comparison to their subcritical counterpart. Although not as common as subcritical flow regimes, transcritical and supercritical flows occur for a variety of situations in rivers. In particular, they can be frequent in natural rivers with moderately to steep slopes, in self-formed streams subjected to very steep hydrographs, and in engineered rivers where flow resistance is low due to smooth boundaries or where the bed geometry has been altered reducing the effective width of the channel. Transcritical- and supercritical-flows are also likely to occur in torrential ephemeral streams, typical of the Mediterranean coast, especially when these streams have been narrowed with vertical rigid walls. Thus, the study of flow, sediment transport and morphology of torrential ephemeral streams, characterized by high sediment load rates, is the practical target of this research.

The aim of this work is to provide empirical evidence, through systematic, well controlled and thoroughly documented laboratory experimentation, of transcritical and supercritical flows over mobile-beds. In terms of bedforms, this work deals with transitional- and upper-regime flows, and compares beds with sand, gravel, and sand-gravel

mixtures. Hence, experimental observations are intended to characterize bedforms and flow resistance in transitional- and upper-regimes, and also to recognize likely effects of sand content in bedform characteristics and sediment transport.

Some supplementary themes treated in this work arose from an a posteriori concern, motivated by experimental observations. These themes include the analysis of the conditions for the formation of short-crested stationary waves; flow hydraulics over stationary, downstream- and upstream-migrating antidunes, and its morphological consequences for each of these three regimes of propagation; and the analysis of the process by which fine particles infiltrate into a bed composed of heterogeneous grain sizes.

In this introductory Chapter some general aspects of the scope of this work are given. First, a general context of the research is presented, within the aim of sedimentation engineering and its current state of knowledge. Later, some notes are given about the choice of an experimental methodology to treat the problem. Next, the general scope of this research is briefly summarized, and finally, in the last Subsection, a general layout of this thesis work is presented.

1.2 GENERAL CONTEXT

Natural alluvial rivers transport water and sediment. River's morphology is tied to the interaction of these two processes in different scales, and thus their study is a matter of concern for a vast range of disciplines and scientists, involved with fluvial environments. Physics, Geography, Geomorphology, Sedimentology, and Ecology are just some examples of scientific disciplines that to some extent are in relation with river morphology. In this work the approach to river morphology is from the point of view of Fluvial Engineering, more precisely, in the scope of Sedimentation Engineering; therefore, the type of general questions intended to be answered are related with the flow characteristics, prediction of sediment transport, and processes involved in changes of channel morphology. Perhaps the most general of these questions can be posed in the following manner: what is the expected water depth and amount of sediment to be transported for a given flow discharge, channel geometry, sediment and fluid characteristics? Recently, a committee of experts in flow and sediment transport over dunes stated that "even for the simplest case (uniform sediment, straight prismatic channel with rigid banks) a general answer to these two questions [prediction of water depth and sediment transport] can only be given with an uncomfortably high degree of uncertainty" (ASCE, 2002). The committee presented a general overview of the advances and most important issues to be solved for increasing the understanding of dunes and transport, in order to direct efforts to reduce uncertainty in the answer to the question posed above.

The study of transitions of bedform states and the effect of sediment heterogeneity on bedform characteristics were among the different issues of practical interest the committee considered that deserve attention of the research community, in order to advance in the current state of knowledge of flow and transport over dunes. The work herein presented intends to contribute to these two aspects, but instead of dunes, the targets here are upper- and transitional-regimes, where plane-beds, antidunes and transitional bedforms can occur. These regimes are less known and they have received much less attention than lower regime. A benchmark in the study of these conditions can be found in the seminal work of Kennedy (1961); he obtained a thorough and well documented data set with medium and fine sand for bedforms in upper regime and lower to upper regime transition. This new work herein intends to continue on the path of Kennedy's work, and thus it aims to extend the available experimental evidence for transitional and upper-regime flows to other ranges and characteristics of sediment.

Different authors have demonstrated that in beds composed of mixtures of sand and gravel, the relative amount of sand in the sediment mixture has a prominent role in flow resistance, bedform dynamics, and mobility of the whole bedload material. Notwithstanding, the limits for which the bed behaves predominantly as a sand-, gravel-, or transitional-bed for a wide range of conditions are not well established. This work pretends to contribute to the recognition of such boundaries for near critical and supercritical flows, under high sediment transport rates; accordingly, sand content has been used as a control parameter between experimental run series with four different sediments, namely, uniform very coarse sand (100% sand content), uniform fine gravel (0% sand content), and two mixtures of this two uniform materials, with a relative proportion of 32% sand content and 45% sand content, respectively.

Referred to the ambit of canonical river classifications, in this work are compared conditions pertaining to sand-bed rivers, gravel-bed rivers, and rivers with sand-gravel mixtures (often called transitional rivers), for a spectrum of flows ranging from the upper subcritical limit to supercritical flow, and for sediment mobility much higher than the threshold for initiation of movement, but below the limits for a generalized suspension of particles. According to these latter features, this work is closer to the sphere of gravel-bed rivers, for which sediment chiefly moves being in contact with the bed surface most of the time.

1.3 METHOD

During the last century, important progress has been achieved in the knowledge of sediment and water dynamics for the understanding of river morphodynamics; many of such achievements were possible through empirically based research. Important advances have been realized through experimentation in laboratory flumes; they have shown to be a valuable tool in the study of river dynamics, since they allow to isolate effects and to reproduce complex processes under controlled conditions. Empirical relationships have thus been developed by researchers, and also theoretical analyses have been assessed by means of physical experimentation.

Nowadays, numerical methods have gained force in the study of physical processes related to rivers, but rather than overshadow flume experimentation, a virtuous complement between both techniques is often recognized by researchers. Experimental data sets from flumes are valuable and indispensable for testing and calibrating numerical models. Even though direct prototype measurements would be most desirable for tuning of numerical models, field data sets are normally scarce, especially for flow and sediment transport, and if available, it is difficult that they cover a wide range of conditions; in some environments, like in ephemeral rivers, monitoring campaigns along many years would be required for acquiring a comprehensive data set, while laboratory experimentation allows for testing a wide range of conditions in a short time. Moreover, accuracy issues and the possibility of isolating effects and causes, warrant the current and future validity of physical experimentation as a relevant tool for the study of river morphodynamics.

Fundamental knowledge in many classical topics of fluvial research in hydraulics and sediment transport has been possible through exhaustive flume experimentation over mobile-beds. Notwithstanding, ranges of relevant variables covered by the whole of accumulated data sets have been restricted to a delimited band of conditions, either because studies have been aimed to the most common environments found in natural streams, or because of practical ranges imposed by typical flume limitations. In consequence, there is firstly a bias toward an abundance of experimental data sets for subcritical flows, which is the most common flow regime found in natural streams; and secondly, there exists a bias

toward beds composed of fine sediment with a uniform grain size distribution. The work herein aims for providing with further empirical evidence, through systematic, well controlled and thoroughly documented laboratory experimentation, for some of the less explored conditions in flumes for the study of river dynamics: transcritical and supercritical flow regimes with low aspect ratios (channel width-to-depth ratio), on beds composed of uniform sediment coarser than fine sand, and beds composed of a mixture of different grain sizes.

The choice for an experimental approach to the topics herein treated comes from a firm conviction that physical experimentation is of great value for understanding physical processes and for the improvement of predictions. Thus, ***the most valuable contribution of this work is the new empirical evidence***. It can be expected that this new data set would contribute to counteract the fact pointed out by Gomez and Church (1989) about sediment transport predictors: "It remains a matter of some concern that there appears to be more bed load formulae than there are reliable data sets by which to test them." After more than twenty years from this statement, more data sets on sediment transport have become available; even so, further efforts to cover with quality data all the likely ranges of variables in rivers are still required.

1.4 SCOPE

The subject of this work is alluvial rivers and their morphodynamic processes, with a main focus on the river-section scale. The experimental data set developed is thus presented in terms of reach average values for mobile-bed equilibrium conditions, and flow resistance and sediment transport are analyzed in terms of these values. Furthermore, some other relevant observations pertain to smaller scales, particularly, in the reach scale or mesoscale level, bedforms are described and their interaction with flow is analyzed; in this same scale, sediment sorting patterns are identified and described. Finally, in the local scale or particle scale level, the process by which fine particles penetrate deep in the bed is analyzed.

The type of sediment-laden flows referred to in this work are non-cohesive and dominated by bedload. Although sediment supply in the experiments performed are herein considered as being extremely high, this must be considered within the context of bedload. The maximum ratio between sediment and water by volume was only slightly higher than 0.5%, i.e., well below the high concentrations required for a hyperconcentrated flow, for which a suspended sediment concentration of at least 20% by volume has been considered as a lower boundary by some authors (Pierson, 2005). Sediment transport rates in the experiments here presented, with unit solid discharges ranging from 0.108 to 1.43 kg/s/m, are much higher than those commonly reported in similar flume experiments in previous literature; in turn, dimensionless sediment discharge rates pertain to the upper ranges measured in field in gravel-bed rivers.

The definitive new experimental data set comprises 22 experimental runs for which the characteristics of flow, sediment transport, grain sorting patterns and bed and water configurations were registered for mobile-bed equilibrium conditions. The channel was 27 m long, and 0.75 m width. Water discharges were in the range of 59 to 80 l/s, mean flow velocities varied from 0.82 to 1.31 m/s, bed slopes from 0.58% to 2.14%, and channel-width to depth ratios from 6.6 to 11. Froude numbers were in the range of 0.73 to 1.49. Four series of experiments were performed feeding sediment to the channel; each series was performed with a different sediment type, namely, coarse sand, fine gravel, and two mixtures of these two materials.

The experimental conditions allowed for the formation of water and bed surface configurations rarely reported in literature, specifically: trains of short-crested stationary

waves, and three-dimensional downstream migrating antidunes coexisting with alternate bars. Stationary waves and bedform characteristics, including bed erosion patterns related to the bedforms, were measured and described. Hence, conclusions are presented about differences in flow resistance and bedform morphology between downstream-migrating and upstream-migrating antidunes, and between bedforms for uniform sand, uniform gravel, and both materials mixed. In turn, empirically based bedform stability diagrams developed for uniform material are tested using the description and classification of bedforms observed experimentally.

Other important results of this research are related with the effect of sand content in sediment mobility, where a conceptual model is presented for considering sand content and bed structure in sediment transport computations; the patterns of bed sorting produced by the transcritical and supercritical flows in the experiments are related with the bed morphology; hydraulics of antidunes are analyzed, and consequences in the characteristics of downstream- and upstream-migrating antidunes are commented; and finally, the infiltration of fine sediment in a bed of heterogeneous material is analyzed with a numerical model, which shows satisfactory results when tested with the experimental data obtained in the experimental work.

Finally, it must be mentioned that even when the approach to fluvial environments in this work is from the point of view of engineering, the elaboration of methods, analysis and discussions makes use of knowledge and experience from different areas of study, namely, Fluvial Morphodynamics, Hydraulics, Fluid Mechanics, Geomorphology and Sedimentology, just to mention some of them. All these diverse disciplines approach to rivers from particular perspectives, but, since the subject of study is the same for all, there is an overlap of common interests between each other, and a diversity of objectives, methods, and terminology. Due to this heterogeneous interest in rivers, advances of the state of knowledge spread over journals, proceedings and reports of diverse fields. Such abundance of positions to the same subjects, namely, river flow, sediment and morphology, can be confusing and ultimately frustrating, for the neophyte in the study of river morphodynamics. In order to counteract such a dispersed development of knowledge, a holistic and interdisciplinary point of view for the study of river environments is required to be promoted. Hydraulic engineers should participate actively in such a unifying vision. The study and interventions in rivers considering the river only as a compendium of physical processes should be avoided; instead, rivers should be considered as a system where physical, ecological and social agents interact in a complex manner. This work pretends to contribute only shortly to the current understanding of physical processes in rivers; albeit, it is expected this contribution could fit as a tiny piece in a broad construction of our knowledge about rivers.

1.5 LAYOUT

This work has been divided in nine Chapters, each one including a brief introduction in order to place the reader in the context of the specific Section; at the end of each Chapter (except Chapter 3), a brief summary is included as well, which highlights the most important aspects treated in that Section. The work is organized in the following sequence: a general overview of the current state of knowledge is first presented, then experimental work is thoroughly described, afterwards the experimental results are presented in detail, and later on they are discussed and used to test theoretical and numerical developments. All these steps are distributed in the different Chapters as detailed below.

The second Chapter presents an overview of the topics treated in this work in light of the current state of the art; particularly, the main characteristics of torrential ephemeral

rivers, the general properties of transitional- and upper-regimes, and the especial features of sediment transport for heterogeneous material are presented therein. Hypothesis and objectives of the research are also included in that Chapter.

The third Chapter presents the experimental work. The experimental set up is described, and justifications for the chosen materials and procedures used are discussed. Afterwards, the treatment of the measured data to obtain the fundamental variables for the definitive data set is explained. Finally, the hydraulic and sediment variables of the definitive data set are summarized.

Flow resistance in the experimental runs is analyzed in Chapter 4. Different shear stress partition methods are applied and compared, and conclusions are obtained about the best results for considering effective shear and form drag forces to be used in subsequent analysis.

Chapter 5 deals with bedforms and presents experimental results in relation to them. A review of bedforms in unidirectional flows is first introduced; later on bedforms observed experimentally are described and classified. Subsequently, experimental results related with the characteristics of stationary waves and bedforms are presented. Finally, results on sediment sorting patterns produced by the passage of bedforms are also presented and described.

In Chapter 6 the experimental results are analyzed and discussed on four main aspects. First, the experimental results are compared with predictors for bedform stability phases found in literature. Afterwards, the effect of sand content in flow resistance is discussed, in relation to form drag, skin friction and total bed shear stress. Later on, a thorough analysis and discussion of sediment transport for the experimental data is presented. Finally, an interpretation of the experimental results is carried out, in relation to stationary waves, bed erosion, sediment sorting patterns and river morphology.

Chapters 7 and 8 can be read as independent works, where theoretical and numerical developments are presented; these two Chapters are linked to the rest of the work by using results obtained from the experimental campaign to test such developments. Particularly, in Chapter 7 the hydraulics of flow over antidunes is analyzed in relation to their direction of movement; morphological consequences for fundamental hydraulic constraints between upstream- and downstream-migrating antidunes are presented. Sediment sorting grain size patterns produced by the infiltration of fine sediment are studied in Chapter 8; a porosity model for binary mixtures is used to identify stages in sediment bed structure as a function of sand content, and a numerical model is presented for computation of the process of clogging, which occurs when fines saturate the bed.

An extended description of the conclusions obtained in this Thesis is presented in Chapter 9, along with suggestions for future research in the topics here treated. The Chapter is separated in individual Sections for describing the general conclusions of each of the most relevant topics.

At the end of the main corpus of this thesis, a list of references cited in the text is given. Finally, nineteen Appendixes are included, with detailed information about the experimental set up, particular computations for the preparation of the experiments, graphs, tables and photos with experimental results, and some deductions that were not completely necessary to be included in the main text.

Partial results and some developments shown in this Thesis were previously published in Conference Proceedings (Núñez-González, F. & Martín-Vide 2009, 2010, 2011b), and in one Journal (Núñez-González, F. & Martín-Vide 2011a), some of them are reproduced in Appendix XIX.

Some practical conventions for making easier the reading of the text are listed as follows:

- Coordinate axis in the experimental channel are: x is the horizontal axis, positive in the upstream direction; y is the transversal to flow axis, positive toward the left-bank; and z is the vertical axis, positive upwards.
- When the text refers to coarse sand, fine gravel or any other characteristic size of sediment with an adjective, reference is given to Table 2.9, where these characteristics are related to a range of grain sizes according to the scale of Wentworth.

CHAPTER 2:

OVERVIEW OF THE PROBLEM

2.1 INTRODUCTION

In this Chapter a general overview is given of the most relevant topics treated in this work. Since most of the Chapters contain a description of the state of the art in the specific topic dealt within each Section, only general concepts and information are here presented. The main practical motivation for this work was the study of the type of flows and fluvial processes likely to occur in torrential ephemeral streams in the Mediterranean coast; hence, a description of the most general characteristics of these types of streams is given first, and some likely consequences of channelisation of these streams are described. Subsequently, in the following Subsection the characteristics of transitional- and upper-regime flows in alluvial beds are described. Later on, relevant features of sediment transport and sorting are presented, with especial emphasis to the effect of sand content in porosity and sediment mobility, and to the predictive methods found in literature. Finally, in the next Subsection the most important hypotheses tested in this work are listed, and later on the objectives that guided the research are presented.

2.2 TORRENTIAL EPHEMERAL STREAMS IN THE MEDITERRANEAN REGION

Rivers with mean bed slopes in the range of 1% to 6%, subjected to a large sediment supply, and prone to sudden, short and violent floods, are called torrential (Ancey, 2001). Torrential streams are ephemeral if the channel is most of the time dry, and water flows occur intermittently. All these characteristics are common of streams proper of the Mediterranean coast, which in Spain are known as "ramblas". The origin of the word "Rambla" is in the Arabic, and is equivalent to the Spanish word "arenal", which means

"sandy area"; the substantive is used also as a verb: "arramblar", which means "to get covered with sand after water flow" but also "to sweep away violently" (Garzón-Heydt et al., 2009). Such etymology informs about the violent character of floods and the large loads of sediment transported through the ramblas; in turn, the oft-used name of "Río Seco" (Dry River) reflects the social perception of the sporadic nature of water runoff through ramblas.

The ramblas are subjected to violent flash-floods, extremely dangerous for human life and property (Barrera et al. 2005, Barnolas et al. 2008). Such floods are sudden. A dry channel can reach peak discharges in only a few minutes or a few hours (Bracken et al. 2008) and runoff concentrates very large volumes of water in short times (see Figure 2.1); these characteristics have been evident in recent studies, which have shown that maximum peak discharges generated in regions under Mediterranean climatic influence are more than twice as high as those in Central Europe (Gaume et al. 2009).

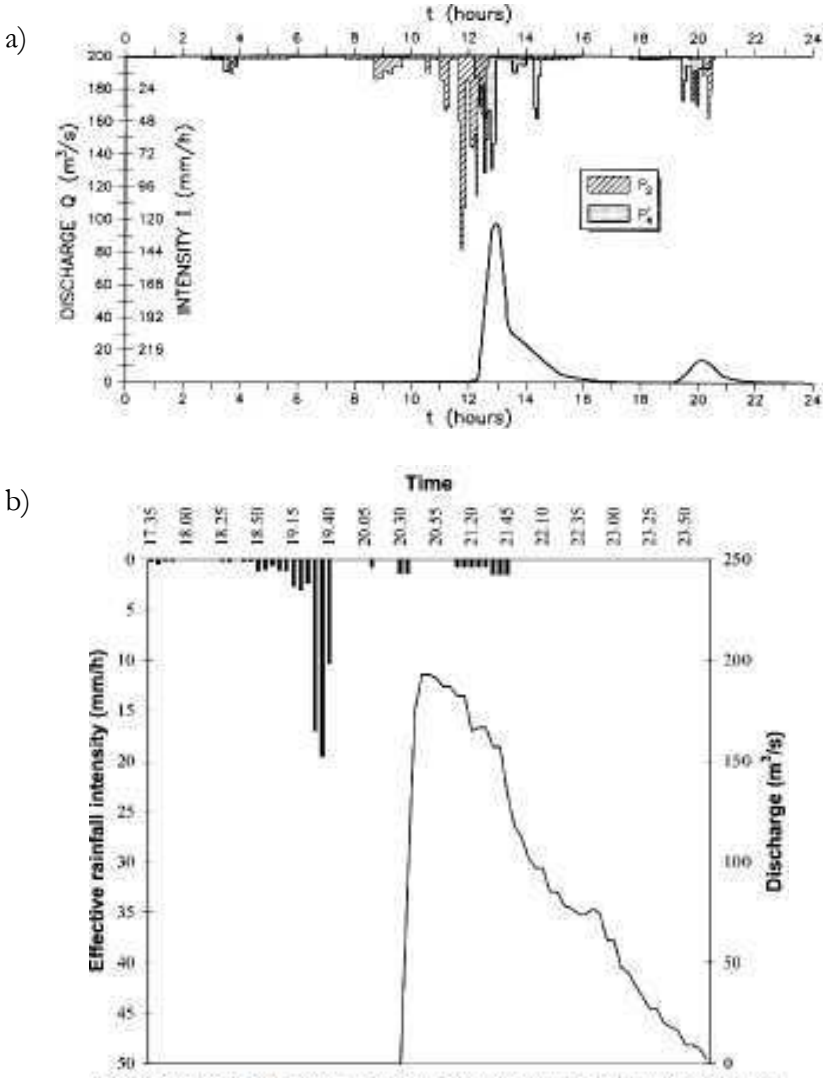

Figure 2.1. Typical flood hydrographs for ephemeral Mediterranean streams, a) Riera de las Arenas in Catalonia (Martín-Vide et al., 1999), and b) Rambla de Poyo in Valencia (Camarasa-Belmonte and Segura-Beltrán, 2001) (time in minutes).

Usually, the ramblas drain small watersheds (several hundred square kilometers) at their lower most basins; channels at the headwaters of these watersheds are deep and narrow (Camarasa-Belmonte and Segura-Beltrán, 2001), and thus encourage the translation of flood and sediment waves to the ramblas, which occur where the valley widens, so that their channels are normally wide and straight. Due to a high sediment supply generated by strong erosive processes at the head of the watershed, the morphology of the channel is usually braided, and it often flows over an alluvial fan. Despite the infrequency of the flood events, channel morphology is highly variable and changeable over time due to the instability of the banks and the strong erosion and sedimentation processes activated during floods (Hooke and Mant, 2000).

Mediterranean ephemeral streams are highly permeable. Camarasa-Belmonte and Segura-Beltrán (2001) found that runoff comprised at most 17% of the rainfall for flood events in three ramblas in Valencia region, while Martín-Vide et al. (1999) found looses of 5% of flood discharge per kilometer of channel length in Riera de Las Arenas, in Catalonia. On the other side, gravel-bedded Mediterranean ephemeral streams do not use to develop a surface armoured layer in comparison to perennial rivers (e.g., García and Martín-Vide 2001); these observations agree with other ephemeral streams in dryland regions (e.g., Laronne et al. 1994). Parker et al. (2003) attributed the lack of a coarse surface layer in dryland gravel-bed rivers to the form of the hydrographs; they suggested that intermediate flows, absent in such ephemeral streams, may be the most relevant ingredient in the development of an armour layer. Laronne and Reid (1993) adduced to this lack of bed armouring as the reason for a much higher efficiency for transporting coarse sediment in dryland ephemeral rivers compared to perennial rivers in humid regions.

Some scenarios of climatic change anticipate that many regions could become drier and more susceptible to extreme flood events; conditions proper of ephemeral streams in drylands, like ramblas, may thus be more widespread in the future (Hooke and Mant, 2000). This circumstance adds significance to the study of processes and dynamics of floods in torrential ephemeral streams, as they can serve as a model to anticipate likely scenarios of flood impacts, sedimentation and morphological response to land use changes. This work fits into this context, as it pretends to increase understanding in hydraulics, sediment transport and morphology of torrential ephemeral streams.

2.2.1 Human intervention in torrential ephemeral streams

Human activity has strongly impacted on rivers in the Mediterranean region during centuries, but mainly during the 20th century considerable transformation of the landscape took place due to accelerated industrialization and concentration of population in urban areas (Hooke, 2006). Sala and Inbar (1992) attributed an increasing frequency of devastating floods in Catalan rivers to a likely three-fold increment of peak discharges due to rapid urbanization. For different basins in Catalonia, they found that urbanized areas increased roughly from two to four times, from the period between years 1947 to 1955 to the period between years 1975 to 1980; for this latter period the degree of urbanization in coastal ramblas was in some cases as high as the 35% of total basin area. From the analysis of records of rain and river discharges, Sala and Inbar found a decrease in lag times and an increment of about 50% in the runoff coefficient for those same periods. By nature, flood hydrographs in torrential ephemeral streams are already sharp and narrow, with short time-lags (Figure 2.1); if as an effect of an increase of impervious areas by extensive urbanization, peak discharges are further increased and lag-times reduced, floods can be catastrophic (see Figure 2.2).

Figure 2.2. Riera de las Arenas in Terrassa, near Barcelona, Catalonia. This is a torrential ephemeral stream, now confined by vertical walls. It is located over a highly urbanized alluvial fan. The images correspond to different periods: after the catastrophic flood event of September, 1962 (top-left), when the river burst its banks and caused more than 800 people dead and considerable damages; after the disastrous flood of September, 1971 (top-right), when important damages to property occurred; state of the Riera in 2006 (down-left), and a recent view from January 2011, (down-right) with the channel covered densely by low vegetation.

Figure 2.3. Riera of Arenys de Munt in Catalonia, in a highly urbanized basin. Train of antidunes along a street of the city, during a flood event in the upper part of the rambla (left); and lower part of the rambla, close to the coast, where it has been channelised and transformed into an impervious channel (right). (Photo to the left: Montserrat Colomer. Photo to the right: J. P. Martín Vide).

Straightening and embankment of river channels has been a common engineering response for flood control during the last century. In turn, channelisation has been carried out to control lateral instability and to use of flood plains. Ramblas, which are often intrinsically unstable, especially if flowing over an alluvial fan, have been thus massively straightened and channelised (see Figures 2.2 to 2.4). River channelisation has a positive social perception when it is performed as a protection measure after a catastrophic flood, since it provides a sense of security to the population (see Figure 2.5). Nevertheless, river straightening and channelisation have a number of effects on the river. Such effects depend on the flow and sediment supply characteristics. Formerly wide, braided and unstable streams, like many ramblas, are constrained into single, narrow, deep channels by straightening and channelisation; hence, the river responds trying to achieve a new equilibrium for the new conditions. This new equilibrium can be obtained through bed incision when the new hydraulic conditions have increased the sediment transport capacity; conversely, if sediment supply is large and the river is channelised with a rigid impervious bottom, channel aggradation can occur, and peak flood discharges might increase as an effect of the total loss of bed permeability. This latter effect is particularly significant in Mediterranean ramblas, for which bed permeability contributes to a high reduction of runoff, as already explained above.

Figure 2.4. Río Seco in Castellón de la Plana, Valencia. Train of three-dimensional antidunes during a flood event on 29th September, 2009 (above left: upstream view; above right: downstream view); and view of the dry channelised river section, some meters downstream from the top views (bottom). Channel width is roughly 35 m. (Upper photos taken from video in: www.youtube.com/watch?v=NVHCgUxfm-Q, last access: January 2012; bottom photo taken from GoogleEarth).

Figure 2.5. Social protests demanded the channelisation of the Llobregat River, in Cornellà, Catalonia, after extreme floods in 1971. Left image, wall graffiti demanding for channelisation: "Channelisation and soon"; right image, poster calling for a demonstration in support of the channelisation in 1977. (Photos from the exhibition: "La memoria del Fang, 40è aniversari de la riuada de 1971". September-October 2011, Cornellá, Catalonia).

2.3 TRANSITIONAL AND UPPER FLOW REGIMES

Flow in alluvial channels can be classified in lower-, transitional- and upper-regimes, according to the type of dominant bedforms. The most general feature that distinguishes bedforms in lower- and upper-regimes is that water surface in lower-regime is out-of-phase with the bedforms, while in upper-regime water surface and bedforms are in-phase. Even though upper- and lower-regimes are closely related to supercritical and subcritical flow, respectively, upper-regime bedforms can occur in subcritical flow, being a Froude number equal to 0.84 a widely accepted minimum condition (e.g., Cheel 2005). In turn, transitional-regime bedforms in gravel have been reported for Froude numbers as low as 0.5 (Carling and Schvidchenko, 2002).

A characteristic of high practical significance is the difference in flow resistance relationships followed by the three flow regimes. Normally, in lower- and upper-regimes bedforms grow in size with flow strength, and so do form resistance, but this does not occur in transitional-regime. In this regime bedforms can flatten as flow strength increases, and, in some cases, eventually bedforms can wash away, giving place to a plane bed, known as transitional plane bed. In consequence, for some ranges of sediment grain sizes, flow resistance relationships show an abrupt discontinuity in the transition from lower- to upper-regime (e.g., Figure 2.6). For this reason, recognition of the limits of the transitional regime is important for the estimation of water stage as a function of water discharge. Notwithstanding, these limits are not well established, especially for coarse and heterogeneous size materials.

The most general sequence of bed configurations in a mobile-bed over an unidirectional flow with increasing flow strength, includes ripples and dunes in lower-regime, transitional bedforms (bedforms with combined characteristics of lower- and upper-regime), plane bed (only for some grain sizes), and for upper-stage antidunes and upper-stage plane bed. Lower-regime bedforms have been widely studied, both theoretically and empirically; conversely, transitional- and upper-regime bedforms have received much less attention.

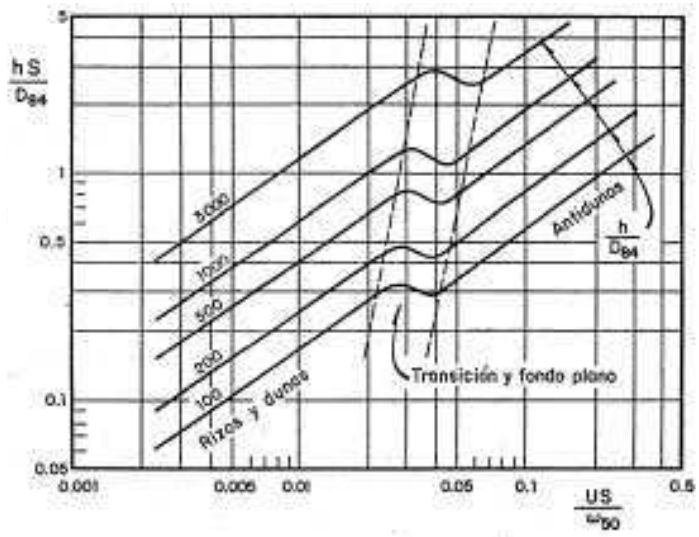

Figure 2.6. Chart for flow resistance in sand-bed rivers, according to Cruickshank and Maza (1973). D_{84} is the grain size diameter for which 84% of the material is finer, h is water depth, S is slope, U is flow velocity, and ω_{50} is falling velocity of median size particles of the bed sediment.

Transitional regime usually occurs for conditions close to the critical flow regime, i.e., for Froude numbers close to one. For this transcritical regime the flow is extremely unstable; analysis of the specific energy-flow depth diagram shows that close to the minimum energy, small disturbances on the bed might produce high variations on water depth. Consequently, large water surface undulations are characteristic of these flows (Chanson, 1999), and the shape of the bedforms also becomes unstable; this could be the reason for a large variety of descriptions found in literature for bedforms within the transitional regime: washed out dunes, asymmetrical antidunes, rhomboid dunes, etc. (e.g., Carling and Shvidchenko, 2002).

Figure 2.7. Trains of stationary waves over antidunes in natural channels; in contrast to antidunes in Figures 2.3 and 2.4, these waves are similar to laboratory bedforms in scale. (Left) Upstream-migrating 2D waves in a coastal sand-bed channel, formed when the tide goes out on a beach of the Basque Country; (right) 3D waves, known as rooster-tails or short-crested waves, in Laonong River, Taiwan (Photo taken from http://www2.ce.ntu.edu.tw/~mh/TaiwanPostcards/LaonongRiver.html, National Taiwan University, last access: January 2012).

Bedforms recognized as antidunes are mesoscale bedforms in-phase with the water surface (Figure 2.7). They can be two-dimensional or three-dimensional, and according to the direction of movement, they can be classified as upstream-migrating, stationary, or downstream-migrating antidunes. The most frequently reported antidunes in flumes and field are upstream-migrating two-dimensional antidunes. Normally, such antidunes are described as part of a cyclical process in which trains of antidunes form from a plane bed, grow in height and length, become unstable, and vanish giving place to a plane bed from which the process begins again (e.g., Alexander et al. 2001).

A thorough study about antidunes and the stationary waves that accompany them was presented by Kennedy (1961). He performed experiments with sand for a wide range of flow conditions, and provided with comprehensive descriptions of upper-regime bed configurations, including all the different types of antidunes listed above. Three-dimensional and downstream-migrating antidunes were observed in some of the experiments of Kennedy, but upstream-migrating two-dimensional antidunes were the most common. Carling and Schivdchenko (2002) collected unpublished data sets from different researchers, for flume experiments in the transitional- and upper-regime with fine gravel; they provided with evidence of downstream-migrating antidunes for a wide range of flow conditions. Data sets like these collected by Carling and Schivdchenko are of great value for the definition of the conditions required for the formation of each type of antidune, such conditions have not been well defined yet; there is still a lack of empirical data for downstream-migrating and three-dimensional antidunes for different grain size ranges and non-uniform size sediment.

Antidunes are rarely preserved, even less in sand and fine gravel (Carling, 1999), since the falling water stages destroy the sedimentary forms. Antidunes are more likely to be preserved if the flow stage decreases rapidly (Carling and Breakspear, 2008), like in the gravel antidunes shown in Figure 2.8. Although less frequently than lower-regime bedforms, different authors have documented evidence of upper-regime bedforms preserved in contemporary flows and in the sedimentological record (e.g., Hand et al., 1969; Foley, 1977; Alexander and Fielding, 1997).

Figure 2.8. Train of presumed antidunes in Fluvià river, a gravel-bed river in Catalonia (Martín-Vide et al., 2012). These antidunes with horseshoe-shaped crestline would have formed during an abrupt avulsion of the river to an older channel. Transient flow in supercritical regime through the steep banks could have formed the train of antidunes with curved crestline, and the abrupt recess of the flow could have enhanced preservation.

Upper-regime bedforms are less frequently observed in field in comparison to their lower-regime counterparts; this is partly related to the fact that supercritical flows are a less common state in natural streams than subcritical regime. Grant (1997) hypothesized that critical flow is a limit condition in mobile-bed channels, so that supercritical flows occur

only over short distances and timescales. He adduced the cyclical pattern of creation and destruction of antidunes as one of the arguments of his thesis. Supercritical regime occurs in some reaches of high gradient streams and in some sections of lower gradient streams (Jarret, 1984; Trieste, 1992); it also must be a common condition during peak flows of flash-floods (Costa, 1987). Hence, due to the steep gradients and sharp and narrow hydrographs characteristic of torrential ephemeral streams, transcritical and supercritical flows are likely to occur during flash-floods in such type of rivers (e.g., Figures 2.3 and 2.4). They would be even more likely to occur in highly urbanized watersheds, where lag times are reduced and consequently peak discharges increased. In turn, in straightened and channelised reaches the flow regime can change from low to rapid due to flow resistance reduction; regular and smooth rigid-boundaries reduce roughness and hinder the growth of vegetation which opposes resistance to flow. In consequence, transcritical and supercritical flows, and thus transitional- and upper-regime bedforms, might be a common feature of engineered torrential ephemeral streams, as Mediterranean ramblas; antidunes shown in Figures 2.3 and 2.4 give examples of such condition.

2.4 SEDIMENT TRANSPORT AND SORTING IN BEDS WITH NON-UNIFORM MATERIAL

The caliber of the bed sediment particles determines to a large extent the morphology of a river. In this sense, a general classification of rivers considers streams of similar bed material as a group of homogeneous characteristics. In the extremes of this classification sand- and gravel-bed rivers are considered. The most distinctive feature between these two streams is the dominant mode in which particles are transported by the flowing water. Suspension is the dominant mode in which the bed particles are transported in sand-bed rivers, while in gravel-bed rivers most of the particles move near the bed surface, sliding, rolling or saltating; for this latter condition it is said that the sediment moves as bedload.

It is generally considered that a river is sand-bedded if the mean diameter of the bed material is lower than 2 mm, while a river is considered as a gravel-bed river if the mean diameter is higher than 2 mm (see Figure 2.9). Such a criterion implicitly assumes that if most of the bed sediment size fractions are in the sand (gravel) range, most of the bed material would be transported predominantly in suspension (as bedload). This criterion has a great practical significance, but it has the limitation of excluding categorically rivers with beds composed of sand and gravel in similar relative proportions. Such rivers, often named transitional, are some times considered as gravel-bed rivers, perhaps on the assumption that morphological changes could be mainly controlled by the transport of the gravel size fractions. Transitional channels, although not so abundant, deserve a classification on their own; some distinctive features of these channels, like the bimodality of their bed material grain size distribution and the high relative proportion of sand in the bed, can exert an important control on sediment transport, not necessarily occurring in rivers with beds frankly in the sand or gravel ranges.

A characteristic that commonly distinguishes transitional and gravel-bedded rivers from sand-bedded rivers is the variety of grain sizes of the bed material. Sediment in sand-bed rivers is normally well-sorted (uniform), while in gravel-bed and transitional rivers it is common that the bed material is poorly-sorted (e.g., composed of a wide variety of grain size classes; see Figure 2.10). As a consequence of the extended sediment grain size distributions, the bed sediment in gravel-bed and transitional rivers can often be sorted in diverse spatial patterns. Such patterns are often related to the different response of each grain size fraction to local flow conditions.

Description of particle size			$\phi = -\log_2$	mm	$\psi = \log_2$
			- 12.0	4096	12.0
	very large		- 11.5	2896	11.5
			- 11.0	2048	11.0
	large		- 10.5	1448	10.5
Boulder			- 10.0	1024	10.0
	Medium		- 9.5	724	9.5
			- 9.0	512	9.0
	small		- 8.5	362	8.5
			- 8.0	**256**	**8.0**
	large		- 7.5	181	7.5
Cobble			- 7.0	128	7.0
	Small		- 6.5	90.5	6.5
			- 6.0	**64**	**6.0**
	very coarse		- 5.5	45.3	5.5
			- 5.0	32	5.0
	coarse		- 4.5	22.6	4.5
		Pebble	- 4.0	16	4.0
Gravel	medium		- 3.5	11.3	3.5
			- 3.0	8	3.0
	fine		- 2.5	5.66	2.5
			- 2.0	4	2.0
	very fine	Granule	- 1.5	2.83	1.5
			- 1.0	**2**	**1.0**
	very coarse		- 0.5	1.41	0.5
			0	1	0
	coarse		+ 0.5	0.707	- 0.5
			+ 1.0	0.500	- 1.0
Sand	medium		+ 1.5	0.354	- 1.5
			+ 2.0	0.250	- 2.0
	fine		+ 2.5	0.177	- 1.5
			+ 3.0	0.125	- 3.0
	very fine		+ 3.5	0.088	- 3.5
			+ 4.0	**0.063**	**- 4.0**
Silt					
			+ 8.0	**0.0039**	**- 8.0**
Clay					
			+ 12.0	**0.00024**	**- 12.0**

Figure 2.9. Size gradation of sediment according to the Wentworth scale (Taken from Bunte and Abt, 2001).

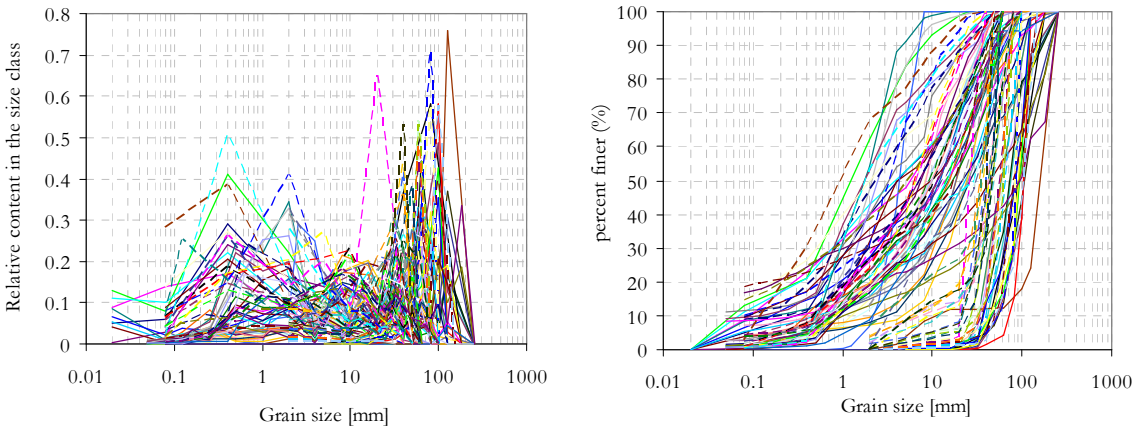

Figure 2.10. Grain size distribution of sediment samples from 100 locations, in different gravel-bed rivers in Catalonia. Coarse well-sorted materials on the rightmost of the cumulative distribution correspond to surface samples taken with the method of Wölman in the same locations. These coarse samples indicate that the bed surfaces were likely armoured.

Of particular importance for the bed morphological changes in gravel-bed and transitional rivers is the vertical sorting feature known as bed armouring. When the bed is armoured, the surface material is coarser than the underlying sediment (see Figure 2.10); this coarse surface layer acts as a cover, that prevents subsurface particles to be in contact with flow, and thus the movement of subsurface sediment with a finer grain size distribution is contingent on the mobilization of the coarser surface sediment particles. Different processes have been adduced to explain the development of bed surface armouring, but in general, there is somehow a consensus about the existence of two types of armoring; one is related to the process known as selective transport, by which flow washes away particles with sizes that it is competent to move, so that eventually a lag surface layer, composed of coarse particles, prevails. Such type of immobile armour layers occurs, for instance, downstream of dams. A second type of armour layer is known as a mobile armour layer; according to an hypothesis known as "equal mobility", owed to Parker and Klingeman (1982), mobile armour layers are formed as a counteracting effect to equalize the mobility of the average load of sand and gravel of a river; coarse particles are intrinsically more resistive to be mobilized than fine particles, and thus they appear overrepresented on the bed surface. The equal mobility hypothesis has been opened to debate in the last 30 years. The reason seems to be the confusion in the interpretation of its main premise. While it can be interpreted that the equal mobility hypothesis implicitly considers that a surface armour layer is not destroyed by floods competent to mobilize all the bed size fractions, the hypothesis rather states that surface armouring is a process related to the passage of many hydrographs, which adjust the sediment supplied load in an annual or long-term basis. Hence, the passage of flows of diverse competence, and not a single flood, is essential for the development and maintenance of bed armouring. Parker and Toro-Escobar (2003) presented field and experimental evidence that verifies this condition.

In rivers composed of fine and coarse material, a particular sorting pattern on the bed surface is the existence of areas of similar grain size material, known as sediment patches. It has been suggested that such patches have a relevant role in bedload and in the morphologic response to changes in sediment supply (Paola and Seal, 1995). Patches of fine material are smooth regions where flow velocity at the bed surface level is increased and the transport of coarse particles is enhanced. Gran et al. (2006) found that the connectivity between fine patches is necessary for maintaining an enhanced bed activity prior to the development of a full bed armour; even when the supply of fine material is low, if the patches are not blocked by gravel jams, the response of a channel can be sand-dominated, i.e., that the mobilization of sand is not dependant on the mobilization of gravel. The conditions for the development of surface patchiness, the methods to characterize a patchy bed, and the consideration of sediment patches in sediment transport estimations and morphodinamic models, are still under discussion.

Contrary to beds composed of uniform material, in beds with heterogeneous sediment different factors add complexity to the study of morphodynamics. Among these are the contrasting mobility between grain size fractions and the grain size sorting patterns displayed at the channel bed. Mobile-bed experiments in flumes must take into account these features, since they lead to a fundamental difference in the mode in which sediment is managed. The most general flume operation modes are sediment-recirculating and sediment-feed. Both modes can simulate morphodynamic processes in rivers, but with different border conditions: sediment-recirculating runs simulate an infinitely large reach, where the sediment supply is self-adjusted according to the initial bed texture and flow capacity; conversely, in sediment-feed flumes hydraulic conditions and bed surface texture are self-adjusted to meet the conditions required to transport an imposed load of sediment. Hence, for sediment-recirculating runs the dynamic equilibrium reached is dependant on

the bed initial conditions (Parker and Wilcock, 1993). Other intermediate modes of sediment operation exist; it can be expected that mobile-bed equilibrium obtained with either operation mode should be equivalent.

2.4.1 Significance of sand content

It is a common trend that the grain size distribution of the bed material in gravel-bed and transitional rivers exhibits two distinctive modes, one in the size range of sand and the other in the size range of gravel (Figure 2.10). Therefore, bed material is often considered as a mixture of sand and gravel (e.g., Wilcock 2001). In turn, it has been demonstrated that the relative proportion of sand in the bed material has implications on flow hydraulics, sediment transport and bed structure. Overall, there is a strong feedback between all these three aspects in close correlation with the bed material sand content.

According to the amount of sand, the bed structure can range from an open-framework gravel, when the bed material is composed only of gravel clasts, to a sand matrix, when gravel is totally absent. In between these two limit conditions, three states can be identified according to the relative sand content: partially filled gravel, filled gravel and matrix gravel (Figure 2.11). The filled gravel is the condition for which the bed porosity is minimum, the bed is supported by gravel clasts and all the voids between coarse particles are filled completely with sand. This condition occurs for sand contents between 25% and 45% (Church et al. 1987). For higher sand contents, the gravel grains are not necessarily in contact between each other, and the bed material grain size distribution is not as sharply bimodal as framework-supported gravels.

Gravel framework	Partially filled gravel	Filled gravel	Matrix gravel	Sand matrix
$\varepsilon = \varepsilon_D$	$\varepsilon = f(\varepsilon_D, \varepsilon_d, r, f_s)$	$\varepsilon_{MIN} = f(\varepsilon_D, \varepsilon_d, r)$	$\varepsilon = f(\varepsilon_D, \varepsilon_d, r, f_s)$	$\varepsilon = \varepsilon_d$
$f_s = 0$	$0 < f_s < f_{sMAX}$	$f_s = f_{sMAX}$	$f_{sMAX} < f_s < 100\%$	$f_s = 100\%$

Figure 2.11. Sketches of different conditions of bed structure and bed porosity, as a function of relative sand content. Variables mean: ε, bed porosity; ε_D, gravel natural porosity; ε_d, sand natural porosity; ε_{MIN}, minimum bed porosity; r, size ratio between sand and gravel grains: r=d/D; f_s, sand content in the sand-gravel mixture; f_{sMAX}, maximum sand content in a gravel framework.

The bed surface for sand contents above the limit for framework-supported gravels (i.e., filled gravel) is smoother than partially filled gravels. Therefore, shear stress and roughness are normally lower over these sandy beds (Ferguson et al. 1989); in turn, such smooth texture has important consequences for sediment transport. Ikeda and Iseya (1988) proved with experimental evidence, that increased sand content can increase the transport rate of gravel. Wilcock (1998) compared transport rates in natural rivers; he found that the shear stress for incipient motion of particles decreases abruptly for sand contents in the transition from a framework-supported gravel to a matrix-gravel. To explain this behavior, he suggested that in matrix-supported beds the gravel particles are more exposed to flow and not influenced by adjacent gravel elements. Hence, their mobility is enhanced as soon as sand content exceeds the limit for a gravel-framework.

As shown in Figure 2.12, the mean diameter of a mixture of sand and gravel decreases as sand content is increased. Therefore, since sand content reduces the

representative size of a mixture, it can be expected that the transport rate of a sand-gravel mixture would increase in the same proportion as the representative diameter changes with sand content. Most of the sediment transport predictors follow this reasoning. Nevertheless, flume experiments from Wilcock et al. (2001) demonstrated that the mobility of a sand-gravel mixture increased with the addition of sand, at a higher rate than what it would be expected from the lower mean diameter associated to the addition of sand. They found that this increment was most rapid over the range of sand content between 15% and 27% for the sediment mixtures they used, which agrees with the range of sand contents for the limit between framework-supported gravel and matrix gravel.

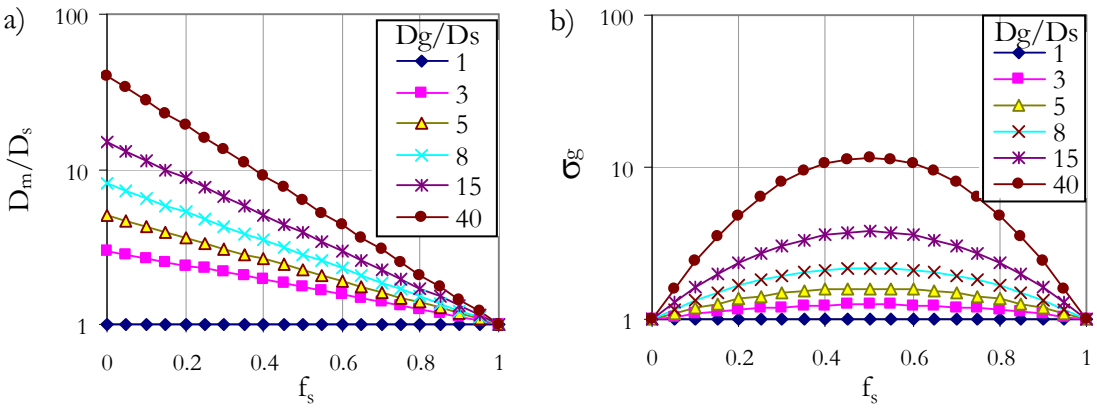

Figure 2.12. Variation with sand content of statistical parameters in a sediment mixture composed of uniform sand and uniform gravel, for different values of the ratio between gravel and sand grain sizes. (a) Geometric mean diameter in relation to the sand grain size; (b) geometric standard deviation. D_g, D_s, and D_m are gravel, sand and mixture geometric mean diameters, respectively, f_s is relative sand content, and σ_g is geometric standard deviation of the mixture.

2.4.2 Sediment transport prediction

Sediment discharge estimates are required for modeling river-bed level changes, and are an input variable of a variety of problems in fluvial engineering practice, e.g., for computing the time in which a dam may silt-up, for the design of stable channels or for the design of sedimentation tanks. Prediction of sediment transport is also relevant in river restoration studies and for the planning and management of fluvial environments from an ecological point of view.

For the study of river morphodynamics in gravel-bed and transitional rivers, it should be consider that not all sediment transported by a stream takes part in the morphological changes produced by sediment imbalances. The wash-load, which is the finest portion of the load, is regulated by the upstream supply and preferentially transported in suspension; thus it is unlikely that wash load is deposited on the bed, and if so, its contribution to the bed level changes is negligible. Fluvial morphology is essentially controlled by the bed-material load, which is the transported load regulated by the flow capacity and composed of bed material moving in suspension or near the bed surface (sliding, rolling or saltating). Frings et al. (2008) defined also a *pore-filling load*, which would be the fine portion of the sediment load that infiltrates between the pores of larger grains and does not contribute to the morphological change. For its importance in fluvial morphology, in this work only the bedload is considered; approaches to compute it using

the bed material characteristics and the hydraulic conditions in the channel are presented in the following Subsections.

2.4.2.1 Characteristics of sediment transport predictors

In many of the sediment transport relations in literature, bed shear stress is the fundamental variable used to characterize the flow conditions that activate the movement of particles. Such relations consider that the mobility of sediment is to a great extend determined by an excess shear stress, which is the difference between the acting stress on the particles and the stress required to put them in motion. This latter shear stress is known as the critical shear stress for initiation of particle motion. One of the most widely used formulas for the estimation of sediment transport in gravel-bed rivers, the empirical function of Meyer-Peter & Müller, employs a power function of this excess shear stress using dimensionless relations. In an extended version of this formula, it can be written as

$$\frac{q_S}{\sqrt{(S_s-1)gD^3}} = \alpha\left(\frac{\tau_b}{(S_s-1)\rho gD} - \frac{\tau_c}{(S_s-1)\rho gD}\right)^{\beta} \qquad (2.1)$$

where D is the diameter of the bed particles, g is the acceleration of gravity, q_S is the volumetric bedload transport rate per unit width, S_s is the relative density of the sediment, ρ denotes the fluid density, τ_b the boundary shear stress on the bed, and τ_c the critical shear stress of the sediment; α and β are constants, that for the Meyer-Peter & Müller formula take the values α=8 and β=1.5. Solving (2.1) for q_S, it is obtained

$$q_S = \frac{\alpha[(S_s-1)g]^{1/2-\beta}}{\rho^{\beta}} D^{3/2-\beta}(\tau_b-\tau_c)^{\beta} \qquad (2.2)$$

Using the exponent β=1.5, as in the Meyer-Peter & Müller formula, it is found that the diameter of the particles is cancelled; thus, it is shown that the sediment transport rate is solely dependant on the critical shear stress (Wilcock 2004). Therefore, the accurate estimation of the critical shear stress is of great importance for the estimation of sediment discharges. Notwithstanding, such relevance of the critical shear value must decrease as the shear stress is higher and thus, at very high flows, it can be expected that the estimation of inaccurate critical stress values would not affect greatly the computation of the sediment discharge.

Cheng (2002) claimed to have developed a simple exponential formula based on the bed shear stress, but disregarded of the critical shear stress concept. Smart (2004) demonstrated that Cheng's formula implicitly contained a dimensionless shear stress equal to 0.05, which is a value close to the value of 0.047 originally suggested by the Meyer-Peter & Müller formula. As in the formula of Cheng, some other sediment discharge predictors implicitly account for the critical shear stress condition.

Estimation of the bed critical shear stress has been the focus of a plethora of studies, as reviewed by Buffington and Montgomery (1997). It has not been free of controversy, since each author has used a different definition of the concept. One of the most significant contributions in this subject was that of Paintal (1971); based on experimental evidence, Paintal stated that there is not a critical stress for incipient motion, but just different degrees of motion as the discharge is increased.

To overcome the problems with the critical shear stress definition, Parker and Klingeman (1982) used a reference value of critical shear stress, i.e., an effective threshold of motion for which sediment transport is so low that its relevance for morphologic changes in the time scale of interest is negligible.

2.4.2.2 Considerations for non-uniform material in sediment transport predictors

When dealing with poorly-sorted sediment, bedload discharge can be computed by dividing the whole mixture in classes of size fractions, and estimating the fractional bedload discharge, that is, the bedload discharge for each size fraction individually. In doing this, it should be considered that there exists an interaction between coarse and fine grains, which is normally taken into account in sediment transport predictors with a correction factor that affects the excess of shear stress exerted on the grains. This correction factor is known as the hiding-exposure function.

The most classical criterion to estimate the grain threshold of motion is that from Shields, which states that the immobility of the bed particles is a function of a dimensionless bed shear stress (defined as $\tau_b/[g\rho D(S_s-1)]$) and the particles Reynolds number. According to Shields, for hydraulically rough flows the predicted value of the critical dimensionless shear stress is 0.06; it has been proved that this criterion tends to overpredict the incipient motion of particles.

For conditions over the limit of hydraulically rough flows, direct application of the Shields incipient motion criterion to a bed material with a large range of particle diameters would indicate that the bed shear stress required to move a particle of the *i*-th size fraction in the sediment mixture would grow linearly with the grain size. That is, that the flow would be selective and finer grains would be preferentially moved by the flow. Actually, grains of different sizes interfere between each other, so that their behavior is slightly different as if they were surrounded by uniform size material. Coarser grains protrude more to flow, so that their area exposed to flow drag is higher than that of the smaller grains, with the consequence that the critical shear stress for coarse particles is reduced. On the other side, finer grains are hidden by coarser grains and therefore tend to have a larger critical shear stress. Hiding-exposure functions are used to correct this effect. A general expression of the hiding-exposure functions is:

$$\frac{\tau^*_{c,i}}{\tau^*_{c,m}} = \left(\frac{D_i}{D_m}\right)^{\gamma} \qquad (2.3)$$

where D_i and D_m are the size of sediment particles for the i-th grain size fraction and the geometric mean diameter of the sediment mixture, respectively; $\tau_{c,i}^*$ and $\tau_{c,m}^*$ are the dimensionless critical shear stress, for the i-th size fraction and for the mean diameter of the mixture, respectively; and γ is an exponent. $\gamma=0$ is the limiting case for no hiding-exposure, on the other side, $\gamma=-1$ is the opposite limiting case for which a condition named "equal mobility" occurs. For this latter condition all particles would begin motion at the same shear stress. Buffington and Montgomery (1997) presented a summary of values for γ obtained by different authors from flumes and field data.

In computing the critical shear stress for the calculation of the fractional bedload transport, the hiding-exposure correction functions take into account the effect of the relative size of each size fraction with respect to the mean diameter in the mixture, but not the form of the grain size distribution. It has been observed that the form of the grain size distribution has an effect in the critical shear stress when distinguishing between unimodal and bimodal mixtures. Unimodal mixtures are close to the equal mobility, that is, that the critical shear stress for all size fractions tends to be similar. Therefore, in computing the bedload discharge, unimodal mixtures might be treated as uniform size grains, using an adequate representative grain size for the whole mixture. Almedeij and Diplas (2003) demonstrated that the mode of a grain size distribution is more stable than other measures of central tendency; hence, they proposed to use the mode as an alternative statistical parameter to represent the bed material, instead of the mean or the median diameters.

It has been observed that bimodal mixtures exhibit a particle size dependence of the critical bed-shear stress. The coarse mode of the mixture shows an increase in mobility with the grain size, thus tending to the size-selective entrainment as in uniform size material. The fine mode behaves more in the equal mobility side, and in some cases it has been observed that the critical stress of the finest fraction is even slightly larger than that of the mean diameter of the mixture. Kleinhans (2002) suggested that this behavior of bimodal mixtures is more likely related to a local size segregation of the bed material, shown as patchiness on the bed surface, than to a simple hiding-exposure concept where it is assumed that the bed surface is thoroughly mixed. In dealing with bimodal mixtures for sediment discharge computations, Almedeij et al. (2006) presented an approach to separate sand from gravel in streams with bimodal sediment.

From the facts described above, it is inferred that determining whether the bed material is unimodal or bimodal is important for performing consistent sediment transport estimations. According to Parker (2004), grain sizes in the range of pea gravel are relatively scarce in natural rivers; albeit gravel-bed rivers often contain large amounts of sand, material between 1 and 8 mm is not common (this trend is true for some of the samples in Figure 2.10). This lack of material in this range of sizes permits a clear differentiation of bimodal sediments, although this is not always the case. For cases where there is not an evident division between modes it would be required to define when a sediment sample could be treated as bimodal and when as unimodal. Wilcock (1993) presented an index of bimodality, based on the distance between the two modes and on the amount of sediment contained in the modes; Sambrook Smith et al. (1997) modified the index of Wilcock, considering logarithmic values for the sizes of the two modes, and using the ratio between the fractional content of each mode, instead of their addition.

As it was exposed in section 2.4.1, the bed material relative proportion of sand might have an important influence on sediment transport rates. Only two relations in literature consider this feature, these are the two-fraction model of Wilcock and Kenworthy (2002), and the model for an arbitrary number of size fractions from Wilcock and Crowe (2003). These two models consider the effect of sand content in a formula for computation of the value of the dimensionless critical shear stress, for the sand and gravel fractions in the former, and for the geometric mean diameter of the sediment mixture in the latter. Those formulas were obtained from limited empirical data. More data and revision of these functions is required, in order to improve the inclusion of sand content in the estimations of sediment transport.

As already explained above, in many gravel-bed rivers the flow sorts the bed grains inversely in the vertical section; in this manner, on the bed surface it is formed a layer with coarser material than the material in the subsurface. This armor layer has a direct effect in the sediment transport, as it hinders underlying finer grains to be in direct contact with the flow. It has been observed that the grain size distribution of the material under the armor layer is similar to that of the bedload when flow is capable of move all grain sizes in the bed. Such characteristic supports the application of formulas that consider a homogeneous distribution of all size fractions in the bed. In that case a sample of the material underlying the pavement serves to fit the model. Surface-based relations, as those from Parker (1990), Wilcock and McArdell (1993) and Wilcock and Crowe (2003), have been developed to take into account bed surface coarsening and also the changes in grain sizes on the bed surface. Almedeij and Diplas (2003) presented a bedload transport relation for unimodal sediment, based on the surface and the subsurface material; they considered that under low to moderate Shields stresses the flow is incapable of breaking the pavement and thus the grain material should be represented by that on the bed surface. On the other side, they considered that under high dimensionless shear stresses there is no pavement layer and equal mobility prevails, in that case, the subsurface material should represent the bedload.

In dealing with the estimation of sediment transport for heterogeneous material, different approaches can be found in literature to consider fractional transport. Molinas and Wu (2000) identified four categories for such approaches, based on the treatment in formulations and the physical considerations in the development. Those categories are described as follows:

i) *Bed material fraction approach*. Considers that bedload for each fraction may be computed with a formula for uniform sediment; total bedload transport would be equal to the sum of fractional bedload transport, each fraction affected by its bulk fractional representation in the bed. This approach has been used widely in numerical models.

ii) *Direct computation by the size fraction approach*. This method is used in formulations that have been originally developed to compute the sediment transport rates by size fractions of non-uniform sediment mixtures. The total bedload is calculated by the summation of fractional sediment transport rates. Pertaining to this category are the formulations of Einstein (1950), Laursen (1958) and Toffaletti (1969).

iii) *Shear stress correction approach*. The capacity of the flow for each size fraction is computed by affecting the threshold shear stress to consider the interaction between different size particles (hiding-exposure functions, sand content effect). Total bedload is calculated by affecting the fractional bedload by the availability of that fraction in the bed and by adding all the fractional rates.

iv) *Transport capacity fraction approach*. A computation is performed by using a model that estimates the total bedload transport from a representative diameter for the whole mixture. Then the computed total is broken into fractional bedload rates by a transport capacity distribution function. This approach is derived under the assumption and observation that total load computations and measurements are more accurate and reliable than those for fractional loads. The transport capacity distribution function takes into account the availability of each fraction in the bed and the physical interaction between different sizes. Methods of this type, are those from Karim and Kennedy (1981) and Wu and Molinas (1996).

According to Molinas and Wu (2000), the advantage of iv)-type approaches is that additional errors are avoided due to summation of transport capacities of individual size fractions and that discrepancies in computing bedloads for individual size fractions are limited. Application of iii)-type approaches is limited to the specific formulations that were developed in that basis. Approaches of the type of i) overlook the effects of interference between different grain sizes; nevertheless, this approach has been used in many applications to numerical models and it is still present in manuals and some texts referred to sediment transport computation.

Perhaps, most of the fractional bedload transport relations have been developed on the basis of iii)-type approaches, which deduction is straightforward and rational. One of the advantages of such approaches is that in correcting the critical shear stress by means of hiding-exposure functions, relations originally developed for unisize sediment may be extended for their applicability to mixtures with a variety of grain sizes. Approaches of the ii)-type take into account the interaction between grains of different sizes tacitly, as would be that from Einstein (1950), but ignore other effects like sand content. In this work, iii)-type approaches are considered.

2.5 HYPOTHESES

From the general revision of the state of knowledge in Subsections 2.2 to 2.4, a general conclusion can be stated as follows: the interaction of flow and sediment in the transitional- and upper-regimes, and the related physical processes, are not completely understood, particularly for conditions in which the distribution of sizes of the bed material is non-uniform; in turn, transitional- and upper-regimes in beds with sediment size heterogeneity are likely to occur in torrential ephemeral streams, particularly, if the watersheds are strongly urbanized and if the streams have been straightened or channelised. Therefore, this work is aimed to contribute to the state of knowledge of transitional- and upper-regime flows, and their distinctive features amongst uniform and non-uniform material. It is expected that a better understanding of these conditions would also contribute to improve the current knowledge of physical processes in torrential ephemeral streams and any other streams with similar morphologic and hydraulic characteristics. In the same vain, the aim of this work is to provide new elements, specifically a new experimental data set, to answer questions of the type:

- Which are the limits of the transitional flow regime for coarse and heterogeneous sediment?
- Are bed configurations in the transitional- and upper-regime with coarse and non-uniform material of similar characteristics to those in uniform fine material? How do these bed configurations affect flow resistance?
- For heterogeneous material, what are the sediment sorting patterns developed by flows in the transitional- and upper-regimes, with no limitations of sediment supply and competent to mobilize all bed size fractions? Do they form surface patches or armoured surface layers?
- Is the effect of sand content in sediment transport near threshold conditions similar in conditions of high sediment transport rates?
- Which are the limits of a transitional river according to sediment transport with respect to sand- and gravel-bed rivers?

In order to establish a methodological route to deal with the concerns raised in the previous questions, a number of hypotheses can be advanced. After the premise that flow regimes have been studied systematically for uniform material before, the most general hypothesis would state that some particular characteristics, not recognized before, of bedforms, bed resistance and sediment transport in the transition- and upper-regimes can occur for non-uniform sediment; these characteristics can be identified with controlled systematic laboratory experimental runs. More particular hypotheses for the phenomena to be studied are summarized in Table 2.1, accompanied by the context in which they are inserted according to the current state of knowledge.

To test the hypothesis in Table 2.1 and to try to respond to the questions raised above as well, an empirical method is used, particularly, an experimental campaign is carried out in a laboratory flume. Besides experimental work, also theoretical and numerical analysis is employed to deal with some particular aspects of the research.

In the next Subsection the objectives of this work are presented, attending to the a priori hypothesis here defined and according to the requirements given by the experimental work. Also, some a posteriori objectives are presented, which arose from experimental observations.

Table 2.1. Formulated hypotheses for the most important topics treated in this work. Methodological hypotheses are marked with cursive.

	Topic	Current state of knowledge	Hypothesis
1.	Unidirectional flows over alluvial beds	If a certain threshold condition is surpassed, particles are transported and the bed is deformed by shear stress action into different types of configurations. Lower-regime flow has been widely studied empirically, while upper-regime has received much less attention, and mainly for fine uniform material.	*Systematic flume experiments would highlight especial features, previously not recognized due to scarce empirical evidence, proper of transitional- and upper-regime flows over coarse and heterogeneous size material.*
2.	Bed Configurations	Bedforms with uniform material have been recognized and classified since long. Bedforms with heterogeneous and coarse material have received less attention. Likewise, lower regime bedforms have been widely studied, but transitional- and upper-regime forms have scarcely been studied systematically in flumes. Particularly, the interactions between stationary waves and bed deformation are not completely understood. In fine uniform sand, the transitional-regime is characterized by transitional bedforms and plane bed. Conversely, for uniform gravel no plane bed occurs.	Bedforms in coarse sand, fine gravel and sand-gravel mixtures for transitional and upper-regime flows will not differ considerably from those in uniform material, but will exhibit distinctive characteristics (form, geometry, resistance to flow, movement, etc.) previously not identified. Therefore, bed configurations for transitional and upper-regime will consist of two-dimensional upstream-migrating antidunes and transitional bedforms, although transitional plane beds will also be likely to occur, especially for beds composed of sand. *Flume experiments would highlight differences between different bed materials, and would help to understand interactions between stationary waves and bed dynamics.*
3.	Transitional regime	For uniform bed material, transitional regime occurs for lower Froude numbers the higher the relative water depth (ratio water depth-sediment grain size) is.	Transitional regime in sand-gravel mixtures will occur for lower Froude numbers the lower the relative depths will be, being relative depth a function of the mean diameter of the mixture.
4.	Bed forms	Bedforms in gravel are shorter and smaller than bedforms in sand.	Bedforms in sand will be steeper than bedforms in gravel. The steepness of bedforms in sand-gravel mixtures will be proportional to the sand content, i.e., for a 30% sand content the bedform steepness will be 30% the steepness of bedforms with sand.
5.	Flow resistance and bedforms	Dunes produce higher drag due to the separation zone developed downstream of the bedform crest. Conversely, antidunes do not develop or develop a weak separation zone, hence they produce less form resistance than dunes.	Form resistance produced by antidunes will be lower than flow resistance commonly reported for dunes with similar steepness.

Table 2.1. (Continued)

	Topic	Current state of knowledge	Hypothesis
6.	Bed resistance in alluvial beds	There exists a wide variety of methods for estimation of bed resistance in sand bed streams. Nevertheless, less information exists for gravel and sand-gravel bed rivers. A common practice is to neglect form resistance in these types of streams. Evidence in field and experiments have shown that steep bedforms can develop in coarse and mixed-size sediment beds, but few efforts have been conducted to elucidate the effect of these forms in form resistance. In turn, sand content can reduce grain resistance, but more evidence and methods are required to quantify this reduction.	Form resistance for bedforms in coarse material will be lower than for fine material bedforms. For mixed size material, bed resistance will be a function of the mean diameter of the mixture. *Bedforms developed in flume experiments for a wide range of flow conditions would allow estimating the portion of bed resistance taken by form drag and by grain roughness for transitional- and upper-regimes.* *The effect of sand content in each flow resistance component could then be quantified, and also this information would allow elucidating if methods for channel bed resistance developed for fine material are valid in coarse and heterogeneous sediment.*
7.	Sediment transport	Sediment transport in uniform material has been widely studied, while heterogeneous material is less understood. The effect of sediment sand content on particle incipient motion has been recently recognized as a fundamental factor in sand-gravel mixtures. The change from gravel-framework to matrix supported bed structure has been recognized to impose a fundamental change in sediment mobility. Most of the studies and measurements are restricted to incipient motion and moderate sediment transport rates.	Sand content will have a negligible effect in sediment transport for high sediment supply loads. *Flume experiments would provide evidence to recognize if the effect of sand content in sediment mobility would vanish under very high sediment transport conditions. Particularly, experiments would help to recognize any important difference between matrix supported and gravel-framework supported beds.*
8.	Sorting of non-uniform sediment	Different sorting patterns occur when the bed material is heterogeneous. The coarsening of the bed surface, known as bed armouring, is a relevant sorting pattern in gravel-bed rivers, due to its implications in sediment transport. Other features include bed surface patchiness, and the formation of open-framework gravels. The process and conditions for the development of different sorting patterns are not completely understood.	A coarse surface layer will not form at high sediment transport rates. The bed surface will be completely mixed by the highly competent flows, but patches of coarse material would occur for less competent flows.
9.	Torrential ephemeral streams	These streams are prone to flash-floods, with steep hydrographs and extremely high water discharges and sediment supply conditions. Difficulties in estimating flow hydraulics due to torrentiallity and lack of reliable field measurements.	*Flume experiments would help to better understand torrential flows in these streams and to assess the role of bedforms in flow resistance.*

2.6 RESEARCH OBJECTIVES

The main objective of this research is to obtain an extensive experimental data set, composed of flow characteristics, sediment transport rates, bed grain size composition and bedform characteristics, in beds composed of sand, gravel and sand-gravel mixtures, for

moderately steep gradients in order to generate flow conditions in the transitional- and upper-regimes. Along with this general aim, some particular objectives are posed as follows. They have been divided in General, Concrete, Incidental and Functional objectives. General objectives refer to the broadest motivations of this work, while Concrete objectives consider especial features that are not completely solved by the current state of knowledge; objectives that arose a posteriori, from observations in the experimental work, have been defined as Incidental, and finally, in Functional objectives have been included those objectives related with auxiliary activities for the fulfillment of the General objectives.

General objectives

- Build on a comprehensive data set for flow over mobile-beds, reproducing flow characteristics, bed configurations, sediment transport and sorting processes in the transitional- and upper-regimes, for uniform sand, uniform gravel and sand-gravel mixtures, under conditions comparable to those generated in laterally confined torrential ephemeral streams characteristic of the Mediterranean coast. Use the new data set to study the interactions between flow and mobile-beds of different grain-size compositions.

Concrete objectives

- Characterize and compare bedforms in the transitional- and upper-regimes for uniform sand, uniform gravel and sand-gravel mixtures, in order to define the limits for the transitional flow regime for different sediment characteristics, and to test the performance with the new experimental ranges of theoretical and empirical bedform stability diagrams for uniform fine material.
- Compare form resistance for bedforms in lower-, transitional-, and upper-regimes.
- Identify likely effects of sand content for high sediment transport rates and torrential flows, in: bed configurations, flow resistance and sediment transport.
- Test the performance of sediment transport predictors for high transport rates.
- Identify grain sorting trends produced by transitional- and upper-regime bedforms in heterogeneous material.

Incidental objectives

- Analyze the hydraulic conditions that determine the direction of movement of antidunes.
- Determine morphological consequences of hydraulic constraints in antidune direction of movement.
- Identify connections between bed structure and sediment sorting processes.
- Develop a numerical model for the grain sorting processes by which fines infiltrate into a bed of heterogeneous material.

Functional objectives

- Adapt, calibrate and test a new flume with enhanced capabilities for performing mobile-bed experiments under high-sediment transport conditions and for different operational modes according to sediment management.
- Develop methods for sampling and characterizing bed material patchiness.
- Compare bed resistance partition methods in a physically coherent basis.

CHAPTER 3:

EXPERIMENTS WITH SAND, GRAVEL AND TWO SAND-GRAVEL MIXTURES

3.1 INTRODUCTION

The paramount objectives of the experimental campaign were, firstly, to develop a comprehensive data set for the study of flow and sediment interactions in mobile-beds subjected to very high sediment supply conditions, and secondly, to reproduce flow characteristics, bed configurations and sediment transport processes comparable to those generated in torrential ephemeral streams characteristic of the Mediterranean coast. Flow in this type of streams, which typically have moderate bed slopes (1 to 3%), is frequently near critical or supercritical, with very high sediment concentrations, while bed compositions include both uniform and non-uniform material. Accordingly, for the experimental runs high flow discharges and sediment transport rates were required, and four different bed compositions were studied, namely, two with uniform size sediment (sand and gravel) and two with mixed-size material (sand-gravel).

In order to meet the experimental requirements, a new laboratory flume was used, which was conceived so as to enable the performance of long-lasting runs with a constant feeding of mixed-size material, without requiring a large stock of sediment. This condition was achieved with a system that is able not only to recirculate the sediment collected at the end of the channel, but it is able also to separate fine- and coarse-fractions, and feed each size-fraction back into the channel at a constant rate using an automatic feeder. This new experimental set-up allowed covering ranges of variables that previously had not been systematically explored in laboratory flumes. The use of this new facility introduced as a secondary objective in the investigation the adaptation, calibration and test of the flume under different operation conditions, to perform experiments using the entire sediment recirculating system for the first time. Appendix I deals in detail with all the issues regarding this objective.

The experiments were designed so as to make the most of the flume capabilities for supplying large sediment-feed rates. Consequently, for the experimental run series performed to build on the new data set, sediment-feed rate was the independent variable, i.e., it was held constant during each run, but varied along a series of runs; while water discharge was used as a parameter which was held within a narrow range of values along the series of runs. Operation of the flume in this manner, imposing water and sediment discharge, resembles a feed type operation. This notwithstanding, the flume operation was not strictly a 'pure' sediment-feed type, but a hybrid between feed and recirculting (named from here on out hybrid-feed operation) since sediment was returned from the end to the head of the flume to be reinserted in the hoppers. This type of operation was chosen in order to perform long-lasting runs with a limited amount of material.

In addition to the runs with a hybrid-feed operation, some few runs were performed using the flume in a sediment-recirculating mode, and two more runs without sediment-supply to the channel, i.e., runs with continuous bed erosion. The sediment-recirculating runs served mainly as a verification of the experimental reproducibility; while the non sediment-supply runs were performed to study the morphodynamics of a bed in constant bed degradation to be contrasted with the mobile-bed equilibrium runs. Nevertheless, since the main interest of the research is set on the morphodynamic equilibrium states, data for non sediment-supply runs will only be described but will not be analyzed further in the current work, as this analysis deserves a study on its own. Moreover, even if emphasis was given to the mobile-bed equilibrium conditions, while the evolution to equilibrium received less attention in this work, this transition to equilibrium in the sediment hybrid-feed runs was documented and described in detail.

The most important measurements performed during the experimental runs had the aim of characterizing the bulk flow conditions of the mobile-bed equilibrium states; in turn, some other measurements were carried out to describe the equilibrium bed and water configurations, and to identify sediment grain-size sorting trends. During runs, videos were taken as well, to record both, the time-evolution of the bed and water surfaces, and the shape of the bedforms and water waves. On the other hand, at the end of the runs additional measurements were conducted and photos were shot, for estimating the maximum bed erosion, for characterizing the final bed configurations and for identifying sediment sorting trends. All together, sieve analysis of almost 1000 sediment samples was undertaken for obtaining grain size distributions of samples taken from the hoppers, from solid discharge samplers used in the channel, and from the bed surface and subsurface.

Six experimental series were performed. The first two series consisted of preliminary test runs with sand and gravel, while each of the other four series was carried out for a different grain size material, namely, gravel, sand and two sand-gravel mixtures. The two sediment mixtures were obtained by mixing the original sand and gravel with an average proportion of 32% sand content for mixture 1 (Mix1) and 44% for mixture 2 (Mix2). Six runs of each of these latter four experimental series (except for the sand series, with only four runs) were conducted operating the flume in the hybrid-feed mode emulating sediment-feed, and their results were used to fill in the definitive data set. The total number of runs carried out for each experimental series and the period of dates when they were performed are summarized in Table 3.1.

This Chapter describes in detail the procedures, materials, methods and criteria used to undertake the experimental runs. Emphasis is given to the 22 sediment hybrid-feed runs conducted to develop the new data set compound of bulk flow properties, solid discharges, bedform characteristics, and grain-size sorting for mobile-bed equilibrium conditions. First a general description of the experimental set-up and the sediment used is presented. Then the aspects taken into account for the design of the experiments are exposed, along with a description of the experimental procedures and type of

measurements conducted. Afterwards, some aspects of the flow and notions of morphodynamic equilibrium are discussed in order to justify the equilibrium criteria used, and for describing the procedures for computation of the bulk flow conditions. In that Section, proofs of the reproducibility of the experimental runs are presented as well. At the end, the experimental data set is summarized for the most important variables, and some aspects of the experimental results are highlighted in a critical review of the experiments.

Table 3.1 Summary of the series of runs conducted during the experimental campaign.

Run series		Total number of runs	Runs used in the data set	Dates	
				Initial	Final
I	Test runs with sand	15	0	January 23rd	February 7th
II	Test runs with gravel	11	0	February 22nd	April 3th
III	Runs with gravel	6	6	April 4th	April 20th
IV	Runs with mixture 1	12	6	April 21st	May 22nd
V	Runs with mixture 2	8	6	May 25th	June 11th
VI	Runs with sand	4	4	June 22nd	June 30th

3.2 EXPERIMENTAL SET-UP AND MATERIALS

The facilities used to carry out the experimental campaign are located in the Hydraulics Laboratory of the University of Castilla-La Mancha, Spain. The experimental set-up consists of a tilting flume, a system for pumping and recirculating water and a sediment-feed and -recirculating system (schematic plans of the experimental facilities are shown in Figures A1.1 to A1.3 of Appendix I, and photos are shown in Section 7 of the same Appendix). The 30 m long (27 m effective length), 0.75 m wide and 0.60 m deep experimental flume is rectangular and can be tilted up to a 0.04 slope by means of three engines under the base of the channel. The walls of the channel are made of one meter long glass-panels, and the planar bottom is made of PVC. Water-discharge in the channel is controlled with an automatic electronic flow-meter and is fed and recirculated independently from the sediment circuit. Water is pumped to the channel by a set of three pumps, each with a capacity up to 90 ls^{-1}. At the downstream end of the channel water is conducted to an underground storage deposit.

The sediment-recirculating system serves to convey the sediment taken from the channel downstream end to the upper head of the channel. A special feature of this system is that it has the ability of separating mixed size sediment into two size fractions: sand and gravel. The sediment circuit works as follows (see diagram in Figure 3.1 and schematic plan in Figure A1.2 of Appendix I): the sediment is collected at the end of the channel by means of a siltation tank, from which sediment with a small amount of water is pumped through a 10 cm diameter PVC pipe to an elevated trommel over the head of the flume. The trommel, made of a fine mesh of 2.24 mm mean diameter ($\pm$0.17 mm), separates gravel from water and sand. Sand and water are subsequently separated through a second siltation tank. Screw conveyors transport the separated size fractions either into independent storage deposits or into independent hoppers above the channel intake. The hoppers can work either as feeders or as a continuous by-pass that returns the sediment to the channel at the same rate as it exits the channel (with a minimum delivery lag time estimated to be approximately 3 minutes for the gravel circuit and 10 minutes for the sand circuit). A conveyor belt and a sluice gate at the base of each hopper serve to control the sediment-feed at a constant rate into the channel. Moreover, with no control (i.e., a high velocity for the conveyor belt and the sluice gate totally open) the empty hoppers work as sediment by-passes for sediment-recirculating operation. A more detailed description of the

experimental facility, and the sediment-feed and –recirculating systems is given in Appendix I.

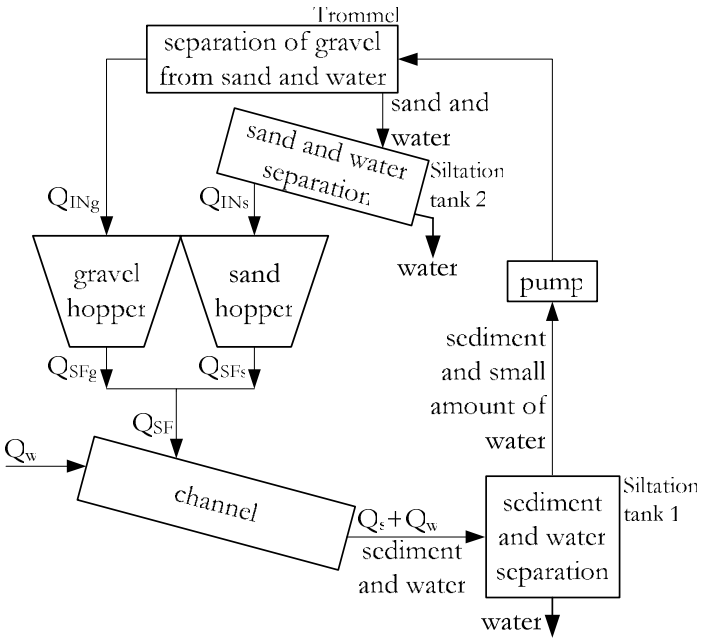

Figure 3.1. Diagram depicting the closed circuit for sediment in the experimental flume. Q_s is the total dry sediment discharge passing through the downstream end of the channel; Q_{INg} and Q_{INs} are the dry gravel and dry sand discharges, respectively, passing through the downstream end of the channel and introduced in the hoppers after recirculation; Q_{SF} is the total dry sediment discharge added to the channel from the hoppers; Q_{SFg} and Q_{SFs} are the dry gravel and dry sand discharges added to the channel, respectively; and Q_w is the constant water discharge in the channel. It is thus fulfilled that $Q_s=Q_{INg}+Q_{INs}$ and $Q_{SF}=Q_{SFg}+Q_{SFs}$. For a sediment-recirculating operation (sediment is not stored in the hoppers), if sediment lag-times in the recirculating system are neglected, it is fulfilled that $Q_{SFg}=Q_{INg}$ and $Q_{SFs}=Q_{INs}$ (i.e., $Q_{SF}=Q_s$); while for a hybrid operation emulating a sediment-feed mode Q_{SFg} and Q_{SFs} are kept constant (i.e., Q_{SF}=constant) and the fulfillment of the condition $Q_{SFg}=Q_{INg}$ and $Q_{SFs}=Q_{INs}$ means that the bed in the channel is in dynamic equilibrium.

One of the main issues to solve when dealing with high sediment transport rates (as it was required for the experiments here described) in mobile-bed experimental flumes is the need of a continuous input of a high volume of sediment to the channel. For sediment-recirculating flumes the problem consists of the capacity of the sediment-recirculating system to take all the material going out of the channel and deliver it again to the channel intake. On the other hand, for sediment-feed flumes the main challenge is the availability of enough fresh material to maintain the channel constantly fed during the experiment, especially during long-lasting runs. Another essential point is the monitoring of sediment loads. For high solid discharges, the volume of any sampler could become unrealistically large to satisfy minimum representative sampling times. The new facility used in these experiments helped to overcome these difficulties by using a hybrid type of sediment operation mode, which combines feed and recirculating configurations. Moreover, a constant monitoring of the weight in the hoppers by means of load cells served as an instantaneous measurement of the solid discharge going out of the channel.

For the hybrid-feed operation, gravel and sand are fed into the channel at a constant rate from their individual hoppers, while the sediment-recirculating system collects sediment from the downstream end of the flume, separates sand and gravel and delivers them to their respective hopper/feeder to avoid shortage of material and thus keep

the channel continuously fed (see Figure 3.1). If Q_{IN} is the rate at which sediment is added in the hoppers (disregarding sediment losses in the recirculating system, Q_{IN} is equal to the solid discharge at the downstream end of the channel), and Q_{SF} is the sediment feed rate supplied by the hoppers, the weight gradient in the hoppers with respect to time is

$$\frac{dW}{dt} = Q_{IN} - Q_{SF} \qquad (3.1)$$

where W is the instantaneous weight in the hoppers and t is time. For a given velocity of the conveyor belt and a given aperture of the sluice gate, the hoppers are able to feed the channel with a constant amount of sediment, independently of the volume of sediment inside the hopper, as it is demonstrated in Section 3.4 of Appendix I. Therefore, for a selected constant value of Q_{SF}, and given certain flow conditions different to those required for the dynamic equilibrium of the bed in the channel, according to eq.(3.1) the weight gradient in the hoppers would be

- $dW/dt<0$ if sedimentation occurs in the channel and $Q_{IN}<Q_{SF}$,
- $dW/dt>0$ if erosion occurs in the channel and $Q_{IN}>Q_{SF}$,
- $dW/dt=0$ if mobile-bed dynamic equilibrium occurs in the channel and $Q_{IN}=Q_{SF}$.

The real-time measurement of the weight in the hoppers makes it possible to have an accurate measurement of the sand and gravel loads passing through the channel ($\approx Q_{IN}=Q_{SF}+dW/dt$), and in search of mobile-bed equilibrium conditions, the system operated in the hybrid mode reflects accurately when dynamic equilibrium has been achieved in the channel. This happens when the bed slope and solid discharge of each size fraction are approximately constant all along the channel, and as a consequence the sediment feed rate is equal to the solid discharge added to the hoppers and thus the weight of the material in the hoppers is constant as well.

An advantage of the hybrid-feed operation is the possibility of performing long-lasting runs without requiring a huge reserve of fresh material. Nevertheless, it should be taken into account that for such an operation mode the dynamic equilibrium reached may be affected by the initial conditions in the bed if mixed-size sediment is used. In a sediment-recirculating flume solid discharge of each size fraction is controlled by the processes in the channel, and thus the initial conditions in the bed affect the equilibrium to be reached; while in a sediment-feed flume sediment discharge is imposed by the operator, and the initial conditions are not relevant for the equilibrium (Parker and Wilcock, 1993). The effect of using a hybrid operation as the one used in these experiments, is that when experiments with poorly sorted material are performed, if the flow conditions in the channel hinder the mobilization of any of the size fractions, after some time it is likely that these 'less' mobilized size fractions would have a lower fractional participation in the total solid discharge in the channel, that is, partial transport of some of the size fractions would occur; as a consequence, these coarser less-mobilized size fractions would be underrepresented in the bulk of sediment recirculated with respect to the initial grain size distribution in the hoppers. The equilibrium thus attained would be different than the equilibrium attained with a pure feed run with the same initial conditions. For the experiments here described, partial transport of any of the sediment size fractions was not likely to occur, first, because the shear stress was so high that all size fractions present in the bed were fully mobilized during all runs, and secondly, because the coarse material was well sorted, i.e., there were no great differences between the coarsest and the finest size fractions, and thus the flow conditions for which partial transport of the coarsest grain sizes would occur was limited to an extremely narrow range of flow conditions. If partial transport occurred in the experimental runs, it must have been quite subtle and thus hidden by the accuracy of the measurements. All things considered, it can be stated that the operation of the flume for the experiments performed to form the new data set, altogether 22 experiments, was of the sediment-feed type.

3.2.1 Adaptation of the flume for the first experimental campaign

The calibration and test of different components of the flume, and several works for adaptation, were carried out during the four months previous to the beginning of the first experimental campaign, for which the flume was used with the sediment-recirculating system altogether for the first time. A detailed description of the calibration of different components of the flume, including the sediment feeders, is given in Appendix I. Additional adaptation works required for the flume implementation are listed and described as follows.

- Water intake. Water discharge was supplied to the channel by means of three flexible hoses connected to a constant head tank (see Figure A1.1 in Appendix I). In order to reduce water agitation in the head of the channel, water discharged by the hoses is conducted through three perforated vertical metal plates. To improve the turbulence reduction, immediately downstream from the vertical sheets, an arrangement of bricks with cavities was set on the base of the channel for the water to pass through. Altogether, the hoses, vertical sheets and bricks took up 3 meters of the upstream side of the channel, leaving free an effective length of 27 m for the sediment bed.
- Sprinklers for the sediment feeders. Sediment in the hoppers is supplied to the channel by means of rotating rubber bands. In order to avoid sediment to get stuck on the rubber bands, these should be continuously moistened. Tubes with orifices were installed over the feeders to be used as sprinklers to moisten the rubber bands (see photos P4a and P4b in Appendix I). Water was supplied to the sprinklers by means of a flexible tube connected to the line that supplies water to the elevated water discharge regulation deposit. The water provided by the sprinklers seeps in the channel and therefore it must be added to the water discharge set for a given experiment. To obtain an average discharge value for the sprinklers, ten tests were performed, which consisted in measuring the volume of water supplied by the sprinklers for a given time. Measured average values were 0.269 l/s for the gravel hopper, and 0.258 l/s for the sand hopper. Therefore, a value of 0.526 l/s was added to the water discharges supplied to the channel in each experiment.
- Sediment management. Although the sediment recirculating system in the flume extends the usual experimental possibilities on sediment transport, this mainly because of its high capacity and its ability to separate two size fractions, some drawbacks of the system are word to be mentioned. First, many problems were found for sucking the sediment out from the siltation tank at the downstream end of the flume (see Figure A1.2 in Appendix I); different arrangements were tested trying to increase the efficiency of the intake, but even so, during the experimental campaign the tank had to be continuously checked to verify, first, if the intake was not stuck, and secondly, if there weren't any large accumulations of sediment in the bottom. Another main cause of the problems with the pumping in the sediment siltation tank was the abrasion of the blades of the pump (see Photos P8 in Appendix I), which had to be changed three times along the experimental campaign. Another drawback of the sediment recirculating system was the operation of the screw conveyors which served to transport sediment from one element of the system to another (see Figure A1.2 in Appendix I); these conveyors were extremely noisy when sediment was being transported, mainly with gravel. It was subsequently verified that the conveyors caused a certain degree of crushing of the gravel grains; therefore, for every run several sediment samples were taken in order to adequately characterize the degree of crushing and to assign a mean grain size distribution representative of feed material in each

specific run. Details of the effects of crushing caused by the screw conveyors are given in Appendix IV.

Before beginning the first experimental campaign, works required for ensuring the sediment continuity in the sediment recirculating system included the identification and plugging of gaps and leaks in zones where sediment could go out of the system because of grains jumping and bouncing with the flume structures. These works included the construction of a tilting ramp to collect the sediment supplied by the two feeders and convey it to the channel (see Photo P5a in Appendix I). The function of the ramp was not only to avoid that sediment grains leaked out of the system, but also to evenly distribute the particles across the channel width and to favor a gentle insertion of the grains in the channel. According to the slope of the channel, the slope of the ramp was adjusted, and thus the point of addition of the material in the channel could change from being 4 to 5 meters downstream of the channel head. Therefore, the length of the sediment bed varied from 25 to 26 m between different experiments.

Adaptation works included the installation of a metal vertical sheet at the downstream end of the channel to be used as a border condition for the sediment bed (see Figure 3.2). The height of this metal plate was 7 cm for the run series I, II and III, and 15 cm for the run series IV, V and VI.

- Rulers on the channel glass panels. The experiments required that the bed and water elevations were continuously surveyed through the channel walls. Therefore, stickers of rulers graduated every 1 mm were attached vertically to the channel walls. After an analysis described in Appendix II, it was found that a separation of one meter between rulers was practical and accurate for measuring the mean bed and water slopes. This analysis considered the bed profile temporal variation because of net erosion or sedimentation, and because of the passage of bedforms. Accordingly, the rulers were spaced one meter apart (each on the mid length of each glass panel), except for the reach between 19.5 and 21.5 m upstream from the end of the channel, where the spacing was of 2 m because no ruler could be installed as the wall is covered by a support for the channel tilting mechanism. In turn, for runs series I and II, rulers were not yet installed in glass panels located 9, 21, 23 and 25 m upstream from the channel end.

Measurements on the 26 rulers installed had to be corrected for errors and referenced to the coordinate system shown in Figure 3.2, whose origin is the pivot about which the channel tilts, approximately 6 cm downstream from the sediment border condition. For the reference coordinate system in Figure 3.2, y axis is perpendicular to the drawing and the origin passes through the center of the channel cross-section. Equations for correcting errors in the rulers and for obtaining the coordinates of the measurements are given in Appendix III. According to these equations, the horizontal and vertical coordinates of a measurement z_h on ruler i, are given by

$$x_i = x_{h,i} \cos\alpha - z_{h,i} \sin\alpha \qquad (3.2)$$

$$z_i = x_{h,i} \sin\alpha + z_{h,i} \cos\alpha + e_{z,i} \qquad (3.3)$$

respectively, where x_h is the horizontal distance between the ruler and the origin of the coordinate system when the channel slope is zero (these values for each ruler are summarized in Table AIII.2 in Appendix III); z_h is the measurement on the ruler (perpendicular distance from the bottom of the channel to the measurement point) already corrected for errors in the rulers with eq.(AIII.1) and functions given in Table AIII.1 in Appendix III; α is the angle between the channel bottom and the horizontal plane; and subscript i refers to the i-th ruler. In eq.(3.3) the correction on the vertical coordinate, e_z, due to deformations of the channel has been included; these

deformations are described in Section 3.3.2 of Appendix I, and rules for computation of the correction e_z are summarized in Table AI.6 of that same Appendix.

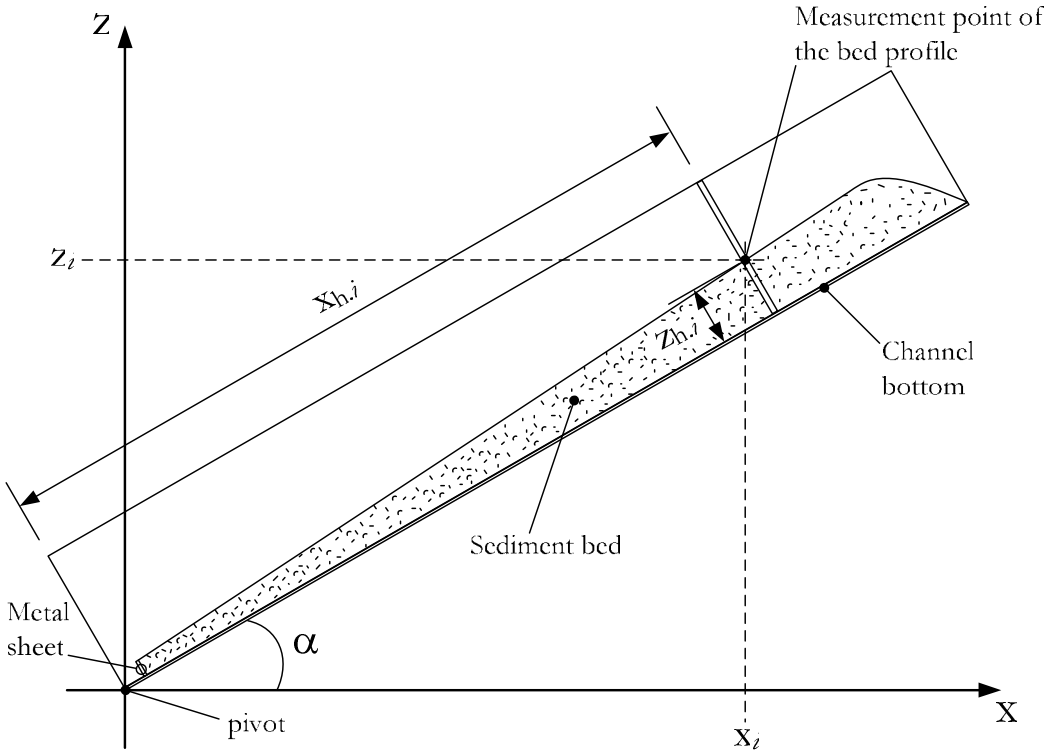

Figure 3.2. Reference coordinate system for the measurements on the channel walls.

3.2.2 Sediment

One of the objectives of the experimental campaign was to develop a data set for high sediment transport conditions under supercritical and near critical flows, with the possibility of identifying the effect of sand content in bed configurations and sediment transport. Accordingly, four sediments were used, namely, sediment with grain sizes in the range of sand for the series of runs I and VI, sediment with grain sizes in the range of gravel for the series of runs II and III, and two sediments prepared by adding the same original sand from the series I and VI to the same gravel from the series II and III. The original gravel ranged in size from 1.25 mm to 10 mm, while sand ranged from 0.08 mm to 2.5 mm. Table 3.2 summarizes the properties of the original sand and gravel, and the procedures for determining each property are described in Appendix IV.

Table 3.2 Summary of the properties of the original sediment before addition to the experimental set-up. D_m is the geometric mean diameter, S_s is the relative density, ε is the porosity, σ_g is the geometric standard deviation of the grain size distribution and σ_{gs} is the geometric standard deviation for a normal size distribution (as defined in Section AIV.3 of Appendix III).

Material	D_m [mm]	σ_g [mm]	σ_{gs}	S_s	ε
Sand	1.51	1.50	1.54	2.63	0.40
Gravel	4.96	1.44	1.44	2.60	0.38

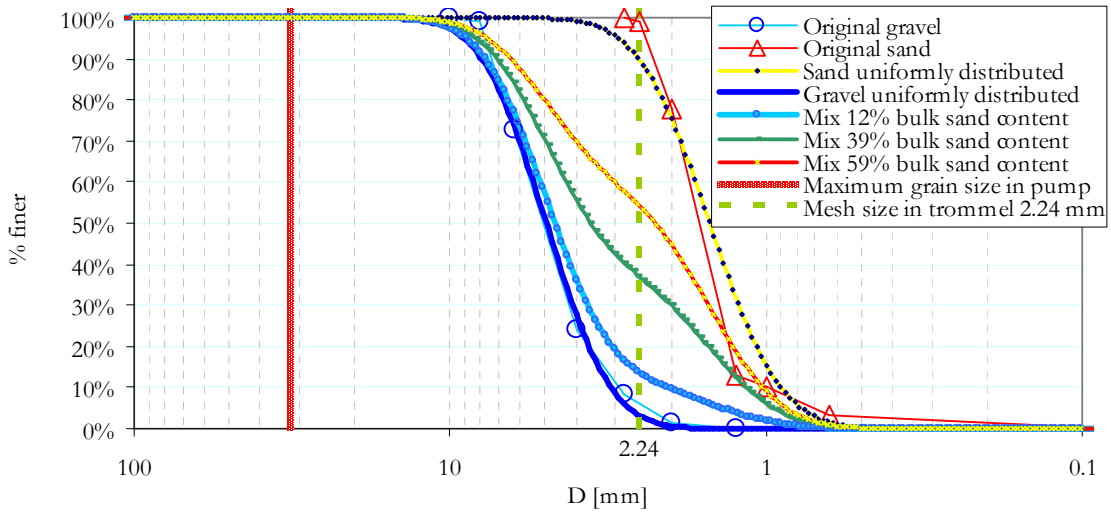

Figure 3.3. Cumulative percent grain size frequency distribution curves for normally distributed grain size density functions for the mean diameter and geometric standard deviations of the original sand and gravel, and theoretical mixtures obtained with these two distributions. Grain size distributions for the original sand and gravel are shown as well.

The sand material used was already available in the laboratory from previous research works. This sand was fitted to be used in the sediment recirculating system, with a maximum grain size close to the maximum opening size of the mesh of the trommel that separated sand from gravel when mixtures were used (see Section 3.4.2 and Figures A1.37 and A1.38 in Appendix I). In selecting the gravel to be used in the experimental campaign, restrictions of the experimental facility and of the objectives of the investigation were taken into account. For the experimental facility, the main limitation was the maximum grain size that could be pumped, indicated as being 32 mm by the manufacturer. In turn, since sediment in natural rivers usually has no gaps between the coarse and fine size fractions, it was desirable that when mixing sand and gravel all of the grain sizes were represented, i.e., that the tails of both grain size distributions superimposed each other. In order to reproduce similar forms to natural grain size distributions, another restriction for the gravel to be selected was that the grain size distribution of the sand-gravel mixtures obtained had to be smooth, with no abrupt slope changes. In searching for gravel grain size distributions that could meet all these requirements, tests were performed by constructing theoretical mixtures using uniformly distributed grain size density functions with the mean diameter and geometric standard deviation of the original sand and of hypothetic gravel samples. Theoretical mixtures with 12%, 39% and 59% of sand added to gravel, for uniformly distributed grain size density functions for the original sand in laboratory and for the selected gravel, are shown in Figure 3.3. Since the grain size distributions of the sand and gravel superpose each other between 1.25 and 2.5 mm, note that the actual sand content (sand considered as all material with D<2 mm) of the theoretical mixtures in Figure 3.3 is 10%, 30% and 45%, respectively.

The series of runs with the sand-gravel mixtures were initially intended to be performed for three different sand contents, but due to time limitations only two sand contents were tested: the first was 30% (run series IV), for which runs were named M1, and the second was 45% sand content (run series V), for which runs were named M2. Since the calibration of the sediment feeders was adjusted with the new data generated during each run, there were slight deviations from the initially intended sand content for every run; Table 3.26 at the end of this Chapter summarizes the actual sand contents estimated for each run and Figures 3.37 to 3.39 show the grain size distributions of the feeding sediment.

In the selection of the sand contents for the mixtures used, different aspects were considered. First, it was necessary that the separation in sand content between mixtures was enough to allow for identifying trends that could be directly attributed to sand content. In the same vein, since it is well documented that bimodality of sediments has a measurable effect on critical shear stress and sediment transport in comparison to unimodal and weakly bimodal sediments (Wilcock 1993, Kuhnle 1993), it was tried to eliminate the influence of bimodality so as not to have an additional variable. From the bimodality parameter of Sambrook-Smith (Sambrook-Smith et al. 1997, this parameter is explained in Section 3.5.1) applied to theoretical mixtures formed with the statistical parameters of the original sand, as those presented in Figure 3.3, it was found that an approximate upper limit of sand content for the mixture to behave as being bimodal was 60%; in consequence, sand contents to test had to be lower than this value.

A second aspect to consider in the selection of sand contents for the mixtures, was that it was desirable not to move away from sand contents that can be usually found in natural rivers. From Figure 2.10 in Chapter 2, it can be obtained that most of the grain size distributions for the natural sediments analyzed had sand contents between 10% and 50%.

A third, definitive criterion, for selecting the proportion of sand in the experimental mixtures, was texture and packing. Wilcock (1998) adduced to the transition from a framework-supported to a matrix-supported gravel bed structure, as a possible cause for the observed variation in some experimental flumes of sediment mobility as a function of sand content in the bed. As indicated in Section 2.4, matrix-supported beds usually occur for sand contents higher than 25% to 45%; in agreement with these values, for flume experiments and field data, Wilcock and Kenworthy (2002) found that the effect of sand in sediment transport was negligible for sand contents above approximately 25%. Hence, the initially selected sand contents for the experimental runs were 10%, 30% and 45%, and were intended to explore the effect of sand content on the sediment mobility at high transport conditions: if the findings of Wilcock and Kenworthy were valid for these conditions, results would show a non-linear response of sediment mobility when comparing the three sand contents with pure gravel and pure sand runs. Since it was not possible to perform the series of runs for 10% sand content, this comparison remained incomplete. This notwithstanding, comparison of runs with 30% and 45% sand contents with runs for pure gravel and pure sand is valuable on its own, and this comparison is still a relevant contribution for understanding the transport of sediment mixtures. Particularly, it is of interest to identify if any important effects can be attributed to different bed structures. In Chapter 8 bed structure is analyzed with empirical bed porosity models; according to these models, bed structure with a mixture of the characteristics of the sand and gravel used in the experiments cannot form a gravel framework (the ratio between sand and gravel grain sizes is too low, see Figure 8.2A). Therefore, if in the experiments there exists a measurable difference in the mobility of the mixture with 30% sand content and the mixture with 45%, with respect to uniform material, then, it could be demonstrated that the effect of sand content in sediment mobility is not necessarily tied to a change from a framework-supported to a matrix-supported gravel bed structure.

3.3 EXPERIMENTAL PROCEDURES AND MEASUREMENTS

The most important issue of the experimental campaign was to create a comprehensive data set for mobile bed equilibrium states, with conditions comparable to those found in Mediterranean torrential streams. Hence, the efforts in the initial phase of each particular run were concentrated in searching for equilibrium states, and afterwards, once the equilibrium was found, the experimental tasks focused in documenting the characteristics

of flow, bed and water configurations and sediment transport. In this regard, the methods and procedures used in the experimental runs were basically not far apart from those used in classical sediment transport flume experiments, from which sediment transport formulas were developed (e.g., Einstein, 1950; Parker et al., 1982a; Wilcock et al., 2001) or from which bedform stability states were studied (e.g., Gilbert, 1916; Kennedy, 1961; Simons et al., 1961); compared to those previous works, the most important added value of the experiments herein reported, is the study of ranges of variables that previously had not been systematically explored in laboratory flumes.

Two main aspects were considered in selecting the most appropriate methods and conditions for the experimental runs. First, it was desired to make the most of the new experimental flume, and secondly, it was required to fulfill the restrictions imposed by the objectives of the research (these are listed in Section 2.6). The selection of a hybrid-feed operation of the flume (combining sediment-recirculating and sediment-feed operations, but resembling the latter as explained in the beginning of Section 3.2) attended to the aspect of making the most of the flume capabilities. The flume could be operated either as sediment-feed or as sediment-recirculating (see Appendix I, Section 5), but the hybrid operation was chosen because of the reasons explained as follows. Since flash floods in perennial rivers often hamper the formation of a coarse layer (e.g., Laronne et al. 1994, García and Martín-Vide 2001), so that bedforms can develop without sediment-supply limitations, it can be assumed that the torrential flows that were intended to be emulated are competent to mobilize all size fractions in the streambed. Then, it was required that no partial transport occurred in the flume; for this condition, it can be expected that there would not be any fundamental difference in the equilibrium states reached, or in the texture of the final bed surface, if the flume is operated either in a feed or in a recirculating mode. For both types of operations, mobile-bed equilibrium states would be equivalent (Parker and Wilcock, 1993) and the only difference would be the path by which equilibrium is reached according to the initial conditions. Consequently, if the selection of either type of flume operation has no fundamental influence on the formation of the data set, the hybrid-feed type was chosen because in this manner it was possible to perform long-lasting runs with a limited amount of sediment (as explained in the beginning of Section 3.2), and in turn, the sediment discharge going out of the channel could be monitored in real-time to record the transient state and accurately identify the instant at which mobile-bed equilibrium was reached. Finally, an additional advantage of selecting the hybrid-feed operation is that it is known that with a sediment-feed flume equilibrium is reached faster than with a recirculating flume (Parker, 2004). Sediment hybrid-feed runs were used for the formation of the data set, but for verification of reproducibility additional few runs were performed in a recirculating mode and two others without sediment-feed neither recirculating.

In search for equilibrium states, when operating the flume in the hybrid-feed mode, sediment-feed rate Q_{SF} and water discharge Q_w are imposed by the user, and for a given initial arbitrary bed slope, sediment discharge Q_s, water depth H, and bed slope S_o in the channel evolve to mobile-bed equilibrium. For the selection of the range of variables to be used in the experimental runs for developing the data set, an *a priori* estimation of the likely equilibrium conditions was performed. Two computations were performed, one for sand and one for gravel, using standard equations for bed resistance and sediment transport, and considering flow over a hydraulically rough plane bed with sediment with the characteristics given in Table 3.2. The results of these computations are summarized in Figures 3.4 to 3.6, while a description of the equations used is given in Appendix V. Actual values of Q_w and S_o for the experimental runs used in the new data set have been plotted in Figure 3.4 as a reference. As already explained above, it was desired to make the most of the flume capabilities, this would allow for exploring ranges of variables previously not

studied in experimental flumes; hence, the range of sediment-feed rates for the experiments was selected trying to cover the spectrum between the minimum and maximum values likely to be managed by the sediment-feeders and the sediment-recirculating system. From Section 4 in Appendix I, it was obtained that the maximum sediment-recirculating rate that the system supports was found to be approximately 1.1 kg/s, while the theoretical minimum sediment-feed rate given by the feeders would be approximately 10 g/s for sand and 36 g/s for gravel; this notwithstanding, for avoiding malfunctions of the feeders, a recommended lower limit would be 45 g/s and 72 g/s, for sand and gravel, respectively, but in the computations here a conservative value of 100 g/s was assumed for the two sediments. In the same manner, computations were restricted to a maximum water discharge of 250 l/s, which is close to the limit of 270 l/s given by the water supply system, although a maximum value of 120 l/s is recommended to avoid water spilling at the entrance of the flume.

Graphics in Figure 3.4, one for sand and one for gravel, describe the combinations of bed slope and water discharge values for the estimated equilibrium states for four solid discharges, namely, the maximum and minimum likely to be supported by the system, and two intermediate values. The regions of likely experimentation, according to the flume limitations and according to restrictions for simulating torrential streams, have been marked with dashed lines in the graphics. Bed slopes in the type of torrential streams that were intended to be studied typically range from 0.010 to 0.030, but a lower value of 0.005 was considered in order to extend the data set to subcritical flows for which bed configurations in the transition between lower and upper regimes occur. Empirical data for defining this transition for sediment grain sizes in the range of coarse sand and gravel, and for sand-gravel mixtures, are not common in literature. The experiments here reported offered an exceptional chance to provide with new empirical evidence for the understanding of the lower to upper flow regime transition. A lower bound to study the transition was set here at Froude numbers equal to 0.7, although transitional bedforms have been reported for Froude numbers as low as 0.5 (Carling and Shvidchenko, 2002). For the equilibrium curves in the graphics in Figure 3.4, Froude numbers higher than 0.7 have been indicated with bold lines. The left limit of the region for likely experimentation is then given either by the imposed lower slope of 0.005 or by the minimum Froude number considered.

The independent variables for the experiments were Q_{SF} and Q_w. Q_{SF} was held constant during each run, but was varied between runs of a same series for a given sediment. For the values of Q_{SF} to be selected, it was desired to cover the whole spectrum of values supported by the flume; conversely, Q_w was taken as a parameter, which was held within a narrow range for all the series of runs. For the selection of a value of Q_w, the widest range of equilibrium bed slopes and all the spectrum of Q_s supported by the flume were tried to be covered within the delimited likely experimental region. For both graphics in Figure 3.4, the optimum for this condition would be roughly between 40 and 65 l/s; this notwithstanding, a value of 80 l/s was selected in order to increase the equilibrium water depths and thus have a better representation of extreme torrential flows. In turn, low water depths might hinder the free development of bedforms. From graphics in Figure 3.5, it is observed that an increase of Q_w from 40 to 80 l/s means an increase of roughly between 60% and 100% the water depth.

Figure 3.6 shows results for the computations of the ratio of Shields stress to critical Shields stress as a function of equilibrium bed slope, with Q_s and Q_w as secondary variables. In the two graphics it is verified that sand and gravel would be set in motion for all the conditions selected with Q_w=80 l/s and Q_s>0.1 kg/s, since it is fulfilled that $\tau_b^*/\tau_c^*>1$ (ratio between the bed Shields stress and the critical Shields stress for the bed sediment). These computations were repeated for the D_{90} grain-size (≈8 mm) in the original

gravel as well, and it was verified that the computed bed Shields stress was always above the critical for initiation of motion (τ^*/τ_c^*=1.24 for Q_s=0.1 kg/s). Therefore, for the conditions that were pretended to be tested, these preliminary computations indicate that no partial transport would occur.

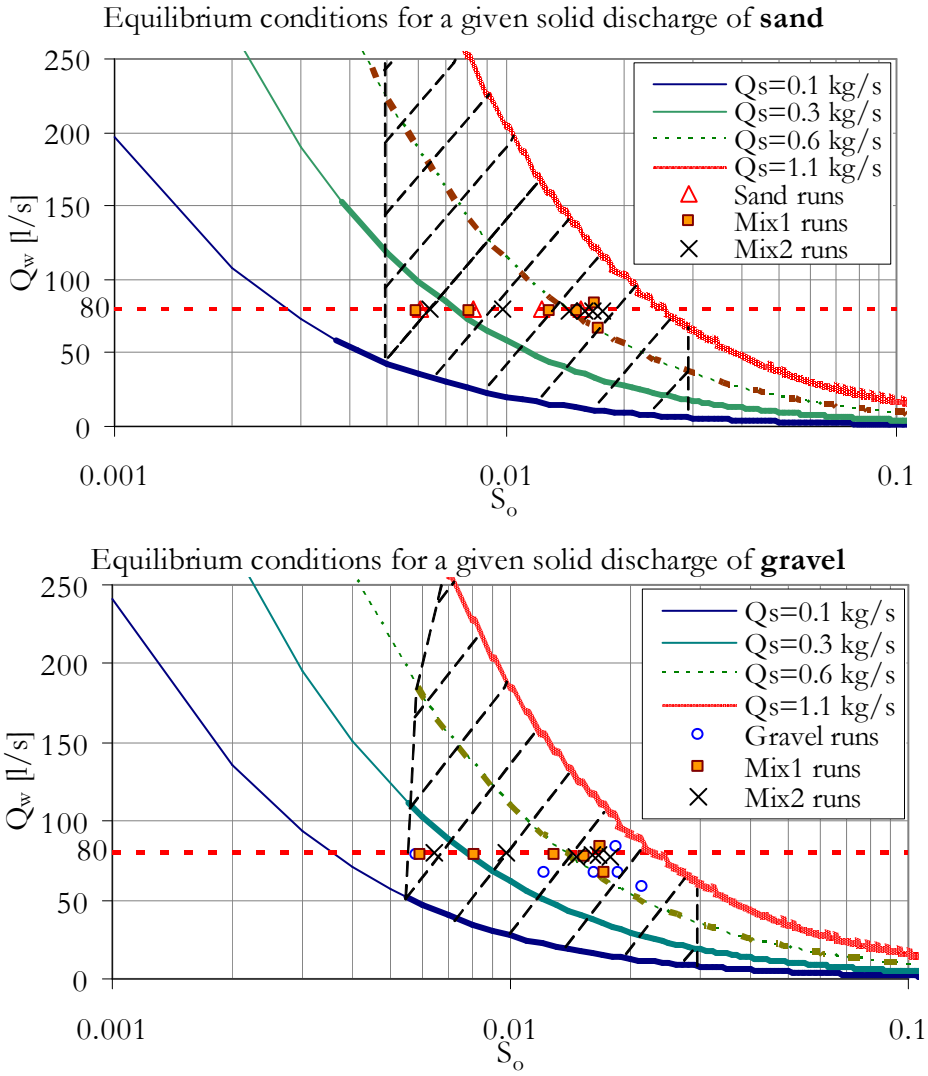

Figure 3.4. Curves for mobile-bed equilibrium conditions for different solid discharges in the experimental flume, as a function of bed slope and water discharge. Computations according to a Meyer-Peter & Müller-type of equation for sediment transport, and according to Manning-Strickler equation for bed resistance over plane beds with the sand and gravel used in the experiments (see Appendix V for a detailed description of the equations). The region hatched with dashed lines delimits the likely combination of variables for the experimental runs according to the limits of the experimental flume for solid and water discharges, and according to the restrictions imposed for reproducing typical flows of Mediterranean torrential ephemeral streams. The actual experimental points for the new data set are plotted as well. Bold lines indicate Froude numbers higher than 0.7.

It should be consider that the computations described above were used just as a first approximation, which was contrasted later with the first two series of test runs. Bedforms were not considered in the computations, and thus the effective shear stress acting on the bed grains was overestimated. If considered, the effect of bedforms in the graphics would be a shift to the right of all curves (higher equilibrium bed slopes) and an increase in water depth. Also, in these computations hiding-exposure effects affecting the

mobility of heterogeneous sediment were not considered. Moreover, only one sediment transport formula was used, and since great variations may be expected when using different formulas, deviations on the computed ratio of Shields stresses could be expected; nevertheless, because of the high flow conditions used, it can be expected, and test runs verified this, that all size fractions were put in motion for all the selected conditions.

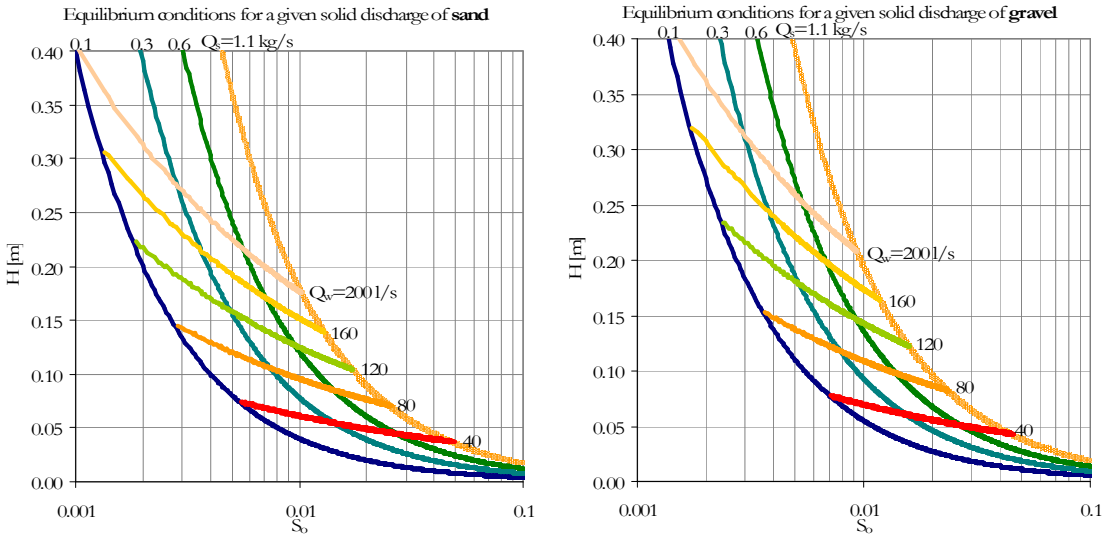

Figure 3.5. Curves for mobile-bed equilibrium conditions for different solid discharges in the experimental flume, as a function of bed slope and water depth, and as a function of the water discharge in the flume. Computations according to a Meyer-Peter & Müller-type of equation for sediment transport and according to Manning-Strickler equation for bed resistance over plane beds with the sand and gravel used in the experiments (see Appendix V for a detailed description of the equations).

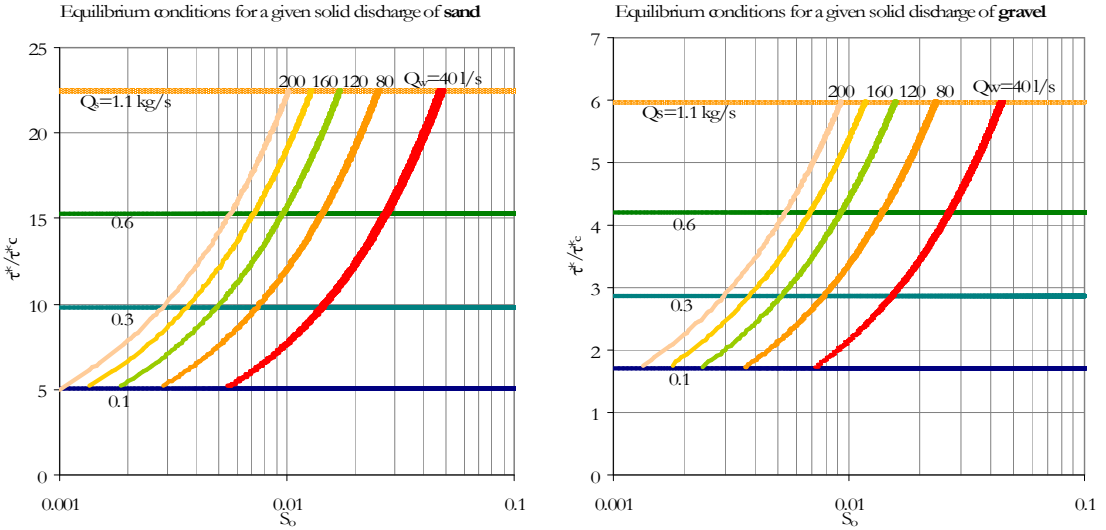

Figure 3.6. Curves for mobile-bed equilibrium conditions for different solid discharges in the experimental flume, as a function of bed slope and the ratio between bed Shields stress and critical Shields stress for the bed sediment. Computations according to a Meyer-Peter & Müller-type of equation for sediment transport and according to Manning-Strickler equation for bed resistance over plane beds with the sand and gravel used in the experiments (see Appendix V for a detailed description of the equations).

In the following Subsections the experimental procedures for each series of runs are described, giving more emphasis to the runs used for developing the experimental data set; later on, the measurements performed during the experiments are described in detail.

3.3.1 Description of experimental runs

Table 3.3 gives a general summary of the six series of runs carried out during the experimental campaign. A more detailed description of each series is presented in the following Sections, but emphasis is given to runs in series III to VI that were used for the final data set with a hybrid-feed operation of the flume. Series I and II are described briefly, since they served as a preliminary approach to perform the definitive runs. For some experimental runs of these two initial series mobile-bed equilibrium states were found, and the most relevant hydraulic variables to characterize these states were measured; nevertheless, runs in series I and II will not be considered in subsequent analysis, neither for the final data set presented in this work, mainly because methods, measurements and procedures were not systematic. For instance, for most of these runs bed configurations were not described, neither recorded in video. A thorough analysis to refine data from runs in series I and II is required, in order to gather extra information for completing the data set of combined hydraulics and sediment transport conditions for mobile-bed equilibrium states, but this analysis will not be presented in this work.

The most significant contributions of runs in series I and II within the whole experimental campaign were:

- They served to try out and to become familiar with all the mechanisms and elements of the flume and sediment-recirculating system, since the complexity of this latter system required especial operation protocols and procedures.
- During these runs many elements of the experimental facility were calibrated. In turn, malfunctions were identified and several improvements were carried out.

Table 3.3 Summary and short description of the series of runs conducted during the experimental campaign.

Run series		Ranges of independent variables		Type of operation	General observations
		Q_w [l/s]	Q_{SF} [g/s]		
I	Test runs with sand	10 - 50	69 - 652	Hybrid-feed: 15 runs	Plane bed in three runs, dunes and antidunes in the rest. Uncertainty of whether equilibrium conditions were actually reached for many of the runs.
II	Test runs with gravel	44 - 104	76 - 884	Hybrid-feed: 11 runs	Antidunes and standing waves. Uncertainty of whether equilibrium conditions were actually reached for many of the runs.
III	Runs with gravel	59 - 84	80 -741	Hybrid-feed: 6 runs	Antidunes and standing waves, and plane bed for one run.
IV	Runs with mixture 1	67 - 84	137 - 862	Hybrid-feed: 7 runs Recirculating: 4 runs No sediment-supply: 1 run	In average 30% sand content. Antidunes and standing waves.
V	Runs with mixture 2	78 - 79	159 - 1070	Hybrid-feed: 6 runs Recirculating: 1 run No sediment-supply: 1 run	In average 45% sand content. Dunes, antidunes and standing waves.
VI	Runs with sand	80	143 - 658	Hybrid-feed: 4 runs	Dunes and antidunes.

- A general overview was obtained of the type of bed and flow configurations for the selected sediment. Moreover, the order of magnitude of the lengths of time required to reach mobile-bed equilibrium states were identified. All this information was helpful in selecting variables and designing the definite experimental runs.
- Methods and procedures for conducting different types of measurements were tested.

Figure 3.7 presents results from runs in Series I and II, of bed slopes obtained presumably during equilibrium states; this notwithstanding, not for all these runs enough measurements or evidence were available to guarantee that equilibrium conditions were attained. A thorough analysis of the data is required to discard doubtful points, but this analysis will not be presented in this work. In spite of the provisional condition of data used in the graph of Figure 3.7, this graph served as a reference for selecting variables when preparing runs in series III to VI.

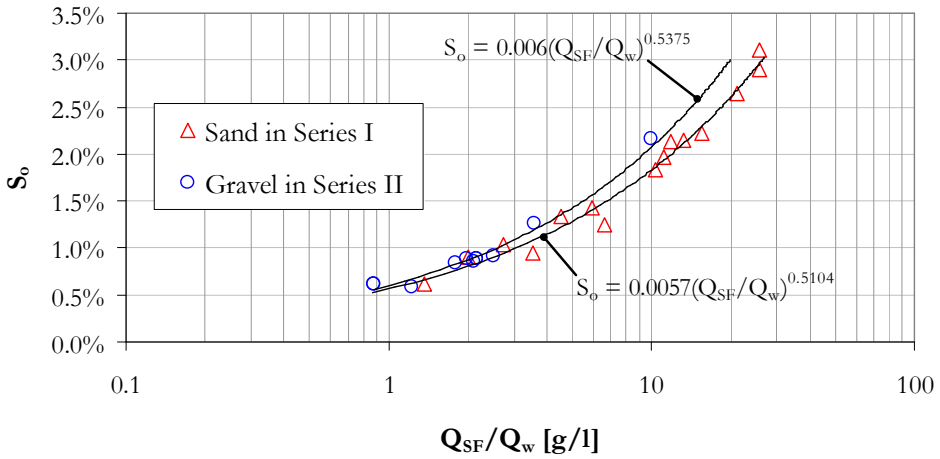

Figure 3.7. Likely equilibrium bed slopes for runs in series I and II as a function of the ratio between sediment-feed rate and water discharge. Best-fit curves are shown for each group of data.

3.3.1.1 RUN SERIES I: Test runs with sand

As already explained before, this series of runs was used as a first approach to the conditions to be tested in the flume with sand. Fifteen runs were performed, with the main goal of searching for mobile-bed equilibrium states. For each run different combinations of constant values of water discharge, sediment-feed rate and channel slope (do not confuse with the bed slope, which was a dependant variable) were imposed. These combinations of variables were arbitrarily selected at the beginning of the run, and therefore, it was not always deliberately controlled if the equilibrium state would be attained by bed erosion or bed aggradation. The evolution to equilibrium states in the channel was monitored by measuring bed and water surface profiles at different time intervals. In addition, the time variation of sediment weight on the hopper was monitored in real-time, but for most of the runs this was not a reliable measurement of the solid discharge in the channel, since the sediment pumping in the sediment-return system failed continuously.

Runs began from different initial conditions. Some runs began from a plane bed obtained by flattening the sand material manually, and after introducing water slowly into the channel; some other runs began introducing water in this same manner, but over the final bed configuration of the preceding run; while some other runs began when water was flowing in the channel with the conditions of the preceding run (whether in equilibrium state or not) and a change was imposed either in water discharge, sand-feed rate, channel slope (using the engines for tilting the channel) or simultaneously on two or the all three of

these variables. Lengths of time required to reach equilibrium states were in the order of a few hours, up to four hours.

Alternate bars, dunes and antidunes were observed in different runs, but no detailed descriptions or measurements of their characteristics were obtained for all of the runs, neither photos nor video recording were taken. There was an initial interest in trying to find plane beds under supercritical or near critical flows, to be used as a reference for bed resistance computations. Only for three runs, with very high sediment concentrations, plane beds were observed; nevertheless, the flow in these runs occurred as a sheet flow (stratified flow in two phases), and thus these conditions are not comparable to the type of flows in the rest of runs of the experimental campaign.

During these series of runs many difficulties were encountered with the sediment management. Solving these difficulties hindered attention to some other experimental tasks and contributed to the lack of consistency in the procedures between runs. Equilibrium states were reached for some runs, but measurements and methods were not systematic, thus avoiding a direct comparison between different runs. Measurements of the bed and water surface profiles were not as rigorous as for the definitive runs in series III to VI: for some runs the initial bed profile was not measured or the running time of the experiment was not taken, and thus it was not possible to obtain a time-evolution of the measured variables to analyze if equilibrium was attained; for three reaches of the channel the separation between measurement points was two meters, instead of one meter, unlike runs in series III to VI, for which the separation was one meter for all the channel length; furthermore, profiles were measured only in the direction of flow, while in the definitive runs these profiles were measured in the opposite direction as well, in order to reduce the effect of the passage of bedforms. For most of the runs no previous computations were performed, and the selection of independent variables was arbitrary. Due to all these exceptions in this series of runs, data obtained will not be used further in this work. Nevertheless, this does not mean that many of the runs in the series are not reliable, thus they can be used to complete the data set. A thorough analysis is required to refine the data, but this analysis is out of the scope of this work and therefore this series of runs will not be included in the final data set.

3.3.1.2 RUN SERIES II: Test runs with gravel

Similarly as series I, the series II was used as a first approach to the conditions to be tested in the flume, but for gravel. Eleven runs were performed, again searching for mobile-bed equilibrium states. Experience gained and improvements performed during runs of the series I, helped for a better performance of the flume and of the protocols implemented. New measurements were required, which were tested along the series of runs, namely, surface and subsurface bed material sampling, solid discharge sampling in the channel with self-made samplers, and bed erosion identification. Because of this trying out of methods and procedures, similarly as with series I, the runs were not systematic but are not discarded for a future incorporation to the data set. Further analysis is required to refine the data, but this analysis is not included in this work.

Most of the runs began from conditions of the preceding run, this means that the bed was not flattened and the initial bed surface was the bed configuration of the previous run. The runs began after introducing water to the flume and restoring the conditions of the previous run, or they began immediately from the conditions of the preceding run in the channel; the run was considered to be initiated when the combination of water discharge, sediment-feed rate and channel slope of the previous run was altered. For most of the runs, equilibrium states were searched by eroding the bed. The evolution toward the equilibrium state was monitored by measuring the bed and water surfaces profiles at

different intervals, and following in real-time the weight variation on the hopper. This notwithstanding, problems with pumping of the sediment-return system prevailed in some of the runs, and the real-time monitoring was thus not always a good measure of the solid discharge in the channel. Equilibrium states were not always attained, some times due to malfunctions of any of the components of the flume for which it was necessary to stop the experiment. Lengths of time required to reach equilibrium states were in the order of a few hours, up to six hours.

Bed configurations observed showed many times trains of three-dimensional antidunes under steep breaking stationary waves, trains of two-dimensional antidunes under gentle stationary waves, long sediment waves in an alternate sequence, and less often plane beds. For some runs, some measurements of the geometry and propagation velocity of the bed features were carried out; videos of the bed surface were taken for some runs as well. At the end of most of the runs, after draining the water from the channel, bed features in an alternate sequence were observed on the bed surface; the wavelength of these features was measured.

These runs were useful for systematizing and standardizing measurements and procedures, which were used in the definitive runs that formed the final data set.

3.3.1.3 RUN SERIES III: Runs with gravel

The six experimental runs in this series were actually part of the sequence of runs in series II, but since the procedures and methods began to be to a certain extent standard, these runs can be considered as a group apart, consistent and homogeneous, so that a direct comparison between runs and between the rest of subsequent series of runs is possible. Because of this continuity between series II and III, the nomenclature was conserved, and thus the designation of the first run of series III begins with the consecutive number following the last run from series II, as can be seen in Table 3.4, where some characteristics of all runs used to form the final data set are presented.

The experimental runs consisted in the search of mobile-bed equilibrium states for given combinations of water discharge and gravel-feed rate. For three runs the evolution to equilibrium was through bed erosion, and for the other three runs through bed aggradation, as indicated in Table 3.4. Before the beginning of an experiment the sediment-recirculating system was initiated (sediment-return pump, screw conveyors and rotating trommel), the channel was moved to a horizontal position and a small water discharge (≈5 l/s) was introduced to inundate the channel without disturbing the bed particles. The experiment began by increasing the water discharge and immediately turning on the gravel-feeder to introduce in the channel the prescribed values of water and sediment-feed rates. A particular run was considered to be started when the selected constant values of Q_w and Q_{SFg} were established. This moment marked the starting point of the running time for that run. Runs G12 and G13 began from stand-still conditions (Q_w was increased from zero to the established value for the run) after the channel was filled with water over the bed configuration of the previous run, while the rest of runs began from the mobile-bed equilibrium conditions of the previous run prevailing in the channel (Q_w or any other variable was changed from the previous established value). Hence, except for run G12, all the experimental runs were divided in two phases: a first phase during which the bed evolved to equilibrium, and a second phase restoring and keeping the stable equilibrium conditions for a certain time. The first phase was over when mobile-bed equilibrium state was attained (see Section 3.4.2 for details on the equilibrium criteria). At this moment, the water discharge was set to zero and the gravel feeder was turned off. Sediment-feed stopped immediately, while it took from one to three minutes to the waning flow being totally brought down. When the water had been totally drained, the bed surface was

photographed (as explained in Section 3.3.2.4), measurements of the preserved bedforms were conducted (as described in Section 3.3.2.4), and bed material samples were taken (following the criteria given in Section 3.3.2.6).

The second experimental phase of a run began from stand-still conditions (except run G12, for which no second phase was performed) from the bed configuration preserved after the first phase. In order to measure the gravel feed-rate supplied to the channel (as it is described in Section 3.3.2.3), at a certain moment during this second phase the hopper was unloaded without cutting off the constant gravel-feed to the channel, and then immediately it was refilled with material from the large deposit (for many of the runs this practice was done during the transition phase). Also in this phase photos were taken of the bed and water surface configurations; samples of the material in the hopper and of solid discharge in the channel were collected (as it is described in Section 3.3.2.5); and measurements of the bedforms and stationary waves were performed (as it is described in Section 3.3.2.4). The second phase lasted one hour and 40 minutes in run G13, 51 minutes in run G14, one hour in run G15, three hours in run G16, and two hours and 43 minutes in run G17. After measurements were performed, the run was finished by changing the combination of values of water discharge, gravel-feed rate and channel slope to give the conditions required for the next run. When this was done (the change in feed rate was instantaneous, while for water discharge and channel slope one to three minutes were required to reach the selected values) the running time was reset and the first phase of the following run started.

Table 3.4 Summary of some characteristics of runs in series III to VI which were used for the definitive data set. For all these runs a hybrid-feed operation of the flume was used. Q_w is water discharge, Q_{SFs} is sediment-feed rate from the sand feeder, Q_{SFg} is sediment-feed rate from the gravel feeder, and S_c is the slope of the flume channel (not the bed slope). The proportion of sediment-feed supplied by the sand feeder is shown in the last column, note that this value is not the same as the actual sand content fed (which is shown in Table 3.26), because separation of sand from gravel in the trommel was not 100% efficient so that the gravel hopper contained some fine particles. Runs ordered in the sequence they were performed, from top to bottom.

Series	Run	Bed evolution	S_c %	Q_w [l/s]	Q_{SFs} [kg/s]	Q_{SFg} [kg/s]	$Q_{SFs}/(Q_{SFs}+Q_{SFg})$
III GRAVEL	G12	Erosion	1.85	59.0	0	0.594	0
	G13	Aggradation	1.50	83.6	0	0.741	0
	G14	Aggradation	1.30/1.50	67.1	0	0.531	0
	G15	Erosion	1.50	67.8	0	0.435	0
	G16	Erosion	1.30	67.8	0	0.266	0
	G17	Aggradation	0.50	78.7	0	0.081	0
IV MIXTURE 1	M1E1	Erosion	1.12	78.9	0.066	0.155	0.299
	M1E2	Erosion	2.24	83.9	0.258	0.604	0.299
	M1E3	Aggradation	2.00	67.1	0.199	0.472	0.297
	M1E4	Erosion	1.97	78.0	0.186	0.430	0.302
	M1E5	Erosion	1.64	78.4	0.131	0.305	0.300
	M1E6	Erosion	1.05	78.4	0.046	0.091	0.336
	M1E7*	Erosion	1.06	78.9	0.042	0.095	0.306
V MIXTURE 2	M2E1	Erosion	2.25	78.0	0.434	0.636	0.406
	M2E2	Aggradation	2.03	78.9	0.365	0.530	0.408
	M2E3	Erosion	2.01	78.4	0.325	0.468	0.410
	M2E4	Erosion	1.77	78.0	0.229	0.324	0.414
	M2E5	Erosion	1.46/1.35	79.4	0.120	0.172	0.411
	M2E6	Erosion	1.03	79.4	0.067	0.092	0.421
VI SAND	S1	Aggradation	1.10	79.7	0.658	0	1.000
	S2	Erosion	1.10	79.7	0.461	0	1.000
	S3	Erosion	1.00	79.7	0.246	0	1.000
	S4	Erosion	0.81	79.7	0.143	0	1.000

*Run to be compared with run M1E6 for testing reproducibility.

Evolution to equilibrium was monitored by measuring the bed and water surface profiles once every hour, and following in real-time the weight variation on the hopper. Graphs of time-variation of some variables for each run are shown in Appendix VII. For these graphs, running-time of a run includes the two experimental phases together. Equilibrium states were attained in 3 to 9 hours (run G14 required less than 2 hours, but this because the channel slope was changed during the transition to equilibrium state using the tilting engines), and the initial bed slopes measured were from 1% to 17% higher or lower than the equilibrium slopes.

During equilibrium state, the flow was steady and uniform all along the channel (except for the flow entrance and exit regions); hence, the measured profiles of the surfaces of the bed and water were roughly parallel. No boundary condition was used downstream, and thus water spilled freely at the downstream end of the channel over the border condition for the sediment, which was a 7 cm height metal plate placed vertically (see Figure 3.2). The bed surface profile was not parallel to the flume bottom, but the distance between the channel bottom and the cross-section average bed-surface elevation was always higher than the height of the border condition for the sediment all along the channel.

The most frequently observed bedforms at the central cross-section were 3D downstream-migrating antidunes under short-crested stationary waves, and only in one run a bed configuration which could be considered as a plane bed (although very low relief sediment waves could be sometimes identified) was observed. Trains of stationary waves appeared in the middle third of the channel length, along which they grew, up to the downstream third, where they remained more or less stable. At the end of the run, the antidunes were erased by the waning flow, and the preserved configuration often showed low relief waves with an alternate sequence; these features were identified as alternate bars. A thorough description of the observed water and bed configurations is given in Chapter 5.

Excluding the first run, the gravel-feed rate was deliberately decreased from run to run in an attempt to cover the whole range of feed rates likely to be supported by the sediment-recirculating system of the flume. Nevertheless, the selection of a specific gravel-feed rate for a given run was somehow arbitrary, while water discharge was hold within values of the fringe covering the maximum range of equilibrium bed slopes in the delimited region of Figure 3.4 (approximately between 50 and 80 l/s). The conditions to be tested were selected depending on the availability of sediment in the hopper and in the channel at the end of the previous run; if there were enough sediment in the channel, evolution to equilibrium was intended to be through bed erosion; conversely, if the volume of gravel in the channel was not high enough, evolution to equilibrium was intended to be through bed aggradation. The best-fit curve for gravel runs in the graph shown in Figure 3.7, with plots of the equilibrium slopes against the ratio between gravel-feed rate and water discharge from runs in series II, was used for estimating likely equilibrium bed slopes for selected combinations of water discharge and sediment-feed rate. The estimated value of the likely equilibrium bed slope was used, together with the bed profile left by the previous run and a given value of the channel slope S_c, to compute volumes of material required in the hopper for aggradation of the bed or to compute the maximum likely bed erosion. The equations and procedure for these computations are shown in Appendix VI. From the computations an initial bed slope was obtained, and if it was found that not enough material was available or if bed erosion could excessively approach to the channel bottom, another value of S_c was tested, until finding one value for an initial bed slope fitting the conditions required. These computations were used just as an approximation; they were prone to a high uncertainty since the feeder calibration had not been performed for all the ranges required, and not all data points used for equations in Figure 3.7 were necessarily representative of mobile-bed equilibrium states. This notwithstanding, as shown in Table AVI.1 in Appendix

VI, for most of the runs reasonable estimations of the required volumes of material in the channel and in the hopper were obtained with this procedure. Only for run G14 the estimations were not entirely good. For this run, during the evolution to equilibrium the hopper ran out of gravel; in order to speed up the approach to the equilibrium state, the channel slope was changed from 1.3% to 1.5%. Therefore, for run G14 the graph in Appendix VII with plots of time-evolution of weights on the hopper shows a discontinuous evolution, with a sudden establishment of equilibrium state approximately one hour after the beginning of the run.

3.3.1.4 RUN SERIES IV and V: Runs with sand-gravel mixtures

Most of the procedures and methods used in runs with a hybrid-feed operation of series IV and V were essentially the same as those used in runs from series III. Each run was divided in a transition and an equilibrium phase, but contrary to series III, every run began from stand-still conditions (Q_w was increased from zero to the established value for the run) with the bed material mixed and almost flat. Therefore, for a given run the experiment was stopped twice, the first time after the transition phase finished, and the second time when the equilibrium phase finished. Such a change in the experimental procedure, with respect to the previous run series, was introduced mainly for two reasons: first, for avoiding any likely influence in the transition to equilibrium due to sediment sorting produced by the previous run, and secondly, for performing measurements of maximum bed erosion during equilibrium state. By mixing the bed sediment before the beginning of any run and starting from stand-still conditions, it was achieved that all runs began from almost identical conditions, in contrast to series III, for which each run began with the conditions of the previous run and grain size sorting was not an important issue since the material was uniform. For measurements of maximum bed erosion, tracer stones were placed after the transition phase was finished, and bed erosion was measured after finishing the equilibrium phase by identifying the stones that were not removed by the flow; these measurements required that there were no water in the channel, as it is described in Section 3.3.2.7. Finally, the choice of stopping the experiment twice for the same run had practical advantages; with this practice, when normal conditions and no unexpected malfunctions of any of the flume elements occurred, all activities required for one run could be performed within two days in average, one for each phase of the run. In this manner, a precise experimental planning was scheduled. Moreover, devoting one full day for the transition phase and one full day for the equilibrium phase make it possible to perform all the experimental activities during working hours, and it was not required to keep the flume running continuously for extremely long periods, which would make it much more prone to breakdowns.

One modification in the channel introduced after run series III, was that the 7 cm height metal plate used as a border condition for the sediment (see Figure 3.2) was changed for a 15 cm height metal plate. This modification was intended to increase the thickness of the sediment bed, to avoid that the erosion produced by the highest and deepest bedforms would reach the channel bottom (for run G16 it was observed that the trough of the highest antidunes sometimes coincided with the channel bottom). Since there was a limited volume of gravel available to be used in the experiments, increasing the height of the downstream border condition imposed an extra difficulty: more gravel was required in the channel to form the sediment bed, and accordingly, there was less gravel available to be used as a reserve in the hopper. This shortage of gravel made of crucial importance a correct anticipation of the equilibrium bed slope and of the volume of sediment required in the hopper for beginning the run and keep a constant gravel-feed all along the experiment. Compared to runs using only sand or only gravel, for the runs with sand-gravel mixtures

more activities were involved and more attention was required to keep an eye on the correct operation of the two hoppers/feeders working simultaneously. The situation of a shortage of gravel added an additional stress and complexity in the performance of runs from these series.

The hybrid-feed runs with sand-gravel mixtures are described in detail below, and afterwards a concise description of the sediment-recirculating and of the no sediment-supply runs is presented as well.

3.3.1.4.1 Hybrid-feed runs

For the definitive data-set only runs performed with the flume operated in a hybrid-feed mode were used; six runs were performed with each mixture for the definitive data-set, while for mixture 1 an additional run (M1E7, using almost the same independent variables as run M1E6), with hybrid-feed operation as well, was performed to verify the experimental reproducibility.

Before beginning with each of the two run series with mixtures, sediment was totally removed from the channel and from the sediment-recirculating system, and all the volume of material available was stored in the hoppers and in the large sediment deposits. Later on, from the feeders sand and gravel were fed to the channel in the proportion stipulated for the corresponding run series.

All runs were performed in two separate phases: one phase to search for mobile-bed equilibrium state, named from here on the transition phase, and another phase to study the equilibrium state, named from here on the equilibrium or stable phase. Previous to the beginning of the transition phase of each run, the sediment deposit left by the preceding run was thoroughly mixed with a hoe all along the channel length, in order to get an approximately homogeneous mixture of sand and gravel. Then, the bed surface was screeded flat and level (see Figure 3.8); for reducing the amount of material used in the sediment bed, the bed surface profile was not parallel to the channel slope, i.e., the channel bottom slope was not the same as the slope of the bed surface. Although some high and low spots were many times apparent on the bed surface, no further efforts were dedicated to produce a perfectly planar surface, since once the run started the flow was able to sweep away these flaws from the very beginning. In order to register the initial conditions of the bed, the bed profile was surveyed to obtain the initial average bed slope with the channel in a horizontal position, and bulk samples of the bed material were taken at different locations along the channel for grain size analysis.

Runs of the same series were performed from higher to lower sediment-feed rates (except the first run of series IV), as shown in Table 3.4; it was better to perform runs with the highest solid discharges first, since the efficiency of the sediment-return pump dropped with time of use due to abrasion. Sediment-feed rates were selected intuitively, trying to cover uniformly the range of values likely to be supported by the flume, while water discharges were held almost constant. For the selected combination of water discharge and sediment-feed rate of a given run, with the procedure explained in Appendix VI a likely equilibrium bed slope was estimated, and an initial bed slope was selected, according to the volume of sediment available and erosion restrictions indicated in Appendix VI. The required channel slope to set the bed profile to the initial bed slope was computed as well. The initial bed slopes were approximately from 1% to 35% higher or lower than the final equilibrium bed slopes. A final computation was performed, to verify if the volume of sediment available in the hoppers was enough to feed the channel during the first three to ten minutes of the run, which was the time required for the material discharged at the downstream end of the channel to be returned to the hoppers through the sediment-recirculating system (see Section 3.4.1.5 in Appendix I).

Figure 3.8. Bed surface before the beginning of the transition phase of run M1E1.

The steps followed to operate the flume before initiating a run are listed as follows:

1. The water pumps were turned on.
2. The tilting gate at the downstream end of the flume (see Figure A1.1 in Appendix I) was almost completely closed, the channel was collocated in a horizontal position and a low water discharge (≈5 l/s) was supplied to fill the channel slowly and in this manner avoid the dislocation of any sediment grains on the bed.
3. Once the channel was full and water was spilling over the tilting gate downstream, the channel slope was adjusted to set the bed profile to the selected initial bed slope.
4. The different mechanisms of the sediment-recirculating system were turned on: rotating trommel, screw conveyors and sediment-return pump.
5. The opening of the sluice gate and the velocity of the conveyor belt that serve to regulate the sediment feed-rate of the feeders were adjusted to the specified conditions for the run.
6. The computer program for the real-time monitoring of the weight on the hoppers was opened. A folder was created, named as the current date, for storing the archives generated by the software during the experimental run. These archives were named as the current run. The program was initiated and simultaneously the running time began to be taken with a chronometer. From there on, all the activities performed were linked to the running time of the chronometer and described in a logbook.
7. Water discharge was increased up to the selected value for the run (this took from 1 to 3 minutes), and immediately the downstream tilting gate was opened. When the water discharge was increasing, the sediment feeders were turned on; this moment was considered as the beginning of the run, from which the actual running time of the run was considered to start.

The transition phase was over when mobile-bed equilibrium state was attained (see Section 3.4.2 for details on the equilibrium criteria); this occurred in average from four to eight hours after the run began. To stop the experiment, water discharge was rapidly decreased to zero (this took normally from one to three minutes) and simultaneously the sediment feeders were turned off; at this moment time given by the chronometer was registered as the time at which the transition phase was finished. The sediment recirculating-system was turned off until no more sediment, or a very small volume of it, was introduced to the feeders by the screw conveyors. In that moment all the mechanisms of the flume were turned off, and the program for monitoring the weight on the hoppers was stopped as well. When water was completely drained from the channel, tracer stones were place in a section 4.5 m upstream from the downstream end of the channel to measure the maximum bed erosion; the procedure to set the stones in layers and perform the measurements are described in Section 3.3.2.7.

The equilibrium or stable phase of a run began from stand-still conditions and over the bed configuration preserved after the transition phase. The steps followed to operate the flume before the beginning of the stable phase were the same listed above for the transition phase. Running time was taken again with the chronometer and all activities were linked to time and registered in the logbook. Once the stable phase began, some time was left for the flow and bed configuration to stabilize, and then different activities were performed: photos were taken and video of the bed and water surfaces was shot at different locations, measurements of different characteristics of the bedforms and the stationary waves were performed (as it is described in Section 3.3.2.4), samples of the sediment in the hoppers and of sediment transport in the channel were taken (as it is described in Section 3.3.2.6), and the hopper was emptied and then refilled, without cutting off the constant sediment-feed, for measuring the feed-rate supplied to the channel (as it is described in Section 3.3.2.3). After finishing with all these activities (which took from three to six hours), the experiment was stopped by setting the water discharge to zero and at the same time turning off the sediment feeders. When the sediment bed was free of water, the bed surface was photographed (as explained in Section 3.3.2.7), measurements of the preserved bedforms were conducted (as described in Section 3.3.2.4), and bed material samples were taken (following the criteria given in Section 3.3.2.6). Finally, a vertical section was opened in the sediment bed, where original bed material had been replaced with the tracer stones, to measure the maximum bed erosion. All together, in average six hours were required to perform the activities without water in the channel.

During the two experimental phases, water depth and bed and water slopes were obtained approximately once an hour, from measurements of the bed and water surface level performed at the channel's glass-paneled walls. In turn, evolution to equilibrium and the equilibrium state were followed through the real-time monitoring of the weight of sediment on the hoppers. Graphs of time-variation of all these variables for each run are shown in Appendix VII. For these graphs, the two experimental phases have been joined, and only the running time for which the water was flowing through the channel has been considered. Graphs with the evolution of weights on the hopper were not always representative of the actual gradient of sediment discharge in the channel, since the suction of sediment from the downstream collecting tank could sometimes stop working adequately. The suction had to be constantly checked, and if it was found that sediment was accumulated in the tank, arrangements had to be performed to fix the problems and suck all the accumulated sediment at once. Hence, for the verification of equilibrium states, data from weights on the hopper had to be examined together with the bed profiles measured during the transition phase.

For the equilibrium states it was verified that flow was uniform all along the channel (except for the flow entrance and exit regions), and thus the measured bed and

water surface profiles were roughly parallel. No boundary condition was used for the flow in the downstream section. The bed surface profile was not parallel to the channel bottom, and for most of the runs the vertical distance between the channel bottom and the cross-section average bed-surface elevation decreased from downstream to upstream. Since the size of the bedforms increased in the flow direction, i.e., they were higher and longer in the downstream sections, it can be expected that the non-uniformity of the bed thickness had no effect on the free development of bedforms.

For most of the runs the evolution to equilibrium state was through bed erosion, except for run M1E3 and run M2E2. For these two runs there was not a good preliminary estimation of the equilibrium bed slope (with the procedure described in Appendix VI), and the initial bed slope was not quite different from the equilibrium bed slope; therefore, it could not be foreseen that equilibrium state would be attained through bed aggradation. This uncertainty in the a priori equilibrium bed slope computed with the procedure given in Appendix VI, and the limited thickness of the sediment bed on the uppermost part of the channel, made that during the transition phase of runs M1E2 and M2E5 the bed erosion reached the channel bottom (for run M1E2 an unexpected power failure also contributed to this undesirable erosion). Accordingly, at the end of the run the upper part of the channel was left without sediment and the length of the bed was reduced from 27 to 22 m in M1E2, and from 26 to 20 m in M2E5. This notwithstanding, even when the upstream boundary condition was displaced, equilibrium state was verified in both of these runs. For the stable phase of run M2E5, the bed sediment on the upper part of the channel was replaced, and the channel slope was reduced from 1.46% to 1.35% to set the bed slope to that obtained in equilibrium state.

Trains of 3D downstream-migrating antidunes, under short-crested stationary waves, were ubiquitous of most of the runs at the channel central cross section. In turn, bed features with an alternate sequence were observed and cataloged as alternate bars. These features were preserved on the bed after the water was drawn down, in contrast to the antidunes, which were washed out by the flow. Plane bed was observed in one run during short intervals, while dunes were the prevailing bedform in one run as well. Bedforms and stationary waves formed within the first 5 to 10 meters of the upper part of the channel. Once formed, water and sediment waves grew in height until approximately the end of the second third of the channel downstream, while coalescence between low-relief sediment waves was commonly observed within the first third of the channel upstream. Bed and water waves were more or less stable at the last third of the channel downstream. A thorough description of the observed water and bed configurations is given in Chapter 5.

3.3.1.4.2 Sediment-recirculating runs

The main goal of these runs was to verify that the flume could be operated in a sediment-recirculating mode with confidence, and that the results would be comparable to those from hybrid-feed operation under similar conditions. Hence, some of the procedures and methods used in these runs were for scouting of the most suitable options. Four runs were performed with mixture 1 and one with mixture 2. Table 3.5 summarizes some of the characteristics of the sediment-recirculating runs.

For a sediment-recirculating operation, it was required that no sediment was stored in the sediment-return system. Hence, the hoppers served just as a by-pass for the sediment, and this was attained by setting the rotating band at the base of the hopper to a very high velocity, so that the sediment incoming in the hopper from the sediment-return system was immediately added to the channel. In contrast to the hybrid-feed operation, for which the hoppers served to measure the solid discharge by means of monitoring the

gradient of weight, using the hoppers as a sediment by-pass prevents from performing a constant measurement of the solid discharge. Accordingly, other methods had to be investigated for measuring the solid discharge using the hoppers. The methods tested, which basically consisted in retaining sediment in the hoppers during short time intervals, are described in Section 5 of Appendix I.

Table 3.5 Summary of sediment-recirculating runs. Energy slopes S were computed with the procedures described in Section 3.4.1.

Run	Bed material	S_c %	S %	Q_w [l/s]	Description
M1R1	Mixture 1	1.06	0.0065	78.9	The run initiated with the bed configuration left by the previous run (run M1E7). Constant water discharge and initial bed slope were the same as those in the previous run. The experiment initiated with hybrid-feed operation in equilibrium state, and this was kept during three hours. Afterwards, the hoppers were emptied and the run continued three more hours with the flume operated as sediment-recirculating. Initial tests for measuring sediment discharge.
M1R2	Mixture 1	1.47	0.0128	78.4	The bed material was mixed, screeded flat and leveled before beginning the run. Only during the first minutes sediment was fed to the channel, afterwards operation in sediment-recirculating. The run was stopped after nine hours to place tracer stones for measuring bed erosion, then the run was reinitiated and kept running for almost four hours. More tests for measuring sediment discharge were performed. The rest of measurements and procedures were almost the same followed for the runs in the series.
M1R3	Mixture 1	1.99	0.0165	84.4	The run initiated with the bed configuration left by the previous run (run M1R2). Only during the first minutes sediment was fed to the channel, afterwards operation in sediment-recirculating during almost four hours. Measurements of sediment discharge with the hoppers.
M1R4	Mixture 1	1.99	0.0159	82.9	The initial bed surface was the same left by the previous run (M1E3). Only during the first minutes sediment was fed to the channel, afterwards operation in sediment-recirculating during almost ten hours. More tests for measuring sediment discharge were performed. The rest of measurements and procedures were almost the same followed for the runs in the series.
M2R1	Mixture 2	1.37	0.0099	78.9	Run trying to reproduce conditions of run M2E5. The initial bed slope was the equilibrium slope for that run. The bed material was mixed, screeded flat and level before beginning the run. Only during the first minutes sediment was fed to the channel, afterwards operation in sediment-recirculating during almost seven hours. More tests for measuring sediment discharge were performed. The rest of measurements and procedures were almost the same followed for the runs in the series.

Another issue to solve was the sediment-supply conditions when initiating a run. Due to the lag times for the sediment when passing through the sediment-return system (see Section 3.4.1.5 in Appendix I), if no sediment were available in the hoppers at the beginning, the initial stages would be without sediment supply. Therefore, it was tried to begin the run feeding sediment during the first stages until the return system began to add to the hoppers sediment returned from the end of the channel. The main difficulty was to

answer which feed rate to use for these initial stages. It was concluded that this amount is not completely relevant for the bed evolution, but most important is that the sand-gravel ratio was conserved in the feeding material. It was then decided to feed during the first minutes using feed rates obtained from similar conditions in previous experiments.

Results from the sediment-recirculating runs are used in Section 3.4.3 to test the experimental reproducibility, by comparing these results with those from hybrid-feed runs for which the independent variables, procedures, methods and measurements were similar.

3.3.1.4.3 No sediment-supply runs

Two runs were performed, M1N and M2N, one for each run series, in which no sediment was fed, neither recirculated to the channel. Accordingly, bed erosion in the channel was continuous, and bed slope and solid discharge decreased with time. The ultimate equilibrium conditions for such type of runs would be asymptotic, with low bed slopes (or even negative bed slopes) and no sediment movement in the channel. Proffitt (1980) performed similar experiments for studying the armouring process and selective transport.

The aim of these runs devoid of a mobile-bed equilibrium state was the comparison of sediment discharges at continuous transient states with sediment discharges in equilibrium states obtained from hybrid-feed runs. Nevertheless, this comparison deserves a study on its own, and will not be presented in this work.

Using the two hoppers/feeders, the runs were prepared by filling the channel with all the gravel available, and sand in the proportion stipulated by the specific run series. The bed material was mixed and screeded flat. Then, an initial bed slope was chosen. For run M1N it was intended to begin the run with similar conditions as those in the equilibrium phase of run M1E5, while for run M2N the initial slope was somehow arbitrary; this slope was the maximum likely slope to be given with the available sediment, in order to avoid that erosion would leave the bottom of the flume uncovered at the end of the run. The characteristics of each run are summarized in Table 3.6.

Prior to the beginning of the runs, water was introduced slowly in the channel. When the channel was full with water, water discharge was increased to the prescribed value (the same water discharges as those used in hybrid-feed runs) and in that moment the bed sediment began to move and the run started. The sediment-recirculating system was used to send the sediment discharged from the channel to the respective sand and gravel hoppers. Bed and water surface elevations were measured on the channel walls, approximately once every 20 to 30 minutes. Figure A1.39 in Appendix I shows the measured profiles during run M2N.

Table 3.6 Summary of runs without sediment-supply.

Run	**M1N**	**M2N**
Bed material	Mixture 1	Mixture 2
S_c %	1.65	0.40
Initial S_o %	1.26	0.75
Final S_o %	0.83	0.29
Q_w [l/s]	78.9	78.9
Run duration (h)	≈2.5	≈6.0

The volume of sediment discharged at the downstream end of the channel was monitored through the real-time record of weights on the hopper. The most important problem to solve was that the volume capacity of the hoppers imposes a limitation for the maximum time during which sediment discharge can be monitored in one run. When the hoppers become full, sediment in the recirculating system must be conducted to the large

deposits (see for instance, Figure A1.37) since the hoppers can only be unloaded on the channel. Hence, when the hoppers become full, volume sediment discharge cannot be monitored anymore. To overcome this difficulty, during run M1N, sediment returned from the recirculating system was conducted in an alternated sequence of controlled intervals to the large deposits and to the hoppers. The curves obtained of increments of weight on the hoppers with time are shown in Figure 3.9; as there can be seen, these curves were fragmented in different segments separated by almost horizontal lines. Even when the curves are not continuous, proceeding this way the sediment discharge could be monitored during the whole run but in spaced intervals.

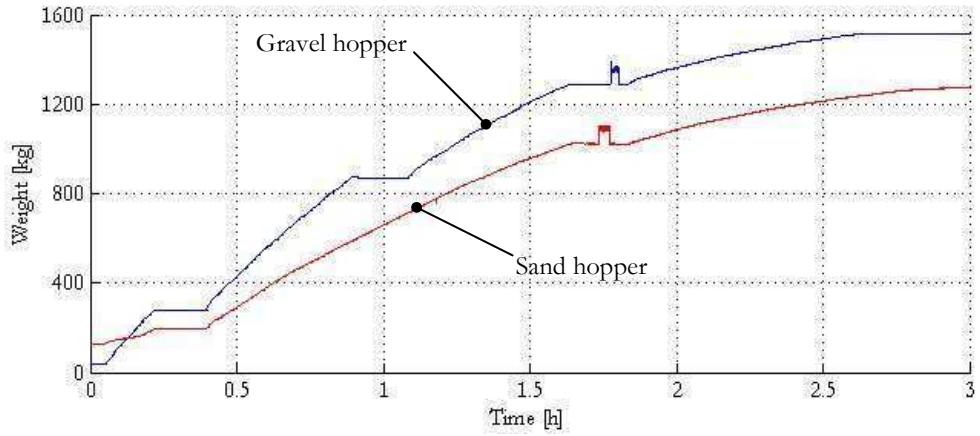

Figure 3.9. Instantaneous weight on the hoppers for run M1N.

For run M2N, sediment was conducted to the hoppers during the whole experiment, but the run was finished when the gravel hopper volume capacity was completely full. Therefore, the run was stopped before equilibrium state had been attained. Figure AI.40 in Appendix I shows the record of weights on the hoppers and the time-evolution of bed slope for run M2N.

Run M1N should be considered more as a scouting run. Bed erosion was not adequately estimated a priori, and thus, due to the limited amount of sediment in the bed, during the run the channel bottom on the upper part of the channel was uncovered. The length of uncovered channel bottom increased with time, and at the end of the run most of the sediment in the channel was washed away and the bed was reduced to a length of only 5 m. Upstream of the remaining bed, over the uncovered bottom, a hydraulic jump was formed.

Experience gained previously with run M1N helped for a better design of run M2N. In order to avoid that erosion reached the channel bottom, the metal plate downstream border condition for the sediment was changed from the 15 cm used for M1N to a 7 cm height plate, and a lower initial bed slope was used. During the run, sediment transport samples were taken in the channel in three series at different intervals, using the two samplers described in Section 3.3.2.4. Samples of the material in the hoppers were taken as well, to obtain the water content. After the run was finished, and water level had been drawn down, the bed surface was photographed, surface and subsurface samples of the bed material were collected at six locations along the channel, and two bedforms were surveyed.

A remarkable feature of these runs was that bed configurations changed from 3D bedforms during the first stages of the run, to 2D bedforms when subcritical flow prevailed in the channel before the run was finished.

3.3.1.5 RUN SERIES VI: Runs with sand

Procedures, methods and activities in this run series were essentially the same as for hybrid-feed runs in series IV and V. Four runs were performed, for three of them equilibrium state was reached through bed erosion and for the other one through bed aggradation. The initial bed slopes were approximately 24%, 42% and 6% higher than the equilibrium slopes for erosion runs, and 27% lower than the equilibrium slope for the bed aggradation run. Even when the material was of uniform size and sediment sorting was not as relevant as with sand-gravel mixtures, the bed was mixed prior to the beginning of the transition phase of each run, as it was done in run series IV and V.

In contrast to runs with gravel and sand-gravel mixtures, short-crested stationary waves were less frequently observed, and bedforms were higher and predominantly 2D. Dunes and antidunes were observed, but no plane beds.

3.3.2 Description of measurements and procedures

The variables to be measured were selected attending to the primordial objective of the experimental campaign, i.e. to create an extensive data set, compound of flow characteristics, sediment transport rates, and grain size compositions of bed and sediment in motion. In turn, procedures and methods to conduct the measurements were selected considering accuracy standards and technical feasibility according to the available resources in the lab and budget for the project. Experiences with this type of experiments in literature and personal communication with researchers that have worked with similar facilities and conditions were also useful to select and adapt procedures and materials for measuring.

Figure 3.10 summarizes most of the variables and measurement procedures. The most important measurements were those related with the minimum information required to characterize bulk flow and sediment transport during mobile-bed equilibrium state, namely, mean slope, mean water depth, mean flow velocity, volume sediment discharge and sediment grain size distribution. With this information grain related mean shear stress can be computed and linked to fractional sediment transport rates. Also important for the computations is water temperature, in order to ascribe appropriate values of water density and viscosity to flow.

Since grain size sorting is a relevant issue in the transport of sediment mixtures on account of selective transport, partial transport or hiding-exposure effects, it was important to characterize grain sorting trends in the experimental runs. Accordingly, sediment samples were taken from the material in the hoppers, from sediment in motion in the channel, and from the bed surface and subsurface. The sand-gravel mixtures in these experiments can be treated as a two fraction mixture, and thus the proportion of sand in the samples suffice to characterize sediment grain sorting for a first level of analysis.

Additional information to complete the data set are the characteristics of the bed and water surfaces configurations, which include the geometry and migration of bedforms and stationary waves, and finally, the maximum bed erosion produced by the passage of bedforms.

It is worth to mention that for ensuring a methodical reproduction of the procedures, the activities to sample and measure during the experimental campaign were performed nearly always by the same persons. Methods and procedures for most of the measurements of the controlled parameters and dependant variables are described in this Section.

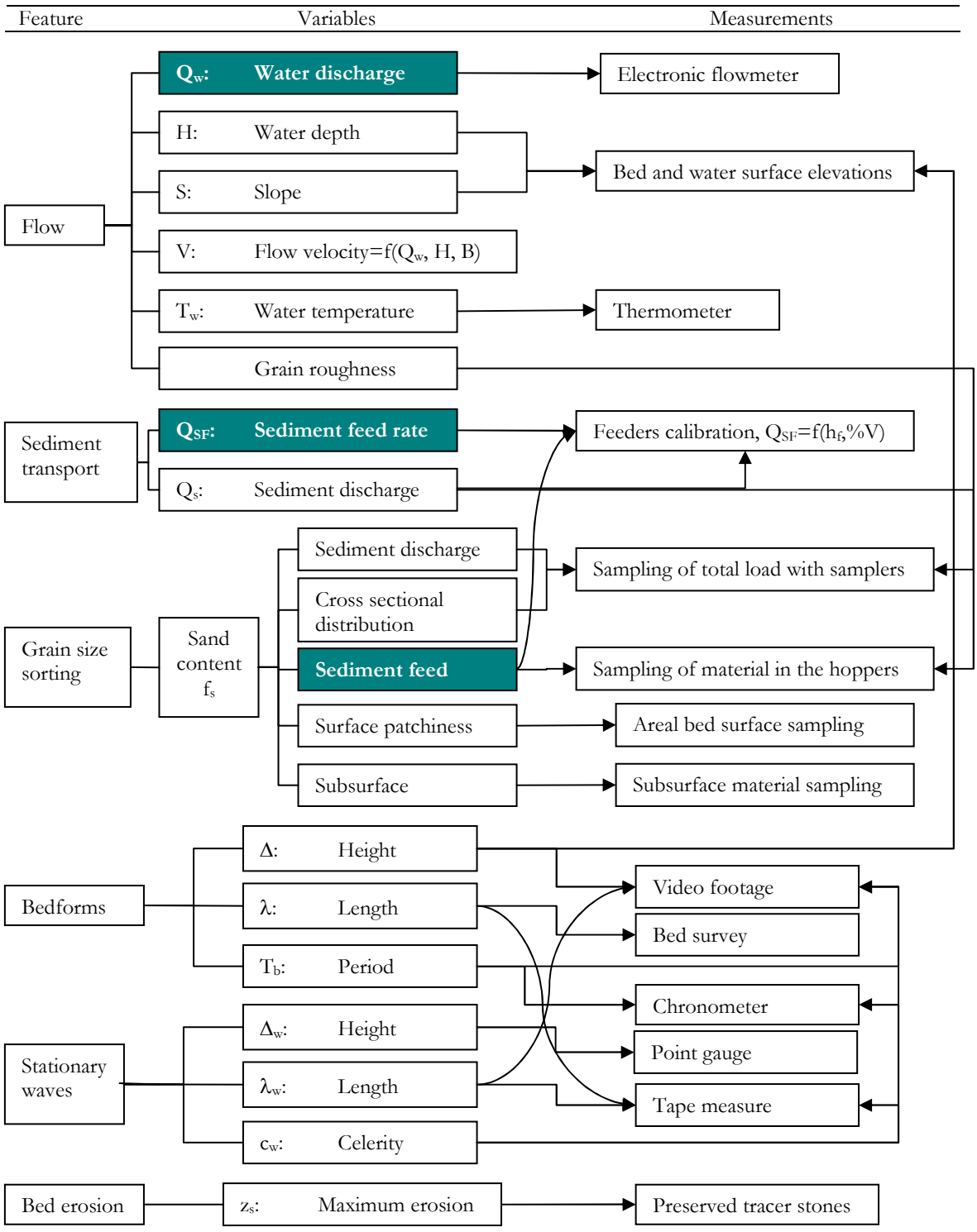

Figure 3.10. Summary of variables measured during the experimental runs and measurement procedures. Independent variables are indicated in shaded boxes.

3.3.2.1 Water discharge and water temperature

Water discharge was supplied by three pumps as described in Section 3.1 of Appendix I, and was controlled by an automatic system which was calibrated using a triangular notch at the downstream end of the channel. Flow discharge was selected on a tactile display. During the experimental campaign it was observed that there were slight variations on the selected water discharge, probably related to the automatic adjustments that the system performs in the valves for controlling the water discharge according to the selected discharge and the discharge measured by the system with a flowmeter. Such variations were not higher than 3% of the selected water discharges.

Water temperature was measured in the channel with a mercury thermometer, but not in all runs. For those runs lacking of a measured value of water temperature, an interpolation from data taken in the other runs was used. Measured water temperature values have been plotted as a function of the days accumulated since the beginning of run series II until run series VI in the graph shown in Figure 3.11. The graph shows an almost linear increment of water temperature with accumulated days from run series II, which began at the end of winter, to run series VI, which ended at the beginning of summer. A best-fit line was obtained, and from this line the lacking values were calculated. The quadratic error for the measured values with respect to the best-fit line was only 0.33 ºC.

Table 3.7 Summary of water characteristics for each run. Water temperature values interpolated with the best-fit line from Figure 3.11 are indicated with an asterisk.

Run	Water temperature T_w [ºC]	Water density ρ [kg/m³]	Kinematic viscosity ν x10⁶ [m²/s]
G12	12.4*	999.4	1.22
G13	13.0	999.4	1.20
G14	13.5	999.3	1.19
G15	13.5	999.3	1.19
G16	13.0*	999.4	1.20
G17	13.8*	999.3	1.18
M1E1	14.5	999.2	1.16
M1E2	14.8*	999.1	1.15
M1E3	15.3*	999.1	1.13
M1E4	15.5	999.0	1.13
M1E5	16.0*	998.9	1.11
M1E6	16.0	998.9	1.11
M2E1	17.9*	998.6	1.06
M2E2	18.0	998.6	1.06
M2E3	19.5	998.3	1.02
M2E4	19.5	998.3	1.02
M2E5	19.2*	998.4	1.03
M2E6	20.0	998.2	1.01
S1	21.0	998.0	0.98
S2	22.0	997.8	0.96
S3	22.0	997.8	0.96
S4	22.0	997.8	0.96

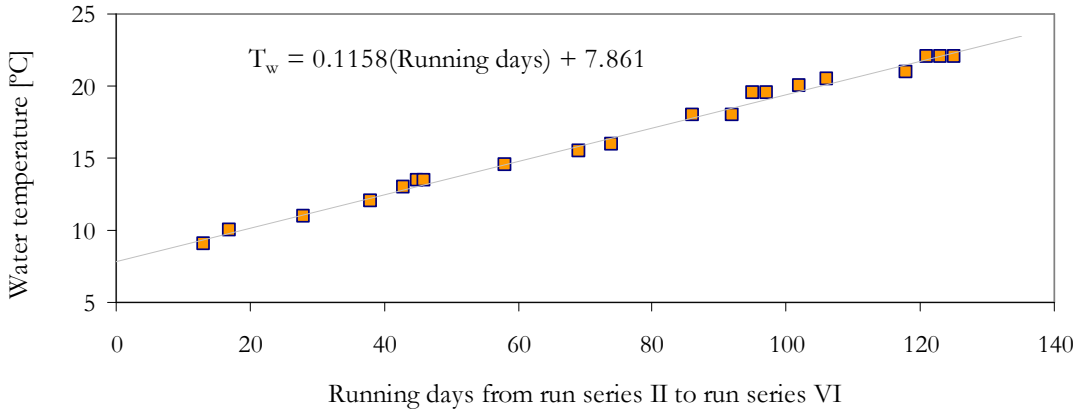

Figure 3.11. Variation of measured water temperature through run series II to VI.

Table 3.7 shows the values of water temperature for each run, indicating which were obtained from the best-fit line. Other columns in that table present the water density and dynamic viscosity calculated from the water temperature. Considering the accuracy in the water temperature as the quadratic error of the fitted-line, it is obtained that the values of water density and kinematic viscosity would be correct within ± 0.06 kg/m^3 and $\pm$ 9.4x10^{-9} m^2/s, respectively.

3.3.2.2 Bed and water surface elevations

As it can be seen in Figure 3.10, recording the bed and water surface elevations was among the most important measurements performed for each experimental run. Not only key variables to characterize flow were deduced from these measurements, namely, hydraulic slope and water depth, but also the complete set of these measurements in a run, linked to the running-time, provided with a reliable overview of the evolution to mobile-bed equilibrium state. Moreover, the scatter of bed elevations around the mean bed profile was useful to obtain a statistical estimation of the average height of bedforms.

Ideally, a continuous survey, in time and space, of bed and water surfaces in the channel would be desirable. Nevertheless, since it was not possible to count with measuring devices that satisfy these conditions, attending to previous experiences in a similar flume (Martin-Vide and Andreatta, 2006), a practical alternative was to perform the measurements through the glass-panel walls of one side of the channel, and spaced in time and in location along the channel length. Using this procedure, it was assumed that the average bed and water elevations near the channel wall were representative of the average cross sectional bed and water profiles. In turn, it was assumed that time-evolution of both profiles was gradual, so that intervals not measured could be deduced from previous and subsequent measurements. An advantage of this approach was that it is not intrusive, an important issue given the high sediment transport rates and speedy bedforms that prevailed in most of the runs.

The measurements were performed on plastic rulers graduated every 1 mm, attached to the channel wall. The basic procedure consisted in moving forward along the channel, while making marks on the channel wall next to the rulers at the same elevation of the water and bed surfaces. Therefore, this procedure did not produce actual instantaneous profiles. It was then required to define the necessary conditions for obtaining representative profiles from these measurements, so that they would adequately characterize the mean flow conditions at a certain moment of a run. In turn, it was

important that the measurements could be performed in an easy manner that allowed for a systematic repetition.

For the sake of easiness and promptness, a low number of rulers would simplify the measuring procedure, nevertheless, with a low density of measurement points the error in the parameters derived is likely to be increased. In this regard, an analysis of the influence of the spacing between rulers in the computation of bed slope, considering the passage of periodic bedforms, is presented in Appendix II. In this same Appendix, it is also analyzed the effect on the measured profiles of time required to perform the measurements due to the temporal variation of the profiles. From the analysis in Appendix II, it was concluded that the error between the computed slope from elevation measurements and the slope obtained from an instantaneous picture of the actual profile is a function of the number of measurement points, of the direction in which the measurements are performed, and of the ratio between the measurement duration and the velocity at which the profile changes. It was found that a maximum spacing of one meter between rulers was appropriate for obtaining accurate representations of the profiles. In turn, it was suggested that for obtaining representative profiles the measurements had to be performed as rapidly as possible, and following first the direction of flow, and immediately afterwards repeating the procedure in the opposite direction.

Attending to the arguments above, the systematic procedure adopted for measuring bed and water elevations is described as follows. Beginning on the wall-panel below the sediment feeders, and proceeding downstream, the bed and water elevations were marked on each of the glass-panel walls, just next to the attached plastic ruler, using a felt-tip pen. Once the last wall at the downstream end had been marked, the process was repeated proceeding upstream, but this time using a felt-tip pen with a different color. On each wall, the bed surface was identified as the top of the particle just next to the ruler when the measurement was made. Since the flow was for most of the runs choppy and thus the water surface was strongly fluctuating, before making the mark with the felt-tip pen the water surface was observed during approximately three to five seconds, and then the mark was made indicating an approximate average elevation of the fluctuations during the observed interval. The running time when the measurement began, when the last wall-panel downstream was marked and when the first wall-panel upstream was marked again, was registered in the logbook of the run. Average time required for completing the procedure was of four and a half minutes. After the walls were marked, the elevations corresponding to each of the four marks on each wall were read on the scale of the rulers and registered in the logbook. The data were immediately plotted to check for errors. Finally, if no anomalies were found, the marks on each wall-panel were erased using a cloth moistened with alcohol to leave the wall clean for the next measurement. Each pair of profiles was named with a letter, following an alphabetical order for consecutive profiles during a run. Running time linked to the measurement was the average between time at the beginning and at the end of making the marks.

The survey of each profile produced two elevation values for each of the 26 rulers on the channel wall. An arithmetic average was applied for obtaining a unique profile representative of the running time at which the measurements were taken; in this manner, for the bed profile, the horizontal and vertical coordinates of the bed surface, x_b and z_b, respectively, referenced to the coordinate system in Figure 3.2, at time n on ruler i are given by

$$x_b\big|_i^n = \frac{x_{bD}\big|_i^n + x_{bU}\big|_i^n}{2} \qquad (3.4), \qquad z_b\big|_i^n = \frac{z_{bD}\big|_i^n + z_{bU}\big|_i^n}{2} \qquad (3.5)$$

where x_{bD} and x_{bU} are the horizontal coordinates for measurements taken in the downstream and upstream directions, respectively, and z_{bD} and z_{bU} are the vertical

coordinates for the values measured following the downstream and upstream directions, respectively. Defining the coordinates for the water profile, it yields

$$x_w\big|_i^n = \frac{x_{wD}\big|_i^n + x_{wU}\big|_i^n}{2} \qquad (3.6), \qquad z_w\big|_i^n = \frac{z_{wD}\big|_i^n + z_{wU}\big|_i^n}{2} \qquad (3.7)$$

where x_w and z_w are the horizontal and vertical coordinates of the water surface at time n on ruler i, and again the subscripts D and U correspond to measurements taken following the downstream and upstream directions, respectively. All measurements of bed and water surfaces were referenced to the coordinate system in Figure 3.2, and corrected for errors in the rulers using eqs.(3.2) and (3.3).

3.3.2.3 Sediment-feed rates and average solid discharge

As already explained before, for the hybrid-feed runs used to create the data set, sediment-feed rates were imposed and kept constant during each run. The a priori selected sediment-feed rate was set in the sediment feeders by adjusting the opening h_f of the sluice gate on the base of the hopper, and the velocity V_f of the rotating band. V_f was given as a percentage of voltage frequency %V on the engine of the band, computed from eq.(AI.11) in Appendix I. A detailed description of the operation of the feeders is given in Section 3.4.1 of Appendix I, and Photos P4 at the end of the same Appendix show images of the hoppers and their components.

Table 3.8 Summary of experimental variables for the sand-feeder in each run of the data set. h_f is the opening of the sluice gate on the base of the hopper, %V is the percentage of voltage frequency on the engine of the rotating band for evacuation of the sediment, and Q_{SFs} is the sand-feed rate. Values used in eq.(3.8) for calculating Q_{SFs} were B_f=0.73, D_m was taken from the values given in Tables 3.27 and 3.28 for each run, V_f was computed from eq.(AI.11) in Appendix I, ε=0.4, ρ_s=2630 kg/m^3, and %w=0. For the ratio in the last column, an average of the measured Q_{SFs} values was used.

Run	h_f [mm]	%V	Q_{SFs} [kg/s]				Q_{SFs}
			Measured 1	Measured 2	Measured 3	Calculated eq.(3.8)	measured/ calculated
M1E1	9.5	2.00	0.065	0.065	-	0.066	0.988
M1E2	10.0	9.20	0.257	0.258	-	0.258	0.999
M1E3	10.0	7.03	0.205	0.202	-	0.199	1.026
M1E4	10.0	6.48	0.180	-	-	0.186	0.971
M1E5	10.0	4.49	0.136	0.135	-	0.131	1.035
M1E6	10.0	1.10	0.045	-	-	0.046	0.979
M2E1	10.0	15.73	0.419	0.403	-	0.434	0.948
M2E2	10.0	13.31	0.368	0.353	-	0.365	0.990
M2E3	10.0	11.65	0.313	0.318	-	0.325	0.971
M2E4	10.0	8.00	0.222	-	-	0.229	0.970
M2E5	10.0	4.04	0.118	0.120	-	0.120	0.991
M2E6	10.0	1.89	0.066	-	-	0.067	0.990
S1	10.0	25.00	0.692	0.667	-	0.658	1.033
S2	10.0	16.96	0.430	0.437	0.456	0.461	0.956
S3	10.0	8.63	0.239	0.233	0.229	0.246	0.949
S4	10.0	4.84	0.138	0.138	-	0.143	0.965
						Standard deviation=	0.027

Table 3.9 Summary of experimental variables for the gravel-feeder in each run of the data set. h_f is the opening of the sluice gate on the base of the hopper, %V is the percentage of voltage frequency on the engine of the rotating band for evacuation of the sediment, and Q_{SFg} is the gravel-feed rate. Values used in eq.(3.8) for calculating Q_{SFg} were B_f=0.73, D_m was taken from the values given in Tables 3.27 and 3.29 for each run, V_f was computed from eq.(AI.11) in Appendix I, ε=0.38, ρ_s=2600 kg/m^3, and %w=0. For the ratio in the last column, an average of the measured Q_{SFg} values was used.

Run	h_f [mm]	%V	Q_{SFg} [kg/s]			Q_{SFg} measured/ calculated
			Measured 1	Measured 2	Calculated eq.(3.8)	
G12	20.0	10.00	0.590	-	0.594	0.994
G13	30.0	7.00	0.720	0.721	0.741	0.972
G14	30.1	5.00	0.542	-	0.531	1.022
G15	30.0	4.00	0.450	-	0.435	1.035
G16	20.0	4.00	0.268	-	0.266	1.008
G17	12.0	2.00	0.077	0.079	0.081	0.966
M1E1	20.0	2.00	0.162	0.157	0.155	1.028
M1E2	20.0	9.75	0.600	0.588	0.604	0.983
M1E3	20.0	7.44	0.459	0.462	0.472	0.976
M1E4	20.0	6.83	0.431	-	0.430	1.002
M1E5	20.0	4.68	0.309	0.310	0.305	1.014
M1E6	20.0	1.00	0.092	-	0.091	1.007
M2E1	20.0	10.00	0.614	0.628	0.636	0.976
M2E2	20.0	8.17	0.533	0.542	0.530	1.014
M2E3	20.0	7.10	0.470	0.477	0.468	1.011
M2E4	20.0	4.76	0.335	-	0.324	1.034
M2E5	20.0	2.19	0.170	-	0.172	0.990
M2E6	20.0	1.00	0.095	-	0.092	1.037
					Standard deviation=	0.023

The required values of h_f and V_f to give the desired sediment-feed rate of the run were obtained from similar charts to those presented in Figures AI.35 and AI.36 in Appendix I. Charts shown in that Appendix summarize all the information gathered along the experimental campaign for the calibration of the feeders: a total number of 116 tests. Conversely, the charts used when each run was prepared contained less information and therefore they were less accurate, since during each run new points for the calibration of the feeders were obtained. On account for this, there were slight variations in the a priori selected sediment-feed rates and the final considered feed rates for each run in the data set.

Tests for calibration of each feeder consisted in unloading a certain volume of sediment from the hopper, using a given combination of h_f and V_f. For every combination of these variables, the rate at which the material unloads is independent of the amount of sediment in the hopper; hence, the weight variation on the hopper with time is linear. For each test, this variation was obtained with the real-time record given by the load cells on the base of the hoppers, connected to a computer. Accordingly, a calibration constant was obtained with the slope of the line describing the weight variation on the hopper. All the lines used to calibrate the two feeders with wet sediment, are shown in Figures AI.28 and AI29 of Appendix I.

During the experimental runs with a hybrid-feed operation, the hoppers were unloaded at a certain moment (mostly during the equilibrium phase of the run) in order to measure the actual sediment-feed rates. The calibration constants thus obtained during all the experimental campaign were used for the final calibration described in Section 3.4.1.6 of Appendix I. The procedure for unloading the hoppers was the following: in the sediment-recirculating system of the flume, which conveys the sediment from the

downstream end of the channel to the upper part, the rotation direction of the screw conveyors that take sand and gravel to their respective hoppers was changed; by doing this, sediment was conducted to the large deposits (see for instance, Figure AI.37 in Appendix I) and the hoppers began to be unloaded. Once the hoppers were almost empty, the rotation direction of the screw conveyors was changed again, and, additionally, sediment from the large deposits was added to the hopper so as to maintain the hopper with a certain amount of sediment for not cutting off the constant feed-rate to the channel at any time. Before changing the rotation direction of the screw conveyor and refilling the hoppers, sediment samples were taken from the rotating band at the base of the hopper. These samples were weighted and then left drying for determining the water content and for performing sieve analysis to obtain a representative grain size distribution of the feeding material. Water content %ω of the samples was obtained as a percentage from the ratio %ω=100*(W_{sh}-W_{sd})/W_{sd}, where W_{sd} is the mass weight of the dry sample, and W_{sh} is the mass weight of the wet sample.

Using dimensional analysis, the fundamental variables that have an influence in the feeding rate of dry sediment from the hoppers were grouped in two non-dimensional numbers. The complete development of the dimensional analysis is presented in Section 3.4.1.1 of Appendix I. Using all the experimental data for different combinations of h_f and V_f, plotted as a function of the dimensionless numbers (see these plots in Figures AI.32 to AI.34 in Appendix I), the following calibration function was fitted

$$\frac{Q_{SF}}{h_f B_f V_f \rho_s (1-\varepsilon)\left(1+\%\varpi/100\right)} = \left(a + b\frac{D_m}{h_f}\right)^{-1} \qquad (3.8)$$

where B_f is the width of the gate at the base of the feeder (≈0.73 m), Q_{SF} is the feeding rate of dry sediment, D_m, ε, ρ_s and %ω are the mean diameter, porosity, density and water content of the sediment in the hopper, respectively, and a and b are calibration constants, being a=1.143 and b=2.496 for the sand hopper when %V≥4, and a=1.009 and b=1.881 for the gravel hopper when %V≥3; Table AI.14 in Appendix I shows the values for these constants for other ranges of %V.

The selected values of h_f and V_f (these latter presented as a function of %V) for each run are shown in Tables 3.8 and 3.9; in these same Tables are shown the feed rates obtained from the calibration tests during the experimental runs, the final considered sediment-feed rates for the data set (these are the same values as those shown previously in Table 3.4) calculated with eq.(3.8) used with the experimental variables, and a comparison between the calculated and the average of the measured values. The standard deviation of the ratio between the average measured and the calculated sediment-feed rates was only 2.7% for the sand feeder and 2.3% for the gravel feeder; these values can be used as a measure of the accuracy of the sediment-feed rates.

The average solid discharge in the channel at any time interval during a run, could be computed with eq.(3.1) solved for Q_{IN}. When average sediment discharge in the channel was roughly equal to the sediment feed-rates of the two hoppers, mobile-bed equilibrium state prevailed in the channel.

3.3.2.4 Bed and water configurations

Characterization of the bed and water surface configurations was not an easy task, since the characteristics of the two surfaces changed not only during the transition to equilibrium states, but also along the channel and throughout time, for some cases very rapidly, during equilibrium and transition phases. In turn, bed and water surfaces were many times strongly three-dimensional and different species of bedforms coexisted on the bed. Therefore, emphasis was set on characterizing configurations during the equilibrium phase

of the run, and particularly more attention was given to the features in the downstream reach of the channel, where the average characteristics of sediment and water waves were more or less stable. A detail description of the bedforms and surface waves observed, and of the criteria used to characterize bed and water surfaces configurations are given in Chapter 5. In that same Chapter the measured characteristics of the waves are presented.

Measurements and observations were performed during the runs when water was flowing, and also after the run was finished and water had been drawn out from the channel. The procedures during both stages are described as follows.

Procedures with water flowing.

During the equilibrium phase of each run, observations were performed for a first assessment of the type of bed and water configurations. These observations included a short description of the bed and water states along the channel considering the shape of the features, whether the forms were symmetric or asymmetric, whether water and bed surfaces were in-phase or not (if in-phase, it was preliminary considered that the bedforms were antidunes), and if the features migrated downstream, upstream or remained immobile. For a later thorough assessment of the bed configurations to be contrasted with those first observations, photos and videos were taken at different locations along the channel. Two or three locations were selected for the videos, trying to capture the evolution of the geometry, shape and velocity of the bedforms along the channel. For these videos the camera was left fixed, framing the bed and water surfaces in an approximately one meter length reach. In turn, some other videos were taken showing the evolution of the bed and water configurations along the channel and the characteristics of the water waves.

Point measurements of some characteristics of the bed and water-surface waves were carried out within the reach where the forms were roughly stable (not growing or decaying, neither coalescing). For bedforms visible through the channel walls, a tape measure was used to measure the height and wavelength of some features (three to six). The period of some of these bedforms was measured as well, for computing their celerity; this was done using a chronometer to take the time required to the bedform to travel a given distance (usually the length of a glass-panel, i.e., one meter). Since for many of the runs the geometry and shape of the bedforms changed constantly, or they vanished suddenly or coalesce with other forms even within the most stable reach downstream, all these measurements were not easy to perform and they should be consider only indicative of the average conditions.

Measurements described above were performed during the equilibrium phase of the runs, and no information of the characteristics of the configurations was collected for the transition phase. This notwithstanding, the dispersion of the measurements of bed surface elevation described in Section 3.3.2.2 served for obtaining an average statistical height of the bedforms passing next to the channel wall, from the transition to the equilibrium state.

On account of the water turbidity, bedforms at the channel central cross section could not be clearly observed during many of the experiments. Since for most of the runs trains of stationary waves formed on the water surface at the centre of the cross section, it was assumed and verified with some few observations, that each surface wave was accompanied by a subaqueous in-phase sediment wave, i.e., by an antidune. Hence, it was considered that the wavelength and celerity of these surface and subaqueous waves were approximately the same; thus, measuring these characteristics for the surface waves served to characterize the central cross section bedforms as well. Wavelengths and celerities for the stationary waves were measured using a tape measure and a chronometer, in a similar way as it was done for the bedforms near the channel walls. Videos and photos described previously were used for measuring wavelengths and celerities later again to verify the confidence of measurements performed during the runs.

For many of the runs, the stationary waves formed on the centre of the channel were steep short-crested waves. For some of these runs, the height of these waves was obtained from measurements of the water surface elevation using three point gauges set on a frame supported on the channel walls. Measurements were performed approximately 5 to 8 meters upstream from the downstream end of the channel. When the crest or trough of a stationary wave passed through the cross section with the point gauges, the water surface elevation was measured at the central and the two lateral sections. On account of the shaking and splashing of the water surface on the crests of the breaking waves, defining the elevation of the crest using the point gauge was difficult and required personal criterion, often prone to subjective appreciations.

Procedures with the dry bed.

Once the water was drawn down in the channel, the channel was set at a horizontal position and the bed surface was photographed, framing one meter long reaches, so that 25 to 26 photographs were taken for each run. The photographs were taken with a digital camera, which was fixed to a wood trestle standing on the upper steel structure of the channel walls. The distance between the camera and the top of the channel walls was one meter. The sequences of photographs for each run are presented in Appendix IX. These photographs served for measuring the length of the preserved bedforms, mainly bars. For some gravel runs white threads were used on the bed surface to indicate the crest of bars and ridges since they were not completely distinguishable in the photographs.

The bed surface was observed and described with simplified schemes in order to identify regions of similar characteristics of bed structure and grain sorting. A representative bedform unit at the downstream end reach was selected for taking photographs with a higher resolution. Finally, three bedform units were selected in three different zones of the channel, and they were surveyed in three or four cross-sections using a point gauge. These measurements served to identify the highest transversal elevation gradients.

Figure 3.12. Instruments used to sample sediment transport: a Helley-Smith-type sampler (right) and a basket-type sampler (left). The ruler on the floor is one meter long.

3.3.2.5 Manual sampling of sediment transport

The real-time record of the weight of sediment in the hoppers does not capture short or instantaneous variations in sediment transport rates in the flume. This occurs because the recirculating system regulates solid discharge and thus cancels out these variations. Moreover, these records do not provide information about cyclic or spatial variations in sediment grain sorting produced by bedforms, as the bedform period is short in relation to the capacity of regulation performed by the sediment recirculating system. Therefore, in order to recognize grain-sorting trends in the cross section and to detect sediment transport variations with time and space, samples of moving material were taken at the downstream end of the channel. These samples were taken during the mobile-bed

equilibrium phase of the runs with two types of instruments: a Helley-Smith type sampler and a basket-type sampler (see Figure 3.12), which are described below.

3.3.2.5.1 Helley-Smith type sampler

Helley-Smith samplers have been widely used in the field in the last 40 years. Their success comes from their proven high efficiency, their simple operation and the fact that they have been extensively calibrated (Van Rijn, 1993). The sampler used in the present work was not a standard Helley-Smith sampler as it was built in the laboratory with slightly different dimensions to those of the standard instrument. The main difference between the samplers are the dimensions of the entrance nozzle, which for the standard version correspond to a square of section 7.60 x 7.60 cm, while for the instrument built for the experiments correspond to a rectangular section of 9.80 x 10.15 cm. The sampler is composed of a nozzle, a sample bag and a handle, as shown in Figure 3.13. The nozzle length is 13% of the channel width.

Helley-Smith samplers are used for sampling bed load. Nevertheless, for the experiments in this work, as the height of the entrance nozzle was sometimes higher than the water depth, the material retained in the sampler could include both, bed load and suspended material.

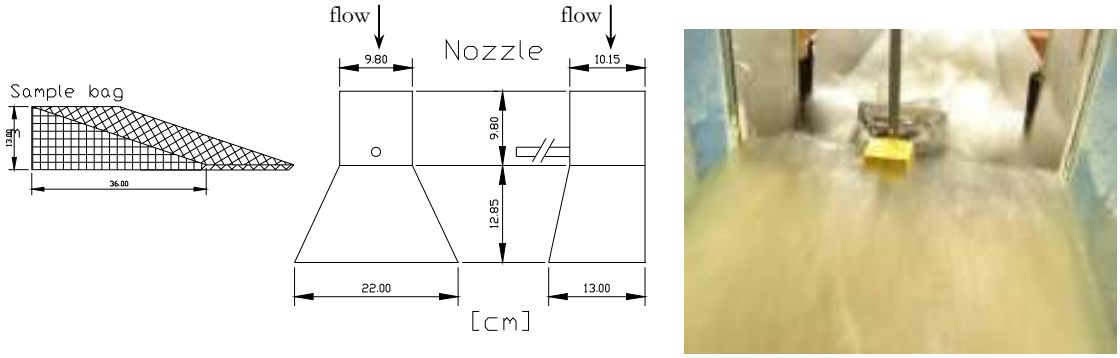

Figure 3.13. Dimensions of the Helley-Smith-type sampler used in the experiments (left). Sampling of sediment at the downstream end of the flume (right).

3.3.2.5.2 Basket-type sampler

The basket-type sampler was built in the laboratory to capture all the sediment passing through the channel at a given time. The sampler intake opening was therefore as wide as the channel, as shown in Figure 3.14. In order to detect sediment transport variations between the central and lateral sections of the channel, the sampler was divided into three sections of equal width. The sampler is composed of a frame, a handle and a structure fitted with a mesh of the same kind as that used in the Helley-Smith-type sampler. For sampling, the sampler was placed at the downstream end of the channel, on the metal channel extension connecting the flume to the silting basin. In this reach, the flow was supercritical and the water depth low to ensure the capture of both suspended load and bed load. Nevertheless, due to the supercritical flow, when the sampler was inserted the water splashed and a certain amount of liquid and sediment jumped over it; on account of this, the sampler was not entirely efficient in collecting all the sediment passing through the cross section.

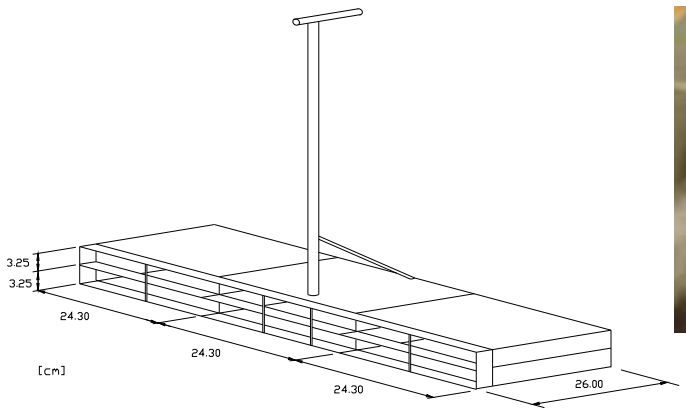

Figure 3.14 Dimensions of the basket-type sampler used in the experiments (left). The sampler just before immersion for sampling at the downstream end of the channel (right).

3.3.2.5.3 Trapping efficiency of the samplers with dry sediment

The same type of mesh (pore size of 1-1.25 mm) was used in the Helley-Smith-type sampler and the basket-type sampler. Tests were performed with dry sand (without water) to test the ability of the mesh to capture and retain different grain size classes. This ability is not only related to the size of the mesh and its irregularities, but also to the irregularities produced by incorrect assemblage between the mesh and the sampler structure. For this analysis, it is convenient to define trapping efficiency as

$$\%T_e = 100\left(\frac{\forall_{ret}}{\forall_{tot}}\right) \qquad (3.9)$$

where $\forall_{ret}$ is the volume of material retained by the sampler and $\forall_{tot}$ is the total volume of material added through the sampler intake opening. A trapping efficiency of 100% would indicate that the sampler is able to retain all the material added.

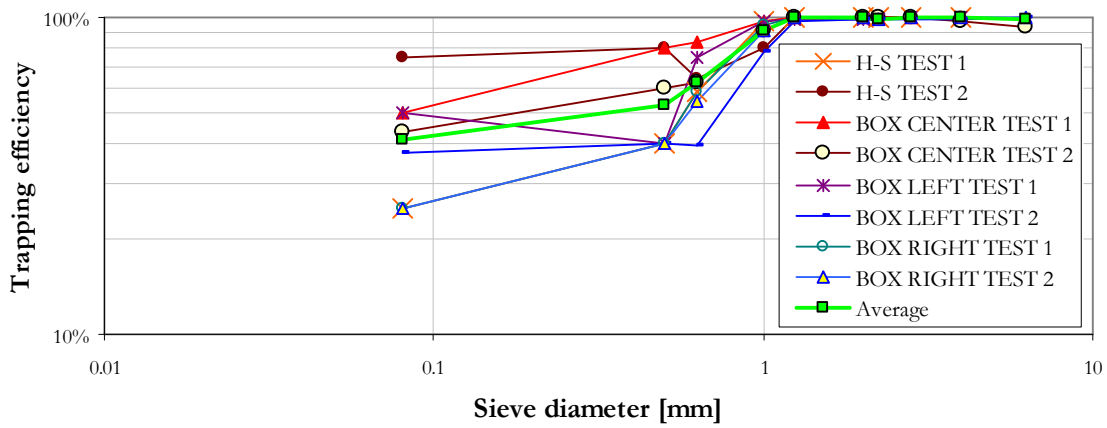

Figure 3.15. Trapping efficiency of the mesh for the sediment transport samplers for each size fraction. 'H-S' refers to the Helley-Smith-type sampler and 'BOX' refers to the basket-type sampler.

Two tests were performed with each sampler to define the trapping efficiency for each sand size fraction used in the experiments. For the tests, two samples of original sand (sand before it was used in the experimental series) weighing 1.58 and 1.05 kg were sieved to obtain their grain size distribution. One of the samples was used in each test. The tests consisted of pouring the sample of sand into the sampler, and without shaking the

samplers, to separately collect the retained and non-retained sediment. The sediment that was not retained by the sampler was weighed and sieved to obtain the grain size distribution. The grain size distribution of the material retained was obtained by subtracting, for each size fraction, the original weight of the size fraction from the weight of material that passed through the sampler. Trapping efficiencies were obtained by applying eq.(3.9). For the basket-type sampler, separate tests were performed for each of the three compartments (left, center, right).

For the basket-type sampler, the percentage of material by weight not retained by the left, right and central compartments was 2.6%, 2.9% and 1.1%, respectively, for the first test, and 12.3%, 9.2% and 7%, respectively, for the second test. For the Helley-Smith-type sampler the corresponding percentages were 2.2% and 6.1% for the first and second tests, respectively.

The mean trapping efficiencies obtained for the bulk of the sand for the basket-type sampler and the Helley-Smith-type sampler were 94.1% and 95.5%, respectively. Figure 3.15 shows the trapping efficiencies per size fraction for all the tests performed. The average trapping efficiencies are shown in Table 3.10. As expected for a mesh size of between 1 and 1.25 mm, the trapping efficiency decreased for grain sizes smaller than 1.25 mm. Conversely, for grain sizes equal to and larger than 1.25 mm the trapping efficiency was practically 100% for both samplers.

Table 3.10 Mean trapping efficiencies per size fraction for the mesh on the samplers.

Size fraction (mm)	0.08	0.50	0.63	1.00	1.25	2.00	2.24	2.80	4.00	6.30
Mean %T_e	41.4	52.5	62.0	90.7	99.4	99.5	99.3	99.8	99.6	99.2

Figure 3.16 shows the grain size distributions obtained by combining the samples from all the tests of the original sands, the material retained by the samplers and the material not retained. These curves show that although trapping efficiency was low for size fractions under 1 mm (%T_e<90% for D_i<1mm), the low participation of these size fractions in the original sand (<10%) meant that the differences between the grain size distribution of the original material compared to the grain size distribution of the material retained by the samplers were almost negligible.

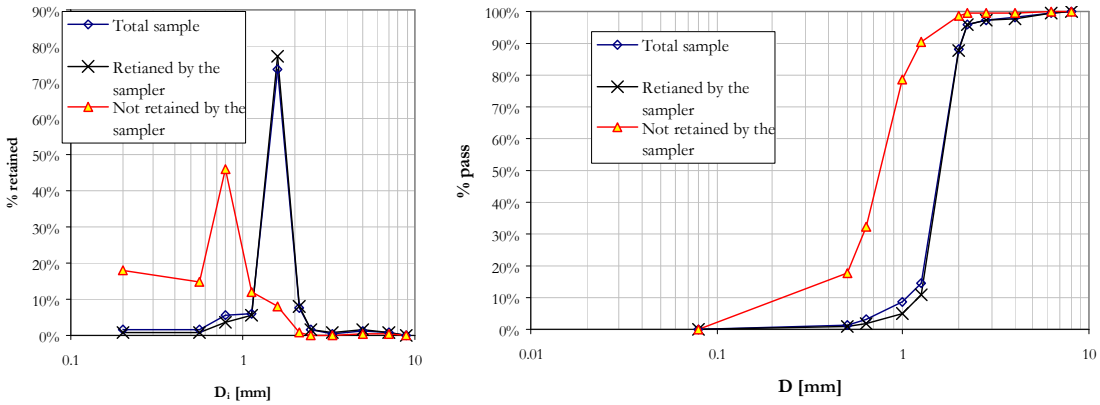

Figure 3.16. Comparison of mean grain size distributions for the original sand sample, the sample retained by the bed load samplers and the sample that the samplers did not retain.

3.3.2.5.4 Sampling procedures

The Helley-Smith-type samples were taken from different points along the last 10 meters of the downstream reach of the channel. All the samples were taken from the center of the channel cross section, except for the gravel run series, for which the samples were taken at the center and at two other lateral sections more or less in the middle of one third of the channel width. The Helley-Smith-type sampler was placed over the bed material, perpendicular to the flow direction. For most of the run series six samples were taken at random intervals whose time-length was a function of the time required to remove the sampler and the collected sediment. For the sand series, the samples were taken at the moment when the greatest amount of sediment passed through the channel section, which concurred with the passage of a bar or dune front.

Figure 3.17. Vertical metal sheets for dividing the flow into three sections at the downstream end of the experimental channel.

Samples collected with the basket-type sampler were taken 0.50 to 1 m downstream of the lower end of the channel. The sampler was placed over the metal channel (which was the same width as the experimental channel) that connected the channel with the siltation basin (see Figure 3.14). At the end of the experimental channel, two vertical metal sheets divided the flow into three sections (see Figure 3.17) so that the total load could be directed to the corresponding compartment of the sampler. Six samples were taken at random intervals whose time-length was a function of the time required to remove the sampler and the collected sediment.

Figure 3.18. Sediment transport samples for run M1E1, taken with the basket-type sampler and left to dry. Each group of three piles of material, from left to right, corresponds to the same sample but each pile to a different section (central or two lateral sections). Note the difference in volume for the different sediment piles even with similar sampling times for all samples (see Table 3.11). These differences in volumes prove the time and spatial variations in sediment transport due to the passing of bed forms.

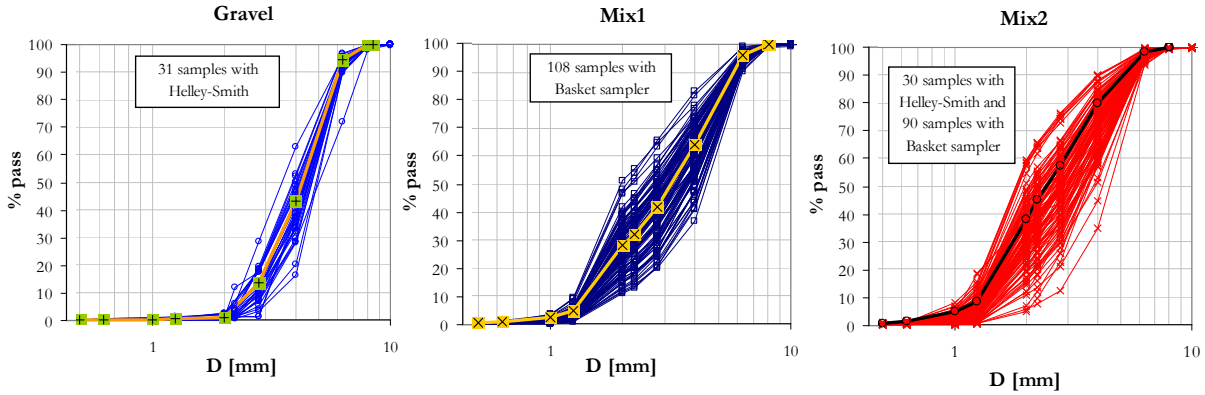

Figure 3.19. Grain size distributions for all the samples taken with the Helley-Smith-type and basket-type samplers for the gravel, mix1 and mix2 run series. Sediment transport samples for the sand run series were not sieved for grain size distribution because this material was considered to be well sorted. For these curves, 259 samples were sieved for grain size analysis. Curves with different symbols in each material are the average samples taken from the hoppers, i.e., the average feeding-material of each run series.

For both samplers, the sampling time was set before sampling, but was altered according to the rate of sediment passing through the section. In other words, the time was increased when the rate was low but reduced when the rate was high and the sampler filled quickly.

Once the sampler was taken out of the water, the sediment was poured onto a plastic sheet, where it was left to dry for a number of days (see Figure 3.18). The material was then poured into labeled plastic bags for subsequent weighing and sieving to obtain the grain size distribution. Tables 3.12 and 3.13 show the dry weights of the samples and Figure 3.19 shows the curves for all the grain size distributions of the sampled materials. Note the great variability between curves for the same sediment mixture in Figure 3.19.

3.3.2.5.5 Computation of sediment transport rates for sampled material

Sediment transport rates in the channel varied with time and across the cross section. In spite of this variability, it can be expected that the average rate of sediment transport through a cross section of the channel would be constant. Therefore, for a long-enough time, the unit load discharge q_S for a given section would be equal to

$$q_S = \overline{q_{Sin}} = \frac{1}{B\Delta t}\int_{t_1}^{t_2}\int_{0}^{B} q_{Sin}(y,t)\,dy\,dt \qquad (3.10)$$

where q_{Sin} and $\overline{q_{Sin}}$ are the instantaneous sediment discharge and the average instantaneous sediment discharge, respectively, t is time, B is the channel-width, y is the coordinate transversal to the flow and Δt is the time-step considered. For mobile-bed equilibrium conditions in the channel, the total load would be equal to the unit sediment feeding rate q_{SF}, such that

$$q_{SF} = q_S = q_{Su} + q_{Sb} \qquad (3.11)$$

where q_{Su} is the suspension load discharge and q_{Sb} is the bed load discharge in the flume. For a discrete *mn* number of samples of instantaneous sediment discharge at a section of the channel, from eq.(3.10) and (3.11) it can be assumed that

$$q_{SF} = \frac{1}{mn}\sum_{\substack{j=1\\k=1}}^{\substack{n\\m}} q_{Sin}^{j,k} \qquad (3.12)$$

where m is the number of samples over time and n is the number of samples across the channel width. The instantaneous sediment discharge is related to the sediment transport rates q_{Ss} obtained with the manual samplers with

Table 3.11. Number of samples and sampling times.

Run	Sampling times (s)											
	Basket-type sampler. Sample number.						Helley-Smith-type sampler. Sample number.					
	1	2	3	4	5	6	1	2	3	4	5	6
G12	-	-	-	-	-	-	72	75	78	42	-	-
G13	-	-	-	-	-	-	71	67	66	-	-	-
G14	-	-	-	-	-	-	46	57	53	54	92	48
G15	-	-	-	-	-	-	63	55	55	49	53	60
G16	-	-	-	-	-	-	73	47	56	59	61	64
G17	-	-	-	-	-	-	90	79	89	84	97	118
M1E1	30	61	38	40	30	31	-	-	-	-	-	-
M1E2	6	8	9	8	7	9	-	-	-	-	-	-
M1E3	6	7	8	7	7	6	-	-	-	-	-	-
M1E4	8	6	6	7	8	6	-	-	-	-	-	-
M1E5	6.5	8.75	10	8	9	8.5	-	-	-	-	-	-
M1E6	17	20	20	20	81	20	-	-	-	-	-	-
M2E1	3.5	4	4	4	4	4	12	15	20	20	20	20
M2E2	7	8.5	7	7	7	7	10	10	10	10	10	10
M2E3	8	10	8.5	8.5	8	8	15	18	15	15	15	15
M2E4	9.5	10	10	10	10	10	20	20	20	30	30	30
M2E5	-	-	-	-	-	-	-	-	-	-	-	-
M2E6	15	20	15	15	15	15	40	40	40	40	40	40
S1	5	5	5	5	5	5	10	10	10	10	10	10
S2	10	10	10	10	10	10	20	20	20	20	20	20
S3	10	10	10	10	10	10	60	60	60	60	60	60
S4	20	20	20	30	30	30	60	70	60	60	60	60

Table 3.12. Dry weight in grams for the samples taken with the Helley-Smith-type sampler.

Run	Sample number/Dry weight (g)					
	1	2	3	4	5	6
G12	2586	3764*	2450*	3302	-	-
G13	2640	2242*	1930*	-	-	-
G14	1554	982*	1346*	3504	5316*	1870*
G15	1906	952*	1656*	3454	2206*	2616*
G16	766	510*	662*	1510	1322*	1628*
G17	206	1618*	2612*	960	1103*	1116*
M2E1	684	578	831	839	913	601
M2E2	1366	557	11	128	686	211
M2E3	1147	87	1150	325	1120	1312
M2E4	74	1804	1128	2370	2056	1018
M2E6	1402	1654	950	1245	1028	994
S1	1434	1504	548	1600	394	926
S2	1028	1474	1952	844	1642	792
S3	2698	2960	3072	3346	3678	2808
S4	2976	2194**	2194**	1914	3224	2938

*Lateral samples, otherwise central samples.

**The weight of both samples is the same and is not an error!

Table 3.13. Dry weight in grams for the samples taken with the basket-type sampler.

	1			2			3			4			5			6		
Run	**right**	**center**	**left**	**right**	**center**	**left**	**right**	**center**	**left**	**right**	**center**	**left**	**right**	**center**	**left**	**right**	**center**	**left**
M1E1	439	948	2238	1262	3545	3680	1932	1408	1678	2494	2855	3266	537	1107	1804	2292	1677	1946
M1E2	1233	912	670	1407	1592	1300	1314	1308	756	1002	1117	1412	1130	885	921	1688	1850	2157
M1E3	1933	1652	1296	962	1047	1491	1241	1228	1747	1393	1561	1274	868	690	1072	1470	1395	1222
M1E4	474	621	1008	1212	1275	1373	985	1165	908	964	535	416	1948	655	426	353	522	615
M1E5	329	266	741	483	254	381	570	801	689	1008	673	672	381	876	1096	1274	793	503
M1E6	102	138	504	795	365	441	360	394	221	402	313	186	242	812	1122	628	380	284
M2E1	1116	976	1098	412	622	1232	1044	909	985	1289	984	764	979	1467	1970	1028	1065	1272
M2E2	1755	2171	2210	2077	1319	1156	1550	1360	1560	928	706	1044	1656	1522	1833	916	652	835
M2E3	1474	1200	968	1670	1771	1334	1696	2581	1740	1195	1413	1559	626	596	1136	1056	1392	2218
M2E4	544	694	934	1692	1502	1382	416	684	796	637	627	510	1664	1664	1698	1514	1229	1104
M2E6	222	292	1116	973	503	733	520	961	745	220	316	375	697	433	528	632	605	509
S1	1254	1324	658	478	624	1320	666**	602	1258	328	538	666**	206	290	596	528	974	1020
S2	244	1000	1810	594*	550	498	704	866	1342	542	430	624	862	708	748	616	1584	2112
S3	702	548	318	272	150	628	476	260	210	220	204	754	106	172	506	118	410	550
S4	826	318	46	178	198	430	102	424	682	1484	508	598	510	824	324	298	524	1222

*Not measured as the sample was lost. This value is an average of the right samples in run S2.
**These samples were accidentally mixed so the mixed sample was divided into two equal samples.

$$\frac{\%\eta}{100} = \frac{q_{Ss}}{q_{Sin}} \tag{3.13}$$

where η is the efficiency of the sampler, and the sediment transport rate per unit length for the samplers can be determined with

$$q_{Ss} = \frac{W_S}{b_s Dt_s} \tag{3.14}$$

where b_S is the width of the intake opening (0.098 m for the Helley-Smith-type sampler and 0.25 m for each of the compartments in the basket-type sampler), Dt_s is the sampling period and W_S is the dry mass of the sediment caught by the sampler. The samples can be considered total load samples as they were composed of both suspended and bed load.

If for given flow conditions (a given run) *mn* samples are taken with random intervals between sampling, for a time long enough to capture all sediment transport variations, then the total load discharge passing through the section can be estimated with

$$q_S \approx \frac{100}{\%\eta b_s}\left(\frac{W_{Ss}^1 + W_{Ss}^2 + ... + W_{Ss}^m}{Dt_s^1 + Dt_s^2 + ... + Dt_s^m}\right) = \frac{100}{\%\eta b_s}\frac{\sum_{j=1}^{m}\sum_{k=1}^{n} W_{Ss}^{j,k}}{\sum_{j=1}^{m}\sum_{k=1}^{n} Dt_s^{j,k}} \tag{3.15}$$

where j and m refer to the samples taken for different time intervals and k and n to samples taken across the channel cross section; as the basket-type sampler was divided into three compartments, n=3, while for the Helley-Smith-type sampler, n=1.

The average unit sediment transport rate for the samplers of all the individual samples $\overline{q_{Ss}}$ can be computed as follows

$$\overline{q_{Ss}} = \frac{1}{mnb_s}\sum_{j=1}^{m}\sum_{k=1}^{n}\frac{W_{Ss}^{j,k}}{Dt_s^{j,k}} \tag{3.16}$$

and the standard deviation of the average solid discharge from the samples can be calculated with

$$\sigma_{Ss} = \sqrt{\frac{\sum_{j=1}^{m}\sum_{k=1}^{n}\left(q_{Ss}^{j,k} - \overline{q_{Ss}}\right)^2}{mn-1}} \tag{3.17}$$

Table 3.14 presents the results after applying eqs.(3.16) and (3.17) to the data in Tables 3.11, 3.12 and 3.13; the results are compared with the constant sediment feeding rates for each run.

To analyze the sediment transport samples it is necessary to study grain size variation between samples. Therefore, it is useful to define the sediment transport relations by grain size fraction. For the i-th size fraction, the average sediment discharge sampled would be

$$\overline{q_{Ss,i}} = \frac{1}{mnb_s}\sum_{j=1}^{m}\sum_{k=1}^{n}\frac{W_{Ss,i}^{j,k}}{Dt_s^{j,k}} \tag{3.18}$$

and the fractional content of the i-th size fraction in the sampled material would be

$$f_{Si} = \frac{\sum_{j=1}^{n}\sum_{k=1}^{m} W_{Ss,i}^{j,k}}{\sum_{j=1}^{n}\sum_{k=1}^{m} W_{Ss}^{j,k}} \qquad (3.19)$$

Table 3.14. Mean sampled solid discharges compared with feeding sediment rate

Run	Feeding q_{SF} [kg/s]	Basket-type sampler			Helley-Smith-type sampler		
		average sample $\overline{q_{Ss}} \pm \sigma_{Ss}$ [kg/s]	$\overline{q_{Ss}} / q_{SF}$	σ_{Ss} / q_{SF}	average sample $\overline{q_{Ss}} \pm \sigma_{Ss}$ [kg/s]	$\overline{q_{Ss}} / q_{SF}$	σ_{Ss} / q_{SF}
G12	0.792	-	-	-	0.500 ± 0.217	0.63	0.27
G13	0.988	-	-	-	0.340 ± 0.041	0.34	0.04
G14	0.708	-	-	-	0.405 ± 0.189	0.57	0.27
G15	0.580	-	-	-	0.397 ± 0.185	0.68	0.32
G16	0.355	-	-	-	0.180 ± 0.075	0.51	0.21
G17	0.108	-	-	-	0.143 ± 0.097	1.33	0.90
M1E1	0.295	0.203 ± 0.082	0.69	0.28	-	-	-
M1E2	1.149	0.639 ± 0.155	0.56	0.13	-	-	-
M1E3	0.893	0.778 ± 0.225	0.87	0.25	-	-	-
M1E4	0.821	0.515 ± 0.260	0.63	0.32	-	-	-
M1E5	0.581	0.310 ± 0.136	0.53	0.23	-	-	-
M1E6	0.183	0.069 ± 0.037	0.38	0.21	-	-	-
M2E1	1.427	1.093 ± 0.337	0.77	0.24	0.433 ± 0.090	0.30	0.06
M2E2	1.192	0.776 ± 0.277	0.65	0.23	0.503 ± 0.510	0.42	0.43
M2E3	1.057	0.669 ± 0.231	0.63	0.22	0.581 ± 0.353	0.55	0.33
M2E4	0.737	0.431 ± 0.187	0.58	0.25	0.564 ± 0.325	0.77	0.44
M2E5	0.389	-	-	-	-	-	-
M2E6	0.212	0.146 ± 0.065	0.69	0.31	0.309 ± 0.071	1.46	0.33
S1	0.877	0.592 ± 0.289	0.68	0.33	1.089 ± 0.531	1.24	0.60
S2	0.615	0.352 ± 0.203	0.57	0.33	0.657 ± 0.241	1.07	0.39
S3	0.328	0.147 ± 0.083	0.45	0.25	0.526 ± 0.062	1.60	0.19
S4	0.191	0.082 ± 0.053	0.43	0.28	0.429 ± 0.101	2.25	0.53
		Average=	0.607	0.26	Average=	0.915/0.688*	0.35

*Excluding sand samples

3.3.2.5.6 Sampler efficiency

Different factors affect the efficiency of sediment transport samplers, including flow disturbances caused by the sampler, mesh size, the portion of sampler capacity filled with sediment, the limited size of the sampler with respect to the channel section or the conditions of movement of sediment particles, which might for instance saltate over the sampler. Here the efficiency of the two sediment transport samplers is estimated using the experimental data collected and eq.(3.13).

If it is considered that for mobile-bed equilibrium conditions in the channel the mean rate of sediment transport through a channel section is equal to the rate of sediment feeding by the hoppers, then, presuming that sampling time is long enough or that a large

enough number of samples is taken, the ratio between the sediment transport rate obtained with the samples and the rate of material fed to the channel (independent variable) would be equal to the efficiency of the sampler. Therefore, eq.(3.13) can be rewritten as

$$\%\eta = 100\frac{\overline{q_{Ss}}}{q_{SF}} \tag{3.20}$$

And for each size fraction the efficiency will be

$$\%\eta_i = 100\frac{\overline{q_{Ss,i}}}{q_{SF,i}} \tag{3.21}$$

Or in an equivalent manner

$$\%\eta_i = 100\frac{\sum_{j=1}^{n}\sum_{k=1}^{m} W_{Ss,i}^{j,k}}{q_{SF,i}\sum_{j=1}^{n}\sum_{k=1}^{m} Dt_s^{j,k}} \tag{3.22}$$

Columns 4 and 7 in Table 3.14 present the computed values of η/100 using eq.(3.20), for each sediment transport sampler and each experimental run. The average value for all runs yields an average efficiency value of **60.7% for the basket-type sampler** and **68.8% for the Helley-Smith-type sampler** (excluding the sand series samples for the Helley-Smith-type sampler, whose efficiencies are higher than 100% because the sampler was always used at the moment of highest sediment transport in an attempt to capture the peak of the sediment wave). As the sampler mesh is unable to retain fines (<1.25 mm), the efficiency was computed excluding these fine fractions as well, but the results are not shown in Table 3.14. The efficiencies thus obtained were 64.4% and 69.3% for the basket-type and Helley-Smith-type samplers, respectively. No major differences were found when the fines were excluded because these size fractions accounted for only a small proportion of the mixtures, as explained previously in Section 3.3.2.5.3 and noted in Figure 3.16.

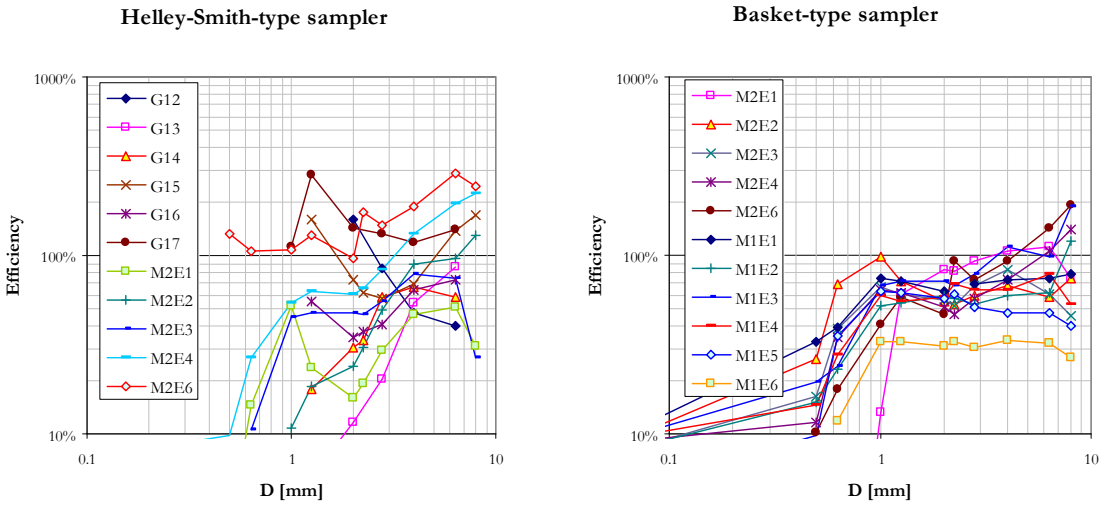

Figure 3.20. Efficiency of the sediment transport sampler by size fraction.

The standard deviation of efficiencies for the Helley-Smith-type sampler (excluding the sand run series) is 37%, which is considerably higher than the 13.5% calculated for the basket-type sampler. Such a difference may be related to the limited length of the Helley-

Smith-type sampler intake, whose entrance spans only 13% of the channel width. The intake entrance of the basket-type sampler, in contrast, spanned the entire channel width. The scatter in efficiency is even greater for the Helley-Smith-type sampler when efficiency is calculated by size fraction using eq.(3.22), as presented in Figure 3.20. The standard deviation for efficiencies computed by size fraction for grain sizes higher than 1.25 mm was 79% for the Helley-Smith-type sampler and 30% for the basket-type sampler. Note in Figure 3.20 the fall in efficiency for grain sizes lower than approximately 1.25 mm, which is congruent with the size for which the trapping efficiency of the mesh drops, as found in Section 3.3.2.5.3.

The average values of sampler efficiency by size fraction are shown in Figure 3.21. Irrespective of the sediment mixture and the sampler, the efficiencies would roughly collapse into a single curve. Higher efficiencies for larger size fractions could be an artifact of the low representation of these size fractions in the mixtures and also related to the preference of these sizes to roll along the bed surface. Finer size fractions, in contrast, can be transported in suspension and could be easily moved out of the trajectory of the sampler entrance.

To compare the sediment discharges obtained with the samples and the feeding sediment rate, a ratio of sediment discharge variation r_{sv} is here defined as

$$r_{sv} = \frac{q_{Ss}}{\left(\%\eta/100\right) q_{SF}} \qquad (3.23)$$

Tables 3.15 and 3.16 present the values of r_{sv} computed with eq.(3.23) considering an efficiency for the samplers of $\%\eta$=60.7% and $\%\eta$=68.8%, for the basket-type sampler and the Helley-Smith-type sampler, respectively, as computed above for the average bulk samples.

Appendix X presents plots of variations in sediment transport obtained with the samplers for each run.

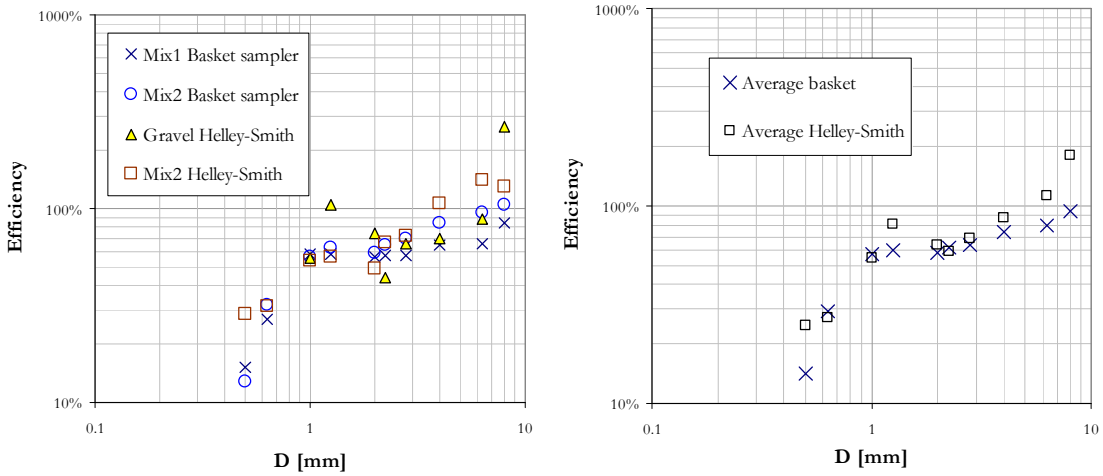

Figure 3.21. Average efficiency of the sediment transport sampler by size fraction.

3.3.2.6 Bed material sampling

In order to identify grain sorting trends in the deposited sediment, the bed material was sampled at selected zones along the channel bed. This was done on the following day or several hours after a run was finished and the water had been drained out of the channel. For each location, surface and subsurface materials were sampled within a bounded circular

area of 19 cm diameter. Surface sampling was areal (see 3.3.2.6.3 for a description of the technique). For the sediment mixture runs, two additional types of bed samples were collected: 1) bulk samples of the original bed material taken from different locations after the bed had been manually mixed before a new run; and 2) bulk samples from two runs (M1E6 and M2E4, six samples each) taken from different depths at a selected reach to identify vertical segregation or strata. The method used is described in Section 3.3.2.6.5. Table 3.17 shows the total number of bed samples taken for each run and Figure 3.22 plots the weight of the samples and the section of the channel from where they were obtained.

Table 3.15. Ratio of sediment discharge variations (eq.3.23) for the samples taken with the Helley-Smith-type sampler.

Run	Ratio of sediment discharge variation							
	Sample 1	Sample 2	Sample 3	Sample 4	Sample 5	Sample 6	Mean	Standard deviation
G12	0.68	0.95	0.59	1.49	-	-	0.93	0.40
G13	0.56	0.51	0.44	-	-	-	0.50	0.06
G14	0.71	0.36	0.54	1.37	1.22	0.82	0.84	0.39
G15	0.78	0.45	0.78	1.82	1.07	1.13	1.00	0.47
G16	0.44	0.46	0.50	1.08	0.92	1.07	0.75	0.31
G17	0.32	2.84	4.07	1.58	1.58	1.31	1.95	1.31
M2E1	0.60	0.40	0.44	0.44	0.48	0.32	0.45	0.09
M2E2	1.72	0.70	0.01	0.16	0.86	0.27	0.62	0.63
M2E3	1.08	0.07	1.09	0.31	1.06	1.24	0.81	0.49
M2E4	0.08	1.83	1.15	1.60	1.39	0.69	1.12	0.65
M2E6	2.48	2.92	1.68	2.20	1.82	1.76	2.14	0.49
S1	2.45	2.57	0.94	2.73	0.67	1.58	1.82	0.89
S2	1.25	1.80	2.38	1.03	2.00	0.96	1.57	0.57
S3	2.05	2.25	2.34	2.55	2.80	2.14	2.35	0.28
S4	3.90	2.46	2.87	2.51	4.22	3.85	3.30	0.78
						Average=	1.00	0.52

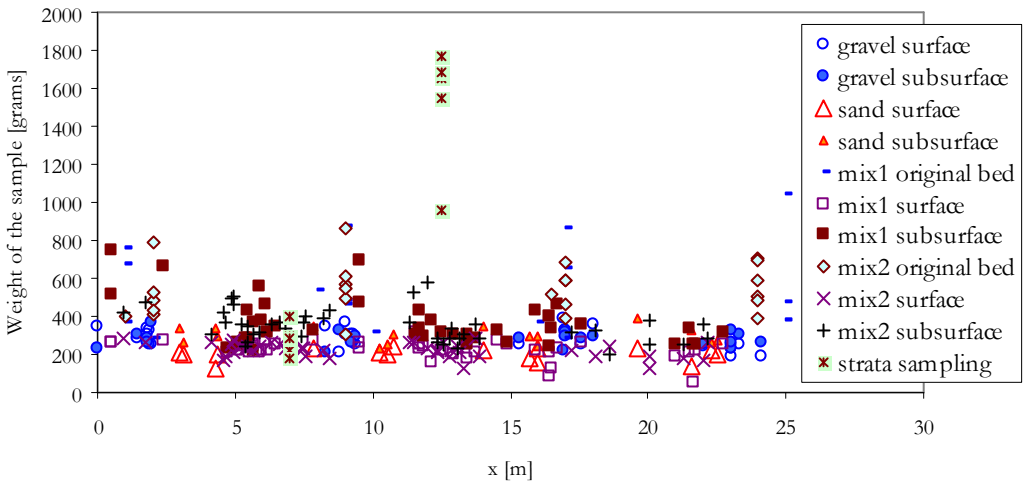

Figure 3.22 Weight of the samples and channel section for all bed samples.

Table 3.16. Ratio of sediment discharge variation (eq.3.23) for the samples taken with the basket-type sampler; r, c and l refer to the right, central and lateral compartments of the sampler, respectively.

Run	Ratio of sediment discharge variation																			
	Sample 1			Sample 2			Sample 3			Sample 4			Sample 5			Sample 6			Mean	Standard deviation
	r	c	l	r	c	l	r	c	l	r	c	l	r	c	l	r	c	l		
M1E1	0.33	0.71	1.68	0.47	1.31	1.36	1.15	0.84	1.00	1.41	1.61	1.84	0.40	0.83	1.36	1.67	1.22	1.42	1.14	0.46
M1E2	1.19	0.88	0.65	1.02	1.15	0.94	0.84	0.84	0.49	0.72	0.81	1.02	0.93	0.73	0.76	1.08	1.19	1.39	0.92	0.22
M1E3	2.40	2.05	1.61	1.02	1.11	1.58	1.15	1.14	1.62	1.48	1.66	1.35	0.92	0.73	1.14	1.82	1.73	1.52	1.45	0.42
M1E4	0.48	0.63	1.02	1.63	1.72	1.85	1.33	1.57	1.22	1.11	0.62	0.48	1.97	0.66	0.43	0.48	0.70	0.83	1.04	0.53
M1E5	0.58	0.47	1.30	0.63	0.33	0.50	0.65	0.92	0.79	1.44	0.96	0.96	0.48	1.11	1.39	1.71	1.07	0.68	0.89	0.39
M1E6	0.22	0.30	1.08	1.45	0.66	0.80	0.65	0.72	0.40	0.73	0.57	0.34	0.11	0.36	0.50	1.14	0.69	0.52	0.62	0.34
M2E1	1.49	1.30	1.46	0.48	0.72	1.43	1.22	1.06	1.15	1.50	1.15	0.89	1.14	1.71	2.29	1.20	1.24	1.48	1.27	0.39
M2E2	1.40	1.73	1.76	1.36	0.86	0.76	1.23	1.08	1.24	0.74	0.56	0.83	1.32	1.21	1.46	0.73	0.52	0.66	1.08	0.39
M2E3	1.16	0.94	0.76	1.05	1.11	0.84	1.25	1.91	1.29	0.88	1.04	1.15	0.49	0.47	0.89	0.83	1.09	1.74	1.05	0.36
M2E4	0.52	0.66	0.89	1.52	1.35	1.25	0.37	0.62	0.72	0.57	0.57	0.46	1.50	1.50	1.53	1.36	1.11	0.99	0.97	0.42
M2E6	0.46	0.61	2.33	1.52	0.79	1.15	1.09	2.01	1.56	0.46	0.66	0.78	1.46	0.90	1.10	1.32	1.26	1.06	1.14	0.51
S1	1.90	2.01	1.00	0.72	0.95	2.00	1.01	0.91	1.91	0.50	0.81	1.01	0.31	0.44	0.90	0.80	1.48	1.55	1.12	0.55
S2	0.26	1.08	1.96	0.64	0.59	0.54	0.76	0.94	1.45	0.59	0.46	0.67	0.93	0.77	0.81	0.67	1.71	2.28	0.95	0.55
S3	1.42	1.11	0.64	0.55	0.30	1.27	0.96	0.53	0.43	0.45	0.41	1.53	0.21	0.35	1.03	0.24	0.83	1.11	0.74	0.42
S4	1.44	0.55	0.08	0.31	0.35	0.75	0.18	0.74	1.19	1.72	0.59	0.69	0.59	0.96	0.38	0.35	0.61	1.42	0.72	0.46
																		Average=	1.00	0.43

Table 3.17 Number of samples and average weight (± standard deviation) of each type of bed sample taken for each run. A total of 304 bed samples were collected and analyzed for grain size distribution. See Subsections in Section 3.3.2.6 for a description of each sample type.

	Number of bed samples						
Run	**surface**	**subsurface**	**fine patches***	**coarse patches***	**mixed patches***	**original bed**	**strata**
G12	4	4	-	-	-	-	-
G13	4	4	-	-	-	-	-
G14	4	4	-	-	-	-	-
G15	4	4	-	-	-	-	-
G16	4	4	-	-	-	-	-
G17	4	4	-	-	-	-	-
M1E1	5	5	2	1	2	4	-
M1E2	8	8	3	3	2	2	-
M1E3	8	8	4	3	1	4	-
M1E4	8	8	3	3	2	4	-
M1E5	8	8	3	3	2	-	-
M1E6	6	6	3	2	1	2	6
M2E1	8	8	3	2	3	4	-
M2E2	7	7	3	2	2	4	-
M2E3	7	7	2	2	3	4	-
M2E4	8	8	3	3	2	4	6
M2E5	6	6	2	2	2	4	-
M2E6	7	7	2	2	3	4	-
S1	4	4	-	-	-	-	-
S2	4	4	-	-	-	-	-
S3	4	4	-	-	-	-	-
S4	4	4	-	-	-	-	-
Total=	126	126	33	28	25	40	12
Average weight of sample (g)=	234.5±53	332.5±96	214.7±50	242.3±43	222.7±34	546.6±179	912.5±692

*Only surface samples are taken into account; subsurface samples were obtained as well.

3.3.2.6.1 Selection of sampling zones

For the sand and gravel runs, four bed sampling zones located 5 to 8 meters apart were selected. See Figure 3.23 for a description of the sampling locations according to the type of bed configuration.

Two or four bulk samples of the original mixed bed were taken at different locations distributed evenly along the channel before the sand-gravel mixture runs. These samples served as a reference for the initial bed material grain size distribution. Once sampled, the bed in the zones from where the samples had been taken was leveled. For samples taken at the end of the sand-gravel mixture runs, the sampling zones were selected on the basis of the bed configuration and grain sorting observed along the bed. Zones with similar morphologies and configurations were identified, and within these bounded zones, representative patches of similar surface grain size sorting were selected for sampling. In general, three or four zones of distinctive bed configuration were identified for all the runs, and within these zones three kinds of patches were selected if identified: one with fine material, another with coarse material and a third with mixed-size material (see Figure 3.24a). The fine and coarse patches were characterized by a high, predominant abundance of sand or gravel, respectively, and the mixed patches were identified by checking with the naked eye for a similar proportion of gravel and sand or for an intermediate mixture of

sand and gravel with respect to the identified fine and coarse patches. Patches were classified as bar trough or bar stoss patches. The former occurred in front of the bar front lobe while the latter occurred on the bar stoss side (see Figure 3.24b).

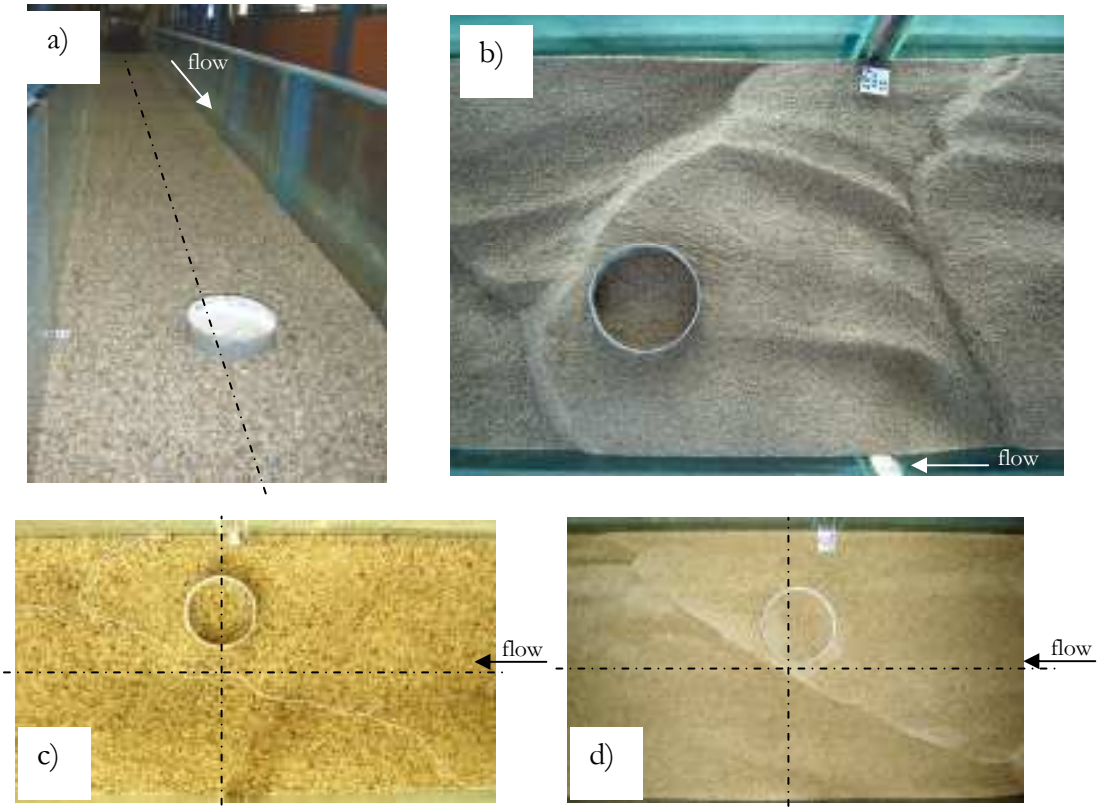

Figure 3.23 Criteria for selecting the locations for bed material sampling in the sand and gravel runs. a) When no bed forms were present, sampling was performed roughly at the center of the channel (image corresponds to run G13); b) when dunes were present, sampling was performed on the stoss side of the dune; for 2D dunes the samples were taken at the channel central cross section and for 3D dunes they were taken near the edge of the dune front lobe (image for run S4); c) when bars were present, sampling was performed on the stoss side of the bar, next to the intersection of the bar front lobe (oblique to the flow direction) and the channel central cross section (image for run G17, the bar crest is marked with a string) d) the same as c) (image for run S2).

3.3.2.6.2 Surface and subsurface samples

In order to detect differences in particle size distributions on the bed surface and between the bed surface and subsurface, it was important to use a technique for sampling the superficial particles only. To achieve this objective, an adhesive method was chosen. Adhesive methods are particularly recommended for areal sampling of bed surfaces with relatively large amounts of sand and fine gravel (Bunte and Abt, 2001). The adhesive used was plaster, as described in detail in 3.3.2.6.3. After the removal of the areal surface sample with plaster, the subsurface material was exposed and sampled using two trowels (Figure 3.25). The chosen depth for subsurface sampling varied with the size of the sample (a rule of thumb was to fill the sampling bags to a limit at which the average sample weight was 332.5 ± 96 g, as shown in Table 3.17) and to a height no greater than the height of the bedforms observed during the run.

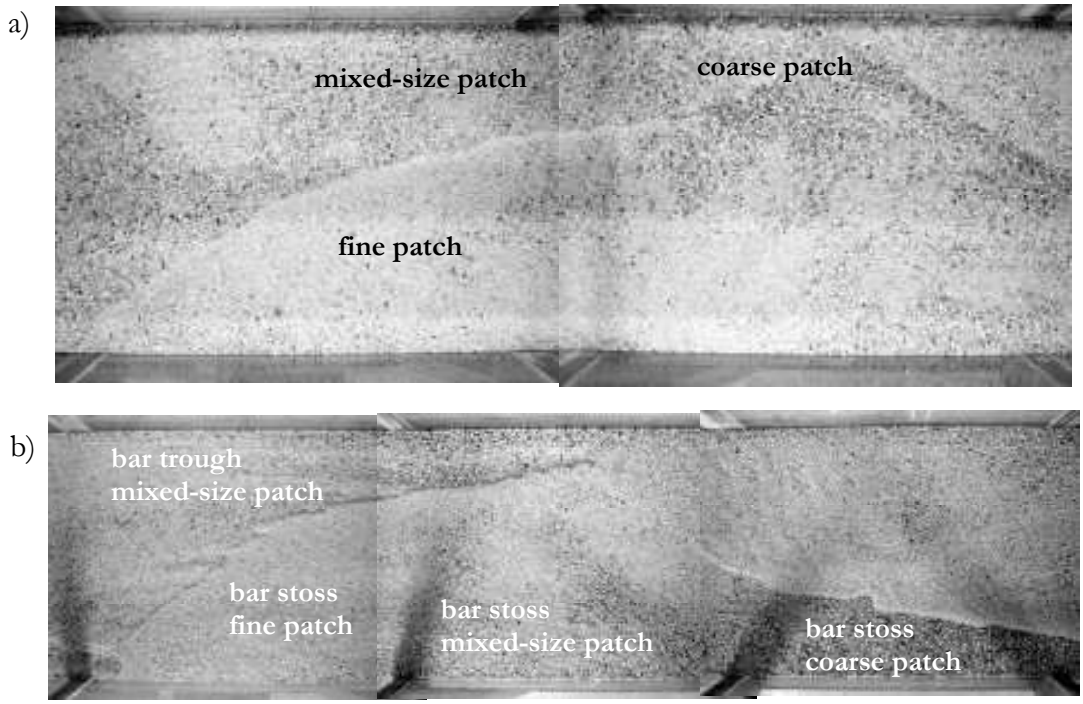

Figure 3.24 Identification of patches of similar grain size distribution on the bed surface for bed configurations with alternate bars. a) Run M1E3, with a reach span of 2 meters, from x=4 to x=6; b) Run M2E1, with a reach span of 3 meters, from x=5 to x=8. Flow from right to left.

Figure 3.25 Sampling of subsurface bed material using two trowels and a plastic bag to store the sample before grain size analysis.

3.3.2.6.3 Areal bed surface sampling

The aim of areal sampling is to collect all particles exposed on the bed surface within a predefined area. Results can vary greatly depending on the sampling procedures used because it is extremely difficult to prevent certain subsurface particles from being included in the sampled material, especially when the bed material is poorly sorted. The procedure chosen in the present work for areal sampling was the application of plaster over the defined area. The plaster acts as an adhesive to which the surface and some subsurface particles adhere when the plaster hardens. By using plaster, it was possible to control the

viscosity and plasticity of the adhesive for low penetration, thus reducing the amount of subsurface material collected. This technique has the added advantage that it is easy and relatively fast to implement, an important issue in this case because of the large number of experiments performed.

The sampling procedure consisted of pouring the previously prepared plaster mixture over the sampling bed surface delimited with a PVC ring (19 cm diameter and 8 cm height), which served as a mold and was placed on the bed surface (Figure 3.26a). The plaster mixture was spread uniformly within the ring and gently pressed with a trowel; it was important to ensure that the plaster touched the walls of the ring to prevent the hardened plaster from breaking when the mold was lifted off. The mixture was left to harden for approximately three minutes or until it was clearly hard (Figure 3.26b); the mold with the adhered plaster cast and particles was then removed (Figure 3.26c). Special care was taken to control the time after which the samples were removed, because an excessive time could cause the plaster to become

extremely hard and would make it difficult to separate the sediment particles. Excessive drying time can also lead to the formation of thick lumps, which are difficult to separate from sediment grains. Once removed, the bed material adhered to the plaster and the mold was placed in a bucket of cold water, where it was separated from the mold and the plaster dissolved by shaking the water and scraping the particles off manually. The water was changed several times to remove the finest plaster particles, and the process was repeated until all plaster residue had been washed away. The clean material was then put in a plastic bag labeled with the run number and the origin of the sample for subsequent sieve analysis.

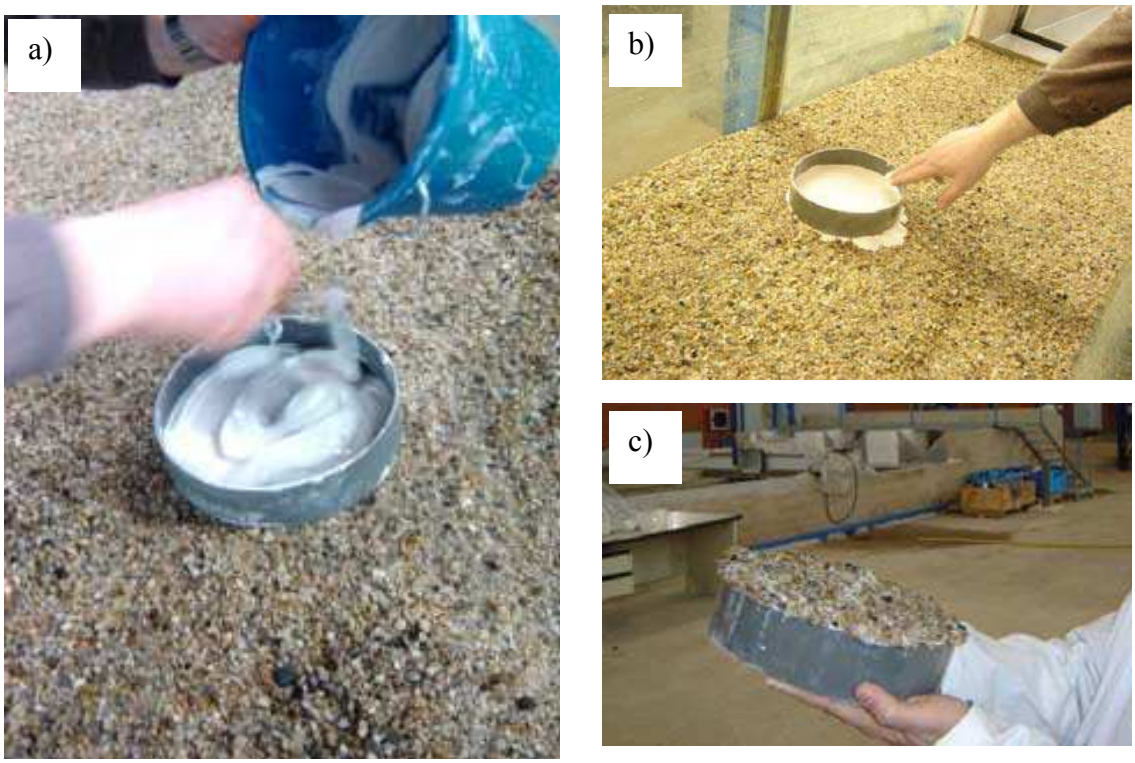

Figure 3.26 Areal bed surface sampling with plaster; a) pouring of the plaster mixture over the bed surface; b) testing of the consistency of the plaster cast after 3 minutes to check whether it was ready to be lifted off; c) plaster cast after being removed from the bed surface; note the sediment grains adhered to the cast.

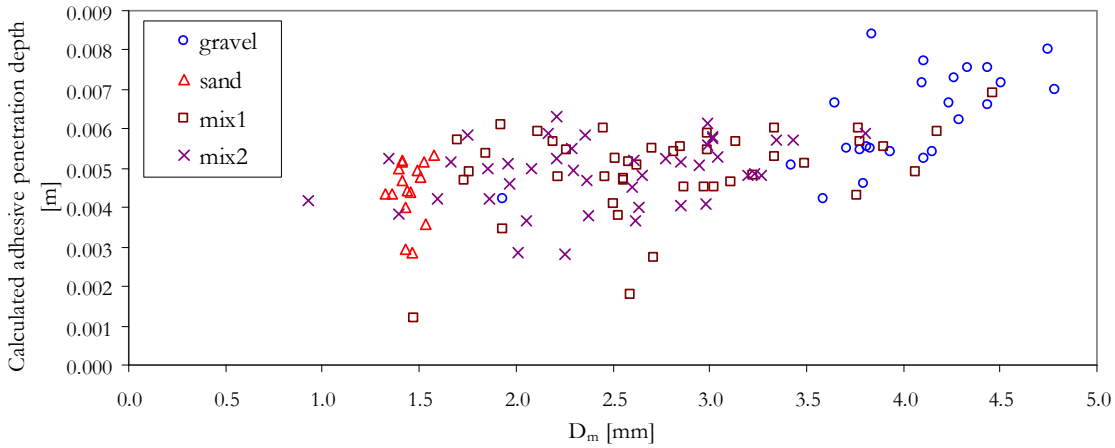

Figure 3.27 Adhesive penetration depths computed with eq.(3.25) shown as a function of the sample mean diameter, for each type of bed material and all surface areal samples taken after each run.

The plaster mixture used for sampling was prepared by mixing 500 ml of water with 330 grams of plaster powder. To ensure adequate consistency, the water-plaster mixture was left to harden for 13 to 14 minutes, or longer if it was observed that the viscosity was still low. Low viscosity can cause the adhesive to penetrate to an excessive depth. Excessive viscosity, in contrast, can make it impossible to pour the mixture over the bed surface.
To reduce variability in the areal sampling procedures, the same operator prepared the adhesive and took the samples for all the runs. To compensate for changes in air humidity, which can affect the consistency of plaster, the operator varied the time the mixture was left to harden to ensure similar consistencies for all runs.

To test the variability of the areal sampling technique used, the penetration depths of the plaster mixture were calculated for all the bed surface samples. These depths were calculated by considering that the adhesive penetrated uniformly within the bounded area, so that the volume of sampled material corresponded to a cylinder with top and bottom areas equal to the area within the PVC ring, and the height was equal to the penetration depth of the adhesive. Accordingly, the weight of the sediment sample can be calculated as

$$W_{ss} = \pi r_s^2 S_d \rho_s (1-\varepsilon) \qquad (3.24)$$

where r_s is the radius of the circular area sampled (=9.55 cm for all samples), S_d is the penetration depth of the adhesive, ε is the bed porosity (as given in Table 3.2) and ρ_s is the sediment density. Solving eq.(3.24) for the penetration depth

$$S_d = \frac{W_{ss}}{\pi r^2 \rho_s (1-\varepsilon)} \qquad (3.25)$$

The computed penetration depths are plotted in Figure 3.27 as a function of the sample mean diameter, and a summary of the average computed penetration depths is provided in Table 3.18. Penetration depths were deeper for gravel samples than for sand and sand-gravel samples, whose penetration depths were similar; the cutoff size separating the average penetration depths from the greatest depths was roughly a mean diameter of 4 mm as seen in Figure 3.27. The increase in penetration depths for gravel samples is presumably related to the higher porosity of the bed with coarser grains and to the absence of fine particles which can fill the small pores, hindering the penetration of adhesive. These results are in agreement with findings by Diplas and Fripp (1992), who concluded that the degree of penetration of molten wax into sediment mixtures was mainly controlled by the finer sizes. Accordingly penetration depths in gravel beds would be deeper because of the absence of sand. Similarly, Diplas and Southerland (1988) found that the absolute size of

grains is also relevant in penetration depth. Consequently, penetration depths would have been deeper for the gravel samples in the current study.

Diplas and Fripp (1992) suggested that the minimum depth for a volumetric sample must be equal to two times the diameter of the maximum grain. Thus for a surface sample, the penetration depth of the adhesive cannot be greater than this maximum value. As seen in Table 3.18, except for the sand runs, the penetration depths of the plaster were less than two times $D_{95.}$ The sand samples were thus more volumetric than areal, while for the rest of materials, for which the penetration depths were comparable to the D_{95}, the samples cannot be strictly considered surface areal samples, as some subsurface particles finer than D_{95} might have been included in the sampled material. Neither, however, can they be considered volumetric.

Table 3.18 Average adhesive penetration depths S_d calculated with eq.(3.2) for all experimental runs. D_m, D_{16} and D_{95} are the mean diameters and the diameters for which 16% and 95% of the surface sample by weight was finer, respectively.

	$S_d \pm \sigma$ [mm]	$S_d/D_m \pm \sigma$	$S_d/D_{16} \pm \sigma$	$S_d/D_{95} \pm \sigma$
Gravel	7.2 ± 2.9	1.84 ± 0.72	2.71 ± 1.19	1.09 ± 0.39
Mix1	5.0 ± 1.1	1.87 ± 0.60	3.14 ± 0.91	0.85 ± 0.24
Mix2	4.9 ± 0.8	2.12 ± 0.70	3.46 ± 1.08	0.97 ± 0.33
Sand	4.4 ± 0.8	3.07 ± 0.53	3.78 ± 0.71	2.19 ± 0.37

For comparison with eq.(3.25), direct measurements of adhesive penetration depths were performed for four surface samples taken after a test run with gravel (run G8). The penetration depths were considered to be equal to the vertical distance between the not-sampled bed surface and the surface of the particles exposed after the surface sample was removed (Figure 3.28). Four to five measurements were performed at different points in each pit; the average depths for each sample were 6.5 ± 3.3, 5.2 ± 2.9, 9.5 ± 2.4 and 9.6 ± 3.5 mm. The depths computed with eq.(3.25), in turn, were 6.8, 6.7, 8.2 and 6.1 mm, and the respective ratios of computed to measured depths were 1.05, 1.30, 0.87, and 0.64. The agreement between measurements and computations can therefore be considered to be reasonable.

Figure 3.28. Measurement of the pit on the bed surface after removal of an areal sample.

3.3.2.6.4 Conversion of surface samples to volumetric samples

It has been long recognized that surface samples are not comparable to volumetric samples (e.g., Kellerhals and Bray, 1971; Church et al., 1987). A conversion method is therefore required to convert surface samples into their volumetric equivalents. While empirical exponential formulas have been proposed for this conversion, they are not reliable when sampling is performed using adhesives such as wax, as these adhesives penetrate into the bed and normally include subsurface fine material in the sample (Diplas and Fripp, 1992). According to the penetration depths calculated in 3.3.2.6.3, as occurs with wax, surface sampling with plaster was not strictly areal, because the mixture would have penetrated to a depth at which finer subsurface grains may have been included.

Marion and Fraccarollo (1997) developed a method to convert surface samples in volumetric samples, computing the penetration depth of adhesive. The method includes the extreme case in which adhesive penetration is so deep that the areal sample is in fact volumetric; in this case the particle size distribution obtained by the algorithm is the same as the initial distribution. According to this method, the penetration depth of the adhesive is computed iteratively from

$$W_{ss} = \frac{\rho_s A_s (1-\varepsilon)}{\sum_{i=1}^{k} \left[f_i^{a-w} / (S_d + D_i/2) \right]} \qquad (3.26)$$

where A_s is the sampling area ($=\pi r_s^2$, where r=9.55 cm for all samples in the present study), D_i is the grain size for the ith size class, f_i^{a-w} is the fractional content by weight of the ith size class of the surface sample, k is the number of size classes, S_d is the penetration depth of the adhesive, W_{ss} is the total weight of the sample, ε is the bed porosity and ρ_s is the density of the sediment. Once the penetration depth is obtained iteratively with eq.(3.26), the percentage of total volume occupied by particles of the ith size fraction $f_{i,0}$ is calculated with

$$f_{i,0} = \frac{f_i^{a-w}(1-\varepsilon)}{(S_d + D_i/2)\sum_{j=1}^{k} \left[f_j^{a-w} / (S_d + D_j/2) \right]} \qquad (3.27)$$

and the converted volumetric fractional content of the ith size fraction is finally obtained by normalizing $f_{i,0}$ as

$$f_i^{v-w} = \frac{f_{i,0}}{\sum_{i=1}^{k} f_{i,0}} \qquad (3.28)$$

The average penetration depths obtained after iterations with eq.(3.26) were 4.3 ± 1.1, 3.6 ± 0.8, 3.5 ± 1.0 and 3.6 ± 0.8 mm, for the gravel, sand, mixture 1 and mixture 2, respectively. These values are 20% to 40% lower than depths obtained with eq.(3.25) shown in Table 3.18. The reason for such differences is the consideration in the method of Marion and Fraccarollo that particles are removed from the bed if they are touched by the adhesive. Accordingly, the penetration depth would be lower than the depth at which the removed particles were located. The simplified model given by eq.(3.25) considers that the penetration depth of the adhesive is the same as the depth at which the particles are removed.

The method of Marion and Fraccarollo (1997) was used to convert the particle size distributions of areal samples to volumetric samples. Using this method, it was found that on average, the D_{50} of the corrected samples was 8% smaller than the original value. The exception was sand, for which the converted samples were almost identical to the original

surface samples, indicating that the penetration depth was sufficient to make the sample volumetric.

3.3.2.6.5 Vertical bed sampling

In order to identify vertical grain size variations, for two of the sand-gravel runs, six successive bed material samples were taken when all other bed sampling and measurements were complete. A zone of the bed was isolated with four metal plates, which were driven into the bed to form a rectangular plan section measuring 0.30 m long × 0.26 m wide for run M2E4 and 0.12m long × 0.12 m wide for run M1E6. Within the isolated section, samples were taken for 1-cm thick layers. As shown in Figure 3.29, the isolated section was located in the channel central cross section, 12.5 m upstream of the downstream end of the channel for run M2E4, and 7 m for run M1E6. The material was collected using two trowels and a set square to indicate the depths of the sampling layers. The samples were stored in plastic bags and labeled for subsequent grain size analysis.

Figure 3.29. Isolation with metal plates driven into the bed of a rectangular section of the bed surface after run M2E4 for sampling bed material at different depths.

3.3.2.7 Bed erosion measurement and inspection for bedding and facies

During the stable phase of the experiments the mean bed profile was approximately constant. Nevertheless, the passage of bedforms produced transitory erosion according to the random variation of bedform height and scour. Due to the three-dimensionality of the bedforms, the erosion was not uniform across the cross section. For measuring the patterns of maximum erosion produced by the bed forms in the cross section, tracer stones were placed in the bed after the transient phase of the experiments (see Figure 3.30). A prismatic pit (0.10 m long, 0.40 m wide and 0.07 m deep) was opened in the bed next to one of the channel walls at 4.5 m upstream of the end of the flume. To open the pit, metal sheets were driven into the bed to isolate the volume to be dug; after extracting all the sediment within the bounded volume, the pit was filled with tracer stones, which consisted

of gravel, set in horizontal layers of a thickness of 0.01 m. The gravel used to fill the pit was of the same characteristics as the original gravel described in Table 3.2, but it was painted with different colors to distinguish between the different layers. The aim of these layers was to trace the cross-sectional profile of maximum bed erosion at one half of the channel width by measuring the variations in depth of the painted gravel not washed away by the flow.

Figure 3.30. Setting of tracer stones to track bed erosion: a) preparation of different colored gravel (three colors) using a cement shaker; b) isolation of the volume with metal sheets; c) extraction of the original bed material; d) leveling of the bed surface after extracting the original material; e) leveling of the bed after adding a layer of colored gravel; f) bed after adding and leveling the layers of colored gravel; g) bed surface showing where the tracer gravel was added, before the stable phase of the run.

The average relative density of the painted gravel was 2.504±0.042, obtained from six experiments with the following individual relative densities: 2.567, 2.507, 2.472, 2.495, 2.531 and 2.450. In other words, the relative density was almost 3% lower than the original gravel described in Table 3.2. It can thus be assumed that this difference was not relevant for the experiments.

After the stable phase of the run was finished, a section was opened in the zone that had been refilled with tracer gravel. The remaining layers of colored gravel allowed the identification of erosion relicts. Horizontal distances were measured from the upper and lower limits of the remaining layers of color gravel, as well as vertical distances to the bed surface. In this section, apparent facies and bedding of the deposited material were observed and photographed. Appendix AXI shows pictures of the sections opened to measure bed erosion and identify bedding and facies.

For run M1E3, another section was opened in the bed at the center of the channel, parallel to the flow direction, to inspect the bedding and facies. Figure 3.31 shows pictures of the cross and transversal sections opened after this run.

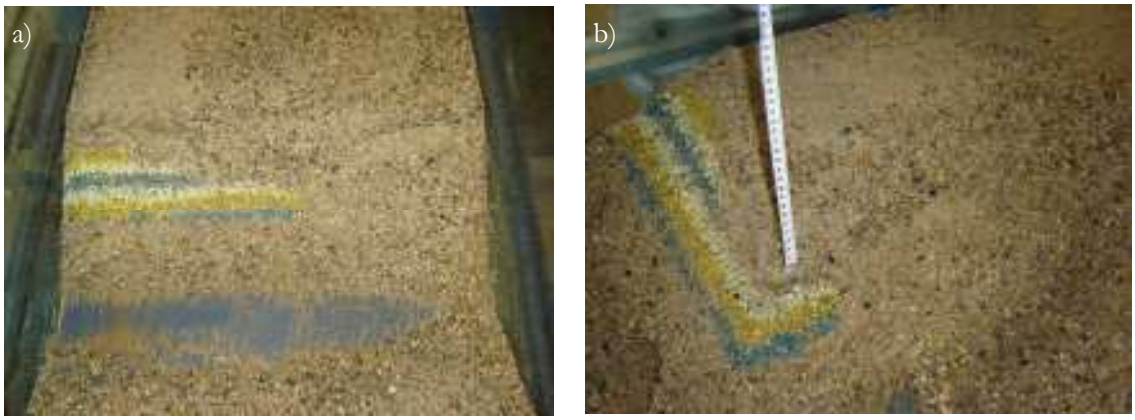

Figure 3.31. Cross and transversal sections opened in the bed after the water was drained for experiment M1E3, in the zone where tracer gravel was added.

3.4 MORPHODYNAMIC INTERACTIONS

Bed and water surfaces for most of the experimental runs were extremely unstable, mainly because the flow regime was close to or in the transition from lower to upper regime. This unstable character of flow, added to the three-dimensionality of bedforms and stationary waves, introduced uncertainty in the measurements performed. For instance, it was found that the degree of confidence of linear regressions for the bed surface profiles, and water surface profiles as well, was inversely proportional to the size of the observed bedforms (see Figure 3.33). This notwithstanding, it was found that average bulk flow conditions were a good representation of the flow state, since the variability between different measured equilibrium profiles of the same run was low. Moreover, tests of reproducibility (see Section 3.4.3) with similar runs showed a low variance of the most important variables to be related with sediment transport.

In this Section the methods used to compute the definitive hydraulic variables for the data set and the criteria used to test morphodynamic equilibrium are described.

3.4.1 Computation of hydraulic parameters

The algorithm for calculating the definitive energy slopes and water depths for the data set using the measured bed and water profiles is described in this Section. The estimation of representative values for these two variables is of especial importance, since bed shear stress, a fundamental variable for sediment transport, is computed from the water depth-slope product. Due to this importance, a rigorous procedure was followed for deriving these variables from the experimental measurements.

For a given time n during an experimental run, the bed and water surface profiles can be defined by the following functions for the bed and water elevations:

$$\eta_b^n(x,z) \quad (3.29), \text{ and } \quad \eta_w^n(x,z) \quad (3.30)$$

respectively, where x and z are the horizontal and vertical coordinates. A simple linear regression can be used to represent η_b and η_w, from which the mean energy slope can be obtained.

To define functions η_b and η_w, best-fit lines were found for the measured profiles using least-squares. Measured profiles are given by eqs.(3.4) to (3.7) applied to the measurements on the rulers. In fitting lines to the measured points, it was necessary to discard some points in entrance and exit regions of the channel, since these were influenced by the local border conditions. For systematizing the computation of average slopes and water depths of the profiles, two methods were used to discard the outliers in the extreme regions of the channel. For both methods, best-fit lines were obtained for different ranges of intermediate points, i.e., for different combinations of the downstream and upstream limits of the profiles. Table 3.18 shows the combinations of the downstream and upstream limit rulers for the reaches considered for line-fitting to the measurements (combinations used were the same for all runs, except for runs M1E2 and M2E5, for which the extend of the bed in the channel was shorter). For the first method 21 reaches were used, while for the second 42. As an example, Figure 3.32 shows the measured profiles, computed energy profiles and best-fit lines to the profiles, for two different runs. The downstream boundary condition for the considered intermediate reaches was not more than 3 meters above the downstream end of the channel, since the reaches upstream of this point used to be more stable (e.g., bedforms were more regular in geometry) and not affected by the exit of the channel.

For the j-th intermediate reach considered in the bed and water profiles measured at time n of a given run (Table 3.22 shows the elapsed time at which each profile was measured during each run), fitted linear functions for the bed and water elevations are given as:

$$\left[\bar{z}_b^n = A_b + B_b x\right]^j \quad (3.31), \text{ and } \quad \left[\bar{z}_w^n = A_w + B_w x\right]^j \quad (3.32)$$

Table 3.18 Pairs of rulers considered as upstream and downstream borders for delimiting a range of measured elevations of the bed and water surface to obtain best-fit lines. For the first method only pairs in shaded boxes were considered (21 reaches), while for the second method all the shown pairs were used. For run M1E2 only the last three columns of the three groups of shaded boxes were used, and the pairs (4,20), (4,19) and (4,18) in both methods; while for run M2E5 in method 1 additional pairs used extended combinations until ruler 14. The x coordinate of each ruler is shown in Table AIII.2 in Appendix III. Ruler 1 corresponds to the downstream end of the channel, while ruler 24 to the upstream.

Downstream ruler	1	1	1	1	1	1	1	1	1	1	1	1	1	1	2	2	2	2	2	2	2
Upstream ruler	24	23	22	21	20	19	18	17	16	15	14	13	12	11	24	23	22	21	20	19	18
Downstream ruler	2	2	2	2	2	2	2	3	3	3	3	3	3	3	3	3	3	3	3	3	3
Upstream ruler	17	16	15	14	13	12	11	24	23	22	21	20	19	18	17	16	15	14	13	12	11

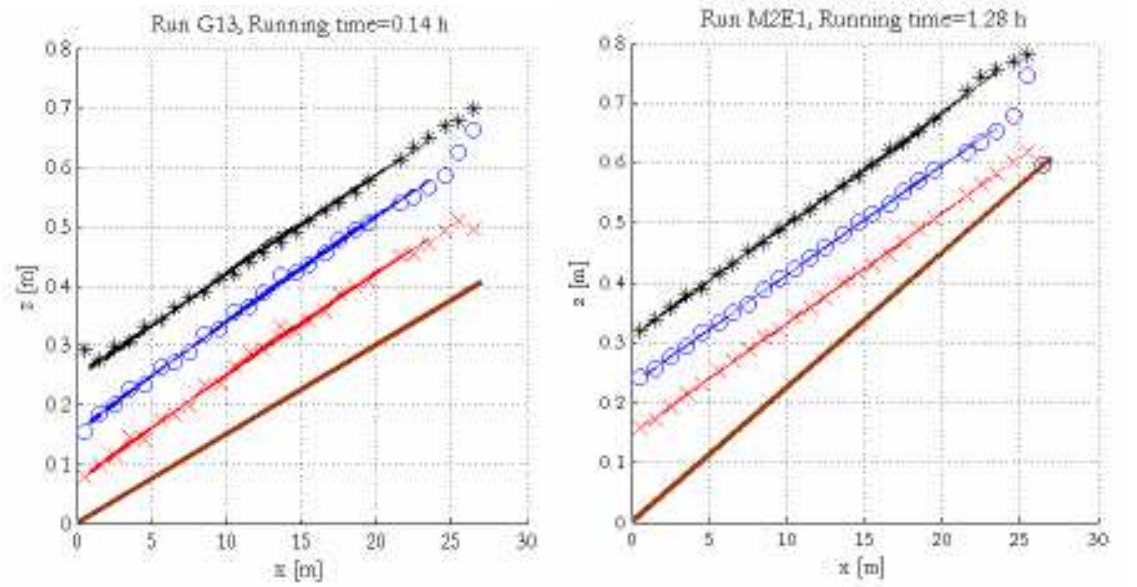

Figure 3.32. Energy gradient profile (black asterisks) determined with eq.(3.33), measured water surface profile (blue circles), measured bed surface profile (red x's), and bottom of the channel (thick continuous line) for one measurement in two different runs. Also shown are all the best-fit lines for the different intermediate ranges of the profiles used to apply the two methods for determining average water depths and energy slopes. Note that scatter of points for bed and water measured elevations is higher for run G13 than for run M2E1, since bedforms were steeper in run G13 than in run M2E1.

respectively, where A_b, A_w, B_b and B_w are fitted constants. The average slope of the bed and water profiles is considered to be equal to B_b and B_w, respectively. In turn, elevation of the energy grade line at each measured point is given by

$$E = z_w + \alpha_c \frac{V^2}{2g} \qquad (3.33)$$

where E is the elevation of the energy grade line, g is gravitational acceleration, V is mean flow velocity, z_w is the elevation of water surface (obtained from eq.[3.7]), and α_c is Coriolis coefficient, which was taken as unity. Introducing the water discharge Q_w and water depth H_e using the continuity principle, i.e. $Q_w=VH_eB$, eq.(3.33) is transformed into

$$E = z_w + \frac{Q_w^2}{2gH_e^2B^2} \qquad (3.34)$$

where B is the channel width (0.75 m). H_e was computed from

$$H_e = z_w - \bar{z}_b \qquad (3.35)$$

which is the difference between the measured water surface elevation [eq.(3.7)] and the mean bed elevation obtained with the best-fit line at the corresponding measurement point [eq.(3.31)]. The mean bed elevation was used instead of the measured bed elevation, in order to soften the high variations produced by the passage of bedforms and thus avoid a large scatter in computed energy values (due to the quadratic exponent of water depth in eq.[3.34]). For the computed values of energy elevations, best-fit lines were obtained by least-squares, given as

$$\left[\bar{E}^n = A_e + B_e x\right]^j \qquad (3.36)$$

where A_e and B_e are fitted constants, being B_e the slope of the energy grade line for the j-th reach at time n. Since it should be expected that uniform flow occurred during mobile-bed equilibrium conditions, an thus it would be satisfied that $B_b \approx B_w \approx B_e$, the final mean slope of

the energy gradient was determined with the average of the computed bed, water and energy slopes, i.e.

$$\overline{S}_j^n = \left[\frac{B_b + B_w + B_e}{3} \right]^{n,j} \tag{3.37}$$

Finally, water depth was determined with the average of water depths in the delimited reach j, i.e.

$$\overline{H}_j^n = \left[\frac{1}{n_p} \sum_{i=1}^{n_p^j} \left(z_{w,i} - z_{b,i} \right) \right]^{n,j} \tag{3.38}$$

where n_p is the number of measured points in the intermediate reach considered, and $z_{b,i}$ and $z_{w,i}$ are the bed and water surface elevations in the i-th ruler given by eqs.(3.5) and (3.7).

Accordingly, for each run at time n, there was a value of energy slope and a value of mean water depth for each intermediate reach j considered (reaches given by the pairs of rulers in Table 3.18). The methods used to obtain the definitive values of energy slope and water depth for the profiles at time n of a run are described as follows.

- Method 1. It was assumed that the best the linear regression adjusted to the data, the most representative it would be of the average conditions in the channel. Hence, the representative energy slope and water depth at time n of a run were obtained as an average of the mean slopes and mean depths of the considered reaches that gave the best linear fits. For evaluating the performance of linear regressions, standard deviations were computed with

$$\overline{\sigma}_b^j = \left(\frac{\sum_{i=1}^{i=n_p} \left[z_{b,i}(x_i) - \overline{z}_b^j(x_i) \right]^2}{n_p - 1} \right)^{\frac{1}{2}} \tag{3.39}$$

$$\overline{\sigma}_w^j = \left(\frac{\sum_{i=1}^{i=n_p} \left[z_{w,i}(x_i) - \overline{z}_w^j(x_i) \right]^2}{n_p - 1} \right)^{\frac{1}{2}} \tag{3.40}$$

where $\overline{\sigma}_b$ and $\overline{\sigma}_w$ are the standard deviations of the measured bed and water elevations (z_b and z_w), respectively, with respect to the lines of best-fit (eqs.[31] and [32]), and n_p is the number of rulers within the reach j considered. Data for all the 21 reaches considered (limits for each reach are shown in Table 3.18) were ordered from the lowest to highest standard deviations in two groups, one for the bed profile and one for the water profile. The first ten reaches of each group were used to obtain the definitive values of energy slope and water depth. Therefore, the definitive energy slope and water depth for the run at time n were obtained as

$$S^n = \frac{\sum_{j=1}^{j=10} \overline{S}_{j(b)} + \sum_{j=1}^{j=10} \overline{S}_{j(w)}}{20} \tag{3.41}$$

$$H^n = \frac{\sum_{j=1}^{j=10} \overline{H}_{j(b)} + \sum_{j=1}^{j=10} \overline{H}_{j(w)}}{20} \tag{3.42}$$

where subscripts (b) and (w) refer to the bed and water groups of data ordered from lower to higher standard deviations. From the 20 values used for calculating the

average slopes and water depths, it is likely that some values were considered in the two groups. With this, the values related to low standard deviations appearing in both, bed and water profiles, were overrepresented and thus had a higher influence in the computed average conditions.

Tables 3.19 and 3.20 show energy slopes and water depths obtained with eqs.(3.41) and (3.42), respectively. The standard deviation of the 20 values of energy slopes considered for each profile can be calculated as

$$\sigma_e^n = \left[\frac{\sum_{j=1}^{j=10} \left(\overline{S}_{j(b)} - S^n \right)^2 + \sum_{j=1}^{j=10} \left(\overline{S}_{j(w)} - S^n \right)^2}{20} \right]^{\frac{1}{2}} \qquad (3.43)$$

This standard deviation is a sort of measure of the uncertainty of the computed energy slopes. The average of this measure, given as a percentage of the energy slope, for all the profiles and runs, was as low as 1.1%±0.7%, with a maximum value of 4.2% in one of the profiles of run S3. The average of a similar deviation but for water depths was as low as 0.5%±0.3%.

- Method 2. Uniform flow prevailed in the channel during the runs (excluding the zones with an influence of the channel entrance and exit); consequently, bed, water and energy profiles were approximately parallel. In this method, the assumed uniform flow condition in the channel was used for determining the representative average energy slopes and water depths. It was considered that the intermediate reaches with the lowest difference between the bed slope and the water slope obtained from linear regression, were the most representative of the average conditions in the channel. The following parameter was used for evaluating the difference between the two profiles

$$B_{dif}^j = \left| 1 - \left(\frac{B_b^j}{B_w^j} \right) \right| \qquad (3.44)$$

B_{dif} was computed for all the 42 intermediate reaches considered, whose limits are shown in Table 3.18. Then, data were sorted out from the lowest to highest B_{dif} values. The first ten reaches in the sorted list were used to obtain averages for the definitive values of energy slope and water depth. Energy slope and water depth for the run at time n were thus obtained as

$$S^n = \frac{\sum_{j=1}^{j=10} \overline{S}_j}{10} \qquad (3.45)$$

$$H^n = \frac{\sum_{j=1}^{j=10} \overline{H}_j}{10} \qquad (3.46)$$

Table 3.21 shows results for the value of B_{dif} ranked tenth, for each profile of every run. The average of this value, as a percentage, considering all the profiles in all runs, was as low as 1.6%±1.64%; hence, the uniform flow assumption can be considered reasonable.

Plots of variables related to the elapsed time during each run, for the results obtained with the two methods described above are shown in Appendix XIII. In these plots it can be seen that there were no important differences between the results obtained with the two methods. The average difference between slopes obtained with method 1 and slopes obtained with method 2 was only 1.15%±1.14%, while for water depths the average

difference was only 0.55%±0.72%. Graphs for time variation of energy slopes and water depths in Appendix XIII are also quite similar to graphs presented before in Appendix VII. For these latter graphs, water depths and bed and water slopes were computed using best-fit lines for a single fixed intermediate reach in each run series. The advantage of the methods presented in the present Section, is that they use most of the information collected in the experimental campaigns, and thus, in a certain way, by doing this the uncertainty of the variables derived is reduced.

In Appendix XIII, graphs with the time variation of the standard deviation of the bed and water profiles with respect to the fitted lines are presented as well (the lowest graph for each run). These graphs serve as a representation of the evolution of the size of the bedforms and water waves during the runs. These standard deviations were determined first with eqs.(3.39) and (3.40) for the different intermediate reaches analyzed, and then the values shown in the graphs were obtained from average values, as it was done for slopes and water depths using eqs.(3.41) and (3.42) for method 1, and using eqs.(3.45) and (3.46) for method 2. A trend was found between the bed elevation scatter shown in those graphs in Appendix XIII and the variation of the computed slopes given by eq.(3.43), which can be seen in Figure 3.33. Somehow, this was an expected trend, which can be interpreted as an increase in the uncertainty of measured energy slopes as the bedforms become steeper.

For the definitive data set, energy gradient slopes and water depths determined with method 1 (Tables 3.19 and 3.20) were considered, since for this method scatter of the variables was slightly lower.

Table 3.19 Average energy slopes obtained from each measured bed and water profile using method 1. Values for considered equilibrium state profiles are shown in shaded boxes.

Profile no.	**1**	**2**	**3**	**4**	**5**	**6**	**7**	**8**	**9**	**10**	**11**	**12**	**Average in equilibrium**	
Run						**S x10²**								
G12	2.30	2.23	2.18	2.14	2.14	-	-	-	-	-	-	-	2.14	±0.000
G13	1.77	1.82	1.90	1.89	1.85	1.78	-	-	-	-	-	-	1.85	±0.052
G14	1.62	1.72	1.89	1.89	1.87	1.86	-	-	-	-	-	-	1.88	±0.016
G15	1.85	1.75	1.68	1.67	1.63	1.63	1.61	1.61	-	-	-	-	1.62	±0.015
G16	1.43	1.36	1.32	1.28	1.26	1.25	1.21	1.22	1.20	1.22	-	-	1.22	±0.008
G17	0.49	0.51	0.53	0.54	0.55	0.56	0.57	0.57	0.58	0.58	0.57	-	0.58	±0.004
M1E1	1.02	0.94	0.85	0.84	0.83	0.82	0.80	0.81	0.82	0.82	0.81	-	0.81	±0.009
M1E2	1.99	1.79	1.69	1.68	1.68	1.64	1.68	1.66	-	-	-	-	1.67	±0.016
M1E3	1.72	1.75	1.74	1.70	1.73	-	-	-	-	-	-	-	1.73	±0.020
M1E4	1.69	1.60	1.54	1.50	1.53	1.54	1.54	1.53	1.53	-	-	-	1.53	±0.014
M1E5	1.41	1.33	1.33	1.31	1.27	1.31	1.32	1.28	1.30	1.29	-	-	1.30	±0.018
M1E6	0.80	0.72	0.65	0.64	0.62	0.60	0.61	0.59	0.58	0.60	0.60	0.60	0.59	±0.009
M2E1	1.91	1.83	1.78	1.78	1.78	1.76	1.78	1.77	-	-	-	-	1.77	±0.008
M2E2	1.63	1.65	1.66	1.66	1.62	1.69	1.64	1.67	1.64	1.63	-	-	1.66	±0.024
M2E3	1.63	1.62	1.60	1.57	1.58	1.60	1.66	1.60	1.57	-	-	-	1.60	±0.033
M2E4	1.47	1.39	1.41	1.43	1.45	1.48	1.46	-	-	-	-	-	1.46	±0.012
M2E5	1.10	1.07	0.97	0.92	0.93	0.99	0.95	1.00	-	-	-	-	0.98	±0.024
M2E6	0.71	0.67	0.65	0.64	0.67	0.63	0.64	0.66	-	-	-	-	0.64	±0.012
S1	1.37	1.46	1.56	1.60	1.66	1.53	1.55	1.65	1.52	1.51	-	-	1.55	±0.056
S2	1.34	1.39	1.16	1.23	1.24	1.27	1.21	1.15	1.23	1.25	1.29	1.23	1.23	±0.041
S3	1.11	1.00	0.97	0.83	0.82	0.87	0.79	0.84	0.86	0.79	0.78	-	0.82	±0.041
S4	0.63	0.60	0.60	0.61	0.59	0.59	0.63	-	-	-	-	-	0.60	±0.020

Table 3.20 Average water depths obtained from each measured bed and water profile using method 1. Values for considered equilibrium state profiles are shown in shaded boxes.

Profile no.	1	2	3	4	5	6	7	8	9	10	11	12	Average in equilibrium
Run	H [cm]												
G12	6.9	6.8	7.0	6.8	6.8	-	-	-	-	-	-	-	6.8 ±0.00
G13	9.0	9.1	9.3	8.8	9.3	9.2	-	-	-	-	-	-	9.2 ±0.21
G14	8.0	7.9	7.7	7.5	7.4	8.0	-	-	-	-	-	-	7.6 ±0.23
G15	7.6	7.8	7.9	7.7	7.9	7.9	7.9	7.9	-	-	-	-	7.9 ±0.02
G16	8.4	8.4	8.5	8.4	8.5	8.6	8.4	8.4	8.6	8.5	-	-	8.5 ±0.11
G17	11.4	11.3	11.2	11.1	11.0	11.0	10.9	11.1	11.0	10.8	10.8	-	10.9 ±0.08
M1E1	9.4	9.8	10.3	10.1	10.2	10.5	10.3	10.3	10.5	10.4	10.2	-	10.4 ±0.10
M1E2	8.4	8.7	8.5	8.6	8.6	8.9	8.7	8.5	-	-	-	-	8.6 ±0.16
M1E3	7.5	7.6	7.5	7.6	7.6	-	-	-	-	-	-	-	7.6 ±0.02
M1E4	8.3	8.7	8.7	8.7	8.4	8.9	8.8	8.7	8.7	-	-	-	8.7 ±0.14
M1E5	8.9	9.0	9.2	9.1	9.0	9.1	8.9	8.8	9.0	9.1	-	-	9.0 ±0.13
M1E6	10.4	11.0	11.2	11.3	11.5	11.4	11.5	11.4	11.3	11.4	11.4	11.26	11.3 ±0.07
M2E1	8.1	8.2	8.2	8.1	8.2	8.1	8.3	8.0	-	-	-	-	8.1 ±0.11
M2E2	8.2	8.3	8.3	8.1	8.1	8.1	8.0	7.8	8.3	7.9	-	-	8.0 ±0.19
M2E3	8.0	8.2	8.3	8.1	8.3	8.3	8.3	8.3	8.5	-	-	-	8.3 ±0.12
M2E4	9.0	9.0	9.3	9.2	9.0	8.6	9.1	-	-	-	-	-	8.9 ±0.27
M2E5	9.6	9.9	10.1	10.5	10.3	10.3	10.6	10.0	-	-	-	-	10.3 ±0.33
M2E6	11.2	11.0	11.3	11.2	11.3	11.3	11.2	11.4	-	-	-	-	11.3 ±0.12
S1	10.0	10.5	10.8	10.4	10.7	10.2	10.4	10.1	10.7	10.0	-	-	10.3 ±0.29
S2	9.3	10.4	10.4	10.3	10.8	10.8	10.9	11.3	11.0	11.3	11.0	10.33	10.9 ±0.31
S3	10.5	10.9	10.5	11.8	11.9	11.9	11.5	12.1	12.2	12.1	11.7	-	11.9 ±0.25
S4	13.0	12.8	12.9	12.5	12.9	13.1	13.5	-	-	-	-	-	13.0 ±0.41

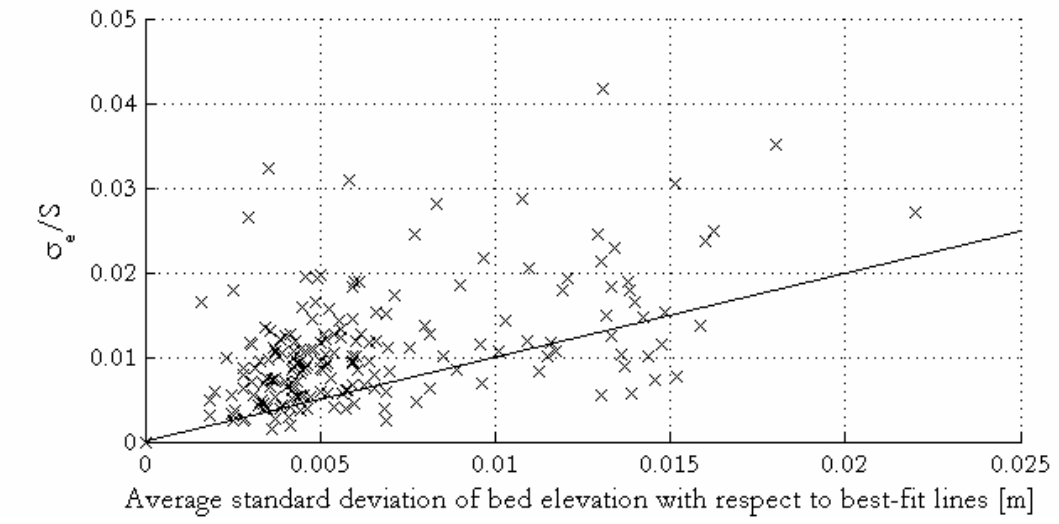

Figure 3.33. Values for all measured bed profiles of the ratio between the energy slope standard deviation and mean value of energy slope, σ_e/S, for the 20 data used to apply eq.(3.41), as a function of the average scatter of the measured bed elevations with respect to the best-fit lines for different intermediate bed reaches. The main trend in the graph can be interpreted as a bias toward higher uncertainty in computed average bed slopes for steeper bedforms in the bed.

Table 3.21 Value of the parameter used to measure the parallelism between bed and water profiles in method 2, for each run and profile. The value presented was the tenth lowest in the list for data obtained with different intermediate reaches in the channel. For data in this Table, eq.(3.44) has been applied without considering the absolute value, i.e., $B_{dif}=1-(B_b/B_w)$, this in order to recognize likely trends on flow acceleration or deceleration.

Profile no.	**1**	**2**	**3**	**4**	**5**	**6**	**7**	**8**	**9**	**10**	**11**	**12**	**Average**
Run						$B_{dif}^{j=10}$ **x10²**							
G12	-0.4	-0.4	-0.2	0.3	0.3	-	-	-	-	-	-	-	-0.04
G13	2.7	-0.3	-0.4	1.3	-2.3	0.5	-	-	-	-	-	-	0.11
G14	0.3	-1.1	-0.2	-0.4	1.7	-1.7	-	-	-	-	-	-	-0.12
G15	-0.2	0.7	0.4	-0.6	0.3	0.2	-0.4	0.7	-	-	-	-	0.09
G16	-1.5	-2.6	-1.0	-2.9	0.4	0.6	1.4	0.5	0.7	-1.0	-	-	-0.45
G17	-7.0	2.8	0.5	-1.1	-1.3	-0.8	-1.6	1.6	-0.8	-0.8	-1.3	-	-0.80
M1E1	0.5	1.0	-1.0	-2.2	-1.3	0.6	-0.6	1.0	-0.8	-1.9	-1.0	-	-0.47
M1E2	0.7	2.1	3.1	5.9	-2.5	1.5	2.8	2.3	-	-	-	-	1.31
M1E3	0.4	0.2	0.3	-0.4	0.4	-	-	-	-	-	-	-	0.08
M1E4	0.9	-0.6	0.1	1.9	-1.5	-0.4	-0.4	0.5	0.5	-	-	-	0.10
M1E5	-1.6	-0.4	-2.2	-2.4	-0.3	0.7	0.7	1.4	0.5	-0.8	-	-	-0.37
M1E6	0.8	-1.9	-1.0	1.7	1.9	1.9	2.4	-1.5	-1.2	2.6	2.2	-3.7	0.34
M2E1	-0.4	0.4	0.2	-0.1	0.4	-0.5	-0.15	0.4	-	-	-	-	0.02
M2E2	1.7	0.4	-1.0	-0.4	2.3	0.3	0.9	-1.1	1.0	2.6	-	-	0.56
M2E3	1.9	0.9	-0.3	0.8	-0.5	0.5	0.2	0.4	0.3	-	-	-	0.35
M2E4	-0.5	-2.9	-0.8	-0.3	-1.9	-0.9	-1.9	-	-	-	-	-	-0.78
M2E5	0.7	1.0	-2.0	2.0	-1.3	-1.1	-3.7	1.5	-	-	-	-	-0.24
M2E6	-1.0	-0.6	-0.8	-0.7	-1.3	2.0	1.1	1.7	-	-	-	-	0.04
S1	1.6	1.4	1.0	-1.2	-5.4	2.0	1.9	1.7	3.4	3.8	-	-	0.85
S2	11.5	3.3	2.1	0.9	-1.7	2.1	3.2	-2.8	3.0	2.7	1.7	2.8	2.40
S3	1.4	-3.2	3.5	4.9	6.2	1.3	-2.2	1.4	-6.6	-2.0	1.8	-	0.53
S4	-2.3	-2.2	-3.7	-2.5	2.4	3.0	-12.8	-	-	-	-	-	-1.50

3.4.2 Equilibrium state

A bed of granular material set in motion by flowing water is said to be in a mobile-bed equilibrium state if average flow and sediment transport conditions remain constant in space and time. Hence, when mobile-bed equilibrium state prevails in a flume, average values of water discharge, volume of solid discharge, flow velocity, water depth and energy slope remain constant. Any important change of any of these quantities would produce morphodynamic disequilibrium, and the evolution of bed and flow toward a new balance condition.

For the experiments described herein, the dependent variable was mobile-bed equilibrium state. The initially imposed conditions of fixed water discharge and sediment-feeding rate produced an imbalance between the sediment supplied to the channel and the sediment transport capacity of the flow; as a response, the bed, hydraulic variables and sediment transport along the channel evolved to eventually reach an equilibrium sate.

3.4.2.1 Criterion for testing equilibrium

The proof in the experiments of mobile-bed equilibrium having been attained was the equality of the constant sediment-feeding rate and the sediment transport rate passing through the downstream end of the channel for each size fraction, and the persistence of

average water-depths, bed- and water-slopes, and bedform dimensions over time. A practical criterion was required to identify the moment at which equilibrium conditions were attained in the channel. An indicative simplified criterion used considered that when equilibrium state was reached, changes in the bed with time were small enough for not being detected by the precision of the measurement devices. Accordingly, with reference to the scheme shown in Figure 3.34, the criterion established considered that the vertical increment of the bed surface during one hour had to be lower than Δz, which is the precision of the bed elevation measurement. The choice of a temporal increment of one hour was somehow arbitrary, but it was reasonable according to the observations in run series I and II. The vertical increment of the bed surface can be transformed into volume of sediment by considering the volume eroded (or aggraded) as a wedge of bed along the effective length of the channel, whose height is Δz. Accordingly, the equilibrium criterion can be expressed as

$$\frac{dW}{dt} \le \frac{0.5\Delta z L_e B(1-\varepsilon)\rho_s}{1\mathbf{h}} \tag{3.47}$$

where B is the channel width (0.75 m), L_e is the bed effective length (≈26 m), W is the instantaneous weight on the hoppers, t is time, Δz is the increment of bed elevation equal to the precision of the bed elevation measurement, ε is the bed porosity (≈0.4), and ρ_s is the density of the bed material (≈2610 kg/m^3). For defining the precision of the bed elevation measurement, it is more reasonable to use the size of the sediment particles rather than the precision of the rulers on the walls. Consequently, a size of 2.5 mm, which is in between sand and gravel grain sizes, was considered. Ascribing values to the variables in eq.(3.47), it was found that equilibrium state could be considered to have been attained when the weight gradient in the hoppers with respect to time was approximately dW/dt<40 kg/1h, which means that during one hour the volume of sediment in the hoppers would change less than 40 kg. This value was compared with the result of eq.(3.1) at every instant during the experiments. For run series with sediment mixtures, the equilibrium condition was tested for the two hoppers, and so the criteria given by eq.(3.47) considered the sum of mass weights of the two hoppers.

In practice, the equilibrium criterion described above was difficult to be implemented, since difficulties and instabilities in the operation of the sediment return system often caused that the measurements of the variation of weight in the hoppers were not completely a precise measure of the sediment load going out of the channel, at least in the resolution required for the equilibrium criterion. Hence, the criterion given by eq.(3.47) was used along with plots of the bed and water slopes evolution during the run to asses if equilibrium state had been attained. Determining whether equilibrium had been accomplished in the run was important, because in that moment the first phase of the experiment was concluded.

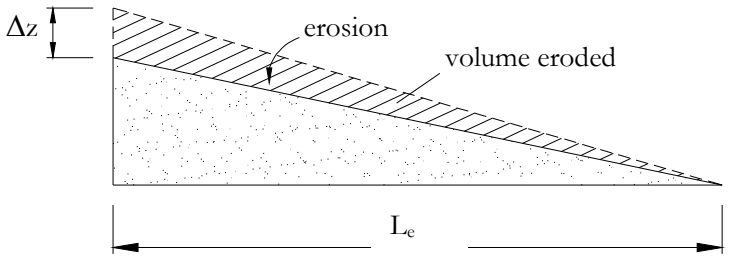

Figure 3.34. Schematic representation of a section of the channel bed and the hypothetic wedge of sediment considered to be removed by erosion during a certain time interval.

3.4.2.2 Average values of variables in equilibrium state

In order to obtain definitive values of hydraulic parameters for the data set, the temporal variation graphs in Appendixes VII and XIII were thoroughly revised to determine which measurements could be considered with confidence as pertaining to the equilibrium state. Definitive values for the data set were obtained by averaging the variables measured during the considered equilibrium state of each run.

A vertical green line in plots of Appendix XIII indicates time considered as that for which the first measurement in equilibrium state was performed. It is known that the process by which the bed approaches to equilibrium, like other time-dependant processes in sedimentation engineering, can be represented with an exponential law. The gradient of the function is steep during the first moments, then the gradient becomes mild, and finally the function describes an asymptotic progression. In determining the benchmark of equilibrium onset, the inflection zone where the function would change from a mild gradient to an asymptotic decay was tried to be identified in time-dependant plots of weight in the hoppers (uppermost graphs in Appendix VII) and of energy slope and water-depth (Appendix XIII). Equilibrium was considered to occur after that inflection. The scatter of the points hindered in some cases the identification of the inflection (e.g., M2E3 and M2E4) and in some others the initial variables were quite close to the equilibrium ones (e.g., run M1E3 and M2E2), so that the path toward equilibrium was covered up by the precision of the measurements. In general, a trend indicating equilibrium state was identifiable in most of the runs, although measurements during equilibrium showed sometimes high fluctuations, which could be attributed to the accuracy of the measurements and the passage of bedforms. In this regard, although a trend could be distinguished in most of the runs toward stabilization of the steepness of the bedforms during equilibrium state, sometimes the bed configuration was extremely unstable and this could have induced important variations in the measured bed slopes and water depths.

It was found that for some runs, the considered onset for equilibrium state did not match with the end of the transition phase of the run, i.e., that for some runs equilibrium was not attained during that phase and some time during the considered equilibrium phase of the run was required to reach actual equilibrium conditions. In general, for just one run, run G12, there was some uncertainty whether equilibrium was reached. Nevertheless, for the definitive values in the data set, it has been assumed that the two last measured profiles in run G12 were very close to equilibrium, and that considering them as being representative of equilibrium state is reasonable; although more time would have been required for reaching actual equilibrium and the actual equilibrium slope would be slightly lower, it is likely that the difference would have not been important.

Table 3.22 shows the elapsed-times for which bed and water surface profiles were measured for each run, and indicates those profiles considered as pertaining to the equilibrium state. For these latter profiles average values of slope and water depth were obtained from representative values presented in Tables 3.19 and 3.20; these average values, presented with their standard deviation in the last column of those same tables, respectively, were considered as the equilibrium state representative values for the definitive data set. The average standard deviation of equilibrium slopes was only 1.70% of the average values, while for water-depth it was only 1.72%. Plots of the measured bed and water profiles in the considered equilibrium state of each run, along with the average best-fit lines to each profile, are shown in Appendix XIV.

Table 3.22 Elapsed-times when bed and water surface profiles were measured during each run. These are the times to which values in Tables 3.19 to 3.21 can be associated. Times for considered equilibrium state profiles are shown in shaded boxes. Time equal to zero would correspond to the beginning of the run.

Profile no.	1	2	3	4	5	6	7	8	9	10	11	12
Run	**Time [h]**											
G12	0.9	1.9	2.9	4.7	5.0	-	-	-	-	-	-	-
G13	0.1	1.2	2.0	2.7	3.5	4.5	-	-	-	-	-	-
G14	0.1	1.0	2.1	3.1	4.1	4.9	-	-	-	-	-	-
G15	0.0	1.0	2.0	3.0	4.0	5.0	6.0	6.5	-	-	-	-
G16	0.1	1.1	2.1	3.1	4.1	5.1	6.1	6.8	7.8	8.8	-	-
G17	0.7	1.7	2.7	3.7	4.7	5.7	6.7	7.7	8.6	9.3	10.3	-
M1E1	0.5	1.3	2.7	3.7	4.8	5.8	6.8	7.8	9.6	11.6	16.2	-
M1E2	0.2	0.9	1.5	2.5	3.6	4.9	5.9	6.8	-	-	-	-
M1E3	0.7	1.7	2.7	3.2	6.2	-	-	-	-	-	-	-
M1E4	0.3	1.3	2.4	3.2	3.7	4.5	5.5	6.5	7.7	-	-	-
M1E5	0.3	1.4	2.4	3.5	4.5	5.4	6.2	7.2	8.2	9.5	-	-
M1E6	0.6	1.6	2.7	3.8	4.8	5.9	7.0	7.5	8.3	9.5	10.5	11.9
M2E1	0.3	1.3	2.3	3.3	4.3	5.2	5.9	7.6	-	-	-	-
M2E2	0.6	1.6	2.6	3.6	3.8	5.1	6.5	8.6	9.7	11.1	-	-
M2E3	0.4	1.4	2.4	3.4	4.4	5.2	6.3	8.2	8.7	-	-	-
M2E4	0.6	1.6	2.6	3.6	5.2	6.7	8.3	-	-	-	-	-
M2E5	0.6	1.6	4.1	5.2	6.2	7.5	9.0	10.9	-	-	-	-
M2E6	1.1	2.2	3.2	4.3	5.3	6.3	7.2	9.8	-	-	-	-
S1	0.4	1.4	2.4	3.5	4.4	5.4	6.5	7.3	9.2	11.0	-	-
S2	0.4	1.4	2.4	3.4	4.4	5.4	6.4	7.3	8.0	10.0	12.3	13.9
S3	0.4	1.4	2.5	3.5	4.5	5.5	6.5	7.1	9.0	12.8	13.3	-
S4	0.6	1.8	2.8	3.8	3.9	4.6	6.3	-	-	-	-	-

3.4.2.3 Variation of bed and water surface elevations in equilibrium state

The variability of the measured values of bed and water surface elevations is closely related to the characteristics of the bedforms and stationary waves, respectively. Hence, the statistical characterization of the variation of these elevations may serve as an indication of the steepness of the undulations next to the channel wall; since the measurement rulers were attached to the wall, the dispersion of the measurements represents only the variation of the bedforms and waves in that section. In the case of the bed surface, the dispersion of the bed elevation can be useful to find correlations for the bed resistance owed to bedforms.

The variability of the elevation measurements was calculated for every measurement point in the channel as a standard deviation of the elevations measured during the considered equilibrium state, i.e., for all profiles marked with shaded boxes in Tables 3.19, 3.20 and 3.22. Accordingly, for a given run the average bed elevation in equilibrium state at the i-th measurement point was computed with

$$\left\langle z_b(x_{b,i})\right\rangle_E = \frac{1}{2n_{PE}}\left(\sum_{n=1}^{n=n_{PE}} z_{bD}^n(x_{b,i}) + \sum_{n=1}^{n=n_{PE}} z_{bU}^n(x_{b,i})\right) \qquad (3.48)$$

where n refers to the considered measured profile among the profiles measured during equilibrium state, n_{PE} is the total number of measured profiles in equilibrium state (summarized in Table 3.23), and z_{bD} and z_{bU} are the vertical coordinates for the values measured on the rulers following the downstream and upstream directions (this are the

same values used for computing the average bed and water elevations in eqs.3.5 and 3.7), respectively, at the i-th measurement point with horizontal coordinate $x_{b,i}$. The standard deviation of measurements in equilibrium at point $x_{b,i}$ was thus obtained from

$$\sigma_{bE}(x_{b,i}) = \left[\frac{1}{2n_{PE}} \left(\sum_{n=1}^{n=n_{PE}} \left[z_{bD}^{n}(x_{b,i}) - \left\langle z_b(x_{b,i}) \right\rangle_E \right]^2 + \sum_{n=1}^{n=n_{PE}} \left[z_{bU}^{n}(x_{b,i}) - \left\langle z_b(x_{b,i}) \right\rangle_E \right]^2 \right) \right]^{\frac{1}{2}} \quad (3.49)$$

Equations equivalent to eqs.(3.48) and (3.49) were obtained for the measurements of water surface elevation.

Figures in Appendix XV show plots with the computed values of σ_{bE} and σ_{wE} (bed and water surface standard deviation, respectively) for each run. An evident trend in these plots is an increase of σ_{bE} and σ_{wE} with the downstream direction. Such a trend is related to the genesis of the bedforms observed during the experiments along the channel. In general terms, at the uppermost part of the bed small perturbations with a high celerity formed, which coalesced and grew in size and decelerate until reaching an approximately stable average size and velocity, roughly in the downstream third of the channel effective length.

For computation of a representative value of the variation of the bed and water surface elevations for each run, the approximate point n_p, at which the bed and water perturbations were, in general terms, stable was considered. For the channel reach comprised between x=0.5 m and $x=n_p$ (for each run, this region is shown in the plots of standard deviations in Appendix XV), to obtain the representative value of bed elevation variation an average was obtained as

Table 3.23 Parameters for computation of bed surface variability in every measured point, and representative values of the variation of bed and water surface elevations for each run during equilibrium state.

Run	n_{EP}	Time for first profile in eq. [h]	Measurement point for stable bedforms n_p [m]	σ_b [mm]	σ_w [mm]
G12	2	4.7	12	3.3	2.5
G13	4	2.0	13	13.0	9.0
G14	4	2.1	14	5.3	4.7
G15	3	5.0	18	4.7	5.0
G16	4	6.1	13	5.0	4.8
G17	3	8.6	15	2.6	2.6
M1E1	5	6.8	16	7.3	5.2
M1E2	6	1.5	18	9.2	8.1
M1E3	4	1.7	10	6.6	5.3
M1E4	6	3.2	13	8.9	7.1
M1E5	6	4.5	11	9.2	7.0
M1E6	4	8.3	10	9.4	4.1
M2E1	5	3.3	14	4.5	3.0
M2E2	5	5.1	13	6.0	4.0
M2E3	5	4.4	18	7.6	5.3
M2E4	3	5.2	16	9.7	8.1
M2E5	3	7.5	18	9.3	7.2
M2E6	3	6.3	16	8.7	4.2
S1	5	5.4	12	17.2	12.8
S2	8	4.4	14	22.9	11.2
S3	6	5.5	10	20.6	8.3
S4	4	3.8	16	20.1	6.9

$$\sigma_b = \frac{1}{n_p}\sum_{i=1}^{i=n_p}\sigma_{bE}^{i} \qquad (3.50)$$

A similar equation was used for the representative water elevation variability. The computed values of σ_b and σ_w are shown in Table 3.23. Elapsed-times for the first profile considered in equilibrium state, and the considered number of measurement point for the onset of stable undulations in equilibrium state n_p, are presented in that table as well.

Figure 3.35 presents the ratio between σ_w and σ_b, as a function of the Froude number, for all the runs in the data set, sediment-recirculating runs and run M1E7 used for testing reproducibility. There is a trend toward an increase of the ratio up to roughly values of F=1, indicating that relative height of water surface waves is larger in transcritical and supercritical flows than in subcritical flows.

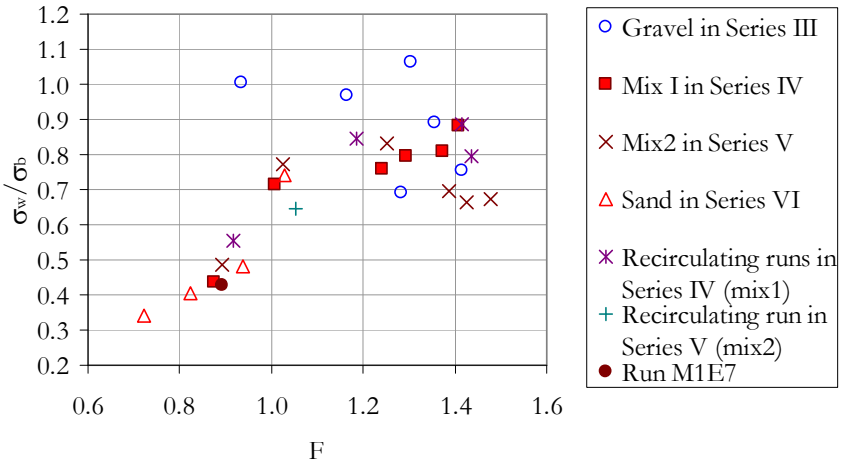

Figure 3.35. Ratio between the variation of the water surface and the variation of the bed surface during equilibrium state, as a function of the Froude number for runs of the definitive data set, sediment-recirculating runs and run M1E7.

3.4.3 Reproducibility

For testing the experimental reproducibility, four runs whose results were used in the definitive data set were compared with additional runs, named here "dummy runs", with similar independent variables. Data from dummy runs are shown in Table 3.24. Except for run M1E7, which was performed explicitly for testing reproducibility at the end of hybrid-feed runs with mixture 1, the rest of dummy runs correspond to runs carried out using the flume in a sediment-recirculating operation; the procedures and characteristics of sediment-recirculating runs are described in Section 3.3.1.4.2. Methods for computing hydraulic variables of the dummy runs were the same as those described in Section 3.4.1. Comparing hybrid-feed runs with sediment-recirculating runs would not be a rigorous test of reproducibility due to the particularities of each of both types of operation, especially for the consequences in sediment segregation and mobility; nevertheless, since equilibrium states reached by sediment-feed and -recirculating modes should be equivalent (Parker and Wilcock, 1993) the comparison here is valid.

Table 3.25 presents the results of comparing dummy runs with four runs of the definitive data set, namely, runs M1E6, M1E5, M1E2, and M2E5. For the comparison, for each variable the ratio between the value of the run of the data set and the value of the dummy run was obtained. Most of these ratios are close to one, and thus suggest that

differences between dummy and data set runs are within the order of magnitude of estimated accuracies of the measurements. It can be concluded from these results that dummy runs reproduced reasonably well the runs of the definitive data set. Only run M1R1 stands out as an exception, since for the comparison with run M1E6 the differences between sediment loads were roughly of 20%, while the difference in Froude number was only of 5%. Such a disparity may be attributed not to the processes in the channel but to the lack of accuracy of the measurements of sediment transport; since M1R1 was the first run performed using the flume in a sediment-recirculating mode, the method for measuring solid discharge with the hoppers had not been tested before and was faulty. This method was improved in subsequent runs, as explained in Section 5 of Appendix I.

Table 3.24 Measured and imposed variables for runs used to test reproducibility ("dummy runs"). Q_{ss}, Q_{sg}, and Q_s are the sand, gravel and total load sediment transport rates passing through the channel, respectively; Q_w is water discharge, H is water depth, S is bed slope, V is mean flow velocity and F is the Froude number.

Run	Q_{ss} [g/s]	Q_{sg} [g/s]	Q_s [g/s]	Q_{ss}/Q_s x 100	Q_w [l/s]	H [m]	S	V [m/s]	F	Q_s/Q_w [g/l]
M1E7	42	95	137	30.7	78.9	0.112	0.0063	0.94	0.89	1.74
M1R1	60	113	173	34.7	78.9	0.110	0.0065	0.95	0.92	2.19
M1R2	101	314	415	24.3	78.4	0.093	0.0128	1.13	1.18	5.29
M1R3	271	546	817	33.2	84.4	0.086	0.0165	1.30	1.41	9.69
M1R4	259	626	885	29.3	82.9	0.085	0.0159	1.31	1.44	10.68
M2R1	121	198	319	37.9	78.9	0.101	0.0099	1.05	1.05	4.04

As a second proof of reproducibility, Figure 3.36 shows the variation of slope as a function of sediment concentration for the runs performed for the data set and the dummy runs. Most of the data with similar characteristics show equal trends in Figure 3.36, giving thus evidence of the reproducibility of the runs.

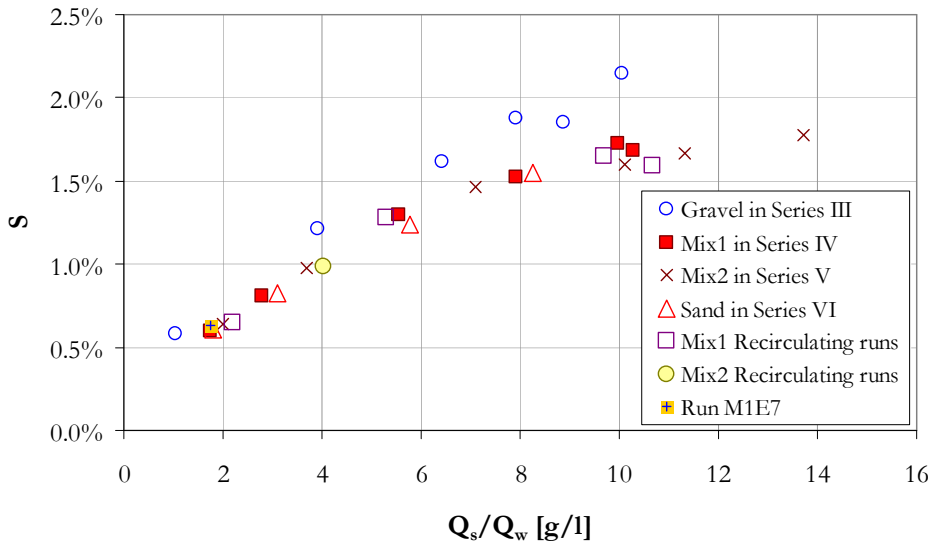

Figure 3.36. Plot of energy slopes vs sediment concentration for 28 of the experimental runs performed during the experimental campaign.

Table 3.25 Comparison between variables for some runs of the definitive data set and dummy runs summarized in Table 3.24. Q_{ss}, Q_{sg}, and Q_s are the sand, gravel and total load sediment transport rates passing through the channel, respectively, and the other variables have already been defined previously.

Run	Ratio between data set run and dummy run									
	Q_{ss}	Q_{sg}	Q_s	Q_{ss}/Q_s	Q_w	H	S	V	F	Q_s/Q_w
M1E6/M1E7	1.10	0.96	1.00	1.10	0.99	1.01	0.94	0.98	0.98	1.01
M1E6/M1R1	0.77	0.81	0.79	0.97	0.99	1.03	0.92	0.97	0.95	0.80
M1E5/M1R2	1.30	0.97	1.05	1.23	1.00	0.97	1.02	1.03	1.05	1.05
M1E2/M1R3	0.95	1.11	1.06	0.90	0.99	1.00	1.02	1.00	1.00	1.06
M1E2/M1R4	1.00	0.96	0.97	1.02	1.01	1.02	1.06	0.99	0.98	0.96
M2E5/M2R1	0.99	0.87	0.92	1.08	1.01	1.02	0.99	0.98	0.97	0.91

Table 3.26 Sediment characteristics, sediment transport and bulk flow conditions during equilibrium state in definitive runs.

Bed material	Run	D_{50} [mm]	σ_g [mm]	f_s (D<2.24 mm)	q_s [kg/s/m]	S	H [m]	V [m/s]	F	T_w [ºC]
GRAVEL	G12	4.8	1.27	0%	0.792	0.0214	0.068	1.16	1.42	12.4
	G13	3.8	1.38	0%	0.988	0.0185	0.092	1.21	1.27	13.0
	G14	4.4	1.35	0%	0.708	0.0188	0.076	1.18	1.37	13.5
	G15	4.1	1.47	0%	0.580	0.0162	0.079	1.14	1.29	13.5
	G16	3.8	1.38	0%	0.355	0.0122	0.085	1.06	1.16	13.0
	G17	4.3	1.37	0%	0.108	0.0058	0.109	0.96	0.93	13.8
SAND-GRAVEL MIXTURE 1	M1E1	3.0	1.78	32%	0.295	0.0081	0.104	1.01	1.00	14.5
	M1E2	3.3	1.74	31%	1.149	0.0167	0.086	1.30	1.42	14.8
	M1E3	3.2	1.70	31%	0.893	0.0173	0.076	1.18	1.37	15.3
	M1E4	3.4	1.78	31%	0.821	0.0153	0.087	1.20	1.30	15.5
	M1E5	3.3	1.74	31%	0.581	0.0130	0.090	1.16	1.23	16.0
	M1E6	3.0	1.80	35%	0.183	0.0059	0.113	0.93	0.88	16.0
SAND-GRAVEL MIXTURE 2	M2E1	2.5	1.87	44%	1.427	0.0177	0.081	1.28	1.44	17.9
	M2E2	2.5	1.71	44%	1.192	0.0166	0.080	1.32	1.49	18.0
	M2E3	2.5	1.75	45%	1.057	0.0160	0.083	1.26	1.40	19.5
	M2E4	2.4	1.75	45%	0.737	0.0146	0.089	1.17	1.25	19.5
	M2E5	2.5	1.74	43%	0.389	0.0098	0.103	1.03	1.02	19.2
	M2E6	2.3	1.70	47%	0.212	0.0064	0.113	0.94	0.89	20.0
SAND	S1	1.6	1.30	100%	0.877	0.0155	0.103	1.03	1.02	21.0
	S2	1.5	1.42	100%	0.615	0.0123	0.109	0.97	0.94	22.0
	S3	1.5	1.46	100%	0.328	0.0082	0.119	0.89	0.82	22.0
	S4	1.5	1.47	100%	0.191	0.0060	0.130	0.82	0.73	22.0

3.5 DEFINITIVE DATA SET

The sediment characteristics, sediment transport and bulk flow conditions of the definitive data set are summarized in Table 3.26. The values of unit solid discharges were computed by dividing the sum of values of sand and gravel transport rates, shown in Tables 3.8 and 3.9, respectively, by the channel width (B=0.75 m). The values for energy gradient slope and water depth were taken from average values in equilibrium state presented in Tables 3.19 and 3.20, respectively. Water temperatures were taken from Table 3.7. Flow velocities were calculated by dividing the water discharge (given in Table 3.4) by the flow area, considered as rectangular, so that $V=Q_w/(BH)$. The Froude number was computed with $F=V/(gH)^{1/2}$. A detailed description of the sediment grain size distributions and their measures of central tendency and dispersion for each run are given in the following

Subsection; the procedure used to calculate the definitive value of sand content of each mixture is described in the next Subsection as well. The data set is complemented with information, photos and graphics presented in Appendices VII to XV. Finally, at the end of this Section a brief critical review of the experiments and data set is presented.

Figure 3.36 is useful for getting a comprehensive and concise summary of the experimental campaign carried out for the current research. The most apparent trend observed in the graph is that the bulk of data form two main groups: one for uniform gravel and one for sand and sand-gravel mixtures; the group for gravel plots above of the second group, suggesting that for the motion of a given sediment concentration, a higher energy gradient slope is required for uniform gravel than for uniform sand and sand-gravel mixtures. By no means should such results be considered as general and conclusive, but as a particular case dependant of the flume and sediment characteristics used in the current work. For a sound generalization of the experimental results, subsequent Chapters analyze the effective shear stress acting on the sediment grains, bed and water surface configurations and sediment sorting for the definitive runs.

Table 3.27 Grain size properties for the experimental runs in the definitive data set. Data obtained from grain size distributions for samples collected in the hoppers throughout the experimental campaigns. Diameters are shown in mm. (Some of the sand content fields in the gravel runs are empty because a 2.24 mm mesh was not used in these cases.)

Run	D_m	σ_g	Mode	D_{16}	D_{50}	D_{84}	D_{90}	Sand content % (D<2mm)	Sand content % (D<2.24mm)
G12	4.69	1.27	3.35	3.59	4.83	6.04	6.28	0	-
G13	3.76	1.38	5.02	2.67	3.77	5.45	5.83	1.05	-
G14	4.23	1.35	5.02	3.00	4.39	5.81	6.11	0.07	1.94
G15	3.94	1.47	5.02	2.85	4.08	5.64	5.98	1.12	2.61
G16	3.82	1.38	3.35	2.62	3.84	5.58	5.96	0.05	-
G17	4.08	1.37	5.02	2.87	4.27	5.75	6.06	0.80	-
Average	**4.09**	**1.37**	**4.46**	**2.93**	**4.20**	**5.71**	**6.03**	**0.51**	**-**
M1E1	2.85	1.78	3.35/1.58	1.57	3.04	5.15	5.67	28.23	32.02
M1E2	2.99	1.74	5.02/1.58	1.58	3.27	5.37	5.83	28.11	31.17
M1E3	2.99	1.70	5.02/1.58	1.60	3.19	5.33	5.82	27.66	31.34
M1E4	3.02	1.78	5.02/1.58	1.57	3.38	5.43	5.86	27.84	31.46
M1E5	3.00	1.74	5.02/1.58	1.58	3.29	5.37	5.81	27.31	31.42
M1E6	2.79	1.80	5.02/1.58	1.52	3.02	5.17	5.67	29.86	34.73
Average	**2.94**	**1.76**	**4.74/1.58**	**1.57**	**3.20**	**5.30**	**5.78**	**28.17**	**32.02**
M2E1	2.43	1.87	3.35/1.58	1.39	2.54	4.68	5.31	38.40	43.89
M2E2	2.50	1.71	3.35/1.58	1.45	2.49	4.58	5.23	37.54	44.30
M2E3	2.43	1.75	3.35/1.58	1.42	2.46	4.38	5.11	38.01	44.50
M2E4	2.37	1.75	3.35/1.58	1.40	2.43	4.20	4.93	38.31	44.90
M2E5	2.42	1.74	3.35/2.12	1.42	2.49	4.32	5.01	35.95	43.43
M2E6	2.40	1.70	3.35/2.12	1.38	2.31	4.39	5.09	37.13	46.56
Average	**2.43**	**1.75**	**3.35/1.76**	**1.41**	**2.45**	**4.42**	**5.11**	**37.56**	**44.60**
S1	1.50	1.30	1.58	1.28	1.56	1.90	1.96	93.18	99.72
S2	1.43	1.42	1.58	1.23	1.53	1.89	1.96	93.59	99.77
S3	1.39	1.46	1.58	1.11	1.51	1.88	1.95	94.10	99.77
S4	1.38	1.47	1.58	1.10	1.51	1.87	1.95	94.31	99.74
Average	**1.43**	**1.41**	**1.58**	**1.18**	**1.53**	**1.88**	**1.95**	**93.80**	**99.75**

3.5.1 Summary of grain size characteristics for each run

The representative grain size distributions for each of the 22 runs selected for the data set are shown in Figure 3.37. These size distributions were obtained by forming a single

sample for each run from the samples collected in the hoppers during the equilibrium phase of the experiments. On average, for each run, three samples were taken from the hopper for the sand and gravel runs, and three from each of the two hoppers for the mixed sand-gravel runs. Table 3.27 summarizes the properties of the grain size distributions that were representative of each run.

Table 3.28 Grain size properties of pure **sand** (D<2.24 mm) in the experimental runs with sand-gravel mixtures. Data obtained from truncating the sand-gravel mixture grain size distributions formed from samples collected in the hoppers during the runs. Diameters are shown in mm.

Run	Number of samples from hopper	D_m	σ_g	Mode	D_{16}	D_{50}	D_{84}	D_{90}
M1E1	3	1.50	1.36	1.58	1.27	1.58	1.95	2.04
M1E2	3	1.49	1.35	1.58	1.27	1.56	1.93	2.00
M1E3	3	1.54	1.29	1.58	1.29	1.59	1.95	2.03
M1E4	1	1.48	1.37	1.58	1.26	1.56	1.94	2.03
M1E5	3	1.49	1.36	1.58	1.26	1.57	1.96	2.05
M1E6	2	1.44	1.49	1.58	1.18	1.56	1.97	2.07
	Average	**1.49**	**1.37**	**1.58**	**1.26**	**1.57**	**1.95**	**2.04**
M2E1	4	1.40	1.48	1.58	1.06	1.53	1.95	2.05
M2E2	4	1.51	1.35	1.58	1.26	1.59	1.99	2.08
M2E3	3	1.46	1.44	1.58	1.19	1.56	1.98	2.07
M2E4	4	1.44	1.46	1.58	1.13	1.55	1.98	2.07
M2E5	3	1.45	1.46	2.12	1.14	1.57	2.02	2.10
M2E6	1	1.47	1.48	2.12	1.15	1.59	2.05	2.12
	Average	**1.45**	**1.45**	**1.76**	**1.16**	**1.57**	**1.99**	**2.08**

Table 3.29 Grain size properties of pure **gravel** (D>2.24 mm) in the experimental runs with sand-gravel mixtures. Data obtained from truncating the sand-gravel mixture grain size distributions formed from samples collected in the hoppers during the runs. Diameters are shown in mm.

Run	Number of samples from hopper	D_m	σ_g	Mode	D_{16}	D_{50}	D_{84}	D_{90}
M1E1	3	3.90	1.35	3.35	2.71	3.87	5.59	5.97
M1E2	3	4.11	1.34	5.02	2.88	4.18	5.75	6.08
M1E3	3	4.04	1.35	5.02	2.83	4.06	5.74	6.10
M1E4	1	4.20	1.33	5.02	2.95	4.33	5.79	6.09
M1E5	3	4.12	1.33	5.02	2.90	4.22	5.74	6.06
M1E6	2	3.98	1.34	5.02	2.80	4.00	5.63	5.98
	Average	**4.06**	**1.34**	**4.74**	**2.85**	**4.11**	**5.71**	**6.05**
M2E1	4	3.79	1.34	3.35	2.69	3.71	5.43	5.83
M2E2	4	3.73	1.33	3.35	2.65	3.64	5.36	5.77
M2E3	3	3.65	1.34	3.35	2.61	3.52	5.26	5.72
M2E4	4	3.57	1.32	3.35	2.58	3.45	5.09	5.56
M2E5	3	3.59	1.32	3.35	2.59	3.48	5.13	5.59
M2E6	7	3.72	1.31	3.35	2.74	3.62	5.26	5.67
	Average	**3.68**	**1.33**	**3.35**	**2.64**	**3.57**	**5.26**	**5.69**

The grain size distributions for the sand-gravel mixtures were constructed by mixing the individual sand and gravel size distributions of the samples from the hoppers in the same proportion in which sand and gravel were fed by the hoppers in the channel (Tables 3.8 and 3.9). The proportion of material fed into the channel from the sand hopper does not concur with the proportion of sand in the mixtures, as is shown in the last column of Table 3.27 compared to the last column of Table 3.4. This is because the gravel collected in the hopper contained a small amount of material in the size range of sand. In

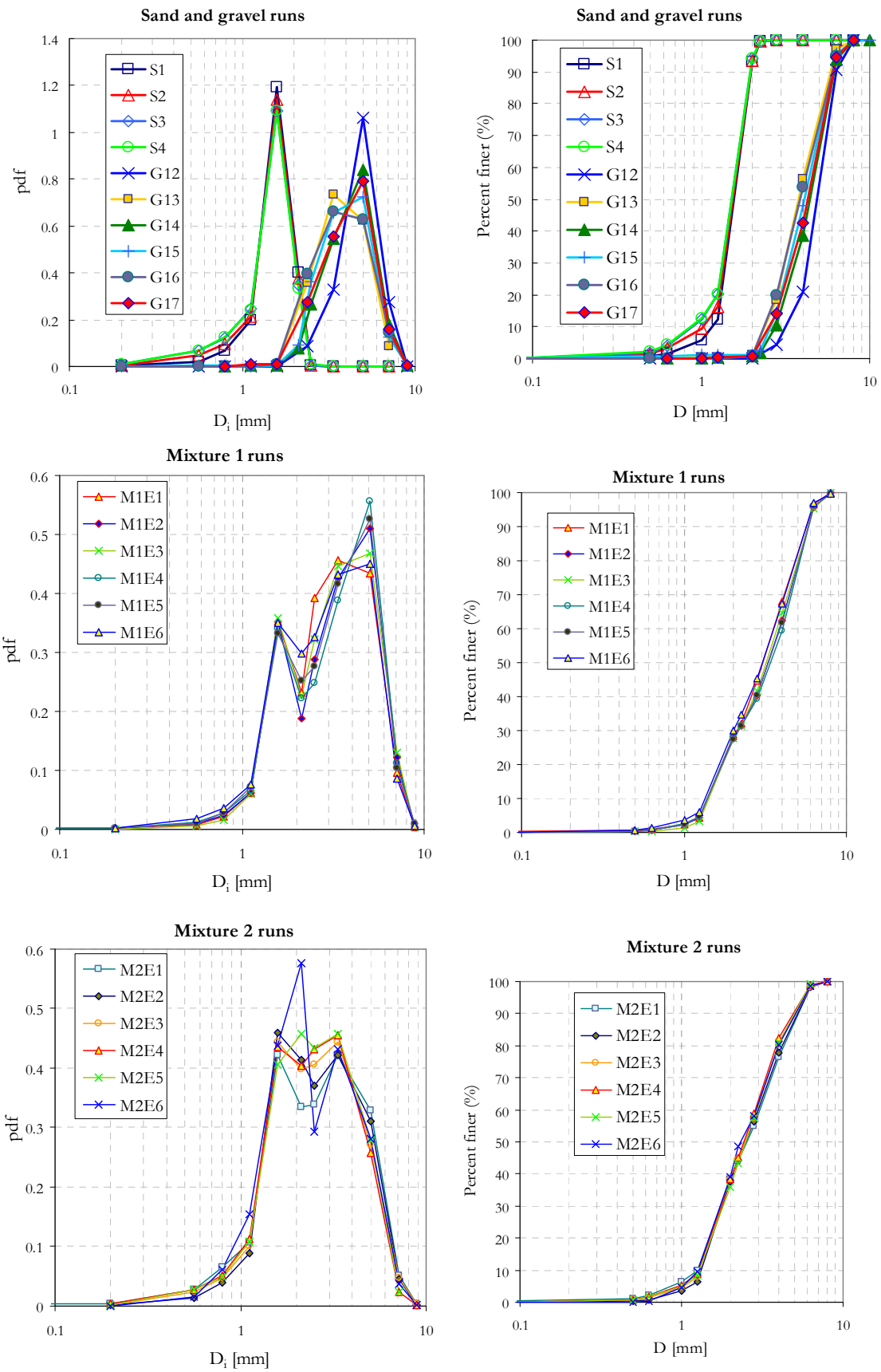

Figure 3.37 Average grain size distributions for the material fed by the hoppers during each experimental run. pdf=Probability density function.

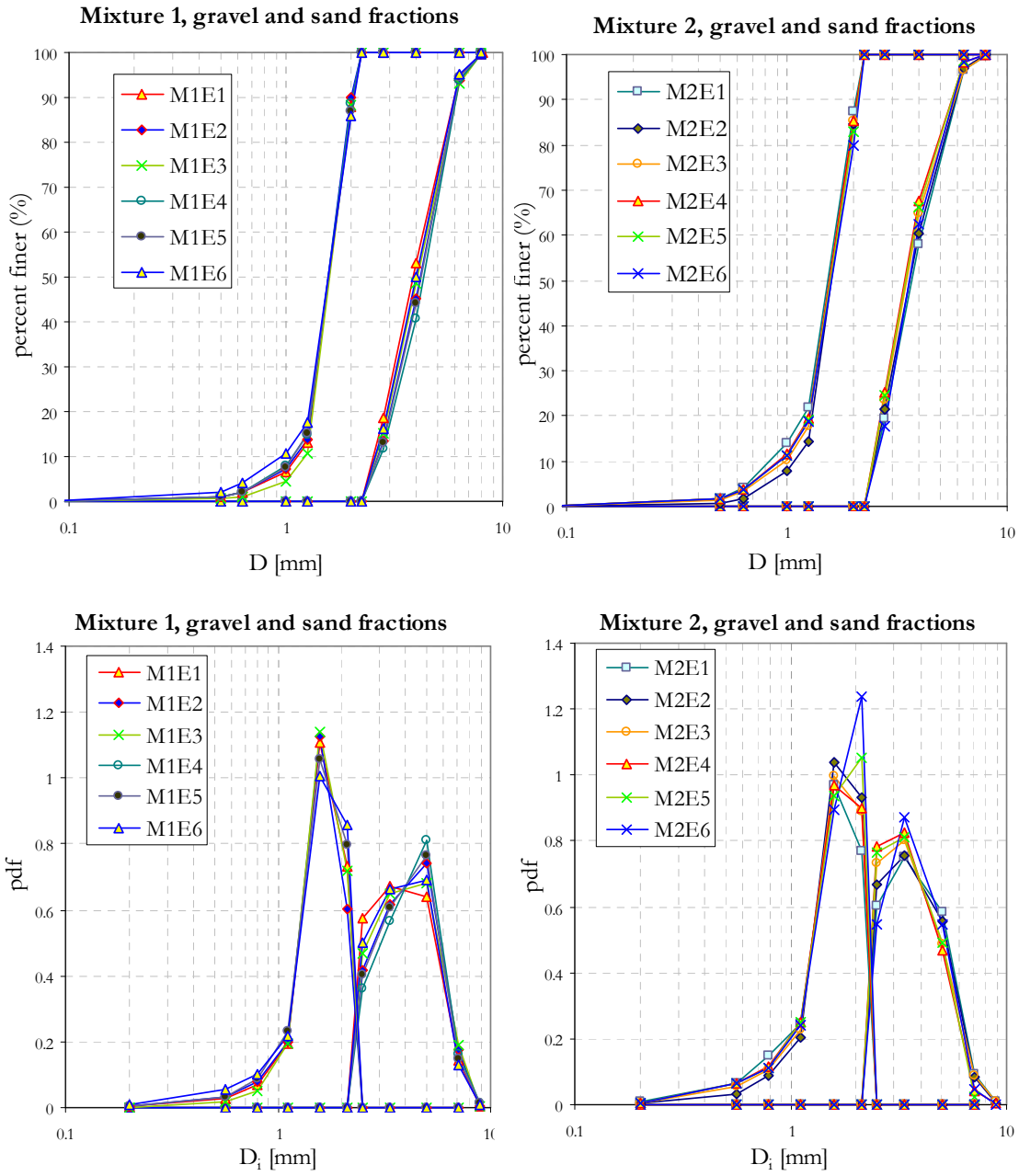

Figure 3.38 Average grain size distributions for sand and gravel fractions of the material fed by the hoppers during each experimental run. pdf=Probability density function.

other words the gravel hopper supplied a small amount of fines, which reduced the representative grain size distribution of the mixtures.

Figure 3.38 shows the grain size distributions of the pure sand and gravel in the feeding mixtures, i.e., these curves were obtained by splitting at diameter 2.24 mm the curves in Figure 3.37. A summary of the properties of the sand and gravel fractions of the mixtures is shown in Tables 3.28 and 3.29.

From the grain size distributions it is evident that the probability density functions for mixture 1 are bimodal, with a dip in the size fraction 2.11 mm. For mixture 2 the probability density functions are slightly bimodal, with a dip in the size fraction 3.35 mm. For some runs such as M2E5, however, the distribution seems more unimodal as the dip between modes is quite subtle.

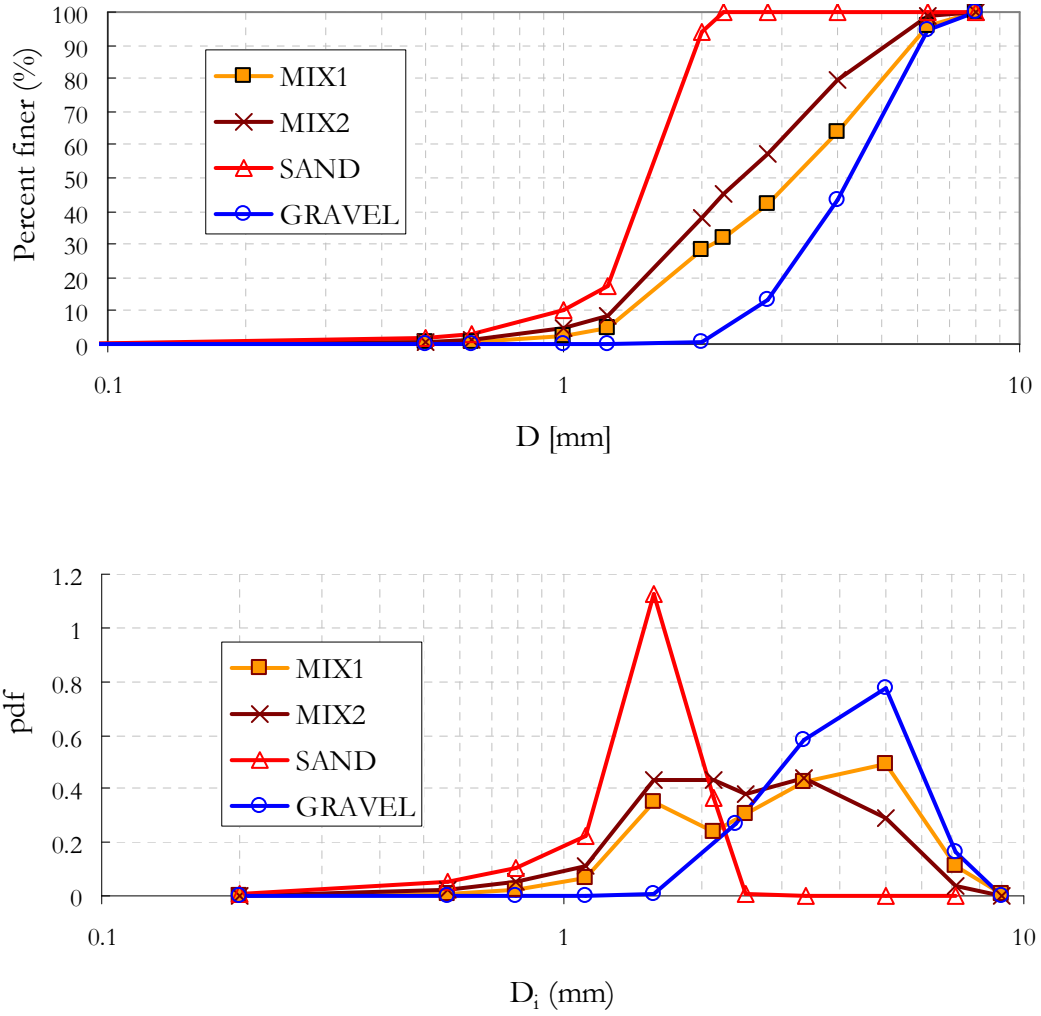

Figure 3.39 Average grain size distributions for the materials fed by the hoppers for the gravel runs, the sand runs, and the mixed sand-gravel runs. pdf=Probability density function.

For a formal definition of the bimodality of the mixtures used in the experiments, indices of bimodality formulated by Wilcock (1993) and Sambrook-Smith et al. (1997) were computed for each mixture. The index described by Wilcock (1993) considers the influence of bimodality on critical shear stress for the beginning of movement of each grain size fraction in the mixture, and is given by

$$B^* = (D_c / D_f)^{1/2}(F_c / F_f) \qquad (3.51)$$

where D_f and D_c are the grain sizes of the fine and coarse modes, respectively, and F_f and F_c are the proportions of sediment in the fine and coarse modes, respectively; a mode is assumed to be of one ϕ unit width (ϕ=-log$_2$[D]=-ln[D]/ln[2]), and thus each mode is defined as the four contiguous ¼ϕ units containing the largest proportion of sediment. According to flume and field data, Wilcock found that for B>1.7 the bimodality of the mixture affected the entrainment and transport of sediment, and therefore concluded that if B<1.7 the mixture could be considered unimodal. Sambrook-Smith et al. (1997) proposed the following bimodality index:

$$B^* = |\phi_2 - \phi_1|(F_2 / F_1) \qquad (3.52)$$

where subscript 1 and 2 refer to the primary and secondary modes, respectively. The limit between unimodal and bimodal mixtures is in the range of 1.5-2.0.

The computed indexes of bimodality for all the sand-gravel mixtures lay in the range of unimodal sediment, with average Wilcock index values of 1.53 and 1.28 for mixture 1 and mixture 2, respectively; the corresponding values of the index defined by Sambrook-Smith et al. were 0.76 and 0.73, respectively.

For comparison, Figure 3.39 shows the average grain size distributions for all the gravel, sand, and mixed sand-gravel runs.

3.5.2 Critical review

The experiments here described provide with a comprehensive data set of flow conditions, bedforms, bed erosion, sediment transport and grain size sorting, that contributes to a better understanding of flows in the transition from lower- to upper-regime for different types of bed materials. This new experimental data set, comprising 22 runs, offers valuable information about flow and sediment interactions for ranges of variables that previously had not been systematically explored in laboratory flumes.

The experiments were intended to reproduce flow conditions, bed configurations and sediment transport processes comparable to those in torrential ephemeral streams prone to flash floods, as those found in the Mediterranean coast. The raw experimental results suggest that antidunes and undular flows must be a frequent feature of these ephemeral streams; furthermore, since flow conditions in the experimental runs produced deep bed erosion, of the same order of magnitude as the flow water depth, these results are relevant for engineering practice and deserve further attention for the study of flow and morphodynamics of flash floods in ephemeral streams.

Within the field of sediment transport, the raw results showed that for the ranges of variables used, for a given energy gradient slope, sediment concentrations were comparable between runs with bed materials composed of uniform sand and runs with bed materials composed of sand-gravel mixtures with volumetric sand contents as low as 30%; conversely, for beds composed of uniform gravel the observed sediment concentrations were lower than for uniform sand and sand-gravel mixtures. Such a trend confirms that there is a non-linear increment of sediment concentration with sand content, as previously observed by other authors (e.g., Wilcock and Kenworthy, 2002). Nonlinearities in the transport of sediment composed of different size fractions are attributed in literature to hiding-exposure effects and other vertical grain-size sorting phenomena like bed armouring (e.g., Parker, 2004). On account of the fact that different species of bedforms were ubiquitous in most of the runs, it is likely that in the experiments here described, besides hiding-exposure, the shear stress taken by the drag on the bedforms and the sediment grain size sorting (longitudinal, vertical and horizontal) resulting from the bedforms progression must have also exerted an important influence in regulating sediment transport and non-linear trends with sand content. To analyze these issues, bed resistance is studied in Chapter 4, bed configurations and bedforms are treated in Chapter 5, and all these topics together are discussed in Chapter 6.

New questions, originally not explicitly considered in the main objectives of the research, arose from the experimental observations. Particularly, the characteristics of bedforms in transcritical and supercritical flows, and the identification and modelling of grain size sorting trends induced by bedforms, were topics to which the progress of the research came out, and which were required to be studied in more detail in order to obtain a holistic view of the processes observed in the experiments. The experimental observations in relation to the first topic above, i.e. bedforms, are analyzed in Chapter 5 and discussed in Chapter 6; in this same vein, Chapter 7 is focused in a simplified

theoretical analysis of the movement of antidunes, as these were the most common bedforms observed in the experiments. Grain size sorting related to bedforms is analized at the end of Chapter 5 and discussed within an entire overview of the processes observed in the experiments in Chapter 6; in that same Chapter, analysis and discussion of the experiments is thoroughly treated; finally, an especial aspect of grain size sorting, the infiltration of fines into the bed, is studied in depth and modelled in Chapter 9.

CHAPTER 4:

ANALYSIS OF CHANNEL BED RESISTANCE

4.1 INTRODUCTION

The amount of sediment that a channel can transport is related to the forces exerted by the fluid flowing over the alluvial particles. In uniform open-channel flows the only force acting on the boundary is the downstream component of the weight of water. Therefore, it is tempting to formulate a general, universal law for sediment transport solely as a function of grain characteristics and the average shear stress acting on the bed. In this manner, bed shear stress would be simple to compute with the downstream component of the weight of a unit-length slice of fluid distributed over the bed surface. Nevertheless, such a straightforward methodology would only be correct for a narrow range of conditions because resistance to the action of fluid weight is influenced by factors other than alluvial grains. Bed load layer height, channel walls, sinuosity and other channel elements, and in several cases bed forms in particular, all have a strong influence on flow resistance and therefore an important effect on feedback between flow resistance and sediment transport. Hence, in order to accurately compute the average shear stress that acts solely on the grains and consequently, is directly responsible for promoting sediment transport, bed resistance to flow must be broken down into different components.

A common practice is to partition bed shear stress into the different elements that oppose resistance to flow. This is essential to evaluating and understanding the mechanics of sediment transport because in this manner sediment transport can be solely associated with the forces that promote grain movement. Nevertheless, some researchers have followed general trends for sediment transport field measurements without reducing bed shear stress to that owed to grain or skin friction. Mueller et al. (2005), for example, studied the beginning of motion in 45 gravel-bed streams and rivers using estimates of total boundary shear stress, i.e., without applying shear stress partition. In doing so, they

appealed to the ease of implementation of a model for estimating the beginning of motion based on morphological properties, believing that the uncertainty associated with such a model would not be worse than that encountered with shear partitioning models.

Some comparisons between the experimental results shown in Chapter 3 and field data on sediment transport using average reach-scale shear stress (i.e., without partition), are shown in Chapter 6. However, as one of the main goals of this work is to study sediment transport functions designed to be of universal applicability (i.e., uniform sediment, all types of sediment mixtures and a wide range of flow conditions), shear stress partition is necessary in the current study. The experimental data in this chapter are thus analyzed for channel bed resistance to flow to obtain the skin friction associated with volume sediment discharge.

A wide range of methods exists for performing shear stress partition to distinguish between shear stress associated with bedforms and that associated with skin friction. Many of these use bedform geometry to compute form drag. As the bed configuration for the experiments reported here was complex, it was decided to apply methods which considered just average flow conditions and a logarithmic velocity profile. It was assumed that this decision would result in a certain degree of error but it was also considered to be the best option as the aggressive supercritical flow conditions and high sediment transport rates in the experiments prevented the performance of velocity profiles measurements and a precise determination of bedform geometry. Possible discrepancies that could arise from such simplifications are discussed briefly at the end of the chapter.

Thus, the main objective of this chapter is to obtain correct shear stress values for the experimental data set that can be directly used when applying sediment transport functions, and in turn, to obtain shear stress values related to the experimental bed states in order to further identify possible trends in bedform resistance associated with the type of flow regime and bed material. To this end, different approaches are applied to compute the effective shear stress (or skin friction) exerted on the sediment particles. A general overview of bed resistance relations is given first. Next, a shear stress correction method for side wall effects is applied to the data set, and then different models to compute skin friction are described and applied to the data set. Later, the models with the best performance are applied to flume data from the literature. Subsequently, a brief discussion is presented with reference to the partition methods used and the assumptions and simplifications implicitly involved when they are applied. Finally, a summary of the chapter is briefly presented.

4.2 FLOW RESISTANCE RELATIONS

To proceed further it is useful to define some hydraulic variables. The most commonly used flow resistance coefficients for steady uniform flow in open channels are

$$f = \frac{8gR_hS}{V^2} \qquad \text{Darcy-Weisbach} \qquad (4.1)$$

$$C = \frac{V}{\sqrt{R_hS}} \qquad \text{Chézy} \qquad (4.2)$$

$$n = \frac{K_n}{V} R_h^{\frac{2}{3}} S^{\frac{1}{2}} \qquad \text{Manning} \qquad (4.3)$$

where f, C and n are the Darcy-Weisbach, Chézy and Manning resistance coefficients, respectively; g is the gravitational acceleration; R_h is the hydraulic radius; V is the cross-sectionally averaged flow velocity, obtained from the water discharge Q_w and the cross-section flow area A as $V=Q_w/A$; S is the energy slope; and K_n is a unit conversion factor

for the Manning flow resistance formula, K_n=1 $m^{1/2}/s$ for V and R_h in SI units. From eqs. (4.1) to (4.3), equivalence between roughness coefficients can be written as:

$$\sqrt{\frac{8}{f}} = \frac{C}{\sqrt{g}} = \frac{R_h^{\frac{1}{6}}}{n}\frac{K_n}{\sqrt{g}} \tag{4.4}$$

If shear velocity, related to the bed shear stress τ_b and the water density ρ, is written as

$$u* = \sqrt{\frac{\tau_b}{\rho}} \tag{4.5}$$

a dimensionless bed resistance coefficient can be defined as (Chaudhry, 1993)

$$C_f = \frac{\tau_b}{\rho V^2} \tag{4.6}$$

which is related to the dimensionless Chézy resistance coefficient C_z as follows

$$C_z = \frac{C}{\sqrt{g}} = \frac{1}{\sqrt{C_f}} = \frac{V}{u*} \tag{4.7}$$

According to the so-called law of the wall, for very wide channels (such that B/H>>1 and thus $R_h \approx H$, where B is the channel width and H is the water depth) the velocity distribution above the bed is well represented by

$$\frac{u}{u*} = \frac{1}{\kappa}\ln\left(\frac{z}{z_o}\right) \tag{4.8}$$

where u is the time-average flow velocity at a distance z above the bed, z_o is the bed roughness length (i.e. the distance above the bed where flow velocity is equal to zero), and κ is the von Karman's constant, which has an approximate value of 0.4. For hydraulically rough flows (which are characteristic of rivers), the next expression for the depth-averaged flow velocity, known as Keulegan's resistance law, is obtained by integrating (4.8) over the flow depth

$$\frac{1}{\sqrt{C_f}} = \frac{V}{u*} = \frac{1}{\kappa}\ln\left(11\frac{H}{k_s}\right) \tag{4.9}$$

where k_s is the Nikuradse equivalent grain roughness, so that k_s=30z_o. According to García (2008), this formulation has been widely used to estimate grain-related resistance in gravel-bed streams. The logarithmic form in eq.(4.9) can be approximated by means of power laws of the Manning-Strikler form, such as the following proposed by Parker (1991):

$$C_z = 8.1\left(\frac{H}{k_s}\right)^{\frac{1}{6}} \tag{4.10}$$

For fixed flat beds with non-uniform granular material, k_s has commonly been approximated by

$$k_s = \alpha_S D_x \tag{4.11}$$

with D_x being a representative grain size for which x percent of bed material is finer and α_S is an empirical coefficient. There is no consensus on the value of k_s, explaining why a wide range of values for α_S and x have been suggested, as shown in Table 4.1.

The equations above reflect the connection between bottom roughness and flow resistance, which in turn, through shear velocity or boundary shear stress, provide a measure of flow intensity and the ability of flow to entrain and move alluvial material. Therefore, equations (4.5) to (4.11) are useful for sediment transport computations. For a flat bed under steady uniform and fully rough turbulent flow in a wide rectangular channel, in the computation of the tangential force per unit bed area, these equations would be equivalent to

$$\tau = \rho g H S \tag{4.12}$$

which is the result of applying the one-dimensional momentum conservation equation.

Table 4.1 Representative diameters and coefficients for estimating the Nikuradse equivalent roughness as proposed by different authors (from Yen 2002).

Researcher	$\mathbf{D_x}$	$\boldsymbol{\alpha_S}$
Ackers and White (1973)	D_{35}	1.23
Strikler (1923)	D_{50}	3.3
Keulegan (1938)	D_{50}	1
Meyer-Peter and Mueller (1948)	D_{50}	1
Thompson and Campbell (1979)	D_{50}	2
Hammond et al. (1984)	D_{50}	6.6
Einstein and Barbarossa (1952)	D_{65}	1
Irmay (1949)	D_{65}	1.5
Engelund and Hansen (1967)	D_{65}	2
Lane and Carlson (1953)	D_{75}	3.2
Gladki (1979)	D_{80}	2.5
Leopold et al. (1964)	D_{84}	3.9
Limerinos (1970)	D_{84}	2.8
Mahmood (1971)	D_{84}	5.1
Hey (1979), Bray (1979)	D_{84}	3.5
Ikeda (1983)	D_{84}	1.5
Colosimo et al. (1986)	D_{84}	3-6
Whiting and Dietrich (1990)	D_{84}	2.95
Simons and Richardson (1966)	D_{85}	1
Kamphuis (1974)	D_{90}	2.0
Van Rijn (1982)	D_{90}	3.0

4.3 LINEAR SEPARATION OF CHANNEL RESISTANCE

A widely accepted approach to separating different sources of flow resistance in an alluvial channel is based on the consideration that the mean boundary shear stress on the channel is equal to the sum of shear stresses due to different sources of resistance. Yang and Tan (2008) expressed this partition in a general form as follows

$$\tau = \tau_w + \tau_b = \tau_w + \tau' + \tau'' \qquad (4.13)$$

where τ is the mean boundary shear stress, τ_w is the side wall shear stress, τ_b is the bed shear stress, τ' is the shear stress associated with grain or skin friction, and τ'' is the shear stress component due to the bed forms. This approach was first proposed by Meyer-Peter and Muller (1948) and Einstein (1950). The direct summation of shear stresses in eq.(4.13) simplifies the analysis required to identify stresses directly related to sediment transport, i.e., those caused by skin friction. In the following Sections, different methods described in the literature are applied to compute the different components of mean boundary shear stress for the experimental data set.

4.3.1 Side wall correction

A standard recognized method for calculating the contribution of the side walls of a channel to total shear stress is that of Vanoni and Brooks (Vanoni 1975), who modified an original method presented by Johnson in 1942. Specifically, the cross section is divided into two areas. In one of these, A_b, flow is resisted by the bed, while in the other, A_w, it is resisted by the side walls of the channel. In this manner, the total area of the cross section is

$$A = A_b + A_w \qquad (4.14)$$

It is assumed that a flow resistance function can be applied to each section. Both sections share equal mean velocity and energy slope, but each has a different boundary roughness. In this manner, the Darcy-Weisbach equation (eq. 4.1) can be divided into one area affected by wall roughness and another affected by bed roughness, such that eq.(4.1) can be rewritten as

$$\frac{V^2}{S} = \frac{8g}{f} R_h = \frac{8g}{f_w} R_{h,w} = \frac{8g}{f_b} R_{h,b} \qquad (4.15)$$

where the subscripts b and w stand for bed and wall, respectively. The hydraulic radius for the section, the wall and the bed would be, respectively,

$$R_h = \frac{A}{P} = \frac{BH}{B+2H}, \qquad R_{h,w} = \frac{A_w}{P_w} = \frac{A_w}{2H}, \qquad R_{h,b} = \frac{A_b}{P_b} = \frac{A_b}{B} \qquad (4.16a,b,c)$$

where B is the channel width, P is the wetted perimeter and H is the mean water depth. Incorporating eq.(4.14) and eq.(4.16) into eq.(4.15), yields

$$\frac{BH}{(B+2H)f} = \frac{BH - A_b}{2Hf_w} = \frac{A_b}{Bf_b} \qquad (4.17)$$

And solving for f_b

$$f_b = f + \frac{2H}{B}(f - f_w) \qquad (4.18)$$

If the definition of the Reynolds number for each section is considered,

$$\mathrm{Re} = \frac{4R_h V}{\nu}, \qquad \mathrm{Re}_w = \frac{4R_{h,w} V}{\nu}, \quad \mathrm{Re}_b = \frac{4R_{h,b} V}{\nu} \qquad (4.19a,b,c)$$

where ν is the kinematic viscosity. V is the same for all sections, therefore:

$$\frac{\mathrm{Re}}{R_h} = \frac{\mathrm{Re}_w}{R_{h,w}} = \frac{\mathrm{Re}_b}{R_{h,b}} \qquad (4.20)$$

From eq.(4.1) these ratios in eq.(4.20) become

$$\frac{\mathrm{Re}}{f} = \frac{\mathrm{Re}_w}{f_w} = \frac{\mathrm{Re}_b}{f_b} \qquad (4.21)$$

The ratio Re/f is known from the average flow conditions, thus Re_w/f_w can be computed from eq.(4.21). If the wall roughness is known, f_w can be computed from a pipe friction diagram. Vanoni and Brooks presented a diagram for smooth walls from which f_w can be obtained directly. Figure 4.1 shows a best-fit curve for this diagram obtained in this study.

The computed value of f_w is used in eq.(4.18) to obtain the bed friction factor, from which the bed hydraulic radius is obtained from eq.(4.15). The bed hydraulic radius serves to compute bed shear velocity, defined as

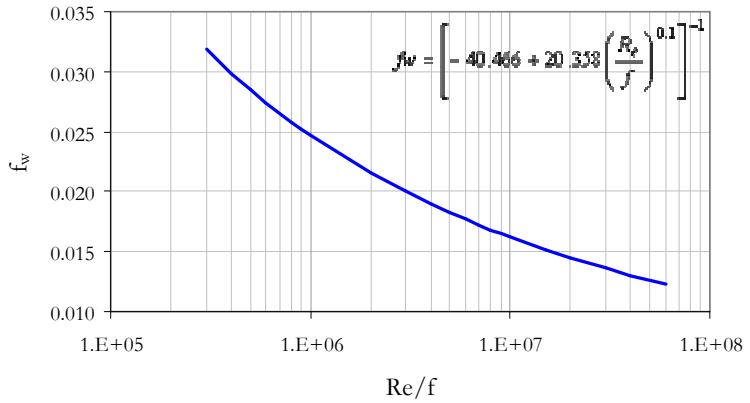

Figure 4.1 Curve for the determination of the Darcy-Weisbach friction factor for a smooth wall. Also shown is the equation obtained for the best-fit curve with respect to the original curve presented by Vanoni and Brooks (1975).

Table 4.2. Experimental data set. Flume width is 0.75 m.

Run	V [m/s]	H [m]	S	ρ* [kg/m³]	ν* x10⁶ [m²/s]
G12	1.16	0.068	0.0214	999.4	1.22
G13	1.21	0.092	0.0185	999.4	1.20
G14	1.18	0.076	0.0188	999.3	1.19
G15	1.14	0.079	0.0162	999.3	1.19
G16	1.06	0.085	0.0122	999.4	1.20
G17	0.96	0.109	0.0058	999.3	1.18
M1E1	1.01	0.104	0.0081	999.2	1.16
M1E2	1.30	0.086	0.0167	999.1	1.15
M1E3	1.18	0.076	0.0173	999.1	1.13
M1E4	1.20	0.087	0.0153	999.0	1.13
M1E5	1.16	0.090	0.0130	998.9	1.11
M1E6	0.93	0.113	0.0059	998.9	1.11
M2E1	1.28	0.081	0.0177	998.6	1.06
M2E2	1.32	0.080	0.0166	998.6	1.06
M2E3	1.26	0.083	0.0160	998.3	1.02
M2E4	1.17	0.089	0.0146	998.3	1.02
M2E5	1.03	0.103	0.0098	998.4	1.03
M2E6	0.94	0.113	0.0064	998.2	1.01
S1	1.03	0.103	0.0155	998.0	0.98
S2	0.97	0.109	0.0123	997.8	0.96
S3	0.89	0.119	0.0082	997.8	0.96
S4	0.82	0.130	0.0060	997.8	0.96

*Theoretical values obtained from the water temperature.

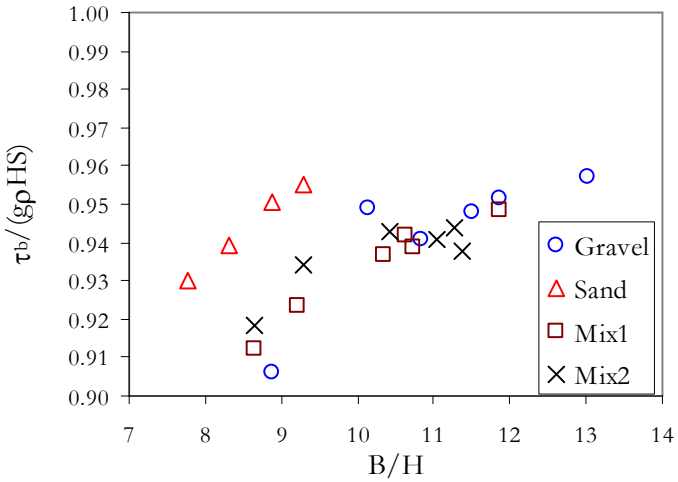

Figure 4.2 Results of Vanoni and Brooks side wall correction as a function of channel aspect ratio, B/H. The ratio $\tau_b/(g\rho HS)$ compares the boundary shear stress for the bed region with the mean boundary shear stress in the channel.

$$u*_b = \sqrt{gR_{h,b}S} \tag{4.22}$$

From which bed shear stress is defined as

$$\tau_b = \rho u*_b^2 \tag{4.23}$$

Table 4.2 shows the experimental data used to compute the wall resistance coefficients and Table 4.3 shows the computation variables and results. The results are also shown in Figure 4.2. In this figure it is evident that bed shear stress decreases as water

depth increases, due to the increase in the size of the area of the side wall opposing the flow. On average, the computed bed shear stress was 6% lower than the mean shear stress computed from the product gρHS.

Table 4.3 Results for side wall correction applied to the experimental data set.

Run	Hydraulic radius	Darcy-Weisbach resistance coefficient	Reynolds number	Re/f	Wall resistance coefficient	Bed resistance coefficient	Bed hydraulic radius	Bed shear stress
	R_h [m]	f	Re x 10^{-5}	x 10^{-6}	f_w	f_b	$R_{h,b}$ [m]	τ_b [Pa]
G12	0.058	0.072	2.2	3.05	0.020	0.080	0.065	**13.7**
G13	0.074	0.073	3.0	4.07	0.019	0.088	0.087	**15.8**
G14	0.063	0.067	2.5	3.74	0.019	0.079	0.072	**13.3**
G15	0.065	0.064	2.5	3.92	0.019	0.071	0.075	**11.9**
G16	0.069	0.059	2.4	4.15	0.019	0.067	0.080	**9.6**
G17	0.084	0.042	2.7	6.59	0.017	0.051	0.099	**5.6**
M1E1	0.081	0.051	2.8	5.59	0.018	0.058	0.096	**7.6**
M1E2	0.070	0.054	3.2	5.83	0.018	0.064	0.081	**13.2**
M1E3	0.063	0.062	2.6	4.28	0.019	0.069	0.072	**12.2**
M1E4	0.071	0.059	3.0	5.09	0.018	0.067	0.082	**12.3**
M1E5	0.073	0.055	3.0	5.51	0.018	0.064	0.084	**10.7**
M1E6	0.087	0.046	2.9	6.26	0.018	0.058	0.103	**6.0**
M2E1	0.067	0.056	3.2	5.70	0.018	0.066	0.076	**13.3**
M2E2	0.066	0.049	3.3	6.66	0.017	0.058	0.075	**12.2**
M2E3	0.068	0.054	3.4	6.25	0.018	0.063	0.078	**12.2**
M2E4	0.072	0.060	3.3	5.48	0.018	0.072	0.084	**12.0**
M2E5	0.081	0.059	3.2	5.52	0.018	0.071	0.096	**9.2**
M2E6	0.087	0.049	3.2	6.55	0.017	0.055	0.104	**6.5**
S1	0.081	0.093	3.4	3.67	0.019	0.117	0.098	**14.9**
S2	0.084	0.087	3.4	3.94	0.019	0.104	0.104	**12.5**
S3	0.090	0.073	3.3	4.56	0.019	0.088	0.112	**9.0**
S4	0.097	0.068	3.3	4.88	0.018	0.085	0.121	**7.1**

4.3.2 Bed shear stress partition

The last column in Table 4.3 shows the computed bed shear stress, i.e., the stress acting solely on the alluvial bottom, as the shear owing to the tangential forces exerted on the channel walls has been removed. Thus, according to eq.(4.13), this bed shear stress can also be decoupled into skin friction τ' and form drag τ". Shear stress related to skin friction will be used in Chapter 6 as a measure of the ability of flow to transport sediment. The form drag component will be used to compute resistance coefficients for the bedforms observed during the experiments to compare them with typical coefficients reported in the literature.

A wide range of methods exists for identifying the separate contributions of grain and form resistance components. The most straightforward, both in terms of conceptual basis and ease of implementation, conceive an equivalent reference plane bed shear, i.e., they consider that grain shear stress would be the same as grain shear stress occurring on a flat bed with the same mean flow velocity (Einstein 1950, Engelund and Hansen 1967, Van Rijn 1982). More sophisticated methods have been designed to provide a more accurate representation of the physics of flow and its interrelation with bedforms and sediment

transport. Among these, the conceptual basis of the formulation presented by Smith and McLean (1977) was the origin for other important developments and generalizations of shear stress partition methods. Smith and McLean considered a longitudinally averaged velocity profile over a wavy bed consisting of logarithmic segments related to the different scales of superimposed bedforms. In contrast to the reference plane bed shear methods, this approach requires bedform geometry as an independent input variable.

Nelson and Smith (1989) found that velocity profiles over bedforms, even averaged profiles, cannot be accurately represented by a plane bed velocity profile. This would be the most contentious issue as far as reference plane bed shear methods are concerned. Nevertheless, the advantage of these methods over others is that they do not require knowledge of the geometrical characteristics of the bedform.

Because of the complexity of the bed configurations observed in the experimental runs described in the following chapter (mostly downstream-migrating antidunes coexisting with alternated bars) and because of the difficulties of characterizing the geometry of bedforms in a simple manner, it was decided to apply methods which do not require bedform characteristics as an input parameter. A more precise computation of the shear velocity is possible when flow velocity profiles are measured; such measurements, however, were not feasible during the experiments because the aggressiveness of the flow and sediment transport made such measurements impracticable, at least for typical techniques used in laboratory flumes. Consequently, the methods selected involve the use of reach-average hydraulic variables.

4.3.2.1 Selected partition models

Four methods were selected, namely those proposed by Einstein (1950), Engelund and Hansen (1967), Van Rijn (1982) and Recking et al. (2008). The main selection criteria were sound theoretical basis and the availability of references on their application, thus providing easy access to experiences or recommendations regarding performance. The exception was the Recking et al. method, which was selected as it had been developed explicitly for gravel-bed rivers and takes into account the additional component to bed resistance introduced by sediment transport. Although this method was developed for plane beds, in this work it is used by extending the concept of a reference plane bed shear as defined above, and also applied in combination with Einstein's model (1950). The rest of the methods selected were developed for sand beds with dunes and are all based on a reference plane bed shear. They are similar in principle and differ mainly in terms of the choice of the value of the effective roughness k_s. Of the first three methods, Benett (1995) found that the Engelund and Hansen method performed best when used to compute depth for plane bed data sets. Bennett also reported that this approach was the most widely used one.

In spite of the conceptual shortcomings of approaches based on a reference plane bed, they offer a convenient and practical means of computing skin friction shear stress when water depth and velocity but not the geometrical characteristics of the bedforms are known. They have been used widely in both field and flume experiments (e.g., in Wilcock and Southard 1989, Kuhnle 1993b, Kleinhans and Van Rijn 2002, Lunt and Bridge 2007). There is a lack of effective means to directly measure the effective shear stress acting on particles entrained by flow. In the same manner, very limited approaches exist to evaluate the accuracy of the partition. Nevertheless, it is expected that by using commonly applied methods, the experimental bed resistance and sediment transport data can be contrasted with different flume conditions and data sets in a relative sense.

Einstein (1950)

Einstein's method introduces a fictitious water depth H_s, which would be the water depth in the absence of bedforms for the same mean velocity and grain (Figure 4.3). Considering normal flow, so that for a plane bed $\tau' = \rho g H_s S$, eq.(4.6) introduced into eq.(4.9) can be rewritten as

$$H_s = \frac{V^2}{gS}\left[\frac{1}{\kappa}\ln\left(11\frac{H_s}{k_s}\right)\right]^{-2} \qquad (4.24)$$

H_s is found iteratively. Einstein suggested that $k_s = D_{65}$. Wilcock and Southard (1988) reported good performance results with this method when applied to unimodal and bimodal sand-gravel mixtures. For bimodal sediments, instead of using the D_{65} of the mixture, Wilcock and Southard used the mean diameter of the coarse mode as, based on their observations, they considered that coarse grains controlled bed roughness.

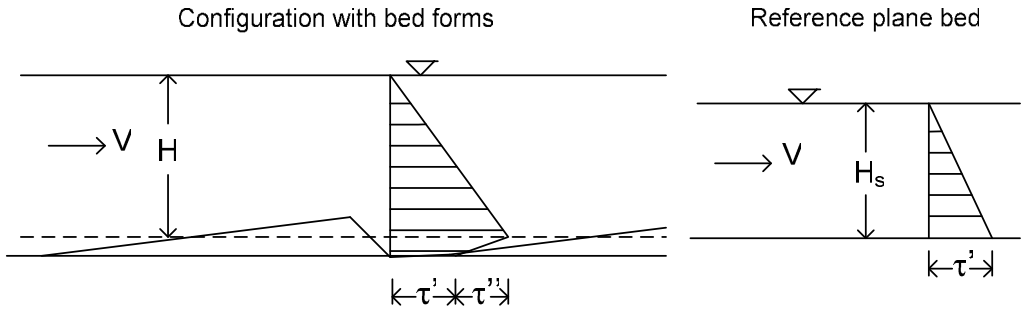

Figure 4.3 Schematic interpretation of the Einstein (1950) method.

Engelund and Hansen (1967)

This method is in essence equivalent to that of Einstein (1950), with an amendment to the suggested value for the equivalent roughness k_s, which Engelund and Hansen suggested should be equal to $2.5D_m$, where D_m is the mean fall diameter. In the presence of dunes, Engelund and Hansen interpreted H_s as the thickness of the boundary layer formed at the end of the dune trough (see Figure 4.4).

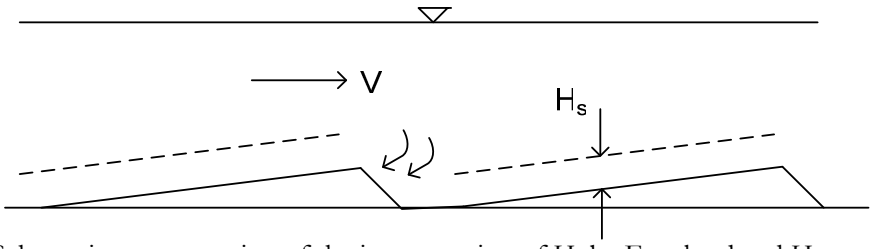

Figure 4.4 Schematic representation of the interpretation of H_s by Engelund and Hansen (1967).

Van Rijn (1982)

Van Rijn proposed a method in which the computation of the Chézy coefficient is performed with the logarithmic velocity profile for a plane bed. The computation uses known flow water depth, which avoids the iterations needed with the Einstein and the Engelund and Hansen methods. The equivalent grain roughness is a function of the Shields number. In this manner, the approach takes into account the increase in roughness caused

by the interaction between flow and the sediment grains in motion. The equation proposed by Van Rijn to compute the Chézy coefficient is

$$C = 18\log\left(\frac{12H}{k_s + 3.3\nu_m/u*}\right) \qquad (4.25)$$

where ν_m is a kinematic viscosity coefficient of the fluid-sediment mixture ($\approx 10^{-5}$ m^2/s in the near-bed region). For the equivalent grain roughness, Van Rijn proposed using the D_{90} of the bed material and a value for the constant α_S in eq.(4.11) as follows:

$$\alpha_s = 3 \qquad \text{for } \tau*<1 \qquad (4.26a)$$

$$\alpha_s = 3\tau* \qquad \text{for } \tau*\geq 1 \qquad (4.26b)$$

where $\tau*$ is the mobility parameter, equivalent to the Shields number: $\tau* = u_*^2/((S_s-1)gD_{50})$. After applying eq.(4.25), the effective shear stress on the grains is obtained from equations (4.6) and (4.7).

Recking et al. (2008)

Recking et al. performed a series of experiments with uniform size gravel particles for a wide range of flow intensities, from no bed material motion to high rates of sediment transport, always under plane bed conditions. Their goal was to develop flow resistance and bed load transport equations that took into account the feedback between both processes. They found three domains for which different resistance laws would be valid: domain 1, for no sediment motion (bed shear stress lower than critical grain shear stress), where the Darcy-Weisbach coefficient decreases with increasing relative depth; domain 2, for intermediate bed load rates (bed shear stress is between 1 and 2.5 times the critical grain shear stress), where the Darcy-Weisbach coefficient increases with slope; and domain 3, for high bed load transport rates (bed shear stress higher than 2.5 times the critical grain shear stress), where the Darcy-Weisbach coefficient decreases with increasing relative depth. Recking et al. developed a model that can be adequately reproduced with Keulegan's equation by replacing the equivalent grain roughness with the following expression to estimate the coefficient α_S in eq.(4.11):

$$\alpha_S = \alpha_{RL}\alpha_{BR} \qquad (4.27)$$

where α_{RL} is a coefficient for the roughness layer and α_{BR} is a coefficient for the bed load roughness layer. Recking et al. obtained roughness layer resistance values for computing coefficient α_{RL} from data presented by Graf (1991). With these data, they found that α_{RL} varies in the range $25>R_h/D>1$, and outside these limits it becomes constant and takes the limit value. The equation presented for this computation is

$$\alpha_{RL} = 4\left(\frac{R_h}{D}\right)^{-0.43} \quad \text{with } 1 \leq \alpha_{RL} \leq 4 \qquad (4.28)$$

Good agreement was found for their own data without sediment transport using eq.(4.28). For α_{BR} they proposed the following equation as a function of the energy slope and relative water depth

$$\alpha_{BR} = 7S^{0.85}\frac{R_h}{D} \quad \text{with } 1 < \alpha_{BR} \leq 2.6 \qquad (4.29)$$

Outside the limits, α_{BR} becomes constant and takes the limit value. The dimensionless Chézy resistance coefficient is computed with

$$C_z = 6.25 + 5.75\log\left(\frac{R_h}{k_s}\right) \qquad (4.30)$$

where k_s is computed from eqs.(4.11) and (4.27), and the effective shear stress on the grains is obtained from equations (4.6) and (4.7). When testing their model with field data corresponding to material of non-uniform size, Recking et al. found good results by using the grain diameter D_{84} in eq(4.11) for data without bed load transport. For flows with

sediment motion they found greater scatter and concluded that under such conditions there were no reasons why D_{84} should be an appropriate diameter for computing flow resistance.

Recking iterative

Recking et al.'s approach (2008) was developed for plane beds. Nevertheless, following the conceptual development of the Einstein model (1950), here it was attempted to extend the applicability of the Recking et al. method to flows with bedforms by considering a reference plane bed shear stress. In this manner, using eqs.(4.6), (4.7) and (4.12), eq.(4.30) can be rewritten as

$$H_s = \frac{V^2}{gS}\left[6.25 + 5.75\log\left(\frac{H_s}{\alpha_{RL}\alpha_{BR}}\right)\right]^{-2} \qquad (4.30)$$

where α_{RL} and α_{BR} are calculated with

$$\alpha_{RL} = 4\left(\frac{H_s}{D}\right)^{-0.43} \quad \text{with} \quad 1 \le \alpha_{RL} \le 4 \qquad (4.31)$$

$$\alpha_{BR} = 7S^{0.85}\frac{H_s}{D} \quad \text{with} \quad 1 < \alpha_{BR} \le 2.6 \qquad (4.32)$$

H_s can be found iteratively, so that the correct value must satisfy eqs.(4.30) to (4.32). The dimensionless Chézy resistance coefficient is computed with

$$C_z = 6.25 + 5.75\log\left(\frac{H_s}{k_s}\right) \qquad (4.33)$$

and the effective shear stress on the grains is obtained from equations (4.6) and (4.7). For the purpose of this study, this method has been called the Recking iterative method as it combines Einstein's iterative model and Recking et al.'s model.

4.3.2.2 Comparison of bed shear stress partition models

The results of applying the shear stress partition methods to the experimental data set are shown in Tables 4.4 and 4.5. For the computations, the hydraulic radius for the bed, as shown in Table 4.3, was used. For comparison purposes, the Recking et al. method was applied for two representative grain size diameters in eqs.(4.11), (4.28) and (4.29); first, using D_{84} and then D_{50}. This procedure was repeated for the Recking iterative method.

Computed k_s values with the selected models differed for some runs by as much as a five-fold factor. Nevertheless, the difference between computed skin friction values never exceeded a factor of two. This is because the equivalent roughness is only present in the log term of the Keulegan formulation. Therefore, the k_s value used has little effect on estimated skin friction. Even when computed skin friction values correspond to the same order of magnitude, there are some evident differences which can provide some clues about the performance of each method. For example, for the iterative methods to be physically coherent, the estimated H_s value would be expected to be lower than flow depth. This was indeed the case for all the models except the Recking iterative model using D_{84}, for which computed H_s values were higher than flow depth for more than half of the runs.

From eq.(4.13) computed skin friction would be expected to be equal to or lower than average bed shear stress. If this does not occur, then the computed bedform shear stress will be negative, which is unrealistic. In other words, the condition $\tau''/\tau_b \ge 0$ must be satisfied, where $\tau'' = \tau_b - \tau'$. As seen in Table 4.5, the models of Van Rijn, Recking et al. with D_{84} and Recking iterative with D_{84} produced many negative values for bedform shear stress. Therefore these three methods were discarded as the results were not physically sound.

Table 4.4 Equivalent roughness height k_s and skin friction portion of water depth (where applicable) H_s, for the selected shear stress partition methods.

Run	Water depth H [m]	Einstein (1950) $k_s=D_{65}$		Engelund and Hansen (1967) $k_s=2.5D_m$		Van Rijn (1992) $k_s=f(D_{35}, \tau^*)$	Reck. (2008) $D_x=D_{84}$	Reck. (2008) $D_x=D_{50}$	Recking iterative $D_x=D_{84}$		Recking iterative $D_x=D_{50}$	
		ks [mm]	Hs [m]	ks [mm]	Hs [m]	ks [mm]	ks [mm]	ks [mm]	ks [mm]	Hs [m]	ks [mm]	Hs [m]
G12	0.068	5.3	0.048	11.7	0.062	18.8	22.6	16.4	21.3	0.074	16.2	0.067
G13	0.092	4.4	0.054	9.4	0.068	17.5	17.2	10.2	17.9	0.080	11.3	0.069
G14	0.076	5.0	0.053	10.6	0.067	18.3	20.5	13.7	19.8	0.080	13.9	0.071
G15	0.079	4.7	0.055	9.9	0.069	17.9	19.3	12.1	18.4	0.082	12.2	0.072
G16	0.085	4.5	0.060	9.6	0.075	17.9	16.8	10.8	17.6	0.089	11.0	0.076
G17	0.109	4.9	0.091	10.2	0.112	18.2	10.2	9.0	10.8	0.112	9.3	0.107
M1E1	0.104	3.8	0.072	7.1	0.086	17.0	12.7	7.9	13.2	0.100	7.9	0.086
M1E2	0.086	4.2	0.063	7.5	0.075	17.5	17.4	8.6	16.5	0.092	8.8	0.076
M1E3	0.076	4.0	0.053	7.5	0.064	17.5	18.1	8.7	17.2	0.080	9.0	0.065
M1E4	0.087	4.3	0.060	7.6	0.071	17.6	17.6	8.9	16.9	0.089	9.3	0.074
M1E5	0.090	4.2	0.064	7.5	0.076	17.4	17.1	8.6	16.3	0.094	8.8	0.077
M1E6	0.113	3.9	0.081	7.0	0.095	17.0	10.2	7.9	10.0	0.103	7.9	0.096
M2E1	0.081	3.3	0.057	6.1	0.066	15.9	14.7	6.6	14.2	0.083	6.6	0.066
M2E2	0.080	3.2	0.062	6.3	0.073	15.7	14.3	6.5	13.5	0.089	6.5	0.071
M2E3	0.083	3.1	0.059	6.1	0.069	15.3	13.2	6.4	12.8	0.084	6.4	0.068
M2E4	0.089	3.1	0.057	5.9	0.066	14.8	12.0	6.3	12.4	0.080	6.3	0.065
M2E5	0.103	3.1	0.063	6.1	0.074	15.0	11.8	6.5	12.3	0.088	6.5	0.073
M2E6	0.113	3.1	0.076	6.0	0.087	15.3	10.2	6.0	10.1	0.098	6.0	0.085
S1	0.103	1.7	0.037	3.8	0.046	5.9	4.9	4.0	4.9	0.049	4.0	0.046
S2	0.109	1.7	0.040	3.6	0.049	5.9	4.9	4.0	4.9	0.053	4.0	0.050
S3	0.119	1.7	0.048	3.5	0.058	5.9	4.9	3.9	4.9	0.062	3.9	0.058
S4	0.130	1.7	0.053	3.5	0.064	5.9	4.9	3.9	4.9	0.069	3.9	0.065

Table 4.5 Results of applying selected bed shear stress partition methods. τ_b' is the bed shear stress skin friction portion; τ_b"/τ_b is the ratio between the form shear stress portion and the total bed shear stress.

Run	τ_b [Pa]	Einstein (1950) $k_s=D_{65}$		Engelund and Hansen (1967) $k_s=2.5D_m$		Van Rijn (1992) $k_s=f(D_{35},\tau^*)$		Recking et al. (2008) $D_x=D_{84}$		Recking et al. (2008) $D_x=D_{50}$		Recking iterative $D_x=D_{84}$		Recking iterative $D_x=D_{50}$	
		τ' [Pa]	τ''/τ_b	τ' [Pa]	τ''/τ_b	τ' [Pa]	τ''/τ_b	τ' [Pa]	τ''/τ_b	τ' [Pa]	τ''/τ_b	τ' [Pa]	τ''/τ_b	τ' [Pa]	τ''/τ_b
G12	**13.7**	10.1	0.26	13.0	0.05	15.7	-0.15	17.0	-0.24	14.4	-0.05	15.5	-0.13	14.0	-0.03
G13	**15.8**	9.7	0.38	12.2	0.23	14.2	0.10	13.8	0.13	10.9	0.31	14.6	0.08	12.6	0.20
G14	**13.3**	9.8	0.26	12.3	0.07	15.2	-0.14	15.8	-0.19	12.9	0.03	14.7	-0.10	13.1	0.02
G15	**11.9**	8.8	0.26	11.0	0.08	13.7	-0.15	14.0	-0.17	11.1	0.06	13.1	-0.10	11.4	0.04
G16	**9.6**	7.2	0.25	9.0	0.06	11.5	-0.19	10.9	-0.14	8.9	0.07	10.6	-0.11	9.1	0.05
G17	**5.6**	5.2	0.07	6.4	-0.14	8.6	-0.53	6.5	-0.16	6.2	-0.10	6.3	-0.13	6.1	-0.08
M1E1	**7.6**	5.7	0.24	6.8	0.10	9.3	-0.22	8.0	-0.05	6.5	0.14	7.9	-0.04	6.8	0.10
M1E2	**13.2**	10.3	0.22	12.2	0.07	16.9	-0.28	16.6	-0.26	12.0	0.09	15.1	-0.15	12.5	0.06
M1E3	**12.2**	9.0	0.26	10.8	0.12	14.8	-0.21	14.8	-0.21	10.5	0.14	13.6	-0.12	11.1	0.09
M1E4	**12.3**	9.1	0.26	10.7	0.13	14.4	-0.17	14.1	-0.15	10.4	0.16	13.3	-0.08	11.1	0.10
M1E5	**10.7**	8.2	0.23	9.7	0.10	13.2	-0.24	12.9	-0.20	9.4	0.12	11.9	-0.12	9.9	0.08
M1E6	**6.0**	4.7	0.21	5.5	0.08	7.6	-0.27	6.0	0.01	5.4	0.10	6.0	0.01	5.5	0.08
M2E1	**13.3**	9.9	0.25	11.4	0.14	16.2	-0.22	15.3	-0.15	10.7	0.19	14.4	-0.08	11.4	0.14
M2E2	**12.2**	10.1	0.17	11.8	0.03	17.2	-0.41	16.1	-0.32	11.4	0.07	14.4	-0.18	11.6	0.05
M2E3	**12.2**	9.3	0.24	10.8	0.11	15.2	-0.25	13.9	-0.14	10.2	0.17	13.2	-0.08	10.7	0.12
M2E4	**12.0**	8.1	0.33	9.4	0.21	12.4	-0.04	11.1	0.08	8.5	0.30	11.4	0.05	9.4	0.22
M2E5	**9.2**	6.0	0.34	7.1	0.23	9.1	0.01	8.0	0.13	6.3	0.32	8.5	0.08	7.0	0.24
M2E6	**6.5**	4.8	0.27	5.5	0.16	7.4	-0.14	6.1	0.07	4.9	0.24	6.1	0.06	5.3	0.18
S1	**14.9**	5.6	0.62	7.0	0.53	6.2	0.59	5.6	0.62	5.2	0.65	7.4	0.50	7.0	0.53
S2	**12.5**	4.8	0.61	5.9	0.52	5.3	0.57	4.9	0.61	4.5	0.64	6.3	0.49	6.0	0.52
S3	**9.0**	3.8	0.58	4.6	0.48	4.4	0.51	4.0	0.56	3.7	0.59	5.0	0.45	4.7	0.48
S4	**7.1**	3.1	0.56	3.8	0.47	3.6	0.49	3.3	0.54	3.1	0.57	4.0	0.43	3.8	0.46

It is noteworthy that the Engelund and Hansen and Recking iterative with D_{50} methods produced quite similar skin friction values. In fact, the average ratio between the computed values for both methods was almost equal to 1, with a standard deviation of 3%. This occurred as the equivalent roughness obtained using these approaches was similar; on average, the k_s for the Engelund and Hansen method was only 10% lower than that for the Recking iterative approach.

4.3.2.3 Comparison with bedload plots

To select an adequate estimate of skin friction for flume experiments with mixed-size sediment, Wilcock and Southard (1988) evaluated the degree to which an estimate diminished scatter in the observed transport rate. They found that Einstein's partition model performed best for their data. Following a similar procedure, best-fit functions were obtained here for the sediment transport rates of each experimental series, i.e., four families of curves were fitted, each for a different bed material. Power functions of the form $Q_{SF}=a(\tau')^b$ were used, where Q_{SF} is the total sediment feeding rate of the run by dry weight, τ' is the grain shear stress obtained using the selected partition models, and a and b are the fitted constants. Figure 4.5 shows the plots for each of the models and Table 4.6 presents the correlation coefficients obtained, defined as:

$$R_{XY} = \frac{\sum (X_i - \overline{X})(Y_i - \overline{Y})}{(n_R - 1)\sigma_X \sigma_Y} \qquad (4.34)$$

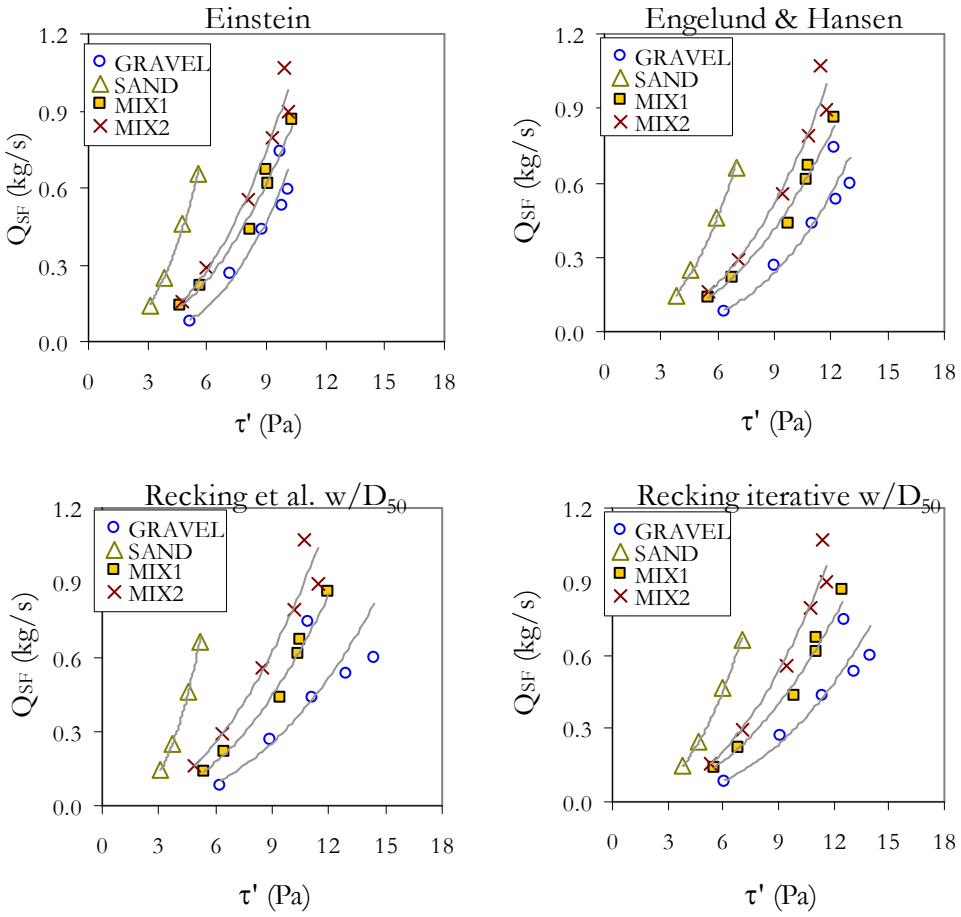

Figure 4.5. Plots of sediment feeding rates and skin friction shear stress for best-performing shear stress partition methods.

Table 4.6 Correlation coefficients for best-fit power functions of the relation between sediment feeding rates and the skin friction computed by the models that performed best.

Method	Correlation coefficient R				Average R	RANKING
	Gravel	Mix1	Mix2	Sand		
Einstein	0.938	0.991	0.979	0.999	0.977	**1**
Engelund and Hansen	0.930	0.994	0.972	0.998	0.974	**2**
Recking w/D_{50}	0.776	0.994	0.962	0.998	0.933	**7**
Recking iterative w/D_{50}	0.906	0.994	0.979	1.000	0.970	**3**

where X and Y are related variables, in this case $X=Q_s$ and $Y=\tau'$, n_R is the number of data and σ_X and σ_Y are the standard deviations for X and Y, respectively.

Overall, because the correlation coefficients are high, the ranking of the performance of the different methods was based on only subtle differences. The highest average correlation coefficients were obtained with Einstein's method. Nevertheless, those obtained for the Engelund and Hansen model and the Recking iterative method using the D_{50} were only slightly lower, so it can be concluded that the three models performed similarly. It is important to note that the Recking model used iteratively as in the Einstein method improved the correlation with respect to the original Recking model. Because the main difference between the methods is related to the selection of k_s, these results prove that a change in k_s or the representative diameter used only moves the sediment transport graphs horizontally with a minimum effect on scatter and bias of the data.

Figure 4.6 contrasts the effect of bed shear stress partition on sediment transport plots compared to the plots in Figure 4.5. As can be seen, using total bed shear stress instead of skin friction, almost a unique power function can adequately describe the trend of the two uniform sediments together and the two mixtures apart. The mixtures plot over the sand and gravel, so that for a given bed shear stress a greater bed load is carried with mixtures than with uniform material. Such behavior is related to the kind of bedforms that the interaction between sediment and flow produces, and to the contribution of such bedforms to total bed resistance. These issues will be discussed in Chapter 6.

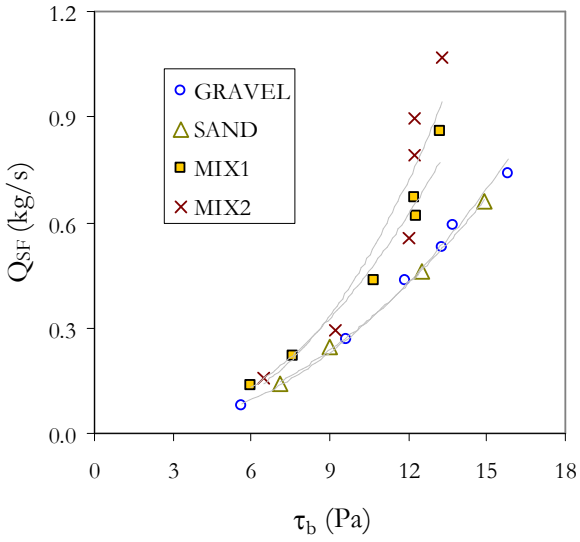

Figure 4.6. Plots of sediment feeding rates and total bed shear stress.

4.3.2.4 Comparison with plane bed runs

Millar (1999) suggested that in defining an estimate for k_s related to grain diameter, rather than deriving a best-fit value, an adequate criterion would be to define a lower bound for the observed flow resistance. This lower bound would correspond to grain resistance in the absence of form roughness. Following this criterion, the dimensionless Chézy friction coefficient C_z, for average flow conditions, was obtained for each run and plotted against the relative submergence R_{hb}/k_s, as shown in Figure 4.7. C_z was computed from eqs.(4.4) and (4.7) using f_b as presented in Table 4.3, so that $C_z=(8/f_b)^{0.5}$. On the other hand, the k_s values used were those obtained from the selected shear stress partition models. In this manner, for each run, four points were plotted with the same C_z value but different relative submergence.

Contrary to the Darcy-Weisbach friction factor, the Chézy coefficient increases with decreased flow resistance. Therefore, a higher bound for the coefficient would define a limit for the lowest possible flow resistance for a given grain diameter. It can be assumed that this higher bound is adequately described by the Keulegan or the Manning-Strickler equations (equations 4.9 and 4.10), which are plotted in Figure 4.7 considering $R_{hb}\approx H$. Furthermore, for a prismatic straight channel, the higher bound should be defined by clear-water plane bed conditions. The dimensionless Chézy factor would be lower (higher roughness) if other elements (bedforms, surface waves, bed load, etc.) consume part of the bed shear stress. Thus, the experimental points with a higher resistance coefficient correspond to a low effective roughness. Therefore, in Figure 4.7, points with the highest dimensionless Chézy resistance coefficient (lowest Darcy-Weisbach coefficient f_b in Table 4.3) correspond to run G17, for which the observed bed configuration was almost plane bed with low sediment transport (in fact this was the run with the lowest sediment feeding rate). On the contrary, all four sand runs, which in contrast to the rest of runs registered very high amplitude bedforms, plot far below the boundary set by the Keulegan formulation.

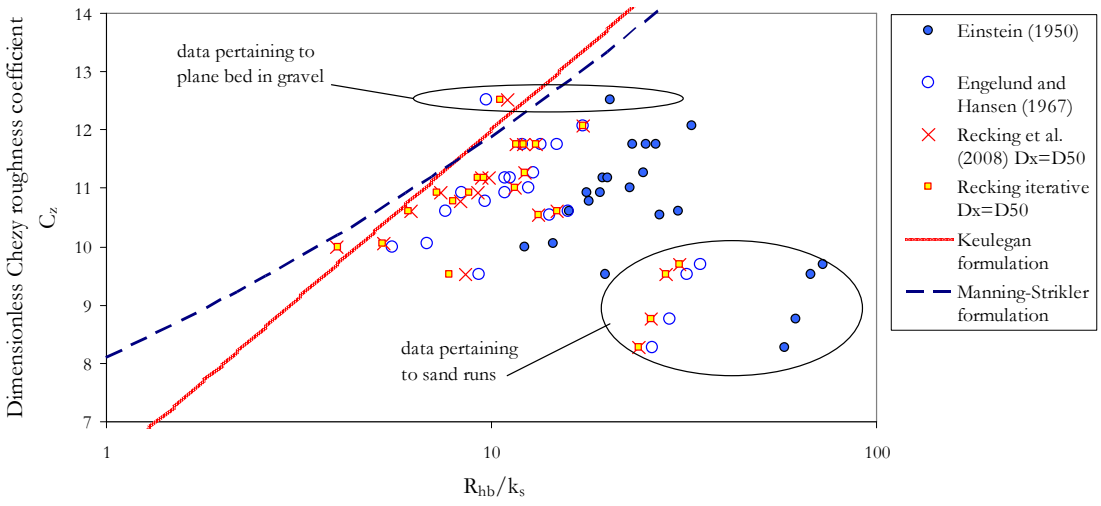

Figure 4.7. Variability of the dimensionless Chézy resistance factor for the experimental runs as a function of relative depth computed with different k_s values proposed by the selected shear stress partition models. The highest C_z values were registered for run G17 with a plane bed and a low sediment transport rate. The lowest values were for the runs with sand with high-amplitude bedforms.

Consistent with the higher bound criterion (lower bound for the Darcy-Weisbach resistant factor), it can be assumed that the further the points plot upwards from the boundary set by the Keulegan formulation, the more likely it is that the equivalent roughness estimate is not adequate. This is related to the negative values for the ratio τ''/τ_b in Table 4.5. As all the selected methods use the Keulegan formulation with the assumption of a plane bed, an erroneous high k_s value predicts a low C_z value, and because $\tau'=\rho(V/C_z)^2$, the skin friction shear stress increases with k_s. Because τ' cannot be higher than τ_b, there is a limit for C_z set by the Keulegan formulation. If the data-points for the shear partition methods of Van Rijn, Recking et al. using the D_{84} and Recking iterative using the D_{84} had been drawn in Figure 4.7, most of them would have fallen above the boundary set by the Keulegan curve.

It can be expected that for plane bed runs, if the correct k_s value for the sediment grains is used, then total bed resistance should be accurately predicted by the Keulegan equation. Otherwise, we would at least expect the estimations to fall inside the fringe of experimental scatter. Wong and Parker (2006) re-analyzed original sediment transport data sets from Gilbert and Meyer-Peter and Müller for plane-bed configurations. Using a value of $k_s=2D_{90}$ they found good agreement with the logarithmic law of Keulegan, as shown in Figure 4.8, where the graph they presented is compared with plots for the present experimental data with k_s as computed using the methods of Einstein, Engelund and Hansen and Recking iterative with D_{50} (these methods were selected as they ranked highest in Table 4.6). For all three models, the plane bed run (i.e., run G17, the point with the highest C_z in the graph) plots close to the curve depicted by the Keulegan formulation, within the region where most of the points in the plot from Wong and Parker fall.

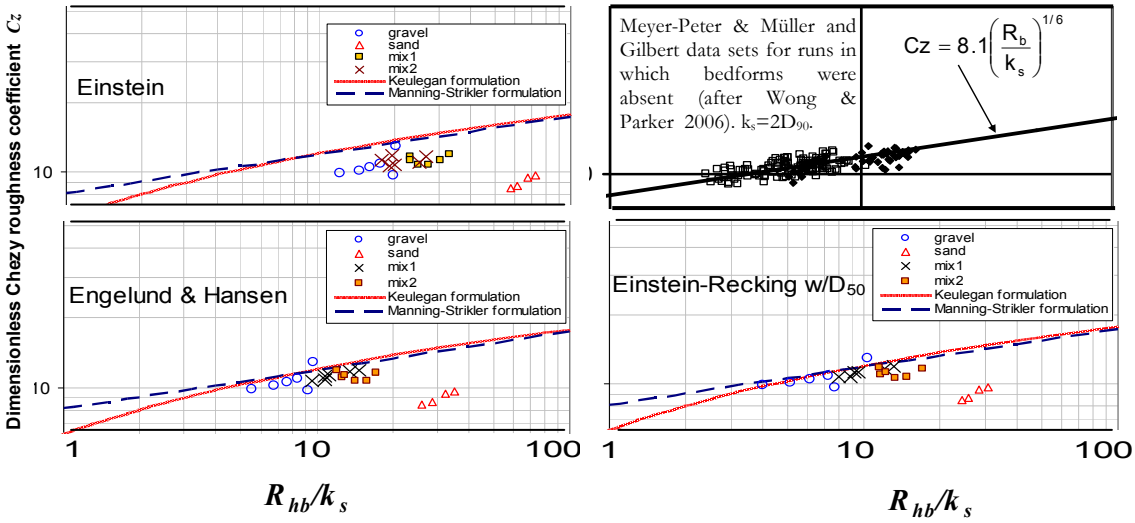

Figure 4.8 Dimensionless Chézy factor for experimental data; plots for k_s estimated with three different criteria, and plot by Wong and Parker (2006) for plane bed data from Meyer-Peter and Müller and Gilbert.

4.3.2.5 Comparison with bed surface level variations

Bedform–related flow resistance is a function of the form drag produced by the bed features; hence, it is linked to the height and length of the bedforms. For comparison and assessment of the selected shear stress partition models, bedform–related shear stress was compared with the standard deviation of the measurements for the bed surface level during

mobile-bed equilibrium conditions, σ_b (see Table 3.23). Because it is a dispersion parameter, the standard deviation of the bed surface concentrates information on the height and length of the bedforms; thus, it should adequately link variations in flow resistance between runs according to the variability of bedform dimensions.

Figure 4.9 compares the three partition methods that performed best when grain shear stress was plotted against sediment transport rates. For the comparison, the ratio between the computed bedform-related shear stress and the total bed shear stress τ''/τ_b, is plotted against the ratio of the bed level variation standard deviation to the bed sediment median diameter σ_b/D_{50}. It can be expected that when $\sigma_b/D_{50}\rightarrow 0$ there would be no bedforms and a plane bed configuration would occur, meaning that $\tau''/\tau_b\rightarrow 0$ would be satisfied. In the same manner, the larger the bed profile standard deviation, i.e., the steeper the bedforms, the more negligible the grain-related shear stress would be, in which case the limit for $\sigma_b/D_{50}\rightarrow\infty$ would be $\tau''/\tau_b \rightarrow 1$.

For all three methods, the data show a clear trend towards $\tau''/\tau_b\leq 0$ for values of $\sigma_{bed}/D_{50}<1$, which coincides with what would be expected for the absence of bedforms. Even though differences in scatter between the three graphs in Figure 4.9 are subtle, at first glance it can be noticed that the data collapse better for the Engelund and Hansen and the Recking iterative methods.

It should be noted that the standard deviation used here corresponds to measurements performed on the channel wall, which means that this parameter does not represent the conditions at the center of the channel. In other words, the three-dimensionality of the bedforms is not taken into account. Nevertheless, in view of the clear bias shown in Figure 4.9, we would expect proportionality to be conserved between the dimensions of the bedforms at the wall and at the center of the channel.

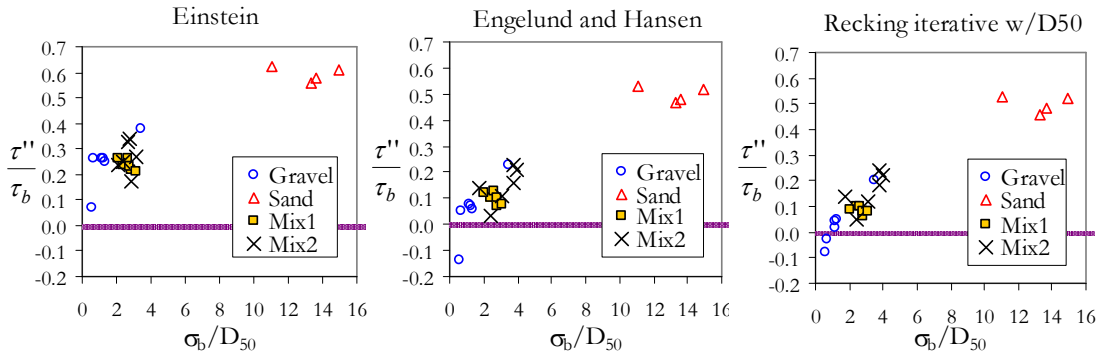

Figure 4.9 Variation of the ratio between bedform–related shear stress and the total bed shear stress, with respect to the standard deviation of the bed surface level (as a ratio of the bed material D_{50}) obtained from measurements of the bed profile. Each graph corresponds to a different shear stress partition method.

4.3.3 Comparison with experimental data from the literature

Using different levels of analysis in the previous Sections, it was found that the shear stress partition methods that performed best when applied to the experimental data were the Engelund and Hansen method and the method designated here as the Recking iterative method. This second method combines concepts and reasoning from Einstein's original model for beds with bedforms (1950) and from Recking et al.'s model for plane beds (2008), which takes into consideration the effect of bed load and bed slope on the value of

equivalent roughness. For the new experimental data set, the Recking iterative model was found to perform better when D_{50} rather than D_{84} was used as a representative diameter.

In order to assess the performance of the Engelund and Hansen model and the Recking iterative model with other ranges of sediment grain diameters and hydraulic conditions, these models were applied to two other data sets, briefly described as follows:

1. Kennedy (1961). 43 experimental runs with uniform sand grains with a mean diameter of 0.23 and 0.55 mm. High Froude numbers, ranging from 0.5 to 2.34. Bedforms described in detail, mostly upper-regime and transitional bedforms, including 12 runs in an upper-regime plane bed.
2. Kuhnle (1993). 30 experimental runs to study the initiation of motion in sand, gravel and three sand-gravel bimodal mixtures with 90%, 75% and 55% sand content. Mean diameters for the sand and gravel were 0.5 and 5.6 mm, respectively. No detailed information was given for the bedforms observed. Plane-bed configurations were observed for low sediment transport rates.

To be analyzed here, for both data sets the method of Vanoni and Brooks was applied to separate side-wall effects (as described in 4.3.1).

Recking et al. (2008) found good agreement with field data when they used D_{84} for no bed load conditions. For field data with bed load they found greater scatter, and were not conclusive about which was the most representative diameter to use in their model with non-uniform size material. To investigate the sensitivity of the model to the representative diameter, plane bed runs were compared with high sediment transport conditions (12 runs for the Kennedy data set) and plane bed runs for near-incipient motion conditions for the bed sediment (8 runs for the Kuhnle data set[1]). The comparisons are shown in Figures 4.10 and 4.11. For Kuhnle's data, only runs identified by Kuhnle as having absent or poorly formed bedforms were included in the comparison. It was observed that for plane bed runs the Recking iterative model with a representative diameter of D_{84} plotted the points closer to the Keulegan formulation than the same model with a diameter of D_{50}. The Engelund and Hansen model produces plots that do not separate much from the Keulegan formulation. It can be concluded that for near-incipient motion conditions, the Recking iterative model performs better with D_{84} than with D_{50}, and that the Engelund and Hansen model performs well. On the other hand, when applying the Recking iterative approach to the Kennedy plane bed runs in upper regime, a better collapse of the data to the Keulegan formulation was found for D_{50} than for D_{84}. This is consistent with the findings of Recking et al. Although they did not suggest a representative diameter to use for such conditions, they stated that there was no reason for D_{84} to control bed roughness when the grains were in motion. Results of the Engelund and Hansen model applied to Kennedy's plane bed data set are not shown as the computed k_s for all the runs differed only by 3.8% from the value computed with the Recking iterative using D_{50}. Finally, half of the runs identified by Kuhnle with absent or poorly formed bedforms plotted over the Keulegan formulation when D_{84} was used; as it is not possible to know which of these runs actually correspond to plane bed runs, we would expect D_{50} to perform better when bedforms appear or when the movement of particles on the bed is generalized. The selection of a representative diameter for this border condition seems to be a function of the bed shear stress. Finding this representative diameter is beyond the scope of this work, but from a trial and error analysis of Kuhnle's data this border would be expected to be between 1.5 and 2 times the critical shear stress of the median bed sediment.

[1] For the Kuhnle data set, in Kuhnle 1993a it is stated that "for all five sediment beds, the experimental runs with the two lowest flow rates lacked visible bedforms"; although for the same data set, in Kuhnle 1993b it is said that "All the 100% sand experiments had bedforms". It has been here considered that no plane bed occurred for the 100% sand bed.

Table 4.7 Summary of results for the Kuhnle (1993a) data set. The Recking iterative model was applied with D_{84} as representative diameter for plane bed runs. Otherwise, D_{50} was used. For most of the plane bed runs, grain-related shear stress was set equal to the bed shear stress obtained using the Vanoni and Brooks method.

Run	R_{hb} [m]	τ_b [Pa]	k_s [mm]	H_s [m]	τ' [Pa]	τ'' [Pa]	τ''/τ_b
SS1	0.089	1.81	1.24	0.044	0.90	0.91	0.50
SS2	0.073	0.29	0.70	0.076	0.29	0.00	0.00
SS3	0.075	0.28	0.71	0.075	0.24	0.04	0.13
SS4	0.078	0.56	1.12	0.074	0.53	0.03	0.06
G3	0.084	6.38	13.13	0.084	6.38	0.00	0.00
G4	0.086	8.73	17.06	0.086	8.73	0.00	0.00
G5	0.088	10.63	20.05	0.088	10.63	0.00	0.00
G6	0.087	11.36	21.28	0.087	11.36	0.00	0.00
GB1B	0.088	3.85	9.74	0.088	3.47	0.37	0.10
GB2B	0.089	3.72	9.71	0.089	3.62	0.10	0.03
GB3	0.088	4.44	9.74	0.088	4.33	0.10	0.02
GB4	0.088	5.32	11.11	0.088	5.23	0.09	0.02
SG10-1	0.080	0.87	1.21	0.073	0.80	0.07	0.08
SG10-2	0.078	0.64	1.21	0.072	0.60	0.04	0.07
SG10-3	0.080	0.44	0.78	0.064	0.36	0.09	0.20
SG10-4	0.077	0.29	1.09	0.077	0.26	0.03	0.09
SG10-5	0.086	2.08	1.21	0.059	1.44	0.64	0.31
SG10-6	0.085	3.10	1.21	0.063	2.28	0.82	0.26
SG25-1	0.078	0.90	1.47	0.075	0.88	0.03	0.03
SG25-2	0.080	0.80	1.29	0.064	0.64	0.16	0.20
SG25-3	0.083	0.60	0.81	0.053	0.38	0.22	0.36
SG25-4	0.079	0.36	6.32	0.079	0.36	0.00	0.00
SG25-5	0.084	1.83	1.47	0.068	1.47	0.36	0.20
SG25-6	0.081	3.24	1.47	0.067	2.65	0.59	0.18
SG45-1	0.086	1.34	1.74	0.059	0.93	0.42	0.31
SG45-2	0.086	1.04	1.23	0.052	0.63	0.41	0.39
SG45-3	0.089	0.79	6.26	0.089	0.60	0.20	0.25
SG45-4	0.085	2.23	2.60	0.069	1.81	0.42	0.19
SG45-5	0.082	3.36	2.60	0.073	2.98	0.39	0.11
SG45-6	0.088	2.96	2.60	0.067	2.26	0.70	0.24

The results after applying the Recking iterative method and the Engelund and Hansen method to all runs in the two data sets are shown in Figure 4.12 and Tables 4.7 to 4.9. Results for Kennedy's data set analyzed with the Engelund and Hansen method are not shown as they were quite similar to results obtained with the Recking iterative method, with a difference in effective shear stresses of less than 1% on average. The considerations explained above regarding the selection of a suitable representative diameter for the plane bed runs, and other considerations were taken into account as follows:

- For plane bed runs with near-incipient motion conditions the representative diameter used was D_{84}. If the computed dimensionless shear stress value exceeded the critical shear stress of the median diameter by 1.5 times, the representative diameter for computing k_s was changed to D_{50}, and all the variables were recalculated. (The appropriateness of this procedure was tested by plotting the bed load data of Kuhnle and finding the least scatter by trial and error, changing the border, from the lowest to

the highest bed load, where the representative diameter changes from D_{84} to D_{50}).

- When the computed grain shear stress was higher than the average bed shear stress, the final grain shear stress was set as equal to the average shear stress.
- For plane bed runs, the original Recking et al. method was applied, with consideration of the previous point.

The points appropriately defined the higher bound set by the Keulegan formulation, and it can thus be concluded that the Recking iterative method performs well for these conditions. It is interesting to note that the k_s value obtained for all the runs from the Kennedy data set was $2.6D_{50}$, which is almost the same as that proposed by the Engelund and Hansen method: $2.5D_m$.

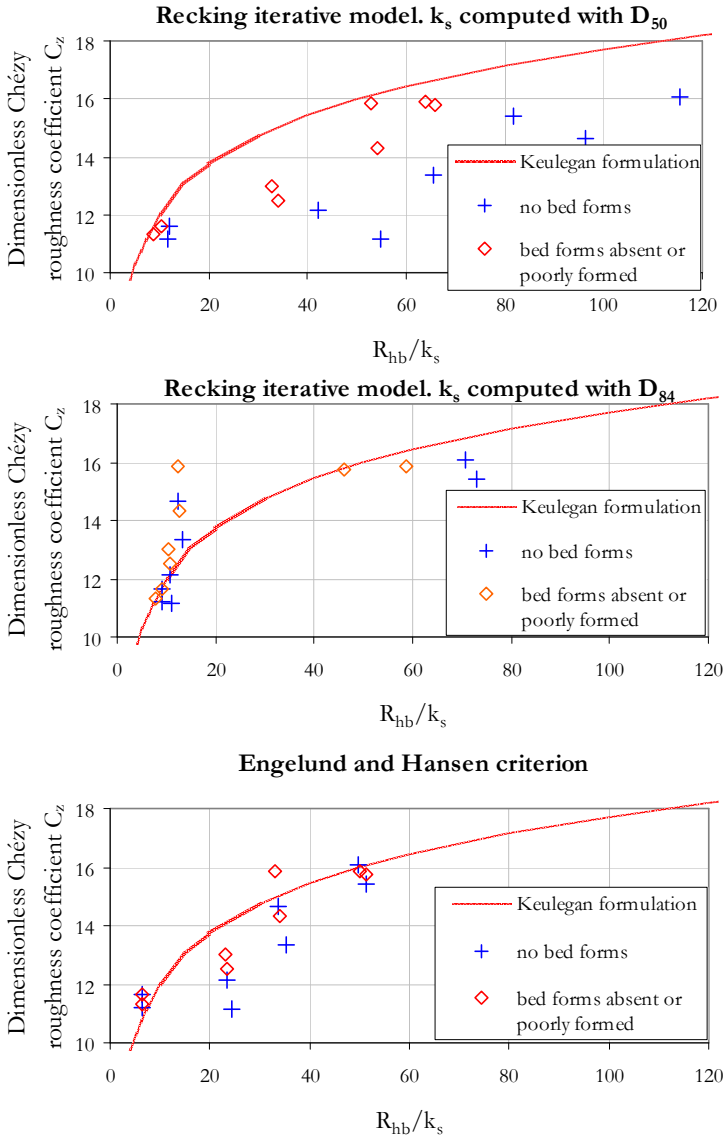

Figure 4.10. Effect of choosing different representative diameters in computing the value of k_s for plane bed runs for the Kuhnle (1993) data set for incipient motion conditions. a) Recking iterative model using D_{50}; b) Recking iterative model using D_{84}; c) Engelund and Hansen model.

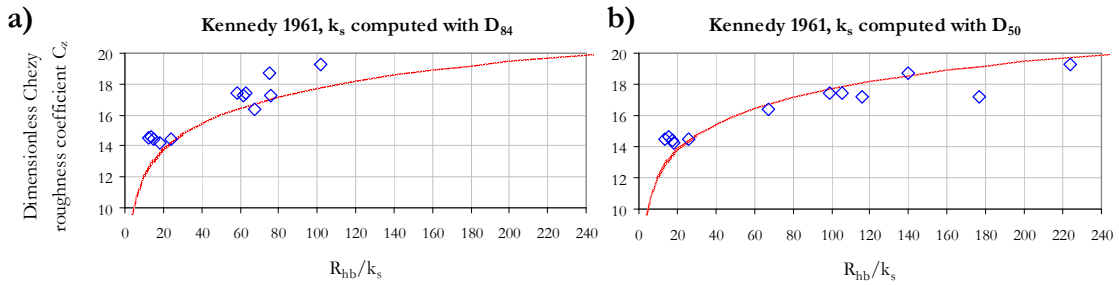

Figure 4.11. Effect of choosing different representative diameters in computing the value of k_s for plane bed runs for the Kennedy (1961) data set for upper regime and high sediment transport rates. a) Recking iterative model using D_{84}; b) Recking iterative model using D_{50}. The curve is for the Keulegan formulation.

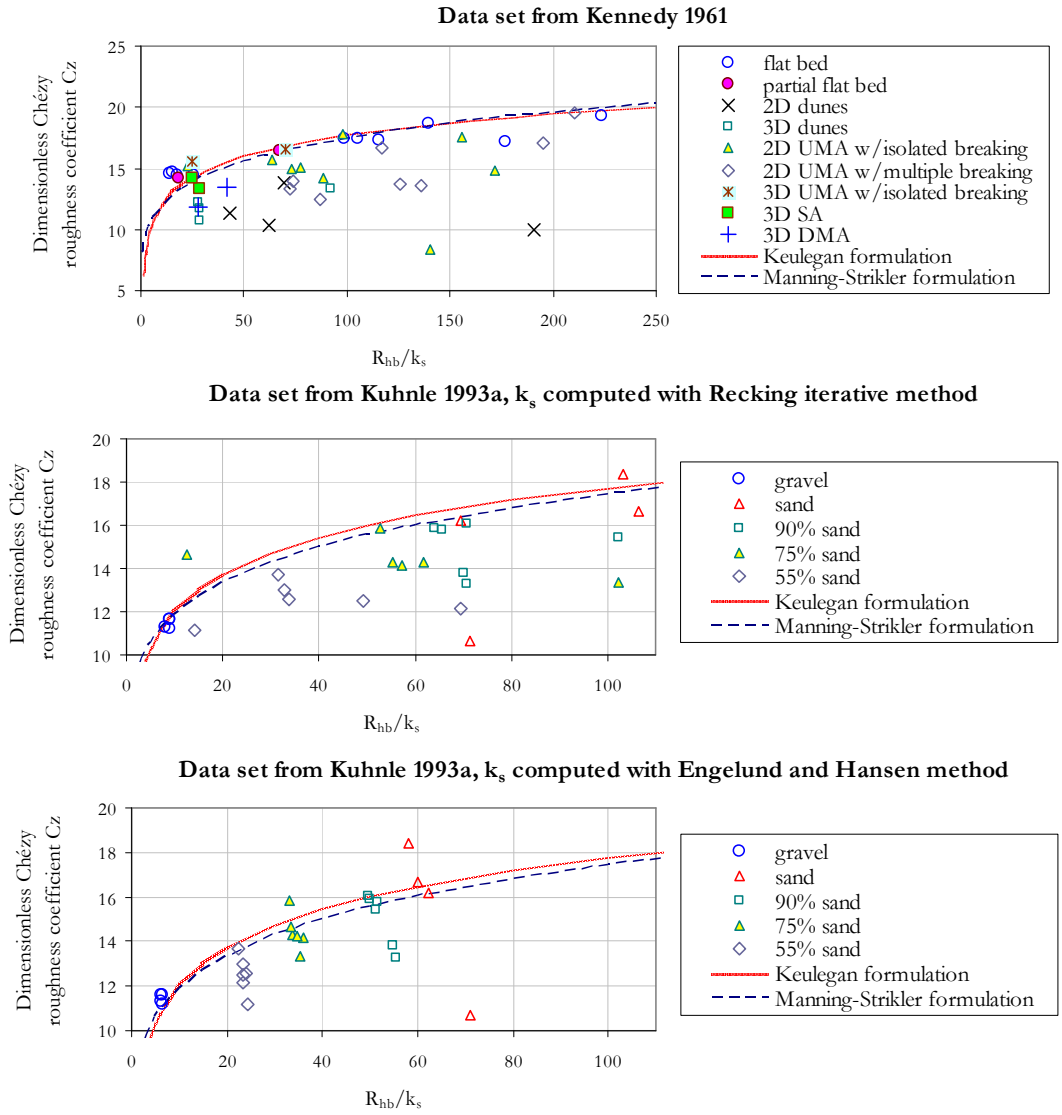

Figure 4.12. Flow resistance coefficients for the Kennedy (1961) and Kuhnle (1993a) data sets, with k_s obtained from the Recking iterative method and the Engelund and Hansen method. For the bedforms in the Kennedy data set: UMA=Upstream-Migrating Antidunes, SA=Stationary Antidunes DMA=Downstream-Migrating Antidunes.

Table 4.8 Summary of results for the Kuhnle (1993a) data set. The Engelund and Hansen model was applied with D_{84} as representative diameter for plane bed runs. Otherwise, D_{50} was used. For most of the plane bed runs, grain-related shear stress was set equal to the bed shear stress obtained using the Vanoni and Brooks method.

Run	R_{hb} [m]	τ_b [Pa]	k_s [mm]	H_s [m]	τ' [Pa]	τ'' [Pa]	τ''/τ_b
SS1	0.089	1.81	1.25	0.044	0.90	0.91	0.50
SS2	0.073	0.29	1.25	0.087	0.29	0.00	0.00
SS3	0.075	0.28	1.25	0.076	0.28	0.00	0.00
SS4	0.078	0.56	1.25	0.075	0.55	0.02	0.03
G3	0.084	6.38	13.98	0.084	6.38	0.00	0.00
G4	0.086	8.73	13.98	0.086	8.73	0.00	0.00
G5	0.088	10.63	13.98	0.088	10.63	0.00	0.00
G6	0.087	11.36	13.98	0.087	11.36	0.00	0.00
GB1B	0.088	3.85	13.98	0.092	3.85	0.00	0.00
GB2B	0.089	3.72	13.98	0.098	3.72	0.00	0.00
GB3	0.088	4.44	13.98	0.097	4.44	0.00	0.00
GB4	0.088	5.32	13.98	0.093	5.32	0.00	0.00
SG10-1	0.080	0.87	1.55	0.077	0.85	0.03	0.03
SG10-2	0.078	0.64	1.55	0.077	0.63	0.01	0.01
SG10-3	0.080	0.44	1.55	0.075	0.42	0.03	0.06
SG10-4	0.077	0.29	1.55	0.078	0.29	0.00	0.00
SG10-5	0.086	2.08	1.55	0.063	1.52	0.56	0.27
SG10-6	0.085	3.10	1.55	0.066	2.42	0.68	0.22
SG25-1	0.078	0.90	2.35	0.084	0.90	0.00	0.00
SG25-2	0.080	0.80	2.35	0.074	0.75	0.06	0.07
SG25-3	0.083	0.60	2.35	0.069	0.50	0.10	0.17
SG25-4	0.079	0.36	2.35	0.076	0.35	0.01	0.04
SG25-5	0.084	1.83	2.35	0.076	1.65	0.19	0.10
SG25-6	0.081	3.24	2.35	0.075	2.97	0.27	0.08
SG45-1	0.086	1.34	3.68	0.072	1.12	0.22	0.16
SG45-2	0.086	1.04	3.68	0.069	0.83	0.21	0.20
SG45-3	0.089	0.79	3.68	0.063	0.56	0.24	0.30
SG45-4	0.085	2.23	3.68	0.076	1.98	0.25	0.11
SG45-5	0.082	3.36	3.68	0.080	3.26	0.11	0.03
SG45-6	0.088	2.96	3.68	0.073	2.47	0.49	0.16

Table 4.9 Summary of results for the Kennedy (1961) data set. The Recking iterative model was applied with D_{50} as representative diameter. For most of the plane bed runs, grain-related shear stress was set equal to the bed shear stress obtained using the Vanoni and Brooks method.

Run	R_{hb} [m]	τ_b [Pa]	k_s [mm]	H_s [m]	τ' [Pa]	τ'' [Pa]	τ''/τ_b
5-11	0.021	4.20	1.51	0.021	4.20	0.00	0.00
5-12	0.023	4.86	1.48	0.023	4.86	0.00	0.00
5-13	0.025	4.57	1.43	0.025	4.57	0.00	0.00
5-18	0.026	4.55	1.43	0.028	4.55	0.00	0.00
5-14	0.033	8.73	1.43	0.037	8.73	0.00	0.00
5-2	0.041	2.22	1.42	0.025	1.39	0.83	0.37
5-10	0.041	3.22	1.44	0.029	2.33	0.88	0.27
5-7	0.040	4.24	1.43	0.030	3.25	0.99	0.23
5-4	0.041	4.98	1.48	0.030	3.67	1.31	0.26
5-9	0.042	5.76	1.50	0.037	5.05	0.71	0.12

Table 4.9 (Continued)

5-16	0.040	5.27	1.56	0.040	5.27	0.00	0.00
5-17	0.039	5.80	1.53	0.038	5.76	0.04	0.01
5-8	0.038	6.97	1.53	0.043	6.97	0.00	0.00
5-3	0.063	3.40	1.46	0.039	2.10	1.30	0.38
5-5	0.060	6.45	1.43	0.048	5.17	1.28	0.20
5-1	0.088	5.76	1.42	0.043	2.83	2.94	0.51
4-25	0.041	1.28	0.44	0.027	0.84	0.44	0.34
4-37	0.038	1.40	0.56	0.036	1.35	0.05	0.04
4-24	0.037	1.73	0.53	0.036	1.68	0.05	0.03
4-29	0.040	2.87	0.54	0.030	2.12	0.74	0.26
4-28	0.038	2.43	0.60	0.035	2.24	0.20	0.08
4-26	0.041	3.76	0.56	0.028	2.60	1.17	0.31
4-27	0.041	6.41	0.47	0.025	3.85	2.56	0.40
4-1	0.053	1.35	0.50	0.053	1.28	0.07	0.05
4-30	0.056	1.41	0.48	0.056	1.28	0.13	0.09
4-31	0.057	2.33	0.57	0.057	2.26	0.07	0.03
4-36	0.055	2.41	0.56	0.056	2.41	0.00	0.00
4-33	0.057	3.63	0.49	0.050	3.18	0.45	0.12
4-32	0.064	5.87	0.47	0.039	3.62	2.25	0.38
4-38	0.068	1.73	0.49	0.068	1.73	0.00	0.00
4-12	0.042	1.40	0.61	0.031	1.03	0.37	0.27
4-10	0.044	1.82	0.61	0.036	1.49	0.33	0.18
4-22	0.043	2.84	0.55	0.035	2.32	0.52	0.18
4-11	0.043	3.44	0.48	0.031	2.51	0.94	0.27
4-7	0.056	4.83	0.45	0.036	3.09	1.74	0.36
4-6	0.065	14.48	0.46	0.019	4.18	10.31	0.71
4-3	0.066	1.69	0.35	0.066	0.45	1.24	0.73
4-19	0.069	1.42	0.39	0.069	1.14	0.27	0.19
4-17	0.069	2.30	0.44	0.062	2.06	0.25	0.11
4-16	0.072	5.03	0.42	0.048	3.37	1.66	0.33
4-13	0.090	2.20	0.46	0.073	1.78	0.41	0.19
4-23	0.092	1.53	0.41	0.092	1.46	0.07	0.04
4-14	0.090	2.83	0.43	0.090	2.82	0.01	0.00

4.4 DISCUSSION AND CRITICISM TO THE SHEAR STRESS PARTITION METHODS USED

From the results in Section 4.3 it has been found that the bed shear stress partition methods that performed best were the method of Recking iterative and the method of Engelund and Hansen. Both produced alike results for the grain shear stress, mainly because the relative roughness values obtained with both were quite similar. However, the computation of the relative roughness with the criterion of Recking iterative requires an additional parameter (bed slope) and more equations than Engelund and Hansen's method. Moreover, the representative grain size of the bed material to use in the computations in the first method is quite sensitive to the sediment transport conditions, while the second method uses only one representative diameter. These aspects reveal that the method of Engelund and Hansen is simpler and more robust than the method of Recking iterative. Because of these two reasons, the results for the grain and bedform shear stresses obtained with Engelund and Hansen will be used for further analysis in the following Chapters. The selection of the Engelund and Hansen method has the additional advantage that it has been widely used in the past.

Different authors have demonstrated that linear decomposition of the total shear stress over the bed, in its components of skin friction and form shear stress, is a realistic approximation. It has been found that measurements over fixed artificial 2D dunes of the total bed shear stress correspond well (within ±10%) to the summation of measured grain and form shear stresses, and that these measurements also agree with the product slope-water depth (e.g., Shen et al. 1990); Maddux et al. (2003) obtained similar results for 3D fixed artificial dunes. In contrast, no information exists in literature about the performance of the reference plane bed method used in Section 4.3 for estimation of the skin friction when compared with empirical data of well-controlled flows.

To test the likely range of uncertainty of skin friction values obtained with the reference plane bed method of Engelund and Hansen, this method has been applied to flow data over fixed dunes from Shen et al. (1990) and Maddux et al. (2003). The data and results are presented in Appendix XVI. Results showed that the grain shear stress measured was in average 50% higher than the computed values for rough 2D dunes, while for smooth 2D dunes the measured grain shear stress was in average 20% of the computed values. For the two data pertaining to 3D rough dunes, the ratio of grain shear stress to total bed shear stress measured was 5% and 38% higher than the same ratio for the calculated values. As already stated, the partition methods compared in Section 4.3, using a reference plane bed, were chosen because of their simplicity and because of the lack of experimental data needed for the implementation of more sophisticated criteria in which the bedform geometry or flow velocity profiles are an input parameter. Therefore, though the method seems crude, the results in Appendix XVI show a reasonable accuracy considering the limited input parameters used (mean flow velocity, water surface slope and relative roughness).

It should not be overlooked that when using a reference plane bed to estimate the skin friction, by considering an average water depth it is assumed that the shear stress over the boundary is uniformly distributed. Such an assumption is fictitious as in the presence of bedforms, especially over complex bed configurations as those in the experiments of this work, local shear stress can be highly variable in space. Such variability is especially important for sediment transport computations, because the rate of transported material obeys to a nonlinear function of the local shear stress acting over the grains. Over dunes very low shear stress values occur in the regions of flow separation, while shear stress increases over the stoss side from a cero value on the reattachment point to a maximum over the crest (Shen et al., 1990). For supercritical flows or close to the critical condition, Chanson (2000) measured boundary shear stresses in flows with standing waves and found that the lowest shear stresses occurred under the wave crests while the highest under the wave troughs.

In discussing the calculation of the bed shear stress in near-critical flows, as those in the experiments here presented, Chanson (1999) warned that there exists little experimental data to estimate accurately form losses in the presence of standing wave bedforms, but that the use of overall bed shear stress correlations is not justified by such a limitation. In a similar sense, Wren et al. (2005) commented that the extension to supercritical flows of relationships developed for subcritical conditions should be undertaken cautiously. This notwithstanding, Wren et al. found that the log law for velocity profiles, which was assumed when applying the reference plane bed method in Section 4.3, was valid for their experimental conditions with slightly supercritical flows over low-relief antidunes. More recently, Breakspear (2008) studied turbulence over fixed artificial symmetric antidunes of three different amplitudes and three different grain roughnesses; contrary to dunes, he did not find a flow separation zone, but an area of retarded flow in the trough region, characterized by high turbulent stresses. He found that turbulence becomes increasingly spatially varied with increasing antidune amplitude. Also, he found lower values of

turbulence stresses (an order of magnitude) over sand antidunes than over gravel antidunes, and hypothesized that there must be an inverse relationship between bed roughness and antidunes amplitude. Breakspear did not analyze form resistance, neither the effective bed shear stresses which could be related to sediment transport.

More experimental data are needed to investigate the validity of the shear stress partition methods under near-critical and supercritical flows. The use in this work of a reference plane bed method to separate form and grain stresses in upper-regime flows can not be entirely justified with a sound theoretical basis; nevertheless, the method proved to be consistent, in that coherent results were obtained, and it allows a direct comparison, in relative terms, with other experimental data sets and methods for which similar approaches have been applied.

Finally, it should be noted that an additional component in flow resistance, not considered in the analysis performed in this Chapter, is wave resistance due to the distortion of the free surface. The relative contribution of wave resistance to energy dissipation is more significant for antidunes than for dunes, and even more significant when the waves break. At present, there exists no means for estimating the contribution of wave resistance to the total energy dissipation.

4.5 SUMMARY

A comprehensive analysis of flow and bed sediment interaction requires the identification of the different components of hydraulic resistance, among which, skin friction is a prime parameter to study sediment transport, while form drag is relevant for relating bed configurations with flow resistance coefficients. In this Chapter, basic flow resistance equations have been presented and a linear separation of boundary shear stress has been undertaken for the analysis of the experimental data described in the previous Chapter. Standard methods have been used to estimate the components of the mean boundary shear stress, namely, side wall, grain and bedform shear stresses. The effective shear stress on the bed was assumed to be equal to the sum of the latter two components. From momentum balance in uniform flow, it is known that the effective bed shear stress can be estimated with the product of the water depth, the bed slope, the water density and the acceleration of gravity. Thus, if one of the components is known, the other can be estimated by the subtraction of the known component to the effective bed shear stress. Following this, the skin friction was estimated with methods found in literature and form drag was obtained from subtracting this skin friction to the total bed shear stress.

Four methods were selected for estimating the grain shear stress. All these methods are based on the consideration that skin friction on the studied bed with bedforms is the same as skin friction over a hypothetic reference plane bed with the same bed slope, mean flow velocity and bed material. These methods were chosen because of their simplicity and because of the lack of experimental data needed for the implementation of more sophisticated criteria. The results obtained with the selected methods were compared between each other using a physical and rational basis. Those methods with results not physically coherent were discarded, for instance, if flow depths computed for the reference plane bed resulted to be higher than the actual mean flow depth for most of the runs the method was discarded. Similarly, methods which resulted in negative values for the bedform shear stress were discarded as well.

Two methods for computing the skin friction were found to perform best. These were the method from Engelund and Hansen, and the method named here as Recking iterative using the D_{50} as representative diameter. This latter method was called in this manner, because the original Recking method was developed for plane bed, and it has been here applied to beds with bedforms by using it in conjunction with the reference plane bed

criterion originally proposed by Einstein. The two best performing methods were applied to two data-sets available in literature to evaluate their performance with other ranges of sediment grain diameters and hydraulic conditions. The performance of both methods was reasonable, given that for the Recking iterative method an adequate representative sediment diameter was chosen. It was found that for the data sets used, the method performed better by using the D_{84} for incipient motion runs, and with the D_{50} for high sediment transport rates. Conversely, the method of Engelund and Hansen performed well irrespective of the sediment transport conditions, showing with this a higher robustness than the method of Recking. For this reason and because it requires less equations to be implemented, the results obtained with the criterion of Engelund and Hansen, as shown in Table 4.5, will be used for further analysis in the following Chapters.

Finally, a brief discussion was presented to expose to criticism the selected shear stress partition methods. By comparison with measurements of the shear stress components in fixed artificial 2D and 3D dunes in literature, it was demonstrated that the linear decomposition of the total bed shear stress is a reasonable approximation. In contrast, computations of skin friction with the reference plane bed method using the relative roughness as proposed by Engelund and Hansen showed some disparities. However, it was concluded that the accuracy of the method is reasonable considering the limited input parameters required to implement it. Additional limitations of the method were exposed, being these the assumption of a uniform shear stress distribution over the bed, the limited empirical evidence for justifying the application of these methods to near-critical and supercritical flows, and not considering the contribution of surface waves to flow resistance which might be an important component in bed configurations with antidunes. In spite of all this drawbacks, it was concluded that using these approaches for partitioning bed shear stress allows a direct comparison, in relative terms, with experimental data sets and methods analyzed and developed on this same basis.

CHAPTER 5:

EXPERIMENTAL BED CONFIGURATIONS AND BEDFORMS

5.1 INTRODUCTION

Bedforms produced by water flowing over an alluvial bed have an important feedback effect on flow and are closely related to sediment transport. Understanding these bedforms is therefore essential for the study of river hydraulics and sediment transport mechanics.

Bedforms that develop in sand beds have been widely studied in experimental flumes and rivers. Those composed of grain-size mixtures, however, have received less attention. In particular, few observations exist for transitional and upper-regime bedforms composed of mixed-size material.

In this Chapter, bed configurations and bedforms are described and classified for the observations made during the experiments reported in Chapter 3 for beds composed of sand, gravel and two sand-gravel mixtures, for flows with Froude numbers close to one. The most common bedforms observed in the experiments were short-crested downstream-migrating antidunes. Such bedforms are rarely described in the literature, where reports of long-crested upstream-migrating antidunes and plane beds (forms normally associated with upper-regime flow) are more common.

In order to recognize the type of bedforms that the state of the art would anticipate for the experimental flows in Chapter 3, a review of bedforms under unidirectional flows and bedform stability diagrams is presented first. Later, the main distinctive characteristics of the bed features formed during the experiments are highlighted and bed configurations are described. With this, bed states for each experimental run are defined to compare with bedform stability diagrams from the literature in the next Chapter. Further on in this Chapter, evidence is presented on the effect of the experimental bedforms in bed erosion patterns, sediment transport variability, grain size sorting, and bed surface texture. All these observations are interpreted and discussed in Chapter 6 to qualitatively relate them with the dynamics and properties of the compound bedforms observed.

5.2 BEDFORMS UNDER UNIDIRECTIONAL FLOWS

The surface of alluvial beds crumples in response to the shear stresses exerted by flowing water; the properties of the forms that develop on the bed surface can thus be associated with prevailing flow conditions and the characteristics of the bed sediment. In this manner, it is possible to classify archetypical bedforms for given ranges of flow and sediment properties. Bedforms are individual topographic elements that develop on an alluvial bed surface; the term bed configuration, in contrast, refers to an assemblage of similar bedforms for a given bed region and time. An ensemble of similar bed configurations is called a bed state. Although bed configurations and forms can change with time, bed states represent the infinity of configurations possible under given conditions of flow and sediment (Southard, 1991). In this manner, on the surface of a granular bed in an experimental flume, a sequence of bedforms can be distinguished as flow velocity is increased and stable conditions are allowed to develop within the range of flow conditions characteristic of each bed state comprised of archetypical bedforms, as described below.

Given an initially flat bed subjected to free surface water flow, as the flow velocity increases and the particles start moving, if smooth turbulent subcritical flow prevails, the bed surface will show forms known as ripples. These have a roughly triangular shape, migrate downstream, and are characterized by the presence of a viscous sublayer. Ripples might not occur for coarse sediment because higher Reynolds numbers are required to set this material in motion, and the viscous sublayer, which is a condition for ripples to exist, might be absent when the coarse material starts moving; alternatively, the viscous sublayer might not be as thick as the diameter of the bed grains. For higher flow velocities and rough turbulent flow, the bed surface shape evolves to dunes, which perhaps are the most common bedforms for subcritical flows in rivers. Like ripples, dunes are roughly triangular in shape and migrate downstream, but they are higher and larger. For even higher flow velocities, which cause flow to become supercritical, the bed might become plane or develop symmetrical bedforms known as antidunes. The name of antidunes is owed to Gilbert (1914), who observed in his flume experiments that contrary to dunes, these symmetrical forms propagated upstream. Subsequent authors pointed out that the main characteristic to distinguish dunes from antidunes was not the direction of movement but rather the interaction between the bed and water surfaces. Consequently, the term antidune is used irrespective of the propagating direction of the bedform.

The sequence of bed features described above corresponds to mesoscale bedforms. Not included in the above classification are large-scale bedforms (macrofroms) known as bars, which have roughly the geometry of a dune but are much larger. Bars occur for high flow and may appear like islands during normal flow conditions in a river (Graf, 1984).

The Froude number is normally used to classify bedforms into three regimes of flow, namely, lower-regime forms ($F<1$), upper-regime forms ($F>1$) and transitional-regime forms ($F\approx1$). It has been found that resistance to flow relationships in sand-bed rivers are generally different for the upper and lower regimes, with a discontinuity in the transition regime; the formation of bedforms is thought to be responsible for this behavior (Engelund, 1966; Cruickshank and Maza, 1973).

In the next Section, particular properties and distinctive features between expected bedforms for the type of flows in the experiments described in Chapter 3 are specified.

5.2.1 Dunes and antidunes

Dunes are the most characteristic bedforms in fully rough turbulent subcritical flows (lower-flow regime). These forms migrate downstream and are asymmetrical in shape, with a gentle stoss side (upstream) slope and a steep slope on the lee side (downstream). The

mechanism by which dunes move downstream is related to the flow separation eddy over the lee side, which induces deposition of material downstream of the slip face. Bedforms typically associated with supercritical flows (upper-flow regime), in contrast, have generally been classed as antidunes. The feature that distinguishes them most from dunes is the fact that the water surface undulations appear roughly in phase with the antidunes. Bearing this defining attribute in mind (an attribute which involves the influence of water surface standing waves on bed shape), antidunes are not only characteristic of supercritical flows, but are also likely to occur even under subcritical flow conditions. Antidunes tend to be more symmetrical than dunes; they are sinusoidal in appearance and move upstream or downstream or remain stationary. Downstream-migrating antidunes are considerably rarer than their upstream-migrating counterparts (Parker, 2004). Instead of the term *antidunes*, some sedimentologists recommend the use of the more general term *in-phase waves* and refer to antidunes only for forms that are in phase with the water surface and migrate upstream (Cheel, 2005). Such a distinction is justified in terms of the different processes and relict sedimentary structures that stationary and upstream- and downstream-migrating antidunes produce.

Antidunes and dunes are classed as two-dimensional (2D) when their crest is straight transverse to flow. Conversely, the shape of three-dimensional (3D) dunes and antidunes is more complex in plan view, and, in contrast to 2D forms, they often develop scour holes in their troughs. Given that the crests of 3D bed features are shorter than those of 2D forms, 3D forms are also called short-crested forms. 3D bedforms occur for higher Froude numbers than their 2D counterparts. There is a shortage of literature available on 3D antidunes (Yokokawa et al., 2008). Short-crested water waves formed over 3D antidunes are known as rooster tails, after Kennedy (1961).

Due to the unstable nature of gravity waves for high Froude numbers and due to the strong feedback between bed and water surfaces in the presence of antidunes, unlike dunes, antidunes tend to be unstable and commonly show a cyclic behavior of formation, growth and destruction. Accordingly, a typical antidune bed state can show for moments symmetrical bedforms, which are later washed away to give place to an ephemeral plane bed until the antidunes form again. Alexander et al. (2001) gave a detailed description of the cyclic genesis of antidunes in sand.

Antidunes are often erased by waning flows and the conditions for their preservation are not yet well understood (Carling and Breakspear, 2007). Notwithstanding, in rivers, the preservation of antidunes can be associated with an abrupt recession of flood flow (Alexander and Fielding, 1997). Furthermore, many authors have suggested that some distinctive low-flow river bed morphologies can be related to relict antidune bedforms. For instance, Whittaker and Jaeggi (1982) related the formation of step pools to gravel antidunes, while Hasegawa and Kanbayashi (1996, in Yokokawa 2008) developed equations and showed experimental evidence for a relationship between step pools and 3D antidunes. Other bed morphologies claimed to originate from antidunes are the so-called transverse ribs, which are ridges of cobble and boulder that are oriented transverse to flow direction (Bridge, 2003).

5.2.2 Bedforms at and close to the transition between lower and upper regimes

The transitional regime, which occurs for Froude numbers close and equal to 1, is characterized by an erratic bed configuration, which may range from developed dunes to a plane bed, or it may consist of the simultaneous presence of heterogeneous forms along the bed profile (Graf, 1984). This regime is extremely unstable; the slightest change in energy (caused, for instance, by an irregularity on the bed) can lead to a considerable change in flow depth (Chanson, 1999).

Wang and White (1993) suggested that bedforms in the transitional regime might occur frequently in natural rivers, and exemplified this with the middle Yangtze River and the lower Yellow River, for which alluvial resistance during much of the flood season is in the transitional regime. Recognizing the limits and characteristics of the transitional regime is relevant from the hydraulics point of view, because, in contrast to what occurs in fully developed lower and upper regimes, in transitional regimes, the resistance coefficient does not necessarily increase with increasing flow strength.

The transition from lower-stage to upper-stage bedforms is usually characterized by a plane bed region if the bed is composed of fine sediment. On the contrary, it has been observed that for coarser grain sizes such a plane bed might not occur, in such a way that the dunes phase may be followed by antidunes. When this occurs, the transitional region may show transitional bedforms, i.e., bed features with intermediate characteristics of well-developed dunes and antidunes. Carling and Shvidchenko (2002) compiled experimental and field data for bedforms in dune-antidune transition in fine gravel. Descriptions of transitional bedforms reported by different authors showed a variety of morphologies and characteristics that resemble those of dunes or antidunes, or both. It is noteworthy that these authors found that transitional bedforms may appear for Froude numbers as low as 0.5. Table 5.1 shows the different bedforms described for the data sets compiled by Carling and Shvidchenko.

Some authors have identified a category of bedforms known as transition or washed-out dunes, which would fall in between the categories of dunes and upper-regime plane beds (Bennett, 1995). For increasing flow strength the lee-side slope of the washed-out dunes becomes gentler and their wavelength longer as compared to those of dunes. The effect is a reduction in flow resistance until the plane bed state is reached (Wang and White, 1993).

Note that plane beds are characteristic of the transition between lower- and upper-regimes for certain sand sizes and flow conditions, but they are also characteristic of the upper-regime for higher flows than those for which antidunes occur. For this second case, the bed configuration is known as upper-stage plane bed. With respect to the upper-stage plane bed, Kennedy (1961) reported particularly interesting findings about the non-uniqueness of water and bed configurations for certain ranges of flow in the upper regime. In experiments with sand, Kennedy observed that for a certain range of Froude numbers, the initially plane bed remained plane if no perturbations were induced on the water surface; instead, if the water surface was disturbed, stationary waves and antidunes formed.

Table 5.1 Descriptions of bedforms observed by different authors in dune-antidune transition with fine gravel. (Taken from data compiled by Carling and Shvidchenko, 2002).

dunes
transitional dunes
low-amplitude transitional dunes
plane mobile bed
rhomboid bedforms on upper stage plane bed
transitional bedforms
transitional bedforms beneath standing waves
downstream-migrating low-amplitude bedforms
downstream-migrating antidunes
downstream-migrating asymmetrical antidunes
downstream-migrating symmetrical antidunes
upstream-migrating low-amplitude antidunes;
upstream-migrating steep antidunes
upstream-migrating antidunes

Some authors have suggested that a true upper-stage plane bed does not actually exist as different very low-relief sediment waves can be distinguished, especially for mixed-size sediment (Bridge, 2003). In experiments with coarse sand, Wren et al. (2005) observed the difficulty of distinguishing between upper-stage plane bed and low-relief bed features by visual observation only; they classed low-relief bedforms, measuring a few millimeters in height, in supercritical flow (F=1.13) as low-relief antidunes.

5.2.3 Bars

Bedforms with wavelengths of the same order of magnitude as channel width or longer, and heights that scale with the mean depth of flow are known as bars. Bars are not necessarily linked with a flow regime, but usually occur for high flows. Different types of bars can be distinguished in rivers, namely:

- **Alternate bars.** These appear in straight streams and are more or less periodical near opposite banks; they can form as single-row alternate bars, double-row alternate bars or bars with higher modes. The formation of alternate bars has been regarded as the beginning of meandering.
- **Point bars.** These form on the intrados of river bends and in meandering streams.
- **Pool bars.** These occur in braided streams.

The formation of bars is related to the three-dimensionality of flow; therefore, contrary to their occurrence in natural streams, their formation in laboratory flumes is seldom achieved because the effect of channel width restricts the development of the three-dimensionality of the flow (Graf, 1984).

The geometry of bars is similar to that of dunes, but dunes always appear as periodic forms in trains, while bars can occur as isolated forms or be periodic, as occurs with alternate bars. A distinguishing feature between dunes and bars is their size; bars are much larger than dunes, and furthermore, dunes scale with water depth, while bars scale with channel width. Nevertheless, confusion between dunes and bars may arise when bedforms scale either with channel width or water depth (for example, in narrow channels), leading to erroneous classification. Typical ratios for bar length to bar width range from 3 to 12, while typical ratios for bar height to bar length are lower than 0.06 (Bridge, 2003). A condition for bar formation is a low ratio between water depth and channel width (Niño, 1996).

5.2.4 Compound bedforms

Different types of bedforms can coexist in a given river reach and cross section. For instance, ripples and dunes often occur on the upstream faces of bars. In this regard, Lunt and Bridge (2007) found that small bedforms on the back of larger bedforms have an important influence on the formation of cross-stratified and open-framework gravel deposits in sand-gravel beds.

The coexistence of different bedform types or bedform scales can also occur in the cross section. For instance, lower-regime bedforms can occur on flood plains subjected to lower flow velocities than in the main flow channel, in which upper-regime bedforms can occur at the same time.

Compound bedforms are common in rivers because of the existence of different scales of flow and sediment transport, but also because of the heterogeneity of sediment characteristics, local flow conditions and especially because of 3D effects. The coexistence of different types of bedforms across the cross section of rivers is seldom reproduced in flumes, because in laboratory channels 3D flows are not easily induced. In the same manner, shear stress in flumes is almost uniformly distributed over the bed, and the side

borders are not erodible (Graf, 1984). Bar formation is thus rarely achieved in the laboratory due to the absence of 3D conditions.

5.2.5 Expected bedforms for coarse and mixed-size sediment

The classification of bedforms presented in Sections 5.2.1 to 5.2.4 is typical of sand beds with uniform-size sediment. Bedforms with coarse and mixed-size material have been less widely documented than those that occur with uniform grain-size sand beds. Notwithstanding, most of the bedforms previously described have been also reported in gravel and in mixed-size sediment, as have other specific features that form only in beds composed of sediment mixtures.

It is known that ripples do not form for bed materials coarser than 0.7 mm because a condition for ripple formation is that flow must be hydraulically smooth (Carling, 1999). Conversely, dunes and antidunes have been observed in gravel beds; Carling (1999) provided a comprehensive review of dunes formed in gravel, while Carling and Breakspear (2007) reviewed reports of gravel dunes and antidunes; these authors highlighted the lack of published data for gravel antidunes. As far as macroscale bedforms are concerned, it can be said that bars are as common in gravel as in sand bed rivers.

For mixed-size sediment beds, different types of bedform have been described in the literature, mostly in relation to bimodal sand-gravel mixtures. Kuhnle et al. (2006) summarized these types of mixed-size sediment bedforms, which include particle clusters, bedload sheets, low-relief bed waves, dunes, antidunes and transverse ribs. A class apart is constituted by bedforms in bimodal mixed-size material which appear when sediment supply is limited and only some of the grain-size fractions available on the bed surface are in motion. Kleinhans et al. (2002) identified three populations for these supply-limited forms, namely, flow-parallel sand ribbons, barchans and dunes.

Little information exists about bedforms at, and close to, the transition between lower- and upper-flow regimes for sediment mixtures. In this sense, it is worth mentioning the work of Chiew (1991), who studied the effect of sediment gradation on the transition between bedform types. While he found no important effects, he did find a tendency towards the absence of antidunes for higher grain-size standard deviations, which he attributed to the formation of a dynamic armored layer.

5.2.6 Bedform stability fields

The range of flow conditions and sediment characteristics under which stable bedforms develop have been studied empirically by different authors, mostly for well-sorted sediment in the size range of fine sand to fine gravel. Diagrams have thus been proposed showing delimited stability fields for the occurrence of the different bedform classes (e.g., Vanoni 1974, Southard and Boguchwal 1990). Nevertheless, because of the lack of observations, some borders between bedform fields have been poorly defined or have been conceived of as intuitive extrapolations from the better-known regions. Furthermore, most stability fields specify neither a clear border between 2D and 3D bedforms, nor the conditions that define the direction of movement of antidunes. Data to confirm the validity of bedform stability diagrams becomes even more scarce and uncertain as grain size and sorting increases, and as the hydraulic conditions approach the upper regime.

In considering the validity of empirical diagrams developed from uniform sand material, Carling (1999) found that stability fields in such diagrams can be extended to grain sizes pertaining to coarse gravel. Likewise, Kleinhans et al. (2002) concluded that these diagrams are also valid for supply-limited bedforms in sand-gravel mixtures if the plots are used with bedload material instead of bed material.

One of the main limitations of diagrams that delimit bedform stability fields is that most of them have been developed from flume data. It is known that channel walls in laboratory flumes constrain bedform size, i.e., bedform height, length, and width can all increase with increasing channel width (Crickmore, 1970; Friedrich et al. 2005). Stability diagrams do not consider channel width to be an important variable. Neither has the effect of limited channel width on the ultimate stable bedform geometries reported in data sets been verified (Southard and Boguchwal, 1990).

Theoretical bedform stability diagrams have been presented by different authors who performed stability analysis of bed disturbances. Kennedy (1963) presented relations for defining bedform stability fields as a function of the Froude number and a non-dimensional wavelength. Engelund and Hansen (1966) analyzed the stability of a sinusoidal sand bed using the continuity equation and the equations of motion of a real fluid; their analysis concluded with a bedform stability diagram as a function of the Froude number and the ratio between mean flow velocity and either sediment shear velocity or sediment critical shear velocity.

5.2.6.1 Bedform stability fields obtained from potential flow theory

Following the original stability analysis outlined by Anderson (1953) and extended by Kennedy (1961), Kennedy (1963) presented relations for defining bedform stability fields based on potential flow theory. Potential flow analysis allows for discrimination between 2D and 3D antidunes. In the same manner, the theory outlines the border between upstream-migrating and downstream-migrating antidunes. Nevertheless, a clear delimitation between upper-stage plane bed and downstream-migrating antidunes is not specified by theory.

The stability field presented by Kennedy (1963) is a function of the Froude number

$$F = \frac{V}{\sqrt{gH}} \tag{5.1}$$

and the wave number $k=2H\pi/\lambda$, where g=gravitational acceleration, H=mean flow depth, λ=wavelength of the sediment wave, and V=mean flow velocity. In this manner, the upper regime occurs when $F>F_u$, where:

$$F_u = \sqrt{\frac{\tanh(k)}{k}} \tag{5.2}$$

Upstream-migrating antidunes are likely to occur for the range $F_u<F<F_p$, with F_p defined by:

$$F_p = \sqrt{\frac{1}{k\tanh(k)}} \tag{5.3}$$

The theory also allows for delimitation between 2D and 3D antidunes, with such a border being given by:

$$F_d = \sqrt{\frac{1}{k}} \tag{5.4}$$

Downstream-migrating antidunes are likely to occur for large wave numbers if $F>F_p$ and $F>F_u$. In such a regime, water and bed surfaces are in phase, but in contrast to upstream-migrating antidunes, water depth is greater over the troughs than over the crests, in a similar way to dunes, so that net sediment deposition occurs over the troughs (Carling and Shvidchenko 2002; Parker 2004).

Upper-stage plane beds for high Froude numbers cannot be predicted by theory. Nevertheless, for $F>F_u$ and low wave numbers ($k\rightarrow 0$), i.e., large wavelengths, antidunes are depressed and upper-stage plane beds are likely to occur (Carling and Shvidchenko, 2002).

According to potential flow theory analysis, the wavelength of antidunes is related to mean flow velocity by:

$$V = \sqrt{\frac{g\lambda}{2\pi}} \tag{5.5}$$

This relation does not hold for 3D waves, which are shorter. Such waves on the water surface are formed by the coincidence of stationary waves in the flow direction and cross-waves transversal to the flow; these waves are also known as rooster tails. According to Hasegawa and Kanbayashi (1996, after Yokokawa, et al. 2008), short-crested antidunes are formed when the wavelengths of 2D antidunes and water-surface diagonal-cross waves are the same. From a previous development by Fuchs (1952, in Kennedy, 1961), Kennedy presented the following functional relation between mean flow velocity and the wavelength of 3D waves, in which he considered that wave celerity and flow velocity were the same

$$V = \sqrt{\frac{g\lambda}{2\pi}}\sqrt[4]{1+\left(\lambda/\lambda_t\right)^2} \tag{5.6}$$

where λ_t=wavelength normal to the direction of flow, which as a first approximation can be taken as channel width.

When contrasting equations (5.5) and (5.6) with experimental data in sand, Kennedy (1961) found a sound correlation between 2D waves but an overestimation trend for flow velocity in the case of 3D antidunes. Kennedy estimated that the discrepancies detected for 3D waves might have been due to the consideration of the transverse wavelength of the rooster tails as equal to channel width.

5.3 EXPERIMENTAL OBSERVATIONS

In this Section extended descriptions are presented of bed and water configurations, bed scour patterns and grain sorting observed for the experiments described in Chapter 3. All descriptions of bed and water configurations during the flowing water stage correspond to the phase in which mobile-bed equilibrium conditions prevailed in the channel, and therefore no important changes in bed slope, water depth, sediment transport or bedform geometry occurred.

Descriptions of water surface configuration are important because for upper regime flows there is a strong feedback between bed and water surfaces. Because it was not always possible to observe the bedforms during the experiments, particularly at the center of the channel, the state of the water surface is helpful for deducing the shape of the moving bed. In the same manner, descriptions of bed configurations preserved after the water was drawn-down from the channel help to relate these to bedforms with flowing water. Such an approach can be used to compare typical morphological features of natural rivers with those found in the laboratory in order to relate high water morphological changes to the appearance of the bed during the passage of normal waters, which is when bed material surveys are usually carried out. The analysis of bed scour patterns after the run and grain sorting provides a better understanding of the dynamics of bedforms and their effect on bed variation.

Appendix VIII shows photographs for the bed and water configurations observed in each experiment, while Appendix IX presents aerial photos of the bed surface configurations at the end of each run.

Figure 5.1. Trains of short-crested stationary waves (rooster tails); (left) run M1E5, F=1.23; (right) run G14, F=1.37. Flow from background to foreground.

5.3.1 Water surface configurations

Trains of rooster tails were observed during most of the runs (see Figure 5.1), with varying characteristics of shape, geometry and stability. All the rooster tails and water waves that were observed showed a net downstream displacement, though a single wave could sometimes, for short periods, remain stationary, migrate upstream or disappear to rebuild again. For Froude numbers lower than approximately 1.3, the splash produced by the short-crested water waves was stronger the higher the Froude number. Such splash was related to the magnitude of the roller formed at the crests. The roller was breaking continuously facing upstream for runs with Froude numbers higher than 1.16 for gravel, 0.94 for sand, 1.01 for Mix1 and 1.02 for Mix2. Even when the roller on the 3D waves produced abundant splash, for most of the runs the rooster tails were stable in the sense that if they broke, they reformed rapidly. Furthermore, despite individual breaks and agitation the train of the rooster tails was not significantly affected.

2D waves (i.e., stationary-waves, as Kennedy 1961 defined waves formed over antidunes to distinguish them from standing waves) formed at the upper part of the channel, some meters downstream from the sediment input, and they then transformed into rooster tails, normally 10 to 15 meters downstream from the sediment-input section. For a varying length of 3 to 6 meters, the 3D waves kept growing in height and length until they stabilized at a more or less fixed geometry, which was conserved until the end of the channel downstream (27 m downstream from the sediment feeding point).

For some of the flows with the highest Froude numbers, the rooster tails gave the water surface a triangular shape in plan, as the central short-crested wave had two shoulders at each side of the crest peak, and the two were slightly upstream oblique with reference to the flow direction (Figure 5.2). Also, in many cases, the region surrounding the wave trough showed a rhomboidal plan-shape. This was due to the alternation between a diverging flow from the channel center line at the wave troughs and a converging flow

toward the peaks of the 3D waves, as also reported by Kennedy (1961) in experiments with sand. Triangular and rhomboidal plan-shapes were less evident for lower Froude numbers, for which rooster tails appeared as a slight protrusion on the water surface.

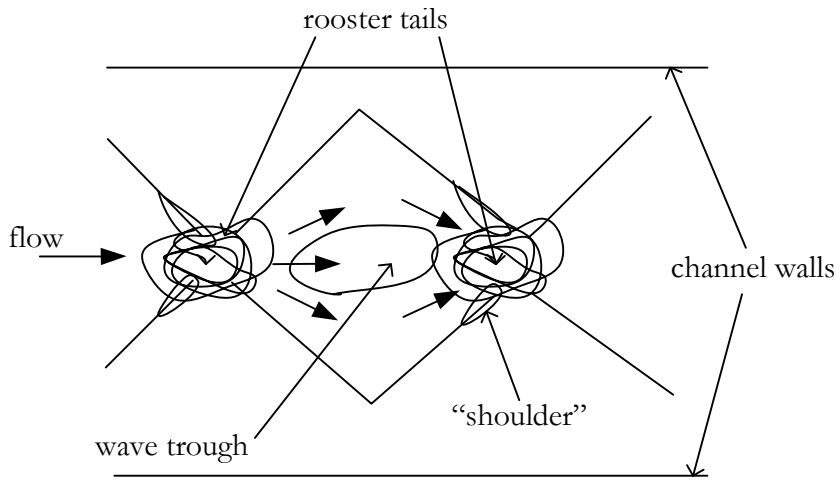

Figure 5.2. Schematic representation of water surface configuration when trains of rooster tails were observed.

5.3.2 Bed configurations

Above all in the case of run series with sediment mixtures, bed states observed during the runs consisted of the coexistence of two types of bedforms. On the one hand, low-amplitude features prevailed next to the channel walls. On the other hand, at the center of the channel cross section, 3D downstream-migrating antidunes occurred under the rooster tails. For sand-runs, low-amplitude bedforms might have been present as well, but possibly remained undetected to the naked eye because of the higher amplitude and lower wavelength of the dominant bedforms.

5.3.2.1 Bed configurations next to the channel walls

As with rooster tails, bed features observed next to the flume walls migrated downstream and evolved along the channel until they reached a stable configuration. Usually, they were first noticeable 3 to 5 meters downstream from the upper sediment-input point. From here to where they reached stability—i.e., 10 to 15 meters downstream from the sediment-input point—the features moved faster, and were shorter and lower than their stable counterparts in the last section of the flume downstream. Though we may refer here to a "stable" configuration, this should be considered within a statistical sense, given that for some runs the bedforms near the wall displayed continuous variations in shape and geometry.

The shape of bedforms near the channel walls and their degree of coupling with the water surface varied with Froude number and bed material. For some conditions, such variations were important even within a single run. In general, unequivocal antidunes (i.e., bedforms which were an in-phase image of the water surface irrespective of their symmetrical or asymmetrical shape, see Figure 5.3) appeared with higher Froude numbers for the gravel and mixtures than they did for the sand-run series. In this manner, the minimum Froude number for antidunes observed near the channel walls were 1.28, 1.3,

1.25 and 0.94 for the gravel, mix1, mix2 and sand run series, respectively. A similar trend was observed for transitional bed states, which are here considered to be those characterized by, firstly, bedforms with a certain degree of coupling between water surface and bed surface and, secondly, those for which the bed configuration alternated between showing dunes and antidunes. The range of Froude numbers for which transitional bedforms occurred near the walls were 0.93-1.28, 0.87-1.3, 0.89-1.25 and 0.73-0.94 for the gravel, mix1, mix2 and sand run series, respectively. The transitional bedforms observed consisted of downstream-migrating features, mainly low-relief waves for the mixtures and gravel, and transitional dunes for the sand. Transitional bedforms were rounder the stronger the coupling with the water surface, and the higher the flow Froude numbers were. Also, a separation eddy on their lee side was more evident for low Froude numbers, for which the features were sharp-crested.

Figure 5.3. Train of downstream-migrating antidunes and stationary waves for run S1 with F=1.02. Flow from left to right. Length of glass panels is 1 meter.

Because most of the bedforms next to the flume walls showed an alternate sequence in plan from side to side, which was clearly evident when the water was drawn down (see photos in Appendix IX), these features can be classed as single-row alternate bars. Alternation reflects an interaction with channel walls, which is a characteristic of bars. Furthermore, the fact that the wavelength of the bedforms next to the walls was of the same order of magnitude as that of channel width confirms the appropriateness of calling them bars.

5.3.2.2 Bed configurations at the center of the channel

In most cases, on account of the turbidity of the water and the local unsteadiness of flow, it was not possible to observe bedforms in the central channel cross section. Nevertheless, based on the few observations available we can assume that if and when rooster tails occurred on the surface, then beneath these rooster tails the bedforms would be in phase with the water wave, and can thus be classed as antidunes. What is more uncertain is the shape and size of these forms. Nonetheless, based on the isolated observations that it was possible to make, and in agreement with observations already made by Kennedy (1961) regarding sand beds, we can infer that the bed under the rooster tails had the same 3D form as the surface waves, with the difference that the bed waves were neither as high nor as sharp as the surface waves.

Figure 5.4. Bed configurations with alternate bars at the end of runs M1E1, M1E3 and M2E5. Note the hold-back water in the thalwegs, showing a zigzag pattern.

For some runs, especially for the sand and gravel series, there were isolated bedforms or a train of bedforms, shaped as a continuous transversal ridge from wall to wall, with a linguoid or straight plan-shape, even when rooster tails prevailed at the center of the channel. Therefore, for these conditions the bed features were not like the steep isolated mounds typically reported underneath rooster tails (Kennedy, 1961; Yokokawa, 2008). In general, the three-dimensionality of the bedforms increased with Froude numbers, although this does not mean that mound-isolated antidunes necessarily formed for high Froude numbers.

Plane mobile beds appeared during some runs at very short time intervals, when waves vanished to rebuild later. The periodicity of such behavior was complex and irregular. More regular plane beds were observed for two runs, one with the lowest Froude number with gravel (G17), and the other with the second highest Froude number for Mix2 (M2E1). For these runs, even though rooster tails were observed, there were long intervals during which the water and bed surface were almost plane. Such a behavior resembles the non-uniqueness of flow configuration, which Kennedy (1961) found for some of his experimental runs according to the presence or not of a perturbation at the channel entrance that gave birth to stationary waves. For the experiments here described, it was not possible to prove if such plane bed states were related to an unsteady more tranquil entrance of water into the channel.

5.3.2.3 Bed configuration at the end of the run

Normally, when the water discharge was drawn down at the end of each run (this usually took between 1 and 2 minutes), most of the bedforms were erased. This type of behavior is typical of antidune configurations and is one of the main reasons why antidunes are so rarely preserved (Carling and Breakspear, 2007). Nevertheless, the plan form of the drained bed surface showed low-relief waves with longer wavelengths than the stationary waves on the water surface observed during the runs (see Appendix IX). Except for the gravel run series, the heights of these bed features increased with a decrease in Froude numbers (see Figure 5.11). For the lowest numbers, the wavelength of the low-relief waves on the dry bed surface was similar to that of the bedforms observed next to the channel wall during the run. Thus, we can accurately relate the preserved forms to those observed when the flow was running. On the other hand, for runs with higher Froude numbers, we suspect

that antidunes and transitional bedforms were superposed to such low amplitude and long alternate waves, but the latter were less evident to the naked eye due to the higher amplitude of the dominant bedforms. Low-relief bed waves at the end of the run were also evident for the gravel run where plane bed prevailed for long periods of time. This supports observations by previous authors (e.g., Best and Bridge, 1992) who have noticed that plane beds are not entirely flat because of the presence of low-relief bed waves.

The most frequent pattern for the final morphologies was an alternating sequence; in a preliminary description the bedforms that produced these features can be classed as alternate bars. As can be seen in Figure 5.4, the thalweg showed a zigzag pattern in most cases, with most of the corresponding morphologies looking like typical pools and riffles as they occur in gravel-bed rivers.

5.3.3 Classification of observed bedforms and bed configurations

The above bed configuration descriptions show that bedform properties changed with channel length, channel width and time, which means that forms with different characteristics coexisted for each experimental run. In spite of this variability, in this Section an attempt is made to classify the bed configurations in each run to define bed states, which will be further associated with mean hydraulic and sediment characteristics for comparison with bedform existence fields. As previously defined, bed states represent all the likely configurations for given flow and sediment conditions. The classification of each experimental run in this manner is also practical for relating flow resistance to prevailing bed states, as will be seen in Chapter 6.

Difficulties arise in the classification of experimental bedforms when trying to distinguish between dunes, antidunes, bars and transitional bedforms for the erratic bed and flow conditions that characterize the transitional regime. To address this complication, reference to definitions given in 5.2 is necessary. In this manner, it will be considered that an antidune bed state occurs if the bed surface and the water surface are in phase, i.e., if the bed is an image of the water waves at all times. Otherwise, even if there is strong feedback between the bed and water surfaces, the bedforms will not be cataloged as antidunes. Dune bed states will be considered states for which bed and water surfaces are not in phase; most of the sediment waves will be approximately triangular and their size will be of the same order of magnitude as water depth. If the bed and water surfaces are not in phase but the bedform wavelength scales with channel width, these forms will be considered to be bars. If the bedforms follow an alternate cyclic path, they will also be considered bars, as this kind of pattern is related to channel width. On the other hand, a bed state consisting of transitional bedforms will be considered to occur when bed features prevail with intermediate states between dunes and antidunes, whether it is in the coupling of water and bed surfaces or in shape. Here, transitional bed sates are also considered to be those for which lower- and upper-regime bedforms coexist, whether they coexist along the same section or alternate periodically for the same flow conditions.

Table 5.2 summarizes the dominant characteristics of the bed configurations observed for each experimental run. Such characteristics are taken into account to define a predominant bedform, as is indicated in the last column. Experimental runs are grouped by bed sediment characteristics and within these groups the runs are ordered from higher to lower Froude numbers. Categories in columns 3 and 4 are the same as those established by Kennedy (1961) to classify his experimental runs for which he registered antidunes and transitional bedforms in sand. These categories and data in each of the columns of Table 5.2 are explained below.

Column 2 presents the Froude number, defined as $F=V/(gH)^{1/2}$, where g is the gravitational acceleration and V and H are the mean flow velocity and water depth, respectively, as presented in Table 3.26.

Table 5.2 Prevailing characteristics of bed and water surfaces for each experimental run. See text for a description of symbols and categories used.

(1) Run	(2) Froude number F	(3) Water surface configuration	(4) Bed configuration		(5) Predominant waves	(6) Dominant bedform or Bed state
			Sides	Center		
G12	1.42	2o(17)3B		i	3D	DMA
G14	1.37	f(20)2o(13)3B		i	3D	DMA
G15	1.29	f(16)3B		i	3D	DMA
G13	1.27	2o(17)3B		i	3D	DMA
G16	1.16	f(13)3B	s	i	3D and 2D	T
G17	0.93	f♦		f	-	PB
M1E2*	1.42	2o(11)3B		i	3D	DMA
M1E3	1.37	f(17)2o(12)3B		i	3D	DMA
M1E4	1.30	f(17)3B		i	3D	DMA
M1E5	1.23	f(20)2o(16)3B	s	i	3D	T
M1E1	1.00	f(15)2b and f(15)3B	m	i	2D	T
M1E6**	0.88	f(14)2b	w	i	2D	D
M2E2	1.49	f(9)2b(6)3B and f(9)3B		i	3D	DMA
M2E1	1.44	f and f(9)2b(5)3B		i	3D	PB and DMA
M2E3	1.40	f(18)2b(12)3B		i	3D	DMA
M2E4	1.25	f(22)2b(16)3B		i	3D	DMA
M2E5	1.02	2b(16)3b(5)3B and 2b(5)3B	s and m	i	3D and 2D	T
M2E6	0.89	2o(13)2b and 2o(13)3b(7)3B	w	i and s	2D	T
S1	1.02	f(21)3B		i	3D and 2D	DMA
S2	0.94	2b(21)3B		i	3D and 2D	DMA
S3	0.82	2b		s	2D	T
S4	0.73	2o		w	2D	D

*Sediment bed began at x=20

** Sediment bed began at x=24

♦Infrequent occurrence of rooster tails at the central cross section

Shaded rows=Downstream-migrating antidunes in all the cross section

D=Dunes; DMA=Downstream-migrating antidunes; T=Transitional bedforms; PB=Plane bed

In column 3 the prevailing water surface configurations are categorized with the following symbols:

- f is used when the water surface was flat;
- numbers 2 and 3 are used for predominantly 2D and 3D waves, respectively;
- the letters b, B or o accompany the numbers 2 and 3 to indicate, respectively, whether most of the waves had isolated breaking, multiple breaking or did not brake.

The variation of the water surface configuration along the flume is considered by numbers in parentheses which indicate the approximate point in meters where the configuration changed (x=0 corresponds to the downstream end of the channel, x=27 to the upstream head). In this manner, for instance, for run M1E4, the expression f(17)3B must be interpreted as a flat water surface occurring upstream from x=17, and 3D waves breaking continuously from there to the downstream end of the channel. Figure 5.5 exemplifies with a scheme the category given to the water surface configuration for run G14. Runs for which two configurations are presented in Table 5.2 correspond to cases where the water

surface interchanged periodically between two conditions. The criterion for distinguishing between 2D and 3D waves was mainly related to the dominant wave observed on the surface. Given that most of the runs showed rooster tails, the criteria used to classify the water surface as 2D rather than 3D was that the rooster tail protruded slightly above the surface compared to other larger 2D stationary waves on which the 3D waves were superimposed—if, that is, such 2D waves were present—or compared to the sediment waves on the bed surface.

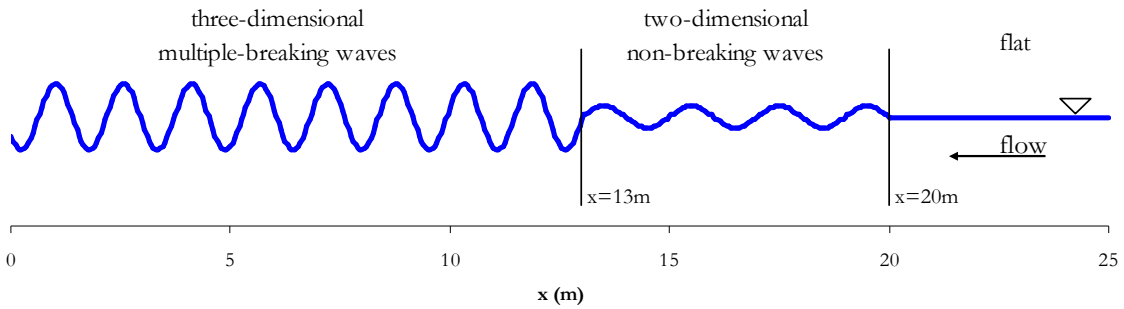

Figure 5.5. Schematic representation of water surface configuration for run G14 categorized with the expression f(20)2o(13)3B in Table 5.2.

Column 4 describes the predominant bed configurations in the zone where the bedforms had reached a stable state, mainly attending to the degree of coupling between the bed and water surfaces. Coupling should be interpreted here as the correspondence between water and bed surfaces in terms of shape and response, e.g., perfect coupling indicates an immediate response of the water (bed) surface to a change on the bed (water) surface, and an in-phase occurrence of both crests and troughs. The letters in column 4 express the following: f indicates that the bed was flat, w, that the dunes were weakly coupled with water surface, m that the dunes were moderately coupled with water surface and s that the dunes were strongly coupled with water surface. The letter i indicates that the bedform was an image of the water surface, i.e., it indicates the occurrence of antidunes. With the exception of sand runs, bed configurations at the center and near the channel walls are considered separately in all cases where two different bedforms coexist.

Column 5 shows whether the prevailing bed features were 2D or 3D in the zone where the bedforms had reached stable conditions. Although in the range of variables investigated the dominant wave forms on the water surface were rooster tails, the bed surface under these essentially 3D waves was not necessarily 3D. Thus this column shows the predominant bedform detected.

Finally, the predominant bedform for the zone where the bedform reached stable mature conditions is presented in column 6. This is considered as the bed state of each run. As can be seen, the most common bedforms were downstream-migrating antidunes (DMA), followed by transitional bedforms (T), dunes (D) and plane bed (PB).

For some runs, the degree of coupling between bed and water surfaces was not easily detectable, particularly in low-relief bedforms and when the water surface was either flat or choppy and unstable. For exemplifying the degrees of coupling, Figure 5.6 presents time series for the bed and water profiles for three different runs for the bedforms near the channel wall. For the graphs in the right column, the mean levels of the bed and water profiles were made equal by subtracting mean water depth from the water surface profile. These graphs clearly show the degree of coupling between both surfaces. For run S1 it is observed that most of the crests and troughs of the bed profile match those of the water profile. This shows without a doubt that the bed configuration can be considered to be

dominated by antidunes. Conversely, profiles for run S4 are evidently out-of-phase; thus the configuration is considered to consist of dunes weakly coupled with the water surface. On the other hand, the graph for run M1E5 shows a mixed behavior; most of the low and short period bedforms appear in phase with the water surface, while higher bedforms with longer periods are out-of-phase; thus, even though the bed configuration has been classed as dunes strongly coupled with water surface, the dominant bed state has been cataloged as transitional because of this alternation between forms with dune and antidune characteristics.

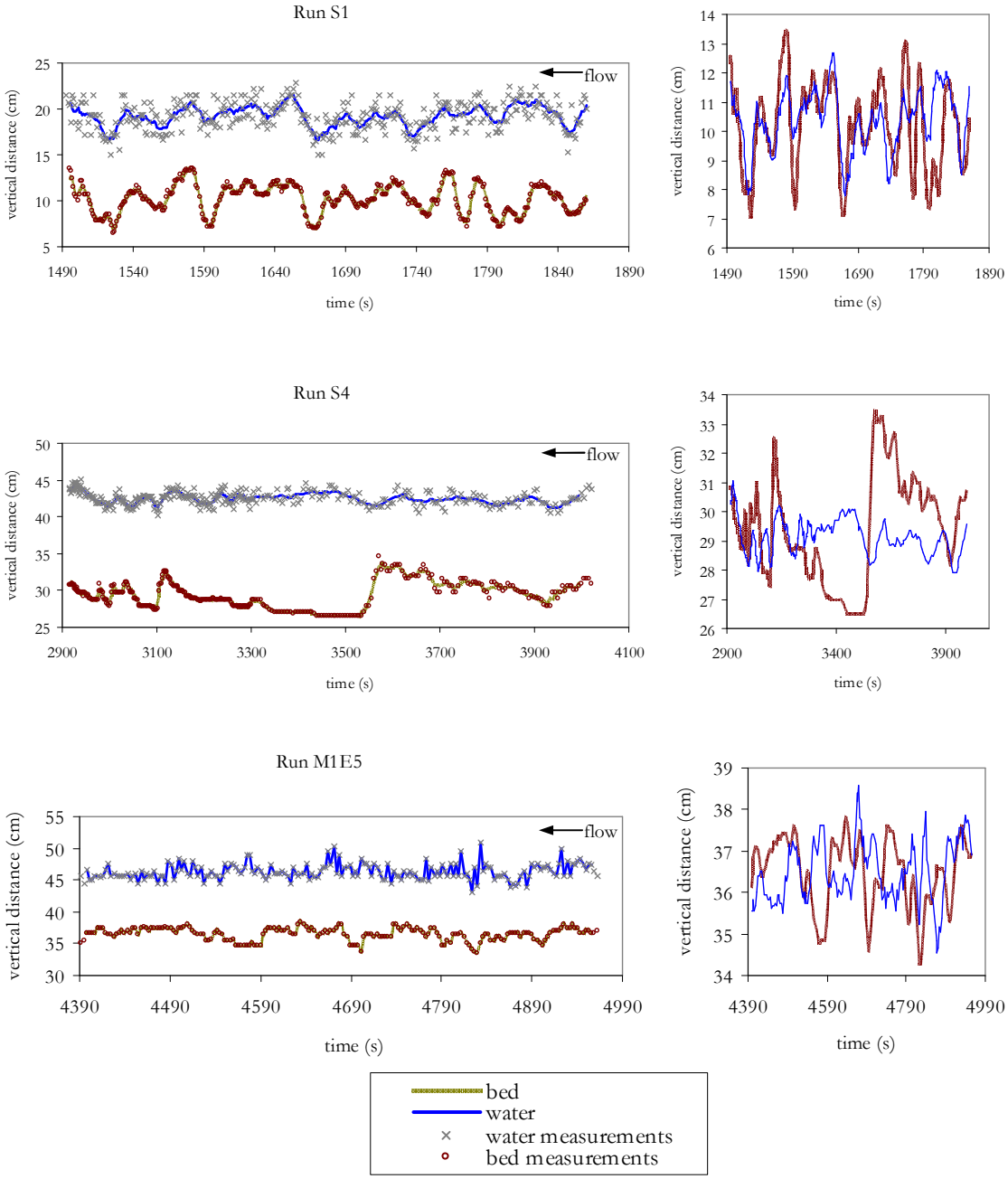

Figure 5.6. Time series for bed and water surfaces near the channel wall at x=1.5 for S1 and S4 and at x=4.6 for M1E5. The sampling time for run S1 is 1 second, 3 seconds for run M1E5 and 1 to 5 seconds for S4. For plots in the left-hand column, points indicate measurements and continuous lines indicate a superimposed moving average of nine points. Plots in the right-hand column correspond to moving averages but mean water depth has been subtracted from the water surface profile.

The graphs in Figure 5.6 show the different degrees of unsteadiness of the water surface based on consideration of the dispersion of the points measured around the softened profiles. The dispersion is much higher for run S1 than for runs S4 and M1E5, even though the Froude number of M1E5 is higher than that of S1. These observations are in agreement with observations by Kennedy (1961), who found that for flows with similar Froude numbers but different sand grain sizes, the wave activity on the water surface increased for the finer more easily transported sand.

Although the bedforms in the last column of Table 5.2 can be considered as those of the dominant bed state, it should be remembered that most of the runs showed compound bedforms. Next to the channel wall, long wavelength bedforms occurred, which for most of the cases can be classed as alternate bars given their wavelength scaled with channel width, as will be demonstrated in the next Section. Therefore, the bed state of each run consisted of the dominant bedforms indicated in the last column of Table 5.2, coexisting, in some cases, with alternate bars.

5.3.4 Properties of experimental stationary waves and bedforms

In this Section some of the characteristics of the stationary waves and bedforms observed in the experimental runs are presented. These characteristics are summarized in Tables 5.3 and 5.4, which are described below. For practical reference purposes, the range of mean flow velocities, water depths and Froude numbers measured during the equilibrium phase of the experimental runs is shown in Figure 5.7. The dominant stationary wave observed at the downstream reach of the channel (2D or 3D) is specified in this Figure according to the third column of Table 5.2.

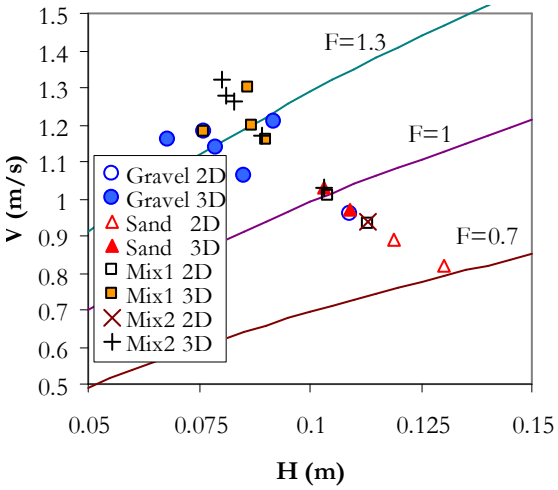

Figure 5.7. Range of experimental data. 2D and 3D refer to the dominant stationary waves observed.

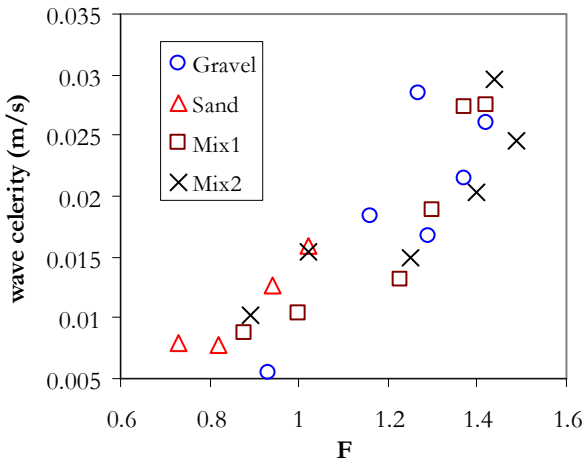

Figure 5.8. Measured celerity for the experimental stationary waves.

5.3.4.1 Stationary waves and antidunes

Kennedy (1961) called surface waves that accompanied antidunes stationary waves to distinguish them from standing waves. Standing waves are immobile surface waves which accompany disturbances at a fixed location. Kennedy's definition for stationary waves is also adopted here. Because, as previously stated, antidunes formed under these stationary

Table 5.3 Characteristics of stationary waves over antidunes in the experimental runs.

(1)	(2)	(3)	(4)	(5)	(6)	(7)	(8)	(9)	(10)
Run	**Number of waves considered for length measurements**	**Mean wavelength** λ **[m]**	**Wavelength measurements standard deviation** σ_a **[m]**	σ_a / λ	**Mean stationary wave height** Δ_w **[m]**	**Maximum stationary wave height** $\Delta_{w,max}$ **[m]**	**Stationary wave steepness** $\Delta_{w,max}/\lambda$	**Wave celerity** **c [m/s]**	**Celerity standard deviation** σ_c **[m]**
G12	5	0.550	0.05	0.09	0.045	0.050	0.091	0.026	0.006
G13	31	0.670	0.07	0.11	0.086	0.105	0.157	0.029	0.011
G14	43	0.602	0.08	0.13	0.077	0.100	0.166	0.021	0.004
G15	26	0.611	0.09	0.15	0.099	0.128	0.210	0.017	0.003
G16	26	0.632	0.03	0.05	0.080	0.115	0.182	0.018	0.008
G17*	5	0.667	0.00	0.00	-	-	-	0.005	0.001
M1E1	61	0.666	0.05	0.08	-	-	-	0.010	0.003
M1E2	33	0.675	0.06	0.09	-	-	-	0.028	0.009
M1E3	15	0.606	0.07	0.12	0.050	0.070	0.116	0.027	0.002
M1E4	50	0.625	0.08	0.13	0.100	0.130	0.208	0.019	0.009
M1E5	38	0.619	0.10	0.16	0.099	0.132	0.213	0.013	0.003
M1E6	12	0.653	0.03	0.04	0.068	0.110	0.169	0.009	0.002
M2E1	31	0.619	0.05	0.07	0.100	0.130	0.210	0.030	0.003
M2E2	24	0.580	0.09	0.16	-	-	-	0.025	0.006
M2E3	35	0.657	0.06	0.10	0.073	0.084	0.128	0.020	0.006
M2E4	38	0.625	0.08	0.12	0.084	0.090	0.145	0.015	0.009
M2E5	41	0.652	0.12	0.19	-	-	-	0.016	0.003
M2E6	43	0.586	0.05	0.08	0.049	0.073	0.124	0.010	-
S1	58	0.533	0.02	0.05	0.055	0.075	0.141	0.016	0.002
S2	43	0.530	0.03	0.06	0.045	0.053	0.100	0.013	0.001
S3	29	0.527	0.05	0.10	-	-	-	0.008	0.001
S4	14	0.561	0.07	0.12	-	-	-	0.008	0.001

*Although plane bed prevailed during the run, for some few short periods very low stationary waves were observed; the measurements correspond to one of these stages.

Table 5.4 Characteristics of bedforms next to channel walls. Bedforms on the bed surface at the end of the run are considered alternate bars for all runs except S3 and S4. Runs G13, G14 and G15 showed no discernible periodic relief on the bed surface at the end of the run.

(1)	(2)	(3)	(4)	(5)	(6)	(7)	(8)	(9)
Run	**Standard deviation of bed surface variation near the wall during run** σ_b **[mm]**	**Bedform height** $\Delta = 2\sqrt{2}\,\sigma_b$ **[mm]**	**Maximum sectional difference in height** Δ_{smax} **[mm]**	**Half-bar mean wavelength[1]** $\lambda_b/2$ **[m]**	**Half-bar wavelength[1] mode (0.2 m intervals)** $\lambda_b/2$ **[m]**	**Mean bedform length/channel width** λ_b/B	**Mean bedform length/mean water-depth** λ_b/H	**Period of a bedform unit** $T_b = \lambda_b/c$ **[s]**
G12	3.30	9.3	-	1.87 ± 0.34	1.00	5.0	55.1	144
G13	13.0	36.8	16.3	-	-	-	-	-
G14	5.3	15.0	24.7	-	-	-	-	-
G15	4.7	13.3	24.3	-	-	-	-	-
G16	5.0	14.1	34.2	1.19 ± 0.34	1.20	3.2	28.0	130
G17	2.6	7.4	30.1	1.04 ± 0.18	1.00	2.8	19.0	382
M1E1	7.3	20.6	40.3	1.20 ± 0.13	1.20	3.2	23.1	233
M1E2	9.2	26.0	22.1	1.55 ± 0.26	1.80	4.1	36.1	113
M1E3	6.6	18.7	28.7	1.38 ± 0.17	1.40	3.7	36.3	101
M1E4	8.9	25.2	38.9	1.48 ± 0.14	1.40	3.9	34.0	157
M1E5	9.2	26.0	38.9	1.16 ± 0.30	1.00	3.1	25.8	176
M1E6	9.4	26.6	49.0	1.14 ± 0.28	1.00	3.0	20.2	259
M2E1	4.5	12.7	23.7	1.62 ± 0.26	1.60	4.3	39.9	109
M2E2	6.0	17.0	13.6	1.80 ± 0.36	1.60	4.8	44.9	147
M2E3	7.6	21.5	30.0	1.47 ± 0.25	1.60	3.9	35.5	144
M2E4	9.7	27.4	20.6	1.11 ± 0.16	1.20	3.0	25.0	148
M2E5	9.3	26.3	55.7	1.02 ± 0.21	1.20	2.7	19.8	132
M2E6	8.7	24.6	55.5	1.18 ± 0.18	1.20	3.1	20.9	231
S1	17.2	48.6	46.3	1.28 ± 0.45	1.20	3.4	24.9	160
S2	22.9	64.8	50.5	0.95 ± 0.32	0.80	2.5	17.4	150
S3	20.6	58.3	82.6	0.33* ± 0.22	0.30*	0.9	5.5	84
S4	20.1	56.9	78.5	0.27* ± 0.23	0.30*	0.7	4.1	67

*Dunes, not bars, so these values correspond to half the dune wavelength. [1]Lengths considered from x=1 to x=12.

waves, it is considered that the wavelength and celerity of the antidunes are the same as those of the surface stationary waves. The measurements described here correspond to the downstream reach of the channel, where the surface waves and bedform properties were approximately stable.

The wavelengths of the stationary waves observed during the experimental runs were obtained from measurements performed using two different methods. The first consisted of the direct measurement, using a tape measure, of the distance between the crests of different waves during the runs. The second method consisted of counting the number of crests over a known distance using photos of the last 10 meters of the channel. The second column in Table 5.3 indicates the number of waves used to obtain the mean wavelengths, which are presented in column 3. Column 4 shows the standard deviation of the wavelength measurements, which on average for all runs was 6 cm. The procedures for obtaining an average wavelength were not completely accurate; firstly, because it was not possible to count many waves owing to the limited length (10 m) of the section observed, which, in turn, limited the number of measurements that could be made of the distance between the wave crests, and, secondly, because the distance between these crests varied significantly from one moment to another. Notwithstanding, as can be observed in column 5, the standard deviations for the measurements were on average 10% of the mean wavelengths. Furthermore, the mean wavelengths obtained from the analysis of time series for the stationary waves of three runs (see Section 5.3.4.3), showed similar values to those presented in Table 5.3.

For some runs, the height of the stationary waves, i.e. the distance from the wave trough to the wave crest, was measured with a tape measure or a vernier scale supported by the channel walls. The mean values of these measurements are shown in column 6 of Table 5.3. The maximum measured height is given in column 7. Although it is not indicated if the measure corresponds to a breaking wave, this maximum value can be related to the maximum height that a surface wave can attain before breaking. Different criteria exist in the literature to calculate the maximum steepness (i.e. the maximum height/length ratio) of a water wave. One of these states that wave height is 0.142 times the wavelength (Michell 1898, after Kennedy, 1961). For comparison, column 8 presents the wave steepness for maximum wave height and mean wavelength. The average ratio is 0.157, which is similar to the theoretical value of 0.142.

Column 9 in Table 5.3 presents the celerity of the surface waves. Because all the observed waves propagated downstream, all the celerity values have the same sign. Celerity was obtained by measuring the distance traveled by a wave over a given time with a tape measure. The results, however, were not accurate and not many measurements were performed; this is reflected by the standard deviation of the celerity measurements, shown in the last column, which was on average 25% of the mean celerity values. In Section 5.3.4.3 the celerity of stationary waves for three runs is obtained following an analysis of time series; in this analysis, it was found that discrepancies with values in Table 5.3 were not important. Figure 5.8 presents the celerity values plotted as a function of the Froude number. Although the scatter is high, a bias toward an increase in celerity as the Froude number increases is noticeable, with a discontinuity approximately between F=1 and F=1.2.

5.3.4.2 Bedforms near the channel wall

As already stated, for most of the experimental runs the bed configuration at the center of the channel was different from the bed configuration near the channel walls. No direct measurements for the bedforms in the central channel cross section were feasible during the runs because of the turbidity and unsteadiness of the bed and water surfaces. Neither

was it possible to measure preserved morphologies of these forms, because they were washed away during the waning flow. Unlike the bedforms in the central channel cross section, those in the side sections were visible through the glass-paneled walls and morphologies remained at the end of the run. In this Section some of the measurable characteristics of the bedforms near the walls are described. These characteristics are summarized in Table 5.4.

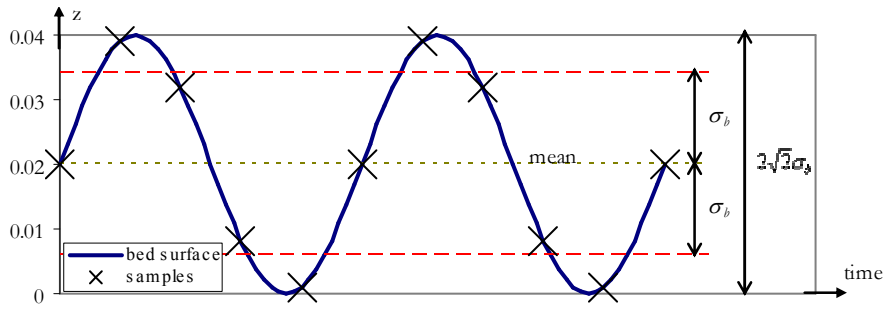

Figure 5.9. Height of sinusoidal bedforms as a function of the standard deviation of bed elevation samples.

The mean height of the bedforms was obtained from the standard deviation of the bed profiles measured (see Chapter 3 for a description of the measurements and Table 3.23 with a summary of the results). Plots of the standard deviation of the bed surface variation along the channel are shown in Appendix XV and summarized in the first column of Table 5.4 for the final downstream section of the channel, where the bedforms reached stable conditions. The mean height of the bedforms, as shown in the third column of Table 5.4, was considered to be given by

$$\Delta = 2\sqrt{2}\sigma_b \qquad (5.7)$$

where Δ is the mean height of the bedforms and σ_b is the standard deviation of the bed surface level; this function depicts the height of idealized sine waves as shown in Figure 5.9 (Willis and Kennedy 1978, after Kuhnle 1993). As shown in Figure 5.10, bedform height increased with sand content in the bed material, a tendency which is in agreement with the findings of Kuhnle (1993) for sand contents of 0, 10, 25 and 45% in sand-gravel mixtures for subcritical flows.

A survey of the bed surface for different cross sections was taken at the end of each experimental run, at different locations of the preserved bars, as is shown in Figure 5.12 for run M2E5. Sections were selected in an attempt to account for representative bedform units of the bed reaches, and for each representative unit at least two cross sections were surveyed. Sequences of these sections exhibited an alternate path of the thalweg along the channel cross section because of the alternate bar sequence. The greatest values for the difference between the highest level and the lowest level for each section in each run are given in the fourth column of Table 5.4 and have been plotted in Figure 5.11 as a function of the run Froude number. As can be seen, these maximum height differences decrease with an increase in Froude numbers. These heights are not only related to bedform height, but also to the scour holes produced by the antidunes and the washing of the bedforms and the fill of the scour holes during the waning flow.

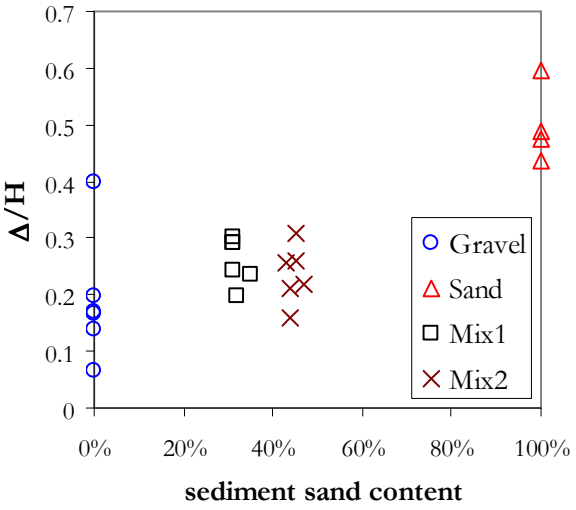

Figure 5.10. Variation of the ratio of mean bedform height and water depth according to the sand content of the sediment mixture.

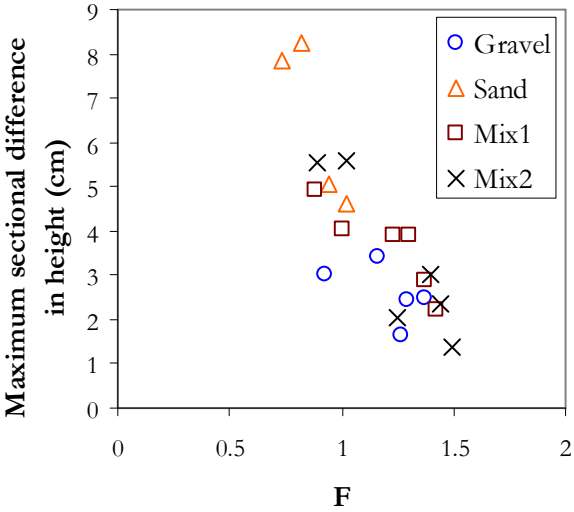

Figure 5.11. Maximum sectional difference in height as a function of the Froude number, for measurements of bed surface elevation at the end of the runs.

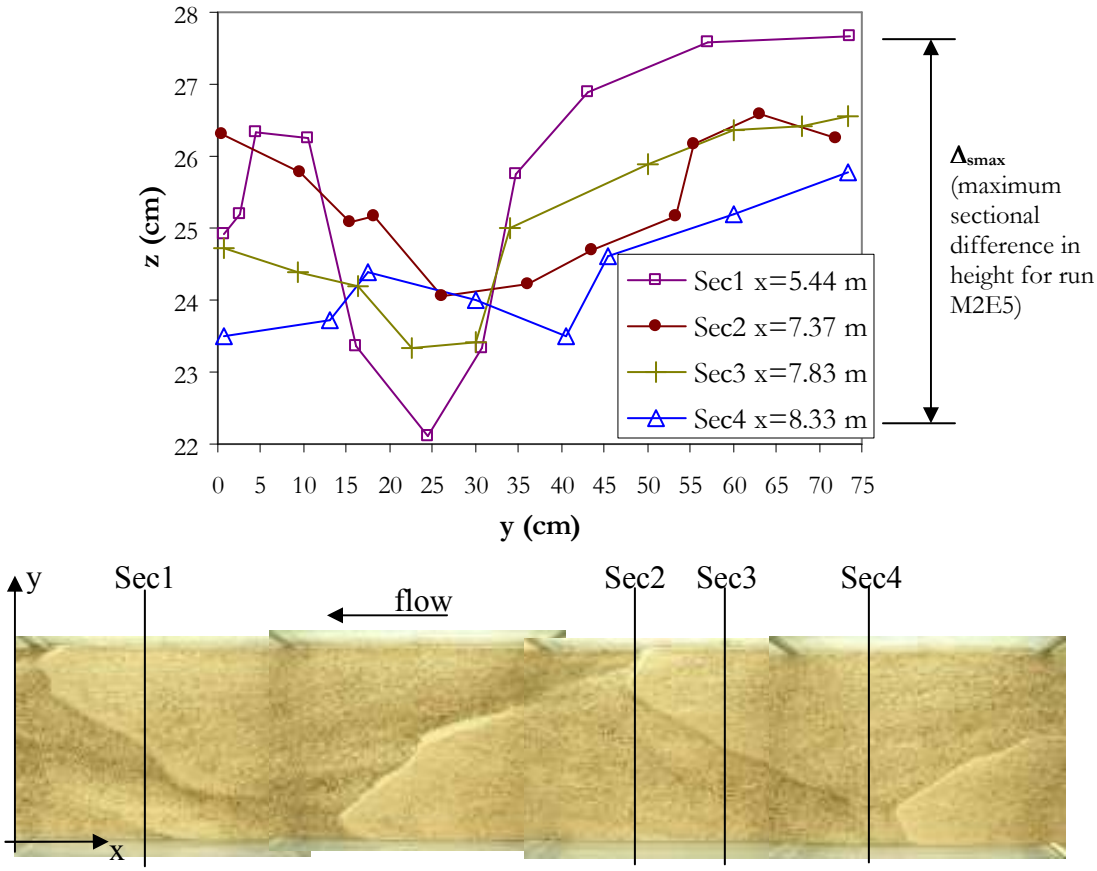

Figure 5.12. Bed surface cross sections for run M2E5.

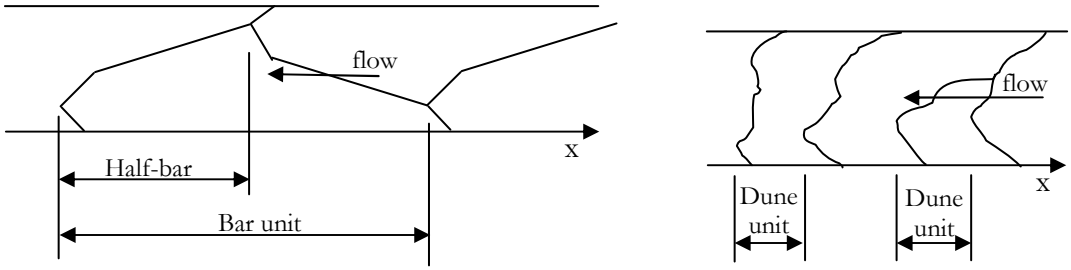

Figure 5.13. Definition of bedform units considered when measuring bedform wavelength from the aerial photos taken at the end of the runs.

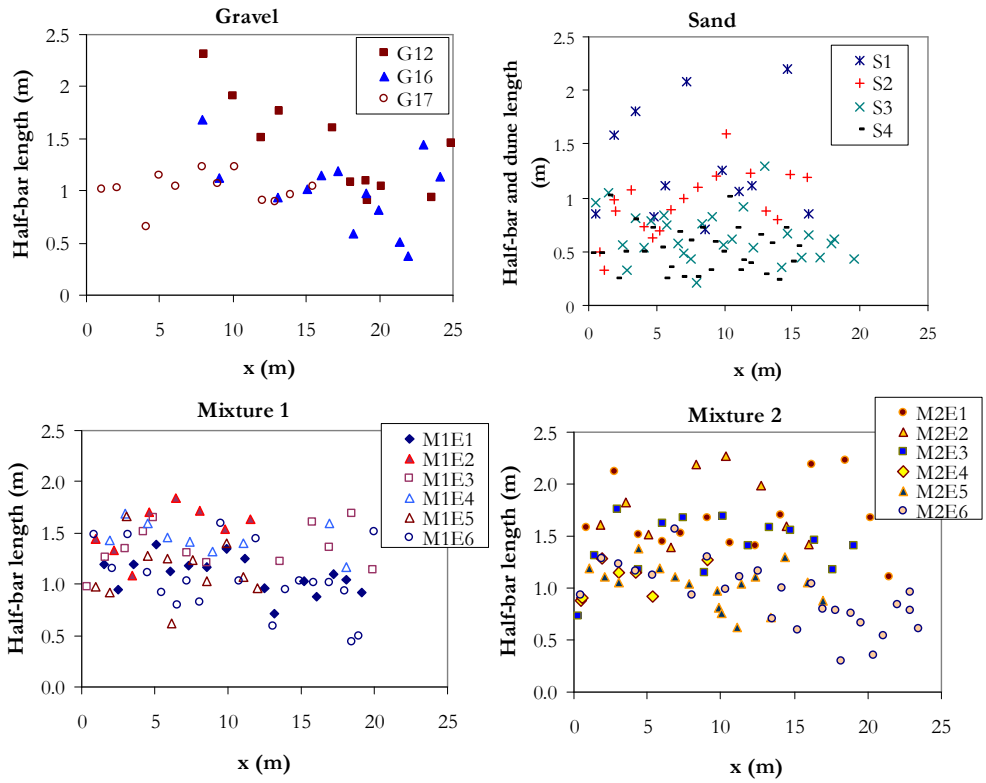

Figure 5.14. Half-bar and dune wavelengths measured from aerial photographs and situated along the channel. For sand runs S1 and S2 the bed configuration was with bars and for runs S3 and S4 with dunes.

The wavelength of the side bedforms was measured from the aerial photographs taken at the end of the runs (shown in Appendix IX). The schemes in Figure 5.13 define the criterion used for considering the wavelength of a morphological unit for bars and dunes and the wavelengths measured along the channel have been plotted in Figure 5.14. It was not possible to measure wavelengths for gravel runs G13, G14 and G15 as the bed surface at the end of the run showed no identifiable bedform morphologies. For these runs the final bed surface was not plane, but rather showed a central depression with a height of the same order of magnitude as the bars in the other runs, as can be seen in Table 5.4 for the maximum sectional differences in height measured, and as shown in Figure 5.11. Column 5 in Table 5.4 presents the average wavelengths of the preserved bedforms for the last 12 meters at the downstream end of the channel length (from x=0 to x=12), as for this final reach the wavelengths showed less variation. The standard deviation of these

measurements was on average 22% of the mean wavelengths. When considering all the bars along the flume, the mode (the most frequent value) of half-bar lengths, presented in column 7, was on average 97% of the average lengths measured in the last 12 meters.

Table 5.4 shows the ratio between bedform wavelength and both channel width (column 7) and water depth (column 8). From the values in these two columns it can be concluded that it is correct to class most side bedforms as alternate bars, because their wavelengths are of the same order of magnitude as channel width and not of water depth. Only bedforms in runs S3 and S4 can be classed as dunes, because their wavelength was of the same order of magnitude as water depth. The ratio between the bedform wavelength and channel width is shown graphically as a function of the Froude number in Figure 5.15; this graph exhibits a bias toward longer wavelengths as the Froude number increased.

In terms of the hydraulics and resistance to flow exerted by the bedforms, an important parameter is bedform steepness, which is the ratio between bedform height and wavelength. Higher bedform steepness would be associated with higher flow resistance related to the bedform. The variation of bedform steepness with Froude numbers is shown in Figure 5.16; in general terms the steepness was higher the lower the Froude number was, and therefore a similar trend for bed resistance produced by the side bedforms in the experimental channel can be expected.

The last column in Table 5.4 presents the computed period of a bedform unit by considering that the bedforms next to the wall had the same celerity as the antidunes at the center of the channel.

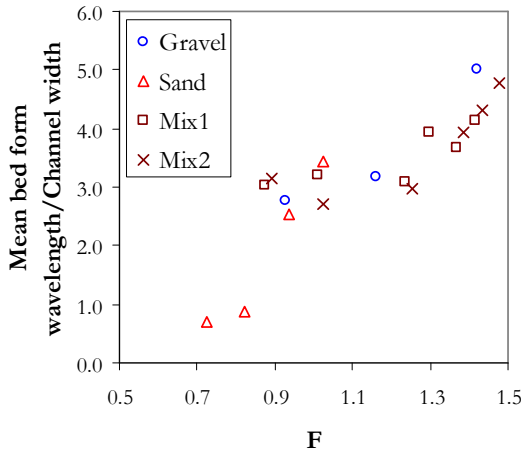

Figure 5.15. Variation in the ratio between bedform wavelength and channel width with Froude number.

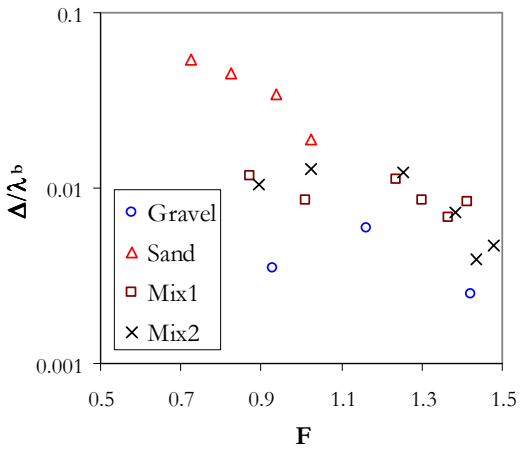

Figure 5.16. Variation in bedform steepness with Froude number.

5.3.4.3 Analysis of time series for selected runs

From videos taken during the experimental runs of the bed and water profiles, time series of the variations in bed surface elevation and displacement of stationary waves were obtained for three runs: S1, S4 and M1E5. The videos were taken through the transparent channel walls during the phase of mobile-bed equilibrium conditions, in the downstream section of the channel where the bedforms and water surface had attained stable properties.

The time series for the displacement of stationary waves are shown in Figure 5.17. These were obtained by recording the instantaneous position of the highest and most stable waves passing in the direction of flow along a reach of the channel, at the center of

the cross section. For the graphs in Figure 5.17, each group of data corresponds to a wave that could be followed more or less continuously, i.e. a wave that remained stable and visible at all times or that rapidly reformed at the same location if it broke or vanished. For runs S1 and M1E5, which showed a 3D water surface (according to the classification in Table 5.2), most of the stationary waves followed when recording the time series corresponded to short-crested waves, i.e., rooster tails, such as those seen in Figure 5.1. For run S4, rooster tails and 2D stationary waves were recorded. The time series reflect many of the features described in Section 5.3.1, as well as the unstable character of the water surface for flows in the transition between lower and upper regimes. Run S1 showed the most stable and organized stationary waves of the three selected runs, which is reflected in Figure 5.17 by almost parallel and periodic groups of data. The region around 1690 s current time is remarkable because the stationary waves vanished but rebuilt rapidly within seconds. Run S4 shows a longer period of time without stationary waves along the reach, between approximately time=3300 and 3500 s; it also shows an upstream displacement for more or less 1 minute for two of the first three waves. The waves on run M1E5 were not as stable as those in run S1, with only a few passing through the observation channel reach without vanishing.

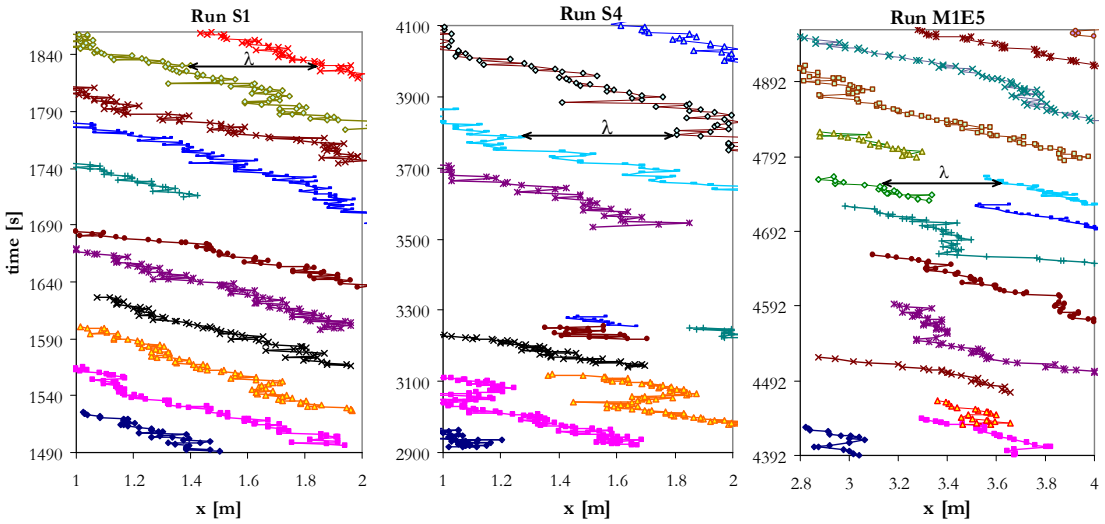

Figure 5.17. Time series for the instantaneous position of stationary waves along a reach of the channel, for runs S1, S4 and M1E5. Each group of data corresponds to a different surface wave. The wavelength λ for a given time is indicated in each graph. Flow from right to left.

From the data presented in Figure 5.17, wavelengths of the stationary waves were obtained by measuring the distance between waves for a given time if two or more waves coincided for that instant within the observation channel reach. Mean values and standard deviations of the measurements are shown in Table 5.5. For comparison, in Table 5.5 the values measured during the run, as presented in Table 5.3, are shown as well. No significant differences were found for measurements during runs and measurements from the time series for runs S1 and M1E5, but for run S4 the difference was higher than 15%. This is related to the non-stationarity of the wavelength measurements for this run, as the wavelengths increased significantly for the last measurements, which correspond roughly to the last 400 seconds of the time series. If for computing the mean wavelength for run S4, only the measurements corresponding to the first 800 seconds are considered, the mean obtained is 0.555 m with a standard deviation of 0.09 m; these values are quite similar to those obtained for the measurements during the run. Sampling for longer time intervals

would be required for run S4 to accurately define the range of wavelengths that could occur for such flow conditions or to verify if such behavior occurs only for short time intervals.

Table 5.5. Mean wavelength, celerity and period of stationary waves for selected runs. The wavelength and celerity values shown were obtained by direct measurements during the runs and from analysis of time series recorded in videos of the experiments.

Run	Stationary waves				
	Mean wavelength λ (m)		Mean wave celerity c (m/s)		Mean period from time series analysis (s) T=λ/c
	Direct measurements (Table 5.3)	Time series	Direct measurements (Table 5.2)	Time series	
S1	0.533 ± 0.02	0.512 ± 0.08	0.016 ± 0.002	0.014 ± 0.002	36.6
S4	0.561 ± 0.07	0.657 ± 0.16	0.008 ± 0.001	0.005 ± 0.002	131.4
M1E5	0.619 ± 0.10	0.619 ± 0.08	0.013 ± 0.003	0.011 ± 0.003	56.3

Wave celerity was obtained for the stationary waves recorded in the time series in Figure 5.17 by applying least-squares linear regression to each group of time-position data for the most stable periods. Because celerity can be defined as an increment in position with respect to time, i.e. c=dx/dt, the slope of the fitted lines is equal to the mean wave celerity. The mean celerity values from the least-squares regressions for each of the selected runs are shown in Table 5.5. For comparison, celerity values measured during the runs are also shown in Table 5.5. It is important to note that the celerity and standard deviations obtained with the two methods are of the same order of magnitude.

Plots of time series for the bed surface level variation near the channel wall are presented in Figure 5.18 for runs S1, S4 and M1E5 (for runs S1 and S4 they are the same plots as those in Figure 5.6). These plots shed light on the superposition of steep bedforms over forms with longer periods. As stated in Section 5.3.2.3, the long bedforms preserved at the end of the runs on the bed surface at the sides of the flume (which appeared in an alternate sequence for most of the runs) might be related to the long bedforms observed through the channel walls when the water was flowing. For demonstrating this correspondence, the characteristics of both bedforms are compared using the bed elevation time series. Figure 5.18 shows the period of discernible long bedforms, which was on average 144, 416 and 181 seconds for runs S1, S4 and M1E5, respectively. If it is considered that the long bedforms at the sides of the channel section propagated at the same celerity as the antidunes underneath the standing waves at the channel central section, the wavelength of the lateral bedforms λ_b can be related to the corresponding period and celerity by

$$\lambda_b = cT \qquad (5.8)$$

Bedform wavelengths obtained by applying eq.(5.8) using mean bedform periods from Figure 5.18 and celerity values obtained from the stationary wave time series shown in Table 5.5, are 2.0, 2.2 and 2.0 m for runs S1, S4 and M1E5, respectively. For runs S1 and M1E5 these results are in agreement with the mode of measured wavelengths for the preserved bedforms as presented in Table 5.4, namely, 2.4 for run S1 and 2.0 for run M1E5. When comparing these values the high variation of the wavelengths measured at the end of the runs, with standard deviations of 0.45 and 0.30 m for S1 and M1E5, respectively, should be taken into account. From these results, it can be considered that for runs S1 and M1E5 the long bedforms observed near the channel walls when the water was flowing can be accurately related to the bedforms preserved after the water was drawn down. On the contrary, for run S4, the measured mode of bedform wavelength is 0.6 m,

quite different to the value of 2.2 m obtained with eq.(5.8). Thus, for this run not all the preserved bedforms can be related to the long period forms identified in Figure 5.18. It is possible that the dunes observed on the bed surface without water at the end of run S4 were superimposed onto the large bedforms shown in Figure 5.18, and that in contrast to the steep bedforms in runs S1 and M1E5, which were washed away by the waning flow, the dunes in S4 were preserved in coexistence with the longer bedforms. This would mean that both types of features were mixed on the bed surface, making it difficult to identify each class of bedform in the aerial photographs shown in Appendix IX.

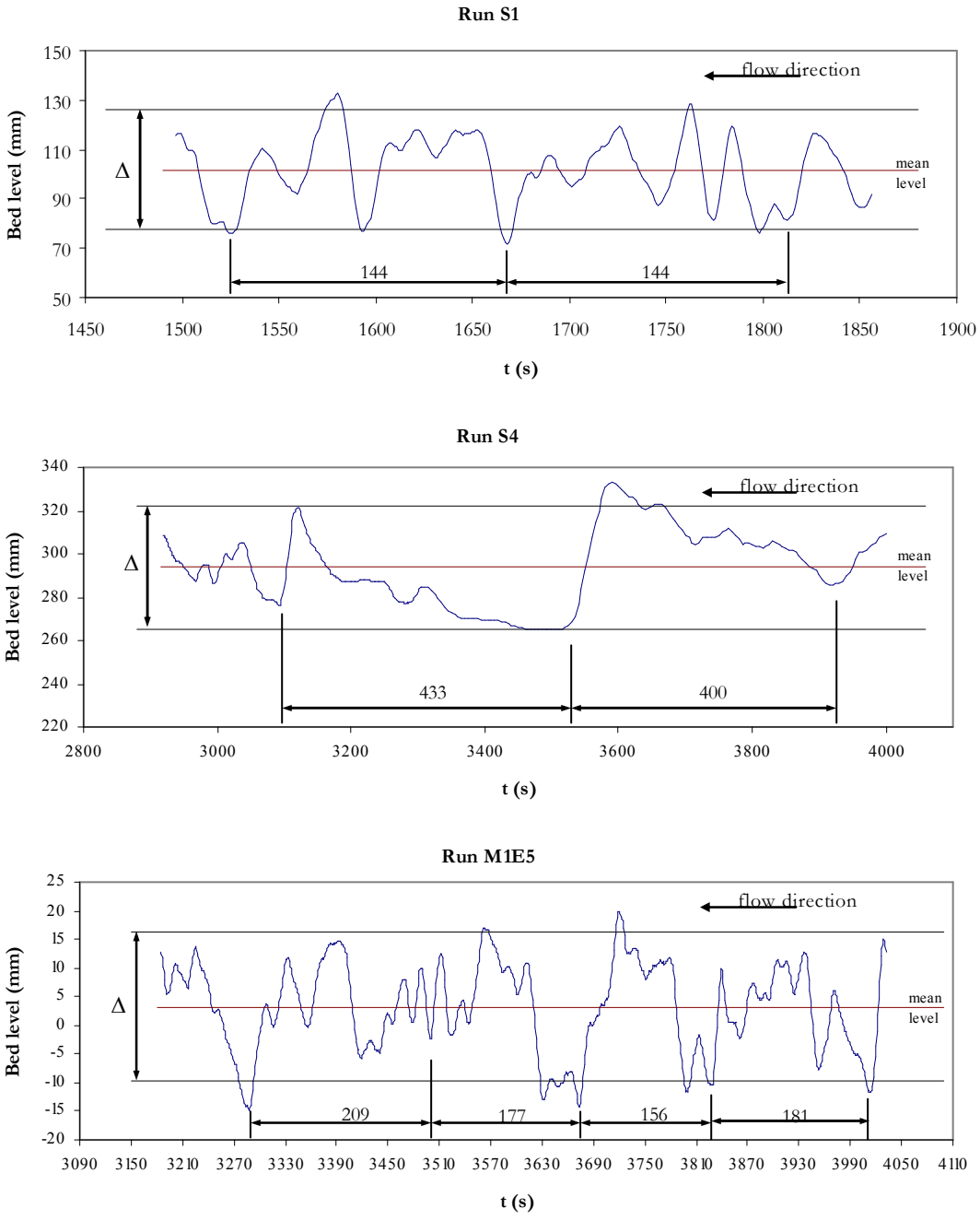

Figure 5.18. Time series for bed level variation. A moving average of 9 was superimposed. Δ refers to the mean bedform height as presented in Table 5.4. The period of the longest periodic forms observed is indicated.

Fourier analysis of the time series in Figure 5.18 resulted in dominant periods of 37, 176 and 171 s for runs S1, S4 and M1E5, respectively. Roughly, these values correspond to a quarter, a half and the mean of the periods identified in Figure 5.18, for the long periodic forms in runs S1, S4 and M1E5, respectively. For run S1 the dominant period obtained with Fourier analysis is the same as that calculated using celerity and wavelengths for the stationary waves in Table 5.5. Meanwhile, for run M1E5 the dominant period corresponds to the long waves, i.e., to the alternate bars. No direct relation can be found for run S4, perhaps because of the great variations in the characteristics of the bedforms.

5.3.5 Bed erosion patterns

Although antidunes and other steep bedforms were washed away when the water discharge was stopped at the end of the run, the resulting transversal profile of maximum erosion was measured for the sand- and mixtures-run series by identifying the buried colored gravel that remained. The colored gravel was placed 4.5 m upstream from the channel end before initiating the mobile-bed equilibrium phase of each run. Photographs of the sections that were opened to measure the erosion depths are shown in Appendix XI. In Figure 5.19 the cross-sectional erosion patterns are compared between runs for each type of bed sediment. For ease of comparison, the final bed elevations near the channel window (y=0) at the end of the run were forced to be equal at level z=0.

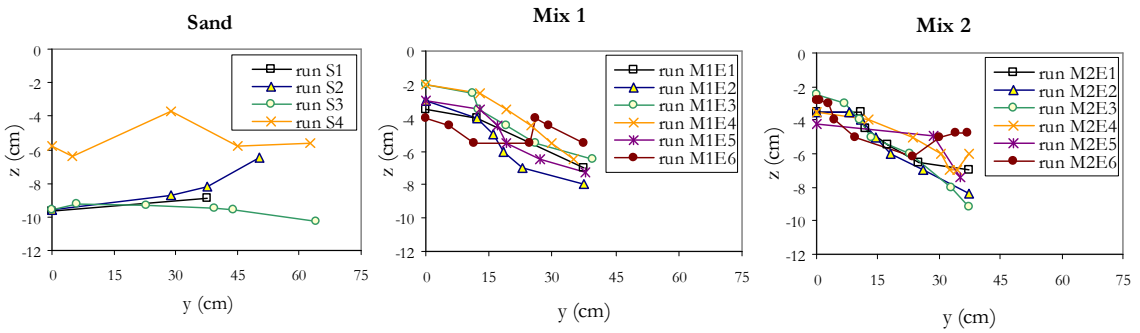

Figure 5.19. Cross-sectional bed erosion patterns. Level z=0 corresponds to the bed surface near the wall at the end of the run. Channel width is 75 cm.

The deepest erosion occurred at the center of the channel for all the runs with mixtures except for those with the lowest Froude numbers (M1E6 and M2E6). Conversely, erosion profiles for the sand runs were approximately uniform, i.e., the depth of erosion was roughly the same across the cross section and even slightly deeper near the walls, as occurred with run S2. Such a pattern reflects the tendency for bedforms in sand runs to be more two-dimensional than those in runs with sediment mixtures, which showed a marked three-dimensionality in the majority of cases.

The active layer is defined here as the bed layer containing the particles put in motion during the run. Therefore, for each run, the active layer for a channel section is equal to the distance between the mean bed surface at the end of the run and the level of maximum erosion, as shown in Figure 5.20. The variations in the mean sectional active layer, the active layer near the channel wall and the maximum active layer as a function of dimensionless shear stress are shown in Figure 5.21. Dimensionless shear stress is given by $\tau_b/[\rho g(Ss-1)D_m]$, where D_m is the mean diameter of the bed sediment, g is the gravitational acceleration, Ss is the relative density of the sediment, ρ is the water density and τ_b is the mean boundary shear stress corrected for side-wall effects (for the computation of τ_b see

Section 4.3.1 and eq.4.23). From Figure 5.21a, it is obtained that the mean active layer varies between 4 and 6 cm for the mixture runs and for the sand run with the lowest shear stress. In the other three sand runs, the mean active layer is higher than 7 cm. As shown in Figure 5.21b, a similar trend occurs for the active layer near the channel wall, but in this case the active layer ranges from 2 to 4 cm for low shear stresses. The maximum active layer in the cross section, described by Figure 5.21c, despite some scatter, exhibits a subtle increasing trend with increasing dimensionless shear stress.

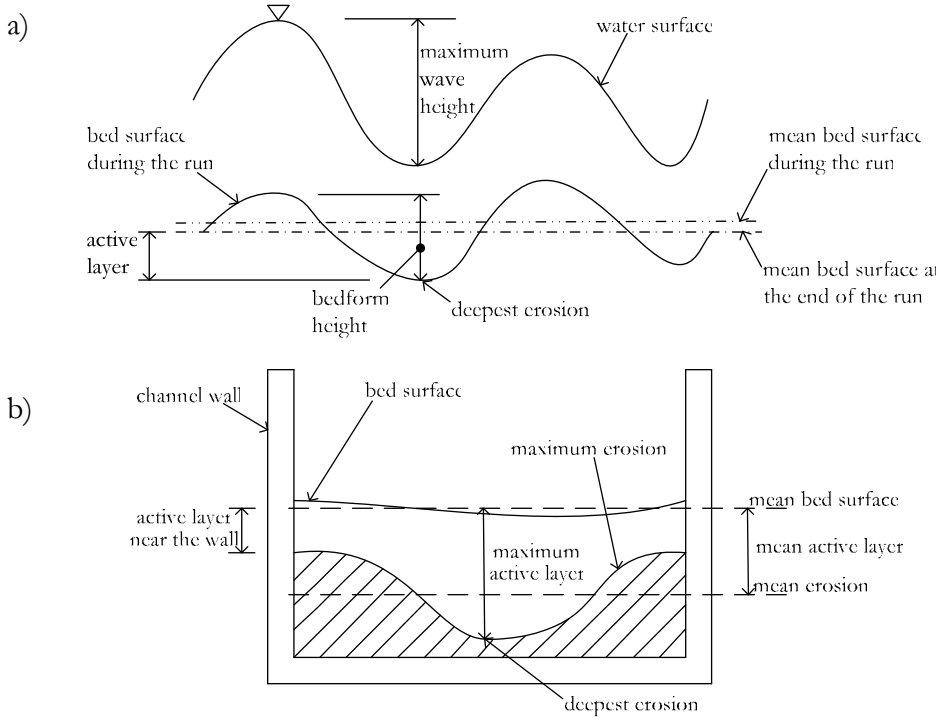

Figure 5.20. Definition of the active layer a) for a section parallel to flow direction, and b) for a channel cross section.

Variations in bed erosion in the cross section can be measured by calculating the ratio between the active layer in the central section and the active layer next to the channel wall. This ratio is presented in Figure 5.22 as a function of the dimensionless shear stress of each run. For the central section, the active layer considered was the maximum active layer measured in the central third of the section. Figure 5.22 shows that the ratio between the central and side sections for the sand runs remains almost constant with shear stress variation; indeed, the active layer in the central section is on average 80% less deep than the layer near the channel wall. Such a small difference between sections reflects the low variation of erosion across the cross section of the channel. The data for mixture 2 (45% sand content) in Figure 5.22 show a different trend. On average, the central section active layer is twice as deep as the layer next to the wall, except for one point at which the ratio is 3.7. Unlike the sand and mixture 2 runs, for mixture 1 (32% sand content), the active layer ratio between the central and wall sections varied notably between runs, and was higher with increasing bed shear stress (Figure 5.19b). Therefore, an increase in mean bed shear stress produced a higher concentration of bed erosion in the central section than in the lateral section, which also means that flow three-dimensionality increased with higher mean shear stress.

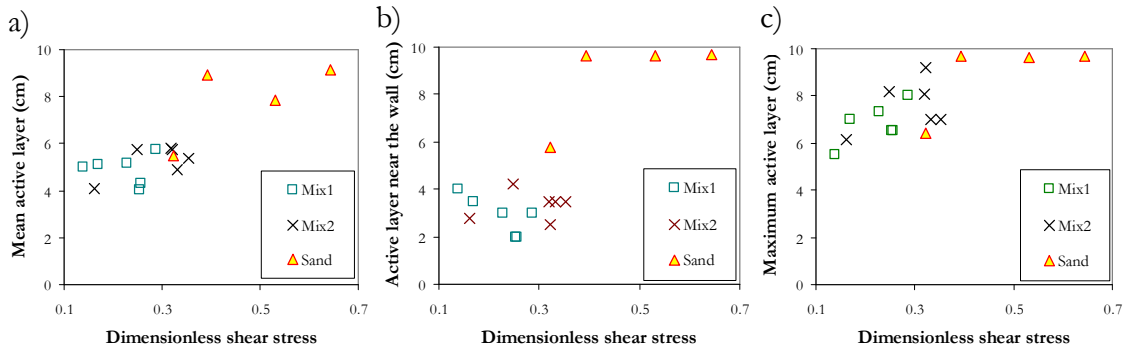

Figure 5.21. Variations in active layer with dimensionless shear stress in the channel cross section; a) mean active layer, b) active layer near the channel wall, and c) maximum active layer.

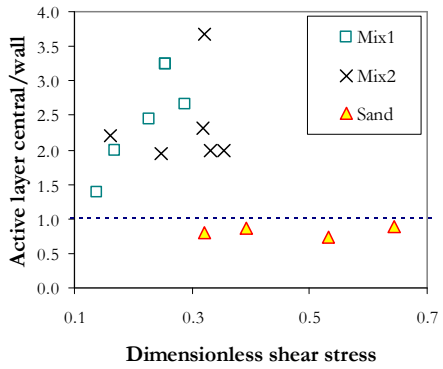

Figure 5.22. Variations, with increasing dimensionless shear stress, in the ratio between the maximum active layer measured in the central third of the section and the active layer next to the channel wall.

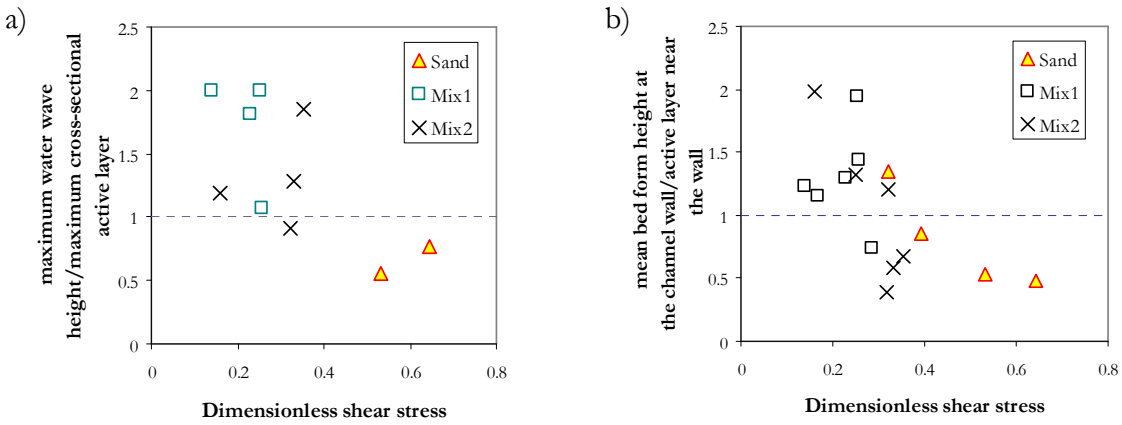

Figure 5.23. a) Variations in the ratio between maximum stationary wave height and the deepest active layer measured in the channel cross section as a function of dimensionless shear stress. b) Variations in the ratio between the mean bedform height obtained from bed profiles measured at the channel walls and the active layer measured at the channel wall, as a function of dimensionless shear stress. See Figure 5.20 for the definitions of active layer, wave height and bedform height.

A comparison of photographic records showed a direct qualitative relationship between the observed height and choppiness of rooster tails during the runs and the depth of the scour in the central section. Notwithstanding, no discernible trends were detected

for the ratio between maximum stationary wave height (Table 5.3) and the maximum active layer measured at the cross section (Figure 5.23a). It should be noted that the height of the active layer in sand runs was 150% higher than that of the maximum stationary waves, while for some sediment mixtures it was only 50% higher.

The ratio between mean bedform height (obtained from measurements at the channel wall, as presented in Table 5.4) and the active layer measured in the channel wall section is presented as a function of mean bed dimensionless shear stress (Figure 5.23b). Despite the scatter of the data points, a subtle trend is noticeable toward lower values of the ratio for higher dimensionless shear stresses. This trend could be related to fluctuations in bedform height; high fluctuations, i.e., the passage of bedforms of a height much greater than that of mean bedform, produce deep instantaneous erosion, and thus would produce an increment in the active layer as defined in Figure 5.20a. Indeed, fluctuations in bedform height may be accentuated in the case of certain flows.

5.3.6 Sediment transport distribution and grain size sorting produced by bedforms

The passage of bedforms produces pulsations on the rate of sediment transport in a fixed section. The passage of the front of a sediment wave through a channel section results in a peak of sediment discharge. If sediment supply is constant over time, it can be expected that the time-average rate of sediment transport through a given channel section during a lapse of time equal to the period of the bedforms would be equal to the constant supply rate. Similarly, the passage of bedforms is associated with grain-sorting patterns, such that the initial grain size distribution of the fed material is locally modified and segregation is observed in the deposited sediment. Nevertheless, the grain size distribution of the bulk deposit and the sediment in motion must be the same as that of the supplied material if an average over sufficient time is considered. In the following Subsections sediment sorting and spatial and temporal variations in sediment transport are analyzed for the experimental runs.

5.3.6.1 Sediment transport variability measured with manual samples

The unsteadiness of sediment transport was measured during the experiments using manual samples taken with two different instruments, as described in Section 3.3.2.5. Plots shown in Appendix X for the ratio between sediment discharge computed with the sampled material and the sediment feeding rate illustrate these temporal and spatial variations in sediment transport. For a qualitative delimitation of this variability, for each run and each of the two manual samplers used, the average, standard deviation, and maximum and minimum values of the ratio of sediment transport, as defined by eq.(3.23) in Section 3.3.2.5.6, are summarized in Table 5.6 (original values for the computations are presented in Tables 3.15 and 3.16).

The average results shown in Table 5.6 for the two samplers are quite similar (see penultimate row), but this is not the case for standard deviation (last row), which was much higher for the Helley-Smith sampler. Such a difference might be related to the span of the intake opening of the sampler in relation to channel width and the sample duration. The width of the intake of each compartment in the basket sampler is 25 cm (see Figure 3.14), i.e., 2.55 times the width of the Helley-Smith intake, which is 9.8 cm (see Figure 3.13). On the other hand, average sampling times for the Helley-Smith sampler were over twice as high as those for the basket sampler (see Table 3.11). These times are related to the time required for the sampling capacity of the sampler to be filled. Because the capacity is higher for the Helley-Smith sampler than for the basket, sampling times could be longer for the

former. A qualitative explanation for the results shown in Table 5.6 would be that peak solid discharges concentrated in time and space (probably produced by antidunes, which are steep) were lessened by the longer sampling times for the Helley-Smith sampler and by a long intake span in the basket sampler, thus producing similar maximums in both cases. Similarly, solid discharges evenly distributed over time but highly concentrated in space (probably produced by bars, which are long) could have been lessened by the width of the basket sampler but not by that of the Helley-Smith sampler, thus yielding high variability (high standard deviations) for this latter sampler. The Helley-Smith sampler, thus, would have been better able to capture point variations in sediment discharge in time and space. Note that the average of the average sediment transport ratios for each run is equal to one because these data were used to calibrate the efficiency of the samplers %η, which was 61% for the basket sampler and 69% for the Helley-Smith sampler.

Table 5.6. Statistical parameters for the computed ratio of sediment transport for each run from sediment transport samples taken with the manual samplers. The ratio of sediment transport is defined as the relation between the sediment discharges computed for manual samples q_{Ss} and the constant sediment feeding rate in the channel q_{SF}, taking into account the efficiency %η of the sampler. For the basket sampler, which was divided into three compartments, each of these compartments was considered an individual sample. Therefore, for each run, statistics were obtained from a total of 18 samples for the basket sampler and 6 samples for the Helley-Smith samples, except for runs G12 and G13, for which the number of samples were 4 and 3, respectively.

Run	Ratio of sediment discharge variation $r_{sv} = \frac{q_{Ss}}{\%\eta / 100\, q_{SF}}$							
	Basket sampler				Helley-Smith sampler			
	Max	Min	Average	σ	Max	Min	Average	σ
G12	-	-	-	-	1.49	0.59	0.93	0.40
G13	-	-	-	-	0.56	0.44	0.50	0.06
G14	-	-	-	-	1.37	0.36	0.84	0.39
G15	-	-	-	-	1.82	0.45	1.00	0.47
G16	-	-	-	-	1.08	0.44	0.75	0.31
G17	-	-	-	-	4.07	0.32	1.95	1.31
M1E1	1.84	0.33	1.14	0.46	-	-	-	-
M1E2	1.39	0.49	0.92	0.22	-	-	-	-
M1E3	2.40	0.73	1.45	0.42	-	-	-	-
M1E4	1.97	0.43	1.04	0.53	-	-	-	-
M1E5	1.71	0.33	0.89	0.39	-	-	-	-
M1E6	1.45	0.11	0.62	0.34	-	-	-	-
M2E1	2.29	0.48	1.27	0.39	0.60	0.32	0.45	0.09
M2E2	1.76	0.52	1.08	0.39	1.72	0.01	0.62	0.63
M2E3	1.91	0.47	1.05	0.36	1.24	0.07	0.81	0.49
M2E4	1.53	0.37	0.97	0.42	1.83	0.08	1.12	0.65
M2E6	2.33	0.46	1.14	0.51	2.92	1.68	2.14	0.49
S1	2.01	0.31	1.12	0.55	2.73	0.67	1.82	0.89
S2	2.28	0.26	0.95	0.55	2.38	0.96	1.57	0.57
S3	1.53	0.21	0.74	0.42	2.80	2.05	2.35	0.28
S4	1.72	0.08	0.72	0.46	4.22	2.46	3.30	0.78
Average	**1.87**	**0.37**	**1.00**	**0.43**	**1.70***	**0.43***	**1.00***	**0.48***
σ	**0.34**	**0.17**	**0.22**	**0.09**	**1.02***	**0.45***	**0.55***	**0.33***

*Excluding sand samples

Sand samples were not included in the computation of the average values for the Helley-Smith sampler in Table 5.6 because these samples were taken when the peak of a sediment wave was passing through the sampling section. While this choice introduced a bias toward higher sediment transport ratios, it allowed the identification of maximum instantaneous sediment transport rates, which can be as high as four times the mean solid discharge in the channel (this is equal to the constant feeding rate), as occurred in the case of run S4. The analysis of samples taken with the basket sampler for the sand runs yielded standard deviations and maximum values for the ratio of sediment transport that were similar to those observed for the runs with sediment mixtures.

The transversal distribution of sediment transport was measured with the basket sampler. Comparisons between the sediment discharges measured in each of the three compartments are shown in Table 5.7 and Figure 5.24. Figure 5.24 shows that for most runs, the ratio between the sediment transport rates measured in the central and lateral compartments is lower than one. Thus, there is a subtle trend (slightly stronger for the lowest Froude numbers) towards higher transport rates in lateral areas of the channel. Nevertheless, the analysis of the average values for all runs, as presented in the last row of Table 5.7, shows that an equal amount of sediment discharge passed through the central and right sections, while the sediment transport in the left section exceeded the other two by 5.5%. Symmetrical sediment transport behavior should be expected between lateral cross sections, given that the processes observed and measured during the runs showed a symmetrical pattern (standing waves, bedforms and bed erosion). Therefore, it is likely that the bias towards higher measured solid discharges for the left side could be related to a systematic error introduced by the sampler or irregularities in the exit of the channel, rather than to the sediment transport processes. This notwithstanding, it is relevant that the average sediment transport rates in the right and central sections were the same, and it can thus be assumed that the distributions of the time-average sediment transport rates across the section were constant.

Table 5.7. Percentage of sediment transport captured in each of the three compartments of the basket sampler.

Run	% of sediment discharge		
	Right	**Center**	**Left**
S1	26.0%	32.6%	41.4%
S2	22.5%	32.4%	45.1%
S3	28.7%	26.4%	44.9%
S4	35.8%	29.4%	34.8%
M1E1	25.5%	32.9%	41.6%
M1E2	34.3%	33.8%	31.9%
M1E3	33.4%	32.2%	34.4%
M1E4	38.4%	30.9%	30.7%
M1E5	34.3%	31.1%	34.6%
M1E6	32.9%	31.2%	35.9%
M2E1	30.5%	31.4%	38.1%
M2E2	35.2%	30.6%	34.2%
M2E3	30.1%	34.9%	34.9%
M2E4	33.5%	33.2%	33.3%
M2E6	31.4%	30.0%	38.6%
Average	**31.5%**	**31.5%**	**37.0%**

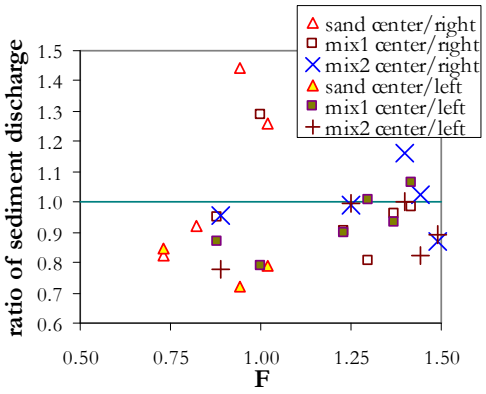

Figure 5.24. Variations with Froude numbers in the ratio between unit sediment discharge in the central section and the lateral sections, based on the samples taken with the basket sampler.

5.3.6.2 Sediment transport variability in bed elevation time series

The sediment transport rate for a bed composed of migrating bedforms can be written as a function of the celerity of the bedforms c, time t and the horizontal coordinate x as

$$q_b = q_b(c,t,x) \tag{5.9}$$

Increments of q_b with respect to x are thus given by

$$\frac{\partial q_b}{\partial x} = \frac{\partial q_b}{\partial c}\frac{\partial c}{\partial x} + \frac{\partial q_b}{\partial t}\frac{\partial t}{\partial x} \tag{5.10}$$

Considering that the bedforms migrate at a constant rate given by $c=\delta x/\delta t$, it results that $\delta c/\delta x=0$, and eq.(5.10) can be rewritten as

$$\frac{\partial q_b}{\partial x} = \frac{1}{c}\frac{\partial q_b}{\partial t} \tag{5.11}$$

Exner's sediment transport continuity equation is given by

$$\frac{\partial z}{\partial t} = -\frac{\partial q_b}{\partial x} \tag{5.12}$$

where z is the vertical coordinate. Introducing (5.12) in (5.11) yields

$$\frac{\partial q_b}{\partial t} = -c\frac{\partial z}{\partial t} \tag{5.13}$$

Eq.(5.13) can be used to transform the time-elevation plots in Figure 5.18 to time-solid discharge plots for comparison with the sediment transport plots for the manually collected samples, which are presented in Appendix X. It should be considered that for the coordinate system in this work, downstream-migrating bedforms have a negative celerity value as the horizontal coordinate increases in the upstream direction. Eq.(5.13) is valid for fully developed bedforms (i.e., bedforms which do not grow or decay in time), for which the sediment grains are transported by rolling and sliding over the bedform along the entire bed profile (i.e., no grains are brought into suspension). In turn, eq.(5.13) is valid for beds in equilibrium, i.e., beds in which no net deposition or erosion occurs and therefore in which the mean bed level is constant over time.

With reference to Figure 5.25 and eq.(5.13), for a given time step Δt, the gradient of sediment transport Δq_b can be computed in a discrete form as

$$\Delta q_b = -c\Delta z(1-\varepsilon) \tag{5.14}$$

where ε is bed porosity, and generalizing

$$q_b^{i+1} - q_b^i = -c\left(z^{i+1} - z^i\right)(1-\varepsilon) \tag{5.15}$$

where i denotes the time step analyzed. Variations in bed elevation with time can be identified from the time series shown in Figure 5.18, and the bedform migration velocity is given in Table 5.5. Therefore, only one boundary condition is required to solve eq.(5.15).

Thus, it can be imposed as a restriction that the average sediment transport rate for the n time steps is equal to the constant sediment feeding rate into the channel q_{SF}, i.e.

$$q_{SF} = \frac{1}{n}\sum_{i=1}^{n} q_b^i \qquad (5.16)$$

Because the equations above are one-dimensional, they do not consider mass transfer between adjacent sections. Nevertheless, their application to the experimental data is valid because the sediment transport variation across the cross section was negligible, as demonstrated in Section 5.3.6.1.

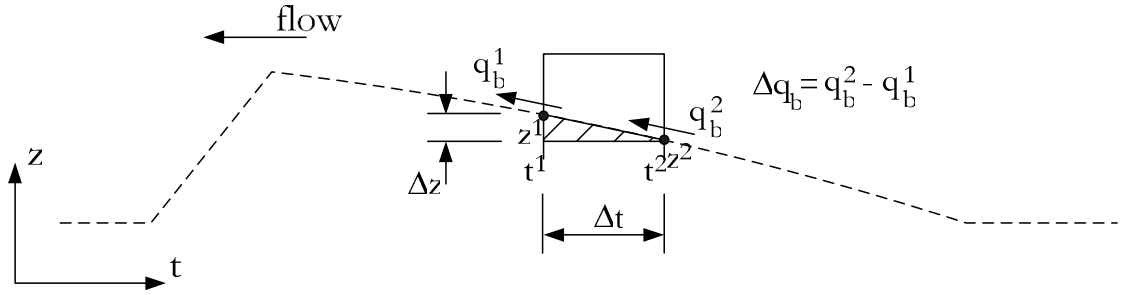

Figure 5.25. Discrete form of variables for a time step of the bed profile for applying eqs.(5.13) to (5.15).

Eqs.(5.14) to (5.16) have been solved iteratively for the time series in Figure 5.18. The bed porosity was considered to be equal to 0.4 for the sand runs and 0.25 for mixture 1. Results for the computed gradients of sediment transport Δq_b and solid discharges q_b are shown in Figure 5.26. From Figure 5.26, it is evident that the average gradient of sediment transport for all three runs is roughly zero, indicating that no net erosion or deposition occurred in the bed, and therefore mobile-bed equilibrium conditions were verified.

For the sake of comparison, the bed profile time series transformed to sediment transport time series with eqs.(5.14) to (5.16) have been plotted in Figure 5.27 together with the sediment transport measured with the manual samplers. Sediment transport is presented in Figure 5.27 as a ratio given by the sediment transport normalized with the constant sediment feeding rate. In this manner, for sediment transport computed from the time series, the ratio of sediment transport is given by q_b/q_{SF}, while for the manual samplers it is given by eq.(3.23), which is the ratio of sediment discharge variation summarized in Tables 3.15 and 3.16. Time in Figure 5.27 is presented as the dimensionless relation

$$\frac{t_m}{T_b} - T_l \qquad (5.17)$$

where t_m is the elapsed time during the run, T_b is the period of a bedform unit (as shown in Table 5.5, except for run S4, for which the period considered is an average of those shown in Figure 5.18) and T_l is a time lag equal to the minimum integer value for the ratio t_m/T_b in the time series. An additional lag of $0.25T_b$ and $0.5T_b$ was used for samples for the central and right compartments of the basket sampler, respectively, with the aim of reproducing the pulses in sediment transport across the cross section because of the passage of alternate bars.

Overall, Figure 5.27 shows that sediment transport ratios obtained with the manual samples are approximately of the same order of magnitude as those computed from the bed elevation time series. Only some samples obtained with the Helley-Smith sampler for

the sand runs presented higher sediment transport rates than the maximum in the time series profiles. This is probably related to the decision to collect these samples when the front of a sediment wave was passing in an attempt to capture peak sediment discharge at the center of the channel.

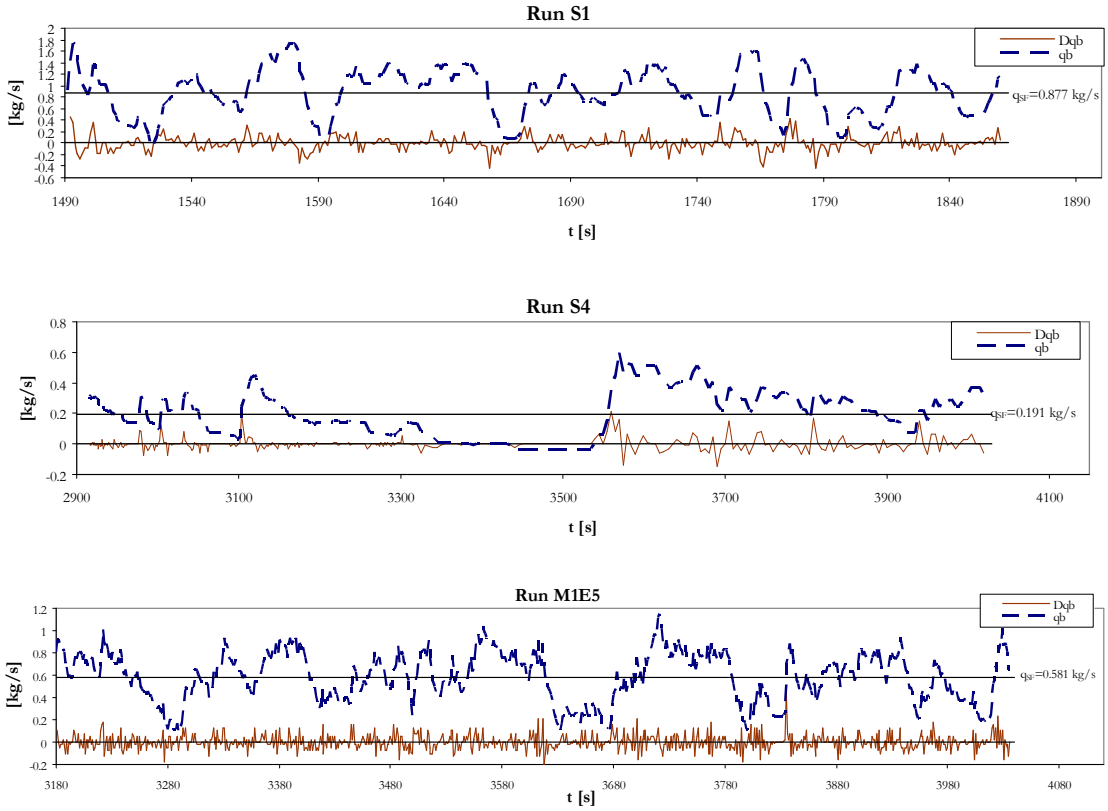

Figure 5.26. Gradient of solid discharge Δq_b and solid discharge q_b computed with eqs.(5.14) to (5.16) for time series of bed elevation for the three selected runs in Figure 5.18.

For a qualitative comparison, Table 5.8 presents standard deviations and maximum values for the ratios of sediment transport obtained with the manual samples and from the time series profiles presented in Figure 5.27. Standard deviations for the basket sampler and the time series are quite similar, while those for the Helley-Smith samples are higher, which again is probably related to the sampling of the fronts of the sediment waves. This would also explain why maximum values are better represented by the Helley-Smith sampler (the basket sampler would not have been able to capture the most localized peaks).

Table 5.8. Comparison of standard deviations and maximum values for the ratio of sediment transport computed for manually collected samples and solid discharge rates obtained from the bed elevation time series.

Run	Manual samples: σ		Time series: σ	Manual samples: maximum		Time series: maximum
	Helley-Smith	Basket		Helley-Smith	Basket	
S1	0.89	0.55	0.54	2.73	2.01	2.15
S4	0.78	0.46	0.81	4.22	1.72	3.54
M1E5	-	0.39	0.38	-	1.71	1.97

The intermittency in sediment transport rates when bedforms are present, as shown in the plots in Figure 5.27, reflects the difficulties in adequately sampling solid discharge and acquiring a reliable cross-channel integrated sediment transport rate with a limited number of samples.

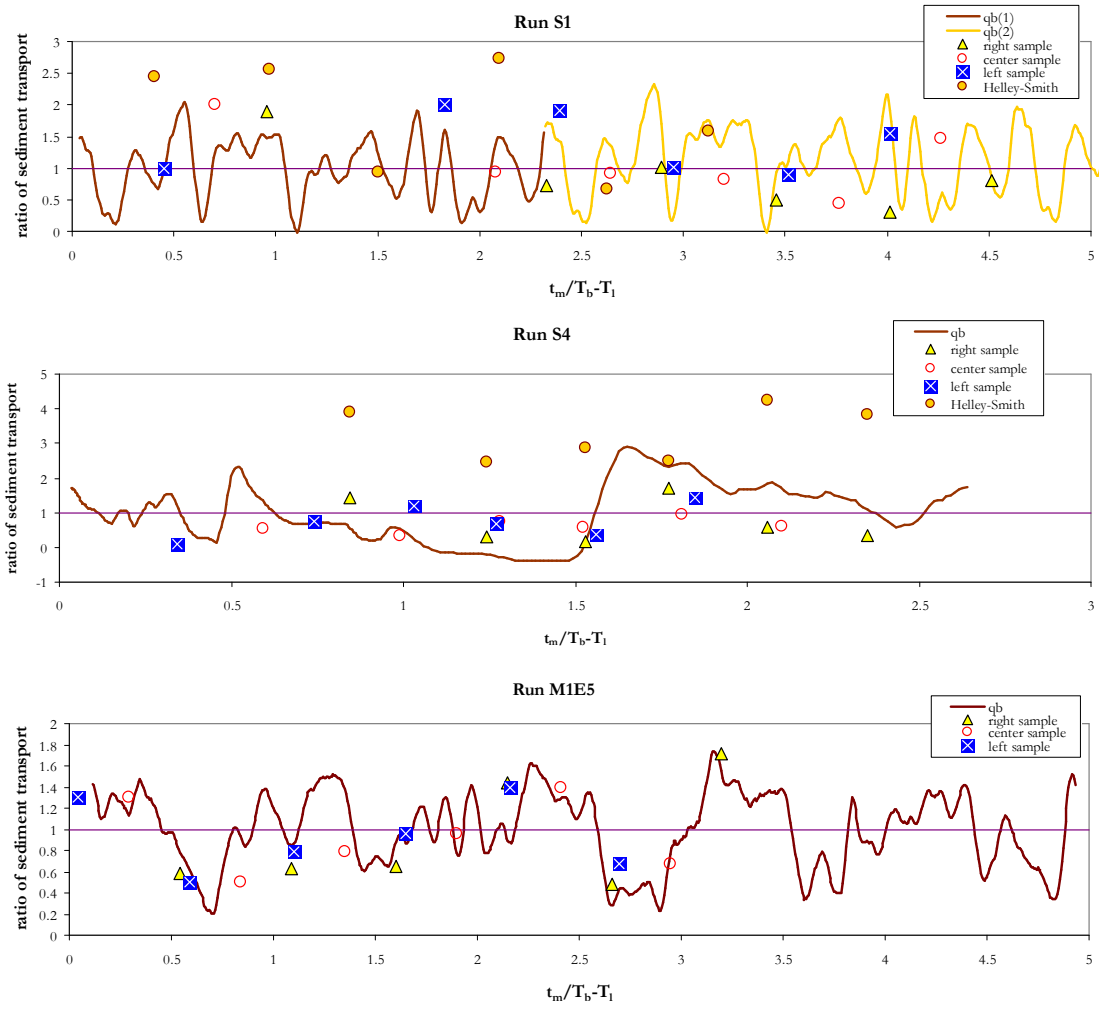

Figure 5.27. Comparison of the ratio of sediment transport (given by the ratio between measured sediment transport and sediment feeding rate) for time series obtained from the bed elevation time series and for sediment transport samples collected manually. t_m is the running time of the experiment, T_b is the period of the dominant bedform and T_l is a time lag. For run S1, qb(1) and qb(2) refer to the repetition, in two intervals, of the same time series. A centered average of nine seconds was used to smoothen the time series, which is evident from comparison with Figure 5.26.

5.3.6.3 Lateral grain sorting measured with the manual samples

A comparison of grain size distributions for the aggregate of samples retained in each of the compartments of the basket sampler was used to identify whether or not transversal grain size sorting occurred for the run series with the sediment mixtures.

The average grain size distributions for the samples collected in each compartment of the basket sampler are shown in Figure 5.28. It is evident that the central compartment had a greater proportion of coarse grains than the other two compartments. The Figure also shows the grain size distribution for samples collected with the Helley-Smith sampler

for runs with mixture 2. These samples were collected at the center of the channel cross section. Their size distribution is similar to that observed for the samples collected in the central compartment of the basket sampler, providing further evidence of the existence of coarser solid discharge in the center of the channel cross section than in the lateral sections. The average grain size distribution for samples collected in the hoppers is also presented in Figure 5.28. For these curves, grain size fractions smaller than 1 mm were excluded to allow comparison with curves corresponding to manual samplers because the mesh of the samplers was not able to retain the smaller grains with adequate efficiency.

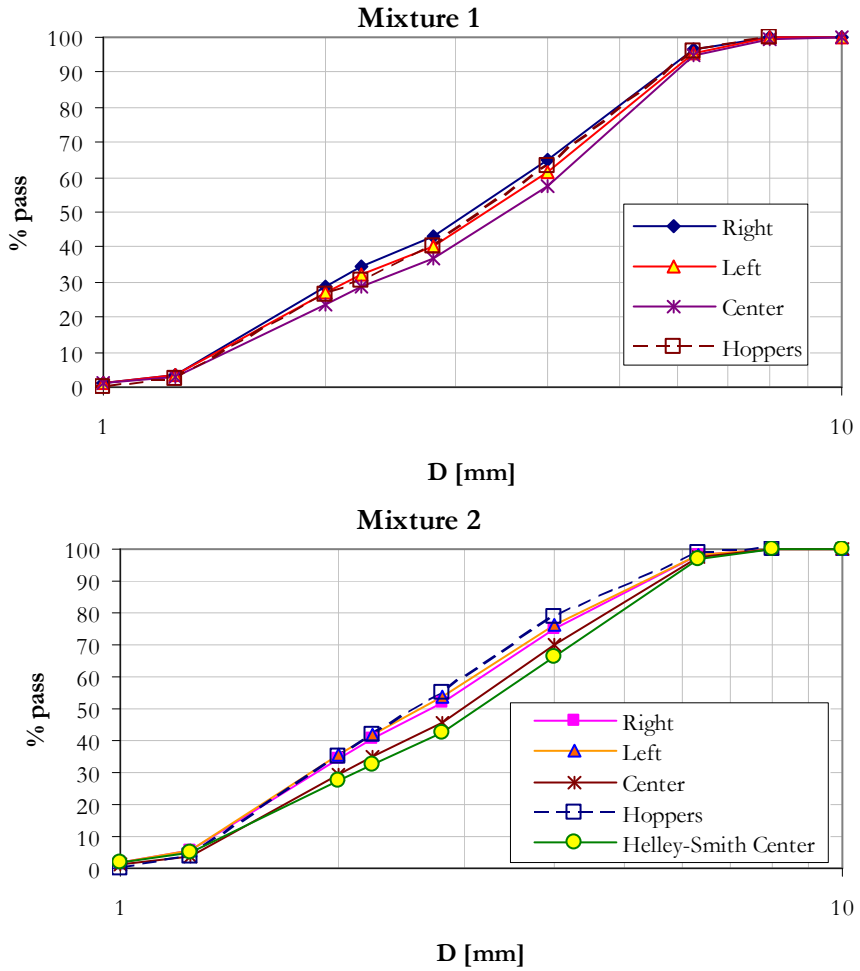

Figure 5.28. Average grain size distributions for manual samples collected in all runs in the left, right and central compartments of the basket sampler. Also shown are the mixture 2 samples collected by the Helley-Smith sampler and the average grain size distributions for the samples collected in the hoppers (excluding grain size fractions for diameters smaller than 1 mm). Note that in both mixtures, the grain size distribution for the central compartment is coarser than the distribution for the left and right compartments.

For comparing grain size distributions in the different compartments, the fractional content of each size fraction was calculated as

$$f_{S,i}^{k} = \frac{\sum_{j=1}^{m} W_{Ss,i,j}^{k}}{\sum_{j=1}^{m}\sum_{i=1}^{l} W_{Ss,i,j}^{k}} \qquad (5.18)$$

where $f_{S,i}^{k}$ is the fractional content of the i-th size fraction in the aggregate of samples for compartment k of the basket sampler (k=1, k=3 and k=2 for the left, right and central compartments, respectively), and $W_{Ss,i,j}^{k}$ is the weight of the i-th size fraction for the j-th sample retained in compartment k of the basket sampler. If $f_{S,i}^{k_1,k_3}$ is the arithmetic average of the fractional content of the i-th size fraction sampled in the lateral compartments, then if $\frac{f_{S,i}^{k_1,k_3}}{f_{S,i}^{k_2}}<1$ the i-th size fraction travels in a greater proportion in the central section; if $\frac{f_{S,i}^{k_1,k_3}}{f_{S,i}^{k_2}}=1$ the i-th size fraction travels in equal proportion in the central and lateral sections; and if $\frac{f_{S,i}^{k_1,k_3}}{f_{S,i}^{k_2}}>1$ the i-th size fraction travels in a greater proportion in the lateral sections than in the central section.

Figure 5.29 presents the ratio between lateral and central fractional contents for each run and size fraction. For grain sizes higher than 1.25 mm, which is the minimum grain size retained by the sampler mesh with an efficiency of 100%, an evident trend (more accentuated for mixture2) in agreement with the curves in Figure 5.28, is that the coarser fractions travel preferentially at the center of the channel cross section. Only the curves for runs M1E1 and M1E5 show an approximate homogeneous distribution between lateral and central sections for most of the size fractions. But even for these runs, there exists a cutoff size for which finer grains are more abundant in the lateral sections and coarser grains are more abundant in the central section. These cutoff sizes are presented in Table 5.9. They have been calculated by interpolating the curves in Figure 5.29 to obtain the grain size for which the ratio of fractional contents is equal to one. Cutoff sizes are coarser for mixture 1 (32% average sand content) than for mixture 2 (44% average sand content). It was found that for most of the runs the cutoff sizes fall in the range between the D_{50} and the D_{65}, as shown in Table 5.7 where the ratios between the cutoff sizes and the D_{50} and D_{65} is approximate to one.

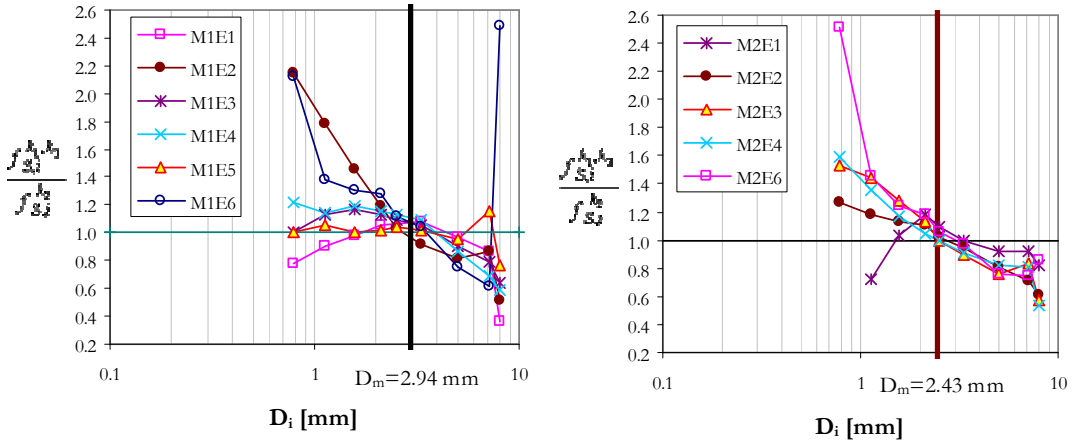

Figure 5.29. Comparisons of fractional contents of the i-th size fractions at each of the compartments of the basket sampler for each run in mixture 1 (left) and mixture 2 (right). The average mean for each mixture is indicated.

Table 5.9. Cutoff sizes for which smaller size fractions are more abundant in the lateral areas and coarser size fractions are more abundant in the central channel area.

Run	Cutoff size D_c [mm]	D_c/ D_{50}	D_c/ D_{65}
M1E1	4.6	1.51	1.20
M1E2	2.7	0.82	0.65
M1E3	3.9	1.24	0.98
M1E4	4.1	1.20	0.95
M1E5	3.9	1.18	0.93
M1E6	3.6	1.18	0.93
M2E1	3.3	1.31	1.01
M2E2	2.7	1.10	0.85
M2E3	2.5	1.01	0.79
M2E4	2.5	1.01	0.80
M2E6	3.1	1.33	0.98

5.3.6.4 Bed material sorting measured with surface and subsurface samples

5.3.6.4.1 Pure sand and gravel runs

Grain sorting on the bed surface was apparent at the end of the runs for the sediment mixtures run series, but not for the pure sand and gravel runs. Therefore, contrary to the mixtures where different patches of similar material were identified for bed sampling, the sampling sites for the sand and gravel runs corresponded to similar morphological regions within the bedforms, as it was explained in Section 3.3.2.6. Subsequent analysis of bed surface and subsurface samples showed subtle grain sorting trends for the sand and gravel runs, as shown in Figure 5.30, where the ratio between surface and subsurface mean diameter and geometric standard deviation have been plotted in relation to the x coordinate where the sample was taken. A subtle trend is evident in Figure 5.30 for the mean diameter of the surface samples being finer than the mean diameter of the subsurface samples. A similar trend is noticeable for the sand samples standard deviation, which tends to be slightly higher for the surface samples than for the subsurface samples. Such trends can be related with the deposition of fines from suspension at the end of the run.

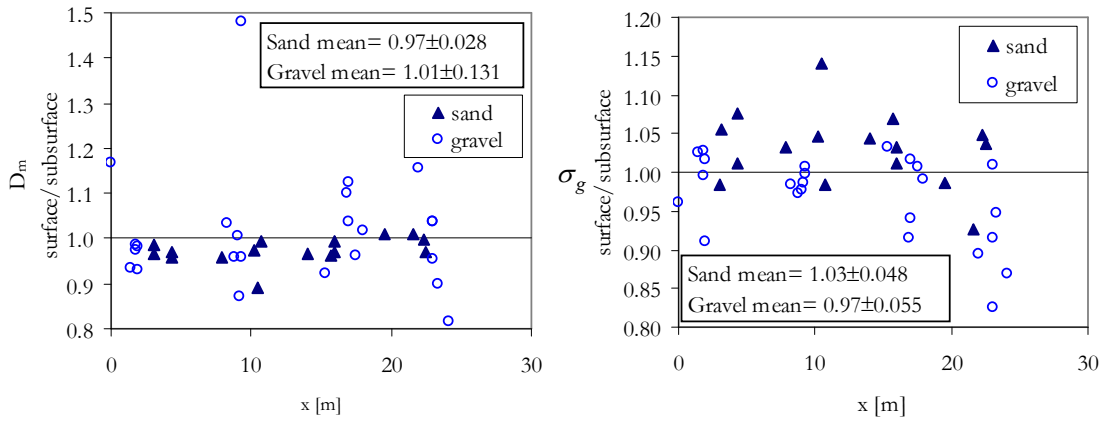

Figure 5.30. Ratio between surface and subsurface mean diameter (left) and geometric standard deviation (right) as a function of the x coordinate where the sample was taken, for pure sand and pure gravel runs. Surface samples converted from aerial to volumetric with the method of Marion & Fraccarollo (1997), (see Section 3.3.2.6.4).

For the gravel runs a sorting trend was found for bed samples being coarser downstream than upstream of the channel, as shown in Figure 5.31. Such a trend was more important for subsurface samples than for surface samples. In average, the median diameter of the gravel subsurface samples was 20% coarser at the downstream end than at the upstream end. This horizontal sorting trend was not found for the sand runs, for which the average of the ratio between the median diameter for the bed samples and the median diameter of the material fed was approximately one, with a standard deviation of 2%.

No statistically significant correlations were found between bed sorting and the bed shear stress for the sand and gravel runs.

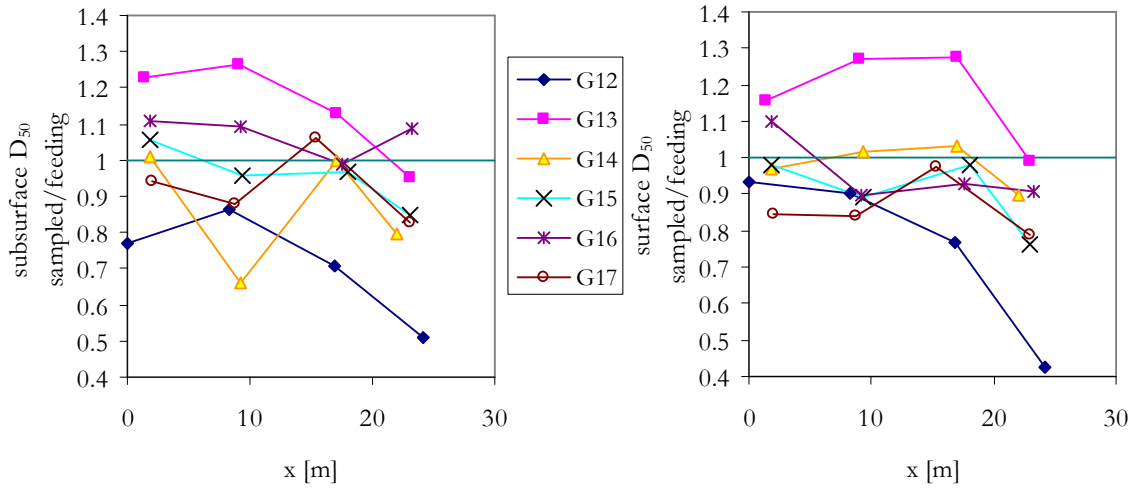

Figure 5.31. Variation along the x coordinate of the channel of the ratio between the D_{50} of the sampled bed material and the D_{50} of the material fed constantly into the channel, for subsurface (left) and surface (right) samples of the gravel runs. x=0 corresponds to the downstream end of the flume. Surface samples converted from aerial to volumetric with the method of Marion & Fraccarollo (1997), (see Section 3.3.2.6.4).

5.3.6.4.2 Runs with sand-gravel mixtures

Unlike the pure sand and gravel runs, planform grain size sorting was distinguishable on the bed surface after each run with sediment mixtures. Such sorting became apparent mainly through the presence of sediment patches of homogeneous relative content of sand and gravel. Sampling of the bed surface took into account this patchiness, as explained in Section 3.3.2.6.1. It can be assumed that comparisons between the relative proportion of sand and gravel of these patches can give a proper description of the bed material grain size sorting trends. The pure sand and gravel used in the experiments were well-sorted materials, and grain size classification within each of both size fractions can be considered not to be significant. Therefore, in order to identify bed material grain size classification trends, the relative content of sand in the bed samples will be used from hereafter for comparisons. The ratio between bed samples sand content and feeding material sand content can be defined as

$$R_{f_s} = \frac{f_{sSAMPLE}}{f_{sFEEDING}} \qquad (5.19)$$

The sand fraction is considered here to contain all grain sizes smaller than 2.24 mm, which was the mean diameter of the mesh that separated sand from gravel in the sediment

recirculating system. All surface samples have been converted from aerial samples to their volumetric equivalent using the method of Marion and Fraccarollo (1997), as described in Section 3.3.2.6.4.

To give evidence of the bed material sorting produced during the experimental runs, R_{fs} has been plotted in Figure 5.32 as a function of the horizontal axis x of the channel, for all bed samples collected before the run started and after the run was finished. For the samples after the run was finished surface and subsurface samples are shown in separate graphics. Only one graphic is presented for the bed material before the run started because for this case only bulk samples were taken. Mean values and standard deviations for the data in Figure 5.32 are shown in Table 5.10. The highest scatter in plots of Figure 5.32 (highest standard deviations in Table 5.10) belongs to the surface samples; in a similar trend, the mean values for the surface samples move away from unity in a higher degree than subsurface samples and samples of the original bed before the runs started. Sand contents for the surface material were as high as three times and as low as 0.15 of the sand content of the feeding material, showing with this variability the high classification of the bed surface grain sizes that was evident to the naked eye when the runs were finished. Note that sediment from subsurface samples was the material uncovered when the surface samples were taken, i.e., for every surface sample there was a pair subsurface sample; therefore, the trends exhibited in Figure 5.32 come from a direct picture of vertical sorting, not biased by sampling of different zones within a bedform unit.

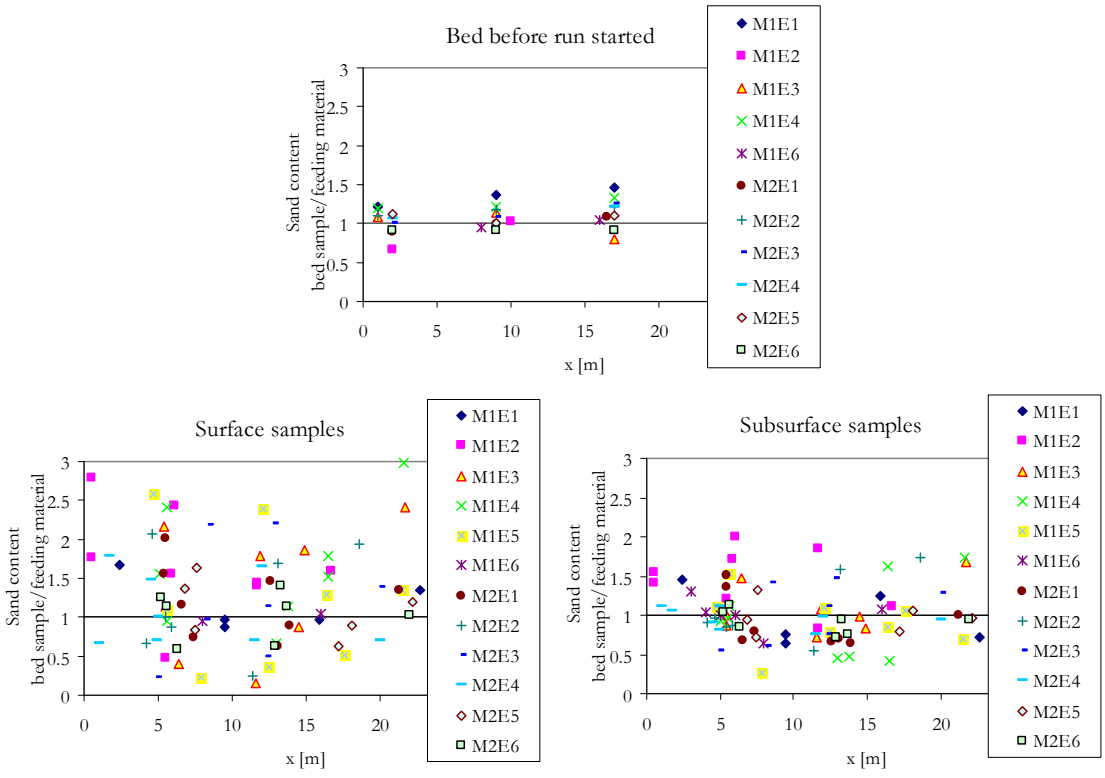

Figure 5.32. Variation of the ratio between the sand content in the bed samples and the sand content of the feeding material along the coordinate x of the channel.

On the other hand, note that the average R_{fs} for samples taken before the run started is not equal to one, showing that the manual mixing of the bed material was imperfect. This imperfection is irrelevant for feeding experiments, because when dynamic equilibrium is reached the bed material in the active layer is constantly replaced by the

feeding material. Important from the samples of the original bed material are the statistics, as these give a measure of the order of magnitude of the random error in the sand content of the material non-worked by the flow. Therefore, manually mixed materials in Table 5.10 have standard deviations of 0.20 and 0.12, for mixture 1 and mixture 2, respectively, which are equivalent to 6.4% sand content for mixture 1 and 5.3% for mixture 2. This variability is low compared to the water worked sediment, for which sand content standard deviations are 22.4% and 22.44%, for surface samples with mixture 1 and mixture 2, respectively, and 13.1% and 12.8% for subsurface samples. Interesting is that the sand content standard deviations are quite similar for both mixtures in each type of sample.

Table 5.10. Average values and standard deviations for the ratio between bed samples sand content and feeding material sand content for bed material samples drawn in Figure 5.32.

Bed material samples	**Average R_{fs} $R_{fs}=f_s$-sample/f_s-feeding**	
	Mixture 1	**Mixture 2**
Bulk, before run started	1.11 ± 0.20	1.08 ± 0.12
Surface (after the run is finished)	1.41 ± 0.70	1.15 ± 0.51
Subsurface (after the run is finished)	1.08 ± 0.41	0.97 ± 0.29

5.3.6.4.3 Analysis of surface patchiness in sand-gravel mixtures

As already explained in Section 3.3.2.6, the bed sampling for the beds composed of sediment mixtures was performed according to the textures of sediment patchiness identified on the bed surface. The classification of patches was prone to an induced bias because the identification of a patch as fine, coarse or mixed was somehow subjective and affected by the composition of the surrounding patches and bed material. For instance, Figure 5.33 shows the areal sampling with plaster, over the stoss side of a bar, of a sediment patch considered as a mixed size patch; after grain size analysis, the surface sample resulted in a 31% sand content. The sample corresponds adequately to a mixture of gravel and sand, nevertheless, it can be considered that the sand content of this sample is low, and could therefore be classed as being a sample of a coarse patch as well. It is therefore necessary to establish a qualitative limit to distinguish between coarse, mixed and fine patchiness.

In order to set a quantitative limit for fine, mixed and coarse patches, the cumulative probability distribution for the sand content of all surface and subsurface samples, obtained after sieving and performing grain size distribution analysis, has been drawn in Figure 5.34. In this Figure, for each bed sample it is indicated the type of patch, the type of mixture of the feeding material and if the sample was taken on the stoss side or trough of the bar. For the sake of clarity, bar trough and bar stoss side have been identified in the picture of a half alternate bar shown in Figure 5.35. The cumulative probability distributions in Figure 5.34 have been obtained with the following expression for the probability of a sample to contain a sand content f_s higher than a given value x

$$P(f_s \geq x) = \frac{m_s}{n_s + 1} \qquad (5.20)$$

where m_s is ranking of the i-th sample according to sand content, and n_s is the total number of samples. Notice that in agreement with results in Table 5.10, in Figure 5.34 it is evident that the cumulative probability distribution of the surface samples has a bias toward higher sand contents than the distribution of subsurface samples; particularly, for sand contents higher than approximately 30% for a given sand content the probability to be exceeded is higher for surface samples than for subsurface samples.

Figure 5.33. Surface areal sampling of a mixed size patch on the stoss side of a bar for run M1E1, at x=9.5 m. Sand content of the surface sample after conversion to a volumetric equivalent sample was 31%. Sand content of the subsurface sample was 24%.

The identification of the patchiness on the bed surface has to be related to the surface samples, as these samples are in direct relation with the observed texture of the bed surface. Careful inspection of the curve for surface samples in Figure 5.34 shows that for sand contents higher than 70% the patches were always identified as fine patches; in the same manner, for sand contents lower than 30% patches were classed only as coarse patches. For the range $30\%<f_s<70\%$, patches were identified either as coarse, fine or mixed. These limits of 30% and 70% have been indicated in Figure 5.34. The agreement between the visual identification of coarse patches with sand contents lower than 30% is not surprising, given that the limit between a bed with a framework-supported gravel (where gravel clasts are in contact between each other) and a bed formed by matrix-supported gravels (where gravel clasts are not necessarily in contact with each other) is roughly 30%; for framework gravel the sand grains occupy the voids between gravel clasts, and thus visually, if some voids are free of sand, the impression to the naked eye is that the bed is coarse and mainly composed of the large material. Otherwise, if the pores are completely filled with sand, as would occur for sand contents higher than 30%, the visual impression is that the bed is composed of a mixture of fines and coarse material.

According to the sand content of the surface samples, bed samples were reclassified as pertaining to a fine patch if $f_s>70\%$, to a coarse patch if $f_s<30\%$, and to a mixed size patch if $30\%<f_s<70\%$. With this reclassification of the samples, Figure 5.36 was drawn, showing the variation of R_{fs} as a function of the dimensionless bed shear stress, in surface and subsurface samples. A subtle tendency is evident for surface coarse patches in the bar trough to be coarser (decreasing sand content) with higher shear stresses. A similar trend is appreciable for fine patches on the bar stoss side, but these fine patches occur only for dimensionless shear stresses higher than roughly 0.22. Mixed size patches show no significant trends in surface samples. The same occurs for all subsurface samples,

irrespective of the superficial patchiness the sand content of subsurface samples seems not to be correlated with the bed shear stress. Average values for data in Figure 5.36 are shown in Table 5.11. It is significant, that the total average for both surface and subsurfaces samples, 0.99 and 1.05, respectively, is close to one (note that these average values don't correspond to averages in Table 5.10 because the number of samples was not the same for each population, i.e. fine, mixed or coarse patch on the bar stoss side or bar trough). Notwithstanding these similar average values, individual average values corresponding to the bar stoss side or trough for the subsurface samples are closer to one than their surface counterparts, showing with this a higher stability. Note, however, that subsurface samples under a fine patch are finer than the feeding material (R_{fs}=1.38) and under a coarse patch are coarser than the feeding material (R_{fs}=0.82).

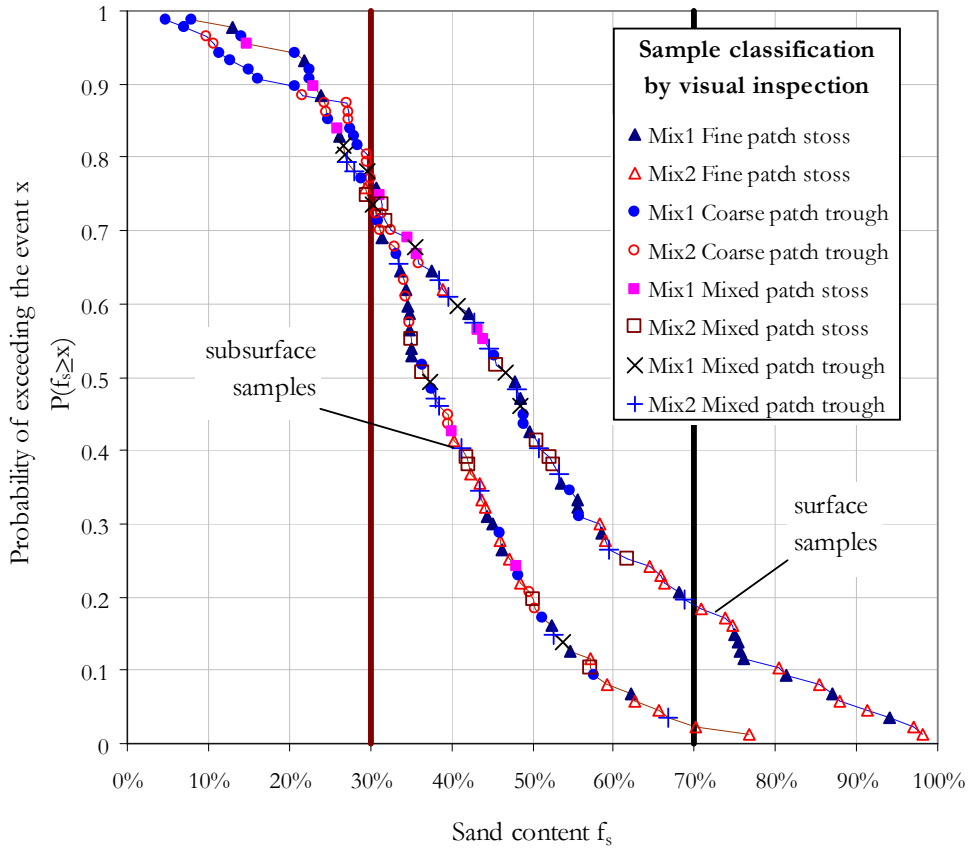

Figure 5.34. Cumulative probability distributions for sand content of surface and subsurface samples for the sediment mixtures run series. 86 samples were used for each curve. For all runs, no fine patches were identified on the bar trough, neither coarse patches on the bar stoss side.

Table 5.11. Average values and standard deviations for the ratio between bed samples sand content and feeding material sand content, for bed material samples used to draw Figure 5.36. Patchiness defined according to the bed surface sand content: fine patch if f_s>70%, coarse patch if f_s<30%, and mixed size patch if 30%<f_s<70%.

Type of patchiness	Average $R_{fs}=f_s$-sample/f_s-feeding					
	Surface			Subsurface		
	Bar stoss side	Bar trough	Average	Bar stoss side	Bar trough	Average
Fine	2.20±0.408	-		1.38±0.310	-	
Mixed	1.31±0.334	1.22±0.325		0.95±0.262	1.05±0.375	
Coarse	-	0.55±0.233		-	0.82±0.286	
Average	1.28	0.70	0.99	1.16	0.94	1.05

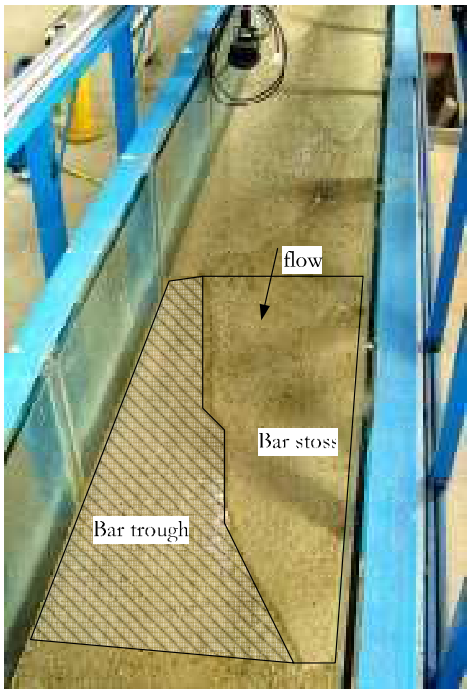

Figure 5.35. Definition of the bar trough and bar stoss side for a half alternate bar. The image corresponds to the bed surface at the end of Run M1E4.

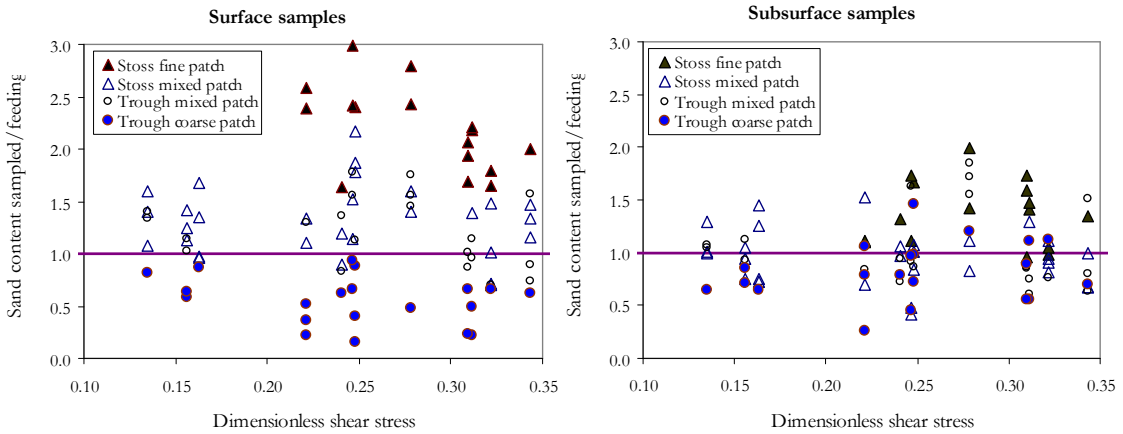

Figure 5.36. Variation of the ratio between bed samples sand content and feeding material sand content as a function of the dimensionless shear stress, for surface (left) and subsurface (right) samples. Definition of fine, coarse and mixed patches is related to the sand content and according to reclassification of samples as explained in text. The dimensionless shear stress is given by $\tau_b/[\rho g(Ss-1)D_m]$, where D_m is the bed sediment mean diameter, g is the gravitational acceleration, Ss is the sediment relative density, ρ is the water density and τ_b is the mean boundary shear stress corrected for side-walls effects (for the computation of τ_b, see Section 4.3.1 and eq.4.23).

5.3.6.4.4 Comparison between surface and subsurface samples

Graphs in Figure 5.37 show a comparison of surface and subsurface samples using the ratio between surface and subsurface sand contents and median diameters. In both graphics it is evident that most of the surface samples for three of the categories of patchiness (fine and mixed size patches in the bar stoss side, and mixed size patch in the trough) were finer than their subsurface counterparts. Only surface samples collected in

coarse patches (f_s>30%) in the bar trough were coarser than samples collected in the underlying material. Best fit lines have been plotted to each category of data in Figure 5.37 to describe tendencies in relation with the dimensionless shear stress. Tendencies shown by best fit lines are similar to those observed in Figure 5.36 for surface samples. This is so because sand contents in the subsurface samples have no apparent relation with variations in the bed shear stress, as it was concluded from Figure 5.36. Samples from the coarse patch in the bar trough and from the fine patch in the bar stoss side show the highest variation with dimensionless shear stress between surface and subsurface material, evidencing with this behavior a coarsening of the bed surface for increasing dimensionless bed shear stress.

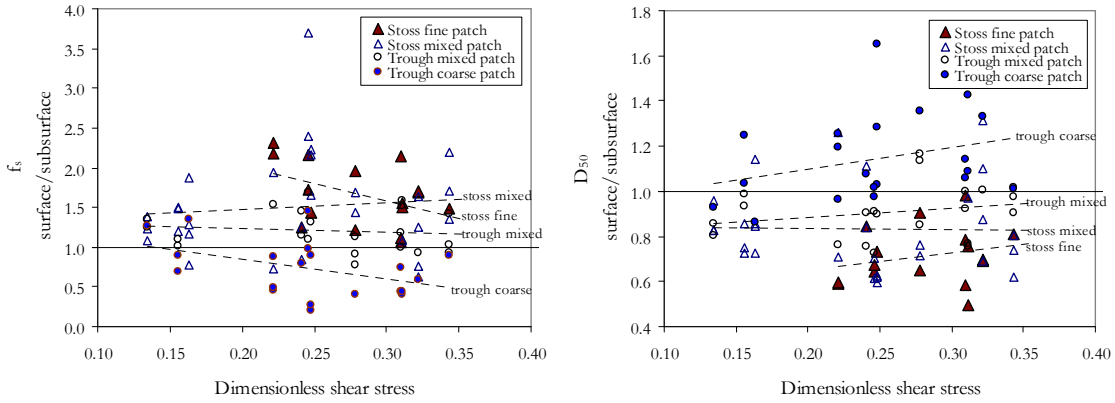

Figure 5.37. Variation with the dimensionless shear stress of the ratio between surface and subsurface bed material sand content (left) and median diameter (right). Definition of fine, coarse and mixed patches is related to the sand content and according to reclassification of samples as explained in text. Samples classified according to the bar region: trough or stoss side, and according to the surface sand content fs: fs<30% coarse patch, fs>70% fine patch, 30%<fs< 70% mixed size patch.

5.3.6.4.5 Comparison between morphological regions

For identifying the morphological region which best represents the grain size distribution of the material transported during the run, the cumulative probability distributions of the ratio between the bed sample and the feeding material sand content, R_{fs}, for each morphological region, type of sample and feeding mixture were obtained using eq.(5.20), as shown in Figure 5.38. A general trend observed after the runs for planform sorting over bars, which is confirmed by curves in Figure 5.38, was that fine patches always occurred on the bar stoss side, while coarse patches always in the region immediately downstream of the bar front, i.e. in the bar trough, in the zones of lowest elevation of the alternate bar unit. Never fine patches were identified on the bar trough, neither coarse patches on the bar stoss side. Mixed size material was found either in the stoss or the trough of the bar. Samples corresponding to the surface of the bar stoss side showed the highest R_{fs} ratios in Figure 5.38, thus showing that this region was the smoothest region of the bar. Remarkable of plots in Figure 5.38 is that the median (50% probability) R_{fs} for subsurface samples of the stoss and for two of the trough curves is roughly equal to one.

Table 5.12 presents mean values and standard deviations for R_{fs} of the curves in Figure 5.38. These values were computed with

$$R_{fsMEAN} = \sum_{i=1}^{n_s+1} \left(R_{fs,i} \left[P(R_{fs,i}) - P(R_{fs,i-1}) \right] \right) \qquad (5.21)$$

and

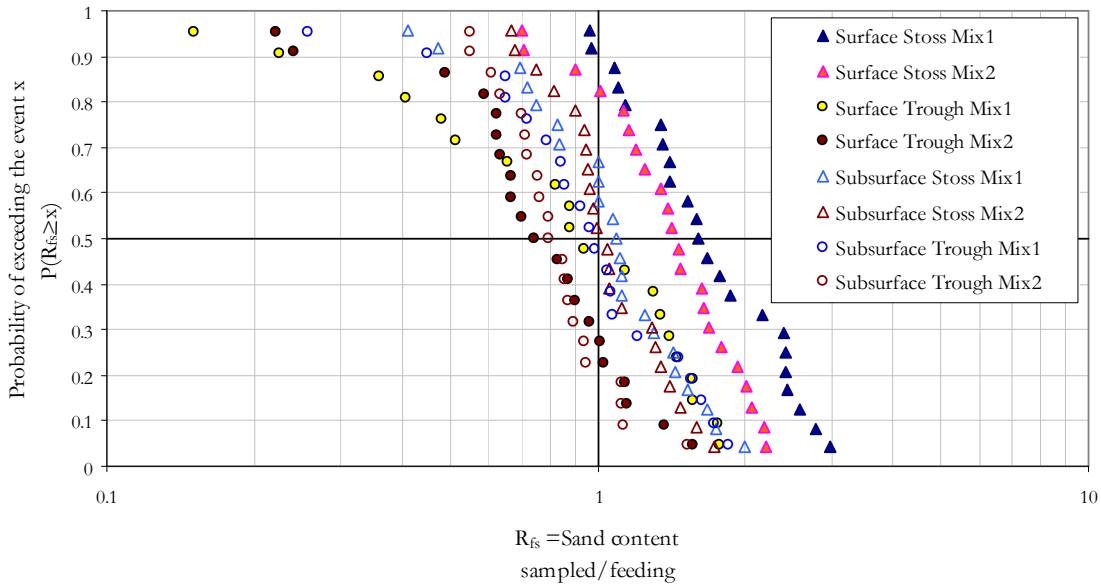

Figure 5.38. Cumulative probability distributions for the ratio of sand content between bed samples and feeding material, for surface (solid symbols) and subsurface (open symbols) bed samples, classified according to the morphological region where the sample was taken (bar stoss side or trough). Each point represents a bed sample.

$$\sigma^2 = \frac{1}{n_s + 1} \sum_{i=1}^{n_s+1} \left(R_{fs,i} - R_{fsMEAN} \right)^2 \qquad (5.22)$$

for the mean and standard deviation, respectively. In spite of the high variability given by the standard deviations, the average of mean values for the subsurface samples approximates to unity. The results in Table 5.12 show the extreme variability of grain sorting and that sampling of only one morphological region do not assure a representative sample of the bed material.

Table 5.12. Mean values for the ratio between the sand content of the bed samples and the sand content of the feeding material, for cumulative probability distributions shown in Figure 5.38.

		Mixture 1	Mixture 2	Average
Surface samples	**Stoss side**	1.79 ± 0.633	1.47 ± 0.453	1.63
	Trough	0.98 ± 0.531	0.82 ± 0.357	0.90
	Average	1.38	1.14	**1.26**
Subsurface samples	**Stoss side**	1.12 ± 0.446	1.10 ± 0.304	1.11
	Trough	1.03 ± 0.463	0.87 ± 0.267	0.95
	Average	1.08	0.98	**1.03**

Table 5.13. Mean values for the ratio between the mean diameter of the gravel fraction of the bed samples and the mean diameter of the gravel fraction of the feeding material, for data in Figure 5.39.

		Mixture 1	Mixture 2	Average
Surface samples	**Stoss side**	0.91 ± 0.091	0.93 ± 0.089	0.92
	Trough	1.01 ± 0.081	1.02 ± 0.062	1.01
	Average	0.96	0.97	**0.97**
Subsurface samples	**Stoss side**	0.95 ± 0.076	0.96 ± 0.065	0.96
	Trough	0.98 ± 0.072	1.02 ± 0.074	1.00
	Average	0.96	0.99	**0.98**

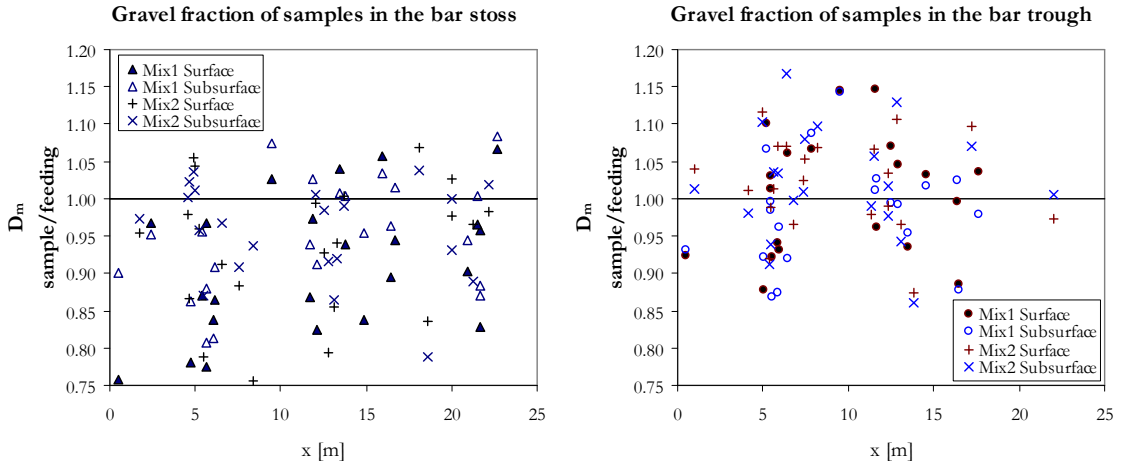

Figure 5.39. Variation along x of the ratio between mean diameters of sampled material and feeding material, considering only the gravel size fractions of the sediment mixture. Graphic on the left for samples taken in the bar stoss side, while graphic on the right for samples taken in the bar trough.

Until here, only the sand content has been analyzed for describing the sediment sorting in the bed material. It was assumed that the sand and gravel fractions were well-sorted materials and thus that the classification within each of the two fractions could be considered negligible. For verifying this assumption for the gravel sizes, for all of the bed samples in the runs with sediment mixtures the gravel size fraction was analyzed. For this analysis the grain size distributions were truncated in the diameter 2.24 mm. Figure 5.39 presents the ratio between the mean diameters obtained for the gravel fraction of the samples and the mean diameter of the gravel fraction of the feeding material (as it was presented in Table 3.29), according to the x coordinate where the samples were taken. The graphic on the left only contains samples taken in the bar stoss side, and the graphic on the right only samples taken in the bar trough. Table 5.13 presents average values for points plotted in Figure 5.39. The results are similar to those in Table 5.12, gravel in the stoss is finer than gravel in the trough for both surface and subsurface samples. Values in Table 5.13 show that the average for the samples taken in the trough approximates to one, while samples from the stoss show that gravel was in average 8% and 4% finer than the feeding gravel, for surface and subsurface samples, respectively.

Table 5.14 shows the ratio between the D_{40} and the mean diameter, and of the D_{16} and the mean diameter of the gravel fraction of the feeding material. In average, the D_{40} is 10% finer than the D_m, and the D_{16} is 30% finer than the D_m, thus, in comparison, it can be said that the average mean diameter in the bar stoss side was not finer than the D_{40} of the feeding material, but could be as fine as the D_{16}.

Table 5.14. Mean diameter, D_{16} and D_{40} of the **gravel fraction** in the feeding material for each run.

Run	D_m [mm]	D_{16}[mm]	D_{40} [mm]	D_{16}/D_m	D_{40}/D_m
M1E1	3.90	2.71	3.49	0.70	0.89
M1E2	4.11	2.88	3.77	0.70	0.92
M1E3	4.04	2.83	3.65	0.70	0.90
M1E4	4.20	2.95	3.96	0.70	0.94
M1E5	4.12	2.90	3.81	0.70	0.92
M1E6	3.98	2.80	3.60	0.70	0.90
M2E1	3.79	2.69	3.38	0.71	0.89
M2E2	3.73	2.65	3.32	0.71	0.89
M2E3	3.65	2.61	3.23	0.71	0.89
M2E4	3.57	2.58	3.17	0.72	0.89
M2E5	3.59	2.59	3.19	0.72	0.89
M2E6	3.72	2.74	3.34	0.74	0.90

5.3.6.5 Vertical grain size variations

Bed material samples at successive depths in the central cross section were taken for runs M1E6 and M2E4, as described in Section 3.3.2.6.5. For both runs, the most superficial of these samples corresponded to a coarse patch. Grain size distributions for these samples in layers are shown in graphs of Figure 5.40. For these graphs the grain size distribution of the original bed material before the runs began is shown as well. For both runs, all samples are coarser than the original bed material, except for the deepest sample. The layer from which this sample comes is analyzed in detail in Chapter 8, where it is hypothesized that this layer was formed by fine sediment successively deposited within voids of gravel. For all the coarsest samples, sand contents vary within a fringe of 10% (from 14.8% to 24.3% for mixture 1, and from 28.7% to 38.8% for mixture 2) and the values correspond to a framework gravel for mixture 1 and to the limit between framework and matrix gravel for mixture 2. These values agree with the facies observed in the cross sections opened in the bed, which are described in Chapter 8. Overall, open-framework gravel patches and gravel patches with low sand content were observed above the central lobe of the erosion profile, while sand patches were more frequent in zones adjacent to the channel walls, although they were evident above the gravel patches as well. Patches of mixed size material were found in different zones, but mainly in the immediate zone under the bed surface.

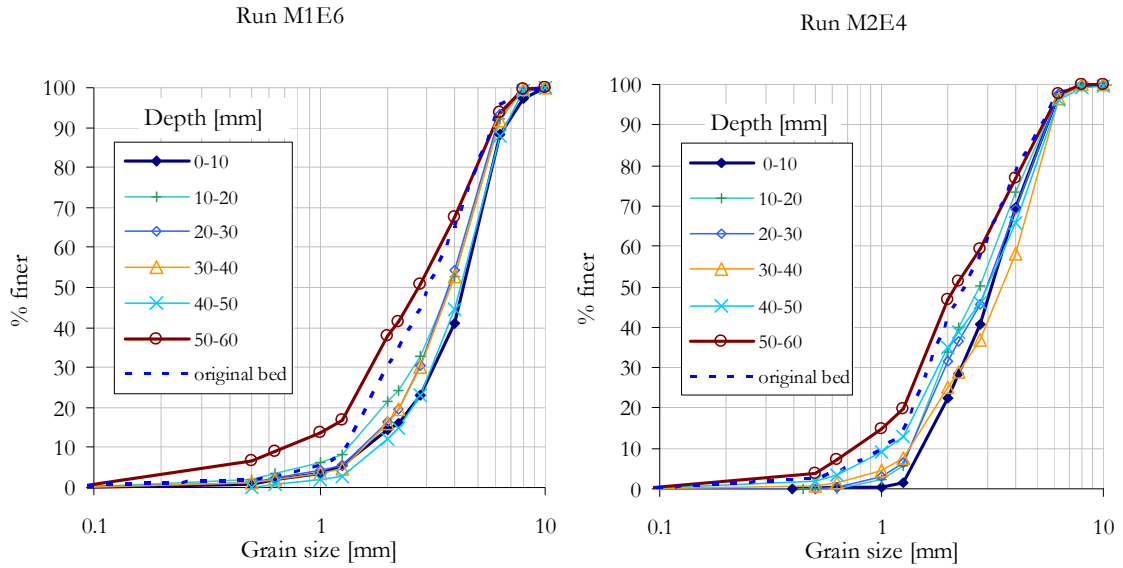

Figure 5.40. Grain size distributions for bed material samples collected at different depths compared with the grain size distribution of the bed material mixed before runs started.

In order to find correspondences between sediment samples, Figure 5.41 shows grain size distributions for the feeding material, the sediment transport samples taken at the central compartment of the basket sampler, subsurface samples underneath bar troughs and the bulk of samples in the vertical. For comparison, size fractions smaller than 1 mm were removed, as these are size fractions which the sampler bag failed to retain. Subsurface samples underneath the troughs have been chosen as these correspond to the deepest bed level where bed material samples were taken; in this manner there is a consistency for comparison, because vertical samples were collected underneath the trough level. The size distribution for the feeding material serves as a reference, because it should be expected that the average grain size distribution of the material in transport during the run should

tend to be equal to the feeding material and the bed material in the active layer at the end of the run too.

From curves in Figure 5.41, it is evident that the coarsest material comes from the bulk of vertical samples, while the finest comes from subsurface samples; nevertheless, in both runs there is a subsurface sample almost as coarse as the bulk of vertical samples. Feeding material and sediment transport central samples are more or less in between the other curves, although the feeding material is finer than the sediment transport load. In Section 5.3.6.3 it was demonstrated that the discrepancies between the transport load and the feeding material are owed to a tendency for coarsest size fractions to travel preferentially through the channel central cross section. The coarse distribution of the material sampled vertically in the central cross section agrees with this conclusion, but additionally, it shows evidence of a vertical sorting trend. The depth at which subsurface layers were taken was not larger than 3 cm, therefore, compared to the maximum erosion depths from Figure 5.19 (roughly 6 and 7 cm, for run M1E6 and M2E4, respectively) subsurface samples corresponded to the superficial layers. The different curves for subsurface material indicate that near the bed surface the bed material could have had either coarse or fine size distributions. Conversely the whole vertical sample, at least in the region of the bed explored, was mainly composed of coarse gravel, with sand contents lower than the limit of a framework and a matrix gravel (roughly 30%). Therefore, it can be stated that the coarsest material traveled preferentially at the channel central cross section and deposited in the lowest levels of the active layer. This was confirmed by observations in the opened sections for erosion and facies description, where patches with open framework gravel were frequent near the deepest traces of erosion. Although strong sorting was evident, Figure 5.41 shows that the average of subsurface samples and vertical samples would approximate to the distribution of the load material at the central section.

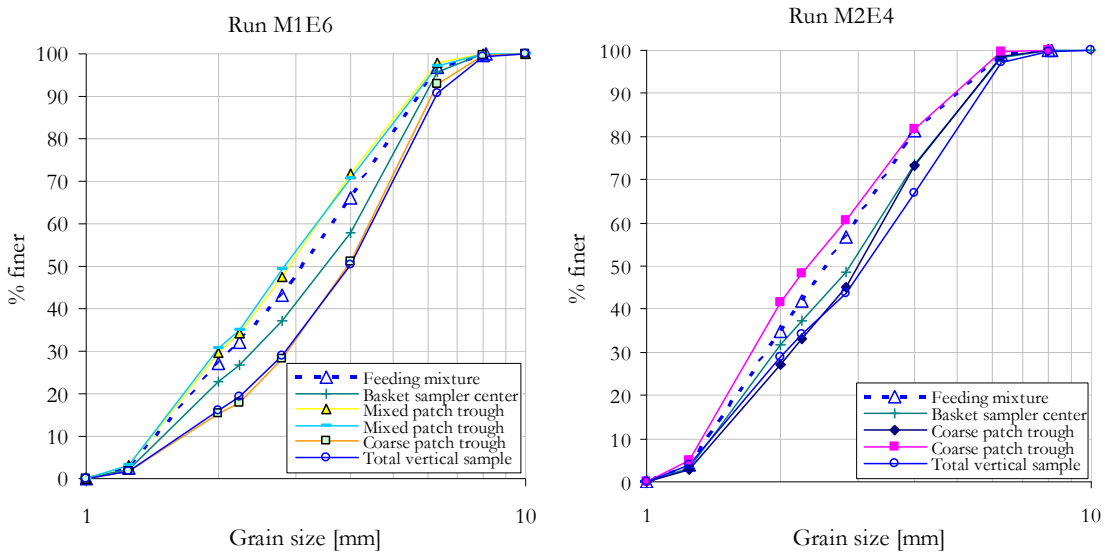

Figure 5.41. Grain size distributions for: feeding material from the hoppers, sediment transport material sampled in the central compartment of the basket type sampler, subsurface samples underneath bar trough level, and the bulk sample formed from individual samples of layers at the central cross section. For the comparison, only size fractions larger than 1 mm have been considered, as this is the size of the mesh of the sampler bag.

5.4 SUMMARY

In this Chapter, bedforms were described which were observed during equilibrium states of the experiments performed for creating the new data set for the study of sediment transport in torrential flows, summarized in Chapter 3; measurements and trends of the characteristics of these bedforms and their effects in bed erosion, sediment transport and sediment segregation were presented in this Chapter as well.

A **general taxonomical review of bedforms** under unidirectional flows was first introduced. In this review, the uncertainty, due to the lack of enough empirical evidence, on the characteristics of the expected bedforms in mixed size beds at and close to the transition between lower and upper regimes was highlighted. Likewise, theoretical developments from Kennedy (1963) in bedform stability analysis using potential flow theory were presented; important is that bedform stability fields obtained by Kennedy not only distinguish between 2D and 3D bedforms, but also the direction of movement of antidunes.

Later on, the observed experimental **bed and water configurations** were described in order to identify their most important characteristics, to class them according to parameters in literature and to label each experimental run as representative of a given bedform state. Most of the bedforms observed were classed as three-dimensional downstream-migrating antidunes, on account of the phase correspondence between bed and water waves. Antidunes at the center of the channel were commonly accompanied by short-crested stationary waves, known as rooster-tails in literature. For most of the runs, stable trains of rooster-tails covered two thirds to half of the channel water surface and progressed downstream. Additionally to the antidunes at the channel central cross section, low relief bed features were regularly observed in the lateral channel sections; these were classed as alternate bars, due to their periodical sequence in opposite channel walls, which was evident at the end of the runs when water was drawn-down. On account of the coexistence of different species of bedforms in bed configurations, for each run a dominant bedform was identified and this was considered as representative of the run bed state. Table 5.2 summarizes the characteristics of the bed and water configurations and indicates the assigned bed state for each run. Besides bars and antidunes, dunes, upper-stage plane beds and transitional bedforms (compound characteristics between dunes and antidunes) were identified as well. Most of the bedforms in gravel and sand-gravel beds were strongly three-dimensional, while for bedforms in sand beds, although the three-dimensional component was present for Froude numbers close to one, this component was not as dominant as in runs with the other bed materials.

Measured **heights, wavelengths and celerities of sediment and water waves** are summarized in Tables 5.3 and 5.4. These data were obtained from direct measurements during the runs, and from measurements using photos and video recordings. For three runs, measurements of the characteristics of the water and sediment waves were compared with measurements obtained using records of time series. Results using both methods were of the same order of magnitude. Celerities, mean wave height and wavelengths of the stationary waves ranged from 5 to 30 mm/s, 4 to 10 cm, and 52 to 67 cm, respectively; while for alternate bars celerity was considered to be equal to that of stationary waves, and mean bar wavelength and height were in the range of 1.8 to 3.7 m and from 7 to 27 mm, respectively. For the **stationary waves** the following trends were apparent:

1. The celerity of the stationary waves increased almost linearly with Froude number, with a discontinuity roughly between F=1 and F=1.2 (see Figure 5.8).
2. The measured aspect ratio or steepness (height/wavelength) of the highest stationary waves was in average 0.157; this value is similar to maximum theoretical aspect ratios that a surface wave can attain before breaking.

For the **bedforms seen through the channel wall** the following trends were apparent:

1. In general, ratios between the average heights of the bedforms and the water depth were the highest for pure sand runs and the lowest for pure gravel runs, while for the two mixtures these ratios were quite similar and slightly higher than for pure gravel runs (see Figure 5.10). An outlier for such trends corresponds to the run with the highest water depth and the highest sediment feeding rate for the run series with gravel (run G13); for this run steep antidunes were formed, slightly shorter than the observed sand antidunes.
2. The maximum difference in bed surface elevations surveyed on bedforms at the end of the runs decreased with Froude number (see Figure 5.11).
3. Bars wavelengths were roughly between 3 to 5 times the channel width; these values assert in the classification of these forms as bars, since they scale with the channel width.
4. A trend toward longer wavelengths with higher Froude numbers was apparent (Figure 5.15); in a consistent vein a decrease of bar steepness with Froude number was evident as well (Figure 5.16).

Direct measurements of the characteristics of the **three-dimensional downstream-migrating antidunes** in the channel central cross section were not feasible; nevertheless, it was assumed that their wavelength and celerity were the same as those measured on the surface stationary waves.

The following general trends were observed from measurements of **maximum bed erosion** at the end of runs with sand and the two sand-gravel mixtures:

1. Mean erosion depths were deeper with sand than with sand-gravel mixtures, almost by a factor of two (Figure 5.19).
2. Erosion with sand was approximately uniform across the cross section, while for mixtures deepest erosion occurred at the center of the cross section, except for runs M1E6 and M2E6, which were runs with the lowest Froude numbers in mixtures (0.88 and 0.89, respectively). Cross sectional variation in erosion was considered as being an effect of the flow three-dimensionality, which was more apparent for mixtures and gravel than for sand.
3. A bias was observed toward a higher concentration of erosion at the channel central cross section for higher bed Shields stresses with mixture 1 (32% sand content). For sand and mixture 2 (45% sand) no evident trends were found with bed Shields stress (Figure 5.21).
4. A qualitative relationship was apparent between the erosion depths in the channel central section and the height and activity of the rooster tails, but no discernible trends were detected when comparing erosion with stationary wave height (Figure 5.23). In turn, non conclusive correlations were found between measured bedform heights and maximum bed erosion.

The development and passage of bedforms with a strong three-dimensional component produced **pulsations on sediment transport**, both in the longitudinal and in the transversal cross sections. Using manual samples of sediment transport it was verified that transversal pulsations were comparable to longitudinal pulsations. In turn, it was verified that average volume load discharges passing through each of three equal length sections in which the transversal section was divided, were almost equal when averaged in time (Table 4.7), with a slight bias toward one of the lateral sections; it was suggested that such a difference could be attributed to an imperfection of the sampling instrument rather than to an asymmetry in the transversal distribution of sediment transport in the channel. With these same manual samples of sediment transport using two different samplers, it was found that the average variation in instantaneous solid discharge due to longitudinal pulsations was in the order of ±45% of the total sediment feeding rates; although, two

maximum values up to more than 4 times the feeding rate were measured, and a minimum as low as 1% of the feeding rate (see Table 5.6). These findings were corroborated by analyzing time series of bed profiles for three runs, for which instantaneous solid discharges were computed using the Exner equation and the measured celerity of the bedforms (Figure 5.27). For the two samplers used, it was found that the most localized peaks in the instantaneous sediment transport rates, related to the passage of steep sediment waves, were better captured by samples taken with a sampler with a short intake span rather than with a sampler with a longer intake span (see Table 4.8).

Besides volume load pulsations related to the passage of bedforms, variations in sediment grain size distributions were identified transversally, vertically, and longitudinally within a bedform unit, especially for the two runs with sand-gravel mixtures. Using the manual samples of sediment transport taken with a sampler divided in three transversal compartments, for runs with sand-gravel mixtures **grain size sorting transversal to flow** was studied. It was found that gravel size fractions were preferentially transported in the channel central cross section, while sand size fractions were more abundant in the lateral sections (Figure 5.28). This trend was more accentuated for runs with mixture 2 (45% sand content) than for mixture 1 (32% sand content). For most of the runs, the proportion of sediment traveling at the central cross section, with respect to the average of the lateral sections, increased with grain size (Figure 5.29); for this trend, the grain size for which the same proportion was transported at the lateral and central sections was approximately between the D_{50} and the D_{65} of the mixtures grain size distributions.

Comparison of **surface and subsurface samples for pure sand and pure gravel runs**, showed a subtle trend for the surface being finer than the subsurface material (Figure 5.30); while the standard deviations for the grain size distributions of most of the gravel samples were lower on the surface than in the subsurface, for sand runs this standard deviations were most of them higher on the surface than in the subsurface. It was hypothesized that this latter trend could be related to the deposition of fines from suspension. For pure gravel a trend toward coarsening in the downstream direction was apparent (Figure 5.31), being the median diameter of the subsurface samples in average 20% coarser at the downstream end of the flume compared to the material at the upstream end.

For analyzing sediment **grain size classification trends in the sediment mixtures**, only the sand content in the bed samples was used for most of the comparisons. Since grain size distributions for pure gravel and pure sand used in the mixtures were uniform, for the sake of simplicity grain size sorting within size fractions of each of these materials can be neglected. From samples of the bed material taken before the runs were begun, a random error for the variation of sand content in the material non-worked by the flow with respect to the feeding material was found to be 5.3% and 6.4% for mixture 1 and mixture 2, respectively. Conversely, for all surface samples taken after runs with the two mixtures this variation was approximately of 22%, while for subsurface samples approximately of 13%, thus showing a much higher variability of the surface material. In turn, it was found that surface samples were in average 41% and 15% finer than the feeding material, for mixture 1 and mixture 2, respectively, while subsurface samples were in average only 8% finer and 3% coarser than the feeding material, respectively.

Sampling of bed material at the end of the runs was performed according to visual identification of **bed surface texture** within three categories: fine, coarse and mixed size patches. For each patch a surface and a subsurface sample were taken. From a statistical analysis of the 172 bed material samples collected, using the cumulative probability distribution of the sand content, it was found that the median sand content for surface samples was approximately 47%, while for subsurface samples it was 37% (Figure 5.34), reasserting that surface material was in average finer than subsurface material. From these

analysis for the surface samples, it was also found that for sand contents higher than 70% the surface texture was always visually identified as corresponding to a fine patch, while for sand contents lower than 30% surface texture was always identified as pertaining to a coarse patch. For the range of sand contents between 30% and 70% the texture was either identified as coarse, fine or mixed size. It was highlighted that there is a clear correspondence of these results with the characteristics of bed structure, since the limit for a gravel framework structure is roughly 30% sand content.

According to the findings from the statistical analysis, all bed samples, surface and subsurface, were reclassified as pertaining to a mixed size patch if sand content was between 30% and 70%, and to a fine (coarse) patch if sand content was lower than 30% (higher than 70%). For the reclassified samples the following trends were found (Figure 5.36):

- Fine patches on the bar stoss side were observed only for dimensionless shear stresses roughly higher than 0.22. These patches showed a slight tendency toward a decrease in sand content with increasing dimensionless bed shear stress.
- A subtle trend was found for sand content in surface coarse patches in the bar trough to decrease with increasing dimensionless bed shear stress.
- Sand contents for surface samples from mixed size patches and for all subsurface samples showed no significant trends with the dimensionless shear stress.
- Average values of the ratio between the sample sand content and feeding material sand content for the subsurface samples were closer to unity than their surface counterparts, showing with this a higher stability.

Comparison of **surface and subsurface samples in mixtures** showed the following tendencies:

- Except for samples collected in coarse patches in the bar trough, for the rest of categories of patches surface samples were finer than their subsurface counterparts.
- Samples from the coarse patch in the bar trough and from the fine patch in the bar stoss side showed the highest variation with dimensionless shear stress between surface and subsurface material, evidencing with this behavior a coarsening of the bed surface for increasing dimensionless bed shear stress.

The following conclusions were obtained from the statistical analysis of **bed material samples with respect to the morphological regions** where they were identified (Figure 5.38):

- Fine patches always occurred on the bar stoss side, while coarse patches always in the region immediately downstream of the bar front, i.e. in the bar trough, in the zones of lowest elevation of the alternate bar unit. Never fine patches were identified on the bar trough, neither coarse patches on the bar stoss side. Mixed size material was found either in the stoss or the trough of the bar.
- Probability distributions of the ratio between sand content of the sample and sand content of the feeding sediment showed that the highest values corresponded to the surface of the bar stoss side, thus giving evidence that this region was the smoothest region of the bar.
- Grain sorting was extremely variable within a bedform unit, therefore, sampling of only one morphological region do not assure a representative sample of the bed material.

Analysis of the **gravel fraction of the bed samples** led to the following results:

- In average, gravel in the bar stoss side was finer than gravel in the trough for both, surface and subsurface samples.
- The average of the ratio between mean diameters for samples taken in the trough and mean diameters of feeding material was close to unity; while for samples from

the stoss side it was found that gravel was in average 8% and 4% finer than the feeding gravel, for surface and subsurface samples, respectively.

Finally, for two runs with sand-gravel mixtures successive **samples taken at different elevations** at the channel central cross section were analyzed. It was found that, except for the sample from the deepest region (roughly at the level of the maximum erosion) all samples were coarser than the original bed material (Figure 5.40). It was hypothesized that the deepest sample was finer than the others because it came from a layer formed by fine sediment successively deposited within voids of gravel, as analyzed in Chapter 8. From comparisons between samples collected in the bed, from material in transport and feeding material (Figure 5.41), it was suggested that the coarsest size fractions traveled preferentially at the channel central cross section and deposited in the lowest levels of the active layer.

CHAPTER 6:

ANALYSIS AND DISCUSSION OF EXPERIMETAL RESULTS

6.1 INTRODUCTION

In this Chapter the experimental results described in Chapters 3, 4 and 5 are analyzed and discussed from different perspectives. First, some aspects of the experimental bedforms classified in Chapter 5 are discussed; particularly, the role of sand content in the morphology of bedforms in the transition from lower to upper regime is discussed, and the ability of empirical and theoretical stability bedform fields proposed by different authors, to predict the experimental bedforms, is assessed. In that same Section, emphasis is given to the formation and persistence of downstream-migrating antidunes, sparsely reported in literature. Further on, fundamental differences between flow resistance in experimental runs with sand in comparison to runs with gravel and sand-gravel mixtures, are analyzed; in turn, form resistance coefficients are obtained and they are compared with other datasets in literature according to dimensionless numbers describing the geometry of the bedforms. Differences between dunes, upstream- and downstream-migrating antidunes are discussed therein, in terms of flow resistance and expansion loses; the effect of sand content in total bed resistance is analyzed as well. Subsequently, sediment transport is exhaustively analyzed in the next Section, first by comparing the experimental data with data sets from field and with sediment transport predictive formulas; later on, the sediment transport experimental data obtained in the present work, along with similar data for sand-gravel mixtures found in literature, are collapsed into a single curve using the reference shear stress method, but slightly modified to consider very high transport rates. Reference shear stress values obtained by the application of this method are used farther on to analyze likely effects of sand content in sediment transport for the extremely high transport rates of the experiments. A conceptual model is presented, based on the changes of bed structure as sand content increases, to account for changes in sediment mobility according to sand

content and relative size of gravel with respect to sand. Additional discussions include the performance of sediment transport predictors and the advantages of the modification of the reference shear stress as presented here, for conditions of very high sediment transport rates. In the last Section of this Chapter an overall interpretation of the experimental results is given. First, the effect of the channel walls in the formation of steep 3D stationary waves is analyzed; theoretical developments are presented for anticipating the wavelength of this waves and a comparison between theory and experimental measurements is presented. The subsequent subsection discusses the relation between the measured bed erosion patterns, bedforms and short-crested stationary waves. Later, the experimental sediment grain sorting trends are discussed, relating these trends to sediment mobility and flow patterns. The last subsection presents comparisons and links between the experimental bed morphologies and typical morphologies and flow conditions in streams in field. Particularly, some similarities with pool-riffle morphologies are presented and links with alternate bars are discussed.

6.2 RELEVANCE FOR BEDFORM STABILITY PHASES

6.2.1 Effect of sand content in the lower to upper regime transition

The most important characteristic for identifying an antidune bed state in Section 5.3.3 was the coupled response between bed and water surfaces. Consequently, for the classification of dominant bedforms in Table 5.2 an unequivocal and fully established antidune bed state was considered to be that for which bed and water surfaces were in-phase, i.e., a maximum (minimum) of the water surface concurred with a maximum (minimum) of the bed surface perturbation. Conversely, dune bed states were identified (only in two runs, S4 and M1E6) when a 180 degrees phase shift between bed and water surfaces occurred and the bed forms showed a triangular shape. All intermediate bed states, with different degrees of coupling of bed and water, and with features resembling those of dunes and antidunes or both, were classed as transitional.

The classification of the bed states considered mesoscale and macroscale bedforms in the most downstream reach of the channel, where roughly stable features occurred. For most of the experimental runs, mesoscale bedforms (lengths of the same order of magnitude as the water depth) were superposed to the macroscale features (lengths comparable with the channel width). The latter were provisionally classed as alternate bars and for some cases were apparent only when the water was drawn-down; this was so because it was common that the heights of the mesoscale and macroscale bedforms were of the same order of magnitude, and thus macroscale features were hidden to the naked eye by the mesoscale bedforms. Overall, mesoscale forms were dominant and had a greater influence in the local hydraulic conditions. A singular condition in the interaction between both features occurred for some bed states classed as transitional, for which mesoscale bedforms were in-phase with the water surface, while troughs and some crests which could be associated with the macroscale features were out of phase with the water surface waves. Run M1E5 exemplifies this condition, as shown in plots of the bed surface evolution in Figure 5.6.

The identification of bed states summarized in Table 5.2 can be used to analyze the effect of sand content in the transition from lower to upper regimes. The experimental data have been plotted in Figure 6.1a as a function of the Froude number and sand content of the feeding material, indicating the type of dominant bedform and sediment as a third parameter. Approximate borders for the transitional regime have been drawn with dashed lines following general trends. In doing this, the lower horizontal line to the left, which marks the limit between transitional bedforms and dunes, was drawn horizontal following

the trend of the upper line dividing transitional bedforms from antidune regime. The line was drawn below the only point for plane bed with gravel (corresponding to run G17) because instead of considering this point as pertaining to lower regime plane bed, it was assumed that it is more realistic to consider that a transitional bed state prevailed for that run since weak rooster tails were sporadically observed at the central cross section; the formation of such features suggests that the flow was not fully established in the lower-regime all across the cross section.

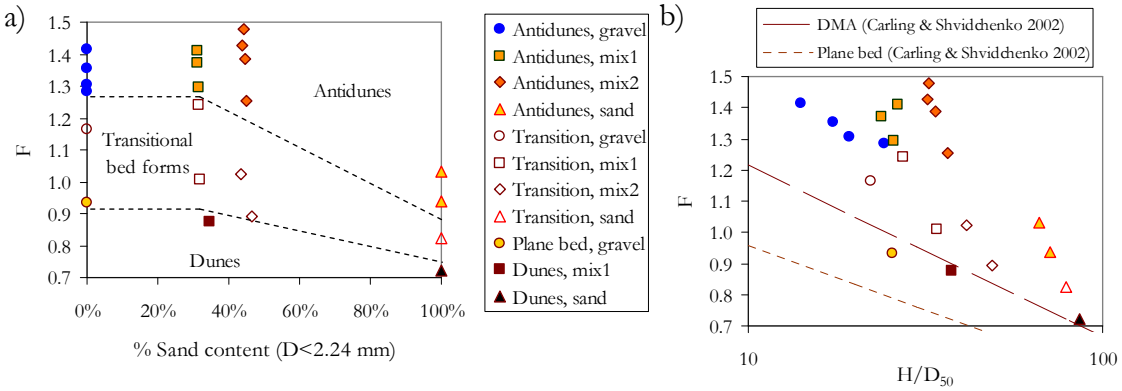

Figure 6.1. Definition of stability phases for dominant bed configurations in the experimental runs, according to a) the Froude number F and sand content of the feeding material, and b) the Froude number F and relative water depth using the median diameter of the mixture; for this latter graph also shown are best fit lines for downstream-migrating antidunes (DMA) and plane bed with fine gravel according to Carling and Shvidchenko (2002).

In spite of the limited number of available data to outline precise boundaries for the transitional regime, some general trends become apparent in Figure 6.1a. The most important effect of an increase in sand content over the dominant bedforms observed was a progressively narrower transition and a shift to lower Froude numbers of the boundary between the transitional and the lower regime. Both effects agree with previous observations and theoretical analysis. Stability theory predicts that the threshold Froude number between dunes and antidunes can be lower than unity as the relative depth increases (Kennedy, 1963), and different authors have provided experimental evidence for such a tendency with uniform material. A commonly used discriminating value of F=0.84 has been widely adopted as a lower boundary for antidune formation (e.g., Southard and Boguchwal, 1990), but experimental data suggest that antidunes can form at Froude numbers as low as 0.75 (e.g., Van den Berg and Van Gelder, 1998). Vanoni (1974) presented bedform stability diagrams for uniform sand as a function of the Froude number and the relative depth (H/D_{50}) where the Froude number for the transition between lower and upper regime declines systematically as relative depth increases (see Figure 6.4); similarly, using fine gravel data sets, Carling and Shvidchenko (2002) found that antidunes can develop at slightly lower Froude numbers as relative water depth increases. For comparison with such previous findings, the categorized experimental bed states have been drawn as a function of the Froude number and the relative depth in Figure 6.1b. Best fit lines obtained by Carling and Shvidchenko (2002) for data sets in the range of transitional regime in fine homogeneous gravel (D<12 mm) have been drawn in this graph as well. The line for downstream-migrating antidunes follows quite well the trend of the lower limit for transitional bedforms of the experimental data in the present work. Therefore, there appears to be agreement in the outline of the transitional regime borders between the

present results with sand-gravel mixtures and those with uniform material in previous studies.

Also in agreement with previous evidence with uniform material is the widening of the transitional regime for lower sand contents or relative depths. According to Carling and Shvidchenko (2002), transitional gravel bedforms have been reported for a range of Froude numbers between 0.5 and 1.8, but cannot be sustained above F≈1.3. Data in Figure 6.1 agree with this limiting value. Carling and Shvidchenko suggested that widening of the transitional regime for gravel reflects lag effects for bedform adjustment to changes in flow, which become more important as the grain size increases.

The median diameter of a sand-gravel mixture is higher the lower the sand content is. Therefore it is congruent that the general trends in the boundaries of the transitional regime for decreasing sand content (wider transition and its lower limit at higher Froude numbers) were similar to those observed by other authors for uniform material when the median size increases. Nevertheless, a somehow unexpected result was that the boundaries of the transition remained almost unchanged for the gravel and the sediment mixtures (this boundaries spanning between approximately F=0.93 and F=1.26), suggesting that a gravel behavior of the transition prevails at sand contents as high as 45%. This would mean that the range of Froude numbers for the transitional regime could be reduced by roughly a factor of three when increasing the sand content from 45% to 100%.

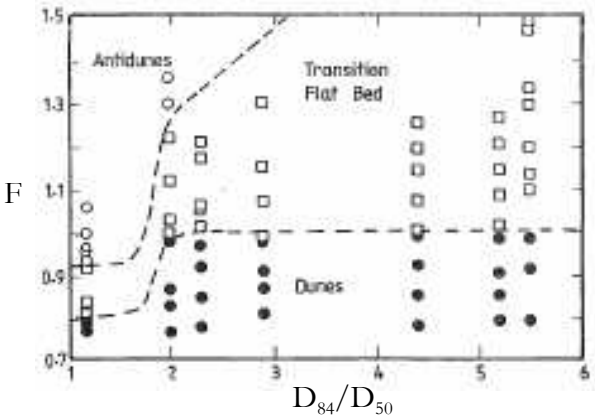

Figure 6.2. Experimental results of Chiew (1991) for occurrence of different types of bedforms according to the Froude number and the variation of the sediment standard deviation. The median diameter of the material was 0.6 mm.

Chiew (1991) performed flume experiments with a 0.6 mm median size material to determine the effect of increasing sediment non-uniformity on the transition between different bedform classes. He used seven mixtures conserving the same median diameter and increasing the geometric standard deviation (defined as $\sigma=D_{84}/D_{50}$) up to a value of 5.5. Figure 6.2 presents the experimental results of Chiew for Froude numbers ranging between 0.75 and 1.5. No important effects of grain sorting were found on the stability fields for lower regime. Nevertheless, as shown in Figure 6.2, for the transition from lower to upper regime, Chiew found that antidunes did not form for geometric standard deviations higher than 2.3, even when the Froude number was as high as 1.5; instead, the plane bed (named flat bed by Chiew), which characterized the transition from dunes to antidunes for the size material used, persisted. Chiew attributed the absence of antidunes to the formation of a dynamic armored layer. For uniform sediment, with $\sigma=1.2$, Chiew found that the transition plane bed occurred for a narrow range of Froude numbers,

roughly from 0.8 to 0.92; this is approximately the same range within which transitional bedforms occurred for pure sand in the present experiments, as seen in Figure 6.1. Conversely, for higher standard deviations, Chiew found that the transition widened and shifted toward higher Froude numbers, occurring these changes in the narrow range between σ=1.2 and σ=2 as seen in Figure 6.2. Such a trend is similar to that described by the dashed lines with tentative boundaries of the transition in Figure 6.1a for the range between pure sand and sand-gravel mixtures. The results of Chiew suggest that an increase in sediment sorting widens the transition from dunes to antidunes, in a similar manner as it has been observed that this transition might widen as the relative depth decreases. Consequently, a double effect is likely to be the reason for the persistence of a wide transitional regime on the two mixtures in the present experiments. First, in mixing sand and gravel the standard deviation of the mixture increases with respect to pure sand and pure gravel (widening of the transition because of an increase in sediment sorting), and secondly, as the sand content is decreased the median diameter of the mixture increases (widening of the transition because of a decrease in relative depth). The combination of both effects would produce a similar range of Froude numbers for the transition in the two mixtures as in pure gravel; following this, it can be expected that both effects would also combine to produce an abrupt narrowing of the transitional regime if sand content increases up to a limiting cutoff value.

The effect of sand content in the height of bedforms is presented in Figure 6.3. In a similar fashion as Figure 5.10, from Figure 6.3 it is evident that the bedform height was higher for pure sand bedforms, but no clear general tendencies can be inferred about the effect of the Froude number. Nevertheless, since data for similar bedforms in gravel and the two mixtures plot in close groups and apart from bedforms with sand, the hypothesis suggested above that the behavior of the mixtures was almost the same as that of the pure gravel is reinforced. Dashed lines in Figure 6.3 are arbitrary and have been drawn for distinguishing between flow regimes.

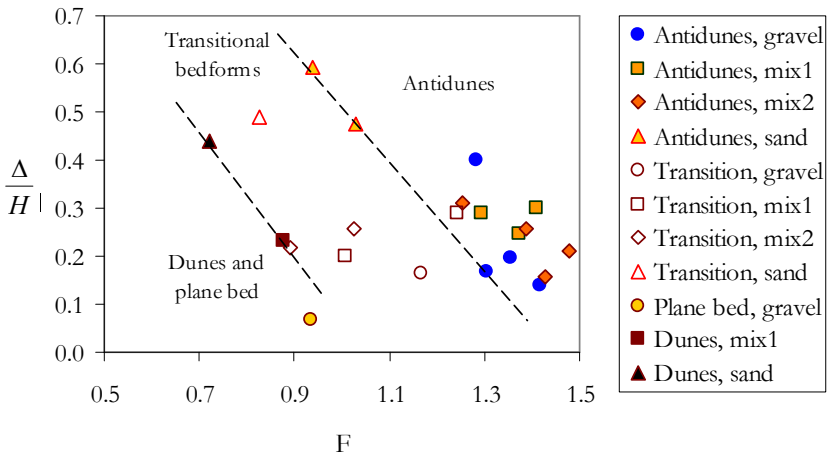

Figure 6.3. Variation with Froude number of the ratio between bedform height and water depth, according to the different types of bedforms observed and feeding material.

The trends exposed above are relevant for the sharp gravel-sand transitions observed in many natural rivers (e.g., Sambrook-Smith and Ferguson, 1995). Such trends would mean that an input of sand material to a gravel bed would not change the limits of the dune-antidune transition unless the supply of sand is large enough to produce the shift from gravel-dominated behavior to sand-dominated. For instance, for a mixed size bed in

lower regime an increase in sand content above the limit for a shift to sand-dominated behavior could produce a change from lower-regime to the more unstable transitional regime, even when the Froude number would remain unchanged. Furthermore, if the shift to sand-dominated bedforms occurs, the height of the bedforms could increase significantly, as is shown in Figure 6.3. The effect of an increase of the bedform height in bed resistance will be discussed further in Sections 6.3.

As a final note, it should be noted that Van Rijn (1993) stated that it is possible that no precise limits neither type of bedforms for the transition can be established, since both depend on the previous flow conditions. So far as this is concerned, it is important to take into account that for the experimental runs here presented, this latter effect was not important since the bedforms were observed during well established mobile bed equilibrium conditions, i.e., that the bedforms were stable and not affected by rising or falling stages. In spite of uncertainties described above, a coherent delimitation of the transitional regime for the experimental runs was feasible by considering the degree of coupling between bed and water surfaces.

6.2.2 Comparison with empirical bedform stability diagrams

Four empirical bedform stability diagrams were chosen for comparison with the experimental data, namely, diagrams from Vanoni (1974), White and Wang (1993), Southard and Boguchwal (1990) and Van den Berg and Van Gelder (1993), as shown in Figures 6.4 to 6.7. The experimental data have been drawn over the original charts presented by the authors, which include the plot of the data sets used to outline the boundaries between bedform phases. Note that the region where the data set of the present work plots in the four selected diagrams remained unexplored or had a poor density of points.

The dimensionless chart of Vanoni (Figure 6.4) was elaborated from the analysis of experimental data with sand, and assumes uniform material with a constant relative density of 2.65. Originally, Vanoni presented five charts, each one for a different range of particle Reynolds numbers, defined as $Re_p=D(gD)^{1/2}/\nu$, where D is the sediment grain size, g is the gravitational acceleration and ν is the kinematic viscosity of water. The chart used for the experimental data in the present work corresponds to $Re_p \geq 48$. From the three stability diagrams selected, the diagram of Vanoni is the only one that uses the Froude number as an independent variable, and thus considers explicitly the lower to upper regime transition. Nevertheless, for the chart shown in Figure 6.4, boundaries between the transition and the upper regime are not indicated, and only the boundary between the lower and the transition or upper regimes is outlined. This boundary is assumed to decrease linearly for high relative depths, which conforms to what was discussed in Section 6.2.1; notwithstanding, the new experimental data plot in a region where this boundary is outlined by a horizontal line. Therefore, for the ranges explored experimentally, the diagram fails to predict the trend observed in the data of a decreasing boundary for higher relative depths.

For determining the upper limit of the transition regime, Wang and White (1993) used over 500 data with bed configurations in the transition and upper regimes, as shown in Figure 6.5. They proposed the following relationship for the border between the transition and the upper regimes

$$F_{rp} = \frac{V}{\sqrt{gD_{50}}} = 2.8\left(\frac{R_h}{D_{50}}\right)^{0.3} \; ; \; \frac{R_h}{D_{50}} \leq 10{,}000 \qquad (6.1)$$

where F_{rp} is the particle Froude number. For $R_h/D_{50}>10{,}000$, $F_{rp}=44.4$. The new experimental data have been plotted in the original chart of Wang and White in Figure 6.5.

Most of the new points plot below the curve given by eq.(6.1), and thus the curve fails to predict accurately the range of values for the transition. According to the new experimental data, the border should be parallel to eq.(6.1) but at slightly lower values of F_{rp}, as indicated with a dashed line in the Figure. It should be noted that Wang and White considered the plane bed between dunes and antidunes as an upper regime feature.

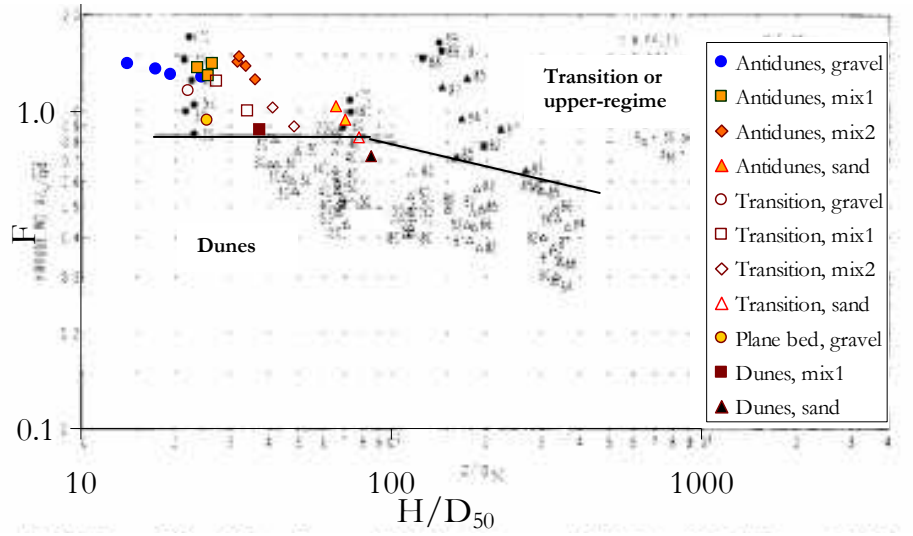

Figure 6.4. Experimental data of bedforms plotted in the bedform chart from Vanoni (1974), for Re_p=83.3, 122, 146, being R_{ep} the particle Reynolds number computed as $Re_p=D(gD)^{1/2}/\nu$. No distinction is given in this chart between transition and antidunes.

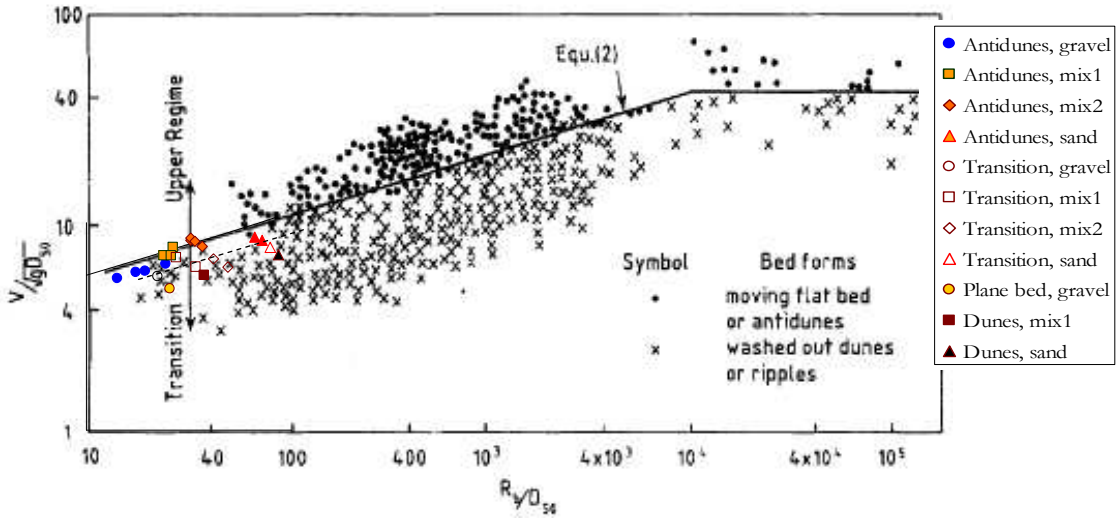

Figure 6.5. Upper limit for the transitional regime according to Wang and White (1993).

Southard and Boguchwal (1990) presented bedform stability diagrams based on different independent variables and for a wide range of particle grain sizes and water depths. The diagram presented in Figure 6.6 uses the sediment representative grain size and the bed shear stress as independent variables. Instead of using dimensionless numbers for the construction of their diagrams, Southard and Boguchwal transformed the variables of the extensive data sets used, to a reference temperature of the water of 10ºC. The present experimental data were drawn in the diagram of Southard and Boguchwal in Figure 6.6

using the median grain size diameter as representative of the sediment, and the bed shear stress after correcting for sidewall effects, as it is described in Section 4.3.1. Transformation to bed shear stresses and grain diameters standardized to a water temperature of 10ºC was also performed as indicated by Southard and Boguchwal. The present work data plot in a region of the diagram where no previous empirical data were available and therefore no boundaries were defined. Nevertheless, if the boundaries were extrapolated following the tendencies for lower grain sizes and shear stresses, specifically the line that divides region IV (dunes) from region V (overlap region of dunes, upper plane bed and antidunes), only would plot in the correct region the data pertaining to the sand experiments, three points for antidunes and the only point for dunes of the mixtures. The rest of data, with transitional bed forms, antidunes and plane bed would plot erroneously in the region for dunes (IV). Thus, it is likely that the boundary between region IV and V would not continue upward with the same linear trend for grain sizes higher than 2 mm. Instead, if the new experimental data are taken into account, the boundary might reach a maximum and then proceed downwards, as has been indicated with a dashed line.

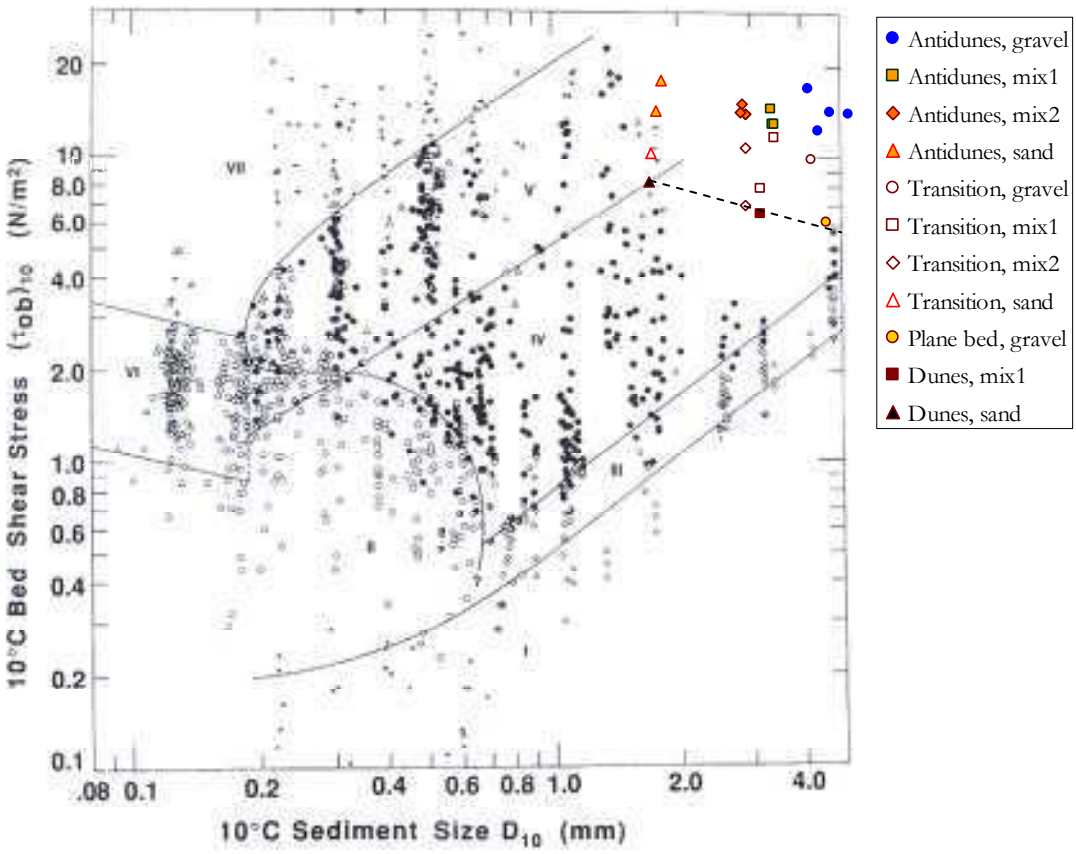

Figure 6.6. Bedform experimental data in the Southard and Boguchwal (1990) bedform stability diagram for 10ºC-equivalent variables. **I**, no movement in plane bed; **II**, ripples; **III**, lower plane bed; **IV**, dunes; **V**, overlap region of dunes, upper plane bed, and antidunes; **VI**, overlap region of ripples, upper plane bed, and antidunes; **VII**, overlap region of upper plane bed and antidunes. D_{10} and $(\tau_{ob})_{10}$ refer to the 10ºC-equivalent representative grain diameter and bed shear stress, respectively.

The diagram presented by Van den Berg and Van Gelder (1993), shown in Figure 6.7, is an extension of a graph originally proposed by Van Rijn (1984). They assumed that the type of bedform for given flow conditions is controlled by the grain shear stress. In

consequence, their chart is a function of a mobility parameter given as a dimensionless grain shear stress, and a non-dimensional particle parameter. The mobility parameter is equivalent to the Shields number for the grain related shear stress τ'*, and is computed with

$$\tau'^* = \frac{\rho V^2}{(\rho_s - \rho) C'^2 D_{50}} \qquad (6.2)$$

where C' is the Chézy coefficient related to grain roughness, which assuming a plane bed and a logarithmic bed profile is given by

$$C' = 18 \log \frac{4H}{D_{90}} \qquad (6.3)$$

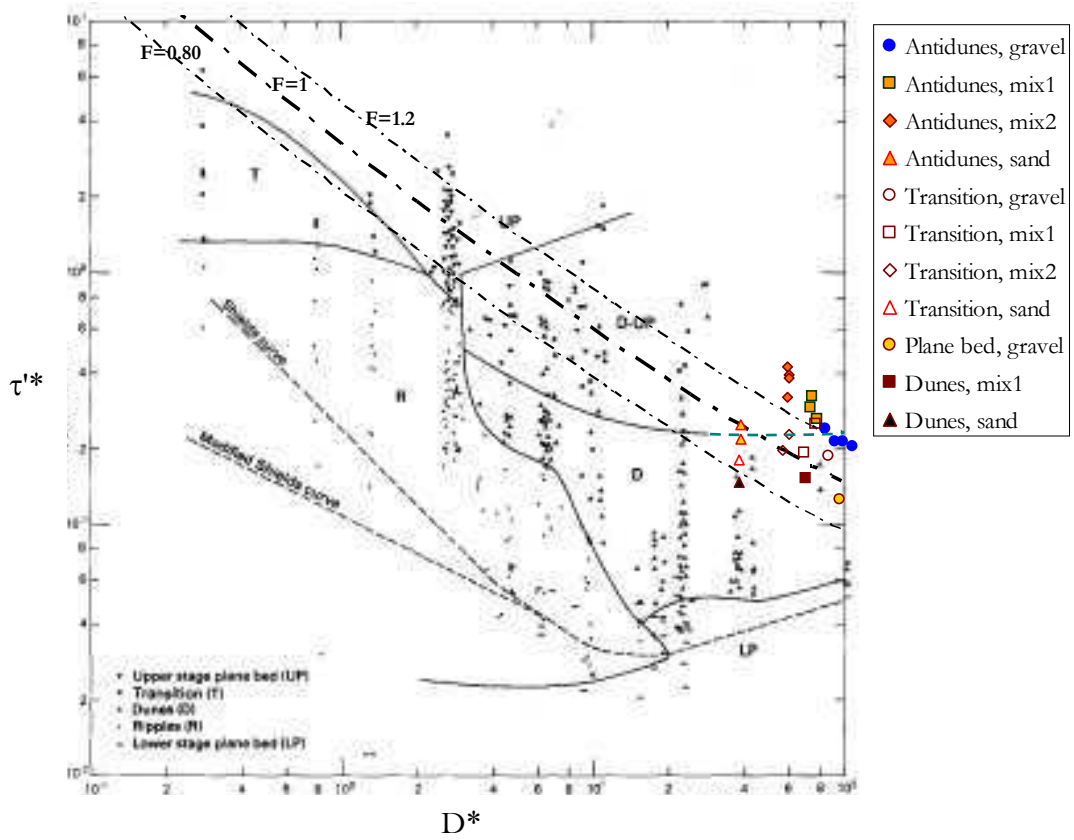

Figure 6.7. Experimental data of bedforms plotted in the bed form stability diagram from Van den Berg and Van Gelder (1993) for shallow water (flume). Lines have been drawn for Froude numbers 0.80, 1.0 and 1.2, for 0.10 m water depth and a ratio D_{90}/D_{50}=1.65.

The particle parameter D_* on the abscissa is calculated as

$$D_* = D_{50} \left(\frac{(\rho_s - \rho) g}{\rho \nu^2} \right)^{1/3} \qquad (6.4)$$

in which ν is the kinematic viscosity of water. Data with antidunes were not used in the elaboration of the diagram; nevertheless, the transition from lower to upper regime can be outlined in the graph with the Froude number, which for a given flow depth and grain sizes D_{50} and D_{90} plots as an almost straight line. Dash-dot lines for three values of the Froude number, namely: 0.8, 1 and 1.2, have been drawn in the graphic for a flow depth of 10 cm and a ratio D_{90}/D_{50}=1.65, which are approximate average values for the new experimental

data. In a similar manner as with the other two stability diagrams, the new data set plots in a region where no previous information existed. Dunes plot in the adequate corresponding bed state stability phase if the original boundaries are extrapolated, as it is shown in the diagram with a fainted dashed line. Although the diagram does not distinguish the transition from lower to upper regime for coarse grain sizes, with the aid of the lines for the Froude numbers the boundaries can be roughly established; for instance, it can be assumed that for a range of Froude numbers between 0.75 and 1.3 transitional bed forms are likely to occur.

The new experimental data set confirms previous observations about the absence of a plane bed in the transition from dunes to antidunes for coarse sediment. Alternative stability charts from Southard and Boguchwal (1990) (not presented here) set the limit for the existence of a plane bed in the transition for grain sizes up to roughly 0.8 mm. This notwithstanding, for two runs, one with gravel (G17 with F=0.93) and one with mixture 2 (M2E1 with F=1.44), plane beds were observed alternating in a complex periodicity with the existence of upper-stage features. The plane beds observed with mixture 2 occurred for a high Froude number, so that it can be assumed with certainty that the flow and bed features belonged to a well established upper-regime flow; the intermittent shift to a plane bed might be associated to the unstable nature of antidunes, which often display a sequence of formation, growth and vanishing (Alexander et al. 2001). Conversely, the plane bed with gravel corresponded to the run with lowest Froude number of that run series. There is no unequivocal evidence to catalog such configuration as a mobile plane bed in the lower regime, neither as a plane bed in the transitional regime. The configuration could be classed as a lower regime plane bed, given that some stability diagrams predict that as relative depth decreases, the transition to antidunes is likely to occur without the intervening phase of dunes. Nevertheless, plotting the experimental point for run G17 in a diagram presented by Southward and Boguchwal (1990) (not presented here) relating mean flow velocity, mean flow depth and grain size as a third parameter, the point plots in the antidune phase, being this phase preceded by the dune and not the lower plane bed phase. The criterion used for classifying such configuration as a transitional plane bed was the occurrence of sporadic rooster tails on the water surface of the central cross section.

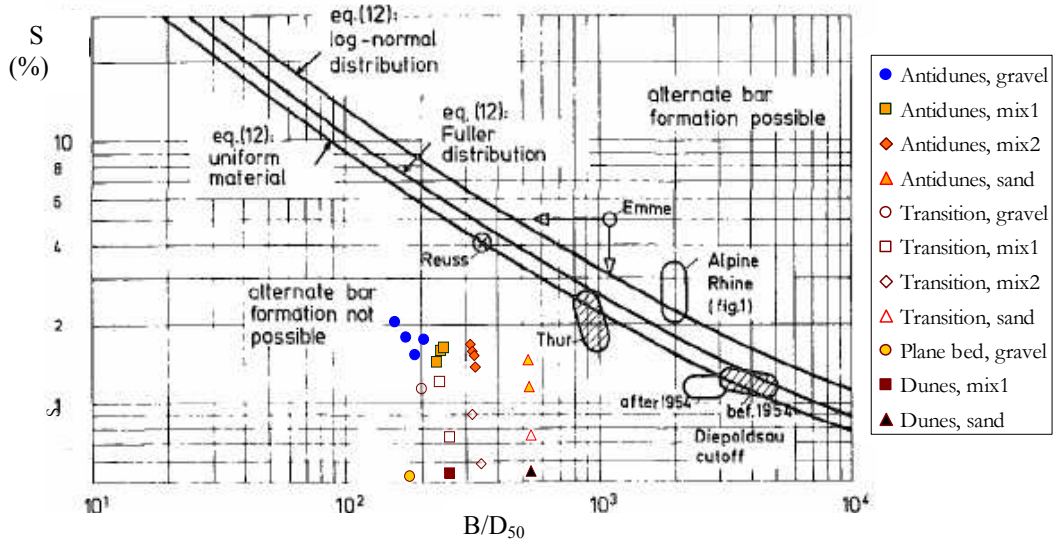

Figure 6.8. New experimental data set plotted in the diagram of Jaeggi (1984) for alternate bar formation.

The bedform stability diagrams above are focused in mesoscale bedforms, but they do not consider macroscale bedforms such as alternate bars. Jaeggi (1984) presented an empirical diagram intended to foresee the conditions for alternate bar formation, using as independent variables the bed slope and the channel width to bed material median size ratio. Such diagram is presented in Figure 6.8, where the experimental data of this work have been plotted. All of the new experimental data plot in the region where the diagram foresees no alternate bar formation. A likely reason for disagreement is that many studies have demonstrated that bar formation is strongly dependant on the channel width to water depth ratio (Chang, 1971; Blondeaux and Seminara, 1985; Niño, 1996; Takebayashi and Egashira, 2002), a variable not considered in the diagram of Jaeggi. This issue will be discussed further in Section 6.5.

6.2.3 Comparison with theoretical developments

In this Section a comparison is performed between the new experimental data for mesoscale bedforms and two bedform stability diagrams developed from theoretical analysis. Bar formation will be discussed in Section 6.5.

6.2.3.1 Comparison with theory developed by Engelund and Hansen

The new experimental data are presented in Figure 6.9 over the diagram developed by Engelund and Hansen (1966) for two options: first, to the left, using as independent variables the Froude number and the ratio between mean flow velocity to critical shear velocity for incipient motion of the bed material; the second option, to the right, uses as independent variables the Froude number and the ratio between mean flow velocity to total shear velocity. In both options, all runs with gravel and mixtures plot erroneously in the bedform phase for upstream-migrating antidunes. For the sand runs, the diagram to the left predicts adequately the occurrence of dunes, but fails to predict correctly the occurrence of transitional bedforms and downstream-migrating antidunes. Conversely, the diagram to the right predicts adequately the existence of downstream-migrating antidunes in sand, but not the sand dunes neither the sand transitional bedforms.

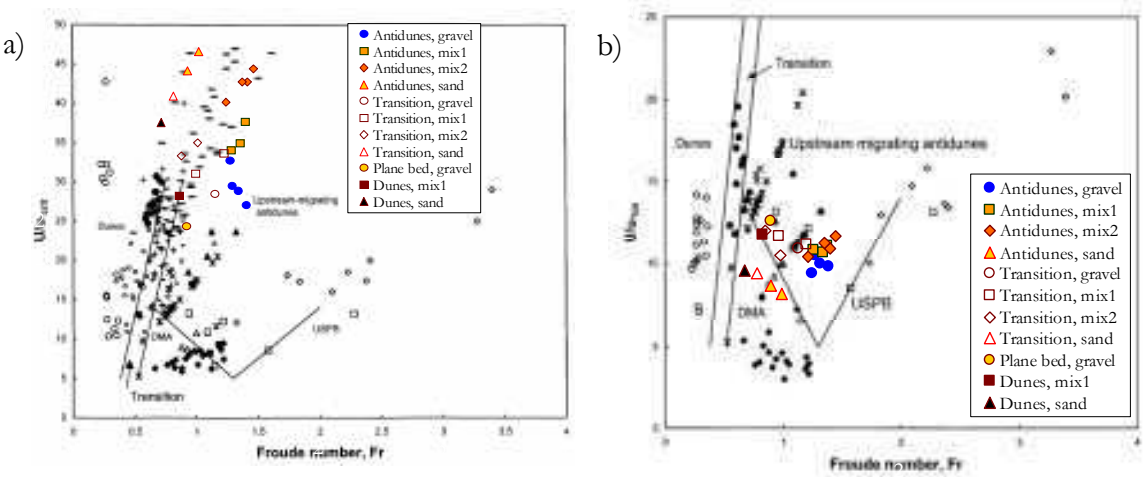

Figure 6.9. Plot of the new experimental data on the theoretical bedform stability diagram of Engelund and Hansen (1966), as a function of a) the Froude number and the ratio between the mean flow velocity and the critical shear velocity for sediment initiation of motion, and b) the Froude number and the ratio between the mean flow velocity and the total shear velocity. Data shown correspond to data sets collected by Carling and Shvidchenko (2002). DMA is downstream-migrating antidunes and USPB is upper stage plane bed.

6.2.3.2 Comparison with potential flow theory as outlined by Kennedy

Figures 6.10 and 6.11 show plots of the new experimental results compared with the developments from Kennedy (1961, 1963) using potential flow theory, as given by eqs. (5.1) to (5.6). Figure 6.10 compares theoretical bedform stability fields with the classification of the bed states observed in each experiment and summarized in Table 5.2. According to theory, dunes are likely to occur in the region below of the curve given by eq.(5.2); from the two experimental points classed as pertaining to the dune phase, only that for sand material plots in this region, while the point for mixture 1 plots above, but not far apart from the upper border for lower-regime given by eq.(5.2). The existence field for upstream-migrating antidunes is defined by the area between curves given by eqs.(5.2) and (5.3), while the existence field for downstream-migrating antidunes corresponds to the zone above the curve for eq.(5.3). All the antidunes observed in the experiments moved in the downstream direction, therefore, these experimental points should plot above the curve for eq.(5.3). Nine of the 13 points for the downstream-migrating antidunes plot correctly above or over this border, while the remaining four, in spite of plotting erroneously below that curve, they remain quite close to it. On the other hand, all bedforms classified as transitional bedforms, which also moved in the downstream direction, plot in the field for upstream-migrating antidunes, except for one point for mixture 1 which plots in the zone for downstream-migrating antidunes. In consequence, it can be concluded that theory performed well in predicting the stable conditions for occurrence of dunes and downstream-migrating antidunes, while transitional bedforms are neglected by the theoretical diagram. Nevertheless, if the observed transitional bedforms would be cataloged as antidunes considering that a certain degree of coupling between bed and water surface existed, since these forms plot in the region for upstream-migrating antidunes then theory failed to predict adequately their direction of movement.

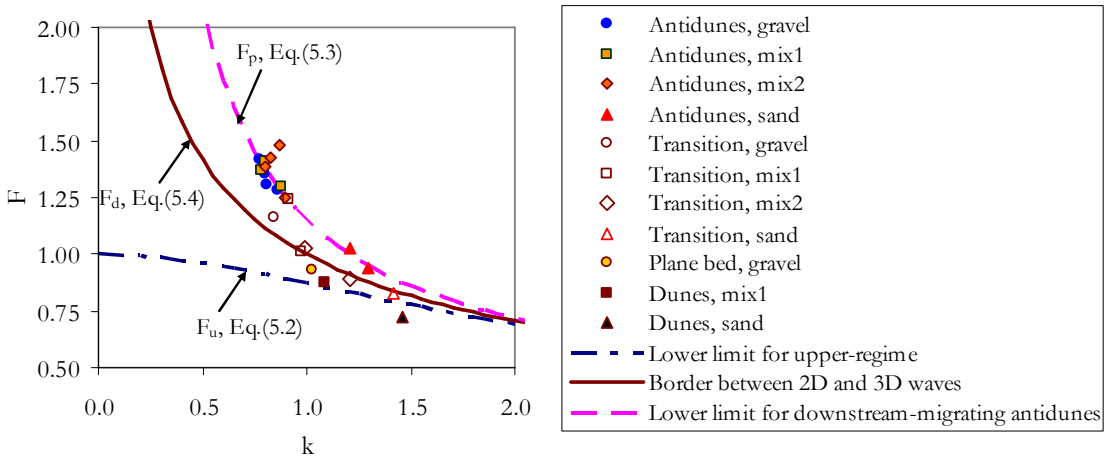

Figure 6.10. Comparison of observed bedforms during the experimental runs with bedform occurrence fields delimited with potential flow theory, as presented by Kennedy (1963).

With respect to the bi- or three-dimensionality of the surface waves summarized in column five of Table 5.2, Figure 6.11a compares the experimental data set with the stability regions given by eq.(5.4) (in this Figure configurations classed as "2D and 3D" in Table 5.2 have been considered as 3D). All of the data for 3D waves appear above of the curve used to, theoretically, delineate the lower limit for 3D antidunes, and all data-points corresponding to 2D waves plot below this border. As a result, and considering the comparison in Figure 6.10 as well, it may be said that theory corresponded adequately to

observations for 3D downstream-migrating antidunes and 2D dunes; conversely, for transitional bed forms, even when theory accurately predicts their bidimensionality, it fails to define their direction of movement correctly.

Figure 6.11b depicts the relation between mean flow velocity and wavelength as given by eqs.(5.5) and (5.6), and shows the experimental data for comparison. In applying eq.(5.6), the transverse wavelength of the 3D wave was considered to be equal to the channel width. For most of the 3D waves, eq.(5.6) underestimates the experimental mean flow velocities. Conversely, eq.(5.5) overestimates flow velocities for most of the 2D waves. Nevertheless, for this equation the agreement is fairly good except for the three points that correspond to dunes and the point for plane bed in gravel.

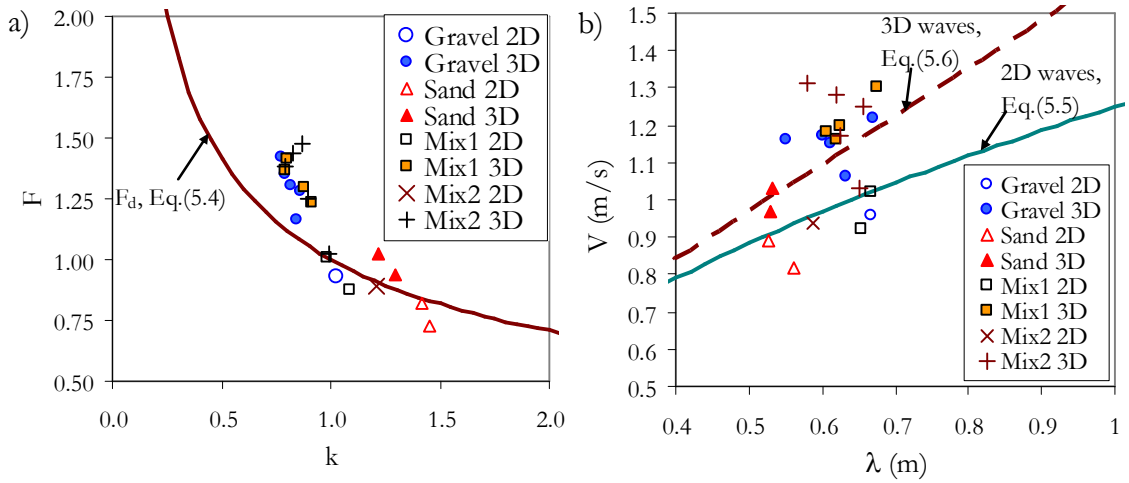

Figure 6.11. Comparison of characteristics of water surface waves observed in the experimental runs with potential flow theory, as presented by Kennedy (1961, 1963); a) comparison with theoretical bedform occurrence fields as a function of the Froude number and the wave number, this defined as $k=2\pi H/\lambda$; b) comparison of flow velocities and wavelengths for 2D and 3D waves.

6.2.3.2.1 Possible reasons for discrepancies

For the comparisons above the wavelength used corresponds to short-crested waves. This was so because trains of short-crested waves (rooster tails) were observed at the center of the channel cross section in all of the experimental runs, even in those runs with the lowest Froude numbers and classed as dune bed states. Nevertheless, these 3D waves varied in size, texture and unsteadiness between runs, and for some runs they appeared only during short time intervals. Normally, the profile of rooster-tails, parallel to the flow, showed a triangular shape, with surf on the crest facing upstream. For the considered 2D waves in Table 5.2 and Figure 6.11, the triangular shape protruded much less on the surface than those considered 3D, or was flattened and rounded like a mound without producing surf. These characteristics were, for instance, observed for the gravel run with the lowest Froude number (G17), for which the bed and water surface were most of the time plane. Wavelengths measured for this run belonged to sporadic trains of low-amplitude rounded stationary-waves that looked like humps on the water surface.

Attending to this variability of the short-crested waves characteristics, though rooster tails were observed in all of the runs, even when they are an essentially 3D feature the bed and water configurations were not always cataloged as three-dimensional. This was so, because based on the experimental observations it was clear that for some runs the dominant bed- and water-configurations were not necessarily 3D, although the water

surface did show short-crested 3D waves. For this reason, some bed and water states were classed as 2D. For these latter cases, if the dominant bed- and water-configurations were 2D, then it would follow that short-crested waves may not be necessarily linked to the bulk flow properties. Conversely, local-flow properties at the central section of the channel would be related to the formation of the rooster-tails, as opposed to the mean flow conditions. As a consequence, for flows with dominant 2D bed- and water-configurations, a different flow velocity than the section mean value should be used in order to coherently test the rooster-tails' existence with potential theory. Such a flow velocity would have to represent the local conditions at the channel central section where the rooster-tails were formed.

It is evident from the tendencies of the data in Figure 6.11 that for a given flow velocity the wavelengths of the configurations labeled as 3D are shorter than wavelengths for 2D configurations. This agrees qualitatively with theory given by eqs.(5.5) and (5.6), and suggests that for the flows labeled as 2D, rooster-tails used for measuring the wavelength must have been superposed to dominant 2D features. On the other hand, one likely reason for disagreement between eq.(5.6) and most of the 3D points can be the selection of the channel width as boundary condition along the sides of the short-crested waves. Although rooster-tails are formed by surface diagonal waves (see Figure 5.1), channel-walls might not be a defining factor for their existence. Kennedy (1961) evidenced this assertion by quoting an experimental run performed at the Colorado State University, for which an isolated train of rooster-tails formed at the center of a 2.4 m wide channel. For this run it was apparent that the vertical channel walls did not exercise any influence on the formation of the short-crested waves. As such, the channel width might not necessarily be equal to the rooster-tail wavelength normal to the direction of flow (λ_t) used in eq.(5.6).

Eq.(5.6) solved for the transversal wavelength of the rooster-tails yields

$$\lambda_t = \frac{\lambda}{\sqrt{V^4\left(\frac{2\pi}{g\lambda}\right)^2 - 1}} \qquad (6.5)$$

In order to ascertain likely values of the transversal wavelength of the rooster tails, the experimental data for measured mean flow velocity and short-crested waves' longitudinal wavelengths were used in eq.(6.5). The results are shown in Figure 6.12 as a function of the grain related shear stress for each run (as computed in Chapter 4) and a ratio between the computed transversal wavelength to the channel width. For most of the 2D waves only imaginary solutions were found, and thus are not considered in this Figure. For each type of sediment, data plotted in Figure 6.12 show a tendency towards lower transversal wavelengths with higher shear stresses. A likely physical explanation would be that such a behavior can be related to the scour holes eroded by the rooster-tails. It is possible that the excavated scour-holes could, in some cases, set a transversal boundary narrower than the channel width. Transversal scour patterns observed had a lobulated or triangular shape with the lobe or apex at the deepest point at the channel central cross section. Nevertheless, not a clear pattern was found to correlate the theoretical transversal wavelengths to the geometry of the scour holes.

Another likely reason for shorter wavelengths of the 3D downstream-migrating antidunes with respect to theory in Figure 6.11b, is given by Carling and Shvidchenko (2002), who suggested that the wavelength of asymmetric downstream-migrating antidunes is shorter than the wavelength of symmetric antidunes. This occurs because the wavelengths of individual downstream-migrating antidunes *are not necessarily well adjusted to the scale of the generating turbulent structures within the flow*. Alluding to experimental data pertaining to Kopalini (1972), Carling and Shvidchenko indicated that the length of turbulence structures is in average 22% longer than the average wavelength of asymmetric downstream-migrating antidunes, and thus, wavelengths in Figure 6.11b should be

increased by this value. Notwithstanding, the observations in which Carling and Shvidchenko based this argument corresponded to unstable antidunes, which collapsed, washed out and reformed continuously. The trains of downstream-migrating antidunes observed in the experiments of the present work were more or less stable, and thus it can be expected that lengths of turbulence structures and bedforms must have been roughly similar.

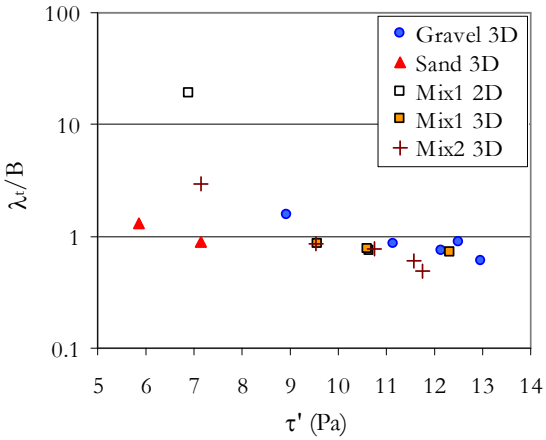

Figure 6.12. Ratio between the computed value of the transversal wavelength of the rooster tails and the channel width as a function of the grain related shear stress for the experimental data. The transversal wavelength was computed using the mean flow depth and the measured longitudinal wavelength in eq.(6.5).

6.2.4 Occurrence of downstream-migrating antidunes

Empirical diagrams used for comparisons in Section 6.2.2 do not distinguish between upstream- and downstream-migrating antidunes, neither do so any empirical stability diagrams in literature to the knowledge of the author. One reason for such an omission is the lack of observations of downstream-migrating antidunes, which have been reported much less frequently than their upstream counterparts. This scarcity of observations, perhaps induced by a requirement of higher Froude numbers for the formation of downstream-migrating antidunes than for upstream-migrating, has probably prevented the identification of a precise stability phase for downstream-migrating antidunes in empirical diagrams.

The scarcity of observations for downstream-migrating antidunes is even higher for grain sizes coarser than sand. Carling and Shvidchenko (2002) pointed out that most of the data for which downstream-migrating antidunes have been reported in literature correspond to sand and not to gravel beds. This is related to the fact that there is a lack of experimental data on coarse material, rather than a tendency for downstream-migrating antidunes to form preferentially in sand beds. The data set obtained in the present work give further evidence of this fact, and because of the absence of upstream-migrating antidunes in all of the experiments performed for this work with coarse sand, fine gravel and sand-gravel mixtures, an opposite tendency could be deduced, i.e. that downstream-migrating antidunes are more likely to form in coarse material. Experimental observations by Kennedy (1961) would agree with this hypothesis. Kennedy performed runs with flow conditions for the development of antidunes and transitional bedforms in a 0.27 cm wide flume with two sand beds. Mean grain-sizes of the sand were 0.55 and 0.233 mm, respectively. From a total of 30 runs with Froude numbers ranging from 0.70 to 2.34, for

the finest sand, transitional downstream-migrating bedforms were observed only for one run and downstream-migrating antidunes were never observed. Conversely, for the coarsest sand downstream-migrating antidunes were observed in two runs and downstream-migrating transitional bedforms were the dominant bedforms in three runs. All these forms were three-dimensional. On the other hand, for 13 runs using the coarser sand in a wider flume (0.85 m wide), neither downstream-migrating antidunes nor transitional downstream-migrating waves were observed for Froude numbers ranging from 0.5 to 1.26. In turn, Carling and Shvidchenko (2002) refer to experimental data sets of different authors, for which downstream-migrating antidunes have been reported in fine gravels. Anyhow, empirical data available are insufficient to conclude if downstream-migrating antidunes could be more frequent than upstream-migrating antidunes in gravel compared to sand beds.

With respect to the three-dimensional nature of the downstream-migrating antidunes observed in the experiments in the present work, these observations agree with those of Kennedy, in that all downstream-migrating antidunes that he registered were 3D. Nevertheless, a conclusive note cannot be given about the tendency of downstream-migrating antidunes for adopting a preferential 3D shape.

Finally, though empirical bedform stability diagrams neglect to distinguish the stable conditions that define the preferential direction of movement of antidunes, theoretical developments do not. In particular, the stability diagram of Kennedy was shown in Section 6.2.3.2 to anticipate correctly the conditions for the formation of the 3D downstream-migrating antidunes in the experiments. Conversely, the diagram of Kennedy failed to anticipate downstream-migrating transitional bedforms. An alternative method for defining the conditions in which the antidunes move upstream or downstream is presented in Chapter 7; it is shown there that in contrast to Kennedy's theory, the new method is able to predict the migration direction of antidunes and transitional bedforms as well.

6.2.5 Summary

The most important feature considered in classifying the experimental bed states in Chapter 5 was the degree of coupling between bed and water surfaces. By adopting this criteria some subjectivity was unavoidable, since the classification was performed by visual inspection of video footage; nevertheless, the criteria was straightforward and allowed to identify the effect of sand content in the transition from lower to upper regime by overlooking other complexities added by the interaction and coexistence of different scales of flow and bedforms.

The most evident effect of sand content in the lower to upper regime transition was a progressively narrower transition and a shift to lower Froude numbers of the boundary between the transitional and the lower regime as the sand content increased. Furthermore, for low sand contents, the range of Froude numbers for the transition remained almost unaltered up to a limiting sand content, located between 45% and 100%, from which this range of Froude numbers was narrowed by roughly a factor of three. Such an abrupt transition was found to be possibly related to two effects of the increase in sand content of the mixture, namely, the reduction in sediment sorting and the increase in relative depth.

Bedforms composed of pure sand were observed to be steeper than bedforms in gravel and in the two sand-gravel mixtures, and as a consequence, bed resistance owed to the bedforms was much larger for the sand runs than for gravel and mixtures runs series, as already shown in Chapter 4. This behavior reflects the relevance of identifying the conditions for which the transitional regime expands or narrows for different bed material conditions, especially when studying the sand-gravel transitions found in rivers. The

experimental evidence here presented contributes to a better understanding of the limits of the lower to upper regime transition for different sand contents in the bed material.

The experimental data were plotted in empirical diagrams for bedform stability phases in uniform material. Nevertheless, it was not possible to test the validity of the diagrams for the conditions tested, either because the experimental data were outside of the limits of the outlined borders between bedform phases, or because the diagram did not consider a distinction for the range of values explored between antidunes and transitional regime. However, as the new data corresponded to previously unexplored regions in the diagrams, it has been hypothesized that the diagrams are valid for gravel and sand-gravel mixtures, and thus approximate extrapolations of the stability phases have been proposed.

Empirical bedform stability diagrams do not consider the occurrence of macroscale bedforms or compound bedforms, neither distinguish separate phases for upstream- and downstream-migrating antidunes or 2D and 3D bedforms. Only one empirical stability diagram was found in literature for macroscale bedforms or bars; this diagram failed to predict the occurrence of bars in the experimental runs. This was probably so, because this diagram does not use the channel width to water depth ratio as a fundamental parameter, while many authors have suggested that this parameter controls bar instability.

The new experimental data set was compared with theoretical bedform stability diagrams developed by Engelund and Hansen (1961) and by Kennedy (1963), both of which consider separated stability fields for upstream- and downstream-migrating antidunes, and the latter distinguishes between 2D and 3D bedforms as well. From both theories, Kennedy's theory performed best, since it was able to predict the occurrence of 3D downstream-migrating antidunes and 2D dunes. However, Kennedy's theory neglects transitional bedforms, and though the experimental 2D transitional bedforms plotted correctly in the region for 2D bedforms, they plotted within the phase for upstream-migrating antidunes, while they actually moved in the downstream-direction.

Equations relating mean flow velocity and wavelength provided by Kennedy's theory, performed well for 2D bedforms, except for dunes, while for 3D bedforms most of the flow velocities were underestimated. It was hypothesized that such differences for 3D bedforms could be owed to the impossibility of defining the adequate transversal wavelength for the rooster tails. It was suggested as well that such a wavelength may be probably related to the extent of the scour holes produced by the short-crested waves in the channel central cross-section.

The classification of bed states and determination if the dominant waves were 2D or 3D was not free of some subjectivity. This subjectivity was introduced by the visual methods used, but mainly by the unsteadiness inherent to flows close to the critical condition, which for some runs produced a temporal and spatial alternation or coexistence of different flow regimes. For instance, short-crested waves, which are 3D upper-regime features, were observed in all of the runs at the channel central cross-section. Such behavior evidence that local flow conditions might differ considerably from the average flow conditions and that large flow variations can be expected in any cross section. This complexity sets a difficulty in establishing the ranges within which transitional bed features are likely to occur.

In short, the new experimental data set provides not only with new relevant knowledge about the effect of sand content in the limits of the lower to upper regime transition, but also contributes with new empirical evidence to outline the borders between bedform stability fields in previously unexplored ranges of the fundamental variables. Furthermore, the new data set contributes with valuable information about the occurrence of the rarely reported 3D downstream-migrating antidunes accompanied by surface short-crested waves (rooster tails). All of this information has a great relevance for river engineering, particularly for the analysis of flow resistance in the lower to upper regime transition.

Particularly, the new data set provides with empirical evidence for flow regimes which are likely to occur in steep ephemeral rivers, for which little experimental and field data are available. Additionally, new information on the bedform stability fields is of great value for sedimentologists when relating fossil sediments with formative environments.

6.3 EFFECT OF SAND CONTENT IN FLOW RESISTANCE

In the last Section, the analysis of the new experimental data set demonstrated that sand content in the bed material has a measurable effect in the range of Froude numbers for which the transitional regime occurred and in the size of the bedforms developed. In this Section the effect of sand content in flow resistance is analyzed. First the increment in total bed shear stress with respect to the increment in skin friction will be compared with published data sets for uniform sand material and mixtures. Next, the form resistance will be analyzed and compared with measurements of bedforms' height and wavelength.

6.3.1 Relation between skin friction and total bed shear stress

It has been recognized for a long time that flow resistance in most sand-bed rivers is characterized by a discontinuity in the transition from lower to upper-regime. Stage-discharge relations in these rivers describe two different functions for lower and upper regime, and both are linked by a transitional stage which can be sensitive on whether the discharge is increasing or decreasing. Different authors have proposed empirical models to account for this behavior, as for instance Cruickshank and Maza (1973), whose model applied to the Rio Grande is shown in Figure 2.6. For the field data in this Figure, the hydraulic radius increases with flow velocity along the lower and upper regime, while it remains almost constant in the transition. Such a discontinuous behavior of flow resistance is an effect of bedforms. Since, for some grain sizes, lower regime can be characterized by dunes and the transitional regime by washed-out dunes and plane bed, when water discharge increases and the bed configuration changes from dunes to washed-out dunes and then plane bed, the consequence is a drop in flow resistance. If water discharge is increased further, the plane bed is replaced by antidunes in upper regime and flow resistance increases again.

As it was discussed in the last Section, plane beds in the transitional regime tend to be infrequent as the bed material coarsens. Therefore, for these beds in which the transitional regime is not characterized by a plane bed, it could be expected that the discontinuity in flow resistance linking lower and upper regimes would behave different or even that flow resistance would not necessarily exhibit a discontinuous behavior. These means that for such cases flow resistance predictors developed for sand-bed rivers, as that from Cruickshank and Maza, would not be valid. The experimental data set for sand, gravel and sand-gravel mixtures obtained in Chapter 3, along with other data sets found in literature, are analyzed in this Section in order to investigate flow resistance trends in these types of beds for which plane bed in the transitional regime does not occur. In doing this, the effect of sediment size and sand content on the effective shear stress is analyzed and discussed.

Engelund and Hansen (1967) analyzed flume data reported by Guy et al. (1966) for uniform sand with grain sizes between 0.19 and 0.93 mm. They used the same shear stress decomposition methods as those exposed in Chapter 4 to obtain the effective shear stress or grain friction. By using similarity principles Engelund and Hansen found a good collapse of the experimental data when plotting the total bed shear stress against the effective shear stress, both made dimensionless with the Shields parameter. For lower regime they

proposed the following expression for describing the relationship between the total and the effective Shields stresses

$$\tau'^* = 0.06 + 0.4\tau_b^{*2} \qquad (6.6)$$

where $\tau_b^* = \tau_b/\rho g(Ss-1)D$ and $\tau'^* = \tau'/\rho g(Ss-1)D$ are the Shields stresses for the total bed shear and the skin friction, respectively. Wang and White (1993) performed experiments with fine and coarse sand, 0.076 and 0.76 mm median size, respectively. By plotting in the diagram of Engelund and Hansen their own data set and additional data from other authors collected in flumes and field, they found a dependence on sediment grain size that was not noticeable in the original plots of Engelund and Hansen because of the limited range of grain sizes used. The original flume data from Wang and White (1993) have been plotted in Figure 6.13a, while one of the diagrams they presented with data from other authors is shown in Figure 6.13b. From the plots of the data sets, it was evident that at least for the lower regime, for a given bed Shields stress value, grain Shields stress is higher the coarser the material is. Therefore, Wang and White concluded that for each grain size there is a single functional relationship that describes the lower regime and a different one for upper regime. Also, they found that for a given grain size, the relation between τ_b^* and τ'^* in the transitional regime depends upon the relative hydraulic radius R_h/D.

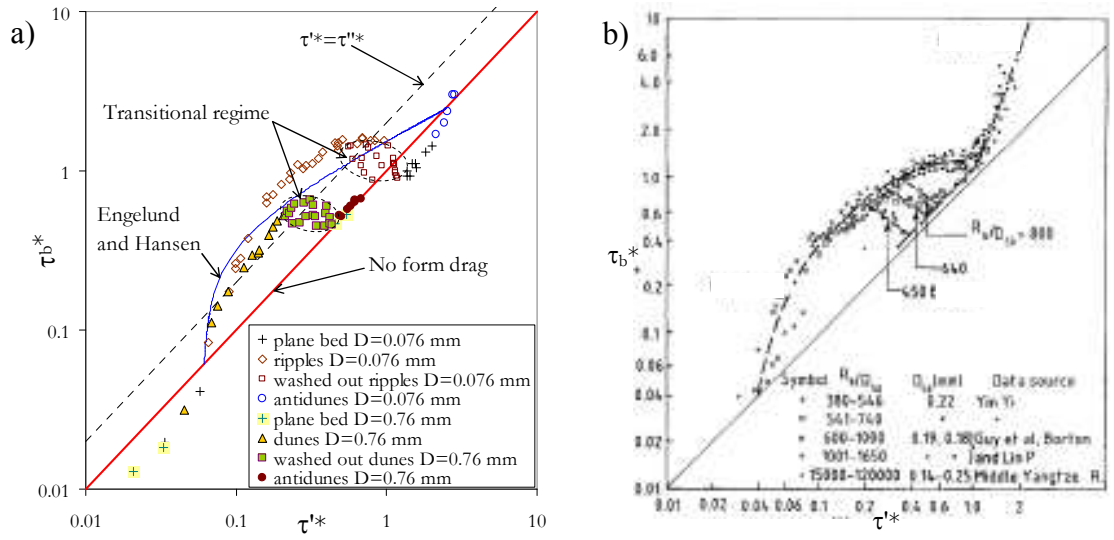

Figure 6.13. Flow resistance diagrams using the same parameters as Engelund and Hansen (1967), i.e., effective Shields stress versus total bed Shields stress, a) with flume data sets from Wang and White (1993) for 0.076 and 0.76 mm grain sizes, and b) with field and flume data (original graph by Wang and White 1993) with grain sizes in the range of 0.22 to 0.25 mm.

The new experimental data set, along with data sets from Kennedy (1961) and Kuhnle (1993a) already described in Chapter 4, are used here to find out if the trends observed by Wang and White are valid for coarser material. Data for uniform material in these three data sets have been plotted in the diagram of Engelund and Hansen, as shown in Figure 6.14. For all the data used in that Figure, skin friction was estimated using the reference plane bed method with $k_s=2.5D_m$, this method was described in Section 4.3.2.1. Except for some few points for coarse sand from the data sets of Kuhnle and Kennedy, for the lower regime it is verified that the coarser the material is, the closer the points plot to the line of no form drag, i.e., the line for bed shear stress equal to skin friction. These observations verify the trends found by Wang and White for very fine and coarse sand, and suggest that

such trends are valid for very coarse sand and fine gravel as well. On the other side, contrary to the data from Wang and White shown in Figure 6.13a, the points of the new data set describe two continuous monotonically increasing relationships, one for sand and one for gravel, even when the data correspond to lower, transition and upper regime. This trend suggests that for coarser material not just a discontinuity in the transition from lower to upper regime is not found, but also that it is likely that for a given grain size a single continuous biunivocal function could describe flow resistance along the three regimes.

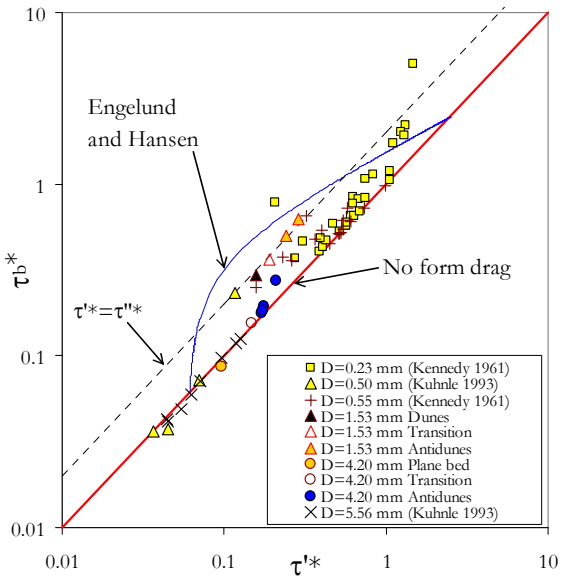

Figure 6.14. Total bed Shields stress versus Shields stress due to skin friction (estimated with the reference plane bed method with $k_s=2.5D_m$) for data obtained by different authors with uniform sand and gravel. For data obtained in the present study the dominant bedform is indicated in the legend.

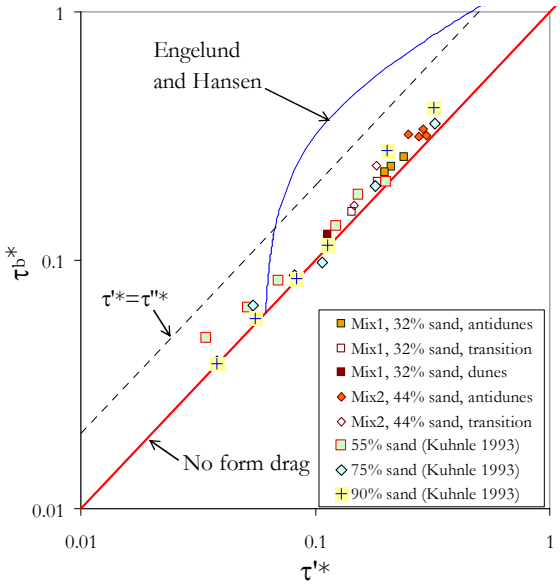

Figure 6.15. Total bed Shields stress versus Shields stress due to skin friction (estimated with the reference plane bed method with $k_s=2.5D_m$) for data obtained by different authors with sand-gravel mixtures. For data obtained in the present study the dominant bedform is indicated in the legend.

Figure 6.15 is similar to Figure 6.14, but extends over a narrower range of values and uses only data for sand-gravel mixtures from experiments in the present study and from the data set of Kuhnle (1993a). In general, all data in Figures 6.13 to 6.15 can be grouped into two similar populations. The first population corresponds to data pertaining to sand, for which in the lower regime the gradient of bed shear stress is high with respect to the gradient of skin friction. This trend is similar to that followed by the relation proposed by Engelund and Hansen, given by eq.(6.6), which has been drawn in all three Figures for reference. The second population of data corresponds to gravel and sand-gravel mixtures. For this data, the increments of bed shear stress are similar to the increments of skin friction, thus indicating an almost negligible contribution of form resistance to the total bed shear stress. Noteworthy is that data for mixtures with sand contents as high as 90% and 75% (from the data set of Kuhnle) plot closer to the points for the rest of mixtures and gravel than to the sand points. These results suggest that, in terms of bed resistance, the shift from gravel to sand behavior would require extremely high proportions of sand in motion with respect to gravel; put in other words, it seems that even small amounts of gravel in motion mute the growth of bedform height and as a consequence sand-gravel mixtures display low form resistance. These findings agree with results obtained for

alternate bars with a stability model by Lanzoni and Tubino (1999), and with experimental runs with a strongly bimodal mixture of fine and coarse sand (67% content of fine sand) by Lanzoni (2000); these authors found that the increase in sediment heterogeneity damps the growth of bar amplitude.

Finally, in Figure 6.15 it can be observed that, similarly as it occurs with uniform very coarse sand and uniform fine gravel, it seems that for sand-gravel mixtures there exists a biunivocal relationship between total and skin friction Shields stresses along lower, transitional and upper regimes.

6.3.1.1 Effect of the Froude number

Graphics for different data sets in Figures 6.14 and 6.15 in the previous Section show that the onset of the transitional regime as shear stress is increased occurs for higher bed Shields stresses the finer the bed material is. In the same manner, as originally observed by Wang and White (1993), for a given grain size the Shields stress for the occurrence of the transitional regime increases with the relative hydraulic radius R_h/D (see for example Figure 6.13b). It can be demonstrated that this correspondence between the transitional regime onset and the sediment grain size and relative hydraulic radius is related with the different response of sediment mobility to flow strength according to the grain size. It is known that the transitional regime is linked to the flow instabilities typical of near critical conditions, for which small bed perturbations can cause high variations in flow depth as seen from the specific energy curve. When near critical flow conditions occur, the mobility of the bed sediment is much greater the finer the grain size is, i.e., if the mobility of the bed material is associated to the Shields stresses, near critical flow conditions (and therefore the transitional regime onset as well) occur for higher Shields stresses for fine material than for coarse material. To prove this assumption, the bed Shields stress related to the critical Froude number, for a bed without bedforms, can be calculated. Using the definition of the Shields parameter for the bed shear stress, $\tau_b^* = \tau_b/\rho g(S_s-1)D$, and eq.(4.6) solved for the bed shear stress, it is obtained that

$$\tau_b^* = \frac{C_f V^2}{g(S_s-1)D} \qquad (6.7)$$

Solving the Froude number for the flow velocity, $V=F(gH)^{0.5}$, and from eq.(4.7) solved for the dimensionless resistance coefficient, $C_f=C_z^{-2}$, where C_z is the dimensionless Chézy resistance coefficient; V and C_f replaced in eq.(6.7) yield

$$\tau_b^* = \frac{F^2 H}{C_z^2 (S_s-1)D} \qquad (6.8)$$

Finally, using eq.(4.10) for the Chézy coefficient, with the relative roughness $k_s=\alpha_S D$, and considering F=1, the bed Shields stress for critical flow conditions is equal to

$$\tau_b^*\big|_{F=1} = \frac{\alpha_S^{1/3}}{65.6(S_s-1)}\left(\frac{H}{D}\right)^{2/3} \qquad (6.9)$$

If it is assumed that α_S and S_s are constants, and that $H\approx R_h$, the dependence of the transitional regime on the relative hydraulic radius R_h/D is proved, and confirms the empirical observations of Wang and White about the transitional regime to occur for higher Shields stresses for finer material.

Wright and Parker (2004b) recognized the dependence on the Froude number in the relationship between skin friction and total bed Shields stresses, and proposed an amendment to eq.(6.6) as follows

$$\tau'^* = 0.05 + 0.7\left(\tau_b^* F^{0.7}\right)^{0.8} \qquad (6.10)$$

These authors justified the incorporation of the Froude number in eq.(6.10) referring to observations by Posada (1995) , Julien and Klaasen (1995) and Wright and Parker (2004a) for large, low slope sand-bed rivers, for which at high flows the original formulation of Engelund and Hansen strongly overestimated the skin friction, as shown in Figure 6.16a (note in this Figure that Wright and Parker changed the axis of the original diagram of Engelund and Hansen, using the grain shear stress as the dependent variable). Wright and Parker argued that the reason for the poor performance of eq.(6.6) was that for such sand-rivers high flows occur at low Froude numbers, so that the transition from lower regime with dunes to plane bed does not occur or occurs seldom. Also, they indicated that for such rivers the transition does not occur at shear stresses as low as those in flume data from which eq.(6.6) was developed. Nevertheless, according to the discussion in the previous Section and to eq.(6.9), it is more likely that the reason for the poor performance of eq.(6.6) when applied to large sand-rivers could be related to the small grain sizes and high relative depths (high H, very low D) typical of those rivers, rather than to their low shear stresses for high flows in comparison to flume data. This is demonstrated by Figure 6.16b, where it can be observed that flume data from Wang and White for 0.076 mm grain sizes plot under the Engelund and Hansen curve, in a similar fashion as the data set for low slope sand rivers in Figure 6.16a.

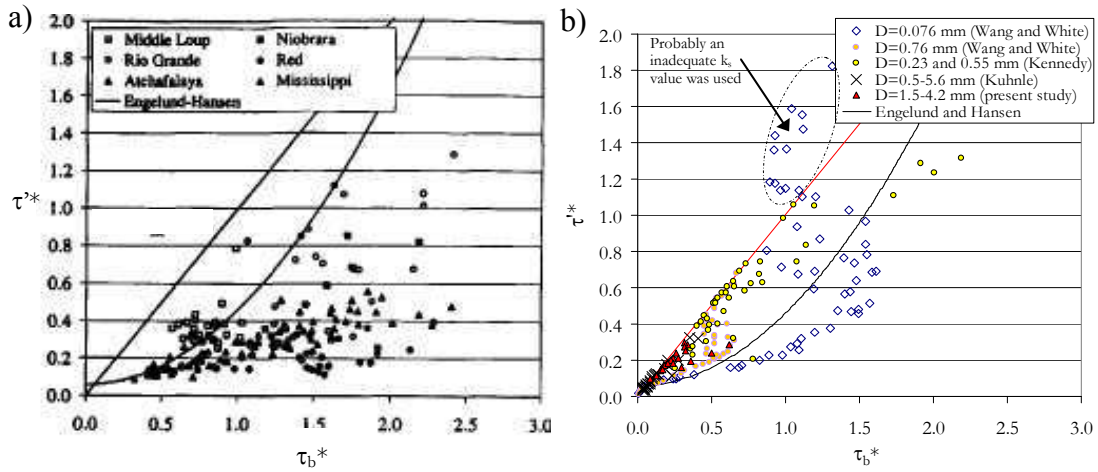

Figure 6.16. Effective shear stress as a function of total bed Shields stress, a) for different sand-bed rivers with grain sizes in the range of 0.09-0.42 mm (original Figure by Wright and Parker, 2004b), and b) for the different flume data sets with sand, gravel and sand-gravel mixtures previously plotted in Figures 6.13a, 6.14 and 6.15. The curve for the Engelund and Hansen formulation is presented in both graphics for comparison.

As opposed to large low slope rivers with fine sand, it can be seen in Figure 6.16b that for a given bed Shields stress the relation of Engelund and Hansen underestimates skin friction for experimental beds with coarse sand, fine gravel and sand-gravel mixtures. This not withstanding, incorporation of the Froude number as a product in the abscissa, with the same exponent introduced in eq.(6.10), makes the data to roughly collapse into a single curve, at least for $\tau'^*<1$, as shown in Figure 6.17. Most of the data plot under eq.(6.10), and thus a best-fit line is given by the relation

$$\tau'^* = 0.03 + 0.7\tau_b^* F^{0.7} \qquad (6.11)$$

This result demonstrates the appropriateness of incorporating the Froude number in the relationship between τ_b^* and τ'^*. On the other hand, the collapse of the experimental data in Figure 6.17 shows much less scatter than the field data for large sand bed rivers

presented by Wright and Parker (2004b). It is likely that for natural rivers with very fine sediment different factors contributed to a larger scatter, among which are included the highest variability and complexity of field in comparison to flumes, and the difficulties in selecting an adequate value for the relative roughness k_s, as well. With respect to this later issue, note that for the highest shear stresses in the finest grain sizes in Figure 6.16b, the estimated skin friction values are higher than the total shear stress, suggesting that an inadequate k_s value has been used. It is likely that an adequate k_s would produce a better collapse of the data with highest shear stresses in Figure 6.17.

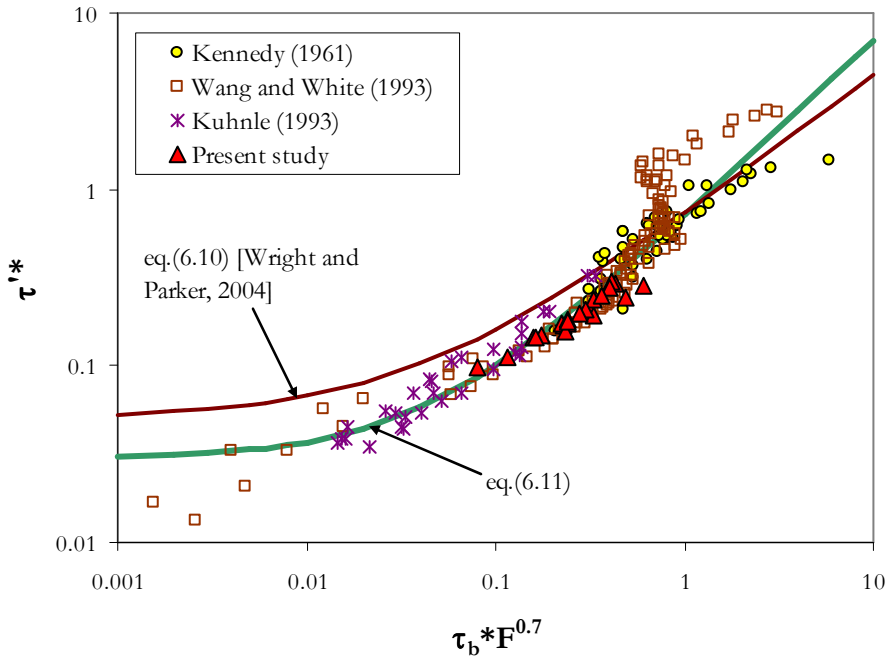

Figure 6.17. Total bed Shields stress versus Shields stress due to skin friction (estimated with the reference plane bed method) for data obtained by different authors with uniform sand, uniform gravel, and sand-gravel mixtures.

6.3.2 Form resistance friction factors

The graphs in the previous Section (Figures 6.13 to 6.15) show that for gravel and sand-gravel beds the main component of bed Shields stress in the lower regime is skin friction, while for sand beds, as the total bed Shields stress increases, the importance of form drag increases rapidly and soon becomes larger than skin friction (see points above the line for $\tau'^*=\tau''^*$ in Figure 6.13a). For grain sizes up to coarse sand, the increasing trend of the form drag encounters a limit in the transitional regime, where the total bed Shields stress decreases or remains constant. On the contrary, for coarse sand, gravel and sand-gravel mixtures, not such a trend is observed, and the total bed Shields stress seems to increase monotonically from lower to upper regime without any intermediate discontinuity. In this Section resistance coefficients owed to the bedforms are calculated and compared with the general trends summarized above.

In a similar manner as eq.(4.6), dimensionless friction factors for the grains and bedforms can be defined as

$$C_f' = \frac{\tau'}{\rho V^2} \qquad (6.12a); \qquad C_f'' = \frac{\tau''}{\rho V^2} \qquad (6.12b)$$

so that form (grain) resistance would be proportional to C_f" (C_f'), i.e., high values of C_f" denote high form resistance and vice versa. From eqs.(4.4) and (4.7), it can be deduced that the relation between the dimensionless resistance coefficients defined by eq.(6.12) and the Darcy-Weissbach resistance coefficient is given by C_f'=f'/8 and C_f"=f"/8. For the new experimental data set, calculated values of the dimensionless resistance coefficient for the bed C_f, effective shear C_f' and form drag C_f" are shown in Table 6.1.

Table 6.1 Experimental conditions for the new data set with gravel, sand and two sand-gravel mixtures. C_f, C_f' and C_f" are the calculated dimensionless resistance coefficients for the bed, effective shear and form drag, respectively; Δ and λ are the bedform height and length, respectively. DMA=Downstream-migrating antidunes, T=Transitional bedforms, and PB=plane bed.

Run	Dominant bed form	Sand content %	D_{50} [mm]	F	Δ [mm]	Δ/H	$\Delta^2/(H\lambda)$	C_f Total x10^3	C_f' Skin x10^3	C_f" Form x10^3	C_f"/ C_f
G12	DMA	0%	4.83	1.42	9.3	0.138	0.002	10.2	9.8	0.4	0.04
G13	DMA	0%	3.77	1.27	36.8	0.401	0.022	10.8	8.4	2.4	0.22
G14	DMA	0%	4.39	1.37	15.0	0.196	0.005	9.6	9.2	0.4	0.04
G15	DMA	0%	4.08	1.29	13.3	0.169	0.004	9.2	8.5	0.7	0.07
G16	T	0%	3.84	1.16	14.1	0.165	0.004	8.5	8.0	0.5	0.06
G17	PB	0%	4.27	0.93	7.4	0.067	0.001	6.1	7.1	-1.1	-0.18
M1E1	T	32%	3.04	1.00	20.6	0.199	0.006	14.1	6.8	0.6	0.09
M1E2	DMA	31%	3.27	1.42	26.0	0.301	0.012	13.3	7.6	0.3	0.03
M1E3	DMA	31%	3.19	1.37	18.7	0.245	0.007	11.4	8.0	0.8	0.09
M1E4	DMA	31%	3.38	1.30	25.2	0.290	0.012	10.6	7.8	0.8	0.09
M1E5	T	31%	3.29	1.23	26.0	0.290	0.012	7.5	7.5	0.4	0.05
M1E6	D	35%	3.02	0.88	26.6	0.234	0.005	7.8	6.7	0.3	0.04
M2E1	PB and DMA	44%	2.54	1.44	12.7	0.157	0.003	8.8	7.1	1.0	0.12
M2E2	DMA	44%	2.49	1.49	17.0	0.210	0.006	8.6	6.9	0.1	0.02
M2E3	DMA	45%	2.46	1.40	21.5	0.259	0.008	8.0	6.9	0.8	0.10
M2E4	DMA	45%	2.43	1.25	27.4	0.309	0.014	6.9	7.0	1.7	0.20
M2E5	T	43%	2.49	1.02	26.3	0.256	0.010	8.1	6.8	1.9	0.22
M2E6	T	47%	2.31	0.89	24.6	0.217	0.009	7.0	6.0	1.3	0.18
S1	DMA	100%	1.56	1.02	48.6	0.475	0.044	7.7	6.8	7.3	0.52
S2	DMA	100%	1.53	0.94	64.8	0.594	0.036	8.8	6.5	6.8	0.51
S3	T	100%	1.51	0.82	58.3	0.489	0.022	8.7	6.0	5.3	0.47
S4	D	100%	1.51	0.73	56.9	0.438	0.023	7.4	5.8	4.8	0.45

6.3.2.1 Drag coefficient

Form resistance is related to a horizontal drag produced by the pressure difference between the stoss and the lee sides of a bedform. Such a pressure imbalance is generated by the flow separation immediately downstream of the crest of the bedform. From elementary theory it is known that pressure drag is equal to

$$F_D = \frac{1}{2} C_D \rho V^2 A_b \qquad (6.13)$$

where A_b is the projected area perpendicular to the flow, so that for 2D bedforms and a unit width A_b=Δ, where Δ is the bedform height; C_D is the drag coefficient, V is the flow velocity and ρ is the water density. From direct measurements in artificial plastic dunes and subcritical flows, Shen et al. (1990) found that surface roughness has no significant

influence on form drag, and therefore they concluded that drag forces depend only on the geometry of the bedform and the flow conditions. It can then be written that

$$\tau'' = \frac{F_D}{\lambda} \tag{6.14}$$

where λ is the bedform length. Combining eqs.(6.13) and (6.14), and introducing them into eq.(6.12), it is found that

$$C_f'' = \frac{1}{2} C_D \frac{\Delta}{\lambda} \tag{6.15}$$

Figure 6.18 shows a graphic presented by Shen et al. (1990) for the form drag coefficient as a function of the relative roughness; the latter defined as the ratio between the bedform height and the water depth. In this graphic, experimental values for artificial and natural dunes obtained by different authors were used. According to Figure 6.18, eq.(6.15) can be rewritten as

$$C_f'' = \frac{\Delta}{2\lambda} C_D\left(\frac{\Delta}{H}\right) \tag{6.16}$$

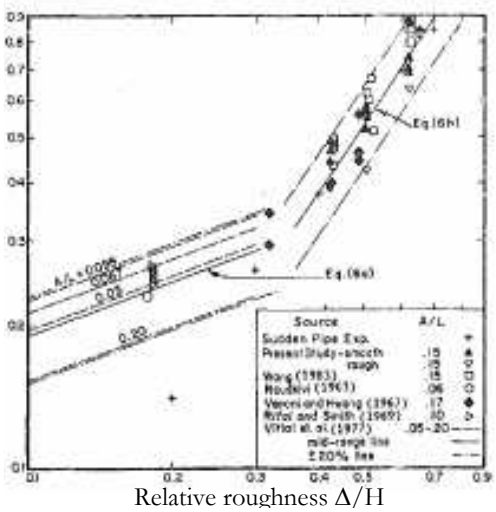

Figure 6.18 Experimental pressure drag coefficient for bedforms as a function of relative roughness (ratio of bedform height to water depth), according to Shen et al. (1990).

Computed values of C_f" for the new data set (presented in Table 6.1), along with values calculated for the experimental data set of Wang and White (1993), are shown in Figure 6.19 as a function of the ratio between the bedform height and the water depth. In this graph, bedforms of the same species plot in similar regions: dunes (except the only point for dunes pertaining to mixture 1) approximately collapse into a steep line to the right; antidunes (except one point for antidunes in gravel) approximately collapse into a mild line in the lower part of the graph; points defined as transitional bedforms in the present study roughly collapse into the same lines as dunes and antidunes, while points from the data set of Wang and White for ripples, washed-out ripples and washed-out dunes show a large scatter in the middle of the graph. The effect of viscosity in the formation of ripples and washed-out ripples might be the reason for the large scatter found for this type of bedforms.

Comparison of Figures 6.18 and 6.19 shows that the lines drawn (by eye) to follow the trend of collapsed points in Figure 6.19 intercept roughly in the same value of 0.35 of the relative roughness as the lines fitted in Figure 6.18. This interception corresponds to an abrupt change of the drag coefficient. Therefore, it can be interpreted that the experimental

data confirm this sudden change of the drag coefficient with a similar effect in bedform resistance; this even when many of the bedforms in the new data set were 3D, and even when the bedform heights of the new data set used to draw Figure 6.19 would not necessarily represent the entire cross section, because they were measured on the lateral section. Since form resistance is strongly dependant on bedform height, as indicated by eq.(6.16), steep bedforms would have an increased effect in bed resistance if the relative roughness exceeds the interception value of the two trend lines in Figures 6.18 and 6.19.

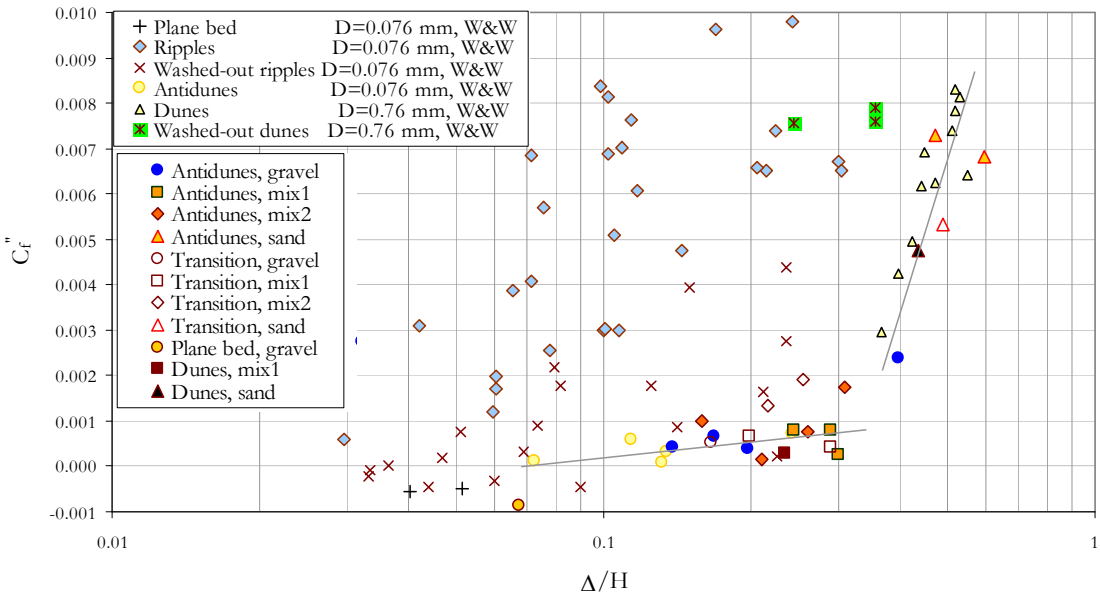

Figure 6.19. Variation of the dimensionless resistance factor due to form drag, computed with eq.(6.12b), as a function of relative roughness of the bedforms, for experimental data obtained in the present study with gravel, sand and two sand-gravel mixtures, and for the data set of Wang and White (W&W) (1993). To avoid negative unrealistic values of C_f", for antidunes in the Wang and White data set the relative roughness was taken as $k_s=0.5D_{50}$ when computing the grain shear stress with the reference plane bed method (see points that erroneously plot below the line for $\tau'^*=\tau"^*$ in Figure 6.13a using $k_s=2.5D_{50}$). Bedform heights for the new data set correspond to measurements of bed surface level on the channel walls, as given in Table 4.4.

6.3.2.2 Form resistance and bedform geometry

With the assumption that $\tau'=\rho gHS'=\rho gH_sS$, where H_s is the skin friction portion of the water depth and S' is the energy slope due grain friction, Engelund and Hansen (1967) proposed that the energy slope can be divided into its components due to grain friction and bedform resistance as follows

$$S = S'+S'' \qquad (6.17)$$

Recalling eq.(4.1) for the Darcy-Weisbach friction factor, if eq.(6.17) is divided by $V^2/8gR_h$, it is obtained that

$$f = f'+f'' \qquad (6.18)$$

On the other hand, the energy gradient for bedform resistance would be equal to the expansion loss produced by the bedform per bedform length, i.e. $\Delta H"/\lambda$; hence, it can be written that

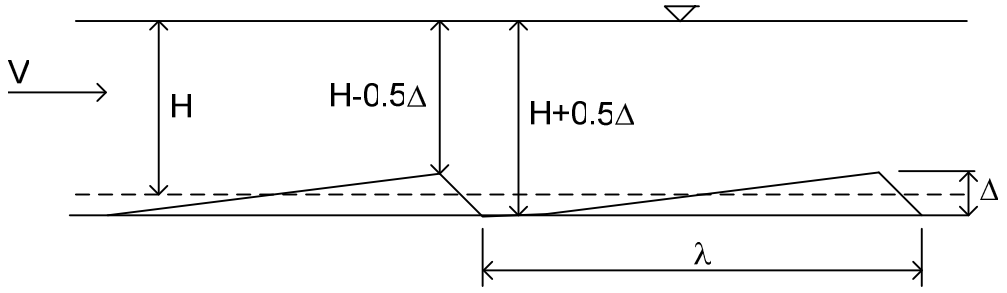

Figure 6.20. Variables for computation of the expansion loss over a bedform, according to Engelund and Hansen (1966).

$$f''=\frac{8gR_h}{V^2}\frac{\Delta H''}{\lambda} \qquad (6.19)$$

For estimating the magnitude of the expansion loss, Engelund and Hansen used the Carnot's formula

$$\Delta H''=\alpha_c\frac{(U_1-U_2)^2}{2g} \qquad (6.20)$$

where U_1 is the mean velocity above the bedform crest, U_2 is the smaller mean velocity downstream from the bedform crest, and α_c is a coefficient that depends on the flow geometry. U_1 and U_2 can be expressed as a function of the unit water discharge q_w, bedform height Δ, and mean water depth H as (see Figure 6.20)

$$U_1=\frac{q_w}{H-0.5\Delta} \qquad (6.21a); \qquad U_2=\frac{q_w}{H+0.5\Delta} \qquad (6.21b)$$

If $V=q_w/H$, introducing eqs.(6.21) into eq.(6.20) and operating, Engelund and Hansen arrived to

$$\Delta H''=\alpha_c\frac{V^2}{2g}\left(\frac{\Delta}{H}\right)^2 \qquad (6.22)$$

Finally, using eq.(6.22) in eq.(6.19), considering that $R_h\approx H$, and recalling that $C_f''=f''/8$, an expression for the dimensionless bedform resistance factor is obtained

$$C_f''=\frac{\alpha_c\Delta^2}{2H\lambda} \qquad (6.23)$$

and equaling eq.(6.23) with eq.(6.16), it is found for the drag coefficient

$$C_D=\alpha_c\frac{\Delta}{H} \qquad (6.24)$$

Eq.(6.23) states that form resistance is a function of bedform geometry, water depth and geometric characteristics of flow. According to this equation, similarity exists between bedforms with the same shape, and consequently, it can be expected that similar bedforms would share a unique value of coefficient α_c. Below, this similarity is tested and is used to compare dunes and antidunes in order to find out if flow resistance produced by downstream-migrating antidunes is comparable to flow resistance generated by dunes.

For the same experimental data in Figure 6.19 and additional flume data for antidunes presented by Simons et al. (1966), the bedform dimensionless friction factor has been plotted in Figure 6.21 as a function of the dimensionless product $\Delta^2/H\lambda$ obtained from eq.(6.23). For the new data set, the bedform wavelength for bedforms labeled as antidunes and transitional bedforms was considered to be equal to the stationary waves wavelength (as shown in Table 4.3), and for bedforms labeled as dunes this wavelength was considered equal to the bedform wavelengths measured at the end of the runs (as shown in the fifth column of Table 4.4). Curves for different values of the coefficient α_c, according to

eq.(6.23), have been drawn in Figure 6.21. The scatter for $\Delta^2/H\lambda<0.01$ hinders the distinction of any possible trend, nevertheless for $\Delta^2/H\lambda>0.01$ an approximate hierarchy for α_c can be distinguished; bedforms from higher to lower values of α_c are: ripples and washed-out dunes, dunes, downstream-migrating antidunes (data from the present work) and washed-out ripples, and antidunes (data from Simons et al.). It is noteworthy that data for ripples and washed-out ripples show less scatter compared to Figure 6.19. This reduction in scatter is owed to the inclusion of the effect of the bedform steepness Δ/λ in Figure 6.21, which is higher for ripples than for dunes and antidunes (from the data set of Wang and White, ranges of Δ/λ for ripples, washed-out ripples, dunes, washed-out dunes and antidunes are 0.05-0.17, 0.08-0.12, 0.045-0.06, 0.039-0.05, and 0.015-0.03, respectively). Again, viscosity effects may contribute to the larger scatter observed for ripples and washed-out ripples.

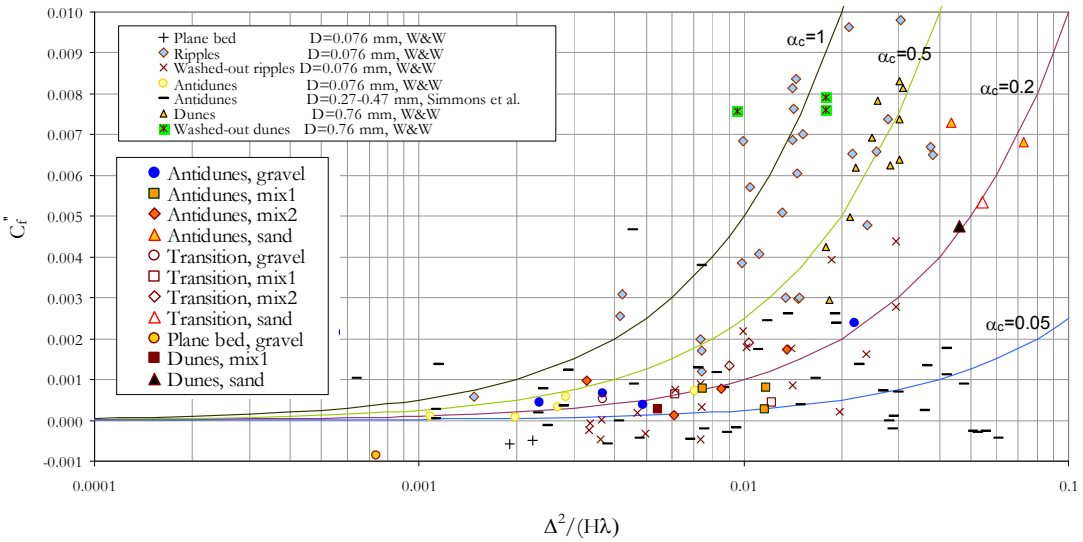

Figure 6.21. Variation of the dimensionless resistance factor due to form drag as a function of the product of the bedform steepness and the bedform relative roughness, for experimental data obtained in the present study with gravel, sand and two sand-gravel mixtures, and for the data sets of Wang and White (W&W) (1993) and Simons et al. (1966). To avoid negative unrealistic values of C_f", for antidunes in the Wang and White data set the relative roughness was taken as $k_s=0.5D_{50}$ when computing the grain shear stress with the reference plane bed method. Bedform heights for the new data set correspond to measurements of bed surface level on the channel walls, as given in Table 4.4.

In Figure 6.21, data for pure sand runs in the present study show larger scatter than in Figure 6.19. This might be attributed to the difficulty of selecting an adequate bedform wavelength. For runs S3 and S4, dune wavelengths were measured at the end of the experiments, but it was not possible to distinguish those dunes which were superposed to larger ones. It is likely that form resistance is best correlated to the later, primary bedforms, rather than to the former secondary bedforms. Figure 6.22 shows images of bedforms during the experimental runs with pure sand. In this Figure, for runs S3 and S4 (considered in Chapter 5 as transitional and dune bed configurations, respectively) secondary bedforms over primary bedforms can be distinguished. In turn, for run S2 (labeled in Chapter 5 as an antidune configuration because bed and water surfaces were in-phase) symmetric antidunes alternated with asymmetric bedforms. Flow separation loses must have been more important for the latter, and thus, when computing the energy gradient due to form drag, the average distance between asymmetric bedforms should be used, rather than the

wavelength of surface stationary waves. After considering these characteristics, a better collapse of the data for pure sand was obtained as shown in Figure 6.23. Corrections consisted in using bedform lengths of twice the stationary waves wavelength for run S2, and twice the bedform length measured at the end of runs S3 and S4.

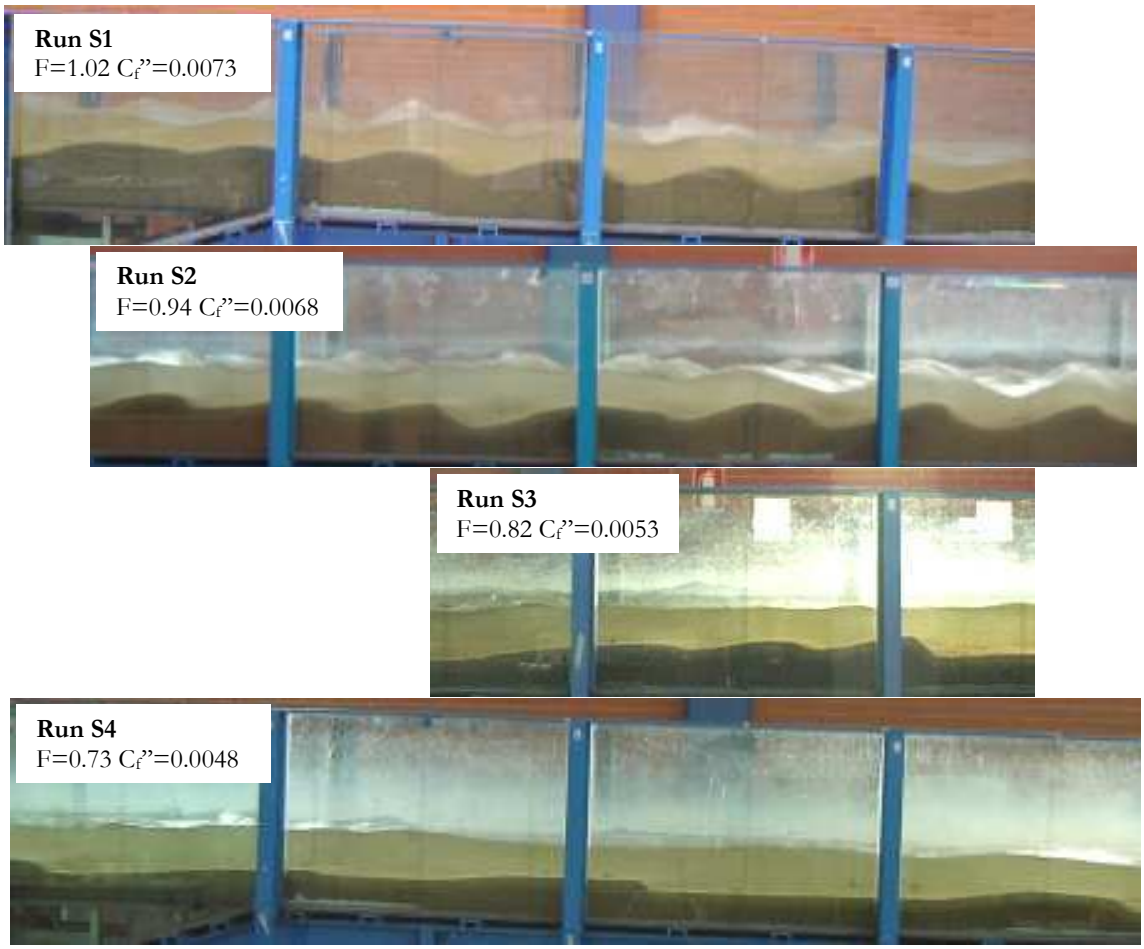

Figure 6.22. Images of representative bedforms for experimental runs with pure sand in the present study. Images have been adjusted to obtain roughly the same scale. Flume panels are 0.6 m deep and 1 m long. Flow from left to right.

According to eq.(6.23), it can be expected that data in Figure 6.23 collapse into groups of comparable geometrical form or aspect, so that their hydrodynamic response to the flow should be similar. In general, the following groups of data can be distinguished: for values of $\Delta^2/(H\lambda)<0.01$, values of α_c for most of the data are lower than 0.3, in this range only one data point pertains to dunes; for values of $\Delta^2/(H\lambda)>0.01$, the highest values of α_c (higher form resistance) correspond to washed-out dunes and some points to antidunes, while the lowest values correspond to most of the data for antidunes. In between the highest and lowest α_c values, dunes show higher values of α_c than downstream-migrating antidunes.

Different authors have observed that symmetrical antidunes produce negligible expansion loses (e.g. Simons 1961); Verbanck (2008) even claims to have measured lower flow resistance values for antidunes than for plane beds. This notwithstanding, Carling and Shvidchenko (2002) indicated that if the antidunes migrate downstream, expansion loses are likely to be important. Most of the antidunes in Figure 6.23 show low form resistance

coefficients, one order of magnitude lower than dunes in sand; this trend includes even those antidunes from the new data set which migrated downstream. Since many of these antidunes correspond to low values of the product $\Delta^2/(H\lambda)$ (<0.01), low form resistance for these antidunes (and maybe for those reported by other authors as well) might be associated to low drag coefficients rather than to a total absence of expansion loses. On the other side, three points for downstream-migrating antidunes in Figure 6.23 (one for pure gravel runs and two for pure coarse sand runs), with high values of the product $\Delta^2/(H\lambda)$ (>0.015), show form resistance coefficients of the same order of magnitude as the points for runs with dunes in sand. Since these antidunes plot below the trend described by dunes, it can be said that these downstream migrating antidunes might have produced severe expansion loses, but not as high as loses produced by dunes. In turn, these downstream-migrating antidunes plot far above from the upstream-migrating antidunes from the data set of Simons et al. with similar $\Delta^2/(H\lambda)$ values. In summary and generalizing, these results suggest that downstream-migrating antidunes produce less expansion losses than dunes with equivalent product between aspect ratio (described by the bedform steepness Δ/λ) and relative height (represented by the ratio between bedform height and water depth Δ/H), but much larger than upstream-migrating antidunes, for which form loses remain low even for high values of the product aspect ratio-relative height.

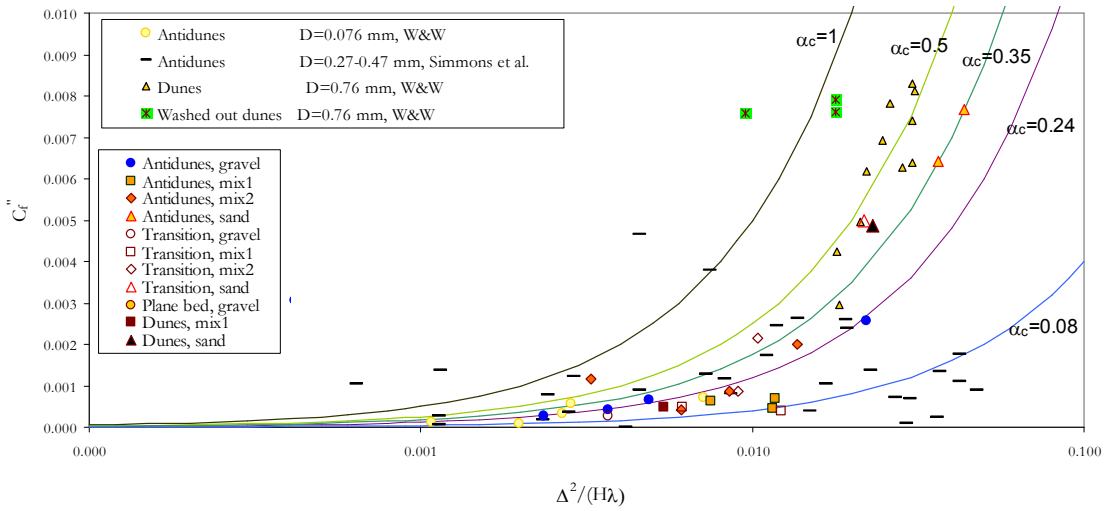

Figure 6.23. Variation of the dimensionless resistance factor due to form drag as a function of the product of the bedform steepness and the bedform relative roughness, for experimental data obtained in the present study with gravel, sand and two sand-gravel mixtures, and for the data sets of Wang and White (W&W) (1993) and Simons et al. (1966). To avoid negative unrealistic values of C_f", for antidunes in the Wang and White data set the relative roughness was taken as $k_s=0.5D_{50}$ when computing the grain shear stress with the reference plane bed method. Bedform heights for the new data set correspond to measurements of bed surface level on the channel walls, as given in Table 4.4. Wavelengths corrected for pure sand runs.

Figure 6.24. Antidunes in runs with sand-gravel mixtures. Note the rooster tails on the water surface in both runs.

6.3.2.3 Flow resistance and sand content

Concerning the effect of sand content in the form resistance coefficient, in Figure 6.23 no discernible differences can be deduced by comparison of most of the data for the two mixtures, but except for some points with values of $\Delta^2/(H\lambda)$ between 0.01 and 0.015, corresponding to runs M1E2, M1E4, M1E5, M2E4 and M2E5. Remarkable is that although the product of bedform steepness and relative height is similar for all these five runs, form resistance coefficients for mixture 2 (45% sand content in average) are roughly 4 times higher than those coefficients for mixture 1 (32% sand content in average). Images of bedforms in runs M2E4 and M1E2 are shown in Figure 6.24 in order to compare their shape and try to find special features that could have had an influence on the large differences in form resistance between both mixtures. Nevertheless, antidunes in both images have similar symmetrical shapes, heights, lengths and lee side mild slopes. In the same manner, both runs showed similar water surface activity with breaking steep rooster-tails, so that the increased flow resistance in run M2E4 cannot necessarily be attributed to larger free surface distortion. Careful comparison of video footage for both runs revealed a slightly higher agitation of the water surface in run M2E4 and a more frequent variation of the bedforms shape than in run M1E2, for which trains of antidunes were mostly similar between each other. It is possible that the larger unsteadiness observed in run M2E4 increased the turbulence production and caused higher energy dissipation than in run M1E2.

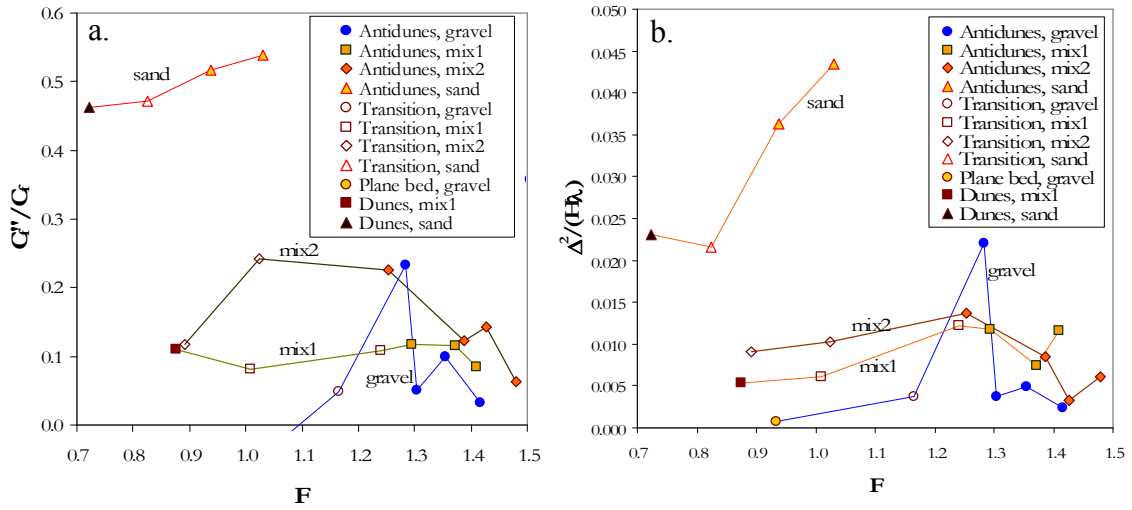

Figure 6.25. Variation with the Froude number of a) the ratio between coefficients for form resistance and total bed flow resistance, and of b) the product of the bedform steepness and the bedform relative height. Points corresponding to the same bed material are connected with lines.

The effect of sand content in form resistance can be more clearly distinguished in Figure 6.25a, where the variation with the Froude number of the ratio between the dimensionless resistance coefficient due to the bedforms and the total bed resistance is shown. This graphic reflects in more detail some of the trends observed in Figures 6.14 and 6.15 for the new data set: for very coarse sand, total bed resistance increases with flow strength along the transitional regime, and more than 40% of the total bed resistance is owed to form drag. Conversely, form resistance in pure gravel and sand-gravel mixtures takes less than 25% of the total bed resistance. In agreement with Figure 6.23, Figure 6.25a

shows that the proportion of bed resistance taken by form drag is higher for mixture 2 than for mixture 1.

Figure 6.25b shows the variation with the Froude number of the parameter $\Delta^2/(H\lambda)$ that describes the geometry of the bedforms. Comparison of Figures 6.25a and Figure 6.25b shows an approximate correspondence between trends for the same sediment, except for mixture 1. For mixture 2, the evolution of the ratio $C_f"/C_f$ with the Froude number describes a bell-shape curve, with a plateau between F=1 and F=1.3; this trend is approximately followed by the graphic to the right, that in the same range of Froude numbers shows a bell-shape curve as well, but without a plateau. Trends for sand and gravel show a similar agreement between both graphics. As far as mixture 1 is concerned, similarly as mixture 2, in the range of Froude numbers tested a bell-shape trend is followed by $\Delta^2/(H\lambda)$, with slightly lower values than mixture 2; however, this trend is not followed by the relative form roughness coefficient in the graphic to the left, which is almost constant for all runs, and circa 0.1. Therefore, contrary to pure sand, pure gravel and mixture 2, for which, as it would be expected, the amount of energy dissipation owed to the bedforms is closely related to the parameter $\Delta^2/(H\lambda)$, for mixture 1 the form resistance coefficient seems to be independent of $\Delta^2/(H\lambda)$. This result suggests the existence of a damping effect on form resistance for low sand contents; it can be argued that the difference in bed structure between mixture 1 and mixture 2 could have had an effect in these results, but since the trend is clear only for some few points this hypothesis cannot be totally proved.

It should be noted, that the computed resistance coefficient $C_f"$ includes not only the effects of drag, but also effects of wave breaking, and therefore it should not be disregarded that the higher values of $C_f"$ for mixture 2 could be related to a higher wave activity on the water surface not detected by simple naked eye observations. For experiments with fine and middle sand, Kennedy (1961) found that wave breaking had a measurable effect in the finer material but was negligible for the experiments with the coarser sand. In the same manner, the higher sand content in mixture 2 could have contributed to an increased effect of wave breaking than with mixture 1, and thus produced higher resistance factors.

Figure 6.26a shows the variation of the grain related friction factor with the Froude number. As expected, gravel beds exhibit the highest grain friction factors, while runs with 32% sand content (mixture 1) show slightly lower friction factors than gravel (roughly 90% lower) for similar Froude numbers. The lowest grain friction factors correspond to sand and to runs with 45% sand content (mixture 2), both materials show a similar trend. This result is meaningful; it suggests that grain resistance on a bed composed of 45% sand and 55% gravel is almost the same as on a bed composed only of sand. Also, since the trend followed by mixture 1 plots closer to sand and mixture 2 than to gravel, it can be stated that with a sand content as low as 32%, grain resistance is more similar to that in a bed with 100% sand than in a bed with 100% gravel. These results can be related to the change in bed structure from gravel-supported to matrix supported, that occurs roughly between sand contents for the two mixtures tested. For a matrix supported bed, coarse grains protrude less than for a gravel framework. Different authors have previously recognized the smoothing effect of sand on the bed surface, e.g. Sambrook-Smith et al. (2005).

Figure 6.26b shows the experimental bed resistance coefficients as a function of the bed Shields stress, error bars have been drawn for the former; these errors correspond to the maximum and minimum coefficients obtained with Monte Carlo-type computations, using different combinations of water discharge, bed slope and water depth within the precision of these variables in the experiments. This Figure shows a clear trend for total bed resistance of runs with uniform material to be higher than for runs with mixtures. As shown in Figure 6.25, bedforms with gravel exhibited similar, or even smaller and lower,

bedform geometries and form resistance coefficients than the runs with mixtures; nevertheless, grain roughness in gravel was higher than in mixtures, with the resulting effect of higher total bed resistance for the former. No significant differences between mixtures are evident in Figure 6.26.

Finally, no attempts were made to clarify the effect of the three-dimensionality of the bedforms in the form resistance coefficient, since the data set did not allowed direct comparisons between 2D and 3D befdforms for similar flow conditions. Maddux et al. (2003) found that 3D artificial dunes produced higher form resistance than 2D dunes, but lower turbulence. It cannot be discarded that an effect of an increased three-dimensionality could also contribute to the higher resistance of mixture 2 in comparison to mixture 1.

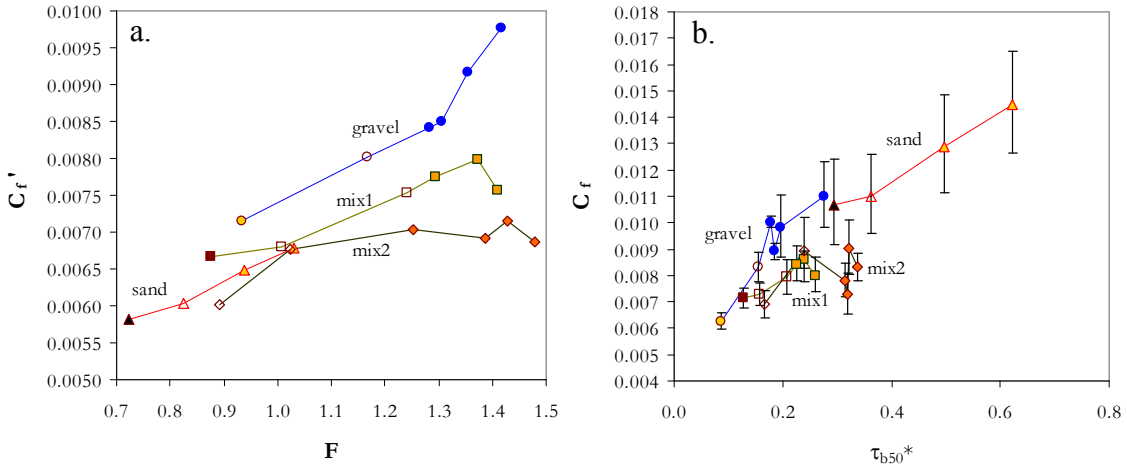

Figure 6.26. a) Variation with the Froude number of the grain related flow resistance coefficient (C_f'=τ'/[ρV²]). b) Total bed resistance dimensionless coefficient (C_f=τ_b/[ρV²]) as a function of the dimensionless shear stress for the median grain size (τ_{b50}^*=τ_b/[ρg(S_s-1)D_{50}]). Points corresponding to the same bed material are connected with lines. Symbols definition is the same as in the legends of Figure 6.25.

6.3.3 Summary

The total bed resistance exhibits an abrupt discontinuity in the transition from lower- to upper-regime in alluvial beds for which this transition is characterized by a plane bed. Thus, such discontinuity occurs when form resistance vanishes, and total bed resistance becomes equal to skin friction. For bed material with grain sizes larger than roughly 0.8 mm, plane beds in the transitional regime do not occur, and thus conventional methods considering a transition through a plane bed are no more valid. Bed resistance has been analyzed in this Section for different bed material grain sizes and sand-gravel mixtures in order to compare and identify trends for the transition from lower- to upper-regime with and without an intervening plane bed.

Adducing to similarity principles, Engelund and Hansen (1967) used a diagram relating total bed Shields stresses τ_b* to grain Shields stresses τ'* to describe bed resistance in sand bed rivers. They suggested that a single universal relationship might exist for the lower-regime trend of this diagram, and another one for the upper-regime. Based on empirical data, these authors proposed a functional relationship between τ_b* and τ'* for the lower-regime. Wang and White (1993) found that for this relationship there exists a dependency on the sediment grain size, not detected by Engelund and Hansen because of the narrow

range of grain sizes that they studied. For this dependency, Wang and White found that as the bed material becomes coarser, the total bed Shields stress tends to be similar to the effective Shields stresses on the grains. In the same manner, these authors also found that for a given grain size, in the transitional regime the relationship between τ_b* and τ'* is dependant on the relative hydraulic radius R_h/D.

The experimental data for very coarse sand and fine gravel in the present study, along with other published data sets for uniform material up to fine gravel grain sizes, corroborated the results of Wang and White partially. It was found that the coarser the grain material was in the lower regime, the closer the points plotted to the line of no drag. Nevertheless, for these materials no dependency on R_h/D was found, since the transition from lower to upper regime was seemingly continuous.

It was found that sand-gravel mixtures, even those with high sand contents, exhibited a similar trend as gravel, with a low contribution of form resistance to the total Shields stresses. These results suggested that the shift from gravel to sand behavior, in terms of bed resistance, would require very high proportions of sand in motion. On the other side, in a similar vain as for uniform fine gravel and uniform very coarse sand, no discontinuity for the bed resistance was noticeable for the transition from lower to upper regime in the mixtures of sand and gravel, i.e., that no intervening plane bed between lower- and upper-regime occurred.

The transitional regime is related to near critical flow conditions. Assuming that this regime occurs for critical flow, and using elemental bed resistance equations and a power law for the vertical distribution of velocity, it was demonstrated that the Shields stress for the onset of the transitional regime is dependent on the relative hydraulic radius, confirming the observations of Wang and White (1993). In turn, incorporating the Froude number in the relationship between τ_b* and τ'*, with the same exponent proposed originally by Wright and Parker (2004b), a good collapse of the flume experimental data was obtained.

Dimensionless resistance coefficients for the bedforms C_f" were calculated for the experimental data set. From elemental theory, it was shown that these coefficients are a function of drag forces, which in turn are dependant upon the bedform height, flow velocity and drag coefficient. From experimental measurements in artificial dunes Shen et al. (1990) found that the drag coefficient is dependent on the bedform relative roughness, defined as the ratio between the bedform height and the water depth. They also found that the drag coefficient shows and abrupt increase for relative roughness values roughly higher than 0.35. For the experimental data in the present work, along with other published data sets, a similar value for a change in trend of the resistance coefficients was obtained. This indicates that if the bedform height increases with sand content, the effect in total bed resistance can be strongly increased if this limit is exceeded.

Engelund and Hansen (1967) computed bedform expansion loses with Carnot's formula. From the original reasoning of these authors, it was here found that the dimensionless form resistance coefficient can be described in terms of the product of the bedform steepness and the bedform relative height ($\Delta^2/H\lambda$). Plots of C_f" versus $\Delta^2/H\lambda$ for different published data sets and the data set obtained in the present work showed a good collapse into groups of similar characteristics. In general, antidunes and dunes showed low and high values of $\Delta^2/H\lambda$ and C_f", respectively, being the values for antidunes approximately one order of magnitude lower than for dunes. Three points for downstream-migrating antidunes, in gravel and sand, were out of these trends, and compared to dunes and upstream-migrating antidunes with similar $\Delta^2/H\lambda$ these points plotted in between. Accordingly, it was concluded that downstream-migrating antidunes produce less expansion losses than dunes with similar steepness and relative height, but much higher losses than upstream-migrating antidunes with similar $\Delta^2/H\lambda$. Similarly, some points for

the two sand-gravel mixtures of the present study showed slightly different trends to the rest of points. Though all of these points had similar values of $\Delta^2/H\lambda$, form resistance coefficients were higher for the mixture with higher sand content. Comparison of the shape and geometry of bedforms in video footage for some of these runs showed no great differences, and thus it was speculated that the differences could be related to an increased turbulence production owed to a higher unsteadiness in the shape of the bedforms and of the water surface. On the other side, from comparison of the ratio between the bedform resistance coefficient and the total bed resistance, it was found that it is likely that low sand contents (or high gravel content) produce a damping effect on form resistance.

Flow resistance coefficients due to sediment grain roughness were similar for runs with sand and mixtures with 45% sand content, while for runs with mixtures with 32% sand content these coefficients were closer to sand than to gravel. It was concluded that these results are related to the smoothing effect of sand over gravel beds, with a sharp transition in grain resistance from a gravel behavior to a sand behavior roughly occurring in the same range of sand contents for which the bed changes from a gravel supported to a matrix supported structure.

Comparison of total bed resistance coefficients for the four different materials tested in the experiments showed that runs with mixtures exhibited lower values than those for uniform material. Even when gravel bedforms were of similar geometry as those in mixtures, gravel runs showed the highest total resistance coefficients since grain roughness was higher for these runs than for runs with mixtures. No significant trends were found between total bed resistance coefficients for the two mixtures.

Finally, it was indicated that the results exposed should be considered with caution since additional components of bed resistance, like wave breaking or the shape of three-dimensional bedforms, were not studied and they might have had an effect on the computed form resistance coefficients.

6.4 SEDIMENT TRANSPORT

In previous Chapters, different plots were presented relating the experimental sediment transport rates to average flow parameters (Figures 3.36, 4.5 and 4.6). Figure 4.6 showed the total sediment discharge as a function of average bed shear stress acting on the bed; from this Figure it could be deduced that for a given bed material load to be transported, higher bed shear stresses were required if the bed was composed of uniform gravel or uniform sand than if it was composed of any of the two mixtures. Approximately, the two mixtures collapsed together in a similar trend and the two uniform materials together following a different pattern; the tendency of the uniform material followed a less steep increase of sediment discharge that clearly separated from mixtures at increasing bed shear values. An explanation for this similar trend between uniform sand and uniform gravel should be found in the portion of shear that bedforms take due to drag, and the residual shear taken by the sediment grains to be set in motion. As shown in Figure 6.25, form resistance for sand beds accounted for more than 45% of the total bed resistance, while for gravel and sand-gravel mixtures it accounted for less than 25%. For the sand and gravel used in the experiments, there seems to be a compensation effect between form drag and skin friction, that produced an approximate equal mobility of the two uniform materials when tested in separated runs; put in other words, for sand grains, whose weight is lower than gravel grains, skin friction was reduced due to the high drag generated by the steep bedforms, while for gravel, the proportion of total shear taken by the grains was much higher in comparison to sand grains because the bedforms were gentler. Both effects compensated to result in an apparently unique sediment transport curve for uniform sand

and uniform gravel. In turn, form drag for mixtures was of the same order of magnitude as for gravel runs, but the mean grain diameter of the mixtures was lower than for gravel; therefore, although shear over the grains was similar for gravel and mixtures, since the average grain size of the mixtures was finer they had a higher mobility than gravel, reflected this with the uppermost and steepest curves in the graph of Figure 4.6.

In contrast to Figure 4.6, plots in Figure 4.5 give a more local description of the physical processes directly involved on the motion of particles. The use of skin friction in Figure 4.5 instead of total shear reflects the intuitive reasoning that the coarser the grain size of the bed material the higher the shear stress required to mobilize the particles. For a more general description of the sediment transport process in the experimental runs, similarity collapse of the family of curves in Figure 4.5 can be pursued by using appropriate dimensionless combinations of the most relevant variables involved. A procedure to achieve similarity will be presented in Section 6.4.2.

Bed slope versus the ratio between solid discharge by weight and water discharge by volume have been used to plot the experimental data in Figure 3.36; although an approximate collapse was obtained, this plot cannot be considered as of universal validity, but just for the flume and bed materials used. The selected non-dimensional variables, namely, bed slope versus the ratio between volume solid and water discharges, do not account for average forces acting on the grains, neither for the characteristics of the sediment. Thus, a more general combination of dimensionless parameters is required for a sound description of the process.

From a dimensional analysis for bedload transport of mixtures in locally quasi-equilibrium flows at a macroscopic scale, Parker (2004b) reduced the unit bedload transport rate to the following functional relation

$$q_i^* = T_b\left(\tau_i'^*, \frac{D_i}{D_r}, \sigma_g, \mathrm{Re}_p\right) \qquad (6.25)$$

where T_b is a dimensionless bed load transport function, D_i is the grain size for the i-th size fraction of the sediment mixture, D_r is a representative diameter for the sediment mixture, q_i^* is a widely used dimensionless number for normalizing unit solid discharge, known as the Einstein number, Re_p is a particle Reynolds number, σ_g is the geometric standard deviation of the sediment mixture, and $\tau_i'^*$ is the Shields number associated with skin friction for the i-th size fraction. The Einstein number is given by

$$q_i^* = \frac{q_i}{F_i\sqrt{(S_s-1)gD_i}D_i} \qquad (6.26)$$

where F_i is the fractional content of the i-th sediment size fraction available to be entrained from the bed, g is the gravitational acceleration, S_s is the relative density of the sediment ($S_s=[\rho_s-\rho]/\rho_s$, with ρ and ρ_s being the water and sediment densities, respectively) and q_i is the unit volume load discharge of sediment in the i-th size fraction, so that

$$q_i = f_i q_S \qquad (6.27), \text{ and} \qquad q_S = \sum_{i=1}^{n} q_i \qquad (6.28)$$

where f_i is the fractional content of the i-th sediment size fraction in the solid discharge, q_S is the total unit load discharge and n the total number of size fractions. The Shields number in eq.(6.25) is given by

$$\tau_i'^* = \frac{\tau'}{\rho(S_s-1)gD_i} \qquad (6.29)$$

where τ' is the shear stress associated with skin friction. Finally, the particle Reynolds number is defined as

$$\mathrm{Re}_p = \frac{\sqrt{(S_s-1)gD_i}D_i}{\nu} \qquad (6.30)$$

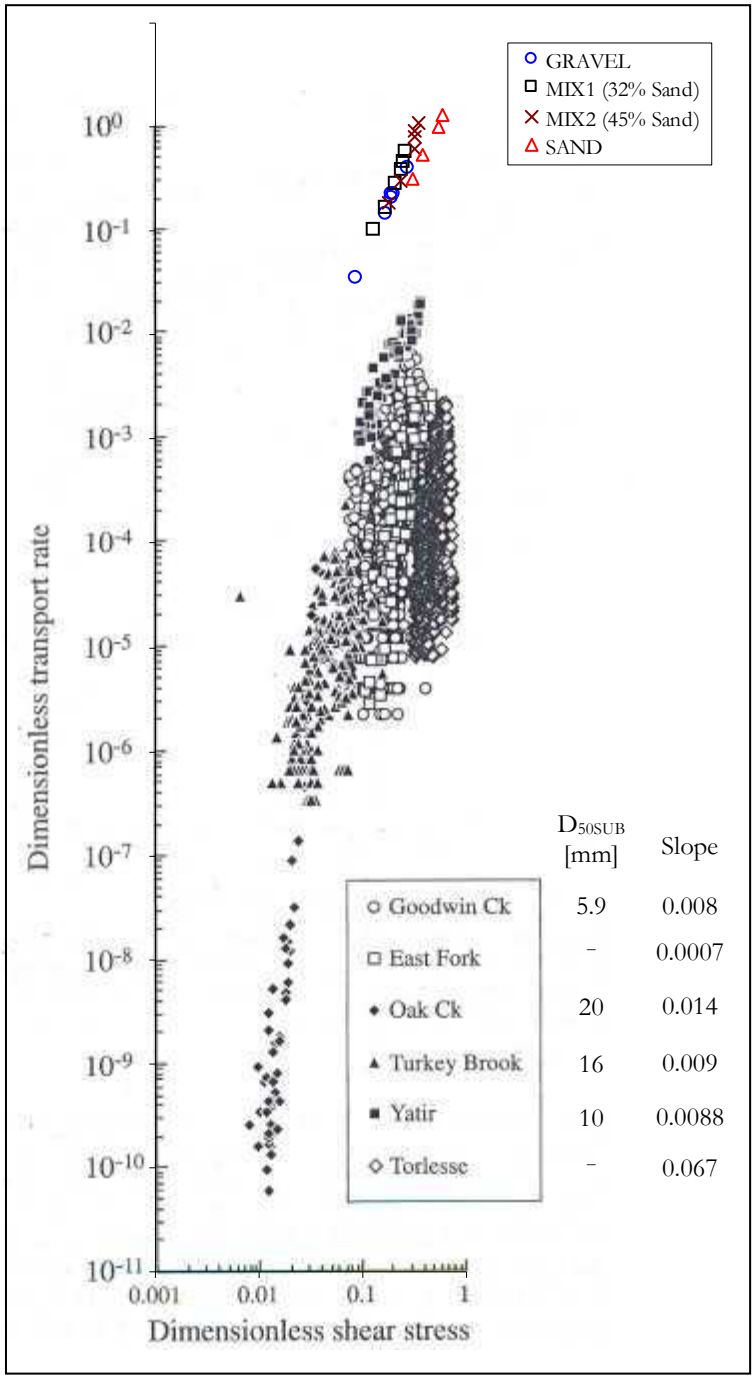

Figure 6.27. Comparison of experimental data in the present work, with data from sediment transport measurements in natural streams (one ephemeral, Yatir; one seasonal, Goodwin Creek; and four perennial streams) presented by Reid and Laronne (1995). Dimensionless shear stress defined as $\tau_b/[\rho g(Ss-1)D_{50}]$, where D_{50} is the median diameter of the bed sediment, g is the gravitational acceleration, S_S is the relative density of the sediment, ρ is the water density and τ_b is the average shear stress in the channel; dimensionless transport rates are defined by $q_S/[g(Ss-1)D_{50}^3]^{0.5}$, where q_S is the total unit solid discharge by volume. D_{50SUB} is the median diameter of the subsurface bed material.

where ν is the water viscosity. For gravel beds, the particle Reynolds number is generally dropped from eq.(6.25) since most of the flows that put in motion particles in the grain size range of gravel customarily are hydraulically rough.

The dimensionless variables given by eqs.(6.26) and (6.29) have been widely used in sediment transport formulas. For comparison of the experimental data with typical ranges of sediment transport measured in some natural rivers, these same variables were used for the plot shown in Figure 6.27. For this Figure, the dimensionless transport rate was calculated using the total sediment load and the median diameter of the bed material, while for the Shields number the median diameter of the sediment, and the total bed shear were used instead of the grain related shear stress. The dimensionless transport rates of the field data, pertaining to ephemeral, perennial and seasonal streams, span over ten orders of magnitude. The new experimental data plot above the bulk of field measurements. It stands out that for similar ranges of dimensionless shear stress, the experimental dimensionless transport rates can be several orders of magnitude higher than those for field data. So far, three main reasons can be invoked to explain this behavior; first of all, the use of total shear stress instead of skin friction hinders a direct comparison based on the physical processes involved in the movement of the sediment grains. The form related shear stress in natural streams can be much larger than in controlled flume experiments since in the former local complexities, like vegetation or channel sinuosity, can increase form drag considerably. Secondly, grain sizes from the field data are coarser than those in the experiments (average mean diameters were 1.5 mm and 4 mm for sand and gravel, respectively); thus, critical shear stress for beginning of movement could be lower for the experimental data, and this would cause the shift to the right with respect to the bulk of field data; and lastly, for some of the seasonal and perennial streams bed armoring could have hindered the complete mobilization of finer grain sizes in the bed, so that transport rates would be below the capacity of the flow.

Among the natural streams in Figure 6.27, those whose characteristics most approach to the characteristics of the experimental data are Goodwik Creek, with a fine gravel and a slope of almost 1%, and Turkey Brook and Yatir streams, both with medium gravel and slopes slightly lower than 1%. The runs with the lowest dimensionless transport rates in the experimental data are of the same order of magnitude as the points with highest transport rates for Yatir stream. Hence, the new experimental data would define an upper bound for dimensionless sediment transport rates in these natural rivers. The plot of the experimental data in Figure 6.27 highlights the exceptionally high sediment-feed rates used in this work.

For the study of selective transport in sediment mixtures, Parker et al. (1982b) introduced the following parameter as a substitute of the dimensionless sediment transport rate

$$W_i^* = \frac{q_i^*}{\tau_i'^{*3/2}} = \frac{(S_s - 1) g q_i}{F_i u_*'^3} \tag{6.31}$$

where u'_* is the shear velocity associated to skin friction given by

$$u_*' = \sqrt{\frac{\tau'}{\rho}} \tag{6.32}$$

Eq.(6.25) can thus be rewritten as

$$W_i^* = T_b\left(\tau_i'^*, \frac{D_i}{D_r}, \sigma_g, \mathrm{Re}_p\right) \tag{6.33}$$

Among the advantages adduced by Parker et al. (1982b) of the use of W^*_i instead of q^*_i is the elimination of any spurious correlation with the sediment size, which appears in the definition of q_i^* and $\tau_i'^*$, but when computing W^*_i is canceled.

Using the dimensionless relations given in eq.(6.33), in search of generalization of the experimental data for sand, gravel and the two mixtures, a collapse of the families of curves

in plots of Figure 4.5 can be expected to be obtained by means of an adequate similarity transformation. In this Section this transformation is pursued and the differences in mobility for the experimental gravel and sand are analyzed when they are isolated and mixed. A comparison between available sediment transport models for sediment mixtures is shown first. Later the effect of sand content in transport and its consideration in prediction models is analyzed, and a brief discussion on the conditions affecting the performance of sediment transport predictors is presented. Finally, some advantages and likely applications of the modified approached used for pursuing the collapse of the data is given.

6.4.1 Comparison with sediment transport predictors

Different formulae exist in literature for computation of sediment transport. In this Section the experimental data are compared with ten of these predictors. It would be desired that a sediment discharge predictor of general applicability could be applied to different hydraulic conditions and types of sediments, whether being of uniform or non-uniform grain-size. Nevertheless, due to the empirical component of these formulations, a widely accepted principle in selecting a formula for predicting sediment discharge is to apply that for which the ranges of variables to use in it are similar to those from the data set from which the formula was derived. Attending to this advice with respect to the characteristics of the sediment, formulae which were developed for being applied to gravel-bed rivers were selected for the comparisons.

Sediment transport predictors developed for gravel-bed rivers must deal with poorly-sorted material. In considering this, some researchers have adapted formulae originally developed for uniform material to consider heterogeneous sizes. The most important and long recognized effect in sediment transport of the coexistence of particles of different sizes in the bed is hiding-exposure (e.g. Egiazaroff, 1965). As it was described in Section 2.4.2.2, hiding refers to the sheltering of the finer particles from flow by the coarser grains, while exposure is related to the greater protrusion toward the flow of coarse granules; the combined effects of hiding and exposure are claimed to be one of the main mechanisms by which the so-called equal mobility of different grain size fractions is achieved, which means that the movement of all particles begins at the same value of shear stress irrespective of their grain size. Hence, to extend the use of formulae originally developed for uniform material to be applied to grain-size mixtures, some authors have included a correction to consider hiding-exposure effects in the critical shear stress for beginning of movement of each size fraction.

Wilcock et al. (2001) presented experimental evidence where besides hiding-exposure, it was demonstrated that fractional sand content f_s in sand-gravel mixtures exerted a measurable influence in the initiation of motion of the different grain size fractions. This effect was subsequently considered in the development of sediment transport formulae by Wilcock and Kenworthy (2002) and Wilcock and Crowe (2003). Until present, these are the only predictors that consider sand content as an explicit variable in the computation of sediment transport.

In the application of sediment transport models, a fundamental question comes up when selecting the characteristics of the sediment to be used in the computations. Since vertical grain sorting is a common feature of gravel-bed rivers, most of them exhibiting a coarse surface layer, an extended practice suggests using the characteristics of the subsurface material in the reasoning that the grain size distribution of this material has been found to be more stable in the long term and normally contains most of the grain size

fractions present in the bed. Nevertheless, there is an inconsistency in using the substrate† material in computing sediment transport, since the material on the bed surface is the material that actually is on direct contact with the flow; the subsurface material is contingent on the superficial texture adjustments to local flow capacity to transport sediment and the upstream sediment supply. Hence, for being physically coherent, a complete computation of sediment transport should be surface based and should account for surface texture changes with a proper implementation of mass conservation equations. The use of surface based sediment transport relations is thus preferred for implementation of numerical models and refined calculations.

Description of an instantaneous bed surface texture to be associated with related flow and sediment transport conditions entails a complex challenge, both in field and in experimental flumes. In developing most of the surface based sediment transport formulae, the researchers overlooked this complexity by relating equilibrium sediment transport conditions under a given flow to a reduced number of bed surface samples taken after water was drawn down. In order to obtain a more accurate picture of the changes in grain sizes on the entire bed surface and to reduce bias associated to common adhesive aerial bed surface sampling methods (as the one described in Section 3.3.2.6.3), Wilcock and McArdell (1993) and Wilcock et al. (2001) performed experiments (those from which the formulae of Wilcock and Kenworthy [2002] and Wilcock and Crowe [2003] were developed) in which each grain size fraction of the sand-gravel mixture used was painted with a different color; when water was stopped, for describing the bed surface texture, direct point counts were feasible of the number of particles of each size fraction on the bed surface. Data sets obtained by these authors are, perhaps, the most reliable in relating surface grain size distribution to sediment transport and flow conditions; however, it should be considered that even these detailed observations do not give an exact picture of the instantaneous bed surface texture with the description of the grain sizes available to be set in motion, since over these superficial particles exposed to flow for entrainment overlapped the sediment that was in motion and conformed the solid load just before the flow was stopped.

Parker et al. (1982c) considered that the use of surface or subsurface material in armoured streams is somehow arbitrary. This is particularly true for bulk computations of sediment transport when the flow is competent to put in motion all grain sizes present in the bed. For such conditions there is a constant interchange between surface and subsurface material, and thus all grain size fractions have a high probability of interacting with the flow. With this in mind, for the experiments of the current work, since all grain size fractions were in motion when mobile bed equilibrium was attained, a condition imposed by the sediment-feed operation of the flume (rigorously "hybrid-feed", see discussion in Section 3.2), the grain size distribution considered for computations in the formulas was that of the feeding material. The bed surface at the end of the runs consisted of patches of approximately homogeneous grain size distributions (see Section 3.3.2.6.1). This final condition cannot be directly related to the surface texture when mobile bed equilibrium prevailed in the channel, since steep and speedy bedforms were ubiquitous and sediment movement was generalized all over the bed surface. Most of the bedforms were washed away by the waning flow and thus the preserved grain size sorting on the bed surface was an artifact of the grain movement during the decreasing water flow. Hence, the final bed surface texture was not necessarily related to the sediment transport and flow conditions during morphodynamic equilibrium. Characterization of the final surface texture serves only as a reference for sorting trends likely to occur after the recession of steep hydrographs and as an initial condition for computation of sediment transport at low flows

† "Subsurface" and "substrate" are used here indistinctly to refer to bed material not directly exposed on the bed surface.

after a very high flow event. On account of this, it is convenient and realistic to consider that the average grain size distribution of the bed material was the same as the grain size distribution of the sediment load, i.e., of the feeding material. In considering this, it is assumed that equal mobility occurred in the channel, which is a prescription of sediment-feed experiments. For accomplishing equal mobility in mobile bed equilibrium state, different mechanisms act to match the sediment feed rate with the local sediment transport capacity, among which are hiding-exposure and surface armouring; in the experiments herein reported, bedforms played an important role in spatially regulating sediment sorting for the achievement of equal mobility.

The selected models for comparison with the experimental results are listed in Table 6.2 with some of their characteristics. Most of them are fully described in Parker (2004a) (except the model of Almedeij and Diplas [2003] and the modified versions of the formula of Meyer-Peter and Müller by Wong and Parker [2006]), and have been applied as indicated therein (except Wilcock and Kenworthy [2002], applied as originally stated by the authors when subsurface material is used; models not described by Parker [2004a] are applied as indicated in the original references) but with the following details:

- Computations for the experiments with mixtures were performed for only two grain size fractions, sand and gravel (except with the model of Almedeij and Diplas [2003], which was designed for computing total load only), while for the experiments with uniform sand and uniform gravel computations were performed with only one size fraction, i.e. only total load was computed. The use of two grain size fractions for the computations with mixtures is justified since the pure sand and the pure gravel were well-sorted materials (σ_g<1.6, see Section 3.5.1). Furthermore, by using only two size fractions disparities between models and their robustness for being applied to either well- or poorly-sorted materials can be more evident. Wilcock (1998) alluded to practical and theoretical advantages of using a two-fraction approach; following this, the model of Wilcock and Kenworthy (2002) was deliberately designed to be applied for two-fractions. Thus, comparisons with this model are of especial interest, also because it considers the effect of sand in the computation of the critical shear stress.
- Sand was not extracted from the grain size distribution in computations with models designed to be used only with size fractions in the gravel range.
- The characteristics of the feeding material (as given in Tables 3.28 and 3.29) were used for the computations, even in surface based formulae.
- The Meyer-Peter and Müller formula was chosen for the comparisons because it has been widely used for computations in gravel-bed streams. Recently, Wong and Parker (2006) reanalyzed the data originally used by these authors and proposed an amendment to the formula in light of recent developments for flow resistance. The corrected formula was used here. Also, this formula was used again considering a computation of the critical shear stress of each size fraction and a correction for hiding-exposure using the criterion of Egiazaroff (1965). For calculation of the critical Shields stress the following equation suggested by Parker (2004b, from original developments by Brownlie [1981] and Neill [1968]) was used

$$\tau_c^* = 0.5\left(0.22\,\mathrm{Re}_p^{-0.6} + 0.06\cdot 10^{-7.7\,\mathrm{Re}_p^{-0.6}}\right) \qquad (6.34)$$

  where Re_p is the particle Reynolds number given by eq.(6.30).

Figure 6.28 shows comparisons between experimental and computed unit solid loads with perfect agreement diagrams, while Figure 6.29 presents a dispersion diagram of the average ratios between computed and measured solid discharges, distinguishing between the two grain size fractions considered and total load. Similarly as with the results of

Gomez and Church (1989), who performed a careful comparison of sediment transport formulae for gravel-bed rivers with field and experimental data, the results here are discouraging; no single model predicts solid load reasonably well for all the different bed materials. Anyhow, some hints can be extracted from these comparisons.

Table 6.2 Characteristics of sediment transport predictors considered for comparison with the experimental results.

Formula	**Bed material**	**Data set**	**Critical or reference Shields stress**	**Observations**
Ashida and Michiue (1972)	Surface	Experimental	For D_m: $\tau^*_c=0.05$	Characteristic grain size is the arithmetic mean of the mixture
Parker, Klingeman and McLean (1982c)	Subsurface	Field	For D_{50}: $\tau^*_R=0.0876$	Applicable only to the gravel fractions
Parker (1990)	Surface	Field	For D_m: $\tau^*_c=0.0386$	Applicable only to the gravel fractions
Wu, Wang and Jia (2000)	Subsurface	Experimental and field	For uniform sediment: $\tau^*_c=0.03$	-
Powell, Reid and Laronne (2001)	Surface and subsurface	Field	For D_{50}: $\tau^*_R=0.03$	Based on data from an ephemeral stream without pavement, thus can be treated as surface or subsurface based. Applicable only to the gravel fractions.
Wilcock and Kenworthy (2002)	Surface and subsurface	Experimental and field	As a function of sand content. For gravel τ^*_R ranging from 0.043 to 0.008; for sand a minimum of 0.045 and maximum related to the ratio between gravel and sand grain size.	Two-fraction model for sand and gravel. Sand content affects critical shear of both fractions. Different coefficients for surface and subsurface material. Here the subsurface version was used.
Wilcock and Crowe (2003)	Surface	Experimental	For D_m as a function of sand content f_s, so that at the extremes: for $f_s=0$, $\tau^*_R=0.036$ and for $f_s=1$, $\tau^*_R=0.021$	Sand content affects critical shear of D_m.
Almedeij and Diplas (2003)	Surface and subsurface	Field	For the mode of the grain size distribution: $\tau^*_c=0.03$	Only for unimodal sediment and for total material load. The representative diameters of the surface and of the subsurface materials intervene in the formula.
MPM* modified by Wong and Parker (2006)	Subsurface	Experimental	For all size fractions: $\tau^*_c=0.047$	-
MPM* modified by Wong and Parker (2006) with Shields and hiding-exposure correction	Subsurface	Experimental	Eq.(6.34) for critical Shear stress of D_{50}, and hiding-exposure correction of Egiazaroff for each size fraction	-

*MPM= Formula originally presented by Meyer-Peter and Müller (1948).

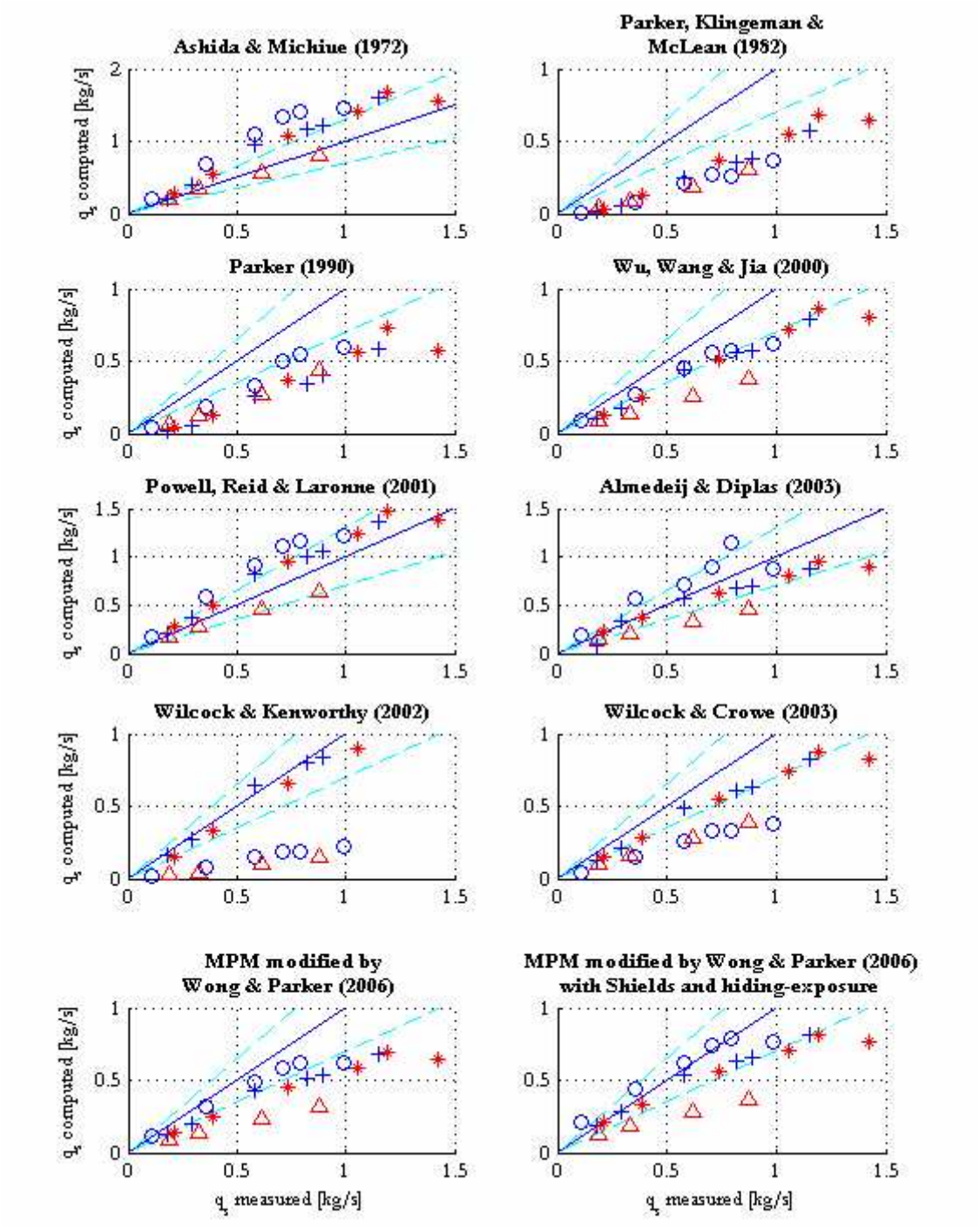

Figure 6.28. Comparison of measured unit sediment discharges (= unit sediment-feed rates) for the 22 experimental runs with computed unit sediment discharges using the ten sediment transport predictors listed in Table 6.2. Symbols for the bed material are: circles=gravel, triangles=sand, crosses=mix1 (32% sand content), and asterisks=mix2 (45% sand content). Dashed lines are for deviations ±30% from perfect agreement.

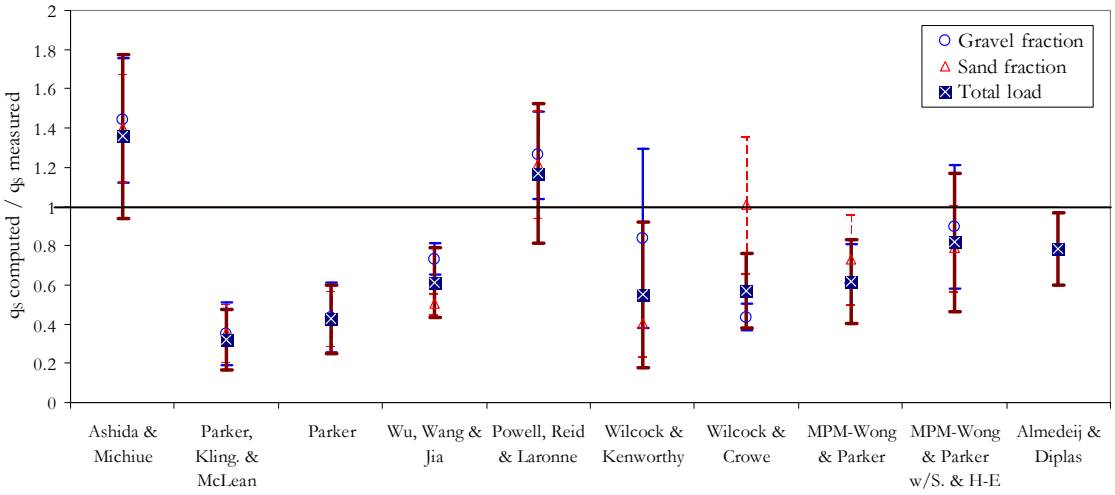

Figure 6.29. Dispersion diagram of the average ratio between computed and measured sediment transport rates for sand fraction, gravel fraction and total load for the ten selected sediment transport predictors. Error bars account for the standard deviation of the 22 experimental runs.

Assessment of the relative performance of the models in order to define the most suitable is not straightforward. From different perspectives particular attributes can be considered as most valuable, and for each of these points of view a different model could result as the best performing. For instance, if the most accurate model in the computation of the total load is considered, perhaps the model of Almedeij and Diplas would be chosen as the best performing, since with this formula for most of the runs the ratio computed-measured (c-m) was within ±30%; in turn, if the most important attribute was not necessarily the accuracy, but the robustness in dealing either with uniform or non-uniform material, probably the model of Parker, Klingeman and McLean and the model of Parker would be the best, since they result in the least deviations of the c-m ratio between bed materials; conversely, if only sand-gravel mixtures were considered, the two-fraction model of Wilcock and Kenworthy would be the best, on account of that most of the computed c-m ratios for runs with mixtures were within ±15%; and, finally, if a compromise between all these aspects is considered, perhaps the model of Wu, Wang and Jia would get ahead of the others.

Due to all these difficulties in the assessment of the models performance, rather than a definition of a best performing model, a thorough analysis of the data to be later faced up to the models seems to be more appropriate. In the following Section the data are thus analyzed, along with similar data sets, giving especial emphasis to clarify the importance of sand content in volume load rates.

6.4.2 Similarity collapse of the data

For the assessment of the likely effects of sand content in sediment transport of the experiments herein reported, first a similarity transformation is here applied using a reference value of the dimensionless sediment transport W^*. This approach, introduced first by Ashida and Michiue (1972, after Parker et al. 1982b), has been widely employed for pursuing approximate similarity collapses of fractional transport rates. The approach is here applied for comparing transport rates of sediment mixtures and uniform material, and is adapted for the current case in which sediment load rates are substantially high, far above critical shear for the onset of sediment motion.

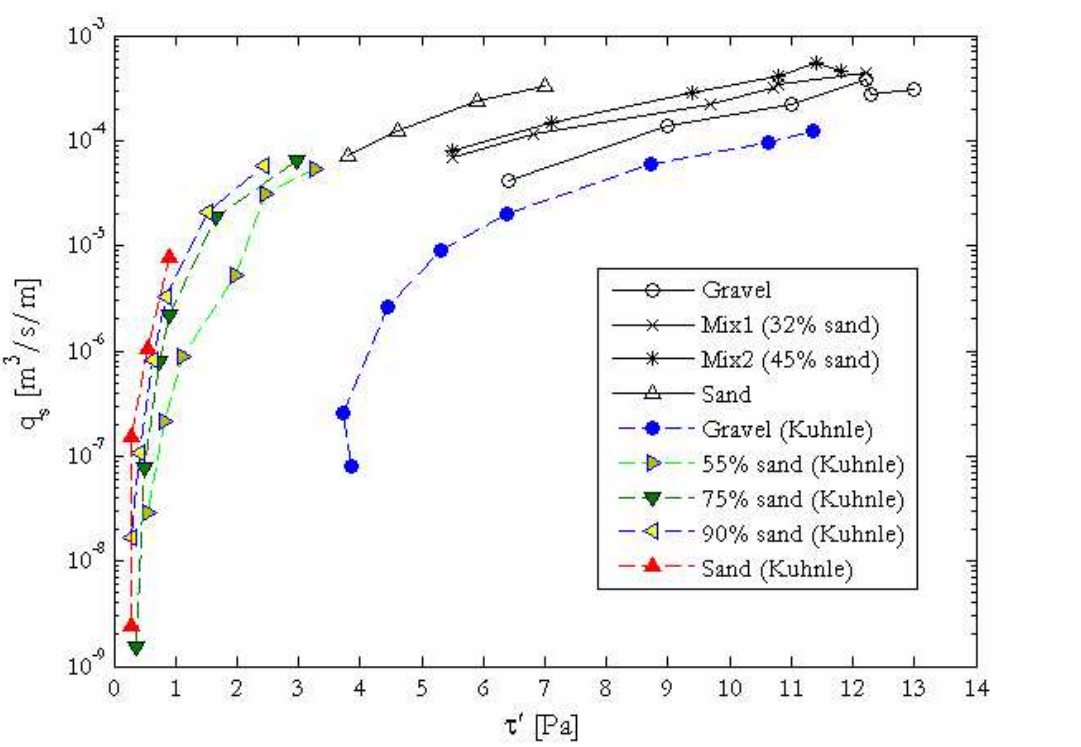

Figure 6.30. Unit sediment transport rates as function of shear stress related to skin friction (obtained with the shear stress partition method described in Chapter 4) for the data set obtained in the present work and for the data set of Kuhnle (1993a).

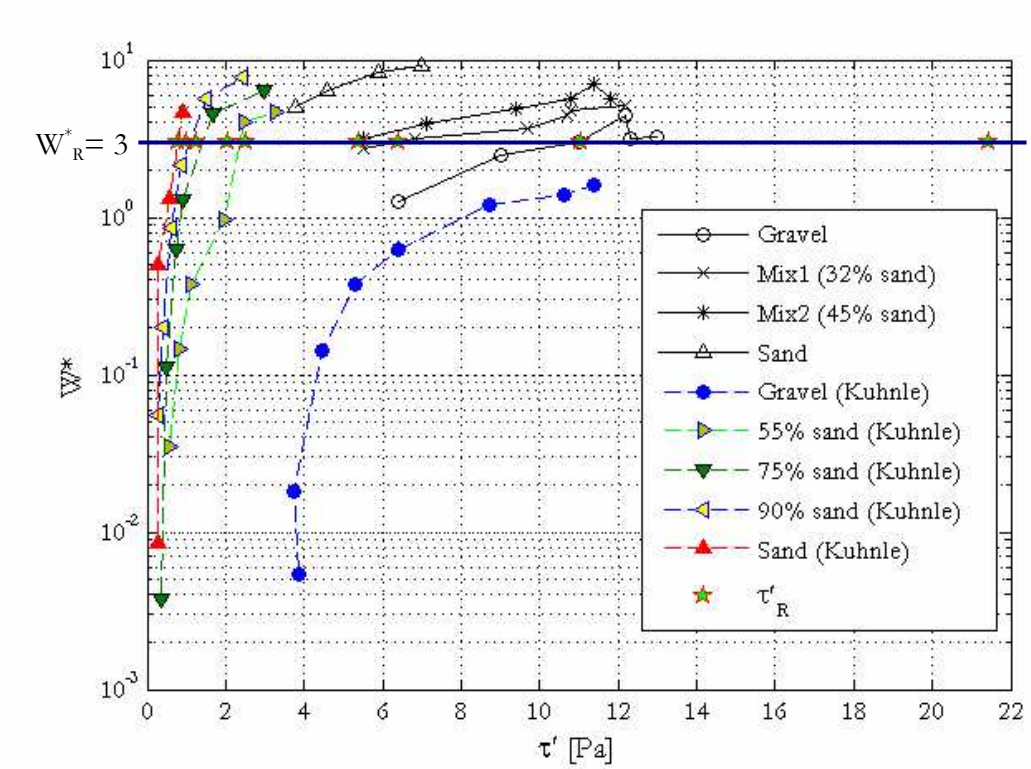

Figure 6.31. Dimensionless sediment transport parameter W^* (given by eq.[6.35]) as a function of shear stress related to skin friction (obtained with the shear stress partition method described in Chapter 4) for the data set obtained in the present work and for the data set of Kuhnle (1993a). The reference values of W^* and τ' considered for similarity transformation are indicated.

The sediment feed rates of the experimental data have been plotted in Figure 6.30 as a function of the grain related shear stress, computed as described in Chapter 4 ('Engelund and Hansen' columns in Table 4.5). Along with the new experimental points, flume data from Kuhnle[‡] (1993a) have been plotted in this Figure as well. The data set of Kuhnle consists of 30 experimental runs, with beds composed of sand, gravel, and three bimodal mixtures of these two materials with 90%, 75% and 55% sand content, respectively. Mean diameters of the pure sand and pure gravel were 0.48 mm and 5.6 mm, respectively; sand and gravel were well-sorted materials (σ_g<1.6), so that, for the bimodal mixtures, grain sizes between roughly 2 and 2.4 mm were not represented in the mixtures. Grain shear stress values used for plots in Figure 6.30 were those obtained in Chapter 4 (Table 4.8).

In Figure 6.30, the groups of data of same bed material describe a monotonic increase of transport rates with shear stress, as general relations for sediment transport do. For these relations, usually three regions can be distinguished: the first at low shear stresses where the increment of sediment transport with respect to shear is steep; the second at intermediate shear values, where the derivative of transport rate with shear stress decreases rapidly; and finally a third region at high shear stresses, where the function has a low gradient and tends toward an upper value of sediment discharge. As it can be seen in Figure 6.30, the groups of data for the current work seem to correspond to the region of low gradient, while data from Kuhnle span from the low shear stress region to the intermediate region. If in Figure 6.30 the groups of points of same bed material were described by curves, it can be expected that these curves would resemble each other in shape. If so, the data can be collapsed into a single curve by applying a similarity transformation.

For pursuing the collapse of the data in Figure 6.30, sediment transport rates are normalized using the dimensionless parameter W^* defined by eq.(6.31). Instead of using it for different size fractions, W^* is used here for the total bed material load since the main interest of the analysis is to recognize likely effects of sand content on the transport of the bulk of grain sizes. Hence

$$W^* = \frac{(S_s - 1) g q_S}{u_*'^3} \qquad (6.35)$$

Note that W^* is independent of grain size, thus, until here there is no relevance whether surface or subsurface material is considered or of which representative grain size should be used. Plots of the data using the dimensionless sediment transport parameter W^* are shown in Figure 6.31.

Different authors have pursued a similarity collapse of fractional transport rates of non-uniform sediments, either with flume data (e.g., Wilcock and Crowe, 2003; Almedeij et al., 2006) or field data (e.g., Parker et al., 1982b; Church and Hassan, 2002). They all have defined an arbitrary low ("but measurable" [Parker and Klingeman, 1982]) reference value of dimensionless sediment transport (normally W^*_R=0.002) and associated to this value they have found a reference shear stress τ_{Ri} for each size fraction D_i from plots of W^*_i versus τ_b or W^*_i versus τ_b^*; this reference shear value has been obtained either by fitting curves by least squares (e.g., Parker et al., 1982b; Diplas, 1987) or by interpolating and extrapolating by eye (e.g., Wilcock and Kenworthy, 2002; Almedeij et al., 2006). The reference shear stress value thus obtained has been considered as a surrogate of critical shear stress for sediment motion onset. If similarity is satisfied, a plot of W^*_i versus τ_b/τ_{Ri} defines a single curve for all the points.

[‡]The data set was corrected for the values of water discharge which were obviously wrong for the data corresponding to pure gravel (runs G3, G4, G5 and G6) bed material composition. Water discharges were thus obtained from the rest of hydraulic data, namely, water depth, slope, and bed material diameter to be used in a flow resistance relation considering flat bed.

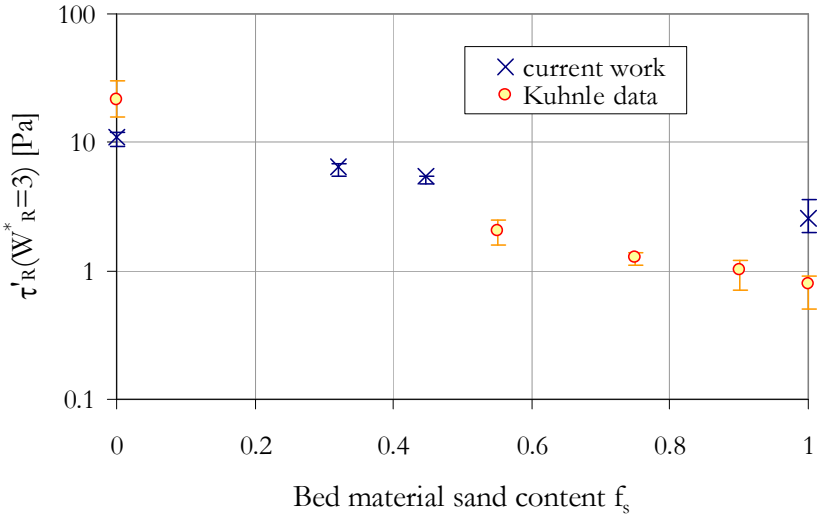

Figure 6.32. Reference shear stress values obtained from data in Figure 6.31 for W^*_R=3, as a function of sand content of the bed material. Error bars indicate likely maximum and minimum values of τ'_R according to the scatter of the data.

For the experiments herein reported, sediment transport rates were extremely high and no runs were performed for low or intermediate shear stress values. A similar situation can be encountered in ephemeral rivers prone to flash floods, as the Yatir stream shown in Figure 6.27: low shear stress events occur seldom, thus data sets might include only information for high sediment transport rates far apart from the initiation of sediment motion. In view of this difficulty, in pursuing the similarity collapse of the data for such cases, it would be convenient to define a reference value of W^* much higher than the commonly used low value of W^*_R=0.002. A value of W^*_R=3 was here considered, since most of the groups of data in Figure 6.31 have points above and below this value; hence, extrapolations were only required for runs with pure sand and with mixture 2 of the current work, and for pure gravel runs in the experiments of Kuhnle. Also, for W^*_R=3 the slope of the trends defined by the groups of data is neither so steep neither extremely tender, making it easier to define a more accurate reference shear value.

Reference shear values τ'_R for each bed material were obtained by interpolating or extrapolating by eye the trend followed by each group of data, to find the value of τ' that matched W^*=3. Only for pure sand of the current experiments and pure gravel of the experiments of Kuhnle, two best-fit curves were obtained to estimate τ'_R; these were a power fit and a logarithmic fit, and an average value of both fits was considered. For pure gravel, following the criterion from Wilcock and Southard (1988), more weight was given to the nearest points to W^*_R, and therefore only the four points with highest W^* values were used in order to represent the upper low gradient trend unbiased by the lower points. The estimated τ'_R values have been indicated in Figure 6.31 (star symbol) and are presented in Table 6.3. Likely maximum and minimum values of τ'_R, according to the scatter of the data, were also obtained by eye for the two data sets; they are shown in Figure 6.32 with τ'_R values as a function of sand content in the bed material. The similarity collapse is shown in Figure 6.33.

Since all the points in Figure 6.33 approximately follow a unique trend, it can be assumed that similarity is satisfied; nevertheless, for $\tau'/\tau'_R<1$ some scatter is evident, mainly due to a certain deviation of the data for mixtures from data for uniform material. Two main reasons can be adduced for this. First, the similarity approach applied does not

take into account likely second order effects; Parker et al. (1982c) noticed that when fitting power functions to plots of W^*_i versus τ^*_i of the different grain size fractions of sediment transport data collected in Oak Creek (a small, steep stream in the U.S.A., represented in Figure 6.27), the exponent of the functions decreased with decreasing grain size; for the same data set, Diplas (1987) proposed a bed load formula that considered these second order effects, while Komar and Shih (1992) indicated that these effects are crucial for the understanding of fractional transport rate variations and the departure from the equal mobility assumption as shear stress decreases. The observations of Parker et al. and Diplas belong to the transport disparities between grain sizes of a unique sediment mixture; nevertheless, no formal reasons can be invoked to discard that such effects could be present when comparing sediment transport trends between different sediment mixtures. Although the trend for the mixtures of the present work in Figure 6.33 exhibit a slightly lower slope than the trend for pure sand, the scatter of the data does not allow for a clear definition of whether second order effects were present or not.

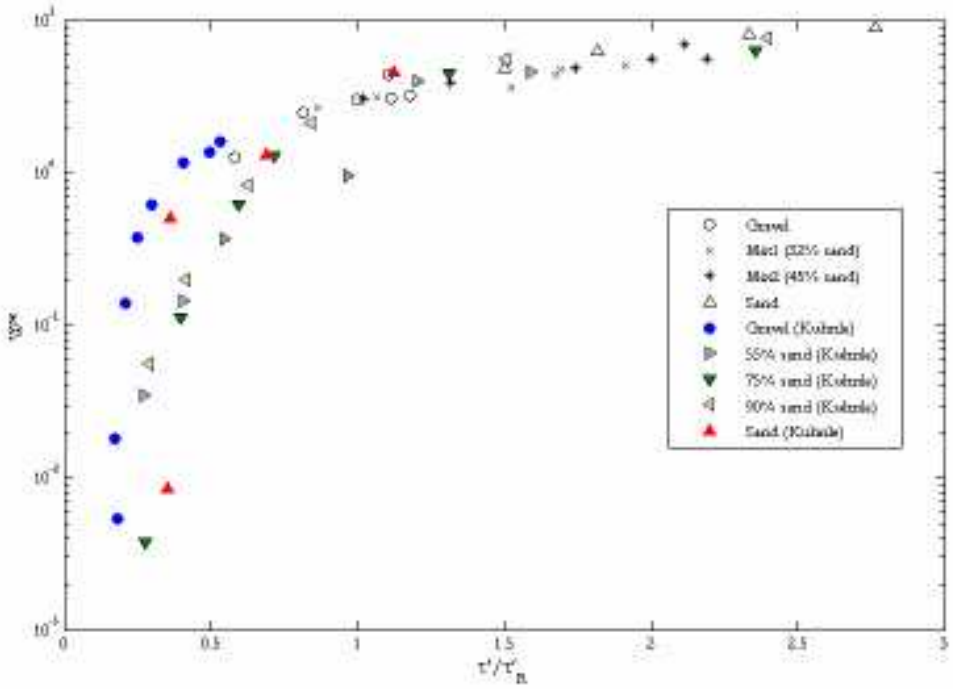

Figure 6.33. Similarity collapse of experimental data in Figure 6.31, using reference shear values for a reference dimensionless sediment transport of $W^*_R=3$.

Instead of second order effects, a likely reason for the scatter in Figure 6.33 is related with partial transport. Since plots in Figure 6.31 are based in eq.(6.35), which does not account for fractional transport rates but for the total bed material load, it is likely that changes in the grain size distribution of the transported material could be the main reason for the failure of an strict perfect similarity. From eq.(6.31) and eq.(6.27), it is obtained that

$$W_i^* = \frac{f_i(S_s - 1)gq_S}{F_i u_*^{'3}} \qquad (6.36)$$

where the ratio f_i/F_i accounts for the differences between the relative availability of the i-th size fraction to be entrained from the bed and the relative abundance of this same size fraction in the material in transport. If $f_i/F_i=1$, the transported material and the bed material contain size i in the same relative proportion. By considering eq.(6.35) for the

similarity transformation, the condition $f_i/F_i=1$ has been implicitly assumed to be fulfilled for all size fractions, i.e., it has been assumed that the grain size distribution of the bed load material and the bed material was the same. This assumption was not entirely true for the experiments of Kuhnle. From grain size distributions of the transported material in the runs with mixtures for the experiments of Kuhnle (presented by Almedeij et al., 2006), it is found that up to a certain shear stress value only the sand fraction of the mixtures participated in the transported material; in turn, the grain size distribution of the transported material was almost the same as that of the bed material only for the two highest shear stresses tested with each mixture. With this in mind, if the mean diameter of the bed material is chosen as a representative grain size (many hiding-exposure functions consider this diameter as the reference grain size, whose incipient motion conditions are similar as for uniform material), for low shear stresses it is likely that $f_i/F_i<1$, and thus, in Figure 6.31 points for mixtures with the lowest W^* values would shift downwards; conversely, for points with intermediate and high W^* values $f_i/F_i\approx1$, and the application of eq.(6.35) in this latter case would be justified. The effect of the downward shift of the lowest points would be an increased steepness of the first segment of the trend described by the groups of points for mixtures, while the upper points would remain unchanged. Reference shear values would thus be slightly higher, and in Figure 6.33 the points for mixtures for $\tau'/\tau'_R<1$ would shift to the left, improving the collapse of the data.

Although partial transport was overlooked by using eq.(6.35), it is worth noting that by selecting a high value of W^* for pursuing the similarity transformation, the similarity collapse at the highest transport rates would have been the same whether or not the analysis would have been performed by size fractions; this is so, because for the upper part of the transport relation the grain size distributions of the bed and the material in motion were almost identical.

6.4.3 Effect of sand content

The reference shear values obtained as described above are used here to analyze if sand content had a measurable effect in sediment transport under the high transport rates imposed in the flume experiments. First, it is necessary to introduce some formal definitions for establishing a reference condition with uniform material to compare the likely deviation in sediment mobility due to sand content.

Consider two different bed materials A and B, with uniform grain sizes D_A and D_B, respectively; with reference to eq.(6.29), at threshold conditions of particle movement, Shields stress of material A with respect to Shields stress of material B is found to be

$$\frac{\tau'^*_{cA}}{\tau'^*_{cB}}=\frac{D_B}{D_A}\frac{\tau'_{cA}}{\tau'_{cB}} \tag{6.37}$$

τ'^*_{cA} and τ'^*_{cB} should respond to a function as that given by eq.(6.34) (which describes a modified version of the Shields incipient motion criterion). For constant viscosity and constant sediment density, eq.(6.34) is a non-linear function of grain size, which for short grain size intervals can be approximated by a power law, so that

$$\tau'^*_c\approx\alpha D^{m_s} \tag{6.38}$$

Hence, with eq.(6.38), eq.(6.37) can be rewritten as

$$\frac{\tau'_{cA}}{\tau'_{cB}}=\left(\frac{D_A}{D_B}\right)^{m_s+1} \tag{6.39}$$

According to eq.(6.34), for coarse uniform material the critical Shields stress becomes constant, and thus if D_A and D_B are coarse enough the exponent in eq.(6.39) is equal to 1 and $m_s=0$. The relative rate of sediment transport in many relations is given as a function

of an excess Shields stress, described by the ratio τ'^*/τ'^*_c; it can be demonstrated that for a given shear stress value $[(\tau'^*_B/\tau'^*_{cB})/(\tau'^*_A/\tau'^*_{cA})]=\tau'_{cA}/\tau'_{cB}$, and therefore eq.(6.39) can be interpreted as a measure of the mobility of material B with respect to material A: if $(\tau'_{cA}/\tau'_{cB})=(D_A/D_B)>1$, B would be transported at a higher relative transport rate than A.

For a mixture composed of materials A and B, with $D_B<D_A$, the representative grain size of the mixture D_{A-B} decreases as the fractional content f_B of material B in the mixture increases. If the mobility of D_{A-B} were the same as that of a uniform material with equal grain size diameter, then eq.(6.39) should be satisfied, i.e.

$$\frac{\tau'_{c(A-B)}}{\tau'_{cB}}=\left(\frac{D_{A-B}}{D_B}\right)^{m_s+1} \qquad (6.40)$$

Otherwise, if the change of representative grain size of the mixture due to the addition of material B is not the only condition affecting the mobility of the mixture, then m_s in eq.(6.40) would take a different value than in eq.(6.39).

Table 6.3 Average characteristics of each experimental bed material, and measured reference shear values compared with computed values for uniform material. Reference shear stresses τ'_R were obtained for $W^*=3$ in Figure 6.31.

Data set	Bed Material	f_s	D [mm]	τ'_R [Pa]	τ'^*_R	m_s [eqs.(6.43)]	τ'_{Ru} [Pa] uniform-material from eq.(6.43b)	τ'^*_{Ru} uniform-material from eq.(6.43b)	τ'^*_R/τ'^*_{Ru}
Using D_m as representative diameter									
This work	**Gravel**	0	4.09	11.0	0.172	0.40	-	-	-
	Mix1	0.32	2.94	6.4	0.138	0.28	7.0	0.150	0.92
	Mix2	0.45	2.43	5.4	0.140	0.43	5.3	0.139	1.01
	Sand	1	1.43	2.5	0.111	-	-	-	-
Kuhnle (1993)	**Gravel**	0	5.59	21.4	0.238	0.36	-	-	-
	SG45	0.55	1.47	2.0	0.086	-0.13	3.5	0.146	0.59
	SG25	0.75	0.94	1.3	0.083	-0.28	1.9	0.124	0.67
	SG10	0.90	0.62	1.0	0.101	0.08	1.1	0.107	0.94
	Sand	1	0.50	0.8	0.099	-	-	-	-
Using D_{50} as representative diameter									
This work	**Gravel**	0	4.20	11.0	0.168	0.45	-	-	-
	Mix1	0.32	3.20	6.4	0.126	0.25	7.4	0.147	0.86
	Mix2	0.45	2.45	5.4	0.139	0.59	5.0	0.130	1.07
	Sand	1	1.52	2.5	0.104	-	-	-	-
Kuhnle (1993)	**Gravel**	0	5.56	21.4	0.239	0.34	-	-	-
	SG45	0.55	1.00	2.0	0.127	0.28	2.1	0.133	0.95
	SG25	0.75	0.57	1.3	0.137	1.64	1.0	0.109	1.25
	SG10	0.90	0.47	1.0	0.133	-12.07	0.8	0.102	1.30
	Sand	1	0.48	0.8	0.103	-	-	-	-

The conditions stated above can be used to verify if sand content had an influence in the mobility of the mixtures for the current experiments and the experiments from Kuhnle. Nevertheless, for comparing with eq.(6.40), which is based on incipient motion conditions, some assumptions must be considered since the reference shear stress values obtained in the previous Section were associated to a reference dimensionless sediment transport rate three orders-of-magnitude above the initiation of particle movement.

For perfect similarity to be satisfied by the sediment transport functions that would fit to points of same bed material in Figure 6.31, these functions should preserve a constant proportionality between each other. Therefore, if perfect similarity is satisfied the ratio between reference shear values obtained for any arbitrary value of W^* should conserve proportionality, i.e.

$$\frac{\left[\tau'_R(W_1^*)\right]_1}{\left[\tau'_R(W_1^*)\right]_2} = \frac{\left[\tau'_R(W_2^*)\right]_1}{\left[\tau'_R(W_2^*)\right]_2} = \frac{\left[\tau'_R(W_n^*)\right]_j}{\left[\tau'_R(W_n^*)\right]_k} \qquad (6.41)$$

where j and k account for two different bed materials and n for any arbitrary dimensionless sediment transport rate. Considering that $\tau'_c \approx \tau'_R (W^* <<)$, then if similarity is satisfied

$$\frac{(\tau'_c)_j}{(\tau'_c)_k} \approx \frac{\left[\tau'_R(W_n^*)\right]_j}{\left[\tau'_R(W_n^*)\right]_k} \qquad (6.42)$$

and it follows that eqs.(6.39) and (6.40) are valid for any reference shear stress associated to a given value of W^*

$$\frac{\left[\tau'_R(W_n^*)\right]_A}{\left[\tau'_R(W_n^*)\right]_B} = \left(\frac{D_A}{D_B}\right)^{m_s+1} \text{ or } \frac{\left[\tau'_R(W_n^*)\right]_{A-B}}{\left[\tau'_R(W_n^*)\right]_B} = \left(\frac{D_{A-B}}{D_B}\right)^{m_s+1} \qquad (6.43a,b)$$

Eqs.(6.43) were used for testing if the mobility of the experimental mixtures was independent of sand content or if sand content induced a deviation from the expected mobility of a uniform material with the same representative grain size. For the comparison, computations were performed using as representative grain size of the bed material the mean diameter first, and later on using the median diameter. Hence, $D_A=D_{mGravel}$, $D_B=D_{mSand}$, and $D_{A-B}=D_{mMixture}$ for a first computation, and $D_A=D_{50Gravel}$, $D_B=D_{50Sand}$, and $D_{A-B}=D_{50Mixture}$ for a second computation. These diameters were selected since in hiding-exposure functions they commonly represent an intermediate size fraction for which the mobility is the same whether within the sediment mixture or surrounded by particles of its same species.

For each bed material, the experimental value of m_s in the exponent of eqs.(6.43) was computed using the corresponding τ'_R and the representative grain size, related both to these same parameters for pure sand of the respective experimental data set. Computed values of m_s are shown in Table 6.3. It can be stated that if the value of m_s obtained from sediment mixtures and sand (eq.[6.42b]) is lower (higher) than m_s obtained from uniform gravel and uniform sand (eq.[6.42a]), then the mobility of the mixture is higher (lower) than the mobility of uniform material with the same grain size diameter as the representative grain size of the mixture, given that $D_{Mixture}>D_{Sand}$. For computations with the mean diameter, most of the exponents for sand-gravel mixtures, from this work and from Kuhnle data, were lower than for their uniform material counterparts; this indicates that mixtures would have a higher mobility than their well-sorted counterparts, except for the mixture with 45% sand content of the current work. For computations with the median diameter this same trend was found for most of the data, except for the mixture with $f_s=0.75$ of the data set of Kuhnle; also, for the mixture with $f_s=0.9$ in this same data set, even when m_s for the mixture was lower than for uniform material, the fact that $D_{Mixture}<D_{Sand}$ made the mixture mobility lower than for the corresponding well-sorted material.

These latter results are clearer in Figure 6.34, where the experimental reference shear values are shown as a function of bed material grain size; grain size is shown as the difference between the representative grain size of each bed material j and the representative grain size of pure sand, normalized by the difference between grain sizes of pure sand and pure gravel; reference shear stresses have been normalized similarly. An arithmetic difference has been used instead of a quotient in the plots, in order to limit the range of all data in both axis to fall within 0 and 1. This allows a more direct comparison between mixtures; it was found that if instead of an arithmetic difference a quotient was used, the results discussed below were roughly the same. In Figure 6.34, eq.(6.43b) has been plotted using the value of m_s obtained with uniform gravel and uniform sand for each data set, so that if points plot below (above) the corresponding curve the bed material has a higher (lower) mobility than uniform material. For most computations with mean diameter

the points plot closely but below the corresponding curve for unisize material, except for sand content of 45% of the current experiments; for mixture 1 (30% sand) of the current experiments the difference in mobility was approximately 7% of the difference in mobility between sand and gravel, while for mixture 2 (45% sand) the mobility can be considered that was almost the mobility of uniform sand and uniform gravel. For the mixtures in experiments from Kuhnle, this difference in mobility was 7%, 4% and less than 1% for mixtures with 55%, 75% and 90% sand content, respectively. For computations with the median diameter the trend was quite similar for the materials in the experiments of this work, but different for Kuhnle experiments. For these latter, except for the 55% sand mixture, the points plot above the curve, within a range of 2% lower mobility than for unisize material in relation to the difference in mobility between sand and gravel. Such disparities with Kuhnle data set, between using mean and median diameters, is owed to the large difference between both representative diameters, being the former from 30% to 65% larger than the latter; the exponent in eq.(6.43b) accentuates this difference.

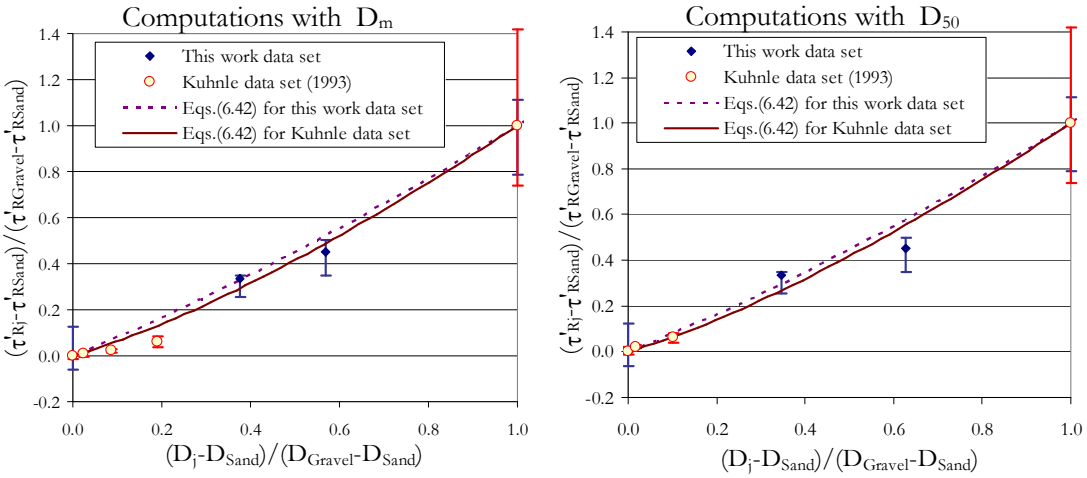

Figure 6.34. Measured reference shear values as a function of bed material grain size (left for j=mean diameter, right for j=median diameter), both represented as an increment with respect to pure sand and normalized by the increment between pure sand and pure gravel. Computed curves for uniform material with same representative grain size as that of the mixture are shown for each of the two data sets.

For a direct comparison of the likely changes in mobility due to sand content in the experimental sand-gravel mixtures, the ratio between measured reference Shields stress (τ'^*_R, related to $W^*=3$) for mixtures and calculated Shields stress for uniform material is shown in the last column of Table 6.3. These values have been plotted in Figure 6.35 as a function of sand content. From these ratios it is obtained that the mixture with 32% sand content of this work increased its mobility roughly between 8% and 14% with respect to uniform material, while the mixture with 45% sand content decreased its mobility from 1 to 7%. For the mixtures in the data set of Kuhnle no general conclusions could be extracted from the results on account of the strong differences between using mean or median diameter. Nevertheless, it can be considered that the use of the mean diameter would be more appropriate, since it is likely that due to the strong bimodality of the mixtures and that the sand mode was much finer than the coarse mode, the use of the median diameter included a strong bias toward the finer mode. This bias could be the cause of an inconsistency such like the median diameter of the mixture with 90% sand content being slightly finer than the median diameter of pure sand. Hence, if computations with the

median diameter are discarded and only those with the mean diameter are considered, mobility was increased as much as 41% with respect to unisize material for the mixture with 55% sand, 33% for the mixture with 75% sand, and for 90% sand content the mixture behaved almost like a uniform material, with an increment of only 6% of mobility with respect to well-sorted material.

The strong non-linearity of the processes here analyzed is apparent on the large difference in results when changing the representative grain size for the computations with the data set from Kuhnle. A difference of slightly less than 0.5 mm (difference between median and mean diameter of the mixture with 55% sand content) could vary the results in computed reference shear stresses for uniform material by more than 60%, which was equivalent to roughly 1 Pa difference. Nevertheless, in spite of the high sensibility of the results to the input data in that case, it is worth noting that confidence in the computations can be found by the fact that the values of m_s in eq.(6.43a) applied to pure sand and pure gravel of the two data sets were quite similar to the values obtained with the Shields criterion for the same range of grain sizes. These values are roughly m_s=0.26 (versus computed value with D_m: m_s=0.40) for the range between sand and gravel of the present work, and roughly m_s=0.22 (versus computed value with D_m: m_s=0.36) for the range between sand and gravel of the Kuhnle data set. In view of the great controversy and variability in the definition of a threshold condition for particle motion (see for example Buffington and Montgomery, 1997), these results add coherency to the findings summarized in Table 6.3. A final prove to support the conclusions above is obtained from the direct comparison of the reference shear values for pure sand of the experiments of this work and the 55% sand content mixture of Kuhnle; the mean diameter for both materials is quite similar (1.43 versus 1.47 mm), as can be seen in Table 6.3. Reference shear stress for the mixture was 24% lower than for uniform material (2.0 Pa versus 2.5 Pa), reinforcing the conclusions of an increased mobility of the bed material as sand content increases.

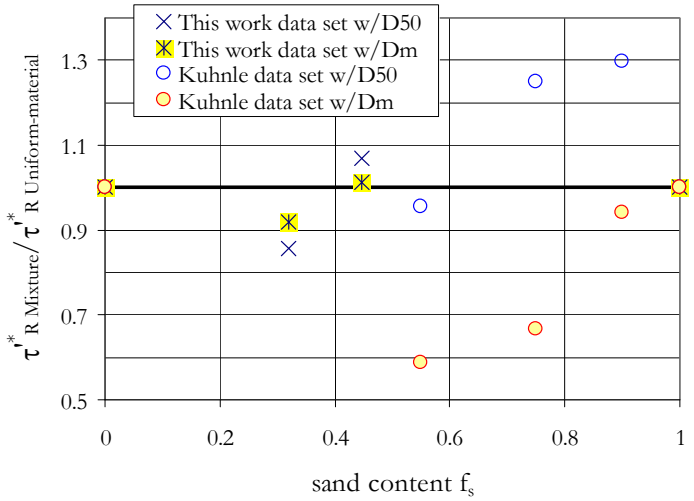

Figure 6.35. Ratio between measured reference Shield stress for mixtures and calculated Shields stress for uniform material as a function of sand content.

6.4.4 Influence of relative grain size on sand content effect

As previously demonstrated by different authors (e.g., Ikeda and Iseya [1988], Wilcock [1998], Wilcock et al. [2001]), it has been here corroborated that sand content has a

measurable effect in sediment transport. Comparisons with the expected trend for uniform material showed that such effect cannot be predicted considering solely the reduction of the representative grain size when sand proportion is increased in the sand-gravel mixture. Wilcock et al. (2001) performed experiments with five sand-gravel mixtures and isolated the effect of sand content on the critical (≈reference, for values of W^*<<) Shields stress for initiation of movement by comparing this dimensionless variable with typical critical Shields values for unisize material with the same bulk median diameter; they found that critical Shields stresses were reduced as sand content increased. For their mixture with 34% sand content, which was the mixture with the highest proportion of sand in their tests, Wilcock et al. estimated a value of critical Shields stress as low as 20% of the critical Shields stress for unisize material. Conversely, critical Shields values were similar to unisize material for mixtures with 6% and 15% sand content. For the two data sets analyzed in the Sections above, the lowest measured reference Shields stress was roughly 59% of its computed uniform counterpart for 55% sand content in the Kuhnle data set, while for the data set of the current work, this value was 86% to 92% of the unisize material for the mixture with 32% sand content. These large differences on the obtained ratios between reference Shields stress of mixtures and uniform material of the data sets analyzed here, compared to the ratios obtained by Wilcock et al. (2001) can be explained with the physical interpretation advanced by Wilcock (1998), and explained below, for the non-linear effects in the transport of mixtures induced by sand. (Note that the notions of "reference" and "critical" Shields stress are used here as equivalent; for the data sets analyzed in the previous Section, this equivalency is only valid in a relative sense, i.e., when comparing between uniform material and mixtures, and considering that perfect similarity of transport rates from which reference shear values were obtained allows that eq.(6.42) be valid. In an absolute sense, reference Shields values obtained in the last Section cannot be compared with the critical Shields stress, since the former are associated to a large value of W^* quite different to that for incipient grain motion.)

The conceptual framework of Wilcock (1998) states that when sand content is low, the limited sand grains on the bed rest in the gaps between gravel clasts, so that they can only be entrained when the gravel is set in motion. Therefore, the beginning of motion of sand and gravel would occur for the same dimensional shear stress value. On the other extreme, when the bed composition is mostly sand with a small amount of gravel, gravel clasts have small influence from surrounding particles and can move easily over the bed made smooth by the fine material filling the pores; for this condition the critical shear stress value for gravel movement would be the lowest. In between this two limiting cases ($f_s \rightarrow 0$ and $f_s \rightarrow 1$), Wilcock considers that there is a transition which is mainly controlled by the change of the bed structure from a gravel-supported framework to a matrix of sand (see Figure 2.11). Since this transition usually occurs for sand contents between 20% and 40%, it can be expected that within this range occurs much of the variation in the mobility of sand and gravel with respect to uniform material.

According to the conceptual model of Wilcock (1998), most of the bed materials from the data sets analyzed here, would be outside of the range where most of the variation in mobility occurs (i.e., their sand content is f_s>40%), and thus the effect in mobility would not differ substantially with respect to the uniform material condition. The values of the ratios between measured reference shear stress and computed reference shear stress for uniform material in the last column of Table 6.3 (between 0.59 and 1.01 when using D_m), in comparison to the minimum of 0.2 reported by Wilcock et al. (2001) for their 34% sand content mixture, respond to this condition. Conversely, for the 32% sand content mixture for the current work data set, which would be within the zone of transition between gravel framework and sand matrix, the high ratio responds to a different condition, which is likely related to the relative size of the sand with respect to the gravel. Wilcock and Kenworthy

(2002) found that changes in the mobility of sand due to the variation of sand content decreased with the ratio between grain size diameters of gravel and sand: the lower the difference in size between sand and gravel is, the lower the effect of sand content in reducing the mobility of sand for low sand contents.

For analyzing the effect of the relative difference between sand and gravel grain sizes in the entire mixture mobility, reference is given to Figure 8.2. In that Figure an empirical model has been used to describe the variation of bed porosity according to the proportional content of the fine fraction in a binary mixture. That Figure shows that bed porosity, and thus bed structure, depends not only on the proportional content of the two size fractions in the mixture, but also on the ratio between the grain sizes of the fine (d) and the coarse (D) size fractions. For low values of this ratio, the porosity variation is low when the proportion of each size fraction changes. Conversely, the variation of porosity increases when the size ratio increases: minimum bed porosity can be reduced up to 70% for d/D=0.08 (which is the size ratio of sand and gravel in Kuhnle runs) with respect to d/D=0.32 (which is the size ratio of sand and gravel in the current work). Since the arguments on the conceptual model of Wilcock (1998) described above, for the effect of sand content in the mobility of sand and gravel, are mostly based on the arrangement of the particles (sand hidden in the pores between gravel for a gravel-framework supported bed; gravel totally exposed to flow for a sand matrix structure), it is here hypothesized that such changes in mobility can be related to changes in bed porosity. The minimum porosity in Figure 8.2 is associated to the shift from a gravel-framework to a sand matrix bed structure, similarly as most of the adjustments in mobility of a mixture would occur in this same transition, as Wilcock (1998) considered. Following these assumptions, it is likely that the effect of sand in the mobility of the 32% sand mixture was not as important as in mixtures from Wilcock et al. (2001) since the ratio between gravel and sand grain sizes was low (≈3), while in the experiments of Wilcock et al. this ratio was much larger (≈12 and ≈24).

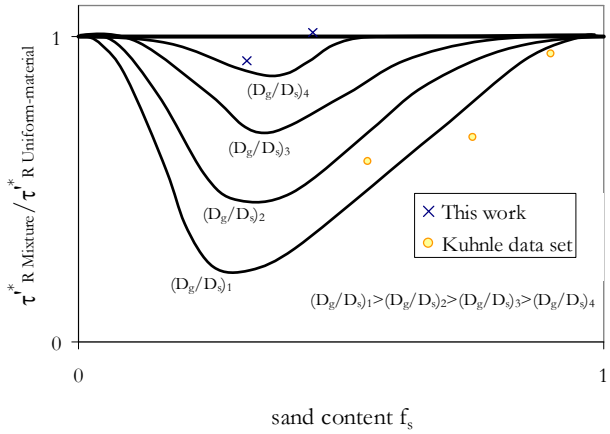

Figure 6.36. Conceptual model for the variation with sand content of the ratio between the reference shear stress of the mixture and the reference shear stress of uniform material with equal representative grain size as that of the mixture. Different curves account for the ratio between gravel and sand grain sizes. The minimum value of each curve would correspond to the sand content for the shift from gravel-framework supported to sand matrix bed structure and to the minimum bed porosity as well. For the sediment in the experiments of this work D_g/D_s≈2.9, while for the experiments of Kuhnle D_g/D_s≈11.

A conceptual diagram is proposed in Figure 6.36 in an attempt to summarize the reasoning above for the effect of relative size and sand content in the mobility of a sand-

gravel mixture. This diagram incorporates the main trends shown in Figure 8.2 for the changes in porosity of a binary mixture of particles, and the conceptual framework of Wilcock (1998). According to the diagram in Figure 6.36, the mobility of a mixture with respect to uniform material of equal representative grain size, would be higher ($\tau'^*_{mixture} < \tau'^*_{uniform\text{-}material}$) the higher the ratio between sand and gravel sizes were. The maximum increase in mobility (minimum values of the curves in Figure 6.36) would occur for the transition from a gravel-framework to a sand matrix, i.e., for the lowest bed porosity in Figure 8.2. Experimental points have been drawn in Figure 6.36 as a reference. Data from Wilcock et al. (2001) would plot in the region of the two lowest conceptual curves.

6.4.5 Sand content in sediment transport predictors

The effect of sand content in the mobility of sediment mixtures is explicitly taken into account in the sediment transport formulas presented by Wilcock and Kenworthy (2002) and Wilcock and Crowe (2003). As it is indicated in Table 6.2, the first formula was designed to perform calculations using two size fractions and incorporates the concepts advanced by Wilcock (1998) already described in previous paragraphs. From Figure 6.28 it can be observed that this formula was the best performing formula when considering only the sediment mixtures, but it failed to perform well for the uniform gravel and uniform sand. A likely reason for the failure of this formula when dealing with uniform material is related to the fixed values assigned to the critical shear stress on the sand content extremes (for subsurface material, $\tau'^*_R=0.043$ for the gravel size fraction when $f_s=0$, and $\tau'^*_R=0.045$ for the sand size fraction when $f_s=1$). These fixed values do not consider the variations in critical shear stress for grain sizes in the range of medium to fine gravel and the whole range of sand sizes, as common incipient motion criteria do, like the modified version of the Shields diagram given by eq.(6.34). Therefore, this formula is likely to be adequate for moderate to medium sand contents, as in the sediment mixtures tested in the experiments of the current work, but it would underestimate the mobility of the mixture for poor and large sand contents.

The formula of Wilcock and Crowe (2003) deals with sediment transport of an arbitraty number of grain size fractions. The formula incorporates sand content in a functional relation for the critical Shields stress of the mean diameter of the mixture; similarly to the formula of Wilcock and Kenworthy (2002), in the extremes of this relation the critical Shields values are fixed as well, being $\tau'^*_R=0.032$ for $f_s=0$ and $\tau'^*_R=0.021$ for $f_s=1$. The functional relation proposed by Wilcock and Crowe (2003) for the critical Shields stress of the mean diameter is shown in Figure 6.37 along with computed reference (≈critical) Shields stress values using eq.(6.34), for uniform material of equal mean diameter as the mean diameter of the mixture (standard values were used for the sediment and water properties: Ss=2.65 and $\nu=1.13\text{x}10^{-6}$ m^2/s)[§]. The mixture was considered to be composed of two size fractions (sand and gravel), and its geometrical mean diameter was computed with

$$D_m = 2^{f_s \log_2 D_s + (1-f_s)\log_2 D_g} \qquad (6.44)$$

where D_s and D_g are the sand and gravel representative grain sizes. For the computations, two sand sizes were tested (0.4 mm and 1.5 mm, similar to the sand size for the Kuhnle and the current work experiments, respectively), and six different values for the ratio between gravel and sand sizes. It is evident from Figure 6.37 that critical Shields stress

[§]Data from the experiments analyzed in previous Sections cannot be plotted in Figure 6.37, since no critical Shear stress values could be obtained from the similarity analysis for a high value of W^*.

values obtained from eq.(6.34) for uniform gravel (f_s=0) and uniform sand (f_s=1) are lower than those suggested by the extremes of the Wilcock and Crowe functional relation. Eq.(6.34) is delimited by an upper constant value of τ'^*_c=0.03 for very coarse gravel; this value and the fixed value of τ'^*_c=0.036 for gravel (or f_s=0) given by the relation of Wilcock and Crowe are within a narrow range of the commonly observed variations in the critical Shields stresses for gravel-bed rivers (Buffington and Montgomery [1997] compiled data with values that spanned from 0.03 to 0.086). In this regard, for coarse material typically found in natural rivers the upper boundary for gravel (or f_s=0) in the Wilcock and Crowe relation seems to be adequate, but not for medium, fine and very fine gravels (pebbles and granules), for which the incipient motion Shields stress has been observed to vary by almost 50% with grain size. In turn, the lower fixed boundary for uniform sand (or f_s=1) in the relation of Wilcock and Crowe does not consider the variations in critical Shields stress due to viscous effects in the sand grain size range. Finally, the formula of Wilcock and Crowe does not take into account the ratio between sand and gravel grain sizes for the computation of the mean diameter incipient motion; this ratio can be relevant for the mobility of a sediment mixture, as it was proved in the previous Section.

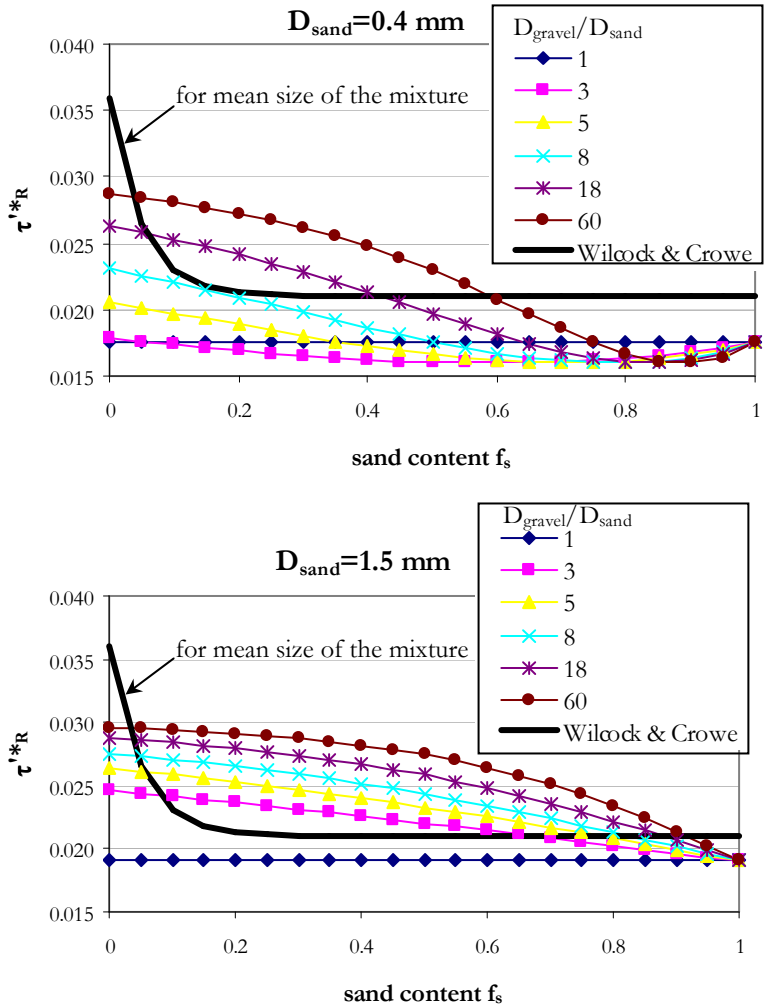

Figure 6.37. Reference Shields stress associated to incipient motion for uniform material (computed with eq.[6.34]) of same grain size as the median diameter of sand-gravel mixtures with different proportional sand contents. The mixtures were considered for two different sand sizes and six different ratios between gravel and sand grain size diameters. Mean diameter of the mixture was obtained from eq.(6.44). The criterion of Wilcock and Crowe (2002) for estimating the reference Shields stress of the surface mean diameter of a sand-gravel mixture is presented for comparison.

Notwithstanding the shortcomings listed above for the critical Shields stress function in the Wilcock and Crowe method, it can be considered that this function represents an average state for typical grain sizes found in natural streams. The fixed value for the critical Shields stress of uniform sand (or $f_s \approx 1$) is in the upper bound of commonly reported values, and therefore, the function will be conservative in the mobility of fine mixtures (sediment movement begins at large values of shear stress for high sand contents); conversely, the fixed Shields stress for uniform gravel (or $f_s \approx 0$) is within the lowest boundary with respect to typical values observed in field and flumes (from 0.03 and 0.086, according to Buffington and Montgomery [1997]), so that the relation would overestimate sediment mobility for coarse mixtures (sediment movement begins at low values of shear stress for low sand contents). In other words, it can be expected that the Wilcock and Crowe relation would overestimate incipient motion shear stress values for mixtures with high sand contents and would underestimate incipient motion shear stress for mixtures with low sand contents.

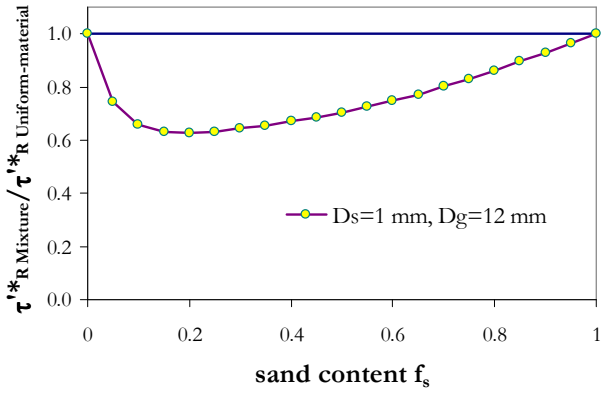

Figure 6.38. Variation with sand content of the ratio between reference Shields stresses for a sand-gravel mixture and for uniform material of equal mean diameter as the mixture. Curve obtained from relating the model of Wilcock and Crowe with eq.(6.44) for given values of sand and gravel grain sizes. See text for explanation of how the results were scaled.

It is likely that the variation of the critical Shields stress of a sediment mixture, with respect to changes in the relative proportion of its different size fractions, could be adequately represented if it is scaled by the mobility of uniform material, as it was presented in the conceptual model of Figure 6.36. A functional relation scaled in this manner could allow variations in the critical Shields stress related to the absolute value of the grain sizes. For this function being of general applicability, it should encompass the family of curves represented in the conceptual model of Figure 6.36, so that it would consider different ratios of grain size between grain size fractions. The relation presented by Wilcock and Crowe (2002), shown in Figure 6.37, would be a particular case of such a general function, for a given size ratio between sand and gravel and given incipient motion conditions of these two size fractions considered isolated. As an example of the form in which such a general relation could be constructed, in Figure 6.38 is presented a curve that describes the ratio between the function of Wilcock and Crowe and the Shields stress for uniform material obtained from eq.(6.44) as in Figure 6.37, for given values of sand and gravel sizes similar to those of the experimental material of Wilcock et al. (2001). The ratio of the two functions was scaled by a weighted average of the relation between the Shields stress values for the extremes of the Wilcock and Crowe function and for uniform sand

and gravel, so that all values would be between 0 and 1. The curve depicted in Figure 6.38 could be considered as one curve of the familiy of curves in Figure 6.36. The complete set of curves could be obtained given that the functions between sand content and reference Shields stress values were known (either theoretically or experimentally) for different ratios between the sizes of sand and gravel.

6.4.6 Discussion on sediment transport predictors

All of the sediment transport formulas used for comparison with the experimental data in Section 6.4.1 consider a critical (or reference) shear stress, with which an excess shear stress ($\tau'^*/\tau'^*_c=\tau'/\tau'_c$ or $\tau'^*-\tau'^*_c$) acting over the sediment grains is computed. Therefore, accurate sediment transport predictions rely, to a great extent, on the correct estimation of the threshold condition of sediment motion. This is so much the case that, as it was demonstrated in Section 2.4.2.1, the original Meyer-Peter and Müller formula can be arranged in such a way that computations of sediment transport rates do not require the sediment grain size as an input parameter, but only a dimensionless critical shear stress value. As it is shown in Table 6.2, each formula defines a different critical (reference) Shields stress, ranging from 0.008 to 0.088, i.e. the suggested values span over one order of magnitude. Due to this broad range of considered critical Shields stress values and to the strong non-linear nature of the transport relations, it must not be astonishing that when applying different sediment transport formulas the results vary by orders of magnitude.

As it was demonstrated in previous Sections, sand content might have an important non-linear effect on critical shear stress of sediment mixtures; nevertheless, this influence had not been recognized but recently, and thus it is not explicitly considered in the great majority of transport relations. In the previous Section, some flaws have been pointed out in the only two relations that include sand content as a relevant parameter in the computation of shear stresses associated with incipient motion. These relations need to be improved to consider more general conditions, and in doing so, as indicated by Parker (2004a), more efforts are needed to quantify the effect of sand content in sediment transport.

In the application of sediment transport relations based on an excess shear stress, as those used in Section 6.4.1, the influence of critical Shields stress in the uncertainty associated to the sediment transport estimations is particularly important for conditions of low bed shear stresses. This is owed to the steep gradient of the sediment transport function in its lower region, as it can be seen in plots of data in Figures 6.30 and 6.31. In this region of low transport rates, small errors in the computation of the critical shear stress, i.e. small errors in the excess shear stress, might lead to high errors on the estimated sediment transport rates. Therefore, the use of adequate critical shear stress values might substantially improve the performance of sediment transport models. On account of this and of all the controversy and disparities in selecting an adequate critical shear stress value for a particular condition, for improving the performance of sediment transport predictors in specific cases, some authors have recommended to calibrate the incipient motion shear stress condition with a limited number of sediment transport samples (e.g., Wilcock, 2001; Habersack and Laronne, 2002).

As opposed to the lower region of the sediment transport function, the slope of the function in the region for high sediment transport rates is mild, and tends toward a limiting value that some authors consider as a constant of $W^*=17$ (Yalin 1972, after Parker and Klingeman 1982). For this region, due to the low increments of sediment transport with respect to the excess shear stress, it can be expected that the impact of a wrong estimation of the critical shear stress would not be as strong as in the lower region of the curve. The data of the experiments in this work, as can be seen in Figures 6.30 and 6.31, correspond to

the vicinity of the upper part of the intermediate region of the transport function, where the function changes from its steep derivative to the mild slope trend. Hence, wrong estimations of the critical Shields stress in this region would still be important in sediment discharge computations, although not as much as for low transport conditions. The poor performance of the formulas used in Section 6.4.1 can thus be associated to a great extent to erroneous estimations of the excess shear stress, although, as it will be shown below, for some conditions this might not be the main source of error in sediment transport predictors. Since it was not feasible to estimate threshold conditions for the movement of the bed material in the experimental data set of this work, it cannot be here assessed as to which extent erroneous excess shear stress values contributed to the differences between measured and computed sediment discharges.

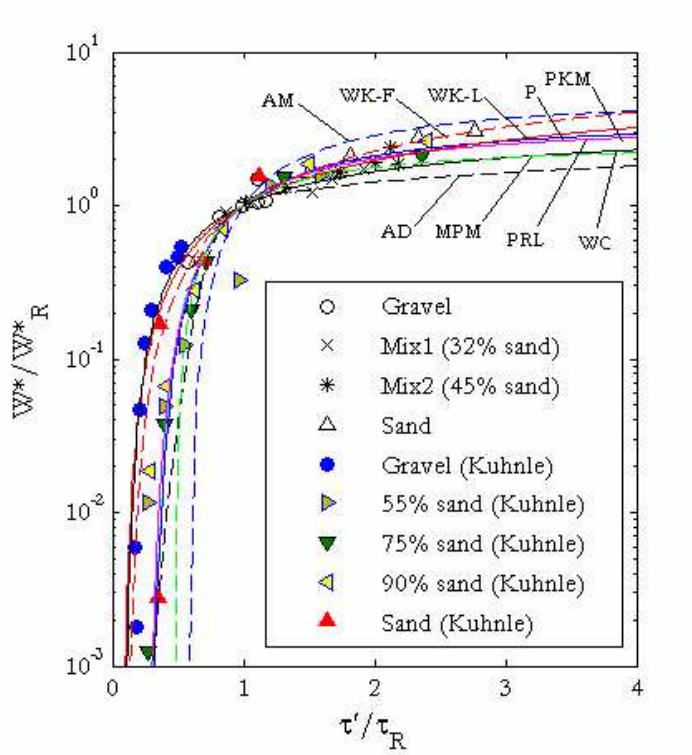

Figure 6.39. Comparison of the collapsed experimental data of this work and those from Kuhnle (1993a) with different sediment transport relations (described in Table 6.2). These relations were transformed to agree with the same reference dimensionless sediment transport of $W^*_R=3$ used for the similarity transformation. AM=Ashida and Michiue; PKM=Parker, Klingeman and McLean; P=Parker; PRL=Powell, Reid and Laronne; WK-F=Wilcock and Kenworthy for field data; WK-L=Wilcock and Kenworthy for laboratory data; WC=Wilcock and Crowe; AD=Almedeij and Diplas; MPM=original formula of Meyer-Peter and Müller.

Even if the estimation of the critical shear stress (or excess shear stress) for a given bed material were reasonable, the prediction of the sediment discharge could be poor according to the form of the sediment transport function of the predictor. This is exemplified in Figure 6.39, where the collapsed experimental data of this work and those of Kuhnle have been plotted along with sediment transport relations of most of the methods used in Section 6.4.1. A suitable transformation was performed to the functional relations in order to make them agree with the selected reference dimensionless sediment transport for the similarity collapse ($W^*_R=3$). In general terms, the trend described by the bulk of data is followed by the curves, and the range over which the set of functions spans encompass the overall dispersion of the experimental points. For a constant value of τ'/τ'_R the difference

in estimates of W^*/W^*_R between the different curves might be up to almost three orders of magnitude, although for $\tau'/\tau'_R>1$ this difference is reduced considerably. For $\tau'/\tau'_R>1$ an upper boundary for the sediment transport relations is outlined by the function of Ashida and Michiue, while the relation of Alemedeij and Diplas outlines a lower boundary. For these two functions, the difference between values of W^*/W^*_R for a constant ratio $\tau'/\tau'_R=4$ is as high as approximately 200%. For $\tau'/\tau'_R<1$ the function of Ashida and Michiue marks the lower boundary, while the upper limit is outlined by the relation of Wilcock and Crowe. A visual inspection of Figure 6.39 shows that for $\tau'/\tau'_R>1$ the data disperse roughly around the relations of WK-L (Wilcock and Kenworthy for laboratory data), P (Parker), PRL (Powell, Reid and Laronne) and PKM (Parker, Klingeman and McLean); all these functions almost overlap and define a unique curve, which is not surprising since all four are based on Parker's (1978) approximation to the original sediment transport function of Einstein (1950) for uniform material.

In general, data and relations in Figure 6.39 show up that even when the excess shear stress is accurately estimated, the error in computed sediment discharge can still be significant according to the form of the transport relation. Since the set of curves in Figure 6.39 roughly expand over the scatter of the experimental data, it is likely that the different trends shown by the curves is related to experimental variability, discrepancies in defining grain shear stress and, for low transport rates, to the difficulties of accurately measure and incorporate partial transport in general dimensionless relations. Improvement of sediment transport relations must tackle with such issues.

6.4.7 Advantages of using a high reference value of dimensionless sediment transport for the similarity collapse

For streams in which bed material is mobilized only during high bed shear stress events, it is not feasible to measure a wide range of sediment discharges, spanning from incipient motion to moderate sediment transport rates, as required by the original similarity analysis method described by Parker and Klingeman (1982) for determining a reference Shields stress value. Such a condition of the bed material being active only at high sediment transport rates is a common feature of ephemeral streams subjected to flash floods, as the ephemeral desert rivers described by Laronne and Reid (1993), with a very high efficiency in transporting coarse material. For one of these streams, Nahal Yatir, Powell et al. (1999) described that from the very beginning stages of a flood event, sediment transport and shear stresses greatly exceed incipient motion values. They related this response to the fine texture of the bed surface, and to the flashy character of the floods that abruptly impose high shear stress values on the dry bed. For such type of currents or for the analysis of data sets for which only the upper part of the sediment transport rating curve is known, the similarity analysis method based on a high value of the reference dimensionless sediment transport W^*, as used here in Section 6.4.2, would be adequate for pursuing the collapse of data.

But pursuing the collapse of data using a high reference dimensionless sediment transport can not only be useful in the case of lack of information for the lower segment of the transport relation. Determining a reference shear value for high transport rates could be more straightforward than for the region in the vicinity of incipient motion conditions, for the reasons explained as follows. Since it is common that bed load becomes coarser as shear stress increases, for high sediment transport rates partial transport of the coarser grain size fractions of the bed material is less likely to occur. For this condition in which all the grain size classes are in motion the ambiguity of scaling transport with surface or subsurface material can be eliminated. Even if a coarse surface layer persisted at high flow rates, if bed load and the bulk of bed material have an equal grain size distribution, i.e. if

equal mobility of all grain size fractions in the bed occurs, this would indicate that all the bed material is exposed to participate in transport and that a distinction between surface and subsurface material is thus irrelevant. Another virtue of using for the data collapse a high transport reference value is a likely reduction in scatter for high sediment transport rates. For the region in the transport function where partial transport persists, higher scatter of the sediment transport observations is more likely to occur, as it is evident in Figure 6.33, where the scatter of the data from Kuhnle decreases at high transport rates. Such a higher dispersion at lower transport rates could be related to the ambiguity in determining the bed material to which relate transport, and to the difficulties in obtaining minimum representative size samples under low sediment transport conditions. Finally, analyzing the upper part of the transport relation would allow for an easier detection of the presence of second order effects.

On account of the qualities mentioned above of using a high dimensionless reference transport for similarity analysis, it can be here advanced that a sediment transport model based on this approach could improve estimations of total bed material load at high sediment transport rates in comparison to models based on a low reference transport related to incipient motion conditions. Collapse of empirical and field data referenced to a high dimensionless sediment transport would elude complexities related to partial transport at low transport stages.

6.4.8 Summary

In this Section, sediment transport of the experimental data has been analyzed in search of general trends and affinities with previous studies. In light of the current knowledge, widely used dimensionless combinations of the most relevant variables were introduced. Using these non-dimensional variables the experimental data were compared with field measurements of sediment transport (Figure 6.27), showing that the data set obtained in this work corresponds to exceptionally high sediment transport rates that define an upper bound for the transport observed in the natural streams used for the comparison. Remarkable of this comparison was that for similar ranges of dimensionless shear stress, the experimental non-dimensional transport rates were higher than those for field data; invoked reasons for such differences were likely form drag effects introduced by flow complexities in field, variations in the critical shear stress due to grain size, and bed armouring in natural streams.

A vast number of methods for estimating sediment transport exist in literature. Those for sediment of heterogeneous grain size include a hiding-exposure function to account for the interactions between different sizes. Recent studies show that sand content can also affect the movement of sediment mixtures, and thus it has been included as an explicit variable in two recently developed models. Ten of these sediment transport predictors developed for heterogeneous material, particularly for gravel-bed rivers, were selected for testing their performance against the experimental data. The use of surface and subsurface material in the sediment transport formulas was discussed, and it was concluded that for the experimental data here obtained the use of the grain size distribution of the feeding material as representative of the bed material was adequate for computations with the sediment transport formulas. The formulas were applied considering two size fractions: sand and gravel. The methods and some of their characteristics were summarized in Table 6.2. Results showed that no single formula performed well in all of the four conditions of bed material tested. It was concluded that defining a best-performing model is rather subjective, as some formulas performed better than others for some particular attributes.

Of particular interest in this work was to analyze the likely effect of sand content in sediment transport. Therefore, for this analysis, a similarity transformation was applied

trying to collapse the data into a single curve. Along with the data set of this work, the data set of Kuhnle (1993a) with sand, gravel and three sand-gravel mixtures (with 0.55, 0.75 and 0.9 sand contents), was also considered. The method used for the transformation has been widely applied in the past for the analysis of fractional transport rates of non-uniform sediment. Here the method was used for comparing different materials at high sediment transport rates. In contrast to the application of the method in previous studies, where a low reference sediment transport rate was considered for estimating a reference shear stress value close to incipient motion conditions, here a high reference transport rate was used. Approximate perfect similarity was found for data with the highest sediment transport rates, while for data with low to moderate transport rates (only data from Kuhnle) more dispersion was evident. Second order effects were discarded as being the reason for these scatter, being more likely owed to partial transport of the gravel size fraction.

Reference shear stress values estimated for the similarity collapse were used for analyzing if sand content has a measurable effect in sediment transport under the high transport rates imposed in the flume experiments. Perfect similarity of the transport relation for each bed material was assumed, and thus it could be considered that for two bed materials a constant proportionality existed between reference shear stresses, given that these were associated to the same dimensionless transport rate. This hypothesis allowed the comparison of the experimental data with the Shields incipient motion criterion for uniform material. The Shields criterion was approximated by means of power laws; the exponent of the function obtained from comparing the mobility of pure sand and pure gravel in each of the experimental data sets served as a reference of the response of uniform material to the experimental conditions. The comparison between sediment mixtures and the corresponding uniform material of the data set showed that the mobility of all of the mixtures was higher than the expected mobility of uniform material with same representative grain size. This was true except for the mixture with 45% sand content of the present work, whose mobility was slightly lower than for uniform material. Reference shear stresses were approximately 8%, 40%, 33% and 6% lower than their computed unisize counterparts in the mixtures with 32%, 55%, 75%, and 90% sand content, respectively. For the data set of Kuhnle, results varied considerably if instead of basing the computations on the mean diameter they were based on the median diameter. Notwithstanding, results based on the median diameter were discarded, assuming that this size was biased toward the fine mode of the grain size distribution.

The variations in mobility for the sand-gravel mixtures with respect to uniform material were compared with results obtained by Wilcock et al. (2001); these authors found an increase in mobility of approximately 80% with respect to the Shields criterion for a sand-gravel mixture of 34% sand content. Such a reduction is much larger than the maximum mobility reduction of 40% obtained with the 55% sand content mixture of Kuhnle. In order to explain such large differences, first the conceptual model of Wilcock (1998) for the variations in mobility of sand and gravel with respect to sand content was adduced, and secondly, an empirical model for the estimation of porosity in a bed composed of a binary mixture was introduced (this model is explained in detail in Chapter 8). According to the model of Wilcock, an abrupt increase in mobility of gravel and sand occurs when the bed changes from a gravel-supported to a sand-matrix structure; this change takes place for sand contents approximately between 20% and 40%. It was here hypothesized, that such a change in mobility can be related to changes in bed porosity; according to the porosity model, bed porosity is minimum for the transition from a clast-supported to a matrix of fines bed structure, and is lower the greater the ratio between the coarse and the fine size fractions is. Therefore, it was concluded that the changes in mobility of the bed material in the studied mixtures, with respect to uniform material, was not as important as in the mixtures of Wilcock et al. (2001), first because sand contents were outside of the range

where most of the mobility changes occur (i.e., the range for which bed structure changes from a gravel-framework to a sand-matrix), and secondly because gravel-sand size ratios were lower than for the mixture of Wilcock. A conceptual diagram was presented (Figure 6.36) which unifies the theory of Wilcock with the bed porosity model for a binary mixture; the diagram depicts the likely variation in mobility of a sand-gravel mixture with respect to uniform material of equal representative grain size, according to sand content. In this conceptual model, a family of curves accounts for different values of the ratio between sand and gravel grain sizes.

A brief discussion was presented regarding the inclusion of sand content effects in the two only sediment transport models that take into account sand content as an explicit variable. These are the models of Wilcock and Kenworthy (2002) and Wilcock and Crowe (2003). Both models consider sand content in functional relations for the incipient motion Shields stress, with fixed values for the extremes of the functions, i.e., for pure sand and pure gravel. It was indicated that such fixed values do not consider variations of the critical shear stress for grain sizes in the range of medium to fine gravel and the whole range of sand sizes. In this respect, it was suggested that the conceptual model depicted in Figure 6.36 would represent a more general interpretation of the effect of sand content on the mobility of sand-gravel mixtures. The relation of Wilcock and Crowe (2003) for computation of the critical shear stress of a mixture as a function of sand content was used along with the sediment incipient motion criterion of Shields given by eq.(6.44) to exemplify a likely approach for developing the conceptual model of Figure 6.36. It was indicated that the relation of Wilcock and Crowe would represent a particular case of this more general model which would take into account variations in critical shear stress due to grain size, and also the ratio between sand and gravel grain sizes.

The performance of the formulas considered for the comparison with the experimental data in Section 6.4.1, relies to a large extent on accurate estimations of the critical shear stress for sediment motion. On account of the lack of consensus for a definitive criterion to compute the critical shear stress, the results obtained with these formulas can vary by orders of magnitude. The recent recognition of sand content as a relevant variable in incipient motion of sand-gravel mixtures might help to improve sediment transport models, but more efforts are needed to assess the qualitative effects for different conditions.

Sediment discharge estimations are more sensitive to erroneous critical shear stress values for low rather than for high transport rates. Nevertheless, at high transport rates the form of the transport relation can also lead to important deviations from actual values. Comparison between the collapsed experimental data (i.e., considering a correct estimation of the critical shear stress) and sediment transport relations shows that even if the critical shear stress were correctly estimated, the estimations between formulas might vary by orders of magnitude. For a constant value of τ'/τ'_R the difference in estimates of W^*/W^*_R between the different curves might be up to almost three orders of magnitude, although for $\tau'/\tau'_R>1$ this difference is reduced considerably.

Finally, some advantages were indicated of the use of a high reference dimensionless transport rate for pursuing the similarity collapse of data. Not only would be this modification of the original approach presented by Parker and Klingeman (1982) adequate for streams or data sets in which no information is available for low sediment transport conditions; this approach could also be adequate for developing an accurate sediment transport model for high transport rates, which would elude the inherent complexities of selective transport and the ambiguities in selecting between surface and subsurface material for computations when an armour layer is formed.

6.5 OVERALL INTERPRETATION OF EXPERIMENTAL RESULTS

The experiments herein reported considered high sediment transport rates and conditions in or close-to the transition from subcritical to supercritical flow. This transition is extremely unstable, water depth can exhibit abrupt changes with small perturbations on the bed. Furthermore, in the passage from subcritical to supercritical flow, bedform stability fields and flow resistance can show important discontinuities. All this complexity makes it difficult to identify clear trends and put forward general conclusions for the experimental observations. Hence, more qualitative rather than quantitative approaches are used in this Section, in pursuing to give a general and holistic interpretation of the most apparent trends in the measured variables.

The experimental data here presented and analyzed pertain to morphodynamic equilibrium states; during these states average values of bed and water slopes, water depth, water discharge and fractional solid discharge, remained approximately constant in time and space. Accordingly, the average characteristics of bedforms, bed resistance and sediment grain size sorting were approximately stable as well. All these variables and processes were linked in complex, yet systematic, interactions; these interactions were the response of the channel to adjust local conditions of bed configuration, flow and sediment transport to the imposed sediment-feed rates and water discharges. The interaction of the most relevant variables is discussed below in light of related experiences and developments in literature; later, as an attempt of synthesis of the overall experimental campaign, a brief discussion is presented on the connection of the experimental flows, morphologies and processes, with streams in field.

6.5.1 Effect of the channel walls in the water surface configuration

A common feature of most of the runs in the data set was the periodic deformation of the water surface in trains of three-dimensional stationary waves, which propagated in the downstream direction in a regular periodic pattern along the channel central cross section. The characteristics of these waves varied with Froude number and bed material, being less active and less steep for subcritical than for supercritical Froude numbers. For the lowest Froude numbers these waves had the appearance of a smooth boil, while for the highest Froude numbers they were violent and broke upstreamwards. The rhomboidal pattern of the water surface configuration on plan view, for the 3D waves with the highest Froude numbers, was similar to oblique standing waves formed under supercritical flows in channel contractions (see sketch in Figure 5.2). In the formation of such type of standing waves the channel walls have a key influence; hence, it is evident that for the 3D stationary waves here reported the channel walls were relevant as well.

Kennedy (1961) indicated that 3D waves above antidunes occur when transversal waves are coupled with the stationary waves produced by antidunes; he suggested eq.(5.6) for estimating flow velocity as a function of the longitudinal and transversal wavelengths of a 3D wave, considering the channel width as a first approximation for the wavelength transversal to the flow. Some disparities were found in Section 6.2.3.2 when applying eq.(5.6) to the experimental data (Figure 6.11b); particularly, for most of the runs with 3D waves, for a given measured wavelength, computed mean flow velocities were under estimated by eq.(5.6); conversely, Kennedy found that eq.(5.6) overestimated mean flow velocities for all of the 3D waves in his own data set with fine sand. He attributed discrepancies between theory and experiments to the use of the channel width as the rooster-tail transversal wavelength λ_t in eq.(5.6); he asserted that the transverse boundary of the 3D waves is quite nebulous and probably not compatible with that used in obtaining

the solution given by eq.(5.6). Accordingly, the role of the channel width in generating the 3D waves is not completely clear.

In an effort to elucidate a likely transversal length different than the channel width for the short-crested waves, using the experimental data in eq.(5.6) solved for the transversal wavelength, as given by eq.(6.5), a trend was observed toward a decrease in the computed transversal wavelength with higher grain shear stress values (Figure 6.12), but no satisfactory explanation was found for such result.

In order to clarify the role of the channel walls in the formation of the experimental 3D waves, the characteristics of oblique standing waves in the formation of transversal cross-waves are analyzed as follows, and a more general formula than that suggested by Kennedy is derived for computing flow velocity as a function of the wavelength of short-crested antidunes and 3D stationary waves.

6.5.1.1 3D waves wavelength

Consider a channel with rigid boundaries and free surface flow in the direction parallel to the channel wall. A disturbance on the water surface produced by an obstacle next to the wall travels at the same velocity c_w in all directions outwards from the wall, while at the same time it is carried downstream at the same velocity as the flow velocity V. When $V>c_w$ (i.e., supercritical flow) successive wave fronts of disturbances produced by the obstacle generate an oblique standing wave on the upstream limit of the wave fronts, as shown in Figure 6.40. This standing wave or shock front is made of the union of all the propagating wave fronts by the only line that is tangent to all of the wave fronts at any time. The origin of this line is the point where the disturbance was originated on the water surface, i.e., point A_n in Figure 6.40. For a given instant, any perpendicular line to the shock front intersects a given wave front (points P1 and P2 in Figure 6.40), and intersects the wall at the center of that same wave front (points A_1 and A_2), which has traveled at a velocity V along the boundary. Hence, considering the trajectory of a given wave front with respect to the front center, and the trajectory of this same center, the following relation can be written

$$\frac{A_1P_1}{A_nA_1} = \frac{c_w}{V} = \sin\beta \qquad (6.45)$$

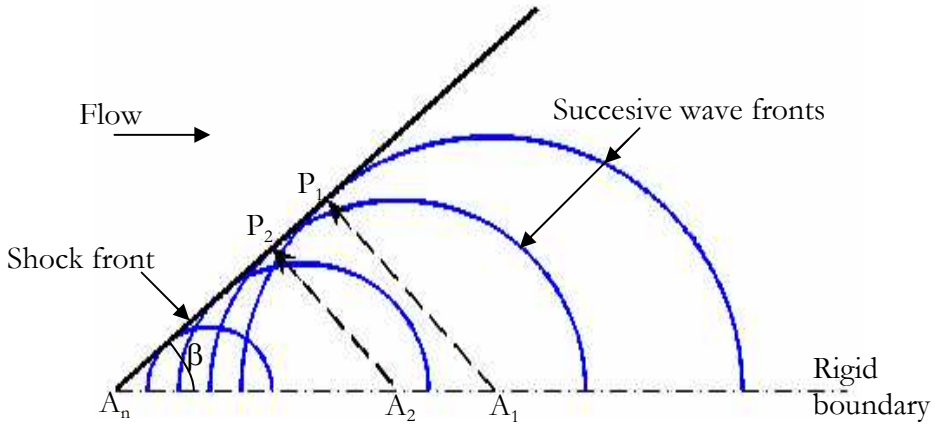

Figure 6.40. Plan view of an oblique standing wave generated by the coincidence of propagation patterns of successive perturbations on the water surface next to a rigid boundary. (Adapted from Figure 7-4 in Henderson, 1966).

where β is the angle formed by the oblique wave and the channel wall. If the surface waves are short, their velocity can be approximated with $(gH)^{1/2}$, where g is gravity and H is mean water depth, and eq.(6.45) can be written as equivalent to the inverse of the flow Froude number. Nevertheless, for finite length waves the propagation velocity must be computed with the general formula

$$c_w^2 = \frac{gL}{2\pi} \tanh \frac{2\pi H}{L} \qquad (6.46)$$

where L is wavelength.

As stated previously, different authors have related the formation of short-crested antidunes to the interaction of oblique standing waves with the bed surface (Kennedy 1961, Yokokawa et al. 2010); the crossing of oblique standing waves forms 3D water surface waves, when the wavelength of these waves matches with the wavelength of antidunes, the surface waves are amplified and the 2D antidunes become 3D (Hasegawa and Kanbayashi, 1996, after Yokokawa, et al. 2010). Here a relationship between wavelength and flow velocity for short-crested antidunes is derived by analyzing the crossing of two transverse waves at mirror symmetrical positions.

Consider the same channel with unidirectional flow in Figure 6.40, and two mirror symmetrical perturbations, each at either wall of the flume, as shown in Figure 6.41. The wave fronts of the two perturbations are mirror symmetric about the channel central cross section, where they concur and form a 3D wave; under this same intersection a short-crested antidune would form. Successive pairs of mirror-symmetric oblique waves crossing form a train of 3D stationary waves (stationary in relation to the bed undulation), "rooster-tails", above short-crested antidunes. The characteristics of these diagonal cross-waves can be computed from eqs.(6.46) and (6.46), and from the geometrical correspondences in Figure 6.41 as explained as follows. If the fundamental mode of vibration is excited in the transverse direction to flow, the angle β formed by the oblique standing waves with the channel wall can be expressed as a function of the distance between 3D waves in the direction of flow, i.e., the wavelength λ_1 in Figure 6.41, as

$$\cos\beta = \frac{\lambda_1}{A_n P_1} \qquad (6.47)$$

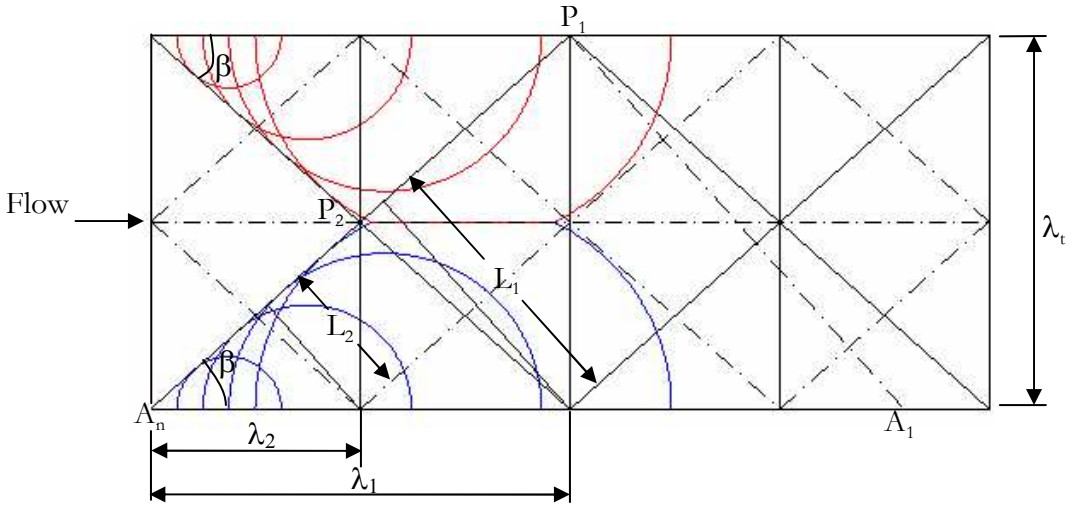

Figure 6.41. Plan view of successive mirror-symmetric oblique standing wave patterns, crossing at the central cross section of a uniform channel, where a train of 3D waves is formed. Cross waves for the fundamental mode of vibration are shown with continuous lines, while broken lines are used for the second mode (adapted from Figure 7-5 in Henderson, 1966).

In order to generalize to any given number of harmonics, the fundamental mode λ_1 can be written as

$$\lambda_1 = m\lambda_m \tag{6.48}$$

where m is any integer and λ_m is the wavelength for the m mode of vibration of the transverse cross waves. Eq.(6.47) can thus take the form

$$\cos\beta = \frac{\lambda_1}{A_n P_1} = \frac{\lambda_m}{A_n P_m} = \frac{\lambda_m}{\sqrt{\lambda_m^2 + \left(\frac{\lambda_t}{m}\right)^2}} = \frac{m\lambda_m}{\lambda_t\sqrt{1+\left(\frac{m\lambda_m}{\lambda_t}\right)^2}} \tag{6.49}$$

where λ_t is the wavelength normal to the direction of flow (Figure 6.41), which can be considered as equal to the width of the channel. In the same manner, it can be written that

$$\sin\beta = \frac{\lambda_t}{A_n P_1} = \frac{\lambda_t}{mA_n P_m} = \frac{\lambda_t}{m\sqrt{\lambda_m^2 + \left(\frac{\lambda_t}{m}\right)^2}} = \frac{1}{\sqrt{1+\left(\frac{m\lambda_m}{\lambda_t}\right)^2}} \tag{6.50}$$

The wavelength for the m mode of the cross waves, to be used in eq.(6.46), can be computed as

$$L_m = \frac{\lambda_t}{m}\cos\beta \tag{6.51}$$

Finally, solving eq.(6.45) for the flow velocity and introducing eq.(6.46) together with eqs.(6.49) to (6.51), it is obtained that

$$V = \frac{c_w}{\sin\beta} = c_w\sqrt{1+\left(\frac{m\lambda_m}{\lambda_t}\right)^2} = \sqrt{1+\left(\frac{m\lambda_m}{\lambda_t}\right)^2}\sqrt{\frac{g\lambda_m}{2\pi\sqrt{1+\left(\frac{m\lambda_m}{\lambda_t}\right)^2}}\tanh\frac{2\pi H}{\lambda_m}\sqrt{1+\left(\frac{m\lambda_m}{\lambda_t}\right)^2}} \tag{6.52}$$

and reducing it yields

$$V^2 = \frac{g\lambda_m}{2\pi}\sqrt{1+\left(\frac{m\lambda_m}{\lambda_t}\right)^2}\tanh\frac{2\pi H}{\lambda_m}\sqrt{1+\left(\frac{m\lambda_m}{\lambda_t}\right)^2} \tag{6.53}$$

Kennedy (1961) advanced a minimum energy hypothesis for flow over antidunes, such that for a given wave amplitude the adopted wavelength would be that for which the total energy of the fluid will be a minimum. He stated that this assumption is possible as the flow deforms the bed to conform to a streamline of the wave. Kennedy demonstrated that this minimum energy assumption corresponds to $H=\infty$, for which $\tanh[2\pi H/\lambda_m]$ approaches unity, and thus eq.(6.53) can be reduced to

$$V^2 = \frac{g\lambda_m}{2\pi}\sqrt{1+\left(\frac{m\lambda_m}{\lambda_t}\right)^2} \tag{6.54}$$

For m=1, eq.(6.54) is equivalent to eq.(5.6), suggested by Kennedy (1961) to be applied to 3D antidunes, and originally developed by Fuchs (1952). Eq.(6.54) is more general than eq.(5.6), since it considers any arbitrary mode of vibration of the diagonal cross-waves in the transverse direction to flow; eq.(5.6) corresponds to the particular case of m=1, i.e., when the fundamental mode is excited.

For large values of λ_t, eq.(6.54) becomes equivalent to eq.(5.5) given by Kennedy (1961) for 2D waves. In turn, if eq.(6.54) is solved for λ_t, as in eq.(6.5), it is found that a real solution is only feasible if

$$V^4\left(\frac{2\pi}{g\lambda_m}\right)^2 > 1 \tag{6.55}$$

This condition defines a lower limit for the formation of 3D waves. Using the definition of the wave number, $k=2H\pi/\lambda_m$, and of the Froude number, $F^2=V^2/gH$, eq.(6.55) can be transformed to

$$F > \frac{1}{\sqrt{k}} \qquad (6.56)$$

that describes the border between 2D and 3D antidunes, and is equivalent to eq.(5.4) presented by Kennedy (1963) for the maximum possible Froude number for a given wave number if the surface waves and bedforms are two-dimensional.

6.5.1.2 Comparison with experimental data

Eq.(5.6), which is equivalent to eq.(6.54) for m=1, i.e. for the fundamental mode of the cross-waves, was compared with the experimental data in Figure 6.11. It was found that eq.(5.6) under estimated the flow velocity for most of the wavelengths of rooster-tails measured. Here, the experimental data are compared with eq.(6.54) to find out if higher order harmonics were excited for the formation of the rooster tails observed.

To determine the order of the transversal oscillations related to the formation of the experimental short-crested waves, it is here hypothesized that the alternate bar configurations observed at the end of most of the runs were related to order one cross-waves. Each half-bar, as depicted in Figure 5.13, would correspond to an oblique standing wave that crosses the channel from one wall to the other. Hence, the ratio between the wavelength of a half-bar $\lambda_b/2$ and the wavelength of a short-crested antidune or rooster tail λ should be indicative of the mode excited in the formation of the 3D waves.

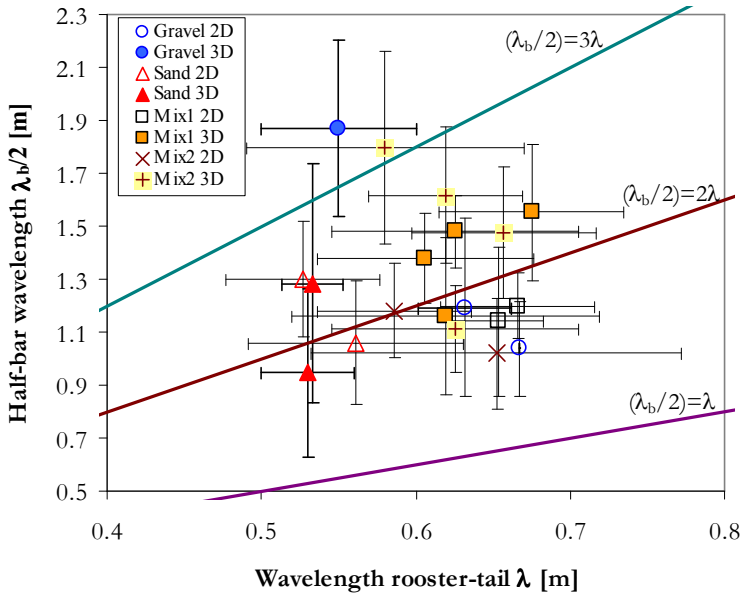

Figure 6.42. Measured wavelengths for 3D waves ("rooster tails"), and half-bar units, with error bars indicating the experimental dispersion. Continuous lines indicate values of the ratio between half-bar and rooster-tail wavelengths of one, two and three. The definition of a bar unit is as described in Figure 5.13.

Measured wavelengths for half-bars and rooster tails have been plotted in Figure 6.42, with the experimental variability indicated with error bars (measured values are those presented in Tables 5.3 and 5.4). Lines corresponding to values of one, two and three of

the ratio between half-bar and rooster tail wavelengths are indicated in the Figure with continuous lines. Since most of the points plot close to the line for $\lambda_b/2\lambda=2$, i.e., the condition for which there were two short-crested waves for each half-bar, rooster tails might have been related to an order two mode of the transversal cross-waves. For only three runs the ratio between the half-bar and rooster tails wavelengths was higher than 2.5, these were runs G12, M2E1 and M2E2. It is likely that for these three runs the third mode of vibration of the transversal cross-waves was excited. Figure 6.43 shows two images from video recordings during the last stages of run M2E2; more than a single row of rooster tails is evident in these images, thus reasserting that higher modes of the cross waves were excited.

Figure 6.43. Water surface configuration during the last stages of run M2E2, recorded in video. More than one row of rooster tails is evident in both images. For the stages of the experiment recorded in these images, rooster tails were present in the last five meters of the channel downstream, while upstream the bed and water surfaces were approximately plane.

For an assessment of the validity of eq.(6.54), this equation was used to compute flow velocities of the experimental data with dominant short-crested waves; for the computations, the measured short-crested waves wavelengths and a value of m=2 were used, except for runs G12, M2E1 and M2E2, for which m=3, according to the conclusions drawn from Figure 6.42. The results are shown in Table 6.4, along with the results using eq.(5.6) (which corresponds to m=1 in eq.[6.53]). Experimental data for short-crested waves in sand beds reported by Kennedy (1961) and by Yokokawa et al. (2010), have been included in Table 6.4. For these two data sets, there was no evidence for higher harmonics being excited, and thus it was considered that m=1.

For experimental data of the current work, computed flow velocities with eq.(6.54) were in average 18% higher than the experimental mean flow velocities, while computed flow velocities with eq.(5.6) (i.e., eq.[6.53] with m=1) were in average 6% lower than the experimental mean flow velocity values. Conversely, for the data sets from Kennedy (1961) and from Yokokawa et al. (2010) the computed flow velocities were in average 21% higher than the experimental mean flow velocities. Figure 6.44a shows these results graphically by comparing experimental and computed flow velocity values with eq.(5.6).

The development of eq.(6.54) in Section 6.5.1.1 considered that water surface waves propagated at a velocity c_w and at the same time they moved downstream at the same velocity as flow. Since flow velocity at the free surface, where the perturbations move, is normally higher than mean flow velocity, it might be more convenient to compare flow velocities computed with eq.(6.54) with flow velocity at the free surface. For computing the

vertical distribution of velocity, the law of the wall, as it is given by eqs.(4.8) and (4.9), is used here. For the free surface velocity eq.(4.8) can be evaluated at the distance above the bed z=H, with a bed roughness length of $z_o=k_s/30$, being k_s the equivalent grain roughness; similarly, the depth average flow velocity can be evaluated with eq.(4.9). From the ratio between eqs.(4.8) and (4.9) it is obtained

$$\frac{V_s}{V}=\frac{\ln\left(\frac{30H}{k_s}\right)}{\ln\left(\frac{11H}{k_s}\right)} \qquad (6.57)$$

where V_s is the flow velocity at the free surface.

Table 6.4 Experimental data for 3D short-crested waves, and comparison with eq.(5.6) (m=1) and eq.(6.54) for computing the flow velocity as a function of wavelength. IT is considered that: $\lambda_t=B$, V_s is calculated with eq.(6.57), λ is the measured wavelength of the 3D waves, λ_b is the measured wavelength of the bar; when applying eq.(6.54), $\lambda_m=\lambda$.

Bed material	Run	B [m]	D_{50} [mm]	H [m]	V [m/s]	V_s [m/s]	λ [m]	λ_b [m]	V Eq.(5.6) [m/s]	$\frac{V_{(Eq.5.6)}}{V}$	m	V Eq.(6.54) [m/s]	$\frac{V_{(Eq.6.54)}}{V_s}$
Gravel	G12	0.75	4.8	0.068	1.16	1.39	0.55	1.87	1.03	0.89	3	1.44	1.04
	G13	0.75	3.8	0.092	1.21	1.43	0.67	-	1.18	0.98	2	1.46	1.03
	G14	0.75	4.4	0.076	1.18	1.41	0.60	-	1.10	0.93	2	1.33	0.95
	G15	0.75	4.1	0.079	1.14	1.35	0.61	-	1.11	0.97	2	1.35	1.00
Mix1	M1E2	0.75	3.3	0.086	1.30	1.53	0.68	1.55	1.19	0.92	2	1.47	0.96
	M1E3	0.75	3.2	0.076	1.18	1.39	0.61	1.38	1.10	0.93	2	1.34	0.96
	M1E4	0.75	3.4	0.087	1.20	1.41	0.63	1.48	1.13	0.94	2	1.38	0.97
	M1E5	0.75	3.3	0.090	1.16	1.36	0.62	1.16	1.12	0.97	2	1.37	1.00
Mix2	M2E1	0.75	2.5	0.081	1.28	1.50	0.62	1.62	1.12	0.87	3	1.61	1.07
	M2E2	0.75	2.5	0.080	1.32	1.55	0.58	1.80	1.07	0.81	3	1.51	0.98
	M2E3	0.75	2.5	0.083	1.26	1.47	0.66	1.47	1.17	0.93	2	1.44	0.98
	M2E4	0.75	2.4	0.089	1.17	1.37	0.63	1.11	1.13	0.96	2	1.38	1.01
Sand	S1	0.75	1.6	0.103	1.03	1.19	0.53	1.28	1.01	0.98	2	1.20	1.01
	S2	0.75	1.5	0.109	0.97	1.12	0.53	0.95	1.01	1.04	2	1.20	1.07
Sand [Kennedy, 1961]	4-24	0.27	0.20	0.04	0.69	0.78	0.28	-	0.79	1.15	1	0.79	1.02
	4-25	0.27	0.17	0.05	0.48	0.54	0.18	-	0.59	1.23	1	0.59	1.09
	4-29	0.27	0.21	0.05	0.75	0.85	0.36	-	0.98	1.30	1	0.98	1.16
	5-2	0.27	0.55	0.05	0.50	0.58	0.18	-	0.58	1.14	1	0.58	1.00
	5-4	0.27	0.57	0.05	0.84	0.96	0.41	-	1.07	1.28	1	1.07	1.12
	5-5	0.27	0.55	0.07	1.08	1.23	0.61	-	1.54	1.42	1	1.54	1.25
	5-7	0.27	0.55	0.04	0.79	0.91	0.30	-	0.85	1.07	1	0.85	0.93
	5-8	0.27	0.59	0.04	1.30	1.50	0.66	-	1.65	1.27	1	1.65	1.10
	5-9	0.27	0.58	0.05	1.01	1.16	0.49	-	1.26	1.24	1	1.26	1.08
	5-10	0.27	0.55	0.05	0.67	0.77	0.26	-	0.75	1.13	1	0.75	0.98
	5-17	0.27	0.59	0.04	1.09	1.25	0.51	-	1.31	1.21	1	1.31	1.05
Sand [Yokokawa, 2010]	4	0.30	0.18	0.04	1.07	1.21	0.46	-	1.15	1.07	1	1.15	0.95

In order to verify the validity of eq.(6.57), Table 6.5 shows flow velocity measurements performed at the free surface during equilibrium state in the run series with sand. Measurements were performed using a piece of rubber and a chronometer; the rubber was

put on the water surface some meters downstream of the uppermost reach of the channel, and time was taken with the chronometer for the floating rubber to travel 20 meters downstream. Five to six measurements were obtained for each sand run. Using eq.(6.57) with the experimental mean flow velocities and water depths, and considering $k_s=D_{50}$, computed superficial flow velocities were 1.19, 1.12, 1.02 and 0.94 m/s for runs S1, S2, S3, and S4, respectively; the difference between measured and computed values is only 1%, 3%, -2% and -6%, respectively, and thus eq.(6.57) can be considered to be a reasonable approach.

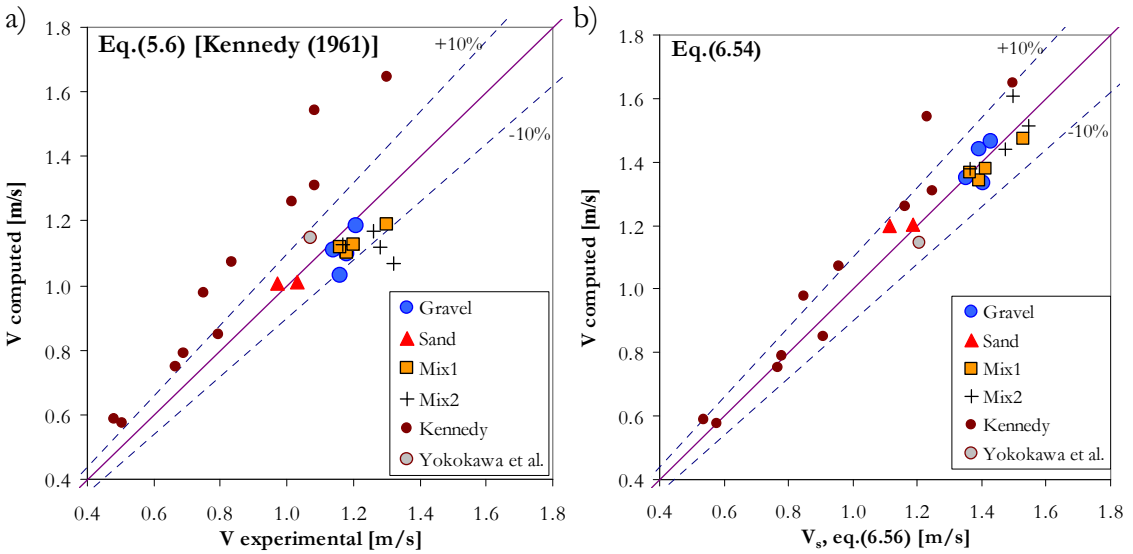

Figure 6.44. Comparison of experimental flow velocities with computed flow velocities using a) eq.(5.6), and b) eq.(6.54), for 3D short-crested stationary waves accompanied by 3D antidunes.

The superficial flow velocity was computed with eq.(6.57) for all experimental data in Table 6.4; results are shown in that same Table. The average ratio between velocities computed with eq.(6.54) and surface velocities for the current work experiments was equal to 1, with a dispersion of 4%, while for the data sets of Kennedy and Yokokawa et al. this same average ratio was 1.06, with a dispersion of 9%. These results are shown graphically in Figure 6.44b, where it is evident that the use of eq.(6.54) considering high order harmonics for the cross-waves to compute the surface velocity improves the results in comparison to eq.(5.6), whose performance is shown in Figure 6.44a.

Table 6.5 Experimental flow velocities for runs with sand.

Run	Mean flow velocity V [m/s]	Measured superficial flow velocity V_s [m/s]						Average V_s [m/s]	V_s/V
S1	1.03	1.11	1.18	1.25	1.18	1.18	-	1.18	1.14 ±0.048
S2	0.97	1.11	0.95	1.18	1.11	1.05	1.11	1.09	1.12 ±0.079
S3	0.89	1.11	1.11	0.91	1.05	1.00	-	1.04	1.16 ±0.096
S4	0.82	1.00	0.95	1.05	0.95	1.03	-	1.00	1.22 ±0.054

6.5.1.3 Discussion

The results above show that rather than the ambiguity in defining a transversal border for the short-crested waves, as Kennedy (1961) interpreted the failure of eq.(5.6) when applied to his experimental results, the poor performance of that equation with the experimental data can be explained by the omission of flow velocity vertical profile, and the consideration of a unique mode of vibration. The decrease of computed transversal wavelength with shear stress in Figure 6.12 can thus be explained as an effect of the velocity gradient, rather than an effect of the bed material and scour wholes, as initially speculated in Section 6.2.3.2.1.

The results above also indicate that the influence of the channel walls was relevant in the formation of steep short-crested waves in the experiments. These waves formed roughly at the end of the first third of the channel upstream (within the first 10 m from the intake), where antidunes were roughly 2D, and grew in height and three-dimensionality as they progressed downstream, until they reached a roughly stable geometry along the middle third of the flume (from 12 to 20 m from the intake). This geometry was approximately conserved until the downstream end of the flume. Since antidunes at their beginning stages on the uppermost reach of the channel grew in length and decreased their speed as they progressed downstream, it is likely that the formation of 3D waves occurred when the wavelength of the antidunes matched with the length of the transversal waves. At those beginning stages the waves were not always stable, but gained stability and height as they progressed downstream. Yokokawa et al. (2010) studied the formation of upstream-migrating 3D antidunes in a 0.3 m width and 10 m long flume with 0.18 mm sand; for one of their experiments (the same summarized in the last row of Table 6.4) they described the formation of 3D stationary waves above 3D antidunes as a process with a strong feed-back between bed and water surface; they identified the following stages in the genesis of rooster-tails: 2D antidunes formed first, which triggered the formation of transversal surface waves; when the wavelength of these waves matched with the wavelength of the antidunes, rooster tails and 3D antidunes formed; finally, the surface waves broke and the bed and water waves were erased. This process was repeated with a periodicity of roughly 1 minute. Unlike the 3D waves described by Yokokawa et al. (2010), similar to those described by Kennedy (1961) as well, which formed and vanished periodically, the waves in most of the current experiments were more or less stable and the trains of waves did not vanished regularly. It is likely that the length of the flume in the current experiments promoted the organization of the flow and sediment interactions to reach a roughly stable pattern in the lowermost reach; Kennedy and Yokokawa et al. used shorter flumes (12 and 18 m the former, 10 m the latter), thus, perhaps their flumes were not long enough for the bedforms to reach stability.

6.5.2 Discussion on bed erosion patterns

The experimental patterns of maximum transversal bed erosion were described in Section 5.3.5. This data are analyzed and discussed here, considering the mean and maximum cross sectional erosion depths equal to the mean and maximum active layers defined in Figure 5.20, respectively. The main difference between erosion patterns for sand and mixtures can be illustrated with the two plots shown in Figure 6.45. The plot to the left shows the ratio between mean transversal erosion z_{sMEAN} and water depth H against the grain related Shields stress τ'^*, while the plot to the right shows the ratio between the maximum transversal erosion z_{sMAX} and water depth against the grain related Shields stress τ'^* as well. It is seen that for all the three bed materials, bed erosion fluctuated in a range from roughly 0.4 to 1.1 times the water depth, with an increasing trend with average Shields stress, as it

would be expected. Careful comparison between the two graphics shows that the erosion ratio for sand remains almost constant for the two graphics, while for mixtures the values on the graph to the right plot slightly higher. This result is an effect of the higher transversal variability observed in runs with sediment mixtures; for sand beds the erosion depth was almost transversally constant (see Figure 5.19 and Appendix XI). For mixed sand-gravel beds the deepest erosion occurred at the central cross section for the runs in which highest rooster tails were observed, while for runs with the lowest Froude numbers transversal variation of maximum erosion was not significant. A qualitative explanation for this difference between sand and mixtures is advanced below.

Chanson (2000) measured velocity profiles under standing waves at supercritical flows, in a flume with fixed bed; he found that for undular flows a high spatial variation on boundary shear stress occurs, with the highest values at the channel central cross-section and under the trough of stationary waves. Such a concentration of shear stress is owed to the curvature of the flow under stationary waves, with pressure gradients larger than hydrostatic for concave flow under the wave trough. Chanson stated that higher concentrations of boundary shear would produce deepest erosion at the channel center of loose boundary flows. The bed erosion patterns for sand-gravel mixtures in the current experiments, with concave upward scour holes at the channel center line and less deep erosion next to the channel walls (see Figure 5.19 and Appendix XI), correspond well to the findings of Chanson; in turn, the deepest erosion region can be linked to the steep short-crested stationary waves at the channel center line. Nevertheless, the almost constant transversal erosion found in sand beds does not agree with the general conclusions from Chanson.

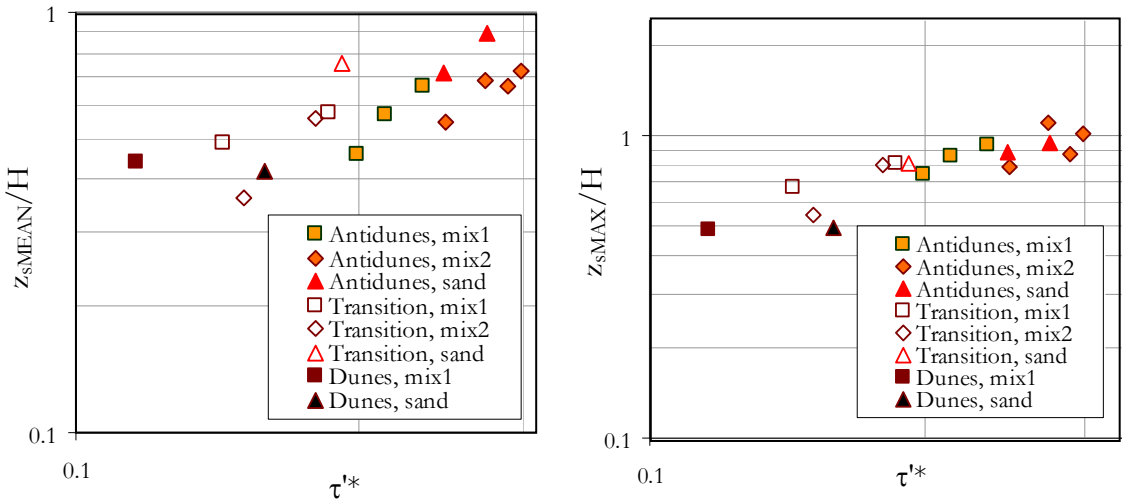

Figure 6.45. Variation with grain related Shields stress of the ratio between mean bed erosion depth and water depth (left), and the ratio between maximum bed erosion and water depth (right) for the experimental runs with sand and sand-gravel mixtures.

The likely reasons for the almost constant transversal erosion pattern found in sand beds can be found on the conclusions obtained by Breakspear (2008) after performing measurements over fixed antidunes at supercritical flows. Breakspear (2008) measured velocity and turbulence over fixed sinusoidal artificial antidunes for three different bedform steepness, and for three different roughness conditions, namely, sand, gravel and openwork gravel. He found that turbulent stresses and the magnitude of instantaneous velocities in

the trough region were positively correlated with the antidune amplitude. Attending to this prominence of the bedform height in boundary shear stresses, it might be expected that bed erosion produced by the passage of bedforms in supercritical flow should also be strongly correlated to bedform height: steep bedforms would be associated with deepest erosion depths. These reasoning agrees with the experimental observations; bedforms in sand beds were approximately two times higher than bedforms in mixtures, consequently, mean erosion in sand was approximately two times deeper than mean erosion in mixtures, as can be seen in Figure 5.19. Then, the reason for an almost constant transversal erosion pattern in sand might be that even when rooster tails were present in the runs with sand, their effect must have been subdued by the steep stationary waves related to the high bedforms extended all along the transversal section. Boundary shear stresses related to the steep bedforms must have been of comparable magnitude to those associated with the rooster tails; accordingly, local mean boundary shear stresses must have been almost equally distributed on the transversal section. Conversely, for runs with mixtures there must have been a high spatial variation of boundary shear stress, with maxima in the channel central section, as found by Chanson (2000) for undular flows. The maximum cross-sectional erosion values for mixtures were close to those in sand, most likely because for mixtures the boundary shear stress in the central cross section was enhanced by the steep short-crested waves.

Figure 6.46a corroborates the reasoning above. This Figure shows the variation of the ratio between the mean short-crested wave height Δ_w and bedform height Δ with Froude number. For sand runs the ratio is close to one, while for mixtures it is much higher than two, thus it is evident that for sand runs the height of the rooster tails was of similar magnitude to the dominant bedforms, and therefore the potential of the former to erode the bed was comparable to that of the stationary waves over the steep bedforms that extended all along the transversal section.

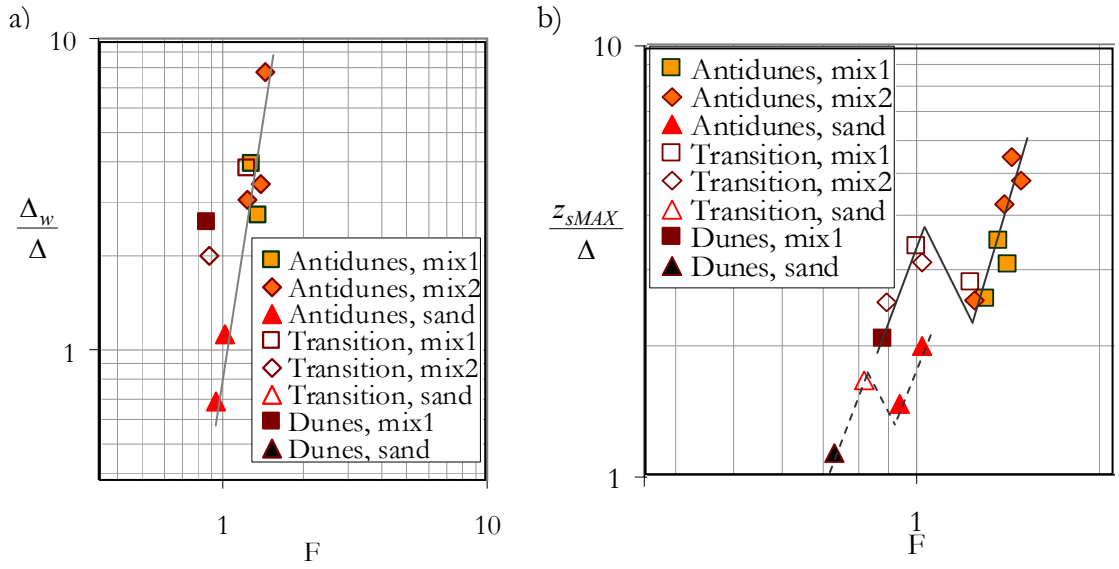

Figure 6.46. Variation with the Froude number of the ratio between a) mean short-crested stationary wave height and bedform height, and b) the ratio between maximum bed erosion and bedform height. Bedfrom height was computed from statistical dispersion of measurements of temporal variation of the bed profile, during equilibrium, on the channel wall, as presented in Table 4.4.

In his measurements over fixed symmetric antidunes, Breakspear (2008) also found that turbulence statistics were one order of magnitude lower over sand antidunes than over gravel and openwork antidunes. Extrapolating these results to the observations in the current experiments, it is likely that the higher grain roughness in runs with mixtures in comparison to sand runs must have contributed to enhance turbulence in the central section. For runs with mixtures, sand was preferentially transported through the lateral sections (see Figure 5.29), consequently, grain roughness must have been higher in the channel central section and this would have favored a higher concentration of turbulent stresses produced under the rooster tails troughs, and accordingly deepest erosion.

A summary of the statements above can be advanced with Figure 6.46b. In that Figure the ratio between maximum transversal erosion and bedform height (as given in the third column of Table 5.4) has been plotted against the Froude number. Overall, a clear trend is evident toward a positive increment of erosion with Froude number in relation to bedform height. Data can be interpreted as collapsing into two distinct groups, one for sand and one for mixtures, and within these two groups two distinct trends are evident: one for data for bedforms labeled as dunes and transitional bedforms, and a second group for antidunes (except for one point for mixture 1, originally labeled as transitional bedform). The slopes of the lines that would fit to the trends exhibited by the four groups are quite similar. For groups of similar material, a sharp discontinuity for roughly Froude numbers close to one separates low regime bedforms from upper regime bedforms. Such a discontinuity, associated to the transitional regime, gives evidence of the distinct processes characterizing bedforms in the lower and upper regime. As opposed to lower regime, for upper regime there is a strong feedback between the water and the bed surface; it can be expected that for upper regime the height of the stationary waves over the bedforms has an important influence on the boundary shear stress, as indicated by Chanson (2000), and thus an important influence on bed erosion. The higher the bedforms, the higher the stationary waves, and thus the positive correlation between boundary shear and bedform height found by Breakspear (2008). Following this, trends in Figure 6.46b could be interpreted as an increase of maximum erosion due to an increase of the stationary waves effect in boundary shear with Froude number; however, if Figure 6.3 is revised, it is found that in fact the trends in Figure 6.46b can be also related to a strong decrease in bedform height with Froude number. For higher Froude numbers such a decrement would tend to the limiting case of upper stage plane bed, for which bed erosion would not be significant, and antidunes and stationary waves would vanish.

In short, from the observations above, it can be concluded that the stationary waves over the bedforms had a fundamental role in the observed bed erosion patterns: the higher the bedforms, the higher the stationary waves, and also the higher the boundary shear stresses associated to bed erosion. In flows for which steep rooster-tails were formed, the deep erosion at the channel central section was related to these 3D stationary waves formed by transversal cross-waves. For the sand runs the bedforms along the cross section were so steep, that even when rooster-tails were present, the stationary waves above the bedforms were dominant, and thus the erosion depths were almost constant all along the cross section.

6.5.3 Interpretation of grain size sorting trends and links to sediment motion and flow

One of the constraints desired for the experimental runs was that the flow were competent to move all sediment size fractions, i.e., avoid partial transport conditions. In a pure feed-flume such a condition is given by the boundary conditions; conversely, for the current experiments in which a hybrid-feed operation was used, as defined in Section 3.2, partial

transport was likely to occur, but for a narrow range of flow conditions. For testing the flow competence in all the experimental runs using criteria found in literature, the grain related Shields stress τ'^* has been plotted against the particle Reynolds number in Figure 6.47, for each size fraction and the conditions of each run. If the flow was competent to move a given grain size class, the data point should plot above the curve for incipient motion. In the Figure the incipient motion criterion of Shields was used, first with the fitted curve to the Shields data suggested by Maza and García (1986), and secondly, using the curve suggested by Parker (2004, given by eq.[6.43]). The latter gives values of τ'^* for the onset of motion roughly half those given by the former curve, for a wide range of Re_p values. The entire experimental data plot above the curves suggested by Parker and by Maza and García, but for the latter curve some data for the two coarsest size fractions fall below. The data plotting below correspond to the center of class for grain size of 7.10 mm for runs G17, M1E6 and M2E6, and to the center of class for grain size of 8.94 mm for runs G17, M1E1, M1E6, M2E5 and M2E6. No clear evidence was found in the sediment transport samples and bed material samples of a lack or drop in the fractional participation of this two size fractions. Since the fractional content of this two size fractions in the bulk of the sediment was too low, if their participation in transport was reduced it must have been hidden by the measurements accuracy, and it can be expected that it must have not affected considerably the dynamics of sediment transport on the bed.

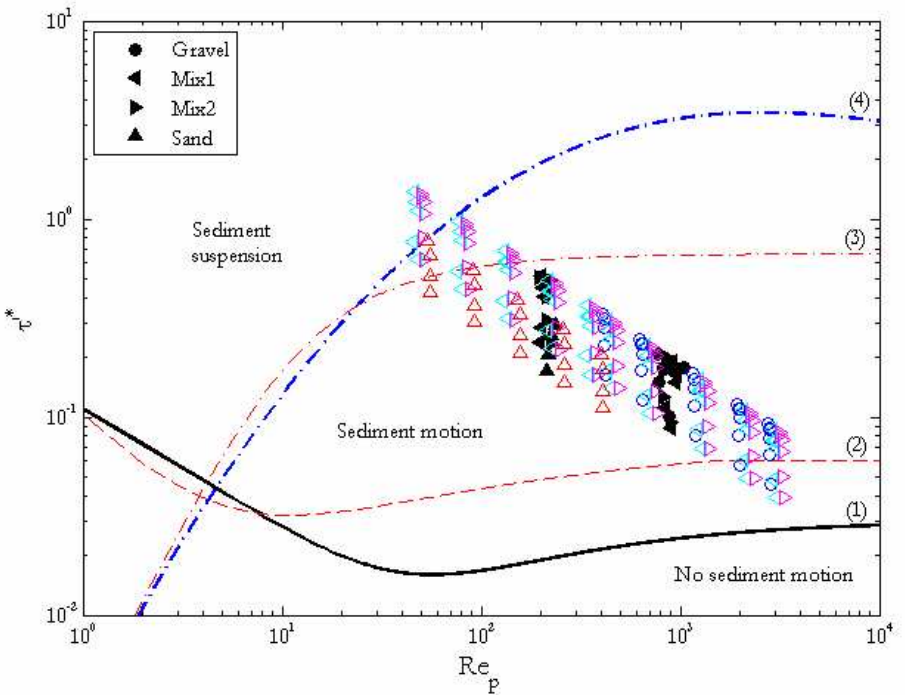

Figure 6.47. Effective Shields stress (eq.6.29) as a function of the particle Reynolds number (eq.6.30) for all the experimental data presented by grain-size fraction. Solid symbols indicate mean diameters, while open symbols indicate grain-size fractions with the following centers of class: 0.56, 0.79, 1.12, 1.58, 2.12, 2.5, 3.35, 5.02, 7.10, 8.94 mm. The curves correspond to (1) the modified Shields incipient motion criterion given by eq.(6.34) as suggested by Parker (2004); (2) the Shields incipient motion criterion as suggested by Maza and García (1986); (3) the onset for sediment suspension using the formula for particle fall velocity of Dietrich (1982); (4) the onset for sediment suspension using the formula for particle fall velocity of Rubey.

In order to test if sediment could have been put into suspension, two criteria for computing settling velocity of particles have been included in Figure 6.47. The first criterion was suggested by Rubey (in Maza-Álvarez and García-Flores, 1996), while the second is owed to Dietrich (1982). If the criterion of Rubey is considered, none grain size fraction would have traveled in suspension, except for the 0.2 mm size fraction in most of the runs with mixtures but two; conversely, the criterion of Dietrich indicates that the size classes of 0.20 and 0.56 mm would have travel in suspension for most of the runs with mixtures and some of the runs with sand. Since these latter size fractions were in the tail of the grain size distributions, their participation in the bulk sediment was too low. By direct observations during the experiments, it was difficult to realize if sediment was brought into suspension. Some of the finest particles followed large trajectories, but they did seem to come in contact with the bed regularly. Therefore, it can be considered that all of the particles were transported most of the time as bedload.

Although most of the particles traveled bouncing, rolling or saltating along the bed, the sand particles could be in motion more frequently than gravel particles, and could travel at higher elevations. Sand grains could be ejected from the bedform crest and travel long distances without coming in contact with the bed. Conversely, gravel grains traveled most of the time rolling, and could be ejected far apart from the bed seldom and only for some of the flows with the highest Froude numbers. These main differences in the motion of sand and gravel can be directly related to two of the most general grain sorting patterns observed and measured:

- **Coarsening of the channel central cross-section and of the bar-trough**. It was found from samples of sediment transport, bed samples at successive elevations, and observations of transversal bed sections opened to measure maximum erosion, that coarse material tended to be more abundant at the channel central section (see Sections 5.3.6.3 and 5.3.6.5). Visually, it was apparent that the coarsest particles were even more abundant, and sand more scarce, in the erosion dips at the channel center line. Lenses of open framework gravel were common at the central transversal section, while next to the channel walls, the bed structure was mostly a sand matrix. In the same vein, bed samples showed that the bar-troughs were coarser than bar stoss-sides (see Figure 5.35 for a definition of trough and stoss bar regions); fine patches were never found in the trough region (see Section 5.3.6.4.5 and Figure 5.38).
- **Fining up- and wallward**. Bed material sampling showed a systematic trend for the upper bed layers being finer than the lower layers. Surface and subsurface bed samples showed that sand content was higher for the former than for the latter (see Section 5.3.6.4.4). In turn, analysis of bed samples showed that the gravel size fraction in samples taken from the stoss side of the bar was finer than gravel taken from the bar trough (see Section 5.3.6.4.4, Figure 5.39, and for a definition of trough and stoss bar regions see Figure 5.35); in other words, gravel forming the bar platform was finer than gravel at a lower elevation in front of the bar oblique front. In the same vein, in many runs patches of fine material were evident on the stoss side, but never on the bar trough. Although upwards fining was evident, a trend toward a subtle decrease of sand content in fine surface patches with bed Shields stress was apparent (see Figure 5.36). Finally, samples of sediment transport showed that fine material traveled preferentially through the lateral sections (see Figure 5.29).

Coarsening of the channel central section and of the trough in a bar unit can be related to the movement of gravel rolling and tending to travel along the lowest topographic elevations. Conversely, surface and wallward fining can be related to the movement of sand bouncing, so that it could reach highest elevations than gravel, being the highest elevations

the crests of the bars next to the wall. For intermediate Shields stress values, fine surface patches were common on the bar stoss surface, but sand content in these patches decreased with increasing Shields stress; this trend can be interpreted as the increment of momentum in gravel that allowed coarser grains to climb further to the bar highs as the sand.

6.5.3.1 Processes of sediment sorting and sediment transport patterns

The observed sediment segregation patterns described above can be linked to processes previously identified by different authors (e.g., review by Powell, 1998). The concentration of coarse particles on low topographic elevations is known as "topographic sorting" (Paola, 1989), and it occurs when a transversal slope exists while bedload is transported downstream. Due to gravity, particles are directed toward the lowest elevation. Coarser particles are more directly deflected laterally toward the base than finer particles, since the weight of a sediment grain scales to the cube of the grain diameter, while drag force, exerted by the downstream flow, scales with the square of the diameter. Topographic sorting must have been relevant to direct and accumulate the coarsest particles of the sand-gravel mixtures into the scour holes opened by the rooster-tails in the channel center line.

Besides topographic sorting, it is likely that a three-dimensional flow field had an important role in the trajectories followed by the particles and their classification, similarly as it occurs in the classification of material in river bends (e.g., Parker and Andrews, 1985). In particular, wallward fining might have been related to a cross-stream sediment flux. It was commonly observed in the experiments that the superficial flow from the crest to the trough of rooster-tails slightly diverged from the channel center line (see Figures 5.1 and 5.2). Considering that at the bed level flow under the rooster tails must have been divergent as well, this flow must have directed laterally the scoured sediment from the channel center. The balance between gravity and drag on the grains, this latter exerted by the lateral and downstream flows, would have controlled the distance traveled by the scoured particles; finer particles would have reached higher elevations on the lateral bars and on secondary bedforms next to the channel walls than coarser grains. In this manner, the bar platform would have accumulated finer material than the material close to the scour holes, and finer than the material on the bar troughs at a lower elevation; this agrees with the observed trends for bed material samples: coarsening of the bar trough, and fining wallward and downstream toward the highest elevation on the sloping bar. The oblique fronts of the alternate bars must have contributed to balance the transversal sediment flux by directing sediment on the lateral sections to the channel center. In summary, the force balance between drag and gravity, and the bed topography constructed by the bedforms, with a minimum at the channel center and a positive slope toward the walls, would have controlled the trend for coarser particles to move along the central channel line, and fine material along the sides; it is likely that intermediate grain-size particles would have a frequent transversal movement, while the trajectories of grain sizes in the tails of the grain size distribution would have followed the main direction of flow more frequently: along the channel central line the coarsest material, and close to the flume walls the finest material.

Whiting and Dietrich (1991) studied the distribution of boundary shear stress over an alternate gravel bar. They found that zones of bed surface coarsening matched with high shear stress zones; in this manner, segregation of coarse material prevented topographic modification of the bar. As already explained in Section 6.5.2, for the current experiments the highest local shear stresses must have occurred under the trough of short-crested stationary waves, in the central transversal section. Similarly as in the measurements of Whiting and Dietrich (1991), coarsening of the bed in this region of maximum shear stress must have prevented the development of deeper scour holes. In turn, concentration of

coarse material in the central section must have exerted an influence in the transversal distribution of sediment transport. In spite of the local concentration of boundary shear stress at the channel center, manual sediment transport samples showed that the average solid discharges passing through the center and lateral cross-channel sections were roughly the same (see Table 5.7 and text in Section 5.3.6.1). Coarsening must have been one of the controls to balance solid discharge transversally, but additionally, the periodical stream-wise distribution of this maximum stress, and lateral flux of sediment must have encouraged such a transversal balance as well. For the assessment of the likely relative influence of bed material coarsening in this balance, computations were performed with a sediment transport predictor, as explained below.

Table 6.6 Average characteristics for sediment taken from manual samples of sediment transport, for runs with sand-gravel mixtures (grain-size distributions in Figure 5.28). D_{50} is the median grain-size, f_s is sand content, and τ' is grain related shear stress computed with the sediment transport formula of Wilcock and Crowe (2003); subscripts $_{cs}$ and $_{ls}$ denote central and lateral cross-channel sections, respectively.

Mix	Lateral sections		Central section		$D_{50,cs}/D_{50,ls}$	$f_{s,cs}/f_{s,ls}$	τ'_{cs}/τ'_{ls}
	$D_{50,ls}$ [mm]	$f_{s,ls}$	$D_{50,cs}$ [mm]	$f_{s,cs}$			
1	3.2	0.34	3.5	0.29	1.09	0.86	**1.07**
2	2.7	0.42	3.1	0.34	1.14	0.80	**1.11**

Powell et al. (1999) analyzed cross-stream variations in bed-load transport rates in two ephemeral coarse-grained streams. They found that, on average, measured solid discharges at the cross-stream center were consistently about twice those measured at the lateral cross-sections. For one of the streams, Powell et al. obtained estimations of local shear stress in relation to channel-average shear stress using measured local transport rates and a channel-average bed-load relation; by doing this they could relate the cross-stream variability in transport rates to a bankward decline in shear stress as an effect of sidewall drag. Using a similar method as that of Powell et al., the sediment transport relation of Wilcock and Crowe (2003) was used here to estimate the average ratio between local bed shear stress in the central and lateral transversal sections from sediment transport samples in the current experiments. This relation was used, since it includes sand content as a relevant variable. Average grain size distributions of sediment transport samples for each mixture were used for the computations (Figure 5.28). Data and results are shown in Table 6.6. For the computations, it was considered that average solid discharges at the lateral and central cross-channel sections were the same, and that no lateral sediment flux occurred, so that each section acted as an independent channel. Results showed that only a difference of 7% and 11% in grain shear stress, for mixture 1 and mixture 2, respectively, would suffice to transport at the same rate the material collected at the lateral (finer material) and central (coarser material) cross-channel sections. These results are contrasting with measurements of boundary shear stress under stationary waves along an undular hydraulic jump, performed by Chanson (2000) in a 0.25 m wide channel. From Figures presented by this author (Figures 7 and 8 in Chanson, 2000), a high variation of boundary shear stress in the cross-channel section is evidenced, being the shear stress values on the central transversal section higher than the values on the lateral section, by a factor even as high as two. The ratio between maximum wave height and water depth in the experiments of Chanson varied from 0.26 to 0.67 (Table 3 in Chanson, 2000). Since in the current experiments for the short-crested waves in the channel center line this ratio ranged from 0.48 to 1.6 (using data given in Table 5.3), it can be expected that similar, and even higher differences between central and lateral shear stress values as those measured by Chanson could have

occurred. Accordingly, the values of 7% and 11% computed with the sediment transport relation seem to be too low in comparison to the measurements of Chanson. Thus, it can be concluded that coarsening of the channel central cross-section might have not been the most important factor to counteract the high concentrations of boundary shear stress at the channel center line in order to achieve equality of transport across the section.

If bed coarsening was not the most important factor that prevented the zone of maximum shear stress from matching with a maximum average solid discharge laterally, it is likely that the high spatial and temporal concentration of this maximum shear stress, and transversal mass transfer were the key factors in promoting a cross-channel balance in time-average solid discharge. As explained above, peak shear stress values on the bed were most likely to occur under the trough of rooster tails on the cross-channel central section; thus, these maximum values would be associated with the same periodicity of the short-crested stationary waves. Accordingly, the boundary shear stress field along the channel center line could be idealized as a succession of pulses in phase with the surface stationary waves. Conversely, in the cross-channel sections close to the flume walls, no important bed shear stress variations would have occurred in correspondence with the gentle stationary waves on the water surface. Hence, at a given channel central section peak shear stresses would have occurred seldom, but with a magnitude much higher than on the lateral sections where shear stress values would have shown low variations in time. The surface integration of local sediment transport rates associated to these local shear stresses along a bar unit should result in the same value for the cross-channel central section and the lateral sections, so that the net cross-channel sediment transport balance were fulfilled. Following this reasoning, it should be expected that the dispersion (e.g., standard deviation) of the time series of sediment transport passing through the channel central cross-section would be higher than for the cross-channel lateral sections: frequent peaks and lows in the center, and an almost constant signal in the lateral sections. Manual samples of sediment transport taken from the channel were not able to capture such variability. Dispersion of the sediment transport rates obtained from samples of each of the three compartments of the basket-type sampler (each compartment captured sediment passing through one third of the cross-channel section, see Section 3.3.2.5.2) exhibited no statistically significant difference, as can be seen in graphs shown in Appendix X. Conversely, for three runs, samples taken with the Helley-Smith type sampler (only used in runs with mixture 2, to sample the cross-channel central section) showed an increase in standard deviation (of 61%, 36% and 55%, from data in Table 5.6) in comparison to samples with the basket-type sampler. As explained in Section 5.3.6.1, the Helley-Smith would have been better able to capture point variations in sediment discharge in time and space due to its short span of the intake opening, while the basket-sampler would have lessened peak solid discharges. Comparison of sampling durations (Table 3.11) with celerities and wavelengths of the stationary waves (Table 5.3) shows that the average sampling duration for the basket-type sampler corresponds to 32% of the period of a rooster tail, and to 68% for the Helley-Smith. Hence, both samplers would not have captured narrowly concentrated peak solid discharges, which could have been associated with the passage of short-crested antidunes under rooster-tails.

Along with the intermittency of maximum shear stresses in the central cross-channel section, lateral sediment transfer must have contributed to a net balance in cross-channel sediment transport as well. It is likely that the bed shear stress vector acting under the rooster tails at the channel center could be slightly directed toward the channel wall. Thus, grains would have been delivered laterally. In order to balance mass transfer, the oblique fronts of the alternate bars would have directed particles toward the channel center.

6.5.3.2 Formation of well-sorted sediment patches and deposits

Sediment sorting during the experiments was closely related to the scour and fill processes inherent to the progression of bedforms. No measurements or evidence was obtained of the bed surface sorting and bed texture changes while the water was flowing in the flume. When the experiment finished and water was drawn down, the scour holes in the channel central section (related to short-crested downstream-migrating antidunes) were filled, and little evidence was preserved on the bed configuration of the steep antidunes migrating through the channel central cross-section. Conversely, the gentle bedforms moving close to the channel walls, and classed as downstream-migrating antidunes and alternate bars, were mostly preserved. At the central section, forms were swept and scour holes were filled, almost immediately, after the water discharge was stopped; on the contrary, lateral bedforms remained almost unaltered when water discharge was stopped, and they even continued moving some time further while the water table declined rapidly. Consequently, the preserved grain sorting conditions on the bed surface were contingent on the stoppage of the experiment. In turn, it can be expected that deposition of most of the substrate bulk material occurred during the stable conditions of the experiment, and thus, that only in some sections the substrate grain size distribution was related, to a certain extent, to the stoppage of flow.

When the experiment was finished, water discharge was stopped, and, in average, two minutes were required for the water discharge, flow velocity and water depth in the channel to recede. It was not possible to control the conditions in which the water stage and discharge declined when the experiment was stopped; nevertheless, it can be assumed that these conditions would resemble the rapid recession of the hydrographs common of flash-floods in ephemeral streams, as can be seen in Figure 2.1 for a measured hydrograph in the Riera de las Arenas. For this hydrograph the transition from the peak discharge to less than half the peak value occurred in just some minutes; if the current experiments were thought as a scaled model of a real ephemeral stream based on Froude similarity, the two minutes in model would represent 14 minutes in prototype for a ratio 1/50 between model and prototype lengths (time scales multiplied by the squared root of the length scale). Further evidence on a good correspondence with field conditions is given by the agreement with sediment sorting trends reported for the surface of bars in natural streams, as will be discussed in Section 6.5.4.2.

The coefficient of variation (standard deviation divided by the mean) for the ratio between sand content in bed samples and sand content in the material fed was 35% higher for surface than for subsurface samples for mixture 1, and 46% for mixture 2 (from data in Table 5.10). In turn, the mean value of this same ratio was close to unity for subsurface material, while for surface material its value was 1.41 and 1.15, for mixture 1 and mixture 2, respectively. These statistics give evidence of the more stable characteristics of the substrate material compared to the surface material. Also, these results reinforce the arguments in favor of the common practice of using substrate material samples for bulk sediment transport computations.

The main control on the sediment deposited in the substrate was set by the bedform progression. The major discontinuity produced by this process was the formation of open-framework gravel deposits. Substrate samples with sand contents lower than 10% give evidence of these deposits, which were more abundant and free of sand in the scour holes in the channel central cross-section of mixture 1. Evidence of this is found in sediment samples shown in Figures 5.40 and 5.41. According to Lunt and Bridge (2007), the formation of open-framework gravel is related to the segregation of sand and gravel at the crests of bars and dunes when the former travels in suspension and the latter as bedload; this segregation is more effective for high aggradation rates and the higher the bedform is.

In the current experiments, open framework gravel formation must have been related to the steep short-crested antidunes at the channel central cross-section, where the flow under the rooster-tails must have been very effective in segregating sand from gravel. The formation mechanism of the open-framework gravel must have been similar to that described by Lunt and Bridge for dunes and bars.

The largest heterogeneity of the surface samples compared to subsurface samples was related to the patchy configuration of the final bed surface. Such heterogeneity was less pronounced in the runs with the lowest Froude numbers, as can be concluded from a careful analysis of grain size distributions in Appendix XII, and from plots in Figure 6.48 below. The Figure has been split in two boxes for a better distinction between types of patches. From this Figure, it is evident that in the two mixtures the whole of samples spanned all over the spectrum of sand contents (from 0 to 100%); nevertheless, it can be found that fine patches (sand content >70%, as it was defined in Section 5.3.6.4.3) were absent roughly for critical and lower than critical Froude numbers. For this same range of Froude numbers, coarse patches (sand content <30%) were on the upper limit of sand content to deserve such a classification. Put in other words, for high Froude numbers coarse patches could be coarser and fine patches could be finer than for runs with the lowest Froude values. This trend gives evidence of the high capacity of supercritical flows to sort bed material and to form well-sorted surface patches irrespective of the sand content of the bulk sediment load. Not a clear trend to distinguish between the two mixtures was found, though a subtle bias toward coarser coarse-patches in mixture 1 is apparent in Figure 6.48. As demonstrated in Section 5.3.6.4.5, fine (coarse) patches were most common on the downstream end of the stoss-side (trough) of bars, but were never found on the trough (stoss) region. This feature could be an artifact of the waning flow washing out fines from the bar trough and depositing them on the bar stoss, but it was not possible to test if this was the case.

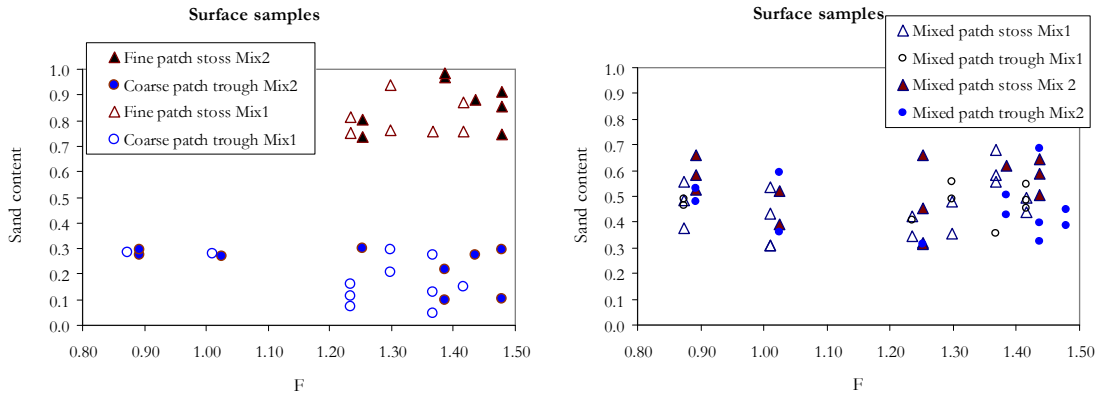

Figure 6.48. Variation with Froude number of sand content in aereal bed surface samples taken from patches of similar texture characteristics.

Despite the relative area occupied on the bed surface by each of the three defined patch classes (fine, coarse and mixed) was not measured, from photomosaics in Appendix IX it is visible that fine patches occupied larger areas the higher the Froude number was. Those photos illustrate how the final bed surface texture was sensitive to different flow conditions and sediment supply rates, even when the grain size distribution of the supplied material was kept constant during all those conditions. These results deserve comparison with experiments performed by Gran et al. (2006). Their experiments were intended to resemble the decline in sand supplied to the Pasig-Potrero river in Filippines, after an

abrupt increment in sand loading over the originally gravel bed due to a volcanic eruption. These authors performed four experiments feeding into the 10 x 0.7 m experimental flume material with sand-gravel mixtures with 40%, 50%, 60% and 70% sand content, respectively. Froude numbers varied from 1.1 to 1.6. They concluded that the connectivity between fine patches parallel to the flow allows that sand-dominated sediment transport conditions in a mixed size bed prevailed for a large range of sand contents. The shift to a gravel-dominated bed occurs when structured gravel deposits clog the connectivity of the sandy transport zone; thus, the transition between a sand- and a gravel-dominated behavior occurs for a narrow range of sand contents (between 10 and 30% sand content, as suggested by Wilcock and Kenworthy [2002]). The current experiments complement those from Gran et al. and their conclusions, in so far as they illustrate the key role of very high flows in the formation of patches of well-sorted material.

6.5.4 Implications for streams in field

The experiments herein reported were intended, as a first objective, to study flow and sediment interactions under high sediment supply and near critical flow conditions; and secondly, they were intended to model torrential ephemeral streams, particularly, under conditions of lateral flow confinement or channelisation. Results and analysis presented previously in this Chapter account for the first objective. For the second objective, in this Section the experimental results and the processes observed are linked to natural streams. First, dimensionless relations are used for comparison of the experimental database with natural rivers; later, morphological and textural correspondences between the experimental results and typical morphologies in field are assessed and discussed.

6.5.4.1 Comparison with dimension-free relations for bankfull flow

The broadest objective of the experiments herein reported was to study high sediment transport conditions under torrential flows; the results exposed along this Chapter represent a valuable evidence of the physical processes in such environments, which previously have been sparsely investigated in a systematic manner in laboratory flumes. A more restricted objective, of practical implications, was to model flow and bed interactions similar to those occurring in torrential ephemeral streams. Many reaches of this type of streams, but not necessarily all, exhibit wide cross-sections, i.e., high ratios between channel width and water depth; in some cases, the banks are diffuse and flood-plains are inexistent. The target of the experiments was the modeling of flow and sediment interactions when this condition of extended width is restricted; this often occurs when these streams have been confined laterally with vertical walls in an attempt to stabilize the banks and provide flood risk protection (see Figures 2.3 and 2.4). From the experimental results, it can be advanced that in some cases one of the most severe effects of flow confinement would be related to the likely formation of 3D stationary waves at supercritical flow, which are highly effective in producing deep bed erosion. Even though the experiments were intended to reproduce flow conditions of altered or engineered rivers, the conditions tested are likely to occur in natural streams as well, e.g., in moderately steep rivers narrowed by geological constraints. A comparison with typical self-formed natural streams is useful for an assessment of the separation of the tested conditions from those in common unaltered alluvial streams. This comparison is presented here.

If the flume and the experiments were considered as a physical undistorted model which can be scaled to prototype dimensions according to Froude similarity, length dimensions in the prototype would be reduced by a factor λ_e in the model. Accordingly, water-depth, channel width, sediment grain size and geometry of the bedforms would be

scaled by this factor, while water discharge would be scaled by $\lambda_e^{5/2}$; slope and Froude number values would be the same in prototype and model, and assuming that sediment and water densities are the same in both systems, Shields stress should also be the same in model and prototype. Since turbulent flow prevailed in the flume, it can be considered that viscous effects were negligible, as in most natural rivers usually occurs, and thus it would not be necessary to satisfy the condition of equal Reynolds number in prototype and model. The establishment of a dynamic mobile-bed equilibrium in the bed was a condition for the experiments (see Section 3.3), hence, in prototype these conditions would be equivalent to river reaches where morphodynamic equilibrium prevails, i.e., that there is no net erosion or deposition in time. Taking into account all these conditions, rigorous dynamic similarity between the experiments and a prototype river can be expected.

Figure 6.49. Sections of the torrential ephemeral stream "Las Arenas y Rubí" in Catalonia, Spain, corresponding to the catastrophic event of September 25th, 1962. This stream is a tributary of the Llobregat River, in the southern limits of Barcelona. (Taken from Helmbrecht and Martín-Vide, 2006).

The experiments were not designed to model a specific prototype stream, but trying to reproduce the generic characteristics of narrowed torrential ephemeral streams, namely, abundant sediment supply and very high sediment transport capacity. Therefore, results cannot be scaled to verify if the conditions tested compare well to *a priori* conditions of a given prototype. Notwithstanding, the similarity of the experimental results to field conditions can be verified by using dimensionless relations of the most significant variables, and comparing these relations with ranges of the same relations typical of natural streams. For a model dynamically similar to its prototype, correlations with appropriate dimensionless variables describing the underlying physics of the processes should be the same in model as in prototype. Attending to this property, a comparison is here presented of the experimental runs with databases of self-formed alluvial streams. To a certain extent, this comparison is an inverse application of the procedure followed by Parker et al. (2003); these authors designed a physical morphodynamic model of mountain streams using correlations between dimensionless variables from measurements in natural streams. Some of the sets of data used by Parker et al. (2003) are also used here.

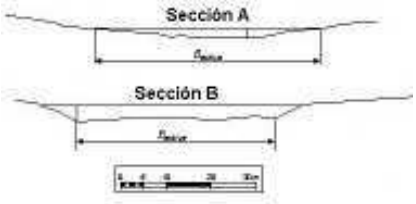

Figure 6.50. Sections for the torrential ephemeral streams "La Galera" (section A) and "Toll Roig" (section B), corresponding to the extreme event of October 23th 2000. Both streams converge to form "La Galera" stream in the province of Tarragona, Catalonia, Spain. (Taken from Helmbrecht and Martín-Vide, 2006).

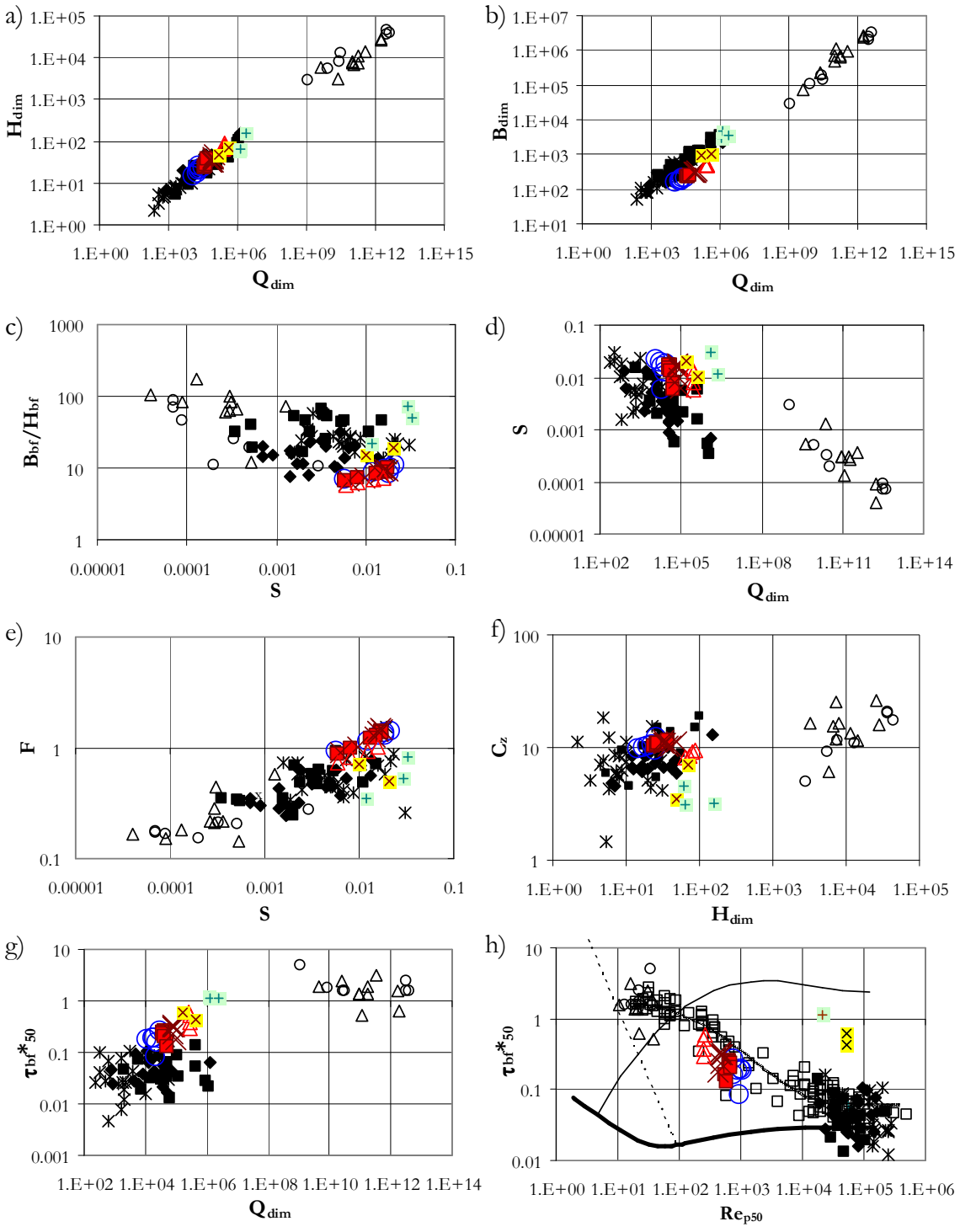

Figure 6.51. Plots of dimensionless relations and flow parameters for bankfull conditions in self-formed natural rivers for comparison with the experimental data.

Table 6.7 Average characteristics for the sections of the two torrential ephemeral streams shown in Figures 6.49 and 6.50. Although here the data have been considered as representative of bankfull flow, actually they correspond to extreme flood events which have been reproduced with a hydrological model. The median grain size refers to the bed surface material.

Section	D_{50} (mm)	Q_{bf} (m^3/s)	H_{bf} (m)	B_{bf} (m)	S
La Galera Section A	55	355	2.7	51	0.0205
La Galera Section B	55	943	3.8	57	0.0101
Riera de Las Arenas and Rubí P-1	30	590	1.8	91	0.0325
Riera de Las Arenas and Rubí P-2	30	610	1.9	139	0.0294
Riera de Las Arenas and Rubí P-3	30	1200	4.8	104	0.0119

In self-formed alluvial rivers, channel morphology is determined by the sediment size and supply, and modulated by the size of the channel (Church, 2006). Bankfull conditions, those for which the water depth in the channel is on the limit to spill onto its floodplain, are strongly related with the size and formative conditions of the channel. Associated to bankfull conditions, there exist a bankfull water discharge Q_{bf}, a bankfull water-depth H_{bf} and a bankfull channel width B_{bf}. According to this prominence of the bankfull characteristics and the sediment caliber in the river morphology, Parker (2004) defined the following dimensionless parameters to characterize bankfull conditions of alluvial streams

$$Q_{\dim} = \frac{Q_{bf}}{\sqrt{gD_{50}}\,D_{50}^2} \quad (6.58), \qquad H_{\dim} = \frac{H_{bf}}{D_{50}} \quad (6.59), \qquad B_{\dim} = \frac{B_{bf}}{D_{50}} \quad (6.60)$$

where Q_{dim}, H_{dim} and B_{dim} are dimensionless bankfull discharge, water depth and channel width, respectively. Hydraulic parameters pertaining to bankfull flow can be defined as well, namely, bankfull Froude number F_{bf}, bankfull Chézy coefficient C_{zbf} and bankfull Shields stress for the median diameter τ^*_{bf50}, given by

$$F = \frac{Q_{bf}}{B_{bf}H_{bf}\sqrt{gH_{bf}}} \quad (6.61), \quad Cz_{bf} = \frac{Q_{bf}}{B_{bf}H_{bf}\sqrt{gH_{bf}S}} \quad (6.62), \quad \tau^*_{bf50} = \frac{H_{bf}S}{(S_s-1)D_{50}} \quad (6.63)$$

The relations in eqs.(6.58) to (6.63) were used for the comparison between the experimental data and natural rivers. For this, the experimental variables were considered as being equivalent to bankfull conditions, while a database with bankfull geometries and flow for self-formed alluvial rivers was used. The database, open to free access in http://vtchl.uiuc.edu/people/parkerg/, was compiled by Parker (2004) from different sources. It includes data from sand- and gravel-bed rivers. The set for sand-bed rivers was originally presented by Church and Rood (1983), and includes data from single- and multiple-channel rivers. The set for gravel-bed rivers includes data from streams in Alberta, Canada (Kellerhals et al. 1972), from British mountain streams (Charlton et al. 1978), and from mountain streams in Idaho, USA (Parker et al. 2003).

Additionally to the databases described above, for the comparison with the experimental results data pertaining to two torrential ephemeral streams in Catalonia, Spain, were used as well. These data were reported by Helmbrecht and Martín-Vide (2006) and correspond to La Galera and Las Arenas streams. Table 6.7 and Figures 6.49 and 6.50 summarize the information used from the two rivers. The data for these two streams correspond to two catastrophic events, therefore, the conditions are not necessarily those related to bankfull flow; however, the selected sections can be considered as not to be far apart from bankfull flow, as can be seen in Figures 6.49 and 6.50. The reported water discharges related to the selected cross-sections were obtained after hydrological analysis using the HEC-HMS model and rain records. The discharges in Table 6.7 correspond to the most "likely" estimates after sensitivity analysis of the basin parameters. For La Galera

stream, an armor layer was found on the bed surface, with a ratio between the surface and subsurface material median diameters ranging from 2.4 to 3.2 (no conversion was performed for the transformation of the surface sample to an equivalent volumetric sample). Conversely, in Las Arenas stream the bed lacked of a coarse surface layer (García and Martín-Vide, 2001), which agrees with other observations from ephemeral streams (e.g., Laronne et al., 1994).

For computations with eqs.(6.58) to (6.63) the bed material considered from the natural streams was the surface median diameter, while for the experiments the material used was the median diameter of the material fed to the flume.

6.5.4.1.1 Links between channel morphology and plots of dimensionless relations

Plots using bankfull dimensionless relations and bankfull flow parameters for the natural streams in the datasets and for the experimental runs are shown in Figure 6.51. The most evident distinction of all these graphics is the separation between sand- and gravel-bed rivers, with the experimental runs plotting close to or within the scatter of data for gravel-bedded streams in most of the graphs.

Sand and gravel streams represent two extreme cases for the dominant mode of movement of the sediment grains in alluvial streams, and also for the morphologies that the flowing water constructs in these streams by setting the bed particles in motion. Put in terms of sediment mobility, sand-bed rivers can be classified as suspension-dominated rivers, while gravel-bed rivers as bedload-dominated. In terms of the stream morphology, bedload-dominated rivers give rise to channels relatively wide and shallow, characterized by a lateral instability since bedload is deposited within the channel and the stream must flow around these accumulations (Church, 2006). Conversely, suspension-dominated rivers are relatively deep and narrow since suspended sediment accumulates vertically on the banks, which gain strength with the accumulation of finer, cohesive particles, and with the rapid growth of vegetation encouraged by the fine sediment (Church, 2006). Channels with intermediate characteristics, between bedload- and suspension-dominated streams, are termed transitional channels.

Some of the characteristics described above for the sand and gravel streams can be identified in the plots of Figure 6.51. These characteristics are briefly discussed below considering three items: hydraulic geometry, flow dynamics and sediment mobility.

Hydraulic geometry

The experimental runs and data from ephemeral streams in Figure 6.51a plot within the scatter of the trend and ranges of values for gravel-bed rivers; hence, relative water-depths H_{dim} in the experiments were comparable to those found normally in field in gravel-bed rivers for the same range of dimensionless bankfull water discharge. By contrast, Figure 6.51b gives another picture; the two ephemeral streams seem to follow the same trend as gravel-bed rivers, but the experimental data do not. A comparison between power-fit regressions for the gravel-bed case and the experimental results shows that the ratio between dimensionless bankfull widths for the experiments and the natural streams ranges from 0.3 to 0.4. This means that, as it was intended, the experiments effectively reproduced a condition of flow confinement with respect to natural streams; for self-formed rivers discharge at bankfull conditions would flow through channels roughly 2.5 to 3 times wider than in the experimental flows. Although less evident, because of the large scatter of the data, the same conclusion can be drawn from Figure 6.51c; experimental width-to-depth ratios (aspect ratios) B_{bf}/H_{bf} are on the lower limit of the values exhibited by natural streams. In this same Figure, two of the points for ephemeral streams, corresponding to sections P-1 and P-2 of the "Riera de Las Arenas y Rubí" (see the two uppermost sections

in Figure 6.49), plot as outliers; it is likely that flow in these two sections was slightly above bankfull conditions, thus, bankfull channel width would be over-represented since a rapid increment of the water surface width, with respect to water-depth, occurs when bankfull flow is surpassed[**]. In average, the aspect ratio of the experimental runs would be roughly half the same ratio for the other three points corresponding to ephemeral rivers.

In comparison to the first two plots described above, the data in Figure 6.51d exhibit a large scatter, similar as in Figure 6.51c; Parker (2004) explains this variability as an effect of the difference in time scales between the response to perturbations of the channel geometry and the bed slope. The channel geometry can be shaped in a unique flood event, while bed slope adjustments might require decades. But not only time scales for bed slope response are larger, also, geological constraints can be more restraining in the adopted bed slope by the channel in comparison to its geometry. Despite of the large scatter, in Figure 6.51d it is evident that for a given slope the experimental data and the points for ephemeral streams plot to the right; this indicates that water discharges evacuated through the selected ephemeral streams are from one to two orders of magnitude higher than the typical discharges flowing through gravel-bed rivers with similar slopes. This reflects the torrential character of the streams intended to be modeled, and the adequate reproduction of this feature in the experimental runs.

Flow dynamics

Figure 6.51e shows that critical and supercritical flows do not occur in natural streams from the selected databases, but that these types of flows were the most common in the experimental runs; in fact, it was intended that the experimental flows were close to and above the critical value. From a straightforward reasoning and concepts of specific energy, it can be demonstrated that channel confinement from an originally subcritical flow reduces unit discharge and increases the value of the critical flow depth if specific energy is conserved; thus, the reduction of the channel width increases the likelihood for the flow to be supercritical.

Critical and supercritical flows can be found in natural streams, for instance, in step-pool and cascade morphologies in mountain channels. These type of streams are not represented in the selected databases above. Step-pool and cascade morphologies commonly occur in beds formed of cobbles and boulders at slopes between 0.03 and 0.065 the former, and higher than 0.065 the latter (Montgomery and Buffington, 1997). Other environments in which supercritical flows have been reported include volcanic channels, e.g., Pasig-Potrero River in Philippines (Gran et al. 2006) and the North Fork Toutle River, Washington (Pitlick 1992); and in ephemeral streams in arid regions, e.g., Nahal Yatir stream in Israel (Reid and Laronne 1995). Also, mediterranean ephemeral streams, which were intended to be modeled in this work, are often characterized by torrential (supercritical) flows.

Data in Figure 6.51f show a large scatter. Even so, the cluster of data for gravel-bed rivers appears well separated from sand-bed rivers, and the experimental data plot within the scatter ranges of the former. Except for the sand runs, the experimental data plot roughly on the upper limit of the data for gravel streams, thus indicating lower flow resistance than most of the natural streams. Data for ephemeral streams plot well below the lowest limit of the gravel points, evidencing a very high flow resistance. Helmbrecht and Martín-Vide (2006) noticed that unusual very high water levels were registered in the flood events of La Galera and Las Arenas streams; such water levels were not in correspondence with the most likely estimates of water discharge by hydrological models. They attributed

[**] Another reason for this effect, is that channel margins in ephemeral streams are often diffuse, and thus in those cases the definition of bank-full conditions is meaningless.

this anomaly to a high flow resistance related to the high concentrations of sediment in the flow.

Sediment mobility

Extending the analysis from Dade and Friend (1998), Church (2006) suggested that the ranges of Shields stresses for bedload-dominated, transitional and suspension-dominated channels are $O[0.01] \leq \tau^* \leq O[0.1]$, $O[0.1] \leq \tau^* \leq O[1]$, and $\tau^* \geq O[1]$, respectively. Data for natural streams in Figure 6.51g agree with such ranges: sand and gravel streams appear clearly separated, being in the range of bedload-dominated channels the former, and suspension-dominated the latter. The experimental data and data for ephemeral streams plot in-between, suggesting that they would correspond to the transitional channels, for which a portion of the bed material moves in suspension and the other portion remains as bedload. Data for Las Arenas ephemeral stream plot in the lower range for suspension-dominated streams, thus evidencing an extremely high sediment transport capacity; in fact, this enhanced capacity is an effect of the lack of a coarse surface layer on the bed surface, which was present in the other ephemeral stream and in all the gravel streams represented in the Figure.

Figure 6.51h gives a complete overview of the mobility of the sediment in the three types of streams, bedload-, suspension-dominated, and transitional. For comparison, in this Figure the Shields curve for sediment incipient motion (as given by eq.[6.34]) has been drawn, along with the same criterion for sediment suspension given in Figure 6.47, and a curve for the maximum conditions for ripple formation according to the thickness of the viscous sublayer. Additional data included by Parker (2004) have also been added in the Figure, these correspond to transitional rivers in Japan, and a curve attributed to Yamamoto (1994) for the trend followed by these rivers (for data from Japan, sediment corresponds to the D_{60} of the bulk material, and water discharge corresponds to the mean annual peak flood flow). The experimental data and the data for ephemeral streams plot roughly between Shields stress values of 0.1 and 1, in the region for bedload sediment transport, where viscous effects are negligible. Thus, the experiments reproduce in the same orders of magnitude the high sediment transport capacity characteristic of ephemeral streams prone to flash-floods. Since the experimental data plot close to the data from transitional rivers in Japan, in the same region where Church (2006) presented data for channels with mixed load (bedload and suspended load), it can be advanced that the mobility of the sediment in the experiments is similar to the mobility of sediment in transitional rivers, i.e., rivers with grain size mixtures, as it was initially intended. According to Church (2006), transitional rivers flow on fine gravels or sandy gravels, or they occur in sand-bed channels on low gradients, in which all grain sizes move but an important portion of the material moves as bedload. From the classification of alluvial rivers from Church (2006), transitional channels are distinguished by a mainly single-thread channel, irregularly sinuous to meandered; this streams develop lateral- and point- bars, and are laterally unstable.

6.5.4.1.2 Summary

Comparison with databases for self-formed natural rivers using dimensionless relations for channel bankfull conditions showed that the experiments herein reported have similarity with the characteristics of some water streams in field. Hydraulic geometries and flow conditions in the experiments, and data for torrential ephemeral streams, resemble to those proper of gravel-bed rivers; the values of the selected dimensionless variables are similar to the ranges of these same variables characteristic of gravel-bed rivers, and quite apart from the ranges common to sand-bed rivers. The experiments reproduce well the condition of

exceptionally high flow discharges and very high sediment transport capacity of ephemeral streams prone to flash-floods. Instead of the wide channels common to ephemeral and gravel-bed streams, the experiments depict a condition of an alluvial straight channel, laterally confined by vertical tough walls. The ratio between dimensionless bankfull channel width for natural streams and experimental runs was from 2.5 to 3, while the experimental aspect ratio (width-to-depth) was roughly half the same ratio for selected ephemeral streams. For this condition of channel width restriction and high to moderately steep slopes, contrary to most of the self-formed streams, supercritical flow conditions are very likely to occur. The experiments modeled this condition, with Froude numbers close to and above the critical value; for similar bed slopes, experimental Froude numbers were in average double the values of the selected natural streams for bankfull flow. Supercritical flows are not common in natural streams, however, flow in flash-flood events in ephemeral streams is often supercritical; the experimental flows reproduced this torrential condition.

In the experiments, sediment mobility, characterized by means of the Shields stress value, was an order of magnitude higher than in gravel-bed streams, and an order of magnitude lower than in sand-bed streams. For bankfull flow in gravel-bedded rivers, it is common that Shields stress values barely surpass the threshold condition for incipient particle motion, with typical values being only 1.6 times the threshold; conversely, for sand-bed rivers, Shields stress can be 50 times the critical conditions. The experiments reproduced the same orders of magnitude of Shields stress values for the selected ephemeral streams; these values ranged approximately between 2 to 18 times the critical Shields condition (considering total bed shear stress, i.e., without partition in grain and form stresses). Moreover, the lack of a coarse surface layer in the experimental bed configurations was in correspondence with observations in ephemeral streams in field. Data from the selected ephemeral streams in Catalonia, and from the experiments, plot in the region where viscous effects are negligible and bedload sediment motion dominates. The ranges of shear stress in the experiments and the considered ephemeral streams are proper of transitional channels, for which a portion of the bed material moves as bedload and the other in suspension. For the experiments, most of the material moved as bedload (see Figure 6.47); nevertheless, experimental morphologies corresponded to those found in transitional channels, which tend to develop lateral bars by lateral and vertical accretion, and are characterized by irregular lateral instability that can evolve in meanders. It is likely that bedforms observed in the experimental runs would not necessarily occur for all conditions in field, since more extended grain size distributions, with coarser particles in the coarse fraction, could prevent their formation.

6.5.4.2 Significance for pool-riffle morphologies

Bed configurations at the end of most of the experimental runs resembled pool-riffle morphologies, typical of gravel-bed rivers with gradients in the range of 0.001 to 0.03 (according to the classification of Montgomery and Buffington, 1997). Pool-riffle morphologies are characterized by a periodic longitudinal sequence of topographic highs (riffles) and lows (pools) along the thalweg (see sketches in Figure 6.52). Figure 6.53 shows an image of the bed surface configuration at the end of run G17 when water had not been totally drained from the bed; in this Figure, some riffles, pools and alternate bars have been identified for comparison with the sketches in Figure 6.52. It is common that in pool-riffle morphologies the thalweg follows a transversally undulating pattern in plan view around alternate bars (see Figures 6.54 and 6.55); for this reason, Church and Jones (1982) refer to this morphology as the pool-riffle-bar triplet. The highest elevations correspond to the bar crests and the deepest to the pools; therefore, it is common that during low flows bars are exposed and water depth on the pools is deeper than in riffles.

The study of pool-riffle morphologies has received considerable attention in recent years, due to the relevance that the alternating sequence of shallow and deep water depths has for habitat diversity. In turn, river restoration concerned with ecological and ambiental issues needs to understand the morphodynamics of pool-riffle morphologies in order to reestablish natural conditions in streams modified by human action. Of particular interest for geomorphologists has been the study of the processes by which pool-riffle morphologies are self-maintained. Different hypothesis have been suggested to explain the conditions that allow riffles not being completely eroded, and pools not being completely aggraded during high and moderately flows. Recently, de Almeida and Rodriguez (2011) explained the pool-riffle maintenance process by a modulation in local fractional sediment transport rates in pools and riffles exerted by grain sorting, selective transport and hydraulic control of contiguous riffles. They found that the rising and falling limbs of a hydrograph and the history of flows have an important role in the self-maintenance process.

Commonly, pool-riffle morphologies have been related to bar instability, the process by which alternate bars are formed; nevertheless, little efforts have been conducted to clarify the links between theories for alternate bar formation and pool-riffle sequences. Wilkinson et al. (2008) highlighted that the ratio of channel width-to-depth for pool-riffle morphologies in field can be lower than the minimum values (roughly 10) suggested by results with mathematical models for the occurrence of bar instability (e.g., linear stability analysis by Colombini et al., 1987). In spite of such disparity, Wilkinson et al. (2008) were able to reproduce pool-riffle sequences in laboratory for width-to-depth ratios as low as 3.8; thus they concluded that bar instability contributes to the formation of pool-riffle sequences. The experimental results in the current work would agree with the results of Wilkinson et al. (2008); alternate bars formed for width-to-depth ratios lower than 10, and as low as 5.8. Nevertheless, the results here presented should be taken with caution, since the analysis of the data until here presented cannot explain the role of the waning flow in the bed configurations preserved at the end of the experiments. An assessment of this shortcoming can be obtained by comparison with the experimental results of Wilkinson et al. (2008).

Wilkinson et al. (2008) performed five experimental runs in a trapezoidal channel 12 m long, with a bed width of 0.32 m and plywood side-walls at 50º to the horizontal. Median diameter of the bed material was 3.4 mm, with a geometric standard deviation of 2.6 mm. Variables used for the experiments were scaled from a prototype pool-riffle sequence, with a ratio between prototype and model lengths of 23. The characteristics of the experimental variables tested by Wilkinson et al., excluding one run for which a portion of the channel width was narrowed, are shown in Table 6.8. In this same Table the average characteristics of each of the current experimental run series are presented as well. Data in Table 6.8 show that the sediment grain size, slopes, Froude numbers and width-to-depth ratios are of the same order of magnitude in the current experiments and those from Wilkinson et al. In both experimental conditions alternate bars formed, with similar ratios of bar wavelength to channel width, and similar bar heights. This similarity between both experimental conditions gives confidence in considering that the patterns of alternate bars observed at the end of the current experimental runs were formed during the main test flow, and also, it gives confidence to neglect the effects of the waning flow in the measured bar geometries. High and long primary bedforms identified in bed elevation time series in Figure 5.18 confirm this conclusion; it can be considered that such bedforms were of the same nature as those preserved after each experimental run was finished.

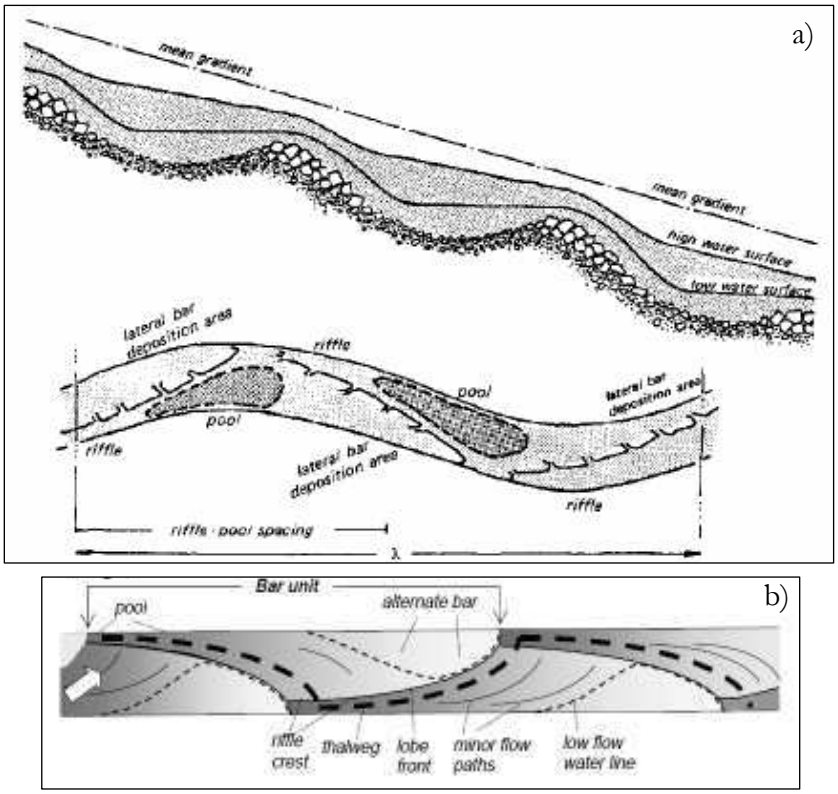

Figure 6.52. Schematic description and definition of elements of pool-riffle sequences, in a meandering (a) and a straight stream (b). (Taken from Bunte and Abt, 2001. Top image was originally presented by Church and Jones, 1982; bottom image was adapted from Dietrich, 1987).

Figure 6.53. Characteristic elements of a pool-riffle morphology, identified on the preserved bed configuration at the end of run G17.

Figure 6.54. Bed configurations with alternate bars, preserved at the end of the first phase (transition to equilibrium) of runs S2 (left) and M1E6 (right). Flow direction is downwards in the image to the left, and upwards in the image to the right.

Figure 6.55. Alternate bar configurations in the Ripoll River in Catalonia (top), and the Loire River in France (bottom). Flow from left to right in both images. Note the change of the size of the bars in the top image as the channel narrows downstream, roughly preserving the same width-to-wavelength ratio as of the bars upstream. Also, note the similitude with experimental configurations in Figure 6.54.

Table 6.8 Average characteristics of experimental runs of this work and those from experiments by Wilkinson et al. (2008). λ_b and Δ_b refer to wavelength and height of alternate bars ($\Delta_b=\Delta_{smax}$ from Table 5.4).

Run series	Total runs	D_{50} [mm]	σ_g [mm]	Q_w [l/s]	H [cm]	S (%)	F	B/H	λ_b/B	Δ_b [mm]
Gravel	6	4.2	1.4	59-84	6.8-10.9	0.58-2.14	0.93-1.21	6.9-11	2.8-5.0	16.3-34.2
Mix1	6	3.2	1.8	67-84	7.6-11.3	0.59-1.73	0.88-1.42	6.6-9.9	3.0-4.1	22.1-49.0
Mix2	6	2.5	1.8	78-80	8.0-11.3	0.64-1.77	0.89-1.49	6.6-9.4	2.7-4.8	13.6-55.7
Sand	2	1.5	1.4	80	10.3-10.9	1.23-1.55	0.94-1.02	6.9-7.3	2.7-2.8	46.3-50.5
Wilkinson et al. (2008)	4	3.4	2.6	15-39	5.1 - 13.7	0.77-1.00	0.57-1.20	3.8-6.9	2.2-5.0	9.6-24.8

From measurements and reports in literature for mountain streams in the Pacific Northwest of the USA, Montgomery and Buffington (1997) found that the spacing between pool-riffle sequences in natural streams is typically between 5 to 7 channel widths. These values correspond well to reported ratios between bar wavelength to bar width in the range 3 to 12 (e.g., Ikeda, 1984). The experimental data in Table 6.8 agree with this latter range, though slightly lower ratios as low as 2.7 were registered in the current experiments, and ratios as low as 2.2 were reported in the experiments by Wilkinson et al. (2008).

Theoretical studies (Colombini et al., 1987; Lanzoni and Tubino, 1999; Takebayashi and Egashira, 2002) have shown that sediment heterogeneity has the effect of suppressing bar height and bar wavelength. Lanzoni (2000a and 2000b) compared alternate bars in laboratory for uniform material (sand with mean diameter of 0.48 mm) and heterogeneous material (mixture with 70% sand content, sand mean diameter was 0.193 mm, and gravel mean diameter was 2.07 mm, both uniform materials) with almost the same mean diameter of 0.48 and 0.49 mm, respectively. Lanzoni found that bars with heterogeneous sediment were smaller than those with uniform material, but he did not found significant changes for bar wavelength between the two materials. Takebayashi and Egashira (2002) performed four experimental runs with beds of sand with 1.1 mm mean diameter; for identical flow conditions they found that wavelengths for poorly-sorted material ($D_{84}/D_{16}=1.93$) were 0.97 and 0.82 times those for well-sorted material ($D_{84}/D_{16}=1.14$) in runs with F=1.22 and F=1.50, respectively; in turn, they found that bar heights with non-uniform material were 0.94 and 0.59 times those for uniform material. Therefore, these authors verified that sediment heterogeneity can reduce bar wavelength and height. For the current experiments, no significant differences or trends were found for the characteristics of the measured bars for the four different materials tested, as can be seen in Figures 5.11, 5.15 and 5.16; for similar flow conditions bars in all four materials were similar.

Alternate bar characteristics of the experimental data in this work are compared with experimental data of alternate bars reported by different authors in graphs of Figure 6.56; most of the data used in this Figure were taken from Ikeda (1984). The channel width-to depth ratio has been used in the abscissa of these graphs, since it is well recognized that this is one of the most significant parameters in bar instability. Data in both graphs span several orders of magnitude, but those pertaining to the present experiments and those from Wilkinson et al. (2008) plot in the left- and down-most extremes of the two graphics. These two datasets would represent a lower limit for the geometry of alternate bars.

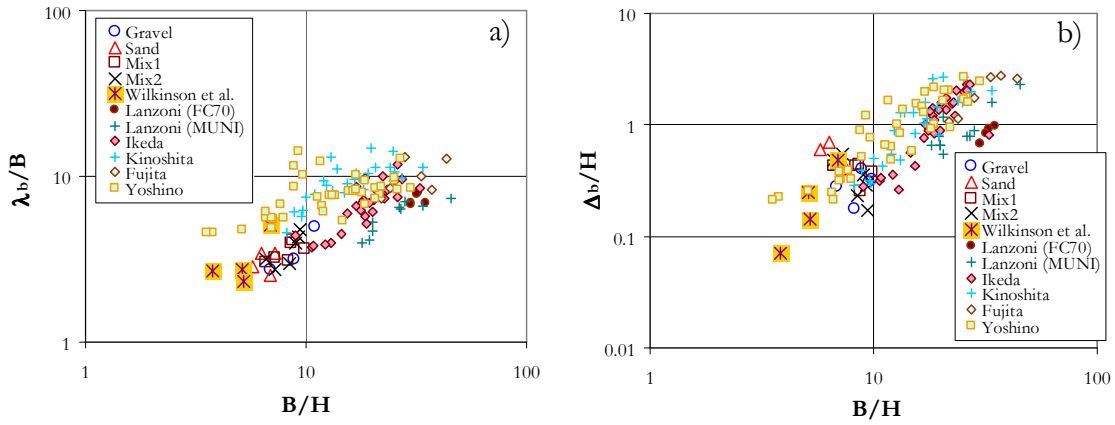

Figure 6.56. Geometrical characteristics of experimental alternate bars measured on the final bed configuration of the current experimental runs, and by other authors, as a function of the aspect ratio. B is channel width, H is water depth, Δ_b is bar height (Δ_{smax} in Table 4.4), and λ_b is bar wavelength. Additional data from: Wilkinson et al. (2008), D_m=3.4 mm; Lanzoni (2000a and 2000b), D_m=0.48 mm; Ikeda (1984), D_{50}=1.3 mm; Kinoshita (in Ikeda, 1984), D_{50}=0.38, 0.765, 1.24 and 1.7 mm; Fujita (in Ikeda, 1984), D_{50}=0.99 mm; and Yoshino (in Ikeda, 1984), D_{50}=2.3, 0.45, 3.55 mm.

Bedforms observed passing close to the channel walls during the experiments were classed as alternate bars, mainly due to their periodic sequence alternating between opposite walls, evident at the end of the experimental runs (Figure 6.54), and secondly, because their wavelengths scaled with the channel width. Graphs in Figure 6.56 show an approximate continuity between the characteristics of alternate bars measured by other authors for high B/H ratios, and the characteristics measured in the current experiments for low B/H ratios; this continuity confirms the adequate classification of such bedforms as alternate bars.

Figure 6.57. Mediterranean ephemeral streams during very low flow dicharges. Riera de las Arenas (left) and Ripoll River near Montcada (right), both in Catalonia, near Barcelona. Note the sinuous pattern of the thalweg bordering bars.

In the current experiments, a subtle trend was observed for the bar height to decrease, and bar wavelength to increase, with increasing Froude numbers (Figures 5.11 and 5.15). The morphological consequence of this trend would be that the stronger the formative

flows, the gentler the bars and the lower the curvature of the thalweg. This can be related to bed configurations observed in some perennial streams (see Figure 6.57); when they are empty no apparent bed forms or sinuosity is evident, but when a small water discharge flows through the channel a sinuous pattern of the thalweg is evident; for slightly higher flows all the channel is inundated and no sinuosity is evident on the water surface width. This pattern could thus be related to low amplitude and long bars formed during very high flow events.

Although there is an approximate correlation with measured alternate bars by other authors, it must be noted that in the current experiments the alternate bars coexisted with short-crested antidunes in most of the experiments. In Figure 6.42 of Section 6.5.1, it was shown that for most of the experimental runs, the wavelength of the short-crested waves was approximately the second harmonic of half the wavelength of a bar unit; also, it was shown in that section, that short-crested waves were related to stationary cross-waves. Accordingly, the observed alternate bars might also be in close correlation with surface cross-waves. Indeed, when applying equations given in Section 6.5.1 for computation of the cross-wave longitudinal wavelength (eqs.[6.56], [6.53] and [6.47], with $\lambda_b=\lambda_1$), the average ratio between computed and measured bar wavelength is 0.95, with a standard deviation of 10%. Applying the same procedure to the data from other authors used in the plots of Figures 6.56, considering only data for supercritical flows, the results showed that there was no correlation with cross-waves; the computed bar wavelengths were found to be from 20 to 80% of the measured values, except for one of the runs of Wilkinson et al. (2008), with a ratio between computed and measured wavelengths of 1.09. Wilkinson et al. did not provide information about bed and water configurations during their experimental runs, and thus it is not possible to know if bars interacted with stationary cross-waves in that specific run. Hence, unlike other experiments in literature where alternate bars formed, the experiments of the present work can be considered as an exceptional case, since alternate bars formed in coexistence with antidunes, and there must have been a strong interaction between stationary transversal waves, antidunes and bars. It is possible that in other experiments low water depths might have suppressed secondary mesoscale bedforms, and that large width-to-depth ratios might have prevented the formation of short-crested stationary waves.

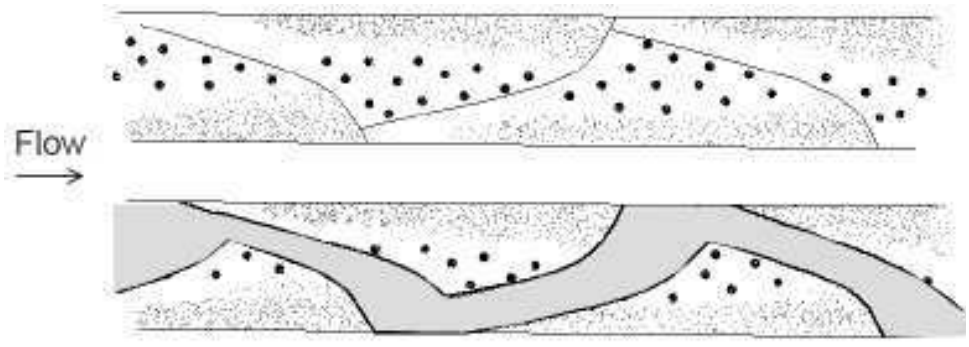

Figure 6.58. Textural characteristics of bed surface material on alternate bars in a straight channel. Coarse material is indicated with coarse dots, fine material with fine dots. Top image corresponds to the channel empty, bottom image to low flow discharge. (Taken from Bunte and Abt, 2001, from an original version by Whiting, 1996).

Finally, some similarities can be pointed out between the experimental sediment sorting patterns on the bed surface, and patterns normally found in pool-riffle morphologies in natural rivers. Figure 6.58 shows a general overview of the spatial variability of sediment sorting in straight reaches with alternate bars; the most general features are a coarse thalweg, and downbar and lateral fining. These general patterns were also found in most of the experimental bed configurations; bar crests were the zones where samples with the highest sand contents were collected, while the coarsest samples were collected from the upstream end of the bars and at the center of the channel cross section. In turn, sand was more abundant near the channel-walls. Overall, it was found that sediment on the bar surface was finer than the feeding material; according to Bunte and Abt (2001), bar surface material is finer than the reach-average sediment size in coarse gravel-bed streams with low sediment supply, thus, the experiments here show that this could also be true for channels with no sediment deficit subjected to very high Shields stresses.

6.5.4.2.1 Summary

Most of the morphologies preserved at the end of the experiments herein reported showed a configuration of alternate bars, and a thalweg with deep zones alternating with topographic highs in an undulating pattern. These morphologies keep close similarities to pool-riffle sequences common of gravel-bed rivers with gradients in the range of 0.001 to 0.03. Figures 6.53 to 6.55 show that the experimental alternate bars were similar to those found in straight reaches in the field. Hence, the experiments here presented supply with further evidence of the conditions required for the formation of pool-riffle morphologies, and their relation with migrating alternate bars.

Measured wavelengths and bar heights on the preserved configurations at the end of the experiments, related to the channel width and water depth, respectively, corresponded to values lower than those commonly reported in literature for experimental alternate bars. Wilkinson et al. (2008) preformed four experimental runs with similar hydraulic and sediment variables as those in the present experiments; these authors observed alternate bars with geometrical characteristics in the same range of magnitude as the ones reported in this work. Wilkinson et al. attributed to low width-to-depth ratios the occurrence of short and small alternate bars, in comparison with previous theoretical and experimental results. Comparison with experimental data obtained by different authors showed that the experimental bars in the current experiments and those from Wilkinson et al. correspond to a lower limit for width-to-depth ratios, bar wavelengths and bar heights. Therefore, these new data set fills the gap of empirical evidence for alternate bar formation in the full range of wavelength-channel width and bar height-water depth ratios observed in natural streams.

Although theoretical models and some experimental evidence in literature indicate that sediment heterogeneity has an effect in reducing bar wavelength and height, the scatter of the data in the experiments of this work did not allow distinguishing significant differences between bars formed with uniform sand and uniform gravel, with those formed with sand-gravel mixtures. More evident were changes in bar geometry with different flow conditions; a slight trend toward a decrease of bar steepness with Froude number was apparent. This could be the reason for ephemeral-streams subjected to steep hydrographs for not showing clear bedforms when they are empty, and a sinuous pattern of the thalweg when very low flows occur. For such streams, even if steep bedforms could occur during very high flow events, these forms would have been erased at the waning flow, and bars would be so low that would only be apparent when low discharges flow through the toe of the gentle bar fronts.

Wavelengths of bars in the current experiments are in close correlation with the length of surface cross-waves, which can be computed with the equations derived in Section 6.5.1. Therefore, there must have occurred a strong interaction between stationary cross waves, antidunes and bars. There are no other reports in literature of alternate bars coexisting with short-crested antidunes, perhaps because high channel width to water depth ratios common of the experimental conditions for alternate bar formation would have prevented the formation of antidunes and short-crested waves; then, so far, the experiments herein reported can be considered as an exceptional case, with alternate bars occurring and strongly interacting with mesoscale bedforms and short-crested stationary waves.

Experimental patterns of bed surface sediment sorting corresponded well to general patterns observed on bars in natural streams. Particularly, downbar and lateral fining, and a coarse thalweg, common features of pool-riffle morphologies in straight channels, were reproduced by the preserved experimental morphologies. Also, the trend for sediment on the bars being finer than the reach-average grain size, which occurs in coarse gravel-bed rivers with low supply, was evident in the experimental beds. These observations have consequences for the selection of sediment sampling locations in ephemeral-streams.

6.5.5 Summary

In this Section an overall interpretation of the experimental results has been advanced according to four main topics, namely, water surface configuration, bed erosion, sediment sorting and morphological links with actual streams in field. Understanding water surface configuration patterns is relevant for the study of upper-regime flows, since for this regime there is a strong feedback between a deformable bed and the undulations of the free surface. During most of the experimental runs, three-dimensional stationary waves (rooster tails) occurred on the water surface at the center of the channel. In Section 6.5.1 it was demonstrated that the development of such features is related to symmetrical oblique standing waves converging at the channel central line, and that the lateral border condition imposed by the channel walls is relevant for their development and characteristics. General equations for these three-dimensional waves were presented and a relation was derived for flow velocity as a function of the wavelength, channel width and mode of vibration. This relation is the same as that originally presented by Kennedy (1961), but more general since it considers more than one mode of vibration, while that presented by Kennedy is applicable only to the fundamental mode. It was here hypothesized that the alternate bars evident at the end of the experimental runs were related to first order cross-waves; in this manner, the mode of vibration excited for the formation of the short-crested waves was computed as the closest integer to the ratio between half-bar wavelength and the wavelength of the 3D stationary waves. It was found that for most of the experimental runs the second mode of vibration was excited. The relation here derived for flow velocity as a function of rooster-tail wavelength, channel width and mode of vibration, performed well with the experimental data of this work, and with other data in literature, provided that the computed flow velocity was compared with the flow velocity on the water surface; for each experiment, this superficial velocity was obtained using a logarithmic approximation of the flow velocity profile.

In the subsequent subsection (6.5.2) experimental cross-sectional bed erosion patterns were discussed. Particularly, the different patterns observed between runs with sand and runs with sand-gravel mixtures were explained in relation to the characteristics of the bedforms and the stationary waves on the surface. The deep concave upward scour holes at the center of the channel in beds with mixtures was then suggested to be related to the higher shear stresses produced by the concave flow under the trough of short-crested stationary waves. Conversely, it was suggested that the almost constant transversal erosion

patterns in beds with sand were related to the stationary waves above the steep bedforms that spanned transversally from wall to wall.

Farther on, sediment sorting trends were discussed in subsection 6.5.3. By comparison with commonly used formulations for incipient motion of particles and the onset of sediment into suspension, it was found that for most of the runs all the sediment size fractions moved as bedload most of the time; nevertheless, the trajectories of sand could be larger than the trajectories for gravel, and sand could travel at higher elevations than gravel by bouncing and being ejected from bedform crests. It was suggested that the most general grain sorting patterns observed in the experiments could be related to this fundamental differences in the motion of sand and gravel. These general patterns were: coarsening of the center of the channel and of the bar trough, and fining up- and wall wards. Coarsening of the central section and of lower bed layers was related to "topographic sorting", the process by which coarser particles tend to move more directly to topographic lows than fine particles; fining up and wallwards must have been related to the bouncing and longer trajectories followed by sand in comparison to gravel. Also, the force balance between drag and gravity could have promoted the trend for coarse particles to move preferentially through the channel center, where deep scour holes were formed by the rooster tails, and to fine material to move preferentially along the sides, where it was able to climb up the positive slope of the bedforms toward the channel walls. In spite of transversal sediment sorting trends and the high concentration of shear stress at the channel center due to the rooster tails, sediment transport was roughly the same along the transversal section. It was first hypothesized that such transversal flux balance could be related to coarsening of the center of the channel; nevertheless, computations with a sediment transport predictor showed that only a difference of 7% and 11% in grain shear stress was required to transport at the same rate the sediment collected from samples at the lateral section (finer) and at the central section (coarser); these values are too low in comparison with measurements by Chanson (2000) for the difference in cross sectional shear stress under stationary waves. Therefore, it was concluded that the periodical distribution of maximum shear stress and a high transversal flux of sediment promoted by the bedforms must have prevented the zone of maximum shear stress (center of the channel) matching with a maximum average sediment transport rate. Nevertheless, sediment transport samples taken in the channel were not able to capture narrowly concentrated peak sediment transport rates, due to extended sampling times. Finally, in subsection 6.5.3.2, the processes related to the formation of patches and deposits of well-sorted material were discussed. It was therein indicated that the stoppage of the experiment must have not affected considerably sediment composition of the bulk substrate material, but it must have significantly influenced the final sediment sorting on the bed surface. Notwithstanding, it was suggested that the rapid recession of flow in the experiments would resemble the type of hydrographs typical of flash-floods in ephemeral streams; indeed, grain sorting trends found on the bars were in good agreement with sorting patterns in field, as demonstrated further in the text in Section 6.5.4.2. Statistics of grain size distributions for bed samples showed that the distributions for substrate material had less variability and were in average more similar to the feeding material than surface material, thus providing support to the common practice of using substrate material characteristics for bulk sediment transport computations. The most important discontinuity in substrate material grain size distributions was found when open-framework gravel deposits formed; sand content in these deposits was much lower than sand content of the feeding material. It was suggested that such deposits were formed by the ejection of sand into suspension on the crests of short-crested antidunes, and the filling with "clean" gravel of scour holes opened by the rooster-tails. Grain sorting of the bed surface was characterized with samples of coarse, fine, and mixed-size patches; it was found that supercritical flows had a higher capacity than subcritical flows to segregate bed

material into well-sorted patches, irrespective of the grain size distribution of the supplied material. The final bed surface texture was sensitive to flow conditions and sediment supply rates even when the grain size distribution of the bed and supplied material was kept constant. The experiments here presented can be considered complementary to those performed by Gran et al. (2006), in which sand content in the supplied material was varied for a narrow range of flow conditions (Froudes between 1.1 and 1.6); these authors found that the shift from a sand- to a gravel-dominated bed occurs for a narrow range of sand contents (between 10 and 30%), while the current experiments demonstrate that patchiness formation is sensitive to flow conditions, being high Froude numbers (or high Shields stresses) more effective in sorting material into patches.

The final subsection (6.5.4) was intended to describe and discuss the connections between the experiments and streams in field. First, dimensionless numbers were used to characterize bankfull conditions in natural streams. Using these dimensionless relations, the experimental data were compared with databases for self-formed sand and gravel-bed rivers, and with data for two torrential ephemeral streams. In general, it was found that the experiments herein reported are a good representation of gravel-bed streams in field. Particularly, it was found that the experiments represent well the high water discharge and sediment transport conditions typical of torrential ephemeral streams, and that, as initially intended, they represent laterally confined flows in those streams. Sediment mobility, characterized by means of the dimensionless Shields stress, was in the same ranges in the experiments as in the bankful conditions of the selected ephemeral streams. These ranges are common of transitional channels, those for which a portion of the bed material moves as bedload and the other as suspended load; such channels tend to develop lateral bars by lateral and vertical accretion, and are characterized by irregular lateral instabilities. In the last subsection it was demonstrated that the experiments performed are a good representation of pool-riffle morphologies, so that they provide with valuable evidence of the conditions required for the formation of these morphologies, and their relation with migrating alternate bars. Comparison with data sets of alternate bars generated in laboratory by other authors, showed that the new experimental data correspond to a lower boundary for width-to-depth ratios under which alternate bars have been reported to form, and for bar wavelengths and heights as well. Although experimental evidence and theoretical results by other authors have shown that sediment heterogeneity has an effect in reducing bar wavelength and height, the present experiments did not allow distinguishing significant differences in the geometry of bars formed with uniform material and those formed with sand-gravel mixtures. More evident were changes with flow conditions; a slight trend toward a decrease in bar steepness with Froude number was apparent. It was suggested that this trend could be the reason for torrential ephemeral streams to show no evident bed configurations when empty of water, but a sinuous pattern at very low flows. Subsequently, it was highlighted that the experiments herein presented can be considered as an exceptional case, in which alternate bars coexisted and interacted with antidunes and short-crested stationary waves; it was suggested that in previous flume experiments by other authors high channel width-to-depth ratios would have prevented short-crested waves to form. Finally, similarities in grain size sorting patterns between alternate bars in field and the experimental bars were indicated. Particularly, downbar and lateral fining, and a coarse thalweg were reproduced by the experimental bars. Also, sediment on the bars was finer than the feeding material, as it occurs in natural streams with coarse material and low sediment supply. All these trends are of practical utility when selecting sediment sampling locations in torrential ephemeral streams.

CHAPTER 7:

HYDRAULIC ANALYSIS OF ANTIDUNE PROPAGATION*

7.1 INTRODUCTION

Among bed features developed by unidirectional water flows in alluvial channels, those features classed as antidunes occur in the so-called upper-regime flow; in contrast to bed forms in lower-regime, which can only move in the downstream direction, antidunes can migrate upstream, downstream or remain stationary. Dunes propagate in the downstream direction mainly because of the separation eddy formed downstream of their slip face. This eddy favors deposition of the sediment grains on the lee side. Conversely, the process by which antidunes move can be entirely different; antidunes are characterized by a strong interaction between bed and water surfaces, so that the undulations of both surfaces are approximately in phase. Because of this correspondence between bed and water surfaces, antidunes tend to be symmetrical with a curved crest in the section parallel to the flow. In contrast with dunes, detachment of streamlines from the bed surface over antidunes may be intermittent and erratic in area and position. Hence, deposition of sediment grains along the flow direction over antidunes could be more related to the gradient of flow velocities along the bed profile, than to sedimentation on regions of flow separation. In this manner, antidunes migrate upstream when the flow velocity decreases from the bed form trough to the bed form crest and increases from the bed form crest to the bed form trough; when this condition occurs, sediment is eroded on the antidune lee side and deposited on the antidune stoss side (Figure 7.1). Likewise, antidunes migrate downstream when the flow accelerates from trough to crest and the material eroded on the stoss side is deposited on the lee side where the flow velocity decreases (Parker 2004, García 2006). Immobility of

*Most of this Chapter is reproduced from:
Núñez-González, F., and J. P. Martín-Vide (2011), Analysis of antidune migration direction, J. Geophys. Res., 116, F02004, doi:10.1029/2010JF001761

antidunes may occur when there is no acceleration of the flow along the bed profile. As the direction of movement of antidunes is related to the sediment depositional pattern, distinctive relict internal sedimentary structures are associated with their migrating direction. As such, some sedimentologists consider that the more generic term "in-phase waves" should be applied to upper-regime bedforms, so that downstream-migrating antidunes and stationary antidunes should be distinguished from upstream-migrating antidunes as different classes of bedforms in their own right (Cheel 2005).

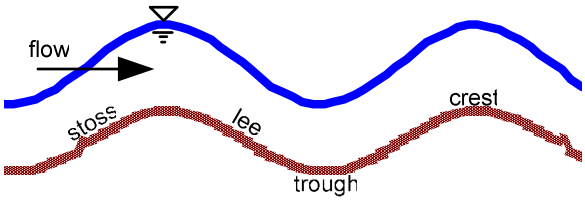

Figure 7.1. Geometry of antidunes

Diagrams that depict the different flow regimes under which stable bedforms develop exist in literature (for instance, Vanoni 1974, Southard and Boguchwal 1990). Most of these diagrams have been obtained from empirical laboratory data, so that in lack of observations for certain ranges of variables, some borders between bedform fields have been poorly defined or have been conceived of as intuitive extrapolations from the better-known regions. Furthermore, empirical diagrams for stability fields do not distinguish the direction of movement of antidunes, or refer solely to the region where upstream-migrating antidunes occur. On the other hand, theoretical bedform stability fields have been presented by different authors by performing stability analysis of bed disturbances. For such type of analysis, some researchers have deduced conditions that define the antidune preferential direction of movement. Particularly, based on the solution of a linearized potential flow over a wavy bed, Kennedy (1963) presented relations for defining bedform stability fields as a function of the Froude number and a non-dimensional wavelength; for the stability fields defined by Kennedy, the distinction between downstream- and upstream-migrating antidunes was included. Similarly, Engelund and Hansen (1966) analyzed the stability of a sinusoidal sand bed using the continuity equation and the equations of motion of a real fluid; they produced a stability diagram where separated regions for upstream- and downstream-migrating antidunes can be distinguished as a function of the Froude number and the ratio between mean flow velocity and the sediment critical shear velocity.

In this Chapter a new analysis and criterion are presented for describing the propagating direction of antidunes. For this analysis, the continuity and Bernoulli equations are applied to an energy balance along a two-dimensional symmetrical bedform. A correction for the pressure head to appropriately consider the curvilinear flow generated over the crest and trough of antidunes is included. Results are compared with experimental data in literature and with the data set obtained for the present study as described in Chapters 3 and 5. The new criterion is also compared with the stability fields developed with potential flow analysis by Kennedy. Finally, a discussion is presented about the limitations of the theory developed and about the possible morphodynamical differences between downstream- and upstream-migrating antidunes as predicted by the new theory.

7.2 HEURISTIC ANALYSIS OF ANTIDUNE MIGRATION

The movement of bedforms in an erodible-bed channel is related to a periodic fluctuation of the bedload sediment transport along the flow direction. The rhythmic erosion and deposition of sediment over preferential regions on the bedform defines the direction of movement. Bedform propagation in downstream direction occurs if sediment is predominantly eroded over the stoss side and deposited over the lee side; conversely, upstream migration results when most of the sediment is deposited over the stoss side and eroded over the lee side.

Considering that the bed profile can be represented by the periodic function

$$\eta = \frac{\Delta}{2}\sin\left(\frac{2\pi x}{\lambda}\right) + \eta_o \qquad (7.1)$$

where x is the horizontal axis, η is the bed-surface level, η_o is the datum for the mean bed-surface level, Δ is the bedform height, and λ is the bedform wavelength, with Δ being much more smaller than the water depth, the sediment conservation equation (Exner) should be satisfied

$$\frac{\partial \eta}{\partial t} = -\frac{1}{1-\varepsilon}\frac{\partial q_s}{\partial x} \qquad (7.2)$$

where q_s is the unit bedload transport rate at a section, and ε is the porosity of the sediment deposit. In the absence of bed perturbations, i.e., η=constant, it can be assumed that the sediment transport rate is the same for all sections and that it takes the value q_o. If periodic bed perturbations are present, likewise, as stated by eq.(7.2), the sediment transport rate should fluctuate periodically, so that at a given time the sediment transport rate can be described by

$$q_s = q_o + q_f \sin\left(\frac{2\pi x}{\lambda}\right) \qquad (7.3)$$

where q_s is the unit bedload transport rate at a section, and q_f is a real number that satisfies the condition $q_f/q_o << 1$.

Eq.(7.3) represents a simplified version of an original heuristic analysis presented by García (2006), who introduced an additional parameter for considering the more general case of developing bedforms, i.e., those bedforms for which geometry changes with time. For simplicity, completely developed bedforms are considered here.

Following the original reasoning of García (2006) for analyzing the relation between the bedload sediment transport fluctuations and the bedform characteristics, three cases can be distinguished according to the value of q_f:

1. $q_f > 0$. The bedload and bed fluctuations are in phase; the bedform moves downstream (see Figure 7.2a). The lowest bedload occurs on the troughs, and the highest at the crests, so that deposition takes place along the lee side because less material is leaving the lee side reach over the trough than the material entering the reach downstream of the crest.
2. $q_f = 0$. The bedload remains constant all along the bed profile; the bedform remains stationary (see Figure 7.2b). No net erosion or deposition occurs.
3. $q_f < 0$. The bedload and bed undulations are one half wavelength out of phase; the bedform migrates upstream (see Figure 7.2c). The lowest bedload occurs over the bedforms' crests and the highest over the troughs, so that deposition of material takes place on the stoss side, i.e., between the trough and the crest.

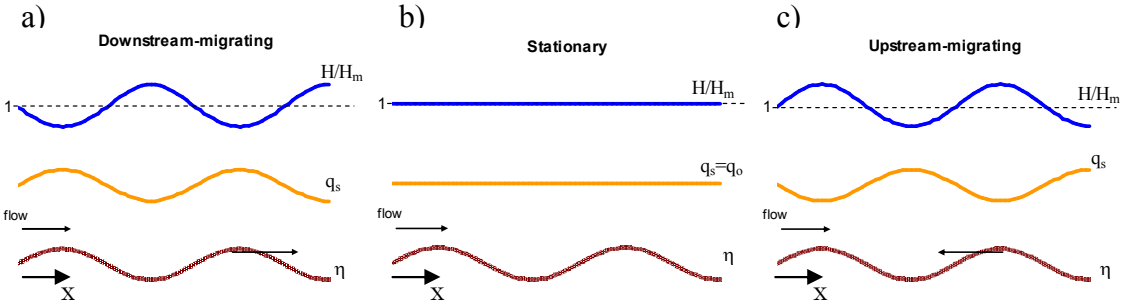

Figure 7.2. Schematic representation of the functions for the fluctuations of the bed surface, bedload transport rate and ratio of water-depths for the different antidune conditions of movement

When antidunes occur, bed and water surfaces are roughly in-phase; nevertheless, the water-depth variation along the bedform can be out of phase with the bed undulations (Parker, 2004b). To investigate the relation between fluctuations at the water-depth, the bed surface and the bedload sediment transport, the following procedure can be used. If it is roughly assumed that the local bedload transport rate at a given channel-section is a function of the mean vertical flow velocity, then local unit bedload transport can be expressed as

$$q_s = m_s V^{n_s} \tag{7.4}$$

with m_s and n_s being constants which depend on the bed material characteristics. Because of the continuity principle, mean flow velocity V is related to the water-depth H at the section and the unit water discharge q_w passing through a unit length channel-section as follows

$$V = \frac{q_w}{H} \tag{7.5}$$

By using eq.(7.5) in eq.(7.4) the unit bedload transport rate is given by

$$q_s = m_s \left(\frac{q_w}{H} \right)^{n_s} \tag{7.6}$$

Now, solving eq.(7.6) for the water depth, it is obtained that

$$H = q_w \left(\frac{m_s}{q_s} \right)^{\frac{1}{n_s}} \tag{7.7}$$

For a uniform flow with the same unit water discharge and total sediment transport rate, but without bedforms, similarly to eq.(7.7), the mean water depth would be given by

$$H_m = q_w \left(\frac{m_s}{q_o} \right)^{\frac{1}{n_s}} \tag{7.8}$$

The ratio between eq.(7.7) and eq.(7.8) yields

$$\frac{H}{H_m} = \left(\frac{q_o}{q_s} \right)^{\frac{1}{n_s}} \tag{7.9}$$

And finally, introducing eq.(7.3) into eq.(7.9), the ratio between local water depth for an undulated bed and mean water depth for a flat bed with the same bedload sediment rate results in

$$\frac{H}{H_m} = \left(\frac{q_o}{q_o + q_f \sin\left(\frac{2\pi x}{\lambda}\right)} \right)^{\frac{1}{n_s}} \qquad (7.10)$$

Eq.(7.10) depicts the water-depth fluctuations with respect to the bed-surface and the sediment transport rate. The upper curves in Figure 7.2 show schematic representations of eq.(7.10) for all three cases of antidune movement. From eq.(7.10) it can be concluded that downstream-migrating antidunes occur if the water surface is in-phase with the bed, but the depth variation is one wavelength out of phase with the bed and with the sediment transport fluctuations. Hence, for downstream-migrating bed features the water depth would be greater over the troughs than over the crests (Figure 7.3). This means that, from crest to trough the flow decelerates and bedload decreases, in such a way that sediment deposition occurs over the lee side of the bedform. Conversely, upstream-migrating antidunes occur if the water surface and water depth variation are in phase with the bed, but one wavelength out of phase with the sediment transport fluctuations. In such a case, the water depth is greater over the crests than over the troughs (Figure 7.3); from trough to crest the flow decelerates and bedload decreases, so that sediment deposition occurs over the stoss side of the bed form. Finally, stationary antidunes would occur when flow depth and bedload transport rate are constant along the bed profile.

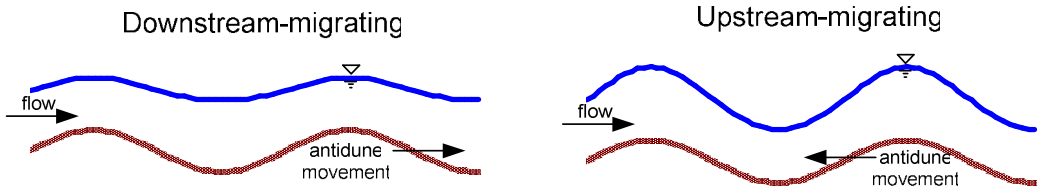

Figure 7.3. Water depth variation over downstream- and upstream-migrating antidunes.

7.3 ANALYSIS TO DEFINE THE ANTIDUNE DIRECTION OF MOVEMENT

If flow over antidunes is idealized as a two-dimensional free-surface flow over a wavy bed-surface as depicted in Figure 7.4, where mean flow velocity V_m and mean water-depth H_m are constant along the flow longitudinal direction (uniform flow hypothesis) and mean bed slope is considered to be small, total energy at the channel section is given by:

$$E = \eta + h + \frac{V^2}{2g} \qquad (7.11)$$

where h is the pressure head on the bed surface, g is the gravitational acceleration, V is the mean sectional flow velocity and η is the bed-surface elevation above the datum η_o for the mean bed-surface level.

If parallel flow occurs, i.e., if the streamlines in the plane of cross section have no substantial curvature, then the pressure distribution can be considered to be hydrostatic, and thus the pressure head in eq.(7.11) would be equal to the water depth. This assumption is valid if the bed and water perturbations are small, so that no important acceleration components appear in the direction normal to the flow. Conversely, if the bed and water perturbations affect the flow filaments, so that the streamlines show a substantial curvature, the flow must be considered curvilinear and the pressure head should be corrected to account for the centrifugal forces produced by the curvature (Chow, 1986). In the study of

the hydraulics of stable antidunes, the parallel flow assumption would not be completely valid, particularly when treating with steep bedforms.

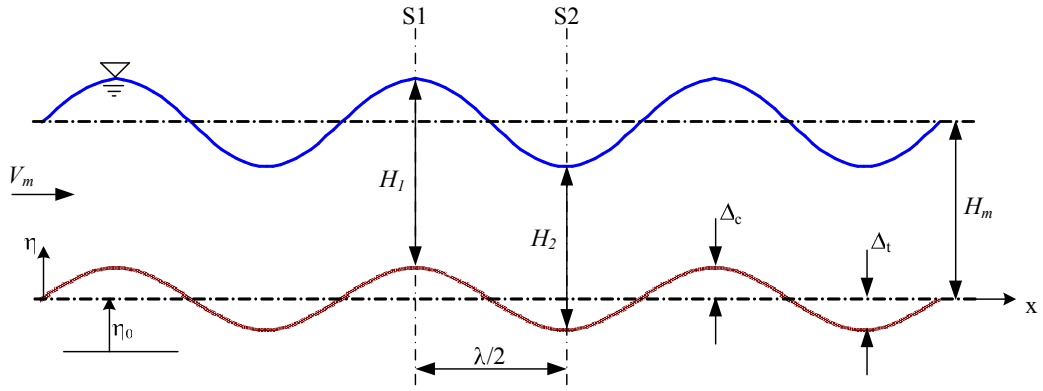

Figure 7.4. Idealized two-dimensional flow over antidunes.

7.3.1 Correction of the pressure head for curvilinear flow

The assumption of hydrostatic pressure distribution over a flow cross-section is valid when parallel flow occurs, i.e., when the streamlines are straight and parallel to the channel bottom. Conversely, if the streamlines are curved, the flow is curvilinear and centrifugal forces should be accounted for. The approximate centrifugal force over a longitudinally curved streamline can be computed by applying Newton's second law, i.e., by the product of mass and acceleration. The mass of a liquid column over a unit cross-section is given by

$$\text{mass} = \rho H \delta A \tag{7.12}$$

where H is the water-depth or the height of the column of liquid having cross-sectional area δA, and ρ is the fluid density. In turn, the centrifugal acceleration can be computed as

$$\text{centrifugal acceleration} = \frac{V^2}{r} \tag{7.13}$$

with r being the radius of curvature of the streamline and V the flow velocity at the point of consideration. In this manner, the centrifugal pressure yields

$$\text{centrifugal force} = \rho H \delta A \frac{V^2}{r} \tag{7.14}$$

Finally, if a unit cross-sectional area is considered, and dividing by the product of fluid density and gravitational acceleration, the pressure head acting at the bottom of the liquid column due to centrifugal acceleration is obtained as (Chaudry, 1993):

$$h_p = \frac{1}{g} H \frac{V^2}{r} \tag{7.15}$$

For concave flows, centrifugal forces act downwards, i.e. in the same direction of gravity, while for convex flows they act upwards, opposing to the gravity.

The piezometric head on the bed-surface of a channel with a longitudinally curved profile can then be computed by including the deviation from the hydrostatic pressure as an algebraic sum of the water depth and the pressure due to the centrifugal forces, i.e. (Figure 7.5):

$$h = H \pm h_p \tag{7.16}$$

Because the centrifugal forces in a concave curvature act in the direction of gravity, their effect is to increase the pressure head, thus in that case h_p takes a positive value; likewise,

for convex curvatures, h_p takes a negative value. In applying eq.(7.15) for solving eq.(7.16), it is assumed that the flow streamlines are attached to the bed, so that the radius of curvature of the bed surface is the same as the radius of curvature of the streamlines. In the same manner, for practical purposes, it can be assumed that V is equal to the average flow velocity over the cross-section.

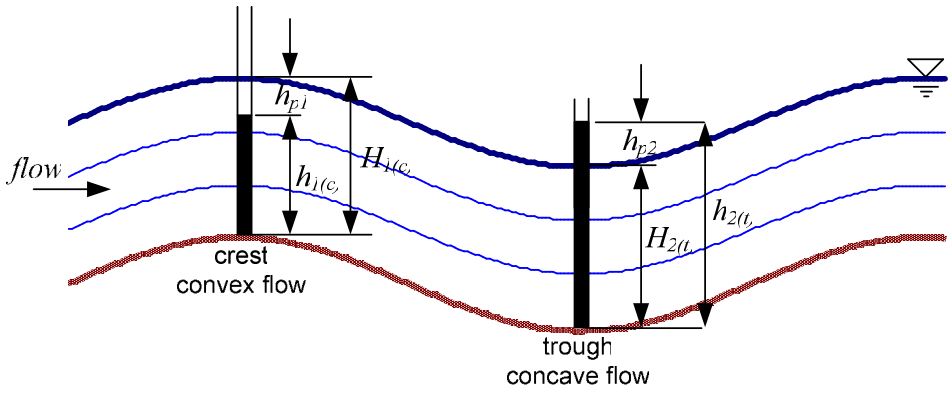

Figure 7.5. Pressure distribution for curvilinear flow over steep antidunes.

7.3.2 Energy balance between the antidune's crest and trough

As it was demonstrated in Section 7.2, the variation of the water-depth along the antidune profile describes whether the antidune migrates downstream, upstream or stays stationary. From Figure 7.2, it was concluded that the antidune moves in the downstream direction if the water depth is higher over the bedform trough than over the crest, and that the antidune moves in the upstream direction if the water-detph is lower over the bedform trough than over the crest (Figure 7.3). Likewise, the antidune remains stationary if the water depth is constant along the flow direction. The hydraulic stable conditions for these three bedform states can be studied by applying the continuity and the Bernoulli energy equations between the crest and trough of the bedform. For this analysis, the problem is reduced to a steady motion by assuming that the reference axes move with the waves.

Applying the principle of conservation of energy, if energy losses are considered negligible, from Figure 7.4 and eq.(7.11), the total energy head at the upstream section S1 over the bedform crest should be equal to the total energy head at the downstream section S2 over the bedform trough, to yield

$$\Delta_1 + h_1 + \frac{V_1^2}{2g} = -\Delta_2 + h_2 + \frac{V_2^2}{2g} \qquad (7.17)$$

where Δ_1 is the distance from the mean bed-surface level to the bedform crest and Δ_2 is the distance from the mean bed-surface level to the bedform trough. Such as it was explained in Section 7.3.1, the pressure head must be corrected to consider the effect of centrifugal forces if the flow is curvilinear. Hence, including eqs.(7.15) and (7.16), and considering a negative head due to centrifugal acceleration at the crest and a positive pressure head due to centrifugal acceleration at the trough, eq.(7.17) becomes

$$\Delta_1 + H_1 - \left(\frac{1}{g} H_1 \frac{V_1^2}{r_1}\right) + \frac{V_1^2}{2g} = -\Delta_2 + H_2 + \left(\frac{1}{g} H_2 \frac{V_2^2}{r_2}\right) + \frac{V_2^2}{2g} \qquad (7.18)$$

Note that for large values of r_1 and r_2, the flow approximates to parallel flow, so that the pressure head is roughly the same as the water depth, i.e., the pressure distribution follows the hydrostatic law when antidunes become low in amplitude and the bed is almost flat.

Considering a unit cross-section, so that the continuity equation satisfies

$$V_1 = \frac{q_w}{H_1} \qquad (7.19a) \qquad \text{and} \qquad V_2 = \frac{q_w}{H_2} \qquad (7.19b)$$

with q_w being the unit water discharge, eq.(7.18) can be simplified to the form

$$(\Delta_1 + \Delta_2) + (H_1 - H_2) = \frac{q_w^2}{g}\left[\left(\frac{1}{H_2 r_2} + \frac{1}{H_1 r_1}\right) + \left(\frac{1}{2H_2^2} - \frac{1}{2H_1^2}\right)\right] \qquad (7.20)$$

A particular case for eq.(7.20) occurs when the bed features are symmetric. For such condition the distances from the mean bed-surface level to the bedform crest and from the mean bed-surface level to the bedform trough are equal, and the radius of curvature of the crest and trough can be considered equal as well, so that

$$r = r_1 = r_2 \qquad (7.21)$$

and

$$\Delta = 2\Delta_1 = 2\Delta_2 = \Delta_1 + \Delta_2 \qquad (7.22)$$

where r is the curvature radius for the crest and trough and Δ is the antidune height. Applying eqs.(7.21) and (7.22) into eq.(7.20), it is obtained

$$\Delta + (H_1 - H_2) = \frac{q_w^2}{g}\left[\frac{1}{r}\left(\frac{1}{H_1} + \frac{1}{H_2}\right) + \frac{1}{2}\left(\frac{1}{H_2^2} - \frac{1}{H_1^2}\right)\right] \qquad (7.23)$$

In order to relate eq.(7.23) to the mean flow characteristics, the definition of the Froude number can be introduced. Considering that the mean water-depth is equal to an arithmetic average of the water-depths over the crest and the trough, i.e.

$$H_m = \frac{H_1 + H_2}{2} \qquad (7.24)$$

and also applying eq.(7.19) with the mean flow velocity, the Froude number can be defined as

$$F = \frac{V}{\sqrt{gH_m}} = \frac{q_w}{\sqrt{gH_m^3}} \qquad (7.25)$$

eq.(7.23) can be transformed into

$$\Delta + (H_1 - H_2) = F^2 H_m^3\left[\frac{1}{r}\left(\frac{1}{H_1} + \frac{1}{H_2}\right) + \frac{1}{2}\left(\frac{1}{H_2^2} - \frac{1}{H_1^2}\right)\right] \qquad (7.26)$$

Eq.(7.26) describes the total energy difference between antidune crest and trough, for a given Froude number and bed form geometry, specified the latter by the curvature radio of the bed undulations.

A particular case for eq.(7.26) exists when water-depth above the crest is equal to the water-depth above the trough, that is, the condition for which the antidune does not migrate either upstream or downstream, but remains stationary. Introducing this condition, i.e., $H_1=H_2=H_m$, into eq.(7.26), and reducing, the following relation is found

$$\frac{2F^2 H_m^2}{r\Delta} = 1 \qquad (7.27)$$

Finally, by taking the squared root of eq.(7.27), a dimensionless number, here defined as the antidune mobility number F_a, is obtained

$$F_a = FH_m\sqrt{\frac{2}{r\Delta}} \qquad (7.28)$$

In this manner, it is established that for $F_a=1$ the antidune remains stationary.

7.3.3 Criterion for antidune migrating direction

Variables involved in eq.(7.26) can be expressed by the functional relation

$$f_a(H_1, H_2, r, \Delta, F) = 0 \qquad (7.29)$$

The number of variables in eq.(7.29) can be reduced by dimensional analysis. According to the Buckingham-Vaschy theorem, because only one reference unit (length) is involved among the five variables, then eq.(7.29) can be reduced to 5-1=4 dimensionless products. In this manner, eq.(7.29) can be rewritten as (see Appendix XVII for an extended version of the dimensional analysis)

$$f_a\left(\frac{H_1}{H_2}, \frac{r}{\Delta}, F, F_a\right) = 0 \qquad (7.30)$$

The ratio H_1/H_2 accounts for the variation of the water-depth between sections, the ratio r/Δ for the geometry of the bedform, the Froude number for the flow hydraulics and F_a for the interaction between all five variables as defined by eq.(7.28). The ratio between the water-depth over the crest and the water-depth over the trough, H_1/H_2, is particularly important for the analysis of antidune movement; according to the findings in Section 7.2 it is satisfied that

for $\frac{H_1}{H_2} > 1$, the antidune migrates upstream

for $\frac{H_1}{H_2} = 1$, the antidune does not move

for $\frac{H_1}{H_2} < 1$, the antidune migrates downstream

Eq.(7.26) has been solved numerically as a function of the dimensionless numbers in eq.(7.30). Results are shown in Figure 7.6 for positive values of F_a and H_1/H_2, and for physically feasible values of r/Δ. For the purpose of defining the stable conditions that determine the direction in which antidunes propagate, from Figure 7.6 it stands out that for $F \geq 1$ the correspondence between H_1/H_2 and F_a is biunivocal; even more meaningful is the fact that for this range if $F_a<1$ then it is always satisfied that $H_1/H_2>1$, and in the same manner, if $F_a>1$ then it is always satisfied that $H_1/H_2<1$. Because of the latter properties of eq.(7.26), the following criterion for antidune direction of movement can be established for critical and supercritical flows:

if $F_a < 1$, then $\frac{H_1}{H_2} < 1$ and upstream-migrating antidunes occur (7.31a);

if $F_a = 1$, then $\frac{H_1}{H_2} = 1$ and stationary antidunes occur, as already known (7.31b);

if $F_a > 1$, then $\frac{H_1}{H_2} > 1$ and downstream-migrating antidunes occur (7.31c).

For Froude numbers close to one and low values of the ratio r/Δ the correspondence between H_1/H_2 and F_a tends not to be biunivocal, i.e., for a given value of F_a there exists more than one value of H_1/H_2 that satisfies eq.(7.26). This would mean that for a certain range of values of F_a and r/Δ downstream-migrating or upstream-migrating antidunes could occur interchangeably. Nevertheless, note that, roughly, values of $r/\Delta<1$ would not be physically feasible, and thus this unstable region would be restricted to a very narrow range, for which F, F_a and H_1/H_2 values are close to one.

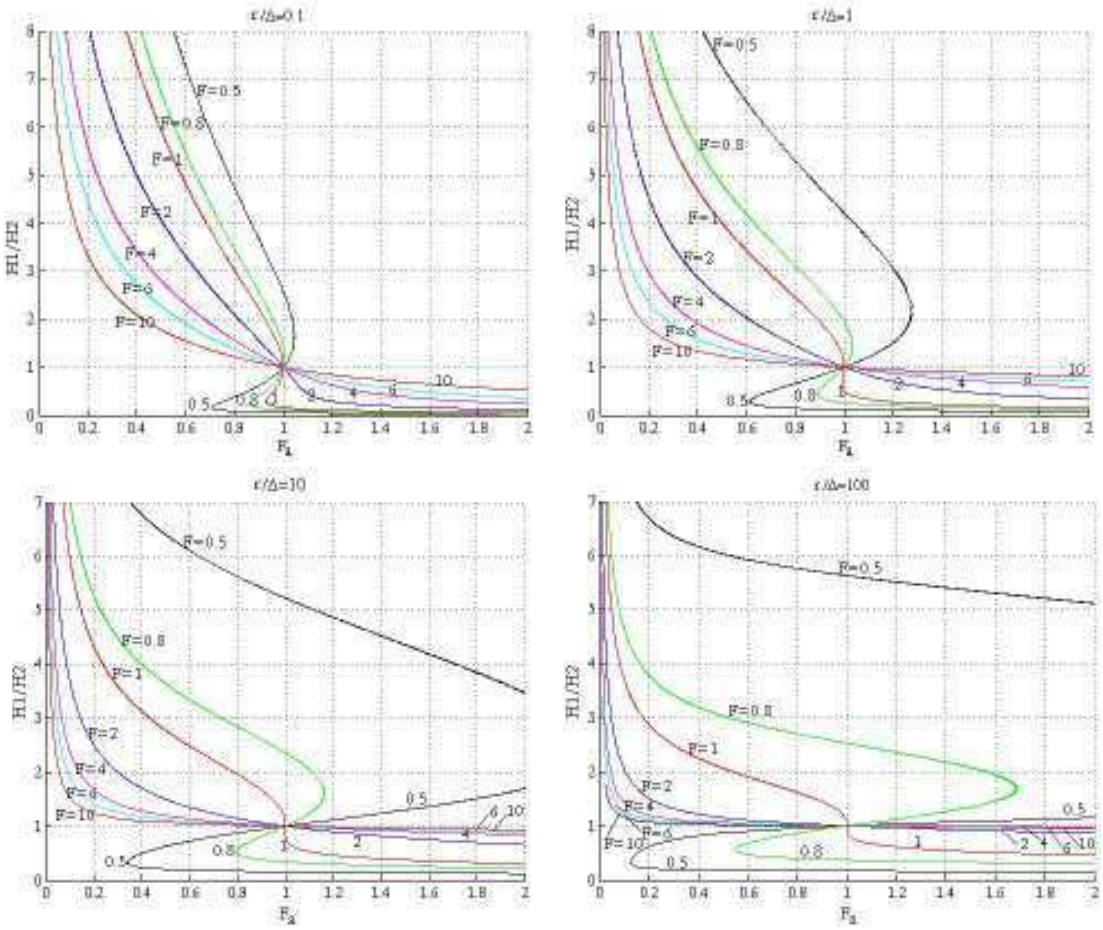

Figure 7.6. Numerical solution for eq.(7.26), as a function of dimensionless numbers in eq.(7.30).

7.3.4 Criterion for antidune propagation as a function of the wave number

The criterion for antidune movement given by eq.(7.31) was stated as a function of the dimensionless number F_a, which in turn is a function of the Froude number, the mean water depth, and the bedform height and radius of curvature, as given by eq.(7.28). However, it is not usual to define the geometry of antidunes in terms of the radius of curvature and the bedform height; more common for this is to use the bedform wavelength instead of the radius of curvature. Therefore, in order to introduce commonly used bedform geometrical parameters for defining F_a, the mathematical definition of radius of curvature is applied to an idealized antidune geometry in the following analysis.

By definition, curvature refers to the amount by which a geometric object deviates from being flat. If it is considered that at a point of a curve the curvature is the same as that of the osculating circle at that point, then the curvature is given by

$$\mathrm{K} = \frac{y''}{\left(1+y'^{2}\right)^{\frac{3}{2}}} \tag{7.32}$$

and the radius of curvature is given by the inverse of the curvature

$$r = \frac{1}{\mathrm{K}} \tag{7.33}$$

The definition of curvature can thus be applied to eq.(7.1), which depicts with a sinusoidal periodic function an idealized bed profile formed by symmetrical antidunes, as is shown in Figure 7.4. In this manner, the first and second derivatives for eq.(7.1) yield

$$\eta' = \frac{\Delta\pi}{\lambda}\cos\frac{2\pi x}{\lambda} \qquad (7.34a) \qquad \eta'' = -\frac{2\Delta\pi^2}{\lambda^2}\sin\frac{2\pi x}{\lambda} \qquad (7.34b)$$

and introducing eq.(7.34) in eq.(7.32), the curvature of the antidune results in

$$\mathrm{K}_a = -\frac{2\Delta\pi^2}{\lambda^2}\frac{\sin\frac{2\pi x}{\lambda}}{\left[1+\left(\frac{\Delta\pi}{\lambda}\right)^2\cos^2\frac{2\pi x}{\lambda}\right]^{\frac{3}{2}}} \qquad (7.35)$$

With reference to Figure 7.4 and eq.(7.17), for the present analysis the curvature of the bed-profile is evaluated at the top of the crest and at the lowest point on the trough, where $x=\lambda/4$ and $x=3\lambda/4$, respectively. As the considered antidune is symmetrical, the curvature is the same on the crest as on the trough but with different sign. Evaluating at the trough, introducing $x=3\lambda/4$ in eq.(7.35), the curvature of the antidune is given by

$$\mathrm{K}_a = -\frac{2\Delta\pi^2}{\lambda^2}\frac{\sin\frac{3\pi}{2}}{\left[1+\left(\frac{\Delta\pi}{\lambda}\right)^2\cos^2\frac{3\pi}{2}\right]^{\frac{3}{2}}} \qquad (7.36)$$

Since $\sin(3\pi/2) = -1$ and $\cos(3\pi/2) = 0$, eq.(7.36) is reduced to

$$\mathrm{K}_a = \frac{2\Delta\pi^2}{\lambda^2} \qquad (7.37)$$

and from eq.(7.33), the radius of curvature for the antidune crest and trough yields

$$r = \frac{1}{2\Delta}\left(\frac{\lambda}{\pi}\right)^2 \qquad (7.38)$$

Introducing eq.(7.38) into eq.(7.28), and reducing, so that the antidune height is cancelled, eq.(7.28) takes the form

$$F_a = FH_m\frac{2\pi}{\lambda} \qquad (7.39)$$

If the wave number k is given by

$$k = H_m\frac{2\pi}{\lambda} \qquad (7.40)$$

then eq.(7.39) can be rewritten as

$$F_a = kF \qquad (7.41)$$

Finally, by introducing eq.(7.41) into the criteria defined by eqs.(7.31), the three states of antidune propagation can be defined in terms of the Froude and wave numbers as follows

if $F < \frac{1}{k}$, upstream-migrating antidunes (7.42a);

if $F = \frac{1}{k}$, stationary antidunes (7.42b);

if $F > \frac{1}{k}$, downstream-migrating antidunes (7.42c).

This criterion, similarly as that given by eqs.(7.31), is valid for critical and supercritical flows.

7.3.5 Maximum antidune and wave steepness

As previously stated in Section 7.3.3, there are some solutions for eq.(7.26) which do not have a physical meaning. Here, two restrictions for the stability of the antidunes' and the water gravity-waves' steepness are introduced in order to set a boundary for the physically feasible solutions of eq.(4.26).

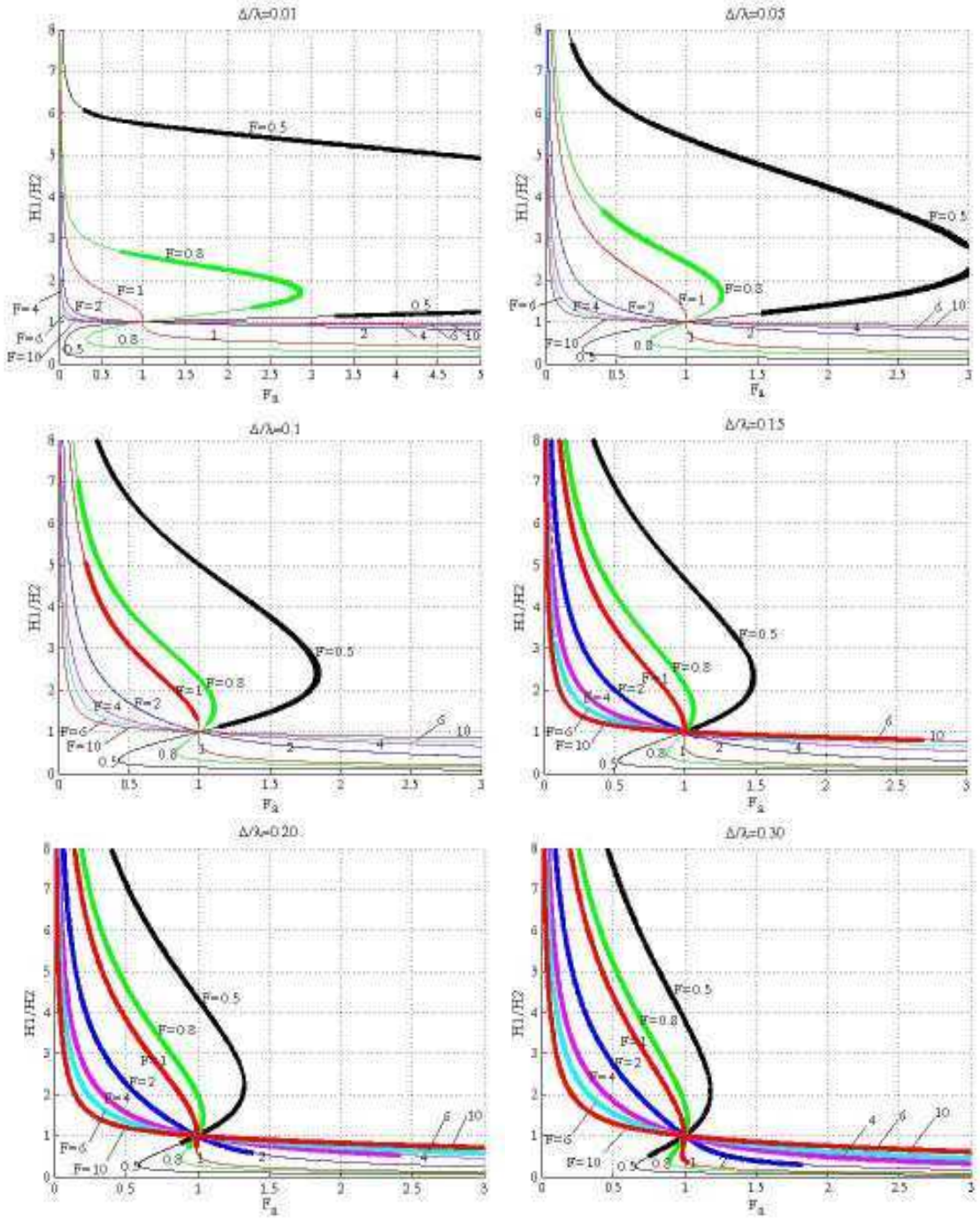

Figure 7.7. Numerical solution for eq.(7.26). Thick lines indicate solutions with no physical meaning due to higher water wave heights than the maximum possible, as given by eq.(7.43).

Because the quotient Δ/λ is related to the steepness of the bedform slip face (i.e., steepness of the slip face $=2\Delta/\lambda$), there exists a maximum Δ/λ value for which the slip face slope would be stable. This maximum value can be related to the submerged angle of repose of the bed material, which value is roughly between 30º to 40º for natural grains. Therefore, for symmetrical antidunes (stoss and lee sides have the same angle with the mean bed level) the maximum ratio between antidune height and length for stability of the slip face slope would range between 0.25 and 0.36. Then, by applying eq.(7.38) it is found that the minimum value that the ratio r/Δ could attained would be between 0.39 and 0.81,

and thus, the graphic in Figure 7.6 with the solution for $r/\Delta<1$, as stated before, would not have any physical meaning.

In the same manner as for the bedform steepness, there exists a limiting value for the steepness of the stationary waves above antidunes. If such a maximum steepness is reached, the waves break. Kennedy (1961) assumed that waves above antidunes have similar characteristics as gravity waves in a fluid of infinite depth, so that the maximum wave height can be estimated from the kinematics of the fluid motion at the wave crests, as studied by Michell (1893, after Kennedy 1961). Michell found that the maximum ratio between the vertical distance from trough to crest, Δ_w, and the wavelength, λ, that can exist for gravity waves is

$$\frac{\Delta_w}{\lambda} = 0.142 \qquad (7.43)$$

For waves above experimental antidunes, Kennedy (1961) reported values of Δ_w/λ that ranged from 0.13 to 0.16, therefore, in good agreement with eq.(7.43).

With reference to Figure 7.4, the height of stationary waves above antidunes can be computed from

$$\Delta_w = \Delta_c + \Delta_t + H_1 - H_2 = \Delta + H_1 - H_2 \qquad (7.44)$$

By combining eq.(7.43) and eq.(7.44), the maximum wave steepness above antidunes can be specified as

$$\frac{\Delta + H_1 - H_2}{\lambda} \leq 0.142 \qquad (7.45)$$

In a similar manner as in Figure 7.6, in Figure 7.7 numerical solutions for eq.(7.26) have been plotted. By applying eq.(7.38), the ratio Δ/λ has been used instead of r/Δ. In addition, by imposing the restriction of a maximum wave steepness, as given by eq.(7.45), Figure 7.7 highlights with thick lines the range of values for which the maximum wave steepness is surpassed, i.e., the range of conditions that would not be physically feasible. Then, from the solutions described by Figure 7.7 it can be put forward that an upper-limit for the steepness of upstream-migrating antidunes would roughly be $\Delta/\lambda=0.15$, as for higher steepness than this value the gravity waves over the antidunes would not be stable. On the other side, physically coherent solutions for downstream-migrating antidunes can occur for even greater ratios of bedform height/bedform length than for upstream-migrating antidunes. Therefore, an upper limit for the solution for downstream-migrating antidunes would roughly be $\Delta/\lambda=0.36$, as this is the maximum possible steepness according to the stability of the bed material, as it was computed above.

7.3.6 Effect of expansion losses

For the energy balance in Section 7.3.2, the loss of energy between the form crest and trough was neglected. Assuming that energy losses owed to skin friction or wave resistance from free surface distortion are not significant, the assumption of insignificant energy loss is at least valid for symmetrical upstream-migrating antidunes, which generate negligible expansion loss (Simons et al., 1961 after Carling and Shvidchenko, 2002). Nevertheless, for downstream-migrating antidunes expansion losses are likely to be appreciable. Therefore, here the expansion losses are considered in the energy balance, in order to evaluate their effect in the criterion for the direction of movement of antidunes developed in Section 7.3.

As an approximation, the expansion loss may be estimated from the velocity head change between sections, as

$$h_e = k_e \frac{(V_1 - V_2)^2}{2g} \qquad (7.46)$$

where k_e is a coefficient. With this, eq.(7.17) can be rewritten as

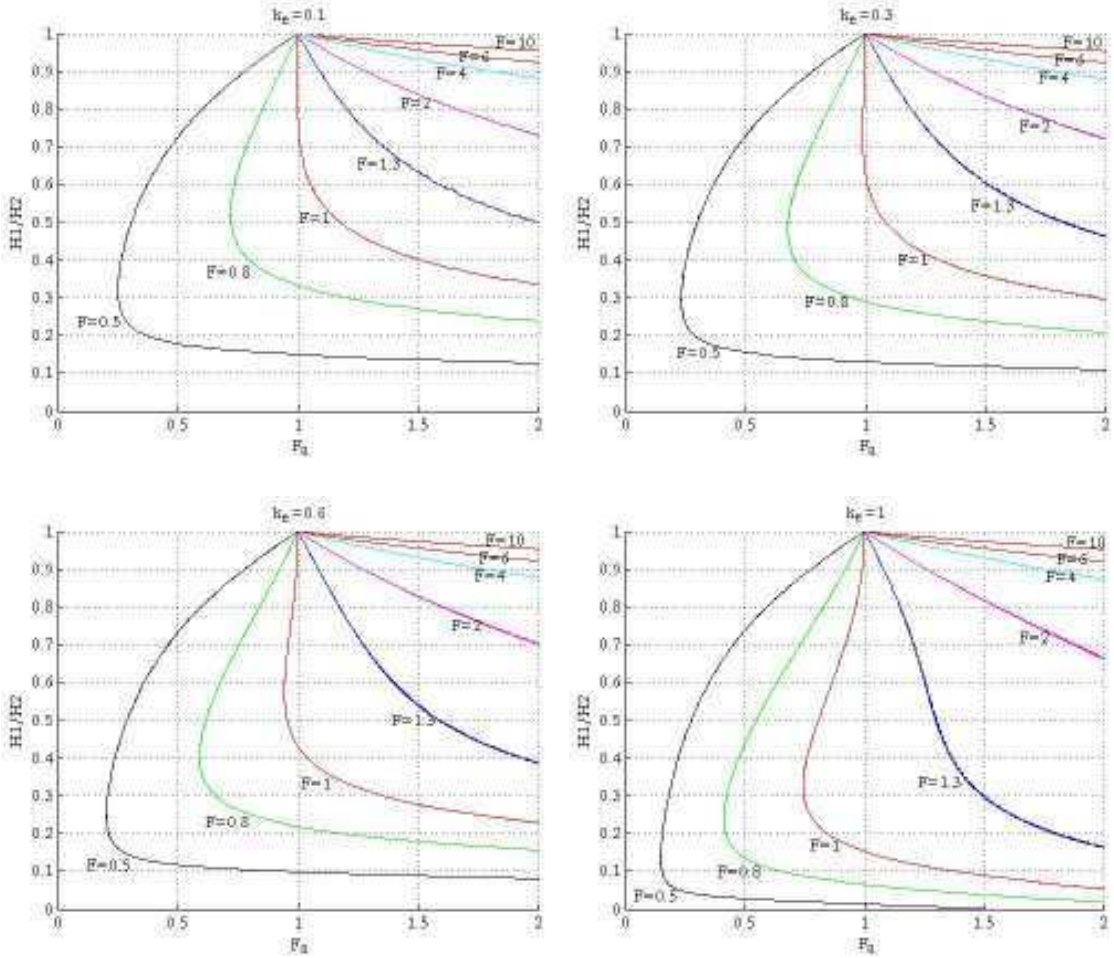

Figure 7.8. Numerical solution for eq.(7.48), for a constant value of Δ/λ=0.05.

$$\Delta_1 + h_1 + \frac{V_1^2}{2g} = -\Delta_2 + h_2 + \frac{V_2^2}{2g} + k_e \frac{(V_1 - V_2)^2}{2g} \qquad (7.47)$$

Following similar simplifications and developments as in eqs.(7.18) to (7.25), eq.(7.26) can be written with the inclusion of expansion loss as follows

$$\Delta + (H_1 - H_2) = F^2 H_m^3 \left[\frac{1}{r}\left(\frac{1}{H_1} + \frac{1}{H_2} \right) + \frac{1}{2}\left(\frac{1}{H_2^2} - \frac{1}{H_1^2} + k_e \left\{ \frac{1}{H_1} - \frac{1}{H_2} \right\}^2 \right) \right] \qquad (7.48)$$

Reduction of eq.(7.48) for stationary antidunes, for which H_1=H_2=H_m, produces the same results given in eqs.(7.27) and (7.28) for the dimensionless number F_a, so that stationary antidunes occur if F_a=1 when H_1=H_2.

Eq.(7.48) would be valid for bed forms where expansion losses and curvilinear flow occur simultaneously, as can be expected for downstream-migrating antidunes. Following the same developments for solving eq.(7.26) as shown in Sections 7.3.4 and 7.3.5, the numerical solution for eq.(7.48) was obtained for different values of the quotient Δ/λ and of the coefficient k_e for the condition H_1/H_2 <1, which corresponds to downstream-migrating forms; we assume that for H_1/H_2 >2 expansion losses are not significant and the solution given in Figure 7.7 would be valid. Results showed that the main effect of including expansion loss is that, as k_e increases, the minimum Froude number for which the correspondence between H_1/H_2 and F_a is biunivocal increases as well. Figure 7.8 shows the solution of eq.(7.48) for Δ/λ=0.05 and for four different values of k_e.

According to the results above, if expansion losses are significant there is a range of values for $F \geq 1$ for which eq.(7.48) is not biunivocal, and the direction of movement of the antidune cannot be established with the criterion given by eqs.(7.31). However, if expansion losses over the bedform are important, it can be expected that downstream propagation would prevail over upstream propagation, because expansion losses are associated to the flow separation over the bedform lee side where deposition would occur. With this in mind, it can be stated here that for critical flows and flows close to the critical, if expansion losses are important, the range for which downstream propagation occurs would not be restricted to $F_a > 1$, as stated in eqs.(7.31), but this range could extend to values of F_a slightly smaller than 1.

7.4 COMPARISON WITH EXPERIMENTAL DATA

The criteria developed above for the propagating direction of antidunes, in the form given by eqs.(7.42), is here compared with experimental data, as shown in Figure 7.9. In addition to the experimental data obtained in the present study, described in Chapters 3 to 5, data from other sources in literature were used as well. Mainly, data referring to bedforms developed in the upper-regime and in the lower- to upper-regime transition were used for the comparison. The data sets and the range of variables are summarized in Table 7.1 and described as follows.

29 data points in Figure 7.9 belong to experiments conducted by Kennedy (1961) to study the mechanics of stationary waves and antidunes in sand beds. Kennedy used two different flumes, one 0.27 m wide and 12 m long and the other 0.85 m wide and 18 m long. Energy slopes ranged from 0.0017 to 0.0272. Downstream-migrating antidunes were observed in only two of the 43 runs performed, while upstream-migrating antidunes were observed in 15 runs; for 7 runs downstream-migrating transitional bedforms with weak to moderately coupling between bed and water surfaces were the dominant bed features registered; only in two runs stationary antidunes formed, and flat beds occurred in 10 runs. For 7 runs with antidunes, the direction of movement was not registered. The bed forms observed by Kennedy were mostly two-dimensional, but in particular most of the transitional bedforms and all of the downstream-migrating and stationary antidunes were three-dimensional. Data used here correspond only to those runs for which the direction of movement was specified and the wave-length was measured.

Table 7.1. Summary of experimental data used for comparison in Figure 7.9.

Author	Flume length [m]	Flume width [m]	Range of flow depths [m]	Range of flow velocities [m/s]	Sediment median size [mm]
Kennedy (1961)	12.0	0.27	0.044-0.106	0.48-1.05	0.23
Kennedy (1961)	18.0	0.85	0.037-0.105	0.50-1.42	0.55
Kopaliani (1972)	30.0	0.50	*	*	2.16 and 6.5
Wieprecht (2000)	*	*	*	*	2 and 3
Alexander et al. (2001)	7.6	0.60	0.068-0.073	1.30-1.41	0.42
Bregoli (2008)	9.2	0.40	0.028-0.036	0.50-1.04	7.34
Recking et al. (2009)	6.0	0.05, 0.102	0.007-0.045	0.29-0.77	2.3, 9 and 23
Present study (gravel)	27.0	0.75	0.068-0.109	0.96-1.16	4.20
Present study (sand)			0.103-0.130	0.82-1.03	1.43
Present study (mix 32% sand)			0.076-0.113	0.92-1.30	3.20
Present study (mix 44% sand)			0.080-0.113	0.94-1.31	2.45

41 data points in Figure 7.9 were obtained from Figure 8 in Carling and Shvidchenko (2002), and correspond to original experimental campaigns by Kopaliani (1972) and Wieprecht (2000). Carling and Shvidchenko (2002) studied the transition between dunes and antidunes in fine gravel, giving emphasis to downstream-migrating antidunes. For this, they collected data sets where transitional bedforms and antidunes were reported. Noteworthy are the data-sets for which downstream-migrating antidunes were observed, as such bedforms have been observed and measured much less often than upstream-migrating antidunes in experimental flumes. 30 data points used in Figure 7.9, all for downstream-migrating bed features, come from Kopaliani's data-set. Kopaliani used very fine and fine gravel in a 30 m long and 0.5 m wide flume with sediment feeding. Bedforms observed were described as downstream-migrating symmetrical antidunes (8 runs), dunes to transitional dunes (4 runs) and downstream-migrating asymmetric antidunes (18 runs). 11 data points from Wieprecht's data set were used in Figure 7.9. All of them correspond to bed features described as upstream-migrating antidunes beneath breaking standing waves. Interesting about the plotted data from Wieprecht's data set is that upstream-migrating antidunes were observed for Froude numbers below 1. No details are given in Carling and Shvidchenko (2002) for the range of water depths, slopes and flow velocities in Kopaliani's and Wieprecht's experiments.

Alexander et al. (2001) performed three runs with medium sand in a 7.6 m long and 0.6 m wide flume to study the relationship between bedforms and relict deposits formed by supercritical flows. Antidunes observed were two-dimensional and migrated upstream. Mean bed slopes ranged from 0.015 to 0.016.

Bregoli (2008) performed 6 experimental runs with fine gravel for supercritical flows and bed slopes of 0.04 and 0.055. The flume used was 9.20 m long and 0.40 m wide. Four data-points in Figure 7.9 correspond to the runs of Bregoli for which antidunes developed. All these antidunes were two-dimensional. Upstream-migrating antidunes were the prominent bedforms observed for three runs, while for one run either downstream- and upstream-migrating antidunes formed; for this latter run the data-point in Figure 7.9 is marked as downstream-migrating.

19 of the data points for upstream-migrating antidunes in Figure 7.9 were obtained by Recking et al. (2009) in a 6 m long flume with two different widths of 0.05 and 0.102 m. Three uniform gravels were used for their experiments, where they investigated the effect of gentle and steep slopes on the antidune wave-length. Observed antidunes were two-dimensional and mean bed slopes ranged from 0.030 to 0.126.

As explained in Chapters 3 to 5, the definitive data set obtained for the present study encompasses 4 run series, each with a different bed material, namely gravel, sand and two sand-gravel mixtures with 32% and 45% sand content, respectively. The flume was 27 m long and 0.75 m wide, and energy slopes ranged from 0.006 to 0.021. All of the bedforms observed moved in the downstream direction, and included three-dimensional antidunes and transitional forms.

In order to emphasize the comparison of the propagating direction of the bedforms, in Figure 7.9 there is no distinction between two- and three-dimensional features, neither between dunes, transitional bedforms and antidunes. Nevertheless, noteworthy is that for $F>1.2$ only antidunes and no dunes nor transitional bedforms were reported in all of the data-sets.

Figure 7.9 shows a consistent agreement between theory and the experimental points. The only two points pertaining to stationary antidunes plot below but close and parallel to the theoretical curve. For a perfect agreement these two points would plot just over the curve. For Froude numbers higher than roughly one, all of the experimental points for upstream-migrating antidunes and most for downstream-migrating forms fall within the region predicted by theory; only 4 downstream-migrating bed features (2 from

Kennedy, one from Kopalini and one from the present study) plot below the theoretical curve, i.e., in the region for upstream-migrating bedforms. Nevertheless, though these points appear quite close to the theoretical curve, their existence below of the predicted position could be related to the expansion losses. As described in Section 7.3.6, if expansion losses are important, the border for downstream propagation could be slightly lower than F_a =1, and thus the theoretical curve in Figure 7.9 would then move slightly below for Froude numbers close to one.

As it was discussed in Section 7.3.3, for Froude numbers close and lower than 1, the theory developed predicts that for a given pair of values of Froude and wave numbers, bedforms are likely to move either upstream or downstream. Data points agree with theory in that for Froude numbers roughly less than 1, downstream- and upstream-propagating forms plot indistinctly above and below from the theoretical curve and overlap between each other. Noteworthy is that most of the data of Wieprecht for upstream-migrating antidunes plot above the theoretical curve, and many of the data-points of Kopaliani for downstream-migrating forms plot below.

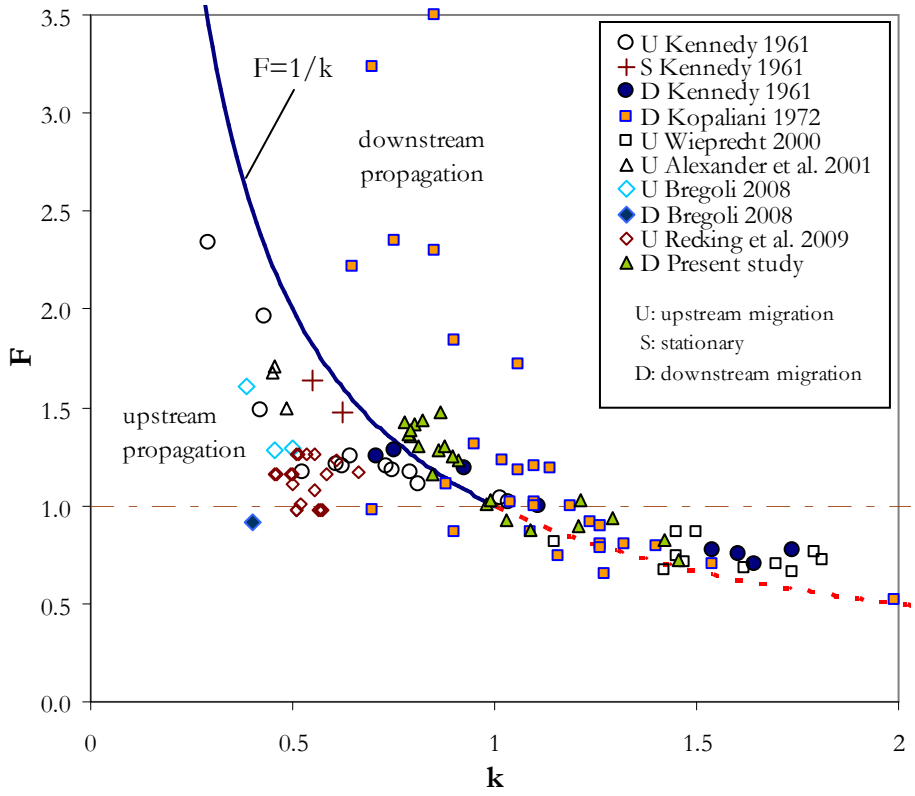

Figure 7.9. Comparison of eqs.(7.42) with experimental data. Continuous line depicts the range of Froude numbers for which theory predicts a unique propagating direction; dashed line depicts the range of Froude numbers for which theory predicts either upstream or downstream propagation. Dashed-dot line outlines the critical Froude number.

7.4.1 Comparison of antidune steepness

Little information exists in literature to test the validity of the range of antidune steepness predicted by the theory developed in Section 7.3. Nevertheless, some information is available, from some of the data sets used to draw Figure 7.9, to compare between

steepness of upstream- and downstream-migrating antidunes. Table 7.2 presents a summary of the bedform characteristics for the data sets for which this information was available. Alexander et al. (2001) presented average values for heights and wavelengths of the upstream-migrating antidunes observed in the three runs they performed. Bregoli (2008) measured antidune wavelengths and heights at different instants during his experiments; average values for each of his runs are presented in Table 7.2. In a similar manner, Recking et al. (2009) measured antidune heights for 12 of their 19 runs. For most of the runs in the data set obtained in the present study (described in Chapters 3 to 5), heights of antidunes were not measured because of the water turbidity and the three-dimensionality of the bed features. Nevertheless, for the sand runs, bedforms were almost two-dimensional, i.e., roughly constant along the channel transversal section, so that their height was observed through the channel wall. In this manner, the average height of the bedforms for the sand runs was computed from the standard deviation of the measured bed profile, σ_b, with $\Delta = 2\sqrt{2}\sigma_b$, as this function depicts the height of idealized sine waves (Willis and Kennedy 1978, after Kuhnle 1993).

Table 7.2. Summary of experimental data for which bedform steepness was computed

Author	Run	Froude number F	Wave number k	mean Δ/λ	Propagating direction
Alexander et al. (2001)	Run1	1.71	0.48	0.053	upstream
	Run2	1.68	0.47	0.050	upstream
	Run3	1.50	0.50	0.052	upstream
Bregoli (2008)	1	0.92	0.40	0.050	downst. and upst.
	2	1.29	0.50	0.106	upstream
	3	1.28	0.45	0.079	upstream
	4	1.61	0.39	0.062	upstream
Recking et al. (2009)	12 runs	0.98, 1.16 and 1.26	0.46 – 0.57	0.025 – 0.062	upstream
Present study (sand)	S1	1.02	1.22	0.092	downstream
	S2	0.94	1.29	0.122	downstream
	S3	0.82	1.42	0.111	downstream
	S4	0.73	1.46	0.101	downstream

By comparing data in the fifth column of Table 7.2, it is remarkable that the steepness of most of the upstream-migrating bedforms is almost half or less than the steepness of the downstream-migrating features. Though this tendency agrees with theory, in that downstream-migrating antidunes could attain steeper shapes than upstream-migrating antidunes, more data for a wider range of conditions would be necessary to test the theoretical findings. For instance, the highest steepness registered in certain measurements in upstream-migrating antidunes for the experiments of Bregoli was as high as 0.15, i.e., an even higher gradient than for any of the downstream-migrating antidunes described in Table 7.2. Such a high steepness reported by Bregoli is in the limit of the highest steepness likely to occur in upstream-migrating antidunes, according to theory as described by Figure 7.7.

Figure 7.10 shows images of experimental bedforms, two upstream-migrating antidunes (A and B), and two downstream-migrating antidunes (C and D). Such images illustrate the distinguishing features of this two propagating conditions, as is specified by the theoretical findings in Section 7.3. Firstly, for the upstream-migrating antidunes the water depth is greater above the crests than above the troughs, while for the downstream-migrating antidunes the opposite occurs. The differences are subtle but measurable.

Secondly, it is evident that downstream-migrating antidunes show highest ratios between flow depth and wavelength, i.e., the wave number k for downstream-migrating antidunes is higher than the wave number for upstream-migrating antidunes, so that for a given Froude number upstream-propagating bedforms plot to the left of the curve in Figure 7.9 and downstream-propagating bedforms to the right. Finally, for the selected pictures the ratio between bedform height and wavelength, i.e., the antidune steepness, is higher for downstream-migrating antidunes than for upstream-migrating antidunes; nevertheless, as stated above, no conclusion can be given about a clear tendency for downstream-migrating antidunes to be able to attain steeper slip faces. The sediment grain size is not considered in the theory developed, and this could have a definite effect on the stability of the bedform slopes and therefore on the bedform steepness.

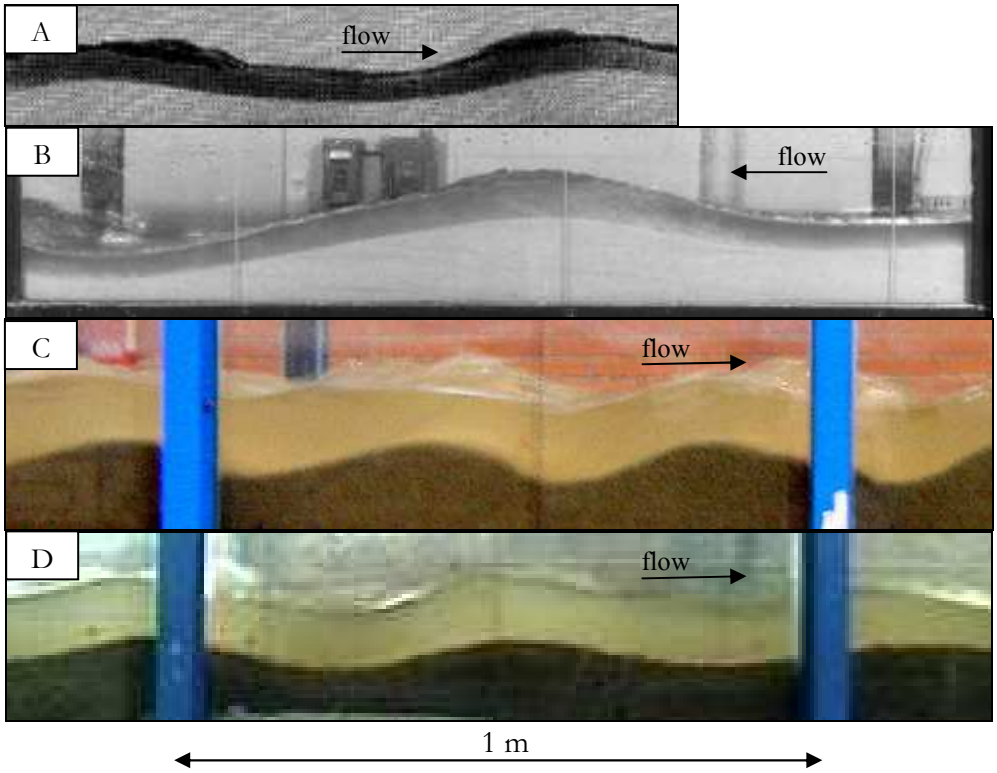

Figure 7.10. Side views for experimental antidunes. A) Kennedy (1961), upstream-migrating antidunes for run 5-14, F=2.34; B) Alexander et al. (2001), upstream-migrating antidune for Run 2, F=1.68; C) Present study, downstream-migrating asymmetric antidunes for run S1 with sand, F=1.02; D) Present study, downstream-migrating symmetric antidunes for run M2E4 with sand-gravel mixture with 44% sand, F=1.25. Scale has been adjusted to be roughly the same for all pictures.

7.4.2 Comparison with potential flow theory

Kennedy (1963) presented bedform stability fields based on the solution of a linearized potential flow over a wavy bed, following original ideas from a stability analysis performed by Anderson (1953) and extended by Kennedy (1961). According to the bedform stability fields developed with potential flow theory, upper-regime occurs when $F > F_u$, where:

$$F_u = \sqrt{\frac{\tanh(k)}{k}} \qquad (7.49)$$

Similarly, theory predicts that downstream-migrating antidunes are likely to occur for large wave numbers if $F > F_p$, F_p given by

$$F_p = \sqrt{\frac{1}{k \tanh(k)}} \qquad (7.50)$$

The existence of upstream-migrating antidunes would be restricted to the range $F_u < F < F_p$. Eq(7.49) and eq.(7.50) have been plotted in Figure 7.11 to be compared with the curve F=1/k, which depicts the criterion for antidune propagating direction developed in Section 7.3. The same experimental data as those used in Figure 7.9 have been plotted in Figure 7.11 as well.

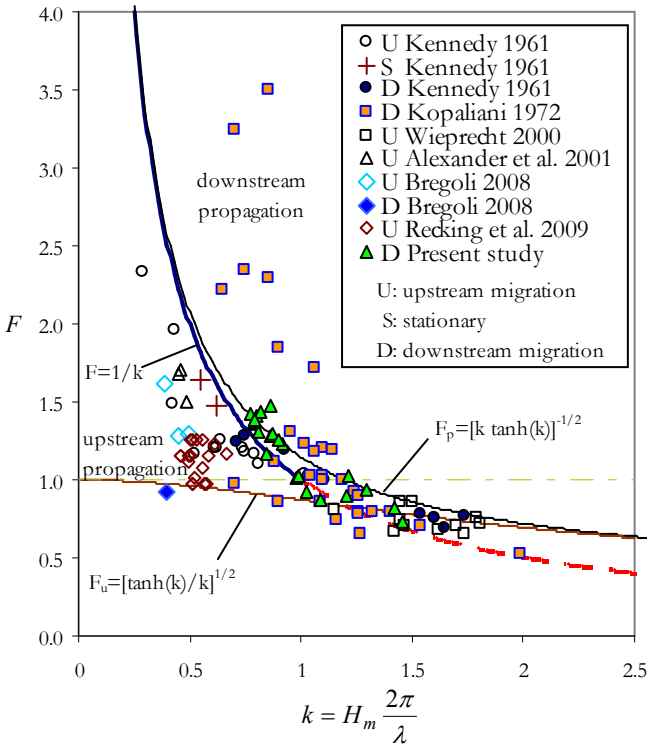

Figure 7.11. Comparison of criteria for distinguishing the antidune propagating direction. Dashed-dot line outlines the critical Froude number.

Most of half of the experimental data-points pertaining to downstream-propagating bed features plot inadequately according to eq.(7.49) and eq.(7.50), while most of the data for upstream-migrating bedforms plot in the predicted region. By comparison, in distinguishing the direction of movement of the bed forms, the criterion developed in the present study performs better than the potential flow analysis.

7.5 LIMITATIONS AND RANGES OF VALIDITY FOR THE CRITERION FOR ANTIDUNE MOVEMENT

The criterion deduced in Section 7.3 for defining the propagating direction of antidunes is based on the application of the Bernoulli equation, so that, a steady irrotational, incompressible, and inviscid flow is implicitly considered.

Most of the bedform stability analysis, like those of Kennedy (1961) and Engelund and Hansen (1966), consider that the bed perturbations are small in comparison to the

wave-length, so that the curvature of the streamlines is considered not to be important. Conversely, the analysis developed in Section 7.3 is based mainly on the inclusion of the correction to the pressure head due to the curvilinear flow. From eq.(7.17), it can be demonstrated that if no curvilinear flow is considered, standing symmetrical antidunes, for which water depths and flow velocity would be constant along the undulated bed profile, cannot be predicted solely with an energy balance; this is so because all variables in the Bernoulli equation would cancel out. The inclusion of the effect of centrifugal forces allows for the balance of energy to be completed. In this manner, for standing antidunes the bedform height results to be equal to the sum of the absolute values of the pressure due to the centrifugal forces on the bedform crest and the trough.

In the limit of validity of the criterion given by eqs.(7.42), i.e., for Froude numbers equal and close to one, the solution of the functions given by eq.(7.26) and eq.(4.47) is quite steep for values of H_1/H_2 and F_a close to one, as can be seen in Figures. 7.6, 7.7 and 7.8. Therefore, it is likely that, for this region, unstable conditions would prevail and transitional bedforms, those bedforms with intermediate or interchanging characteristics of well-developed dunes and antidunes, would occur. When comparing with runs in the present study, for which F, F_a and H_1/H_2 were all close to one (run M1E1 and run M2E5) it is observed that in fact, transitional bedforms occurred (rooster tails at the center of the channel, dunes and antidunes alternatively interchanging near the channel wall) but that bedforms always migrated downstream and antidunes at the center of the channel were quite stable. Prevailing of downstream migration over upstream migration might be related to the asymmetry of the transitional bedforms, which favors the detachment of the streamlines over the bedform slip face and thus deposition over the bedform trough.

Referring to Figure 7.9, for a given Froude number and bedform wavelength, downstream-migrating features would require higher values of flow depth (higher k values) compared to upstream-migrating antidunes. For this, larger water discharges would be necessary. This could explain, in a certain manner, the rare formation of downstream-migrating antidunes in experimental flumes compared to their upstream counterpart; downstream-migrating antidunes would require higher water discharges to be formed and experimental flumes are often limited to low discharges.

Finally, the theory here developed for distinguishing the movement direction of an antidune does not give clues about the cyclic nature of sand upstream-migrating antidunes, which grow and decay with an apparently arbitrary periodicity (Alexander 2001). Downstream-migrating antidunes observed in the present study (as described in Chapter 5) were mostly stable, although the bed features could sometimes vanish, trains of antidunes were most of the time visible under rooster tails. This behavior could be related to the grain size; as the cyclic grow and decay of the antidunde has been associated with the energy produced by the breaking of the standing wave (Kennedy 1961, Alexander 2001), which destroys the bedform and gives place to a transient plane bed, it is possible that for coarse materials such wave-breaking is not capable of destabilizing the antidune. Bregoli (2008) gives descriptions of stable upstream-migrating antidunes with gravel (Table 7.1), but no details are given about the genesis of these forms. More observations are required for expanding the knowledge of downstream-migrating antidunes and to recognize the role of grain size and grain size heterogeneity in antidune morphology and genesis.

7.6 SUMMARY

Antidunes are bedforms characteristic of supercritical unidirectional flows. Contrary to bedforms developed in subcritical flows, like dunes and ripples, antidunes can not only propagate in the downstream direction, but can propagate upstream or remain stationary as

well. In this Chapter, the stable hydraulic conditions that determine each of the three antidune movement possibilities have been analyzed, and a new theory was developed for distinguishing the stability fields of occurrence of each of these three conditions. The new theory is based on fundamental hydraulics and allows discriminating the antidune movement direction as a function of the wavelength and the bulk flow parameters, namely, Froude number and mean water depth. The theory was developed from an energy balance over a symmetrical antidune; for this, the Bernoulli equation was applied between the antidune crest and antidune trough, and the pressure head was corrected to account for the centrifugal forces generated by curvilinear flow over the in-phase bedform. Manipulation of the fundamental equations produced an antidune movement dimensionless number (F_a), whose critical value (F_a=1) corresponds to the stationary condition of the antidune, while values higher and lower than the critical correspond to downstream- and upstream-propagation, respectively. Comparison with experimental data shows good agreement between the new theory and experimental observations. A better agreement than the predicted by bedform stability analysis based on potential flow theory was found as well. By introducing a restriction for the maximum standing-wave height above antidunes, theory predicts ranges of hydraulic variables and bedform steepness for which antidunes are likely to occur. According to this restriction, downstream-migrating antidunes could attain steeper height-wavelength ratios than upstream-migrating antidunes. Likewise, theory predicts that for a given Froude number, downstream-migrating antidunes are formed for higher water depth-wavelength ratios than upstream-migrating antidunes, which could be a likely reason why downstream-propagating antidunes have been less documented than their upstream-propagating counterparts in laboratory flumes.

CHAPTER 8:

FINES INFILTRATION IN MIXED-SIZE BEDS

8.1 INTRODUCTION

Horizontal lamination under the migration path of downstream migrating antidunes was observed at transcritical- and supercritical-flows in the flume experiments with sand-gravel mixtures described in Chapter 3. The observed laminae were defined by the continuity of fine sand layers, named here sub-bottom sets, which were formed by the preservation of fines in the bedforms troughs surface and subsurface. Fines were preserved in the near surface as they found shelter in between coarse grains or penetrated to where the flow was not able to winnow or wash them away. On the other side, the process by which fines did not penetrate deep into the bed was the bridge building of the in-filling grains on the pores of the sediment framework. By this process the grains formed a seal from which subsequent settling fines filled the bed upwards. The bridge building process, hitherto poorly understood, is addressed in this work to explain the formation of fine sand layers under bedforms. To study this process, data in literature where the infiltration of fines is reported are analyzed, and calculations with porosity empirical models for particle mixtures are presented. A numerical model is also developed, which calculates the saturation limit of the bed by fines and analyzes the infilling process in temporal steps. Results show that for bimodal mixtures the bridging potential is controlled by the ratio of the maximum and minimum grain diameters, of the fine and coarse fractions, respectively; the bed vertical sorting can be appropriately described using porosity models for binary mixtures and the relative content of the in-filling matrix in the bed. For less bimodal or unimodal sediments, the bridging process is more complex. Consistent results for the bridging potential for such sediments were found applying a multifractional porosity model to compute a cutoff size for grains that make up the bed structure and those that fill the voids. Results proved the utility of porosity models for understanding the interactions between the bed structure and the in-filling matrix in natural gravel-bed rivers.

8.2 FINES INFILTRATION AND PRESERVATION UNDER THE EXPERIMENTAL SAND-GRAVEL BEDFORMS

Sediment sorting in beds with heterogeneous size material is frequently controlled by grain size segregation processes exerted during bedform migration. A well-known grain sorting mechanism in downstream migrating bedforms occurs when flow separation at the crest of the bedform produces the segregation of the bedload coarse fraction from suspended fines (Carling and Glaister 1987, Julien et al. 1993, Bridge 2003). Such a mechanism is the origin of open-framework gravel deposits (Lunt and Bridge 2007) and cross-stratified strata, which could be characterized by three basic depositional units (Figure 8.1): a topset, a foreset and a bottomset (Kleinhans 2004).

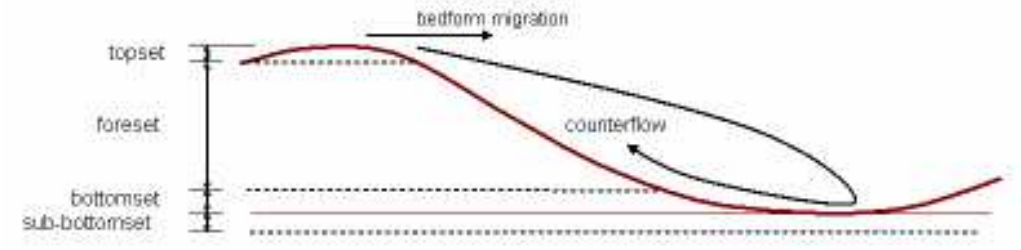

Figure 8.1. Basic depositional units in a bedform.

Coarse bottomsets may form if fine material is mainly transported in suspension or if fines put in suspension at the bedform crest are carried off to the stoss side of the next bedform downstream. In such conditions, only coarse particles settle down on the bedform trough and alternating coarse and fine laminae may form, as observed by McBride et al. (1975) using sand in laboratory experiments with downstream migrating in-phase wave bedforms. In turn, bottomsets composed of fine sediment are produced if sand in suspension deposited on the bedform trough is preserved and not washed away by the counterflow generated in the flow separation region. Thus, usually they are not associated with high shear stress flows. A sort of bottomset rich in fines, called here "sub-bottomset", may eventually form, even at high shear stress flows, if fine grains deposited on the trough region are preserved by finding shelter in between coarse surface grains or by shallow percolation in the bed subsurface. Continuity of sub-bottomsets in the bed may define a band or lamina bounding the migration path of the bedforms (Figure 8.1). Bridge and Best (1997) observed a lamina of fine sediment formed by this process under experimental low-height sand waves, and also Lunt and Bridge (2007) reported the formation of planar strata or cross strata bounded below by a sand or sandy-gravel band formed by the infiltration of fines deposited in bedforms troughs.

Lamination produced by fines enrichment of fluvial beds is relevant for the study of hyporreic flows. Such lamination may be formed of densely packed sediment which could interrupt the continuity of ground water flows into high permeable deposits. This effect would be particularly harmful for flooding in torrential ephemeral streams; a high percentage of the flood flow is lost by infiltration in the highly permeable beds of such streams. In turn, understanding the conditions in which sub-bottomsets form would be of interest for paleohydraulics reconstruction from relict deposits; sub-bottomsets are not related to the bedform height, so they should not be considered within the cross-set thickness when applying methods (as those presented by Paola and Borgman 1991 and Leclair and Bridge 2001) to relate ancient fluvial deposits with formative bedforms geometry. Moreover, as sediment transport depends on particle size, anticipation of the size composition of laminae formed by fines infiltration is important for grain sorting

models as that presented by Kleinhans (2005), which relates sediment transport with vertical sorting mechanisms in dunes.

The experimental formation of sandy-gravel sub-bottomsets under downstream migrating in-phase wave bedforms (downstream-migrating antidunes) is described and analyzed in this Section. Continuity of the sub-bottomsets defined thin laminae parallel to the mean bed level. The experiments revealed that at hydraulic conditions higher than the critical flow, laminae may form by the preservation of fine particles under the surface of beds composed of sand-gravel mixtures, whose sand contents are close to the optimum required for a maximum packing density. Preservation of fines near the bed surface is determined by the possibility of the settling grains to fit in the pores in between bed particles and bridge the gaps, a process which is poorly understood and therefore addressed in this work to understand the formation of the observed fine sand layers under the bedforms. Calculations with porosity models for binary and multifractional particle mixtures are presented to explain the shallow percolation of fines that defined the laminae.

8.2.1 Infiltration of fine particles and bed porosity

When turbulent fluctuations in the zone of flow separation at the lee-side of a bedform are strong enough to remove the fine particles deposited in the trough region, these grains are washed away unless they penetrate deep in the bed or find shelter in between other surface particles. Thus, the ability of the grains to infiltrate through the bed is an important factor for their preservation. According to Diplas and Parker (1992) the main controls over the maximal depth at which fines may infiltrate below the surface of a coarse bed are the size ratio $r=d/D$ of the pore-filling sediment d and the bed material D, and the boundary shear stress. Very low size ratios allow a deep penetration of the fine sediment in the substrata, which starts filling the pores from the bottom up, as observed in laboratory by Einstein (1968) and in a field experiment at Turkey Brook by Frostick et al. (1984). On the other hand, moderate size ratios hinder the in-filling sediment penetration, so that fines occlude the pores to form a seal or plug close to the bed surface, which may be pushed deeper in areas of higher Shields stress. Penetration depths observed by different authors are shown in Table 8.1. In an armored bed, the seal may form in the substrata after the fines infiltrate through the pavement, thus the infiltration depth would be controlled by the pavement thickness and the size ratio between the infilling sediment and the substrate (Frostick et al. 1984). As found by Allan and Frostick (1999), penetration of fines into subsurface pores is enhanced when the framework lifts and dilates if the flow is competent to mobilize the surface gravel layer.

A near surface seal forms when the fine grains build bridges on the pores between the bed coarse grains; in that case, a continuous supply of fines will fill the bed from the seal bottom upwards to the bed surface, until they saturate it and no more gaps are left to be occupied by fine grains. By analogy, the process of pore-filling of a gravel framework by a matrix of sand can be described in an idealized manner with the particle packing theory for binary mixtures as follows. For a bed of unit volume composed of a skeleton of self-supporting large particles with size D, in which the voids are subsequently and uniformly filled with small particles of size d, such that $r=d/D\rightarrow 0$, variation of porosity ε of the mixed bed will be a function of the proportion by volume between particles and of the pure porosities of the large and small fractions alone, ε_D and ε_d, respectively. The total volume of solids in the unit volume would be $1-\varepsilon$ and the volume of large particles $1-\varepsilon_D$. Maximum packing density would be reached when the bed saturates and all the voids in between coarse grains have been completely filled with fines; for that condition, the volume of small particles in the unit volume would be $\varepsilon_D(1-\varepsilon_d)$ and the minimal porosity in the entire mixture would be given by

Table 8.1. Fines penetration depths observed by different authors. r is the size ratio between representative diameters D and d, of the coarse (framework bed material) and fine (bed load) materials, respectively; D_x and d_x are the grain diameters for which x% of the particles by weight are finer.

Author	Bed material	Bedload material	$r=d_{50}/D_{50}$	Penetration depth
Einstein (1968)	poorly sorted gravel	silt	0.0002*	No seal formation
			0.0008*	No seal formation
Beschta & Jackson (1979)	well-sorted gravel	well-sorted sand	0.033	2.5 - 5D_{90}
			0.013	No seal formation
Carling (1984)	well-sorted gravel	well-sorted sand	0.010	No seal formation
			0.012	No seal formation
			0.090	Not given
Carling & Glaister (1987)	well-sorted gravel	bimodal mixtures of well-sorted sand and well-sorted gravel	0.035	2 – 3.5D_{90}
Lisle (1989)**	well-sorted gravel	poorly sorted sand and gravel	0.21-0.31	2.6D_{90}
Diplas & Parker (1992)	poorly sorted unimodal mixture of sand and gravel	poorly sorted sand-gravel mixture + fines (silica flour)	0.027†	5D_{90}
			0.037†	3D_{90}
Schälchli (1992)	poorly sorted unimodal mixture of sand and gravel	well-sorted sand	0.007	2D_{90}
Allan & Frostick (1999)	well-sorted gravel	well-sorted sand	0.076	2D_{max}
Lunt & Bridge (2007)	poorly sorted unimodal mixture of sand and gravel	same as bed material	0.202††	D_{mean} – 2D_{mean}

* Average of minimum and maximum diameters

** Field experiment with buried cans

† Here subpavement is considered as bed material and silica flour as bedload

†† Size ratio of sand and gravel fractions

$$\varepsilon_{MIN} = \varepsilon_D \varepsilon_d \tag{8.1}$$

The capacity of the bed to be filled with fine grains before becoming saturated may be represented with the maximum fractional content by volume of small particles f_{dMAX} that can occupy the voids left by the large particles framework. f_{dMAX} is given by the relation between the volume of fine particles in the mixture and the volume of solids, as follows

$$f_{dMAX} = \frac{\varepsilon_D (1-\varepsilon_d)}{1-\varepsilon_{MIN}} \tag{8.2}$$

and using (8.1) it is obtained

$$f_{dMAX} = \frac{\varepsilon_D - \varepsilon_{MIN}}{1-\varepsilon_{MIN}} \tag{8.3}$$

For $\varepsilon \leq \varepsilon_{MIN}$, the proportion of large particles by volume f_D, defined as the relation between the volume of large particles in the mixture and the volume of solids, becomes

$$f_D = \frac{1-\varepsilon_D}{1-\varepsilon} \tag{8.4}$$

Using the proportion of fine particles by volume $f_d=1-f_D$, and operating, from (8.4) it is obtained

$$\varepsilon = \frac{\varepsilon_D - f_d}{1-f_d} \tag{8.5}$$

which describes the change in bed porosity as the voids in the large particles framework are subsequently filled with small grains.

On the other side, as (8.1) is a singular case for which $\varepsilon=\varepsilon_{MIN}$, doing (8.1) equal to (8.5) and operating, it is found that

$$\varepsilon_D = \frac{f_d}{1-\varepsilon_d(1-f_d)} \tag{8.6}$$

and substituting into (8.1), considering that $\varepsilon=\varepsilon_{MIN}=\varepsilon_D\varepsilon_d$, the following relation is obtained

$$\varepsilon = \frac{\varepsilon_d f_d}{1-\varepsilon_d(1-f_d)} \tag{8.7}$$

This equation describes the dependency of bed porosity to the fractional content of small grains in the mixture when these constitute a matrix where large particles are embedded and not necessarily in contact between each other.

Equations (8.5) and (8.7) define an idealized model for a densely packed mixture of two particle sizes. Both equations have been plotted in Figure 8.2A, using porosity values of ε_D=0.4 and ε_d=0.38. Note that the unique point where both equations are equal corresponds to f_{dMAX} and ε_{MIN}.

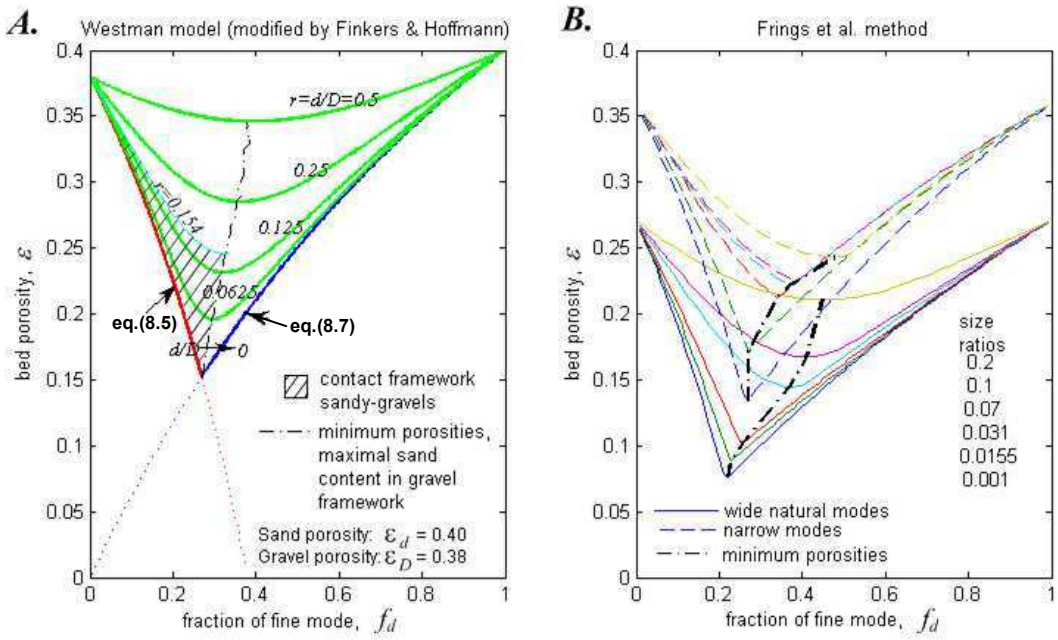

Figure 8.2. Bed porosity for different particle size ratios according to A) Westman's model, as corrected by Finkers and Hoffmann (1998) for spherical and non-spherical particles with a narrow size distribution; B) Frings et al. (2008) model for multifractional mixtures, standard deviations used for the fine and coarse fractions of the wide natural modes was 1; the size ratios are listed in the same order (from top to bottom) as the lines.

8.2.2 Empirical bed porosity models

The model expressed by equations (8.1)-(8.7) for binary mixtures represents a particular case for a more general condition that considers the effect of the particle size ratio in the bed packing density. Different authors have proposed empirical relations to account for this effect. One of the most consistent empirical models found in literature is that from Westman for spherical particles, presented in 1936 (see Appendix XVIII). Finkers and Hoffmann (1998) modified the Westman's model to extend its applicability to non-spherical grains (see Appendix XVIII). The model of Westman as modified by Finkers and

Hoffmann has been plotted in Figure 8.2A for different values of the particle size ratio, using original porosity values of ε_D=0.4 and ε_d=0.38. Curves in Figure 8.2A show that as the values of r increase, the transition in the region of minimum porosity turns smoother. Dias et al. (2004) related this behavior to a more pronounced interaction between fractions when $0.1<r<1$. They demonstrated that for such moderate values of the particle size ratio, at the region around minimum porosity (roughly $0.25 <f_d < 0.35$), the arrangement of small and large particles is unstable and thus the packing density is strongly dependant on the mixing procedure. If the mixture has been obtained by filling with small particles a self-supporting skeleton of large grains, a densely packed mixture may be obtained; otherwise, if the mixing procedure is particle displacement and rotation the overall bed porosity may increase because small grains are able to wedge between large ones.

In analogy with the packing of sediment mixtures composed of sand and gravel, in Figure 8.2A a region where a gravel framework in natural sediments is most likely to occur has been shaded. The region is bounded at the right-hand side by the dashed line that joins the minimum porosity values for each sand-gravel size ratio, defining the border for the maximum sand content that might fill the pores of a bed supported by gravel clasts. The upper boundary is given by the maximum size ratio for which the sand particles fit in the pores of the gravel framework. Larger size ratios would mean that also the sand grains make up the bed structure. For tightly packed spheres, such a maximum size ratio is between 0.154 (for tetrahedral packing) and 0.414 (for cubic packing); for natural grains with random tight packing it would be close to the former, and thus that value was used to mark out the region in Figure 8.2A. Outside of the bounded area, matrix supported gravel occurs, in which large clasts are not necessarily in contact. Thus, the maximum sand content that could fit in a gravel framework, or the capacity of a coarse bed to be filled with fines, will depend upon the packing arrangement of the gravel framework, the grains size ratio and the original porosity of both fractions. In terms of the factors that control the intrusion of sediment in the bed, the gravel framework region is bounded at the right-hand side by the volumetric capacity of the bed to be filled with sand and at the upper limit by the presence of pores large enough to allow sand grains to penetrate in the bed. Pore size would control the possibility for a given sand grain to fit and penetrate in the pockets, while volumetric capacity would define the amount of pockets available.

Packing porosity models for binary mixtures consider that the small and large particles are of uniform size or that their size distribution is narrow. In contrast, the particle sizes of fine and coarse fractions of natural sediment mixtures are not uniform, so that their size distributions usually overlap and size fractions interact between each other; as a consequence, the bed framework normally consists of more than one size fraction. Even though the Finkers and Hoffmann model considers the particle size distribution, it only distinguishes two general cases of narrow and wide size distributions (See Appendix XVIII). A more precise computation of bed porosity would consider the size heterogeneity of natural sediments. Frings et al. (2008) presented a multifractional porosity model based on an original model developed by Yu and Standish (1991). The Frings et al. model has been plotted in Figure 8.2B* for different size ratios and for two different sediment mixtures. The model is based on a detailed empirical description of the interaction between binary sediments, like the Finkers and Hoffmann model, which is then extended to arbitrary mixtures. The model was verified by Yu and Standish (1991) on a great number of ternary mixtures and by Frings et al. (2008) on natural sand-gravel mixtures. The applicability to arbitrary mixtures makes it highly valuable to sedimentology where extremely bimodal sediments such as those covered by the Finkers and Hoffmann model

*These computations were performed by Maarten Kleinhans using the original Matlab code used by Frings et al. (2008); other computations with that same model in this Section were performed with that same code, which was kindly provided to the author by Maarten Kleinhans.

are rare. In Figure 8.2B model results are plotted for both artificially narrow binary mixtures and for bimodal sediments with natural wide modes, each with an arithmetic standard deviation of 1. The mixture is the sum of two modes. Along the x-axis the fine mode increases in proportion and various curves are drawn for different size ratios of the modes. The specified size-independent initial porosity for a unisize random close packing is 0.36. Accordingly, the curves for the mixtures of artificial narrow modes all have a modeled porosity of 0.36 for 0 or 100% of fines. However, for the natural mixtures the porosity of each mode alone is smaller than 0.36 according to the model because their smaller grains fill the pores of their larger grains. Hence the natural mode lines plot increasingly lower than the artificial narrow ones for increasing standard deviations.

Frings et al. (2008) used their model to predict a boundary, the cutoff grain size, between the smallest grain size that is still part of the bed structure and the largest grain size that is not. In other words, the model predicts where the boundary is between grains (not necessarily gravel) that are part of the contact framework and grains that just fill the pores. For unimodal mixtures these are a very small percentile of the sediment, but for bimodal mixtures with less than the pore-filling proportion of sand the boundary is a grain size between the two modes. The cutoff grain size is used by Frings et al. for a novel distinction between sediment that is and is not contributing to morphological change as an alternative to the term wash load which has several meanings. The cutoff size will be used in this Chapter to predict the tendency of a sediment to form bridges.

According to Parker (2004), grain sizes in the range of pea gravel are relatively scarce in natural rivers; albeit gravel-bed rivers often contain large amounts of sand, material between 1 and 8 mm is not common. Using the latter values, a limiting condition for a maximum size ratio between sand and gravel in gravel-bed rivers is obtained, $r_{MAX}=1/8=0.125$, which falls below the upper limit of the contact framework gravels region in Figure 8.2A. Applying the Finkers and Hoffmann porosity model with the same porosity values used in Figure 8.2A, maximum sand contents obtained for a gravel framework are 27% for $r\rightarrow 0$ and 32% for $r=0.125$, which is a similar range to the 22-32% range obtained by Plumley (1948, after Church et al. 1987) with calculations for a deposit of two sizes of spheres, and also agrees well with field–determined estimates (Church et al. 1987). A similar verification for the application of their porosity model to natural sediments was presented by Frings et al. (2008).

From the concepts described above, it might be expected that the bed vertical sorting for bimodal sediments with low size ratios can be well predicted based on f_d. As the fine fraction would not be part of the bed structure, it would percolate until reaching a denser or silted up strata. Nevertheless, for natural sediments with less bimodal or unimodal size distributions vertical sorting prediction is uncertain, as it is unknown how deep the fine sediment would percolate. In this Section the experiments described in Chapter 3 are used to analyze the sediment infiltration process; the experiments were performed under flows higher than the hydraulic critical condition, and with mixtures of uniform sand and uniform gravel with high size ratios. The observed penetration of the fine fraction in the bed during the experiments was restricted to the surface layer, describing near-horizontal laminae for all runs. Unlike the percolation data summarized in Table 8.1, the experiments described herein report the penetration of fines in the bed under high sediment transport conditions with mobile bedforms. The shallow penetration of the fine fraction is analyzed with packing model calculations and compared with data from literature shown in Table 8.1.

8.2.3 Experimental observations

Four runs from the experimental campaign, namely, M1E3, M1E5, M2E3 and M2E4, are use here for a general description of sedimentological features of the strata formed by the passage of bedforms. Average sand content by weight in these four mixtures was 31% for the first two experiments, and 45% for the other two. Average grain size distributions for the mixtures are shown in Figure 8.3, and the characteristics of the sand and gravel, feeding rates and conditions at each run are shown in Table 8.2. Measured porosity for the original sand and gravel was 0.4 and 0.38, respectively, which were the same values used to plot the curves in Figure 8.2A.

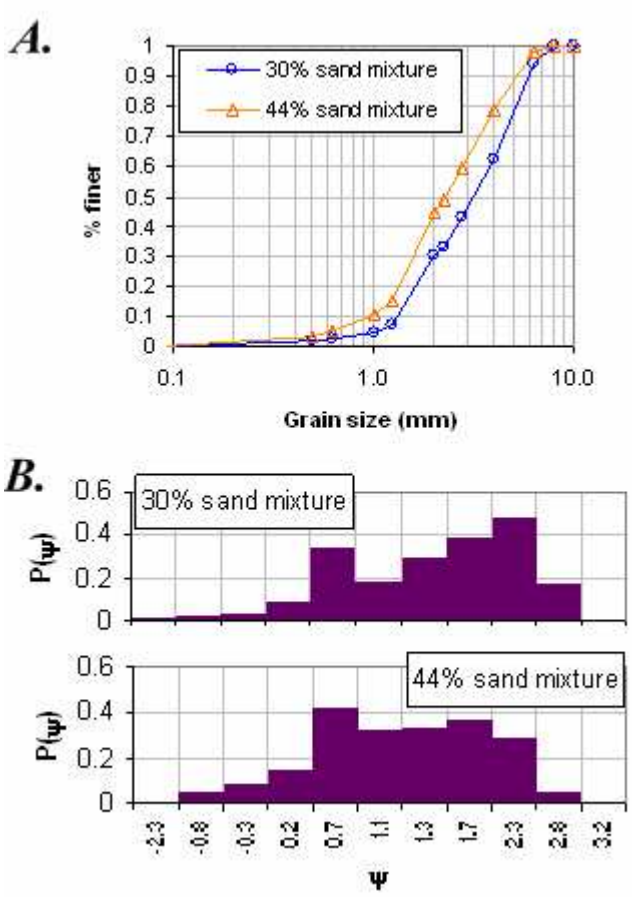

Figure 8.3. Characteristics of the bed material used in the experiments, A) cumulative particle size distributions; B) discrete probability density functions in ψ scale units.

Table 8.2. Experimental conditions and characteristics of the sediment fed.

Run	Water discharge (l/s)	Mean water depth (m)	Froude Number	% sand fed	Feeding rate (kg/s)	Gravel fraction (≥ 2 mm)		Sand fraction (< 2 mm)	
						D_{50} (mm)	σ_g (mm)	d_{50} (mm)	σ_g (mm)
M1E3	67.0	0.076	1.37	31%	0.670	4.01	1.38	1.57	1.30
M1E5	78.4	0.090	1.23	31%	0.436	4.17	1.36	1.55	1.39
M2E3	78.4	0.083	1.40	45%	0.793	3.43	1.37	1.53	1.45
M2E4	78.0	0.089	1.25	45%	0.553	3.35	1.36	1.52	1.48

For all the four selected runs, except run M1E5, the bed and water surface were in-phase, thus, bedforms were cataloged as downstream-migrating antidunes (see Figure 8.4); for run M1E5 the configuration was labeled as transitional, since the water and be surface were not completely in phase. All bedforms had a strong three dimensional component, with deep trough scour at the center of the channel; scour holes were covered by a lag deposit during the receding discharge at the end of the experiment. As explained in Chapter 5, when the water was drawn down the bed surface showed a pattern of alternate bars.

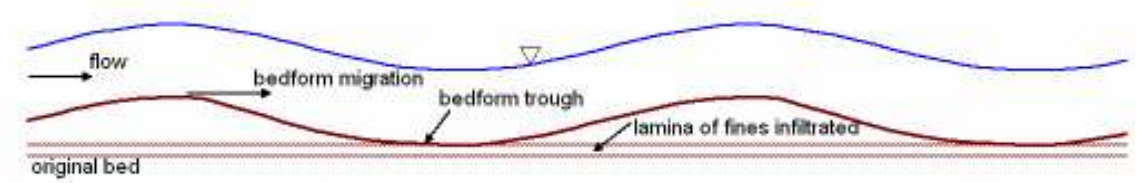

Figure 8.4. Sketch view of the profile of the downstream migrating antidunes at the flume walls section.

8.2.3.1 Layering in the preserved bed

Visual inspection of the internal strata in the foresets near the channel transparent walls showed no evident cross-stratification for the four runs, but a planar simple strata bounded by a lamina of sand on the topset. The lower bounding surface for the runs with 30% sand content was a well defined sandy-gravel band or lamina, with regular continuity along the channel and roughly parallel to the mean bed surface (Figure 8.5). The minimum thickness of the lamina was roughly the mean diameter of the gravel, that is approximately 4 mm, and the maximum could be even slightly higher than 2 times the D_{90} (roughly 15 mm). A lag deposit covered the upper surface of the lamina on the bedform troughs; careful observation in video recordings showed that during the experiments the top of the lamina was at the same level of the deepest scour troughs (Figure 8.4). Thus, the top of the band matched the migration path of the bedforms and the plane of erosion over which bedforms displaced. In this manner, the band marked the boundary between coarse sediment that was not put in motion during the experiment and a layer with a continuous exchange of grains. The latter was confirmed by the coincidence of the top of the band with the top of the preserved colored gravels that traced the maximum bed erosion (see Section 3.3.2.7).

The sandy-gravel lamina was easily discernible through the flume transparent walls because in most of its length there were no appreciable voids between grains, nor even between the grains and the walls; thus, the material inside seemed to be more compact than the material in the upper and lower layers. Furthermore, high concentration of fines was noticed because of its uniform and slightly clearer shade in comparison to gravel, which shades were heterogeneous and darker.

Unlike the experiments with 30% sand, for the experiments with 45% sand there was not such an evident division between the basal surface over which the bedforms migrated and the underlying sediment that was not put in motion during the run. A more detailed inspection of the bed allowed distinguishing a subtle thin band with a higher concentration of very fine particles that seemed more compact than the upper and lower layers.

For all four runs, cross sections in the bed normal to the flow direction, where the colored gravel layers had been put (see Section 3.3.2.7), showed a symmetrical scoop-shaped bounding surface, with the deepest scour roughly in the middle of the channel (see

Figure 3.31 and Photos in Appendix XI). Bounding surfaces were distinguished at one half-side by the preservation of the colored gravel, while at the other half, by slight differences between the texture and color of the adjacent layers. In the latter, more often in the 30% sand content mixture than in the 45%, a subtle lamination with high concentration of compacted fines marked the border between sediment deposited and the material that did not moved during the passage of water. Thickness of the lamina was difficult to measure, although it seemed not to be greater than $2D_{90}$. Distinction of the bounding surface was enhanced by the difference in sand content of the deposited material and the underlying original mixture. Open-framework gravel patches could be observed above the central scour lobe for all runs; thus, at the center of the section the strong contrast between the underlying original mixture with high content of sand and the upper openwork gravel deposited during the experiments, outlined the shape of the bounding surface. Sand content within the deposited material increased wallwards, contributing to a more diffuse bounding surface; nevertheless, the bounding surface was perceptible due to the different and irregular concentrations of sand in the deposited mixture with respect to the homogeneous original underlying material, and also due to the lamina defined by the fines infiltrated and compacted in the underlying mixture, which was slightly more evident for the 30% sand content runs.

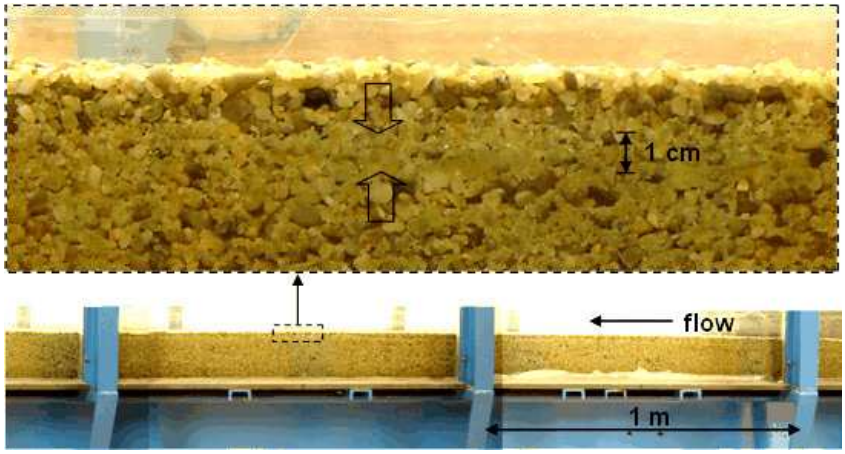

Figure 8.5. Lamination for experiment 1 after the channel had been drained.

Sections opened in the bed at the center line of the channel and parallel to the flow direction, showed a similar trend as in the normal to the flow cross-sections. The bounding surface was evident by a subtle continuous lamina with highly compacted sandy gravel, roughly parallel to the mean bed surface. Lamination being more evident for the 30% sand runs. In this section, for all experiments, internal structures were complex; even so, cross strata at a lower angle than the sediment repose angle were sometimes distinguished. As in the cross sections, open-framework gravel patches and patches with sand and gravel mixed with varying proportions were also observed. They were bounded by planar sand-rich upper and lower laminas, parallel to the mean bed surface. Large surfaces of openwork gravel were commonly found above the migration path at the central cross section. Thickness of the internal stratification at the central section, i.e. the section of maximum scour, varied from 4 to 7 cm within runs.

8.2.3.2 Fines deposition

Observations of video recordings through the transparent walls of the channel proved that the formation of the sandy-gravel lamina was related to the accumulation and preservation of fine grains. These grains settled on the bed surface, and then got trapped or infiltrated within the voids left by other bed particles. Two processes were observed, by which fine particles reached the level at which the lamina developed. The first one is related to the deposition of fine particles on the bedform toe, in a similar manner as it occurs in dunes, as described by different authors (Bridge 2003, Kleinhans 2004, Carling and Breakspear 2006). For sediment transported over dunes three main types of sediment movement and deposition in the lee side can be identified: individual grains moving down the lee slope, grain flows and grain falls. All three of them were identified to occur in the experiments, being grain falls the main mechanism by which fine grains reached the level where the lamina formed. In a dune, grain falls occur when at the brink point a flow separation layer develops where fines are put in suspension and coarser grains roll down over the dune slope or slipface, which angle is roughly equal to the repose angle of the sediment. Fine particles in suspension may travel further downstream than coarse grains in the flow direction, so that they may deposit away from the slipface and form a bottomset. If the counter flow in the separation zone is not strong enough to put fine particles again in suspension, the bottomset is preserved buried by the coarse grains that deposit on the dunes toe. Also, in the same way as in dunes, at the lee side of downstream migrating antidunes, the flow separates and favors the development of a deposition zone. Unlike dunes, in the observed antidunes the slipface angle was lower than the repose angle of the sediment, so that grain flows were less frequent than grain falls. When fine particles reached the bed by any of the deposition mechanisms described, they remained in the bed until the flow reattachment point of subsequent bedforms coincided with its position, or until an antidune with deeper trough passed and eroded all material above. If no deeper antidune passed, small particles could remain if they were hidden by coarser grains or if they could find a pocket to penetrate in the substrate where subsequent passage of bedforms would not affect them.

A less frequent process observed, by which fine grains were placed in the sandy lamina, occurred when fine sediment settled down on the lower part of the slipface, or even of the antidunes stoss, and the underlying deposit was an openwork gravel or had a low sand content. In that case it could occur that the finest sand particles percolated through the bed and reached the level where the sandy-gravel lamina was developing. Also, such a percolation was observed during the erosion of the antidune stoss: random movements of large particles, dilation of the bed or impact from other grains in movement enhanced a bed adjustment that facilitated the finest particles to infiltrate through the bed, in a similar way as reported by Middleton et al. (2000).

8.2.3.3 Vertical grain sorting

Figures 5.40 and 8.6 show the vertical sorting measured for experiment M2E4. At the section where the vertical samples were taken the bed surface exhibited a coarse layer and the maximal erosion observed below was 5.5 cm. In Figures 5.40 and 8.6 a normal sorting trend (vertically, downwards coarsening) can be observed under the surface coarse layer, until a maximum gravel content is reached, roughly at two thirds of the maximum scour depth measured in that section. From there on, a reverse sorting trend (vertically, downwards fining) prevailed and extended even below the maximum scour depth. It is worth to mention that the finest grain fraction share in the bed (diameter <1 mm) increased with depth, with its maximum value under the maximum depth of erosion.

Trends observed in Figures 8.40 and 8.6 are based only in one sample at each level; they confirm the observations of the lamina rich in fines, although they would not be statistically representative for an accurate quantification of its grain size distribution.

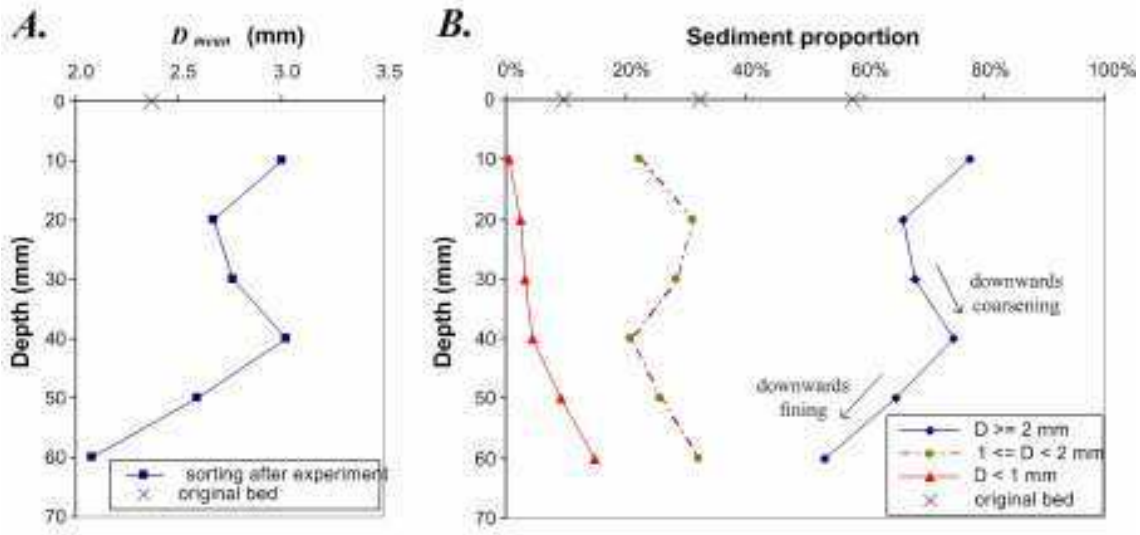

Figure 8.6. Vertical grain sorting obtained for experiment M2E4; A) mean diameters and B) bed fractional composition for different depths. Bed surface corresponds to the upper part of the graphics.

8.2.4 Discussion on experimental observations

8.2.4.1 Analogy with the active layer concept

From the stratigraphical planes explored in the bed, it can be inferred that the observed lamina of highly compacted sandy gravel defined a continuous surface, with its deepest level at the center line of the channel. During the experiments, at the channel walls, the upper boundary of the lamina matched the deepest scours excavated by the migrating bedforms. Because of the continuity of the lamina at the planes explored (bed cross sectional and longitudinal planes) and the visual contrast between sediment worked by the flow and grains not removed during the experiments, it can be assumed that such trend could be generalized for the cross sections. Therefore, it can be expected that such a lamina would mark a transition in the bed between a layer with sediment that exchanged grains with sediment in transport and a substrate of particles that had no direct interaction with sediment transport during the experiment. In this way, the layer over the lamina would partly approach to the active layer concept, i.e., a layer that contains those grains available to exchange directly with the sediment in motion. Theoretical definition of the active layer refers to a well-mixed layer with no vertical structure, a condition not fulfilled in reality, since vertical sorting fluxes occur through the migration of bedforms and through the variability in trough elevations (e.g., Blom et al. 2003); in the experiments herein reported these two conditions occurred and they must have had a key role on the vertical segregation of sediment (see Figures 5.40 and 8.6).

8.2.4.2 Lamina preservation

Preservation of fines that defined the thin lamina after the continuous passage of bedforms was related to the ability of the grains to hide or penetrate through the bed surface, to a

level where no further eroding flows would affect them. Because a main factor controlling the infiltration of particles is the relationship of grain size and shape to pore size, smaller particles have a higher chance to find a pocket in the bed or to penetrate further below. The particle size ratios between the median diameters of the sand and gravel fractions used in the experiments (in average for all four runs r=0.416) was higher than the limiting value for small size particles to penetrate through the larger pores of a natural bed of self-supported large grains (r=0.154). So, as could be expected, sand grains were not able to penetrate deep in the bed and those which made it to find a space in between other particles clogged the pores and formed a seal near the bed surface. Clogging of pores occurred slightly below the level of the deepest scour holes. Thus, the sandy lamina developed over this level. As subsequent bedforms passed, the bed saturated and the opportunity for grains to find shelter in the bed diminished. In this way a dense packed band formed by receiving fine grains infilling the decreasing size hollows. Continuity of the seal near the deepest scour holes surface along the channel defined the lamination. In this process the smallest size fractions of sand had an important role, because even when their transport mode should have been preferentially in suspension, and also even when their participation in the bulk mixture was not high (roughly, 8% and 5% of the sediment in the 45% and 30% sand content mixtures, respectively, had diameters smaller than 1.25 mm; see Figure 8.3), when they settled down they had a greater chance than coarser grains to find shelter. Particles that settled down at the level of the deepest scour holes and found a void where to hide prevailed and formed the lamina.

Formation of the lamina was favored by the fact that there was no net deposition in the bed. The passage of a single bedform could supply fines to form an incipient lamina, but it was better formed if several bedforms with similar trough depth passed. Even if after the passage of a single bedform no fines were preserved, it was very likely that another deep bedform passed later on leaving fines that would hide and could be preserved in the bed. Thus, enrichment of the band with fine particles (and thus, its notoriety) was enhanced by the passage of several bedforms with similar scour depth levels.

An aspect that could have favored a better definition of the lamina in some sections would be related with deficiencies in the mixing procedure of the bed before each experiment. Obtaining a strictly homogeneous bed along the channel is a quite difficult task, and some segregation of the material is unavoidable. The existence of some patches with lower sand content would have favored the formation of a sporadic well defined lamina. Also, a wall effect would have also been important for a better defined lamina along the channel walls than in the explored cross and transversal sections, as it is known that the porosity of packed beds is higher at solid walls (Finkers and Hoffmann 1998 and Dias et al. 2004).

8.2.5 Discussion on the bridge building process

As stated above, formation of a lamina of fine particles near the bed surface is related to the potential penetration and bridging of the gaps in the bed by the settling sediment. The experimental data found in literature and described in Table 8.1 are used here to analyze this process.

According to the characteristics of the sediment used, experimental data referred to the penetration of fines into a coarse bed can be classified as those performed with bimodal sediment for which the sizes of fine and coarse fractions do not overlap, and those with unimodal or bimodal sediment for which fine and coarse fractions do overlap (Table 8.3).

For bimodal sediments with no coarse and fine modes overlapping, the experiments of Einstein (1968), Beschta and Jackson (1979), Carling (1984) and Allan and

Frostick (1999) were performed feeding fine sediment over a bed formed with coarse material (gravel). For the experiments of Carling and Glaister (1987) all size fractions were in motion and had a contemporary deposition; a negative step favored the coarse and fine fractions segregation and the formation of a prograding bar-front. Infiltration of fines was observed in the openwork framework formed upstream of the brinkpoint.

Table 8.3. Classification of experiments where fines infiltration has been observed.

Experiments where fine and coarse fractions do not overlap	Experiments where fine and coarse fractions do overlap
Einstein (1968)	Diplas and Parker (1992)*
Beschta and Jackson (1979)	Schälchli (1992)
Carling (1984)	Lunt and Bridge (2007)
Carling and Glaister (1987)	Present work
Allan and Frostick (1999)	

*Additional feeding of fines with slight or no overlap to the sand-gravel mixture.

Grain sizes of fine and coarse modes of the bed material in natural streams usually overlap between each other. Therefore, experiments that take this feature into consideration are expected to be more realistic. From this group of experiments, Diplas and Parker (1992) supplied fine sediment in different concentrations to mobile sand-gravel beds previously worked by the flow. The size of the supplied fine grains did not overlap or overlapped little with the grain sizes in the bed and bedload mixtures. Schälchli (1992) supplied well sorted sand to a bed composed of a unimodal mixture of sand and gravel. Lunt and Bridge (2007) observed fines infiltration in the upper layers of an aggrading bed at the toe of bedforms; the sediment supplied was the same as that conforming the bed, which exhibited different grain sorting features produced by bedforms.

8.2.5.1 Porosity calculations

Porosity calculations for the experimental data listed in Table 8.1 were performed using the models of Finkers and Hoffmann (1998) and Frings et al. (2008). For sediment with no size overlapping between fine and coarse modes, porosity was calculated for different fractional contents of the fine mode in the sediment mixture, as shown in Figure 8.7 for two of the data sets. Similar trends as those observed in Figure 8.7 occurred for the rest of the data; porosities computed with the model of Frings et al. were always lower than porosities obtained with the Finkers and Hoffmann model. The left branch of curves in Figure 8.7 might be seen as a description of the filling process of the coarse framework with fines until it is "full" when the minimum porosity (the densest packing) is reached.

Table 8.4. Results of porosity models applied to the bed material for sediment with size overlapping between fine and coarse fractions. r is the size ratio between representative diameters D and d, of the sand and gravel fractions in the bed, respectively; D_x and d_x are the grain diameters for which x% of the bed particles by weight are finer.

Author	$r=d_{50}/D_{50}$	Bed porosity, ε	
		Finkers & Hoffmann*	Frings et al.
Diplas and Parker (1992)	0.230	0.2774	0.2212
Schälchli (1992)	0.007	0.2749	0.1287
Lunt and Bridge (2007)	0.202	0.3068	0.1991
Present work	0.311	0.3079	0.2759
	0.322	0.3098	0.2696

*Initial porosities= 0.38 & 0.4 (narrow size distribution considered)

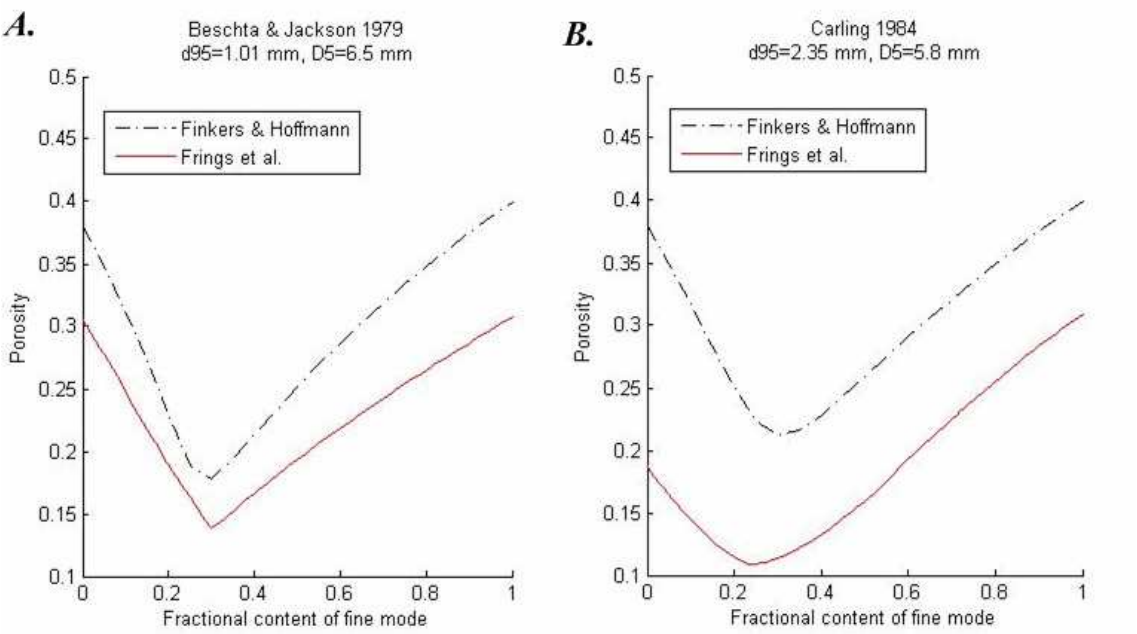

Figure 8.7. Application of porosity models to the sediment used in the experiments by A) Beschta and Jackson (1979) and B) Carling (1984). Finkers and Hoffmann model was applied with initial porosities of 0.4 and 0.38, for the fine and coarse fractions, respectively.

In applying the porosity models to data with grain size overlapping between fine and coarse modes, when using the Finkers and Hoffmann model sediment was divided in its sand and gravel modes. Results are shown in Table 8.4. Again, Frings et al. method gives lower porosities; as the separation of the sediment in coarse and fine fractions for applying the Finkers and Hoffmann model is artificial, particularly for unimodal sediment, the Frings et al. model would be more suitable to represent the packing of the sediment.

Computed porosities for the experimental data in the present work were similar for both mixtures used. Visual definition of the laminae formed in the experiments with a lower sand content (30%) was better than for those with a higher sand content (45%). Thus, it may be expected that this feature was not related to the porosity of the bed, but rather to the visual contrast between the original underlying materials and the rich in fines mixture that formed the thin band.

8.2.5.2 Bridging potential when there is no overlapping between fine and coarse modes

For a bed composed of large particles with uniform size D, smaller uniform size particles d will not be able to penetrate if the size ratio $r=d/D$ is larger or equal than 0.154 (tetrahedral packing). In the same manner, it can be expected that free penetration of the fine particles in the bed, without bridging the gaps in the framework, would occur for size ratios smaller than 0.154/2=0.077, which is the minimum size ratio for which two small particles could clog a gap in the bed. Therefore, the size ratio range for which the small particles of uniform size may form a near surface seal would be $0.077 \leq r < 0.154$ (Lisle 1989). Similarly, for a bed formed of coarse particles with different sizes D_i, a critical condition for uniform fine particles of size d to penetrate freely without bridging the gaps is given by $d/D_{min}<0.077$, where D_{min} is a representative diameter of the finest particles in the coarse framework, say, for example, the D_5, for which 5% of the bed particles by weight are finer. On the other side, if the fine particles consist of different sizes that do not overlap to the sizes of the coarse grains, the critical condition for free infiltration is given by

d_{max}/D_{min}<0.077, where d_{max} is a representative diameter of the coarsest particles in the fines population, for example, the d_{95}. In this manner, we may expect that a near surface plug comprised of jammed fines in the pores would form if $d_{95}/D_5 \geq 0.077$. This condition is confirmed for the experimental data, as shown in Table 8.5; the minimum size ratio for which a seal formed was 0.155 for the experiments of Beschta and Jackson (1979), while the maximum size ratio for free penetration to the bottom of the bed was 0.06, for one of the runs from Carling (1984).

Table 8.5. Experimental data for bimodal sediment with no overlapping between sizes of fine and coarse fractions.

Author	Seal formation	d_{95} (mm)	D_5 (mm)	d_{95}/D_5	$D_{c,p}$ (mm)	$d_{95}/D_{c,p}$
Einstein (1968)	No	0.03	25.4	0.0012	*	*
	No	0.03	6.3	0.0048	*	*
Beschta and	Yes	1.01	6.5	0.155	0.877	1.15
Jackson (1979)	No	0.31		0.048		0.35
Carling (1984)	No	0.21	5.8	0.036	2.83	0.07
	No	0.35		0.060		0.12
	Yes	2.35		0.400		0.83
Carling and Glaister (1987)	Yes	0.90	3.1	0.290	1.41	0.64
Allan and Frostick (1999)	Yes	1.86	2.49	0.747	2.18	0.85

The potential bridge formation may also be evaluated using the Frings et al. (2008) porosity model to calculate the bed material cutoff grain size $D_{c,p}$, which marks the boundary between particles that make up the bed structure and those that just fill the pores. Thinking of the cutoff size as the size of the largest pores in the bed framework, a limiting condition for the bridging of a gap would occur when two of the settling particles get clogged, i.e., fine particles may penetrate freely through the coarse bed if $2d_{max}/D_{c,p}<1$. With the d_{95} as representative of the maximum size of the small fraction, it can be expected that a near surface seal can form if $d_{95}/D_{c,p} \geq 0.5$. All data in Table 8.5, for which grain size distributions were available to compute the cutoff size with the Frings et al. model, fulfill this condition.

8.2.5.3 Bridging potential when fine and coarse modes overlap

The use of a unique size ratio to evaluate the potential penetration and retention of particles in the uppermost bed layers becomes somehow useless when the bed is formed of particles of different sizes. In that case, the use of the cutoff size would be more appropriate as it defines the bed size fraction that does not take part of the bed structure and therefore the grain sizes that are prone to penetrate through the bed pores. Thus, it can be stated that if a grain size d_x in the bedload exists, so that $d_x<D_{c,p}$, the formation of a seal near the bed surface is possible. As shown in Table 8.6, such a grain size existed for all experimental data with fine and coarse modes overlapping. No one of the authors reports the free penetration of fines through the bed and the filling of the pores from the bed bottom up, as occurred for low size ratios for experiments where fine and coarse sediments did not overlap. It seems that the availability of grains with a wide range of sizes turns bridge building extensive and avoids deep penetration even of the finest particles.

Table 8.6. Experimental data for unimodal or bimodal sediment with fine and coarse material sizes overlapping. All data refer to the formation of a near surface seal.

Author	Bed load size ranges (mm)	Cutoff size, $D_{c,p}$ (mm)
Diplas and Parker (1992)	1-8 and 0.08	0.25
	1-8 and 0.11	
Schälchli (1992)	0.06-1	0.125
Lunt and Bridge (2007)	0.06-16	0.126
Present work	0.08-10	0.200

8.2.6 Summary

Observations from the experiments with sand-gravel mixtures demonstrated that at high sediment transport conditions, under supercritical flows, horizontal lamination under the bedforms migration path may occur by continuity of a sub-bottom set, formed by the preservation of fine grains near the bed surface at the bedforms trough. Shallow preservation of fines without being winnowed or washed away was possible due to the shelter offered by coarser immobile grains. On the other side, maximum lamination thickness is controlled by the infiltration depth of pore-infilling particles, which are not able to penetrate deep into the bed since the coarsest grains in the fine fraction bridge the gaps within the framework material. Subsequent settling fines fill the bed from the bridge upwards forming a band with compact texture. Such a grain sorting mechanism may be exhibited under bedforms in gravel-bedded rivers when all the bed size fractions have been set in motion.

For bimodal sediments the bridging potential can be described based on the ratio of the maximum and minimum grain size diameters, of the fine and coarse fractions, respectively; also, for bimodal sediments empirical bed-porosity models for binary mixtures, as that from Finkers and Hoffmann (1998), give valuable insights to describe the bed texture and potential vertical sorting features based on the relative abundance of the matrix infilling the bed framework. In contrast, for less bimodal or unimodal sediments as commonly found in nature, the bridging process is more complex as grains of the fine fraction may be part of the bed contact framework. Calculations performed with an empirical porosity model for multifractional mixtures (Frings et al., 2008) to estimate a cutoff size for grains that make up the bed structure and those that just fill the voids were consistent with experimental data found in literature where bridge building processes have been observed. Results proved the utility of bed porosity models for understanding the interactions between the bed structure and the infilling matrix in natural gravel-bed rivers.

8.3 VERTICAL SIZE DISTRIBUTION OF AN IMMOBILE BED OF HETEROGENEOUS PARTICLES, SUBJECTED TO FINE SEDIMENT INFILTRATION: NUMERICAL MODELING

The aim of the model here presented is to compute the evolution of the bed sediment grain size distribution along time and depth, when particles moving on the bed surface progressively penetrate into the bed, until an equilibrium state is reached when the deposit is saturated with fine material. Such a saturation limit can occur on the upper bed layers when fine grains block the pore throats between coarse particles and form a seal that avoids further penetration of fines. The model is conceived to simulate the infiltration of fine sediment into a coarse bed; hence, this model may be useful for applications in sediment transport simulations with vertical sorting computations (e.g., as those assessed by Blom, 2008), to predict the size distribution of the bed material in different layers when

the particles settle down and are entrained periodically. In the same vein, this model may serve to explain and analyze the formation and characteristics of low permeability laminae under migrating bedforms, like the lamina formed in the experiments performed in this work, described and analyzed in Section 8.2.

According to the discussion in Section 8.2.5, two different situations may occur in the infiltration process, in relation with the size distributions of the potentially infiltrated sediment (filling material) and the receiving bed:

1. Non-overlapping: All of the size fractions of the filling material are smaller than any of the size fractions in the original bed.
2. Overlapping: Any, some or all of the size fractions of the potential filling material are present in the original bed.

Non-overlapping would occur when fines in large amounts are suddenly introduced into a gravel bed river, for example, because of mining residuals, dam removal or because of a volcanic eruption that produces a sudden availability of fines. On the other hand, overlapping commonly occurs when all size fractions present in the bed are in motion and the smaller size fractions are capable of moving into the bed, for example, at the lee side of a dune. In comparison with other models in literature (e.g., semi-empirical model by Wooster et. al. 2008), which were developed only for non-overlapping conditions, the model herein presented is applicable to both conditions, non-overlapping and overlapping. Furthermore, it improves other models as it is capable of computing the fines saturated bed size distribution rather than only the bed maximum fines content.

Improvements to previous models are here feasible by incorporating a model for computing the bed cutoff size, i.e., the grain size for particles capable of fitting in the pore throats between the bed coarse grains. The cutoff size allows the prediction of the maximum size of particles that can penetrate into the bed at every instant. As the bed is filled with fines the pore throats and thus the cutoff size become smaller, until no more fines are admitted when a saturation limit is reached.

Equations used by the model are an extension to sediment mixtures of those for uniform size material presented firstly by Sakthivadivel and Einstein (1970), and later revised by Cui et al. (2008). For solving the equations it is necessary to distinguish the size fractions prone to penetrate into the bed and the maximum fractional content that they can attain in the bed. For this, the model is based on three different algorithms: one for computing the bed cut-off size given the bed material size distribution; a second one for computing the bed saturation limit given the bed material size distribution and the characteristics of the material prone to infiltrate into the deposit; and the third one is an algorithm to solve numerically the equations for the theory of fine sediment infiltration into an immobile bed, involving this the other two algorithms.

8.3.1 Computation of the saturation limit

Since fine material infiltrated into an immobile coarse bed occupies the voids between particles without altering the bed structure, the bed porosity serves as a measure of the maximum amount of fines that can be admitted into the bed. Here, the model applied is used in chemical research for computing the porosity of randomly packed particles (Yu and Standish, 1991). This model was adapted by Frings et al. (2008) for estimation of the bed porosity and cut-off size in natural sediments. The bed cut-off size is defined as the grain size in the boundary between size fractions that are part of the bed structure and those that can percolate through the pores without disturbing the 'skeleton' of the large grains. The concept of the cut-off size is here useful as it allows identifying which size fractions in the potentially infiltrating sediment can actually get into the pore space available between large grains.

8.3.1.1 Theoretical concepts

For a given immobile bed, infiltration of fine sediment can occur if on the bed surface there is deposition of material smaller than the bed cutoff size D_c. If the size fractions smaller than the cutoff size percolate into the bed progressively, at a certain point the bed will become saturated and no more sediment will fit within the voids, unless the bed structure is disturbed. Therefore, the saturated condition is attained when:

1. The bed arrives to a minimum porosity. This means that the pore space available at the initial conditions has been occupied by fines progressively percolated into the bed. As the bed is filled, the porosity decreases. There is a point when for accommodating more grains the porosity must be higher, but this means that the bed structure must be affected: that large grains loose contact between each other and the bed structure became more that of a matrix framework. As this condition is not possible when the sediment infiltrates from the bed surface, unless dilation of the large particles structure occur, reaching a minimum value for the porosity may be used as a sign of having attained the bed saturation limit.
2. Limitation of available fines. While fine grains intrude progressively into the bed, the cutoff size decreases (the pore space available between grains decreases as the amount of percolated material increases), until a limit is reached when there are no more size fractions available on the bed surface smaller than the bed cutoff size.

One of the two conditions must be satisfied when the bed is saturated with fine sediment.

Under some sediment transport conditions the bed material may be prone to dilation, as shown by Allan and Frostick (1999). Such dilation favors the penetration of fine grains into the bed, since there is an arrangement of particles and an expansion of pore throats. For the model here presented, the effect of bed dilation is considered negligible; therefore, the bed porosity is not reversible, i.e., as the sediment fills the pores, porosity would always tend to decrease, and the original bed structure would remain intact until the end of the infiltration process.

It is worth to mention, that even when the model uses porosity calculations for computing the saturation limit, the actual porosities of the original sediment samples and final mixtures are not important for the final result. In contrast with the semi-empirical model of Wooster et al. (2008), for which porosity obtained from experiments is an implicit fundamental parameter, our model removes the additional sources of error that a wrong estimation of porosity could introduce.

8.3.1.2 Methodology for computing the bed saturated condition

Given a finite bed volume, composed of an originally unit volume of particles of multiple grain sizes, and a sediment mixture depositing on the bed surface, prone to penetrate into it, the fractional content by volume of grain size D_i when a volume ΔV_s of the depositing material fills partially the bed pores is:

$$f_{b,i} = \left(\frac{\Delta V_s}{\Delta V_s + 1} \right) f_{d,i} + \left(1 - \frac{\Delta V_s}{\Delta V_s + 1} \right) f_{b,i}^{\,0} \qquad (8.8)$$

where $f_{d,i}$ and $f_{b,i}$ are the grain size fractions for the grain size D_i of the depositing sediment and the bed, respectively, and the index '0' refers to the original conditions in the bed, i.e., before the sediment on the bed surface penetrates. Grain sizes D_i cover the range of sediment sizes available in the bed and in the collapsing material, with i=1 for the finest grain size and i=nf for the coarsest, nf being the total number of size fractions.

If the finite bed volume is progressively filled with the depositing material at constant increments of its fractional content in the bed, $\Delta f_d = \left(\frac{\Delta V_s}{\Delta V_s + 1} \right) < 1$, using eq.(8.8) the process can be described as

$$f_{b,i}^{\,j+1} = (j+1)\Delta f_d f_{p,i} + [1-(j+1)\Delta f_d] f_{b,i}^{\,j} \qquad (8.9)$$

where j is an integer number that refers to the consecutive steps for the increments of the fractional participation of the depositing material in the bed, so that $j = 0,1,2,...,\left(1/\Delta f_d - 1\right)$; and $f_{p,i}$ is the fractional content of the grain size D_i for the collapsing material that is able to penetrate into the bed. We consider that $f_{p,i}$ is restrained by the cutoff size D_c of the bed material, because only the grains with a smaller size than the cutoff diameter would be able to infiltrate into the bed. Therefore, $f_{p,i}$ is controlled by the following expressions:

$$f'_{p,i} = \begin{cases} f_{d,i} & for \quad D_i \le D_c \\ 0 & for \quad D_i > D_c \end{cases}; \quad (8.10a) \qquad f_{p,i} = \frac{f'_{p,i}}{\sum_{i=1}^{nc} f'_{p,i}} \quad (8.10b)$$

nc is the number of size fractions for which $D_i \le D_c$.

For the bed structure to remain unaltered the following condition for the bed porosity P_b must be satisfied

$$P_b^{j+1} < P_b^{j} \qquad (8.11)$$

when the bed reaches a maximal j value for which any of the following conditions is satisfied

$$P_b^{j} < P_b^{j+1} \quad (8.12a) \text{ or } \quad D_1 > D_c \quad (8.12b)$$

the bed is considered to be saturated with respect to the sediment depositing on the bed surface, i.e., there are no more pores available with size enough to be filled by any size fraction of the material on the bed surface.

As the cutoff size may decrease when the volume of infiltrating sediment increases, if at any step j the cutoff size for the bed differs from the cutoff size at step j-1, the value of j is set to cero and eqs.(8.10a) and (8.10b) are recalculated with the new cutoff size value. Eq.(8.9) is then computed again with j progressively increasing, until the saturated bed is found.

8.3.1.3 Some considerations for the implementation of the algorithm

The bed cutoff size and porosity are computed with the Frings et al. model†, which is an adaptation of the Yu and Standish model for multifractional mixtures of spherical particles. Due to the discretization of the grain size distribution, the model defines the cutoff size at one class limit between grain size fractions. Eq.(8.10a) considers that a size fraction may infiltrate if it is smaller than the cutoff size, but because the cutoff size is defined by the Frings et al. model at one class limit, it would be more pertinent to compare between class limits, rather than between centers of class. If the fine and coarse class limits of the grain size D_i are defined as $D_{i(N)}$ and $D_{i(N+1)}$, respectively, it can be assumed conservatively that if $D_{i(N+1)} > D_c$ the grain size fraction D_i cannot penetrate into the bed. This criterion is in agreement with the Frings et al. model, but is opposite to the assumptions taken by the original model by Yu and Standish, who would set the limit for filling fines at $D_{i(N)} > D_c$. Thus, eqs.(8.10a), and (8.12b) can be rewritten as

†The code used for all the computations of the cutoff size presented in this Chapter is the same code in Matlab used by Frings et al. (2008); this code was kindly provided to the author by Maarten Kleinhans.

$$f'_{p,i} = \begin{cases} f_{d,i} & for \quad D_{i(N+1)} \le D_c \\ 0 & for \quad D_{i(N+1)} > D_c \end{cases} \qquad (8.13)$$

nc in (8.10b_3b) would be the number of size fractions for which $D_{i(N+1)} \le D_i$;

$$D_{N2} > D_c \qquad (8.14)$$

After some tests, it was found that an adequate value for the increments of the infiltrating material is Δf_d=0.01. No important variations were found when using smaller increments. On the other hand, for the sediment original size distributions, class width should be, at most, 0.5 phi to obtain accurate predictions of the cutoff size, as recommended by Frings et al.

8.3.1.4 Application to experimental data

The model has been tested with the results of two of the experimental runs described in Chapter 3. For these runs, M1E6 and M2E4, successive vertical samples were obtained at the end of the experiment, as described in Section 3.3.2.6.5. At the end of both experiments, a thin lamina, 1 cm thick in average, was evident through the flume windows. Such lamina, as explaine in Section 8.2, was formed by the accumulation of fine sediment. The lamina described the migration path of the bedforms, so that its surface coincided with the bedforms trough, but remained buried under the bedforms foreset. The observed lamina was formed by penetration and preservation of fine sediment near the bed surface. The fine material in motion was put in suspension on the bedform slipface and deposited on the bedform trough. Deposition of fines at a fixed point on the bed surface was a periodical process that occurred every time that a bedform trough passed. Because of this continuous deposition of fines along the run, it can be expected that the upper part of the bed arrived to its saturation limit. Figures 8.8 and 8.9 show the size distributions of the sediment sampled at the depth where the lamina formed.

The fines saturation model was applied to the experimental data using the same size distribution for the bed and the potentially infiltrated material. As the mesh diameters used for the size distribution analysis after the experiments had a higher separation than 0.5 phi between each other, an interpolation was performed to introduce more detailed data in the model. Results for the run with 31% sand are compared with measured values in Figures 8.8a and 8.8b. Figure 8.8a shows results when using all the size classes, while Figure 8.8b shows results when the finest size class was left out (corresponding to a mesh diameter of 0.06 mm). It can be observed that results without considering the finest size fraction are closer to the model results. Likely reasons for a better performance of the model when not considering the finest size fraction are the following:

1. Material retained on the 0.06 mm mesh weighted less than 2 grams (from a compound sample weighting 908 grams), which is the same value as the precision of the balance used to measure the retained material at each mesh. Thus, it can be considered that the accumulated sediment in that mesh was negligible, as it corresponded to less than 0.22% of the total weight in the sample.
2. It can be expected that the grains with a smaller diameter than 0.08 mm traveled during the experiment in suspension. So, though this size class was present in the original bed material, it may have not come in touch with the bed until the end of the run, and thus should not be considered as part of the potentially infiltrated sediment.

Figure 8.9 shows the results after applying the model to data from the run with 45% sand content. The initial sand content for this run was high and therefore the bed was

close to its saturation limit, which was reached with a low amount of additional fines. The model reproduced this behavior adequately.

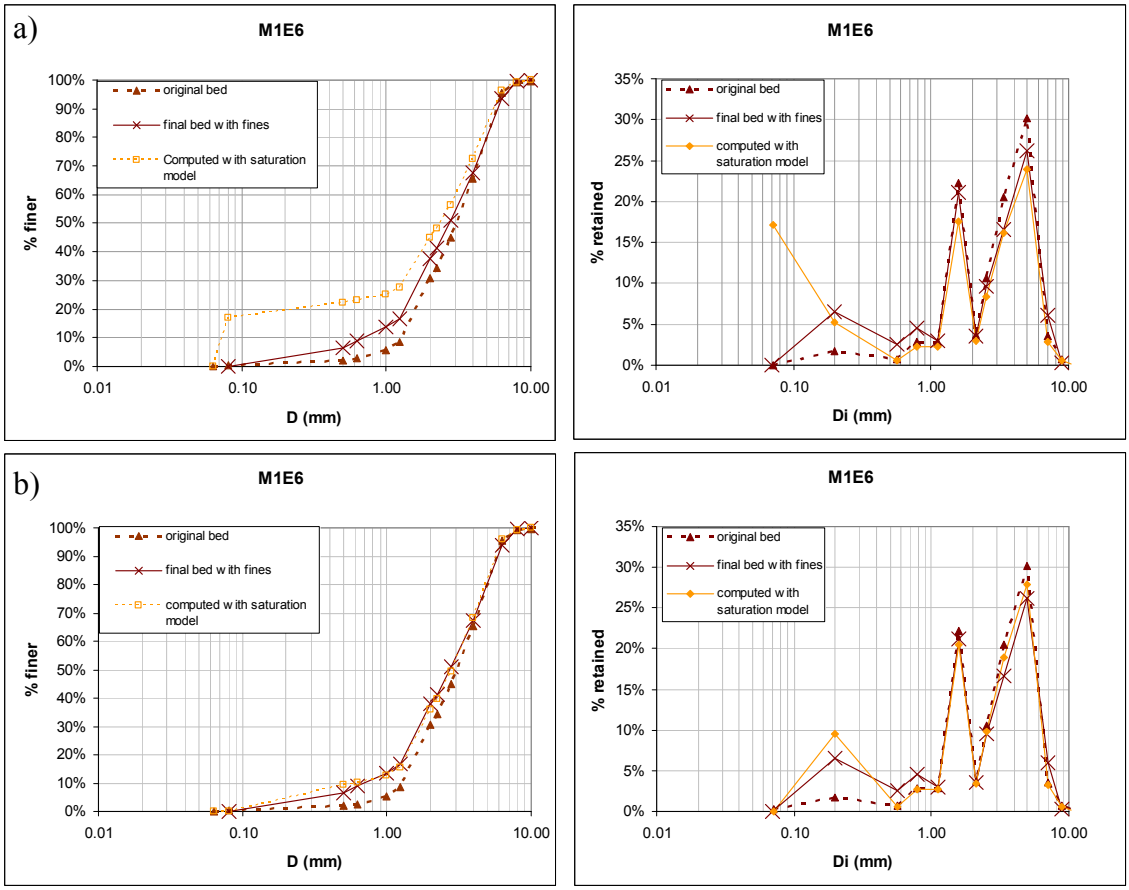

Figure 8.8. Bed grain size distributions, measured and computed with the saturation model, for data from run M1E6. a) Considering the smallest size fraction. b) Omitting the smallest size fraction.

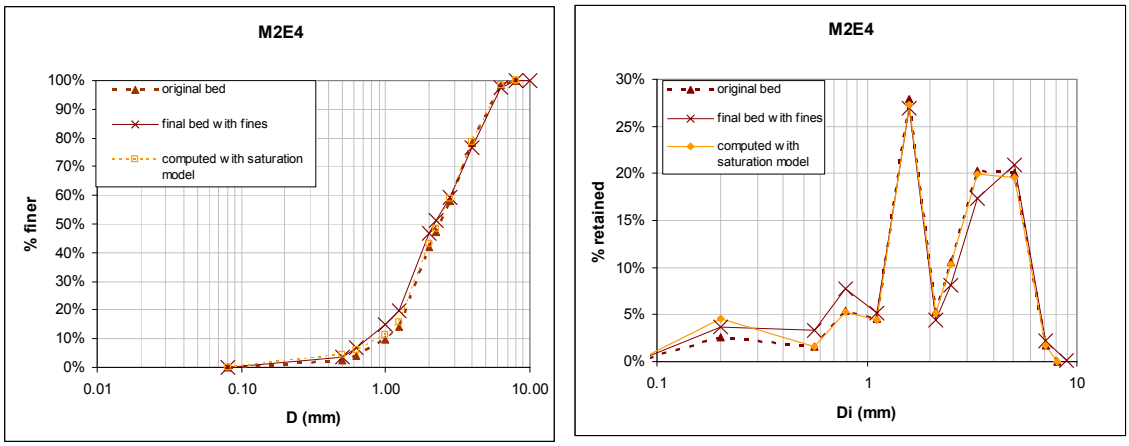

Figure 8.9. Bed grain size distributions, measured and computed with the saturation model, for data from run M2E4.

8.3.1.5 Application to data in literature

Most data available in literature for the infiltration process are restricted to conditions of non-overlapping between the size distributions of the potentially infiltrating fines and the bed material. Several authors have found that a common trend is that the filling sediment remains near the bed surface and forms a seal that avoids deeper progress of the material.

When the infiltrating grains are much finer than the bed grains, some researchers have observed that the fines penetrate all the way down until reaching an impervious stratum (the flume bottom) and begin to fill the bed from below. Cui et al. (2008) demonstrated that such a condition is an effect of short experimental beds, so that it may be expected that even very low relations between infilling and bed material diameters may block the bed at a certain depth. Beschta and Jackson (1979) observed both process in an experimental bed with gravel of 13.45 mm mean geometric diameter. Sand with median size of 0.5 mm was fed into the channel for 18 runs, while sand with median size of 0.2 mm was fed for 2 runs. The finest sand infiltrated until the flume bottom, 30.5 cm under the gravel bed surface, while the coarsest sand grains remained trapped near the bed surface, within the upper 10 cm. Measured values of the intruded sand, expressed as a percent of total volume, varied from 2 to 8% for the 0.5 mm sand, and was of 25% for the 0.2 mm sediment.

The saturation model was applied to the experimental data of Beschta and Jackson (Figure 8.10). Figure 8.11 shows the results and comparisons for the size distribution of the intruded sediment for the 0.5 mm sand experiments. The model performs well, as it was capable of predicting accurately the mode of the infiltrating material. On the other hand, the model predicts a saturated condition of 27.1% and 27.7% fines content, for the 0.2 and 0.5 mm sands, respectively.

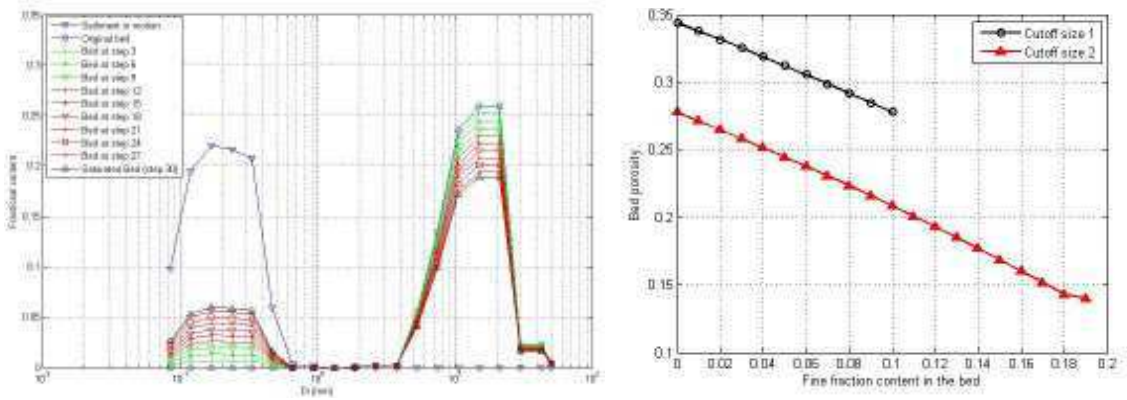

Figure 8.10. Application of the saturation model to the data from Beschta and Jackson. Size fraction steps for sand with 0.2 mm mean diameter.

Wooster et al. (2008) performed 3 experimental runs, feeding uniform sand with a mean diameter of 0.35 mm to a bed divided in 10 zones with gravel with different size distributions. Figure 8.12 shows the accumulated grain size distributions of the materials used by Wooster et al. (as sand grain size distribution was not available, it has been drawn considering a log-normal distribution). At the end of each run, samples at each zone were taken at different bed levels, and the amount of intruded sand was obtained. Results for the top subsurface bed layer (where Wooster et al. hypothesized that the bed had reached the saturated condition) for run 1, are shown in Table 8.7 (data taken from Figure 7 in Wooster et al. 2008). Table 8.7 also shows the results of applying the saturation model. It is evident that for all cases the model over-predicted the amount of trapped fines in the bed.

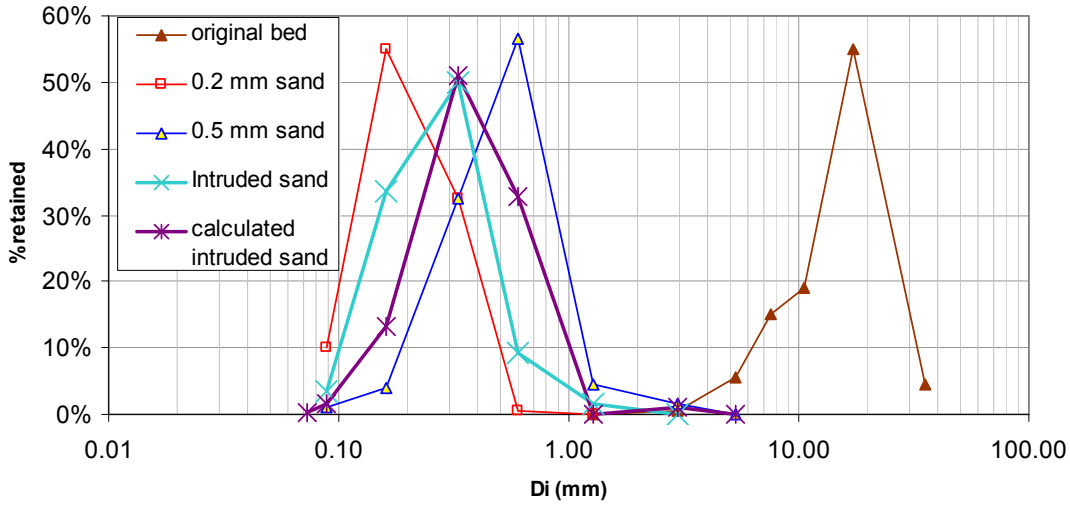

Figure 8.11. Application of the saturation model to the data from Beschta and Jackson. Grain size distribution for original bed, fine material in motion, and final bed with intruded material for the 0.5 mm sand in motion. Calculated intruded sand refers to the 0.5 mm sand.

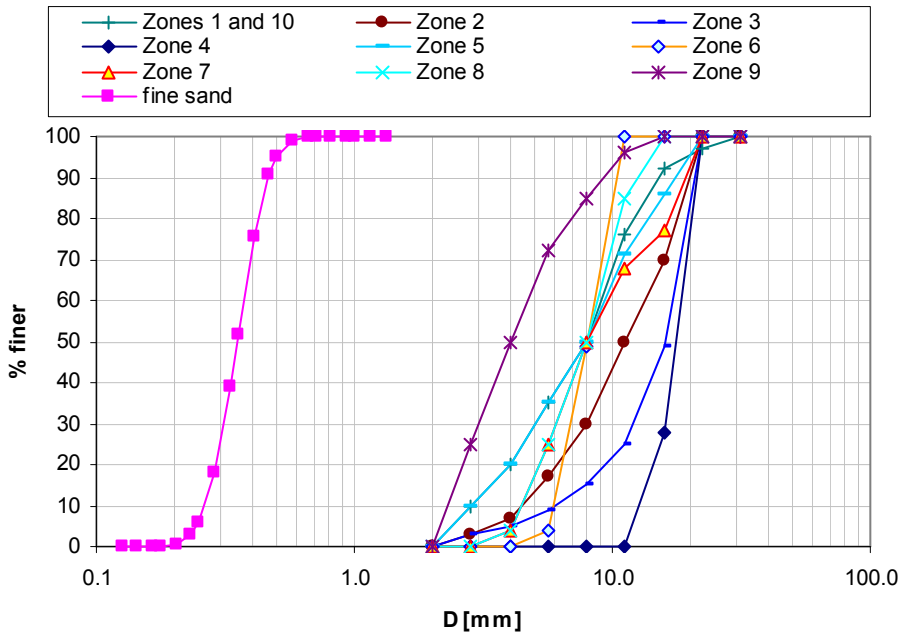

Figure 8.12. Grain size distributions of the fine sand and the bed material in the 10 zones in which the bed was divided in the experiments of Wooster et al. (2008).

Table 8.7. Results from Wooster et al. (2008) for the saturated top subsurface bed layer. Values indicate the fines saturation fraction.

Zone	1	2	3	4	5	6	7	8	9	10
Maximum measured	**8%**	**18%**	**15%**	**16%**	**5%**	**14%**	**11%**	**9%**	**5%**	**8%**
Mean measured	**6%**	**11%**	**12%**	**16%**	**4%**	**12%**	**6%**	**5%**	**5%**	**6%**
Model	**25%**	**26%**	**25%**	**31%**	**25%**	**31%**	**26%**	**29%**	**20%**	**25%**

8.3.1.6 Comparisons

As shown before, the model performs well in predicting the size distribution of the infiltrated sediment (Figures 8.8b, 8.9 and 8.11), but it seems to overestimate the fractional content of fines for the bed saturated condition. Figure 8.13 compares the measured and predicted saturated fines content, for the data in literature and the experimental data collected for the present study. Only three points appear close to the perfect agreement line: two correspond to the present study and the other to the runs of Beschta and Jackson performed with the 0.2 mm sand, which filled the bed from the bottom upwards. The rest of points, which seem to exhibit no apparent trend, are related to similar experimental characteristics: non-overlapping fine and coarse size distributions and formation of a sediment seal near the bed surface. The authors reporting such data informed that the measurements corresponded to the saturated condition. Different complexities inherent to this type of experiments make it difficult to precisely distinguish if the saturated condition is measured, among which are: the removal of fines from the bed surface, where the saturation normally occurs, because of turbulent effects; difficulties of obtaining unaltered bed samples; and the decay of infiltrated fines with depth, so that the vertical thickness of samples is proportional to a bias toward underestimation of fines content. The model computes a top limit value of fines that can fit in the bed, a value which is difficult to measure. As will be shown below, the use of the model with the sediment infiltration equations produces reasonable results, comparable to the experimental measurements, so that the rapid decrease in fines with depth appears to be a plausible explanation for the saturated condition overestimations.

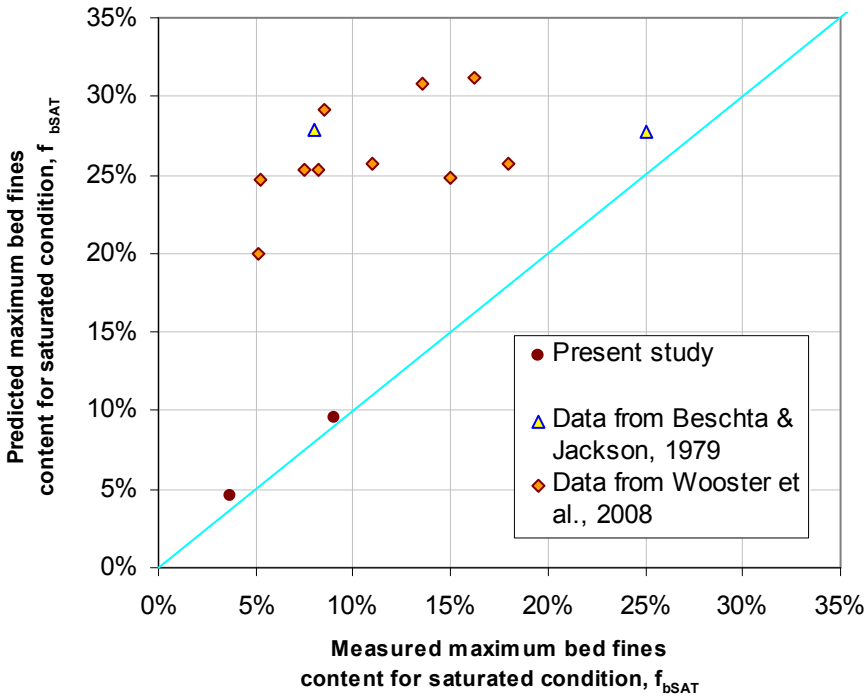

Figure 8.13. Perfect agreement diagram for comparison between measured and computed fines content with the saturation model.

8.3.2 Computation of the vertical variation of bed material grain size distribution during the infiltration of fines

A model is here described to compute the variation of the bed grain size distribution along the vertical as a constant rate of sediment infiltrates through the bed surface. The model uses the equations of the theory of fine sediment infiltration, as presented by Cui et al. (2008) (slightly different from those originally derived by Sakthivadivel and Einstein, 1970), and extends their applicability to sediment mixtures.

8.3.2.1 Governing equations

The continuity equation for sediment of the *i*-th size fraction penetrating a finite volume of bed, with unit area and depth Δz (Figure 8.14), is

$$\frac{\partial f_{b,i}}{\partial t} + \frac{\partial q_i}{\partial z} = 0 \qquad (8.15)$$

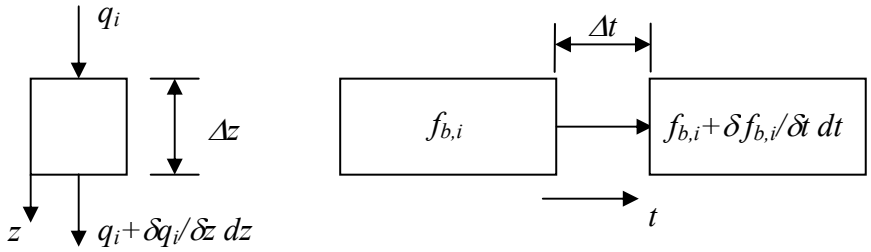

Figure 8.14. Schematic representation of the sediment flux variation for a depth increment, when sediment infiltrastes through a finite volume of unit area (left); and schematic representation of the variation in the fraction occupied by grains with size D_i in the finite volume, for a time step (right).

where $f_{b,i}$ is the fraction of the finite volume occupied by grains with size D_i; q_i is the sediment flux through the bed per unit area, t is time and z is depth. $f_{b,i}$ and q_i are dependant on time and space, and they satisfy

$$f_{b,i} = f_{b,i}(z,t) \quad (8.16a); \qquad \sum_{i=1}^{nc} f_{b,i} = 1 \qquad (8.16b)$$

$$q_i = q_i(z,t) \qquad (8.17a); \qquad \sum_{i=1}^{nc} q_i = q_{TOT} \qquad (8.17b)$$

where q_{TOT} is the total solid volume passing downwards through the finite volume per unit time and per unit area; and $nc = i_{\max}$, is the total number of size fractions in the bed and the material penetrating.

For the *i*–th sediment size fraction to be able to penetrate through the bed, two conditions must be satisfied:

1. The grain size must not be coarser than the cutoff size of the bed. As the cutoff size D_c represents the coarse limit for the grain sizes that can fit and occupy the pore spaces in the bed, the sediment flux can only contain grains finer than this limit, i.e.:

$$q_i(z,t) = 0 \qquad \text{for } D_i > D_c \qquad (8.18)$$

The cutoff size is a function of the grain size distribution in the bed, and of time and space:

$$D_c = D_c(z,t,f_{b,1},f_{b,2},...,f_{b,nc}) \qquad (8.19)$$

2. The bed has not attained its saturation condition for that size fraction. As the bed is filled with fine sediment it arrives to a limit where the porosity is minimum and no more sediment can penetrate, for this:

$$q_i(z,t) = 0 \qquad \text{for} \qquad f_{b,i} = F_{SAT_i} \qquad (8.20)$$

where F_{SATi} is the maximum fractional content of the infilling sediment that can admit the bed, i.e., the saturated limit for that size fraction. The saturation condition is a function of the bed and penetrating material grain size distributions, and of time and space as both size distributions continuously vary in the space during the process:

$$F_{SAT_i} = F_{SAT_i}(z,t,f_{b,1},f_{b,2},...,f_{b,nc},f_{d,1},f_{d,2},...,f_{d,nc}) \qquad (8.21)$$

where $f_{d,i}$ is the volume fraction of the sediment with grain size D_i penetrating into the bed, so that:

$$f_{d,i} = \frac{q_i}{q_{TOT}} \qquad (8.22)$$

8.3.2.2 Trap efficiency

The trap efficiency β is defined as the ratio of the portion of the incoming sediment retained in the bed to the total incoming sediment flux into the finite volume, when the material travels vertically a unit distance. If the volume of sediment of the *i*–th fraction, entering into the bed finite volume during time interval Δt is:

$$\Delta V_{E,i} = q_i \Delta t \qquad (8.23)$$

then, the volume of sediment trapped would be:

$$\Delta V_{T,i} = \beta q_i \Delta t \Delta z \qquad (8.24)$$

The units of the trap efficiency β can be given as a percentage per unit of vertical length; for easiness, these units are defined here as a percentage per mm. For abbreviating, only the percentage is indicated further on in this Chapter.

The trap efficiency defined above applies to the sediment traveling downwards into a bed initially clean of fines, so that the bed saturates first from the upper layers. As stated by Lauck (1991) and demonstrated by Cui et al. (2008), saturation of the bed may also occur proceeding upwards if the bed is limited below by an impervious strata or by the flume bottom in the case of laboratory experiments. For these conditions, besides the volume of sediment trapped computed with (8.24), the finite volume also retains a volume $\Delta V_{R,i}$ that corresponds to the amount of sediment rejected from the bed below, that is, the sediment that cannot penetrate further in the bed if the condition stated in (8.20) is satisfied. Furthermore, if the condition stated in (8.18) is satisfied, no sediment for that size fraction would be able to proceed downwards out of the finite volume. Thus, the volume of sediment $\Delta V_{L,i}$ that goes out from the finite volume would be

$$\Delta V_{L,i} = \begin{cases} \Delta V_{E,i} - \Delta V_{T,i} - \Delta V_{R,i} & for \quad D_i \le D_c(z+1,t-1) \\ 0 & for \quad D_i > D_c(z+1,t-1) \end{cases} \qquad (8.25)$$

where $D_c(z+1,t-1)$ refers to the cutoff size for the finite volume immediately below and at a time step before. The amount of rejected sediment $\Delta V_{R,i}$ would depend on the space available $\Delta V_{A,i}$ in the finite volume immediately below, i.e., on the capacity to receive the sediment not trapped in the finite volume above: $(\Delta V_{E,i}-\Delta V_{T,i})$. Therefore, the rejected sediment can be computed as

$$\Delta V_{R,i} = \begin{cases} \Delta V_{E,i} - \Delta V_{T,i} - \Delta V_{A,i} & for \quad \left(\Delta V_{E,i} - \Delta V_{T,i}\right) > \Delta V_{A,i} \\ 0 & for \quad \left(\Delta V_{E,i} - \Delta V_{T,i}\right) \le \Delta V_{A,i} \end{cases} \tag{8.26}$$

and the available volume in the finite volume below is:

$$\Delta V_{A,i} = \left(F_{SAT_i}(z+1,t-1) - f_{b,i}(z+1,t-1)\right)\Delta z \tag{8.27}$$

Approximating the vertical increment of sediment flux as a function of the incoming and outgoing sediment volumes from the finite volume for time and depth intervals, it can be written

$$\frac{\partial q_i}{\partial z} = \frac{\left(\Delta V_{L,i} - \Delta V_{E,i}\right)}{\Delta z \Delta t} \tag{8.28}$$

and operating with (8.23) to (8.27) into (8.28) it is obtained:

$$\frac{\partial q_i}{\partial z} = \begin{cases} 0 & for \quad D_i > D_c(z+1,t-1) \\ -\beta q_i & for \quad q_i(1-\beta\Delta z) \le \left(F_{SAT_i}(z+1,t-1) - f_{b,i}(z+1,t-1)\right)\dfrac{\Delta z}{\Delta t} \\ & and \quad D_i \le D_c(z+1,t-1) \\ \dfrac{\left(F_{SAT_i}(z+1,t-1) - f_{b,i}(z+1,t-1)\right)}{\Delta t} - \dfrac{q_i}{\Delta z} & for \\ & q_i(1-\beta\Delta z) > \left(F_{SAT_i}(z+1,t-1) - f_{b,i}(z+1,t-1)\right)\dfrac{\Delta z}{\Delta t} \\ & and \quad D_i \le D_c(z+1,t-1) \end{cases} \tag{8.29}$$

And from (8.15) the bed size distribution at any time can be obtained as

$$\frac{\partial f_{b,i}}{\partial t} = -\frac{\partial q_i}{\partial z} \tag{8.30}$$

In the equations above β is equivalent to the trapping coefficient introduced by Cui et al. (2008) and for which Wooster et al. (2008) derived a semi-empirical relation assuming that the trapping coefficient is independent of the fine sediment fraction in the bed deposit. Below a calibration of the trap efficiency for sediment mixtures is pursued with the same assumptions used by Wooster et al. (2008) for their trapping coefficient and also considering that β is constant for all size fractions.

8.3.2.3 Numerical implementation

Equation (8.30) is solved using a scheme in finite differences. The bed saturation limit is computed at each step using the methodology described above in Section 8.3.1. The bed cutoff size is computed using the model presented by Frings et al. (2008).

Initial conditions

Consider an alluvial bed, with *k* different strata along its depth, each with a different size distribution, so that at the initial time the bed conditions at any depth are:

$$f_{b,i}(z,0) = f_{b,i}\Big|^{k(z)} \tag{8.31}$$

Also, at the initial time there is no sediment flux into the bed:

$$q_i(z,0) = 0 \tag{8.32}$$

Boundary conditions

It is here assumed that grains deposited on the bed surface penetrate into the bed substrate at any time $t>0$ if they are not coarser than the cutoff size, but also if the bed is not

saturated. Then, if a given grain size present on the bed surface is smaller than the cutoff size, the amount of material that passes through the interface water-bed surface at a certain time interval would only be conditioned to the availability of space to receive the incoming grains. Distributing the volume available in time, equation (8.27) can be written as

$$\frac{\Delta V_{A,i}}{\Delta t} = \left(F_{SAT\,i} - f_{b,i}\right)\frac{\Delta z}{\Delta t} \tag{8.33}$$

With $q_{0,i}$ being the constant flux of sediment downwards on the bed surface for the *i*-th size fraction, and considering (8.33), the sediment incoming rate into the upper bed layer is then given by

$$q_i(0,t) = \begin{cases} 0 & for \quad D_i > D_c(0,t-1) \\ q_{0,i} & for \quad q_{0,i} \le \left(F_{SAT\,i}(0,t-1) - f_{b,i}(0,t-1)\right)\dfrac{\Delta z}{\Delta t} \quad and \quad D_i \le D_c(0,t-1) \\ \left(F_{SAT\,i}(0,t-1) - f_{b,i}(0,t-1)\right)\dfrac{\Delta z}{\Delta t} & for \quad q_{0,i} > \left(F_{SAT\,i}(0,t-1) - f_{b,i}(0,t-1)\right)\dfrac{\Delta z}{\Delta t} \\ & \quad and \quad D_i \le D_c(0,t-1) \end{cases} \tag{8.34}$$

where

$$F_{SAT\,i}(0,t-1) = F_{SAT\,i}\left(\left[f_{b,i}, f_{b,1}, f_{b,2}, ..., f_{b,nc}\right]_{t-1}^{t=0}, \left[f_{d0,1}, f_{d0,2}, ..., f_{d0,nc}\right]\right) \tag{8.35}$$

and

$$f_{d0,i} = \frac{q_{0,i}}{\sum_{i=1}^{nc} q_{0,i}} \tag{8.36}$$

Note that as for the second and third cases in (8.34), q_i is dependant on depth and time intervals, the following condition must be satisfied to avoid a numerical effect on the final results: $\dfrac{\Delta z}{\Delta t} > q_{0,i}$.

If an infinite depth is considered, no any other boundary condition needs to be specified. Otherwise, if depth is limited by an impervious border at a certain level z_{max}, the following boundary condition must be introduced:

$$q_i(z_{\max}, t) = 0 \tag{8.37}$$

Propagation of the sediment flux into the bed

The sediment conservation in the finite volume can be described as a function of the incoming and outgoing sediment flux, q_i and $q_{L,i}$, respectively, for a given vertical interval as follows:

$$\frac{\partial q_i}{\partial z} = \frac{\left(q_{L,i} - q_i\right)}{\Delta z} \tag{8.38}$$

Using (8.38) with (8.29) the governing equation for the outgoing sediment of the finite volume is obtained

$$q_{L,i}(z,t)=\begin{cases}0 & for \quad D_i > D_c(z+1,t-1)\\ q_i(z,t)(1-\beta\Delta z) & for \quad q_i(z,t)(1-\beta\Delta z)\le\left(F_{SAT_i}(z+1,t)-f_{b,i}(z+1,t-1)\right)\dfrac{\Delta z}{\Delta t}\\ & \quad and \quad D_i \le D_c(z+1,t-1)\\ \dfrac{\left(F_{SAT_i}(z+1,t)-f_{b,i}(z+1,t-1)\right)}{\Delta t}-\dfrac{q_i(z,t)}{\Delta z} & for\\ & \quad q_i(z,t)(1-\beta\Delta z)>\left(F_{SAT_i}(z+1,t)-f_{b,i}(z+1,t-1)\right)\dfrac{\Delta z}{\Delta t}\\ & \quad and \quad D_i \le D_c(z+1,t-1)\end{cases} \tag{8.39}$$

where

$$F_{SAT\,i}(z+1,t)=F_{SAT\,i}\left(\left[f_{b,i},f_{b,1},f_{b,2},...,f_{b,nc}\right]_{t-1}^{z+1},\left[f_{d,1},f_{d,2},...,f_{d,nif(z,t)}\right]\right) \tag{8.40}$$

and

$$f_{d,i}=\frac{q_i(z,t)}{\sum_{i=1}^{nif(z,t)}q_i(z,t)} \tag{8.41}$$

being *nif* the number of size fractions with a diameter smaller than the cutoff size: $D_i \le D_c(z+1,t-1)$; and the sediment incoming into the finite volume is

$$q_i(z,t)=q_{L,i}(z-1,t) \tag{8.42}$$

Finally, the bed fraction for the *i*-th size is obtained from (8.38) and (8.30) as

$$f_{b,i}(z,t)=f_{b,i}(z,t-1)-\left(q_{L,i}(z,t)-q_i(z,t)\right)\frac{\Delta t}{\Delta z} \tag{8.43}$$

Trap efficiency β in (8.39) is a function of the bed and incoming sediment characteristics. Calibration of β is pursued as follows.

8.3.3 Calibration of the trap efficiency β

Wooster et al. (2008) derived a semi-empirical relation for a trapping coefficient, as a function of the bed material and infiltrating fine sediment geometric mean grain sizes and the bed material geometric standard deviation. They assumed that the trapping coefficient is weakly dependant on the degree of saturation of the bed, i.e., that the fraction of infiltrating sediment trapped in an initially clean deposit is conserved constant as the bed becomes progressively filled with fines. Cui et al. (2008) provided further evidence for the appropriateness of these assumptions. The bed grain sizes used by Wooster et al. to derive their relation did not overlap with the infilling material grain sizes, which had a moderately uniform distribution; furthermore, the methodology used to derive the trapping coefficient relation was based on another semi-empirical formula for estimating the bed saturated condition with fines. Because of the latter, the empirical relation of Wooster et al. would not be compatible with the trap efficiency described herein for sediment mixtures with overlapping between fine infiltrating and coarse bed grain sizes; neither with the methodology described in 8.3.1 to estimate the bed saturated condition based on the cutoff size. Therefore, here a parametric relation for the trap efficiency is derived, applicable to the infiltration of heterogeneous size sediment into a bed where the grain diameters in the filtrating mixture are already present. The relation is compatible for application with the model for fines infiltration described in 8.3.2.

8.3.3.1 Application of the fines infiltration model to experimental data

In deriving a general functional relation for the trap efficiency, applicable to sediment mixtures irrespective of the existence or not of a gap between fine infilling and coarse bed grain sizes, it is convenient to include, besides representative diameters of both materials and the standard deviation of the bed material, the infilling sediment geometric standard deviation as an additional variable; in this manner, the trap efficiency can be described by the following functional relationship:

$$\beta = \beta\left(D_m, d_m, \sigma_g, \sigma_s\right) \tag{8.44}$$

where D_m and d_m are the bed and infiltrating materials geometric mean diameters, respectively, and σ_g and σ_s are the bed and infiltrating materials geometric standard deviations, respectively. As an initial guess it can be hypothesized that the assumptions used by Wooster et al. are also valid for sediment mixtures, in particular, that the fraction of sediment trapped in an initially clean deposit is conserved constant as the bed becomes progressively filled with fines. In this way, for infiltrating sediment composed of size fractions already present with a given fractional content in the bed deposit (and smaller than the bed cutoff size), it can be considered that the trap efficiency for the penetrating material related to the bed material does not change whether the deposit is clean of the infilling size fractions or already with a certain grade of saturation. By this assumption, the trap efficiency can be computed by considering the bed deposit clean of the fines infiltrating. To further simplify the derivation of a parametric functional relation for the trap efficiency applicable to sediment mixtures, it can also be considered that β is constant for all size fractions, i.e., that the size distribution of the sediment retained is the same as that of the infiltrating material. With this hypothesis, all the importance for producing a downwards sorting effect is given to the cutoff size.

Below, calibration of the trap efficiency is tried using experimental data from Wooster et al. (2008) and Beschta and Jackson (1979). Though both data-sets were obtained for sediment with no-overlapping between fine and coarse size distributions, because of the hypotheses exposed above, it can be considered that the data serve also for application to sediment mixtures with overlapping size distributions. The derived functional relation for the trap efficiency is further tested in Section 8.3.4 with experimental data for sediment mixtures.

Trap efficiency for data from Beschta and Jackson (1979)

Beschta and Jackson performed 23 runs with two different sands fed over a gravel bed 30.5 cm thick. They observed the formation of an upper seal, within the upper 10 cm of the bed, for the 21 runs performed with their coarsest sand; on the contrary, for the 2 runs with the finest sand the bed filled until saturation from the bottom upwards. Original sediment grain size distributions are shown in Figure 8.11. Measured values of the intruded sand, expressed as a percent of total volume, were from 2 to 8% for the 0.5 mm sand in the upper 5 to 10 cm, and was of 25% for the 0.2 mm sediment. For each of both sands, the model was applied to compute the evolution of the bed grain size distribution along the gravel deposit as the sediment infiltrated. Different values of the trap efficiency were tested trying to reproduce with the model the experimental observations. Figures 8.15 to 8.20 show results for different trap efficiency values. Results are summarized as follows:

1. Fine sand, mean diameter=0.2 mm. A maximum value of β=0.29% was found for reproducing the complete bed saturation from the bottom upwards (Figure 8.15). Higher values than this resulted in the formation of a sediment seal near the bed surface, which prevented the bed total saturation (Figure 8.16). Lower values always produced a complete saturation proceeding from the bottom upwards (Figure 8.17). For complete fines saturation the fractional fines content equals 27.1%,

similar to the measured value of 25%. Note in Figures 8.15 to 8.17 that for the lowest trap efficiency, equilibrium is reached faster than for the highest and the intermediate trap efficiency values, requiring the latter the longest time.

2. Coarse sand, mean diameter=0.5 mm. A minimum value of β=2.5% was found for reproducing the formation of an upper sand seal with no accumulation of sediment on the flume bottom (Figure 8.18). Comparing with the measured 2 to 8% fines content on the upper 5 to 10 cm, model results showed an average of 15% and 9% fines content in the upper 5 cm and 10 cm, respectively. Lower trap efficiency values resulted on accumulation of sediment on the bottom, being β=1.2% an approximate lower limit for a trap efficiency that produced 8% fines content in all the vertical (Figure 8.19), which is a value similar to those measured experimentally. Accumulation of 22% of fines occurred in the upper 5 cm. A top limit to reproduce similar sand contents as those measured was β=5%, for which sand content on the upper 5 cm was 8.5% and no fines accumulated on the bottom (Figure 8.20).

Trap efficiency for data from Wooster et al. (2008)

For 3 different experimental runs, Wooster et al. measured in detail the vertical variation of infiltrated uniform sand into a gravel bed divided in 10 zones with different size distributions. Grain size distributions for these zones are shown in Figure 8.12 (since the size distribution for the sand was not available, it was considered to be log-normal). All of the 10 zones were prepared with a surface top layer, 2 cm thick, coarser than the subsurface gravel, to simulate the pavement that usually forms on the bed surface of gravel-bed rivers. Wooster et al. believed that in their experiments, the bed saturated condition with sand occurred on the limit between the coarse surface layer and the subsurface layer since fines were removed by the flow from the surface coarse layer due to turbulent effects. Considering the latter, the model here developed was applied to the data set from Wooster et al. supposing that the sand penetrated freely the pavement surface layer and saturated the upper subsurface layer. By testing different values of the trap efficiency, and visually comparing with the measurements (see Figure 8.21), an approximate mean value of the trap efficiency has been here obtained. This is the value that best represented the infiltration process observed at each of the 10 zones. Also, two extreme values were obtained for which most of the points fall within. In Figure 8.21 the model results have been drawn over the original Figure 10 presented by Wooster et al.; although the data show a large dispersion, the model is capable of anticipating the infiltration trends when the adequate trap efficiency is used.

Table 8.8 summarizes the results obtained after applying the model for fines infiltration to both experimental data sets, in search of an adequate trap efficiency value. Results for the best "fit" trap efficiency values are plotted in Figure 8.22 as a function of the mean diameters ratio of infiltrating-sand to bed-gravel. Extreme minimum and maximum values are also indicated. For comparison, the trapping coefficients computed with the semi-empirical relation developed by Wooster et al. have been plotted in Figure 8.22 as well. Trapping coefficients by Wooster et al. are always much smaller than the trap efficiencies here obtained, mainly because the saturation limit from Wooster et al. was always smaller than for the model used herein (see Figure 8.13).

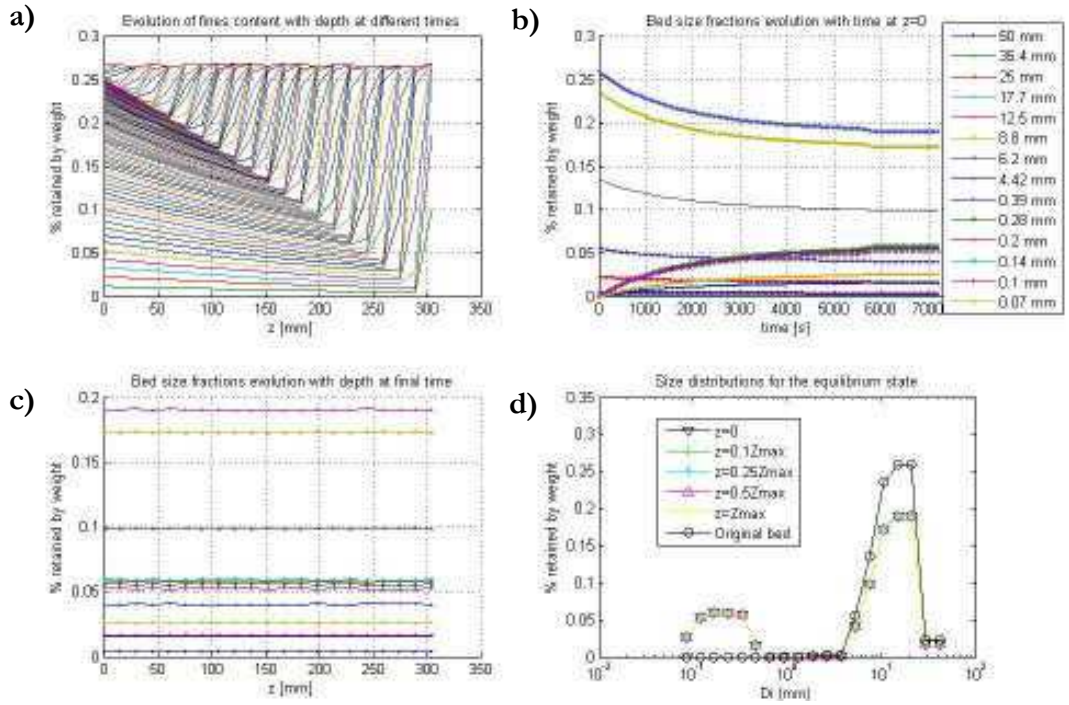

Figure 8.15. Model results for β=0.29%, Δt=72 s, Δz=15.25 mm, q_{0TOT}=0.212 mm³/s. Fine sand with 0.2 mm mean diameter, data set from Beschta and Jackson. a) Time and depth evolution of total fractional content of fines; each curve for a given time, time increasing from below upwards and from right to left. b) Time evolution of each bed size fraction near the bed surface. c) Bed sizes fractional content at equilibrium time; horizontal lines indicate complete bed saturation. d) Grain size distribution at different depths for the equilibrium state.

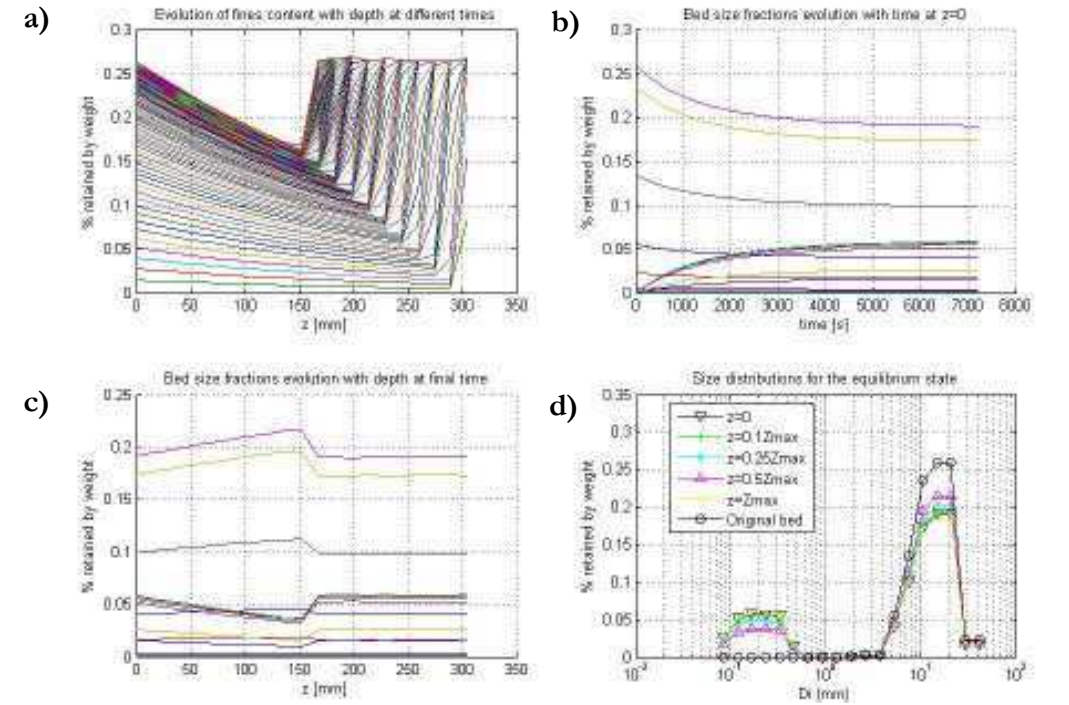

Figure 8.16. Model results for β=0.35%, Δt=72 s, Δz=15.25 mm, q_{0TOT}=0.212 mm³/s. Fine sand with 0.2 mm mean diameter, data set from Beschta and Jackson. a) Time and depth evolution of total fractional content of fines; each curve for a given time, time increasing from below upwards and from right to left. b) Time evolution of each bed size fraction near the bed surface (diameters as in Figure 8.15). c) Bed sizes fractional content at equilibrium time. d) Grain size distribution at different depths for the equilibrium state.

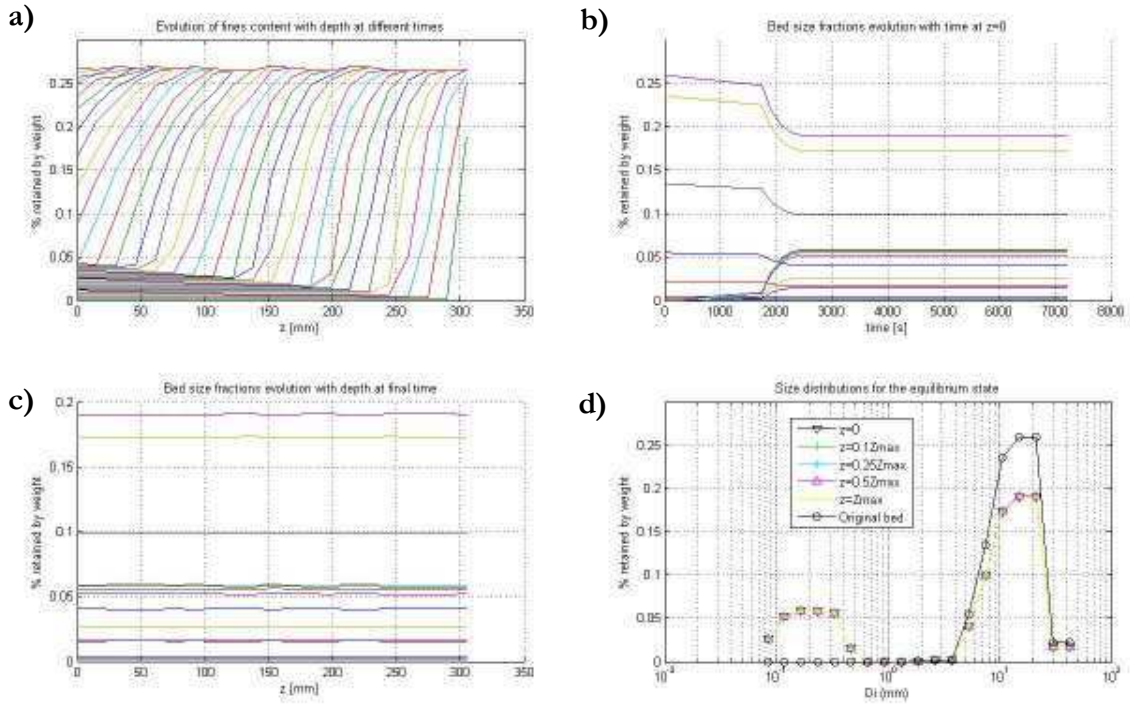

Figure 8.17. Model results for β=0.05%, Δt=72 s, Δz=15.25 mm, q_{0TOT}=0.212 mm^3/s. Fine sand with 0.2 mm mean diameter, data set from Beschta and Jackson. a) Time and depth evolution of total fractional content of fines; each curve for a given time, time increasing from below upwards and from right to left. b) Time evolution of each bed size fraction near the bed surface (diameters as in Figure 8.15). c) Bed sizes fractional content at equilibrium time; horizontal lines indicate complete bed saturation. d) Grain size distribution at different depths for the equilibrium state.

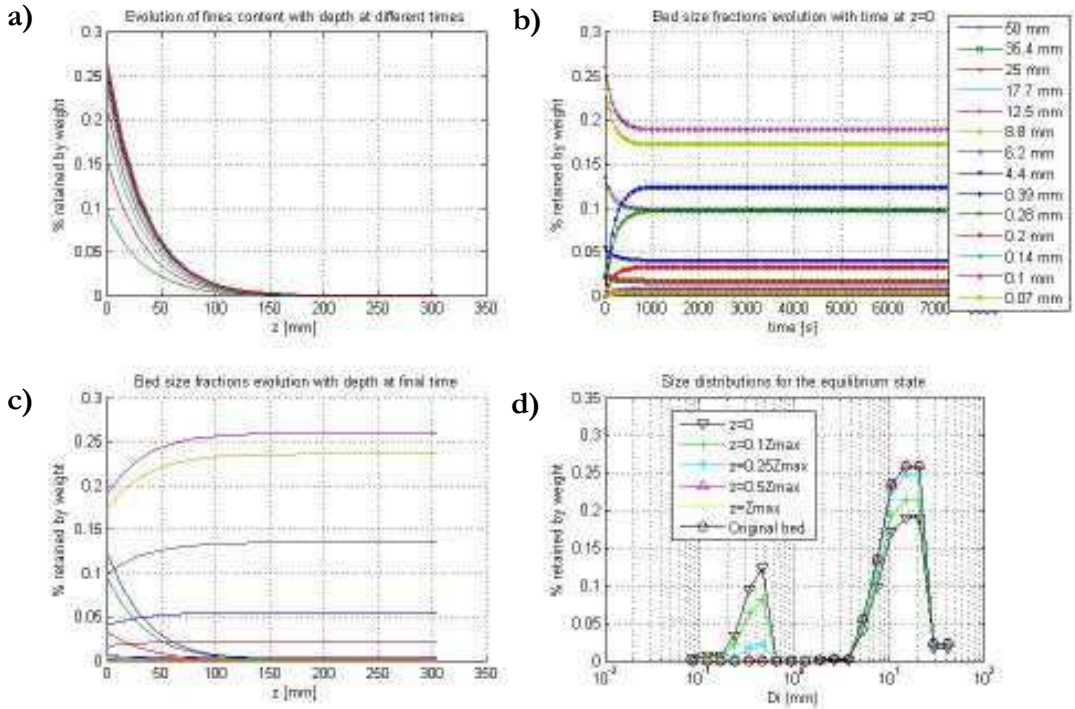

Figure 8.18. Model results for β=2.5%, Δt=72 s, Δz=15.25 mm, q_{0TOT}=0.212 mm^3/s. Fine sand with 0.5 mm mean diameter, data set from Beschta and Jackson. a) Time and depth evolution of total fractional content of fines; each curve for a given time, time increasing from below upwards. b) Time evolution of each bed size fraction near the bed surface. c) Bed sizes fractional content at equilibrium time. d) Grain size distribution at different depths for the equilibrium state.

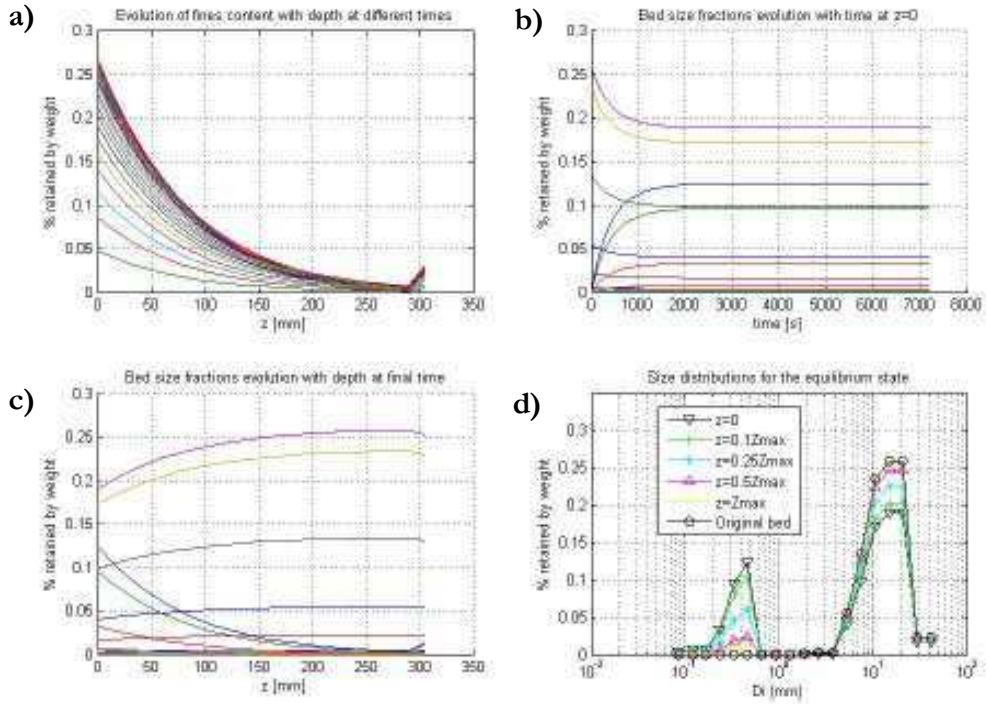

Figure 8.19. Model results for β=1.2%, Δt=72 s, $\Delta\tilde{z}$=15.25 mm, q_{0TOT}=0.212 mm^3/s. Fine sand with 0.5 mm mean diameter, data set from Beschta and Jackson. a) Time and depth evolution of total fractional content of fines; each curve for a given time, time increasing from below upwards. b) Time evolution of each bed size fraction near the bed surface (diameters as in Figure 8.18). c) Bed sizes fractional content at equilibrium time. d) Grain size distribution at different depths for the equilibrium state.

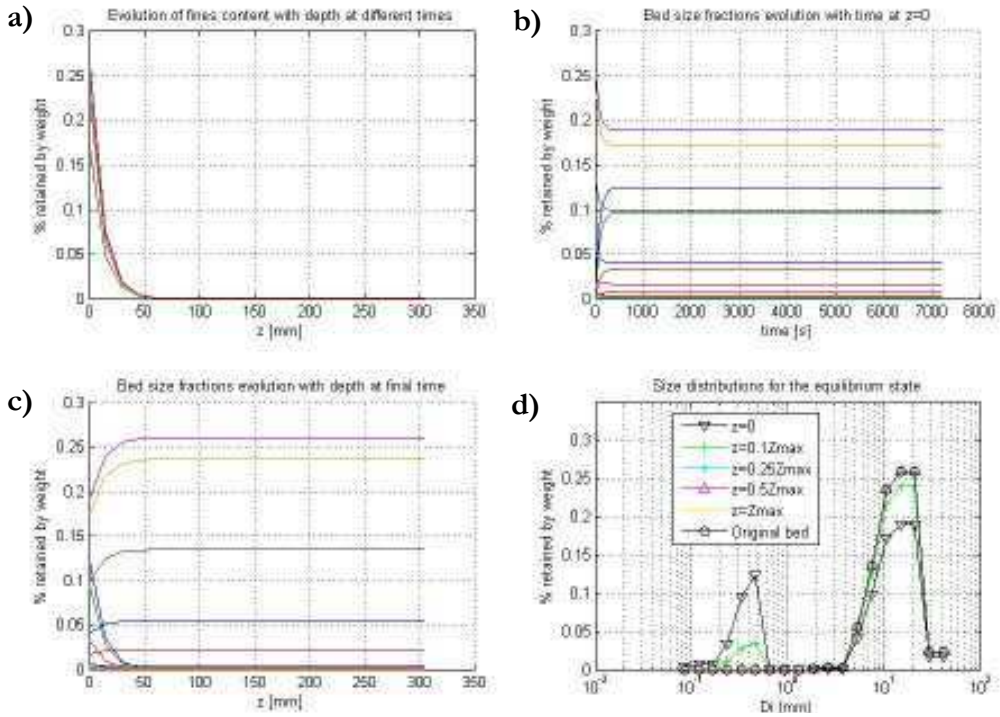

Figure 8.20. Model results for β=5%, Δt=72 s, $\Delta\tilde{z}$=15.25 mm, q_{0TOT}=0.212 mm^3/s. Fine sand with 0.5 mm mean diameter, data set from Beschta and Jackson. a) Time and depth evolution of total fractional content of fines; each curve for a given time, time increasing from below upwards. b) Time evolution of each bed size fraction near the bed surface (diameters as in Figure 8.18). c) Bed sizes fractional content at equilibrium time. d) Grain size distribution at different depths for the equilibrium state.

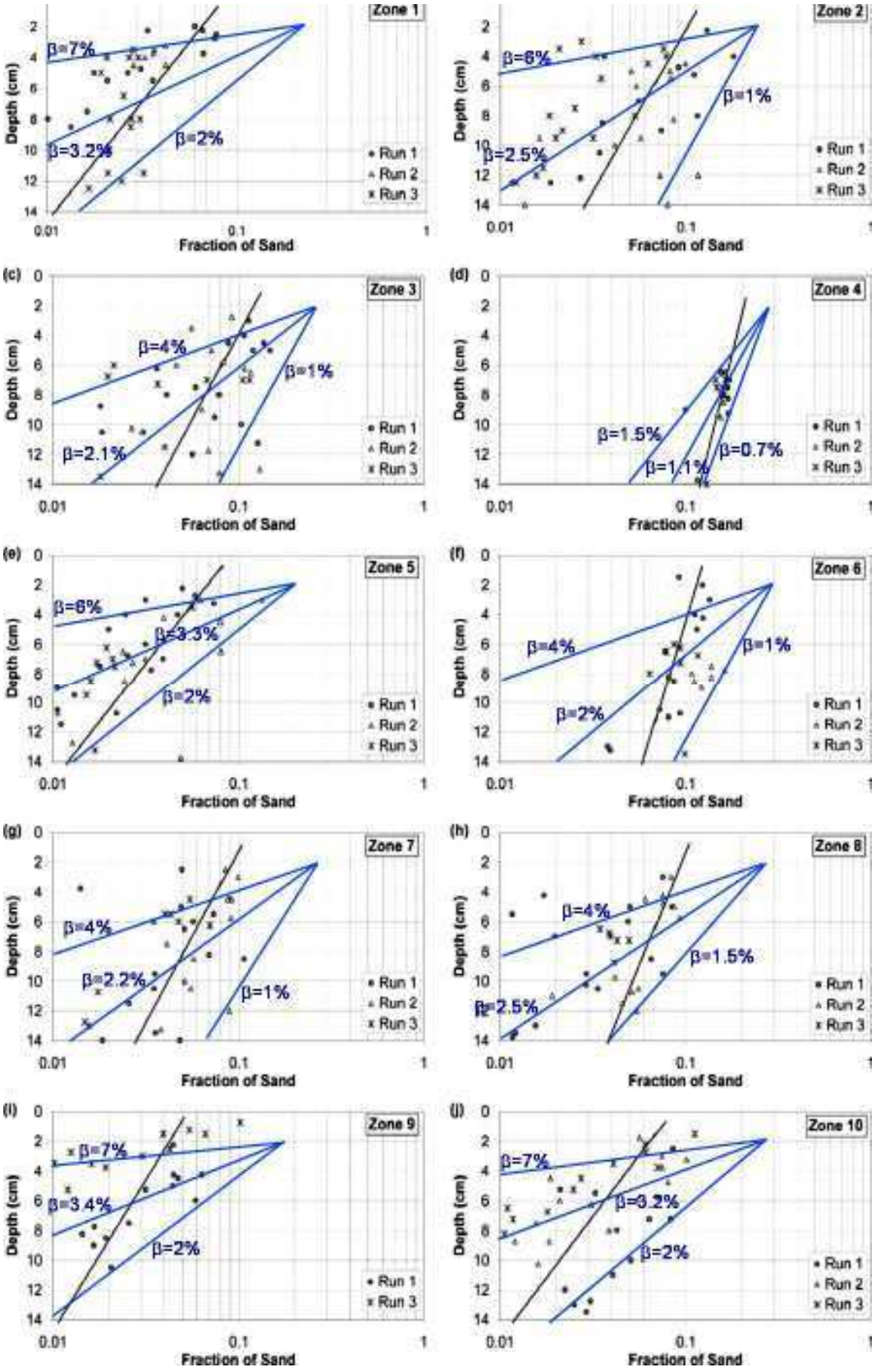

Figure 8.21. Comparison of model results for different trap efficiency values, with measurements from the experiments of Wooster et al. (2008). The black line in each graph is the best fit line originally drawn by Wooster at al.

Table 8.8. Characteristics of the sediment used for calibration of the trap efficiency. W-Z*x* refers to data set from Wooster et al. (2008) at zone *x*. B&J-S1 and B&J-S2 refer to data set from Beschta and Jackson (1979) for sand with 0.2 and 0.5 mm mean diameters, respectively.

Data	Gravel bed		Fines infiltrating		Bed initial cutoff size D_c [mm]	β Trap efficiency		
	D_m [mm]	σ_g	d_m [mm]	σ_s		minimal	mean	maximal
B&J-S1	13.5	1.57	0.20	1.55	0.778	0.005%	0.29%	0.29%
B&J-S2	13.5	1.57	0.50	1.61	0.778	1.2%	2.50%	5.0%
W-Z1	7.2	1.87	0.35	1.24	0.499	2.0%	3.20%	7.0%
W-Z2	10.2	1.77	0.35	1.24	1.995	1.0%	2.50%	6.0%
W-Z3	13.1	1.68	0.35	1.24	1.995	1.0%	2.10%	4.0%
W-Z4	17.2	1.17	0.35	1.24	7.959	0.7%	1.10%	1.5%
W-Z5	7.4	1.9	0.35	1.24	1.995	2.0%	3.30%	6.0%
W-Z6	7.9	1.22	0.35	1.24	3.979	1.0%	2.00%	4.0%
W-Z7	8.7	1.71	0.35	1.24	2.814	1.0%	2.20%	4.0%
W-Z8	7.6	1.46	0.35	1.24	2.814	1.5%	2.50%	4.0%
W-Z9	4.3	1.65	0.35	1.24	0.250	2.0%	3.40%	7.0%

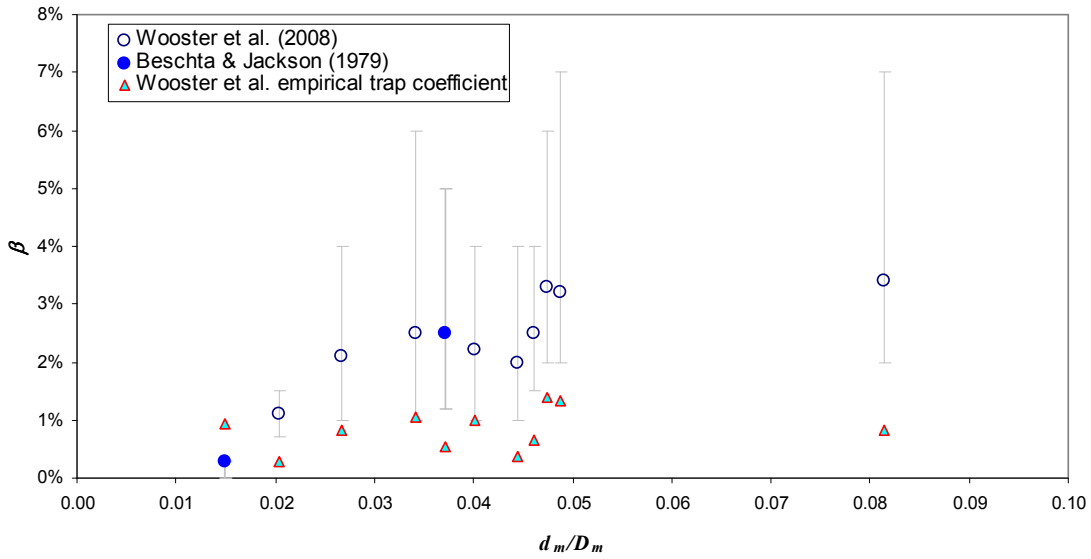

Figure 8.22. Best "fit" trap efficiency values obtained by applying the fines infiltration model to experimental data sets.

8.3.3.2 Functional relation for the trap efficiency

As stated in equation (8.44), a general functional relation for the trap efficiency must include measures of dispersion of the grain size distributions, like the geometric standard deviation, of the sediment in the bed and the fines infiltrating. Two processes with opposite effects, related to the dispersion around the mean diameter of the grain sizes in the bed and the filling sediment, control the amount of sediment trapped in the bed:

1. Pore throats occlusion. The opportunity for the incoming material to remain lodged and not progressing further below increases when the incoming particles clog the bed pore-throats, forming a bridge or platform between gaps where fines can be retained. The coarsest grains of the incoming fines have a higher chance for clogging the pores, which are narrower the finer the particles in the bed are. Hence,

the coarser the incoming fines and the finer the coarse bed grains, the higher the trap efficiency is.

2. Free percolation. The chance for the incoming grains to proceed further downwards increases when they encounter broader pores to pass through. The finest grains of the incoming material have a higher chance than the coarser ones to proceed deeper in between pores, which are wider the coarser the particles in the bed are. Hence, the finer the incoming material and the coarser the bed grains, the lower the trap efficiency is.

A measure of the pore throats occlusion can be obtained with the ratio of the coarsest grain sizes in the infilling material to the finest grain sizes present in the bed; this ratio can be described as a function of the mean diameter of the coarse half of the size distribution of the incoming material and of the mean diameter of the fine half of the size distribution of the bed material, which for log-normally distributed materials would be given by the diameters d_{84} and D_{16}, respectively. Similarly, a measure of the free percolation potential could be given by the ratio of the finest grain sizes in the incoming material to the coarsest grain sizes in the bed, that is, d_{16}/D_{84}. In this manner, eq.(8.44) can be rewritten as

$$\beta = \beta\left(\frac{d_{84}}{D_{16}}, \frac{d_{16}}{D_{84}}\right) \qquad (8.45)$$

For log-normally distributed material, as it often occurs with natural sediments, the following relations are valid:

$d_{84} = d_{50}\sigma_s$ (8.46a); $d_{16} = d_{50}\sigma_s^{-1}$ (8.46b); $D_{16} = D_{50}\sigma_g^{-1}$ (8.46c); $D_{84} = D_{50}\sigma_g$ (8.46d)

Hence, assuming that $d_{50} = d_m$ and $D_{50} = D_m$, the following equation would be equivalent to eq.(8.45), reagrouping the same variables that appear in (8.44):

$$\beta = \beta\left(\frac{d_m\sigma_s}{D_m\sigma_g^{-1}}, \frac{d_m\sigma_s^{-1}}{D_m\sigma_g}\right) \qquad (8.47)$$

The first group of variables in (8.45) and (8.47) is directly proportional to the trap efficiency, while the second one is inversely proportional. The product of both ratios could be a reasonable measure of the capacity of the incoming sediment to remain trapped in the bed. In that form, (8.45) and (8.47) could be reduced to

$$\beta = \beta\left(\frac{d_{84}d_{16}}{D_{16}D_{84}}\right) \quad (8.48); \qquad \beta = \beta\left(\left[\frac{d_m}{D_m}\right]^2\right) \quad (8.49)$$

Representative grain sizes and the groups of variables in equations (8.48) and (8.49), for the experimental data, are shown in Table 8.9. The grain size distributions for the sediment used in the experiments are close to be log-normally distributed, as is evidenced by the similarity between the product of the values of the independent variables in (8.48) and (8.49), for each of the experimental data; thus, for both data-sets, (8.48) and (8.49) are approximately interchangeable.

The independent variable in eq.(8.48) has been plotted in Figure 8.23a against the mean trap efficiencies obtained for the experimental data sets. A clear bias is observed toward a direct proportionality between parameter $[(d_{16}/D_{84})(d_{84}/D_{16})]$ and trapping efficiency, with a rapid increase of the trapping efficiency for low values of $[(d_{16}/D_{84})(d_{84}/D_{16})]$ and the approximation to a plateau of constant β at high values of the pàrameter.

Small values of $(d_m/D_m)^2$ would denote domination of free percolation against pore throat occlusion, so that for infinitely small values pore throat occlusion would not occur and it can be expected that $\beta \approx 0$. On the other side, for increasing values of $(d_m/D_m)^2$ a continuous increase of β can be expected, but since the bed structure imposes a geometric restriction for the grain sizes that can percolate through the pores, there must exist an

upper limit for the higher values of β. For sediment mixtures such a limit could be described with the bed cutoff size, so that an upper boundary would be given for, say $d_5/D_c \approx 1$, for which few grains would percolate and the trap efficiency would approach to its maximum. On the other hand, for uniform material, for which $d_{16} \approx d_{50} \approx d_{84}$ and $D_{16} \approx D_{50} \approx D_{84}$, the maximum possible trap efficiency would be given for $(d_m/D_m)^2 = 0.414^2 = 0.171$ or $(d_m/D_m)^2 = 0.155^2 = 0.024$, which are the maximum size ratios for percolation of small grains through the pores of larger grains, in case of cubical and tetrahedral packing, respectively. Consequently, in search of a functional relation for the variables in eqs.(8.48) and (8.49), a lower and an upper boundaries for the trap efficiency should be considered. A good agreement is obtained when using a lower boundary on $\beta = 0$ and an upper boundary on $\beta = 3.5\%$, with an exponential function of only two parameters, as shown in Figure 8.23a. With this function trap efficiency can be computed as

$$\%\beta = 3.5 \exp\left[-0.0005 \frac{D_{16} D_{84}}{d_{84} d_{16}} \right] \qquad (8.50)$$

Table 8.9. Characteristic grain sizes and trap efficiency for the experimental data sets. W-Zx refers to data set from Wooster et al. (2008) at zone x. B&J-S1 and B&J-S2 refer to data set from Beschta and Jackson (1979) for sand with 0.2 and 0.5 mm mean diameters, respectively.

Data	D_{16} [mm]	D_{84} [mm]	d_{16} [mm]	d_{84} [mm]	$(d_{84}/D_{16})(d_{16}/D_{84})$	$(d_m/D_m)^2$	β
B&J-S1	8.07	21.59	0.11	0.33	0.0002	0.0002	0.3%
B&J-S2	8.07	21.59	0.3	0.75	0.0013	0.0014	2.5%
W-Z1	3.47	13.39	0.28	0.43	0.0026	0.0024	3.2%
W-Z2	5.41	18.72	0.28	0.43	0.0012	0.0012	2.5%
W-Z3	8.27	20.16	0.28	0.43	0.0007	0.0007	2.1%
W-Z4	13.73	20.79	0.28	0.43	0.0004	0.0004	1.1%
W-Z5	3.47	15.26	0.28	0.43	0.0023	0.0022	3.3%
W-Z6	6.16	10.08	0.28	0.43	0.0019	0.0020	2.0%
W-Z7	4.85	17.73	0.28	0.43	0.0014	0.0016	2.2%
W-Z8	4.85	11.09	0.28	0.43	0.0022	0.0021	2.5%
W-Z9	2.48	7.78	0.28	0.43	0.0062	0.0066	3.4%

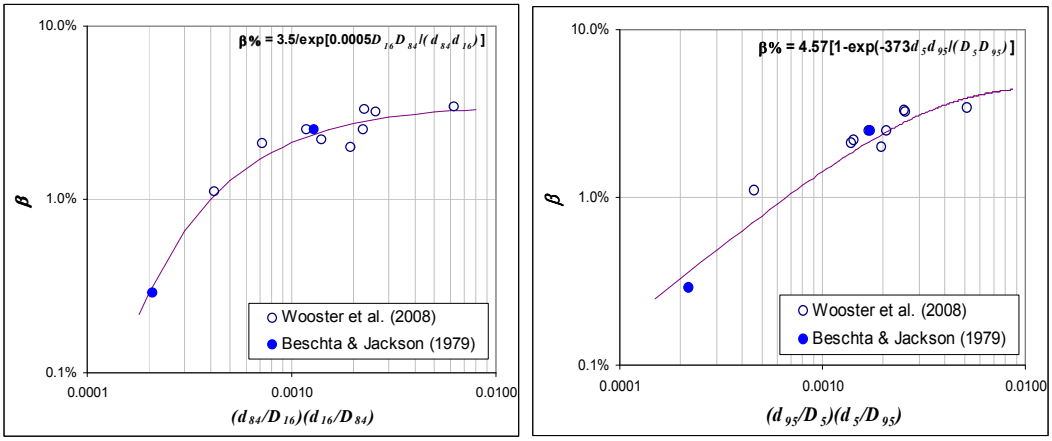

Figure 8.23. Best "fit" trap efficiency values obtained by applying the fines infiltration model to the experimental data-sets, related to the infiltrating and bed materials characteristic grain size ratios. a) Using 16th and 84th percentiles of the grain size distributions; b) using the 5th and 95th percentiles of the grain size distributions.

or considering a log-normal grain size distribution

$$\%\beta = 3.5\exp\left[-0.0005\left(\frac{D_m}{d_m}\right)^2\right] \qquad (8.51)$$

These functions were forced to an arbitrary upper limit of β=3.5%, nevertheless, more data would be needed to define a more realistic upper limit for the trap efficiency.

Gibson et al. (2009) performed experiments to study the infiltration of four different fine sediments into a unique coarse bed. The grain size distributions of the sediments used by Gibson et al. are shown in Figure 8.24. Gibson et al. found that the bridging formation process is quite sensitive to the coarse tail of the grain size distribution of the infiltrating fines. Two of the fine materials they tested had similar median diameters (IFS2 and IFS3 in Figure 8.24), but one of them (IFS2) had a larger tail for the coarse diameters, i.e., a higher maximum diameter than the other material. For the material with a larger tail (IFS2) a plug near the bed surface was formed. On the other side, the material with lower maximum diameter (IFS3) penetrated deep until the flume bottom and filled the bed from the bottom upwards. Considering these observations, an alternative to improve the trap coefficient function would be the use of minimum and maximum diameters of the grain size distributions, say, the 5th and 95th percentiles, instead of the 16th and 84th percentiles. Figure 8.23b shows the results with this correction. The best fit exponential function obtained in this case is

$$\%\beta = 4.57\left[1-\exp\left(-373\frac{d_5 d_{95}}{D_5 D_{95}}\right)\right] \qquad (8.52)$$

or considering a log-normal grain size distribution

$$\%\beta = 4.57\left[1-\exp\left(-373\frac{d_m}{D_m}\right)\right] \qquad (8.53)$$

For these functions, the upper limit for the trap coefficient is given by $(d_m/D_m)^2$=0.024, i.e., for a tetrahedral packing of the bed particles. This is shown in Figure 8.25, where the derivatives of the function are shown.

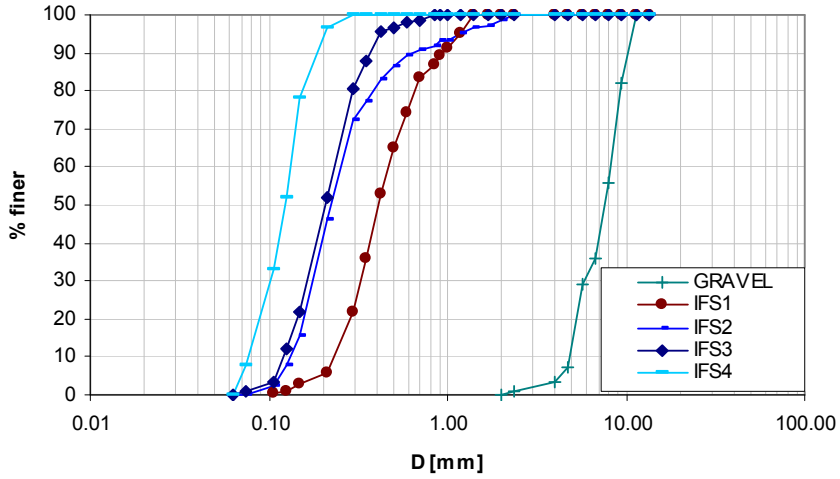

Figure 8.24. Grain size distributions of coarse bed material and the four infiltrated fines used in the experiments by Gibson et al. (2009).

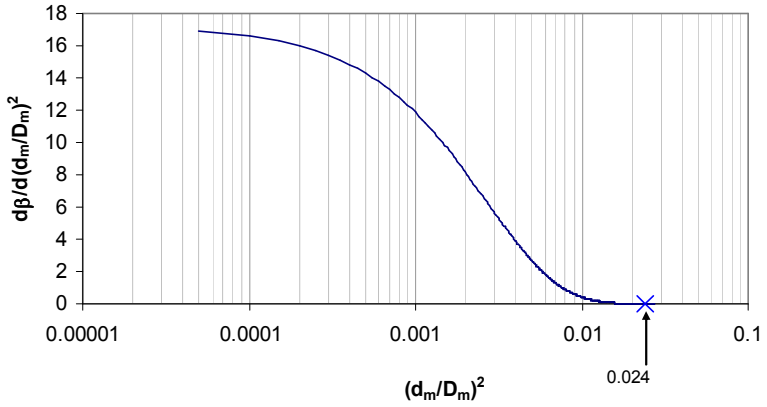

Figure 8.25. Derivative of eq.(8.53) with respect to the quadratic ratio of mean diameters of the coarse and fine materials. The derivative is zero for $(d_m/D_m)^2$=0.024, which corresponds to tetrahedral packing of the bed.

8.3.4 Application of the model to flume experiments

The model developed and described along Sections 8.3.1, 8.3.2 and 8.3.3, is here applied and compared to results from flume experiments in which infiltration of fine material into a static bed was observed.

Runs M1E6 and M2E4 of experiments in this work

As it was described in Section 8.2.3, in the experimental campaign presented in Chapter 3 the finest size fractions penetrated into the most superficial layers of the bed, at the level of the plane of erosion over which bedforms displaced. The infiltrated material formed a layer composed of a high content of fine material (Figure 8.5). The infiltration model was applied to runs M1E6 and M2E4, the two runs for which the grain size distribution was measured at different depths. Those grain size distributions are shown in Figure 5.40. Results of the model are shown in Figures 8.26.

Comparison of cumulative grain size distributions in Figure 8.26, with those of the original bed and for the bed at depths at which the lamina of fines formed (50-60 mm) in Figure 5.40, show a great similarity; for run M1E6, with an initial sand content in the bed of 30%, infiltrated fine material was larger than for run M2E4, with 45% initial sand content in the bed. The model reproduced this trend accurately.

Schälchi (1992)

Schälchi reported on experiments in which fine sand penetrated into an immobile bed with poorly-sorted material. The maximum penetration depth was twice the D_{90} bed grain size, which is 152.2 mm. Since the bed material was not well-sorted and the grain size distribution far from being log-normally distributed (see the original grain size distribution in Figure 8.27), eq.(8.52) was used for computation of the trap efficiency.

Results of applying the fines infiltration model are shown in Figures 8.27 and 8.28. The maximum penetration depth can be obtained from the upper-left graph in Figure 8.28a, which is roughly 130 mm, a value quite similar to the 152.2 mm measured in the experiments.

Gibson et al. (2009)

Gibson et al. performed experiments with the bed materials shown in Figure 8.24. Four different sands were used over a unique bed of gravel. Two of the sands (IFS1 and IFS2, in experiments 1 and 2, respectively) produced bridging near the bed surface, which

prevented that a large amount of fines penetrated deeper into the bed; while the other two sands (IFS3 and IFS4, in experiments 3 and 4, respectively) penetrated deep until the flume bottom, and filled the bed from the bottom upwards. This latter process was called "unimpeded static percolation" by these authors. Gibson et al. measured the variation of the median diameter along the vertical at the end of the experiments.

Results after application of the fines infiltration model are shown in Figures 8.29 to 8.32. For all the four experiments, the model predicted accurately the vertical distribution of sand content and the maximum content of fines (saturated condition, which occurs near the bed surface for most of the runs); conversely, the median grain size of the deposited sand along the vertical was largely underestimated by the model.

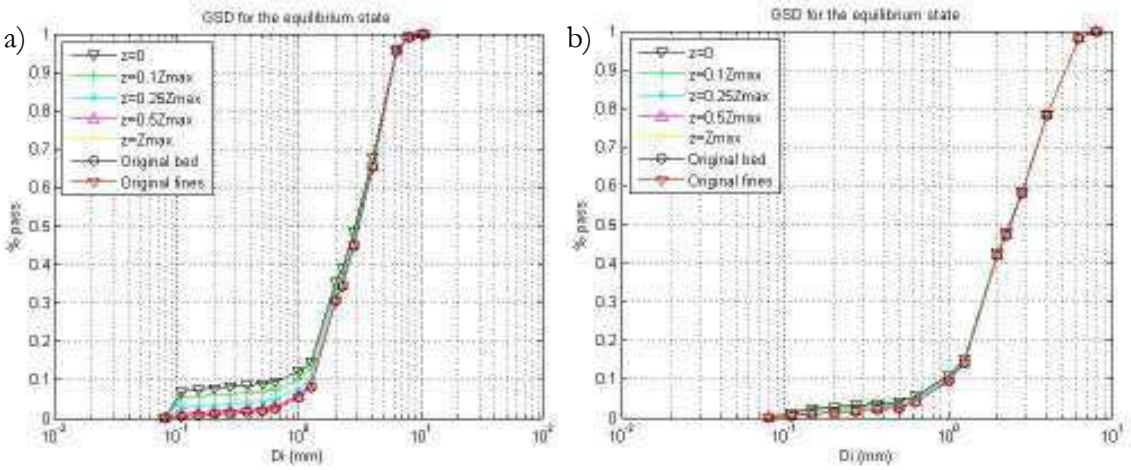

Figure 8.26. Grain size distributions at different depths, when the bed has reached the saturated condition with the infiltration model; a) run M1E6, b) run M2E4. Compare these two graphs with the deepest samples of the bed at the end of the experiments, shown in Figure 5.40.

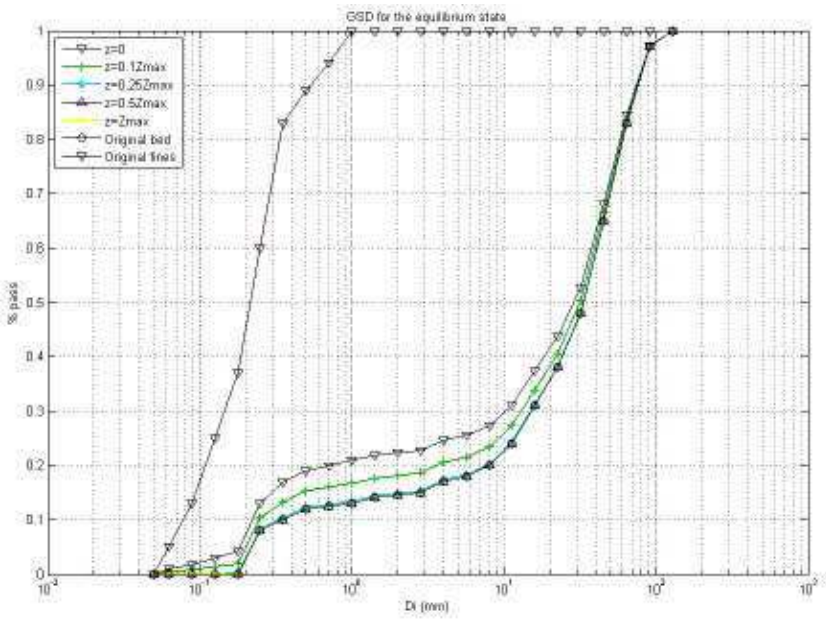

Figure 8.27. Grain size distributions at different depths, when the bed has reached the saturated condition with the infiltration model, for experimental data from Schälchi (1992).

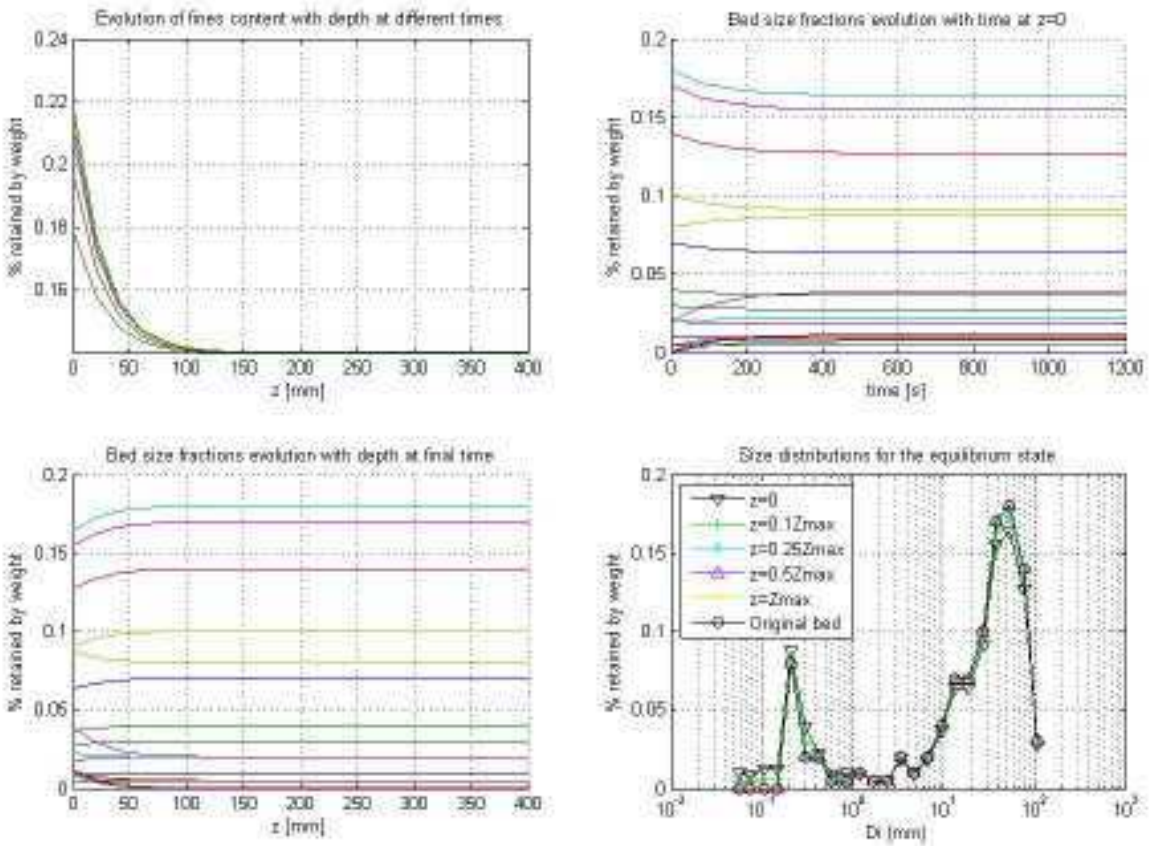

Figure 8.28. Model results for experimental data from Schälchi (1992). a) Time and depth evolution of total fractional content of fines; each curve for a given time, time increasing from below upwards. b) Time evolution of each bed size fraction near the bed surface. c) Bed sizes fractional content at equilibrium time; horizontal lines indicate complete bed saturation. d) Grain size distribution at different depths for the equilibrium state.

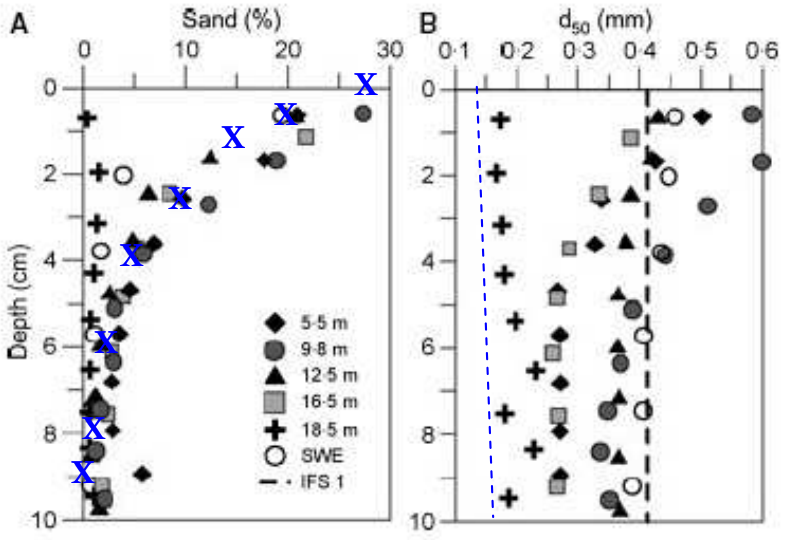

Figure 8.29. Comparison of measured vertical variation of sand content (A) and median diameter of infiltrated fines (B) for experiment 1 of Gibson et al. (2009), and results of the infiltration model (left: blue x's, right: dashed blue line). The five different experimental points refer to samples taken at different flume positions, the number in the legend indicates the distance downstream of the sediment source; SWE refers to still water experiments; IFS refers to the fine sediment used in the experiment in relation to Figure 8.24.

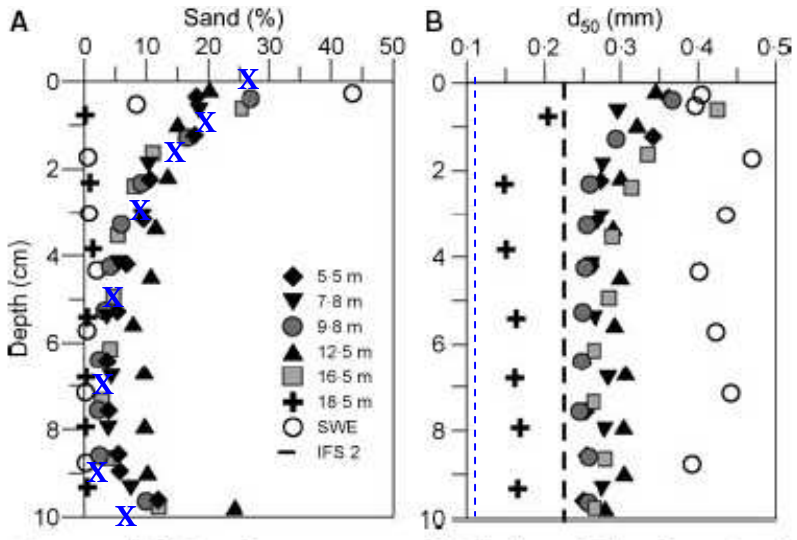

Figure 8.30. Comparison of measured vertical variation of sand content (A) and median diameter of infiltrated fines (B) for experiment 2 of Gibson et al. (2009), and results of the infiltration model (left: blue x's, right: dashed blue line). The five different experimental points refer to samples taken at different flume positions, the number in the legend indicates the distance downstream of the sediment source; SWE refers to still water experiments; IFS refers to the fine sediment used in the experiment in relation to Figure 8.24.

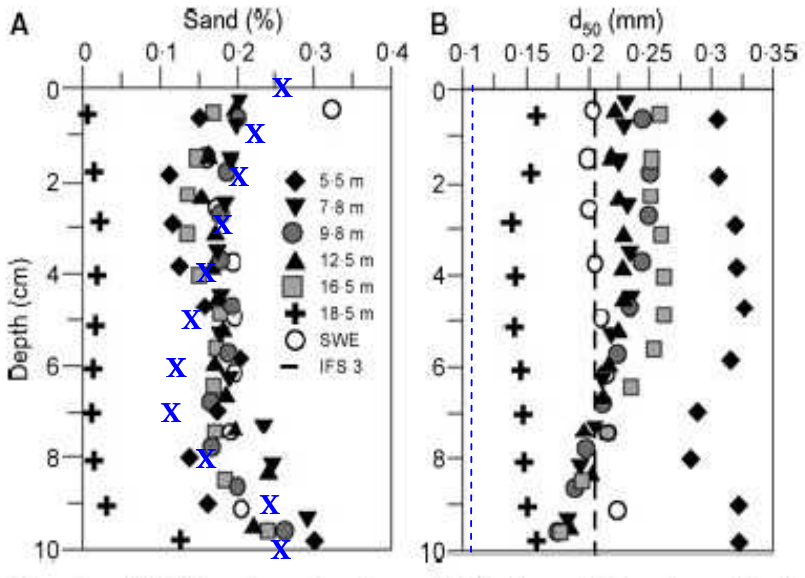

Figure 8.30. Comparison of measured vertical variation of sand content (A) and median diameter of infiltrated fines (B) for experiment 3 of Gibson et al. (2009), and results of the infiltration model (left: blue x's, right: dashed blue line). The five different experimental points refer to samples taken at different flume positions, the number in the legend indicates the distance downstream of the sediment source; SWE refers to still water experiments; IFS refers to the fine sediment used in the experiment in relation to Figure 8.24.

It was found that the median size of the infiltrated fines computed with the model were much smaller than the measured values, due to limitations of the Frings et al. (2008) model for computation of the cutoff size. According to that model, the cutoff size value drops substantially when even a small amount of fines is added to the coarse fraction. For instance, as shown in Table 8.10, for materials IFS2, IFS3 and IFS4 the initial cutoff size of

the gravel is 2 mm, but if only 0.5% of fines are added to the gravel the cutoff size drops to a value of 0.335 mm. The effect of this feature is that the infiltration model predicts finer grains penetrating into the bed than those measured. The model of Frings et al. (2008) must be revised to improve this fault.

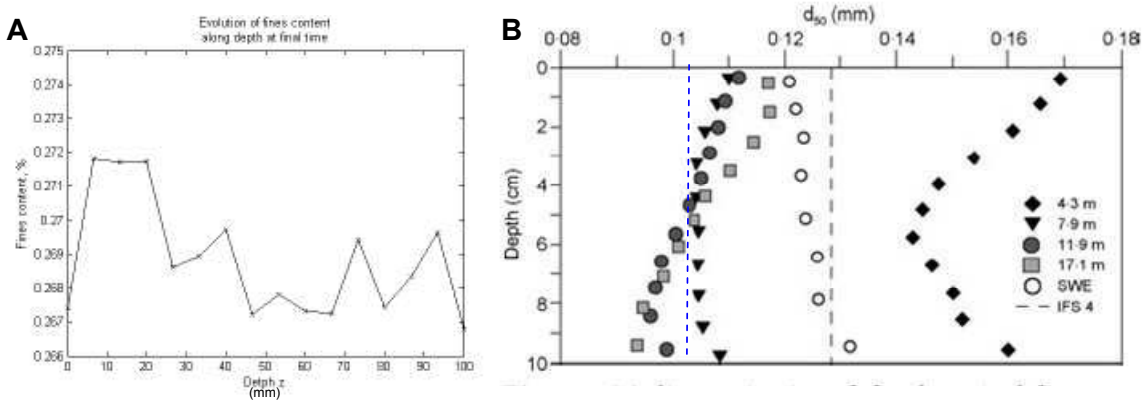

Figure 8.31. Variation of sand content computed with the infiltration model for experiment 4 of Gibson et al. (2009) (A); comparison of measured vertical median diameter of infiltrated fines (B) for experiment 4 of Gibson et al. (2009), and results of the infiltration model (dashed blue line). The five different experimental points refer to samples taken at different flume positions, the number in the legend indicates the distance downstream of the sediment source; SWE refers to still water experiments; IFS refers to the fine sediment used in the experiment in relation to Figure 8.24

Table 8.10 Variation of the cutoff size as sand content of infiltrated material increases in the bed, according to the model of Frings et al. (2008). The cutoff size is the maximum grain size that is able to penetrate through the pores in a bed with a given grain size distribution. The computed cutoff size for the initial gravel bed is 2 mm.

Fine material	Cutoff size for 0.5% fines content added to gravel [mm]	Cutoff size for 1% fines content added to gravel [mm]	Cutoff size for 2% fines content added to gravel [mm]
IFS1	0.5000	0.3535	0.2847
IFS2	0.3535	0.2847	0.2847
IFS3	0.3535	0.2847	0.2847
IFS4	0.3535	0.2847	0.2847

In short, the fines infiltration model predicts with accuracy the fines content distribution along depth and the bed saturated condition, but it underestimates the size of the infiltrated material. This is owed to a defect in the model for computation of the cutoff size, i.e., the maximum diameter that can fit in between the pores of the bed.

8.4 SUMMARY

This Chapter dealt with sediment grain size sorting patterns produced by the infiltration of particles into a static bed of mixed size material. First, in relation to the experiments with sand-gravel mixtures presented in Chapter 3, the characteristics of a thin horizontal lamina formed under the migration path of bedforms were described. It was concluded that such lamina was formed by the shallow percolation into the bed of the finest size fractions of the material in motion. It was suggested that the thickness of the lamina was related to the maximum depth reached by the infiltrated particles; at such limiting depth, the infilling

particles bridged the gaps between the bed static material, so that subsequent material that penetrated into the bed filled the bed from the bridge upwards. Hence, the lamina was formed by a horizontally continuous region, with a high concentration of fines and extremely low bed porosity. For describing the process by which the bed is occluded by infiltrating sediment, reference to observations and measurements by other authors was given; in turn, empirical bed porosity models for binary and multifractional mixtures were used to analyze the bridging potential. Bed packing models were used as well to describe the structure of beds with natural sediment, and to analyze the infiltration of fine material into a bed of coarse particles. A fundamental difference was found between bimodal and less bimodal or unimodal sediment for the process of sediment infiltration. For the latter, the bridging process is more complex, as grains of the fine fraction may be part of the bed contact framework; conversely, for the former, the infiltration of fines can be explained based on the relative abundance of the matrix infilling the bed framework. Results proved the utility of bed porosity models for understanding the interactions between the bed structure and the infilling matrix in natural gravel-bed rivers.

In the second part of this Chapter, general equations were presented and an a numerical model was developed, for simulating the process by which different size fractions of sediment infiltrate into a bed composed of poorly-sorted material. The model consists of three main components: an empirical model for bed packing porosity, an algorithm for estimating the bed saturated condition, and a model to solve the equations of the sediment percolation process. The first component, i.e., the packing porosity model, is used in the computations of the two other components, and it is the same model presented originally by Frings et al. (2008). Such model allows estimating the bed cutoff size, which is the maximum size of particles that can fit in the voids between particles in a static bed. The second component of the sediment infiltration model computes the variation of the cutoff size as the bed is filled with fine material; in this manner, the maximum volumetric capacity of the bed to store sediment with a given grain size distribution can be obtained. The third component of the infiltration model solves the continuity equation for infiltrating sediment; in this manner, the temporal variation of fine material content along depth can be calculated. This component uses computations of cutoff size and maximum bed capacity at different time steps. To be implemented, the sediment infiltration model uses a trapping coefficient, which depends on the characteristics of the bed and infiltrating materials. It was found that the trapping coefficient is quite sensitive to the coarse and fine tails of the sediment grain size distributions. Therefore, for its calibration using experimental data from literature, a good correlation was found when using the ratio between the product of the maximum and minimum diameters of the infiltrated sediment and the product of the maximum and minimum diameters of the bed material $[(d_5 d_{95})/(D_5 D_{95})]$. Such correlation was parameterized with an exponential function. When compared with experimental data reporting infiltration of fine material, the numerical model for fines infiltration showed good agreement for reproducing the bed saturated condition and the variation of infiltrated fines along the vertical. Nevertheless, the performance of the model was poor for reproducing the grain size distribution of the infiltrated material. It was found that this poor performance was related to limitations of the cutoff size computed by the packing porosity model. Such model requires to be improved for a better performance of the numerical model for fines infiltration herein developed.

CHAPTER 9:

CONCLUSIONS AND FUTURE RESEARCH

9.1 OVERVIEW

The research presented in this work tackled issues in the realm of flow over mobile boundaries from an experimental perspective, with the aim of contributing to increase the current understanding of river morphodynamics. An experimental campaign was carried out in a laboratory flume to generate flow and sediment transport states in morphodynamic equilibrium conditions, i.e., conditions for which average values of bed and water slopes, water depth, and fractional solid discharges remained approximately constant in time and space. The experiments considered high sediment transport rates and water flows in the transition, or close-to the transition, from subcritical to supercritical flow.

More than 60 experimental runs were performed with four different sediments in a channel with 27 m of effective length, and 0.75 m width. The sediments used were coarse sand, fine gravel, and two mixtures of these materials, with 32% and 45% average sand content by weight. Constant sediment feed rates added to the channel in each run were in average of 500 g/s, and were as high as 1070 g/s; these values are one order of magnitude higher than commonly reported sediment transport rates tested in laboratory flumes in previous studies found in literature. In turn, for the definitive runs, the ratio between bed shear stress and critical shear stress for the median sediment size ranged from 3 to 30, with an average value of 12.

From the experimental campaign a definitive data set was obtained, comprising 22 runs with characteristics of flow, stationary waves, bedforms, sediment transport, erosion and grain size sorting. This new experimental data set offers valuable information about flow and sediment interactions for ranges of variables that previously had not been systematically explored in laboratory flumes. For the definitive data set, water discharges were in the range of 59 to 80 l/s, water depths varied from 6.8 to 13 cm, mean flow velocities varied from 0.82 to 1.31 m/s, bed slopes from 0.58% to 2.14%, and Froude

numbers were in the range of 0.73 to 1.49.

A practical purpose of the experimental campaign was to reproduce flow conditions, bed configurations and sediment transport processes comparable to those in torrential ephemeral streams prone to flash floods, as those found in the Mediterranean coast. The processes proper of such type of streams were intended to be reproduced for the particular situation in which flow is laterally confined by vertical walls. Most of the experimental flows were characterized by three-dimensional stationary waves and antidunes, it can be expected that these same configurations could occur in laterally confined ephemeral streams; furthermore, since these configurations in the experimental runs produced deep bed erosion, of the same order of magnitude as the flow water depth, these results highlight the relevance of the study of stationary waves in transitional and supercritical flows for engineering practice, and the need for further attention to the study of flow and channel morphodynamics for the conditions imposed by flash floods in ephemeral streams.

Nine general hypotheses were initially considered for the flume experiments; they were summarized in Table 2.1 of Chapter 2. Overall, the experimental results confirmed partially five of those nine a priori hypotheses and verified completely three. The hypotheses and the experimental results are contrasted in Table 9.1

Analysis of the experimental data set showed that different variables and processes were linked in complex, yet systematic, interactions; these interactions were the response of the channel to adjust local conditions of bed configuration, flow and sediment transport to the imposed sediment-feed rates and water discharges. Conclusions from this analysis, along with original contributions and improvements to the current state of knowledge, are summarized in the following Sections. Each Section corresponds to each of the most general topics to which this research is related. Finally, in the last Section an overview is given of future trends of research in the topics treated in this work, in order to give subsequent continuity to the developments herein presented.

9.2 EXPERIMENTAL CHARACTERISTICS, TECHNIQUES AND OBSERVATIONS

The experimental methods and procedures used in this work were fundamentally similar to those used by other authors in flume experiments with loose-boundary beds and unidirectional flows for developing sediment transport relations, study bedforms or analyzing the morphodynamics of alluvial beds; compared to the extensive laboratory experiments in literature, the most important added value of the experiments herein reported is the study of ranges of variables that previously had not been systematically explored in laboratory flumes. The following conditions characterized the experiments performed for this work:

- Flows near critical conditions.
- Low channel width to water depth ratios, compared to previous studies.
- Loose-boundary beds of four different compositions, two of these materials (sand and gravel) were well-sorted, and two poorly-sorted (sand-gravel mixtures with 32% and 45% sand content, respectively).
- Flow conditions were such that no partial transport of any of the grain size fractions in the poorly-sorted material occurred.
- Mobile-bed equilibrium states were attained; flow and bed characteristics were registered for such states.

Table 9.1. Test of a priori formulated hypotheses compared with experimental results, for the most important topics treated in this work.

	Topic	Hypothesis	Experimental results
1.	Unidirectional flows over alluvial beds	*Systematic flume experiments would highlight especial features, previously not recognized due to scarce empirical evidence, proper of transitional- and upper-regime flows over coarse and heterogeneous size material.*	**Verified:** The experimental results highlighted differences between bedforms in uniform and heterogeneous material. Of particular interest was the formation of three-dimensional stationary waves and stable three-dimensional downstream migrating antidunes, which have been sparsely reported in literature.
2.	Bed Configurations	Bedforms in coarse sand, fine gravel and sand-gravel mixtures for transitional- and upper-regime flows will not differ considerably from those in uniform material, but will exhibit distinctive characteristics (form, geometry, resistance to flow, movement, etc.) previously not identified. Therefore, bed configurations for transitional and upper-regime will consist of two-dimensional upstream-migrating antidunes and transitional bedforms, although transitional plane beds will also be likely to occur, especially for beds composed of sand. *Flume experiments would highlight differences between different bed materials, and would help to understand interactions between stationary waves and bed dynamics.*	**Partially verified:** Three-dimensional downstream-migrating antidunes and transitional bedforms prevailed in most of the runs, and they coexisted with alternate bars. Plane beds were observed only in two runs, and it is likely that they were upper-regime plane beds. Bedforms in sand were steeper than those in gravel and sand-gravel mixtures and dominantly two-dimensional. The experiments provided valuable data about three-dimensional stationary waves and antidunes.
3.	Transitional regime	Transitional regime in sand-gravel mixtures will occur for lower Froude numbers the lower the relative depths will be, being relative depth a function of the mean diameter of the mixture.	**Partially verified:** Froude numbers in which transitional regime occurred were lower and in a narrower range of values for sand than for gravel. But the ranges for sediment mixtures were similar to gravel.
4.	Bed forms	Bedforms in sand will be steeper than bedforms in gravel. The steepness of bedforms in sand-gravel mixtures will be proportional to the sand content, i.e., for a 30% sand content the bedform steepness will be 30% the steepness of bedforms with sand.	**Partially verified:** Sand bedforms were steeper than gravel bedforms; bedforms with mixtures were similar to gravel bedforms, so that no linear relationship between bedform steepness and sand content existed.
5.	Flow resistance and bedforms	Form resistance produced by antidunes will be lower than flow resistance commonly reported for dunes with similar steepness.	**Partially verified:** antidunes produced less drag, although steep downstream-migrating antidunes could produce similar drag as dunes.

Table 9.1. (Continued)

	Topic	Hypothesis	Experimental results
6.	Bed resistance in alluvial beds	Form resistance for bedforms in coarse material will be lower than for fine material bedforms. For mixed size material, bed resistance will be a function of the mean diameter of the mixture. *Bedforms developed in flume experiments for a wide range of flow conditions would allow estimating the portion of bed resistance taken by form drag and by grain roughness for transitional- and upper-regimes.* *The effect of sand content in each flow resistance component could then be quantified, and also this information would allow elucidating if methods for channel bed resistance developed for fine material are valid in coarse and heterogeneous sediment.*	**Partially verified:** Bed resistance in gravel was considerably smaller than in sand. Bed resistance for mixtures was even slightly lower than for gravel. The experiments allowed determining the portion of shear taken by forms and grains. Bed resistance methods were also tested with the new data set.
7.	Sediment transport	Sand content will have a negligible effect in sediment transport for high sediment supply loads. *Flume experiments would provide with evidence to recognize if the effect of sand content in sediment mobility would vanish under very high sediment transport conditions. Particularly, experiments would help to recognize any important difference between matrix supported and gravel-framework supported beds.*	**False:** For the high transport rates in the experiments, sand had a larger mobility than gravel, and it was verified that sand content slightly enhanced transport of the bed material in comparison to uniform material, at least for the mixture with 32% and content. The experiments allowed determining the effect of sand content in sediment mobility.
8.	Sorting of non-uniform sediment	A coarse surface layer will not form at high sediment transport rates. The bed surface will be completely mixed by the highly competent flows, but patches of coarse material would occur for less competent flows.	**Verified:** Patches of different characteristics were observed on the bed surface, some of them were coarse, so it can be said that bed armouring occurred in some regions of the bed, but that patchiness was generalized.
9.	Torrential ephemeral streams	*Flume experiments would help to better understand torrential flows in these streams and to assess the role of bedforms in flow resistance.*	**Verified:** The data set developed with the experiments can be compared with flows in torrential ephemeral streams, and contributes to the understanding of these types of rivers.

- Measurements included flow characteristics, sediment transport rates, grain size compositions of sediment in motion and final bed material, maximum bed erosion, and characteristics of bedforms and stationary waves.

The collected data can be considered as exceptional, since sediment feed rates were unusually high, in ranges not common for laboratory flumes. These conditions allowed the development of bed and water configurations rarely reported in literature, particularly, downstream-migrating antidunes, and three-dimensional stationary waves, known as rooster tails.

Uncommon high sediment feed rates for laboratory channels were feasible due to the use of a new flume with extended capabilities for the operation of sediment. This new flume can be operated in a hybrid type of configuration, which combines sediment-feed and -recirculating modes; this hybrid operation consists in recirculating sediment at the downstream end of the channel to be reintroduced at the channel head, but unlike sediment-recirculating mode, sediment is reintroduced at a constant feed-rate. For the experiments herein presented, this hybrid operation is in fact a surrogate of sediment-feed operation, given that no partial transport of any size fraction occurred in the channel. This novel operation mode allowed the performance of long-lasting runs without requiring large stocks of sediment, and by means of load cells installed under the sediment-feeders it also allowed for an instantaneous measurement of the solid discharge passing through the downstream end of the channel. This latter feature provided with an additional source of information to verify if equilibrium state had been attained.

Novel experimental techniques and methods developed for the experimental campaign were the following:

- Characterization of bed surface texture patchiness. A method was developed for a rapid characterization of the bed surface texture in runs with sand-gravel mixtures; the method consisted in identifying channel reaches with similar morphological and textural characteristics. Within each of these reaches, three types of patches were visually identified: fine, coarse and mixed. Samples were taken for each of this type of patches, and the morphological region where they were collected was registered.
- Bed surface material sampling with plaster. For a qualitative characterization of bed surface texture, areal bed surface samples were collected using an adhesive made of plaster. This method allowed controlling the viscosity and plasticity of the adhesive for low penetration, thus reducing the amount of subsurface material collected. In turn, the technique used was easy and relatively fast to implement.
- Measurement of bed erosion. The experiments were performed in two phases: a transitory phase and a stable phase. The transitory phase was finished when equilibrium state prevailed in the channel. In that moment the experiment was stopped. This allowed for the introduction of tracer stones, in layers of different colors, in a section of the bed; at the end of the stable phase, it was possible to measure the patterns of maximum bed erosion produced by the passage of bedforms by recognizing the tracer stones not removed by the flow.

A general summary of experimental observations for the runs that comprised the new data set is given as follows:

- The most frequent water surface configuration in most of the experimental runs consisted of trains of short-crested stationary waves; in turn, the most frequent bed surface configuration consisted of trains of three-dimensional downstream-migrating antidunes.
- Three-dimensional antidunes at the channel central cross-section coexisted with alternate bars and two-dimensional downstream-migrating antidunes on the cross sections close to the channel walls.
- Dominant bedforms in sand beds were predominantly two-dimensional, while dominant bedforms in gravel and sand-gravel mixtures were three-dimensional.
- Bedform height increased and bedform celerity decreased from the upstream end of the channel to roughly the second third of the channel length.
- The average height of stable sand bedforms was roughly half the water depth, while stable bedform height for gravel and sand-gravel mixtures was roughly 15% and 25% of the water depth, respectively.
- Wave celerity increased almost linearly with Froude number, with a discontinuity roughly between F=1 and F=1.2.

- Average wavelength of short-crested stationary waves was 80% of the channel width, with a coefficient of variation of 8%.
- For the highest stationary waves, the ratio between height and wavelength was in average 0.157, while the ratio between wave height and water depth ranged from roughly 0.5 to 1.
- Alternate bars wavelength was between 2.5 to 5 times the channel width.
- Antidunes were washed away when the experiment was stopped, while alternate bars were preserved.
- Maximum erosion depths in sand beds was almost double the erosion depths in sand-gravel mixtures.
- Almost constant cross-sectional erosion patterns were found for sand beds, while patterns of deeper erosion at the channel center than at the lateral sections were found for sand-gravel mixtures.
- Sediment transport samples showed that average variation in instantaneous solid discharge due to longitudinal pulsations was in the order of ±45% of the average sediment feeding rates; although, two maximum values up to more than 4 times the feeding rate were measured, and a minimum as low as 1% of the feeding rate.

The following patterns in sediment sorting were observed in experiments with sand-gravel mixtures:

- Average sediment transport rates were the same for each of three equal length segments in which the channel cross section was divided for sediment transport sampling. Coarse material traveled preferentially through the central cross section, and fine material traveled preferentially through the laterals. This trend was sharper in runs with the mixture with 45% sand content.
- The bed surface at the end of the experiments showed patches of similar sediment texture. Patches of well-sorted material on the bed surface were more common for dimensionless shear stresses roughly higher than 0.22.
- Fine patches were common on the bar crest, while coarse patches were common on the region of low elevation in front of the bar front. A general trend of downbar and wallward fining was apparent, while coarse material was commonly concentrated in the lowest regions and at the center of the channel.
- Surface material was finer than subsurface material.
- Grain size distribution of subsurface material was similar to the distribution of the feeding-material, showing to be more stable and more representative of the entire bed composition than surface material.

9.3 STATIONARY WAVES AND ANTIDUNES

The experiments herein reported considered high sediment transport rates and conditions in or close-to the transition from subcritical to supercritical flow. This transition is extremely unstable, water depth can exhibit abrupt changes with small perturbations on the bed; therefore, standing waves, named here stationary when they accompany migrating bedforms, are characteristic of this transitional regime. Three-dimensional stationary waves accompanied by three-dimensional downstream-migrating antidunes were common in most the experiments in the new data set herein presented. This data set can be considered a complement or continuation of the seminal work of Kennedy (1961), who obtained a data set for stationary waves and antidunes with uniform fine- and coarse-sands. The new data set covers the gap of empirical evidence for stationary waves and antidunes in very coarse sand, fine gravel and sand-gravel mixtures. Relevant of this new data is the contribution with descriptions, flow conditions and characteristics of downstream-

migrating antidunes, which are rarely reported in literature. A summary of the most significant conclusions obtained in this work regarding stationary waves and antidunes is advanced as follows.

- The formation of three-dimensional stationary waves and short-crested antidunes could be related to the interaction of converging diagonal cross waves with an erodible bed. Such diagonal cross waves are originated by the shock fronts of successive perturbations, spaced at a distance equal to the wavelength of antidunes; for the experiments here presented the lateral border condition imposed by the channel walls was relevant for the development and characteristics of short-crested waves.
- From the general potential flow solution for the propagation velocity of waves of finite length and geometrical considerations, the following equation was derived relating mean flow velocity V to short-crested wave longitudinal wavelength λ_m, short-crested wave transversal wavelength (channel width) λ_t, and mode of vibration m,

$$V^2 = \frac{g\lambda_m}{2\pi}\sqrt{1+\left(\frac{m\lambda_m}{\lambda_t}\right)^2}$$

  This relation is the same as that originally presented by Kennedy (1961), but more general since it considers more than one mode of vibration, while that presented by Kennedy is applicable only to the fundamental mode.
- The relation above performed well when compared to experimental data of this work, and with other data in literature, provided that the computed flow velocity was compared with the flow velocity on the water surface, and considering that for the experiments of the new data set alternate bars were related to first order cross-waves; in this manner, the mode of vibration excited for the formation of the short-crested waves was computed as the closest integer to the ratio between half-bar wavelength and the wavelength of the three-dimensional stationary waves. It was found that for most of the experimental runs of this work, in the formation of short-crested waves the second mode of vibration of diagonal cross waves was excited, while for experiments of other authors, with narrower flumes, only the first mode was excited.
- Deep concave upward scour holes at the channel central section in beds with mixtures was related to steep rooster tails on the water surface, while almost constant transversal erosion patterns in beds with sand were related to two-dimensional stationary waves above the steep bedforms that spanned transversally from wall to wall.
- For bedforms with similar steepness and relative height, bed configurations with downstream-migrating antidunes produce less expansion losses than dunes (roughly 70% lower), but much higher losses than upstream-migrating antidunes (roughly 4 times higher).
- Downstream-migrating antidunes could attain steeper geometries than upstream-migrating antidunes, due to hydraulic constraints imposed by the maximum stationary wave steepness before breaking.

Conclusions related to the distinction of lower-, transitional- and upper-regime bedforms, and to the flow conditions required for the formation of stable bedforms of a given species (bed phases), are summarized as follows:

- The degree of coupling between bed and water surfaces can serve as an objective and straightforward criterion to distinguish antidunes (bed and water surfaces in phase) from dunes (180 degrees phase shift between bed and water surfaces) and transitional bed forms (different degrees of water and bed surfaces coupling). This

was the main criterion used in this work for classification of bedforms. Notwithstanding, some subjectivity is unavoidable due to the unsteadiness inherent to flows close to the critical condition, which can produce a temporal and spatial alternation or coexistence of different flow regimes; local flow conditions might differ considerably from the average flow conditions and large flow variations can be expected in any cross section. This complexity sets a difficulty in establishing the ranges within which transitional bed features are likely to occur.

- The validity of empirical diagrams for bedform stability phases found in literature could not be tested with data from the experiments of this work, either because the ranges of variables of the new experimental data were outside of the limits of the borders between bedform phases in the diagrams, or because the diagrams did not consider a distinction for the range of values explored between antidunes and transitional regime. However, approximate extrapolations of the borders of stability phases were proposed to extend the ranges of validity of the diagrams.
- Empirical bedform stability diagrams do not distinguish separate phases for upstream- and downstream-migrating antidunes or for two-dimensional and three-dimensional bedforms. Conversely, theoretical bedform stability diagrams developed by Engelund and Hansen (1961) and by Kennedy (1963), consider separated stability fields for upstream- and downstream-migrating antidunes, and the latter distinguishes between two-dimensional and three-dimensional bedforms as well. Comparison with the experimental data of this work showed that Kennedy's theory performed best, since it was able to predict the occurrence of three-dimensional downstream-migrating antidunes and two-dimensional dunes. However, Kennedy's theory neglects transitional bedforms, and although the experimental transitional bedforms were correctly anticipated as being two-dimensional by theory, it erroneously predicted they would move upstream, while they actually moved in the downstream direction.
- A new theory was presented for explaining the direction of movement of antidunes. This theory is based on a simplified analysis of flow hydraulics over antidunes. Results indicated that the boundary between downstream- and upstream-migrating antidunes is given by

$$F > \frac{1}{k}$$

where F is the flow Froude number and k is the wave number, given by $k=2\pi H/\lambda$, being H the mean water depth and λ the antidune wavelength. The new criterion performed well when compared with experimental data of this work, including transitional bedforms, and with data from other authors; accordingly, it was shown that this new criterion supersedes the original criterion presented by Kennedy (1963) for discriminating antidune direction of movement (see Núñez-González and Martín-Vide 2011b).

9.4 FLOW RESISTANCE

For the analysis of flow resistance a linear separation of boundary shear stress was undertaken for the experimental data. Conventional methods were applied for estimating side wall, grain and bedform shear stresses. For the effective shear stress on the bed (skin friction) the reference plane bed method was used, according to the modifications of four different authors. This method was first introduced by Einstein (1950). The results obtained with the different variants of the method were compared between each other using physical and rational basis. According to this comparison, the best performing variant

was that suggested by Engelund and Hansen (1967), considering an equivalent roughness equal to $2.5D_m$, being D_m the mean diameter of the bed material.

The following conclusions were obtained from analysis of the estimated grain related shear stress and form drag for the experimental data, and analysis of other experimental data in literature:

- For bed material coarser than roughly 0.8 mm, plane beds in the transition from lower to upper regime do not occur, and thus conventional flow resistance methods for alluvial beds considering a transition through a plane bed are not valid anymore.
- Form shear stress decreases as bed material becomes coarser, so that the coarser the material the more similar the total bed Shields stress and the effective Shields stresses on the grains are.
- For bed materials finer than coarse sand (<1 mm), approximately, for a given grain size there exist two monotonically increasing relationships between bed Shields stress and grain Shields stress, one for lower-regime and one for upper-regime. Both relationships are separated by a discontinuity in the transitional regime, dependant on the relative water depth (ratio water depth to bed material grain size).
- For bed materials coarser than coarse sand (>1 mm), approximately, for a given grain size there is no discontinuity in the relationship between bed Shields stress and grain Shields stress in the transition from lower- to upper-regime.
- Sand-gravel mixtures exhibited a similar trend as uniform fine gravel and uniform very coarse sand, with no plane bed between lower- and upper-regime, and no discontinuity in the transition from lower- to upper–regime for the relationship between bed Shields stress and grain Shields stress.
- Since upper-regime can be roughly related to critical flow conditions, from elemental bed resistance equations and a power law for the vertical distribution of velocity over a plane bed, it was demonstrated that the Shields stress for the onset of the transitional regime can be estimated with

$$\tau_b *\big|_{F=1} = \frac{\alpha_S^{1/3}}{65.6(S_s - 1)}\left(\frac{H}{D}\right)^{2/3}$$

  where D is the representative grain size of the bed surface, H is mean water depth, S_s is sediment relative density, F is Froude number, and α_S is a constant (≈2.5).
- The following equation was proposed for grain shear stress computations, valid for grain shear stress values lower than unity and for grain sizes in the sand and gravel ranges

$$\tau'* = 0.03 + 0.7\tau_b * F^{0.7}$$

  where F is Froude number, τ'^* is grain Shields stress, and τ_b^* is bed Shields stress.
- For the experimental data, shear stress related to the bedforms was obtained from subtracting skin friction to the total bed shear stress. By computing resistance coefficients, it was found that form resistance for sand beds accounted for more than 45% of the total bed resistance, while for gravel and sand-gravel mixtures it accounted for less than 25%.
- Analysis of resistance coefficients related to bedforms showed that the coefficient of expansion loses due to bedforms is roughly 0.5 for dunes, between 0.2 and 0.4 for downstream-migrating antidunes, and less than 0.2 for upstream-migrating antidunes.

9.5 SEDIMENT TRANSPORT

Conclusions from the analysis of solid discharges in the experimental runs can be summarized as follows:

- From the comparison of the new experimental data with field measurements of sediment transport using dimensionless relations, it was shown that the data set obtained in this work corresponds to exceptionally high sediment transport rates that define an upper bound for the transport observed in natural streams, including ephemeral, seasonal and perennial streams. For similar ranges of dimensionless shear stress, the experimental non-dimensional transport rates were higher than those for field data.
- The performance of ten sediment transport predictors for heterogeneous size material was tested using the new experimental data set. Results showed that no single formula performed well with all of the four bed materials used. It was concluded that defining a best-performing model is rather subjective, as some formulas performed better than others for some particular attributes.
- The performance of most sediment transport formulas relies to a great extent on accurate estimations of the critical shear stress for sediment motion. Sediment discharge estimations are more sensitive to erroneous critical shear stress values for low rather than for high transport rates. Nevertheless, at high transport rates the structure of the transport relation can also lead to important deviations from actual values. Even if the critical shear stress was correctly estimated, the estimations between formulas might vary up to three orders of magnitude.
- The collapse of the experimental data of this work, along with other data in literature for sand-gravel mixtures, was pursued using the reference shear stress method. Unlike the original method, a high reference dimensionless sediment transport rate was considered here. Approximate collapse was found for data with the highest sediment transport rates. Data with low to moderate transport rates showed more dispersion, which was here attributed to partial transport of the gravel size fraction.
- The use of a high reference dimensionless transport rate for pursuing the collapse of data, as it was done in this work, would be adequate for streams or data sets in which no information is available for low sediment transport conditions; this approach could also be adequate for developing an accurate sediment transport model for high transport rates, which would elude the inherent complexities of selective transport and the ambiguities in selecting between surface and subsurface material for computations when an armour layer is formed.
- From comparison with the Shields incipient motion criterion, it was found that the mobility of all of the sediment mixtures analyzed in this work was higher than the expected mobility of uniform material with same representative grain size, except for the mixture with 45% sand content of the present work, whose mobility was slightly lower than for uniform material. Reference shear stresses were approximately 8%, 40%, 33% and 6% lower than their computed unisize counterparts in mixtures with 32%, 55%, 75%, and 90% sand content (data for the three latter mixtures pertain to experimental data from Kuhnle, 1993a).
- A conceptual model was developed to explain different changes in mobility due to sand content observed in the experiments of this work compared to the observations of other authors. The model is based on bed porosity changes with sand content; bed porosity is minimum for the transition from a clast-supported to a matrix of fines bed structure, and is lower the greater the ratio between the coarse and the fine size fractions is. Qualitatively, the model was in agreement with

experimental observations. It was found that the two relations found in literature that consider sand content as an explicit variable would represent a particular case of this more general model, which would take into account variations in critical shear stress due to grain size, and also the ratio between sand and gravel grain sizes.

9.6 SEDIMENT GRAIN SIZE SORTING

Conclusions of the analysis of sediment grain size sorting patterns in the experimental runs with sand-gravel mixtures are summarized as follows:

- Experimental bed surface textures were characterized by patches of similar sediment composition, which were visually identified and sampled. An *a posteriori* analysis of samples from the bed surface patches showed that visual identification of coarse, fine and mixed size patches had a direct correspondence with sand content; for sand contents lower than 30% patches were always classed visually as coarse patches; for sand contents higher than 70% the patches were always visually identified as fine patches; and in the range of 30% and 70% sand content the patches were visually identified either as coarse, fine or mixed. A direct correspondence exists between this visual characterization of the bed surface in patches of similar sediment composition, and the limit between a bed with a framework-supported gravel and a bed formed by a sand matrix; for framework gravel the sand grains occupy the voids between gravel clasts, and thus visually, if some voids are free of sand, the impression to the naked eye is that the bed is coarse and mainly composed of the large material. Otherwise, if the pores are completely filled with sand, as would occur for sand contents higher than 30%, the visual impression is that the bed is composed of a mixture of fines and coarse material.
- A new practical method was developed to characterize the bed surface texture according to sand content. The basis of the method was the limit for a change in bed structure, from gravel-supported to sand matrix, according to sand content. Fine, coarse and mixed patches visually identified during the experiments were reclassified as pertaining to a fine patch if sand content was higher than 70%, to a coarse patch if sand content was lower than 30%, and to a mixed size patch if sand content was in the range of 30% and 70%. With this method it was possible to introduce a qualitative basis in the subjective visual characterization of bed surface texture. The method showed to be practical and allowed a direct comparison between samples taken on different runs.
- The most general sediment sorting patterns observed in the experiments, i.e. coarsening of the centre of the channel and of bar troughs, and fining up- and wall-wards, were related to the different conditions of movement of sand and gravel. Sand and gravel moved as bedload in most of the experimental runs, but the trajectories of sand particles could be larger than the trajectories of gravel grains. Furthermore, sand could travel at higher elevations than gravel by bouncing and by being ejected from bedform crests. Fining up and wallwards was related to the bouncing and longer trajectories followed by sand in comparison to gravel, while coarsening of the central section and of lower bed layers was related to the process by which coarser particles tend to be more directly directed to topographic lows than fine particles; also, the force balance between drag and gravity could have promoted the trend for coarse particles to move preferentially through the channel center, where deep scour holes were formed by the rooster tails, and to fine

material to move preferentially along the sides, where it was able to climb up the positive slope of the bedforms toward the channel walls.

- Bed erosion patterns evidenced that the highest local bed shear stresses occurred at the center of the channel, promoted by the steep rooster tails. Nevertheless, two main factors prevented the zone of maximum shear stress matching with a maximum average sediment transport rate; these factors were the periodical distribution of maximum shear stress in isolated peaks, and a high transversal flux of sediment promoted by bedforms. Coarsening of the center of the channel contributed to a lesser extent to the transversal mass transfer balance.
- Grain size distributions for substrate material had less variability and were in average more similar to the feeding material than surface material, thus providing support to the common practice of using substrate material characteristics for bulk sediment transport computations.
- The most important discontinuity in substrate material grain size distributions was found when open-framework gravel deposits formed; sand content in these deposits was much lower than sand content of the feeding material.
- The final bed surface texture was sensitive to flow conditions and sediment supply rates even when the grain size distribution of the bed and supplied material was kept constant in between runs.
- Supercritical flows (or bed Shields stresses higher than 0.22) had a higher capacity than subcritical flows to segregate bed material into well-sorted patches, irrespective of the grain size distribution of the supplied material. These results are complementary to results by Gran et al. (2006) for experiments in which sand content in the supplied material was varied for a narrow range of flow conditions (Froude numbers between 1.1 and 1.6); these authors found that the shift from a sand- to a gravel-dominated bed occurs for a narrow range of sand contents (between 10 and 30%), while the current experiments demonstrate that patchiness formation is sensitive to flow conditions, being high Froude numbers (or high Shields stresses) more effective in segregating material into well-sorted patches.
- A particular pattern of sediment sorting in the experiments produced an almost horizontal lamina composed of fine material at the basal surface of the migrating bedforms. It was demonstrated that such lamina was formed by the infiltration of the finest particles in motion into the bed material. Equations were derived and a numerical model was developed for analyzing the infiltration of fines in a bed composed of an heterogenoues mixture of grain sizes. The model showed good agreement when compared to the experimental results of this work, and data in literature.

9.7 CHANNEL MORPHOLOGY

Conclusions regarding the relevance of the research in this work for channel morphology are summarized as follows:

- The ranges of Shields stresses in the experiments were typical of transitional channels, for which a portion of the bed material moves as bedload and the other in suspension. For the experiments, most of the material moved as bedload, thus, experimental morphologies corresponded to those found in transitional channels and gravel-bed rivers. Such channels tend to develop lateral bars by lateral and vertical accretion, and are characterized by irregular lateral instability that can evolve in meanders.

- Experimental hydraulic geometries and flow conditions resembled to those typical of gravel-bed rivers, particularly most of the morphologies preserved at the end of the experiments showed a configuration of alternate bars, and a thalweg with deep zones alternating with topographic highs in an undulating pattern. These morphologies keep close similarities to pool-riffle sequences common of gravel-bed rivers with gradients in the range of 0.001 to 0.03. Hence, the experimental results supply with further evidence of the conditions required for the formation of pool-riffle morphologies, and their relation with migrating alternate bars.
- The experimental bars in the current experiments corresponded to a lower limit for channel width-to-depth ratios, bar wavelengths and bar heights, for those values commonly reported in literature for experimental alternate bars. This new data set fills the gap for alternate bar formation in the full range of wavelength-channel width and bar height-depth ratios observed in natural streams.
- Although theoretical models and some experimental evidence in literature indicate that sediment heterogeneity has an effect in reducing bar wavelength and height, the scatter of the data in the experiments of this work did not allow distinguishing significant differences between bars formed with uniform sand and uniform gravel, with those formed with sand-gravel mixtures. More evident were changes in bar geometry with different flow conditions; a slight trend toward a decrease of bar steepness with Froude number was apparent.
- Bar wavelength was in close correlation with the length of surface short-crested waves; there must have occurred a strong interaction between stationary cross waves, antidunes and bars. Since there are no other reports in literature of alternate bars coexisting with short-crested antidunes, the experiments herein reported can be considered as an exceptional case, with alternate bars occurring and strongly interacting with mesoscale bedforms and short-crested stationary waves. Also, these experiments give evidence of formative bedforms for pool-riffle morphologies in supercritical and transcritical flows.
- Experimental patterns of bed surface sediment sorting corresponded well to general patterns observed on bars in natural streams. Particularly, downbar and lateral fining, and a coarse thalweg, common features of pool-riffle morphologies in straight channels, were reproduced by the preserved experimental morphologies. Also, the trend for sediment on the bars being finer than the reach-average grain size, which occurs in coarse gravel-bed rivers with low supply, was evident in the experimental beds. These observations have repercussions for the selection of sediment sampling locations in ephemeral-streams.

9.8 TORRENTIAL EPHEMERAL STREAMS

The new experimental data are useful for the study of flow regimes which are likely to occur in moderately steep ephemeral rivers, for which few experimental and field data are available. The following conclusions regarding torrential ephemeral streams can be advanced according to the analysis of the experimental results:

- The experiments were able to adequately reproduce the condition of exceptionally high flow discharges and very high sediment transport capacity of ephemeral streams prone to flash-floods. Instead of the wide channels common to ephemeral and gravel-bed streams, the experiments depicted a condition of an alluvial straight channel, laterally confined by vertical walls. Channel widths for the experiments were in average 30% to 40% those in gravel-bedded and ephemeral streams.

- Supercritical flows are not common in natural streams, however, flow in flash-flood events in ephemeral streams can be supercritical; the experimental flows reproduced this torrential condition, with Froude numbers close to and above the critical value.
- The experiments reproduced the same orders of magnitude of Shields stress values in torrential ephemeral streams. These values ranged approximately between 3 to 30 times the critical Shields condition (considering total bed shear stress, i.e., without partition in grain and form stresses). Moreover, the lack of a coarse surface layer in the experimental bed configurations was in correspondence with observations in ephemeral streams in field.

9.9 EFFECT OF SAND CONTENT

The experiments comprising the new data set included four run series, each for a different type of sediment; two run series were performed with uniform material, namely, sand and gravel, and the rest with two mixtures of the two uniform materials. Comparison between run series allowed distinguishing trends that can be related to the sand content of the material, whose average experimental values were 0%, 32%, 45% and 100%. In general, it was found that the shift from sand to gravel behavior in different process is strongly non-linear, with sharp transitions not in correspondence with the gradual increments in sediment mean diameter as sand content increases. The following conclusions were obtained from comparison of run series with different sand contents, and from links to other data in literature:

- Transitional regime, in between lower- and upper-regimes, covers progressively narrower ranges of Froude numbers and occurs for lower Froude numbers the higher the sand content of the sediment in motion is. Results suggested that between 45% and 100% sand content, the range of Froude numbers in the transitional-regime would be reduced by a factor of 3.
- Bedforms in sediment with 100% sand are steeper than bedforms in gravel and in sand-gravel mixtures. Even small amounts of gravel can suppress the development of steep bedforms.
- Bedforms in 100% sand beds are steeper than bedforms in gravel and sand-gravel mixtures. Hence, flow resistance related to form drag can be significantly higher for very high sand contents in comparison to gravel and mixtures with moderately to high sand contents. The shift from gravel to sand behavior, in terms of form resistance, would require very high proportions of sand in motion.
- For sand contents higher than roughly 30%, flow resistance related to grain roughness is much more similar to a bed composed of 100% sand, than to a bed composed only of gravel. This is the same boundary for the change in bed structure between a gravel framework and a sand matrix.
- Total bed resistance is lower for sand-gravel mixtures than for uniform gravel and uniform sand. This is related to the low form drag in mixtures compared to sand beds, and to the lower grain resistance for mixtures than for pure gravel beds.
- The mobility of bed material is increased with sand content, with an abrupt increment for roughly 30% sand contents. The higher the ratio between the gravel and the sand, the higher the increment in sediment mobility.

9.10 FUTURE RESEARCH

The conclusions presented above are modest contributions to topics that deserve deeper developments in order to provide more fundamental advances to the current state of knowledge in fluvial morphodynamics. General ideas are summarized as follows, for future developments in these different topics and also to improve the work herein presented.

Mobile-bed experiments

- The experimental techniques and the flume operation used in this work can be applied to study other sediment transport regimes. Particularly, the new flume has enhanced capabilities to study bed coarsening and fining processes for variations in the grain size composition of the supplied material. Also, the opportunity of obtaining real-time measurements of the sediment load in the channel with the load cells of the hoppers would allow performing experiments to study the sediment transport and bed texture adjustments to changes in the grain size distribution of the feeding material.
- For development of the conceptual model for incipient motion of heterogeneous material as a function of sand content (presented in Chapter 6), an experimental campaign would be required to test sediment mixtures with different grain size ratios between sand and gravel; along the same line, more relative proportions of sand in the mixtures should be tested in order to obtain a better quantitative definition of the effect of sand content in the mixture mobility for a wide range of conditions.

Stationary waves and antidunes

- Theoretical bedform stability analyses have been performed by different authors to study bedforms and bar instability, nevertheless, no theory has been developed to study the coexistence of different species of bedforms. For the particular case of antidunes, such an analysis would be useful to elucidate the likely interactions between transversal cross-waves, antidunes and alternate bars.
- The role of the sediment characteristics in the formation of either downstream- or upstream-migrating antidunes deserves theoretical and experimental attention. Particularly, a thorough description of the fundamental differences in movement and deposition patterns of particles for either type of bedform is needed. New experimental techniques, like high-speed video, would be useful for such investigation.

Sediment transport

- To validate the use of the reference shear method for the collapse of sediment transport data with a high reference dimensionless sediment transport value, as it was used here, the method must be applied to larger data sets of field and experimental measurements. Of particular interest would be to determine a reference sediment transport value for which the effects of partial transport and bed surface coarsening are no more relevant.
- Analysis of data sets in literature and performance of further experimental campaigns with sand-gravel mixtures would be required to develop the conceptual model presented in this work for sediment mobility based on sand content and bed porosity. Also, a thorough theoretical development would be required to obtain practical functions for such a model, including hiding-exposure and sand content effects in the same model.

Sediment grain size sorting

- No analysis was performed in this work of the effect of flow conditions on the relative area occupied by each class of surface texture patches. This analysis could be performed by measuring approximate areas on the areal photographs taken at the end of the experiments.
- The numerical model developed for analysis of fine sediment infiltration can be used for different conditions. For instance, to test in which conditions fines infiltration would affect the total sediment load, or to study the maximum volumes of fines supplied to a river to alter the habitat of particular species.
- For perennial rivers prone to extreme floods, bed surface texture after such extreme events can be similar as that found in the experiments of this work. For low flows incipient motion and bed resistance could be affected by the history of flows. For gaining knowledge on bed and flow dynamics, future research could study the sensitivity of hiding-exposure coefficients for sediment transport and of bed resistance coefficients after the passage of extreme events with high sediment supply and supercritical flows.

Channel morphology

- The morphologies observed in the experiments resembled morphologies typical of gravel bed rivers; nevertheless, the sand and gravel used in the experiments were uniform materials, while in most natural rivers it is more common that coarse and fine fractions exhibit an extended grain size distribution. Future developments could be directed to explore theoretically and experimentally the effect of sediment heterogeneity in channel morphology for transcritical and supercritical flows.
- The dataset here obtained is useful for testing morphodynamic models. Future research can be oriented to model numerically the processes observed in the experiments.
- This work focused on mobile-bed equilibrium states, future work could study transient morphological states, i.e. the path to attain equilibrium, in different aspects. Of particular interest is the interaction between flow, bed surface texture, and bedforms, to answer questions of the type: how determinant is this interaction in the type of equilibrium attained? Does flow resistance produced by the transient bedforms determine the pathway to equilibrium?

Torrential ephemeral streams

- Future work should consider the collection of field data for characterizing channel geometry, flow and sediment transport of torrential ephemeral streams, in order to identify morphological similitude and equivalent processes with typical gravel-bed rivers.
- The analysis of the experiments performed here was focused on uniform flow and morphodynamic equilibrium states; typical hydrographs in torrential ephemeral streams are steep; an analysis on its own would be required for the transient state, and its effect on ephemeral streams morphodynamics.

REFERENCES

Alexander, J.; Bridge, J. S.; Cheel, R. J. & Leclair, S. F. (2001), 'Bedforms and associated sedimentary structures formed under supercritical water flows over aggrading sand beds', *Sedimentology* **48**, 133-152.

Alexander, J. & Fielding, C. (1997), 'Gravel antidunes in the tropical Burdekin River, Queensland, Australia', *Sedimentology* **44**, 327-337.

Allan, A. F. & Frostick, L. (1999), 'Framework dilation, winnowing, and matrix particle size; the behavior of some sand-gravel mixtures in a laboratory flume', *Journal of Sedimentary Research* **69**(1), 21-26.

Almedeij, J. H. & Diplas, P. (2003), 'Bedload transport in gravel-bed streams with unimodal sediment', *Journal of Hydraulic Engineering* **129**(11), 896-904.

Almedeij, J. H.; Diplas, P. & Al-Ruwaih, F. (2006), 'Approach to separate sand from gravel for bed-load transport calculations in streams with bimodal sediment', *Journal of Hydraulic Engineering* **132**(11), 1176-1185.

Ancey, C. (2001), 'Debris Flows and Related Phenomena', *in Geomorphological Fluid Mechanics, edited by N.J.Balmforth and A. Provenzale, Lecture Notes in Physics (Springer, Berlin)* **582**(DOI: 10.1007/3-540-45670-8_21), 528-547.

Anderson, A. G. (1953), 'The characteristics of sediment waves formed by flow in open channels', *Third Midwest Conference on Fluid Mechanics, University of Minnesota, Minneapolis, Minn.*.

ASCE, Task Force (2002), 'Flow and transport over dunes', *Journal of Hydraulic Engineering* **128**(8), 726-728.

Ashida, K. & Michiue, M. (1972), 'Study on hydraulic resistance and bedload transport rate in alluvial streams', *Transactions, Japan Society of Civil Engineering, No. 20, Oct.*, 59-69.

Barnolas, M.; Atencia, A.; Llasat, M. C. & Rigo, T. (2008), 'Characterization of a Mediterranean flash flood event using rain gauges, radar, GIS and lightning data', *Advances in Geosciences*(17), 35-41.

Barrera, A.; Barriendos, M. & Llasat, M. C. (2005), 'Extreme flash floods in Barcelona County', *Advances in Geosciences*(2), 111-116.

Benett, J. P. (1995), 'Algorithm for resistance to flow and transport in sand-bed channels', *Journal of Hydraulic Engineering* **121**(8), 578-590.

van den Berg, J. H. & van Gelder, A. (1998), 'Disscussion to: Flow and sediment transport over large subaqueous dunes: Fraser River, Canada', *Sedimentology* **45**, 217-221.

van den Berg, J. H. & van Gelder, A. (1993), 'A new bedform stability diagram, with

emphasis on the transition of ripples to plane bed in flows over fine sand and silt', *Spec. Publs Int. Ass. Sediment.* **17**, 11-21.

Beshta, R. L. & Jackson, W. L. (1979), 'The intrusion of fine sediments in a stable gravel bed', *Journal of the Fisheries Research Board of Canada* **36**, 204-210.

Blom, A. (2008), 'Different approaches to handling vertical and streamwise sorting in modeling river morphodynamics', *Water Resources Research* **44**(W03415), 16 pp.

Blom, A.; Ribberink, J. S. & Vriend, H. J. (2003), 'Vertical sorting in bed forms: Flume experiments with natural and a trimodal sediment mixture', *Water Resources Research* **39**(2), 1025, 13 pp.

Blondeaux, P. & Seminara, G. (1985), 'A unified bar-bend theory of river meanders', *Journal of Fluid Mechanics* **157**, 449-470.

Bracken (née Bull), L. J.; Cox, N. J. & Shannon, J. (2008), 'The relationship between rainfall inputs and flood generation in south–east Spain', *Hydrological Processes* **22**, 683-696.

Breakspear, R. (2008), 'Hydrodynamics and sedimentary structures of antidunes in gravel and sand mixtures', *PhD Thesis* University of Southampton.

Bregoli, F. (2008), 'Setting of an experimental flume and first experiments in gravel-bed river's morphodynamics' (in Italian), *Corso di Laurea Specialistica in Ingegneria per la Tutela dell'Ambiente e del Territorio, Università degli Studi di Firenze, Facoltà di Ingegneria.*

Bridge, J. & Best, J. (1997), 'Preservation of planar laminae due to migration of low-relief bed waves over aggrading upper-stage plane beds: comparison of experimental data with theory', *Sedimentology* **44**(253), 253-262.

Bridge, J. S. (2003), *Rivers and Floodplains. Forms, Processes and Sedimentary Record.* Oxford: Blackwell Publishing, 416 p.

Brownlie, W. R. (1981), 'Prediction of flow depth and sediment discharge in open channels', *Report No. KH-R-43A, W. M. Keck Laboratory of Hydraulics and Water Resources, California Institute of Technology, Pasadena, California, USA*, 232 p..

Buffington, J. M. & Montgomery, D. R. (1997), 'A systematic analysis of eight decades of incipient motion studies, with special reference to gravel-bedded rivers', *Water Resources Research* **33**(8), 1993-2029.

Bunte, K. & Abt, S. R. (2001), *Sampling surface and subsurface particle-size distributions in wadable gravel- and cobble-bed streams for analyses in sediment transport, hydraulics, and streambed monitoring.* General Technical Report RMRS-GTR-74. Fort Collins,CO: U.S. Department of Agriculture, Forest Service, Rocky Mountain Research Station. 428 p. http://www.fs.fed.us/rm/pubs/rmrs_gtr74.html

Camarasa-Belmonte, A. M. & Segura-Beltrán, F. (2001), 'Flood events in Mediterranean ephemeral streams (ramblas) in Valencia region, Spain', *Catena*, 229-249.

Carling, P. A. (1999), 'Subaqueous gravel dunes', *Journal of Sedimentary Research* **69**(3), 534-

545.

Carling, P. A. (1984), 'Deposition of fine and coarse sand in an open-work bed', *Canadian Journal of Fisheries and Aquatic Sciences* **41**, 263-270.

Carling, P. A. & Breakspear, R. M. D. (2007), 'Gravel dunes and antidunes in fluvial systems', *River, Coastal and Estuarine Morphodynamics: RCEM 2007 – Dohmen-Janssen & Hulscher (eds)Taylor & Francis Group, London, ISBN 978-0-415-45363-9*.

Carling, P. A. & Breakspear, R. M. D. (2006), 'Placer formation in gravel-bedded rivers: A review', *Ore Geology Reviews* **28**, 377-401.

Carling, P. A. & Glaister, M. S. (1987), 'Rapid deposition of sand and gravel mixtures downstream of a negative step: the role of matrix-infilling and particle-overpassing in the process of bar-front accretion', *Journal of the Geological Society* **144**(4), 543-551.

Carling, P. A. & Shvidchenko, A. B. (2002), 'A consideration of the dune:antidune transition in fine gravel', *Sedimentology* **49**, 1269-1282.

Chang, Y.; Simons, D. & Woolhiser, D. A. (1971), 'Flume experiments on alternate bar formation', *J. Waterways Harbors Coastal Eng. Div. Am. Soc. Civ. Eng.* **97**, 155–165

Chanson, H. (2000), 'Boundary shear stress measurements in undular flows: Application to standing wave bed forms', *Water Resources Research* **36**(10), 3063-3076.

Chanson, H. (1999), 'Critical flow constrains flow hydraulics in mobile-bed streams: A new hypothesis - Comment', *Water Resources Research* **35**(3), 903-907.

Charlton, F. G.; Brown, P. M. & Benson, R. W. (1978), 'The hydraulic geometry of some gravel rivers in Britain', *Rep. No. INT 180, Hydraulics Research Station, Wallingford, England, 48*.

Chaudhry, M. H. (1993), *Open-Channel Flow*, Prentice Hall, 483 p.

Cheel, R. J. (2005), *Introduction to clastic sedimentology,* Course Notes. Department of Earth Sciences, Brock University, Ontario, Canada

Cheng, N. S. (2002), 'Exponential formula for bedload transport', *Journal of Hydraulic Engineering* **128**(10), 942-946.

Chiew, Y. M. (1991), 'Bed features in nonuniform sediments', *Journal of Hydraulic Engineering* **117**(1), 116-120.

Chow, V. T. (1986), *Open-channel hydraulics*, McGraw-Hill, 680 p.

Church, M. (2006), 'Bed material transport and the morphology of alluvial river channels', *Annual Review of Earth and Planetary Sciences* **34**, 325-354.

Church, M. A.; McLean, D. G. & Wolcott, J. F. (1987), 'River Bed Gravels: Sampling and Analysis', *Sediment Transport in Gravel-bed Rivers, Edited by C.R. Thorne, J.C. Bathurst and R.D. Hey*. John Wiley Sons Ltd., 43-88.

Church, M. & Hassan, M. A. (2002), 'Mobility of bed material in Harris Creek', *Water Resources Research* **38**(11).

Church, M. & Jones, D. (1982), 'Channel bars in gravel-bed rivers', *In: Gravel-bed Rivers. Fluvial Processes, Engineering and Management. R.D. Hey; J.C. Bathurst and C.R. Thorne (eds.), John Wiley and Sons, Chichester*, 291-338.

Church, M. & Rood, K. (1983), 'Catalogue of alluvial river data', *Report, Dept. Geography, University of British Columbia, Vancouver, B. C.*.

Colombini, M.; Seminara, g. & Tubino, M. (1987), 'Finite-amplitude alternate bars', *Journal of Fluid Mechanics* **181**, 213-232.

Costa, J. E. (1987), 'Hydraulics and basin morphometry of the largest flash floods in the conterminous United States', *Journal of Hydrology* **93**, 313-338.

Crickmore, M. J. (1970), 'Effect of flume width on bed-form characteristics', *Journal of Hydraulic Engineering* **96**, 473-496.

Cruickshank, C. & Maza, J. A. (1973), 'Flow resistance in sand bed channels', *International Symposium on River Mechanics, IAHR, Bangkok, Thailand, A30:1-9*.

Cui, Y.; Wooster, J. K.; Baker, P. F.; Dusterhoff, S. R.; Sklar, L. S. S. & Dietrich, W. E. (2008), 'Theory of fine sediment infiltration into immobile gravel bed', *Journal of Hydraulic Engineering* **134**(10), 1421-1429.

Dade, W. B. & Friend, P. F. (1998), 'Grain-size, sediment-transport regime, and channel slope in alluvial rivers', *Journal of Geology* **106**, 661-675.

de Almeida, G. A. M. & Rodríguez, J. F. (2011), 'Understanding pool-riffle dynamics through continuous morphological simulations', *Water Resources Research* **47**(W01502, doi:10.1029/2010WR009170).

Dias, R. P.; Teixeira, J. A.; Mota, M. G. & Yelshin, A. I. (2004), 'Particulate binary mixtures: Dependence of packing porosity on particle size ratio', *Industrial & Engineering Chemical Research* **43**, 7912-7919.

Dietrich, E. W. (1982), 'Settling velocity of natural particles', *Water Resources Research* **18**(6), 1626-1982.

Dietrich, W. E.; Kirchner, J.; Ikeda, H. & Iseya, F. (1987), 'The origin of the coarse surface layer in gravel-bedded streams: The role of sediment supply', *Geol. Soc. Am. Abstr. Programs* **19**, 642.

Diplas, P. (1987), 'Bedload transport in gravel-bed streams', *Journal of Hydraulic Engineering* **113**(3), 277-292.

Diplas, P. & Fripp, J. B. (1992), 'Properties of various sediment sampling procedures', *Journal of Hydraulic Engineering* **118**, 955-970.

Diplas, P. & Parker, G. (1992), 'Deposition and removal of fines in gravel-bed streams',

Proc. 3rd Internat. Workshop on Gravel-Bed Rivers, Florence.

Diplas, P. & Sutherland, A. J. (1988), 'Sampling techniques for gravel sized sediments', *Journal of Hydraulic Engineering* **114**(5), 484-501.

Egiazaroff, I. V. (1965), 'Calculation of nonuniform sediment concentrations', *Journal of the Hydraulics Division* **91**(HY4), 225-248.

Einstein, H. A. (1968), 'Deposition of suspended particles in a gravel bed', *Journal of the Hydrauics Division, ASCE* **94**(HY5), 1197-1205.

Einstein, H. A. (1950), 'The bedload function for bedload transportation in open channel flows', *Technical Bulletin No. 1026, U.S.D.A., Soil Conservation Service*, 1-71.

Engelund, F. (1966), 'Hydraulic resistance of alluvial streams', *Journal of the Hydraulics Division ASCE* **92**(2), 315-326.

Engelund, F. & Hansen, E. (1967), 'A monograph on sediment transport', *Technisk Forlag, Copenhagen, Denmark.*

Engelund, F. & Hansen, E. (1966), 'Investigations of flow in alluvial streams', *Acta Polytech. Scand., Ci-35*.

Ferguson, R. I.; Prestegaard, K. L. & Ashworth, P. J. (1989), 'Influence of sand on hydraulics and gravel transport in a braided gravel bed river', *Water Resources Research* **25**(4), 635-643.

Finkers, H. J. & Hoffmann, A. C. (1998), 'Structural ratio for predicting the voidage of binary particle mixtures', *AIChE Journal* **44**(2), 495-498.

Foley, M. G. (1977), 'Gravel-lens formation in antidune-regime flow-A quantitative hydrodynamic indicator', *Journal of Sedimentary Petrology* **47**(2), 738-746.

Friedrich, H.; Melville, B. W.; Nikora, V. & Coleman, S. E. (2005), 'Flume influence on developing dune beds', *XXXI IAHR Congress, Water Engineering for the Future: Choices and Challenges, Seoul, Korea, September 11-16*.

Frings, R.; Kleinhans, M. & Vollmer, S. (2008), 'Discriminating between pore-filling load and bed-structure load: a new porosity-based method, exemplified for the river Rhine', *Sedimentology* (doi: 10.1111/j.1365-3091.2008.00958.x).

Frostick, L.; Lucas, P. M. & Reid, I. (1984), 'The infiltration of fine matrices into coarse-grained alluvial sediments and its implications for stratigraphical interpretation', *Journal of the Geophysical Society* **141**(6), 955-965.

Fuchs, R. A. (1952), 'On the theory of short-crested oscillatory waves. Gravity Waves', *National Bureau of Standards Circular 521*, 187-200.

García, C. & Martín-Vide, J. P. (2001), 'Caracterización granulométrica del lecho móvil de un río de gravas efímero: Aplicación a un tramo de la riera de Les Arenes', *Acta Geologica Hispanica* **36**(1-2), 137-147.

García, H. M. (2007) *Sedimentation engineering: processes, management, modeling, and practice. ASCE manuals and reports on engineering practice No. 110*.

García, H. M. (2006), 'Sediment transport', *Lecture Notes, Ven Te Chow Hydrosystems Lab., Department of Civil and Environmental Engineering, University of Illinois at Urbana-Champaign*.

García, M. H. & Niño, Y. (1993), 'Dynamics of sediment bars in straight and meandering channels: Experiments on the resonance phenomenon', *Journal of Hydraulic Research* **31**(6), 739-761.

Garzón-Heydt, M. G.; Ortega-Becerril, J. A. & Garrote-Revilla, J. (2009), 'Las avenidas torrenciales en cauces efímeros: ramblas y abanicos aluviales. (Torrential floods in ephemeral streams: wadies and alluvial fans.)', *Enseñanza de las Ciencias de la Tierra* **17**(3), 264-276.

Gaume, E.; Valerie, B.; Bernardara, P.; Newinger, O.; Barbuc, M.; Bateman, A.; Blaskovicova, L.; Bloschl, G.; Borga, M.; Dumitrescu, A.; Daliakopoulos, I.; Garcia, J.; Irimescu, A.; Kohnova, S.; Koutroulis, A.; Marchi, L.; Matreata, S.; Medina, V.; Preciso, E.; Sempere-Torres, D.; Stancalie, G.; Szolgay, J.; Tsanis, I.; Velasco, D. & Viglione, A. (2009), 'A compilation of data on European flash floods', *Journal of Hydrology* **367**(1-2), 70-78.

Gibson, S.; Abraham, D.; Heath, R. & Schoellhamer, D. (2009), 'Vertical gradational variability of fines deposited in a gravel framework', *Sedimentology* **56**(doi: 10.1111/j.1365-3091.2008.00991.x), 661-676.

Gilbert, G. K. (1914), 'The transportation of debris by running water', *U.S. Geological Survey, Profesional Paper No. 400*.

Gomez, B. & Church, M. (1989), 'An assessment of bed load sediment transport formulae for gravel bed rivers', *Water Resources Research* **25**(6), 1161-1186.

Graf, W. H. (1991), 'Flow resistance over gravel bed: its consequence on initial sediment movement', *Fluvial Hydraulics of Mountain Regions, Lect. Notes Earth Sci. Ser.* **37**, Springer, New York, 17-32.

Graf, W. H. (1984), 'Hydraulics of sediment transport', *Water Resources Publications*.

Gran, K. B.; Montgomery, D. R. & Sutherland, D. G. (2006),'Channel bed evolution and sediment transport under declining sand inputs', *Water Resources Research* **42**(10).

Grant, G. E. (1997), 'Critical flow constrains flow hydraulics in mobile-bed streams: A new hypothesis', *Water Resources Research* **33**(2), 349-358.

Guy, H. P.; Simons, D. B. & Richardson, E. V. (1966), 'Summary of alluvial channel data from flume experiments, 1956-1961', *U.S. Geol. Survey, Prof. Paper 462-j*.

Habersack, H. M. & Laronne, J. B. (2002), 'Evaluation and improvement of bed load discharge formulas based on Helley–Smith sampling in an alpine gravel bed river', *Journal of Hydraulic Engineering* **128**(5), 484-499.

Hand, B. M. (1969), 'Antidunes as trochoidal waves', *Journal of Sedimentary Petrology* **39**(4), 1302-1309.

Hand, B. M.; Wessel, J. M. & Hayes, M. O. (1969), 'Antidunes in the Mount Toby Conglomerate (Triassic), Massachusetts', *J. Sediment. Petrol.* **39**, 1310-1316.

Hasegawa, K. & Kanbayashi, S. (1996), 'Formation mechanism of step-pool systems in steep rivers and guide lines for the design of construction', *Journal of Hydroscience and Hydraulic Engineering* **40**, 893-900.

Helmbrecht, J. & Martín-Vide, J. P. (2006), 'Principios y ejemplos de cálculo hidráulico torrencial', *Ingeniería Civil, CEDEX,* **141**(Enero), 137-141.

Henderson, F. M. (1966), 'Open channel flow', *McMillan.*

Hooke, J. (2006), 'Human impacts on fluvial systems in the Mediterranean region', *Geomorphology* **79**, 311-335.

Hooke, J. M. & Mant, J. M. (2000), 'Geomorphological impacts of a flood event on ephemeral channels in SE Spain', *Geomorphology* **34**, 163-180.

Ikeda, H. & Iseya, F. (1988), 'Experimental study of heterogeneous sediment transport', *Environmental Research Center Papers* Rep. No. 12, Univ. of Tsukuba, Tsukuba, Japan, 50 pp.

Ikeda, S. (1984), 'Prediction of alternate bar wavelength and height', *Journal of Hydraulic Engineering* **110**, 371-386.

Jaeggi, M. N. R. (1984), 'Formation and effects of alternate bars', *Journal of Hydraulic Engineering* **110**(2), 142-156.

Jarrett, R. D. (1984), 'Hydraulics of high-gradient streams', *Journal of Hydraulic Engineering* **110**(11), 1519-1539.

Julien, P. Y. & Klaassen, G. J. (1995), 'Sand-dune geometry of large rivers during floods', *Journal of Hydraulic Engineering* **121**(9), 657-663.

Julien, P. Y.; Lan, Y. & Berthault, G. (1993), 'Experiments on stratification of heterogeneous sand mixtures', *Bulletin of the Geological Society of France* **164**(5), 649-650.

Karim, M. F. & Kennedy, J. F. (1981), 'Computer-based predictors for sediment discharge and friction factor of alluvial streams', *Iowa Institute of Hydraulic Research Report No. 242, University of Iowa; Iowa City, Iowa.*

Kellerhals, R. & Bray, D. I. (1971), 'Sampling procedures for coarse fluvial sediments', *Journal of the Hydraulics Division ASCE* **97**(8), 1165-1180.

Kellerhals, R.; Neill, C. R. & Bray, D. I. (1972), 'Hydraulic and geomorphic characteristics of rivers in Alberta', *River Engineering and Surface Hydrology Rep.* **72-1,** Research Council of Alberta.

Kennedy, J. F. (1963), 'The mechanics of dunes and antidunes in erodible bed channels',

Journal of Fluid Mechanics **16**, 521-544.

Kennedy, J. F. (1961), 'Stationary waves and antidunes in alluvial channels', *Rep. no. KH-R-2, W. M. Keck Laboratory of Hydraulics and Water Resources, California Institute of Technology*.

Kleinhans, M. G. (2005), 'Dune-phase fluvial transport and deposition model of gravelly sand', *Spec. Publs int. Ass. Sediment* **35**, 75-97.

Kleinhans, M. G. (2004), 'Sorting in grain flows at the lee side of dunes', *Earth-Science Reviews* **65**, 75-102.

Kleinhans, M. G. (2002),'Sorting out sand and gravel: sediment transport and deposition in sand-gravel bed rivers', PhD thesis, Netherlands Geographical Studies 293, The Royal Dutch Geographical Society/Faculty of Geographical Sciences, Utrecht University.

Kleinhans, M. G.; Wilbers, A. W. E.; De-Swaaf, A. & Berg, J. H. V. D. (2002), 'Sediment supply-limited bedforms in sand-gravel bed rivers', *Journal of Sedimentary Research* **72**(5), 629-640.

Kleinhans, M. G. & van Rijn, L. C. (2002), 'Stochastic prediction of sediment transport in sand-gravel bed rivers', *Journal of Hydraulic Engineering* **128**(4), 412-425.

Komar, H. & Shih, S. (1992), 'Equal mobility versus changing bed load grain sizes in gravel-bed streams', *in Dynamics of Gravel-bed Rivers, edited by P. Billi et al., Chap. 5, John Wiley, New York*, 73-106.

Kuhnle, R. A. (1993a), 'Incipient motion of sand-gravel sediment mixtures', *Journal of Hydraulic Engineering* **119**(12), 1400-1415.

Kuhnle, R. A. (1993b), 'Fluvial transport of sand and gravel mixtures with bimodal size distributions', *Sedimentary Geology* **85**, 17-24.

Kuhnle, R. A.; Horton, J. K.; Bennett, S. J. & Best, J. L. (2006), 'Bed forms in bimodal sand–gravel sediments: laboratory and field analysis', *Sedimentology* **53**(3), 631-654.

Kuhnle, R. A. & Southard, J. B. (1990), 'Flume experiments on the transport of heavy minerals in gravel-bed streams', *Journal of Sedimentary Petrology* **60**(5), 687-696.

Lanzoni, S. (2000), 'Experiments on bar formation in a straight flume 1. Uniform sediment', *Water Resources Research* **36**(11), 3337-3349.

Lanzoni, S. (2000), 'Experiments on bar formation in a straight flume 2. Graded sediment', *Water Resources Research* **36**(11), 3351-3363.

Lanzoni, S. & Tubino, M. (1999), 'Grain sorting and bar instability', *Journal of Fluid Mechanics* **393**, 149-174.

Laronne, J. B. & Reid, I. (1993), 'Very high rates of bedload sediment transport by ephemeral desert rivers', *Nature* **366**(11), 148-150.

Laronne, J. B.; Reid, I.; Yitshak, Y. & Frostick, L. E. (1994), 'The non-layering of gravel

streambeds under ephemeral flood regimes', *Journal of Hydrology* **159**, 353-363.

Laursen, E. M. (1958), 'The total sediment load of streams', *Journal of the Hydraulics Division ASCE* **84**(HY1), 1-36.

Leclair, S. F. & Bridge, J. S. (2001), 'Quantitative interpretation of sedimentary structures formed by river dunes', *Journal of Sedimentary Research* **71**, 713-716.

Lisle, T. E. (1989), 'Sediment transport and resulting deposition in spawning gravels, North Coastal California', *Water Resources Research* **25**(6), 1303-1319.

Lunt, I. A. & Bridge, J. S. (2007), 'Formation and preservation of open-framework gravel strata in unidirectional flows', *Sedimentology* **54**, 71-87.

Maddux, T. B.; McLean, S. & Nelson, J. M. (2003), 'Turbulent flow over three-dimensional dunes: 2. Fluid and bed stresses', *Journal of Geophysical Research* **108**.

Marion, A. & Fraccarollo, L. (1997), 'New conversion model for areal sampling of fluvial sediments', *Journal of Hydraulic Engineering* **123**(12), 1148-1151.

Martín-Vide, J. P.; Rodríguez-Máñez, E.; Ferrer-Boix, C.; Núñez-González, F. & Vilalta, M. (2012), 'Estudio morfodinámico del río Fluvià. Alcances y métodos frente a la escasez de datos.', *Tecnología y Ciencias del Agua* **3**(3).

Martín-Vide, J. P. & Andreatta, A. (2006), 'Disturbance caused by bed sills on the slopes of steep streams', *Journal of Hydraulic Engineering* **132**(11), 1186-1194.

Martín-Vide, J. P.; Niñerola, D.; Bateman, A.; Navarro, A. & Velasco, E. (1999), 'Runoff and sediment transport in a torrential ephemeral stream of the Mediterranean coast', *Journal of Hydrology* **225**, 118-129.

Maza-Álvarez, J. A. & García-Flores, M. (1996), 'Transporte de Sedimentos', *Capítulo 10 del Manual de Ingeniería de Ríos, Serie del Instituto de Ingeniería No. 584*.

Maza-Álvarez, J. & García-Flores, M. (1986), 'Distribuciones de los tamaños de los sedimentos del fondo en cauces naturales', *Porcs. XII Congreso Latinoamericano de Hidráulica, Vol 3, Sao Paolo, Brasil*, 104-109.

McBride, E. F.; Shepherd, R. G. & Crawley, R. A. (1975), 'Origin of parallel, near-horizontal laminae by migration of bed forms in a small flume', *Journal of Sedimentary Research* **45**(1), 132-139.

Meyer-Peter, E. & Muller, R. (1948), 'Formulas for bedload transport', *Proceedings of the 2nd Congress, IAHR, Stockholm*, 39-64.

Michell, J. H. (1893), 'The highest waves in water', *Phil. Ma.* **36**, 430-437.

Middleton, R.; Brasington, J.; Murphya, B. J. & Frosticka, L. E. (2000), 'Monitoring gravel framework dilation using a new digital particle tracking method', *Computers & Geosciences* **26**, 329-340.

Millar, R. G. (1999), 'Grain and form resistance in gravel-bed rivers', *Journal of Hydraulic Research* **37**(3), 303-312.

Molinas, A. & Wu, B. (2000), 'Comparison of fractional bed-material load computation methods in sand-bed channels', *Earth Surface Processes and Landforms* **25**, 1045-1068.

Montgomery, D. & Buffington, J. M. (1997), 'Channel-reach morphology in mountain drainage basins', *Geological Society of America Bulletin* **109**(5), 596-611.

Mueller, E. R.; Pitlick, J. & Nelson, J. M. (2005), 'Variation in the reference Shields stress for bed load transport in gravel-bed streams and rivers', *Water Resources Research* **41**(W04006, doi:10.1029/2004WR003692).

Neill, C. R. (1968), 'A reexamination of the beginning of movement for coarse granular bed materials', *Report INT 68, Hydraulics Research Station, Wallingford, England.*.

Nelson, J. M. & Smith, J. D. (1989), 'Mechanics of flow over ripples and dunes', *Journal of Geophysical Research* **94**(C6), 8146-8162.

Niño, Y. (1996), 'Inestabilidades en un lecho granular móvil: análisis matemático de formas de fondo', *Ingeniería del Agua* **3**(4), 25-36.

Núñez-González, F. & Martín-Vide, J. P. (2011a), 'Analysis of antidune migration direction', *Journal of Geophysical Research* **116**, F02004, doi:10.1029/2010JF001761.

Núñez-González, F. & Martín-Vide, J. P. (2011b), 'Experiments on erosion and sediment sorting produced by antidunes and alternate bars', *Two-Phase modelling for Sediment dynamics, THESIS 2011 26-28th April, 2011 – Chatou FRANCE.*

Núñez-González, F. & Martín-Vide, J. P. (2010), 'Downstream-migrating antidunes in sand, gravel and sand-gravel mixtures', *River Flow 2010, International Conference on Fluvial Hydraulics, Braunschweig, Germany.*

Núñez-González, F. & Martín-Vide, J. P. (2009), 'Bed resistance and sediment transport experiments in sand, gravel and sand-gravel antidunes', *33th IAHR Congress, Water Engineering for a Sustainable Environment, Vancouver, Canada.*

Paintal, A. S. (1971), 'Concept of critical shear stress in loose boundary open channels', *Journal of Hydraulic Research* **9**, 91-113.

Paola, C. (1989), 'Topographic sorting', *EOS* **70**, 323.

Paola, C. & Borgman, L. (1991), 'Reconstructing random topography from preserved stratification', *Sedimentology* **38**(4), 553-565.

Paola, C. & Seal, R. (1995), 'Grain size patchiness as a cause of selective deposition and downstream fining', *Water Resources Research* **31**, 1395-1407.

Parker, G. (2004a), 'Transport of gravel and sediment mixtures', Chapter 3, Manual 54: 'Sedimentation Engineering', American Society of Civil Engineers.

Parker, G. (2004b), '1D sediment transport morphodynamics, with applications to rivers and turbidity currents', *E-book in: http://cee.uiuc.edu/people/parkerg/*, St. Anthony Falls Laboratory, University of Minnesota.

Parker, G. (1991), 'Selective sorting and abrasion of river gravel. II: Applications.', *Journal of Hydraulic Engineering* **117**(2), 150-171.

Parker, G. (1990), 'Surface-based bedload transport relation for gravel rivers', *Journal of Hydraulic Research* **28**(4), 417-436.

Parker, G. (1978), 'Self-formed rivers with stable banks and mobile bed: Part I, the sand-silt river', *Journal of Fluid Mechanics* **89**(1), 109-126.

Parker, G. & Andrews, E. D. (1985), 'Sorting of bedload sediments by flow in meander bends', *Water Resources Research* **21**, 1361-1373.

Parker, G.; Dhamotharan, S. & Stefan, H. (1982a), 'Model experiments on mobile, paved gravel bed streams', *Water Resources Research* **18**(5), 1395-1408.

Parker, G. & Klingeman, P. C. (1982b), 'On why gravel bed streams are paved', *Water Resources Research* **18**(5), 1409-1423.

Parker, G.; Klingeman, P. C. & McLean, D. G. (1982c), 'Bedload and size distribution in paved gravel-bed streams', *Journal of Hydraulic Engineering* **108**(4), 544-571.

Parker, G. & Toro-Escobar, C. M. (2002), 'Equal mobility of gravel in streams: the remains of the day', *Water Resources Research* **38**(11), 46-1.

Parker, G.; Toro-Escobar, C. M.; Ramey, M. & Beck, S. (2003), 'Effect of floodwater extraction on mountain stream morphology', *Journal of Hydraulic Engineering* **129**(11), 885-895.

Parker, G. & Wilcock, P. R. (1993), 'Sediment feed and recirculating flumes: fundamental difference', *Journal of Hydraulic Engineering* **119**(11), 1192-1204.

Pierson, T. C. (2005), 'Hyperconcentrated flow transition process between water flow and debris flow', *In: Jakob M., Hungr O. (eds) Debris flow hazards and related phenomena. Springer-Verlag, New York*, 159-196.

Pitlick, J. (1992), 'Flow resistance under conditions of intense gravel transport', *Water Resources Research* **28**, 891-903.

Plumley, W. J. (1948), 'Black Hills terrace gravels, a study of sediment transport', *Journal of Geology* **56**, 526-577.

Posada-García, L. (1995), 'Transport of sands in deep rivers', *Ph.D. Dissertation, Department of Civil Engineering, Colorado State University, Fort Collins, Colorado.*

Powell, D. M. (1998), 'Patterns and processes of sediment sorting in gravel-bed rivers', *Progress in Physical Geography* **22**(1), 1-32.

Powell, D. M.; Reid, I. & Laronne, J. B. (2001), 'Evolution of bedload grain-size distribution with increasing flow strength and the effect of flow duration on the caliber of bedload sediment yield in ephemeral gravel-bed rivers', *Water Resources Research* **37**(5), 1463-1474.

Powell, D. M.; Reid, I. & Laronne, J. B. (1999), 'Hydraulic interpretation of cross-stream variation in bedload transport rate in two straight alluvial channels', *Journal of Hydraulic Engineering* **125**(12), 1243-1252.

Proffitt, G. T. (1980), 'Selective transport and armouring of non-uniform aluvial sediments', PhD thesis, Dept. Civil Eng., Univ. of Canterbury, New Zealand, Res. Rept. 80/22.

Recking, A.; Bacchi, V.; Naaim, M. & Frey, P. (2009), 'Antidunes on steep slopes', *Journal of Geophysical Research* **114**(F04025, doi:10.1029/2008JF001216).

Recking, A.; Frey, P.; Paquier, A.; Belleudy, P. & Champagne, J. Y. (2008), 'Feedback between bed load transport and flow resistance in gravel and cobble bed rivers', *Water Resources Research* **44**(W05412).

Reid, I. & Laronne, J. B. (1995), 'Bedload sediment transport in an ephemeral stream and a comparison with seasonal and perennial counterparts', *Water Resources Research* **31**(3), 773-782.

van Rijn, L. (1993), *Principles of sediment transport in rivers, estuaries, coastal seas and coastal seas*, University of Utrecht, Department of Physical Geography, Aqua Publications.

van Rijn, L. C. (1984), 'Sediment transport. Part III: bed forms and alluvial roughness', *Journal of Hydraulic Engineering* **110**(12), 1733-1754.

van Rijn, L. C. (1982), 'Equivalent roughness of alluvial bed', *Journal of Hydraulic Engineering* **108**(10), 1215-1218.

Sakthivadivel, R. & Einstein, H. A. (1968), 'Clogging of porous column of spheres by sediment', *Hydraul. Div. Am. Soc. Civ. Eng.* **94**(5), 1197-1205.

Sala, M. & Inbar, M. (1992), 'Some hydrologic effects of urbanization in Catalan rivers', *Catena* **19**(363-378).

Sambrook Smith, G. H. & Nicholas, A. P. (2005), 'Effect on flow structure of sand deposition on a gravel bed: Results from a two-dimensional flume experiment', *Water Resources Research* **41**(W10405, doi:10.1029/2004WR003817).

Sambrook Smith, G. H. & Ferguson, R. I. (1995), 'The gravel-sand transition along river channels', *Journal of Sedimentary Research* **65**(2a), 423-430.

Sambrook, S. G. H.; Nicholas, A. P. & Ferguson, R. I. (1997), 'Measuring and defining bimodal sediments: Problems and implications', *Water Resources Research* **33**(5), 1179-1185.

Saunderson, H. & Lockett, F. (1983), 'Flume experiments on bedforms and structures at the dune-plane bed transition', *In: International Association of Sedimentologists: Special Publication*

6 Modern and Ancient Fluvial systems, Eds. Collinson, J.D. and Lewin, J., 49-58.

Schälchli, U. (1992), 'The clogging of coarse gravel river beds by fine sediment', *Hydrobiologia* **235-236**(1), 189-197.

Shen, H. W.; fehlman, H. M. & Mendoza, C. (1990), 'Bed form resistances in open channel flows', *Journal of Hydraulic Engineering* **116**(6), 799-815.

Simons, D. B. & Richardson, E. V. (1966), 'Resistance to flow in alluvial channels', *U.S. Geol. Surv. Prof. Pap., 422J, J1-J61*.

Simons, D. B.; Richardson, E. V. & Albertson, M. L. (1961), 'Flume studies using medium sand (0.45 mm)', *US Geol. Survey Water Supply Paper No. 1498-A*, 76 pp.

Singh, A.; Fienberg, K.; Jerolmack, D. J.; Marr, J. & Foufoula-Georgiou, E. (2009), 'Experimental evidence for statistical scaling and intermittency in sediment transport rates', *Journal of Geophysical Research* **114**(F01025, doi:10.1029/2007JF000963).

Smart, G. (2004), 'Exponential formula for bedload transport: discussion', *Journal of Hydraulic Engineering* **130**(5), 473.

Smith, J. D. & McLean, S. R. (1977), 'Spatially averaged flow over a wavy surface', *Journal of Geophysical Research* **82**(12), 1735-1746.

Southard, J. B. (1991), 'Experimental determination of bed-form Stability', *Annual Review of Earth and Planetary Sciences* **19**, 423-455.

Southard, J. B. & Boguchwal, L. A. (1990), 'Bed configuration in steady unidirectional water flows; Part 2, Synthesis of flume data', *Journal of Sedimentary Petrology* **60**(5), 658-679.

Takebayashi, H. & Egashira, S. (2002), 'Alternate bars formed on beds with non-uniform sediment', *Journal of Hydroscience and Hydraulic Engineering* **20**(2), 131-140.

Toffaleti, F. B. (1969), 'Definitive computations of sand discharge in rivers', *Journal of the Hydraulics Division ASCE* **95**(HY1), 225-248.

Trieste, D. J. (1992), 'Evaluation of supercritical-subcritical flows in high-gradient channel', *Journal of Hydraulic Engineering* **118**(8), 1107-1118.

Vanoni, V. A. (1975), *Sedimentation Engineering, ASCE Manual No. 54*. New York.

Verbanck, M. A. (2008), 'How fast can a river flow over alluvium?', *Journal of Hydraulic Research* **46**(Sp. Iss. 1), 61-71.

Wang, S. & White, W. R. (1993), 'Alluvial resistance in transition regime', *Journal of Hydraulic Engineering* **119**(6), 725-741.

Whiting, P. (1996), 'Sediment sorting over bed topography', *In: Advances in Fluvial Dynamics and Stratigraphy, P.A. Carling and M.R. Dawson (eds.), John Wiley and Sons, Chichester*, 203-228.

Whiting, P. S. & Dietrich, W. E. (1991), 'Convective accelerations and boundary shear

stress over a channel bar', *Water Resources Research* **27**, 783-796.

Whittaker, J. G. & Jaeggi, M. N. R. (1982), 'Origin of step-pool systems in mountain streams', *Journal of Hydraulic Division, Proceedings of ASCE* **108**(HY6), 758-773.

Wilcock, P. R. (2004), 'Sediment transport in gravel-bed rivers, with implications for channel change (Lecture notes)', *Summer Short Course: "The principles and practice of stream restoration", August 2004. Univ. of California - Berkeley.*

Wilcock, P. R. (2001), 'Toward a practical method for estimating sediment-transport rates in gravel-bed rivers', *Earth Surface Processes and Landforms* **26**, 1395-1408.

Wilcock, P. R. (1998), 'Two-fraction model of initial sediment motion in gravel-bed rivers', *Science* **280**, 410-412.

Wilcock, P. R. (1993), 'Critical shear stress of natural sediments', *Journal of Hydraulic Engineering* **119**(4), 491-505.

Wilcock, P. R. & Crowe, J. C. (2003), 'Surface-based transport model for mixed-size sediment', *Journal of Hydraulic Engineering* **129**(2), 120-128.

Wilcock, P. R. & Kenworthy, S. T. (2002), 'A two-fraction model for the transport of sand/gravel mixtures', *Water Resources Research* **38**(10), 1194.

Wilcock, P. R.; Kenworthy, S. T. & Crowe, J. (2001), 'Experimental study of the transport of mixed sand and gravel.', *Water Resources Research* **37**(12), 3349-3358.

Wilcock, P. R. & McArdell, B. W. (1993), 'Surface-based fractional transport rates: mobilization thresholds and partial transport of a sand-gravel sediment', *Water Resources Research* **29**(4), 1297-1312.

Wilcock, P. R. & Southard, J. B. (1988), 'Experimental study of incipient motion in mixed-size sediment', *Water Resources Research* **24**(7), 1137-1151.

Wilkinson, S. N.; Rutherfurd, I. D. & Keller, R. J. (2008), 'An experimental test of whether bar instability contributes to the formation, periodicity and maintenance of pool-riffle sequences', *Earth Surface Processes and Landforms* **33**(11), 1742-1756.

Willis, J. C. & Kennedy, J. F. (1978), 'Sediment transport in migrating bed forms', *Proc. Verification of Mathematical and Physical Models in hydraulic Engineering, ASCE, College Park, Md.*, 551-560.

Wong, M. & Parker, G. (2006), 'Reanalysis and correction of bed-load relation of Meyer-Peter and Müller using their own database', *Journal of Hydraulic Engineering* **132**(11), 1159-1168.

Wooster, J. K.; Dusterhoff, S. R.; Cui, Y.; Sklar, L. S.; Dietrich, W. E. & Malko, M. (2008), 'Sediment supply and relative size distribution effects on fine sediment infiltration into immobile gravels', *Water Resources Research* **44**(W03424, doi:10.1029/2006WR005815)

Wren, D. G.; Bennett, S. J.; Barkdoll, B. D. & Kuhnle, R. A. (2005), 'Distributions of

velocity, turbulence, and suspended sediment over low-relief antidunes', *Journal of Hydraulic Research* **43**(1), 3-11.

Wright, S. & Parker, G. (2004a), 'Density stratification effects in sand-bed rivers', *Journal of Hydraulic Engineering* **130**(8), 783-795.

Wright, S. & Parker, G. (2004b), 'Flow resistance and suspended load in sand-bed rivers: simplified stratification model', *Journal of Hydraulic Engineering* **130**(8), 796-805.

Wu, B. & Molinas, A. (1996), 'Modeling of alluvial river sediment transport', *Proceedings of the International Conference on Reservoir Sedimentation, Vol. I, Albertson M.L., Molinas A., Hotchkiss R (eds.). Colorado State University: Fort Collins, Colorado*, 281-325.

Wu, W.; Wang, S. S. Y. & Jia, Y. (2000), 'Nonuniform sediment transport in alluvial rivers', *Journal of Hydraulic Research* **38**(6), 427-434.

Yalin, M. S. (1992), *River Mechanics*, Pergamon Press.

Yalin, M. S. (1972), *Mechanics of sediment transport*, Pergamon, New York.

Yamamoto, K. (1994), 'The study of alluvial rivers', *Sankaidou (in Japanese)*.

Yang, S. & Tan, S. (2008), 'Flow resistance over mobile bed in an open-channel flow', *Journal of Hydraulic Engineering* **134**(7), 937-947.

Yen, B. C. (2002), 'Open Channel Flow Resistance', *Journal of Hydraulic Engineering* **128**(1), 20-39.

Yokokawa, M.; Hasegawa, K.; Kanbayashi, S. & Endo, N. (2010), 'Formative conditions and sedimentary structures of sandy 3D antidunes: an application of the gravel step-pool model to fine-grained sand in an experimental flume', *Earth Surface Processes and Landforms* **35**, 1720-1729.

Yokokawa, M.; Hasegawa, K.; Kanbayashi, S. & Endo, N. (2008), '3D antidunes preserved on fine-grained sand bed in an experimental flume: Genetic conditions and their sedimentary structures', *Marine and River Dune Dynamics - 1-3 April 2008 - Leeds, United Kingdom*, 345-351.

Yu, A. B. & Standish, N. (1991), 'Estimation of the porosity of particle mixtures by a linear-mixture packing model', *Ind. Eng. Chem. Res.* **30**, 1372-1385.

UNIVERSITAT POLITÈCNICA DE CATALUNYA

Escola Tècnica Superior d'Enginyers
de Camins, Canals i Ports

Departament d'Enginyeria Hidràulica, Marítima i Ambiental
Secciò d'Enginyeria Hidràulica i Hidrològica

TESI DOCTORAL

BEDLOAD TRANSPORT OF SAND-GRAVEL MIXTURES WITH ANTIDUNES
FLUME EXPERIMENTS

VOLUME II: APPENDIXES

Francisco Núñez-González

Director de Tesi:
Juan Pedro Martín Vide

Tesi presentada per obtenir el títol de doctor per la
Universitat Politècnica de Catalunya

Barcelona, Abril 2012

TABLE OF CONTENTS

VOLUME I

VOLUME II

APPENDIXES

APPENDIX I

CALIBRATION OF THE EXPERIMENTAL FLUME

CALIBRATION OF AN EXPERIMENTAL FLUME FOR EXPERIMENTS WITH SAND-GRAVEL SEDIMENT MIXTURES

Francisco Núñez González

UPC-UNIVERSIDAD POLITÈCNICA DE CATALUNYA
UCLM-UNIVERSIDAD DE CASTILLA-LA MANCHA

Barcelona, March 2007

CONTENTS

LIST OF SYMBOLS

SYMBOL	VARIABLE	Reference units	SI Units
A_1, A_2	Areas of the two bases of a truncated pyramid, used to calculate the volume of the sediment feeding hopers	$[L^2]$	m^2
a	Constant	-	-
B	Width of the tilting gate	[L]	M
B_f	Width of the gate at the base of the sediment feeder	[L]	M
b	Constant	-	-
C_d	Discharge coefficient for the tilting gate	-	-
c	Constant	-	-
D	Sieve diameter of sediment in the hopper	[L]	m
E_Q	Error between the actual water discharge entering the flume and the selected discharge on the flowmeter display	[L]	m^3/s
E_m	Error between the mean of the fluctuations along time for the actual water discharge entering the flume, and the selected discharge on the display	[L]	m^3/s
e_K	Mean quadratic error for lines fitted to data for calibration of the unloading constant of the feeders	$[M\ T^{-1}]$	kg/s
e_z	Error between the actual and calculated vertical displacement of the channel, for a given slope and horizontal coordinate	[L]	m
g	Acceleration of gravity	$[L\ T^{-2}]$	m/s^2
H	Head of water over the tilting gate	[L]	m
H_c	Water depth in the channel	[L]	m
h	Altitude or perpendicular height of a truncated pyramid, used to calculate the volume of the sediment feeding hoppers	[L]	m
h	water height over the joint of the tilting gate	[L]	m
h_f	Openning of the sluice gate on the base of the hoppers	[L]	m
h_v	Head of water at the triangular notch weir above the apex notch	[L]	m
i	Slope of the channel selected on the digital display	$[L\ L^{-1}]$	m/m
i_o	Actual slope of the channel	$[L\ L^{-1}]$	m/m
K_f	Unloading constant for the sediment feeder/hoppers	$[M\ T^{-1}]$	kg/s
K_{fS}	Unloading constant for the sand feeder/hopper	$[M\ T^{-1}]$	kg/s
K_{fG}	Unloading constant for the gravel feeder/hopper	$[M\ T^{-1}]$	kg/s
L	Length of the tilting gate	[L]	m
n	Manning's roughness coefficient	$[L^{1/6}]$	$m^{1/6}$
n	Run number	-	-
P_a	Opening percentage of the titling gate	-	-
Q_a	Actual instantaneous water discharge entering the channel	$[L^3\ T^{-1}]$	m^3/s
$\overline{Q}_a$	Actual mean water discharge entering the channel	$[L^3\ T^{-1}]$	m^3/s
Q_f	Water discharge given by the flowmeter	$[L^3\ T^{-1}]$	m^3/s
Q_{SF}	Feeding rate of dry sediment by the hoppers	$[M\ T^{-1}]$	kg/s
Q_V	Water discharge calculated at the triangular notch weir	$[M\ T^{-1}]$	kg/s
Q_w	Water discharge	$[L^3\ T^{-1}]$	m^3/s
S_o	Slope of the channel	$[L\ L^{-1}]$	m/m
t	Time	[T]	s
$\%V$	Voltage frequency for the rotating band display	-	-
V_f	Velocity of the rotating band of the hoppers	$[L\ T^{-1}]$	m/s
V_S	Voltage from the load cells in the hoppers	-	V
W	Weight	[M]	kg

W_a	Actual weight in the hopper	[M]	kg
W_d	Measured weight in the hopper	[M]	kg
W_{di}, W_{df}	Initial and final measured weight in the hopper	[M]	kg
W_{dMean}	Mean weight between the initial and final measured weights in the hopper	[M]	kg
W_t	Instantaneous total weight of sediment in the hopper	[M]	kg
w_c	Maximum weight used for the calibration of the load cells	[M]	kg
x	Horizontal coordinate at the channel, with cero at the joint where the flume tilts	[L]	m
y	Vertical coordinate at the channel, with cero at the same level of the channel bottom where the joint at which the flume tilts	[L]	m
Za	Actual vertical displacement of the flume for a given slope and horizontal coordinate	[L]	m
Z_b	Vertical distance from the bottom of the channel to an horizontal plane	[L]	m
Zm	Calculated vertical displacement of the flume for a selected slope at the digital display and a horizontal coordinate	[L]	m
Zw	Water stage upstream from the tilting gate	[L]	m
α	Opening angle of the tilting gate	-	degrees
ε	Porosity of sediment	-	-
ρ_s	Density of sediment	[M L^{-3}]	kg/m^3
$\%\omega$	Water content of the sediment as a percentage by weight, $\%\omega=100*(weight\ of\ water/weight\ of\ solids)$	-	-
ΔW_a	Increment of the actual weight in the hopper	[M]	kg
ΔW_d	Increment of the measured weight in the hopper	[M]	kg

M=units of mass
T=units of time
L=units of length
F=units of force: [F]=[M L T^{-2}]

1. INTRODUCTION

Flumes are an important tool for studying different aspects of streamflow and sediment transport in rivers. Most advances in our knowledge of rivers' morphodynamics and the phenomena involved with the sediment they transport have been possible through experimentation using these devices. The simplest arrangement of a flume would consist of a channel or deposit and a system to introduce and extract water from it. From these three basic elements the system may grow in complexity and size in different manners according to the experimental necessities. In particular, flumes for studying sediment transport phenomena have an additional complexity, as they must deal with granular material, for which management, transport and disposal usually require more complicated solutions than those for water.

In the hydraulics laboratory of the Civil Engineering School of the University of Castilla-La Mancha (UCLM), in Ciudad Real, Spain, a new flume for experiments with mobile granular beds has been constructed. The flume, with a 30 m long channel, has been conceived for carrying out experiments related with the transport of sediment with mixed grain sizes. For the automatic and continuous management of large amounts of sediment, the flume has been equipped with a sediment-recirculating system, whose main innovative feature, which makes it different from usual systems, is that it is capable of separating sand and gravel after they leave from the downstream end of the flume channel and are recirculated to the upper part of the flume. This feature allows a more precise determination of the transport of each of the size fractions. Such a flume opens the experimental perspectives for a wide range of research possibilities, relevant for the study of phenomena related with rivers with non-uniform size sediment beds and for the study of the structures constructed in their channels. Nowadays, research efforts in understanding these phenomena are a relevant issue for river hydraulics fundamental knowledge.

The design of the flume and its sediment-recirculating system was conceived by Professor Juan Pedro Martín Vide and his collaborators in the UCLM (Martín-Vide 1999). The complete project was finished in year 2004. A first experimental campaign using all facilities together in function was carried out during the first half of year 2006. For this, during the autumn and winter of 2005 the whole experimental set-up was tested, calibrated and prepared to fulfill the requirements of the experimental research programmed. In this document a description of the experimental set-up is presented with information about the activities and works performed to prepare it for that first campaign, which was carried out by the author.

The document is organized in the following manner; first, a general description of the flume and its sediment-recirculating system is given; later, a more detailed description of some of the experimental set-up components is exposed, with information about their calibration, testing and works performed to adjust them to the experimental requirements. Next, the range of values for different variables in the flume is summarized, together with the accuracy of the variables given by the instrumentation used for measuring. Finally, some examples are introduced of the operation of the flume using the sediment-recirculating-system. These examples cover the most general cases of mobile-bed experiments in fluvial engineering. At the end, a list of references and a selection of photos of the different elements of the flume are included.

2. GENERAL DESCRIPTION OF THE EXPERIMENTAL SET-UP

The experimental set-up for mobile-bed experiments in the hydraulics laboratory of the UCLM consists of a system for water feeding (Figure A1.1); a tilting flume with a 30 m long channel (27 m useful length), made of glass walls and PVC bottom, with a rectangular cross section 0.75 m wide and 0.65 m deep; and a system for sediment feeding and recirculation. A general sketch of the flume and the sediment feeding and recirculating-system is shown in Figure A1.2 (see also photo P1).

Water is fed to the flume from an elevated regulation deposit with constant water height, which in turn takes the water from an underground general deposit, 1.5 m deep (Figure A1.1), by means of three pumps with a capacity of 90 l/s each. Water is conducted from the regulation deposit to the flume through three horizontal PVC pipes and then through three flexible hoses arranged vertically. As the upper part of the channel is occupied by the flexible hoses and a series of perforated metal screens and superimposed bricks to tranquilize the incoming water, the useful length of the channel is reduced to 27 m. The hydraulic circuit is closed when water leaves the channel and is reintroduced into the underground deposit after spilling over a triangular notch weir (Figures A1.1 and A1.3). Water discharge entering the flume is selected by the user with a tactile screen that is connected with three magnetic flowmeters and an automated system, which according to the required discharge regulates the aperture of the valves in each of the pipes connected to the regulation deposit.

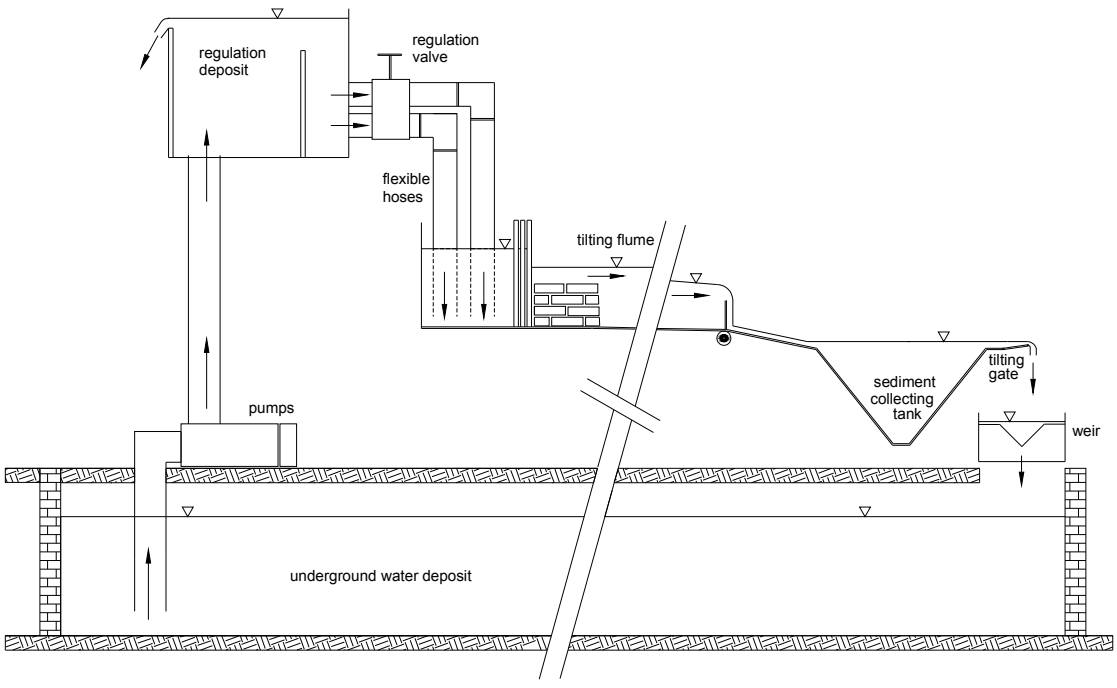

Figure A1.1 Hydraulic circuit

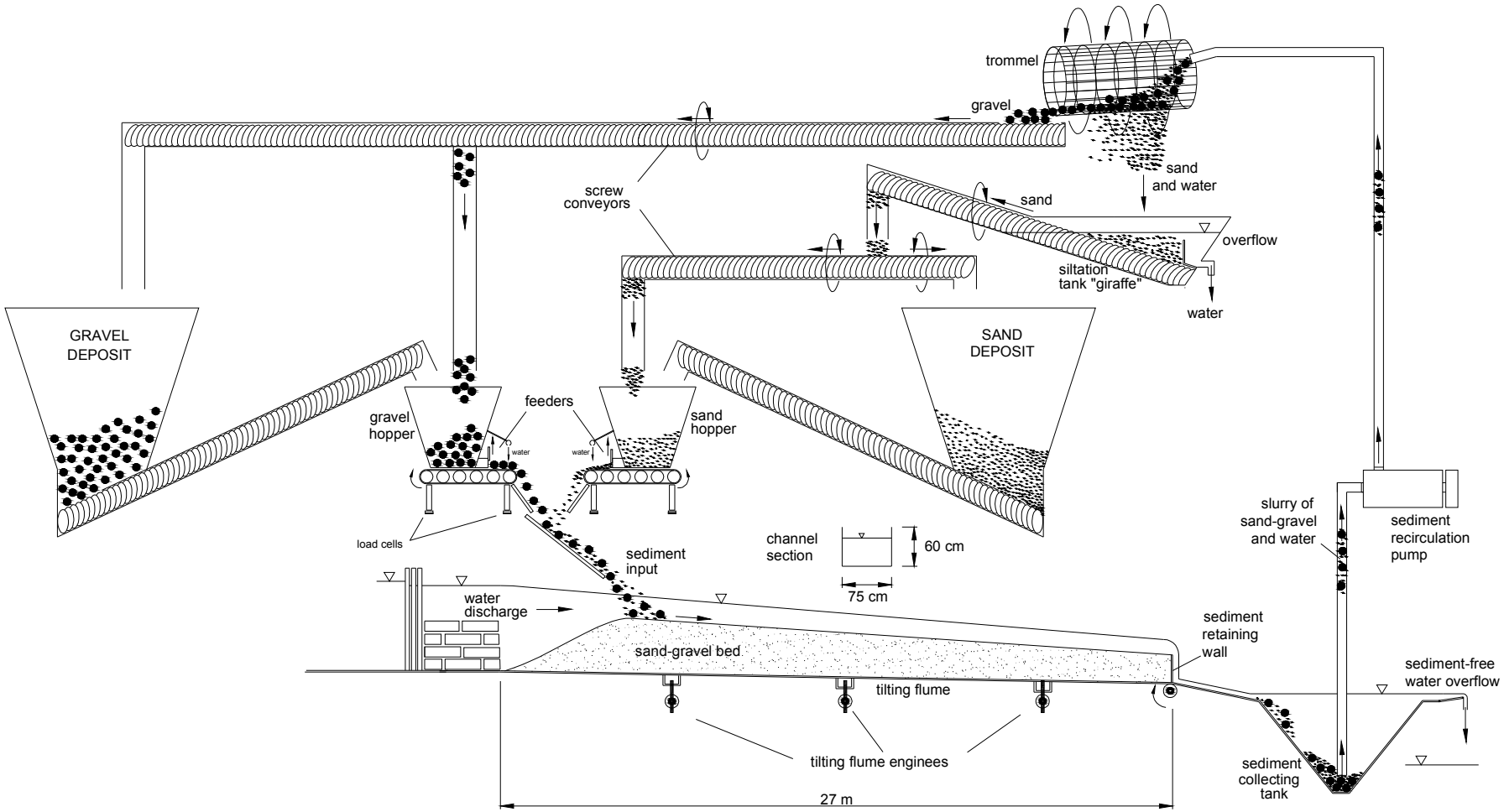

Figure A1.2 Schematic view of the experimental set-up

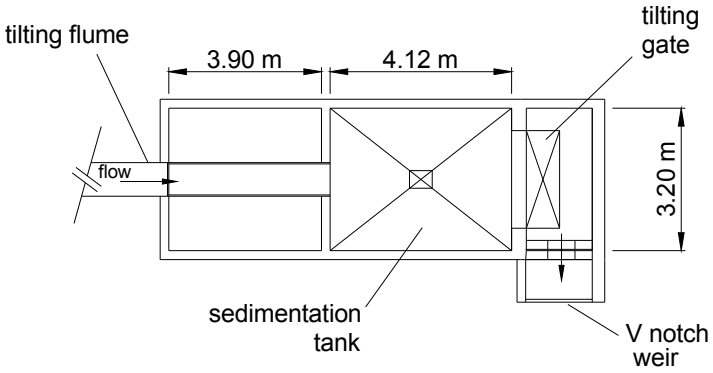

Figure A1.3 Plan view of the downstream end of the experimental set-up

When experiments with water and sediment are performed, at the downstream end of the flume sediment is separated from water by means of a siltation tank, i.e., a deep deposit where sediment settles down and water overflows (see Figures A1.2 and A1.3). The shape of the sediment collecting tank is that of an inverted truncated-squared pyramid, so that sediment would deposit at the center of the tank. A pumping system suctions the sediment from the collecting tank with a small amount of water, and conducts them through a 10 cm diameter pipe to the head of the flume, where an elevated trommel with a fine mesh separates gravel from water and sand. Sand and water pass through the trommel and are then separated in a siltation tank, called “giraffe”. By means of screw conveyors, gravel and sand are taken either to independent deposits or to independent hoppers just above the channel. At the base of the hoppers a rotating band and a gate serve as a regulation system, which allows that the hoppers may be used as sediment-feeders to insert a fixed and constant rate of sediment to the channel or as a continuous by-pass that returns the sediment to the channel at the same rate as it is deposited in the silting tank (although with a lag effect due to the time required for the sediment to go around the recirculation circuit. As will be described further below, it was found that the lag time for the sand fraction was longer than for the gravel).

The sediment-recirculating system and the feeding controls in the hoppers give the flume an enhanced flexibility to adjust to different operational modes, and thus to different experimental conditions. The flume may be operated either in a sediment-feed or a recirculating mode, but also as a hybrid system which combines feed and recirculating; that is, gravel and sand in their individual hoppers are fed to the channel at a constant rate, while the recirculating system collects sediment from the downstream end of the flume, separates sand and gravel and delivers them to their respective hopper/feeder to avoid shortage of material to feed the channel during the experiment. An advantage of this hybrid operation is the possibility of performing long-lasting runs without requiring a huge reserve of fresh material. Also, because the hoppers are mounted on load cells that allow for a real-time measurement of their weight, it is possible to get a precise measurement of the sand and gravel solid discharges by computing the difference between the incoming rate of sediment to the hopper and the constant output (this considering that suction of sediment from the collecting tank at the downstream end of the flume is continuous, avoiding material accumulation). In search of mobile bed equilibrium states in the flume channel, the system operated in this manner

reflects precisely when the equilibrium has been achieved, because this condition occurs when the weight of the material in the hoppers becomes constant (feeding rate turns equal to sediment transport rate in the channel).

It should be taken into account that one of the constraints of operating the flume in the hybrid mode described before, combining feed and recirculating modes, is that if in search of an equilibrium state any size fraction of material in the bed has no mobility (i.e., partial transport occurs, as defined by Wilcock & McArdell 1993) or its representation in the solid discharge is weaker than in the initially fed sediment, the volume rate of this fraction leaving the flume may decrease, and its presence in the hoppers may diminish. In that case, the equilibrium state achieved would be different from that obtained by feeding fresh material. For experiments in which the flow mobilizes all size fractions in the original mixture, tending to the equal mobility (as defined by Parker 1982) such an effect will become negligible. Operation of the flume in the hybrid mode will be equivalent to a "pure" feed operation when all size fractions in the channel are mobilized by the flow. For instance, this condition can be more likely to be attained if a well-sorted coarse fraction in the sediment mixture is used; in that case, partial transport within the gravel fraction of the mixture would be limited to a very narrow range of hydraulic conditions.

3. DESCRIPTION AND CALIBRATION OF SPECIFIC COMPONENTS

Following are described different calibration procedures performed before the first experimental campaign with sediment feed and recirculation was carried out in the flume.

3.1 Flow discharge

Selection of the water discharge that enters the flume is done by means of an automated system that uses a flowmeter to compare the passing discharge with the desired discharge. The desired discharge is selected on a tactile display and the system adjusts the flow to this value by controlling the opening of three valves in the tubes connected to the regulation deposit. For a constant discharge selected on the display, error can be defined as the difference between the actual discharge entering to the flume and the selected discharge on the flowmeter display (Figure A1.4): $E_Q = Q_a - Q_f$; in turn, a mean error may be defined as the difference between the mean of the discharge fluctuations along time and the selected discharge (Figure A1.4): $Em = \overline{Q}_a - Q_f$.

For different discharge values selected on the flowmeter display, measurements were performed at the triangular notch weir at the end of the flume (Figure A1.3) to get and estimate of the error for the discharge values selected. According to de Almeida (2007), the discharge at the triangular notch weir in m^3/s is expressed by

$$Q_V = 1.3647\left(h_v + 0.00085\right)^{5/2} \qquad \text{(A1.1)}$$

where h_v is the head of water at the weir above the apex notch, in meters. Measurements of h_v were carried out when water discharge stabilized after going from one discharge value to another, and were performed with a vernier which precision was ±0.1 mm. Table A1.1 shows values of measured heads of

water at the weir and the corresponding calculated discharges for different selected discharges on the display. Table A1.2 shows the same variables, but for measurements performed for a constant discharge of 80 l/s selected at the display. In Figure A1.5 the error between measured and selected discharges has been plotted against the selected discharges at the flowmeter display for data in both tables.

Dispersion of the measured data observed in Figure A1.5 may be related to fluctuations in the incoming flow discharge to the flume, but also to fluctuations in water level at the weir (and thus in measured h_v values) due to eddies formed at the sedimentation tank and under the tilting gate overflow. Mean error is assumed to be well represented with a line fitted to the data in Figure A1.5, so that

$$Em = -0.016 Q_f - 0.31 \qquad \text{(A1.2)}$$

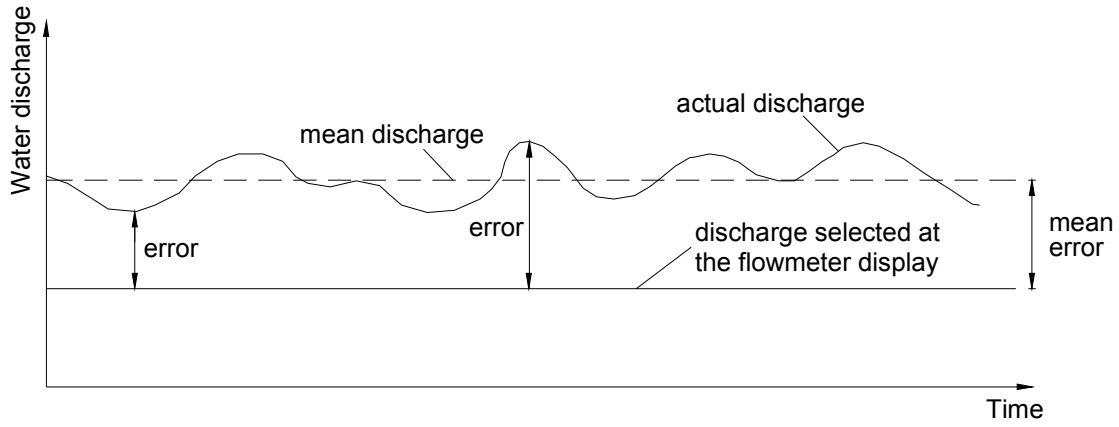

Figure A1.4 Definition of error for the flow discharge passing through the flume

Run	**Q_f = discharge selected (flowmeter) [l/s]**	**h_v = Measured head of water in the weir above apex of notch [mm]**	**Q_V = discharge calculated at the weir [l/s]**	$E = Q_V - Q_f$ **[l/s]**
1	10.00	136.5	9.54	-0.46
2	10.00	136.6	9.56	-0.44
3	12.00	146.0	11.28	-0.72
4	14.50	160.3	14.23	-0.27
5	17.50	170.4	16.56	-0.94
6	21.50	188.8	21.38	-0.12
7	25.00	198.1	24.09	-0.91
8	25.00	199.2	24.43	-0.57
9	26.00	202.1	25.32	-0.68
10	31.00	216.0	29.88	-1.12
11	45.00	254.5	44.97	-0.03
12	45.00	250.5	43.22	-1.78
13	55.00	273.1	53.61	-1.39
14	69.50	300.4	67.98	-1.52
			Average =	-0.78
			Standard Deviation =	0.53

Table A1.1Measured discharges at the triangular notch weir for different selected flow discharges on the flowmeter display.

Run	h_v **= Measured head of water in the weir above apex of notch [mm]**	Q_V **= discharge calculated at the weir [l/s]**	$E = Q_V - Q_f$ **[l/s]**
1	320.3	79.76	-0.24
2	318.4	78.59	-1.41
3	317.6	78.10	-1.90
4	317.8	78.22	-1.78
5	318.4	78.59	-1.41
6	316.9	77.67	-2.33
7	318.1	78.40	-1.60
8	317.8	78.22	-1.78
9	317.6	78.10	-1.90
10	319.0	78.96	-1.04
11	317.9	78.28	-1.72
12	317.8	78.22	-1.78
	Average =	78.43	-1.57
	Standard Deviation =	0.53	0.53

Table A1.2 Measured discharges at the triangular notch weir for a constant discharge Q_f = 80 l/s selected on the flowmeter display.

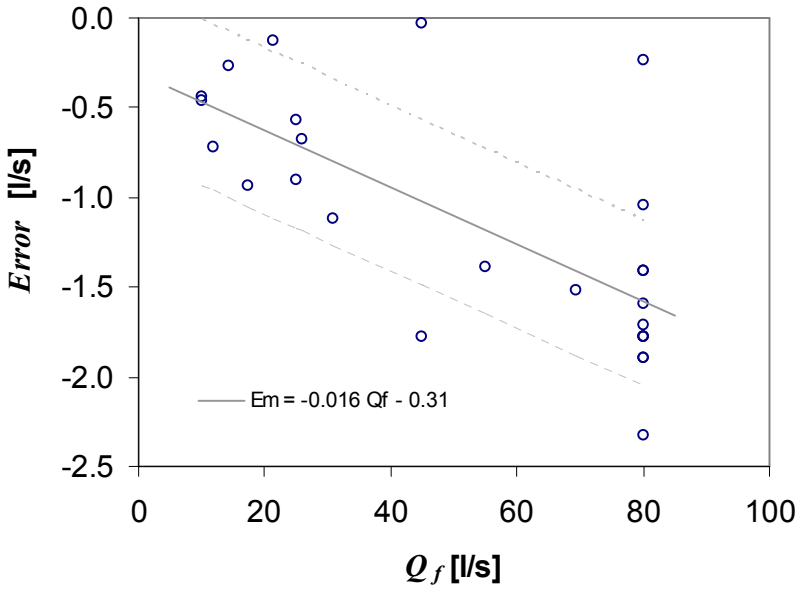

Figure A1.5 Error for measured data in Tables A1.1 and A1.2

We may use the standard deviation of the whole data set related to the estimated mean error function as a measure of the flow discharge precision. Such value is 0.46 l/s, similar to the standard deviations of 0.53 l/s for the individual data sets in tables A1.1 and A1.2. Dashed lines in Figure A1.5 mark the limit of uncertainty for flow discharge values using the standard deviation of the error. Thus, the actual mean discharge passing through the flume may be estimated from:

$$\overline{Q}_a = 0.984 Q_f - 0.31 \pm 0.46 \text{ [l/s]} \qquad \text{(A1.3)}$$

3.2 Tilting gate

Water depth in the channel can be controlled by means of the tilting gate located downstream of the sedimentation tank (see Figures A1.1 to A1.3). Experiments in search for steady uniform flow conditions usually require that the normal water depth prevails along the entire channel. The tilting gate is useful for reaching these conditions, as it can be operated to adjust a water stage in the sedimentation tank that coincides with the water height at the end of the channel. In this manner, the formation of a gradually varied flow in the immediate region upstream from the channel end is avoided.

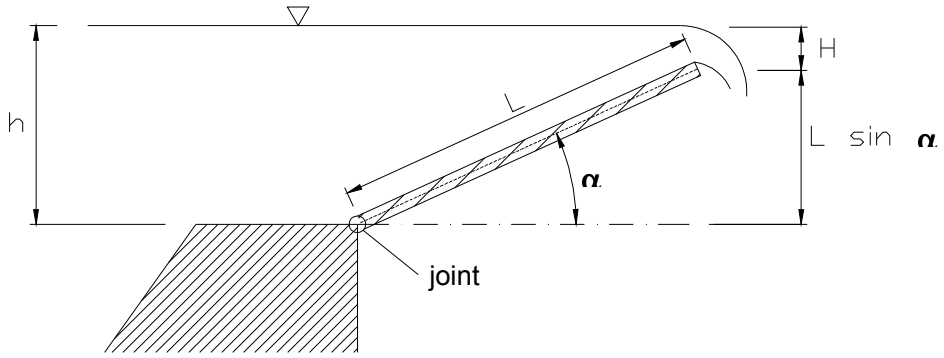

Figure A1.6 Geometric parameters for calculation of the water discharge over the tilting gate

Calibration of the gate was performed with the aim of getting approximate values of the gate opening angle when searching for uniform flow conditions in the channel. The gate is operated electronically, with the disadvantage that the selection of the opening angle required is performed with a manual device which precision is low. The steps for different tilt angles are a function of a percentage of aperture (0% for the gate totally closed at an angle of 60º, 100% for the gate totally fold down, see Figure A1.6) shown digitally only with whole numbers but no decimals.

The relation between the opening percentage of the gate P_a, as shown on the digital display, and its tilt angle α (Figure A1.6) was found to be well described by $\alpha = 60 - 0.75P_a$. For determining the variation of the discharge coefficient due to different gate opening angles, 20 runs were performed with 4 different tilt angles, letting pass given constant water discharges through the flume, measured at the triangular notch weir (Figure A1.1). Data for all runs are shown in Table A1.3. Water stage Z_w upstream from the gate (on the sedimentation deposit) was measured with a pipe attached to the wall of the deposit and tilted 45º. From the geometry of the deposit and the position of the tube, the relation between Z_w and the water height over the joint of the gate h (see Figure A1.6) is $h = 0.027 + \left(\frac{Z_w - 2.1}{\sqrt{2}} \right)$, with Z_w and h in m. Also, from the geometry of the flume we also know that if the water stage at the end of the channel is the same as over the joint of the gate, the relation between the flow depth H_c at the channel and the water head over the joint of the gate is given

by: h=0.1985+H_c, where H_c and h are in meters. The water height over the gate, or head of water, H is calculated from $H = h - L\sin\alpha$, with L=0.76 m. Discharge coefficients C_d were obtained from the rectangular notch weir equation:

$$Q_w = \frac{2}{3} C_d B H^{3/2} \sqrt{2g} \qquad \text{(A1.4)}$$

where B is the notch width, equal to 2.06 m in the flume. Calculated values of the discharge coefficient plotted as a function of the water head over the gate are shown in Figure A1.7.

Run	*Measured values*			*Calculated parameters*					C_d	P_a % (eq. A1.5)
	h_v (cm)	Z_w (cm)	P_a %	Q_v (m^3/s) (eq. A1.1)	h (m)	α °	$L\ sin(\alpha)$ (m)	H (m)		
1	19.5	23.8	65	0.023	0.180	11.25	0.148	0.032	0.65	64
2	27.4	26.7	65	0.054	0.201	11.25	0.148	0.053	0.72	64
3	30.9	28.4	65	0.073	0.213	11.25	0.148	0.065	0.72	65
4	34.1	29.3	65	0.093	0.219	11.25	0.148	0.071	0.80	65
5	33.7	29.9	65	0.091	0.224	11.25	0.148	0.075	0.71	65
6	19.5	45.0	50	0.023	0.330	22.5	0.291	0.040	0.47	50
7	27.0	47.9	50	0.052	0.351	22.5	0.291	0.060	0.58	50
8	30.8	49.3	50	0.073	0.361	22.5	0.291	0.070	0.64	51
9	32.8	50.5	50	0.085	0.369	22.5	0.291	0.078	0.63	50
10	33.8	51.3	50	0.091	0.375	22.5	0.291	0.084	0.61	50
11	19.5	69.5	30	0.023	0.504	37.5	0.463	0.041	0.45	30
12	27.0	72.5	30	0.052	0.524	37.5	0.463	0.062	0.55	30
13	30.4	73.8	30	0.070	0.534	37.5	0.463	0.071	0.60	30
14	32.4	74.9	30	0.082	0.542	37.5	0.463	0.079	0.60	30
15	33.7	76.2	30	0.091	0.551	37.5	0.463	0.088	0.56	29
16	19.3	85.2	15	0.022	0.615	48.75	0.571	0.043	0.40	16
17	23.9	86.9	15	0.038	0.627	48.75	0.571	0.055	0.48	15
18	27.0	88.2	15	0.052	0.636	48.75	0.571	0.064	0.52	15
19*	30.7	90.0	15	0.072	0.649	48.75	0.571	0.077	0.54	14
20*	33.8	91.1	15	0.091	0.656	48.75	0.571	0.085	0.60	15

**water spills over the lateral walls*

Table A1.3 Measured data for calibration of the discharge coefficient for the tilting gate. h_v is the head of water above the apex notch at the triangular weir (Figures A1.6 and A1.7).

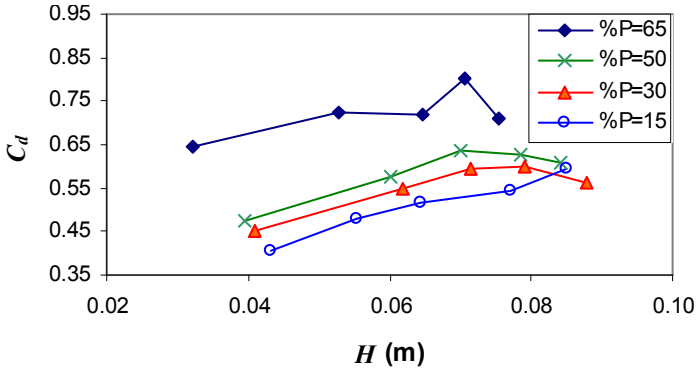

Figure A1.7 Variation of the discharge coefficient with the head of water for different tilt angles of the gate.

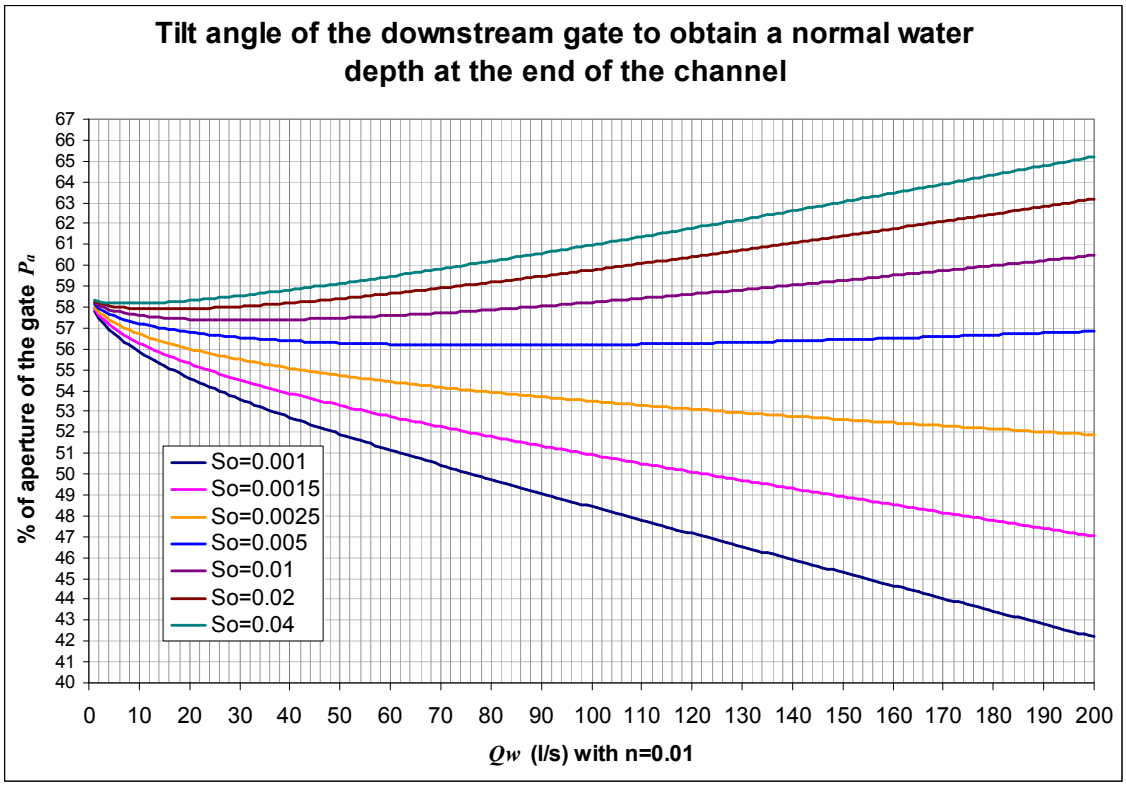

Figure A1.8 Theoretical relations for estimating the gate tilting for uniform flow in the channel when the Manning roughness coefficient is 0.01. S_o being the slope of the channel.

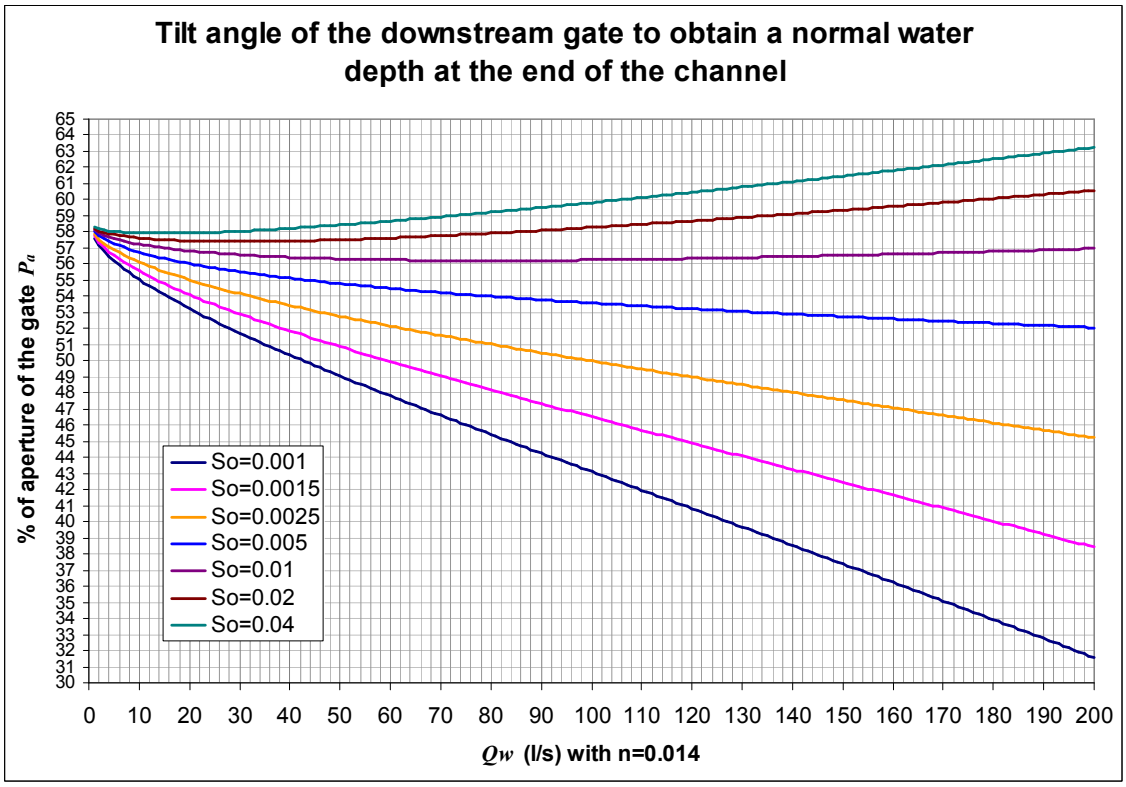

Figure A1.9 Theoretical relations for estimating the gate tilting for uniform flow in the channel when the Manning roughness coefficient is 0.014. S_o being the slope of the channel.

An estimate of the necessary tilt angle of the gate for a given water discharge passing through the flume, such that the water surface for the normal flow depth occurring at the channel coincides at the same level with the water stage in the tank (neglecting the effects of the section widening), may be obtained from Figures A1.8 and A1.9. Such figures were calculated by applying the Manning flow resistance formula (each figure for a different roughness coefficient value, n=0.01 and n=0.014) to get the normal water depth in the channel, and by fitting an equation to the data in Table A1.3 to get a practical functional relation between water head over the joint of the gate, water discharge and tilt angle, as follows

$$P_a = 71.184 + 69.233Q_w - 118.36h^{3/2} \qquad \text{(A1.5)}$$

The last column in Table A1.3 shows P_a estimates by applying this function to the data. Figures A1.8 and A1.9 are useful to get a first estimate for positioning the gate when searching for uniform flow conditions in the channel.

3.3 Mechanism to tilt the flume

The flume tilts by means of three engines located under the base of the channel at 6, 13 and 20 m from its downstream end (Figure A1.2). Each of the engines acts like a jack to raise or lower the channel to the height required for the desired slope. The engines are controlled automatically by a system where the slope is selected on a digital screen. It takes less than 4 minutes to the system to tilt the flume from one slope to another, being 4% the maximum slope that the channel can reach.

3.3.1 Horizontal channel

Measurements with a theodolite and a ruler set on the channel next to one of the lateral glass-walls were performed to verify the horizontality of the bottom of the channel when the tilting mechanism was set to a null slope. Table A1.4 and Figure A1.10 summarize the results. x refers to the horizontal distance from the point of measurement to the downstream end of the channel and z_m is the measured vertical distance from the bottom of the channel to an horizontal plane defined by the theodolite. Differences in height measurements along the channel are related to local unevenness on the bottom. As shown on the last column of Table A1.4, in average the slope of the channel is negative when the tilting mechanism is set to cero, but it is so mild (-0.01%), that we can consider it negligible.

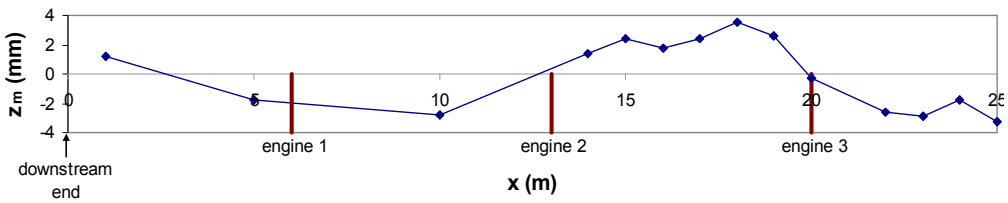

Figure A1.10 Difference in height along the bottom of the channel with respect to an horizontal plane at Z_b=0

x (m)	Z_b vertical distance from the bottom to an horizontal plane (m)	$Z_i = (Z_b)_i - \overline{Z_b}$ (mm)	Partial slopes $(z_i - z_{i-1})/(x_i - x_{i-1})$ (m/m)	Slopes with respect to x=1m $(z_i - z_{x=1m})/(x_i - 1)$ (m/m)
1	0.421	1.2		
5	0.418	-1.8	-0.0008	-0.0008
10	0.417	-2.8	-0.0002	-0.0004
14	0.421	1.4	0.0010	0.0000
15	0.422	2.4	0.0010	0.0001
16	0.422	1.7	-0.0007	0.0000
17	0.422	2.4	0.0007	0.0001
18	0.423	3.5	0.0011	0.0001
19	0.422	2.6	-0.0009	0.0001
20	0.420	-0.3	-0.0029	-0.0001
22	0.417	-2.6	-0.0012	-0.0002
23	0.417	-2.9	-0.0003	-0.0002
24	0.418	-1.8	0.0011	-0.0001
25	0.417	-3.3	-0.0015	-0.0002
Average=	**0.420**	**0.0**	**-0.0003**	**-0.0001**

Table A1.4 Data for verifying the horizontality of the bottom of the channel

3.3.2 Flume slopes verification

An evaluation of the precision of the slope given by the automated system was carried out before and during the first experimental campaign. Though the system is highly accurate, errors between the desired slope selected on the screen and the actual slope may arise because of differences between the engines for different slopes and because of deflections on the channel structure in between engines for different weights of water and sediment.

Measurements of the channel vertical displacements were performed related to the channel elevation when the tilting mechanism was set to cero. Measurements were performed for three selected slopes, 0.5%, 1% and 2.5%, at four points along the channel, at 6, 13.5, 20 and 27.4 m from the joint around which the channel turns. Displacements were measured with fixed metal rulers graduated every mm, i.e., with a precision of ±0.5 mm. Results of the measurements are shown in Table A1.5. Tests refer to the first and second verifications, performed before the first experimental campaign the former and during that campaign the latter.

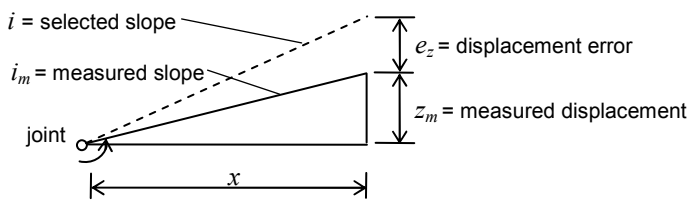

Figure A1.11 Definition of error for the vertical displacements of the channel

As shown in Figure A1.11, the error for the vertical displacement e_z was defined as the difference between the measured value z_m and the expected value z_e, the

latter calculated from $z_e=xi$, where i is the selected slope on the digital screen and x is the distance from the measured point to the joint. Values and plots of the error along the horizontal axes are shown in Figure A1.12 and Table A1.5.

One third of the absolute errors are $\leq$ 0.5 mm, i.e., of the same order of the precision of the rulers with which the measurements were done. Average error is -0.7 mm. The higher errors are negative, and are found for both, the highest slopes and the highest x coordinate. An interpretation for this is that the upper extreme of the channel has no support, so, as it rests in cantilever, it is possible that a subtle deformation appears at the channel structure, being higher the higher the x coordinate. Positive errors might be due to inverse deflections on the channel structure along the span between engines.

Differences between the selected slopes and the slopes calculated with the measured displacement values are presented in Table A1.5. Also, on the last two columns a comparison is presented between selected slopes and slopes calculated by fitting a line to the four measured data along the channel for each slope. Average relative errors for both slope estimations are 0.09% and 0.37%, respectively.

Test	selected slope	distance to the joint	Vertical displacement			Measured slope		Slope fitted	
			expected	measured	error	measured	relative error	fit to measured data	error
	i	x (m)	z_e (mm)	z_m (mm)	$e_z=z_m-z_e$ (mm)	$i_m = z_m/x$ (m/m)	$(i_m-i)/i_m$	i_f (m/m)	$(i_f-i)/i_f$
1st	0.005	5.984	29.9	30.0	0.1	0.50%	0.3%	0.0050	0.0%
1st	0.005	13.509	67.5	67.5	0.0	0.50%	-0.1%		
1st	0.005	20.148	100.7	102.0	1.3	0.51%	1.2%		
1st	0.005	27.376	136.9	136.0	-0.9	0.50%	-0.6%		
1st	0.01	5.984	59.8	59.5	-0.3	0.99%	-0.6%	0.0099	-1.0%
1st	0.01	13.509	135.1	134.5	-0.6	1.00%	-0.4%		
1st	0.01	20.148	201.5	202.0	0.5	1.00%	0.3%		
1st	0.01	27.376	273.8	272.5	-1.3	1.00%	-0.5%		
1st	0.025	5.984	149.6	149.0	-0.6	2.49%	-0.4%	0.0249	-0.4%
1st	0.025	13.509	337.7	336.0	-1.7	2.49%	-0.5%		
1st	0.025	20.148	503.7	501.0	-2.7	2.49%	-0.5%		
1st	0.025	27.376	684.4	683.0	-1.4	2.49%	-0.2%		
2nd	0.005	5.984	29.9	30.0	0.1	0.50%	0.3%	0.0050	0.0%
2nd	0.005	13.509	67.5	68.0	0.5	0.50%	0.7%		
2nd	0.005	20.148	100.7	100.5	-0.2	0.50%	-0.2%		
2nd	0.005	27.376	136.9	135.5	-1.4	0.49%	-1.0%		
2nd	0.01	5.984	59.8	61.5	1.7	1.03%	2.7%	0.0100	0.0%
2nd	0.01	13.509	135.1	136.0	0.9	1.01%	0.7%		
2nd	0.01	20.148	201.5	201.0	-0.5	1.00%	-0.2%		
2nd	0.01	27.376	273.8	272.5	-1.3	1.00%	-0.5%		
2nd	0.025	5.984	149.6	148.5	-1.1	2.48%	-0.7%	0.0248	-0.8%
2nd	0.025	13.509	337.7	337.0	-0.7	2.49%	-0.2%		
2nd	0.025	20.148	503.7	500.0	-3.7	2.48%	-0.7%		
2nd	0.025	27.376	684.4	680.0	-4.4	2.48%	-0.6%		
				Average	-0.7		-0.09%		-0.37%
				Standard deviation	1.4		0.80%		0.45%

Table A1.5 Measurements for slope verification

The error for the slopes in the channel seems not to be of great magnitude; nevertheless, for essays in which a high accuracy in channel slope determination is a main feature, it may be important to take this error into account. A correction for the error in vertical displacements was found using a linear function fitted to the measured data. The origin of the function was fixed to coincide with the joint of the channel, where displacement, and thus the error, is supposed to be null. Thus, error on the vertical displacements may be estimated from:

$$e_z = -4.372xi \qquad \text{(A1.6)}$$

with x in m and e_z in mm. Plots of the function are shown in dashed lines in the graphs of Figure A1.12. For slopes higher than 1%, correction of vertical displacements might be estimated with equation (A1.6) for all points along the channel; for slopes lower than 1% the error is low when x < 15 m, so for those slopes equation (A1.6) would be better to be applied only to the second half of the channel.

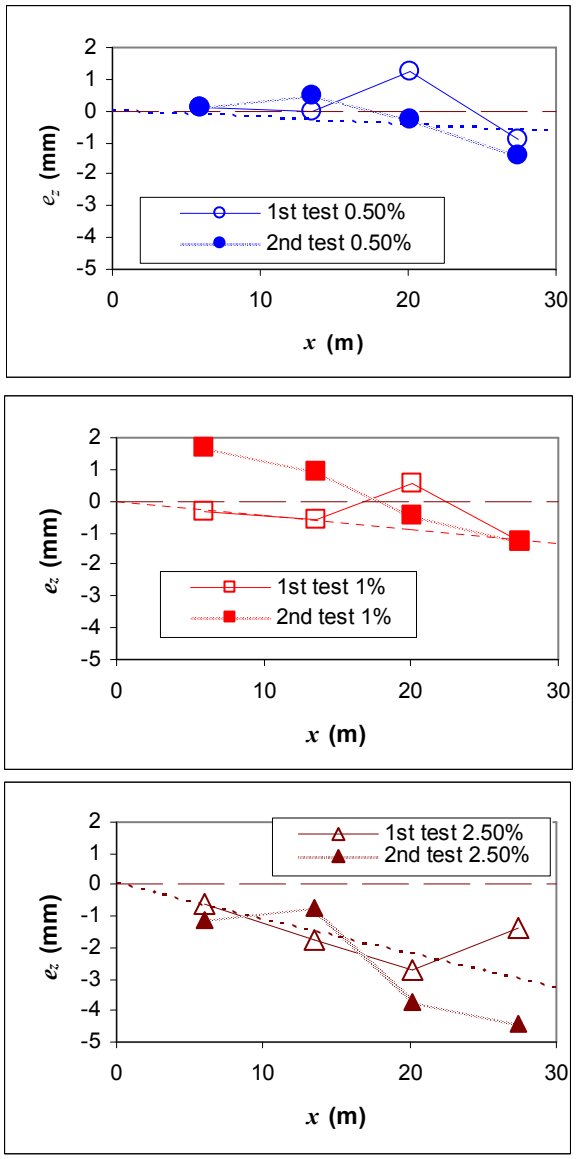

Figure A1.12 Variation of the vertical displacement error along the channel

Table A1.6 summarizes the relation between actual vertical displacements and those expected from a given slope selected at the tilting mechanism. The standard deviation of the error after applying the corrective function (eq. A1.6) to the data from Table A1.5 is shown as a measure of the precision for the vertical displacement associated to a selected slope.

Condition	Correction	Mean e_z (mm)	σ (mm)
$i \leq 1\%$, $x<15$ m	No correction	0.3	0.7
$i \leq 1\%$, $x>15$ m	$Za=ix+e_Z$ *i=selected slope, Za=actual displacement*	0.0	0.8
$i > 1\%$		0.1	1.0
	Average=	**0.1**	**0.9**

Table A1.6 Mean errors and standard deviations for corrected displacements. e_z is calculated with eq.(A1.6)

3.4 Sediment-feed and -recirculating system

Mobile-bed experiments with sediment feeding require a continuous and constant supply of sediment to the channel. To achieve this, the experimental flume contains two feed or "lung" hoppers at the head of the channel, one for sand and the other for gravel (Figure A1.13 and Photos P3 and P4). Each hopper can be supplied with fresh material by a screw conveyor connected to a large deposit (see Photos P1 and P2). Also, each hopper can receive material from a screw conveyor connected to the sediment-recirculating system. Material in the hoppers is fed to the channel through a sluice gate by means of a rubber rotating band (see Photo P4a). Sprinkler systems moisten the rubber bands to avoid that sediment got stuck (especially sand). Before entering the channel, the material slips over a ramp below each feeder and then over a tilting ramp where sand and gravel mix (see Photo P5a). This ramp avoids that material spills out of the system and also allows a gentle insertion of the particles in the channel to avoid an excessive distortion of the flow. A continuous measurement of the weight of each hopper is obtained with 4 load cells (see Photo P3b). Following, some of these components are described in detail, and also the procedures employed for their calibration and operation.

3.4.1 "Lung" hoppers and feeders

The term "lung" hoppers is used here (as used by Ferrer-Sansa 1994 and Martin-Vide et al. 1998) in allusion to their capability for regulating the volume of sediment delivered to them by the recirculating system and, at the same time, to pour into the channel a controlled amount of sediment. The hoppers also might be used independently from the recirculating system, to act only as feeders that may be replenished through the screw conveyors connected to the large deposits. The disadvantage of using the system in the "pure" feed mode is that the required amount of sediment for a long lasting or high sediment transport run may be excessive, and the volumetric capacity of the hopper could be short for supplying the required volume. Such an inconvenient is overcome using the whole recirculating system working together, so that the material that leaves

from the channel end is reused. In doing this, the hoppers become the main element of the recirculating circuit.

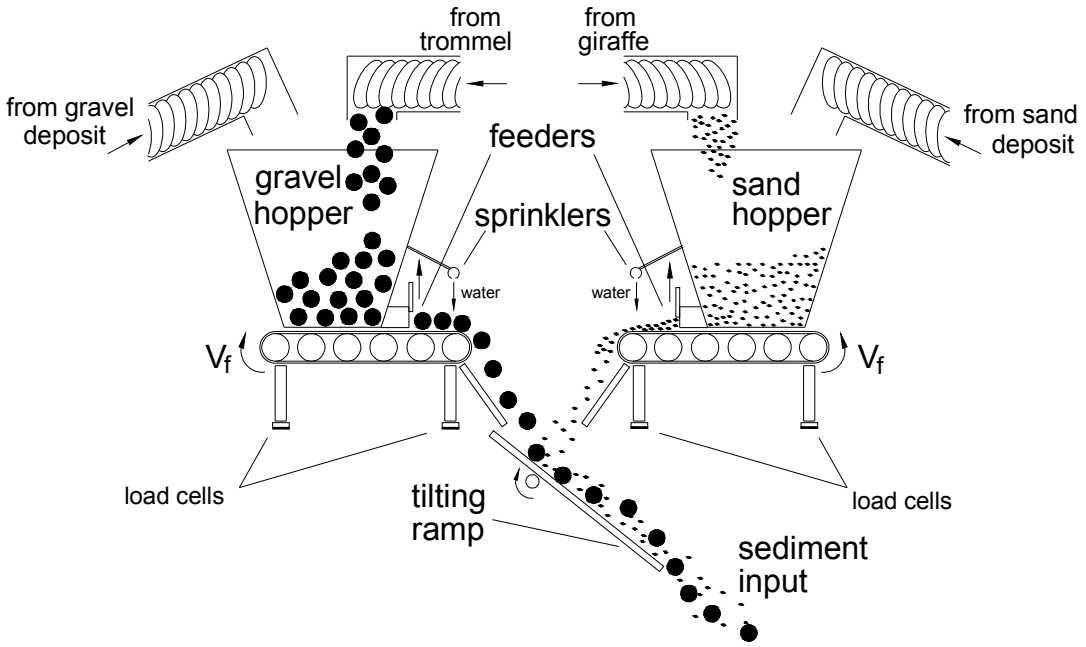

Figure A1.13 Elements of the sediment feed system

As shown in Figure A1.14, the capacity of each hopper is 1.1 m^3 (≈1.5 to 2 tons of sediment). The feeding rate Q_{SF} is regulated by adjusting the opening h_f of the sluice gate at the base of the hopper and the velocity V_f of the rotating band. As the accuracy of the feeding rate is one of the most important variables for runs to study sediment transport, a reliable calibration for establishing the feeding rates for different combinations of h_f and V_f for each hopper is required. An analysis of the main variables is presented as follows.

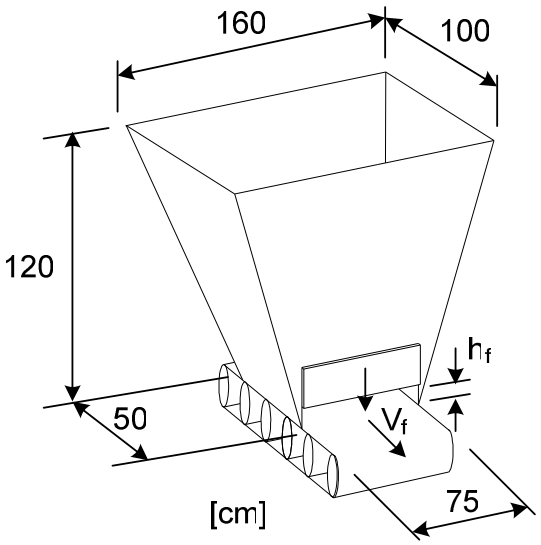

$$\textbf{Volume} = \frac{\mathbf{1}}{\mathbf{3}}\mathbf{h}\left(\mathbf{A_1} + \sqrt{\mathbf{A_1 A_2}} + \mathbf{A_2}\right)$$

A_1 = 0.50*0.75 =0.375 m^2

A_2 = 1.60*1 = 1.60 m^2

h = 1.2 m

Volume = 1.10 m^3

Figure A1.14 Dimensions and elements of the lung hoppers

3.4.1.1 Variables that condition the feeding rate

An important property of the sediment unloading from the hoppers, verified with similar facilities in the Universidad Politécnica de Cataluña by Ferrer-Sansa 1994 and Martin-Vide et al. 1998, is that the rate of sediment evacuation depends only on the combination of h_f and V_f, and is independent of the volume of material in the hopper. Expressed in a differential form, for a given combination of h_f and V_f, and a volume of dry sediment with homogeneous characteristics, it is satisfied that:

$$Q_{SF} = \frac{dW_t}{dt} = K_f \qquad \text{(A1.7)}$$

where K_f is an "unloading" constant, Q_{SF} is the feeding rate of dry sediment, W_t is the instantaneous weight of sediment in the hopper and t is time. Therefore, if we know the function $W_t=f(t)$ we may find the constant K_f for calibration of the feeder.

Generalizing for different combinations of gate openings and band velocities, and for sediment with different characteristics, we may summarize all variables that influence the feeding rate of dry sediment with the next functional relation:

$$Q_{SF} = f\left(B_f, D, h_f, V_f, \%\varpi, \rho_s, \varepsilon\right) \qquad \text{(A1.8)}$$

where B_f is the width of the gate at the base of the feeder (B_f =0.73 m), D, $\%\omega$, ε and ρ_s are a representative diameter, the water content, porosity and density of the sediment in the hopper, respectively.

From dimensional analysis, eq.(A1.8) may be reduced to

$$\frac{Q_{SF}}{h_f B_f V_f \rho_s} = f\left(\frac{h_f}{B_f}, \frac{h_f}{D}, \varepsilon, \%\varpi\right) \qquad \text{(A1.9)}$$

We drop the aspect ratio of the gate h_f/B_f, considering that both feeders in the flume have the same geometry. On the other hand, we know that the flux of dry sediment through the sluice gate is equal to: $h_f B_f V_f \rho_s (1-\varepsilon)$; if the sediment is wet, as is the case when the whole recirculating system is running, the flux of mass through the gate includes the water content; thus, we may write:

$$\frac{Q_{SF}}{h_f B_f V_f \rho_s (1-\varepsilon)\left(1+\%\varpi/100\right)} = f\left(\frac{h_f}{D}\right) \qquad \text{(A1.10)}$$

Different tests were performed with the sand and gravel feeders to find the value of constant K_f in eq.(A1.9) and the functional relation in eq.(A1.10). Moreover, data obtained during the first experimental campaigns were used to increase the data set for the calibration.

3.4.1.2 Calibration of the velocities of the rotating-band

The velocity of the rubber rotating-band on the base of the hopper is controlled by regulating the voltage of an engine that activates the rotating rollers, whose friction with the band produces its movement. Selection of the voltage is performed with a digital display and is shown as a percentage of the maximum rotating speed, i.e., 0% for no motion and 100% for the maximal voltage or rotating speed.

%V	5	5	5	10	10	10	25	25	25	25
t (s)	136.6	136.9	137.0	73.7	73.6	73.6	31.1	31.0	31.0	30.7
V_f *(m/s)*	0.019	0.019	0.019	0.036	0.036	0.036	0.085	0.086	0.086	0.086

%V	50	50	50	50	50	100	100	100
t (s)	16.2	15.3	15.5	15.9	15.5	8.4	8.3	8.5
V_f *(m/s)*	0.164	0.173	0.171	0.166	0.171	0.315	0.318	0.311

Table A1.7 Calibration data for the rotating band

Eighteen runs were performed to calibrate the relation between the velocities of the band and the selected percentages of voltage for the engine $\%V$. A chronometer was used to measure the time required for the band to complete a turn around the rollers. In this manner, the velocity of the band V_f for each run was calculated by dividing the length of the band, equal to 2.65 m, by the measured time. Results are shown in Table A1.7 and plotted in Figure A1.15. A best-fit function that relates the measured voltage percentages with the band velocities is:

$$V_f = 0.0042\%V^{0.94} \qquad \text{(A1.11)}$$

with V_f in m/s. The standard deviation for the error associated with eq.(A1.11) was 3.14 mm/s.

Calibration was performed when the hopper was empty. We may consider that no sliding between the rollers and the rubber band would occur even if the hopper is filled with sediment, i.e., that the velocity is kept constant independently of the mass weight on the band.

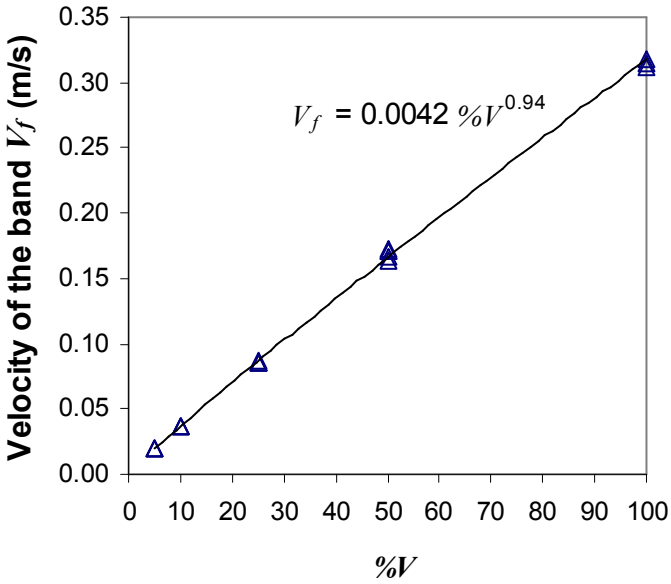

Figure A1.15 Calibration curve for the rotating band

3.4.1.3 Calibration of the load cells for the sand hopper with the analogical display

Each hopper rests on four load cells which allow a continuous monitoring of the weight they support. The signal from the load cells is added and displayed by an analogical system. Also, a real-time data acquisition system (RTDAS)

connected to a personal computer was installed to record the signal digitally. Here we will refer to the calibration of weights given by the analogical display of the sand hopper before the RTDAS was installed.

Prior to the calibration, we made sure that there were no obstacles exerting any external force on the hopper. According to the manufacturer protocol, calibration of the load cells with the analogical display system required to place a known weight in the hoppers, in the order of 80% of the maximal weight to be normally measured. Since the volumetric capacity of the hoppers allows a maximum volume of sediment of 1.1 m^3 (Figure A1.14), then, for sediment with a density of 2630 kg/m^3 and a porosity of 0.4, as the sand available in the laboratory, the maximum weight to fit in the hopper filled flush with its upper height would be approximately 1.1 m^3*2630 kg/m^3*(1-0.4)=1.74 tons; the 80% of that value is 1.39 ton. In practice, it was extremely complicated to place 1.39 tons in the hopper and control its weight precisely with another measurement device. Therefore, the hopper was filled with a volume of sand, which weight was accurately measured (weighted in four batches with a scale with precision ±4 grams) equaling 136 kg, and also one person, with 115.5 kg of weight (weighted in a scale with precision ±100 grams) got into the hopper. Following the calibration procedure detailed by the manufacturer, the analogical display was calibrated by matching together the zero value for the hopper empty and the value of 115.5+136=251.5 kg for the hopper loaded.

A test was performed to estimate the error when weighting higher values than the weight of 251.5 kg used in the calibration. Beginning with the hopper totally empty, it was successively filled with sand in 4 steps of 310, 608, 840 and 1011 kg, as marked on the analogical display. For each step, the person that participated in the calibration (weight =115.5 kg) got inside of the hopper and the increment of weight on the display was registered. Results are shown in Table A1.8.

Run n	Displayed initial weight W_{di} [kg]	Displayed final weight W_{df} [kg]	Measured increment ΔW_d [kg]	Actual weight increment ΔW_a [kg]	Mean weights displayed $W_{dMean}=(W_{di}+W_{df})/2$ [kg]	$\Delta W_a/\Delta W_d$
1	-0.350	115.500	115.850	115.500	57.575	0.997
2	310.100	424.800	114.700	115.500	367.450	1.007
3	607.900	721.300	113.400	115.500	664.600	1.019
4	839.800	951.900	112.100	115.500	895.850	1.030
5	1011.100	1122.200	111.100	115.500	1066.650	1.040

Table A1.8 Tests for the estimation of error in incremental weights for different load conditions in the hopper.

The weight increments ΔW_d, obtained from the measurements at the analogical display, are not constant for different loads in the hopper. An interpretation for this tendency is related with the characteristics of the sensors. It is well known that for this kind of devices the relation between the signal and the acting force is not linear but slightly curved, thus, error produced when extrapolating to higher values than the maximal value used for the calibration introduces higher errors the higher apart the measured value is from the

calibrated region. Figure A1.16 presents schematically the error between the actual weighted values and the measured values when the calibration is considered linear, as the analogical display calibration protocol probably does.

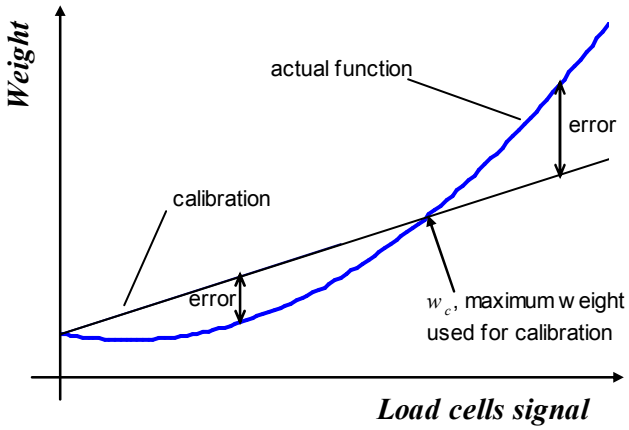

Figure A1.16 Schematic plot of the error between the calibration with a linear function and the actual function that relates the load cells signal with the weight in the hoppers.

If we assume that the functional relation between the load cells signal and the actual weights set in the hopper is quadratic, the function that relates the actual weights W_a and the weights measured with the analogical display W_d may be written as:

$$W_a = aW_d^2 + bW_d + c \qquad \text{(A1.12)}$$

From the calibration, we know that for W_a=0, W_d=0, and therefore for eq(A1.12) the value of constant c=0. In the same manner, we can expect that for W_a=w_c, with w_c being the maximum weight used in the calibration (w_c=251.5 kg), W_d=w_c, and thus from eq(A1.12) we can write

$$b = 1 - aw_c \qquad \text{(A1.13)}$$

To find the value of constant a we use the data in Table A1.8. From eq(A1.12), for each run j of the n=5 runs, actual increments of weight in the hopper would be related to the displayed initial and final weights, ΔW_{di} and ΔW_{df}, respectively, as:

$$\Delta W_a = \left(aW_{df}^2 + bW_{df}\right) - \left(aW_{di}^2 + bW_{di}\right) \qquad \text{(A1.14)}$$

Considering all runs in Table A1.8 in a single equation, we have

$$n\Delta W_a = a\sum_{j=1}^{n}\left(W_{df}^2 - W_{di}^2\right)_j - b\sum_{j=1}^{n}\left(W_{df} - W_{di}\right)_j \qquad \text{(A1.15)}$$

Including eq(A1.13) in eq(A1.15) and arranging, we have

$$a = \frac{n\Delta W_a + \sum_{j=1}^{n}\left(W_{df} - W_{di}\right)_j}{\sum_{j=1}^{n}\left[W_{df}^2 - W_{di}^2 - w_c\left(W_{df} - W_{di}\right)\right]_j} \qquad \text{(A1.16)}$$

Replacing the variables in eq(A1.16) and eq(A1.13) with data in Table A1.8, we find the following values for the constants in eq(A1.12):

a=0.000019 ; b=0.9952; c=0

Eq.(A1.12) has been applied to obtain the plots shown in Figure A1.17. Figure A1.17a describes the variation of the relation between the measured weight increments ΔW_d and the constant actual weight increment ΔW_a=115.5 kg for different load conditions, these obtained by averaging the initial and final displayed weights, and compares the measured values to the values obtained when applying eq(A1.12). Figure A1.17b shows the variation of the error between actual and displayed weights for different load conditions in the hopper. From this Figure we find that for total weights in the hopper lower than 350 kg the absolute errors would be lower than 0.6 kg, i.e., of the same order of magnitude as the approximate precision of the analogical display of ±300 grams. Although the error in measured weights for the whole capacity of the hopper can be corrected with eq(A1.12), further calibration of the feeders is preferred to be performed for weights below 350 kg to minimize possible error propagations.

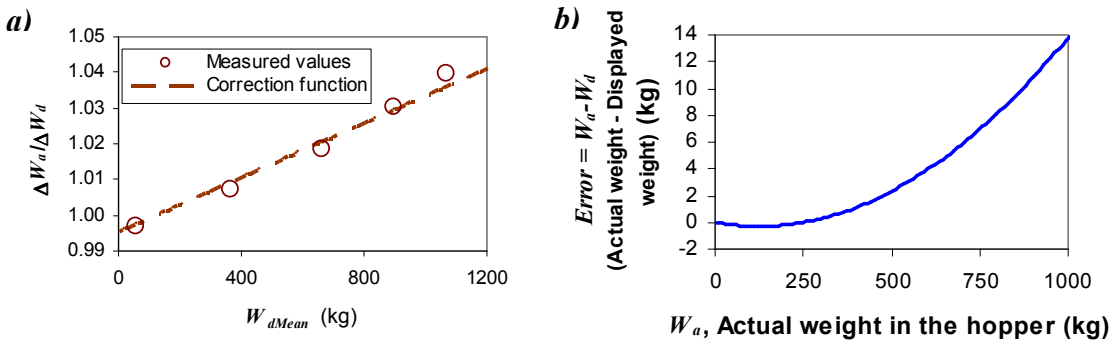

Figure A1.17 a) Comparison between actual weight increments and measured weight increments with respect to the degree of volumetric capacity occupied in the hopper. b) Error variations for the measured weights in the analogical display with respect to the actual weight in the hopper

3.4.1.4 Calibration of the load cells with the Real-Time Data Acquisition System (RTDAS)

A disadvantage of the analogical display is that the variations of weight in the hoppers during one experiment cannot be recorded continuously. Therefore, the RTDAS was installed to obtain a digital, continuous and instantaneous record of the variation of weight in the sand and gravel hoppers. The RTDAS takes the signal from the load cells before it goes through the analogical display; thus, a calibration different from that performed for the analogical display was required.

Figure A1.18 depicts the components of the RTDAS, from which the most important element is the data acquisition card from National Instruments PCI-6034E, which had 8 differential analog channels and 16 bits. It was found that the different electronic devices to bring into operation the sediment feeding and recirculating system, produced certain noise in the signal of the load cells. Therefore, noise that affected the signal was treated with two filters, a signal filter and a digital filter. The software used for registering and visualizing the signal from the load cells was Matlab 7.1 with the Simulink Toolbox.

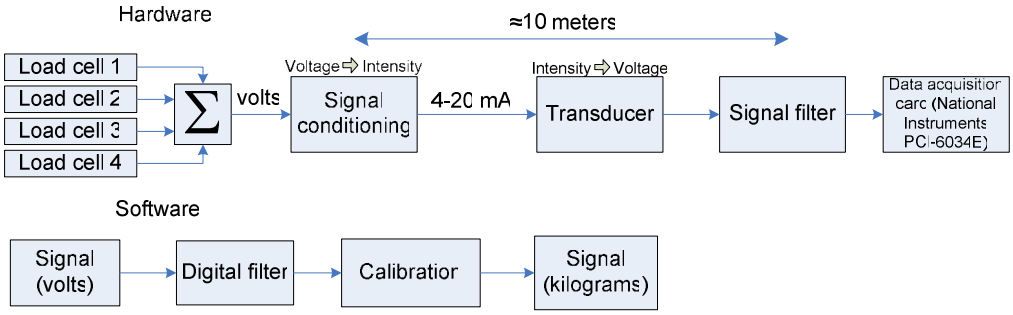

Figure A1.18 Flowchart for the components of the Real-Time Data Acquisition System, RTDAS

Calibration for the sand hopper

Calibration consisted in assigning a corresponding value in mass units to the signal in voltage given by the load cells. Prior to the calibration, a revision was performed to move away any obstacles exerting external forces on the hopper and to make sure that the only contact between the hopper and the structure of the recirculating system was through the four load cells. Figure A1.18 shows the continuous record of the signal for one of the 6 tests performed to calibrate the load cells for the sand hopper. The RTDAS was set to record the signal every half a second. Different weights were set in the hopper and measured with the analogical display (corrected with eq.[A1.12]) if they were higher than 150 kg, and with a small scale with precision ±100 grams for weights smaller than 150 kg. From the recorded signal, time averages were taken for the most stable region of each constant weight set in the hopper, seen as plateaus in Figure A1.18. In this Figure, the ramp with positive slope corresponds to the loading of the hopper with sand from the large deposit using the screw conveyor; on the other hand, ramps with negative slope correspond to the unloading of the hopper using the feeder (rotating band and sluice gate). Results for the 6 tests performed are registered in Table A1.9.

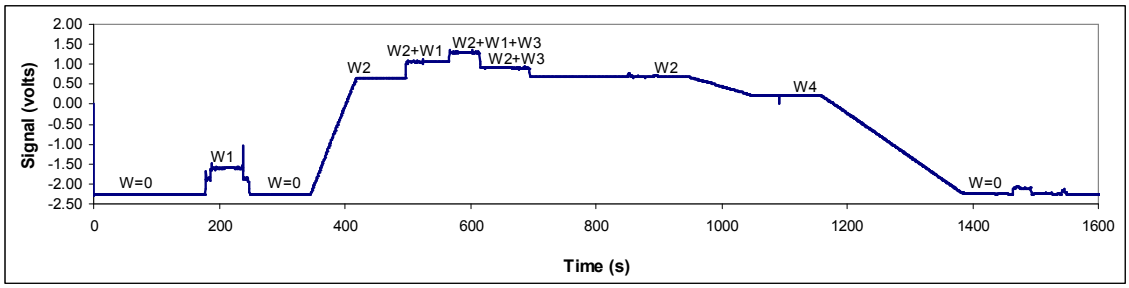

Figure A1.18 Continuous record of the load cells signal given by the RTDAS for the sand hopper loaded with different weights W for calibration in tests 2 and 3 shown in Table A1.9

Calibration points obtained with the data in Table A1.9 are plotted in Figure A1.19. Although visually the relation between the signal voltage and the weight in the hopper seems linear, a more detailed analysis showed that the signal has a slight curvature (see Figure A1.16). A good correlation was obtained by fitting the next quadratic function:

Test	Average signal (volts)	Δt (s)	Standard deviation (volts)	W_a Actual weight (kg)	ΔW_a (kg)	W_d Calculated weight (eq. A1.17) (kg)	ΔW_d (kg)	$e_r = \left\| \frac{\Delta W_a - \Delta W_d}{\Delta W_a} \right\|$
1	-2.277	41	0.00078	0.000		-1.116		
1	-1.865	11	0.00178	117.350	117.350	115.763	116.522	0.71%
1	-1.612	10	0.00076	189.350	72.000	187.383	71.841	0.22%
1	-2.024	30	0.00023	72.000	-117.350	70.478	-117.094	0.22%
1	-2.278	25	0.00011	0.000	-72.000	-1.399	-71.550	0.63%
2	-2.266	165	0.00064	0.000		1.943		
2	-1.848	6	0.05383	116.500	116.500	120.458	118.182	1.44%
2	-1.606	13.5	0.00093	185.950	69.450	189.039	68.808	0.92%
3	-2.266	85	0.00063	0.000		1.826		
3	0.663	78	0.00057	852.693	852.693	849.707	847.798	0.57%
3	1.066	35.5	0.00270	969.193	116.500	970.165	120.151	3.13%
3	1.296	22	0.00372	1038.643	69.450	1038.855	68.896	0.80%
3	0.907	28	0.00057	922.143	-116.500	922.536	-116.506	0.01%
3	0.673	38	0.00055	852.693	-69.450	852.743	-69.522	0.10%
3	0.205	40	0.00069	711.511	-141.183	712.870	-138.469	1.92%
3	-2.263	56	0.00065	0.000	-711.511	2.793	-711.387	0.02%
4	-2.288	21	0.00013	0.000		-4.307		
4	-1.872	21	0.00037	117.100	117.100	113.605	117.531	0.37%
4	-1.624	18.5	0.00013	186.900	69.800	183.948	70.548	1.07%
4	-2.040	11	0.00381	69.800	-117.100	66.020	-118.088	0.84%
4	-2.288	21	0.00006	0.000	-69.800	-4.315	-69.998	0.28%
5	-2.266	10	0.00009	0.000		1.970		
5	-1.854	21	0.00054	117.100	117.100	118.858	116.554	0.47%
5	-1.609	14.5	0.00051	186.900	69.800	188.276	69.642	0.23%
5	-2.022	16	0.00445	69.800	-117.100	71.222	-117.249	0.13%
5	-2.266	10	0.00008	0.000	-69.800	1.976	-68.941	1.23%
6	-2.267	15	0.00007	0.000		1.732		
6	-1.855	23	0.00058	117.100	117.100	118.540	116.472	0.54%
6	-2.267	8.5	0.00007	0.000	-117.100	1.763	-116.441	0.56%
	Mean=		0.00094				Mean=	0.71%

Table A1.9 Data for calibration of the sand hopper load-cells. Actual weights W_a refer to weights measured with a scale (if W<150 kg) or in the calibrated analogical display (if W>150 kg).

$$W = 2.6303 Voltage^2 + 293.646 Voltage + 653.878 \text{ [kg]} \qquad \text{(A1.17)}$$

As presented in Table A1.9, for each calibration test, weight increments between consecutive loads were obtained for the actual weights and also for weights calculated from eq.(A1.17) applied to the average signal values. The mean relative error, here defined as the absolute value of the difference between the actual and calculated increment divided by the actual value, was as low as 0.71%.

Using the best-fit curve given by eq.(A1.17) to transfer the average standard deviation of the signal (=0.00094 volts, see Table A1.9) to its value in mass units, we obtain a range from **266 to 283 grams**, i.e., values of the same order of magnitude as the approximate precision of the analogical display of ±300 grams. The highest standard deviations in Table A1.9 are due to

oscillations of the hopper, as most of the calibration tests were performed with the weight of two people that produced high vibrations when they climbed up and got into the hopper.

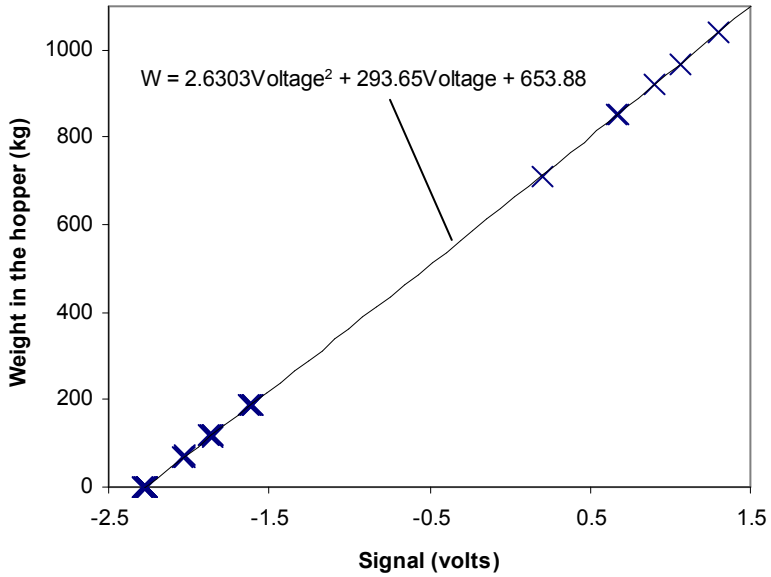

Figure A1.19 Calibration of the load cells to relate the signal voltage to its corresponding weight on the sand hopper

During the experimental campaign, the calibration of the load cells was verified three times. Data for these verifications have been plotted in Figure A1.20 using the ratio of the increment of weight to the increment of voltage as a function of the mean signal voltage. These variables were chosen since they allow distinguishing more easily changes between verifications than with the plot signal vs weight shown in Figure A1.19. In general, no important changes are observed between verifications, since it is apparent that the standard deviation of the measurements is roughly conserved for the different tests. Using the whole of the data, a best fit line was obtained, whose standard quadratic error was 1.84. Therefore, the ratio between weight and voltage increments in the sand hopper can be given by

$$\frac{\Delta W}{\Delta signal} = \left(295.565 + 5.674 Voltage\right) \pm 1.843 \quad \text{[kg/volts]} \quad \text{(A1.18)}$$

A line representing the original calibration has been plotted in Figure A1.20. This line plots slightly below and parallel to the line fitted to the entire data set.

Usiung eq.(A1.18), it is found that roughly an increment of 1 volt is equivalent to an increment of 295 kg of weight on the sand hopper for a mean signal of cero volts. Hence, using these values for the error of eq.(A1.18) it is found that the error in measurements of weight increment with the RTDAS is roughly of 1.84 kg for an increment of 295 kg, i.e., 6 grams every 1 kg, and therefore of approximately 0.62%, which is quite reasonable.

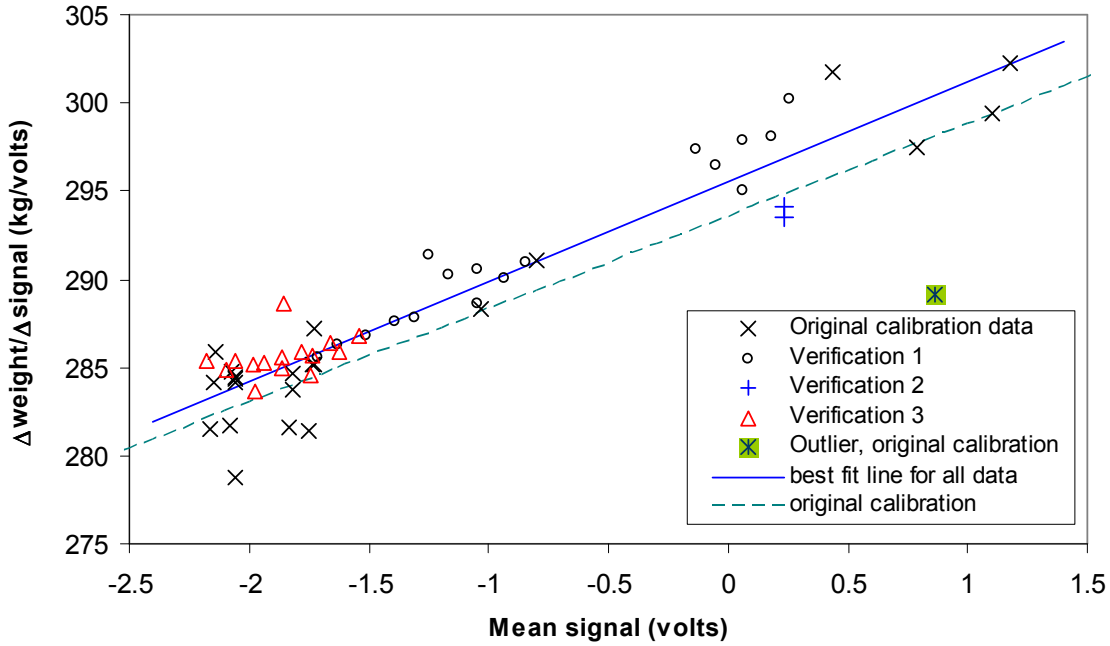

Figure A1.20 Calibration of the load cells to relate the signal voltage to its corresponding weight on the sand hopper

Calibration of the gravel hopper

The calibration procedure was essentially the same as that followed for the sand hopper, with the only difference in that for the gravel hopper no previous calibration of the analogical display was performed. Therefore, for the calibration of the RTDAS, it was not possible to use heavy weights which could be weighted with another instrument. Maximal weights used were of 190 kg, which was the sum of weights, measured with a scale, of two persons that got into the hopper for the calibration.

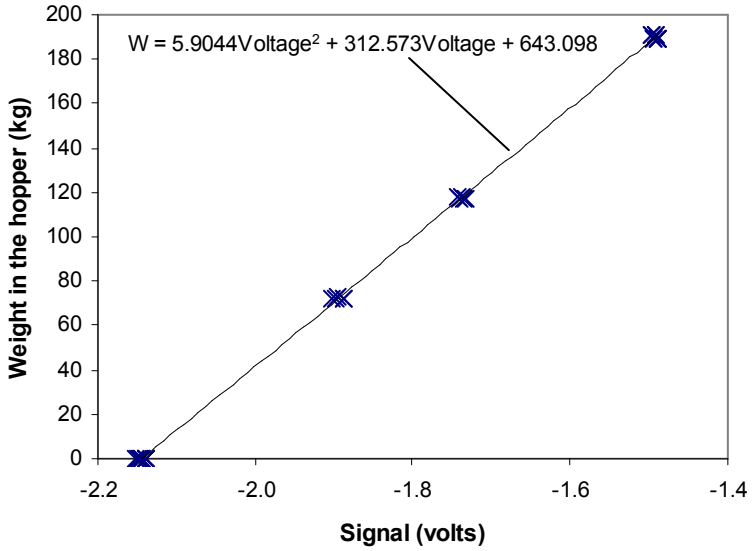

Figure A1.21 Calibration of the load cells to relate the signal voltage to its corresponding weight on the gravel hopper

Test	Average signal (volts)	Δt (s)	Standard deviation (volts)	W_a Actual weight (kg)	ΔW_a (kg)	W_d Calculated weight (eq.A1.16) (kg)	ΔW_d (kg)	$e_r = \left\| \frac{\Delta W_a - \Delta W_d}{\Delta W_a} \right\|$
1	-2.139	33	0.00034	0.000		1.508		
1	-1.734	41	0.00481	117.100	117.100	118.867	117.358	0.22%
1	-1.488	16	0.00995	189.550	72.450	191.112	72.245	0.28%
1	-1.887	16	0.00115	72.450	-117.100	74.198	-116.913	0.16%
1	-2.139	70	0.00033	0.000	-72.450	1.574	-72.624	0.24%
1	-1.488	16	0.00995	189.550	189.550	191.112	189.537	0.01%
2	-2.139	100	0.00025	0.000		1.521		
2	-1.734	40	0.00471	117.100	117.100	118.830	117.309	0.18%
2	-1.489	13	0.00800	189.550	72.450	190.693	71.863	0.81%
2	-1.887	16	0.00115	72.450	-117.100	74.198	-116.495	0.52%
2	-2.139	50	0.00034	0.000	-72.450	1.552	-72.646	0.27%
2	-1.489	13	0.00800	189.550	189.550	190.693	189.141	0.22%
3	-2.147	33	0.00026	0.000		-0.734		
3	-1.741	20	0.00499	117.150	117.150	116.754	117.488	0.29%
3	-1.495	25	0.00091	189.350	72.200	189.015	72.261	0.08%
3	-1.898	29	0.00144	72.200	-117.150	71.201	-117.814	0.57%
3	-2.146	150	0.00019	0.000	-72.200	-0.629	-71.830	0.51%
3	-1.495	25	0.00091	189.350	189.350	189.015	189.644	0.16%
4	-2.145	135	0.00027	0.000		-0.163		
4	-1.738	27	0.00330	118.000	118.000	117.548	117.711	0.24%
4	-1.491	11	0.00061	190.550	72.550	190.311	72.763	0.29%
4	-1.895	30	0.00037	72.550	-118.000	72.005	-118.306	0.26%
4	-2.145	51	0.00029	0.000	-72.550	-0.188	-72.192	0.49%
4	-1.495	11	0.00061	190.550	190.550	190.311	190.498	0.03%
5	-2.150	7	0.00040	0.000		-1.712		
5	-1.744	16	0.00044	118.150	118.150	116.020	117.732	0.35%
5	-1.497	50	0.00293	190.600	72.450	188.314	72.294	0.22%
5	-1.903	13	0.00021	72.450	-118.150	69.597	-118.717	0.48%
5	-2.152	60	0.00025	0.000	-72.450	-2.216	-71.813	0.88%
5	-1.497	50	0.00293	190.600	190.600	188.314	190.530	0.04%
		Mean=	0.00234				Mean=	0.31%

Table A1.10 Data for the calibration of the gravel hopper load cells

Calibration data obtained with 5 tests are shown in Table A1.10. Plots of the calibration points are shown in Figure A1.21. Taking into account the findings for the sand hopper (Figures A1.16 and A1.19), a quadratic function was used instead of a linear fit, as follows:

$$W = 5.9044 Voltage^2 + 312.573 Voltage + 643.098 \text{ [kg]} \qquad \text{(A1.19)}$$

In applying eq.(A1.19) to the calibration data in Table A1.10, the mean relative error, here defined as the absolute value of the difference between the actual and calculated weight increment divided by the actual value, was as low as 0.31%.

Similarly as with the sand hopper, during the experimental campaign, the calibration of the load cells of the gravel hopper was verified three times. Data for these verifications have been plotted in Figure A1.22 using the ratio of the increment of weight to the increment of voltage as a function of the mean signal

voltage. For these verifications, weights higher than 200 kg (approximately higher than -1.46 volts) were obtained by filling the hopper with sand, using increments of known weights. In Figure A1.22 it is evident that, in contrast to the sand hopper, verifications showed a slight deviation from the original calibration. One reason for such variations may be the change in ambient temperatures, because the first calibration was performed in winter and the others in late spring. Nevertheless, it was not clear which could have been the real reason for such variation, as the sand hopper did not show a similar effect.

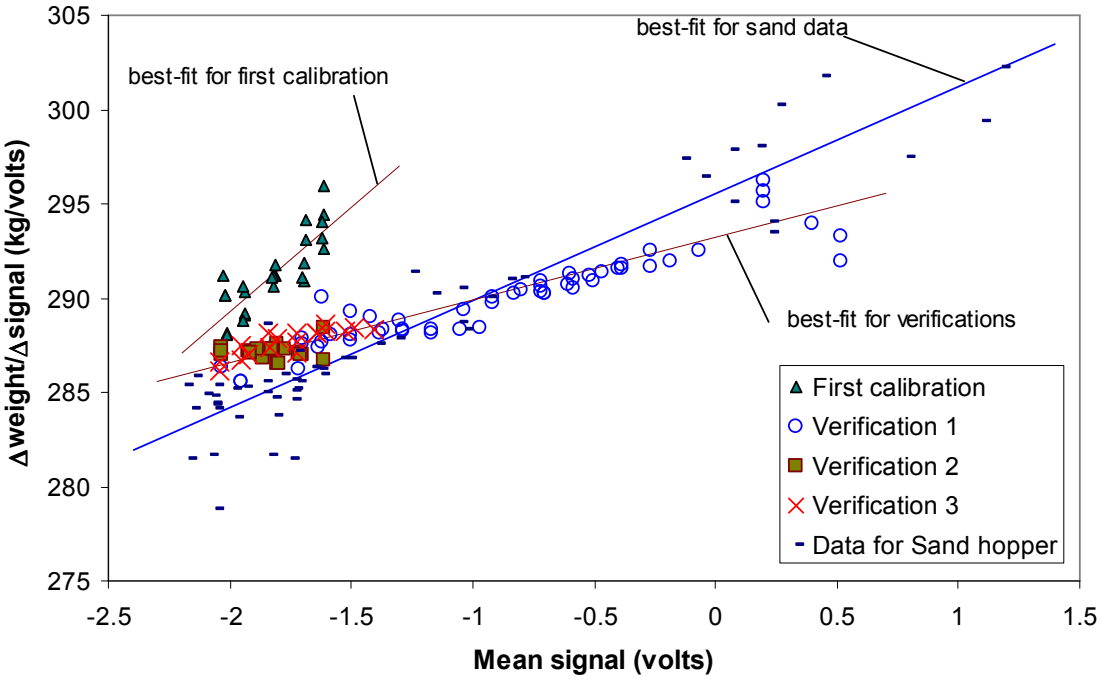

Figure A1.22 Calibration of the load cells to relate the signal voltage to its corresponding weight on the gravel hopper. Data and best-fit curve for the sand hopper are shown for comparison as well.

The best-fit line for the data for the original calibration was

$$\frac{\Delta W}{\Delta signal} = 311.306 + 11 Voltage \text{ [kg/volts]} \qquad \text{(A1.20)}$$

All three verifications showed no important differences between each other, therefore a unique best-fit line was obtained for the three:

$$\frac{\Delta W}{\Delta signal} = 293.232 + 3.332 Voltage \text{ [kg/volts]} \qquad \text{(A1.21)}$$

The standard quadratic error for the original calibration was 1.09, while for the verifications it was 0.775. Using eqs.(A1.20) and (A1.21), it is found that an increment of 1 volt is equivalent to an increment of 311 kg and 293 kg of weight on the gravel hopper, respectively. Hence, using these values for the error of both equations it is found that the error in measurements of weight increment with the RTDAS is roughly of 0.35% and 0.26%, for the original calibration and the verifications, respectively.

3.4.1.5 Operation of the Real-Time Data Acquisition System (RTDAS) with the sediment feeding and recirculating system

In this section some examples are shown of the operation of the RTDAS joint with the sediment feeding and recirculation-systems. Eqs.(A.17) and eq.(A1.19) were used to transfer the signal of the load cells from voltage to mass in kg, for the sand and gravel hoppers, respectively.

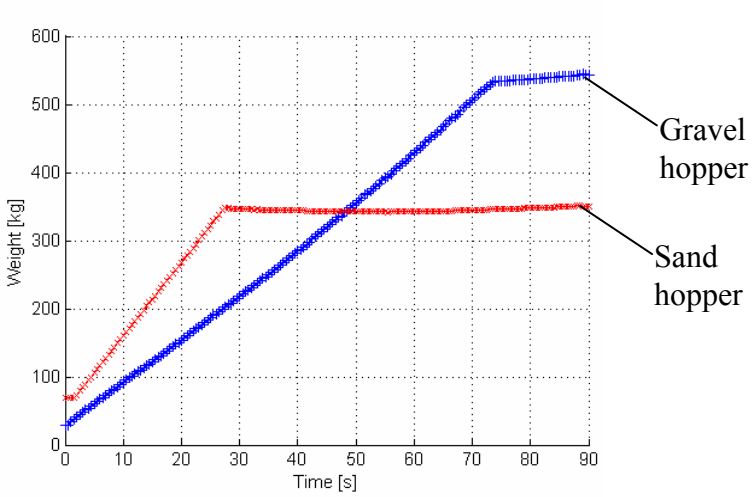

Figure A1.23 Monitoring with the RTDAS of the filling of the sand and gravel hoppers with sediment conveyed by the screw conveyors connected to the storing deposits.

Sediment to be used in the experimental flume can be stored in two large deposits (one for sand and one for gravel, see Figure A1.2 and Photos P1 and P2), from which the material can be supplied to the respective hopper by means of screw conveyors driven each by a motor. Figure A1.23 shows the filling operation of the sand and gravel hoppers registered by the load cells with the RTDAS. Note that the operation is quite fast, with an approximate rate of 10 kg/s for sand and 6 kg/s for gravel. Only slightly more than 70 seconds are needed to load the gravel hopper from being almost empty to contain half a ton.

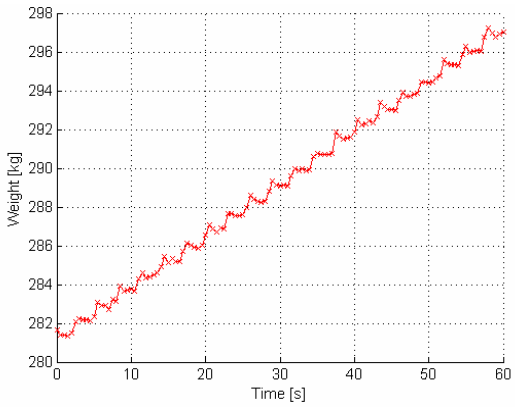

Figure A1.24 Monitoring with the RTDAS of the filling of the sand hopper with sediment conveyed by the screw conveyor connected to the sediment-recirculating system.

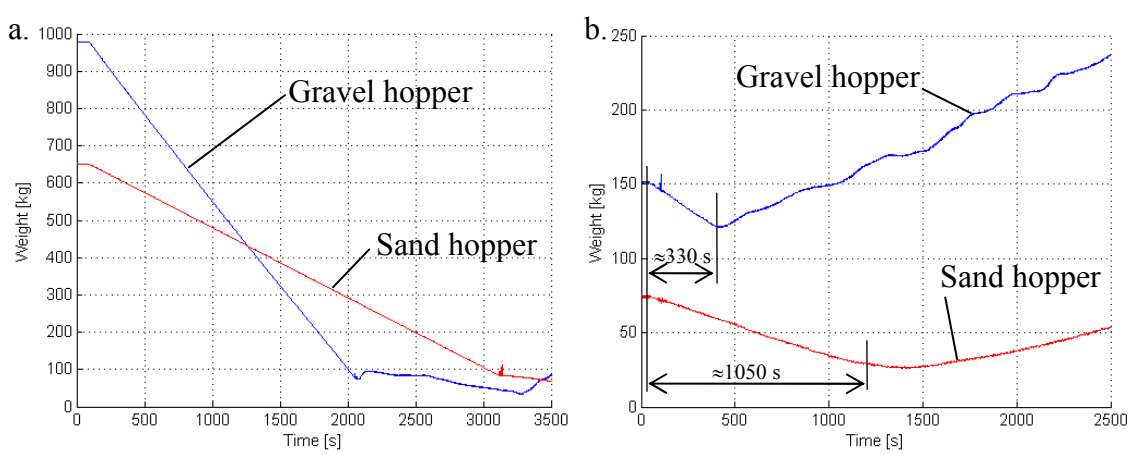

Figure A1.25 Monitoring of the weights in the hoppers with the RTDAS; a) constant sediment feeding to the channel with no addition of material to the hoppers; b) lag-time for the sediment to arrive in the hopper after leaving the downstream-end of the channel and traveling through the circuit of sediment recirculation.

Material that comes from the sediment-recirculating system is delivered to the hoppers by means of screw conveyors that receive the material from the trommel and from the giraffe, for gravel and sand, respectively. These screws deliver the material in pulses and rotate more slowly than those to take the material from the large deposits to the hoppers. Figure A1.24 shows the operation registered with the RTDAS for the filling of the sand hopper with material delivered by the screw conveyor (see also Photo P3a) for a condition in which the hopper is not feeding material to the channel and it is only being filled. Note that the RTDAS is able to register the sediment pulses produced by the rotation of the screws, which occur approximately every 3 seconds.

The main function of the hoppers is to operate as feeders and supply a constant amount of sediment to the channel. Figure A1.25a shows the operation of the hoppers as feeders, registered with the RTDAS. For this Figure there is only sediment unloading and no supply from the recirculating system. In the example, the gravel hopper unloads 880 kg in 2000 seconds, i.e., 440 g/s, while the sand hopper unloads 550 kg in 3000 seconds, i.e. 183 g/s (feeding rate with 29.4% of sand content). Note the linearity of the unloading process, verifying that the sediment feeding is constant irrespective of the amount of sediment in the hopper.

When the RTDAS is used for a real-time monitoring of the rate of solid discharge in the channel, sediment that leaves from the downstream-end of the channel needs to travel all the way in the recirculating system to be registered by the load cells when arriving in the hoppers. Therefore, rigorously the changes in weight registered on the hopper are not a real-time measurement of the sediment transport rate in the channel, since there is a lag-time equal to the time needed for the sediment to travel through the recirculating system. Lag-times have been measured for the sand and gravel in the example shown in Figure A1.25b. This example corresponds to a run for which sediment was constantly fed but at the same time the material leaving the downstream-end of the channel was recirculated and returned back to the hoppers. Both hoppers begin to feed material at the same time as the experiment with water flowing and moving sediment through the channel begins. The experiment corresponds

to a run for which the imposed hydraulic conditions caused bed erosion, therefore, at the beginning of the run the hoppers lost weight gradually but then, when the sediment leaving the channel arrived, the weight on the hoppers began to recover. In the Figure it is evident that lag-times for the sand circuit (≈1050 s=17 min) were longer than lag-times for the gravel (≈330 s=5 min). This difference is due to the larger trip for the sand, which after being separated from the gravel in the trommel, it has to enter in the siltation tank called “giraffe” to be separated from water. Lag-times could vary some minutes for each of the two circuits depending on the selected velocity of rotation of the screws, the efficiency of the recirculating pump for the imposed conditions, the efficiency of the suction in the sediment collecting tank, and, at the beginning of a run, depending on the sediment concentration from previous runs in the system.

3.4.1.6 Calibration of the sediment feeders

A total number of 136 runs, 84 for the sand hopper and 52 for the gravel hopper, were performed to obtain the unloading constant K_f in eq.(A1.7) for different combinations of the opening h_f of the sluice gate at the base of the hopper and the velocity V_f of the rotating band. The tested hopper was filled with sediment and for a selected opening h_f and velocity frequency $\%V$ of the band, the hopper was unloaded and the variation of weight with time was registered. Some examples of the unloading curves for wet sand are shown in Figure A1.26. All runs shown in this Figure began approximately with the same weight of sediment on the hopper (≈650 kg) and for all of them the run ended when the hopper was totally empty. Note that for these curves it is verified that the rate of sediment feeding during the unloading process is approximately constant and therefore, independent of the weight on the hopper (excluding the last part of the curve when the hopper was almost empty).

For runs with wet material, sediment samples were collected from the rotating band on the base of the hopper when the unloading process was about to finish. These samples were weighted and let to dry to obtain the water content first, and secondly, for being sieved to obtain the mean diameter of the sediment. For each run, a best-fit line was calculated using least-squares. K_f was equal to the slope of this line. For line fitting, the unloading curves were truncated at their lowest part to exclude segments with a slight curvature due to a poor sediment distribution along the width of the sluice gate. This feature occurred when the hopper was almost empty and sediment near the gate was limited. Similarly, the unloading curves were truncated at their upper part to consider only weights close to or within the range of weights used in the calibration of the load cells. Figures A1.27 to A1.29 show the unloading curves and the best-fit lines for the calibration of the feeding rates.

For the first 20 runs performed the analogical display and a chronometer were used to measure the variation of weight with time. From these 20 runs, 15 runs were performed with dry sand and 5 runs with wet sand. Table A1.11 shows the combinations of h_f and $\%V$ used and the values obtained for K_f. The mean quadratic error for the weights computed with the fitted trend line are shown as well. Figure A1.27 shows the unloading curves for the dry sand and the obtained best-fit lines by least-squares. The minimum weight on the hopper considered for line fitting was 50 kg, and the maximum weight was 400 kg.

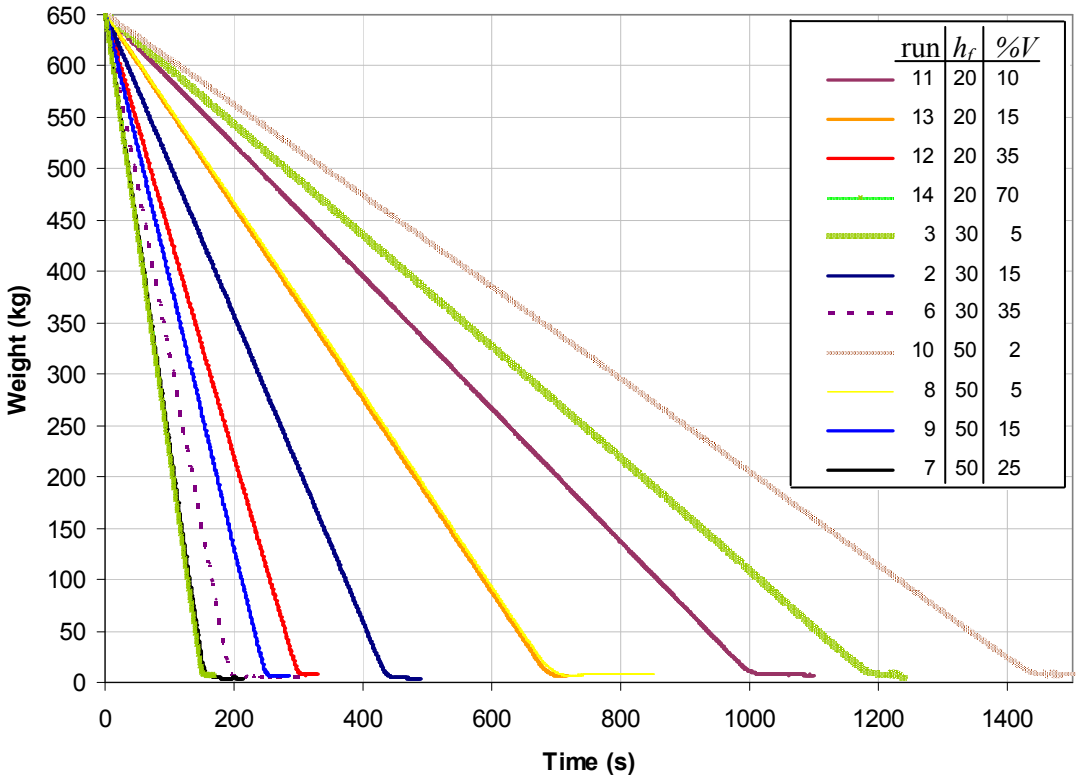

*Figure A1.26 Runs performed with **wet sand** to obtain the rate of sediment feeding. Weight and time measurements were taken with the RTDAS. h_f is the sluice gate opening in mm and %V is the voltage frequency for the velocity of the rotating band.*

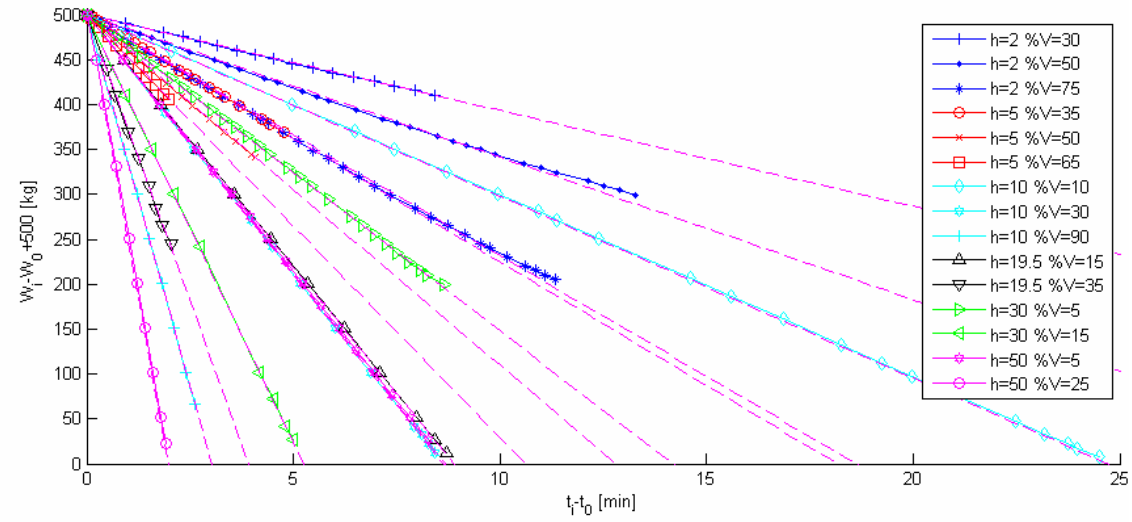

*Figure A1.27 Runs performed with **dry sand** to obtain the value of coefficient K_f in eq.(A1.7). Dashed lines correspond to best-fit lines for measured weights on the hopper between 50 and 400 kg. Weight measurements were taken on the analogical display and time was measured with a chronometer. Subscript i refers to the number of measurement in the run, so that W_0 is the initial weight on the hopper, corresponding to time t_0.*

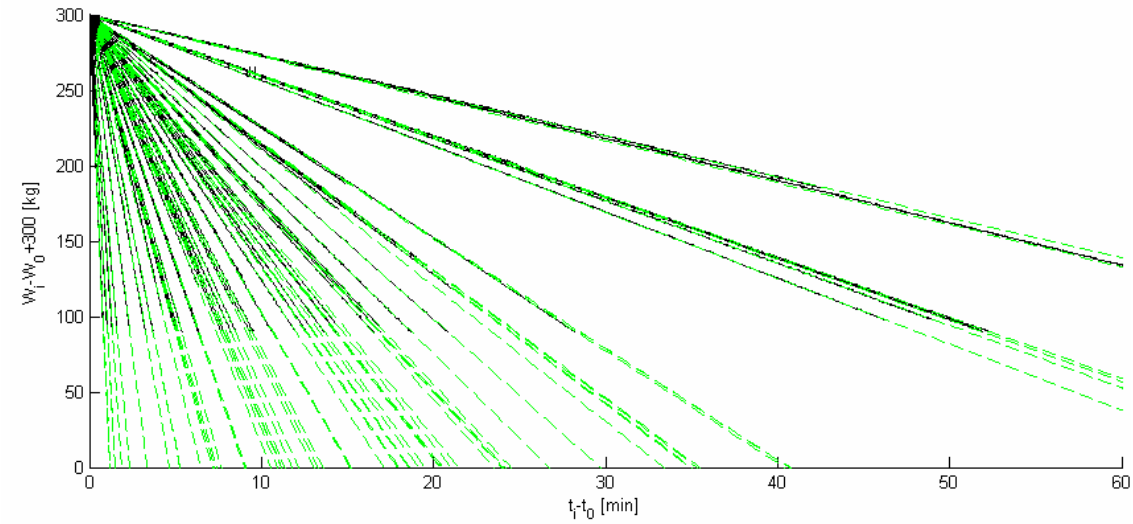

*Figure A1.28 Runs performed with **wet sand** to obtain the value of coefficient K_f in eq.(A1.7). Dashed lines correspond to best-fit lines for measured weights on the hopper between 90 and 300 kg. Weight and time measurements were taken with the RTDAS. Subscript i refers to the number of measurement in the run, so that W_0 is the initial weight on the hopper, corresponding to time t_0.*

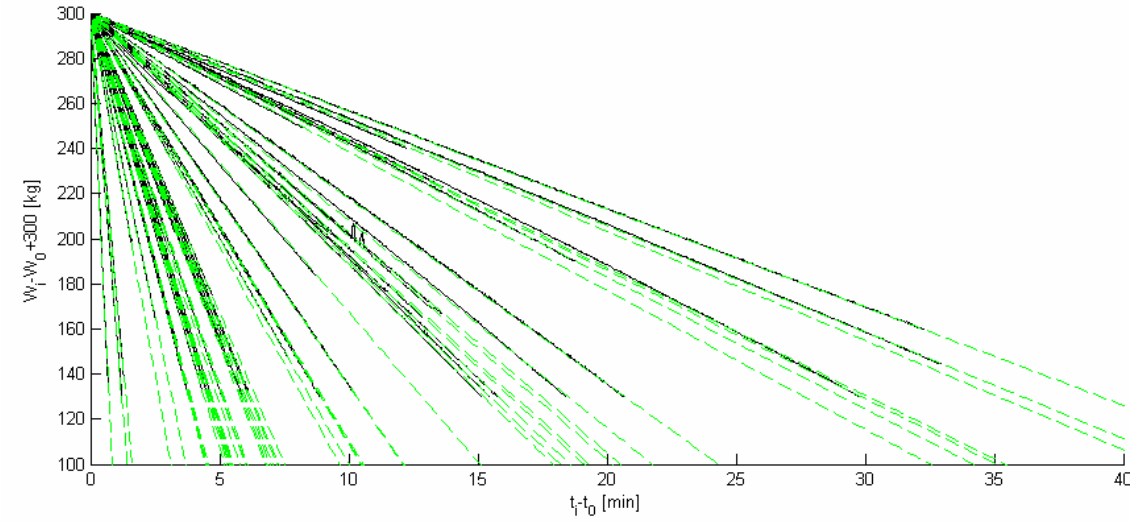

*Figure A1.29 Runs performed with **wet gravel** to obtain the value of coefficient K_f in eq.(A1.7).). Dashed lines correspond to best-fit lines for measured weights on the hopper between 80 and 250 kg. Weight and time measurements were taken with the RTDAS. Subscript i refers to the number of measurement in the run, so that W_0 is the initial weight on the hopper, corresponding to time t_0.*

The Real time Acquisition System was used to automatically measure the time variation of weight in 64 runs on the sand hopper with wet material, and in 52 runs on the gravel hopper with wet material as well. Most of these runs were performed when experimental runs with the whole flume in operation were carried out during the first experimental campaign. To achieve this, the feeding of sediment from the recirculating system to the hopper was stopped until the hopper was almost empty. The range of weights used for line fitting to the data was between 90 and 300 kg for the sand hopper, and between 80 and 250 kg

for the gravel hopper. Tables A1.12 and A1.13 show the combinations of h_f and $\%V$ used, and the values of K_f obtained by least-squares line fitting. The mean quadratic error for the weights computed with the fitted function is shown as well in the tables, while Figures A1.28 and A1.29 show the unloading curves and the lines fitted by least-squares.

Run number	Gate aperture	Rotating band voltage freq.	Water content	Mean diameter	Unloading constant	Mean quadratic error of the fitted line
n	h_f (mm)	$\%V$	$\%w$	D_m (mm)	K_{fS} (kg/s)	e_K (kg/s)
9	2.0	30	0	1.53	-0.178	0.148
10	2.0	50	0	1.53	-0.264	0.215
14	2.0	75	0	1.52	-0.447	0.201
12	5.0	35	0	1.52	-0.459	0.060
11	5.0	50	0	1.53	-0.650	0.133
15	5.0	65	0	1.52	-0.785	0.076
2	10.0	10	0	1.55	-0.337	0.121
3	10.0	30	0	1.55	-0.966	0.187
4	10.0	90	0	1.54	-2.760	0.162
7	19.5	15	0	1.54	-0.937	0.121
8	19.5	35	0	1.53	-2.129	0.726
13	30.0	5	0	1.52	-0.587	0.118
1	30.0	15	0	1.55	-1.587	0.304
5	50.0	5	0	1.54	-0.961	0.084
6	50.0	25	0	1.54	-4.233	0.190
17	5.0	50	3.3%	1.51	-0.543	0.100
16	5.0	65	3.6%	1.51	-0.732	0.115
19	10.0	10	3.7%	1.51	-0.276	0.045
18	10.0	30	4.0%	1.51	-0.818	0.059
20	10.0	90	3.1%	1.50	-2.417	0.309

Table A1.11 Combination of variables for the 20 runs performed for calibration of the sand feeder using the analogical display. The run number refers to the consecutive order in which the runs were performed. Runs with dry sand are indicated by a water content equal to zero. Weights in the hopper for obtaining K_f were between 50 and 400 kg.

For the calibration of the feeders, weight measurements on the analogical display were corrected with eq.(A1.12), while for the transfer of the load cells electric signal to mass units, when using the RTDAS, eqs.(A1.17) to (A1.21) were applied and solved numerically. The weight W for time i was obtained with

$$W_i = W_{i-1} + (V_{Si} - V_{Si-1})\left[a + b\left(\frac{V_{Si} + V_{Si-1}}{2}\right)\right] \qquad \text{(A1.22)}$$

where a and b are constants in eqs.(A1.18), (A1.20) and (A1.21), and V_{Si} is the voltage from the load cells signal for time i. $W_{i=1}$ was calculated with eq.(A1.17) for the sand hopper, and with eq.(A1.19) for the gravel hopper. For applying eq.(A1.22) to the gravel hopper, constants in eq.(A1.20) were used for runs 1 to 28, while constants in eq.(A1.21) were used for runs 29 to 52. The reason for using one or another were the changes in the original calibration, which were

likely caused by the use of both hoppers together when runs mixing sand and gravel were performed. The difference found between using only eq.(A1.20) and only using eq.(A1.21) with all data for computed values of K_f was in average of only 1.7%.

Run number	Gate aperture	Rotating band voltage freq.	Water content	Mean diameter	Unloading constant	Mean quadratic error fitted line
n	h_f (mm)	$\%V$	$\%w$	D_m (mm)	K_{fS} (kg/s)	e_K (kg/s)
1	5.0	25.00	2.0%	1.55	-0.261	0.011
32	9.5	2.00	2.8%	1.44	-0.067	0.003
33	9.5	2.00	3.4%	1.48	-0.068	0.003
42	10.0	1.00	4.1%	1.38	-0.045	0.004
41	10.0	1.10	3.0%	1.44	-0.046	0.006
53	10.0	1.89	3.4%	1.44	-0.069	0.003
19	10.0	2.00	5.0%	1.54	-0.073	0.004
52	10.0	4.04	2.7%	1.41	-0.123	0.006
51	10.0	4.04	3.8%	1.37	-0.123	0.005
39	10.0	4.49	3.9%	1.46	-0.142	0.006
40	10.0	4.49	4.1%	1.49	-0.141	0.007
62	10.0	4.84	3.4%	1.31	-0.143	0.004
63	10.0	4.84	3.7%	1.39	-0.143	0.002
20	10.0	5.00	5.0%	1.53	-0.150	0.003
38	10.0	6.48	3.9%	1.47	-0.187	0.005
37	10.0	7.03	3.3%	1.49	-0.209	0.008
36	10.0	7.03	3.5%	1.56	-0.213	0.007
50	10.0	8.00	5.0%	1.36	-0.233	0.011
59	10.0	8.63	2.8%	1.30	-0.246	0.004
61	10.0	8.63	3.8%	1.42	-0.238	0.004
60	10.0	8.63	4.6%	1.41	-0.244	0.003
35	10.0	9.20	4.2%	1.46	-0.269	0.013
34	10.0	9.20	4.5%	1.50	-0.268	0.006
21	10.0	10.00	3.6%	1.53	-0.279	0.015
22	10.0	10.00	3.6%	1.52	-0.278	0.004
49	10.0	11.65	3.5%	1.38	-0.329	0.016
48	10.0	11.65	5.4%	1.45	-0.330	0.013
46	10.0	13.31	4.2%	1.47	-0.384	0.010
47	10.0	13.31	4.2%	1.42	-0.368	0.007
18	10.0	15.00	3.6%	1.54	-0.411	0.003
44	10.0	15.73	5.0%	1.49	-0.440	0.011
45	10.0	15.73	5.3%	1.31	-0.425	0.019
57	10.0	16.96	2.5%	1.48	-0.447	0.006
58	10.0	16.96	4.0%	1.45	-0.474	0.018
56	10.0	16.96	4.4%	1.39	-0.449	0.005
16	10.0	20.00	3.6%	1.55	-0.554	0.014
54	10.0	25.00	1.2%	1.45	-0.701	0.006
55	10.0	25.00	3.3%	1.46	-0.689	0.022
17	10.0	25.00	3.6%	1.54	-0.677	0.006
43	10.0	30.62	3.8%	1.50	-0.773	0.071
31	10.0	40.00	3.1%	1.49	-1.073	0.019
25	15.0	2.00	3.8%	1.51	-0.124	0.009
26	15.0	4.00	2.4%	1.51	-0.204	0.003

27	15.0	4.00	3.6%	1.51	-0.207	0.002
28	15.0	4.00	3.8%	1.50	-0.208	0.003
30	15.0	5.00	4.0%	1.50	-0.245	0.003
29	15.0	5.00	4.2%	1.50	-0.243	0.006
23	15.0	6.00	3.6%	1.52	-0.292	0.014
24	15.0	8.00	3.6%	1.52	-0.376	0.015
64	19.0	5.00	2.4%	1.47	-0.328	0.019
15	20.0	2.00	3.6%	1.55	-0.168	0.003
11	20.0	10.00	8.3%	1.55	-0.651	0.008
13	20.0	15.00	6.0%	1.55	-0.947	0.008
12	20.0	35.00	3.6%	1.55	-2.168	0.018
14	20.0	70.00	3.6%	1.55	-4.350	0.035
5	30.0	2.00	3.6%	1.55	-0.256	0.005
3	30.0	5.00	3.6%	1.55	-0.549	0.005
2	30.0	15.00	6.6%	1.55	-1.494	0.010
4	30.0	35.00	3.6%	1.55	-3.385	0.044
6	30.0	35.00	3.6%	1.55	-3.366	0.029
10	50.0	2.00	6.0%	1.55	-0.457	0.005
8	50.0	5.00	3.6%	1.55	-0.948	0.009
9	50.0	15.00	3.6%	1.55	-2.637	0.032
7	50.0	25.00	3.6%	1.55	-4.257	0.048

Table A1.12 Combination of variables for the 64 runs performed for calibration of the sand feeder using the RTDAS. The run number refers to the consecutive order in which the runs were performed. Weights in the hopper for obtaining K_f were between 90 and 300 kg.

Run number	**Gate aperture**	**Rotating band voltage freq.**	**Water content**	**Mean diameter**	**Unloading constant**	**Mean quadratic error fitted line**
n	h_f **(mm)**	$\%V$	$\%\omega$	D_m **(mm)**	K_{fG} **(kg/s)**	e_K **(kg/s)**
14	10.0	3.00	2.1%	4.76	-0.072	0.002
28	12.0	2.00	2.2%	4.50	-0.081	0.004
27	12.0	2.00	2.4%	4.18	-0.079	0.005
15	15.0	3.00	2.6%	4.04	-0.137	0.006
13	15.0	4.00	2.2%	4.20	-0.179	0.004
11	15.0	4.00	2.2%	4.23	-0.186	0.007
12	15.0	4.00	2.4%	4.60	-0.183	0.012
10	15.0	4.00	2.8%	4.28	-0.172	0.022
9	15.0	5.00	3.1%	4.42	-0.221	0.005
50	20.0	1.00	2.6%	3.25	-0.098	0.007
38	20.0	1.00	2.6%	3.98	-0.094	0.006
39	20.0	1.04	2.7%	3.82	-0.095	0.014
40	20.0	1.04	11.0%	3.82	-0.103	0.006
29	20.0	2.00	2.0%	3.73	-0.165	0.019
8	20.0	2.00	2.8%	4.44	-0.153	0.014
30	20.0	2.00	3.2%	3.59	-0.162	0.004
49	20.0	2.19	2.8%	3.52	-0.174	0.008
26	20.0	4.00	2.6%	3.83	-0.275	0.004
25	20.0	4.00	2.7%	3.96	-0.275	0.009
36	20.0	4.68	2.1%	3.89	-0.316	0.009
37	20.0	4.68	2.5%	4.14	-0.317	0.005
48	20.0	4.76	3.1%	3.11	-0.345	0.005

6	20.0	5.00	1.8%	4.38	-0.333	0.003
7	20.0	5.00	3.2%	4.38	-0.318	0.008
35	20.0	6.83	2.8%	4.15	-0.443	0.011
47	20.0	7.10	3.1%	3.42	-0.491	0.013
46	20.0	7.10	3.4%	3.16	-0.486	0.011
33	20.0	7.44	2.8%	3.97	-0.471	0.010
34	20.0	7.44	3.4%	3.57	-0.478	0.012
45	20.0	8.17	2.9%	3.53	-0.558	0.011
44	20.0	8.17	3.1%	3.16	-0.549	0.016
31	20.0	9.75	2.0%	3.91	-0.612	0.034
32	20.0	9.75	2.4%	3.93	-0.603	0.043
16	20.0	10.00	2.1%	4.37	-0.620	0.008
3	20.0	10.00	2.4%	4.38	-0.622	0.006
42	20.0	10.00	2.6%	3.72	-0.629	0.011
43	20.0	10.00	2.7%	3.31	-0.645	0.008
17	20.0	10.00	2.8%	4.69	-0.607	0.012
4	20.0	15.00	2.4%	4.38	-0.900	0.007
41	20.0	17.00	2.3%	3.65	-1.070	0.020
2	20.0	35.00	3.7%	4.38	-2.081	0.017
1	20.0	40.00	2.9%	4.38	-2.344	0.020
5	20.0	70.00	2.1%	4.38	-4.038	0.025
23	30.0	4.00	2.6%	4.03	-0.462	0.005
24	30.0	4.00	2.8%	3.69	-0.457	0.010
22	30.0	5.00	4.2%	3.53	-0.577	0.019
51	30.0	7.00	0.0%	3.85	-0.731	0.011
52	30.0	7.00	0.0%	3.85	-0.739	0.010
20	30.0	7.00	2.8%	4.13	-0.748	0.011
18	30.0	7.00	3.1%	4.06	-0.742	0.009
19	30.0	7.00	3.3%	3.64	-0.745	0.013
21	30.1	5.00	2.5%	4.01	-0.556	0.005

Table A1.13 Combination of variables for the 52 runs performed for calibration of the gravel feeder using the RTDAS. The run number refers to the consecutive order in which the runs were performed. Weights in the hopper for obtaining K_f were between 80 and 250 kg.

Comparison of mean quadratic errors in Tables A1.11 to A1.13 show a difference of two orders of magnitude between runs performed with the analogical display and runs using the RTDAS. Hence, it is evident that the RTDAS improved the precision of the measurements. This notwithstanding, comparison of runs with dry sand using the same combination of h_f and $\%V$ with both instruments, showed no important differences. These are runs 21 and 22 for the RTDAS and run 19 for the analogical display, for which h_f=10 mm and $\%V$=10; computed values of K_f were 279 and 278 g/s for the RTDAS runs, and 276 g/s for the analogical display, that is a difference of almost 1%.

Comparison between dry and wet sand

For the hopper filled up to a certain volume, the unloading curve for wet sediment would be steeper than the curve for dry sediment if the porosity remains the same for both conditions, as it is schematized in Figure A1.30. Martín-Vide et al. (1998) verified this effect for a hopper similar to those in the present work, filled with sand with a median diameter of 0.86 mm. This

notwithstanding, this behaviour is not necessarily verified for all materials since moisture can produce a cohesive behaviour on the sediment or affect the arrangement of the particles and thus the porosity of the bulk material. For the sand used in the present work the condition presented in Figure A1.30 was not valid.

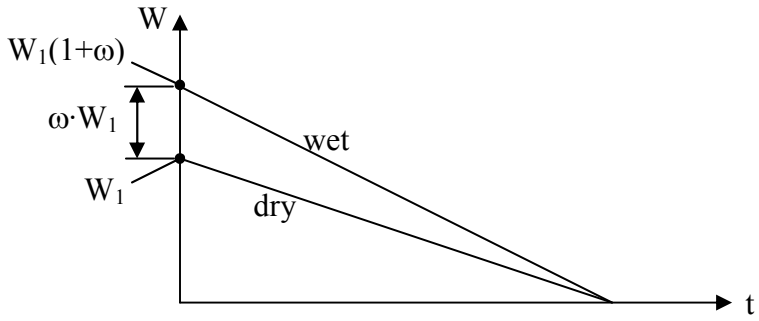

Figure A1.30 Theoretical representation of the unloading curves for wet and dry sand when porosity is the same for both conditions and does not change during the unloading process. ω is water content.

Unloading curves for dry and wet sand in the present work, with equal h_f and $\%V$, are compared in Figure A1.31. The curves for dry sand are steeper than those for wet sand, thus indicating that for the sand tested sediment feeding is more efficient when the material is dry.

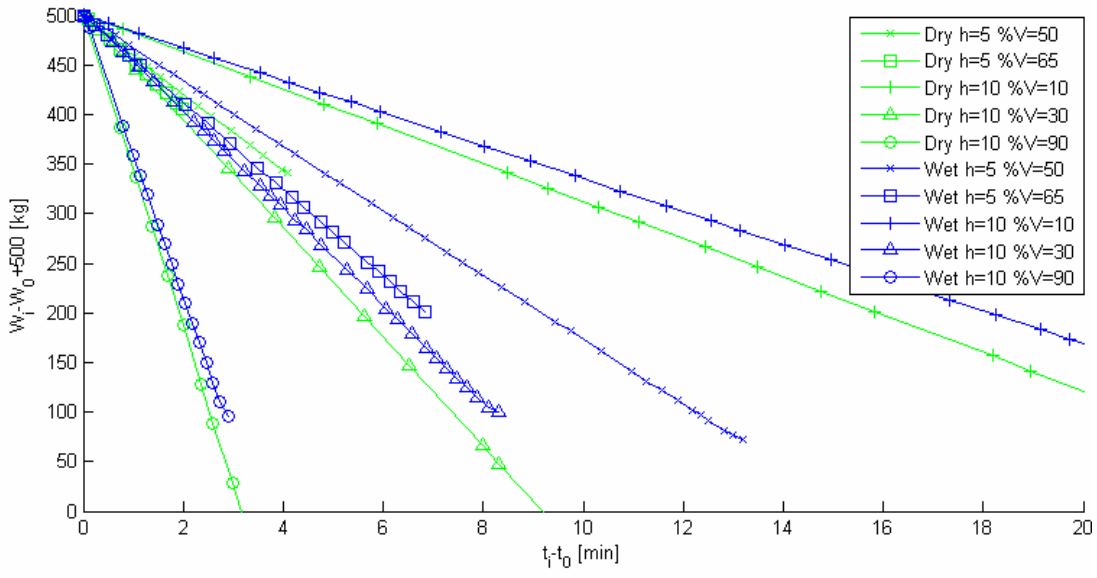

Figure A1.31 Comparison between runs with dry and with wet sand. Weight measurements were taken on the analogical display and time was measured with a chronometer. Subscript i refers to the number of measurement in the run, so that W_0 is the initial weight on the hopper, corresponding to time t_0. Note that for equal h_f and $\%V$, the slope of lines for wet-sand runs is milder, indicating a lower feeding efficiency than for runs with dry sand.

As can be seen in Tables A1.11 to A1.13, a higher number of tests were performed with wet material than with dry material; this was so because when the hoppers are operated with the sediment-recirculating system the sediment returning to the hoppers necessarily contains a certain amount of moisture. We were particularly interested in calibrating the hopper for this condition.

Calibration of the general equation for sediment feeding

The data for all runs in Tables A1.11 to A1.13 have been plotted in Figure A1.32 using the dimensionless numbers in eq.(A1.10). For each run it was considered that $Q_{SF}=K_f$, the velocity of the rotating band was calculated with eq.(A1.11) using $\%V$, the mean diameter D_m was used as the representative diameter of the sediment, and the values used for density and porosity were 2630 kg/m^3 and 0.4 for the sand, and 2600 kg/m^3 and 0.38 for the gravel, respectively.

It was observed that data for low velocities of the rotating band plotted as outliers, therefore, for each hopper, data for wet material were grouped in 3 classes according to different ranges of the $\%V$. This response must have been related to a highly nonlinear tail of the function relating the voltage frequency and the velocity of the rotating band. As far as data for dry sand is concerned, it was remarkable that these data showed a much larger scatter than wet sand and gravel, but no trends were found to explain the outliers. It is likely that such a larger scatter was related to the higher errors found for data measured with the analogical display than with the RTDAS. Measurements on the analogical display were obtained visually using a chronometer, and as it was already indicated, from comparisons of Tables A1.11 and A1.12, mean quadratic errors for the best-fit lines obtained for data measured with the RTDAS were two orders of magnitude lower than data measured with the analogical display and the chronometer.

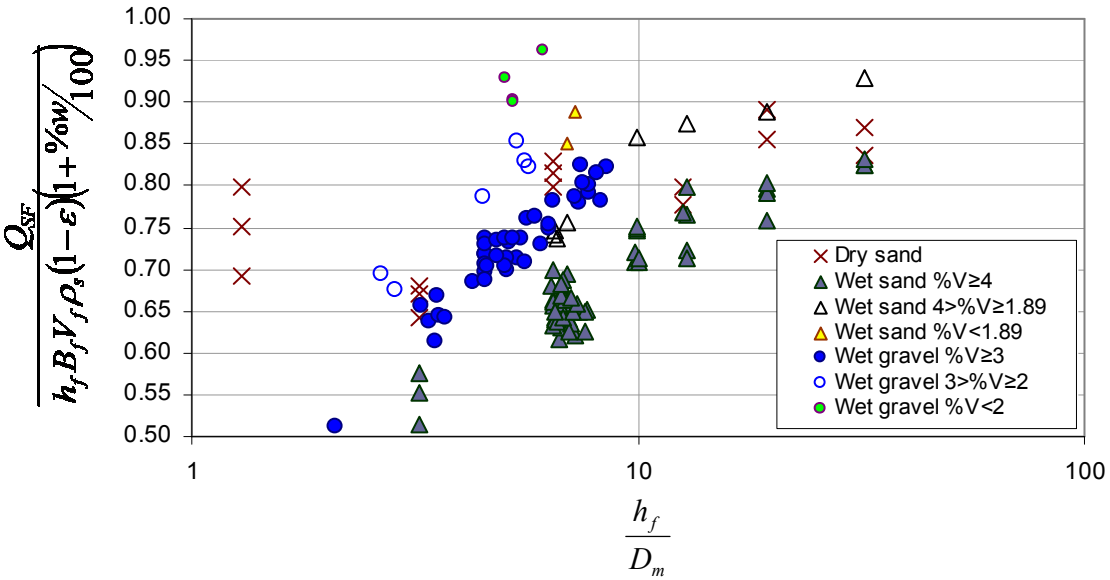

Figure A1.32 Data for calibration of the sand and gravel feeders as a function of dimensionless numbers in eq.(A1.10).

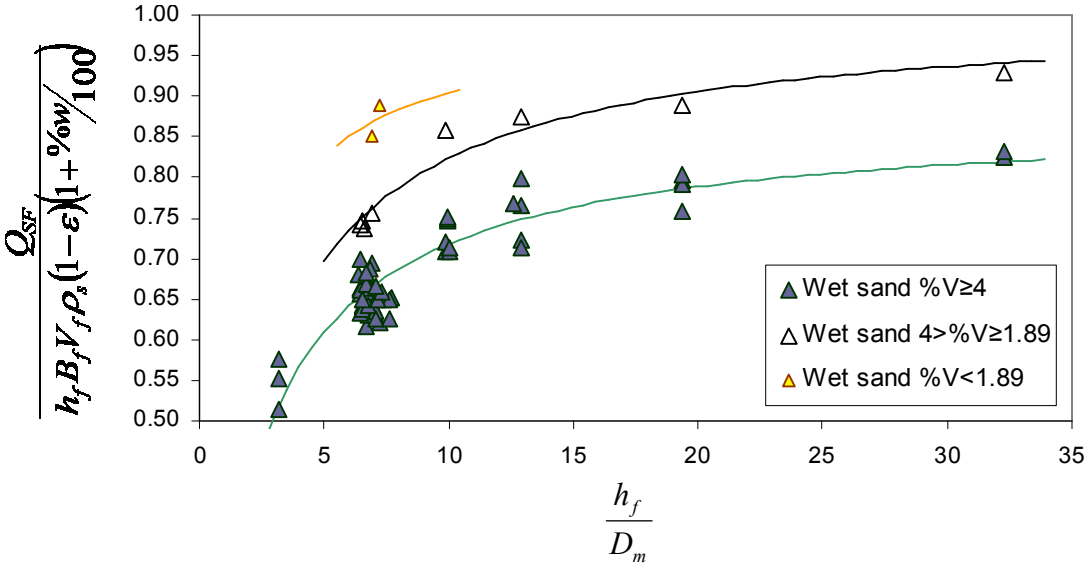

Figure A1.33 Data and calibration curves for the sand feeder with wet material. Curves are given by eq.(A1.23) and coefficients in Table A1.14.

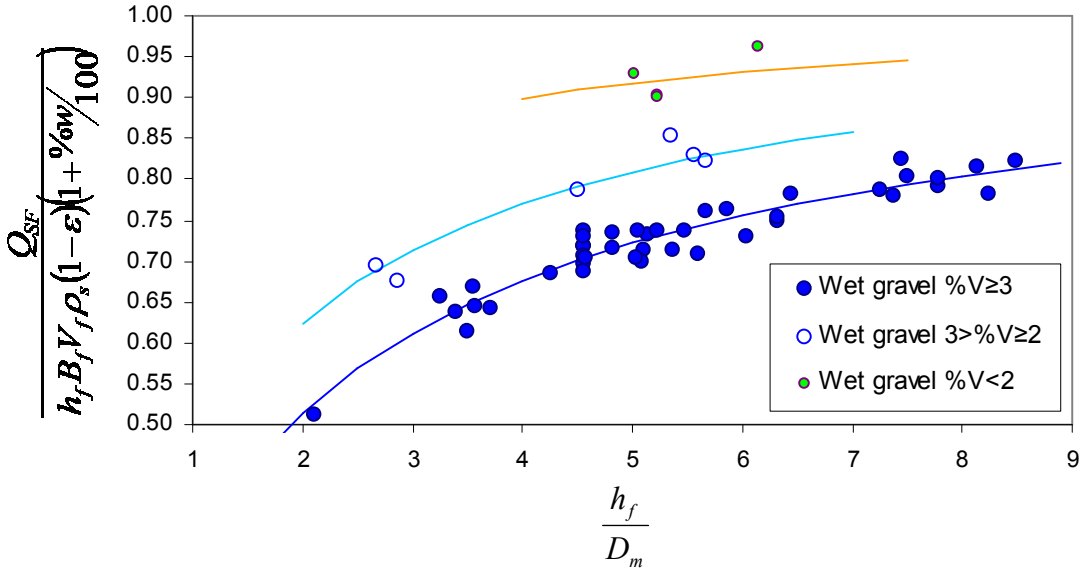

Figure A1.34 Data and calibration curves for the gravel feeder with wet material. Curves are given by eq.(A1.23) and coefficients in Table A1.14.

Coefficients in (A1.23)	Dry sand	Wet sand			Wet gravel		
		%V≥4	4>%V≥1.89	%V<1.89	%V≥3	3>%V≥2	%V<2
a	1.096	1.143	0.995	0.999	1.009	0.990	0.996
b	1.187	2.496	2.198	1.059	1.881	1.231	0.465
Mean quadratic error	±0.116	±0.025	±0.017	±0.067	±0.017	±0.019	±0.021

Table A1.14 Coefficients for eq.(A1.23) according to the characteristics of the sediment and the range of velocities of the rotating band.

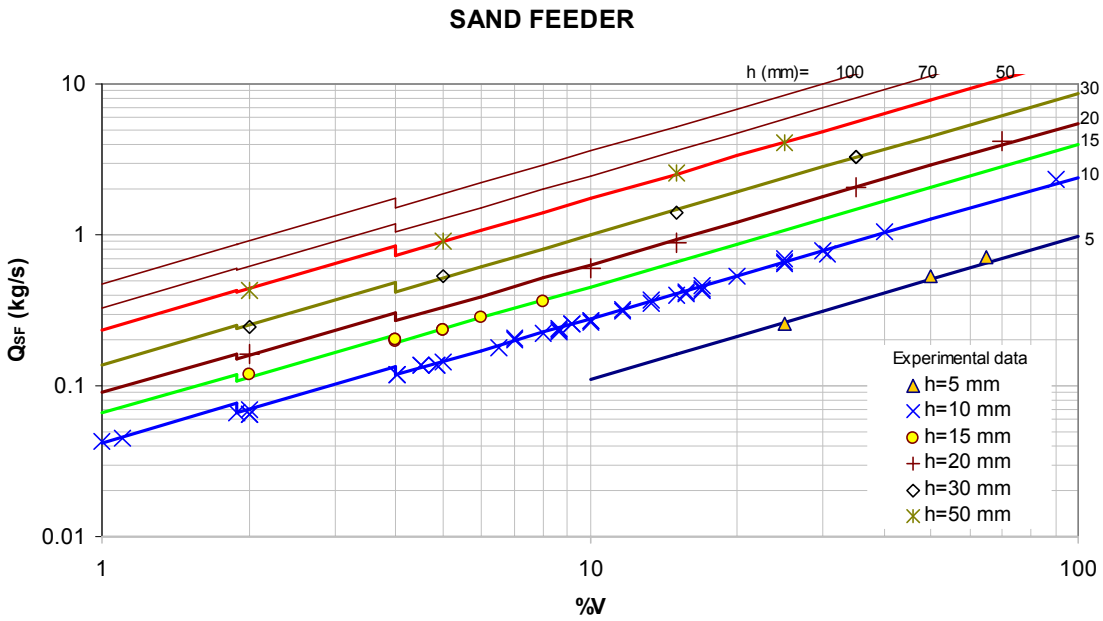

Figure A1.35 Chart for feeding rates of the sand hopper as a function of %V and h_f, according to eq.(A1.23). Values obtained for B_f=0.73 m, ρ_s=2630 kg/m^3, ε=0.4, %ω=3.9%, and D_m=1.5 mm.

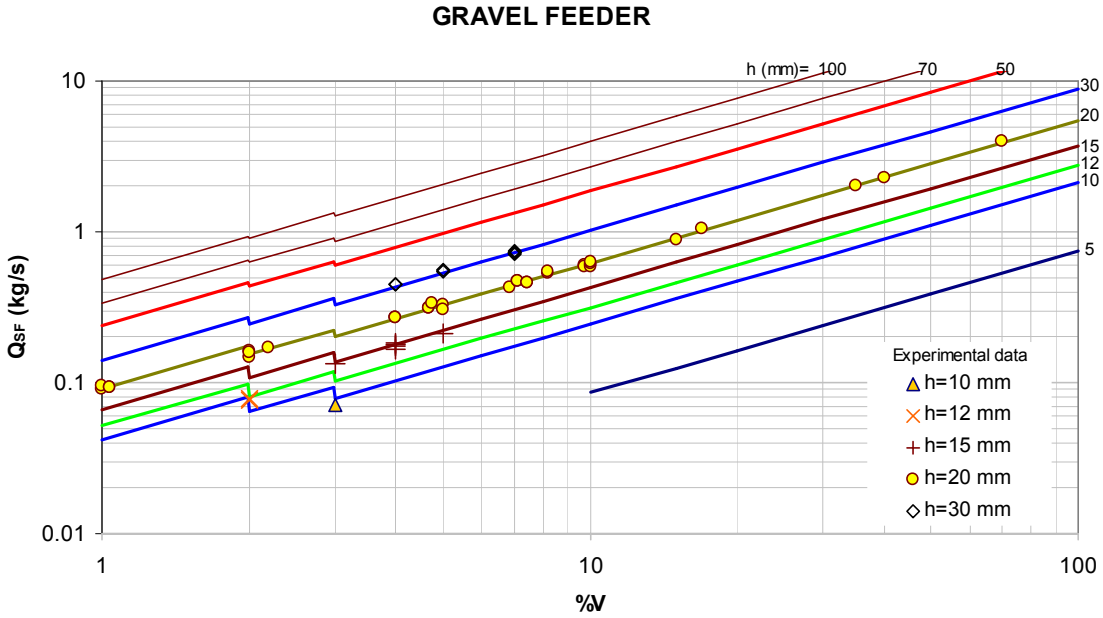

Figure A1.36 Chart for feeding rates of the gravel hopper as a function of %V and h_f, according to eq.(A1.23). Values obtained for B_f=0.73 m, ρ_s=2600 kg/m^3, ε=0.38, %ω=2.7% and D_m=4.0 mm.

Best-fit functions were searched for the data in Figure A1.32. Good correlations were found using a function of the type $y=(a+b/x)^{-1}$, with a trend toward an asymptotic limit at $y \sim a \sim 1$ for $x \sim \infty$. Using this function, eq.(A.10) yields

$$\frac{Q_{SF}}{h_f B_f V_f \rho_s (1-\varepsilon)\left(1+\%\varpi/100\right)} = \left(a + b\frac{D_m}{h_f}\right)^{-1} \qquad \text{(A1.23)}$$

The values obtained for a and b for the seven classes of data are shown in Table A1.14, and Figures A1.33 and A1.34 show the data for wet sand and wet gravel with the fitted functions. Note that eq.(A1.23) verifies that for $D_m/h_f \to 0$, $Q_{SF} \approx h_f B_f V_f \rho_s (1-\varepsilon)(1+\%\varpi/100)$. Mean quadratic errors are also shown in Table A1.14. It can be considered that the fitted function given by eq.(A1.23) concentrates all the variability of the measured parameters, and thus mean quadratic errors in Table A1.14 can be used as a measure of the error for Q_{SF}; consequently, for wet sand and wet gravel maximum errors in the feeding rate would be within ±6.7% and ±2.1%, respectively, being this maximum values related to the lowest velocities of the rotating band.

For practical purposes, the charts shown in Figures A1.35 and A1.36 were obtained for average values of the variables to be used in the first experimental campaign. Note that low feeding rates (<100 g/s) are restricted to low values of the velocity of the rotating band, which for the sand hopper are related to the highest error in Table A1.14. Since for a correct operation of the feeders necessarily h_f/D_m>1 must be fulfilled, there exists a restriction for low values of Q_{SF}, in the order of 20 to 50 g/s (for h_f/D_m<5 some tests showed that the excessive friction between the sediment grains and the sluice gate could affect the rotating of the band and even make its velocities slower). On the other extreme, although the hoppers would be able to feed sediment at rates higher than 10 kg/s (h_f=100 mm and $\%V$>30), the sediment-recirculating system would not be able to move all this amount of material from the lower section of the flume to the upper part where the trommel receives the recirculated material. This sets an upper limit for the ranges of operation of the system. It was observed that for an operation with a new pump and ideal suction conditions, the system was able to recirculate more than 1.10 kg/s, it is likely the maximum capability of the system must not be quite above this value.

3.4.2 Other elements of the sediment-recirculating system

The aim of the recirculating system is to take the sediment from the end of the channel, convey it, and deliver it with low water content either to the hoppers or to the large sediment deposits at the head of the flume. For an optimal operation when the hoppers are used, it is desirable that there were no sediment accumulation along the system during operation, that is, that the same amount of sediment that goes out from the channel is delivered to the hoppers (after lag-time, as shown in Figure A1.25b). However, this condition was not always achieved during the first experimental campaign since many problems were encountered with the suction of sediment from the sediment collecting tank. Abrasion of the blades of the pump (see Photos P8) produced a decrease in the suction efficiency with the accumulated time of operation, and thus the impeller had to be replaced from time to time. Therefore, for a good operation without sediment accumulation in the collecting tank (except for the beginning stages of a run, when small amounts of sediment inevitably accumulate on the bottom), experiments with sediment feeding rates in the range of the highest values that the system can manage, must be performed when the impeller has been recently replaced.

The interconnected elements to convey the sediment from the end of the channel to the head of the flume are listed as follows and can be identified in Figure A1.2 and photos in section 7.

Ramp to connect the channel with the sediment collecting tank

The downstream-end of the channel is separated from the sediment collecting tank by a rectangular pool of 3.2 x 3.9 m (see Figure A1.3). Inside of the pool a metal ramp with a rectangular section was installed to conduct to the collecting tank the water and sediment that goes out from the channel (Photo P7a). This ramp was joined to the channel with a rubber seal (see Photo P6a) to allow the displacement of the joint produced when the slope of the channel is changed. The slope of the ramp was roughly 9%, this high gradient guarantees that sediment is not accumulated and thus is rapidly evacuated to the downstream-end.

Sediment collecting tank, suction and pump

The sediment collecting tank has the geometry of an inverted truncated-squared pyramid that allows that sediment delivered from the ramp to the top of the tank slips by gravity to the bottom where it is suctioned with a PVC pipe (see Figures A1.1 and A1.3, and Photos P6b and P7b). The top of the tank has a rectangular geometry, 3.2 x 4.5 m, and the tank's depth (i.e., the distance from the deepest point on the bottom to the plane of the top) is 2 m. Water at the downstream-end of the tank overflows over the tilting gate described in section 3.2, to be conducted to the underground deposit as shown in Figure A1.1.

Many problems were found during the preparation of the first experimental campaign to suck efficiently the sediment on the bottom of the tank. Different suction arrangements were tested, but the most practical was found to be to use a PVC pipe leaning on one of the edges of the truncated pyramid. This pipe had a flexible joint on the upper part which allowed moving the mouth of the pipe around the bottom.

The main difficulties for efficiently suck the sediment from the bottom of the tank were found to be produced by the abrasion of the blades of the pump impeller. Photos P8 show a comparison of a new and a worn out impeller. The suction efficiency declines with the degree of abrasion, until the blades are completely worn out and no suction of sediment is possible.

The maximum sediment diameter that the pump is able to move is 32 mm, according to specifications of the manufacturer. According to tests performed, when sucking sediment from the bottom of the siltation tank, the pump uses approximately 12 l/s of water when the propeller is brand-new.

Trommel

The pump on the downstream-end of the flume sucks a slurry of water and sediment from the collecting tank. This slurry is conveyed through a 10 cm diameter PVC pipe to the head of the flume at its highest elevation. The slurry is delivered to the trommel, which is a cylindrical revolving drum whose walls are made of a wire mesh (see Photos P9). The coarse fraction of sediment (gravel) in the slurry is separated from water and from the fine fraction (sand) by the trommel, being the cutoff size of the mixture the mesh opening size. Water and fine material pass through the mesh and are deposited in the giraffe. In order to avoid the fine material to be stuck to the mesh and to the structure of the

trommel, a series of sprinklers spray water continuously to the trommel, as can be seen in Photo P9a. The axis of the trommel is slightly tilted to let the coarse material retained on the mesh to be carried to the opposite end of the drum by gravity and by the impulse given by the rotation (see Figure A1.37). The coarse material that slips down from the end of the trommel is collected in a screw conveyor that conveys the material either to the hopper or to the large deposit according to the selected turning direction.

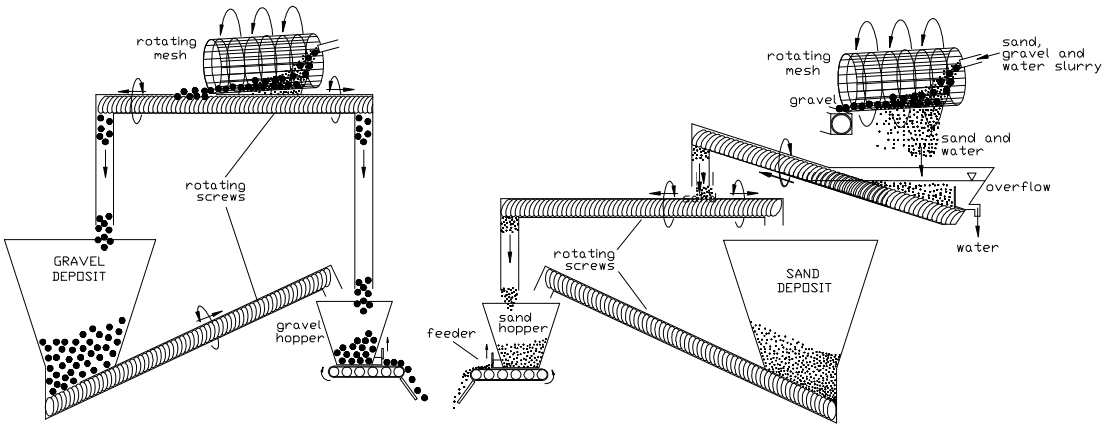

Figure A1.37 Schemes for the end of the sand (right) and gravel(left) circuits in the sediment-recirculating system.

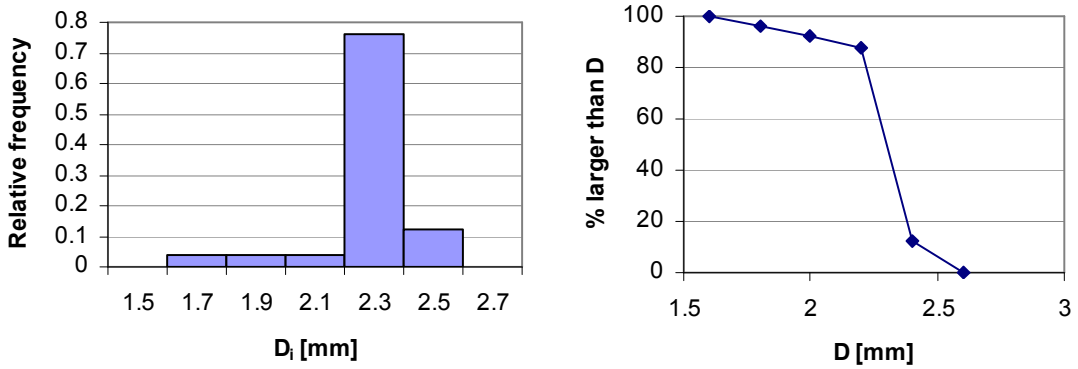

Figure A1.38 Statistics of the measured opening sizes D of the mesh of the trommel for the first experimental campaign with sand and gravel mixtures.

The mesh opening used for the first experimental campaign was slightly larger than 2 mm. Figure A1.38 shows the statistics for 25 measurements of randomly selected openings of the mesh. The measurements were performed with a vernier with an accuracy of ±0.05 mm. The average measured opening value was **2.24 mm**, with a standard deviation of 0.17 mm. As can be seen in Figure A1.37, only 12% of the measured openings were larger than 2.4 mm and none was larger than 2.6 mm. Sieve analysis of samples of material taken in the sand hopper during the first experimental campaign (a total number of 34 samples for runs with sand-gravel mixtures, 6 runs with 32% sand content and

6 runs with 44% sand content), i.e., material that had passed through the trommel and through the giraffe, showed that in average only 1.24% of the sand contained particles coarser than 2.24 mm.

Siltation tank for fine particles: “Giraffe"

The fine particles and water that pass through the mesh of the trommel fall inside of a siltation tank, called “Giraffe” because of its form with a long neck, as can be seen in Figure A1.37 (See also Photos P10). Sediment deposits on the bottom of the tank, directly over a screw conveyor. This screw conveys the material out of the tank and pours it in another screw conveyor that conveys it either to the hopper or to the large deposit according to the selected turning direction. Water overflows and is conducted to the underground deposit. As opposed to gravel, sand must pass not only through the trommel, but also through the giraffe, and this additional station in its route through the sediment-recirculating system causes an additional delay, and therefore causes that the lag time for sand to be longer than for gravel, as seen in Figure A1.25b.

4. RANGE OF VARIABLES AND PRECISIONS

According to the characteristics of the flume, Table A1.15 summarizes the maximum values of some of the variables that can be used as parameters in experiments with mobile-bed conditions. Notice that although the feeders have an extremely high capacity for supplying sediment to the channel, the upper limit for the duration of experiments with high sediment feeding rates would be given by the volume of sediment available in the hopper (maximum capacity=1.1 m^3) and in the large storing deposits (maximum capacity=12 m^3 each, and maximum rate for supplying sediment from the large deposit to the hopper $\approx$10 kg/s, as shown in Figure A1.23). Alternatively, when using the feeders simultaneously with the recirculating system, the upper limit would be given by the maximum capacity of the pump. For a new propeller in the pump this limit could be slightly higher than the value of 1.1 kg/s given in Table A1.15, which corresponds to the maximum value attained during the experiments in the first experimental campaign.

Variable	**Maximum value**
Water discharge (l/s)	250 (For avoiding water spilling at the entrance of the flume: 120)
Channel slope (%)	4
Water depth (m)	0.70 (without sediment)
Sediment feeding rate (kg/s)	$\approx$20 =0.0075 m^3/s
Sediment-recirculating rate (kg/s)	$\approx$1.1 =0.0004 m^3/s

Table A1.15 Maximum values of some variables for performing mobile-bed experiments according to the capacities of the experimental set-up.

While the feeders can easily provide large feeding rates, a restriction is found for feeding low rates of sediment in the range of values usually found on published data for mobile-bed experiments. Minimum feeding rates attained with the calibration runs given in Table A1.12 were 45 g/s and 72 g/s for the

sand and gravel, respectively (h_f=10 mm, $\%V$=1 for the sand feeder, and h_f=10 mm, $\%V$=3 for the gravel hopper). For lower values of h_f than those used to obtain these latter lower limit feeding rates, the rotating band might get stuck by grains jammed between the sluice gate and the band. A minimum condition could be set at h_f=2D, for which, using eq.(A1.23) with %V=1 and average conditions encountered during the first experimental campaign using the recirculating system, the minimum estimated feeding rates are 10 g/s for sand and 36 g/s for gravel. Different solutions should be tested for attaining lower sediment feeding rates, like for instance reducing the width of the gate. Nevertheless, it should be considered that when exploring low feeding rates and water discharges care should be taken to avoid unexpected accumulations of sediment in certain zones of the system, like for example the ramp connecting the channel with the siltation tank.

Table A1.16 summarizes the calibration functions and precision for some of the variables that can be used as parameters with mobile-bed experiments in the flume.

Variable	Measuring device	Actual value	Measured value	Calibration function	Accuracy
Water Discharge	flowmeter	$\overline{Q}_a$	Q_f	$\overline{Q}_a = 0.984Q_f - 0.31$ in [l/s]	± 0.46 [l/s]
Flume vertical displacement	Tilting mechanism display	Za	$Zm=ix$ (i=selected slope at the display; x=horizontal coordinate)	$Za=Zm$, for $i \leq 1\%$, $x<15$m	± 0.7 [mm]
				$Za=Zm+e_Z$, for $i \leq 1\%$, $x>15$m $e_z = -0.0044xi$ in [mm]	± 0.8 [mm]
				$Za=Zm+e_Z$, for $i>1\%$ $e_z = -0.0044xi$ in [mm]	± 1 [mm]
Channel Slope	Tilting mechanism display	i_o	i (=selected slope at the display)	i_o =0.9963 i	± 1%
Velocity of the rotating band	Analogical display selector	V_f	$\%V$	$V_f = 0.0042\%V^{0.94}$ in [m/s]	± 0.0031 [m/s]
Weight in the sand hopper	Analogical display	Wa	Wd	$W_a = aW_d^2 + bW_d$ in [kg], a=0.000019; b=0.9952	± 0.3[kg]
	RTDAS	W	$Voltage$	$W = 2.6303Voltage^2 + 293.65Voltage + 653.88$ in [kg]	± 0.3[kg]
Weight in the gravel hopper	RTDAS	W	$Voltage$	$W = 5.9044Voltage^2 + 312.573Voltage + 643.098$ in [kg]	± 0.3[kg]
Feeding rate	Feeder	Q_{SF}	$\%V$, h_f, B_f, ρ_s, ε, $\%\omega$ and D_m	$\frac{Q_{SF}}{h_f B_f V_f \rho_s (1-\varepsilon)\left(1+\%\varpi/100\right)} = \left(a + b\frac{D_m}{h_f}\right)^{-1}$ (For values of a and b see Table A1.14)	± 2.7%

Table A1.16 Calibration functions and accuracy for some of the parameters in the experimental flume.

5. EXAMPLES OF OPERATION OF THE EXPERIMENTAL FLUME WITH THE SEDIMENT-RECIRCULATING SYSTEM

Four examples of the operation of the experimental flume using the sediment-recirculating system are described in this section. These examples represent some of the most general conditions that can be tested with the experimental set-up.

Bed erosion with no sediment supply

This type of experiment represents conditions similar to those occurring when sediment supply is interrupted by the construction of a dam in a river. Downstream of the dam, bed erosion would occur until a new fluvial equilibrium is reached. In the flume channel, for given initial conditions of bed slope higher than the equilibrium bed slope, shear stress produced by a constant flow discharge would progressively erode the bed and volume sediment discharge would decrease until becoming zero. Using the sediment-recirculating system and the Real-Time Data Acquisition System, the time-variation of solid discharge (for two different size fractions) going out of the channel can be measured by monitoring the increment of weight on the hoppers. For an experiment with these conditions, Figure A1.40 shows the evolution of the bed and water surface profiles, while Figure A1.39 shows the time-variation of weight on the hoppers and of bed slope. A limitation for the continuous measurement of volume sediment discharge going out of the channel in such an experiment is set by the volume of the hoppers: in order to monitor the solid discharge variation during the entire duration of the experiment, it should be verified that the total volume of material eroded would not exceed the volumetric capacity of both hoppers.

Bed erosion with sediment supply

A river reach for which the capacity of the flow is able to transport a higher amount of sediment than that supplied by the reach upstream would suffer erosion. This condition can be modeled by feeding sediment at a constant rate to the channel and fixing a flow strength with a high sediment transport capacity. To achieve long-lasting runs without requiring huge amounts of material, the sediment can be recirculated and reintroduced in the hoppers. The hoppers would progressively be filled with the eroded material until reaching mobile-bed equilibrium, for which condition the volume of material in the hoppers would remain constant, i.e., the material feeding rate would be equal to the rate at which sediment goes out from the channel. Figure A1.41 shows the evolution of the bed and water surface profiles for an experiment with these characteristics. For this same experiment, Figure A1.42 shows the time-evolution of weight on the hoppers and of bed slopes. Notice that lag-times for sand and gravel are evident at the beginning of the experiment.

Bed aggradation with sediment supply

This condition is similar to that in the latter example, but instead of a deficit there is an excess of sediment supplied by the upstream reach, and therefore instead of erosion, bed aggradation occurs. This condition can be modeled in the same manner as in the latter example, but imposing a flow with lower capacity to transport the bed material than the flow for mobile-bed equilibrium conditions. The hoppers would progressively be emptied, and the material stored in the channel would construct a bed with a higher gradient. Figure A1.43 shows the bed and water surface profiles for an experiment with this characteristics using only gravel. When equilibrium is reached, and thus bed slope is roughly constant, the volume of material in the hoppers would remain constant. Figures A1.44c and A1.44b show the time-evolution of the bed slopes and of the weight in the hoppers, respectively, for the same run in Figure A1.43.

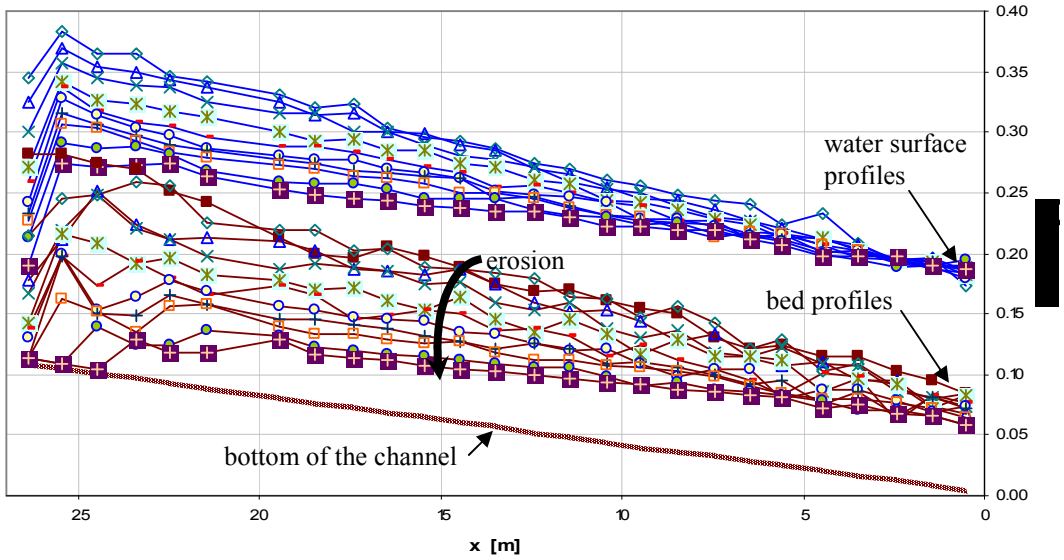

Figure A1.39 Bed and water surface profiles measured for run M2N of the first experimental campaign. ***Bed erosion with no sediment supply*** *upstream.*

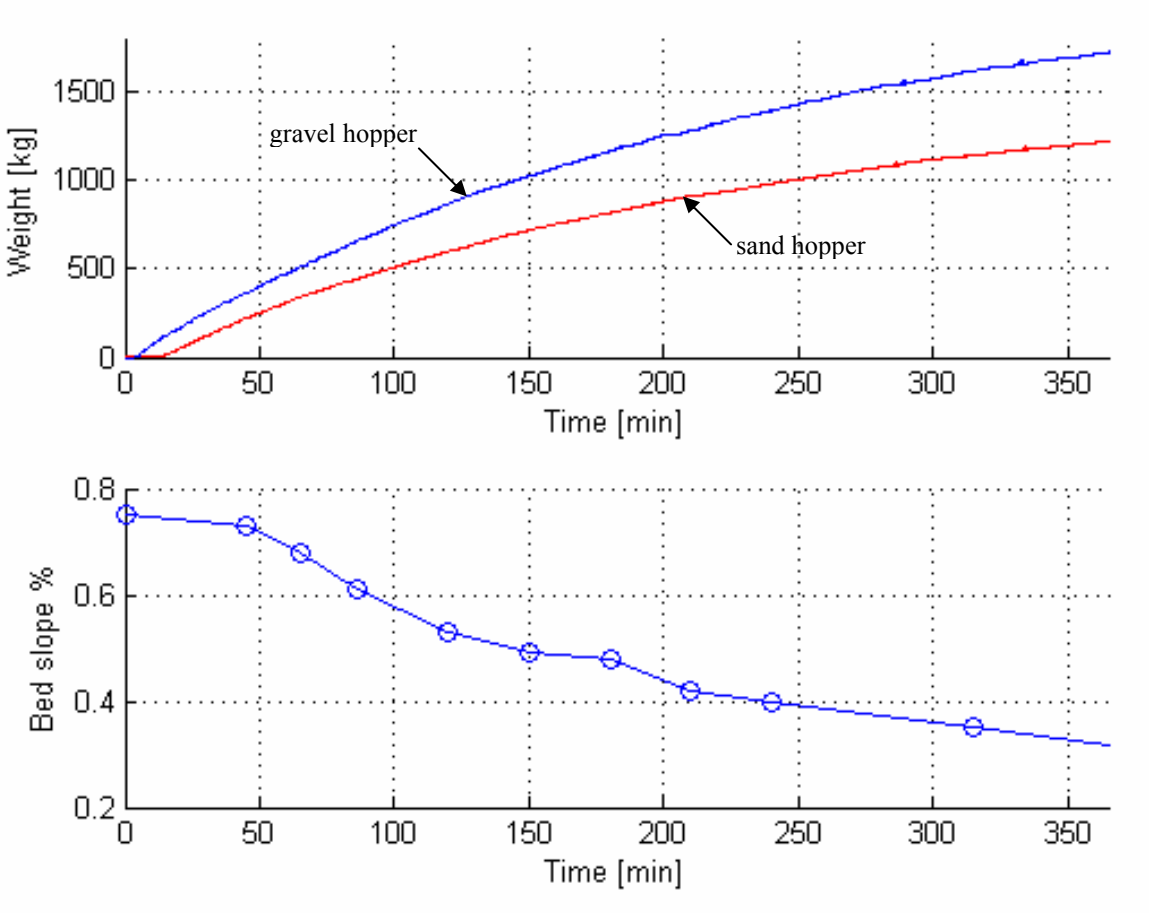

Figure A1.40 Time-variation of weight on the hoppers and of measured bed slope for run M2N of the first experimental campaign. ***Bed erosion with no sediment supply*** *upstream. Bed material consisted of a sand-gravel mixture with 44% sand content.*

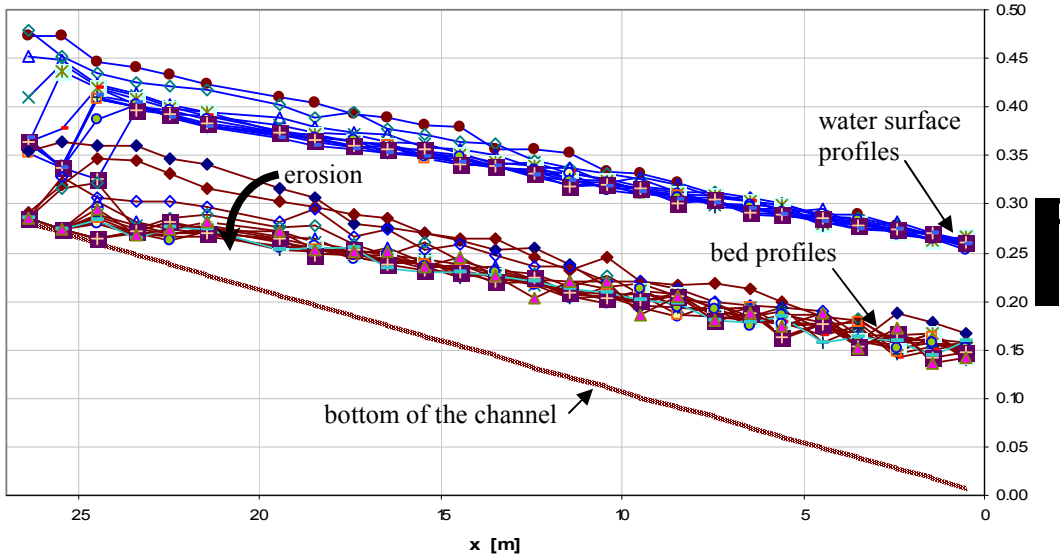

Figure A1.41 Bed and water surface profiles measured for run M1E6 of the first experimental campaign. ***Bed erosion with constant sediment supply*** *upstream.*

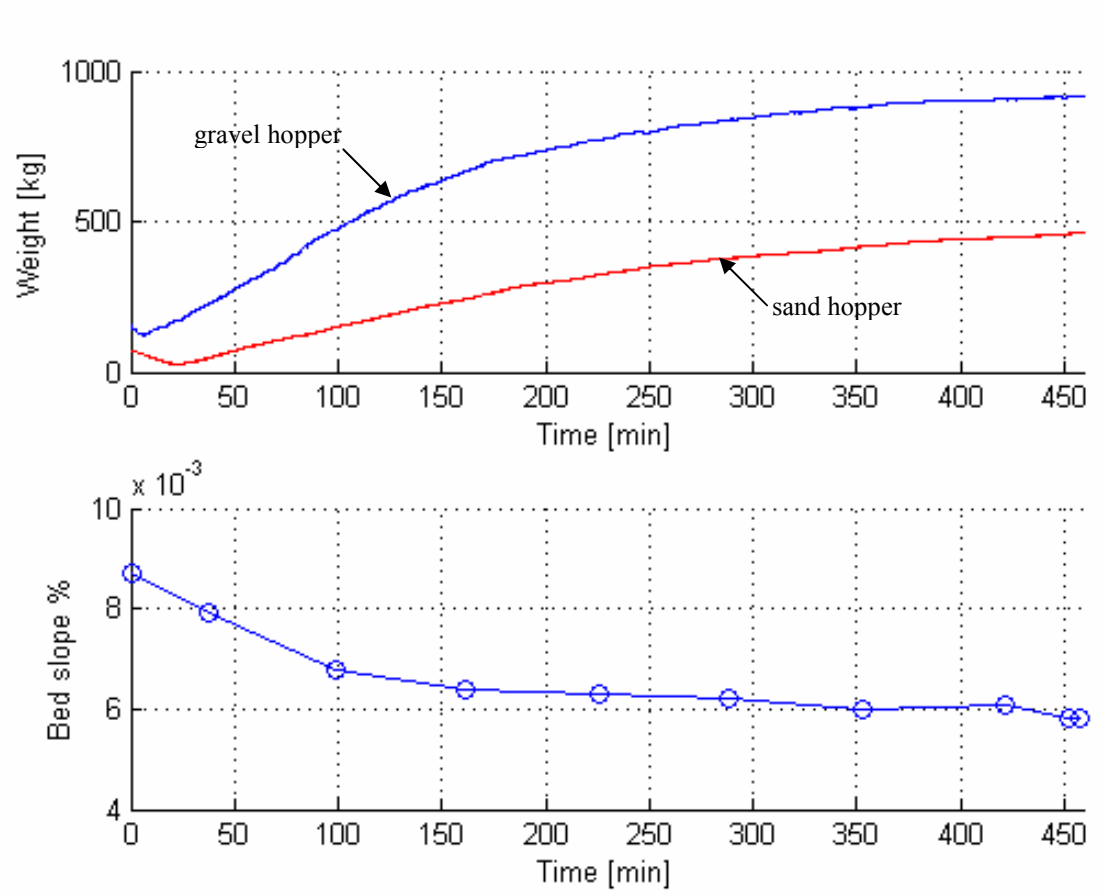

Figure A1.42 Time-variation of weight on the hoppers and of measured bed slope for run M1E6 of the first experimental campaign. ***Bed erosion with constant sediment supply*** *upstream. Bed material consisted of a sand-gravel mixture with 32% sand content.*

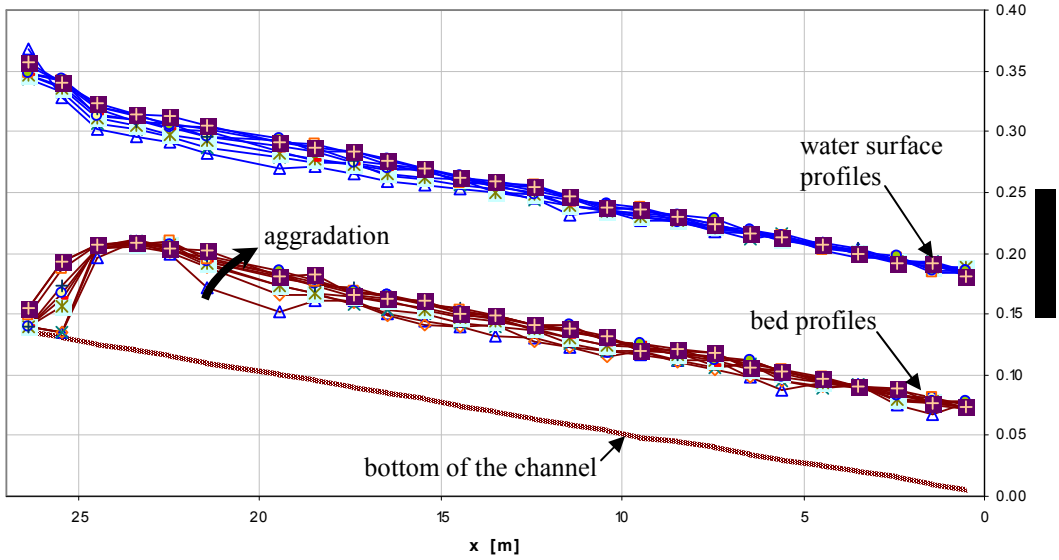

Figure A1.43 Bed and water surface profiles measured for run G17 of the first experimental campaign. ***Bed aggradation with constant sediment supply*** *upstream.*

Figure A1.44a shows the original record of the time-evolution of weight on the hopper. In this Figure, almost straight vertical lines in the continuous record describe sediment inputs from the large deposits; this material was added to avoid that the hopper were totally emptied. In turn, a ramp with negative slope in the record describes the emptying of the hopper when diverting the recirculated material to the large deposit; this was done to measure the feeding rate supplying the channel, which was equal to the slope of the ramp. Figure A1.44b was obtained from adjustments to times in Figure A1.44a to describe the actual difference between sediment added to the channel and sediment going out of the channel. Notice that the curvature of the record in Figure A1.44b is concave in contrast to the convex curvature in Figure A1.42 for the bed erosion case.

Sediment recirculating

In a pure recirculating flume the total amount of water and sediment in the flume are conserved, all the water and all the sediment are taken from the downstream end of the channel and reinserted in the upstream end. For this condition, the operator sets the water discharge and water depth, while bed slope and volume sediment transport evolve to equilibrium values (Parker, 2004). With small modifications the flume here referred to would be able to operate in this manner, but the recirculation pump would set a limit for the maximum water discharges likely to be tested. A more flexible operation is obtained by recirculating sediment and feeding water; for this case, the operator sets water discharge and bed slope, while water depth and volume sediment transport evolve toward values for the equilibrium conditions. Changes in bed profiles are negligible. For operating in this manner, the gate of the feeders is opened to its maximum and the rotating band is set to a high velocity. This assures that sediment is not stored but by-passed through the hoppers. Volume sediment transport going out of the channel can be measured using the hoppers, by storing the incoming material during short-time intervals (as short as possible to avoid disruptions to the dynamics in the channel, but sufficiently

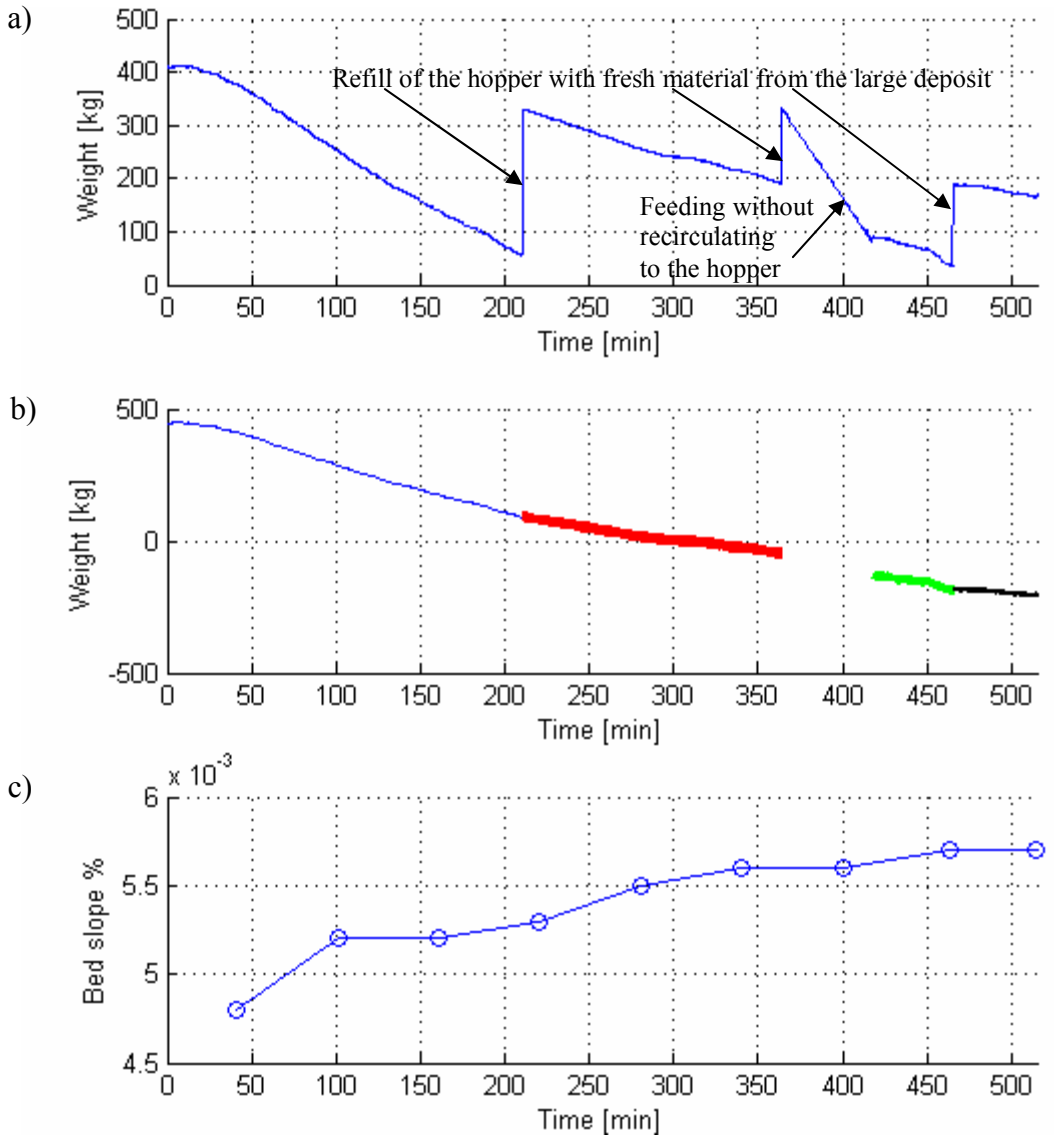

Figure A1.44 Time-variation records for run G17 with gravel, in the first experimental campaign. ***Bed aggradation with constant sediment supply*** *upstream; a)original record of time-evolution of weight on the hopper; b)adjusted record to describe the actual difference between sediment added to the channel and sediment going out of the channel; c)time-evolution of bed slopes in the channel.*

large to be a representative measurement). This is attained by stopping the rotating band and measuring the increments of weight on the hopper. Figures A1.45 and A1.46 show two examples of sediment sampling with the hoppers and the RTDAS, for measuring sediment discharge during different sediment recirculating runs when equilibrium conditions had been attained. For the example in Figure A1.45, one sample in each hopper was taken during one minute, while in Figure A1.46 three samples are shown, which were taken every hour. For this latter example, sampling consisted in stopping the rotating band during five intervals one-minute length, with a lag of one-minute between each other (during the lag the rotating band was turned-on and sediment stored was reinserted in the channel). Figure A1.47 shows the time-evolution of weight on

the sand hopper for one of the samples in Figure A1.46. Best-fit lines and their slopes for the filling intervals are shown. These slopes are equal to the sediment transport rate for sediment going out of the channel, being for this example in average 311 g/s. Since the material deposited in the hoppers contains a certain amount of water, to obtain the solid discharge for dry material the water content must be subtracted. Water content for samples of material taken from the sand hopper during the first experimental campaign was 4% in average. Accounting for the water content with this value, the average dry sediment discharge for the example in Figure A1.47 is 299 g/s.

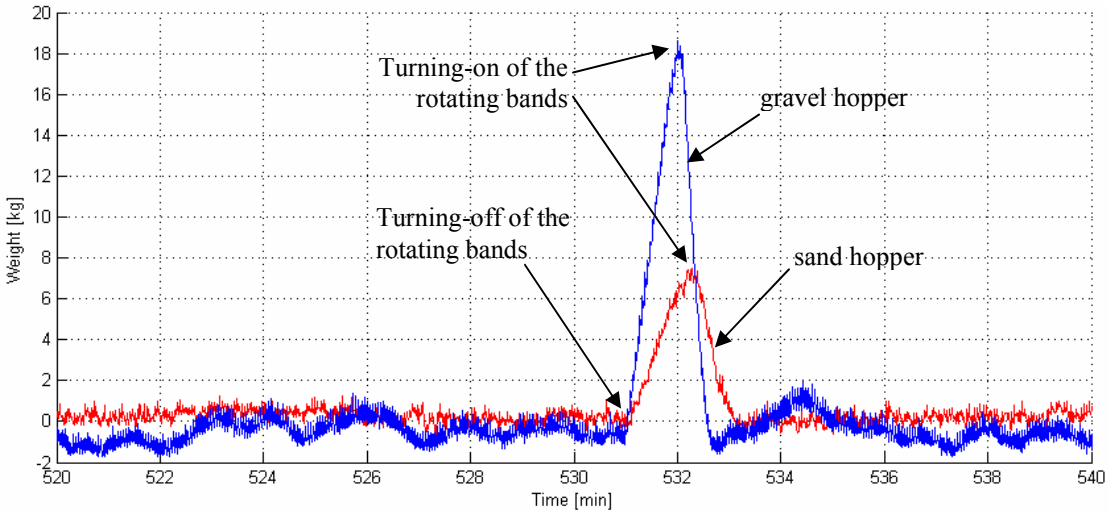

*Figure A1.45 Sampling of volume sediment transport using the hoppers and the RTDAS, during a **sediment-recirculating** run (Run M1R2 of the first experimental campaign). Sampling consisted in stopping the rotating band on the base of the hoppers during one minute to record the increment of weight.*

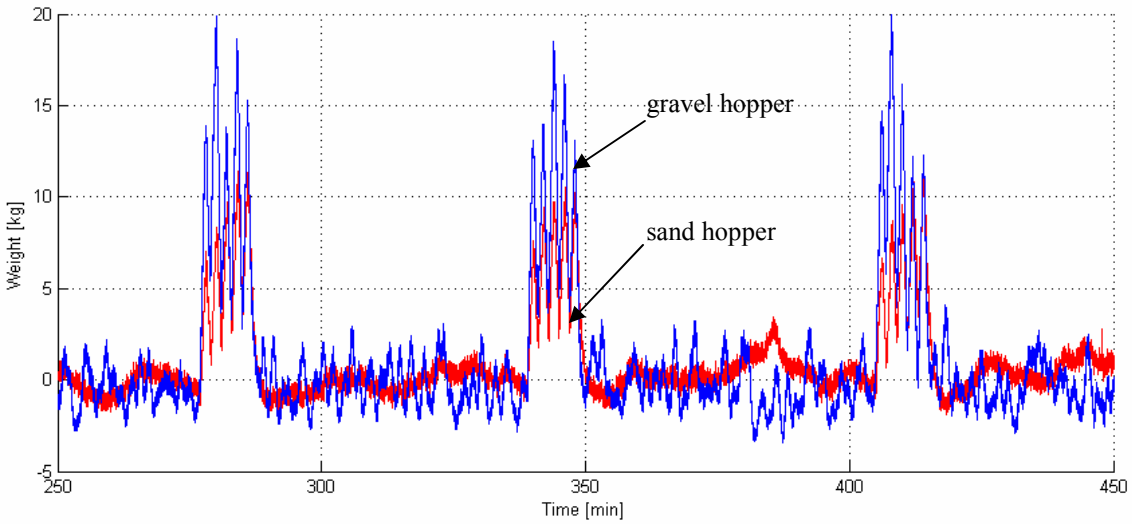

*Figure A1.46 Sampling of volume sediment transport using the hoppers and the RTDAS, during a **sediment-recirculating** run (Run M1R4 of the first experimental campaign). Samples were taken every hour, and consisted in stopping the rotating band on the base of the hoppers during five one-minute intervals with one minute lag between each other.*

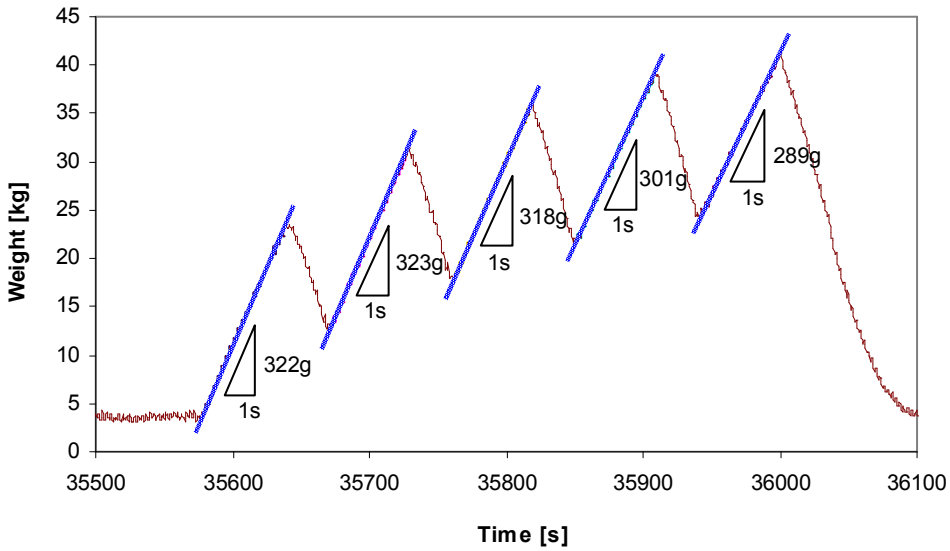

*Figure A1.47 Measurement of volume sediment transport of the sand fraction for samples taken with the hopper and the RTDAS, during a **sediment-recirculating** run (Run M1R4 of the first experimental campaign). Best-fit lines to the increment of weight in the hopper when the rotating band was stopped are shown. Average sediment discharge obtained with the slopes of the five best-fit lines is 311 g/s. After discounting average water content (≈4%), the computed dry sediment discharge is 299 g/s.*

When operating the flume in a sediment-recirculating mode, it should be recalled that sand and gravel have different lag times in their way through the recirculating system, as it was shown in Figure A1.25b. This feature could affect the transient process toward mobile-bed equilibrium, nevertheless the equilibrium attained would have to be equivalent to equilibrium obtained operating as a feed flume (Parker and Wilcock, 1993).

6. REFERENCES

Echávez-Aldape, G. *Introducción a los modelos hidráulicos de fondo fijo y a la ingeniería experimental*. Universidad Nacional Autónoma de México, CONACYT y AMH, México, **1996.**

Ferrer-Sansa, R. *Estudio hidráulico en modelo reducido de la estación de aforos y trampa de sedimentos de la riera de las arenas*. Tesina de especialidad, Universidad Politécnica de Cataluña, **1994.**

Martín-Vide, J. P. *Proyecto para la construcción de un canal con recirculación de mezcla de sedimentos*. Reporte interno, Escuela Técnica Superior de Ingenieros de Caminos, Canales y Puertos, Universidad de Castilla-La Mancha, **1999.**

Martín-Vide, J. P.; Bateman, A.; García-Revilla, C.; López-García, E. & Solans, D. *Estudio experimental en lecho vivo de la estabilización del perfil longitudinal de un cauce de gran pendiente*. XVIII Congreso Latinoamericano de Hidráulica, Oaxaca, México, **1998.**

de Almeida, G. A. M. *Influencia de la geometría de una protección fluvial de escollera en su fallo por arrastre. Estudio experimental*. Tesis doctoral, Escola Tècnica Superior d'Enginyers de Camins, Canals i Ports, Universidad Politècnica de Catalunya, **2007**.

Parker, G. *1D sediment transport morphodynamics, with applications to rivers and turbidity currents*. E-book In: http://cee.uiuc.edu/people/parkerg/, St. Anthony Falls Laboratory, University of Minnesota, **2004.**

Parker, G. & Wilcock, P. R. *Sediment feed and recirculating flumes: fundamental difference.* Journal of Hydraulic Engineering, 119(11),1192-1204, **1993.**

Parker, G. & Klingeman, P. C. *On why gravel bed streams are paved*. Water Resources Research, 18(5),1409-1423, **1982.**

Wilcock, P. R. & McArdell, B. W. *Surface-based fractional transport rates: mobilization thresholds and partial transport of a sand-gravel sediment*. Water Resources Research, 29(4),1297-1312, **1993**.

7. PHOTOS

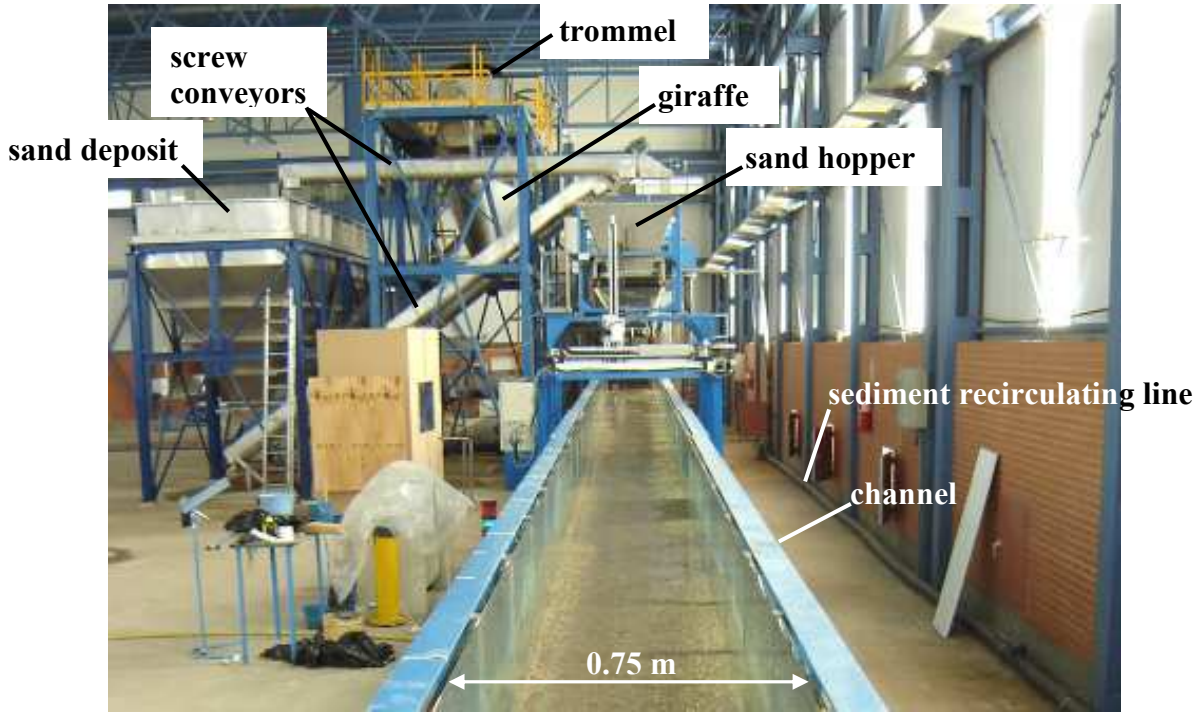

Photo P1. General view of some of the elements to control sediment storing, feeding and recirculation in the experimental flume.

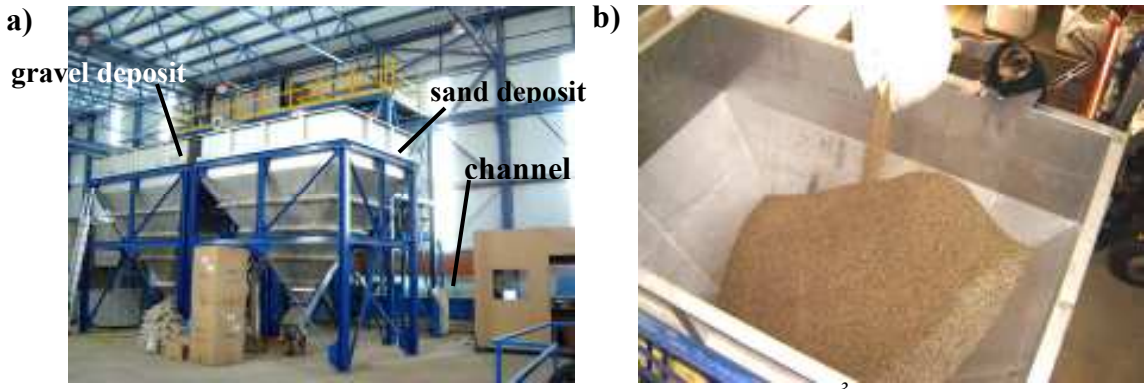

Photos P2. Large deposits for sediment, with a capacity of 12 m^3 each; a) general view of the two deposits; b) filling of one of the deposits with fresh gravel using a crane.

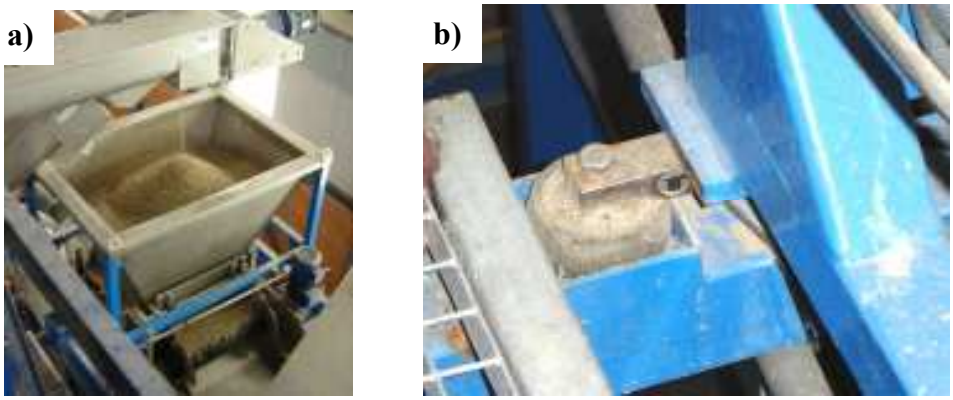

Photos P3. Sediment hoppers/feeders; a) filling of the gravel hopper with material coming from the trommel; b) load cell under one of the supports of the sand hopper.

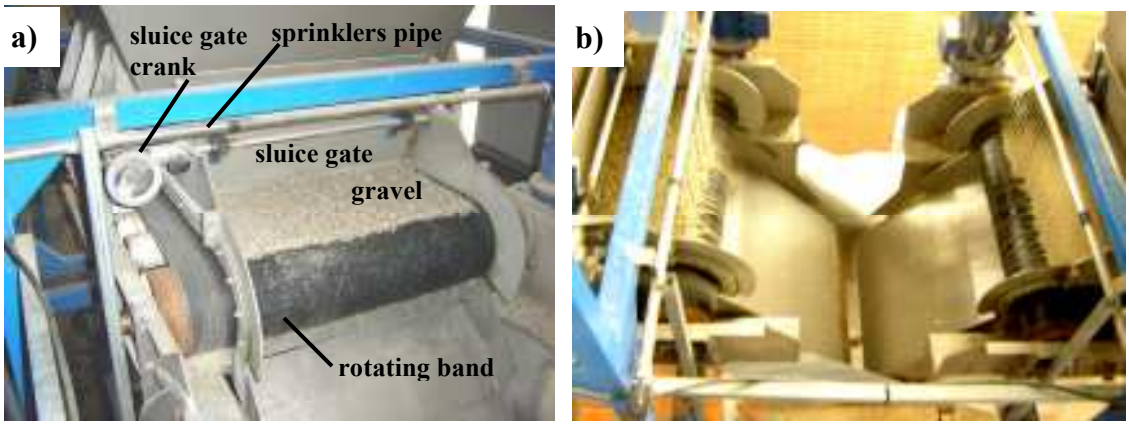

Photos P4. Sediment hoppers/feeders; a) components of the gravel hopper for feeding sediment; b) sand and gravel hoppers feeding material to the channel.

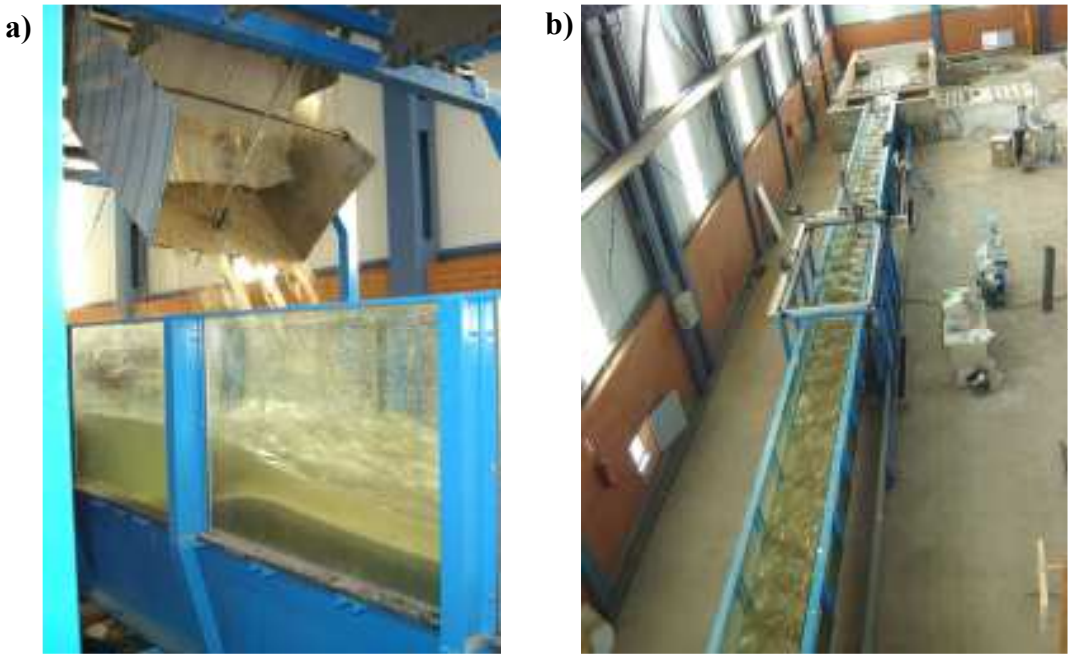

Photos P5. a) Tilting ramp for adding sediment to the channel (for low channel slopes increasing the ramp slope decreases the distance between the ramp and the channel); b) downstream view of the channel from the elevation of the trommel.

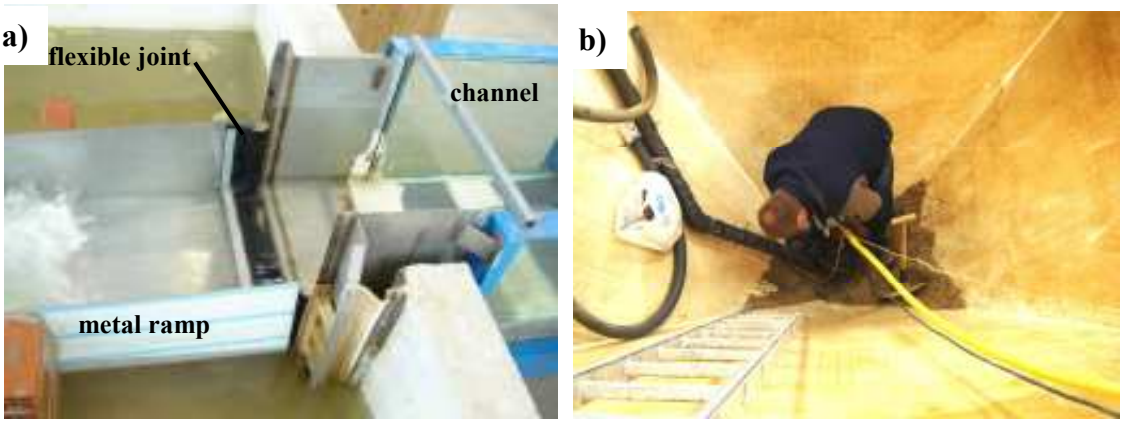

Photos P6. a) Ramp to connect the channel with the sediment collecting tank; b) cleaning of the sediment collecting tank after siltation due to a pump failure.

a) b)

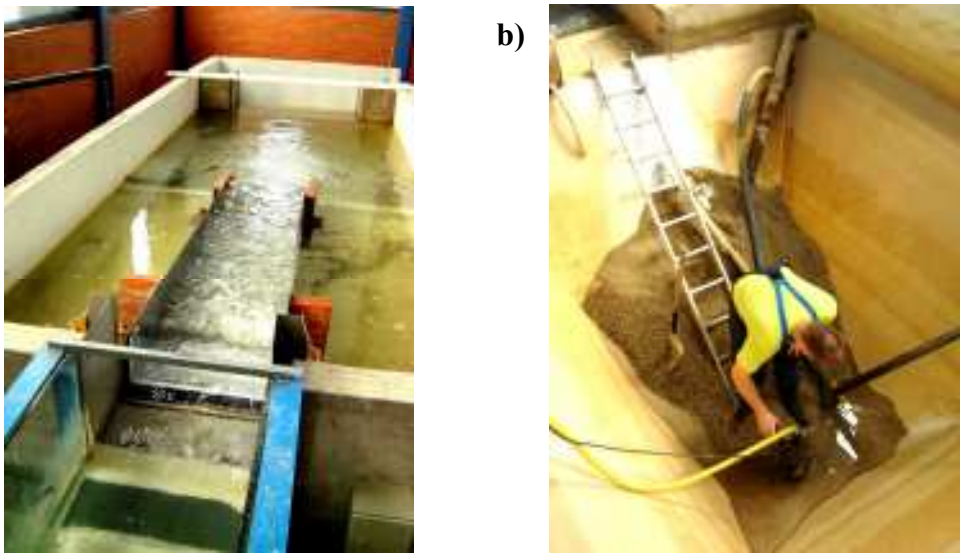

Photos P7. a) Downstream end of the channel, metal ramp and sediment collecting tank; b) cleaning of the sediment collecting tank after siltation due to a pump failure.

Photos P8. Sediment recirculating pump (left) and views of the propeller affected by abrasion (center) compared with a new propeller (right).

a) b)

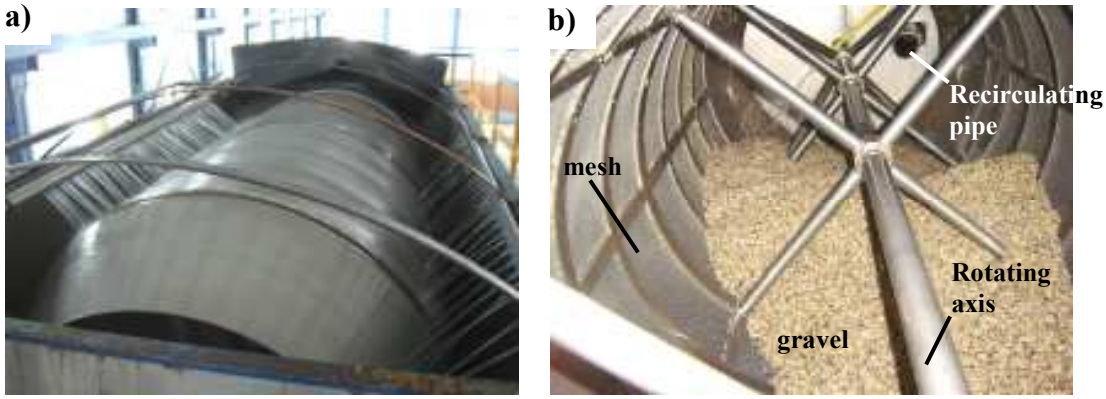

Photos P9. Rotating trommel, used for separating sand from gravel in the sediment-recirculating system; a) view of the trommel rotating and being sprinkled with water to avoid sediment get stuck on the wire mesh; b) view of the trommel from inside, filled with gravel.

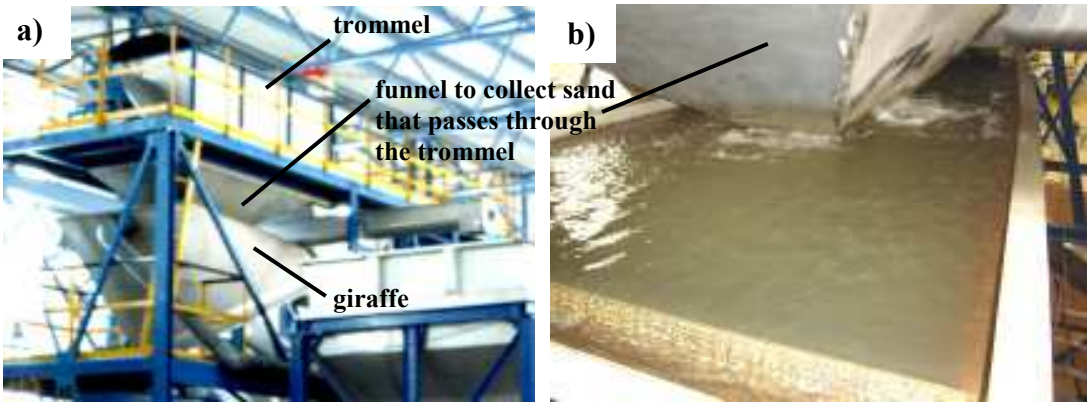

Photos P10. Siltation tank for sand, "giraffe"; a) view of the giraffe under the trommel; b) funnel to collect sand falling from the trommel and water overflowing over the giraffe.

Photos P11. a) Screw conveyor to transport gravel from the trommel; b) control panel for screw conveyors, recirculating pumps and feeders.

Photo P12. Channel section showing one of the supports with one of the engines to tilt the channel.

APPENDIX II

ANALYSIS OF THE EFFECT OF THE BED AND WATER SURFACES TEMPORAL VARIATION AND BEDFORM MIGRATION ON THE MEASUREMENT OF THE BED AND WATER SURFACES PROFILES

Introduction

The average slopes of the bed and water surfaces are two of the most important variables to be obtained from the measurements of the bed and water surfaces profiles. In the evolution to an equilibrium state, these profiles change with time, not only because of the net erosion or sedimentation on the bed, but also because of the passage of periodic bedforms. In this appendix an analysis is performed of the effect of these two processes on the measured bed profiles, and recommendations are given for performing the measurements and to define the separation between measurement points.

The relative error e_r of the measured slope can be defined as the ratio of the difference between the actual slope i_R and the measured slope i_M to the actual slope, i.e.,

$$e_r = \frac{i_R - i_M}{i_R} \qquad \text{(AII.1)}$$

For the following analysis, the measured slope was considered to be equal to the slope of the best-fit line to the measured data of bed elevations along the channel. In doing this, the least-squares method was used, forcing that an obligated point of the bed profile is the downstream end of the channel. In the channel, bed and water surface profiles were measured by making marks on the transparent channel walls to indicate the position of the bed (or water) surface. Only one person performed the measurements, and this was done by walking along the channel length; therefore, there is a finite time associated with the measurement of the whole profile, i.e., the identification of the vertical position of the bed for all measured points was not simultaneous.

The relative error of the measured slope is analyzed for the temporal variation of the bed profile first, and secondly, it is analyzed for the passage of periodic bedforms.

Relative error due to the temporal variation of the bed profile

Considering a plane bed and an instantaneous constant slope of the bed profile, when the measurement begins the actual bed profile can be defined by the variation of the bed elevation y_0 with the horizontal coordinate x as

$$y_0 = i_0 (x - L_c) \qquad \text{(AII.2)}$$

where i_0 is the bed slope and L_c is the effective channel length (≈25.5 m from the point of sediment feed to the downstream end of the channel). When the channel is eroding or aggrading, bed slope is a function of time t; therefore, because a certain finite time is required to measure the bed profile, the bed slope at the beginning of the measurement would not be the same as when the measurement is finished (see Figure AII.1, where i_{FS} and i_{FE} are the bed slopes at the end of the measurement when the bed aggrades and erodes, respectively).

For the increment of time required to measure the profile, it can be considered that the rate of variation of the slope is almost constant (this is correct the closer the bed is to the dynamic equilibrium condition); therefore, the bed profile as a function of time can be defined by

$$y(t) = (i_0 + v_i t)(x - L_c) \qquad \text{(AII.3)}$$

where v_i is the rate of variation of the bed slope.

The bed profile measurement consists of marking the vertical position of the bed surface on the channel wall, progressing in the flow direction or in the opposed direction. If the person performing the marks progresses along the channel at a velocity v_M, his position along the channel at time t (and therefore the position of the point being measured in that instant) can be described with

$$x = x_M + v_M t \qquad \text{(AII.4)}$$

where x_M is the point on the horizontal axis where the measurements begin and v_M is the velocity at which the person measuring walks along the channel; v_M is positive if the person walks in the same direction of the flow and negative for the inverse direction.

If eq.(AII.4) is solved for time, and substituted in eq.(AII.3), the measured profile is obtained as

$$y_M = \left(i_0 + \frac{v_i}{v_M}\left(x - x_M\right)\right)\left(x - L_c\right) \qquad \text{(AII.5)}$$

Eq.(AII.5) has been plotted in Figure AII.2 for an aggradation run, with i_0=0.01, v_i/v_M=0.0005 and L_c=25 m, for a measurement following the flow direction (x_M=0) and for a measurement in the opposite direction to flow (x_M=25 m, v_i/v_M =-0.0005). Measurements were spaced one meter apart. The measured profile is convex if the measurement is performed in the flow direction, and concave if performed in the opposite direction. If the run were an erosion run, the measured curves would be the same as those shown in Figure AII.2, but the convex curve would correspond to the measurement following the opposite direction to flow and vice versa. These results prove that the direction in which the measurement is performed can produce an error in the interpretation of the profiles, since the profile can be erroneously considered as being curved when this curvature would be an effect of the measurement method. Nevertheless, it can be expected that the velocity at which the measurements are performed would always be much higher than the rate of change of the bed profile, and therefore it is likely that the effect of the direction of measuring would be hidden by the accuracy of measurements and by the passage of bedforms.

When a best-fit line is obtained for the bed profile measured points, the relative error, as defined by eq.(AII.1), is found to be a function of the relation v_i/v_M. This can be observed in Figure AII.3 for two values of the initial bed slope i_o. The fastest the measurement is performed with respect to the rate of change of the bed slope, the lower the relative error between the actual slope (defined here as the average between the initial and final slopes) and the measured slope is.

From Figure AII.2 it is observed that the two curves obtained for the measured points in the two opposed directions are symmetric, being the symmetry axis the average profile between the initial and the final profiles. The average of the measured curves is equal to the average actual bed profiles. This means that if the measurement is performed, simultaneously or consecutively, in the two directions the relative error would cancel, and the velocity at which the measurement is performed would not be important (remembering that it has been considered that the rate of change of the bed slope is constant).

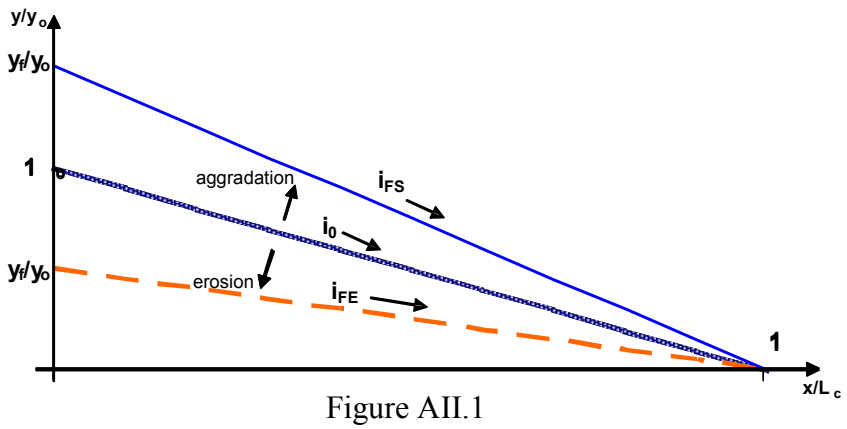

Figure AII.1

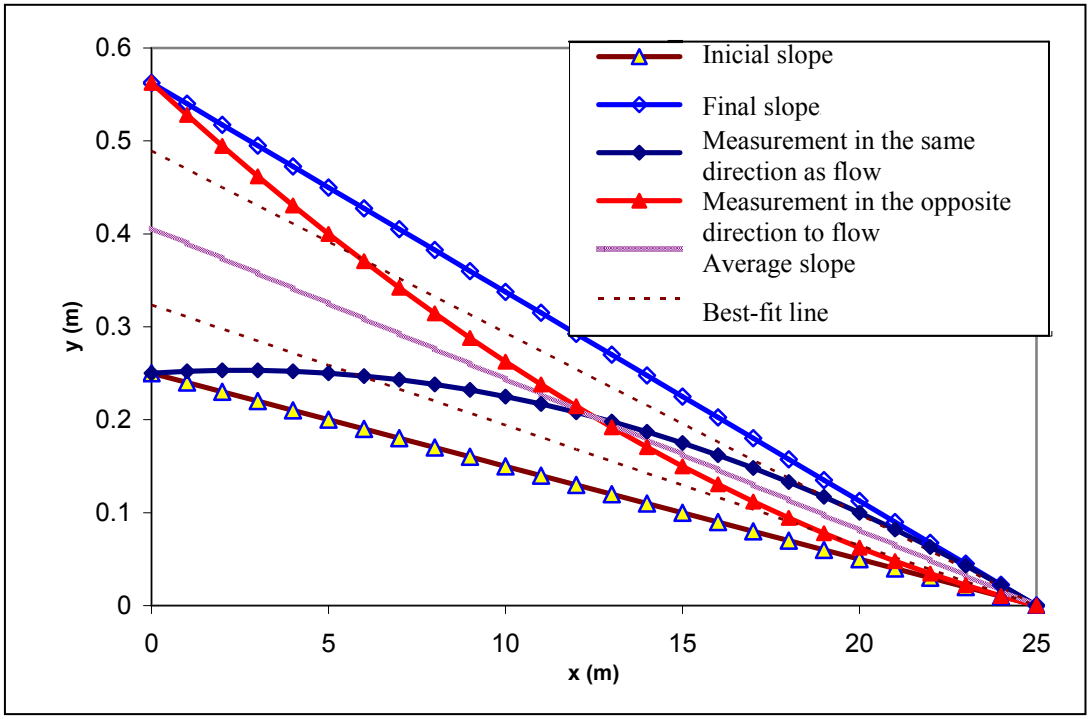

Figure AII.2

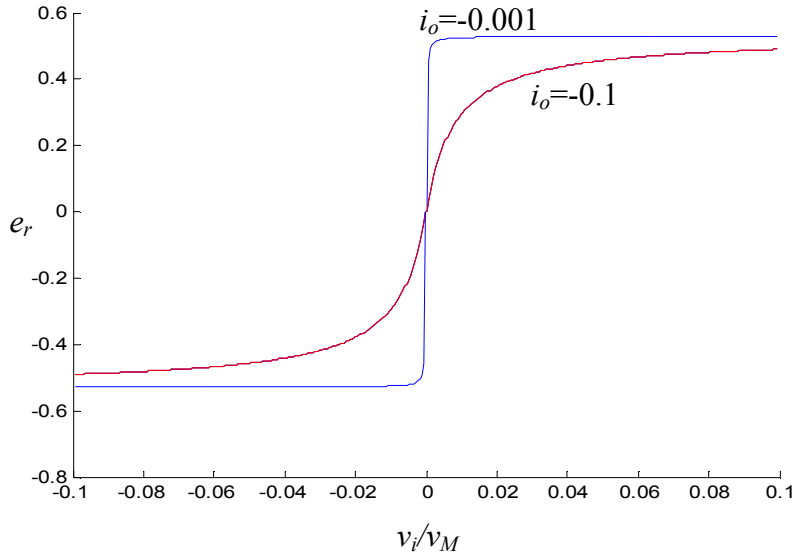

Figure AII.3

Relative error due to the passage of bedforms

The time variation of the bed profile due to the passage of bedforms can be analyzed by idealizing the bedforms as symmetrical and periodic undulations (this hypothesis is quite reasonable for antidunes) using a sinusoidal equation as

$$y = a \quad Sin\left[2\pi \frac{(x - ct - b)}{L}\right] \qquad \text{(AII.6)}$$

where L is the bedform wavelength, a is the bedform height, b is the function phase-lag, c is the bedform velocity and t is time. For this profile the bedfroms are considered to migrate in a horizontal bed.

The velocity at which the bed profile is measured can be expressed as the relation between the distance covered when measuring (i.e., the length of the channel) and the total time needed for measuring all the profile, i.e.

$$v_M = \frac{(L_c - x_M)}{t_M} \qquad \text{(AII.7)}$$

If eq.(II.4) for the position of the measured point is solved for time

$$t = \frac{(x - x_M)}{v_M} \qquad \text{(AII.8)}$$

using (AII.7) and (AII.8) in (AII.6) yields

$$y_M = a \quad Sin\left[\frac{2\pi}{L}\left(x - \frac{ct_M(x - x_M)}{(L_c - x_M)} - b\right)\right] \qquad \text{(AII.9)}$$

which is the equation for the measured profile with bedforms.

As it was demonstrated in the previous section, in order to cancel out the error in the measured slope due to the time evolution of the bed slope, it is necessary to perform the measurement in two parts: first following the flow direction, and next following the opposite direction to flow. If this rule is applied, the total measurement time is doubled and therefore eq.(AII.9) for the measurements in the same direction as flow turns into

$$y_{M1} = a \quad Sin\left[\frac{2\pi}{L}\left(x - \frac{ct_M(x - x_M)}{2(L_c - x_M)} - b\right)\right] \qquad \text{(AII.10)}$$

while for the measurements in the opposite direction to flow, considering (AII.7) and (AII.8), eq.(AII.9) turns into

$$y_{M2} = a \quad Sin\left[\frac{2\pi}{L}\left(x - c\left[\frac{t_M(x_M - x)}{2x_M} + \frac{t_M}{2}\right] - b\right)\right] \qquad \text{(AII.11)}$$

By considering that the measurements performed in the same direction as flow begin in the upstream end of the channel, where x_M=0 according to Figure AII.2, and that measurements performed in the opposite direction to flow begin in the downstream end of the channel, where x_M=L_c, Eqs.(AII.10) and (AII.11) can be reduced to

$$y_{M1} = a \quad Sin\left[\frac{2\pi}{L}\left(x - \frac{ct_M x}{2L_c} - b\right)\right] \qquad \text{(AII.12)}$$

$$y_{M2} = a \quad Sin\left[\frac{2\pi}{L}\left(x - \frac{ct_M}{2}\left[2 - \frac{x}{L_c}\right] - b\right)\right] \qquad \text{(AII.13)}$$

Eqs.(AII.6), (AII.12) and (AII.13) have been plotted in Figure AII.4 for the following values (these values are similar to those found for bedforms in gravel during the preliminary tests in the channel):

- characteristics of the bedforms: L=2 m, a=0.025 m, c=0.005 m/s, b=0;

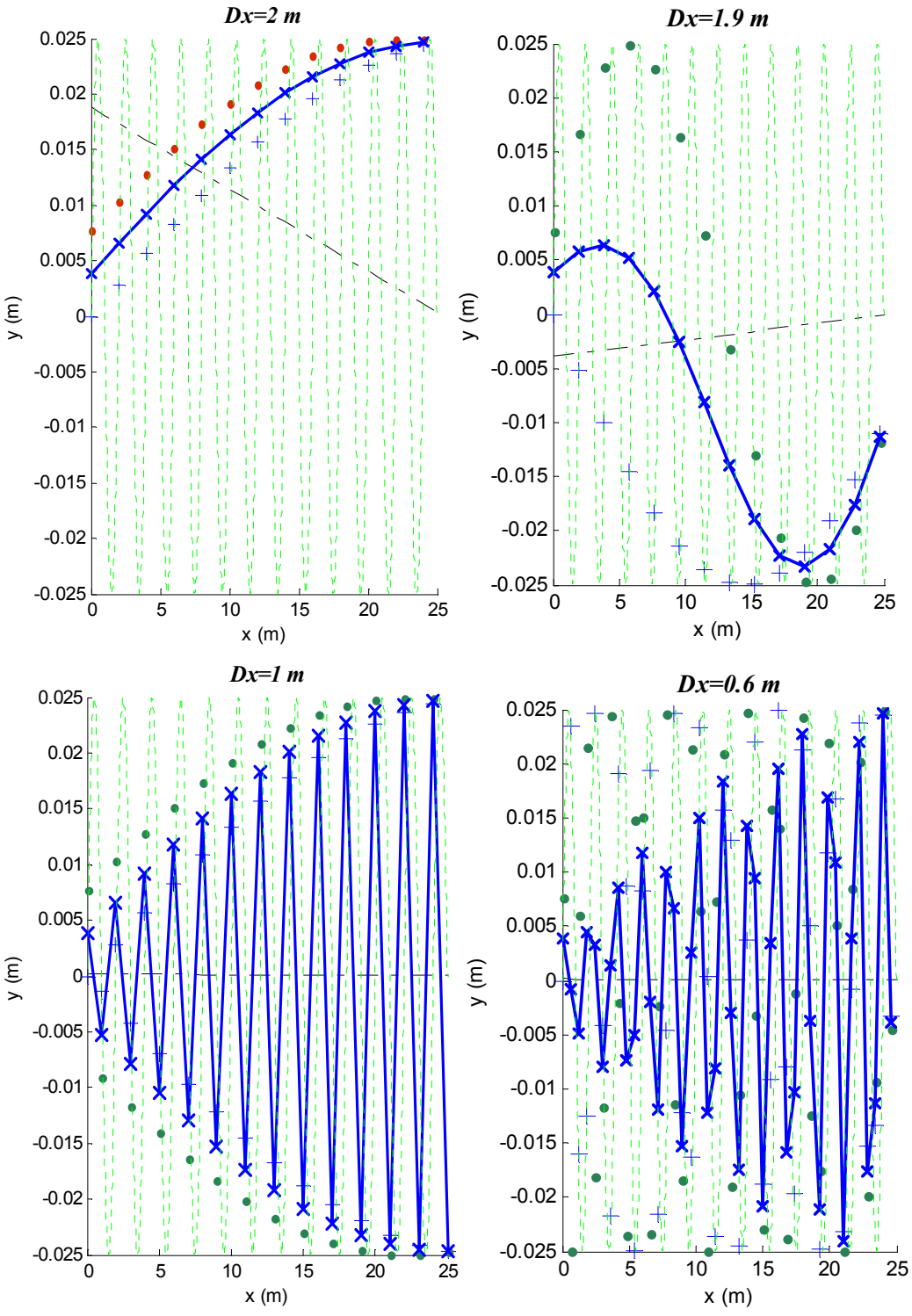
Dx=2 m
Dx=1.9 m
Dx=1 m
Dx=0.6 m
y (m)
x (m)
Best-fit line to the measured points
Measured points in the flow direction
Measured points in opposite direction to flow
Average for measured points
Actual profile for t=0

Figure AII.4

- characteristics of the measurements: t_M=180 s, Dx= spacing between measurement points;
- Effective length of the channel: L_c=25.5 m.

As can be seen in Figure AII.4, the form of the measured profile is strongly dependant on the distance between measurement points Dx. A higher resolution in the measurements is desired in order to decrease the error in the measured slope, but on the other side, an excessive number of measurements can be impractical and time-consuming. The results in Figure AII.4 can be used to select a minimum spacing between measurements for the experimental campaign. For data in this Figure, which are similar to those expected to be found in the experiments, spacing of one meter seems to be reasonable. Furthermore, tests indicated that performing measurements with a spacing of one meter took between 4 to 5 minutes (considering that measurements are performed in the direction of flow and in the opposite direction, and also considering approximately 5 seconds of observation in each point), which is practically reasonable.

Dashed lines in Figure AII.4 show the best-fit lines to the measured points. These lines were obtained with the least-squares method, with a fixed point at the downstream end of the channel where x=25.5 and y=0. If the best-fit line is horizontal, then it can be considered that there is no error between the actual bed slope and the measured slope. The best-fit lines for Dx=1 m and Dx=0.6 m are approximately horizontal, while for Dx=2 m and Dx=1.9 m the slope of the line of best fit is higher than zero.

In order to study the maximum likely error in the measured bed slope due to the passage of bedforms, eqs.(AII.12) and (AII.13) have been plotted in Figure AII.5, for different ranges of the relevant variables, and as a function of the dimensionless products in the following functional relation:

$$\frac{iL_c}{a} = f\left(\frac{ct_M D_x}{LL_c}\right) \qquad \text{(AII.14)}$$

where i is the value of the slope obtained from the best-fit line to the measured points, using the least-squares method with a fixed point at x=25.5 m and y=0. The ranges of data used were chosen according to the expected values in the experimental channel, these were:

$\frac{ct_M}{L} \in [0.0001,5]$, with steps of 0.1

$\frac{b}{L} \in [0,0.9]$, with steps of 0.1

$Dx \in [0.4,5]$, with steps of 0.2

$a \in [0.005,0.1]$, with steps of 0.005

L_c=25 m

The maximum value found for the dimensionless product $\frac{iL_c}{a}$ was 1.4; this means that for a bedform with a height of 5 cm, the maximum likely measured “fictitious” slope could be ±0.0028.

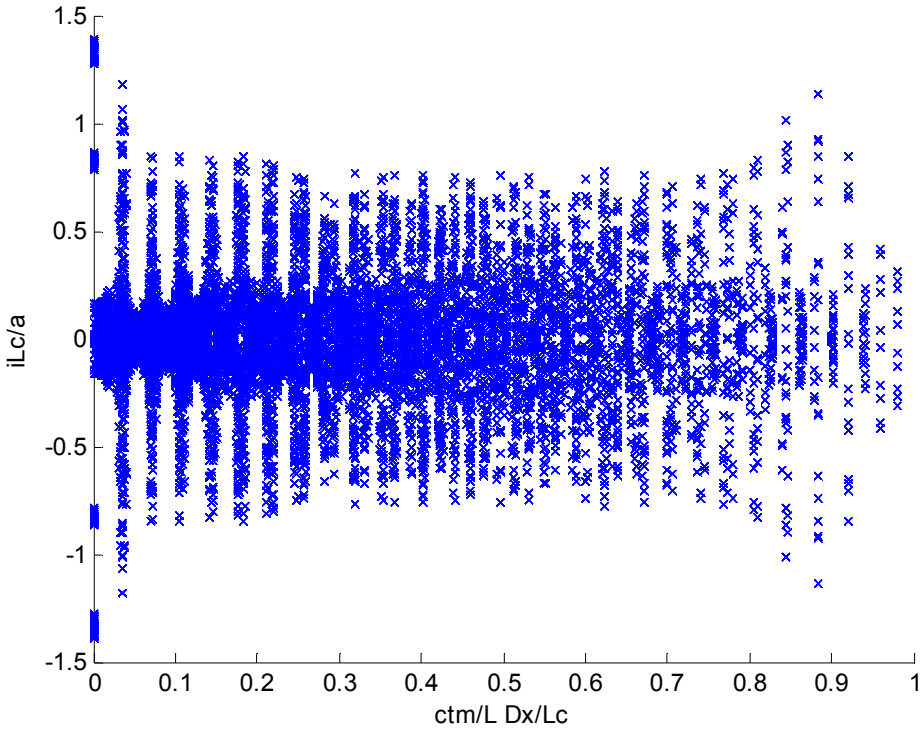

Figure AII.5

Conclusions

From the analysis above the following recommendations for the measurements of the bed and water surface profiles can be written:

- Consider a maximum spacing of one meter between measurement points.
- The measurement of the profiles must be performed following first the direction of flow, and secondly in the opposite direction (or vice versa). It is desirable that the total time required to perform the measurement were registered.
- Perform the measurements as rapidly as possible, but when marking the water surface profile take at least 5 seconds to observe the water surface variations and mark an approximate average.
- Register the main characteristics of the bedforms: height, wavelength and velocity.

APPENDIX III

CORRECTIONS TO MEASUREMENTS ON RULERS ATTACHED TO THE CHANNEL WALLS

Introduction

In this appendix the corrections and computations required to obtain the actual values of measurements on the rulers attached to the flume walls, with reference to the coordinate system in Figure 3.2, are presented. First corrections due to irregularities on the installation and manufacture of the rulers are considered, and secondly, a description is given of the computation of the coordinates of a measured value with respect to the reference coordinate system when the channel is tilted.

Corrections to measurements on the rulers

Twenty-six Rulers, 50 cm length, were attached to the channel walls for measuring the vertical distance from the channel bottom to the bed and water surfaces. The rulers were made of an adhesive film sheet, over which a graduation scale, with marks spaced 1 mm, was printed. The measurements on the rulers were found to contain three sources of error:

1. Error in the graduation of the scale.
2. Error because of stretching of the ruler during installation.
3. Error because of differential distance to the channel bottom.

The first type of error had its origin in the production of the rulers; it was found that for some rulers, between the marks for 25.0 cm and 25.5 cm, there were only three 1 mm marks, instead of four. Also, the actual length of some of the rulers was not exactly 50 cm. A metal ruler was used to found the error e_s between the actual distance and the measured distance to the ruler origin, due to the first and the second type of errors. Figure AIII.1 shows graphs with the errors obtained for all the 26 rulers; best-fit curves for the error are shown in the graphs as well. The functions for the error curves are presented in Table AIII.1, where $z_{hmo,i}$ is the measured distance on the i-th ruler, and $z_{hm,i}$ is the actual distance to the origin of the ruler on the i-th ruler measurement.

The third type of error was due to small vertical displacements of the rulers. Accordingly, each ruler had a different distance from its origin to the base of the channel. A datum plane was established 42.2 cm over the average channel bottom (see Figure AIII.2) and the vertical distance from that plane to the origin of the rulers (C_h in Figure AIII.2) was measured. Table AIII.2 shows the values of C_h for each ruler. Consequently, the vertical distance from the average channel bottom to the measurement point $z_{hm,i}$ for the i-th ruler is

$$z_{h,i} = D_d - \left(C_{h,i} - z_{hm,i}\right) \qquad \text{(AIII.1)}$$

where D_d is the distance from the channel bottom to the datum (D_d=42.2 cm) and $z_{hm,i}$ is the measurement on the i-th ruler corrected for the other errors as indicated in Table AIII.1.

Coordinates computation when the channel is not horizontal

Figure AIII.3 describes all the variables necessary to obtain the coordinates (x, z) of a measurement z_{hi} on the rulers for the i-th ruler (after correction with eq.[AIII.1]), when the channel is tilted α degrees. The coordinates are referenced to the coordinate system given in Figure 3.2, for which the origin is approximately at the joint of the channel. x_h is the distance from the ruler to the origin of the coordinate system when the channel is horizontal. Values of x_h for all the 26 rulers are shown in Table AIII.2.

With reference to Figure AIII.3, the coordinates of a measurement z_h are given by

$$z = \Delta z_1 + \Delta z_2 \qquad \text{(AIII.2)}$$

$$x = x_h - \Delta x_1 - \Delta x_2 \qquad \text{(AIII.3)}$$

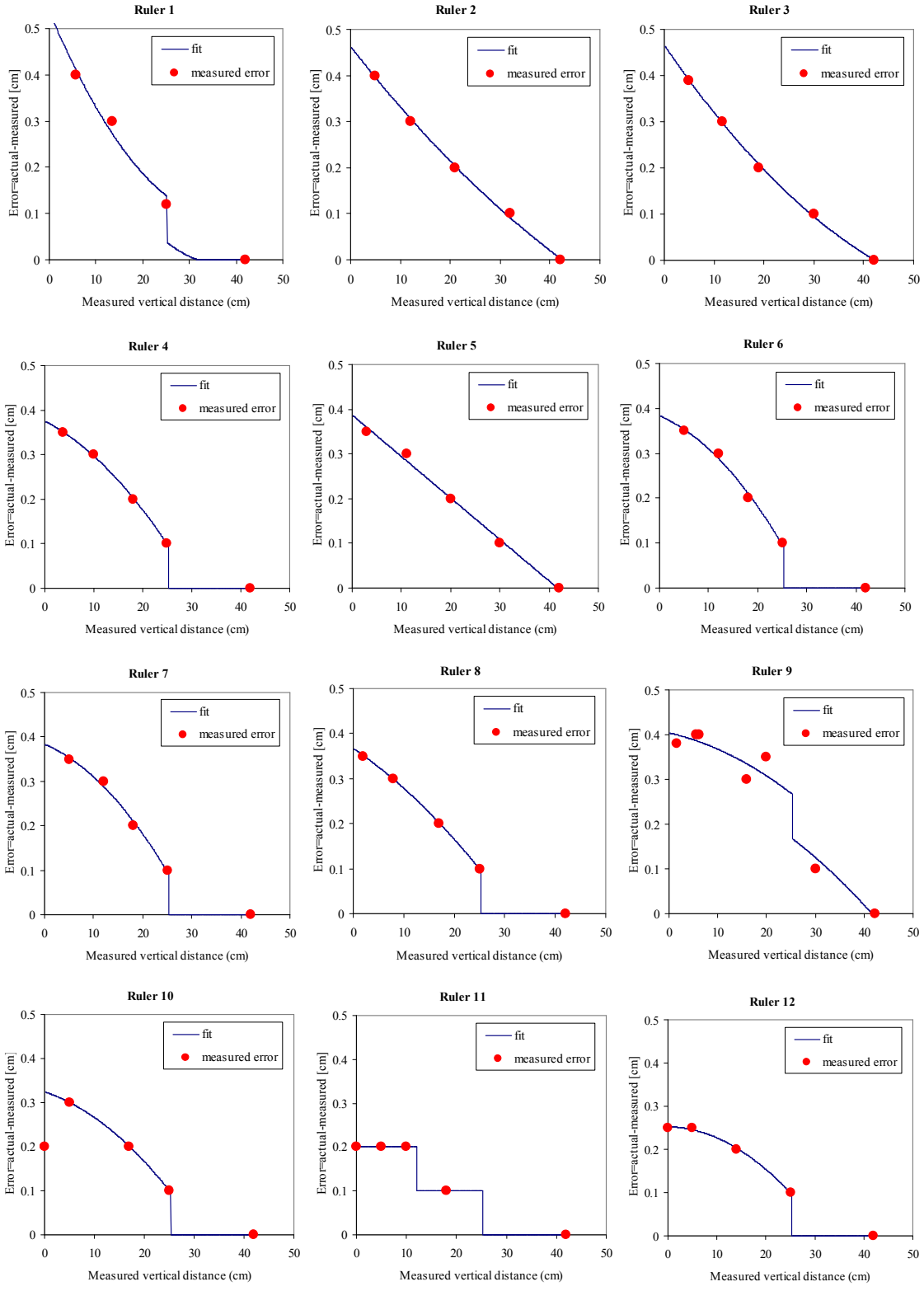

Figure AIII.1

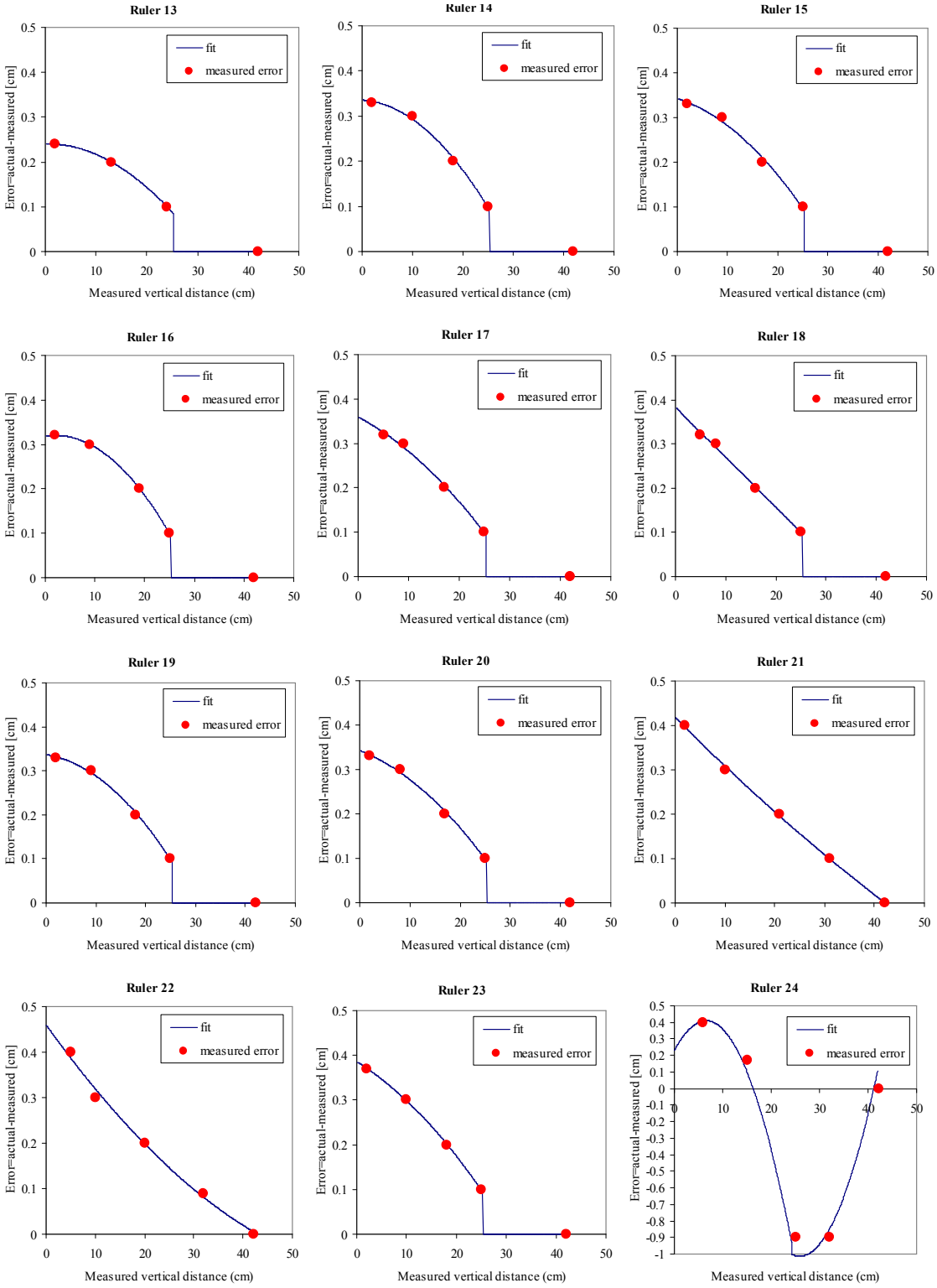

Figure AIII.1 (cont.)

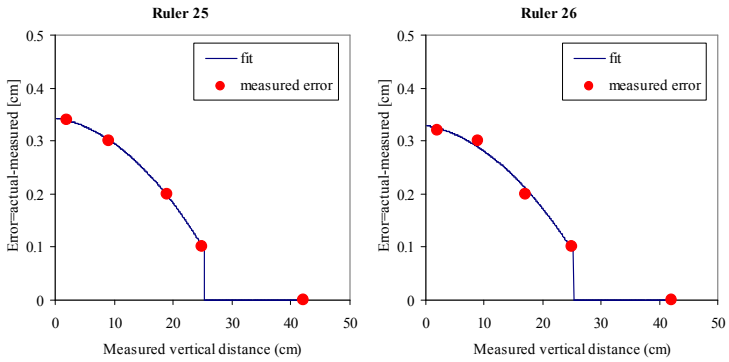

Figure AIII.1 (cont.)

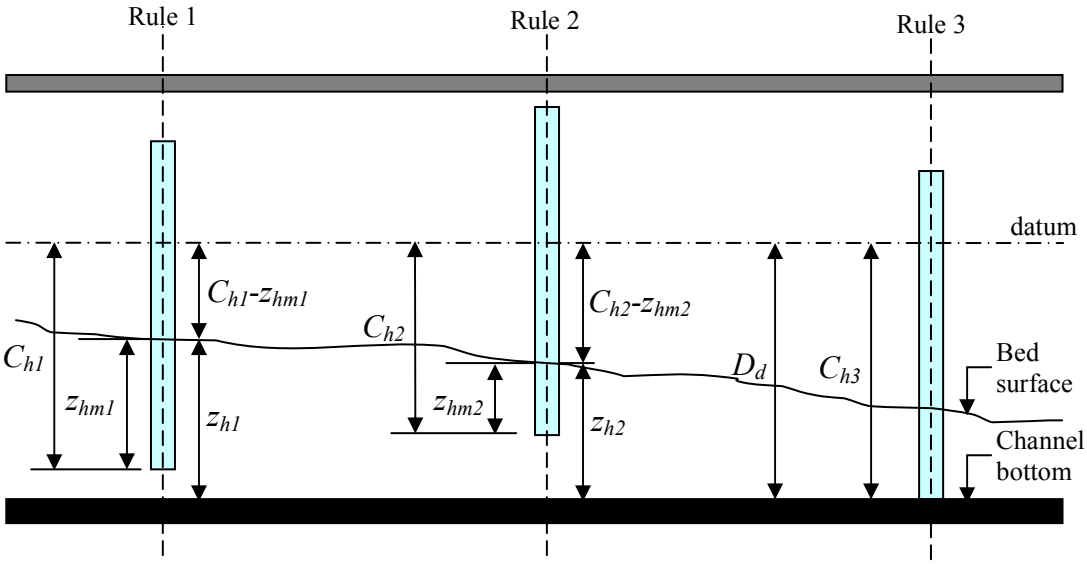

Figure AIII.2

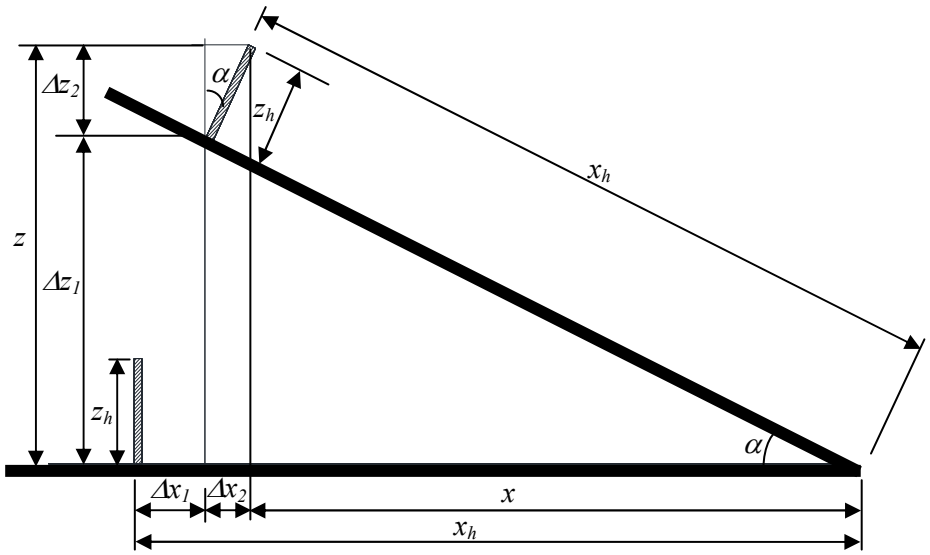

Figure AIII.3

Table AIII.1

Ruler	Actual vertical distance	Computation of error
1	If $z_{hmo,1} \geq 31.7$ $z_{hm,1} = z_{hmo,1}$ If $z_{hmo,1} \geq 25.2$ $z_{hm,1} = z_{hmo,1} + e_s$ If $z_{hmo,1} < 25.2$ $z_{hm,1} = z_{hmo,1} + e_s + 0.1$	$e_s = a + b\ z_{hmo,1} + c\ z_{hmo,1}^2$ a=0.43651; b=-0.2387; c=0.000318
2	$z_{hm,2} = z_{hmo,2} + e_s$	$e_s = a + b\ z_{hmo,2} + c\ z_{hmo,2}^2$ a=0.46260; b=-0.01381; c=0.00007
3	$z_{hm,3} = z_{hmo,3} + e_s$	$e_s = a + b\ z_{hmo,3} + c\ z_{hmo,3}^2$ a=0.46557; b=-0.01570; c=0.00011
4	If $z_{hmo,4} \geq 25.2$ $z_{hm,4} = z_{hmo,4}$ If $z_{hmo,4} < 25.2$ $z_{hm,4} = z_{hmo,4} + e_s + 0.1$	$e_s = a + b\ z_{hmo,4} + c\ z_{hmo,4}^2$ a=0.27490; b=-0.000568; c=-0.00021
5	$z_{hm,5} = z_{hmo,5} + e_s$	$e_s = a + b\ z_{hmo,5}$ a=0.38682; b=-0.00928
6	If $z_{hmo,6} \geq 25.2$ $z_{hm,6} = z_{hmo,6}$ If $z_{hmo,6} < 25.2$ $z_{hm,6} = z_{hmo,6} + e_s + 0.1$	$e_s = a + b\ z_{hmo,6} + c\ z_{hmo,6}^2$ a=0.28331; b=-0.00460; c=-0.00027
7	If $z_{hmo,7} \geq 25.2$ $z_{hm,7} = z_{hmo,7}$ If $z_{hmo,7} < 25.2$ $z_{hm,6} = z_{hmo,6} + e_s + 0.1$	$e_s = a + b\ z_{hmo,7} + c\ z_{hmo,7}^2$ a=0.28332; b=-0.00460; c=-0.00027
8	If $z_{hmo,8} \geq 25.2$ $z_{hm,8} = z_{hmo,8}$ If $z_{hmo,8} < 25.2$ $z_{hm,8} = z_{hmo,8} + e_s + 0.1$	$e_s = a + b\ z_{hmo,8} + c\ z_{hmo,8}^2$ a=0.26659; b=-0.00759; c=-0.00012
9	If $z_{hmo,9} \geq 25.2$ $z_{hm,9} = z_{hmo,9} + e_s$ If $z_{hmo,9} < 25.2$ $z_{hm,9} = z_{hmo,9} + e_s + 0.1$	$e_s = a + b\ z_{hmo,9} + c\ z_{hmo,9}^2$ a=0.30372; b=-0.00246; c=-0.00012
10	If $z_{hmo,10} \geq 25.2$ $z_{hm,10} = z_{hmo,10}$ If $z_{hmo,10} < 25.2$ $z_{hm,10} = z_{hmo,10} + e_s + 0.1$	$e_s = a + b\ z_{hmo,10} + c\ z_{hmo,10}^2$ a=0.22396; b=-0.00375; c=-0.00021
11	If $z_{hmo,11} \geq 25.2$ $z_{hm,11} = z_{hmo,11}$ If $z_{hmo,11} > 12.0$ $z_{hm,11} = z_{hmo,11} + 0.1$ If $z_{hmo,11} < 12.0$ $z_{hm,11} = z_{hmo,11} + 0.2$	-
12	If $z_{hmo,12} \geq 25.2$ $z_{hm,12} = z_{hmo,12}$ If $z_{hmo,12} < 25.2$ $z_{hm,12} = z_{hmo,12} + e_s + 0.1$	$e_s = a + b\ z_{hmo,12} + c\ z_{hmo,12}^2$ a=0.15238; b=-0.00022; c=-0.00024
13	If $z_{hmo,13} \geq 25.2$ $z_{hm,13} = z_{hmo,13}$ If $z_{hmo,13} < 25.2$ $z_{hm,13} = z_{hmo,13} + e_s + 0.1$	$e_s = a + b\ z_{hmo,13} + c\ z_{hmo,13}^2$ a=0.14083; b=-0.00008; c=-0.00025
14	If $z_{hmo,14} \geq 25.2$ $z_{hm,14} = z_{hmo,14}$ If $z_{hmo,14} < 25.2$ $z_{hm,14} = z_{hmo,14} + e_s + 0.1$	$e_s = a + b\ z_{hmo,14} + c\ z_{hmo,14}^2$ a=0.23536; b=-0.00077; c=-0.00035
15	If $z_{hmo,15} \geq 25.2$ $z_{hm,15} = z_{hmo,15}$ If $z_{hmo,15} < 25.2$ $z_{hm,15} = z_{hmo,15} + e_s + 0.1$	$e_s = a + b\ z_{hmo,15} + c\ z_{hmo,15}^2$ a=0.24179; b=-0.00351; c=-0.00025
16	If $z_{hmo,16} \geq 25.2$ $z_{hm,16} = z_{hmo,16}$ If $z_{hmo,16} < 25.2$ $z_{hm,16} = z_{hmo,16} + e_s + 0.1$	$e_s = a + b\ z_{hmo,16} + c\ z_{hmo,16}^2$ a=0.21823; b=-0.00173; c=-0.00042
17	If $z_{hmo,17} \geq 25.2$ $z_{hm,17} = z_{hmo,17}$ If $z_{hmo,17} < 25.2$ $z_{hm,17} = z_{hmo,17} + e_s + 0.1$	$e_s = a + b\ z_{hmo,17} + c\ z_{hmo,17}^2$ a=0.25910; b=-0.00596; c=-0.00018
18	If $z_{hmo,18} \geq 25.2$ $z_{hm,18} = z_{hmo,18}$ If $z_{hmo,18} < 25.2$ $z_{hm,18} = z_{hmo,18} + e_s + 0.1$	$e_s = a + b\ z_{hmo,18}$ a=0.28236; b=-0.01130
19	If $z_{hmo,19} \geq 25.2$ $z_{hm,19} = z_{hmo,19}$ If $z_{hmo,19} < 25.2$ $z_{hm,19} = z_{hmo,19} + e_s + 0.1$	$e_s = a + b\ z_{hmo,19} + c\ z_{hmo,19}^2$ a=0.23637; b=-0.00171; c=-0.00031
20	If $z_{hmo,20} \geq 25.2$ $z_{hm,20} = z_{hmo,20}$ If $z_{hmo,20} < 25.2$ $z_{hm,20} = z_{hmo,20} + e_s + 0.1$	$e_s = a + b\ z_{hmo,20} + c\ z_{hmo,20}^2$ a=0.24256; b=-0.00441; c=-0.00021
21	$z_{hm,21} = z_{hmo,21} + e_s$	$e_s = a + b\ z_{hmo,21} + c\ z_{hmo,21}^2$ a=0.41846; b=-0.0113; c=-0.00003
22	$z_{hm,22} = z_{hmo,22} + e_s$	$e_s = a + b\ z_{hmo,22} + c\ z_{hmo,22}^2$ a=0.46037; b=-0.01520; c=-0.00010
23	If $z_{hmo,23} \geq 25.2$ $z_{hm,23} = z_{hmo,23}$ If $z_{hmo,23} < 25.2$ $z_{hm,23} = z_{hmo,23} + e_s + 0.1$	$e_s = a + b\ z_{hmo,23} + c\ z_{hmo,23}^2$ a=0.28518; b=-0.00690; c=-0.00018
24	If $z_{hmo,24} \geq 25.2$ $z_{hm,24} = z_{hmo,24} + e_{s1}$ If $z_{hmo,24} < 25.2$ $z_{hm,24} = z_{hmo,24} + e_{s2} + 0.1$	$e_{s1} = a + b\ z_{hmo,24} + c\ z_{hmo,24}^2$ a=2.08237; b=-0.23078; c=-0.00430 $e_{s2} = a + b\ z_{hmo,24} + c\ z_{hmo,24}^2$ a=0.06754; b=0.06446; c=-0.00428
25	If $z_{hmo,25} \geq 25.2$ $z_{hm,25} = z_{hmo,25}$ If $z_{hmo,25} < 25.2$ $z_{hm,25} = z_{hmo,25} + e_s + 0.1$	$e_s = a + b\ z_{hmo,25} + c\ z_{hmo,25}^2$ a=0.24309; b=-0.00152; c=-0.00032
26	If $z_{hmo,26} \geq 25.2$ $z_{hm,26} = z_{hmo,26}$ If $z_{hmo,26} < 25.2$ $z_{hm,26} = z_{hmo,26} + e_s + 0.1$	$e_s = a + b\ z_{hmo,26} + c\ z_{hmo,26}^2$ a=0.22949; b=-0.00194; c=-0.00029

Table AIII.2

i-th ruler	1	2	3	4	5	6	7	8	9
x_h [m]	0.573	1.512	2.501	3.568	4.509	5.647	6.535	7.498	8.555
C_h [m]	0.422	0.422	0.421	0.422	0.422	0.422	0.422	0.422	0.422
i-th ruler	10	11	12	13	14	15	16	17	18
x_h [m]	9.560	10.505	11.503	12.463	13.578	14.562	15.490	16.548	17.463
C_h [m]	0.423	0.422	0.422	0.423	0.422	0.422	0.422	0.422	0.421
i-th ruler	19	20	21	22	23	24	25	26	
x_h [m]	18.538	19.500	21.546	22.525	23.459	24.561	25.512	26.452	
C_h [m]	0.422	0.422	0.422	0.421	0.421	0.421	0.421	0.421	

It is found that

$$\Delta z_1 = x_h \sin\alpha \qquad \text{(AIII.4)}$$

$$\Delta z_2 = z_h \cos\alpha \qquad \text{(AIII.5)}$$

and

$$\Delta x_1 = x_h\left(1-\cos\alpha\right) \qquad \text{(AIII.6)}$$

$$\Delta x_2 = z_h \sin\alpha \qquad \text{(AIII.7)}$$

Including eqs.(AIII.4)-(AIII.7) in eqs.(AIII.2) and (AIII.3) the coordinates of the point measured on the ruler are

$$x = x_h \cos\alpha - z_h \sin\alpha \qquad \text{(AIII.8)}$$

$$z = x_h \sin\alpha + z_h \cos\alpha \qquad \text{(AIII.9)}$$

APPENDIX IV

SEDIMENT PROPERTIES

AIV.1 Introduction

Table 3.2 summarizes the properties of the original sand and gravel used in the investigation, namely, mean diameter, geometric standard deviation, relative density and porosity. The procedures for determining each of these properties are described in this Appendix. The effect of abrasion produced by the sediment recirculating system and pump are discussed in this Appendix as well.

AIV.2 Relative density and porosity

The relative density ($S_s=[\rho_s/\rho]$, where ρ is water density and ρ_s sediment density) of the sediment was determined with

$$S_s = \frac{A}{A+B-C} \qquad \text{(AIV.1)}$$

where A is the weight of the dry sample, B is the weight of a container filled with water to a certain mark and C is the weight of the container with the sample and the water up to the same mark as for B. Fourteen tests were performed for the sand samples and 11 for the gravel samples; the temperature of the water was 25.5ºC. The relative frequencies for the different relative density classes are shown in Figure IV.1. The mean relative densities were 2.63 and 2.60 for sand and gravel, respectively.

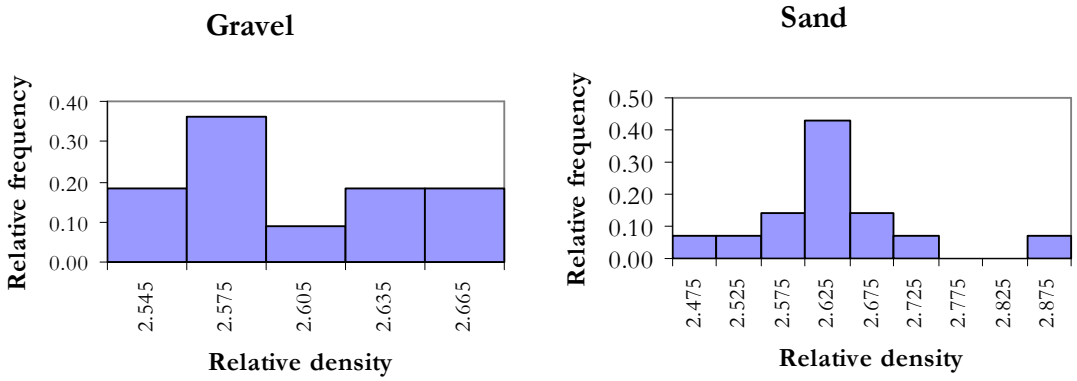

Figure IV.1 Frequency histograms for the relative densities of the sand and gravel used in the experiments.

To determine porosity, the sediment sample was added to a container, which was then filled with water to the same level of the sediment. Porosity was calculated as the ratio of the volume of water added to the container to the volume of the container occupied by the sediment sample. The average porosity values obtained were 0.40 and 0.38 for the sand and gravel, respectively.

AIV.3 Sieve analysis of sediment samples

Of the 1,073 sediment samples collected in all the experimental runs, 979 were sieved to determine grain size distribution. The sieved samples yielded a total weight of 656.34 kg.

The samples were stored in plastic bags labeled with the run number and the origin of the sample. Before sieving, the samples were taken out of the bags and left to dry.

Eleven sieves (whose sieve openings are shown in Table IV.1) were used for the size analysis. An additional sieve, with a 2.24 mm opening, was added to analyze sediment mixture samples; 2.24 mm is the sieve size of the trommel used to separate sand and gravel in the sediment recirculating system of the experimental set-up.

Table IV.1 Sieve diameters D_b and centers of class D_i between sieves for the sieves used to analyze the grain size distribution of the sediment samples. Geometric diameters are shown in the first and second rows and diameters in ψ scale are shown in the second and third; $\psi=\log_2(D)=\ln(D)/\ln(2)$.

D_i [mm]	0.20	0.56	0.79	1.12	1.58	2.37	3.35	5.02	7.10	8.94	-
D_b [mm]	0.08	0.50	0.63	1.00	1.25	2.00	2.80	4.00	6.30	8.00	10.00
ψ_i	-2.32	-0.83	-0.33	0.16	0.66	1.24	1.74	2.33	2.83	3.16	-
ψ_b	-3.64	-1.00	-0.67	0.00	0.32	1.00	1.49	2.00	2.66	3.00	3.32

Each sample was added to the series of standard laboratory sieves, which were shaken for 8 to 10 minutes with a standard machine. Sediment retained between successive sieves was weighed on a digital scale, with a precision of ±2 g. Figure IV.2 shows the grain size distribution of all the samples analyzed.

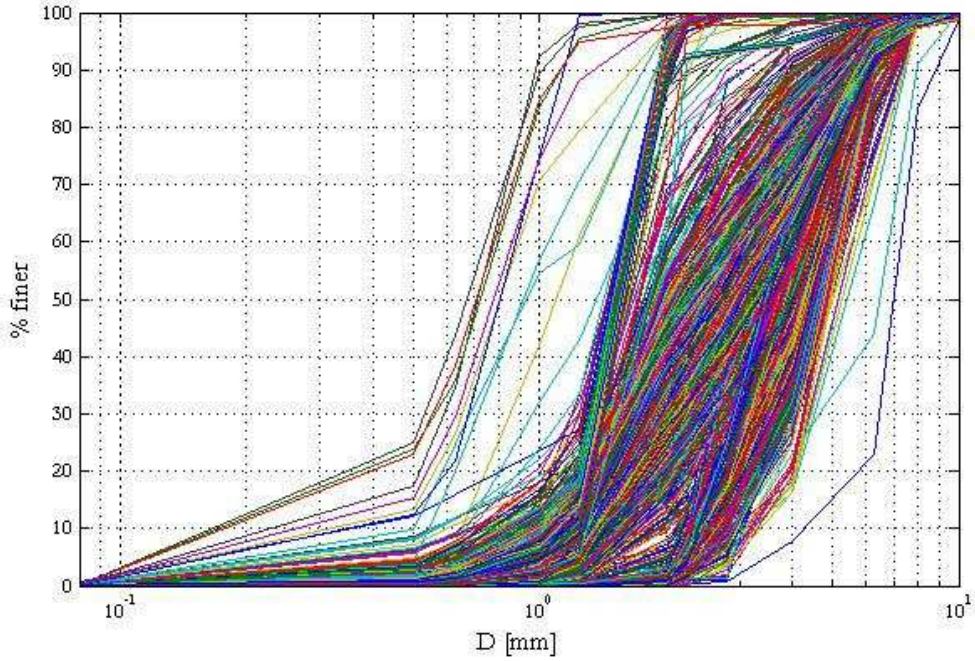

Figure IV.2 Grain size distributions for the 979 samples sieved.

The mean grain sizes and standard deviations of the sediment samples were calculated on a ψ scale, for which $D=2^{\psi}$, so that the mean diameter is given by

$$\overline{\psi} = \sum_{i=1}^{n} \psi_i f_i \qquad \text{(AIV.2)}$$

where f_i is the fractional content of the i-th size fraction and ψ_i is the center of class for the i-th size range, given by $\psi_i=0.5(\psi_{b,i}+\psi_{b,i+1})$. In the same manner, the standard deviation was computed as

$$\sigma^2 = \sum_{i=1}^{n} (\psi_i - \overline{\psi})^2 f_i \qquad \text{(AIV.3)}$$

Geometric mean sizes and standard deviations were then calculated from

$$D_m = 2^{\overline{\psi}} \qquad \text{(AIV.4)}, \qquad \text{and} \qquad \sigma_g = 2^{\sigma} \qquad \text{(AIV.5)}$$

It is considered that sediment is well sorted when σ_g<1.6 (Parker, 2004). Therefore, the sand and the gravel used in the experiments were well sorted.

By definition, if the distribution of grain sizes follows a normal law, the standard deviation is equal to

$$\sigma_{gs} = \left(D_{84} / D_{16} \right)^{0.5} \qquad \text{(AIV.6)}$$

where D_{84} and D_{16} are sizes for which 84% and 16% of the sample is smaller, respectively. As seen from the values in Table 3.2, σ_g and σ_{gs} are quite similar in both the sand and the gravel, showing that both materials were normally distributed.

In determining the number of grain size modes of a sediment sample it is convenient to show grain size distribution as a probability density function, which in a discrete form can be calculated as

$$P(\psi_i) = \frac{f_i}{(\psi_{b,i+1} - \psi_{b,i})} \qquad \text{(AIV.7)}$$

where f_i is the fractional content by weight of the i-th size fraction, $\psi_{b,i}$ is the sieve diameter where the ψ_i size class is retained, and $\psi_{b,i+1}$ is the sieve diameter of the closest sieve to $\psi_{b,i}$ with a greater diameter.

AIV.4 Crushing and abrasion produced by the sediment recirculating system

After the performance of some experimental runs, it was noted that the grain size characteristics of the gravel had changed. These changes were found to be due to the unexpected crushing of the material by screw conveyors in the sediment recirculating system and to abrasion by the water-sediment recirculating pump. The effects of crushing and abrasion on gravel grain sizes are shown in Figure IV.3, where a sample of the original gravel (before it was added to the experimental set-up) is compared with a sample of gravel taken from the gravel hopper after run M2E6, which was one of the last runs performed with the sand-gravel mixtures. The main effect was a displacement to the left in terms of grain size distribution, with a change in mode from 5.02 to 3.35 mm.

Table IV.2 shows the effect of crushing and abrasion on mean diameter, geometric standard deviation, and characteristic gravel diameters. On average, crushing and abrasion reduced the size of the original gravel by 20%, but the geometric standard deviation remained almost the same.

Table IV.2 Effect of crushing and abrasion by the sediment recirculating system on mean diameter, geometric standard deviation and characteristic gravel grain sizes. Diameters in mm.

Characteristic diameter	D_m	σ_g	D_5	D_{10}	D_{16}	D_{25}	D_{50}	D_{60}	D_{75}	D_{84}	D_{90}
Original gravel	4.58	1.39	2.34	2.73	3.09	3.67	4.77	5.21	5.93	6.48	7.05
Gravel in hopper after run M2E6	3.53	1.40	2.11	2.28	2.49	2.83	3.51	3.82	4.57	5.17	5.61
Ratio Original/Hopper-M2E6	0.77	1.01	0.90	0.83	0.81	0.77	0.74	0.73	0.77	0.80	0.80

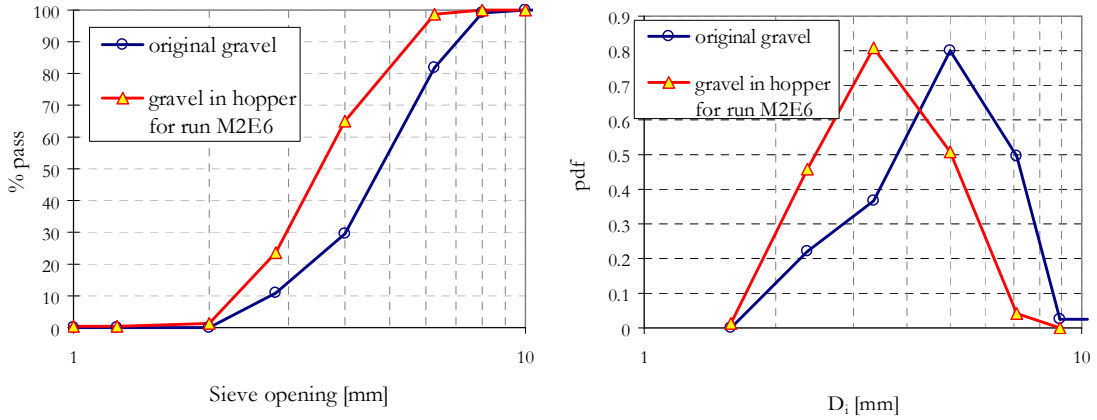

Figure AIV.3. Comparison of grain size distributions for samples of the original gravel before it was added to the experimental set-up and samples of gravel taken from the gravel hopper after run M2E6, which was one of the last runs performed with the sand-gravel mixtures.

AIV.4.1 Crushing by the screw conveyor from the deposit to the hopper

Considerable crushing of gravel particles was found to occur just after the sediment was added to the experimental set-up. The gravel was crushed by the screw conveyor that transported the material from the big deposit to the hopper (see Photo P1 in Appendix I for an image of this screw). Figure AIV.4 shows a comparison of grain size distributions and probability density functions for the original gravel before it was added to the system and after it had passed through the screw conveyor.

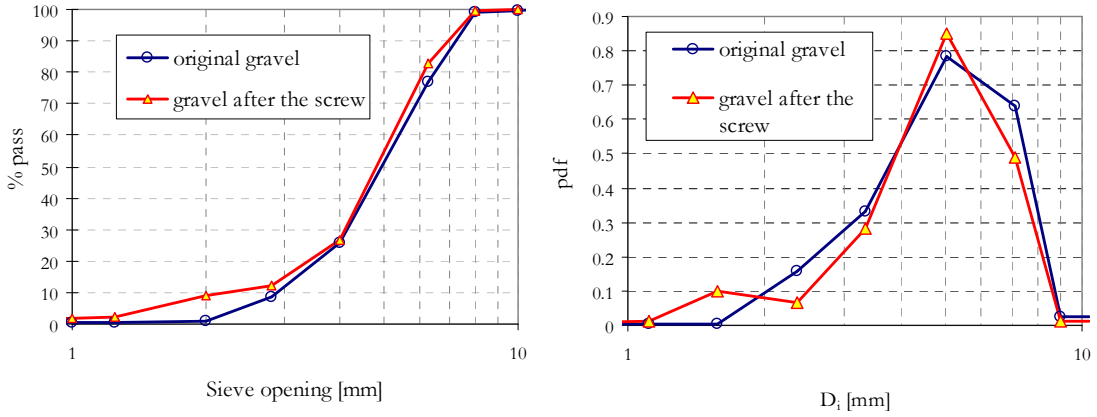

Figure AIV.4 Comparison of grain size distributions for the gravel samples before they were added to the experimental set-up and after they had passed by the first screw conveyor that transported the sediment from the deposits to the hoppers.

The effect of crushing produced by the screw conveyor was an increase in the fractional content of the mode (=5.02 mm) and a reduction in the participation of the other size fractions. The exception was the fraction size 1.58 mm, which, before crushing, was practically absent and after crushing, accounted for almost 7% of the fractional content of the sample by weight. This new size fraction must have been automatically removed from the gravel circuit in the recirculating system by the trommel after its first passage

through the channel. Accordingly, it would have ended up forming part of the sand material in the system and having a minimum effect on the grain size distribution of this material, as the mode of the original sand was also 1.58 mm. Although the mixing of the crushed gravel with the sand might have not had an important effect on sand grain size distribution, it might have had an effect on the shape of the grains.

The geometric standard deviation of the gravel was 1.44 before crushing and 1.75 after crushing. Nevertheless, the geometric standard deviation for normal distribution (σ_{gs}) remained virtually unchanged (1.44 for the original sample and 1.45 after crushing). Table AIV.3 shows characteristic grain sizes before and after crushing by the screw. The ratio for the original sample and the crushed sample in the last line shows that the most affected diameters were those with sizes lower than the D_{16}, explaining why the geometric standard deviation for normal distribution was not altered by the crushing of the material.

Table AIV.3 Effect of crushing by screw conveyor on characteristic grain sizes of the gravel.

Characteristic diameter	D_5	D_{10}	D_{16}	D_{25}	D_{50}	D_{60}	D_{75}	D_{84}	D_{90}	D_{95}
Original gravel [mm]	1.51	2.22	3.07	3.83	4.83	5.24	5.92	6.43	7.00	7.51
Crushed gravel [mm]	2.40	2.89	3.27	3.95	4.96	5.42	6.19	6.80	7.25	7.66
Ratio crushed/original	0.63	0.77	0.94	0.97	0.97	0.97	0.96	0.95	0.96	0.98

AIV.4.2 Changes in grain size during the experimental campaign

Changes in gravel grain size due to crushing occurred from the moment the material first entered the system, as shown in IV.4.1 for the screw conveyor that transports the gravel from the deposit to the hopper. The material continued to be affected by crushing and abrasion during its recirculation through the system throughout the experimental campaign, as can be seen in Figure AIV.5. This Figure shows most of the sediment samples taken throughout the experimental campaign, with an analysis of gravel size fraction only (D>2.24 mm). On the abscissa the corresponding runs are shown in the order in which they were performed. The graph shows how the characteristic diameters decreased more or less steadily as the runs were performed, but the standard deviation remained almost constant. These trends are apparent, even when many of the samples must have undergone grain size sorting effects within the same gravel size fraction due to flow and transport processes. Subtle recoveries in grain sizes were produced by the supply of fresh material to the system; this material was routinely supplied at the beginning of the pure gravel runs (G), but for most of the runs with mixtures, no additional fresh material was fed into the system. The last part of the graph shows a slight recovery in grain sizes because of the fresh material added for some of the last runs with mixture 2.

Figure IV.6 is similar to Figure IV.5 but it shows the sand size fraction of the samples. The trend for all grain sizes was roughly horizontal, demonstrating that crushing and abrasion had a lesser impact on the sand than on the gravel.

Although the changes in grain size produced by crushing and abrasion were distinguishable between experimental runs, it can be considered that they were almost negligible within individual runs. Therefore, **each run can be characterized by an average representative grain size distribution. For this characterization, the exhaustive sampling of sediment during the experimental campaigns served to accurately determine the mean properties of the material for each run**.

Crushing and abrasion reduced not only the size of the gravel but also the volume of the gravel within the system. This created an additional problem in the planning of the runs when the bed was eroded in search of equilibrium conditions. Because the amount of gravel was limited, the erosion of the bed had to be reduced to the minimum. Therefore,

the prediction of the stable bed slope for the imposed hydraulic conditions of a given run turned to be of great importance.

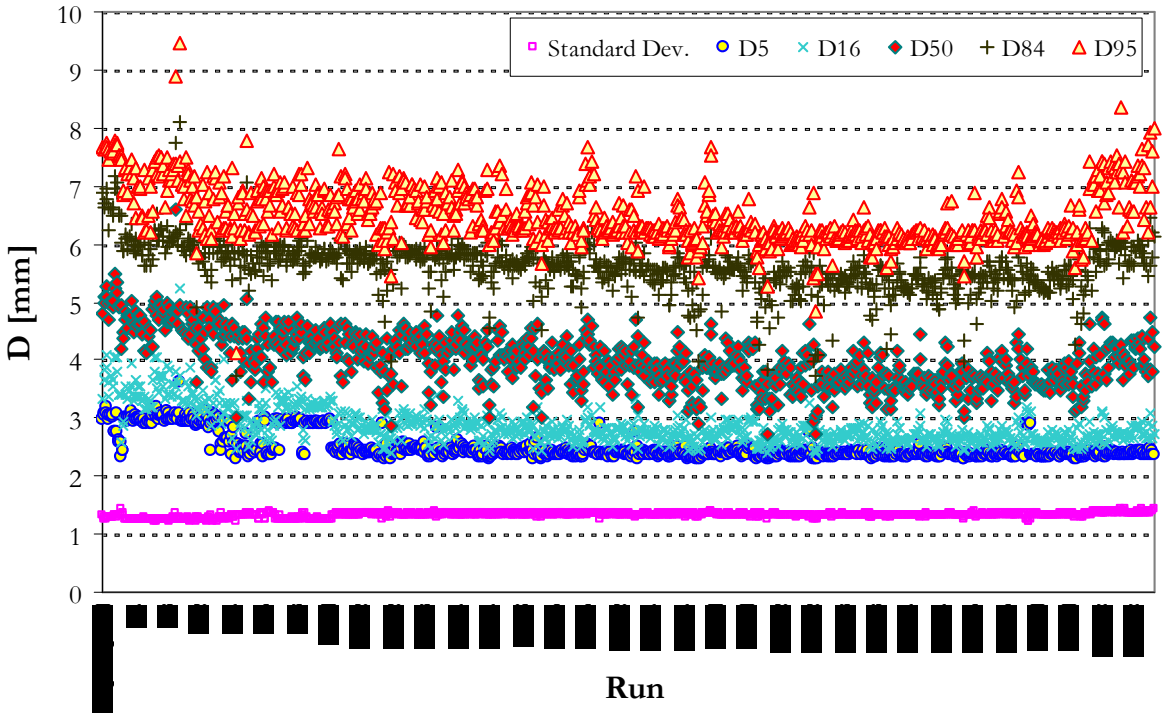

Figure AIV.5 Characteristic grain sizes and standard deviations for the **gravel** fraction (D>2.24 mm) of the sediment samples taken during all the experimental runs (samples from the sand run series and the sand hopper were excluded, as were samples containing less than 30 grams of gravel). The runs are shown in order of performance.

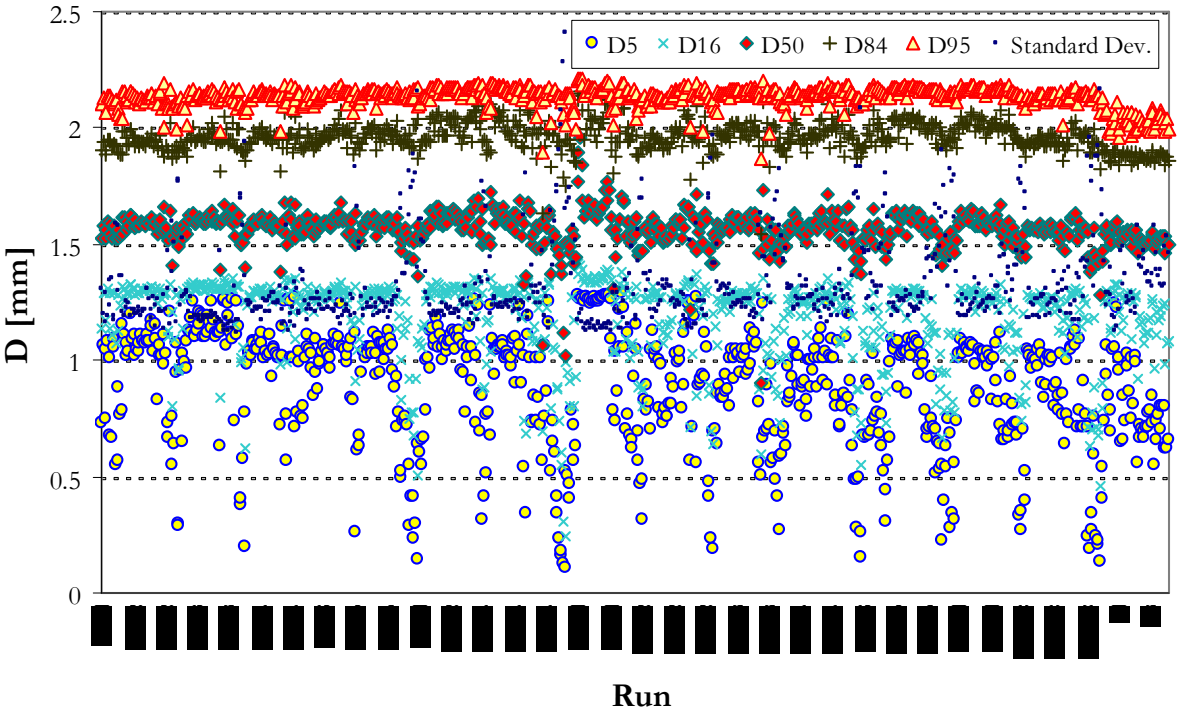

Figure AIV.6 Characteristic grain sizes and standard deviations for the **sand** fraction (D<2.24 mm) of the sediment samples taken during all the experimental runs (samples from the gravel run series and from the gravel hopper were excluded, as were samples containing less than 20 grams of sand). The runs are shown in order of performance.

APPENDIX V

HYDRAULICS AND SEDIMENT TRANSPORT COMPUTATIONS FOR SELECTING THE RANGES OF VARIABLES

Introduction

The equations used for obtaining an initial notion of the ranges of variables that could be used in the experimental flume are presented in this Appendix. These equations included a hydraulic resistance equation, the mass continuity equation for water, a sediment transport capacity equation, and a criterion for initiation of sediment motion.

Hydraulic resistance

Considering flow over a hydraulically rough plane bed, flow mean velocity can be computed from the Manning equation given as

$$V = \frac{R_h^{\frac{2}{3}} S_o^{\frac{1}{2}}}{n} \qquad \text{(AV.1)}$$

where n is a resistance coefficient, which can be obtained from the approximation of Strickler

$$n = \frac{D_{50}^{\frac{1}{6}}}{21} \qquad \text{(AV.2)}$$

with D_{50} being the median grain size of the bed sediment; R_h is the hydraulic radius, which for a rectangular cross-section is given by

$$R_h = \frac{BH}{B+2H} \qquad \text{(AV.3)}$$

with B being the channel width (B=0.75 for the channel in the experiments herein reported), and H being the mean water-depth; and S_o is the energy slope, which for steady uniform flow can be assumed equal to the bed and water surface slopes.

Sediment transport

A sediment transport capacity equation was used, which is similar to the formula presented by Meyer-Peter and Müller. The formula used is essentially the same as that presented by these authors, but only the critical Shields stress was not considered constant. The formula is the following

$$q^* = a_m \left(\tau_b^* - \tau_c^*\right)^{b_m} \qquad \text{(AV.4)}$$

where a_m and b_m are empirical constants; q* is the Einstein number given by the relation

$$q^* = \frac{Q_s}{B\sqrt{(S_s - 1)gD_{50}^3}} \qquad \text{(AV.5)}$$

where g is the gravitational acceleration, Q_s is the sediment transport rate by volume, and S_s is the relative density of the bed sediment; τ^*_b is the Shields stress acting on the bed, computed with

$$\tau_b^* = \frac{\tau_o}{(S_s - 1)\rho g D} \qquad \text{(AV.6)}$$

where ρ is the density of the water, τ_o is the average shear stress on the bed surface, which for uniform flow can be computed from

$$\tau_o = \rho g H S_o \qquad \text{(AV.7)}$$

and τ^*_c is the critical Shields of the bed material for initiation of motion.

Critical Shields stress

Brownlie (1981) presented an approximation to the original empirical Shields curve that defines the critical boundary shear stress for the beginning of movement of the streambed sediment, given the sediment grain size; this approximation was subsequently amended by Parker et al. (2003). The equation is given by

$$\tau_c^* = 0.22\,\mathrm{Re}_p^{-0.6} + 0.06 \cdot 10^{-7.7\,\mathrm{Re}_p^{-0.6}} \qquad \text{(AV.8)}$$

where Re_p is the particle Reynolds number computed from

$$\mathrm{Re}_p = \frac{\sqrt{(S_s - 1)gD}D}{\nu} \qquad \text{(AV.9)}$$

where ν is the dynamic viscosity of water.

Determination of the water discharge for a given sediment transport rate

For mobile-bed equilibrium conditions in a granular bed with a given sediment transport rate and bed slope, water depth can be computed by combining eqs.(AV.4) to (AV.7), yielding after arrangement and solving for H

$$H = \frac{(S_s - 1)D}{S_o}\left(\left[\frac{Q_s}{a_m B\sqrt{g(S_s - 1)D^3}}\right]^{\frac{1}{b_m}} + \tau_c^*\right) \qquad \text{(AV.10)}$$

In turn, considering the water continuity equation as follows

$$Q_w = AV = BHV \qquad \text{(AV.11)}$$

where A is the flow area and Q_w is the water discharge, combining eq.(AV.11) with eqs.(AV.1) to (AV.3), water discharge can be calculated as

$$Q_w = \frac{21BHS_o^{\frac{1}{2}}}{D_{50}^{\frac{1}{6}}}\left(\frac{BH}{B + 2H}\right)^{\frac{2}{3}} \qquad \text{(AV.12)}$$

Figures 3.4 to 3.6 in Chapter 3 were obtained after applying eqs.(AV.10) and (AV.12) for a range of bed slopes between 0.001 and 0.1, and for four solid discharges, namely, 0.1, 0.3, 0.6, and 1.1 kg/s. Sediment characteristics used were those summarized in Table 3.2, considering the mean diameter D_m as the representative grain size for all the computations. For these sediments, critical Shields stresses computed with eq.(AV.8) were τ_c^*=0.020 for sand, and τ_c^*=0.025 for gravel. The coefficients used for eq.(AV.4) were a_m=4 and b_m=1.5, as originally proposed by Meyer-Peter and Müller.

References

Brownlie, W. R., 1981, Prediction of flow depth and sediment discharge in open channels, *Report* No. KH-R-43A, W. M. Keck Laboratory of Hydraulics and Water Resources, California Institute of Technology, Pasadena, California, USA, 232 p.

Parker, G., Toro-Escobar, C. M., Ramey, M. and S. Beck, 2003, The effect of floodwater extraction on the morphology of mountain streams, *Journal of Hydraulic Engineering*, 129(11), 885-895.

APPENDIX VI

ESTIMATION OF THE GRADIENT OF SEDIMENT VOLUMES IN THE CHANNEL

Introduction

An estimation of the likely volumes of sediment to be eroded or deposited in the channel bed was performed previous to each experimental run. The equations and procedure for these calculations are presented in this Appendix.

The independent variables selected prior to the beginning of every run were water discharge, sediment-feed rate and initial bed slope. Water discharge and sediment-feed rate were established according to criteria given in section 3.3, while for the selection of an initial bed slope three restrictions had to be taken into account. First, for bed aggradation runs it was required to verify if the sediment available in the hopper would be enough to develop a sediment deposit with the expected equilibrium bed slope. Secondly, for bed erosion runs it was necessary to verify if the bed degradation would not approximate excessively to the channel bottom. A third restriction for bed erosion, not as important as the other, was that the volumetric capacity in the hopper had to be enough to store the volume of eroded material. If these restrictions were not satisfied, the initial bed slope had to be changed, and this was done by adjusting the channel slope. Computations were repeated until finding an adequate channel slope.

Computation of the gradient of sediment volume

For the developments here described, the sketch shown in Figure VI.1 was used as a reference. Assuming that the angle α between the channel bottom and the horizontal plane is low, so that the approximation $\cos\alpha \approx 1$ is valid, the increment of volume of sediment $\Delta\forall$ in the channel, when evolving from an initial bed slope S_o to a final bed slope S_f, can be calculated with

$$\Delta\forall = \frac{1}{2} L \Delta z B (1-\varepsilon) \qquad \text{(AVI.1)}$$

where B is the width of the channel (0.75 m), L is the length of the sediment deposit in the channel (≈26 m), Δz is the vertical increment in bed elevation of the uppermost part of the deposit, and ε is the sediment porosity in the channel (0.40 for sand and 0.38 for gravel). Δz can be computed from

$$\Delta z = z_f - z_i \qquad \text{(AVI.2)}$$

where z_i is the initial bed elevation and z_f is the final bed elevation, which can be calculated with

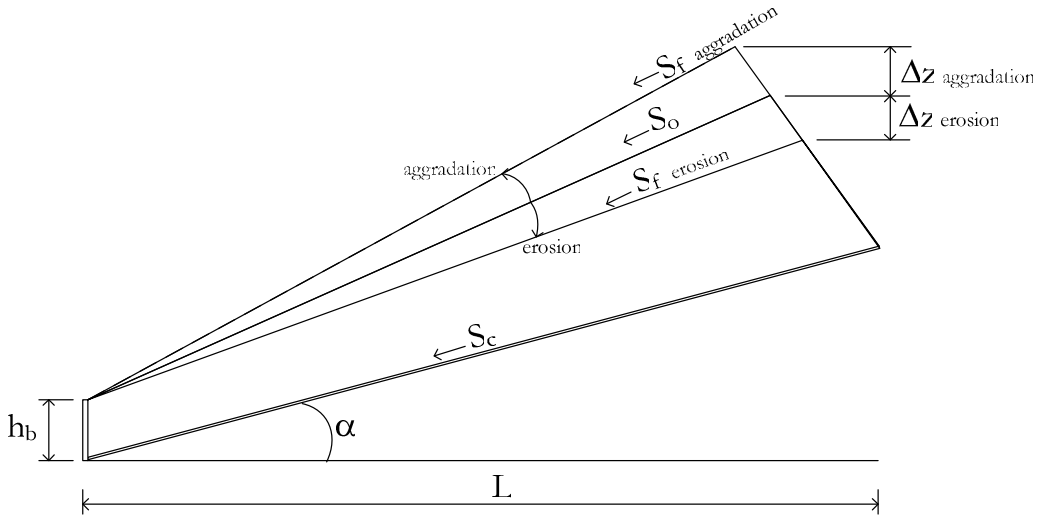

Figure AVI.1

$$z_i = h_b + S_o L \qquad \text{(AVI.3)}$$

and

$$z_f = h_b + S_f L \qquad \text{(AVI.4)}$$

respectively, being h_b the height of the border condition for the sediment (7 cm for run series I to III, and 14 cm for run series IV to VI).

The final bed slope is the expected bed slope for mobile-bed equilibrium conditions. A practical functional relation for the equilibrium bed slope in the experimental channel can be written as

$$S_f = f\left(\frac{Q_{SF}}{Q_w}\right) \qquad \text{(AVI.5)}$$

where Q_{SF} is the sediment-feed rate and Q_w is the water discharge. From test runs in run series I and II, the functional relation in eq.(AVI.5) was found to be well represented with a power-law function. Best-fit functions, one for sand and one for gravel, are shown in Figure 3.7 with the experimental points in run series I and II. These functions were used for anticipating equilibrium bed slopes in runs from series III and VI. For runs series IV and V with sand-gravel mixtures, a weighted average of the two functions was used, according to the sand content of the mixture. Additionally, the estimations were judged and refined by the incorporation of new data in the assessment of final expected values.

Finally, in order to put the initial bed slope as a function of the channel slope S_c, which is the variable that could be controlled, the bed slope with the channel in a horizontal position S_{oc}, as shown in Figure AVI.2, is used as follows

$$S_o = S_{oc} + S_c + \frac{h_b}{L} \qquad \text{(AVI.6)}$$

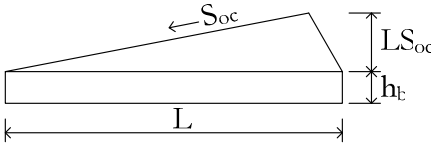

Figure AVI.2

Comparison with restrictions

Eq.(AVI.1) was used to anticipate the volume of sediment deposited in the channel for aggradation runs, and the volume of sediment extracted from the channel for erosion runs. These volumes were compared with the volume of sediment available in the hopper for the former, and with the capacity of the hopper for the latter. Hence, for aggrading runs it should be fulfilled that $\Delta\forall < \forall_{mh}$, where $\forall_{mh}$ is the volume of material in the hopper; while for erosion runs it should be fulfilled that $\Delta\forall < (\forall_h - \forall_{mh})$, where $\forall_h$ is the total volumetric capacity of the hopper.

Table AVI.1 show results of the application of eqs.(AVI.1) to (AVI.6) to experimental data from run series III. If computed weights of material displaced from/to the channel, presented in the penultimate column, are compared with the temporal variation graphs of weight in the hoppers, shown in Appendix VII, it can be concluded that the equations gave a reasonable and valuable approach for selecting variables and preparing the definitive experimental runs.

Table AVI.1

Run	Q_{SF}/Q_w	S_c	S_{oc}	S_o	S_f	Δz	$\Delta\forall$ [m^3]	$\Delta\forall$ [kg]	y_s [m]
G12	0.0039	0.0185	0.0025	0.0237	0.0209	-0.074	-0.4475	-1185.8	0.131
G13	0.0034	0.0150	0.0003	0.0180	0.0195	0.039	0.2334	618.5	0.187
G14	0.0030	0.0130	0.0008	0.0165	0.0181	0.042	0.2556	677.4	0.203
G15	0.0025	0.0150	0.0011	0.0188	0.0164	-0.063	-0.3790	-1004.3	0.105
G16	0.0015	0.0130	-0.0015	0.0142	0.0126	-0.042	-0.2521	-668.0	0.059
G17	0.0004	0.0050	-0.0035	0.0042	0.0061	0.051	0.3065	812.2	0.099

The second restriction to be taken into account was that bed erosion should not progress deeply, so that the sediment bed would not end being extremely thin or would not vanish. In choosing a value for the initial bed slope of a run, the criteria used was that in equilibrium state it should be fulfilled that $y_s \geq h_b$, where y_s is the vertical distance from the channel bottom to the bed surface on the uppermost part of the bed, and can be calculated from

$$y_s = h_b + L\left(S_f - S_c\right) \qquad \text{(AVI.7)}$$

Results of the application of eq.(AVI.7) to data from run series III are shown in the last column of Table AVI.1. For runs with sediment mixtures, this restriction was relaxed, since not enough gravel was available for some runs.

APPENDIX VII

TIME-EVOLUTION GRAPHS

Introduction

In this appendix five graphs are presented for each run, which describe the evolution with time of some of the variables measured during the experimental runs. Descriptions of each graph and details on treatment of the data to obtain the plots are provided as follows.

Gradient of weight on the hoppers

The uppermost graph of the column of five graphs for each run describes the variation of weight W on the hopper with time t. The curves in these graphs (one curve for pure sand and pure gravel runs, two curves for runs with mixtures: one for gravel in blue, and one for sand in red) are not always continuous in all time intervals because they are not exactly the same curves of the original record of the real-time variation of weight on the hoppers. The reason for this difference is that some intervals have been removed and some have been displaced. Since during the runs there were disruptions and discontinuities in the addition of sediment coming from the channel end into the feeders, manipulation of the curves for the graphs here presented was performed in order to obtain an approximate description of the weight variation on the hoppers if there wouldn't have been any disruptions or discontinuities. Disruptions and discontinuities occurred because of three main reasons:

- by-passing of the sediment to the large deposits for measuring the actual sediment-feed rate supplied by the feeder;
- introduction of fresh material from the large deposits;
- malfunctions in the system.

The method used to remove disruptions and discontinuities from the graphs is exposed as follows using as an example the by-passing of sediment and subsequent addition of fresh material in run G15. For most of the runs, at a certain moment the sediment coming from the channel end instead of being conducted to the hopper(s) it was guided to the large deposit(s). In this manner, the hopper(s) began to empty at a constant rate; the record of the gradient of weight when the hopper was emptying served to measure the actual constant feed rate added to the channel during the run, and supplied an additional point for the calibration curve of the feeder as well, as explained in Section 3.3.2.3. Once the hopper was almost empty, sediment from the large deposit was added to refill the hopper, and the material returning from the channel end was again conducted to the hopper. Figure AVII.1 below shows this procedure reflected in the continuous record of weight on the hopper for run G15. For generating the approximate record without disruptions, the increment of weight ΔW was added to all the record of weights for times higher than t_2, which is the running time at which the disruption was ended. ΔW was obtained from extrapolating to a time $t=t_1+(t_1+t_2)/2$ best-fit curves to the original record at intervals before t_1 and after t_2, where t_1 is the running time when the disruption began. To obtain the final curve, data between t_1 and t_2 were erased.

Even when the graphics have been altered as described above, some discontinuities remained, which should not be attributed to changes in solid discharge in the channel, but to malfunctions and effects of the flume operation. For instance, many times during the experimental runs there were problems with the suction and pumping of sediment from the sediment collecting tank downstream of the channel; these problems produced accumulation of sediment in the tank. When the problems were solved and sediment accumulated was sucked and conducted to the hoppers, the effect in the real-time record was a sudden increment of weight on the hopper. In the same vein, starting and stopping the sediment-return system produced discontinuities, which can be noted in some of the graphs at the beginning and end of the runs.

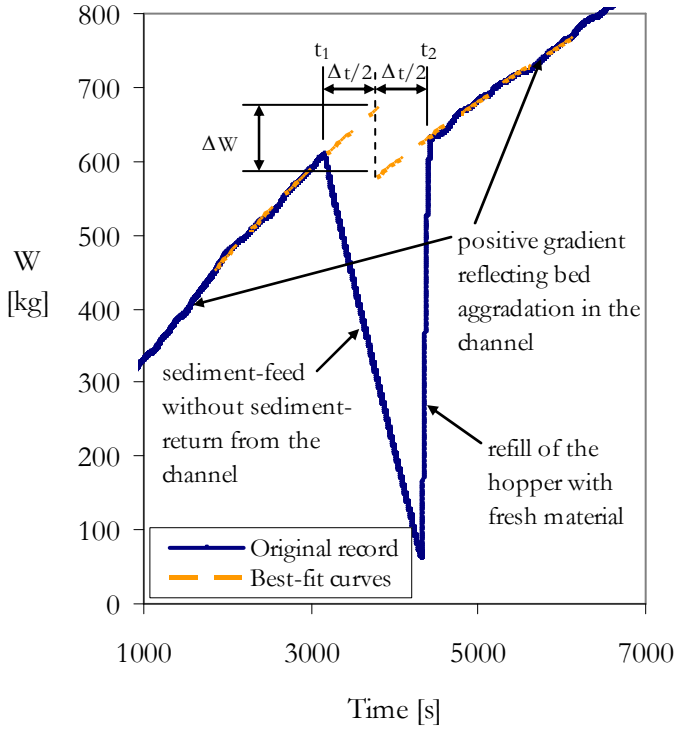

Figure AVII.1

In order to synchronize the records of time variation of weights on the hoppers with measurements of bed and water surface elevations, lag-times reflecting the delay of the sediment passing through the sediment-return system were considered (see section 3.4.1.5 in Appendix I). Lag-time for sand was considered to be 10 minutes, while for gravel it was 3 minutes; according to observations along the experimental campaign, these values were approximately representative of the minimum times required for a grain of sand and a grain of gravel, respectively, to travel all the way through the sediment-return system.

The second uppermost graph for each run gives the rate of change of weight in the hopper(s) with respect to time; if the record of weight were continuous, this would be the derivative with respect to time of the uppermost graph, i.e. dW/dt. It should be expected, that at equilibrium state in the channel, the solid discharge would be equal to the feeding rate, and thus dW/dt=0.

For a discrete record, the average increment of weight with respect to time for a given running time t_i can be approximated with

$$\frac{dW}{dt} \approx \frac{\Delta W}{\Delta t} = \frac{W_{t_i+(\Delta t/2)} - W_{t_i-(\Delta t/2)}}{\Delta t} \qquad \text{(AVII.1)}$$

where $W_{ti+(\Delta t/2)}$ and $W_{ti+(\Delta t/2)}$ are the values of weight for running times $t_i+(\Delta t/2)$ and $t_i-(\Delta t/2)$, respectively, and Δt is a time interval. For selecting the value of Δt, tests were performed which consisted in calculating dW/dt with eq.(AVII.1) using different values of Δt for a W(t) record (run S1 between t=6 h and t=7 h) for which the average variation of weight with time was approximately zero. Figure AVII.2 shows the results in a plot of time vs dW/dt. The variation of the record is lower the highest Δt is. To characterize this variability, the standard deviation was used. Figure AVII.3 shows the variation of the standard deviation with Δt. A value of Δt =400 s was chosen for plotting the graphs

in this Appendix, for this value the standard deviation of the computed dW/dt was lower than 2 g/s.

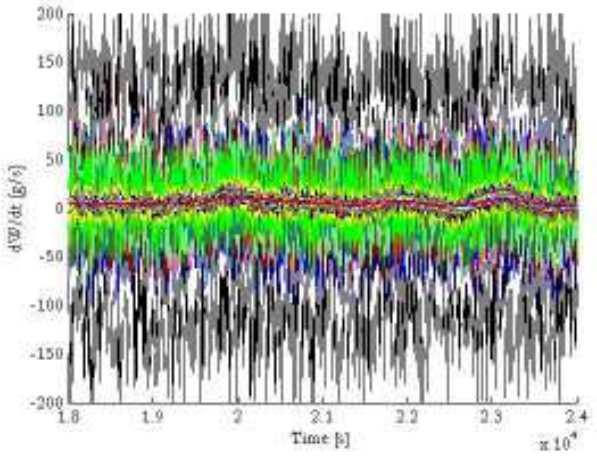

Figure AVII.2

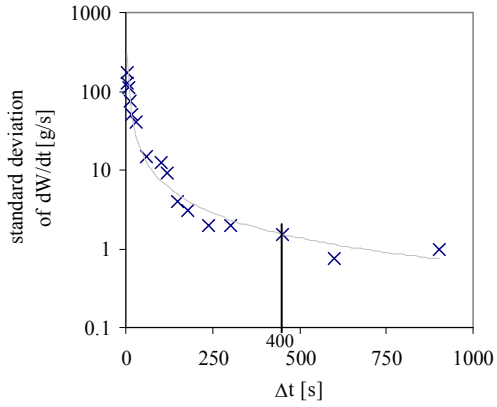

Figure AVII.3

Bed and water surface profiles

The three lowest graphs in the column for each run present the time evolution of variables obtained from the measured bed and water surface profiles. They are described as follows in downwards order:

1. Bed and water elevation at a constant horizontal coordinate. These graphs show the vertical variation of the bed and water surface elevation during the run at the same measurement point, which was selected to be 17.5 m upstream from the channel end. Water surface elevation Z_w is indicated with circles, while bed surface elevation Z_b is indicated with x's.

2. Water depth. For all the bed and water surface profiles, best-fit lines were obtained using intermediate points (from x=3 to 21 m for the gravel runs; from x=5 to 20 m for the mixtures runs, except run M2E5, for which the range x=2 to 16 m was used; from x=5 to 22 m for sand runs). The extremes were eliminated because they were affected by the entrance and exit of the water near the border conditions. In order to associate a water depth to each pair of profiles, the bed and water surfaces were evaluated with the best-fit functions at the intermediate horizontal point of the range taken for fitting the lines. The difference between the obtained water surface and bed surface elevations was the water depth H used in the graphs.

3. Slope of the bed and water profiles. Slopes used in the graphs were those obtained from the best-fit lines described above. Water slope S_w is shown with circles and bed slope S_o with x's.

Some profiles were measured when there was no water in the channel, and therefore only the bed profile was obtained; accordingly, for some instants in the graphs for the surface elevations and for the slopes only the point corresponding to the bed profile is shown.

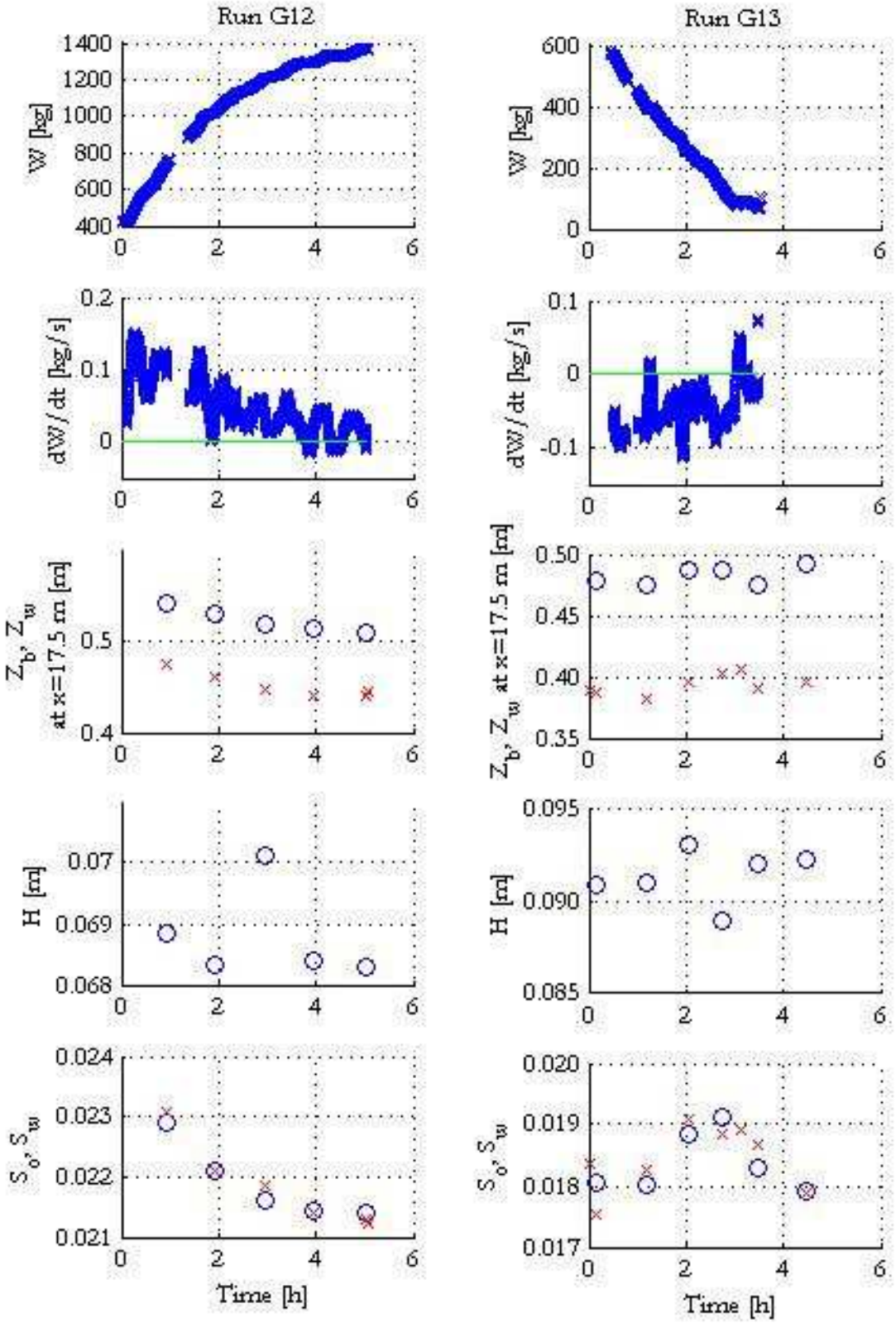
Run G12
Run G13
W [kg]
dW / dt [kg/s]
Z_b, Z_w at x=17.5 m [m]
H [m]
S_o, S_w
Time [h]

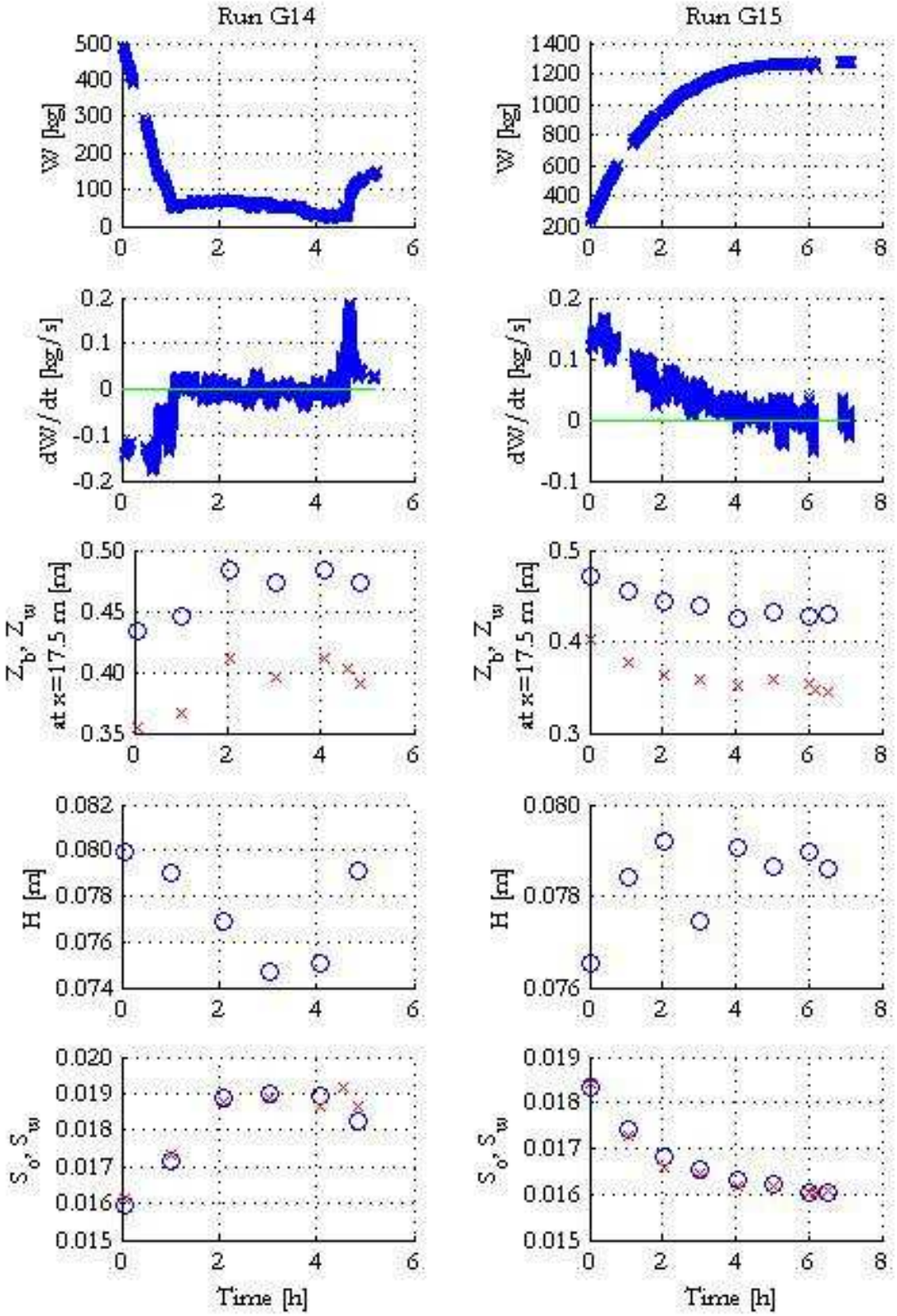
Run G14
Run G15
W [kg]
dW/dt [kg/s]
Z_b, Z_w at x=17.5 m [m]
H [m]
S_o, S_w
Time [h]

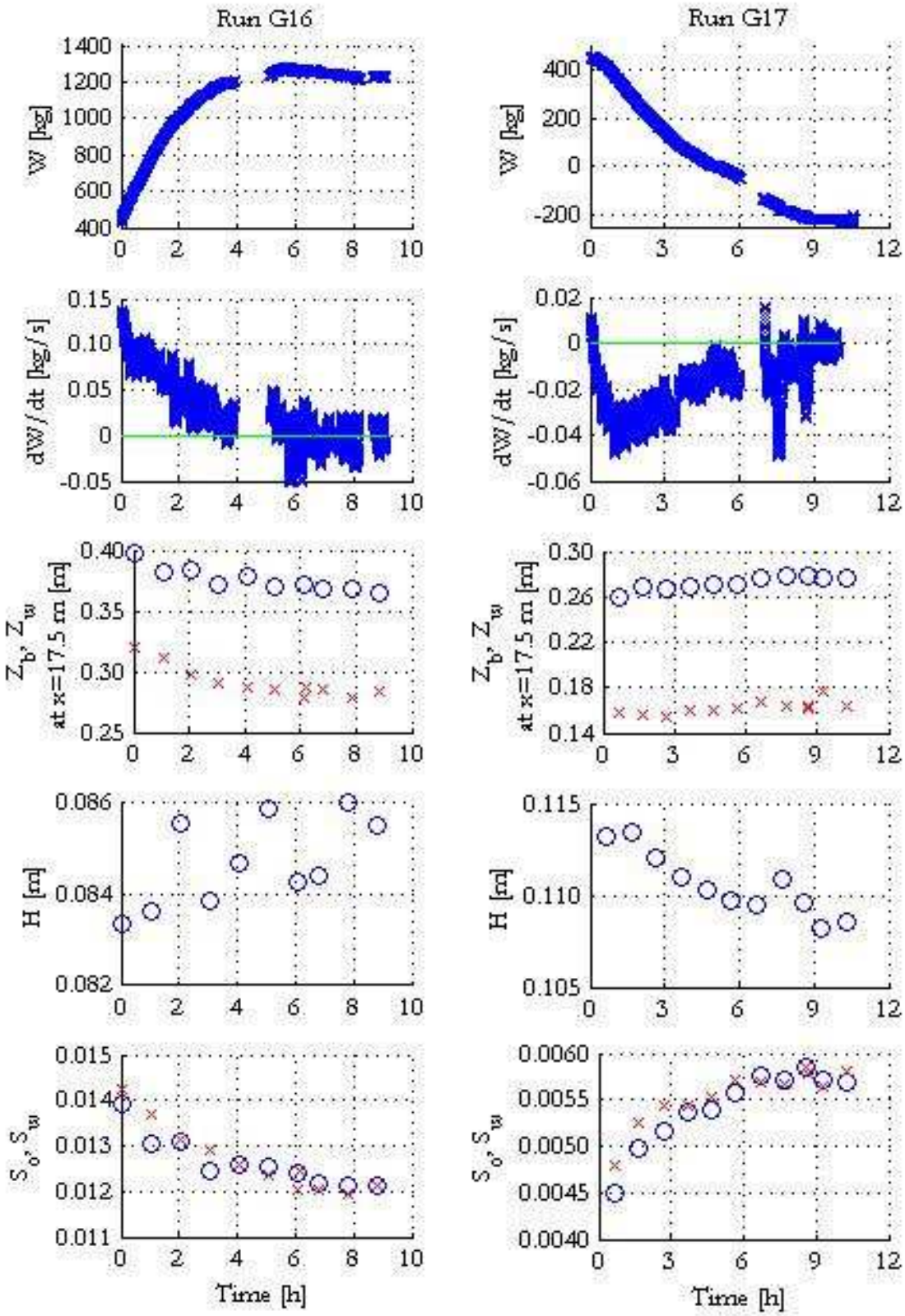
Run G16
Run G17
W [kg]
dW/dt [kg/s]
Z_b, Z_w at x=17.5 m [m]
H [m]
S_o, S_w
Time [h]

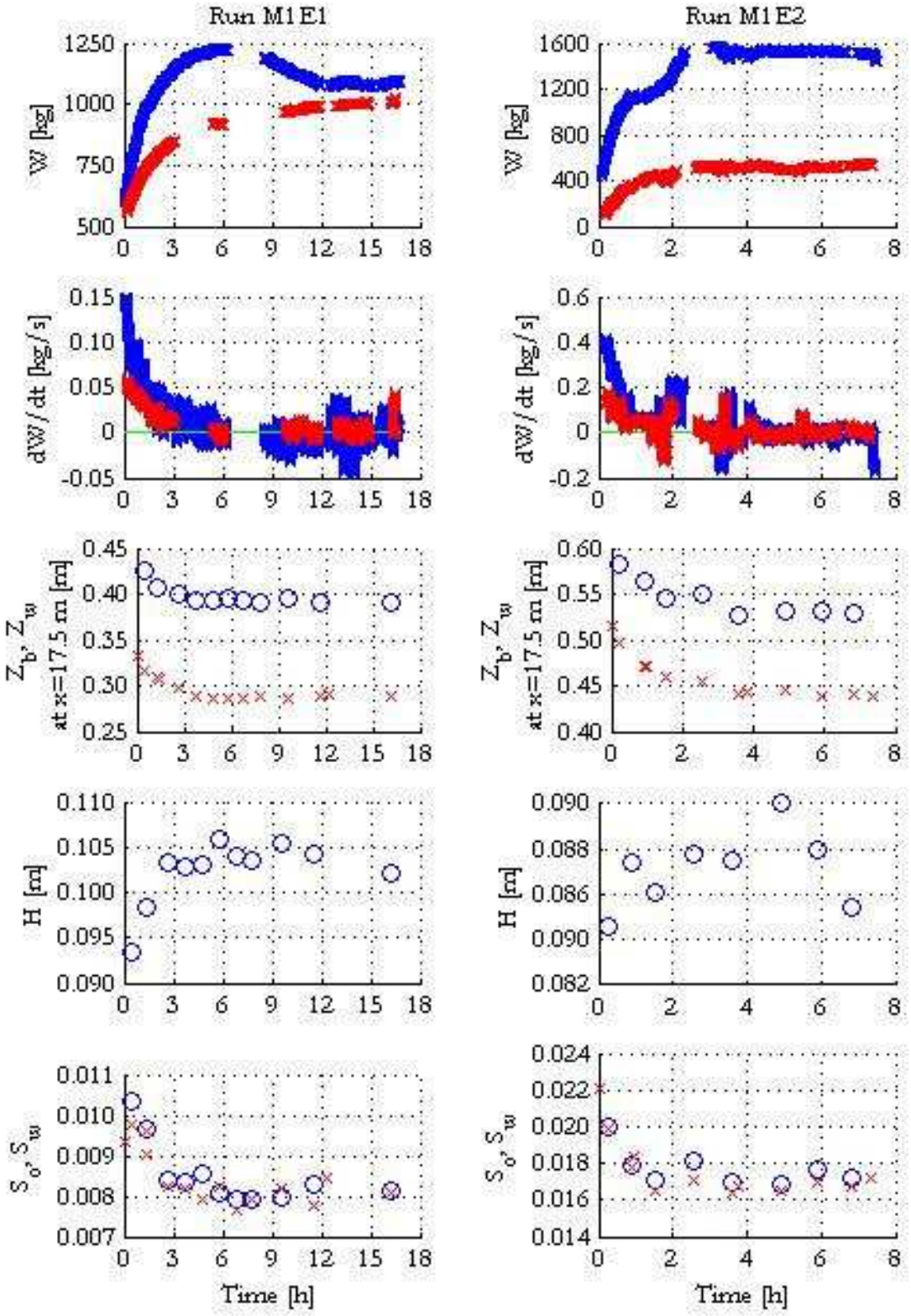
Run M1 E1
Run M1 E2
W [kg]
dW / dt [kg / s]
Z_b, Z_w at x=17.5 m [m]
H [m]
S_o, S_w
Time [h]

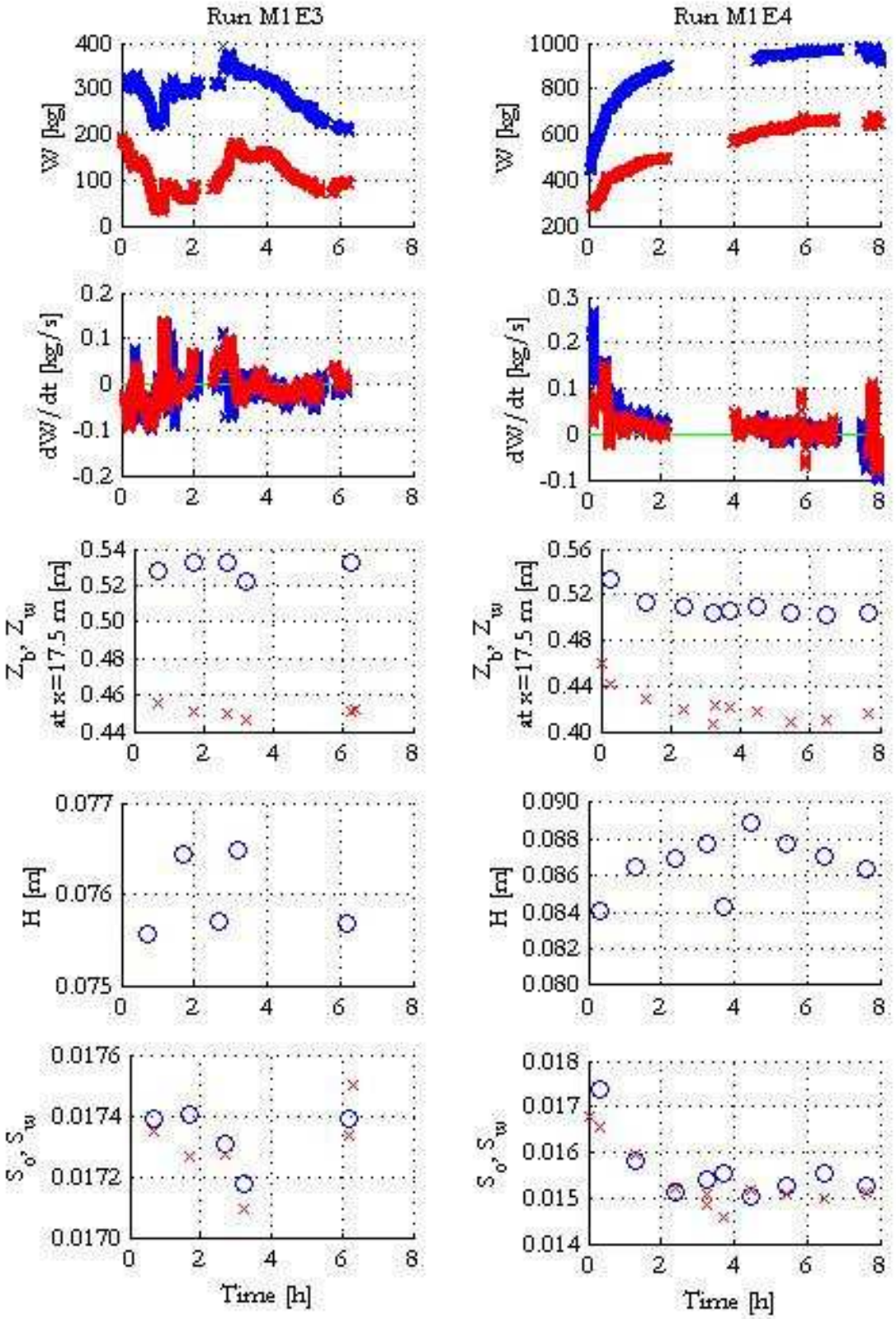
Run M1 E3
Run M1 E4
W [kg]
dW / dt [kg/s]
Z_b, Z_{ss} at x=17.5 m [m]
H [m]
S_o, S_{ss}
Time [h]

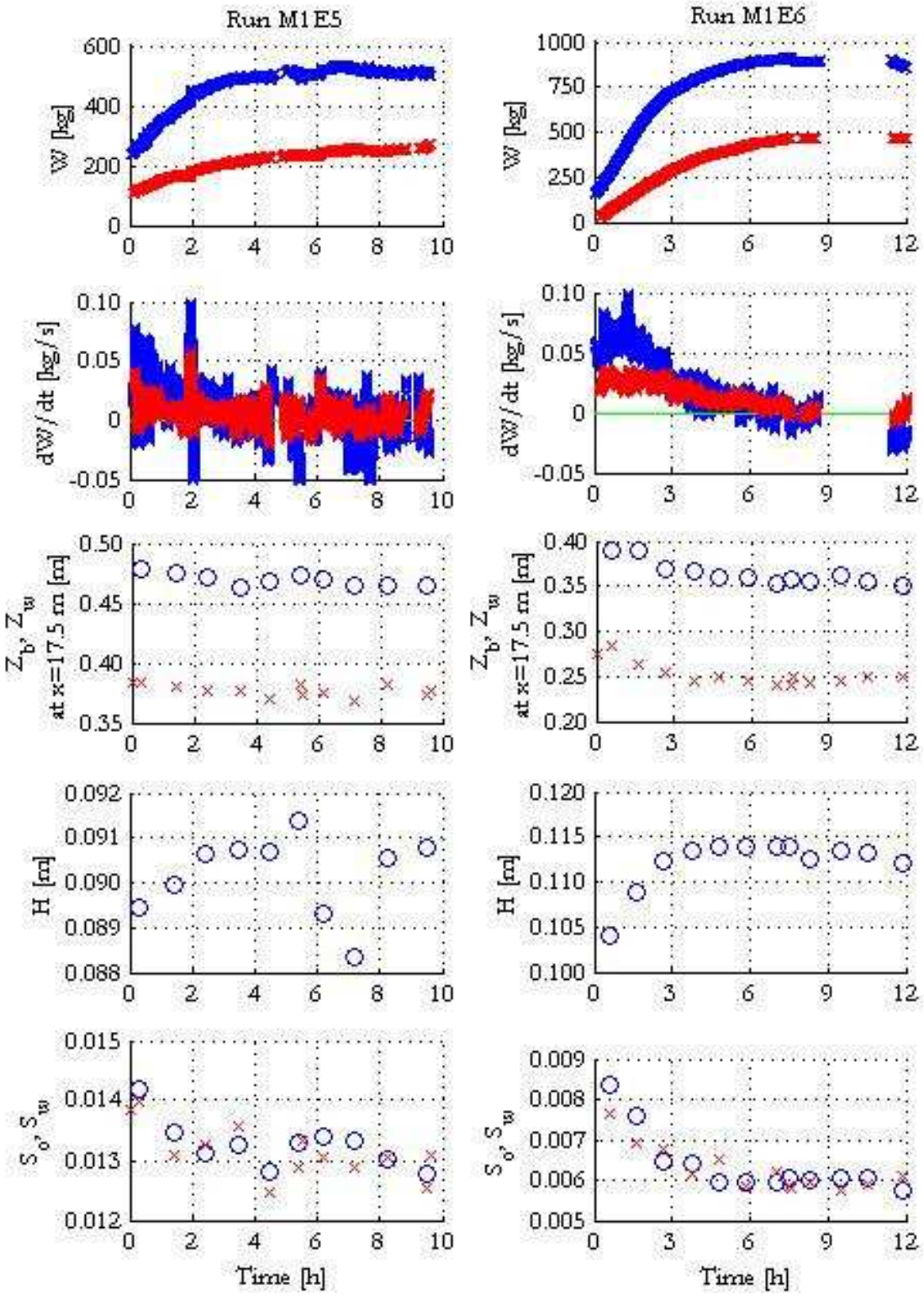
Run M1E5
Run M1E6
W [kg]
dW/dt [kg/s]
Zb, Zw at x=17.5 m [m]
H [m]
So, Sw
Time [h]

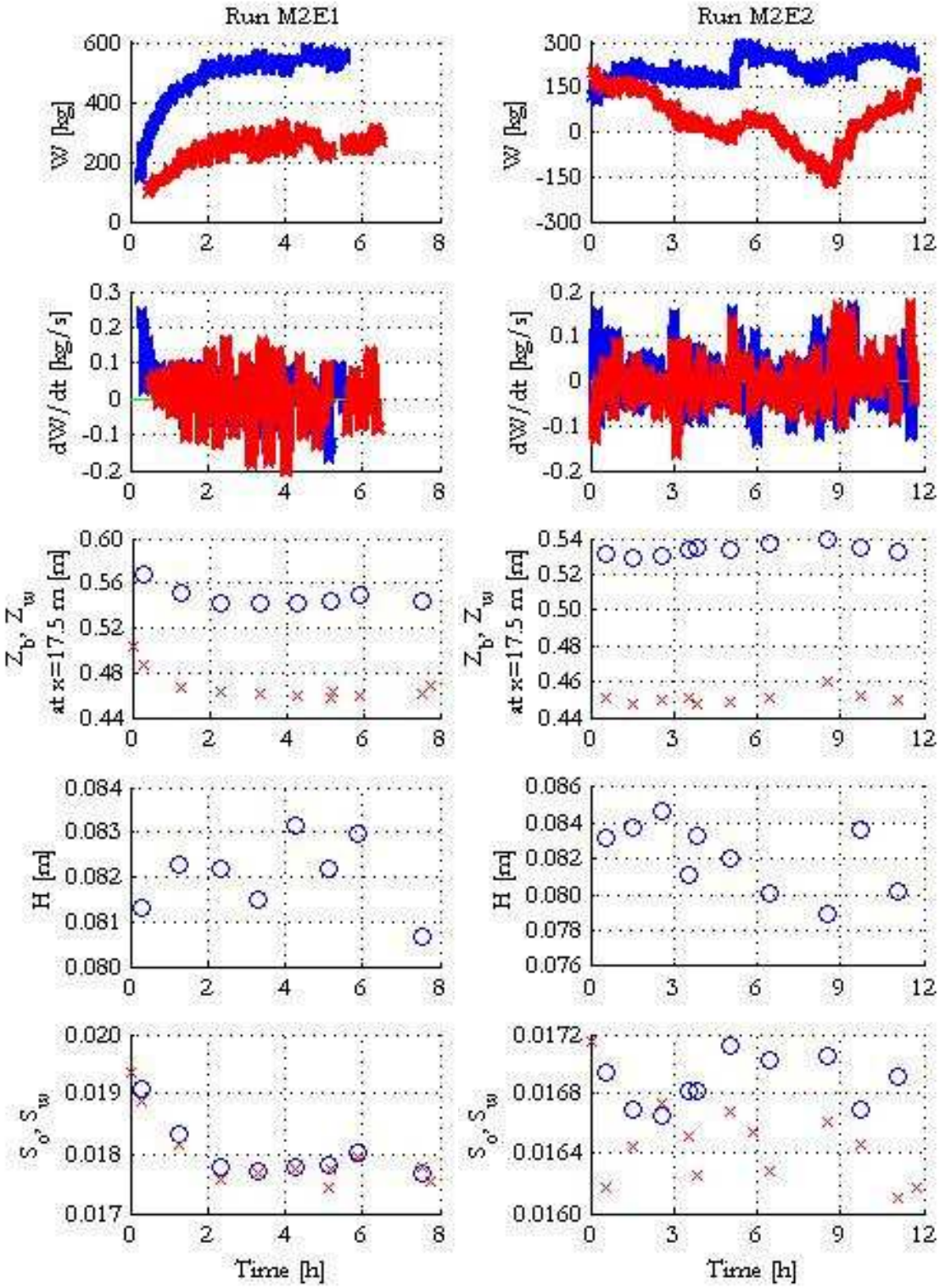
Run M2E1
Run M2E2
W [kg]
dW / dt [kg/s]
Z_b, Z_w at x=17.5 m [m]
H [m]
S_o, S_w
Time [h]

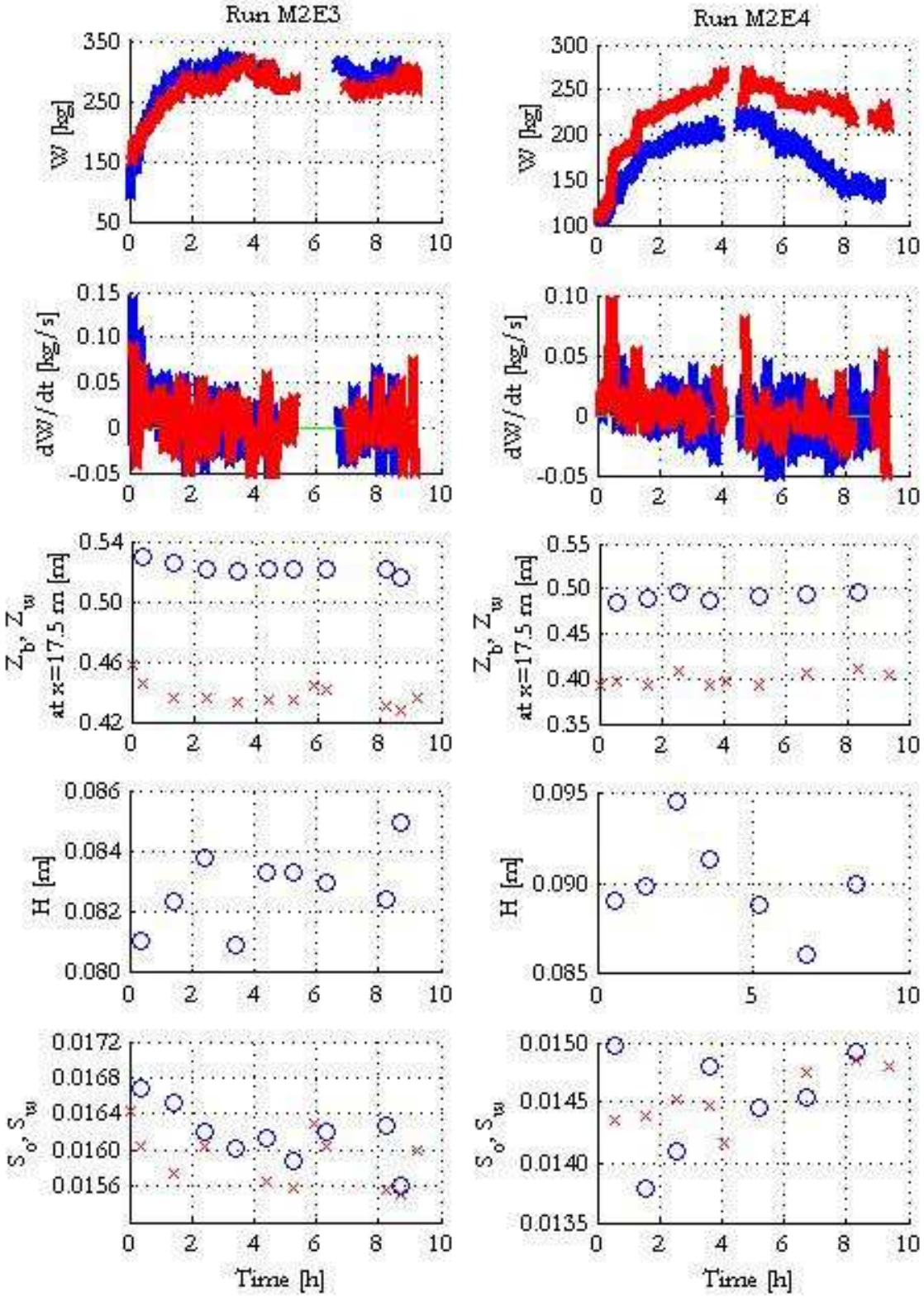
Run M2E3
Run M2E4
W [kg]
dW/dt [kg/s]
Zb, Zw at x=17.5 m [m]
H [m]
So, Sw
Time [h]

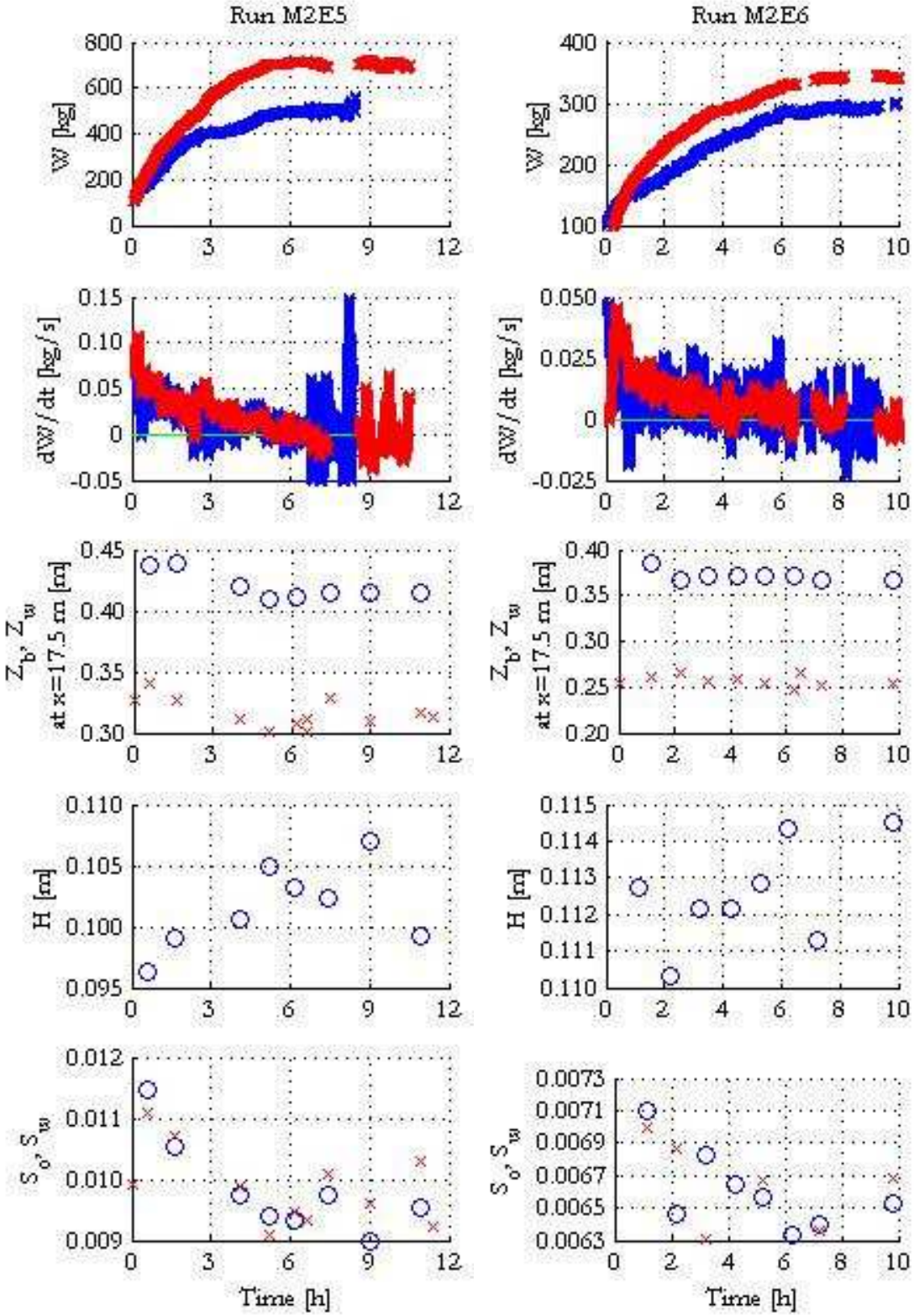
Run M2E5
Run M2E6
W [kg]
dW / dt [kg/s]
Z_b, Z_w at x=17.5 m [m]
H [m]
S_o, S_w
Time [h]

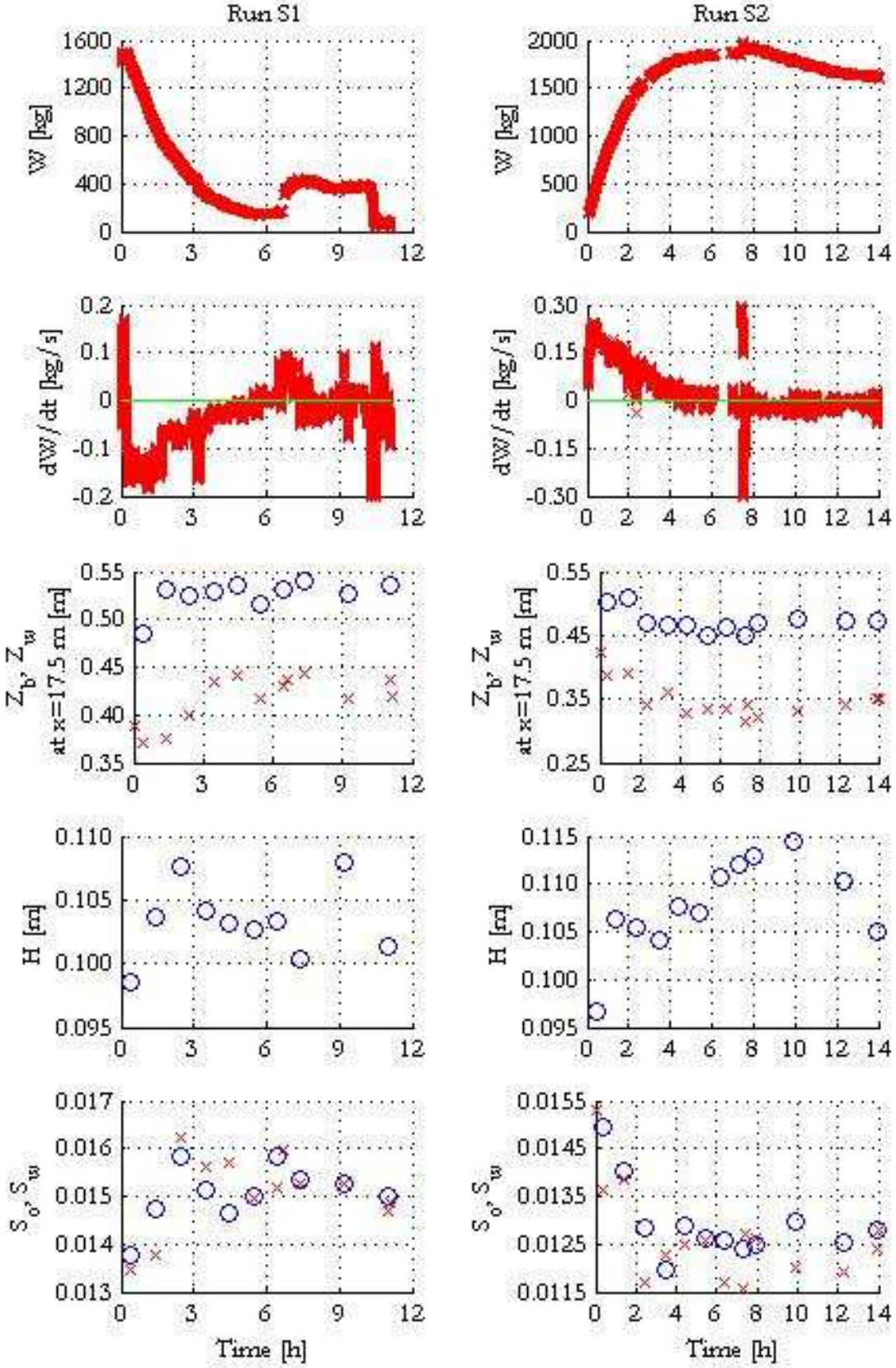
Run S1
Run S2
W [kg]
dW/dt [kg/s]
Z_b, Z_w at x=17.5 m [m]
H [m]
S_o, S_w
Time [h]

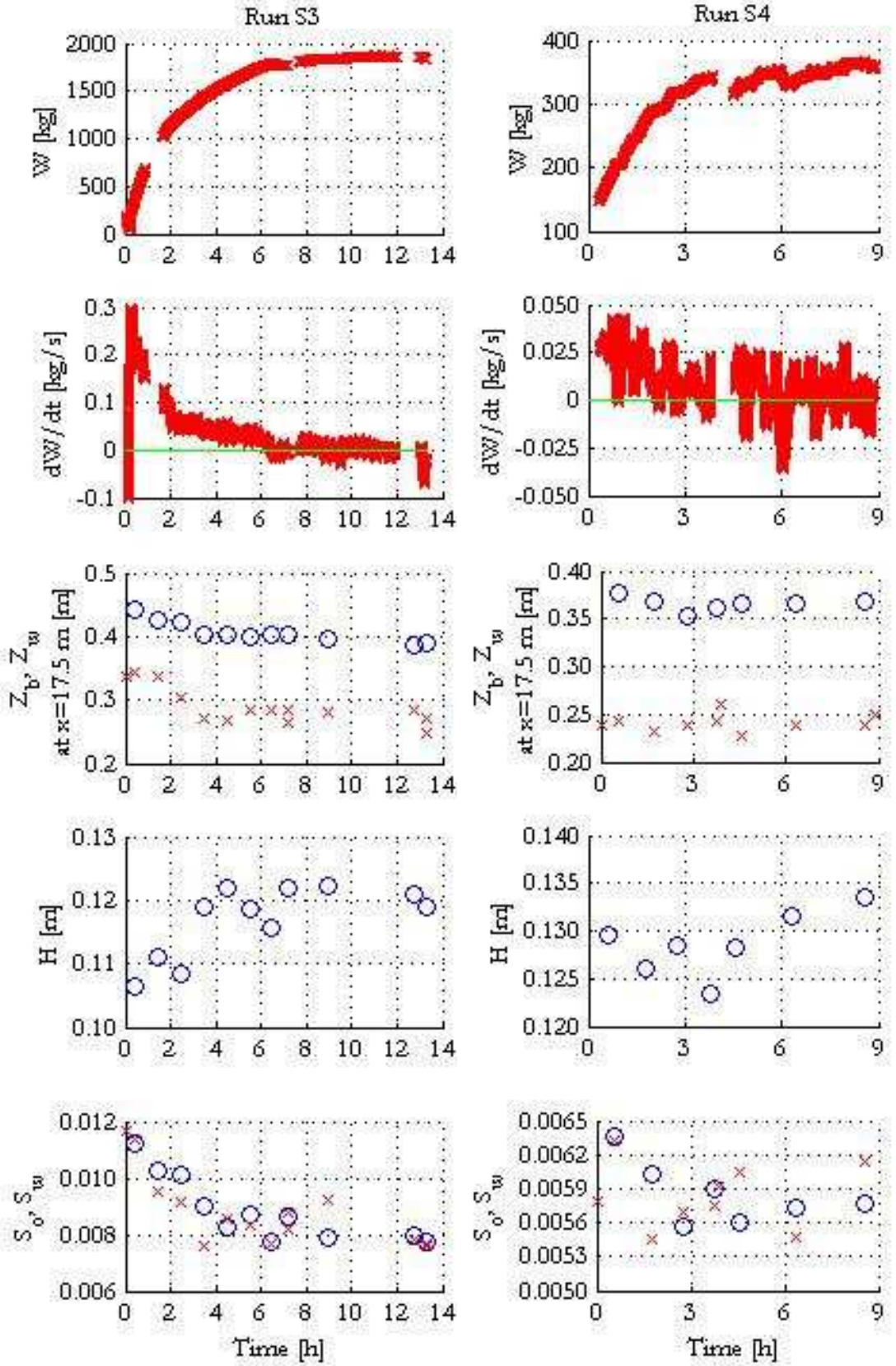
Run S3
Run S4
W [kg]
dW/dt [kg/s]
Z_b, Z_w at x=17.5 m [m]
H [m]
S_o, S_w
Time [h]

APPENDIX VIII

PHOTOGRAPH ALBUM FOR EXPERIMENTAL BED AND WATER SURFACE CONFIGURATIONS

GRAVEL

*Runs ordered from higher to lower sediment concentration.
*No photos available for Run G12 configurations.

RUN G13

H=0.092 m, V=1.22 m/s, S=0.0185, F=1.28, q_s=3.8x10^{-4} m^2/s, D_m=3.8 mm, Q_{SF}/Q_w=8.9 g/l.







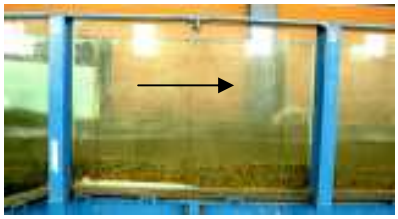

RUN G14

H=0.076 m, V=1.17 m/s, S=0.0188, F=1.36, q_s=2.72x10^{-4} m^2/s, D_m=4.2 mm, Q_{SF}/Q_w=7.9 g/l.




RUN G15

H=0.079 m, V=1.15 m/s, S=0.0162, F=1.31, q_s=2.23x10^{-4} m^2/s, D_m=3.9 mm, Q_{SF}/Q_w=6.4 g/l.

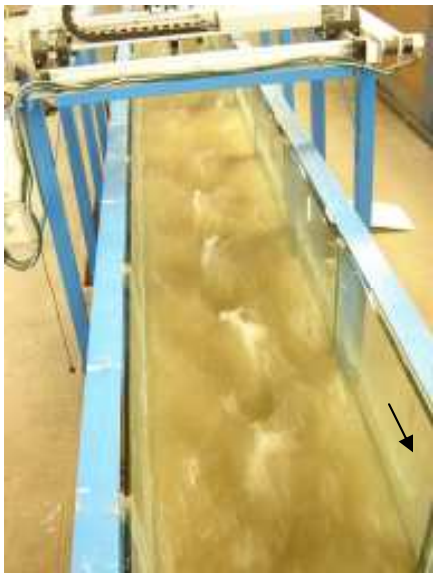

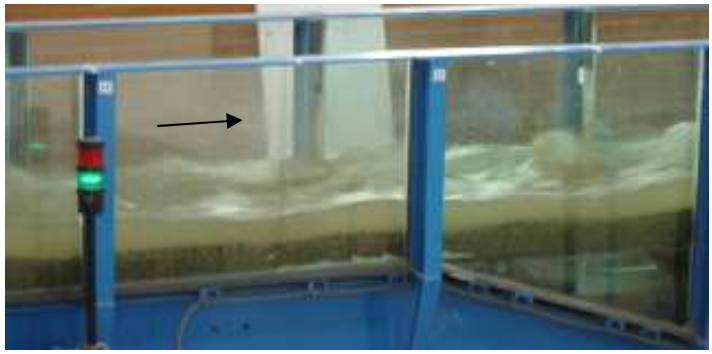

RUN G16

H=0.085 m, V=1.06 m/s, S=0.0122, F=1.16, q_s=1.36 x10^{-4} m^2/s, D_m=3.8 mm, Q_{SF}/Q_w=3.9 g/l.

RUN G17

H=0.109 m, V=0.96 m/s, S=0.0058, F=0.93, q_s=4.16 x10^{-5} m^2/s, D_m=4.1 mm, Q_{SF}/Q_w=1 g/l.

MIXTURE 1

*Runs ordered from higher to lower sediment concentration.

RUN M1E2

H=0.086 m, V=1.30 m/s, S=0.0168, F=1.42, q_s=4.41 x10^{-4} m^2/s, D_m=3.0 mm, Q_{SF}/Q_w=10.3 g/l.

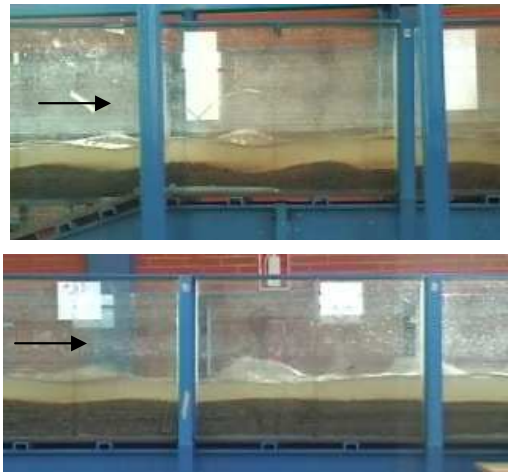

RUN M1E3

H=0.076 m, V=1.18 m/s, S=0.0173, F=1.37, q_s=3.43 x10^{-4} m^2/s, D_m=3.0 mm, Q_{SF}/Q_w=10.0 g/l.

RUN M1E4

H=0.087 m, V=1.20 m/s, S=0.0153, F=1.3, q_s=3.15 x10^{-4} m^2/s, D_m=3.0 mm, Q_{SF}/Q_w=7.9 g/l.

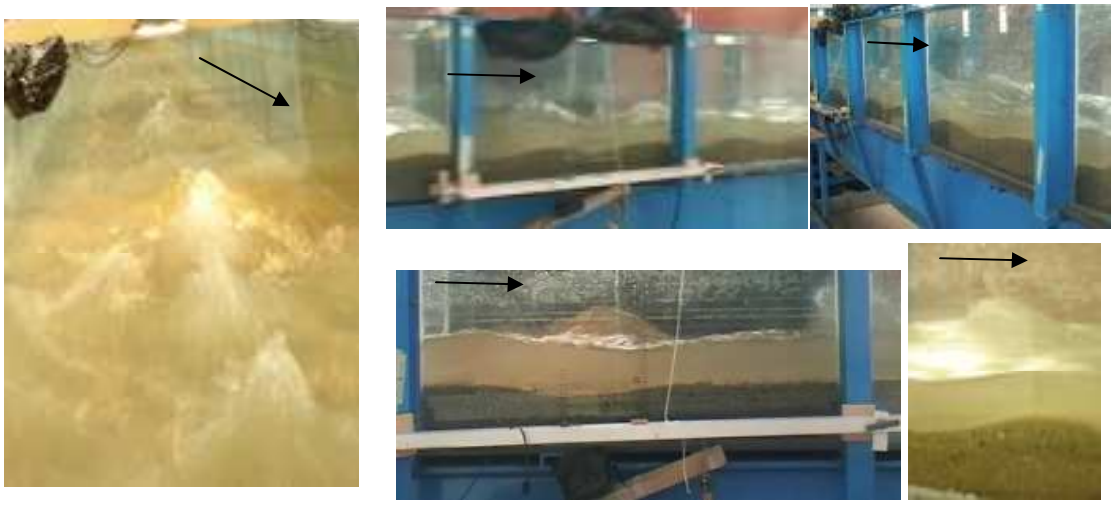

RUN M1E5

H=0.090 m, V=1.16 m/s, S=0.0130, F=1.23, q_s=2.23 x10^{-4} m^2/s, D_m=3.0 mm, Q_{SF}/Q_w=5.6 g/l.

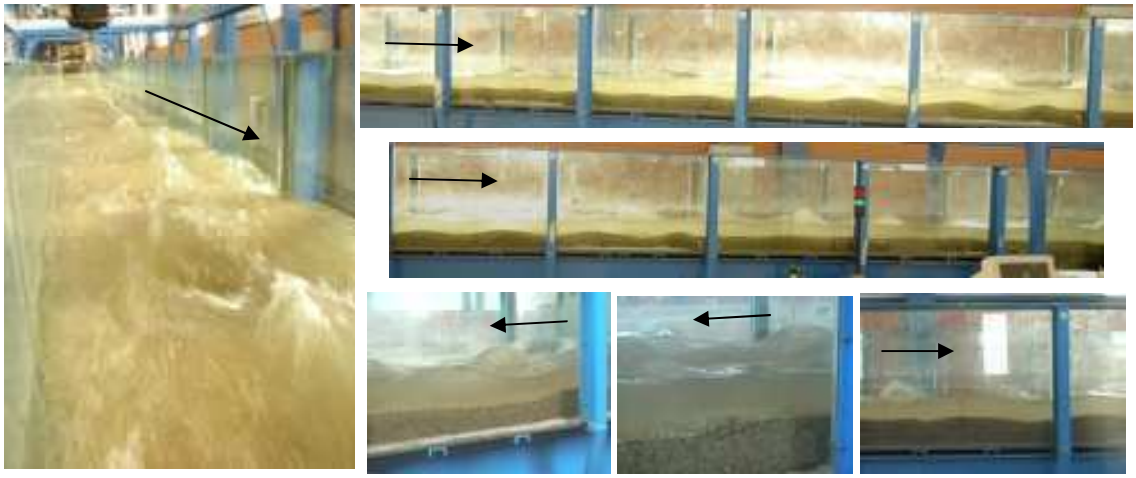

RUN M1E1

H=0.104 m, V=1.02 m/s, S=0.0081, F=1.01, q_s=1.13 x10^{-4} m^2/s, D_m=2.9 mm, Q_{SF}/Q_w=2.8 g/l.

RUN M1E6

H=0.113 m, V=0.92 m/s, S=0.0059, F=0.87, q_s=7.00 x10^{-5} m^2/s, D_m=2.8 mm, Q_{SF}/Q_w=1.7 g/l.

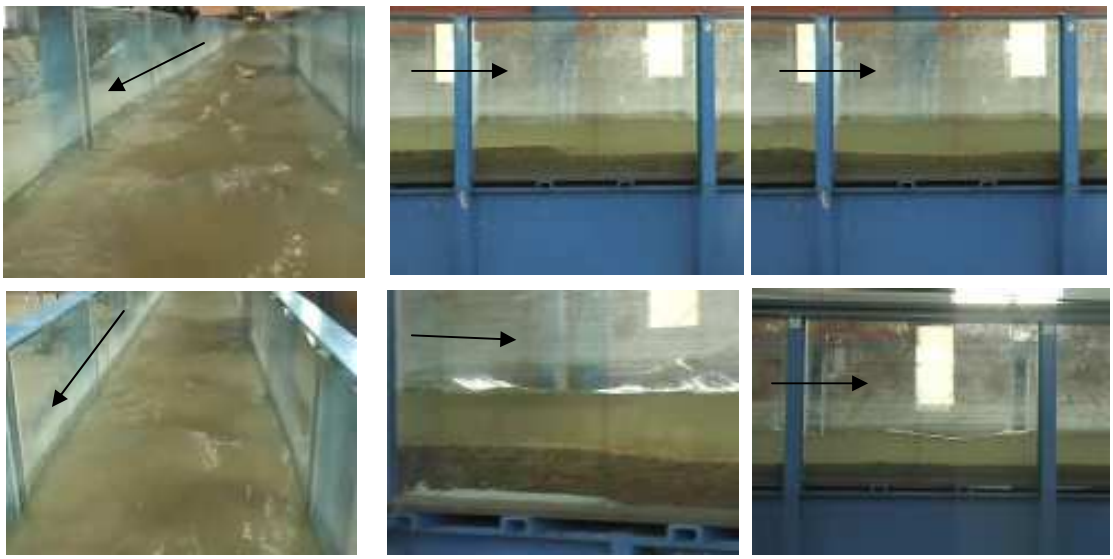

MIXTURE 2

*Runs ordered from higher to lower sediment concentration.

RUN M2E1

H=0.081 m, V=1.28 m/s, S=0.0177, F=1.44, q_s=5.47 x10^{-4} m^2/s, D_m=2.4 mm, Q_{SF}/Q_w=13.7 g/l.

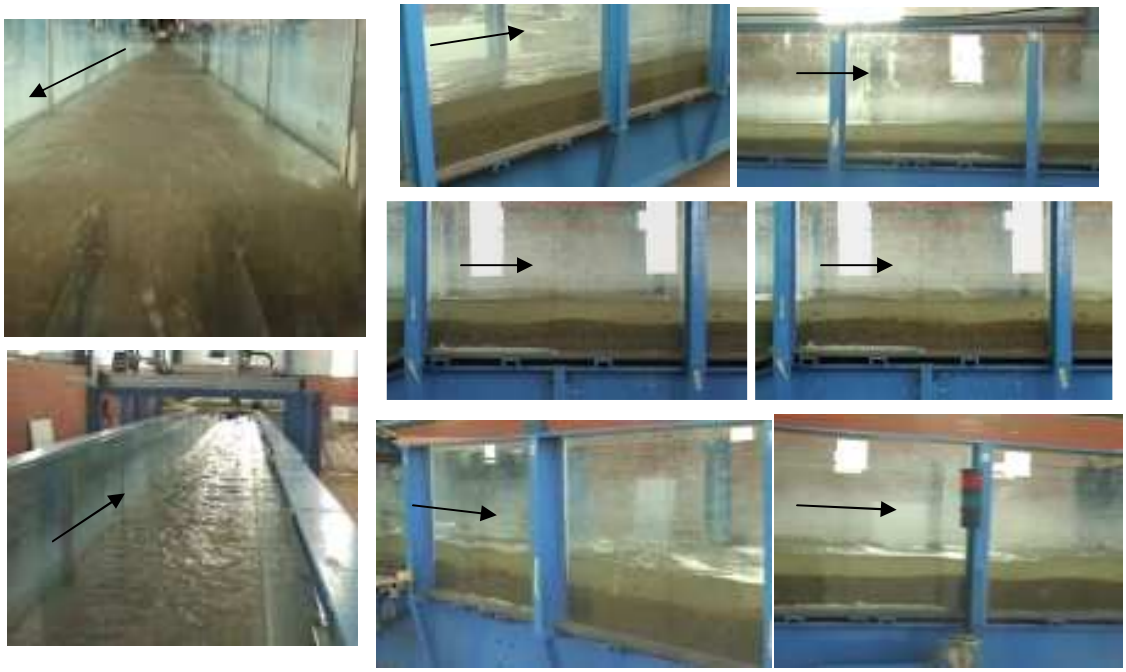

RUN M2E2

H=0.080 m, V=1.31 m/s, S=0.0167, F=1.48, q_s=4.57 x10^{-4} m^2/s, D_m=2.5 mm, Q_{SF}/Q_w=11.3 g/l.

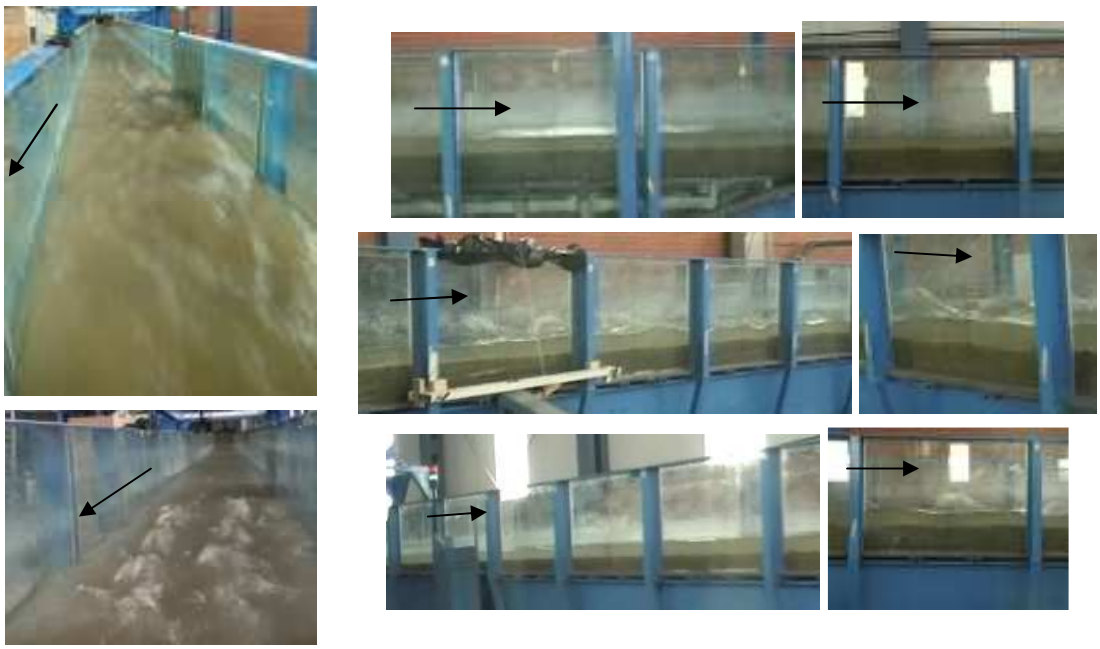

RUN M2E3

H=0.083 m, V=1.25 m/s, S=0.0160, F=1.39, q_s=4.05 x10^{-4} m^2/s, D_m=2.4 mm, Q_{SF}/Q_w=10.1 g/l.





RUN M2E4

H=0.089 m, V=1.17 m/s, S=0.0146, F=1.25, q_s=2.83 x10^{-4} m^2/s, D_m=2.4 mm, Q_{SF}/Q_w=7.1 g/l.






RUN M2E5

H=0.103 m, V=1.03 m/s, S=0.0098, F=1.02, q_s=1.49 x10^{-4} m^2/s, D_m=2.4 mm, Q_{SF}/Q_w=3.7 g/l.

RUN M2E6

H=0.113 m, V=0.94 m/s, S=0.0064, F=0.89, q_s=8.12 x10^{-5} m^2/s, D_m=2.4 mm, Q_{SF}/Q_w=2.0 g/l.

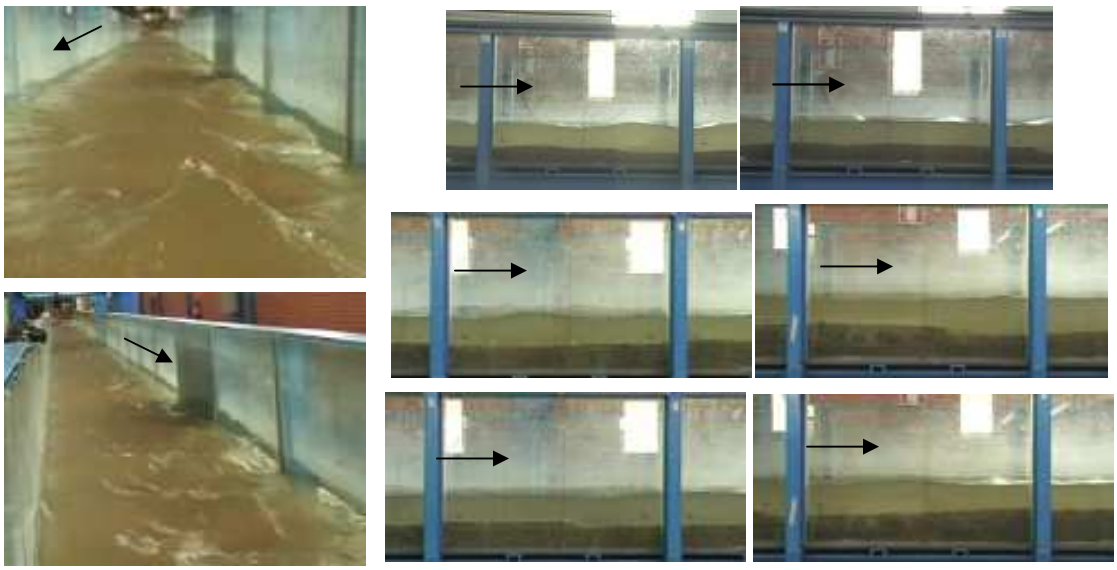

SAND

*Runs ordered from higher to lower sediment concentration.

RUN S1

H=0.103 m, V=1.03 m/s, S=0.0155, F=1.02, q_s=3.34 x10^{-4} m^2/s, D_m=1.5 mm, Q_{SF}/Q_w=8.3 g/l.

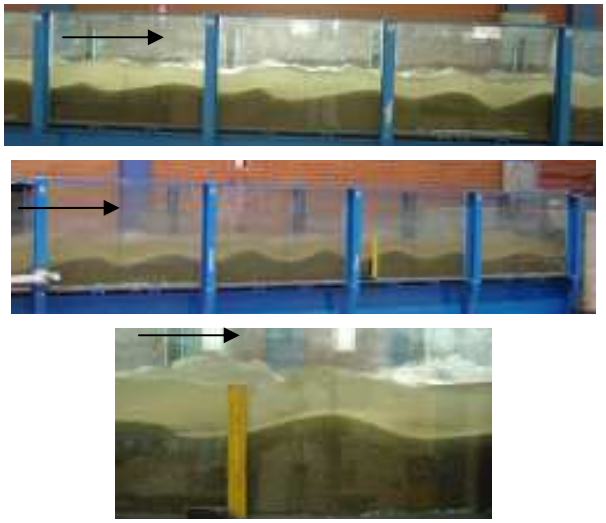

RUN S2

H=0.109 m, V=0.97 m/s, S=0.0123, F=0.94, q_s=2.34 x10^{-4} m^2/s, D_m=1.4 mm, Q_{SF}/Q_w=5.8 g/l.

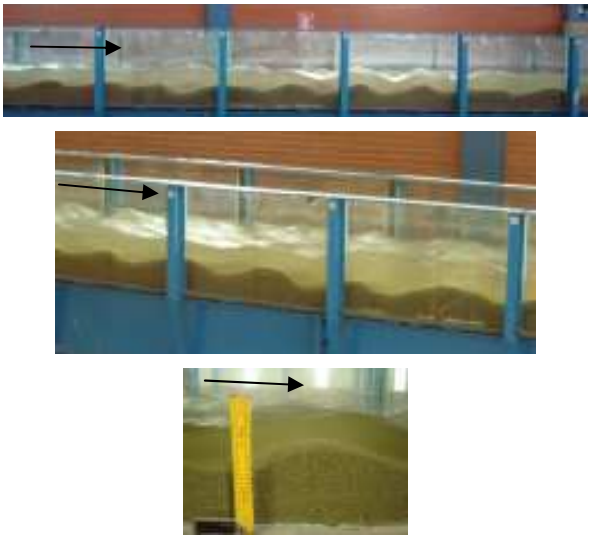

RUN S3

H=0.119 m, V=0.89 m/s, S=0.0082, F=0.82, q_s=1.25 x10^{-4} m^2/s, D_m=1.4 mm, Q_{SF}/Q_w=3.1 g/l.

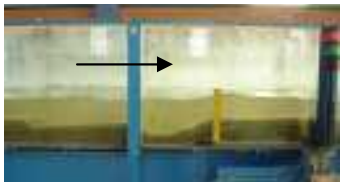

RUN S4

H=0.130 m, V=0.82 m/s, S=0.0060, F=0.73, q_s=7.27 x10^{-5} m^2/s, D_m=1.4 mm, Q_{SF}/Q_w=1.8 g/l.

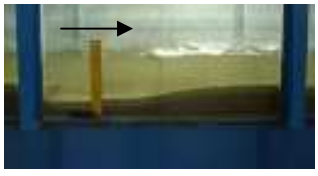

APPENDIX IX

PHOTOGRAPH ALBUM FOR BED-SURFACE CONFIGURATIONS AT THE END OF THE EXPERIMENTS

GRAVEL

*Runs ordered from higher to lower sediment concentration.

RUN G12

H=0.068 m, V=1.16 m/s, S=0.0215, F=1.42, q_s=3.0x10^{-4} m^2/s, D_m=4.7 mm, Q_{SF}/Q_w=10.1 g/l.

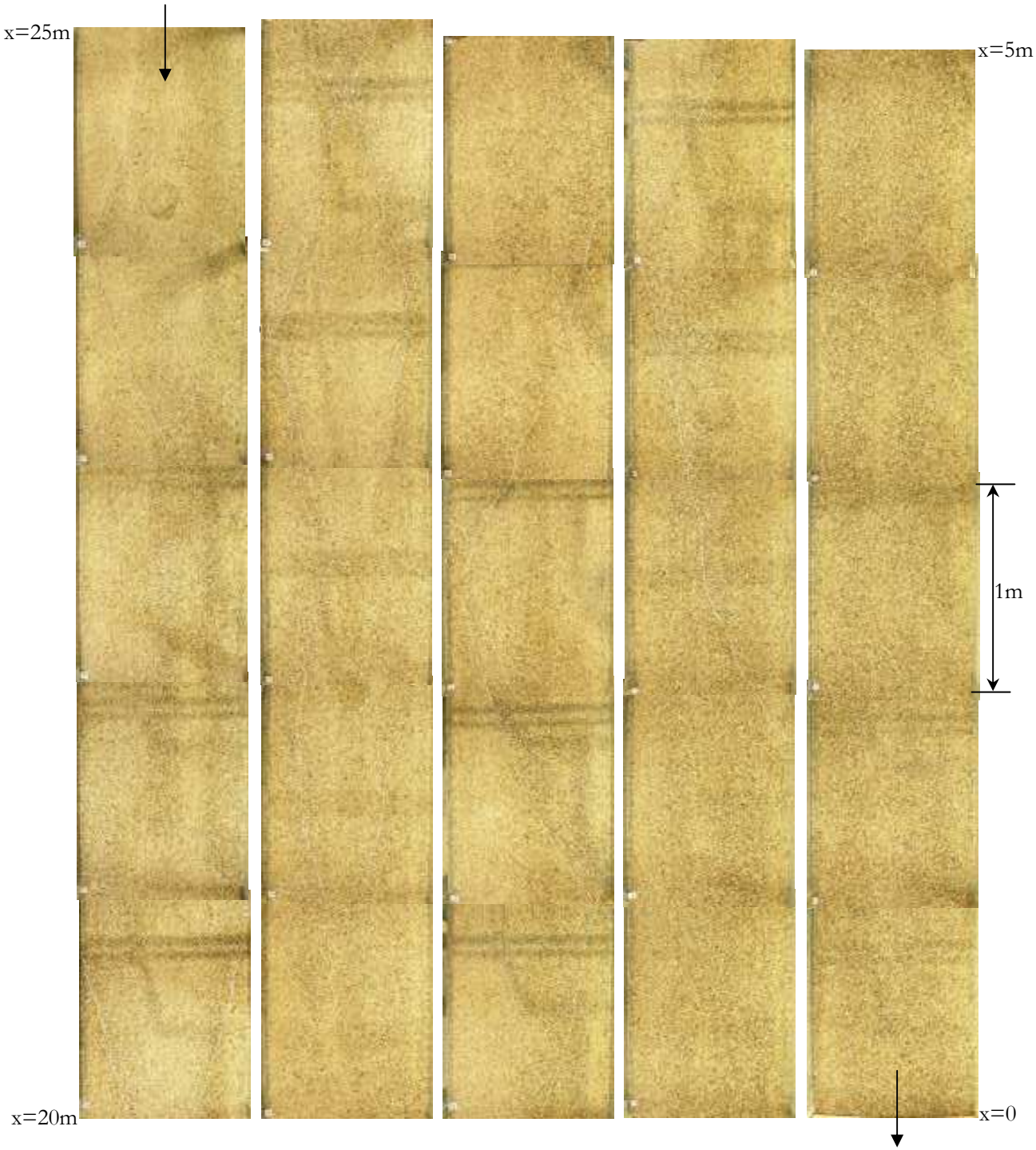

RUN G13

H=0.092 m, V=1.22 m/s, S=0.0185, F=1.28, q_s=3.8x10^{-4} m^2/s, D_m=3.8 mm, Q_{SF}/Q_w=8.9 g/l.

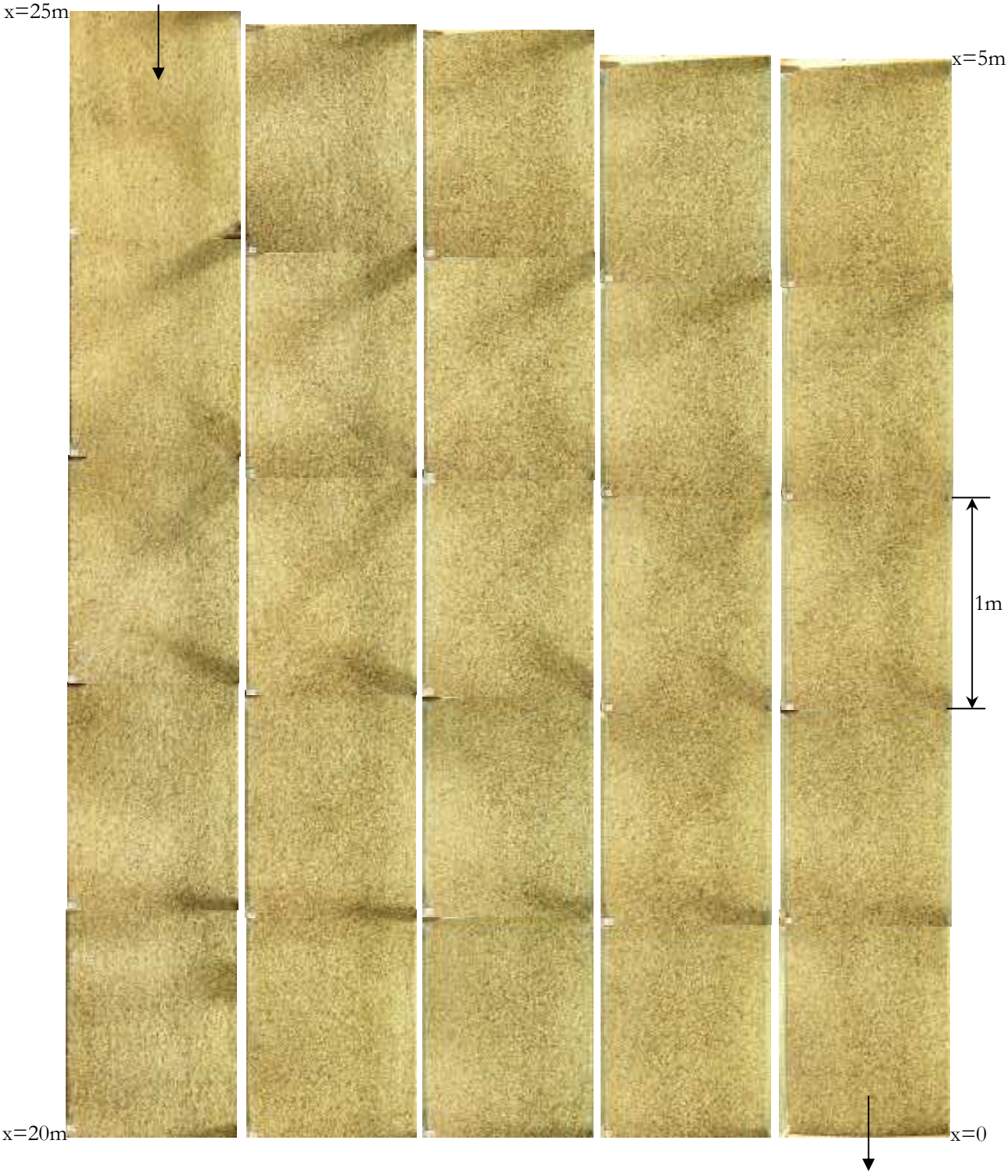

RUN G14

H=0.076 m, V=1.17 m/s, S=0.0188, F=1.36, q_s=2.72x10^{-4} m^2/s, D_m=4.2 mm, Q_{SF}/Q_w=7.9 g/l.

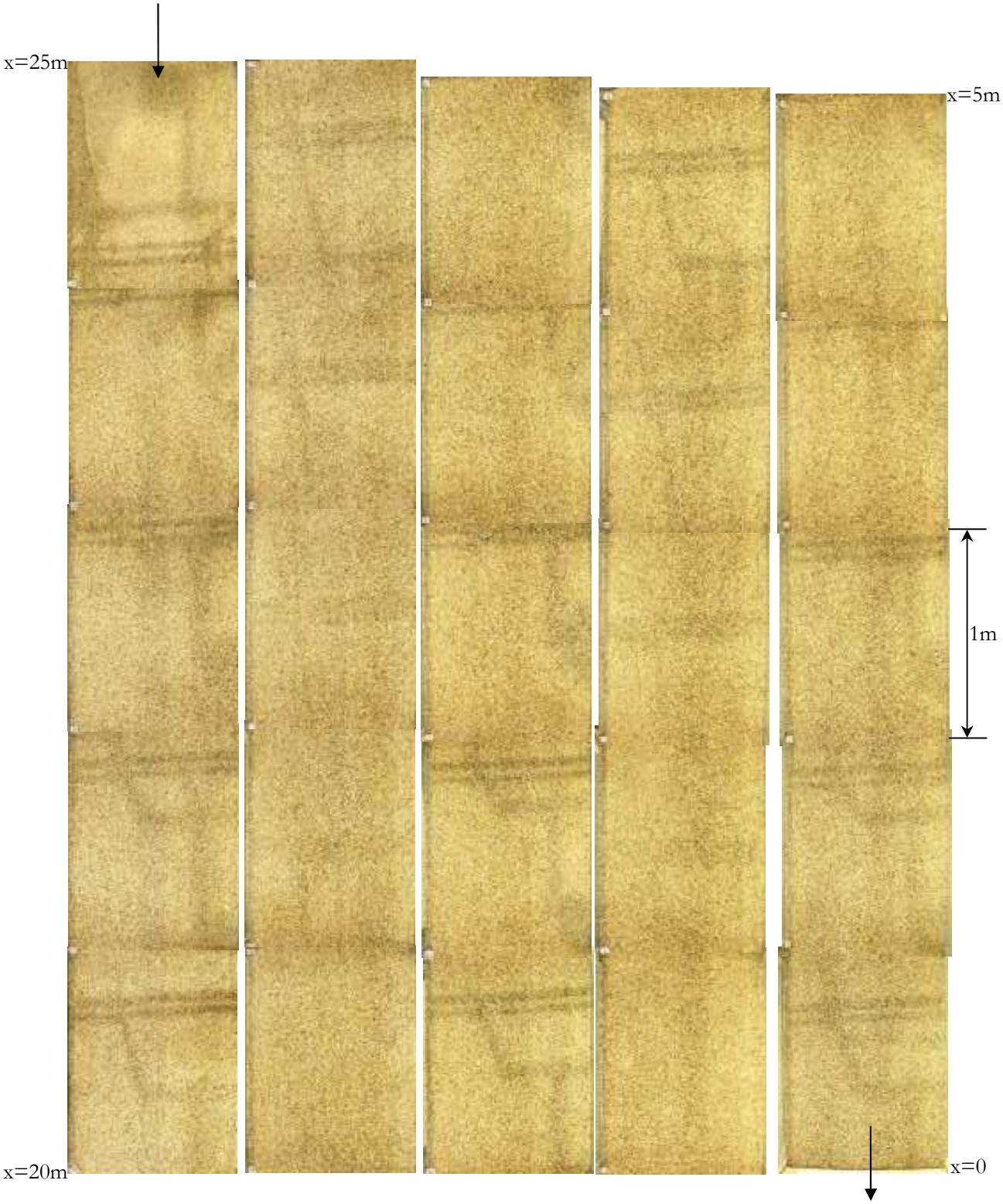

RUN G15

H=0.079 m, V=1.15 m/s, S=0.0162, F=1.31, q_s=2.23x10^{-4} m^2/s, D_m=3.9 mm, Q_{SF}/Q_w=6.4 g/l.

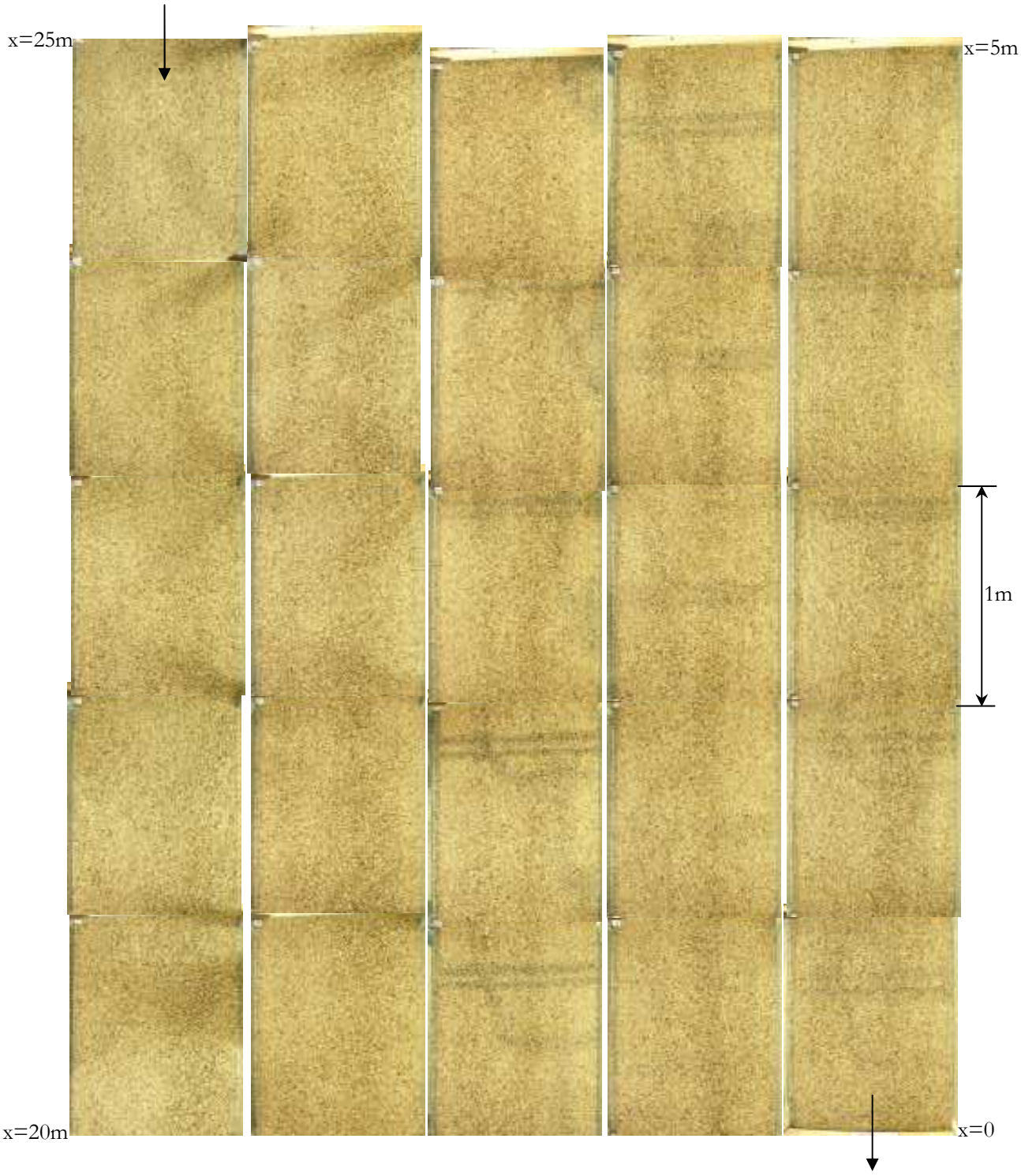

RUN G16

H=0.085 m, V=1.06 m/s, S=0.0122, F=1.16, q_s=1.36 x10^{-4} m^2/s, D_m=3.8 mm, Q_{SF}/Q_w=3.9 g/l.

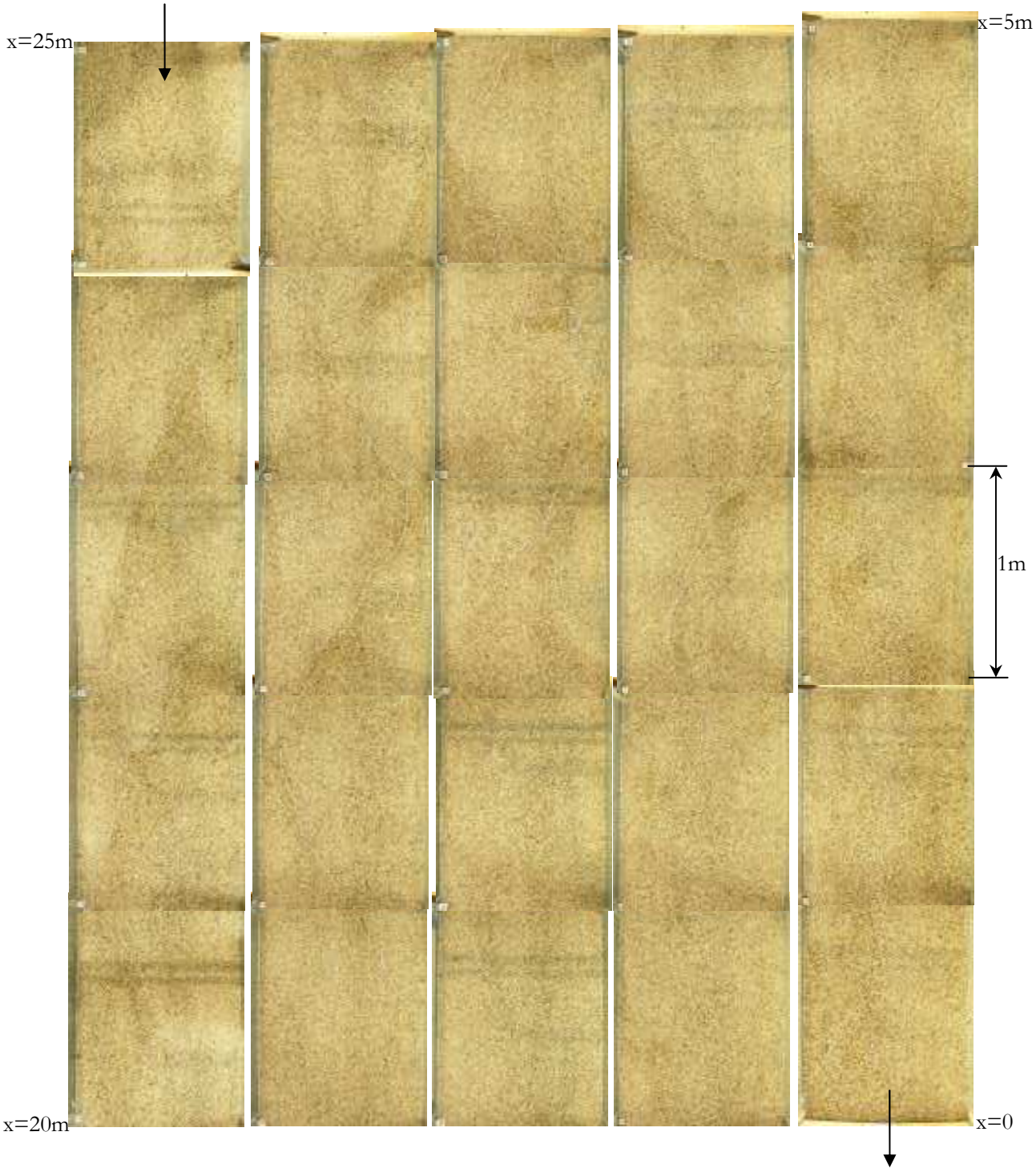

RUN G17

H=0.109 m, V=0.96 m/s, S=0.0058, F=0.93, q_s=4.16 x10^{-5} m^2/s, D_m=4.1 mm, Q_{SF}/Q_w=1.0 g/l.

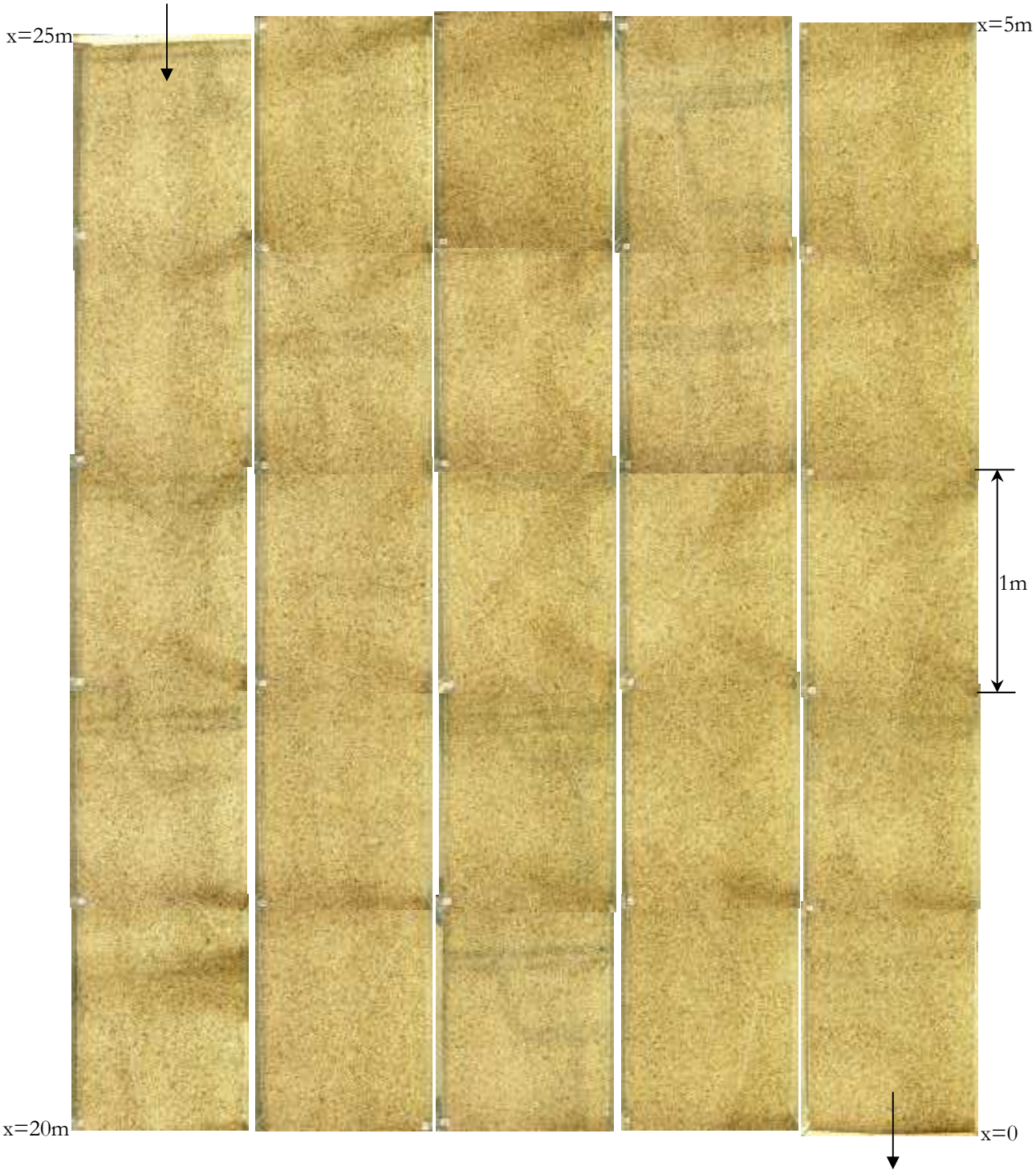

MIXTURE 1

*Runs ordered from higher to lower sediment concentration.

RUN M1E2

H=0.086 m, V=1.30 m/s, S=0.0168, F=1.42, q_s=4.41 x10^{-4} m^2/s, D_m=3.0 mm, Q_{SF}/Q_w=10.3 g/l.

RUN M1E3

H=0.076 m, V=1.18 m/s, S=0.0173, F=1.37, q_s=3.43 x10^{-4} m^2/s, D_m=3.0 mm, Q_{SF}/Q_w=10.0 g/l.

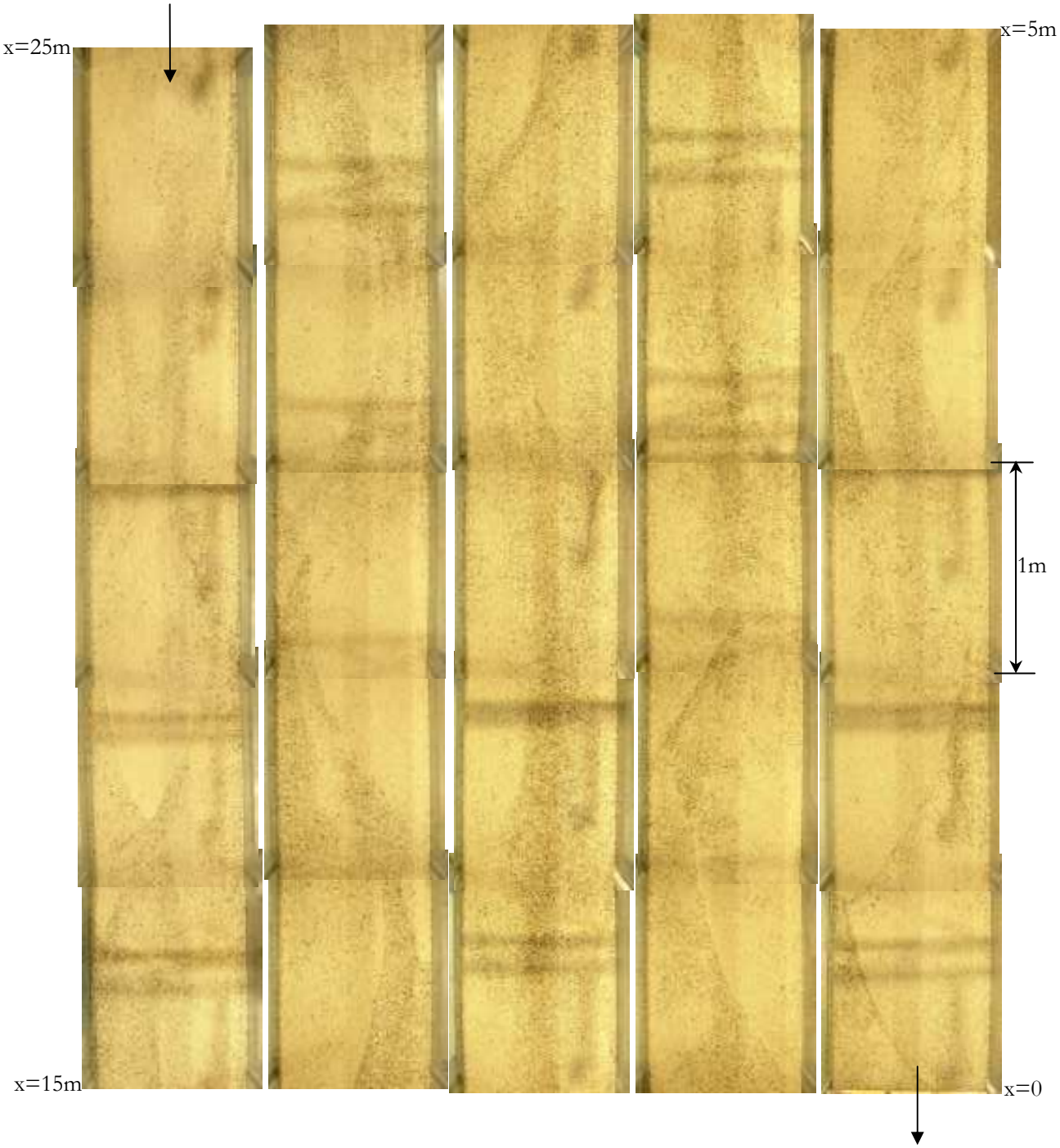

RUN M1E4

H=0.087 m, V=1.20 m/s, S=0.0153, F=1.3, q_s=3.15 x10^{-4} m^2/s, D_m=3.0 mm, Q_{SF}/Q_w=7.9 g/l.

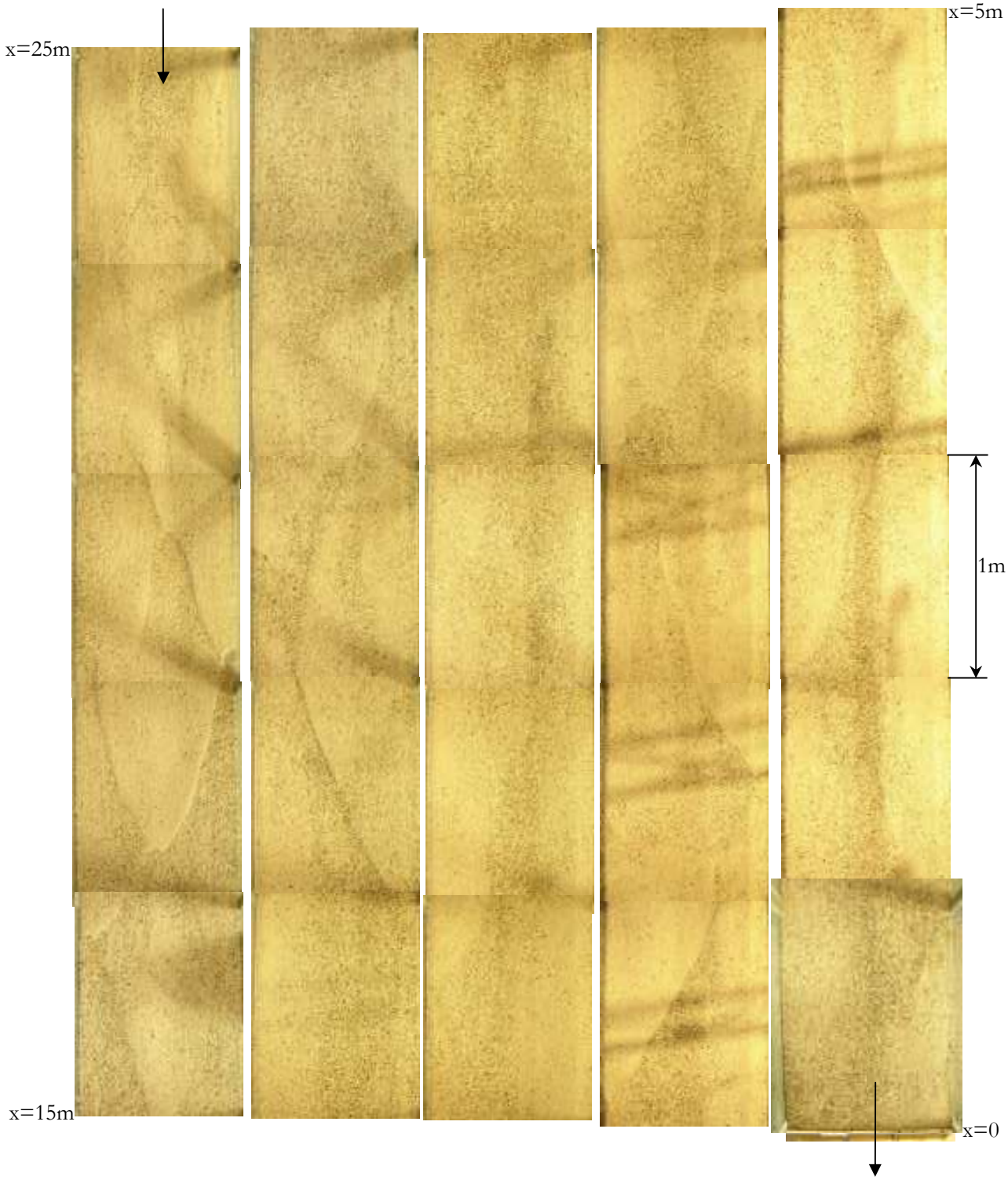

RUN M1E5

H=0.090 m, V=1.16 m/s, S=0.0130, F=1.23, q_s=2.23 x10^{-4} m^2/s, D_m=3.0 mm, Q_{SF}/Q_w=5.6 g/l.

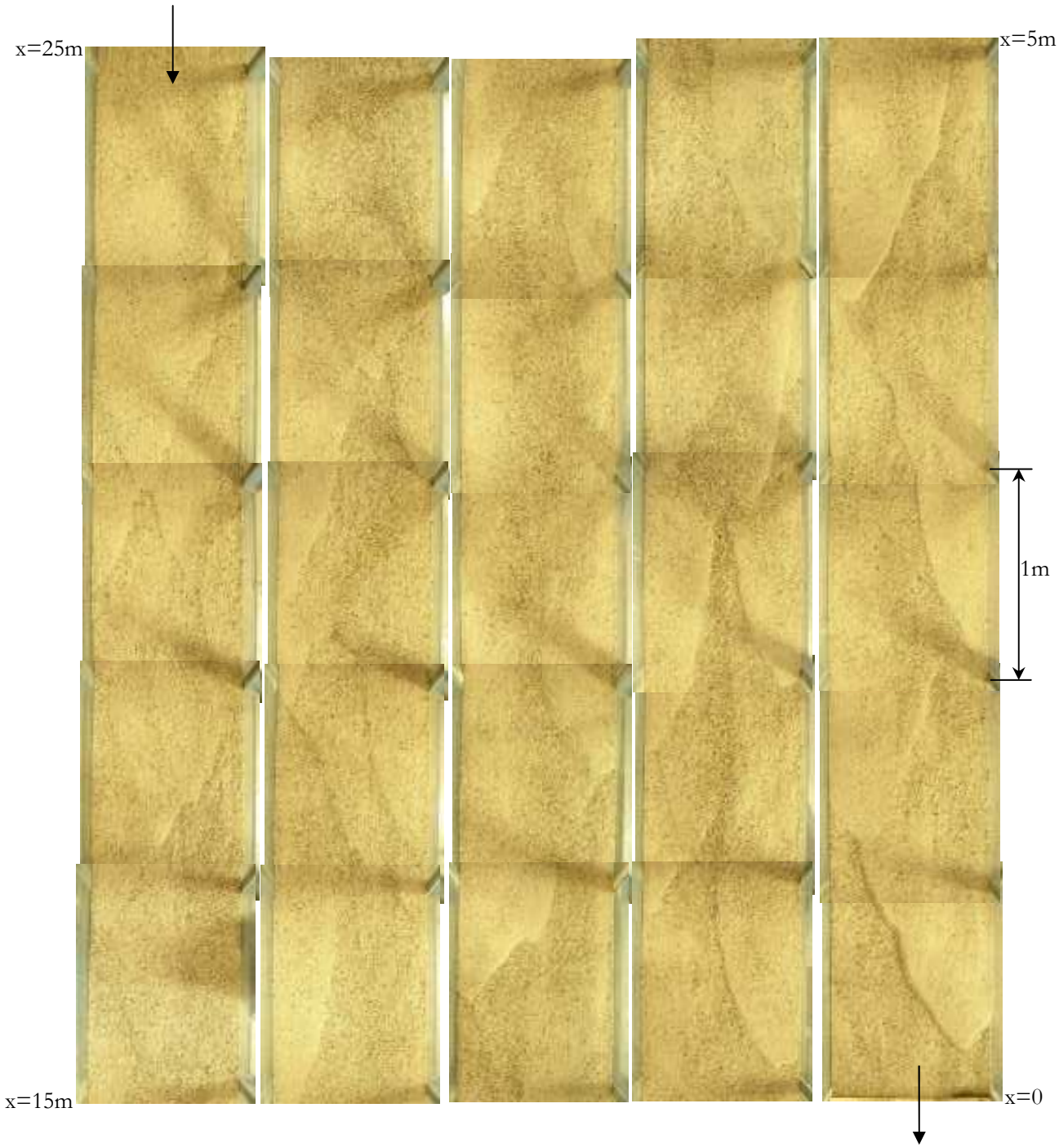

RUN M1E1

H=0.104 m, V=1.02 m/s, S=0.0081, F=1.01, q_s=1.13 x10^{-4} m^2/s, D_m=2.9 mm, Q_{SF}/Q_w=2.8 g/l.

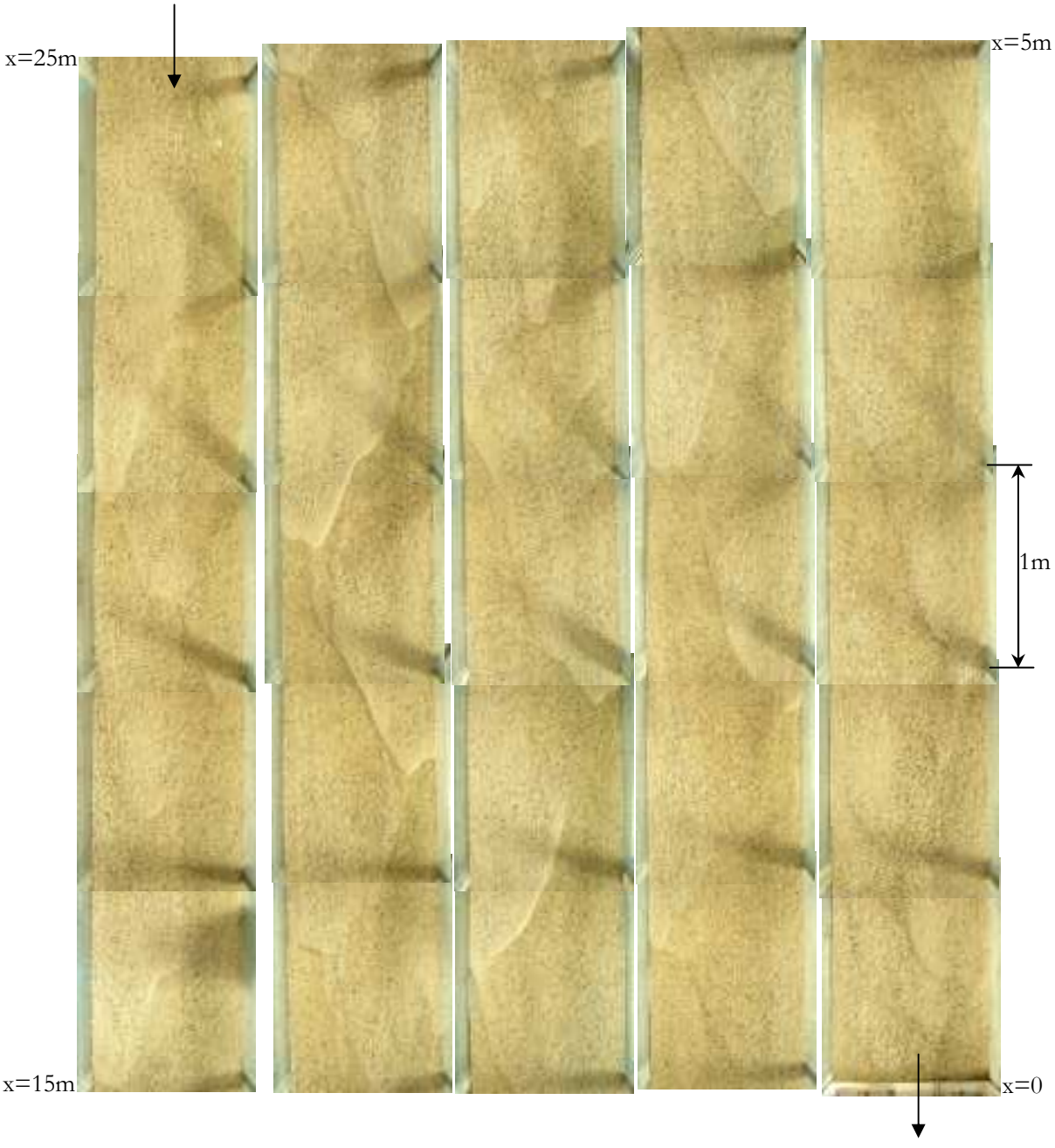

RUN M1E6

H=0.113 m, V=0.92 m/s, S=0.0059, F=0.87, q_s=7.00 x10^{-5} m^2/s, D_m=2.8 mm, Q_{SF}/Q_w=1.7 g/l.

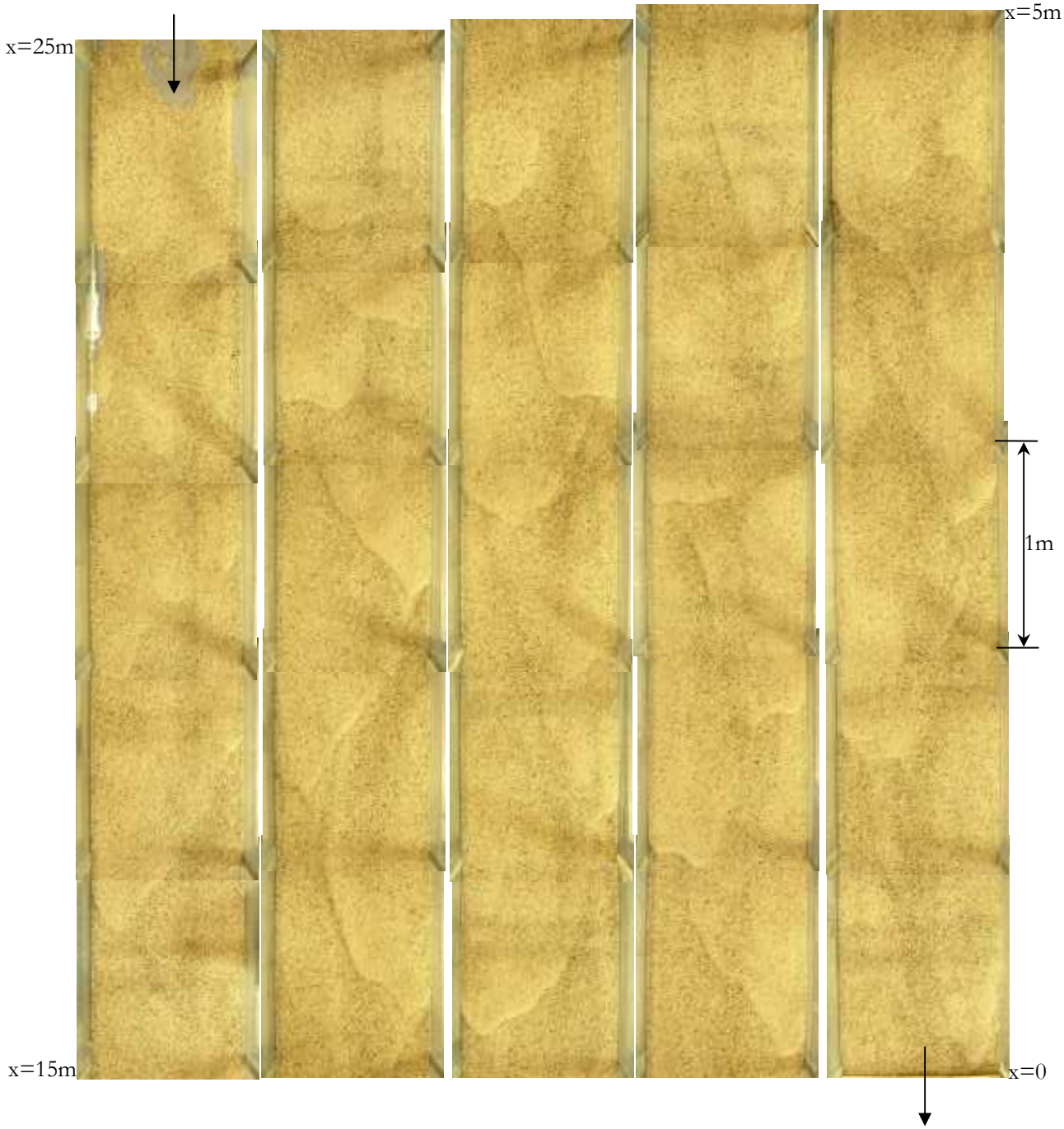

MIXTURE 2

*Runs ordered from higher to lower sediment concentration.

RUN M2E1

H=0.081 m, V=1.28 m/s, S=0.0177, F=1.44, q_s=5.47 x10^{-4} m^2/s, D_m=2.4 mm, Q_{SF}/Q_w=13.7 g/l.

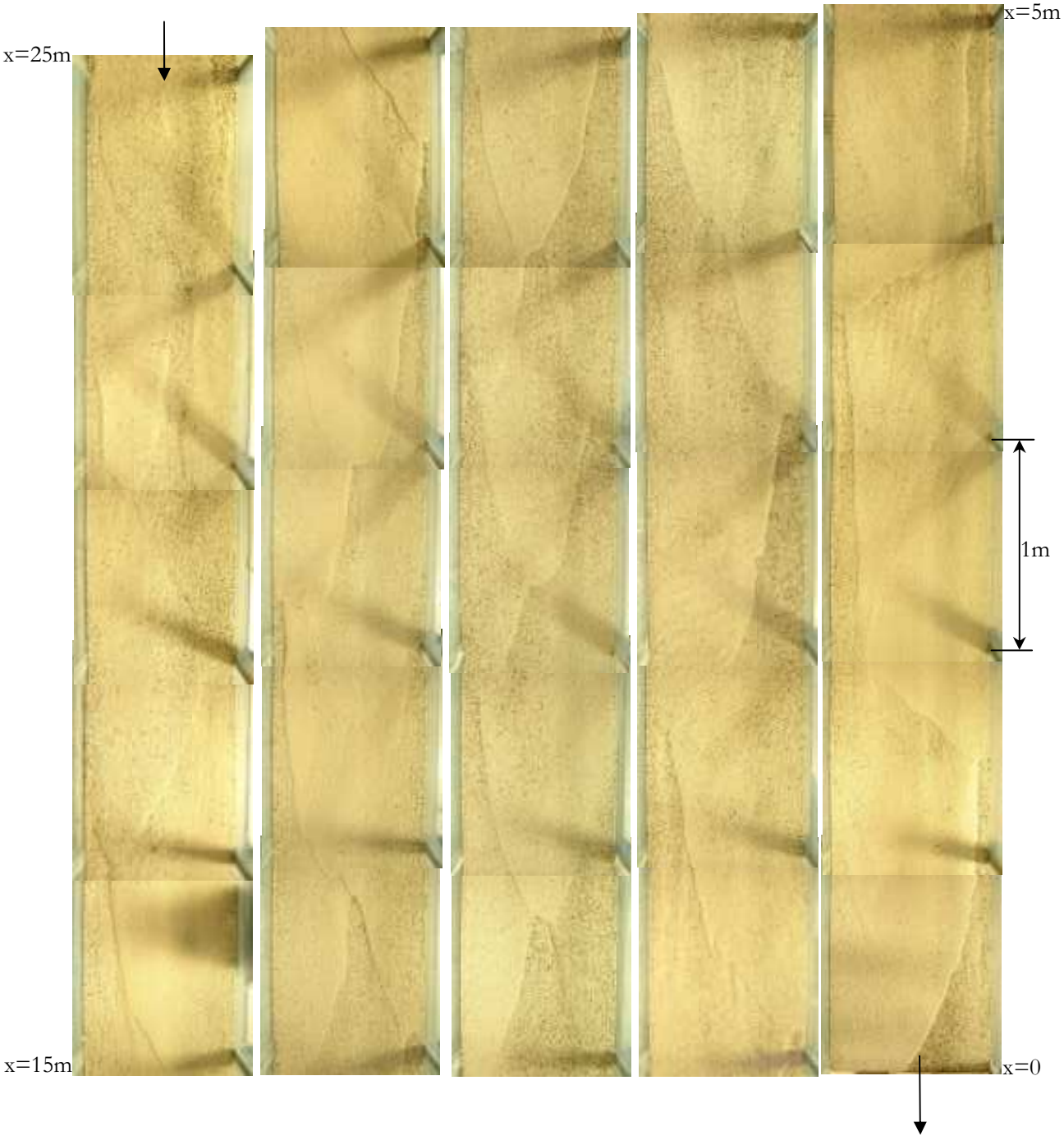

RUN M2E2

H=0.080 m, V=1.31 m/s, S=0.0167, F=1.48, q_s=4.57 x10^{-4} m^2/s, D_m=2.5 mm, Q_{SF}/Q_w=11.3 g/l.

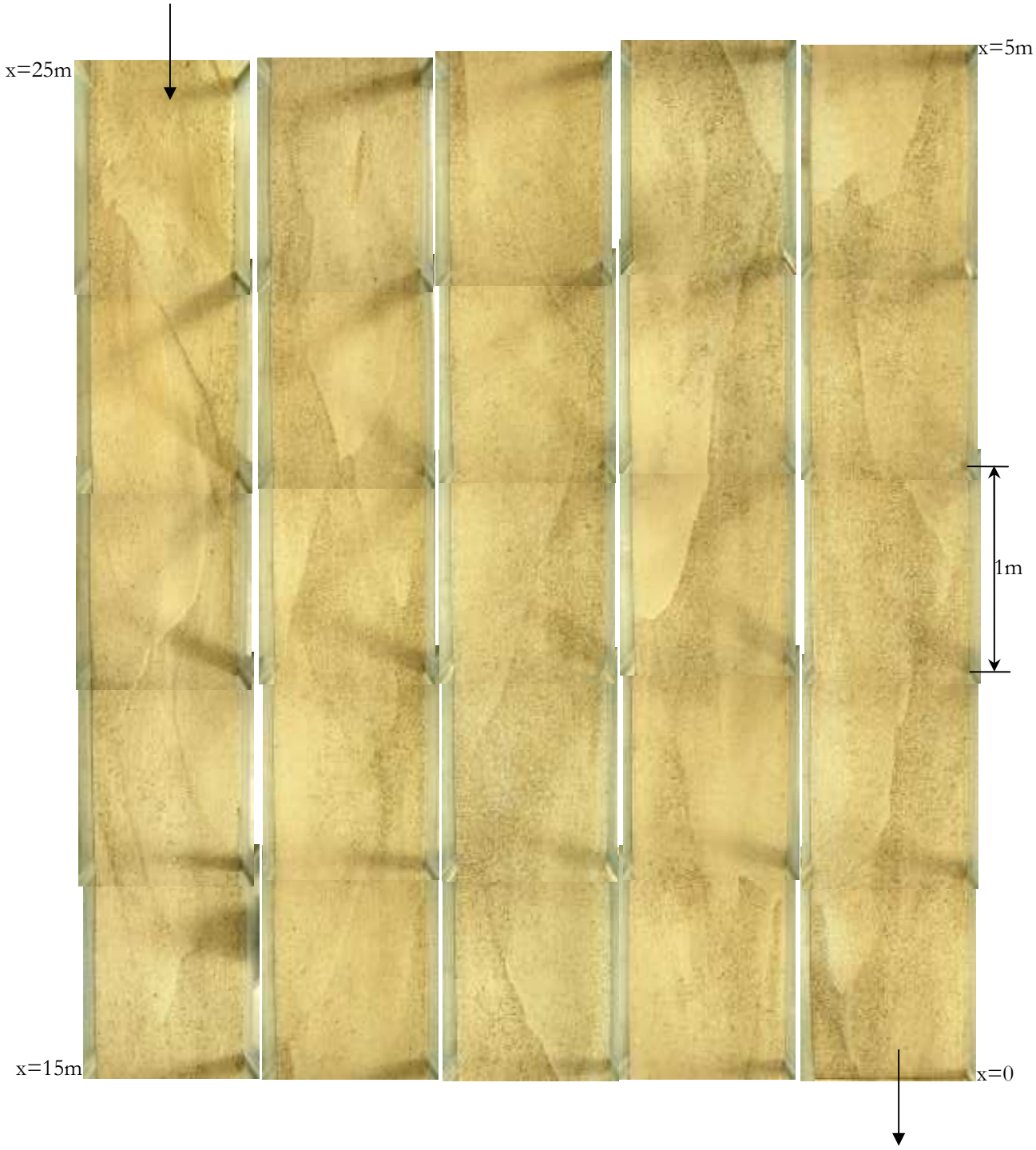

RUN M2E3

H=0.083 m, V=1.25 m/s, S=0.0160, F=1.39, q_s=4.05 x10^{-4} m^2/s, D_m=2.4 mm, Q_{SF}/Q_w=10.1 g/l.

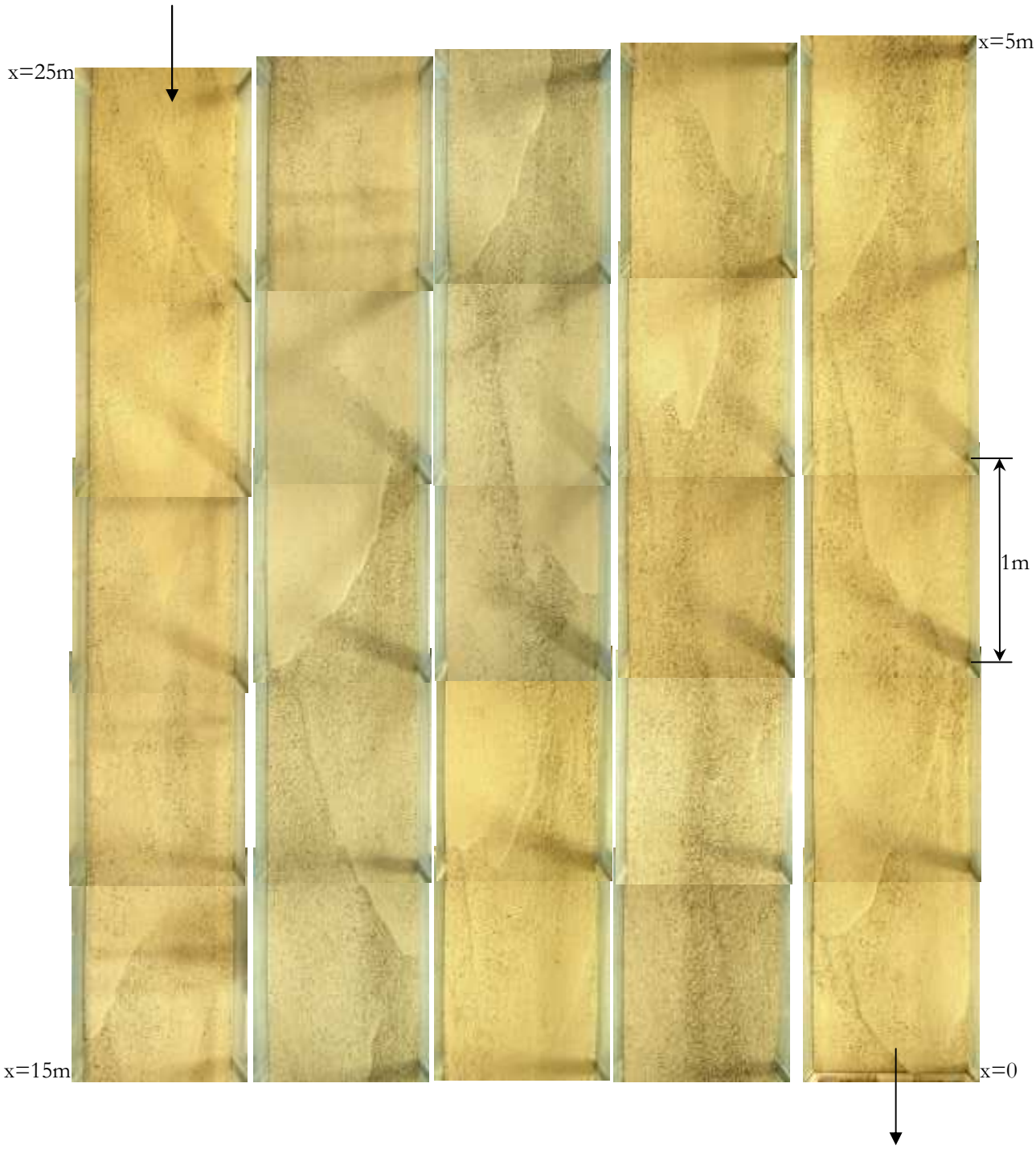

RUN M2E4

H=0.089 m, V=1.17 m/s, S=0.0146, F=1.25, q_s=2.83 x10^{-4} m^2/s, D_m=2.4 mm, Q_{SF}/Q_w=7.1 g/l.

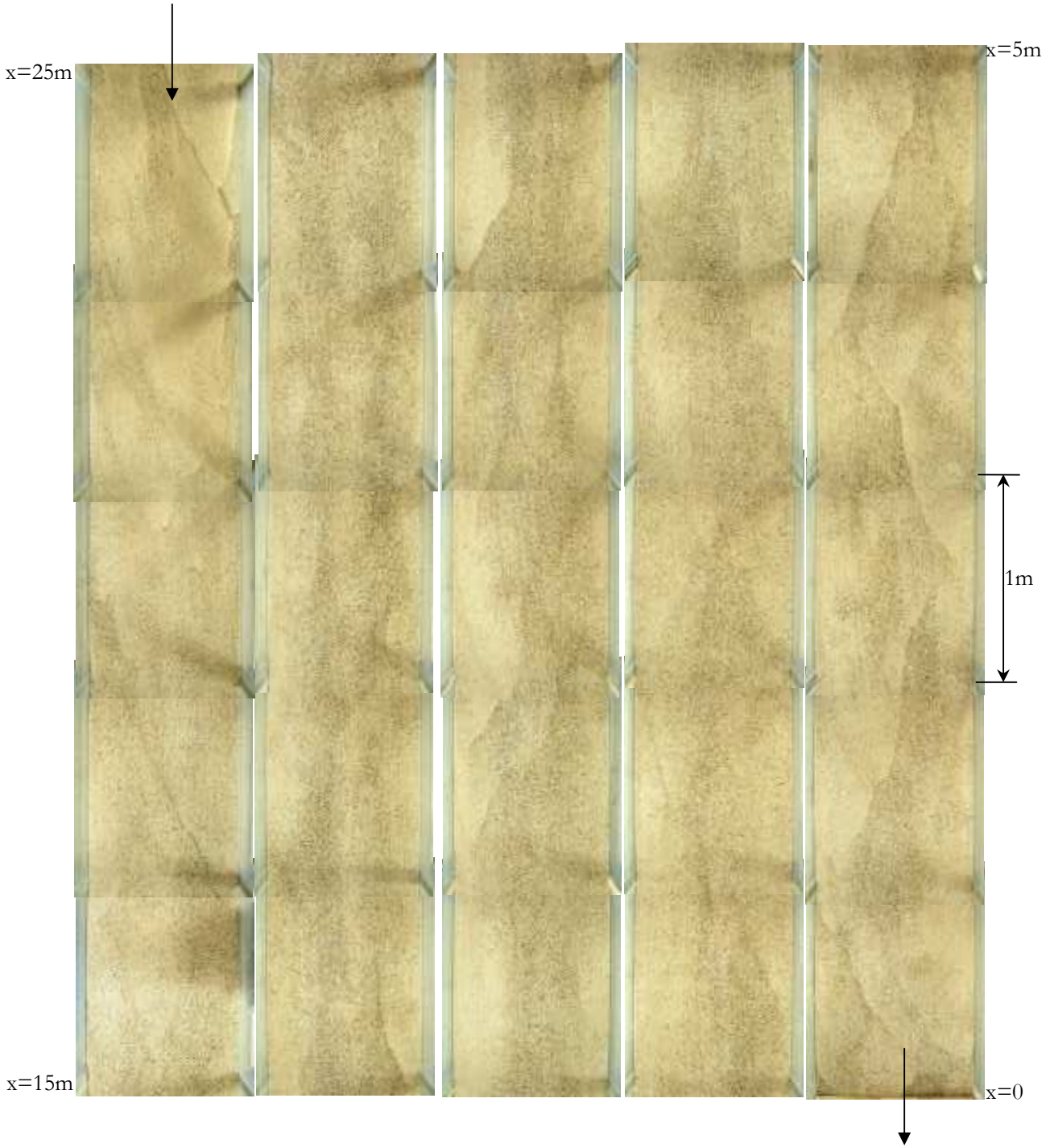

RUN M2E5

H=0.103 m, V=1.03 m/s, S=0.0098, F=1.02, q_s=1.49 x10^{-4} m^2/s, D_m=2.4 mm, Q_{SF}/Q_w=3.7 g/l.

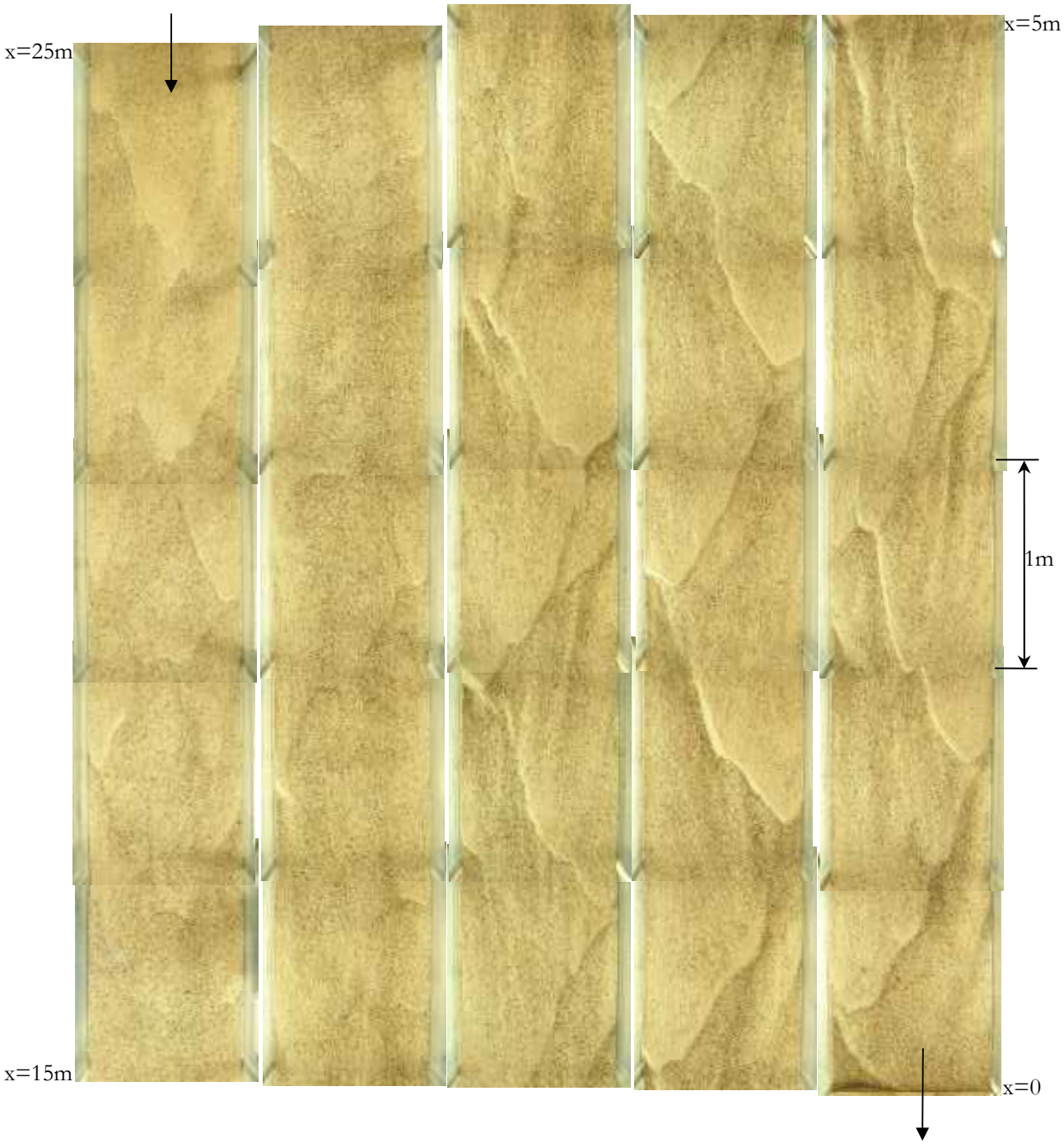

RUN M2E6

H=0.113 m, V=0.94 m/s, S=0.0064, F=0.89, q_s=8.12 x10^{-5} m^2/s, D_m=2.4 mm, Q_{SF}/Q_w=2.0 g/l.

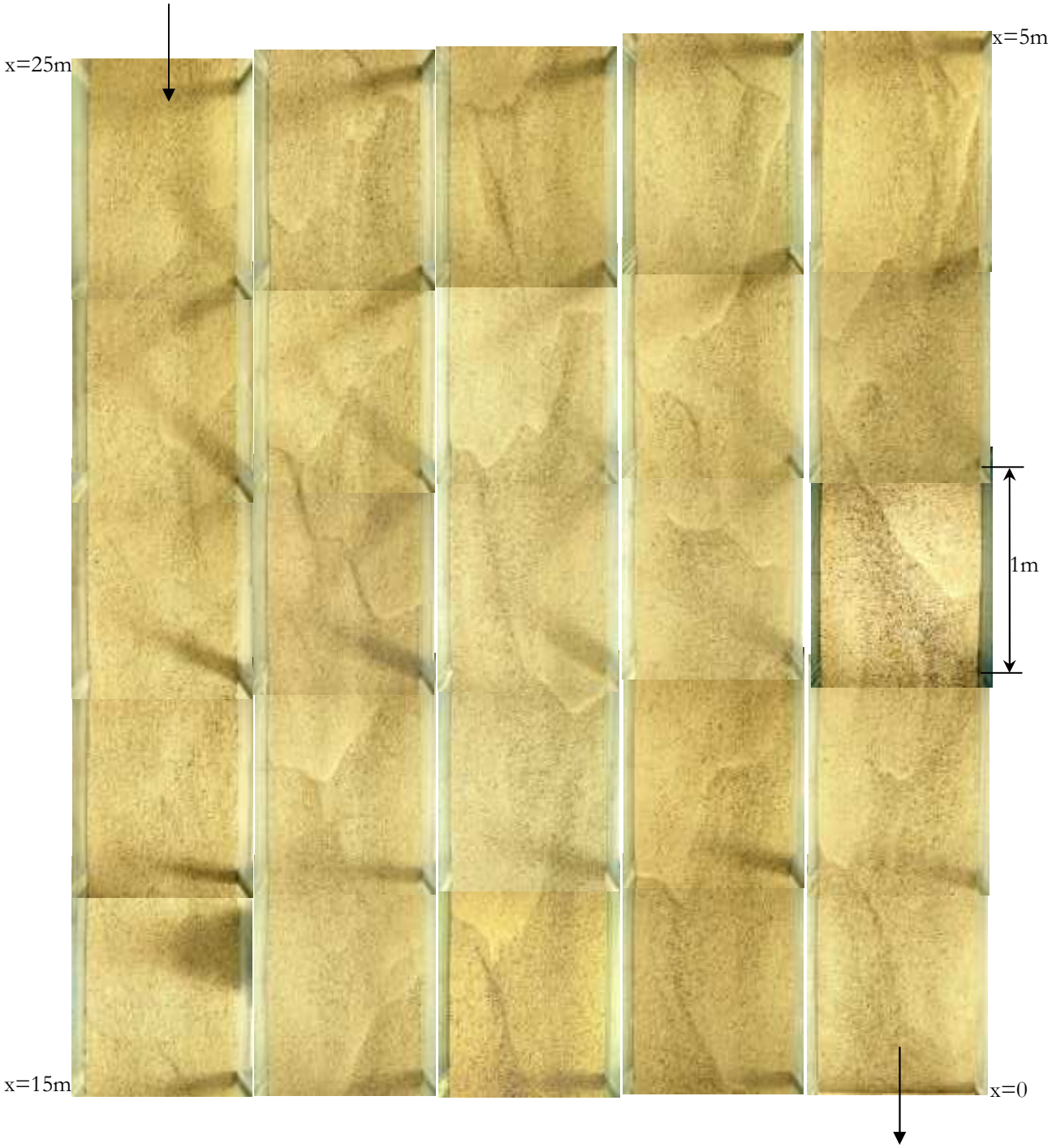

SAND

*Runs ordered from higher to lower sediment concentration.

RUN S1

H=0.103 m, V=1.03 m/s, S=0.0155, F=1.02, q_s=3.34 x10^{-4} m^2/s, D_m=1.5 mm, Q_{SF}/Q_w=8.3 g/l.

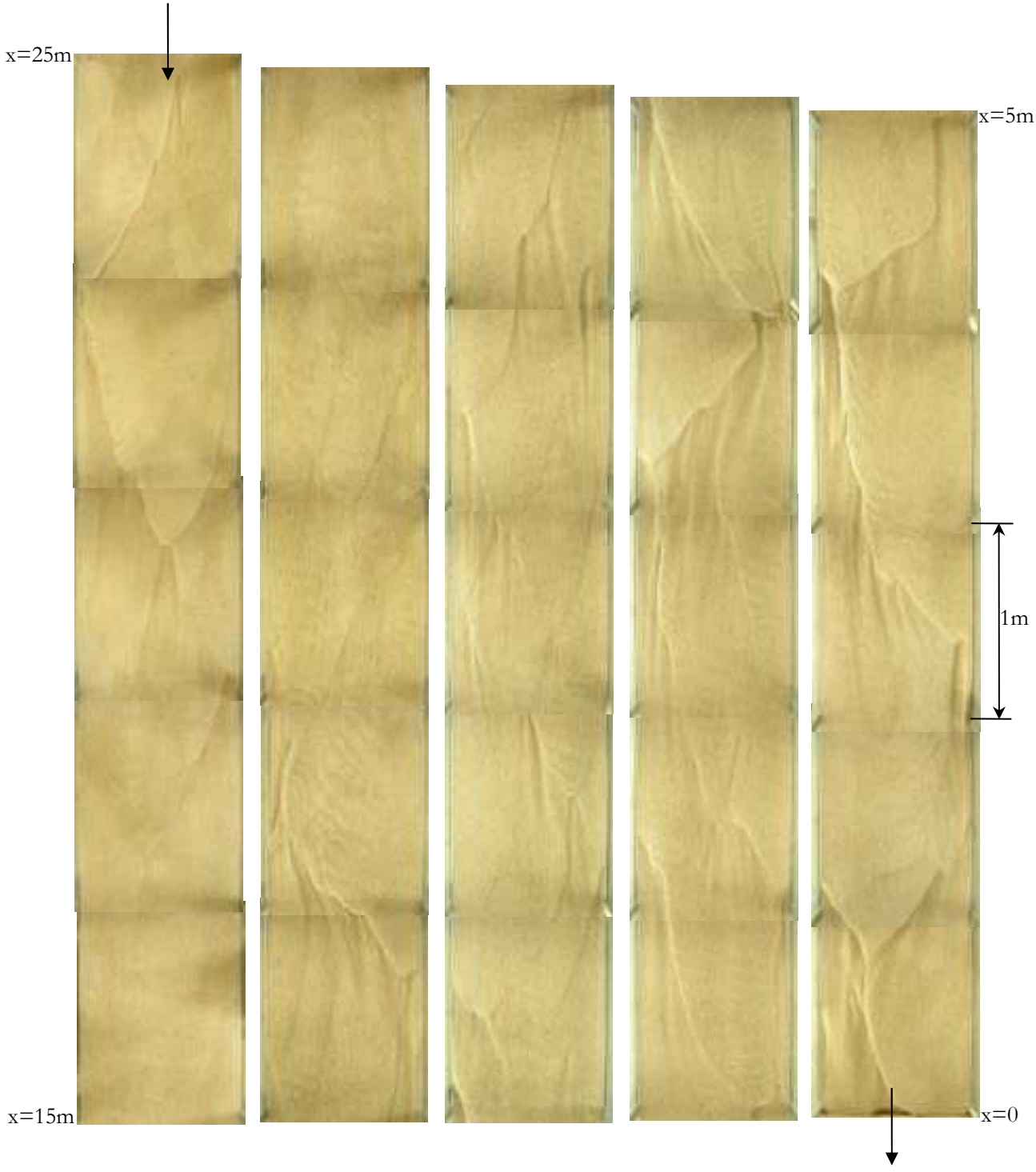

RUN S2

H=0.109 m, V=0.97 m/s, S=0.0123, F=0.94, q_s=2.34 x10^{-4} m^2/s, D_m=1.4 mm, Q_{SF}/Q_w=5.8 g/l.

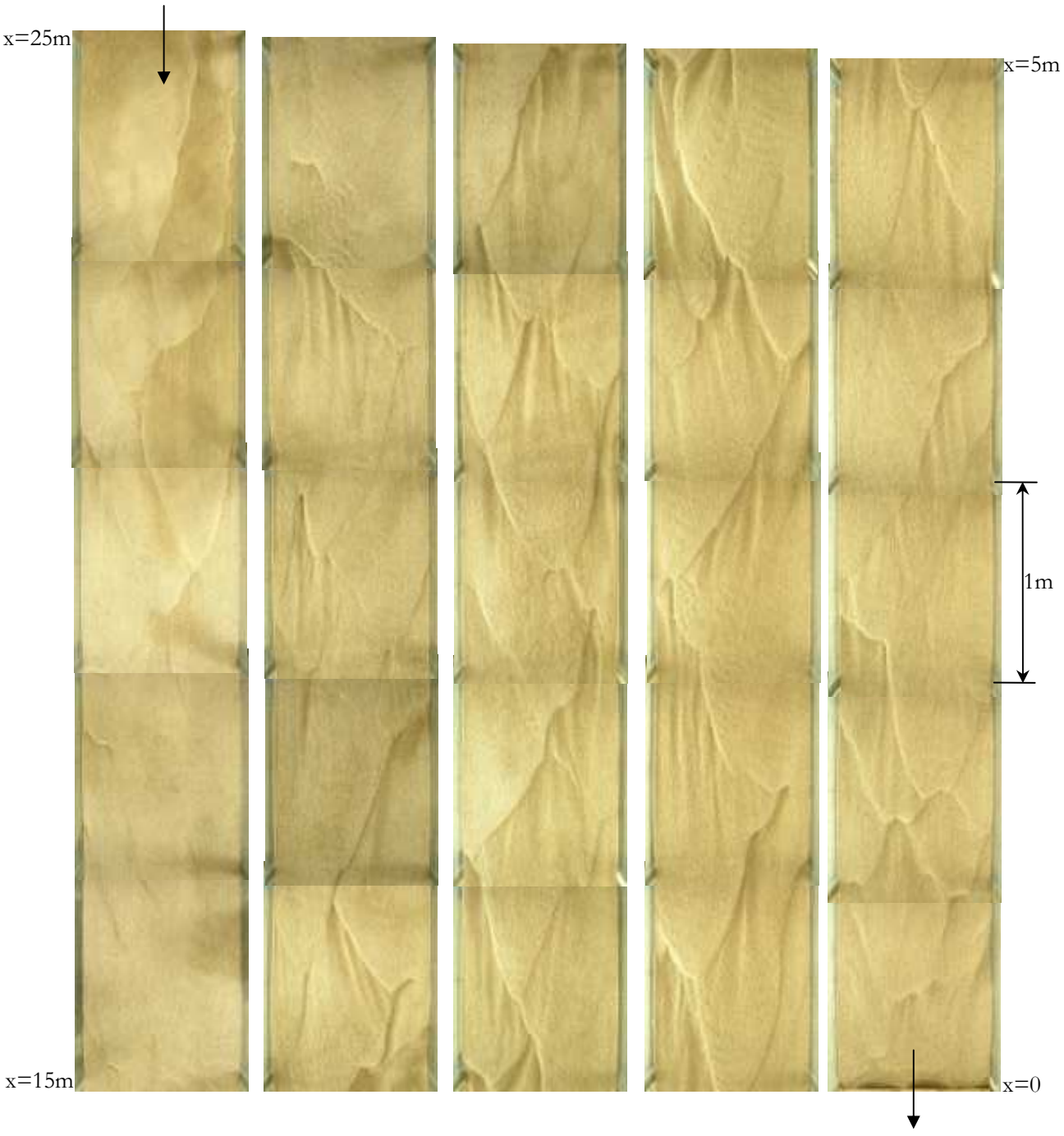

RUN S3

H=0.119 m, V=0.89 m/s, S=0.0082, F=0.82, q_s=1.25 x10^{-4} m^2/s, D_m=1.4 mm, Q_{SF}/Q_w=3.1 g/l.

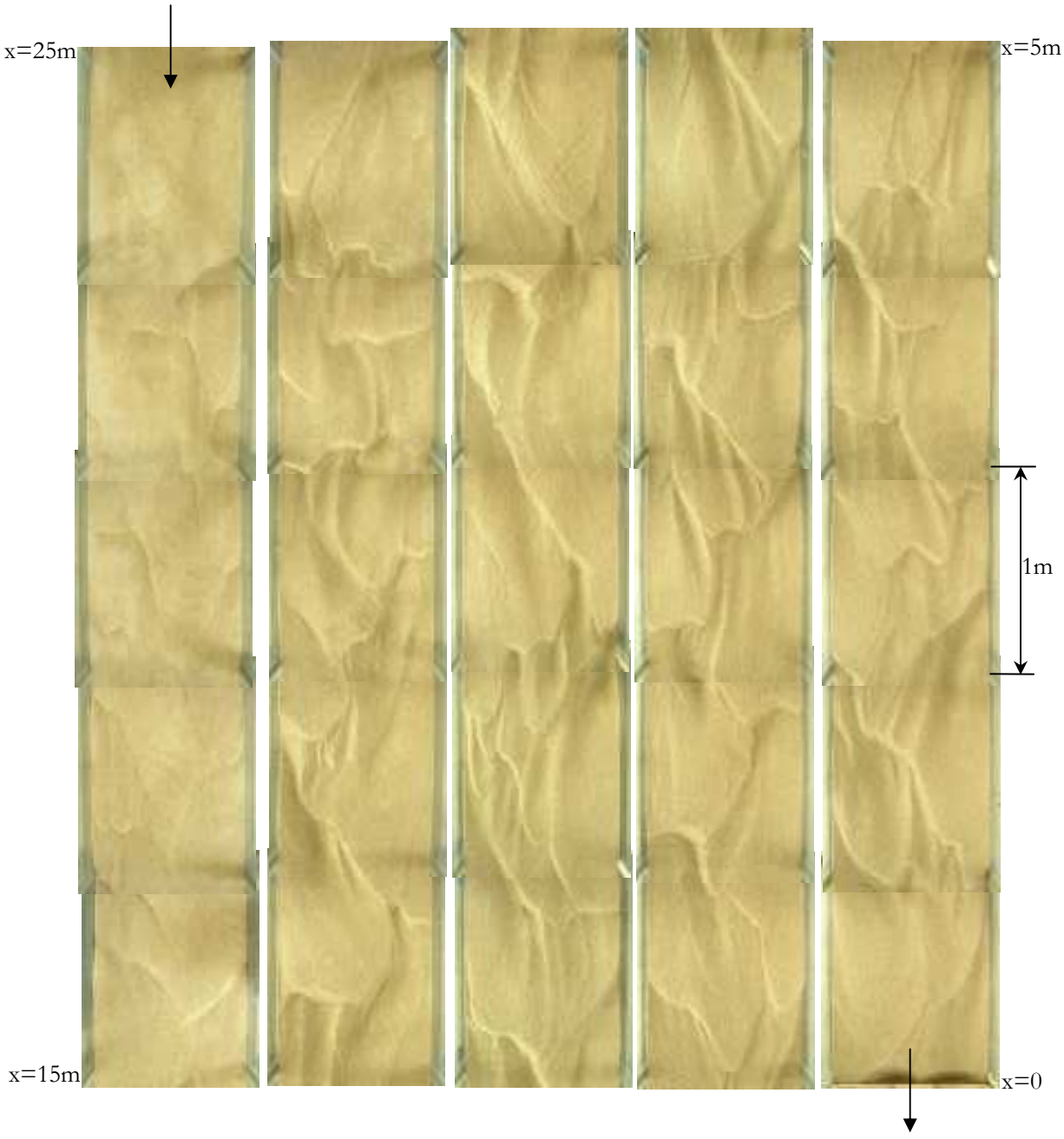

RUN S4

H=0.130 m, V=0.82 m/s, S=0.0060, F=0.73, q_s=7.27 x10^{-5} m^2/s, D_m=1.4 mm, Q_{SF}/Q_w=1.8 g/l.

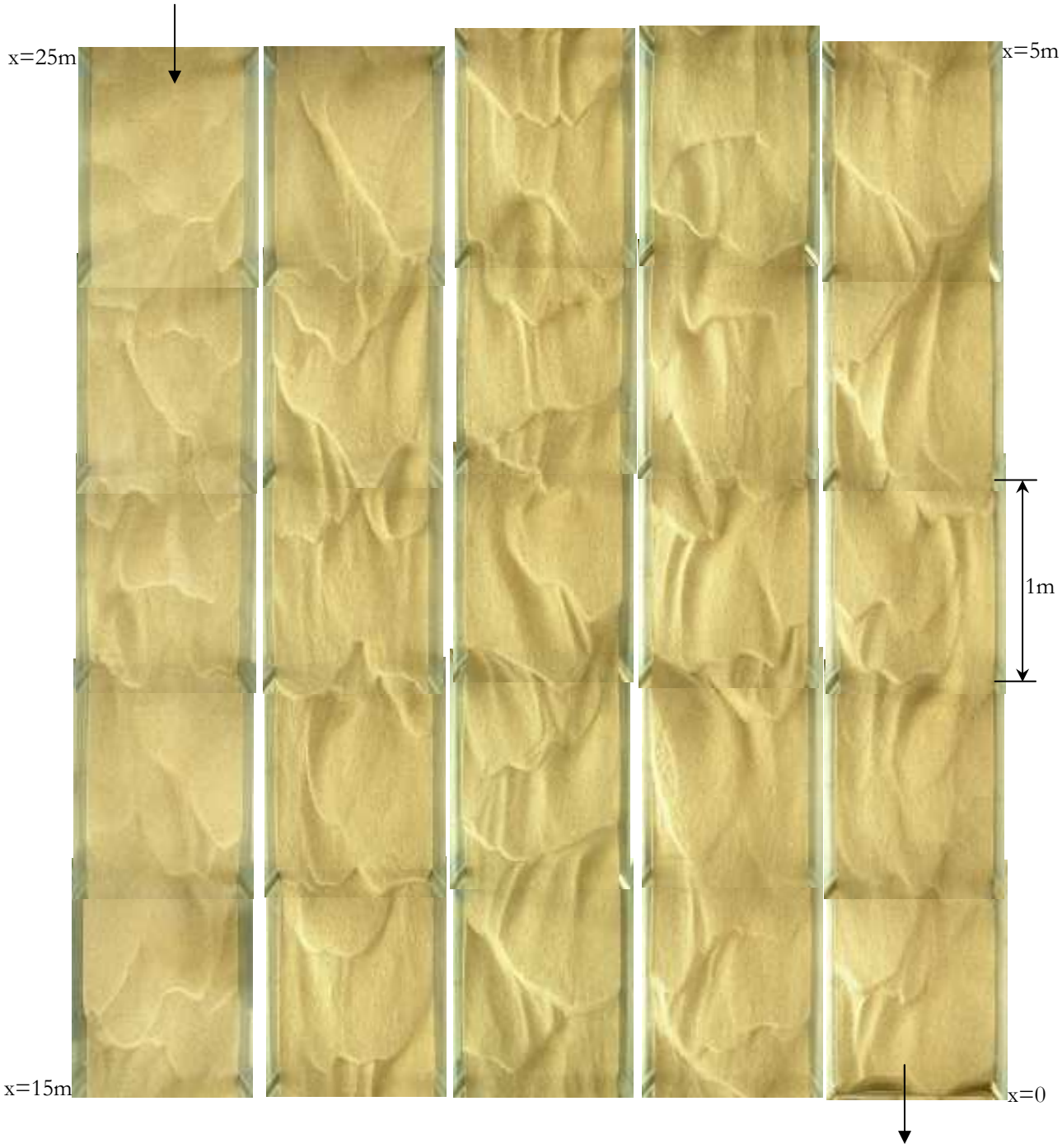

APPENDIX X

MANUAL SEDIMENT TRANSPORT SAMPLES

BASKET TYPE SAMPLER

Sediment transport and median grain size

The basket sampler was divided in three compartments of equal width, so that each of these compartments caught the sediment passing through one third of the channel cross-section. Unit solid discharges obtained from sediment samples caught in each of the compartments are plotted below as a function of a ratio of sediment transport and time normalized by the bedform period. The sediment transport ratio is defined as

$$\text{Ratio of sediment transport} = \frac{q_{Sin}}{3q_{SF}} \qquad \text{(AX.1)}$$

where q_{SF} is the constant unit rate of sediment feeding to the channel and q_{Sin} is the instantaneous unit sediment discharge computed from the sediment transport samples for each compartment using eqs.(3.13) and (3.14) and considering an efficiency for the sampler of $\%\eta=60.7\%$, as obtained in section 3.3.2.5.6. Eq.(AX.1) is equivalent to a third of the ratio of sediment discharge variation defined in eq.(3.23) and given in Table 3.16 for each run. The partition by three in eq.(AX.1) is introduced in order to feature a better visualization of the segmentation of the solid discharge in the cross-section compared to the total solid discharge. The ratio of sediment transport for the total solid discharge is shown in the plots below as well; it was obtained as the sum of the three individual ratios of sediment transport for each compartment.

Time of sampling on the horizontal axes in the plots is presented as the quotient of the elapsed time t_m during the run, registered when the sample was taken, and the period of a bedform unit T_b (as shown on the last column of Table 5.4).

For runs with sediment mixtures, the grain size distribution is also presented in the plots by means of a ratio of grain size, defined as

$$\text{Ratio of grain size} = \frac{D_{50s}}{D_{50F}} \qquad \text{(AX.2)}$$

where D_{50s} is the median diameter of the grain size distribution of the sample formed by the sum of the material retained in the three compartments, and D_{50F} is the median diameter of the material fed constantly into the channel.

Horizontal lines have been drawn on the plots as a reference for values of 0.33 and 1 of the ratio of sediment transport. Error bars have been included for each sample to indicate the length of the sampling time.

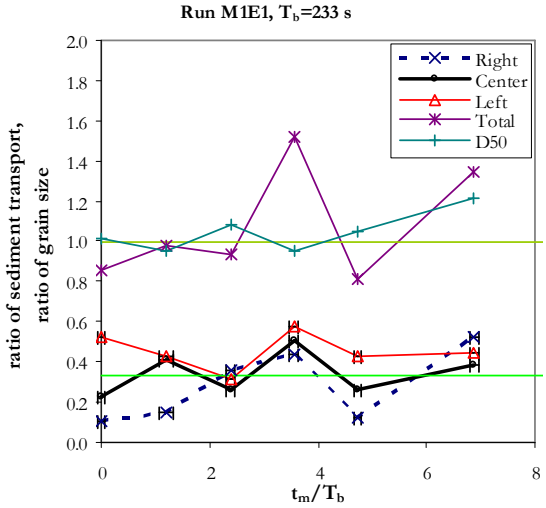
Run M1E1, T_b=233 s
ratio of sediment transport, ratio of grain size
t_m/T_b
Right
Center
Left
Total
D50

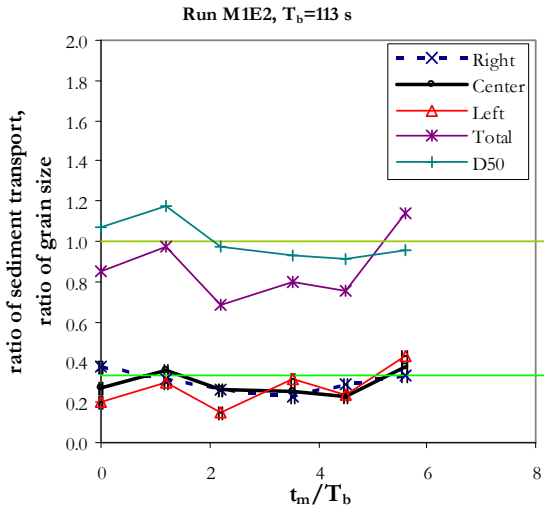
Run M1E2, T_b=113 s
ratio of sediment transport, ratio of grain size
t_m/T_b
Right
Center
Left
Total
D50

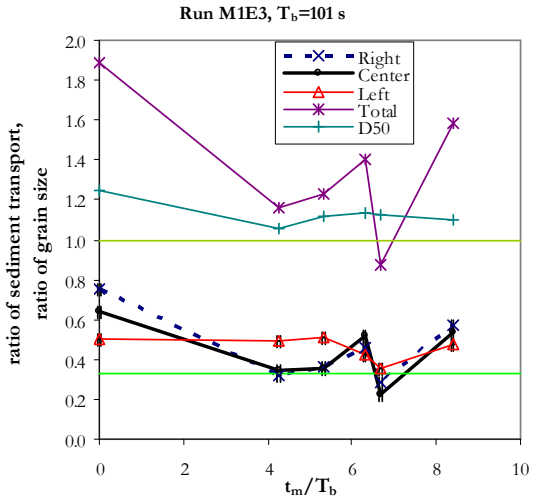
Run M1E3, T_b=101 s
ratio of sediment transport, ratio of grain size
t_m/T_b
Right
Center
Left
Total
D50

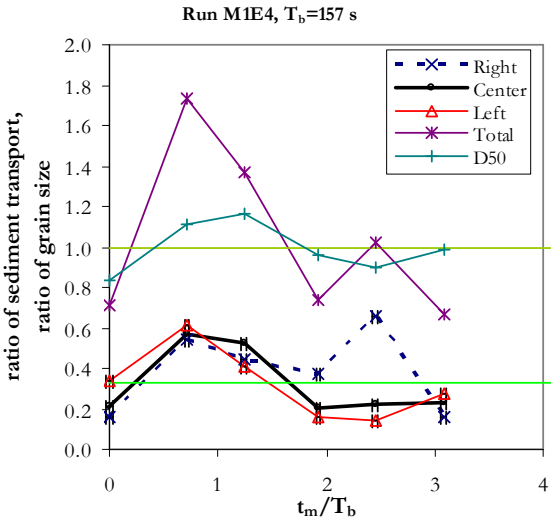
Run M1E4, T_b=157 s
ratio of sediment transport, ratio of grain size
t_m/T_b
Right
Center
Left
Total
D50

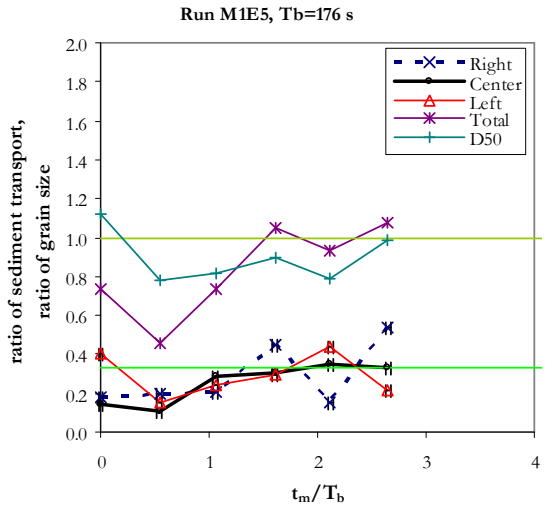
Run M1E5, Tb=176 s
ratio of sediment transport, ratio of grain size
t_m/T_b
Right
Center
Left
Total
D50

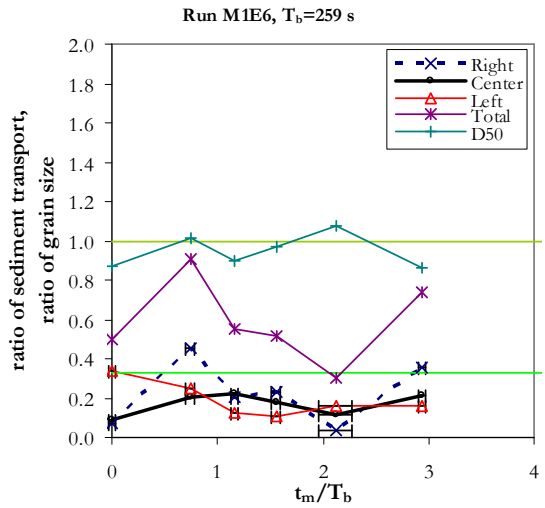
Run M1E6, T_b=259 s
ratio of sediment transport, ratio of grain size
t_m/T_b
Right
Center
Left
Total
D50

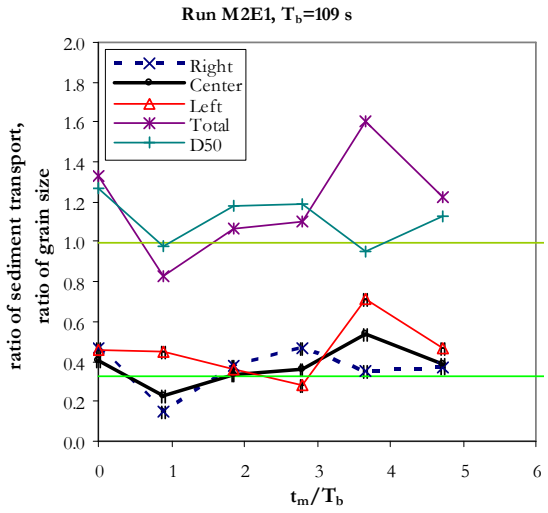
Run M2E1, T_b=109 s
ratio of sediment transport, ratio of grain size
t_m/T_b
Right
Center
Left
Total
D50

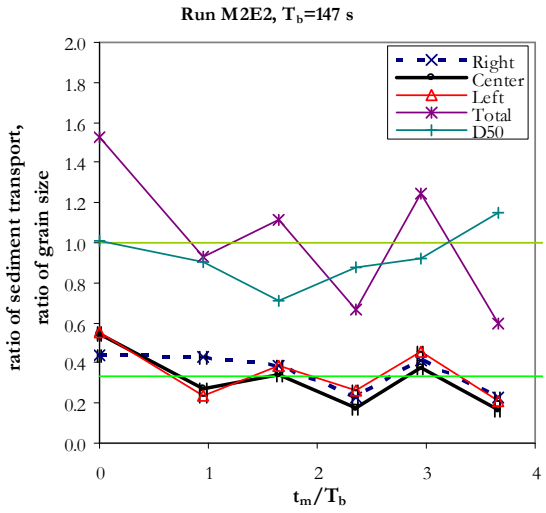
Run M2E2, T_b=147 s
ratio of sediment transport, ratio of grain size
t_m/T_b
Right
Center
Left
Total
D50

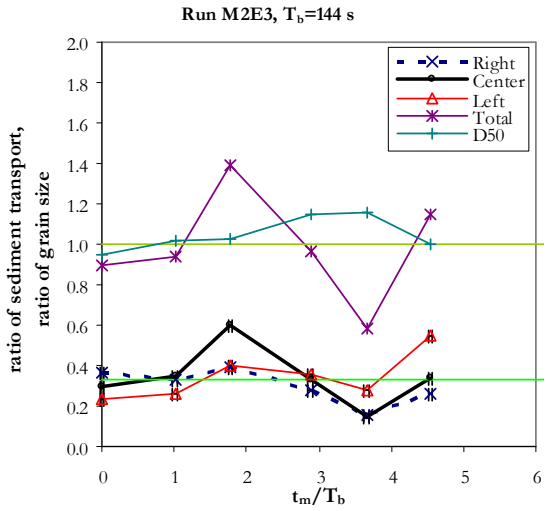
Run M2E3, T_b=144 s
ratio of sediment transport, ratio of grain size
t_m/T_b
Right
Center
Left
Total
D50

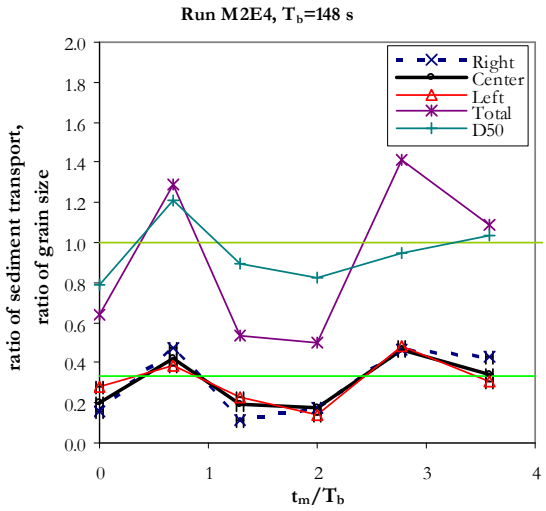
Run M2E4, T_b=148 s
ratio of sediment transport, ratio of grain size
t_m/T_b
Right
Center
Left
Total
D50

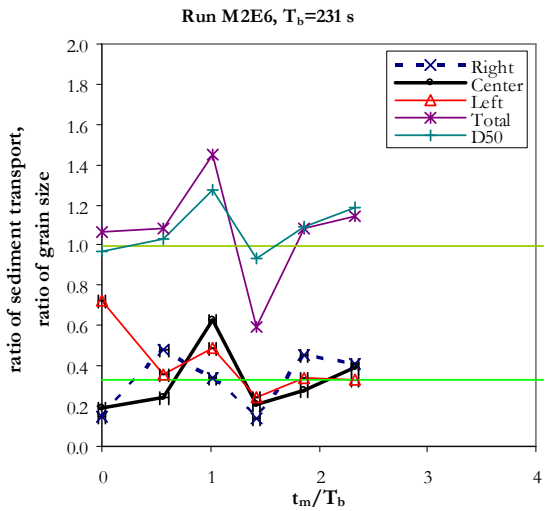
Run M2E6, T_b=231 s
ratio of sediment transport, ratio of grain size
t_m/T_b
Right
Center
Left
Total
D50

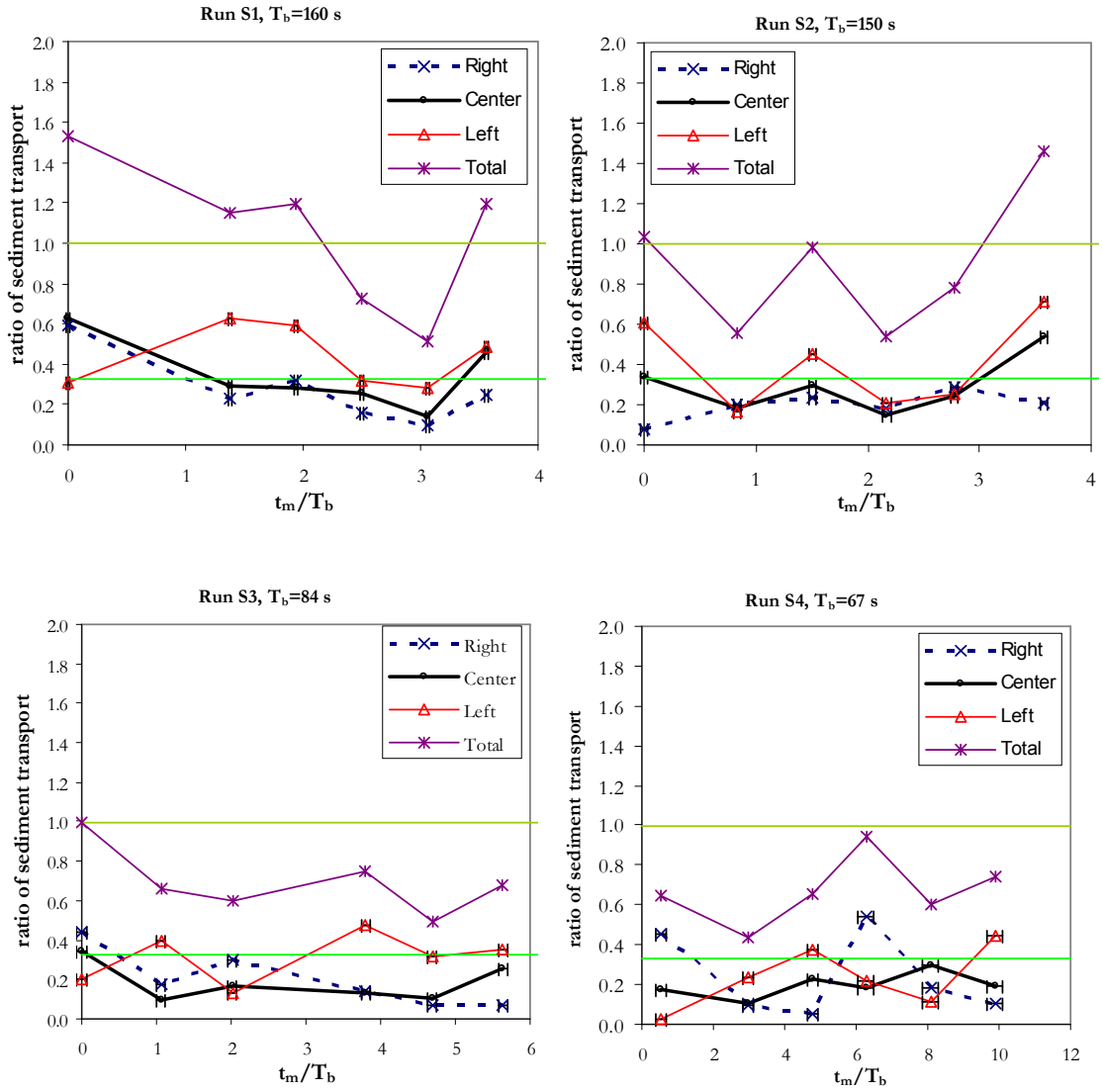

Sand content

For runs with sediment mixtures, a ratio of sand content for the sediment transport samples was defined as

$$\text{Ratio of sand content} = \frac{f_{ss}}{f_{sF}} \qquad \text{(AX.3)}$$

where f_{ss} is the fractional content in the sediment transport sample of the size fraction with 1.25 mm diameter and f_{sF} is the fractional content for the same size fraction in the feeding sediment. Variation of the ratio of sand content is shown on the plots below for the sediment transport samples taken with the basket type sampler.

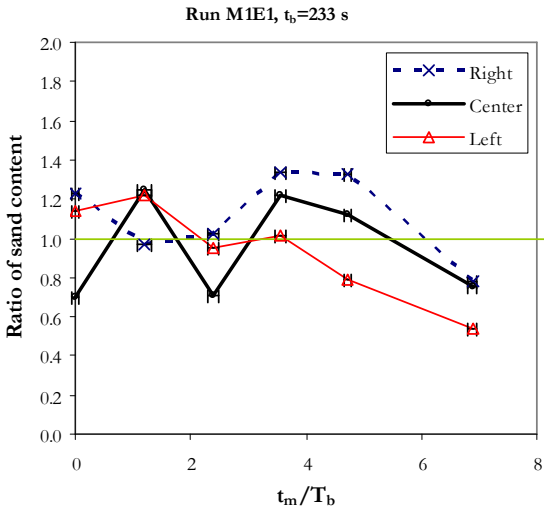
Run M1E1, t_b=233 s
Ratio of sand content
t_m/T_b
Right
Center
Left

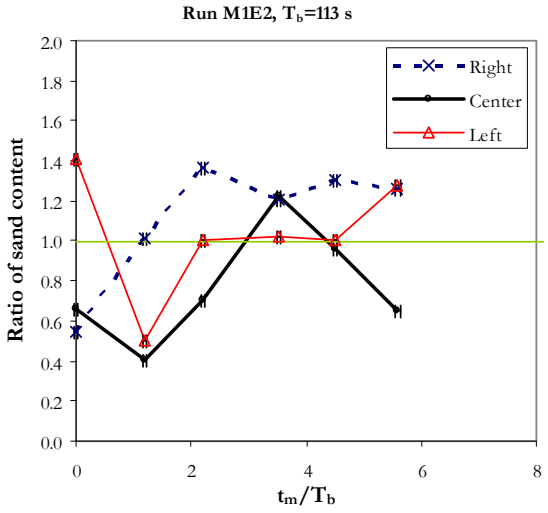
Run M1E2, T_b=113 s
Ratio of sand content
t_m/T_b
Right
Center
Left

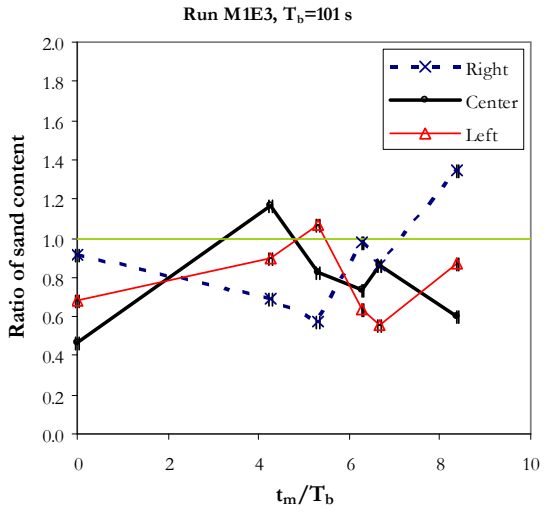
Run M1E3, T_b=101 s
Ratio of sand content
t_m/T_b
Right
Center
Left

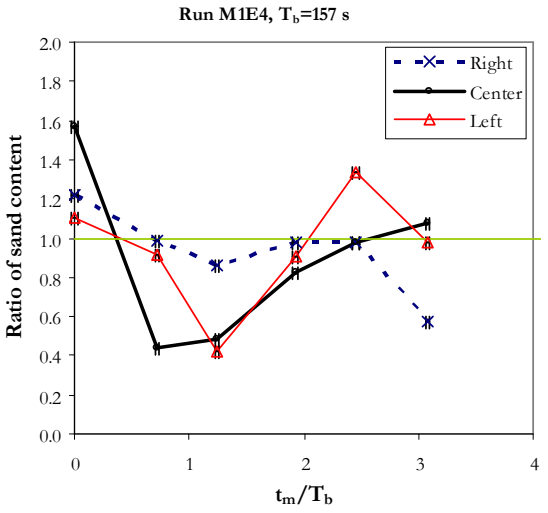
Run M1E4, T_b=157 s
Ratio of sand content
t_m/T_b
Right
Center
Left

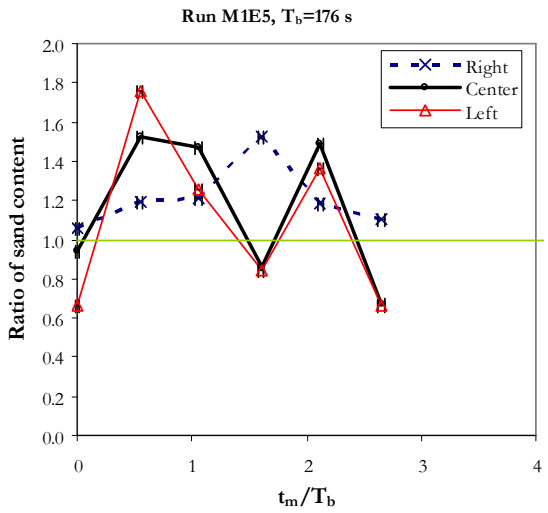
Run M1E5, T_b=176 s
Ratio of sand content
t_m/T_b
Right
Center
Left

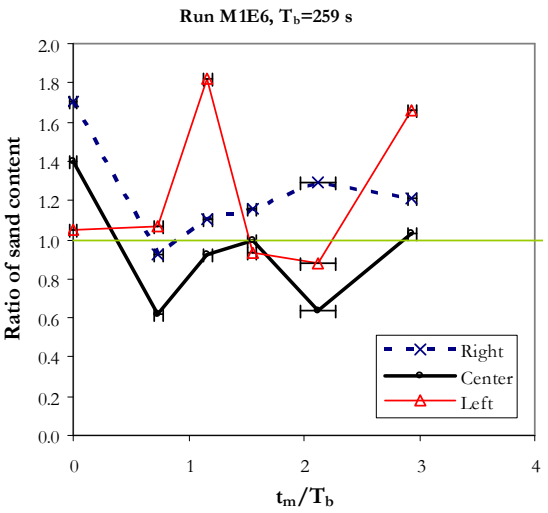
Run M1E6, T_b=259 s
Ratio of sand content
t_m/T_b
Right
Center
Left

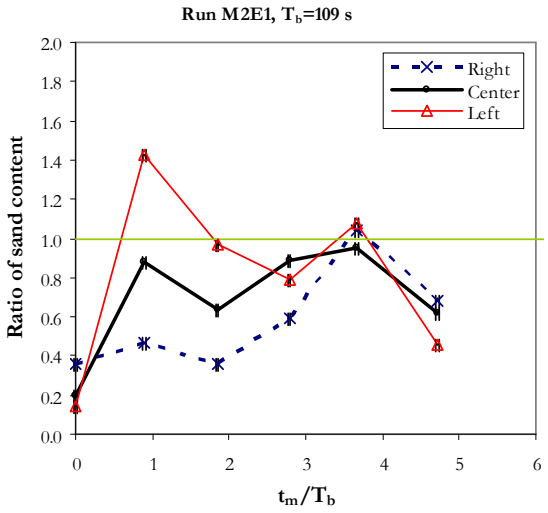
Run M2E1, T_b=109 s
Ratio of sand content
t_m/T_b
Right
Center
Left

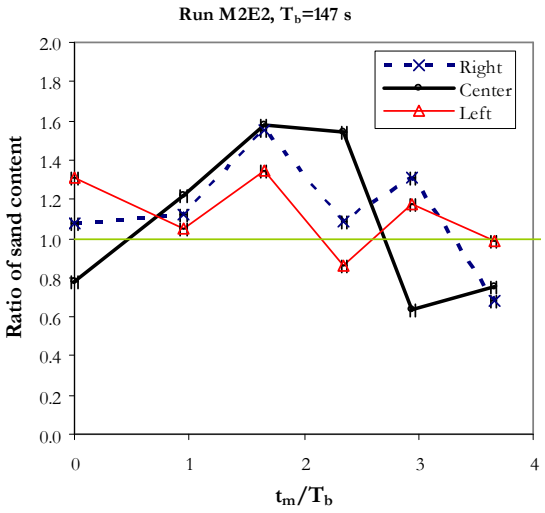
Run M2E2, T_b=147 s
Ratio of sand content
t_m/T_b
Right
Center
Left

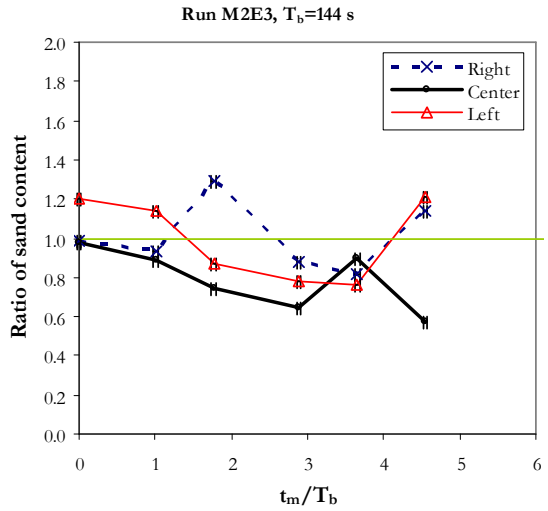
Run M2E3, T_b=144 s
Ratio of sand content
t_m/T_b
Right
Center
Left

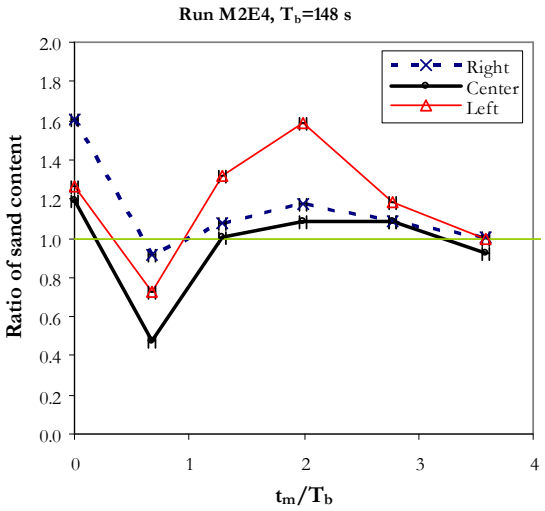
Run M2E4, T_b=148 s
Ratio of sand content
t_m/T_b
Right
Center
Left

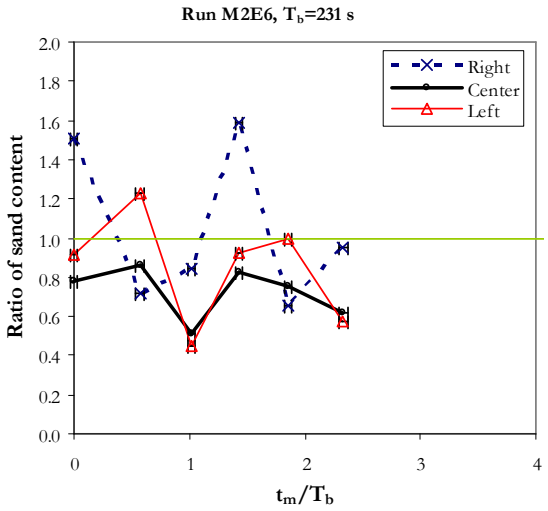
Run M2E6, T_b=231 s
Ratio of sand content
t_m/T_b
Right
Center
Left

HELLEY-SMITH SAMPLER

Similarly to the plots above for the basket sampler, below are presented plots of sediment transport for the Helley-Smith sampler as a function of a ratio of sediment transport and the time when the sample was registered as a function of the bedform period. For this, the sediment transport ratio is defined as

$$\text{Ratio of sediment transport} = \frac{q_{Sin}}{q_{SF}} \qquad \text{(AX.4)}$$

where q_{SF} is the constant rate of sediment feeding to the channel and q_{Ss} is the instantaneous unit sediment discharge computed from the sediment transport samples using eqs.(3.13) and (3.14) and considering an efficiency for the sampler of $\%\eta=68.8\%$, as obtained in section 3.3.2.5.6. Eq.(AX.4) is equivalent to the ratio of sediment discharge variation defined in eq.(3.23) and given in Table 3.15 for each run.

Time of sampling on the horizontal axes is presented as the quotient of the elapsed time t_m during the run, registered when the sample was taken, and the period of a bedform unit T_b (as shown on the last column of Table 5.4). For runs G13, G14 and G15, for which the bedform period was not possible to be computed, the horizontal axis is given by the elapsed time of the run when the sample was taken.

Variables accounting for the grain size distribution are presented as a ratio of grain size and a ratio of sand content, as defined in eqs.(AX.2) and (AX.3). For the gravel samples the zone of the channel transversal section where the sample was taken is indicated (central, right or left third), for the sand and mixtures run series all samples were taken on the central cross section.

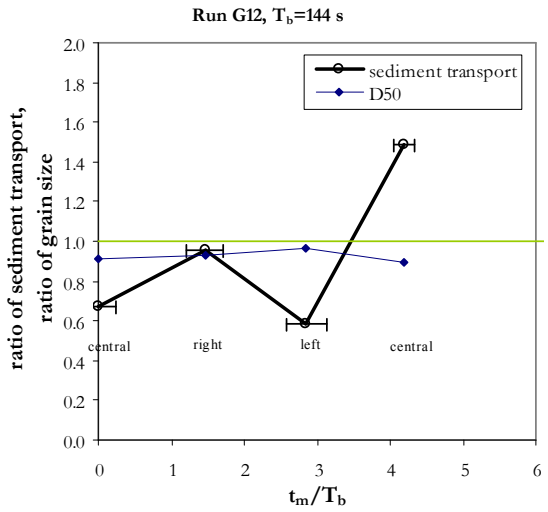
Run G12, T_b=144 s
sediment transport
D50
ratio of sediment transport, ratio of grain size
central
right
left
central
t_m/T_b

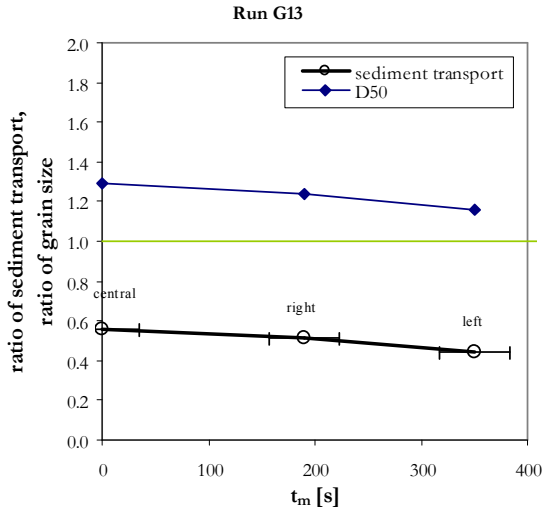
Run G13
sediment transport
D50
ratio of sediment transport, ratio of grain size
central
right
left
t_m [s]

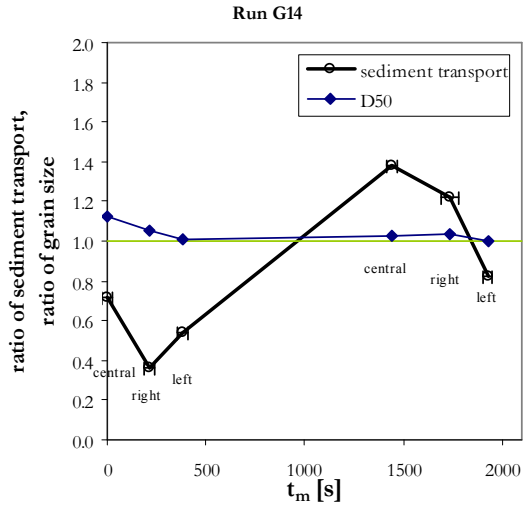
Run G14
sediment transport
D50
ratio of sediment transport, ratio of grain size
central
right
left
central
right
left
t_m [s]

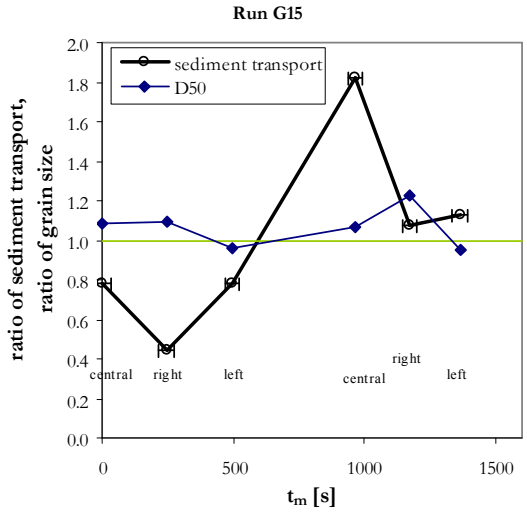
Run G15
sediment transport
D50
ratio of sediment transport, ratio of grain size
central
right
left
central
right
left
t_m [s]

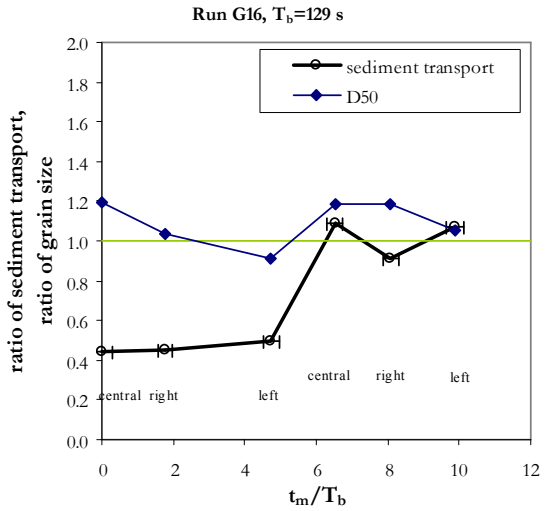
Run G16, T_b=129 s
sediment transport
D50
ratio of sediment transport, ratio of grain size
central
right
left
central
right
left
t_m/T_b

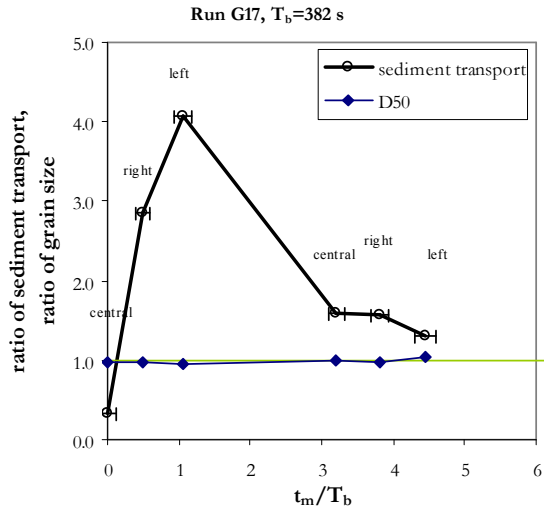
Run G17, T_b=382 s
sediment transport
D50
ratio of sediment transport, ratio of grain size
left
right
central
right
left
central
t_m/T_b

Run M2E1, T_b=109 s

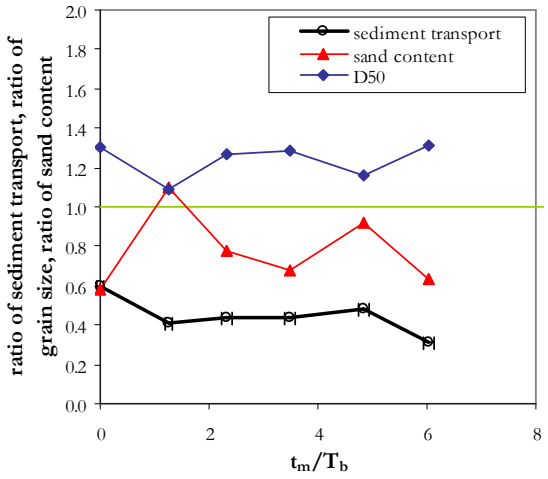

Run M2E2, T_b=147 s

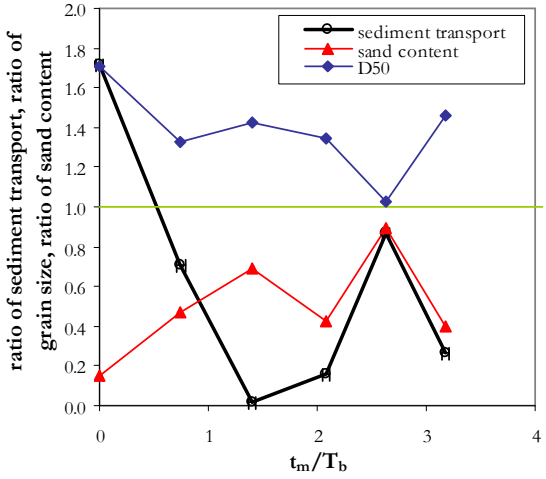

Run M2E3, T_b=144 s

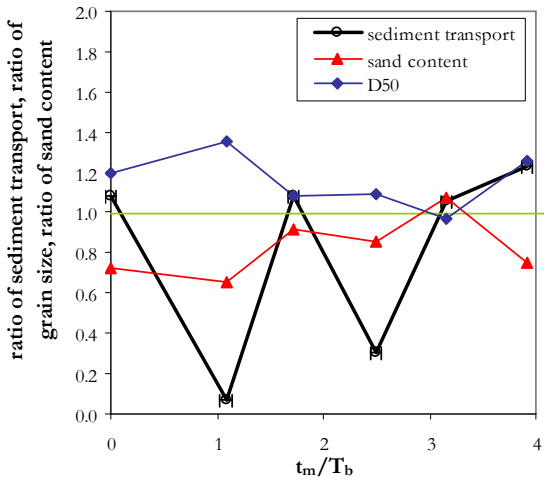

Run M2E4, T_b=148 s

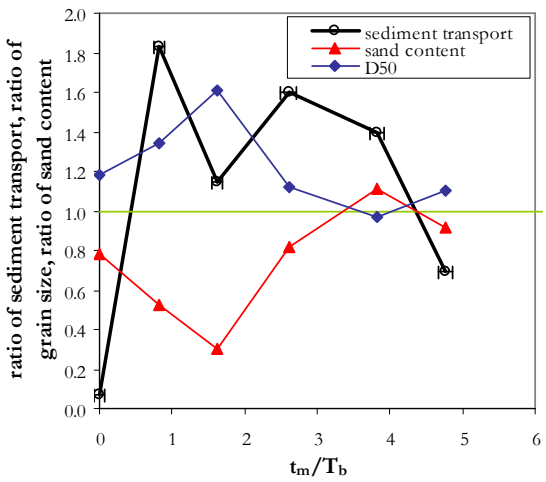

Run M2E6, T_b=231 s

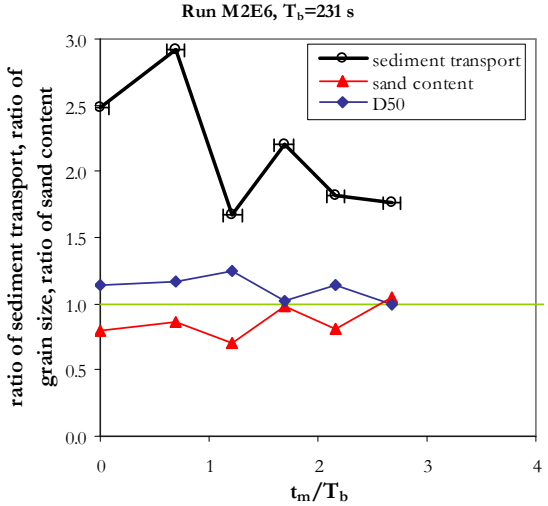

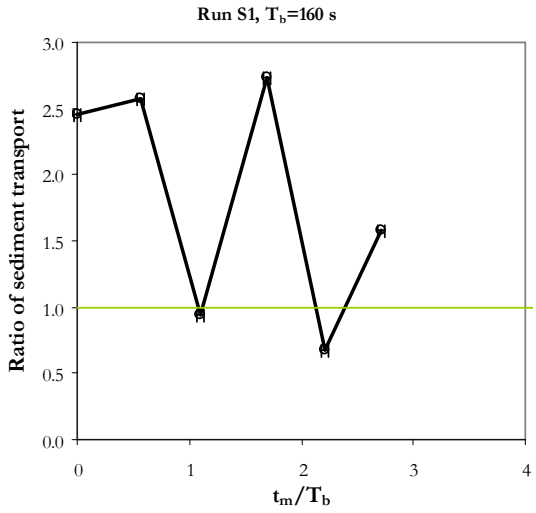
Run S1, T_b=160 s
Ratio of sediment transport
t_m/T_b
0.0
0.5
1.0
1.5
2.0
2.5
3.0
0
1
2
3
4

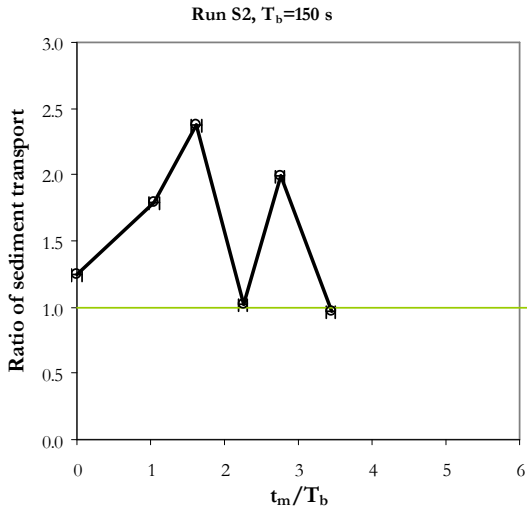
Run S2, T_b=150 s
Ratio of sediment transport
t_m/T_b
0.0
0.5
1.0
1.5
2.0
2.5
3.0
0
1
2
3
4
5
6

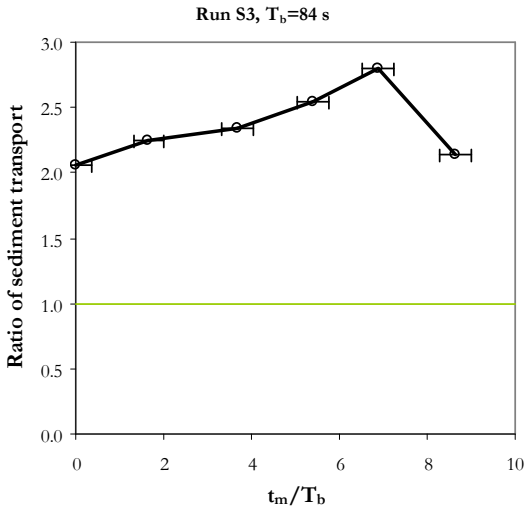
Run S3, T_b=84 s
Ratio of sediment transport
t_m/T_b
0.0
0.5
1.0
1.5
2.0
2.5
3.0
0
2
4
6
8
10

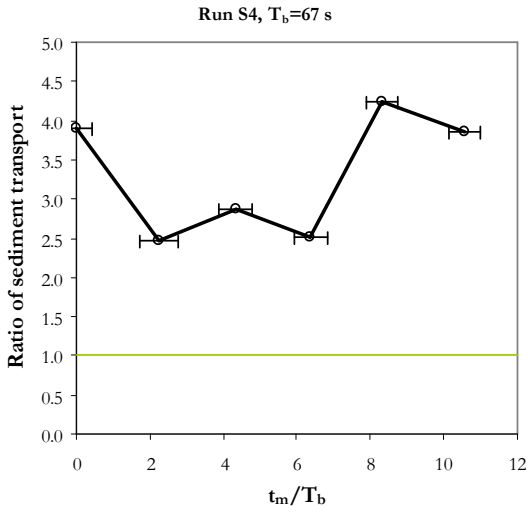
Run S4, T_b=67 s
Ratio of sediment transport
t_m/T_b
0.0
0.5
1.0
1.5
2.0
2.5
3.0
3.5
4.0
4.5
5.0
0
2
4
6
8
10
12

APPENDIX XI

BED EROSION PATTERNS

*Runs within the same series ordered from higher to lower sediment concentration.

MIXTURE 1 RUNS

RUN M1E2

RUN M1E3

RUN M1E4

RUN M1E5

RUN M1E1

RUN M1E6

MIXTURE 2 RUNS

RUN M2E1

RUN M2E2

RUN M2E3

RUN M2E4

RUN M2E5

RUN M2E6

SAND RUNS

RUN S1

RUN S2

RUN S3

RUN S4

APPENDIX XII

GRAIN-SIZE DISTRIBUTIONS FOR RUNS WITH SAND-GRAVEL MIXTURES

Grain size distributions presented in this Appendix correspond to runs performed with the two sand-gravel mixtures; sediment fed contained an average 32% sand content for mixture 1, and 45% sand content for mixture 2. Sieve analysis was performed as indicated in Appendix IV.

Grain size distributions correspond to the following classes of samples:

Feeder:	Bulk of samples collected form the sediment feeders throughout each run.
Original bed:	Bulk of samples collected from the bed material before the beginning of each run.
Basket-sampler, Center:	Bulk of sediment transport samples collected with the basket-type sampler in the central compartment.
Basket-sampler, Sides:	Bulk of sediment transport samples collected with the basket-type sampler in the two lateral compartments.
Helley-Smith:	Bulk of sediment transport samples collected with the Helley-Smith type sampler.
Bed substrate:	Bulk of samples collected from the subsurface bed material at the end of each run.
Bed surface:	Samples collected from the surface material at the end of each run. The corresponding morphological region is indicated and the longitudinal coordinate x, along the channel, where the sample was taken, as well. All these samples were converted to a volume-by-weight sample using the Marion and Fraccarollo (1997) conversion (see Section 3.3.2.6.4).

*Runs within the same series ordered from higher to lower sediment concentration.

MIXTURE 1

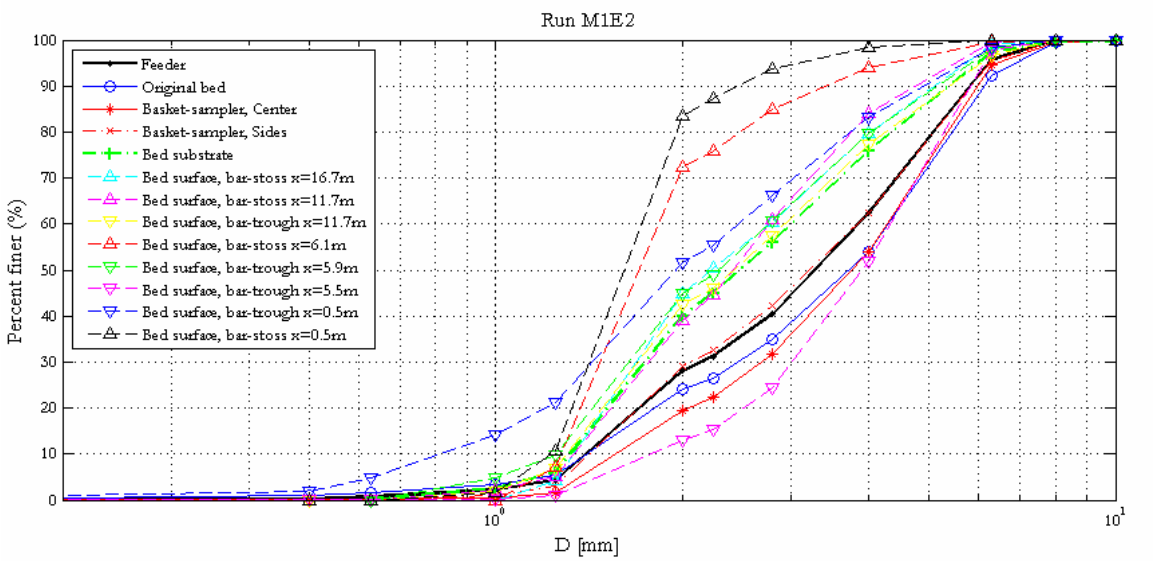
Run M1E2
Feeder
Original bed
Basket-sampler, Center
Basket-sampler, Sides
Bed substrate
Bed surface, bar-stoss x=16.7m
Bed surface, bar-stoss x=11.7m
Bed surface, bar-trough x=11.7m
Bed surface, bar-stoss x=6.1m
Bed surface, bar-trough x=5.9m
Bed surface, bar-trough x=5.5m
Bed surface, bar-trough x=0.5m
Bed surface, bar-stoss x=0.5m
Percent finer (%)
D [mm]

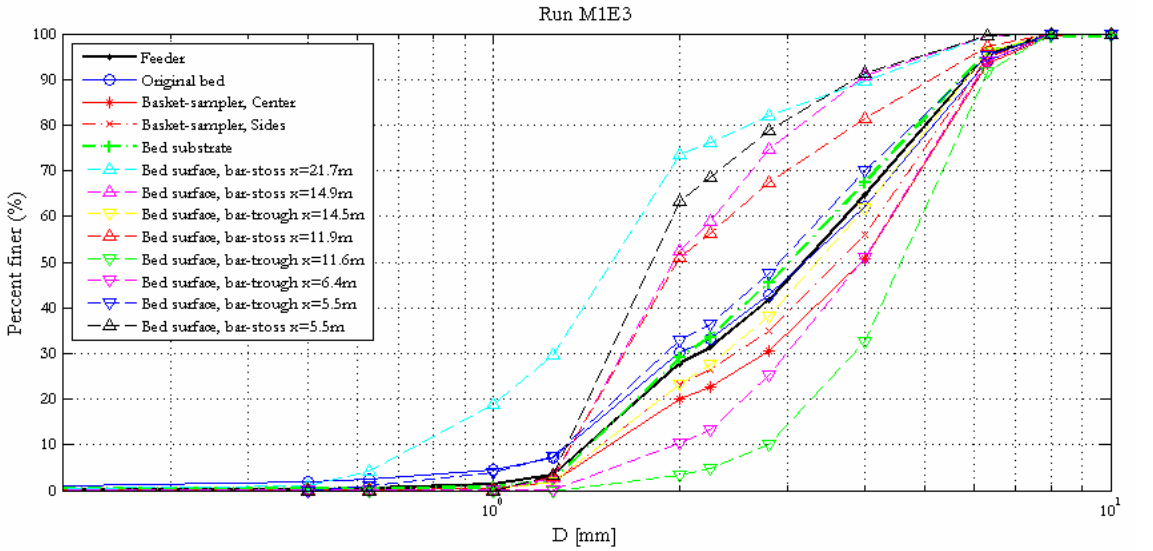
Run M1E3
Feeder
Original bed
Basket-sampler, Center
Basket-sampler, Sides
Bed substrate
Bed surface, bar-stoss x=21.7m
Bed surface, bar-stoss x=14.9m
Bed surface, bar-trough x=14.5m
Bed surface, bar-stoss x=11.9m
Bed surface, bar-trough x=11.6m
Bed surface, bar-trough x=6.4m
Bed surface, bar-trough x=5.5m
Bed surface, bar-stoss x=5.5m
Percent finer (%)
D [mm]

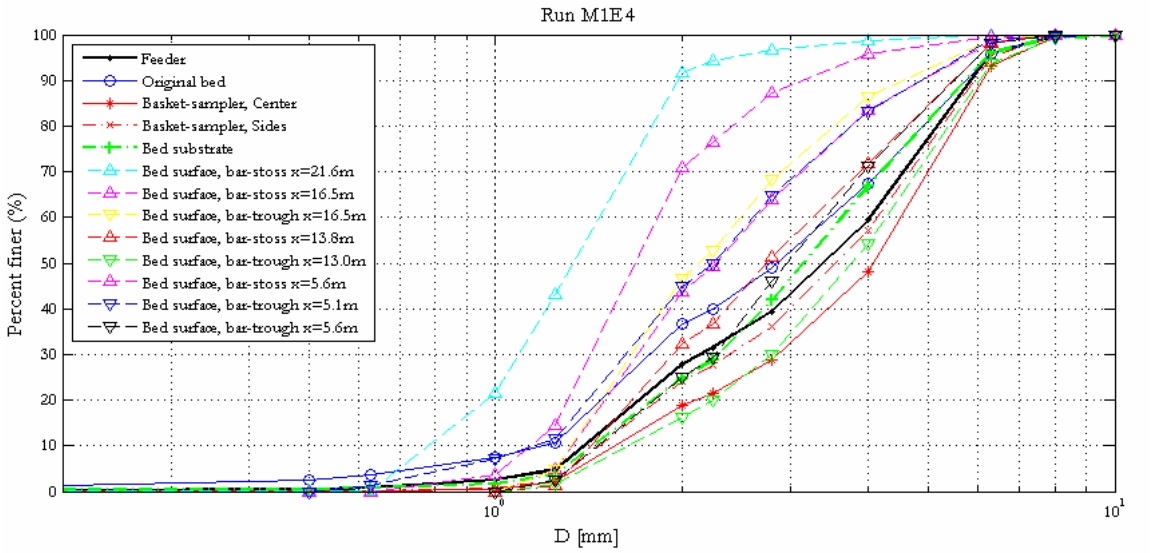
Run M1E4
Feeder
Original bed
Basket-sampler, Center
Basket-sampler, Sides
Bed substrate
Bed surface, bar-stoss x=21.6m
Bed surface, bar-stoss x=16.5m
Bed surface, bar-trough x=16.5m
Bed surface, bar-stoss x=13.8m
Bed surface, bar-trough x=13.0m
Bed surface, bar-stoss x=5.6m
Bed surface, bar-trough x=5.1m
Bed surface, bar-trough x=5.6m
Percent finer (%)
D [mm]

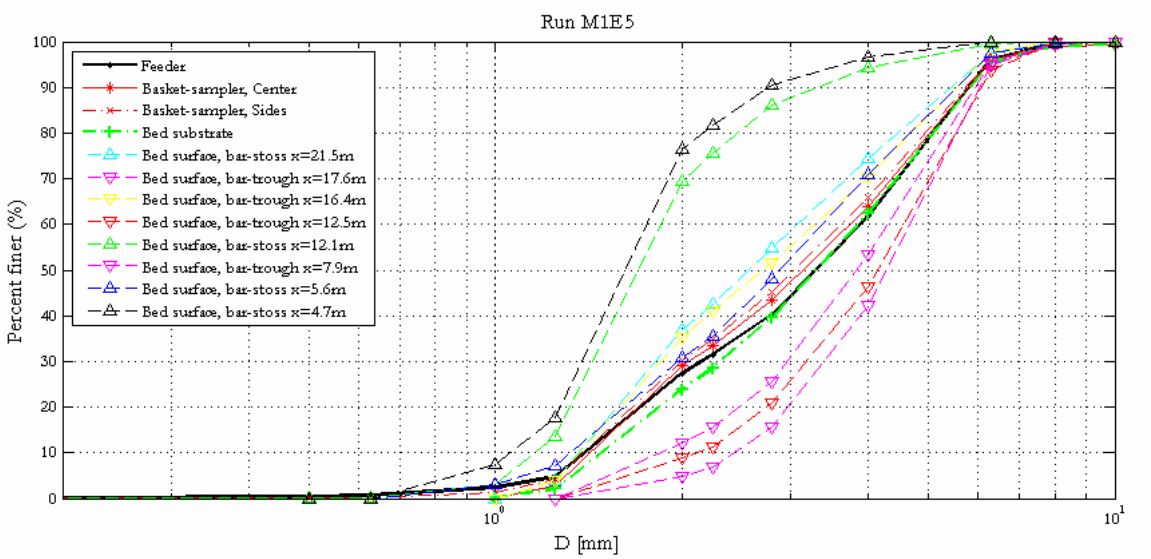
Run M1E5
Feeder
Basket-sampler, Center
Basket-sampler, Sides
Bed substrate
Bed surface, bar-stoss x=21.5m
Bed surface, bar-trough x=17.6m
Bed surface, bar-trough x=16.4m
Bed surface, bar-trough x=12.5m
Bed surface, bar-stoss x=12.1m
Bed surface, bar-trough x=7.9m
Bed surface, bar-stoss x=5.6m
Bed surface, bar-stoss x=4.7m
Percent finer (%)
D [mm]

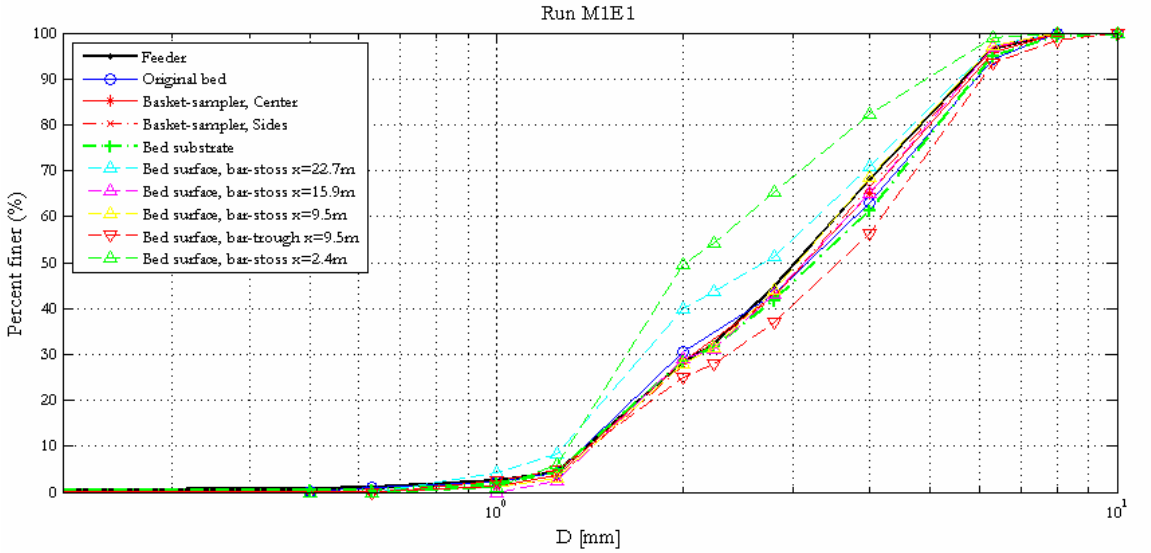
Run M1E1
Feeder
Original bed
Basket-sampler, Center
Basket-sampler, Sides
Bed substrate
Bed surface, bar-stoss x=22.7m
Bed surface, bar-stoss x=15.9m
Bed surface, bar-stoss x=9.5m
Bed surface, bar-trough x=9.5m
Bed surface, bar-stoss x=2.4m
Percent finer (%)
D [mm]

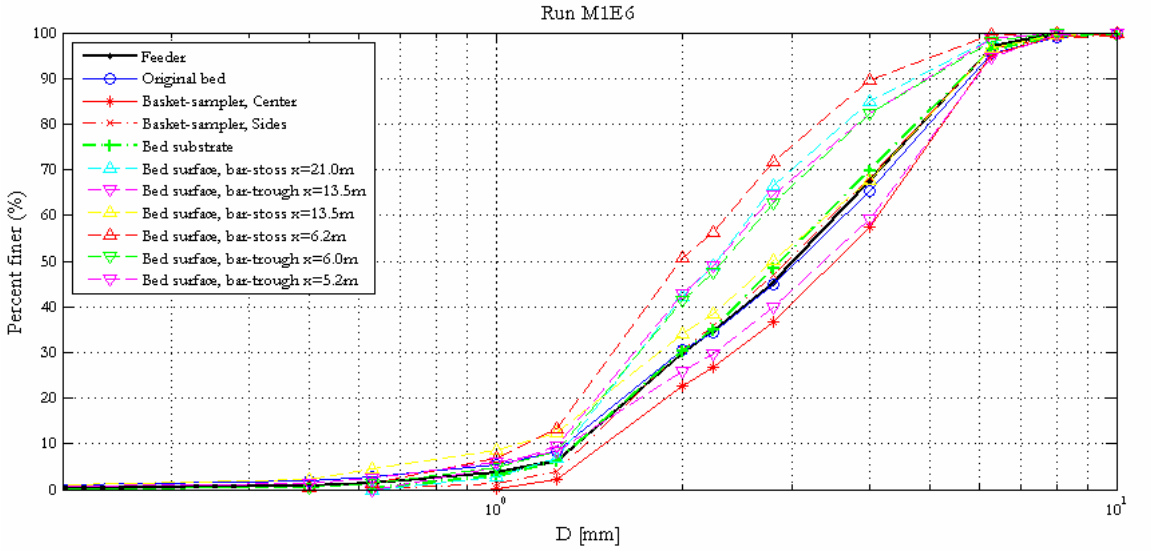
Run M1E6
Feeder
Original bed
Basket-sampler, Center
Basket-sampler, Sides
Bed substrate
Bed surface, bar-stoss x=21.0m
Bed surface, bar-trough x=13.5m
Bed surface, bar-stoss x=13.5m
Bed surface, bar-stoss x=6.2m
Bed surface, bar-trough x=6.0m
Bed surface, bar-trough x=5.2m
Percent finer (%)
D [mm]

MIXTURE 2

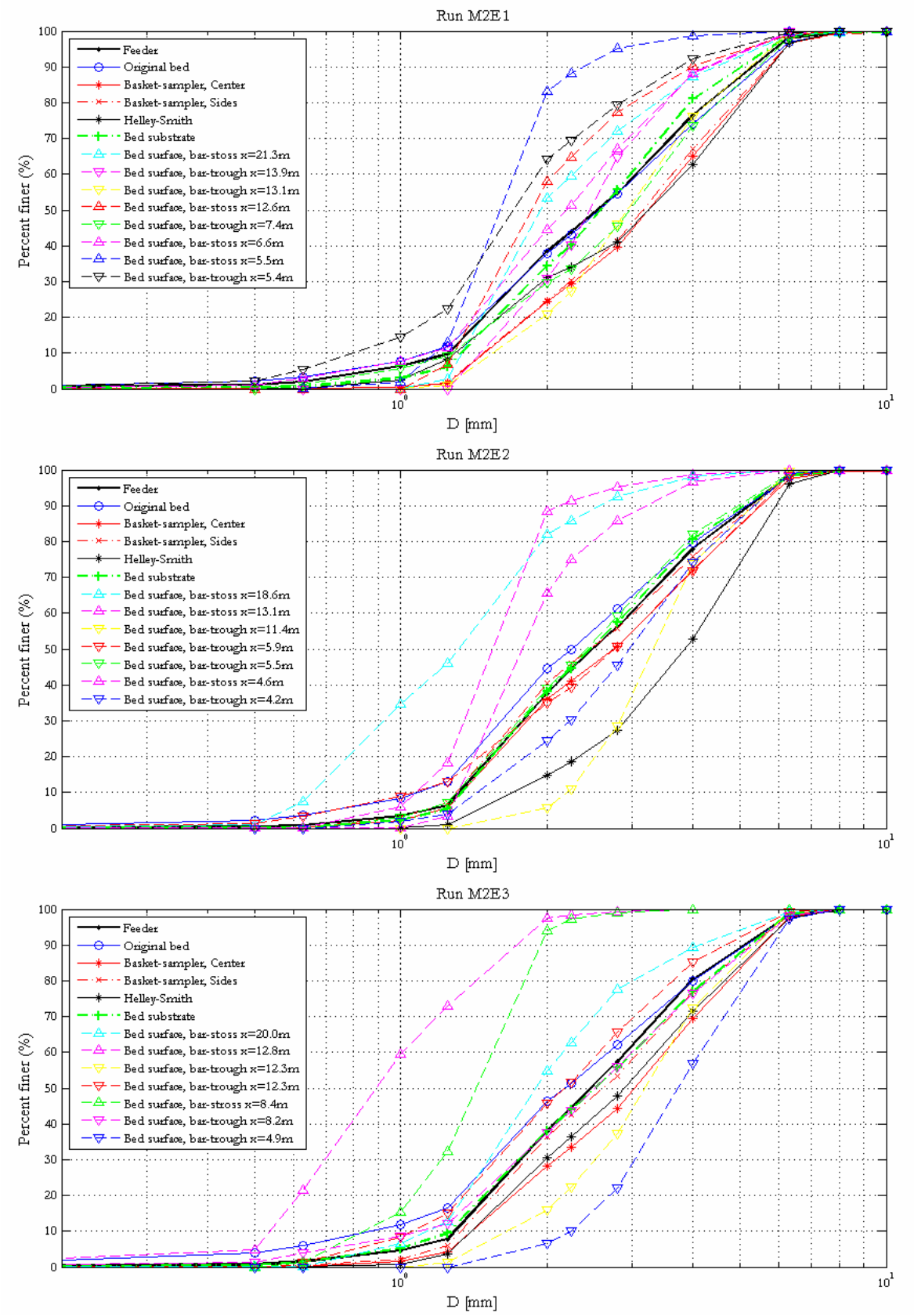
Run M2E1
Feeder
Original bed
Basket-sampler, Center
Basket-sampler, Sides
Helley-Smith
Bed substrate
Bed surface, bar-stoss x=21.3m
Bed surface, bar-trough x=13.9m
Bed surface, bar-trough x=13.1m
Bed surface, bar-stoss x=12.6m
Bed surface, bar-trough x=7.4m
Bed surface, bar-stoss x=6.6m
Bed surface, bar-stoss x=5.5m
Bed surface, bar-trough x=5.4m
Percent finer (%)
D [mm]
Run M2E2
Feeder
Original bed
Basket-sampler, Center
Basket-sampler, Sides
Helley-Smith
Bed substrate
Bed surface, bar-stoss x=18.6m
Bed surface, bar-stoss x=13.1m
Bed surface, bar-trough x=11.4m
Bed surface, bar-trough x=5.9m
Bed surface, bar-trough x=5.5m
Bed surface, bar-stoss x=4.6m
Bed surface, bar-trough x=4.2m
Percent finer (%)
D [mm]
Run M2E3
Feeder
Original bed
Basket-sampler, Center
Basket-sampler, Sides
Helley-Smith
Bed substrate
Bed surface, bar-stoss x=20.0m
Bed surface, bar-stoss x=12.8m
Bed surface, bar-trough x=12.3m
Bed surface, bar-trough x=12.3m
Bed surface, bar-stross x=8.4m
Bed surface, bar-trough x=8.2m
Bed surface, bar-trough x=4.9m
Percent finer (%)
D [mm]

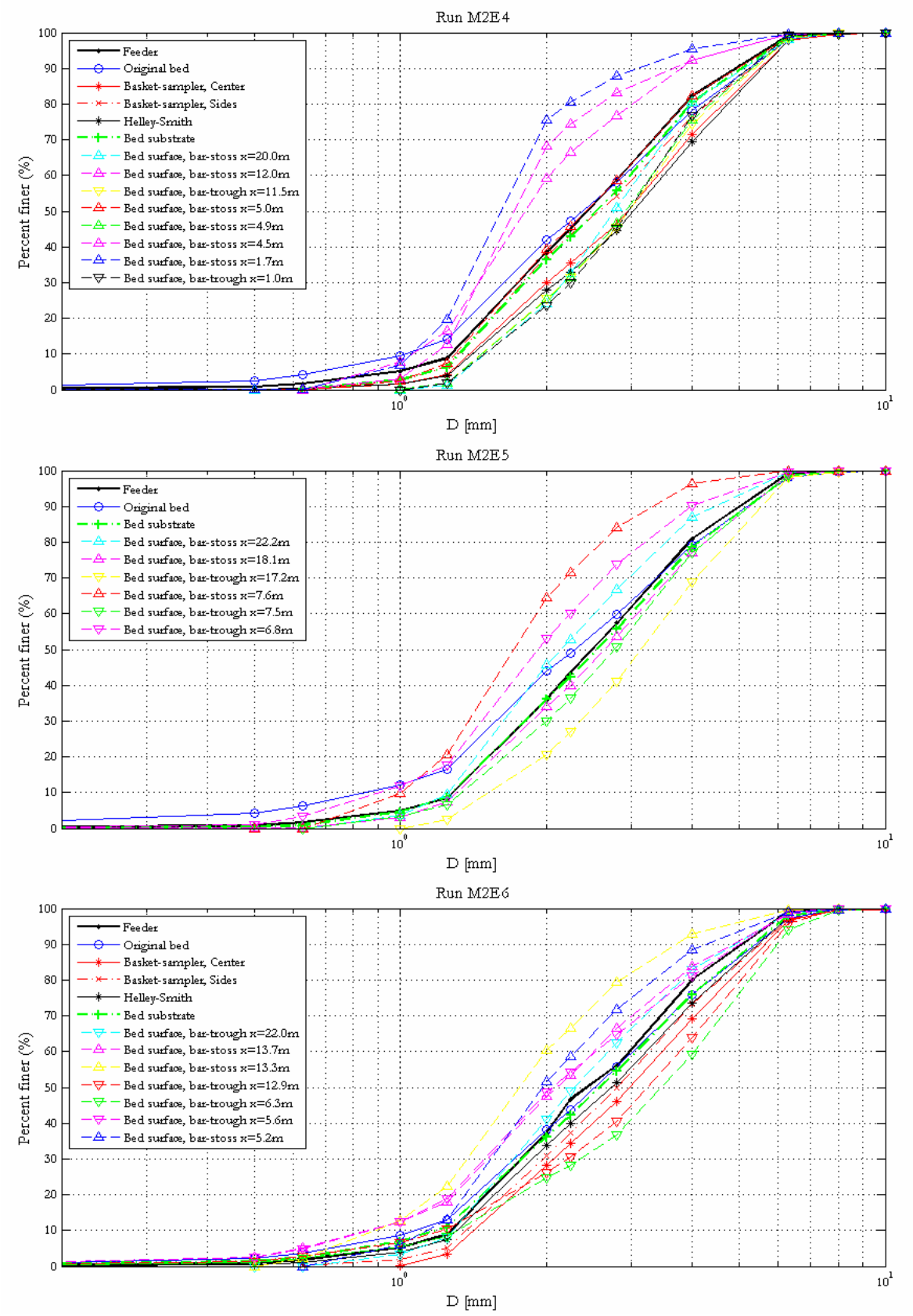
Run M2E4
Feeder
Original bed
Basket-sampler, Center
Basket-sampler, Sides
Helley-Smith
Bed substrate
Bed surface, bar-stoss x=20.0m
Bed surface, bar-stoss x=12.0m
Bed surface, bar-trough x=11.5m
Bed surface, bar-stoss x=5.0m
Bed surface, bar-stoss x=4.9m
Bed surface, bar-stoss x=4.5m
Bed surface, bar-stoss x=1.7m
Bed surface, bar-trough x=1.0m
Percent finer (%)
D [mm]
Run M2E5
Feeder
Original bed
Bed substrate
Bed surface, bar-stoss x=22.2m
Bed surface, bar-stoss x=18.1m
Bed surface, bar-trough x=17.2m
Bed surface, bar-stoss x=7.6m
Bed surface, bar-trough x=7.5m
Bed surface, bar-trough x=6.8m
Percent finer (%)
D [mm]
Run M2E6
Feeder
Original bed
Basket-sampler, Center
Basket-sampler, Sides
Helley-Smith
Bed substrate
Bed surface, bar-trough x=22.0m
Bed surface, bar-stoss x=13.7m
Bed surface, bar-stoss x=13.3m
Bed surface, bar-trough x=12.9m
Bed surface, bar-trough x=6.3m
Bed surface, bar-trough x=5.6m
Bed surface, bar-stoss x=5.2m
Percent finer (%)
D [mm]

APPENDIX XIII

TIME-VARIATION OF PARAMETERS FROM BED AND WATER PROFILES

See section 3.4.1 for a detail description of procedures used to determine the variables for the plots presented in this Appendix. These plots were obtained from the experimentally measured bed and water surface profiles. Each graph presents results for two different methods applied to the same set of data. Description of symbols used for each method and each variable is given in the following table:

Method	**Lines**	**Slope and water depth**	**Bed standard deviation**	**Water standard deviation**
1	Continuous	Red line with crosses	Red line with crosses	Blue line with open circles
2	Dashed	Blue line with open squares	Red line with asterisks	Blue line with open squares

A green vertical line indicates time for which the first profile in equilibrium state was considered.

*Runs ordered from higher to lower sediment concentration.

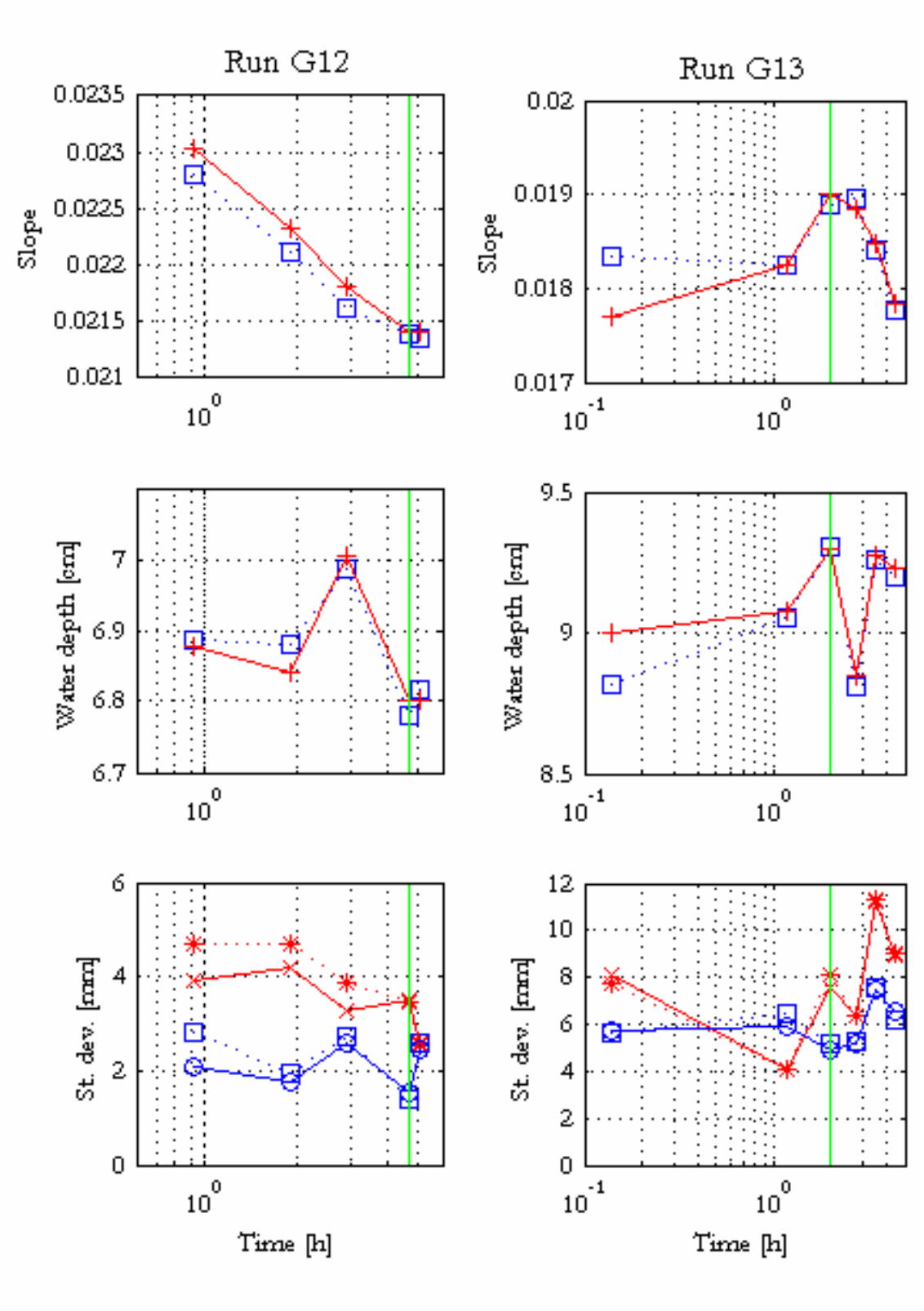
Run G12
Run G13
Slope
Water depth [cm]
St. dev. [mm]
Time [h]

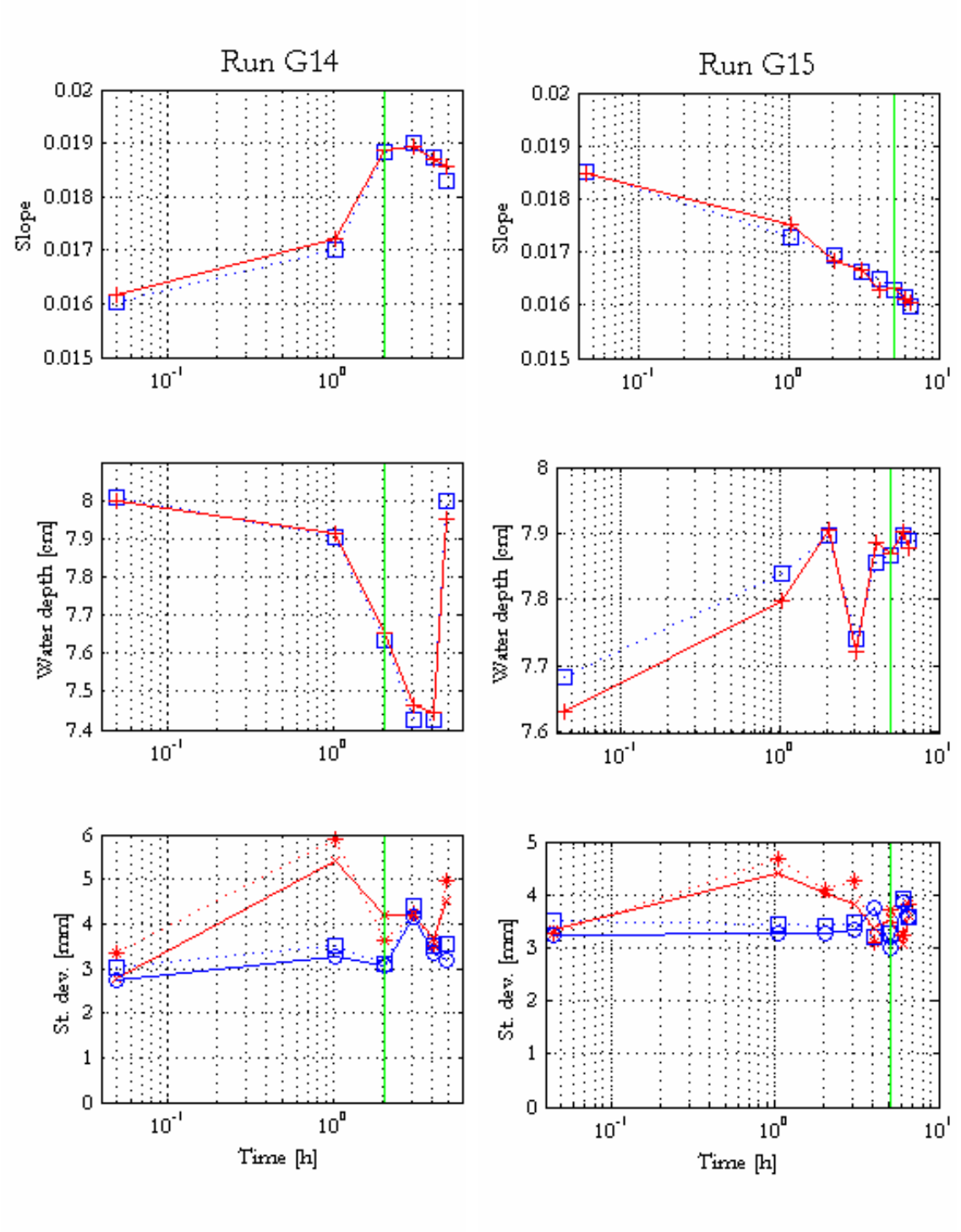
Run G14
Run G15
Slope
Water depth [cm]
St. dev. [mm]
Time [h]

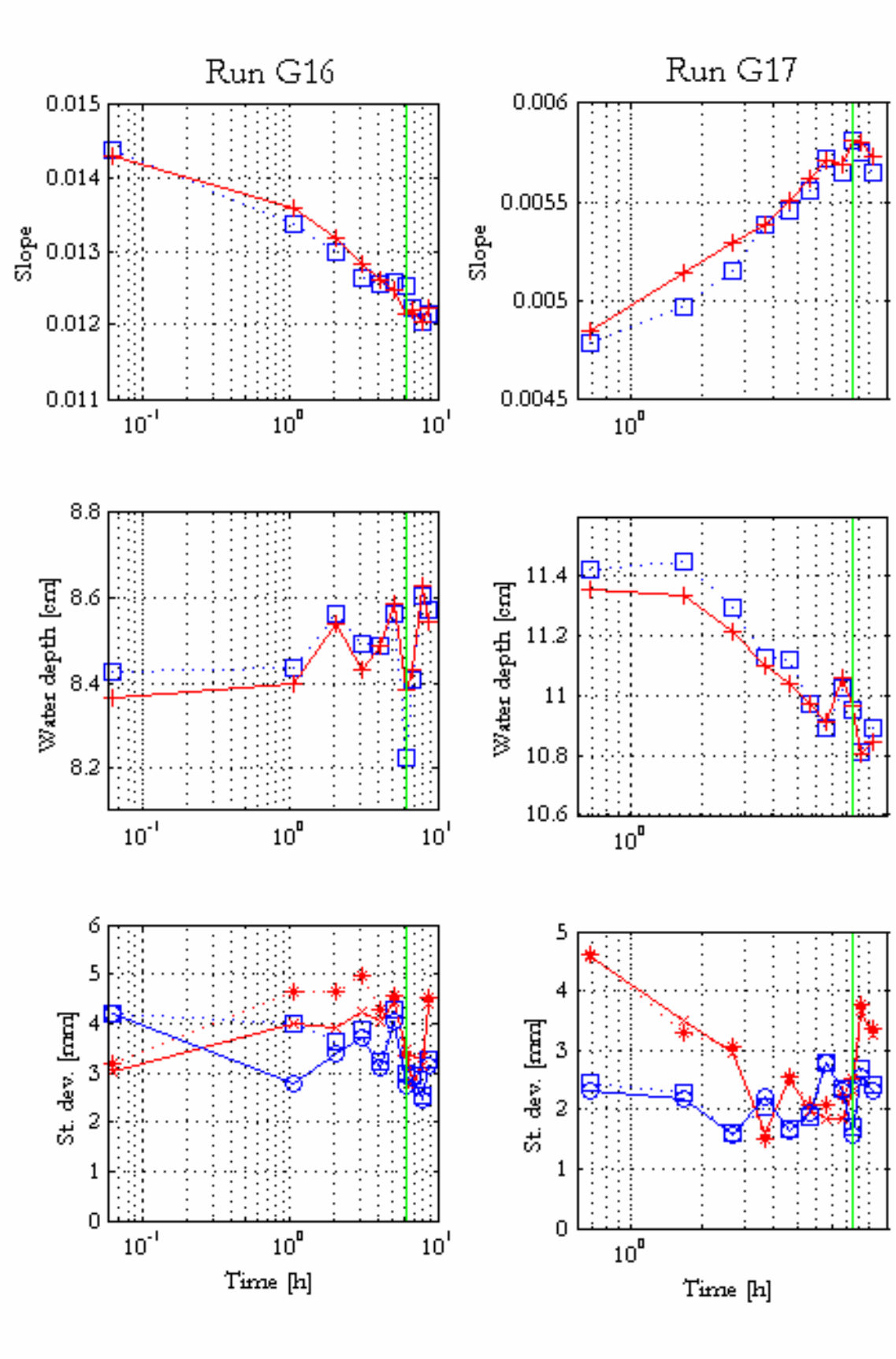
Run G16
Run G17
Slope
Water depth [cm]
St. dev. [mm]
Time [h]

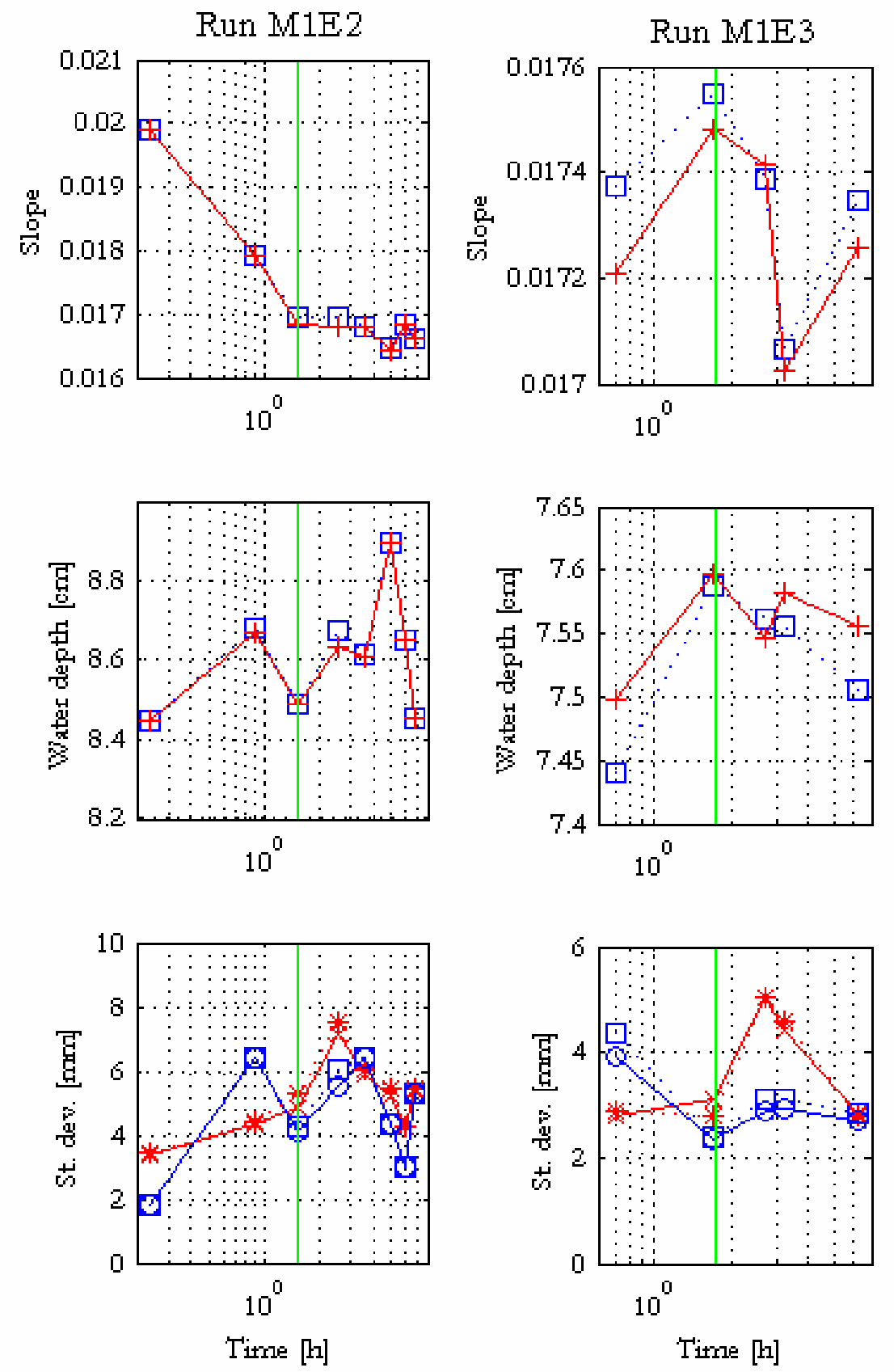
Run M1E2
Run M1E3
Slope
Water depth [cm]
St. dev. [mm]
Time [h]
0.021
0.02
0.019
0.018
0.017
0.016
0.0176
0.0174
0.0172
0.017
8.8
8.6
8.4
8.2
7.65
7.6
7.55
7.5
7.45
7.4
10
8
6
4
2
0
10^0

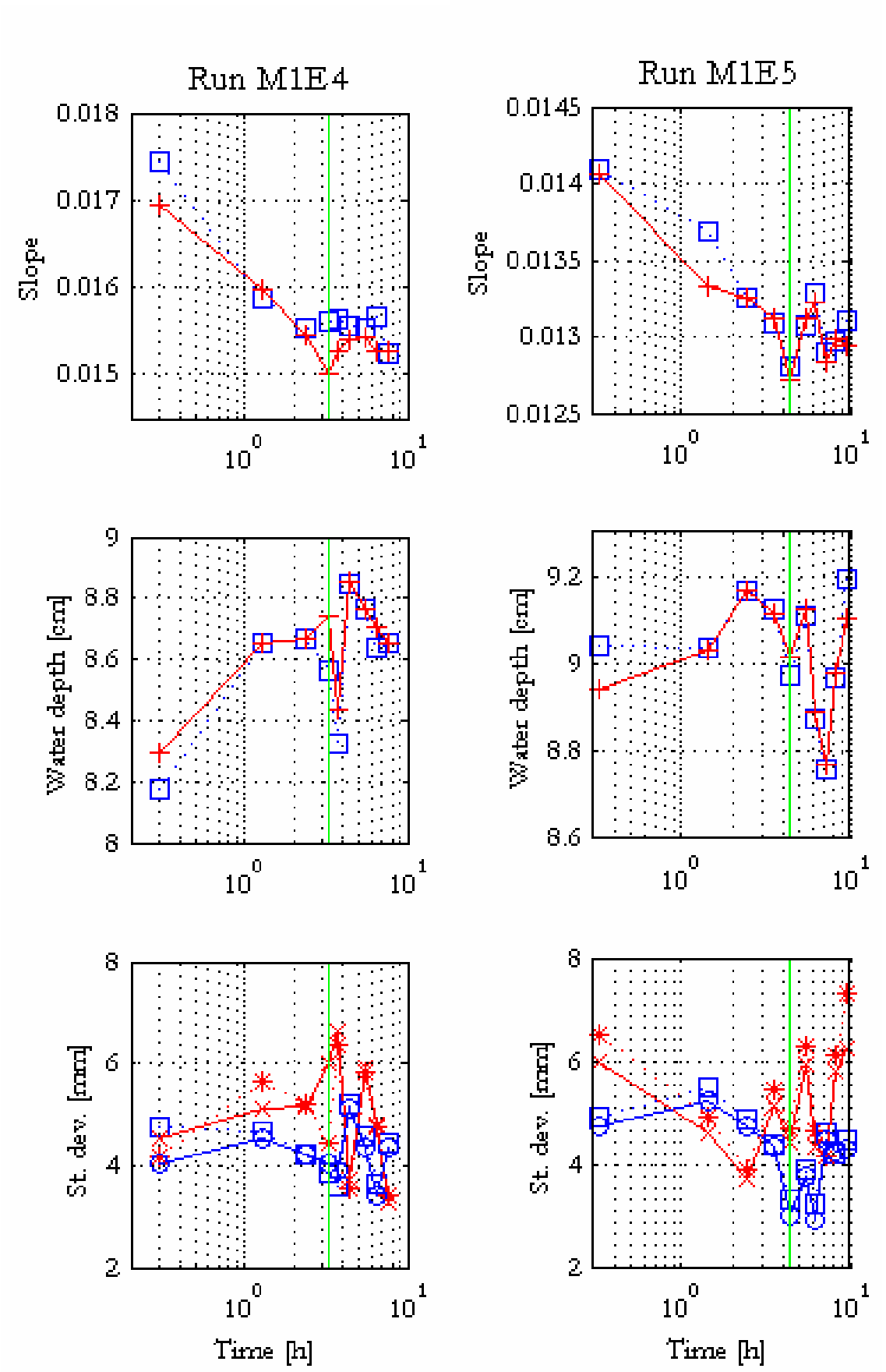
Run M1E4
Run M1E5
Slope
Water depth [cm]
St. dev. [mm]
Time [h]

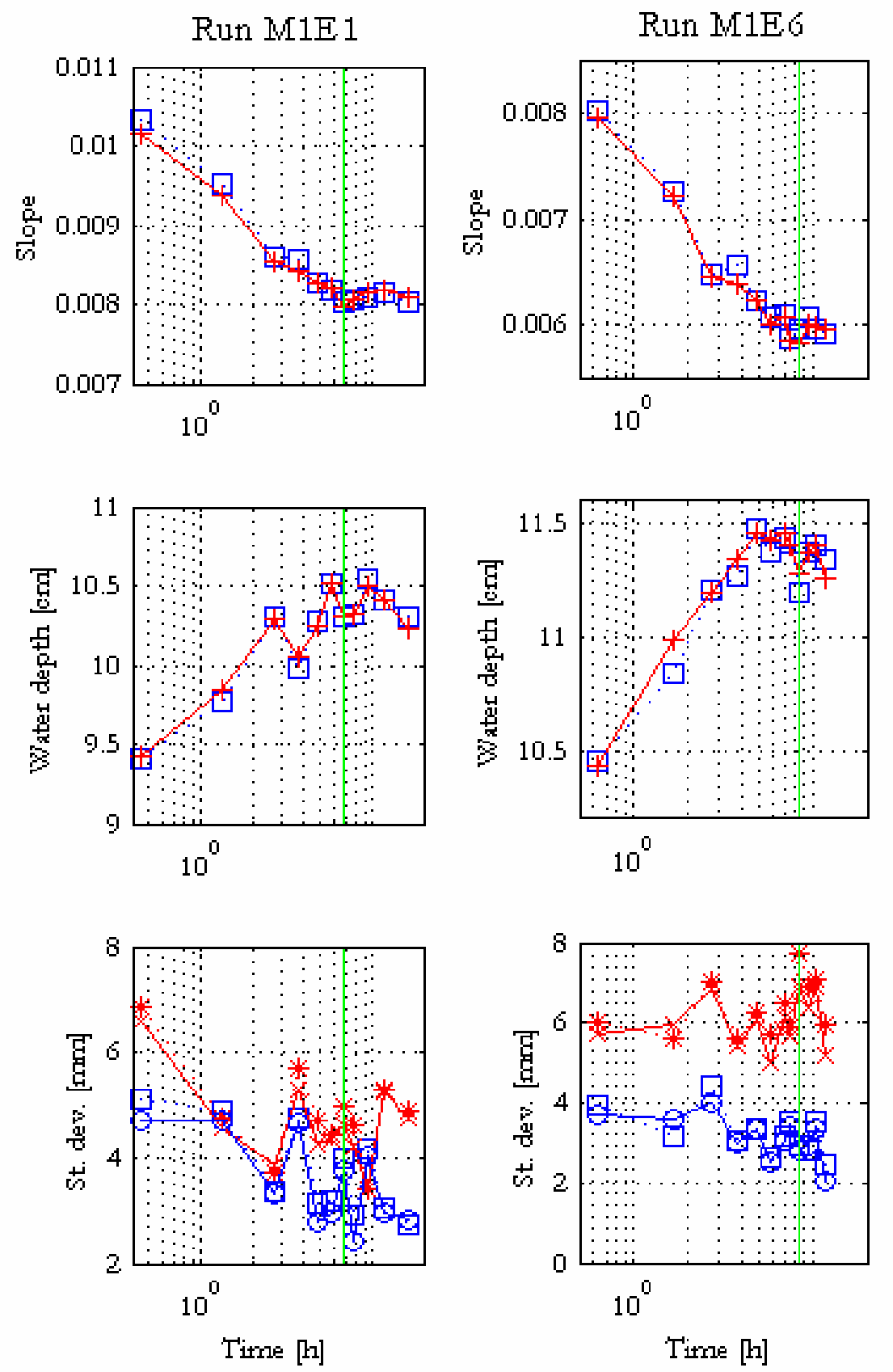
Run M1E1
Run M1E6
Slope
Water depth [cm]
St. dev. [mm]
Time [h]
0.011
0.01
0.009
0.008
0.007
0.006
11
10.5
10
9.5
9
11.5
8
6
4
2
0
10^0

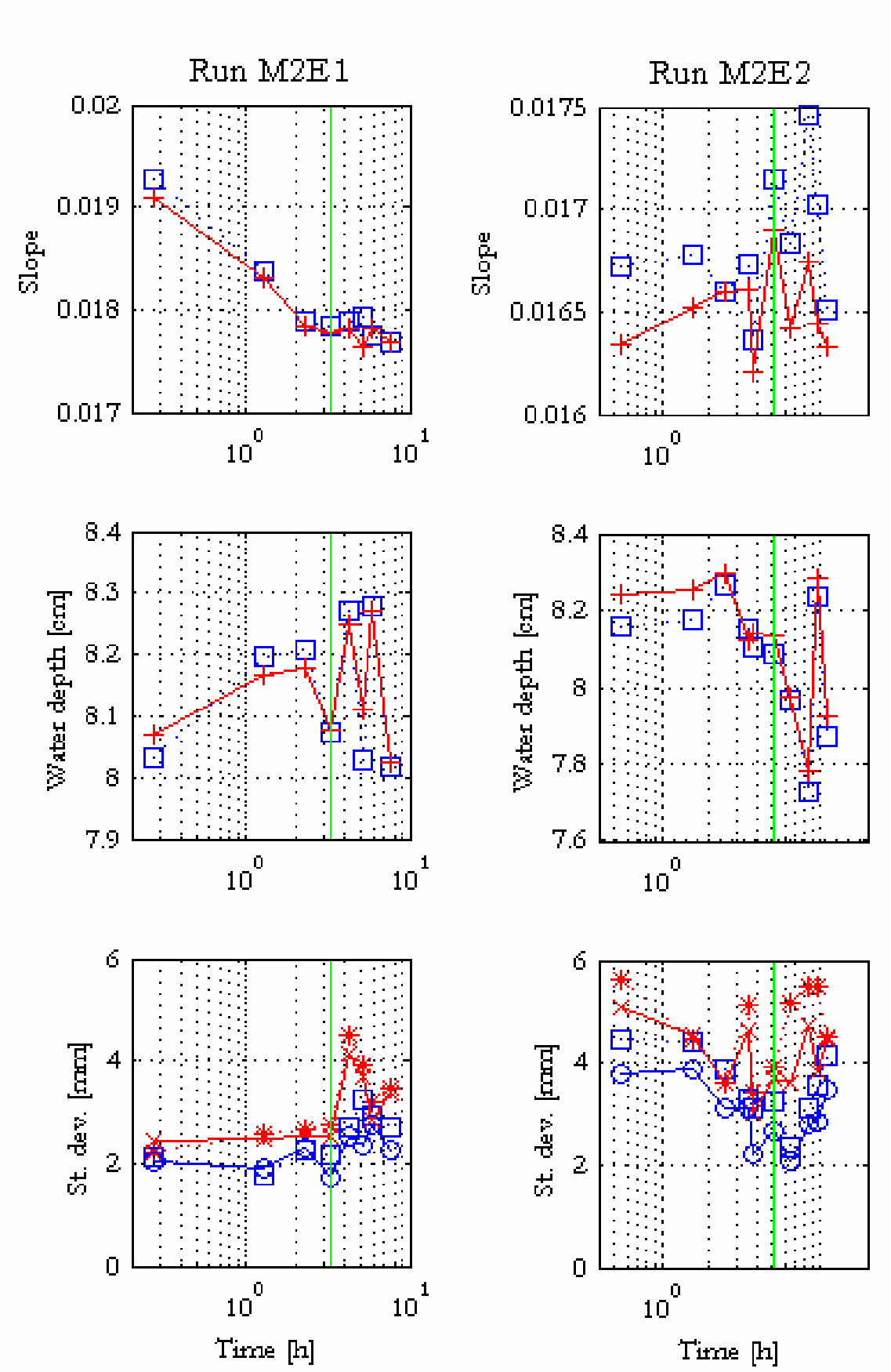
Run M2E1
Run M2E2
Slope
Water depth [cm]
St. dev. [mm]
Time [h]
0.02
0.019
0.018
0.017
0.0175
0.016
0.0165
8.4
8.3
8.2
8.1
8
7.9
7.8
7.6
6
4
2
0
10^0
10^1

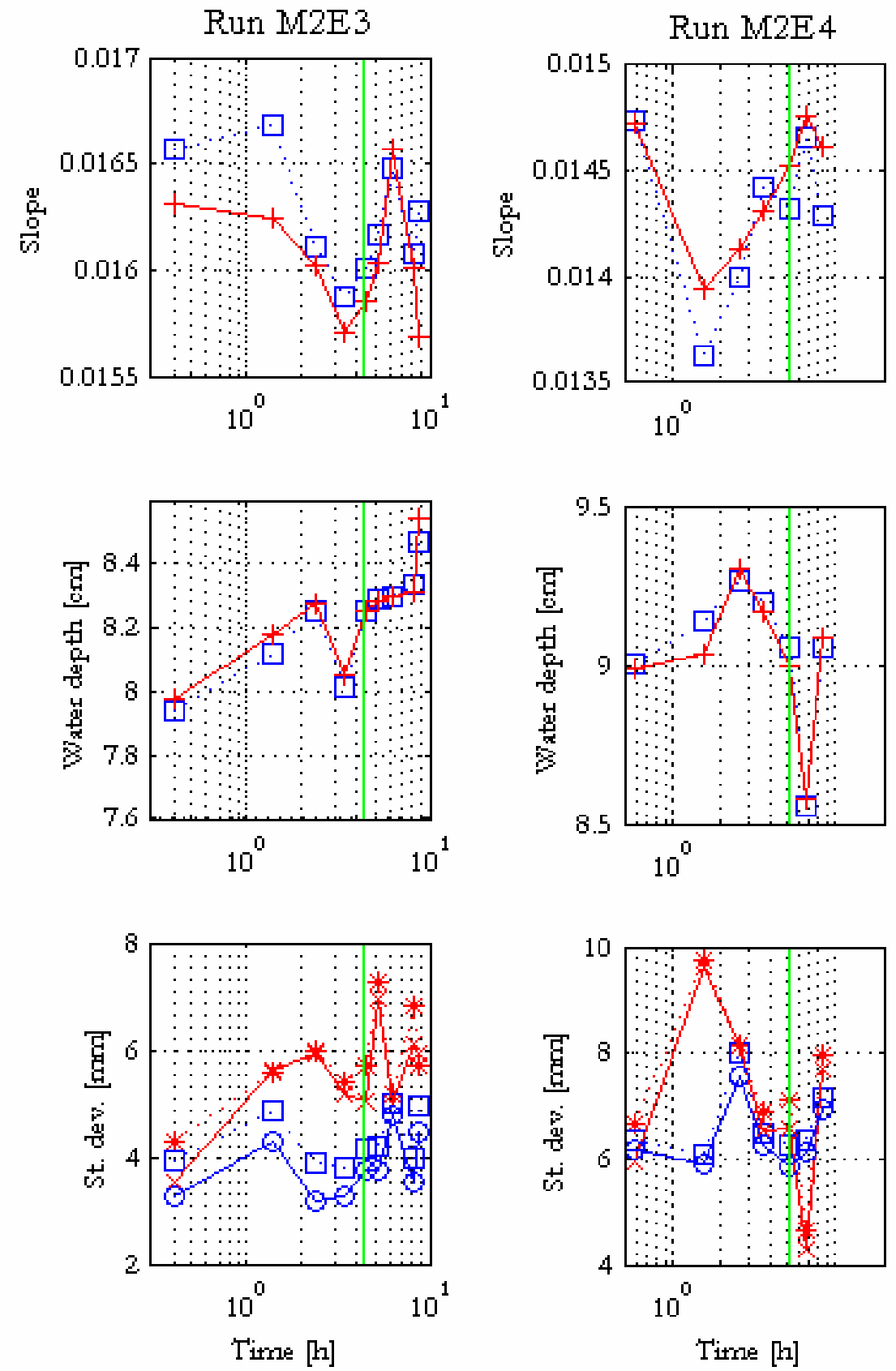
Run M2E3
Run M2E4
Slope
0.017
0.0165
0.016
0.0155
0.015
0.0145
0.014
0.0135
Water depth [cm]
8.4
8.2
8
7.8
7.6
9.5
9
8.5
St. dev. [mm]
8
6
4
2
10
8
6
4
10^0
10^1
Time [h]

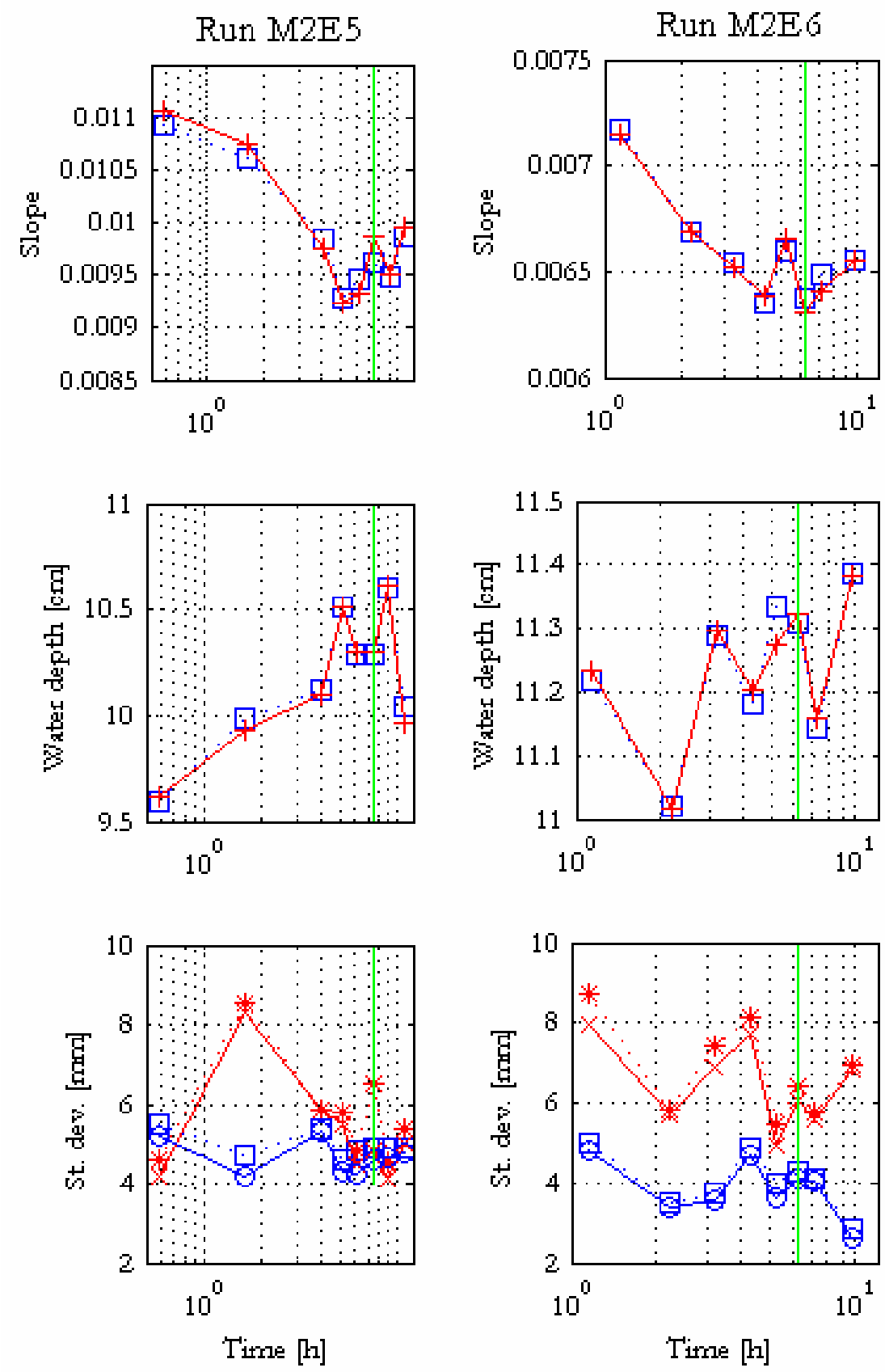
Run M2E5
Run M2E6
Slope
Water depth [cm]
St. dev. [mm]
Time [h]

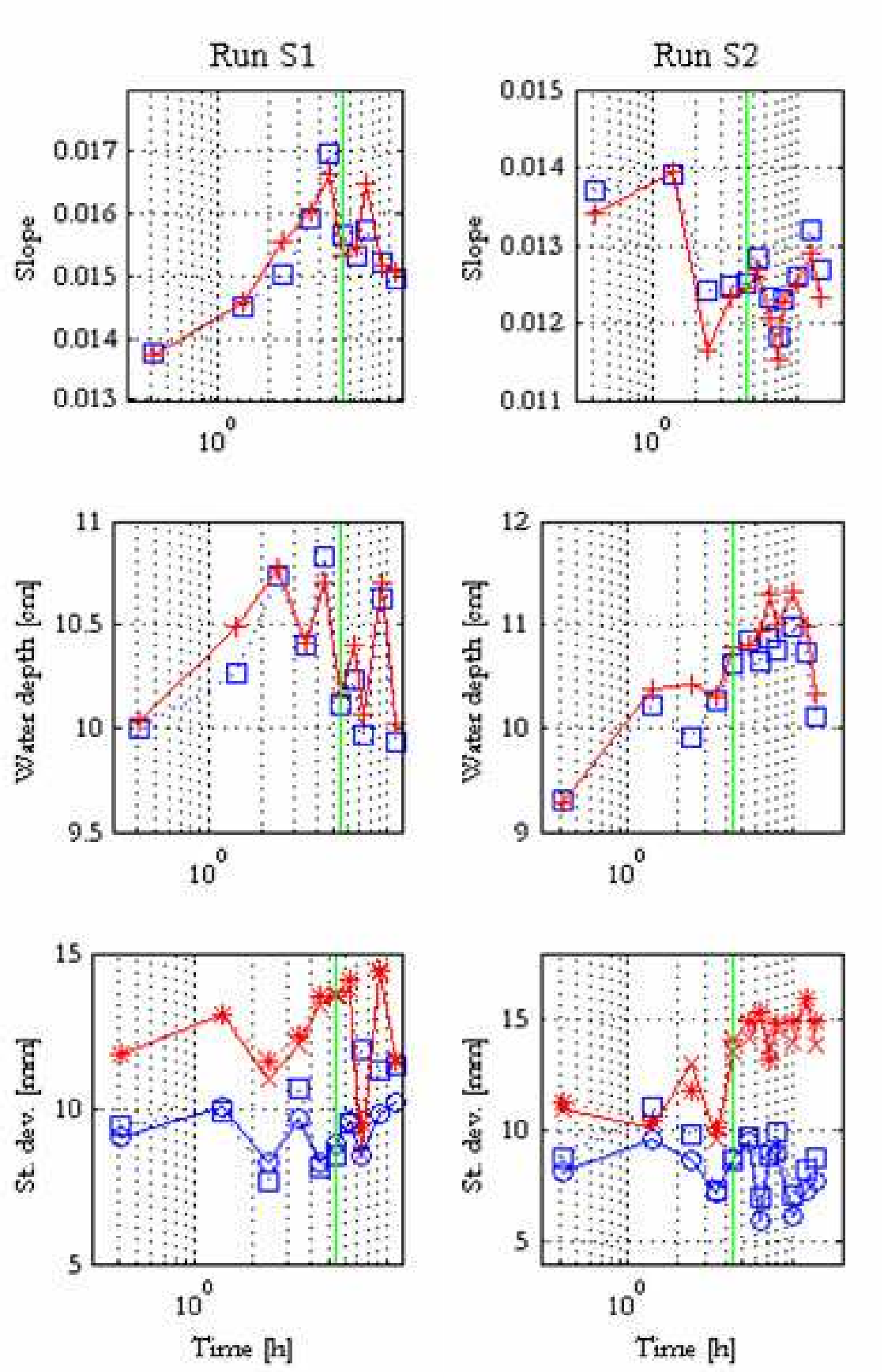
Run S1
Run S2
Slope
0.017
0.016
0.015
0.014
0.013
0.015
0.014
0.013
0.012
0.011
Water depth [cm]
11
10.5
10
9.5
12
11
10
9
St. dev. [mm]
15
10
5
15
10
5
10^0
Time [h]

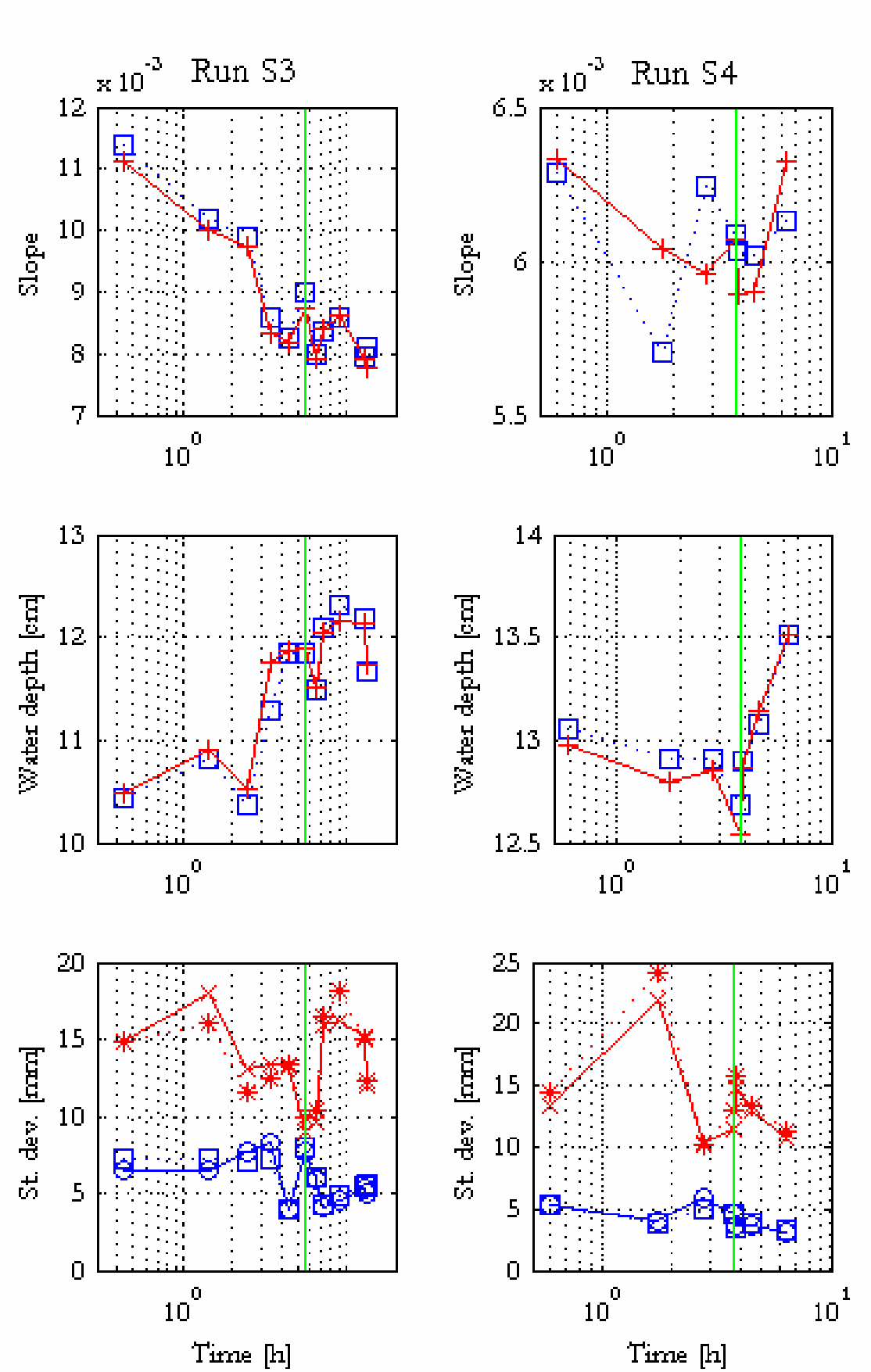
x 10^-3 Run S3
Slope
x 10^-3 Run S4
Slope
Water depth [cm]
Water depth [cm]
St. dev. [mm]
St. dev. [mm]
Time [h]
Time [h]

APPENDIX XIV

EQUILIBRIUM STATE
BED AND WATER PROFILES

Graphs in this Appendix correspond to measurements performed strictly during the considered equilibrium state (see section 3.4.2 for a description of criteria used to test equilibrium). The graphs show the measured bed and water surface elevations, and the computed elevation of the energy gradient. Additionally, best-fit lines are shown for each of the profiles measured in equilibrium state and an average best-fit line representative of equilibrium state.

Explanation of symbols used in the graphs:

- Black asterisks: Elevation of the energy gradient, determined with eq.(3.33)
- Blue circles: Measured water surface elevation
- Red x's: Measured bed surface elevation
- Thick continuous line: Bottom of the channel
- Dashed lines: best-fit lines for each of the profiles in equilibrium state
- Black continuous lines: Average best-fit line representative of equilibrium state

Runs within the same series, ordered from higher to lower sediment concentration.

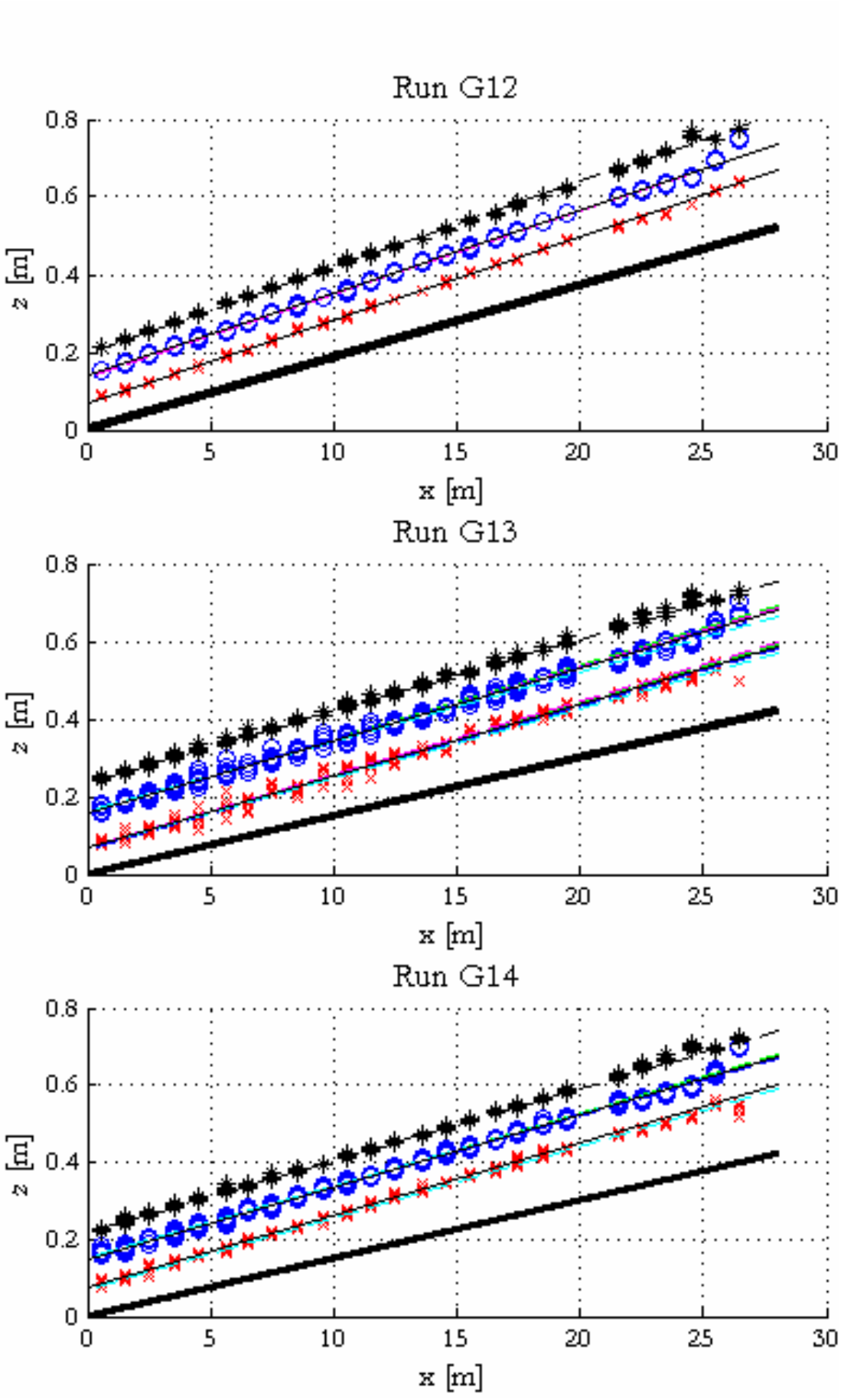
Run G12
z [m]
x [m]
Run G13
z [m]
x [m]
Run G14
z [m]
x [m]

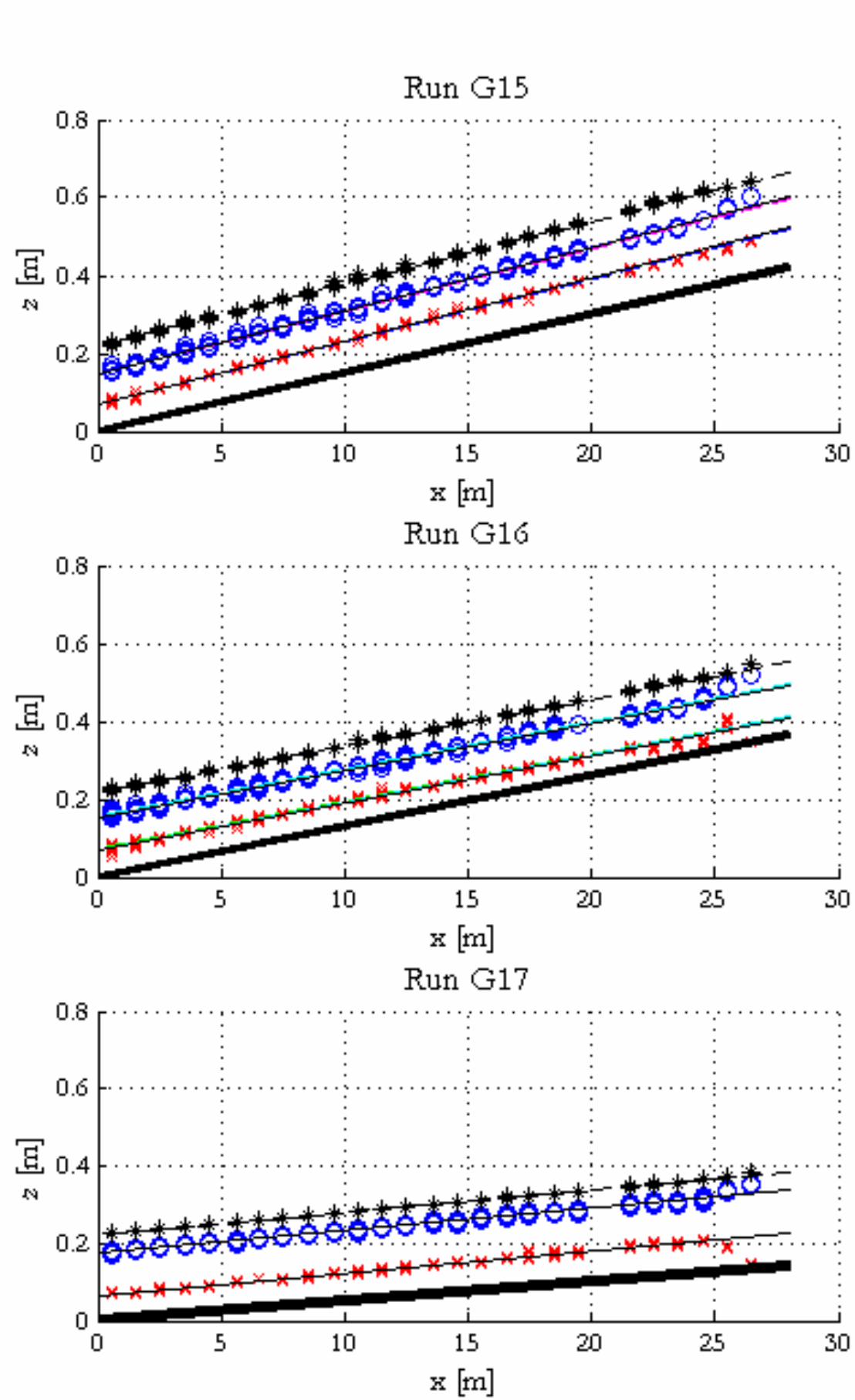
Run G15
z [m]
x [m]
Run G16
z [m]
x [m]
Run G17
z [m]
x [m]

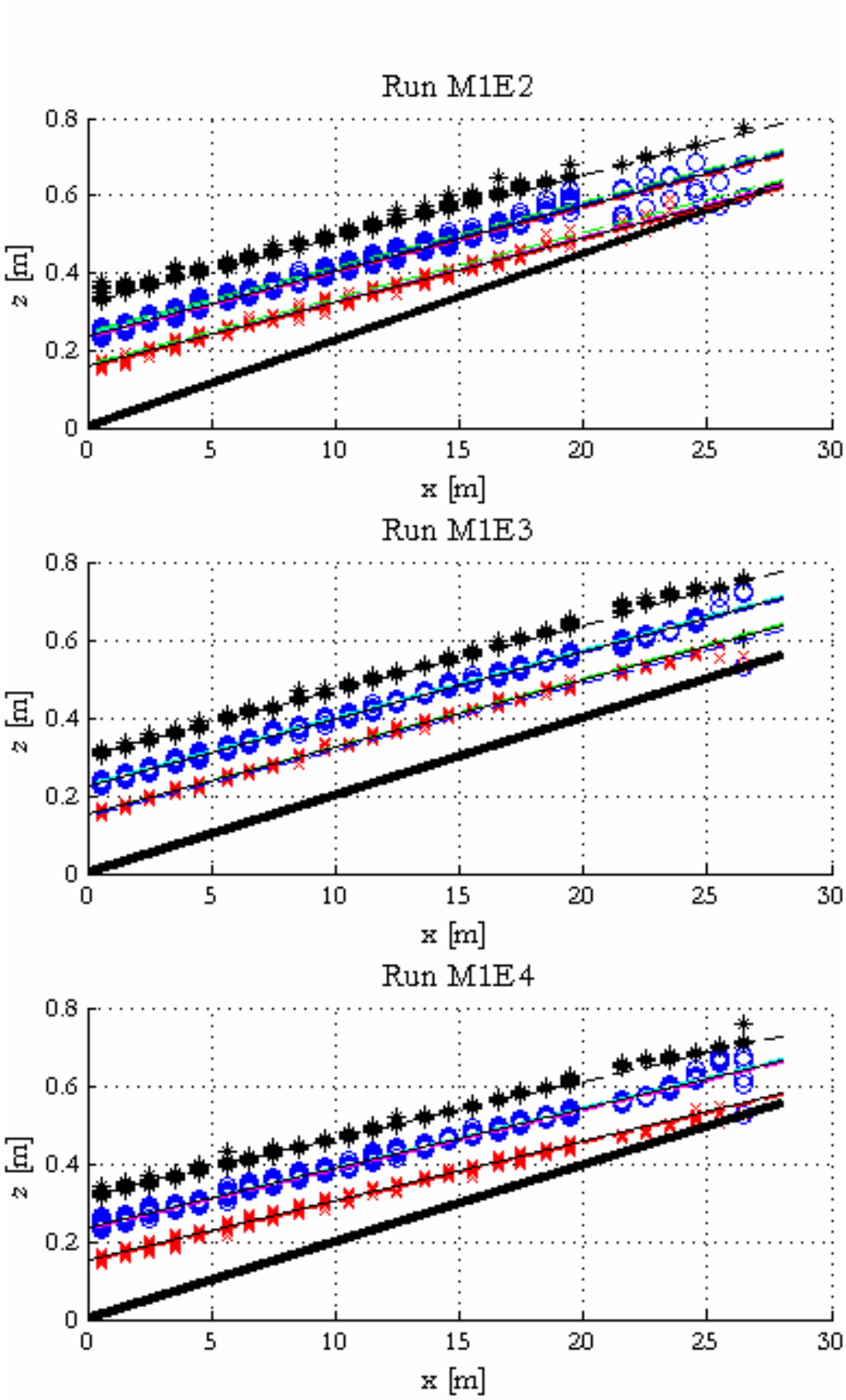
Run M1E2
z [m]
x [m]
Run M1E3
z [m]
x [m]
Run M1E4
z [m]
x [m]

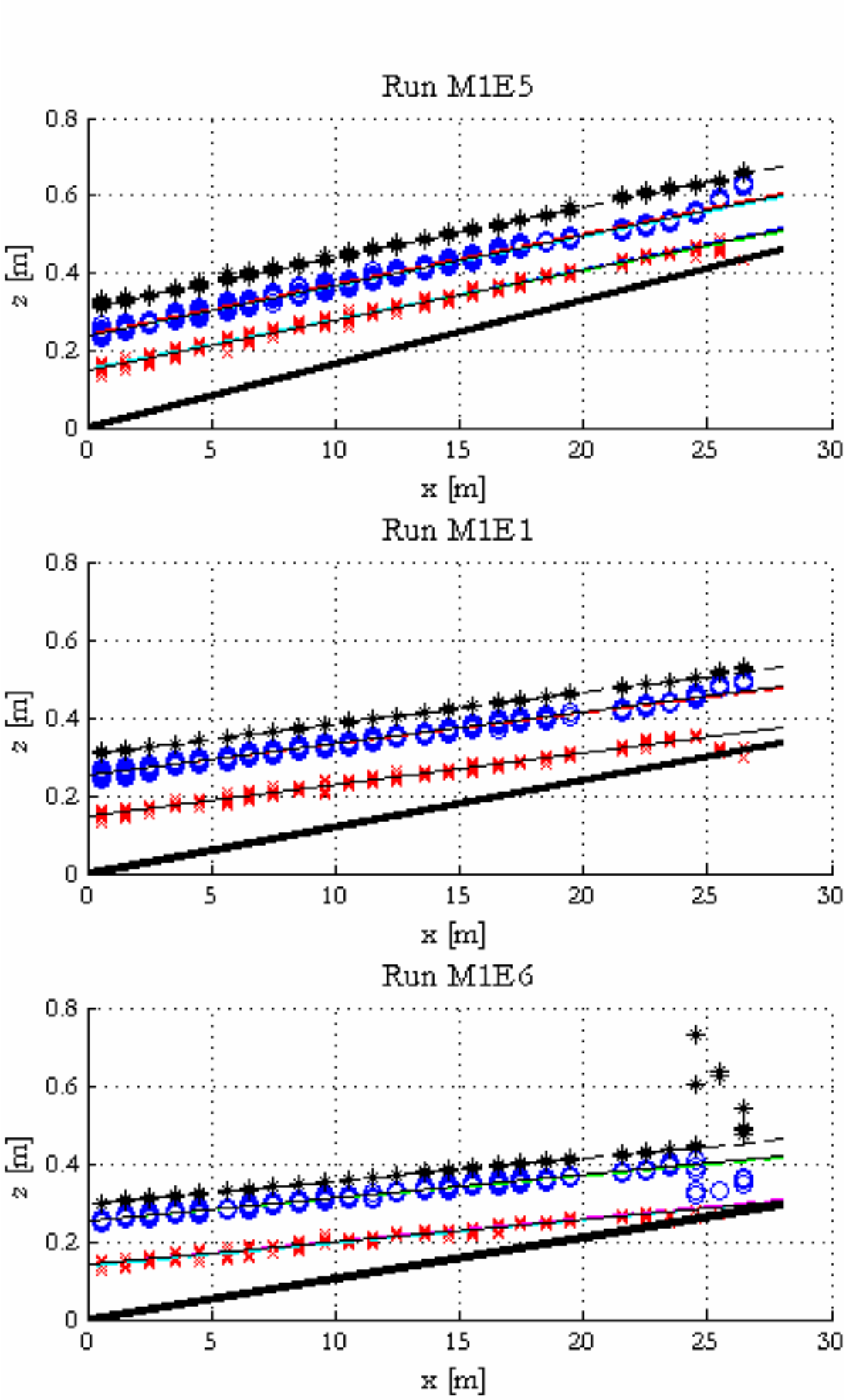
Run M1E5
z [m]
x [m]
Run M1E1
z [m]
x [m]
Run M1E6
z [m]
x [m]

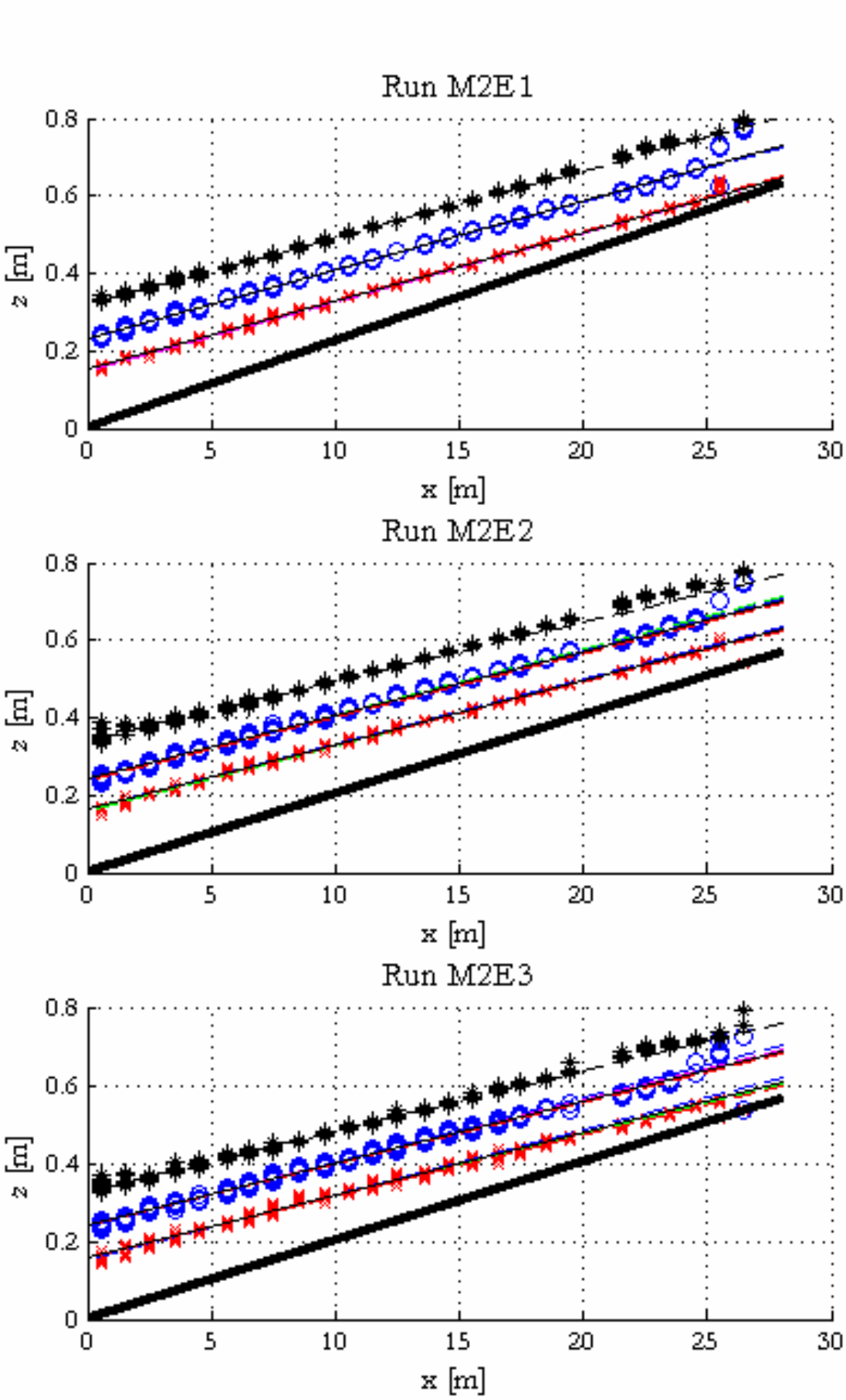
Run M2E1
z [m]
x [m]
Run M2E2
z [m]
x [m]
Run M2E3
z [m]
x [m]

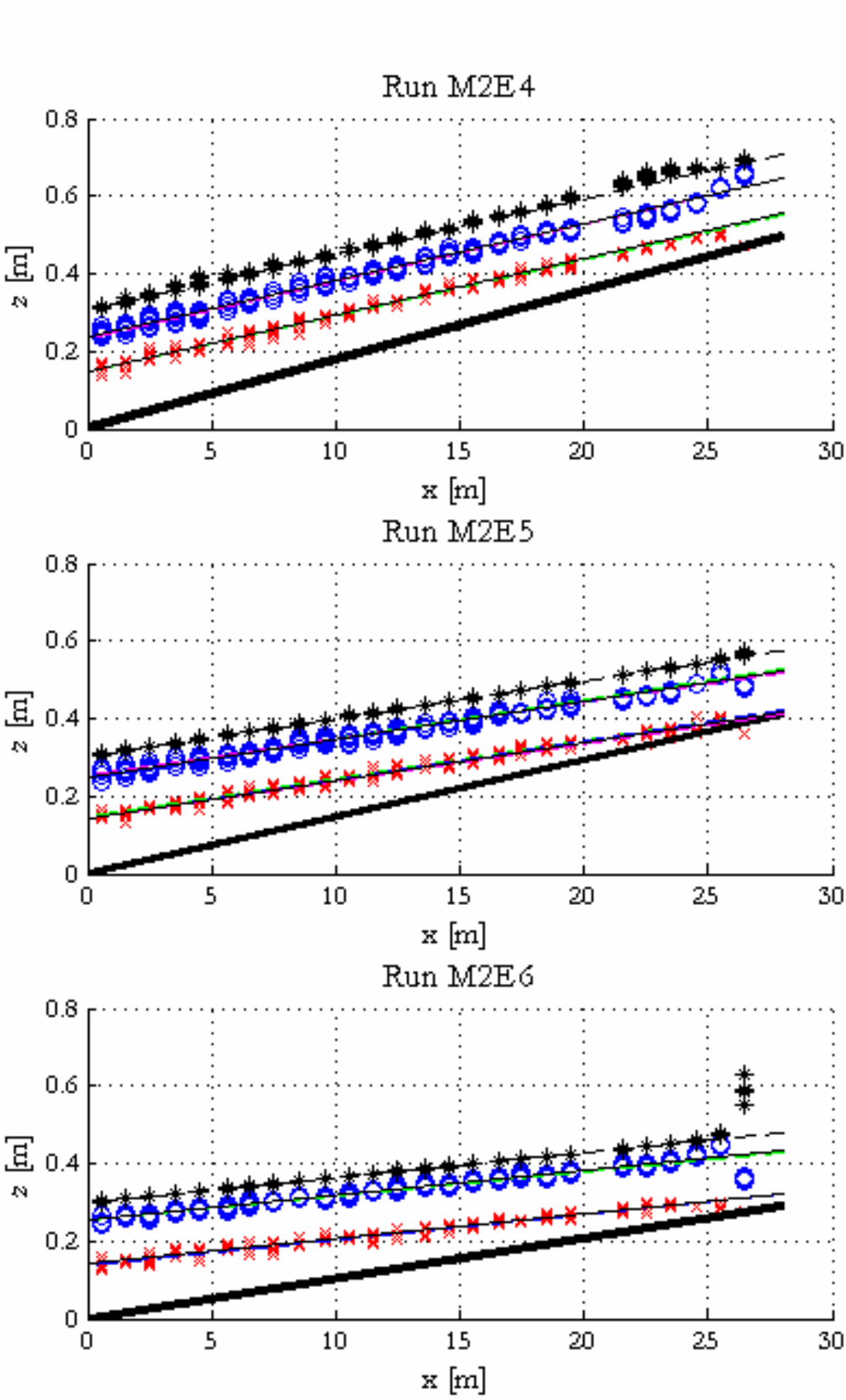
Run M2E4
z [m]
x [m]
Run M2E5
z [m]
x [m]
Run M2E6
z [m]
x [m]

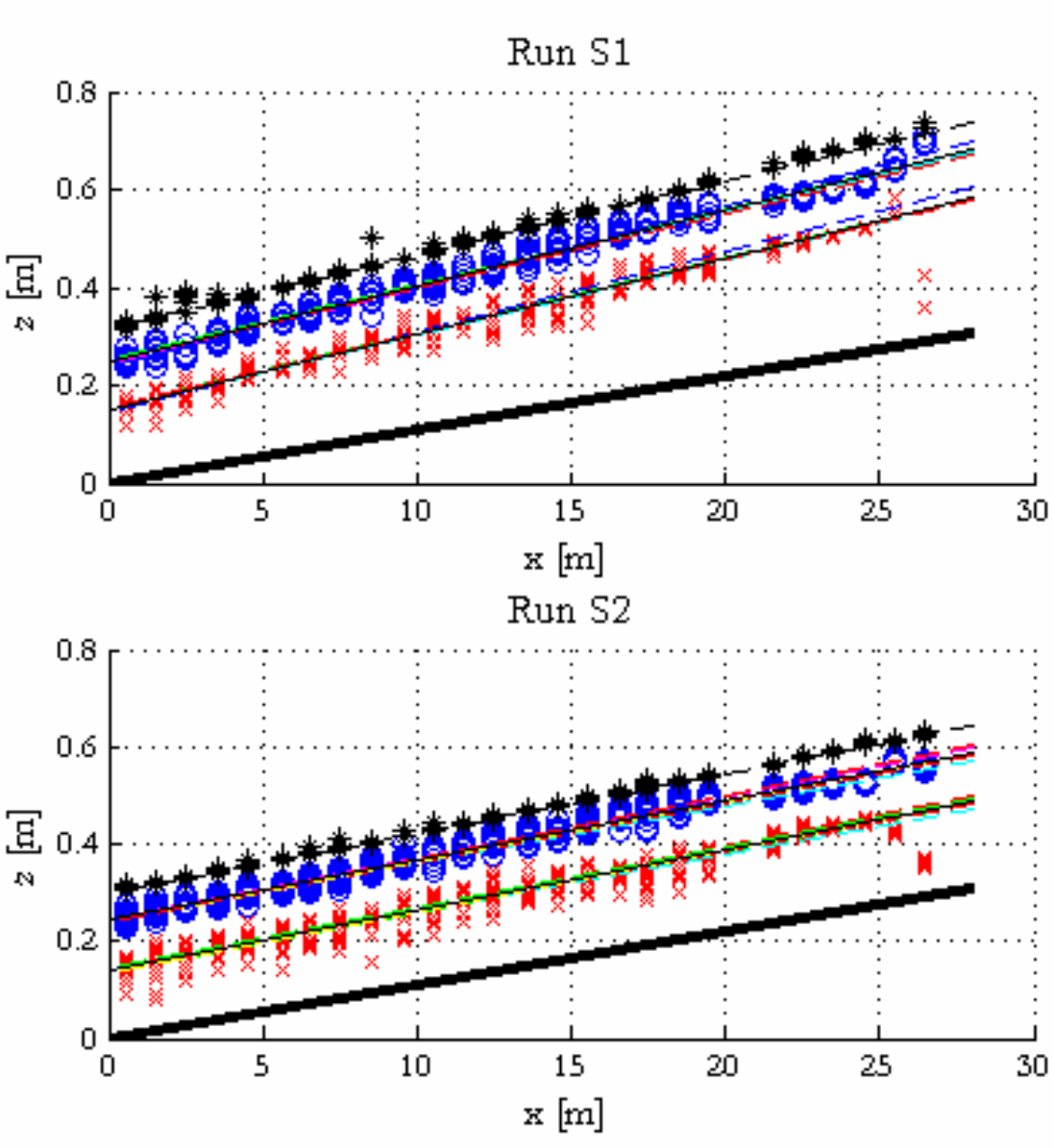
Run S1
z [m]
x [m]
0
0.2
0.4
0.6
0.8
0
5
10
15
20
25
30
Run S2
z [m]
x [m]
0
0.2
0.4
0.6
0.8
0
5
10
15
20
25
30

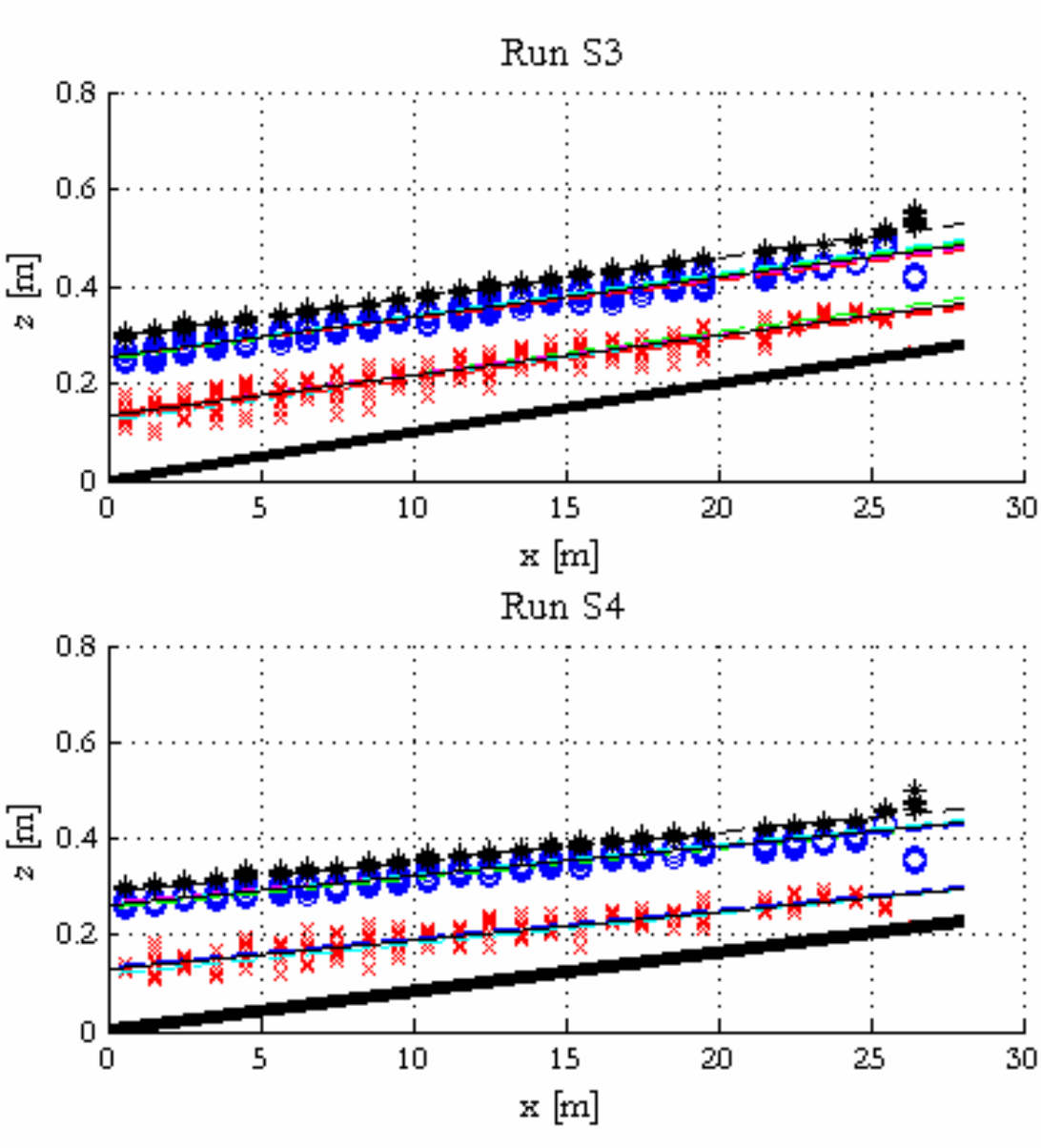
Run S3
z [m]
x [m]
0
0.2
0.4
0.6
0.8
0
5
10
15
20
25
30
Run S4
z [m]
x [m]
0
0.2
0.4
0.6
0.8
0
5
10
15
20
25
30

APPENDIX XV

DISPERSION OF BED AND WATER SURFACE ELEVATIONS IN EQUILIBRIUM STATE

Graphs in this Appendix correspond to measurements performed strictly during the considered equilibrium state (see section 3.4.2 for a description of criteria used to test equilibrium). The graphs show the standard deviations of all measurements of bed and water surface elevations, performed at each measurement point along the channel during equilibrium state. These standard deviations were computed using eq.(3.49) applied to all the measured bed and water elevations plotted in graphs of Appendix XIV. Continuous lines for each group of data (bed and water) were obtained using a moving average of five points. Also shown in the graphs are vertical lines to delimit the internal bed region considered for computing the average standard deviation to be used as a representative value of the run, given by eq.(3.50).

Explanation of symbols used in the graphs:

- Blue circles: Standard deviation of water surface elevation, σ_{wE}
- Red x's: Standard deviation of bed surface elevation, σ_{bE}
- Blue continuous line: Moving average for σ_{wE}
- Red continuous line: Moving average for σ_{bE}
- Vertical continuous green line: Lower and upper limits for region with stable bedforms

Runs within the same series, ordered from higher to lower sediment concentration.

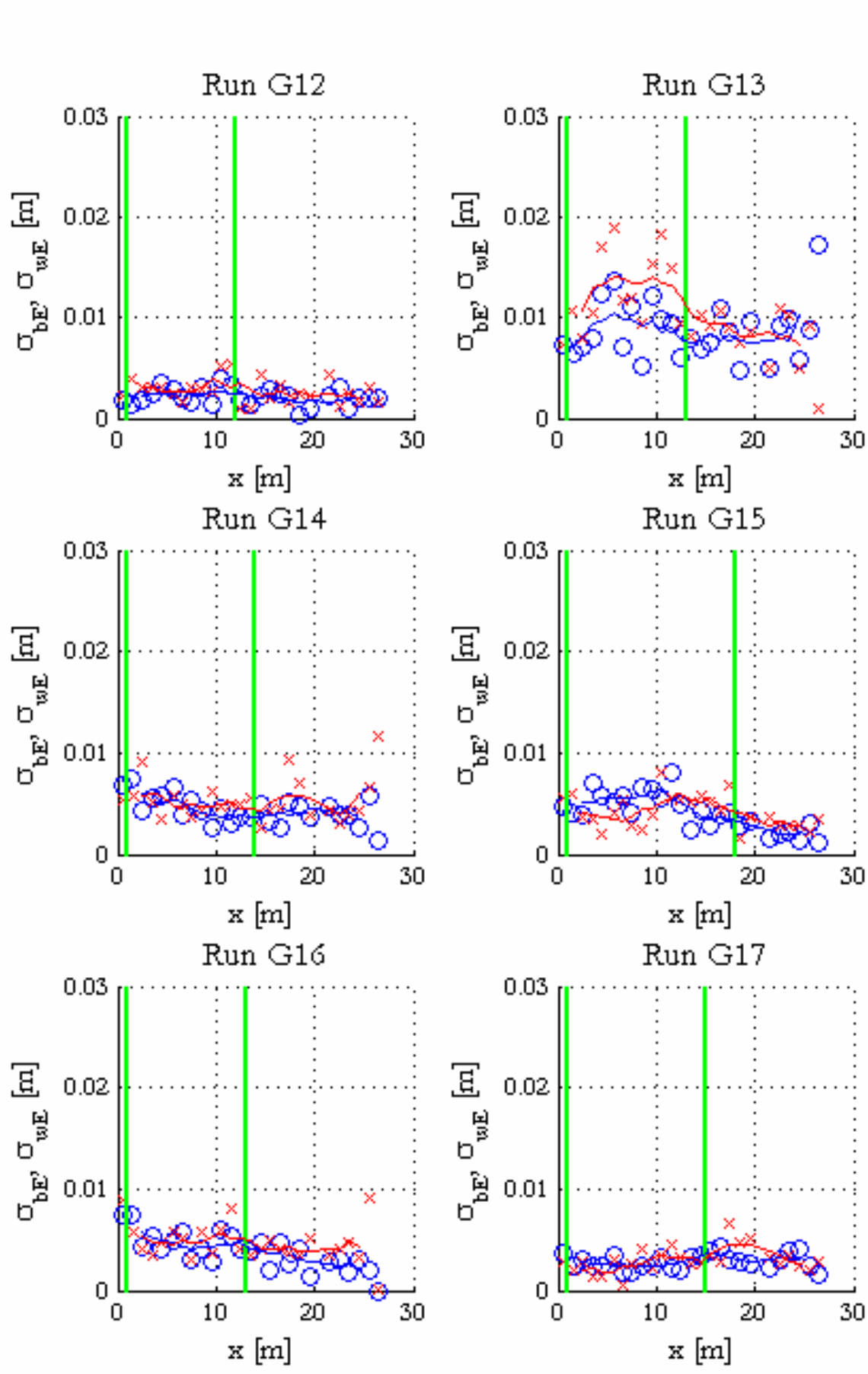
Run G12
Run G13
Run G14
Run G15
Run G16
Run G17
σbE', σwE [m]
x [m]
0.03
0.02
0.01
0
0
10
20
30

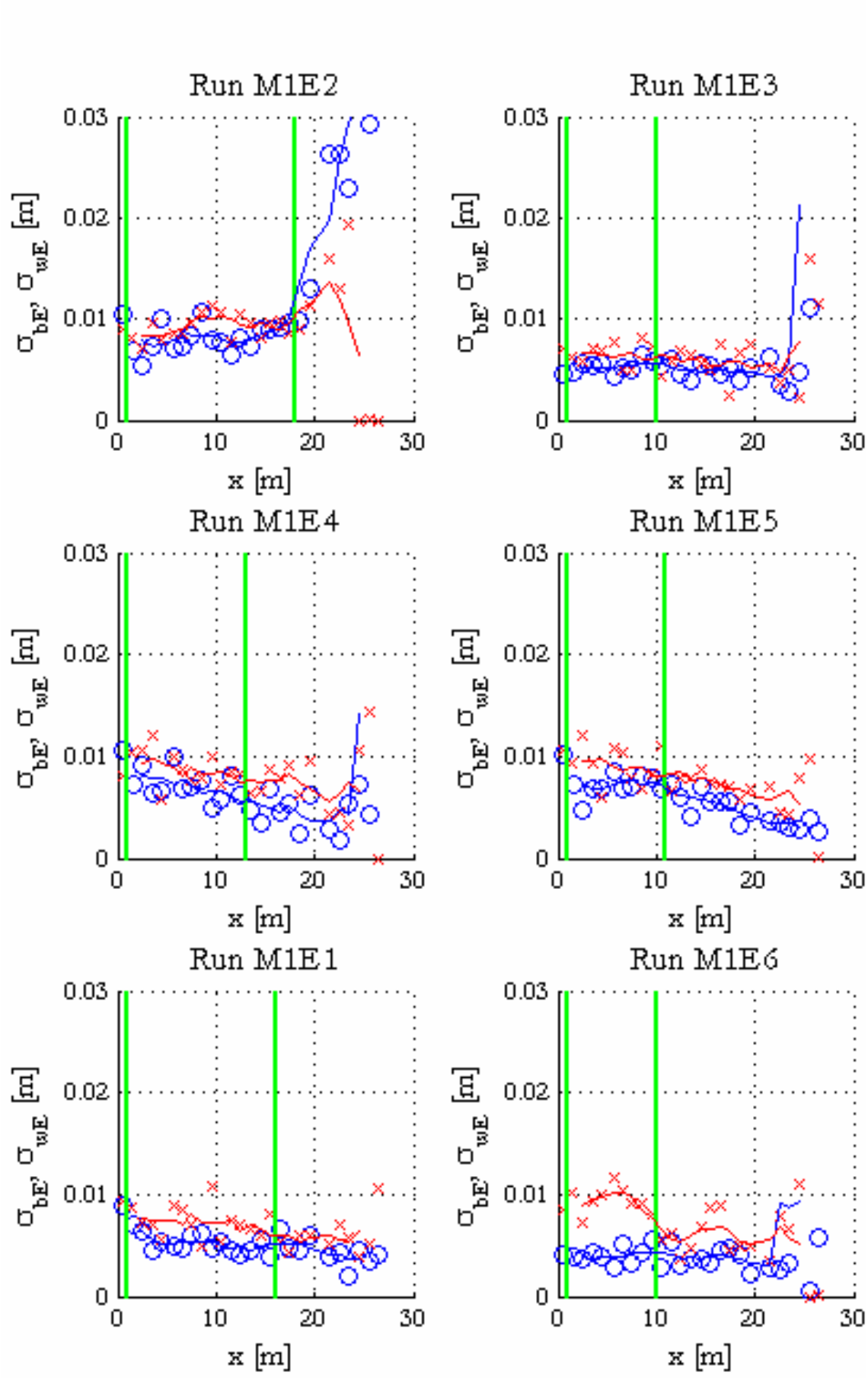
Run M1E2
Run M1E3
Run M1E4
Run M1E5
Run M1E1
Run M1E6
σ_{bE}, σ_{wE} [m]
x [m]
0.03
0.02
0.01
0
0
10
20
30

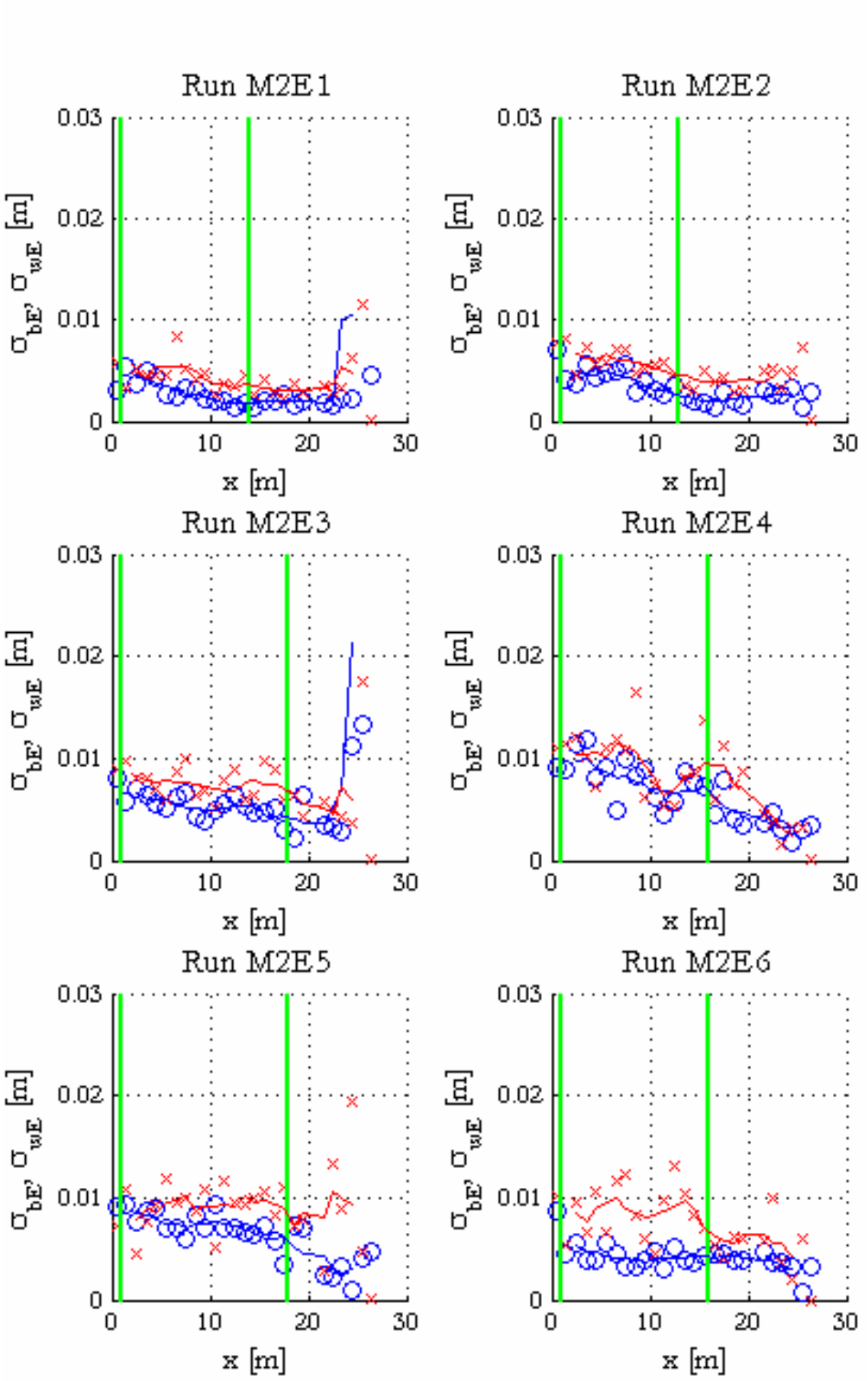
Run M2E1
Run M2E2
Run M2E3
Run M2E4
Run M2E5
Run M2E6
σbE', σwE [m]
x [m]
0.03
0.02
0.01
0
0
10
20
30

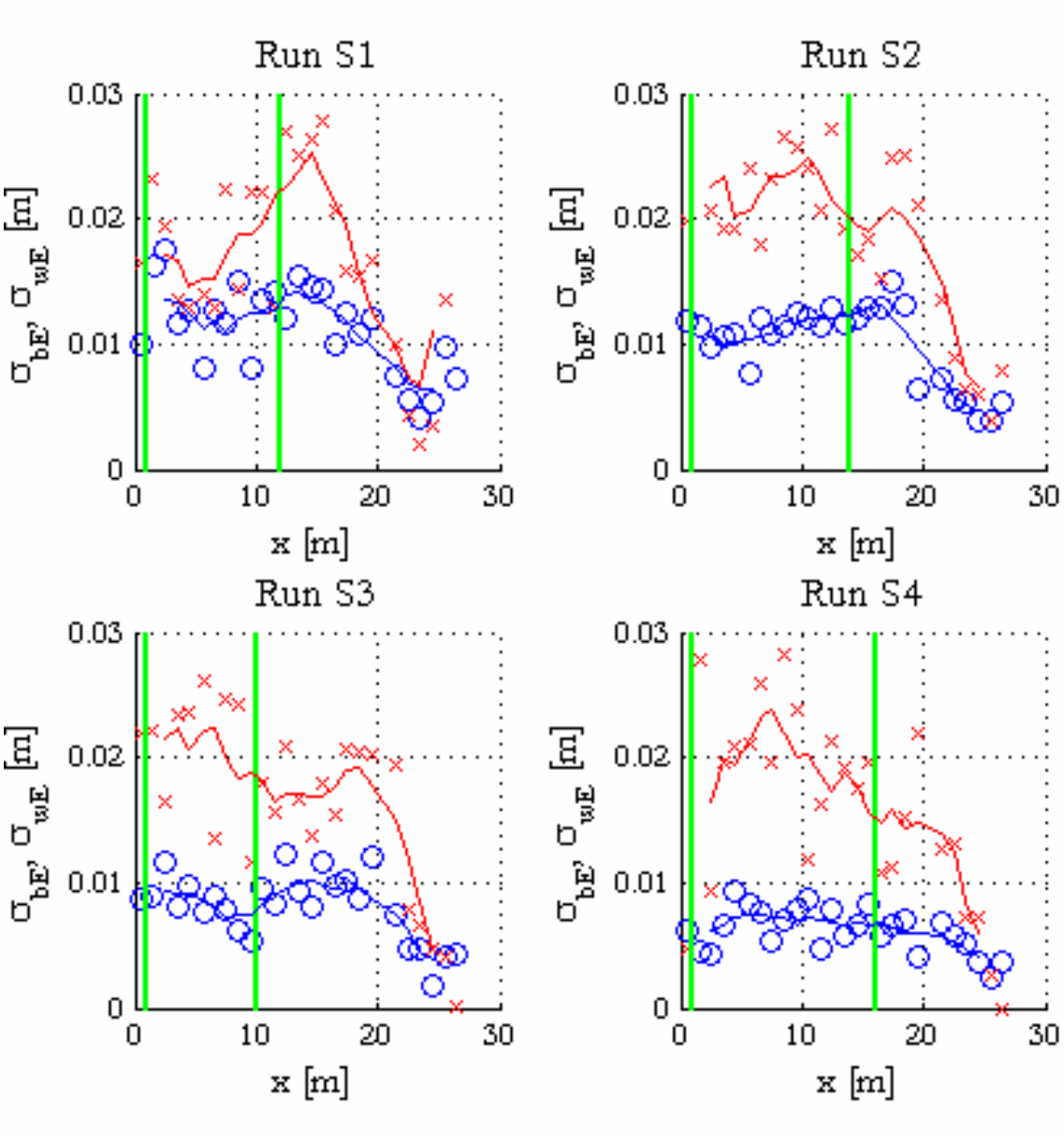
Run S1
Run S2
Run S3
Run S4
σ_{bE}, σ_{wE} [m]
x [m]
0.03
0.02
0.01
0
0
10
20
30

APPENDIX XVI

COMPARISON OF SHEAR STRESS MEASUREMENTS AND THE REFERENCE PLANE BED METHOD

In this Appendix the reference plane bed method for estimation of the skin friction in the presence of bedforms is compared with two experimental data-sets in literature. This method was described and applied in section 4.3.2 to the experimental data-set presented in Chapter 3. The two experimental data-sets for the comparison here correspond to measurements over fixed artificial dunes in subcritical flows. The first data-set (Shen et al. 1990) corresponds to two-dimensional dunes, while the second (Maddux et al. 2003) corresponds to three-dimensional dunes. The reference plane bed method is applied here using a relative roughness $k_s=2.5D_m$ after Engelund and Hansen. The total bed shear stress was corrected for side wall effects using the method of Vanoni and Brooks as it is described in section 4.3.1.

Shen et al. (1990).

Shen et al. presented independent measurements of skin resistance, form resistance and total resistance over an instrumented dune in a train of rigid two-dimensional dunes of equal size. The dunes were made of aluminum and plastic, and were triangular in shape with a height of 0.137 m and a length of 0.915 m. The upstream slope of the dunes was of 11.5º and the downstream angle of 30º. The flume was 0.61 m wide and 15.25 m long. Two series of experiments were performed, the first series used dunes with a smooth surface and the second series used dunes with a rough surface; for the latter, sand grains with a median size of 1.75 mm were glued over the dunes surface. Total shear stress was obtained from measurements of the deflections of the instrumented dune, using a force transducer. Form resistance was calculated from pressure measurements performed with pressure taps connected to individual pressure transducers. Skin friction was estimated from shear measurements along the dune using a Preston tube.

Maddux et al. (2003).

Maddux et al. performed detailed measurements of turbulent open channel flow over fixed, artificial asymmetric three-dimensional dunes. The mean wavelength of the dunes was 0.8 m and the mean height at the crest was 0.04. The angle of the lee slope was 30º. The dunes were constructed form a wooden frame and cover with leader sheets on the upstream side and acrylic plastic on the downstream side. The surface of the dunes was covered with sand 1 mm diameter. Fourteen dunes were place in a flume 22 m long and 0.9 wide. Estimations of total boundary shear stress were obtained from the spatially average equations of motion using averaged mean flow and turbulence fields. In the same manner, estimates of skin friction were obtained from the distribution of the near-bed mean velocity field.

Table AXVI.1 Experimental results and application of the reference plane bed method as presented by Engelund and Hansen (1967) for the data-set of Shen et al. (1990), for 2D fixed artificial dunes. The letter after the run number indicate Smooth surface run series if S and Rough surface if R.

Run	Measurements								Calculations					Measured/calculated		
	Temp ºC	H [m]	V [m/s]	S	F	τ_b [Pa]	τ' [Pa]	τ'' [Pa]	R_h [m]	τ_b [Pa]	k_s [m]	H_s [m]	τ' [Pa]	τ_b	τ'	τ''
Shen 1S	20	0.221	0.147	0.0006	0.10	1.32	0.03	1.17	0.126	0.75	0.001	0.022	0.13	1.76	0.24	1.90
Shen 2S	20	0.272	0.163	0.0006	0.10	1.15	0.03	1.03	0.168	0.91	0.001	0.028	0.15	1.27	0.21	1.36
Shen 3S	22	0.323	0.178	0.0004	0.10	0.93	0.03	0.93	0.187	0.69	0.001	0.041	0.15	1.36	0.21	1.74
Shen 4S	19	0.221	0.294	0.0024	0.20	4.89	0.11	4.55	0.171	3.93	0.001	0.023	0.52	1.24	0.22	1.33
Shen 5S	23	0.272	0.326	0.0019	0.20	4.67	0.11	4.33	0.204	3.88	0.001	0.030	0.57	1.20	0.19	1.31
Shen 6S	22	0.323	0.356	0.0019	0.20	4.07	0.11	4.39	0.238	4.38	0.001	0.035	0.65	0.93	0.17	1.18
Shen 7S	19	0.221	0.442	0.0056	0.30	10.5	0.22	9.96	0.183	10	0.001	0.022	1.19	1.05	0.19	1.13
Shen 8S	16	0.272	0.490	0.0036	0.30	10.4	0.24	10.4	0.210	7.47	0.001	0.035	1.23	1.39	0.20	1.67
Shen 9S	18	0.323	0.534	0.0039	0.30	9.96	0.25	9.39	0.248	9.35	0.001	0.038	1.42	1.07	0.17	1.18
Shen 10S	22	0.221	0.589	0.0100	0.40	22.6	0.34	23.2	0.189	18.4	0.001	0.022	2.12	1.23	0.16	1.42
Shen 11S	23	0.272	0.653	0.0063	0.40	18.8	0.53	18.4	0.217	13.3	0.001	0.035	2.17	1.41	0.24	1.65
Shen 12S	23	0.323	0.71	0.0064	0.40	18.7	0.38	18.5	0.253	15.8	0.001	0.039	2.47	1.18	0.15	1.39
													Average=	1.26	0.20	1.44
Shen 1R	18	0.221	0.146	0.0008	0.10	1.49	0.38	1.16	0.212	1.62	0.004	0.027	0.20	0.92	1.88	0.82
Shen 2R	18	0.272	0.163	0.0007	0.10	1.27	0.35	0.85	0.258	1.68	0.004	0.034	0.22	0.76	1.56	0.58
Shen 3R	18	0.323	0.178	0.0004	0.10	1.19	0.29	0.91	0.296	1.26	0.004	0.052	0.22	0.94	1.29	0.88
Shen 7R	18	0.221	0.442	0.0064	0.30	12.6	2.72	9.2	0.213	13.4	0.004	0.029	1.80	0.95	1.51	0.79
Shen 8R	18	0.272	0.490	0.0047	0.30	11.9	2.68	9.77	0.258	11.8	0.004	0.041	1.87	1.01	1.43	0.99
Shen 9R	17	0.323	0.534	0.0047	0.30	10.6	2.57	8.29	0.304	13.9	0.004	0.046	2.11	0.77	1.22	0.70
													Average=	0.89	1.48	0.79

Table AXVI.2 Experimental results and application of the reference plane bed method as presented by Engelund and Hansen (1967) for the data-set of Maddux et al. (2003), for 3D fixed artificial dunes.

Run	Measurements						Calculations					
	H [m]	V [m/s]	S	F	τ_b [Pa]	τ'/τ_b	R_h [m]	τ_b [Pa]	k_s [m]	H_s [m]	τ' [Pa]	τ'/τ_b
Maddux T2	0.173	0.357	0.00106	0.274	1.40-1.60	0.42	0.159	1.66	0.0025	0.064	0.67	0.40
Maddux T3	0.561	0.261	0.00024	0.111	0.61-1.07	0.36	0.478	1.12	0.0025	0.122	0.29	0.26

APPENDIX XVII

DIMENSIONAL ANALYSIS FOR STABLE CONDITIONS OF ANTIDUNE PREFERENTIAL PROPAGATION DIRECTION

EXTENDED DIMENSIONAL ANALYSIS FOR ANTIDUNE MIGRATION

A17.1. Dimensional Analysis of eq.(7.26)*

In order to shorten the text in Chapter 7, some important steps of the dimensional analysis were omitted or obviated. To clarify the issue, below, a detailed working out of the dimensional analysis is presented.

A17.2 Formation of dimensionless products

Dimensional analysis was invoked for studying the properties of the fundamental equation (7.26), which describes the total energy difference between antidune crest and trough. This equation was written as

$$\Delta + (H_1 - H_2) = F^2 H_m^3 \left[\frac{1}{r}\left(\frac{1}{H_1} + \frac{1}{H_2} \right) + \frac{1}{2}\left(\frac{1}{H_2^2} - \frac{1}{H_1^2} \right) \right] \quad \text{(A17.1)}$$

where F is the flow Froude number, H_1 and H_2 are the water depths over the crest and trough of the antidune, respectively, H_m is the mean flow water depth, r is the radius of curvature of the stream lines over the crest and trough and Δ is the antidune height.

By introducing the definition of the Froude number as $F=V_m/(gH_m)^{0.5}$, with V_m being the mean flow velocity and g the gravitational acceleration, eq.(A17.1) is equivalent to

$$\Delta + (H_1 - H_2) = \frac{V_m^2}{g} H_m^2 \left[\frac{1}{r}\left(\frac{1}{H_1} + \frac{1}{H_2} \right) + \frac{1}{2}\left(\frac{1}{H_2^2} - \frac{1}{H_1^2} \right) \right] \quad \text{(A17.2)}$$

In this manner, for the dimensional analysis of the variables involved in eq.(A17.2), the following functional relation can be stated

$$f(H_1, H_2, H_m, r, \Delta, V_m, g) = 0 \quad \text{(A17.3)}$$

The mean water depth H_m can be defined as a function of the local water depths on the crest and trough as

$$H_m = f_h(H_1, H_2) \quad \text{(A17.4)}$$

Dimensional analysis theory considers that variables which can be stated as a function of other variables involved in the problem are superfluous. Because we know the function that relates H_m, H_1 and H_2, one of these variables is redundant in eq.(A17.3) and can be eliminated. We drop H_m, as we are interested in keeping H_1 and H_2 for analyzing the antidune movement with relation to the ratio between water depths on the crest and the trough. By doing this, the relation (A17.3) is transformed to

$$f(H_1, H_2, r, \Delta, V_m, g) = 0 \quad \text{(A17.5)}$$

For a detailed dimensional analysis we may apply the Theorem of Buckingham-Vaschy. By forming the matrix from the exponents X of the dimensions of the n fundamental quantities (in this case n=6) we may find out the minimum number of dimensionless variables to which we can reduce eq.(A17.5). The exponents matrix is formed for the variables in eq.(A17.5) as follows:

Dimension/Variables	H_1	H_2	r	Δ	V_m	g
Mass [M]	0	0	0	0	0	0
Length [L]	1	1	1	1	1	1
Time [T]	0	0	0	0	-1	-2

* Numbering of equations beginning with 7 refers to equations in Chapter 7, while using a 'A17' presiding the number of equation refers to equations in this Appendix.

The rank of the matrix is r=2, so we may express eq.(A17.5) as a combination of n-r=6-2=4 non-dimensional products, i.e., eq.(A17.5) can be restated as

$$F(\pi_1, \pi_2, \pi_3, \pi_4) = 0 \qquad \text{(A17.6)}$$

where the π_i are dimensionless parameters constructed from the physical variables and from exponents X_k, where X_k is the exponent of the variable k. Using the elements in the matrix, the following system of equations is formed:

$$[L] \qquad X_1 + X_2 + X_3 + X_4 + X_5 + X_6 = 0 \qquad \text{(A17.7a)}$$

$$[T] \qquad -X_5 - 2X_6 = 0 \longrightarrow X_5 = -2X_6 \qquad \text{(A17.7b)}$$

Because the number of variables is higher than the number of equations, we may assign values to the redundant variables to solve the system. Also, we may resort to the formation of known dimensionless products which satisfy the system. For instance, we can form dimensionless numbers relating variables with length dimensions; therefore, a solution is given by

$X_3=X_4=X_5=X_6=0$, $X_1=1 \longrightarrow X_2=-1$: $\pi_1 = \dfrac{H_1}{H_2}$;

$X_1=X_2=X_5=X_6=0$, $X_3=1 \longrightarrow X_4=-1$: $\pi_2 = \dfrac{r}{\Delta}$;

To form the third non-dimensional product we may introduce a Froude number, for instance, as

$X_5=1 \longrightarrow X_6=-0.5$, and $X_2=X_3=X_4=0 \longrightarrow X_1=-0.5$,: $\pi_3 = \dfrac{V_m}{\sqrt{gH_1}}$

But in search of a more general solution, we may form the Froude number using both water depths, which are related by eq.(A17.4), so that

$$\pi_3 = \frac{V_m}{\sqrt{g f_h(H_1, H_2)}}$$

For this dimensionless number, the exponents take the values $X_3=X_4=0$, $X_5=1 \longrightarrow X_6=-0.5$, and thus it must be satisfied that $X_1+X_2=-0.5$, which implies that the function f_h must be a dimensionally homogeneous product. The exponents of H_1 and H_2 in f_h can be found according to the restrictions for satisfying π_3 as follows; if f_h is considered to be a product of the two water depths as

$$f_h(H_1, H_2) = H_1^{Y_1} H_2^{Y_2} \qquad \text{(A17.8)}$$

by introducing (A17.8) into π_3 it may be stated

$$\pi_3 = H_1^{-0.5Y_1} H_2^{-0.5Y_2} V_m^1 g^{-0.5} \qquad \text{(A17.9)}$$

and

$$-0.5Y_1 - 0.5Y_2 = -0.5 \qquad \text{(A17.10)}$$

Finally, if we assume that $Y_1=Y_2$, then it is found that $Y_1=Y_2=0.5$, and (A17.8) yields

$$f_h(H_1, H_2) = \sqrt{H_1 H_2} \qquad \text{(A17.11)}$$

which is the geometric mean of H_1 and H_2.

For the remaining dimensionless product, we can turn to eq.(A17.2), for which it was found that a particular condition occurs when $H_1=H_2=H_m$ (see Section 7.3.2 in Chapter 7). This assumption gives rise to the dimensionless product (eq.7.28)

$$F_a = FH_m \sqrt{\frac{2}{r\Delta}}$$

Taking into account eq.(A17.4), in a more general form we may state F_a as the fourth dimensionless product given by

$$\pi_4 = \frac{V_m}{\sqrt{g f_h(H_1, H_2)}} f_h(H_1, H_2)\sqrt{\frac{2}{r\Delta}}$$

For this product, the exponents of the variables take the values $X_5=1 \longrightarrow X_6=-0.5$, $X_3=X_4=-0.5$, and it must be satisfied that $X_1+X_2=0.5$. Note that although F_a was obtained by assuming $H_1=H_2=H_m$ in eq.(A17.1), it is a valid dimensionless product to be included in eq.(A17.6) if the system satisfies (A17.7). Following the same procedure as with π_3 for finding the exponents of H_1 and H_2 in (A17.8), we can conclude

$$0.5Y_1 + 0.5Y_2 = 0.5 \qquad \text{(A17.12)}$$

Again, assuming that $Y_1=Y_2$ it is found that $Y_1=Y_2=0.5$ and f_h is given as in (A17.11).

According to the analysis above, eq.(A17.1) can be represented as a relationship of non-dimensional products with

$$F\left(\frac{H_1}{H_2}, \frac{r}{\Delta}, \frac{V_m}{\sqrt{g f_h(H_1, H_2)}}, V_m\sqrt{\frac{2 f_h(H_1, H_2)}{r\Delta g}}\right) = 0 \qquad \text{(A17.13)}$$

where f_h must be a dimensionally homogeneous product. Considering that H_m is well represented by the geometric mean of H_1 and H_2, i.e. by eq.(A17.11), we can finally represent eq.(A17.1) as

$$F\left(\frac{H_1}{H_2}, \frac{r}{\Delta}, \frac{V_m}{\sqrt{g(H_1H_2)^{0.5}}}, V_m\sqrt{\frac{2(H_1H_2)^{0.5}}{r\Delta g}}\right) = 0 \qquad \text{(A17.14)}$$

or equivalently as

$$F\left(\frac{H_1}{H_2}, \frac{r}{\Delta}, F, F_a\right) = 0 \qquad \text{(A17.15)}$$

which was labeled as eq.(7.30) in Chapter 7.

A17.3 Discussion

The mean water depth in Chapter 7 was defined as the arithmetic mean of the local water-depths H_1 and H_2 [eq.(7.24)], instead of the geometric mean given by eq.(A17.11). For the more detailed dimensionless analysis presented above, an arithmetic mean would not fulfill the requirements of f_h being a dimensional homogeneous product. Therefore, the dimensional analysis used in Chapter 7 would not be completely rigorous. Notwithstanding, this weak point is not crucial for the analysis of eq.(7.26) and thus it has little influence on the results obtained for determining the conditions that govern the direction of movement of antidunes. To prove this, the entire analysis was performed again changing the definition of the mean water depth from an arithmetic mean to a geometric mean, i.e., $H_m=(H_1H_2)^{0.5}$ instead of $H_m=0.5(H_1+H_2)$. Comparison of Figures 7.6 to 7.8 using the geometric mean showed that the biunivocal properties of eq.(7.26) for F>1 are conserved, and only the shape of the curves is changed, particularly for F<1. Therefore, the use of an arithmetic mean does not alter the final results and conclusions in Chapter 7.

APPENDIX XVIII

WESTMAN POROSITY MODEL

Westman's empirical model for predicting the voidage of binary particle mixtures is given by the equation

$$\left(\frac{V - V_D f_D}{V_d}\right)^2 + 2G\left(\frac{V - V_D f_D}{V_d}\right)\left(\frac{V - f_D - V_d f_d}{V_d - 1}\right) + \left(\frac{V - f_D - V_d f_d}{V_d - 1}\right)^2 = 1$$

where G is a fitting parameter; V is the specific volume calculated from 1/(1-ε), with ε being the porosity of the mixture; V_D and V_d are the specific volumes for large and small particles, respectively, calculated with the porosities ε_D and ε_d of beds of the pure particle fractions; f is the volume fraction and the subscripts D and d refer to the large and small particles, respectively.

For spherical and non-spherical particles, Finkers and Hoffmann (1998) proposed to calculate G as

$$G = r_{str}^k + \left(1 - \varepsilon_D^{-k}\right)$$

where k is a constant, which empirically was found to take the value -0.63 for monosized particles or with a narrow size distribution, and -0.345 for particles with a wider size distribution; r_{str} is the structural ratio, i.e., the ratio of the volume of a small particle with its associated interstitial region to the volume of the interstitial region associated with a large particle, calculated from:

$$r_{str} = \frac{\left(\frac{1}{\varepsilon_D} - 1\right) r^3}{1 - \varepsilon_d}$$

where r is the ratio of particle diameters, i.e., $r=d/D$.

The equations for the Yu and Standish model are modified and provided in detail in Frings et al. (2008).

References

Finkers, H. J. and Hoffmann, A. C. (1998), 'Structural ratio for predicting the voidage of binary particle mixtures', *AIChE Journal* **44**(2), 495-498.

Frings, R.; Kleinhans, M. and Vollmer, S. (2008), 'Discriminating between pore-filling load and bed-structure load: a new porosity-based method, exemplified for the river Rhine', *Sedimentology,* doi: 10.1111/j.1365-3091.2008.00958.x.

Yu, A. B. and Standish, N. (1991), 'Estimation of the porosity of particle mixtures by a linear-mixture packing model', *Ind. Eng. Chem. Res.* **30**, 1372-1385.

APPENDIX XIX

PUBLICATIONS

Analysis of antidune migration direction

Francisco Núñez-González[1] and Juan P. Martín-Vide[1]

Received 6 May 2010; revised 7 January 2011; accepted 2 February 2011; published 16 April 2011.

[1] Antidunes are bed forms characteristic of upper regime unidirectional flows. Contrary to bed forms developed in lower regime flows, antidunes not only can propagate in the downstream direction but can propagate upstream or remain stationary. In this work we analyze the stable hydraulic conditions that determine each of the three antidune movement possibilities, and a new theory is developed for distinguishing the occurrence of each of these conditions. The theory is developed from an energy balance over a symmetrical antidune; for this, the Bernoulli equation is applied between the antidune crest and antidune trough, and the pressure head is corrected to account for the centrifugal forces generated by curvilinear flow. Manipulation of the fundamental equations produces an antidune mobility dimensionless number (F_a), dependent on the Froude number, the mean water depth, and the antidune wavelength. The critical value of the antidune mobility number ($F_a = 1$) corresponds to the stationary condition, while values higher and lower than the critical correspond to downstream and upstream propagation, respectively. Theory predicts that for a given Froude number, downstream-migrating antidunes are formed for higher water depth–wavelength ratios than for upstream-migrating antidunes. Likewise, by introducing a restriction for the maximum stationary wave height above antidunes, theory predicts that downstream-migrating antidunes could attain steeper height–wavelength ratios than upstream-migrating antidunes. Comparison with published experimental data in literature largely showed agreement between theory and experimental observations.

Citation: Núñez-González, F., and J. P. Martín-Vide (2011), Analysis of antidune migration direction, *J. Geophys. Res.*, *116*, F02004, doi:10.1029/2010JF001761.

1. Introduction

[2] Among bed features developed by unidirectional flows in alluvial beds, those features classed as antidunes occur in the so-called upper regime flow; in contrast to bed forms in lower regime, which can only move in the downstream direction, antidunes can migrate upstream, downstream or remain stationary. Dunes are lower regime bed forms which propagate in the downstream direction mainly because of the separation eddy formed downstream of their slip face. This eddy favors deposition of the sediment grains on the lee side. Antidune migration may be related to the detachment of streamlines as well, so that flow separation over the upstream slope may be associated with upstream migration while separation over the downstream slope will be associated with downstream migration. In contrast with dunes, streamline detachment over antidunes may be intermittent and erratic in area and position. This unsteadiness is related to the strong interaction between bed and water surface that characterizes transitional and supercritical flows. In the presence of real antidunes the undulations of both surfaces are approximately in phase. On account of this, antidunes, especially those migrating upstream, tend to be symmetrical with a curved crest in their profile parallel to flow.

[3] Diagrams that depict the different flow regimes under which stable bed forms develop have been obtained empirically by different authors [e.g., *Vanoni*, 1974; *Southard and Boguchwal*, 1990]. Such empirical diagrams for stability fields do not distinguish the direction of movement of antidunes, or refer solely to the region where upstream-migrating antidunes may occur. On the other hand, theoretical bed form stability fields have been presented by different authors who have carried out stability analysis of bed disturbances. For such methods of analysis, some researchers have deduced conditions that define the antidune preferential direction of movement. Particularly, based on the solution of a linearized potential flow over a wavy bed, *Kennedy* [1963] presented relations for defining bed form stability fields as a function of the Froude number and a nondimensional wavelength. For the stability fields defined by Kennedy, the distinction between downstream and upstream-migrating antidunes was included. Similarly, *Engelund and Hansen* [1966] analyzed the stability of a sinusoidal sand bed using the continuity equation and the equations of motion of a real fluid; they produced a stability diagram where separated regions for upstream- and downstream-migrating antidunes can be distinguished as a function of the Froude number and the ratio between mean flow velocity and the sediment critical shear velocity.

[1]Hydraulics Department, Technical University of Catalonia, Barcelona, Spain.

0148-0227/11/2010JF001761

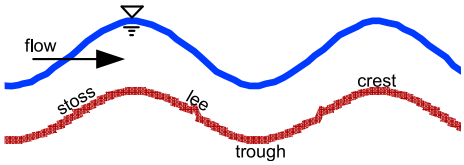

Figure 1. Geometry of antidunes.

[4] Many other researchers have explored theoretically the flow over bed forms, their formation, and characteristics. For instance, consecutive contributions using potential flow analysis are given by *Reynolds* [1965] and *Hayashi* [1970], and more recently by *Coleman and Fenton* [2000], while rotational flow models have been proposed, for instance, by *Engelund* [1970], *Fredsøe* [1974], *Richards* [1980], and *Smith* [1970] and lately by *Colombini and Stocchino* [2008] and *Bose and Dey* [2009]. For most of these studies, tackling the conditions of bed form migration direction was not the main objective that was being pursued; as a result, no explicit criteria were developed to distinguish between the three regimes (upstream, downstream, and no migration).

[5] In this work a new analysis and criterion are presented for determining the propagation direction of antidunes. Unlike the previous theoretical developments (such as those mentioned above) that, for the most part, provide a detail analysis of the genesis and stability of bed forms, the object of the present work is restricted to the formulation of a simplified theory of the antidune movement direction, based on flow hydraulics. The problem is addressed by resorting to the simplified theoretical framework of *Kennedy* [1963], for which the bed form direction of movement may be related to the gradient of mean flow velocities over the bed forms. In this manner, antidunes migrate upstream when the near-bed flow velocity decreases from the bed form trough to the bed form crest and increases from the bed form crest to the next bed form trough; when this occurs, sediment is eroded from the lee side of one antidune, it is transported both as bed load and suspended load, and deposited on the stoss side of an antidune downstream (Figure 1). Likewise, antidunes migrate downstream when the near-bed flow accelerates from trough to crest and decelerates from crest to the next trough; the material eroded on the stoss side is transported and deposited on the lee side where the near-bed flow velocity decreases [*García*, 2006; G. Parker, St. Anthony Falls Laboratory, University of Minnesota, 1D sediment transport morphodynamics, with applications to rivers and turbidity currents, 2004, e-book available at http://cee.uiuc.edu/people/parkerg/]. Immobility of antidunes occurs when there is no acceleration of the flow along the bed profile. This principle may be altered by spatial lags between flow acceleration and sediment transport, particularly for suspended load. Owing to the fact that sediment transport variations are most influenced by boundary shear stress, these phase lags may originate from shifts of shear stress in relation to mean velocity and from shifts of the sediment transport in relation to shear stress [*McLean*, 1990]. For the analysis presented here no phase shifts are considered between the mean flow velocity and sediment transport.

[6] The theory developed here is based on the continuity and Bernoulli equations applied to a symmetrical bed form. This represents a very simplified approach in which sediment grain size and transport are not directly involved, but only the flow hydraulics are invoked as the bare, essential basis for describing the migration. In spite of its limitations, the developed criterion was compared successfully with published experimental data, and it is shown to perform better than bed form stability fields developed with potential flow analysis by *Kennedy* [1963]. Such results show an alternative for describing the antidune migration regime. Subsequent analysis of the equations explores possible connections of migration direction with the geometry of antidunes and the influence of expansion losses in the event of flow separation.

2. Analysis of Antidune Direction of Movement

[7] Bed form propagation in downstream direction occurs if sediment is predominantly eroded over the stoss side and deposited over the lee side; conversely, upstream migration takes place when most of the sediment is deposited over the stoss side and eroded over the lee side [*García*, 2006]. Such a rhythmic sediment transport pattern can be related to the near-bed flow acceleration along the bed form and also to the water depth variation. In such a manner, sediment deposition would occur where the near-bed flow decelerates and flow depth increases, and erosion would occur where the near-bed flow accelerates and flow depth decreases. Consequently, when the antidunes migrate downstream, the water depth is less over the crest than over the trough (Figure 2a), whereas when the antidunes migrate upstream the water depth is greater over the crest than over the trough (Figure 2b). Finally, for stationary antidunes (those not propagating in any direction) the flow depth is constant along the bed profile. Images of experimental upstream- and downstream-migrating antidunes are shown in Figure 3, for which the differences in water depth over the crest and trough, though subtle, are noticeable.

[8] The following analysis of the stable hydraulic conditions over antidunes considers the water depth variations along the antidune profile as the most important property for defining the antidune migration direction.

2.1. Total Energy Over a Wavy Bed Surface

[9] If flow over completely developed antidunes is idealized as a two-dimensional free surface flow over a wavy bed

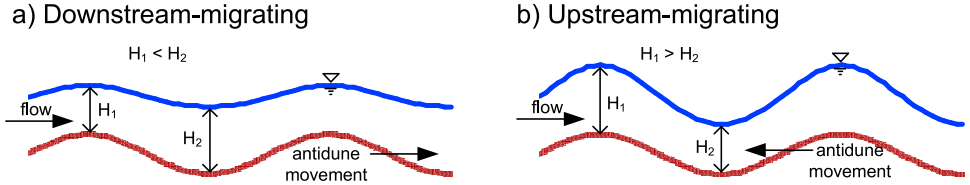

Figure 2. Water depth variation over (a) downstream- and (b) upstream-migrating antidunes.

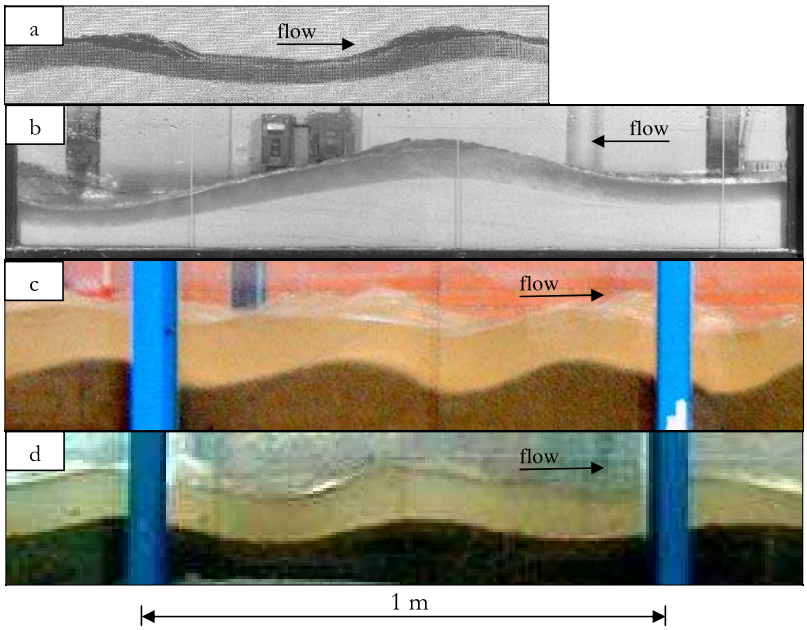

Figure 3. Side views for experimental antidunes. (a) *Kennedy* [1961], upstream-migrating antidunes for run 5-14, $F = 2.34$; (b) *Alexander et al.* [2001], upstream-migrating antidune for run 2, $F = 1.68$; (c) *Núñez-González and Martín-Vide* [2010], downstream-migrating asymmetric antidunes for run S1 with sand, $F = 1.02$; (d) *Núñez-González and Martín-Vide* [2010], downstream-migrating symmetric antidunes for run M2E4 with sand-gravel mixture with 44% sand, $F = 1.25$. (Scale has been adjusted to be approximately the same for all images.)

surface as depicted in Figure 4, where V_m is the mean flow velocity, H_m is the mean water depth, and the mean bed slope is considered to be small, total energy per unit weight is then given by

$$E = \eta + h + \frac{V^2}{2g} \tag{1}$$

where h is the pressure head-on the bed surface, g is the gravitational acceleration, V is the mean sectional flow velocity, and η is the bed surface elevation above the datum η_0 for the mean bed surface level. Equation (1) is the Bernoulli equation, which implicitly considers a steady irrotational, incompressible, and inviscid flow.

[10] If parallel flow occurs, i.e., if the streamlines have no substantial curvature, then the pressure distribution can be considered to be hydrostatic, and thus the pressure head in equation (1) would be equal to the water depth. This assumption is valid if the bed perturbations and water perturbations are small, so that no important acceleration components appear in the direction perpendicular to the flow. Conversely, if the bed and water perturbations affect the flow filaments in such a way that the streamlines show a substantial curvature, the flow must be considered curvilinear and the pressure head should be corrected to account for the centrifugal forces produced by the curvature [*Chow*, 1959]. In the study of the hydraulics of stable antidunes, the parallel flow assumption would not be completely valid, particularly when dealing with steep bed forms.

2.2. Correction of the Pressure Head for Curvilinear Flow

[11] According to *Chaudhry* [1993], for a curvilinear, irrotational, and inviscid flow the pressure head acting at the

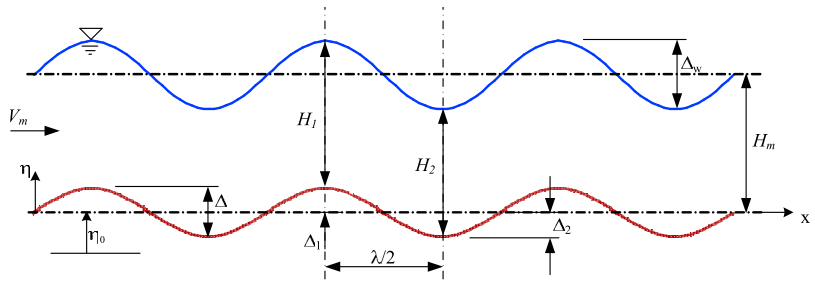

Figure 4. Idealized two-dimensional flow over antidunes.

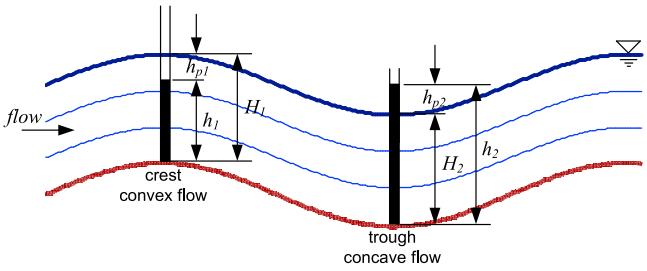

Figure 5. Pressure distribution for curvilinear flow over steep antidunes.

bottom of a liquid column due to centrifugal acceleration is given by

$$h_p = \frac{1}{g} H \frac{V^2}{r} \tag{2}$$

where H is the water depth, V is the flow velocity, and r is the radius of curvature of the streamline, which is here defined as the distance between a point on the curved streamline and the center of the osculating circle of the streamline at that point; a mathematical definition of r is given in section 3. For concave flows, centrifugal forces act downward, i.e., in the same direction of gravity, while for convex flows they act upward, opposed to gravity.

[12] The piezometric head on the bed surface of a channel with a longitudinally curved profile can then be calculated by including the deviation from the hydrostatic pressure as an algebraic sum of the water depth and the pressure due to the centrifugal forces, i.e. (Figure 5),

$$h = H \pm h_p \tag{3}$$

Given that the centrifugal forces in a concave curvature act in the direction of gravity their effect is to increase the pressure head, in which case h_p takes a positive value. Likewise, for convex curvatures, h_p takes a negative value. For practical purposes, it is assumed that the flow streamlines are attached to the bed, so that the radius of curvature of the bed surface and the streamlines are the same. In a similar vein, it can be assumed that V is equal to the average flow velocity over the cross section.

2.3. Energy Balance Between the Antidune's Crest and Trough

[13] As is shown in Figure 2, the variation of the water depth along the antidune profile describes whether the antidune migrates downstream, upstream or stays stationary. The hydraulic conditions for the three cases can be studied by applying the continuity and Bernoulli equations between the crest and trough of the bed form. In this analysis, the problem is reduced to a steady motion by assuming that the reference axes move with the waves.

[14] If energy losses are considered negligible, from Figure 4 and equation (1), the total energy head at the upstream section S1 over the bed form crest should be equal to the total energy head at the downstream section S2 over the bed form trough, to yield

$$\Delta_1 + h_1 + \frac{V_1^2}{2g} = -\Delta_2 + h_2 + \frac{V_2^2}{2g} \tag{4}$$

where Δ_1 is the distance from the mean bed surface level to the bed form crest and Δ_2 is the distance from the mean bed surface level to the bed form trough. Including equations (2) and (3), and considering a negative pressure head due to centrifugal acceleration at the crest and a positive pressure head due to centrifugal acceleration at the trough, equation (4) becomes

$$\Delta_1 + H_1 - \left(\frac{1}{g} H_1 \frac{V_1^2}{r_1}\right) + \frac{V_1^2}{2g} = -\Delta_2 + H_2 + \left(\frac{1}{g} H_2 \frac{V_2^2}{r_2}\right) + \frac{V_2^2}{2g} \tag{5}$$

Note that for large values of r_1 and r_2, the flow approximates to parallel flow, so that the pressure head is roughly the same as the water depth; that is, the pressure distribution follows the hydrostatic law when antidunes become low in amplitude and the bed is almost flat.

[15] Considering the continuity equation

$$q_w = V_m H_m = V_1 H_1 = V_2 H_2 \tag{6}$$

with q_w being the unit water discharge, equation (5) can be simplified to the form

$$(\Delta_1 + \Delta_2) + (H_1 - H_2) = \frac{q_w^2}{g}\left[\left(\frac{1}{H_2 r_2} + \frac{1}{H_1 r_1}\right) + \left(\frac{1}{2H_2^2} - \frac{1}{2H_1^2}\right)\right] \tag{7}$$

A particular case of equation (7) occurs when the bed features are symmetric. For such condition the distances from the mean bed level to the bed form crest and from the mean bed level to the bed form trough are equal, and the radius of curvature of the crest and trough can be considered equal as well, so that

$$r = r_1 = r_2 \tag{8}$$

and

$$\Delta = 2\Delta_1 = 2\Delta_2 = \Delta_1 + \Delta_2 \tag{9}$$

where r is the curvature radius for the crest and trough and Δ is the antidune height. Applying equations (8) and (9) into equation (7), the following is obtained:

$$\Delta + (H_1 - H_2) = \frac{q_w^2}{g}\left[\frac{1}{r}\left(\frac{1}{H_1} + \frac{1}{H_2}\right) + \frac{1}{2}\left(\frac{1}{H_2^2} - \frac{1}{H_1^2}\right)\right] \tag{10}$$

In order to relate equation (10) to the mean flow characteristics, the definition of the Froude number can be introduced. Using equation (6) with the mean flow velocity and mean water depth, the Froude number can be defined as

$$F = \frac{V_m}{\sqrt{gH_m}} = \frac{q_w}{\sqrt{gH_m^3}} \tag{11}$$

and equation (10) can be subsequently transformed into

$$\Delta + (H_1 - H_2) = F^2 H_m^3 \left[\frac{1}{r} \left(\frac{1}{H_1} + \frac{1}{H_2} \right) + \frac{1}{2} \left(\frac{1}{H_2^2} - \frac{1}{H_1^2} \right) \right] \quad (12)$$

where the mean water depth can be considered to be equal to a geometric mean of the water depths over the crest and the trough, i.e.,

$$H_m = \sqrt{H_1 H_2} \quad (13)$$

Equation (12) describes the total energy difference between antidune crest and trough when both the Froude number and the bed form geometry are given, whereby the latter is specified according to the curvature radio as well as the amplitude of the bed undulations.

[16] A particular case for equation (12) exists when water depth above the crest is equal to the water depth above the trough, that is, the condition for which the antidune does not migrate either upstream or downstream, but remains stationary. Introducing this condition, i.e., $H_1 = H_2 = H_m$, into equation (12), and reducing, the following relation is found:

$$\frac{2F^2 H_m^2}{r\Delta} = 1 \quad (14)$$

Finally, by taking the squared root of (14), the dimensionless number

$$F_a = F H_m \sqrt{\frac{2}{r\Delta}} \quad (15)$$

called here the antidune mobility number F_a is introduced. In this manner, when $F_a = 1$, then the antidune remains stationary.

2.4. Criterion for Antidune Migration Direction

[17] Fundamental variables involved in equation (12) can be expressed by the functional relation

$$f_a(H_1, H_2, H_m, r, \Delta, V_m, g) = 0 \quad (16)$$

Because equation (13) relates H_1, H_2 and H_m, one of these variables is redundant in equation (16) and can be eliminated. H_1 and H_2 are retained, as they describe the water depth variation between the antidune crest and trough which is considered here the defining property of the migration direction; thus, H_m can be dropped. By doing this, equation (16) is transformed to

$$f_a(H_1, H_2, r, \Delta, V_m, g) = 0 \quad (17)$$

The number of variables in equation (17) can be reduced by dimensional analysis. Because two dimensions (length and time) are involved among the six variables, equation (17) can be reduced to 6–2 = 4 dimensionless products. In this manner, an alternative for representing equation (17) as a combination of nondimensional products is given by

$$f_a\left(\frac{H_1}{H_2}, \frac{r}{\Delta}, F, F_a \right) = 0 \quad (18)$$

The ratio H_1/H_2 accounts for the variation of the water depth between sections, the ratio r/Δ for the geometry of the bed form, the Froude number for the flow, and F_a for the interaction between all six variables as defined by equation (15). The ratio between the water depth over the crest and the water depth over the trough, H_1/H_2, is particularly important for the analysis of antidune movement. Consequently, according to Figure 2, it is established that for $H_1/H_2 > 1$, the antidune migrates upstream; for $H_1/H_2 = 1$, the antidune does not move; and for $H_1/H_2 < 1$, the antidune migrates downstream.

[18] Equation (12) has been solved numerically with the aid of the dimensionless numbers in equation (18). Results are shown in Figure 6 in a F_a versus H_1/H_2 plot, with families of Froude numbers, and for four values of r/Δ. For the purpose of defining the conditions that determine the direction in which antidunes propagate, what is conspicuous based on Figure 6 is that for $F > 1$ the correspondence between H_1/H_2 and F_a is biunivocal, i.e., for constant F and r/Δ, each value of F_a is related to only one value of the ratio H_1/H_2, which in turn is solely related to that same value of F_a. What is even more significant is the fact that for this range (i.e., $F > 1$) when $F_a < 1$, then $H_1/H_2 > 1$. Conversely, if $F_a > 1$, then $H_1/H_2 < 1$. On account of the latter properties of equation (12), the following criterion for antidune direction of movement can be established for supercritical flows ($F > 1$):

$$\text{if } F_a < 1, \text{ then } \frac{H_1}{H_2} > 1 \quad (19a)$$

and upstream-migrating antidunes occur;

$$\text{if } F_a = 1, \text{ then } \frac{H_1}{H_2} = 1 \quad (19b)$$

and stationary antidunes occur, as already known;

$$\text{if } F_a > 1, \text{ then } \frac{H_1}{H_2} < 1 \quad (19c)$$

and downstream-migrating antidunes occur.

[19] For Froude numbers close to one and low values of the ratio r/Δ the correspondence between H_1/H_2 and F_a tends not to be biunivocal; that is, for a given value of F_a, there exists more than one value of H_1/H_2 that satisfies equation (12). This would mean that for a certain range of values of F_a and r/Δ downstream-migrating or upstream-migrating antidunes could occur. Nevertheless, it is important to note that values of r/Δ which are approximately less than one would not be physically feasible, and thus this unstable region would be restricted to a very narrow range, for which F, F_a and H_1/H_2 values are close to one.

3. Criterion for Antidune Propagation as a Function of the Wave Number

[20] The criterion for antidune movement given by equations (19a)–(19c) was stated as a function of the dimensionless number F_a, which in turn depends on the flow Froude number, the mean water depth, and the bed form height and radius of curvature, as given by equation (15). Notwithstanding, description of the bed form geometry in terms of the radius of curvature is not common; instead, the bed form wavelength is widely used, with the advantage that

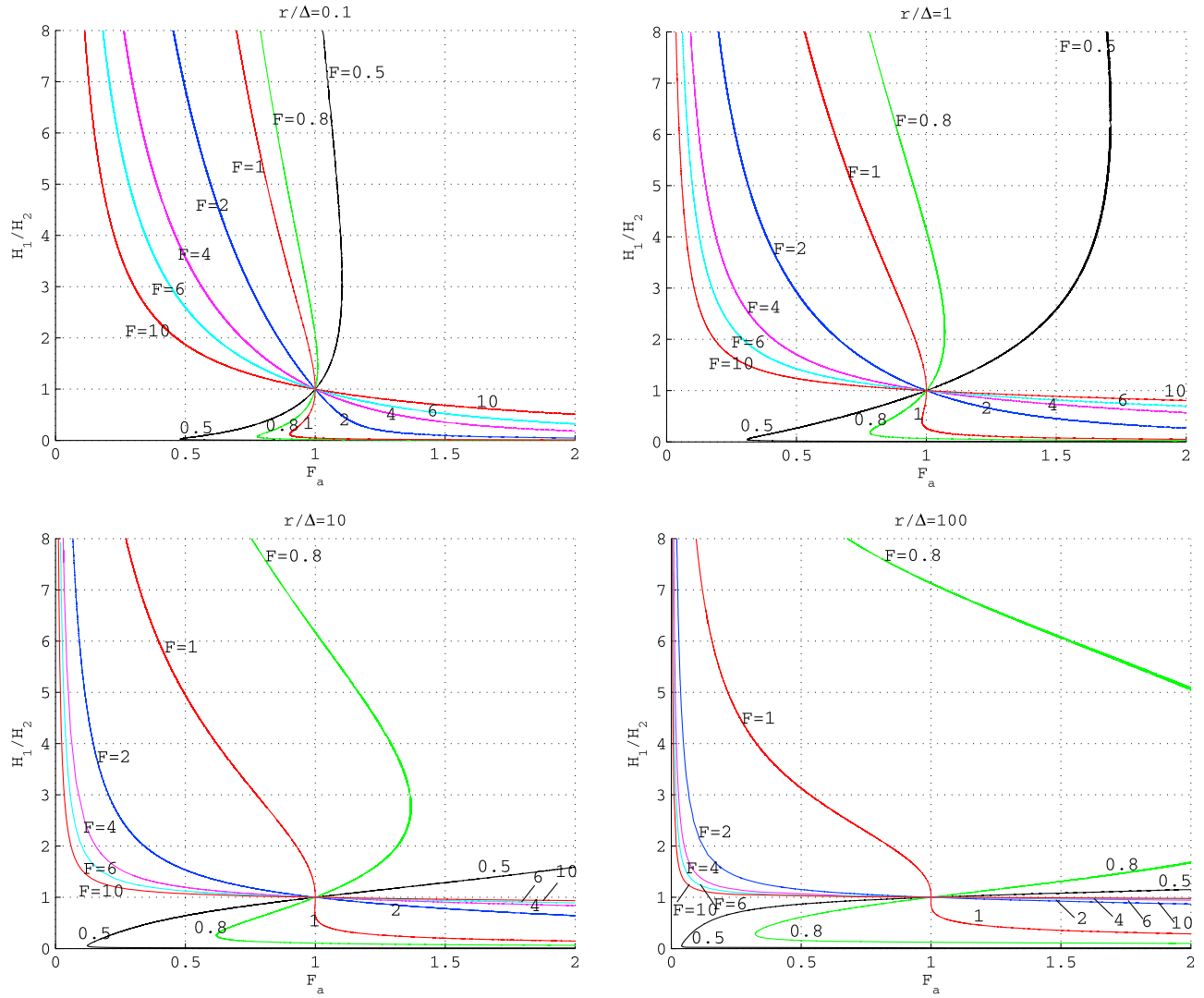

Figure 6. Numerical solution for equation (12), in terms of dimensionless numbers in equation (18).

for practical purposes in flumes and field the wavelength is easier to measure than the curvature radius. Therefore, in order to introduce commonly used bed form geometrical parameters for defining F_a, the mathematical definition of radius of curvature is applied here to an idealized antidune geometry in the following analysis.

[21] By definition, the curvature of a geometric object refers to its deviation from being flat. If it is considered that at a point of a curve the curvature is the same as that of the osculating circle at that point, then the curvature is given by

$$\mathrm{K} = \frac{y''}{\left(1 + y'^2\right)^{\frac{3}{2}}} \tag{20}$$

where y′ and y″ are the first and second derivatives of the curve function. The radius of curvature is given by the inverse of the curvature

$$r = \frac{1}{\mathrm{K}} \tag{21}$$

The idealized bed profile of a train of symmetrical antidunes, as shown in Figure 4, can be represented by the sinusoidal periodic function

$$\eta = \frac{\Delta}{2}\sin\left(\frac{2\pi x}{\lambda}\right) + \eta_o \tag{22}$$

where x is the horizontal axis, η is the bed surface level, η_0 is the datum for the mean bed surface level, Δ is the bed form height, and λ is the bed form wavelength. The definition of curvature can thus be applied to equation (22), whereby the curvature of the antidune results in

$$\mathrm{K} = -\frac{2\Delta\pi^2}{\lambda^2}\frac{\sin\left(2\pi x/\lambda\right)}{\left[1 + \left(\Delta\pi/\lambda\right)^2\cos^2\left(2\pi x/\lambda\right)\right]^{3/2}} \tag{23}$$

With reference to Figure 4 and equation (4), for the present analysis the curvature of the bed profile is evaluated at the top of the antidune crest and at the lowest point on the antidune

trough, where $x = \lambda/4$ and $x = 3\lambda/4$, respectively. As the considered antidune is symmetrical, the curvature is the same on the crest as on the trough but with a different sign. Evaluating at the trough with the introduction of $x = 3\lambda/4$ into equation (23), the curvature of the antidune is found to be

$$K = \frac{2\Delta\pi^2}{\lambda^2} \tag{24}$$

and from equation (21), the radius of curvature for the antidune crest and trough yields

$$r = \frac{1}{2\Delta}\left(\frac{\lambda}{\pi}\right)^2 \tag{25}$$

Introducing equation (25) into equation (15), and reducing, so that the antidune height is canceled, equation (15) takes the form

$$F_a = FH_m\frac{2\pi}{\lambda} \tag{26}$$

If the wave number k is given by

$$k = H_m\frac{2\pi}{\lambda} \tag{27}$$

then equation (26) can be rewritten as

$$F_a = kF \tag{28}$$

Finally, by introducing equation (28) into the criteria defined by equations (19a)–(19c), the three cases of antidune propagation can be defined in terms of the Froude number and wave number as follows: if

$$F < \frac{1}{k} \tag{29a}$$

upstream-migrating antidunes; if

$$F = \frac{1}{k} \tag{29b}$$

stationary antidunes; and if

$$F > \frac{1}{k} \tag{29c}$$

downstream-migrating antidunes. This criterion is similar to that given by equations (19a)–(19c) insofar as it is also valid for supercritical flows.

4. Maximum Antidune and Stationary Wave Steepness

[22] As stated in section 2.4, there are some solutions for equation (12) which do not have a practical significance. Here, restrictions for the stability of the antidunes' and the water gravity waves' steepness are introduced in order to set a boundary for the physically feasible solutions of equation (12).

[23] Because the quotient Δ/λ is related to the steepness of the bed form lee side (i.e., lee slope steepness equals $2\Delta/\lambda$), there exists a maximum Δ/λ value for which the lee slope angle would be stable. This maximum value can be related to the submerged angle of repose of the bed material, whose value is roughly between 30° and 40° for natural grains (G. Parker, e-book, 2004). Therefore, for symmetrical antidunes (stoss and lee sides have the same angle with the mean bed level) the maximum ratio between antidune height and wavelength for stability of the lee slope would range between 0.25 and 0.36. Then, by applying equation (25) it is found that the minimum value that the ratio r/Δ could attain would be between 0.39 and 0.81, and thus, the graphic in Figure 6 with the solution for $r/\Delta = 0.1$, would not have any practical significance.

[24] In the same manner as for the bed form steepness, there exists a limiting value for the steepness of the stationary waves above antidunes. If such a maximum steepness is reached, the waves break. *Michell* [1893] [after *Kennedy*, 1961] found that the maximum ratio between the vertical distance from trough to crest, Δ_w, and the wavelength, λ, that can exist for gravity waves is

$$\frac{\Delta_w}{\lambda} = 0.142 \tag{30}$$

For waves above experimental antidunes, *Kennedy* [1961] reported values of Δ_w/λ that ranged from 0.13 to 0.16, findings which correspond well to equation (30).

[25] With reference to Figure 4, the height of stationary waves above antidunes can be calculated from

$$\Delta_w = \Delta_1 + \Delta_2 + H_1 - H_2 = \Delta + H_1 - H_2 \tag{31}$$

By combining equation (30) and equation (31), the maximum wave steepness above antidunes can be specified as

$$\frac{\Delta + H_1 - H_2}{\lambda} \le 0.142 \tag{32}$$

In a similar manner as in Figure 6, in Figure 7 numerical solutions for equation (12) have been plotted. By applying equation (25), the ratio Δ/λ has been used instead of r/Δ. In addition, by imposing the restriction of a maximum wave steepness, as given by equation (32), Figure 7 highlights with bold lines the range of values for which the maximum wave steepness is surpassed, i.e., the range of conditions that would not be physically feasible. As such, from the solutions described by Figure 7 it can be put forward that an upper limit for the steepness of upstream-migrating antidunes would roughly be $\Delta/\lambda = 0.15$, since sharper steepness than this value would result in the gravity waves over the antidunes being unstable. On the other hand, physically coherent solutions for downstream-migrating antidunes can occur for even greater ratios of bed form height/bed form wavelength than they can for upstream-migrating antidunes. An upper limit for the solution for downstream-migrating antidunes could be set at $\Delta/\lambda = 0.36$, as this is the maximum possible steepness which ensures the stability of the bed material, as calculated above.

5. Effect of Expansion Losses

[26] For the energy balance in section 2.3, the loss of energy between the form crest and trough was not taken into consideration. If it is assumed that energy losses owed to skin friction are not significant, the hypothesis of insignificant

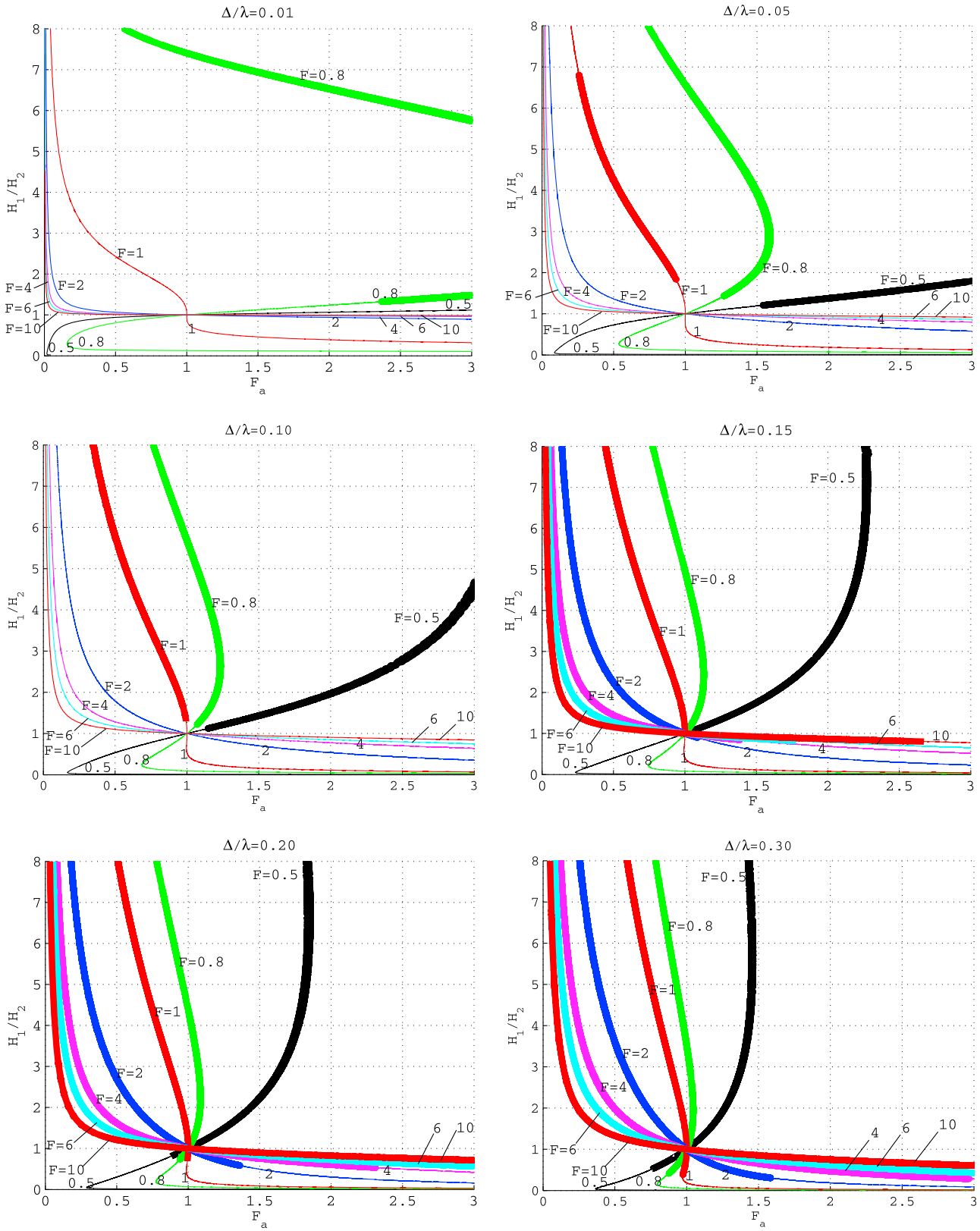

Figure 7. Numerical solution for equation (12). Bold lines indicate solutions with no practical significance due to the fact that the height of the waves physically exceeds what equation (32) has established as being the maximum possible height.

energy loss is at least valid for symmetrical upstream-migrating antidunes, which are known to generate negligible expansion loss [*Simons et al.*, 1961; after *Carling and Shvidchenko*, 2002]. Nevertheless, for downstream-migrating antidunes expansion losses are likely to be appreciable. This is confirmed by the analysis presented in Appendix A, where it is shown that separation of the boundary layer can be more important over downstream-migrating antidunes than over upstream-migrating antidunes. Here the expansion losses are considered in the energy balance in order to evaluate their effect on the criterion (developed in section 2) for determining the direction of movement of antidunes.

[27] As an approximation, the expansion loss may be estimated from the velocity head change between sections, as

$$h_e = k_e \frac{(V_1 - V_2)^2}{2g} \tag{33}$$

where k_e is a dimensionless coefficient. With this, equation (4) can be rewritten as

$$\Delta_1 + h_1 + \frac{V_1^2}{2g} = -\Delta_2 + h_2 + \frac{V_2^2}{2g} + k_e \frac{(V_1 - V_2)^2}{2g} \tag{34}$$

Following similar simplifications and developments as in equations (5) to (11), equation (12) can be written with the inclusion of expansion loss as follows:

$$\Delta + (H_1 - H_2) = F^2 H_m^3 \left[\frac{1}{r} \left(\frac{1}{H_1} + \frac{1}{H_2} \right) + \frac{1}{2} \left(\frac{1}{H_2^2} - \frac{1}{H_1^2} + k_e \left\{ \frac{1}{H_1} - \frac{1}{H_2} \right\}^2 \right) \right] \tag{35}$$

Reduction of equation (35) for stationary antidunes, for which $H_1 = H_2 = H_m$, produces the same results given in equations (14) and (15) for the antidune mobility number F_a, so that stationary antidunes occur if $F_a = 1$ when $H_1 = H_2$.

[28] Equation (35) would be valid for bed forms where expansion losses and curvilinear flow occur simultaneously, as can be expected for downstream-migrating antidunes. Following the same developments for solving equation (12) as shown in section 3, the numerical solution for equation (35) was obtained for different values of the quotient Δ/λ and of the coefficient k_e for the condition $H_1/H_2 < 1$, which corresponds to downstream-migrating forms; we assume that for $H_1/H_2 > 1$, i.e., upstream-migrating forms, expansion losses are not significant (see Appendix A) and the solution given in Figure 7 is valid. Results showed that the main effect of including expansion loss is that, as k_e increases, the minimum Froude number for which the correspondence between H_1/H_2 and F_a is biunivocal also increases. Figure 8 shows solutions of equation (35) for $\Delta/\lambda = 0.05$ and for four different values of k_e.

[29] According to the above results, if expansion losses are significant there is a range of values for $F \geq 1$ for which equation (35) is not biunivocal, and the direction of movement of the antidune cannot be established with the criterion given by equations (19a)–(19c). However, if expansion losses over the bed form lee side are important, it can be expected that downstream propagation will prevail over upstream propagation because expansion losses are caused by flow separation which, in turn, favors sediment deposition. Bearing this in mind, it can be stated here that for critical flows and flows close to the critical, if expansion losses are important, the range for which downstream propagation occurs would not be restricted to $F_a > 1$, as stated in equations (19a)–(19c); rather, this range could extend to values of F_a slightly smaller than 1.

6. Comparison With Experimental Data

[30] The criterion developed above for defining the propagating direction of antidunes, in the form given by equations (29a)–(29c), is here compared with experimental data, as shown in Figure 9a. Selected data sets for the comparison refer to bed forms developed in the upper regime and in the lower to upper regime transition. The data sets and the range of variables are summarized in Table 1 and are described below.

[31] Regarding *Kennedy*'s [1961] findings, the data set corresponds to experiments where the mechanics of stationary waves and antidunes in sand beds were studied. Downstream-migrating antidunes were observed in only 2 of the 43 runs performed, while upstream-migrating antidunes were observed in 15 runs. For 7 runs downstream-migrating transitional bed forms with weak to moderate coupling between bed surface and water surface were the dominant bed features registered. In only 2 runs stationary antidunes formed, while flat beds occurred in 10 runs. For 7 runs with antidunes, the direction of movement was not registered. The bed forms observed by Kennedy were mostly two dimensional, but in particular most of the transitional bed forms and all of the downstream-migrating and stationary antidunes were three dimensional. Data used here correspond only to those runs for which the direction of movement was specified and for which the wavelength was measured.

[32] *Carling and Shvidchenko* [2002] studied the transition between dunes and antidunes in fine gravel, giving emphasis to downstream-migrating antidunes. For this study, they collected data sets (some previously unpublished) where transitional bed forms and antidunes were described. What is noteworthy are the data sets they collected for which downstream-migrating antidunes were observed, given that such bed forms have been observed and measured much less often than upstream-migrating antidunes in experimental flumes. Data points from original experimental campaigns by *Kopaliani* [1972] and *Wieprecht* [2000] presented by *Carling and Shvidchenko* [2002, Figure 8] were used here in Figure 9. All data from Kopaliani's data set correspond to downstream-migrating bed features, which he described as downstream-migrating symmetrical antidunes, dunes to transitional dunes, and downstream-migrating asymmetric antidunes. Data points from Wieprecht's data set correspond to bed features described as upstream-migrating antidunes beneath breaking standing waves. What is interesting about the plotted data from Wieprecht's data set is that upstream-migrating antidunes were observed for Froude numbers below one. No details are given by *Carling and Shvidchenko* [2002] for the range of water depths, slopes and flow velocities in Kopaliani's and Wieprecht's experiments.

[33] *Alexander et al.* [2001] performed three runs with medium sand to study the relationship between bed forms and

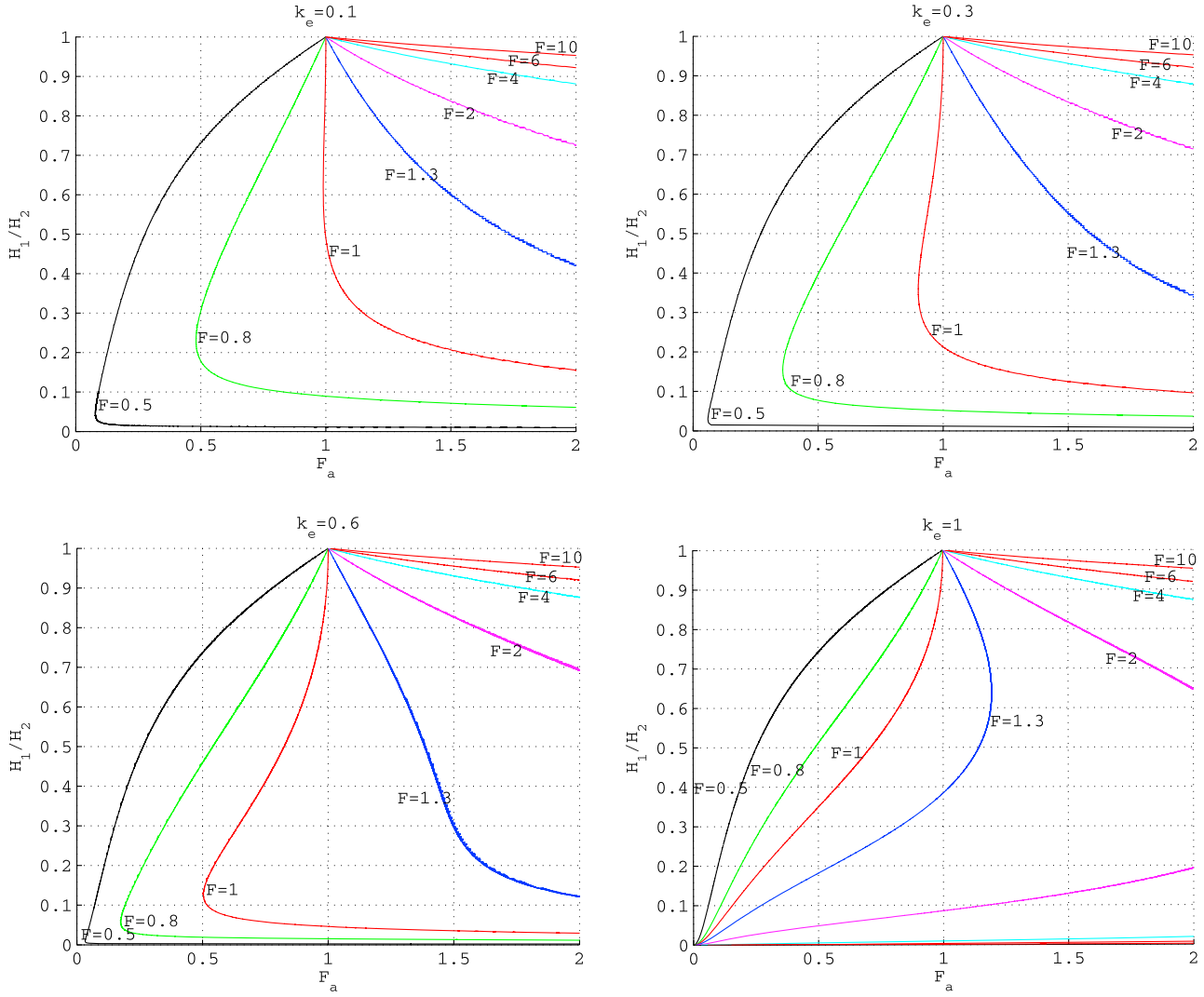

Figure 8. Numerical solutions for equation (35), for a constant value of $\Delta/\lambda = 0.05$.

their internal structures under supercritical flows. Antidunes observed were two-dimensional and migrated upstream.

[34] *Bregoli* [2008] performed six experimental runs for supercritical flows with fine gravel. Two-dimensional antidunes developed in four of the runs for which upstream-migrating antidunes were the prominent bed forms observed for three of them, while for one run either downstream or upstream-migrating antidunes formed. For this latter run the data point in Figure 9 is marked as downstream migrating.

[35] *Recking et al.* [2009] investigated the effect of gentle and steep slopes on the antidune wavelength using three uniform gravels. Observed antidunes were two-dimensional upstream migrating.

[36] Trains of downstream-migrating antidunes were observed by *Spinewine et al.* [2009] when conducting experiments aimed at reproducing the formation of wedge-shaped deposits by decelerating turbidity currents in the marine environment. Salt was used as a substitute for fine mud transported by actual turbidity currents. Evidence to class the observed bed forms as antidunes was the phasing of the interface between the saline current and the ambient water above relative to the bed.

[37] *Núñez-González and Martín-Vide* [2010] described three-dimensional antidunes and transitional forms that propagated in the downstream direction for flows at, and close to, the transition between lower and upper regimes. Four run series were performed, each with a different bed material, namely gravel, sand and two sand-gravel mixtures with a sand content of 32% and 44%, respectively.

[38] In order to emphasize the comparison of the propagating direction of the bed forms, in Figure 9 there is no distinction between two- and three-dimensional features, nor between dunes, transitional bed forms, and antidunes. Nevertheless, what is noteworthy is that when $F > 1.2$ only antidunes, and not dunes or transitional bed forms, were described in all of the data sets.

[39] Figure 9a shows a consistent agreement between theory and the experimental points. The only two points pertaining to stationary antidunes plot below, albeit close and parallel to, the theoretical curve. For Froude numbers higher than approximately one, all of the experimental points for upstream-migrating antidunes and most for downstream-migrating forms fall within the region predicted by theory; only four downstream-migrating bed features for $F > 1$ (two

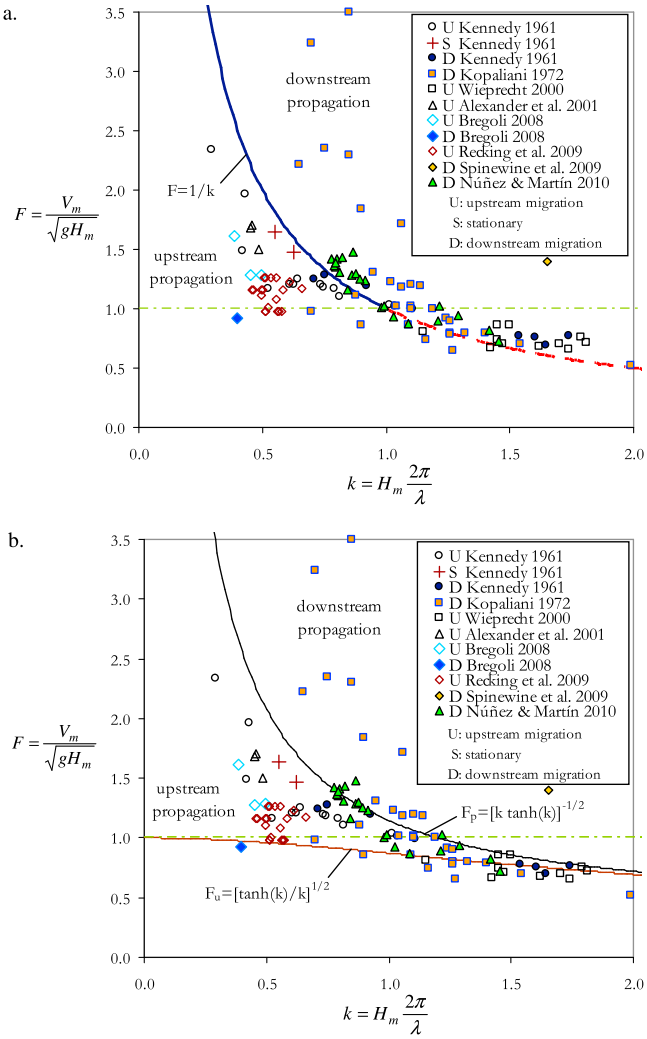

Figure 9. Comparison of criteria for discriminating antidune propagation direction with experimental data. (a) Criterion developed in the present work, given by equations (29a)–(29c); solid line for the function $F = 1/k$ depicts the range of Froude numbers ($F \geq 1$) for which theory predicts a unique propagating direction, whereas the dashed line depicts the range of Froude numbers ($F < 1$) for which theory predicts either upstream propagation or downstream propagation; (b) bed form occurrence fields developed from potential flow theory as given by *Kennedy* [1963]; F_u gives the lower limit for upper regime and F_p gives the higher limit for upstream-migrating antidunes and lower limit for downstream-migrating antidunes. The horizontal dash-dotted line corresponds to the critical Froude number.

from Kennedy, one from *Kopaliani* [1972] and one from *Núñez-González and Martín-Vide* [2010]) plot below the theoretical curve, i.e., in the region for upstream-migrating bed forms. Nevertheless, though these points appear quite close to the theoretical curve, their existence below the predicted position could be related to the expansion losses. As described in section 5, if expansion losses are important, the border for downstream propagation could be slightly lower than $F_a = 1$, and thus the theoretical curve in Figure 9a would then move slightly below for Froude numbers close to one.

[40] As was discussed in section 2.4, for Froude numbers close and lower than one, the theory developed predicts that for a given pair of values of Froude and wave numbers, bed forms would move either upstream or downstream. Data points agree with theory in the sense that for Froude numbers roughly less than one, downstream- and upstream-propagating forms plot indistinctly above and below the theoretical curve, and they even overlap. What is conspicuous is that most of the data provided by *Wieprecht* [2000] for upstream-migrating antidunes plot above the theoretical curve, and many of the data points of *Kopaliani* [1972] for downstream-migrating forms plot below it.

6.1. Comparison With Potential Flow Theory

[41] *Kennedy* [1963] presented bed form stability fields based on the solution of a linearized potential flow over a wavy bed, following original ideas from a stability analysis performed by *Anderson* [1953] and extended by *Kennedy* [1961]. According to the bed form stability fields developed with potential flow theory, upper regime occurs when $F > F_u$, where

$$F_u = \sqrt{\frac{\tanh(k)}{k}} \tag{36}$$

Similarly, theory predicts that downstream-migrating antidunes are likely to occur for large wave numbers if $F > F_p$, where F_p is given by

$$F_p = \sqrt{\frac{1}{k \tanh(k)}} \tag{37}$$

The existence of upstream-migrating antidunes would be restricted to the range $F_u < F < F_p$. Equations (36) and (37) have been plotted in Figure 9b to be compared with the curve $F = 1/k$ in Figure 9a, which depicts the criterion for antidune propagating direction presented in section 3.

[42] More than half of the experimental data points pertaining to downstream-propagating bed features plot inadequately according to equations (36) and (37), while most of the data for upstream-migrating bed forms plot in the predicted region. In comparison, in distinguishing the direction of movement of the bed forms, the criterion developed in the present study performs better than the potential flow analysis.

6.2. Comparison of Antidune Steepness

[43] Little information exists in literature to test the validity of the range of antidune steepness predicted by the theory developed in sections 2, 3, and 4. Nevertheless, some information is available from some of the data sets used to draw Figure 9 to compare between steepness of upstream- and downstream-migrating antidunes. Table 2 presents a summary of the bed form characteristics for the data sets for which this information was available. *Alexander et al.* [2001] presented average values for heights and wavelengths of the upstream-migrating antidunes observed in the three runs they performed. *Bregoli* [2008] measured antidune wavelengths and heights at different instants during his experiments; average values for each of his runs are used in Table 2. In a similar manner, *Recking et al.* [2009] measured antidune heights for 12 of their 19 runs, and *Spinewine et al.* [2009] presented the range of aspect ratios (wavelength divided by

Table 1. Summary of Experimental Data Used for Comparison With Theory in Figure 9

Source	Flume Length (m)	Flume Width (m)	Sediment Median Size (mm)	Range of Flow Depths (m)	Range of Flow Velocities (m/s)	Range of Mean Slopes
Kennedy [1961]	12.0	0.27	0.23	0.044–0.106	0.48–1.05	0.0026–0.0272
Kennedy [1961]	18.0	0.85	0.55	0.037–0.105	0.50–1.42	0.0017–0.0229
Kopaliani [1972]	30.0	0.50	2.16 and 6.50	-	-	-
Wieprecht [2000]	-	-	2.0 and 3.0	-	-	-
Alexander et al. [2001]	7.6	0.60	0.42	0.068–0.073	1.30–1.41	0.015–0.016
Bregoli [2008]	9.2	0.40	7.34	0.028–0.036	0.50–1.04	0.040–0.055
Recking et al. [2009]	6.0	0.05 and 0.102	2.3, 9.0 and 23.0	0.007–0.045	0.29–0.77	0.030–0.126
Spinewine et al. [2009]	15.0	0.45	0.21[a]	0.05[b]	0.15	0.095–0.140
Núñez-González and Martín-Vide [2010] (gravel)	27.0	0.75	4.20	0.068–0.109	0.96–1.16	0.006–0.021
Núñez-González and Martín-Vide [2010] (sand)	27.0	0.75	1.43	0.103–0.130	0.82–1.03	0.006–0.016
Núñez-González and Martín-Vide [2010] (mix 32% sand)	27.0	0.75	3.20	0.076–0.113	0.92–1.30	0.006–0.017
Núñez-González and Martín-Vide [2010] (mix 44% sand)	27.0	0.75	2.45	0.080–0.113	0.94–1.31	0.006–0.018

[a]Plastic sediment with a specific density of 1.53.
[b]Mean flow thickness for the turbidity current.

wave height) for the antidunes observed in their experiments. For two-dimensional sand antidunes, *Núñez-González and Martín-Vide* [2010] measured wavelengths and obtained average heights from the standard deviation of the measured bed profiles.

[44] By comparing data in the fifth and sixth columns of Table 2, it is remarkable that the steepness of most of the upstream-migrating bed forms is almost half, or less than half, of the steepness of the downstream-migrating features. Though this tendency agrees with theory, insofar as downstream-migrating antidunes could attain steeper shapes than upstream-migrating antidunes, more data for a wider range of conditions would be necessary to test the theoretical findings. For instance, the highest steepness registered in certain measurements in upstream-migrating antidunes for the experiments of Bregoli was as high as 0.15, i.e., an even higher gradient than for any of the downstream-migrating antidunes described in Table 2, except one. Such sharp steepness described by Bregoli is within the limit of the most abrupt steepness likely to occur in upstream-migrating antidunes, according to theory as described by Figure 7.

[45] Images of experimental bed forms in Figure 3 illustrate some of the distinguishing features of upstream- and downstream-migrating antidunes, as is specified by the theoretical findings developed above. First, it is evident that downstream-migrating antidunes show highest ratios between flow depth and wavelength; that is, the wave number k for downstream-migrating antidunes is higher than the wave number for upstream-migrating antidunes, so that for a given Froude number, upstream-propagating bed forms plot to the left of the curve in Figure 9a, whereas downstream-propagating bed forms plot to the right. Second, for the selected pictures the ratio between bed form height and wavelength, i.e., the antidune steepness, is higher for downstream-migrating antidunes than for upstream-migrating antidunes. Nevertheless, as stated above, no conclusion can be given with respect to a clear tendency for downstream-migrating antidunes being able to attain steeper lee slope angles. The sediment characteristics are not considered in the theory developed, and this could have a decisive effect on the stability of the bed form slopes and therefore on the bed form steepness. Furthermore, note that images in Figure 3 refer to instantaneous bed conditions; it is common that the bed behavior associated with antidunes exhibits a complex periodic pattern, for which not only the form and shape of the antidunes, but also the bed state, may change considerably from time to time for given flow conditions. The antidunes reproduced in Figure 3 might not, therefore, correspond to an ultimate stable condition representative of the particular mean flow.

7. Discussion

[46] Most of the bed form stability analyses, like those of *Kennedy* [1961] and *Engelund and Hansen* [1966], consider that the bed perturbations are small in comparison to the wavelength, so that the curvature of the streamlines is con-

Table 2. Summary of Experimental Data for Which Bed Form Steepness Was Measured

Source	Run	Froude Number F	Wave Number k	Mean Δ/λ	Propagating Direction
Alexander et al. [2001]	1	1.71	0.48	0.053	upstream
	2	1.68	0.47	0.050	upstream
	3	1.50	0.50	0.052	upstream
Bregoli [2008]	1	0.92	0.40	0.050	downstream and upstream
	2	1.29	0.50	0.106	upstream
	3	1.28	0.45	0.079	upstream
	4	1.61	0.39	0.062	upstream
Recking et al. [2009]	12 runs	0.98, 1.16 and 1.26	0.46–0.57	0.025–0.062	upstream
Spinewine et al. [2009]	2 runs	1.40[a]	1.57–1.74	0.111–0.167	downstream
Núñez-González and Martín-Vide [2010] (sand)	S1	1.02	1.22	0.092	downstream
	S2	0.94	1.29	0.122	downstream
	S3	0.82	1.42	0.111	downstream
	S4	0.73	1.46	0.101	downstream

[a]Densimetric Froude number of the turbidity current.

sidered unimportant. Conversely, the analysis developed in this study is based mainly on the inclusion of the correction to the pressure head due to the curvilinear flow. From equation (4), it can be demonstrated that if no curvilinear flow is considered, stationary symmetrical antidunes, for which water depths and flow velocity would be constant along the undulated bed profile, cannot be predicted solely with an energy balance; this is the case considering that all variables in the Bernoulli equation would cancel each other out. The inclusion of the effect of centrifugal forces allows for the balance of energy to be completed. In this manner, for stationary antidunes the bed form height turns out to be equal to the sum of the absolute values of the pressure head due to the centrifugal forces on the bed form crest and the trough.

[47] In the limit of validity of the criterion given by equations (29), i.e., for Froude numbers equal and close to one, the solution of the functions given by equations (12) and (34) is quite steep for values of H_1/H_2 and F_a close to one, as can be seen in Figures 6, 7, and 8. Therefore, for this region the developed theory fails to predict the direction of movement. Notwithstanding, it can be hypothesized that downstream propagation of the bed forms could prevail over immobility and upstream migration; this might be so because a transitional regime occurs for flows close to and at the critical condition, for which the bed configuration is erratic, and bed forms with intermediate or interchanging characteristics of well-developed dunes and antidunes are formed. The irregularity and asymmetry of these transitional bed forms favors the detachment of the streamlines over the bed form slip face, and thus, deposition over the bed form trough and downstream migration might be more likely to occur than upstream migration. This is confirmed by Figure 9, where all data points with values of H_1/H_2 and F_a close to one, except for one, correspond to downstream-migrating antidunes.

[48] The flow regime for which antidunes develop is extremely unstable, often characterized by a sequence in which the water surface and bed change continuously; a thorough description of the cyclic behavior of antidunes in sand was given by *Alexander et al.* [2001]. This unsteadiness may favor a constant change of the shape and geometry of antidunes, especially if the breaking of the stationary waves over the antidunes occurs. The theory developed here comes up against, at this point, a limitation, as it considers a steady flow over a steady sinusoidal bed. Furthermore, it could be queried whether the hypothesis of incompressibility of the flow remains applicable for the case in which wave breaking leads to a large amount of air entrained into the water.

[49] A probable drawback of the theory developed here would seem to be that sediment transport is not adduced as a fundamental variable for tackling the problem of the antidune movement direction. However, it should be noted that sediment transport has been indirectly considered by assuming that erosion (deposition) occurs along the region of the bed form where flow accelerates (decelerates). By neglecting possible spatial lags between bed shear stress and sediment transport, such a hypothesis is reasonable and allows for a straightforward analysis.

[50] As a final point, it can be noted that the theory developed here for distinguishing the movement direction of an antidune does not consider the characteristics of the bed sediment. The grain size distribution, shape and sorting may have an important effect on the bed form steepness and on the variation of the bed load sediment transport along the antidune. More investigation is required for expanding the knowledge of downstream-migrating antidunes and to recognize the role of sediment grain characteristics in antidune morphology and genesis.

8. Conclusion

[51] A new theory has been developed for identifying the conditions for which antidunes move preferentially upstream, downstream or remain stationary. The new theory is based on fundamental hydraulics by considering an energy balance over an idealized symmetrical sinusoidal antidune. In order to carry out this energy balance, the Bernoulli equation has been applied between the antidune crest and antidune trough, and the pressure head has been corrected to account for the centrifugal forces generated by curvilinear flow over the in-phase bed form. The biunivocal character of the deduced function for the supercritical flow range allows for the establishment of a criterion to identify the preferential direction of movement of antidunes, according to an antidune dimensionless mobility number (F_a). Such a mobility number depends only on the flow Froude number, the mean water depth, and the antidune wavelength. The critical value of the antidune mobility number ($F_a = 1$) denotes the stationary condition; when the values are higher than the critical they correspond to downstream antidune propagation, while those values which are lower than the critical correspond to upstream antidune propagation. For Froude numbers and ratios of the flow depth over the crest and over the trough close and equal to one, the criterion is no longer valid, especially if expansion losses are important. Nonetheless, for this range, it can be expected that the margin for which downstream propagation occurs would extend to values of the mobility number slightly smaller than one.

[52] By introducing a restriction for the maximum stationary wave height above antidunes, the developed theory predicts that downstream-migrating antidunes could attain steeper height-wavelength ratios than upstream-migrating antidunes. Likewise, the theory predicts that for a given Froude number, downstream-migrating antidunes are formed for higher water depth-wavelength ratios than upstream-migrating antidunes.

[53] Comparison with published experimental data in literature provided a considerable degree of agreement between the developed theory and experimental observations. Furthermore, the new theory gives a better definition of the fields of occurrence of each of the three antidune mobility regimes than does potential flow theory.

[54] The theory here developed does not consider the sediment characteristics; further investigation is required to study the influence of grain size diameter, shape and grain size standard deviation in the preferential propagating direction of antidunes and their morphology. Moreover, the influence of wave breaking on antidune migration is not considered in the analysis; this issue also deserves attention for future work.

Appendix A: Effect of the Pressure Gradient on Boundary Layer Detachment

[55] Prandtl demonstrated that boundary layer separation occurs when the flow should move downstream against an

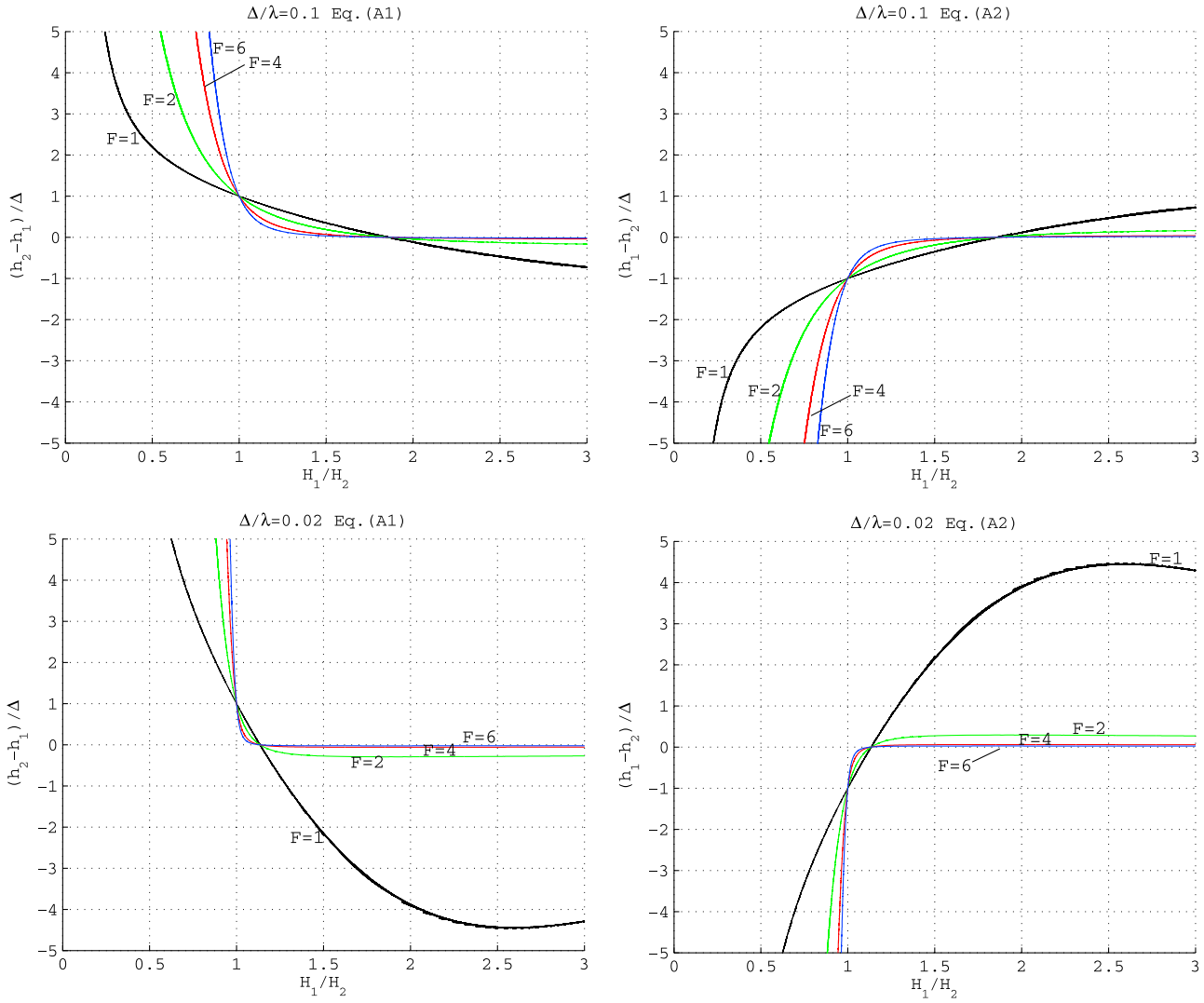

Figure A1. Numerical solutions for equation (A1) and equation (A2) applied with equation (12).

adverse pressure gradient [*White*, 1979], i.e., dp/dx < 0, with p being the pressure head. If pressure decreases, i.e., dp/dx > 0, it is said that there exists a favorable gradient and separation does not occur. To study the flow separation on the stoss and leesides of antidunes for the three conditions of movement, here we analyze the pressure gradient over a train of symmetric antidunes, as depicted in Figure 4.

[56] Considering curvilinear flow by applying equations (2) and (3), introducing the Froude number with equations (6) and (11), and using the definition of the radius of curvature given by equation (25), the pressure gradient from the antidune crest to trough is found to be

$$h_2 - h_1 = (H_2 - H_1) + 2F^2 H_m^3 \Delta \left(\frac{\pi}{\lambda}\right)^2 \left(\frac{1}{H_1} + \frac{1}{H_2}\right) \qquad \text{(A1)}$$

Table A1. Conditions for Flow Separation Along an Antidune According to the Pressure Gradient

Pressure Gradient	Downstream Migrating ($H_1 < H_2$)	Stationary ($H_1 = H_2$)	Upstream Migrating ($H_1 > H_2$)
Crest to trough (h_2–h_1)	dp/dx > 0 High adverse gradient.	dp/dx > 0 Adverse gradient = Δ.	dp/dx > 0 and dp/dx < 0 Weak adverse gradient < Δ and weak favorable gradient > −Δ.
	Separation	Separation might or might not occur	Increased probability of separation the lower H_1/H_2 is and the higher Δ/λ is
Trough to crest (h_1–h_2)	dp/dx < 0 High favorable gradient.	dp/dx < 0 Favorable gradient = −Δ.	dp/dx < 0 and dp/dx > 0 Weak favorable gradient > −Δ and weak adverse gradient < Δ.
	No separation	No separation	Increased probability of separation the higher H_1/H_2 is and the lower Δ/λ is

where the subscripts 1 and 2 refer to the crest and trough, respectively. Likewise, the pressure gradient from trough to crest yields

$$h_1 - h_2 = (H_1 - H_2) - 2F^2 H_m^3 \Delta \left(\frac{\pi}{\lambda}\right)^2 \left(\frac{1}{H_1} + \frac{1}{H_2}\right) \qquad \text{(A2)}$$

[57] For four families of Froude numbers and two values of Δ/λ, Figure A1 shows numerical solutions for equations equation (A1) and equation (A2) used with equation (12), as a function of the quotients H_1/H_2 and $(h_1-h_2)/\Delta$. According to Figure A1, Table A1 presents the conditions for which flow separation would occur taking into account that there is no separation when the pressure gradient is favorable, when it is zero, and when it is adverse but weak.

[58] The higher the adverse gradient is, the higher the effect of flow separation. From Figure A1 it can be observed that $d[(h_2-h_1)/\Delta]/d(H_1/H_2)$ and $d[(h_1-h_2)/\Delta]/d(H_1/H_2)$ are higher for $H_1/H_2 < 1$ than for $H_1/H_2 > 1$; hence flow separation can be expected to be more intense in downstream-migrating antidunes than in upstream-migrating ones.

Notation

E total energy at the channel section [L].
F Froude number [dimensionless].
F_a antidune mobility number [dimensionless].
f_a functional relation.
g gravitational acceleration [L T^{-2}].
H cross-section water depth [L].
H_m reach average water depth [L].
h pressure head on the bed surface [L].
h_e expansion loss [L].
h_p pressure head due to centrifugal acceleration [L].
k wave number [dimensionless].
k_e coefficient for expansion losses [dimensionless].
K curvature [L^{-1}].
p pressure head [L].
q_w water discharge [L^2 T^{-1}].
r radius of curvature [L].
V cross-sectionally averaged flow velocity [L T^{-1}].
V_m reach average flow velocity [L T^{-1}].
x horizontal axis [L].
y vertical coordinate [L].
Δ bed form height [L].
Δ_1 distance from the mean bed surface level to the bed form crest [L].
Δ_2 distance from the mean bed surface level to the bed form trough [L].
Δ_w vertical distance from trough to crest of water stationary wave [L].
η bed surface level [L].
η_o datum for the mean bed surface level [L].
λ bed form length [L].

[59] **Acknowledgments.** The first author was supported by the Programme Alßan, the European Union Programme of High Level Scholarships for Latin America (E04D048796MX), and by Conacyt, México (179047). The authors thank Gary Parker for providing them with a digital copy of Kennedy's original study on antidunes. The writers also acknowledge the constructive reviews by the Editor, Associate Editor, and three anonymous referees, whose helpful comments and suggestions largely contributed to the improvement of earlier versions of this manuscript.

References

Alexander, J., J. S. Bridge, R. J. Cheel, and S. F. Leclair (2001), Bedforms and associated sedimentary structures formed under supercritical water flows over aggrading sand beds, *Sedimentology*, *48*, 133–152, doi:10.1046/j.1365-3091.2001.00357.x.

Anderson, A. G. (1953), The characteristics of sediment waves formed by flow in open channels, paper presented at Third Midwest Conference on Fluid Mechanics, Univ. of Minn., Minneapolis, Minn.

Bose, S. K., and S. Dey (2009), Reynolds averaged theory of turbulent shear flows over undulating beds and formation of sand waves, *Phys. Rev. E*, *80*(3), 036304, doi:10.1103/PhysRevE.80.036304.

Bregoli, F. (2008), Setting of an experimental flume and first experiments in gravel-bed river's morphodynamics (in Italian), Graduate thesis, Eng. Fac., Univ. of Florence, Florence, Italy.

Carling, P. A., and A. B. Shvidchenko (2002), A consideration of the dune: antidune transition in fine gravel, *Sedimentology*, *49*, 1269–1282, doi:10.1046/j.1365-3091.2002.00496.x.

Chaudhry, M. H. (1993), *Open-Channel Flow*, Prentice Hall, Englewood Cliffs, N. J.

Chow, V. T. (1959), *Open-Channel Hydraulics*, McGraw-Hill, New York.

Coleman, S. E., and J. D. Fenton (2000), Potential-flow instability theory and alluvial stream bed forms, *J. Fluid Mech.*, *418*, 101–117, doi:10.1017/S0022112000001099.

Colombini, M., and A. Stocchino (2008), Finite-amplitude river dunes, *J. Fluid Mech.*, *611*, 283–306, doi:10.1017/S0022112008002814.

Engelund, F. (1970), Instability of erodible beds, *J. Fluid Mech.*, *42*, 225–244, doi:10.1017/S0022112070001210.

Engelund, F., and E. Hansen (1966), *Investigations of Flow in Alluvial Streams*, *Acta Polytech. Scand.*, vol. 35, Akad. for de Tek. Videnskaber, Copenhagen.

Fredsøe, J. (1974), On the development of dunes in erodible channels, *J. Fluid Mech.*, *64*, 1–16, doi:10.1017/S0022112074001960.

García, H. M. (2006), *Sediment Transport, Lecture Notes*, Ven Te Chow Hydrosyst. Lab., Dep. of Civ. and Environ. Eng., Univ. of Ill. at Urbana-Champaign, Urbana.

Hayashi, T. (1970), Formation of dunes and antidunes in open channels, *J. Hydraul. Div. Am. Soc. Civ. Eng.*, *96*(2), 357–366.

Kennedy, J. F. (1961), Stationary waves and antidunes in alluvial channels, *Rep. KH-R-2*, W. M. Keck Lab. of Hydraul. and Water Resour., Calif. Inst. of Technol, Pasadena.

Kennedy, J. F. (1963), The mechanics of dunes and antidunes in erodible bed channels, *J. Fluid Mech.*, *16*, 521–544, doi:10.1017/S0022112063000975.

Kopaliani, Z. D. (1972), Laboratory study of dune movement of coarse sediments (in Russian), *Trans. State Hydrol. Inst.*, *204*, 61–74.

McLean, S. R. (1990), The stability of ripples and dunes, *Earth Sci. Rev.*, *29*(1–4), 131–144.

Michell, J. H. (1893), The highest waves in water, *Philos. Mag.*, *36*, 430–437.

Núñez-González, F., and J. P. Martín-Vide (2010), Downstream-migrating antidunes in sand, gravel and sand-gravel mixtures, in *River Flow 2010*, vol. 1, edited by A. Dittrich et al., pp. 393–400, Bundesanst. für Wasserbau, Braunschweig, Germany.

Recking, A., V. Bacchi, M. Naaim, and P. Frey (2009), Antidunes on steep slopes, *J. Geophys. Res.*, *114*, F04025, doi:10.1029/2008JF001216.

Reynolds, A. J. (1965), Waves on the erodible bed of an open channel, *J. Fluid Mech.*, *22*, 113–133, doi:10.1017/S0022112065000630.

Richards, K. J. (1980), The formation of ripples and dunes on an erodible bed, *J. Fluid Mech.*, *99*, 597–618, doi:10.1017/S002211208000078X.

Simons, D. B., E. V. Richardson, and M. L. Albertson (1961), Flume studies using medium sand (0.45 mm), *U.S. Geol. Surv. Water Supply Pap. 1498-A*, 76 pp.

Smith, J. D. (1970), Stability of a sand bed subjected to a shear flow of low Froude number, *J. Geophys. Res.*, *75*, 5928–5940, doi:10.1029/JC075i030p05928.

Southard, J. B., and L. A. Boguchwal (1990), Bed configuration in steady unidirectional water flows; Part 2, Synthesis of flume data, *J. Sediment. Petrol.*, *60*(5), 658–679.

Spinewine, B., O. E. Sequeiros, M. H. Garcia, R. T. Beaubouef, T. Sun, B. Savoye, and G. Parker (2009), Experiments on wedge-shaped deep sea sedimentary deposits in minibasins and/or on channel levees

emplaced by turbidity currents. Part II. Morphodynamic evolution of the wedge and of the associated bedforms, *J. Sediment. Res.*, *79*(8), 608–628, doi:10.2110/jsr.2009.065.

Vanoni, V. (1974), Factors determining bed forms of alluvial streams, *J. Hydraul. Eng.*, *100*(3), 363–367.

White, F. M. (1979), *Fluid Mechanics*, McGraw-Hill, New York.

Wieprecht, S. (2000), *Development and Behaviour of Bed Forms of Coarse Bed Material* (in German), vol. 74, 153 pp., Inst. of Hydraul., Univ. of Fed. Armed Forces, Munich, Germany.

J. P. Martín-Vide and F. Núñez-González, Hydraulics Department, Technical University of Catalonia, Jordi Girona 1-3, D1, E-08034, Barcelona, Spain. (fngon@yahoo.com)

River Flow 2010 - Dittrich, Koll, Aberle & Geisenhainer (eds) - © 2010 Bundesanstalt für Wasserbau ISBN 978-3-939230-00-7

Downstream-migrating antidunes in sand, gravel and sand-gravel mixtures

F. Núñez-González & J. P. Martín-Vide
Hydraulics Department, Technical University of Catalonia, Jordi Girona 1-3, D1, 08034 Barcelona, Spain

ABSTRACT: Downstream-migrating antidunes occur at upper-regime flows, but in contrast to the upstream-migrating antidunes, there have been a scarce number of reports about them in literature. Likewise, little is known about the characteristics of upper-regime and transitional bedforms when the bed sediment is not composed of a unique grain-size. In this study, flume experiments are described, for which mobile-bed equilibrium conditions were obtained for flows at, and close to, the transition between lower- and upper-regimes. High sediment feeding rates, even as high as 1 kg per second, were required for reproducing such conditions, for which three-dimensional downstream-migrating antidunes were the most frequent bedforms observed. Bed material for the experimental runs was composed of sand, gravel and two sand gravel mixtures, with average sand contents of 32% and 44%, respectively. A good agreement was found when comparing experimental results with bedform existence fields developed with potential flow theory, with the exception of the direction of movement of transitional bedforms, which theory failed to predict adequately. Mean flow velocity-wave length theoretical equations did not perform well for three-dimensional downstream-migrating antidunes, possibly because of the difficulties of defining adequately a transversal border condition.

Keywords: Bedforms, Upper-regime, Antidunes, Sand, Gravel, Sediment-mixtures

1 INTRODUCTION

Bedforms produced by water flowing over an alluvial bed have an important feedback effect on flow and are closely related to sediment transport. The understanding of them is, therefore, essential for the study of river hydraulics and sediment transport mechanics.

Bedforms developed in sand beds have been widely studied in experimental flumes and rivers. Bedforms composed of grain-size mixtures, however, have received less attention. In particular, few observations exist for transitional and upper-regime bedforms composed of mixed-size material.

In this study we report experimental bedforms in beds composed of sand, gravel and two sand-gravel mixtures, for flows with Froude numbers near to 1. The most frequent bedforms observed in the experiments were short-crested downstream-migrating antidunes; such bedforms are rarely reported in literature in comparison to the long-crested upstream-migrating antidunes and flat bed, with which upper-regime flow is normally associated.

The main distinctive characteristics of the bed features formed during the experiments are highlighted, and a comparison is presented with potential flow theory.

1.1 *Dunes and antidunes*

Dunes are the most characteristic bedforms in fully-rough turbulent subcritical flows (low Froude numbers). These forms migrate downstream and are asymmetrical in shape, with a gentle stoss-side slope and a steep slope on the leeside. The mechanism by which dunes move downstream is related to the flow separation eddy over the leeside, which induces deposition of material in front of the slip-face. On the other hand, bedforms typically associated with supercritical flows have been generally classed as antidunes, and the feature that most distinguishes them from dunes is the fact that the water surface undulations appear in-phase with the antidunes.

Bearing this defining attribute in mind, an attribute which involves the influence of the water surface standing-waves over the bed shape, antidunes are not only characteristic of supercritical flows, they are also likely to occur even under subcritical flow conditions.

Antidunes tend to be more symmetrical than dunes, showing a sinusoidal appearance, and move either upstream, downstream or remain stationary. As the direction of movement of antidunes is related to the sediment depositional pattern, distinctive relict internal sedimentary structures are associated with their migration direction. As such, some sedimentologists consider that the more generic term "in-phase waves" should be applied to upper-regime bedforms, so that downstream-migrating antidunes (DMA) and stationary antidunes should be distinguished from upstream-migrating antidunes (UMA) as different classes of bedforms in their own right (Cheel 2005).

Antidunes and dunes are classed as two-dimensional (2D) when their crest is straight transverse to the flow. Conversely, the shape of the so-called three-dimensional (3D) dunes and antidunes is more complex in plan form, and, in contrast to 2D forms, they often develop scour holes in their troughs. Given that the crests of 3D bed features are shorter than in 2D forms, 3D forms are also named short-crested. 3D bedforms occur for higher Froude numbers than their 2D counterparts. There is a scarce amount of literature available regarding reports on 3D antidunes.

1.2 *Bedform stability fields*

The ranges of flow conditions and sediment characteristics under which stable bedforms develop have been studied empirically by different authors, mostly for uniform sand-size material. Diagrams have thus been suggested with delimited stability fields for the occurrence of the different bedform classes (e.g., Vanoni 1974, Southard and Boguchwal 1990). Nevertheless, because of the lack of observations, some borders between bedform fields have been poorly defined or have been conceived of as intuitive extrapolations from the better-known regions. Furthermore, most stability fields specify *neither* a clear border between 2D and 3D bedforms, *nor* the conditions defining the direction of movement of antidunes.

In considering the validity of empirical diagrams developed from uniform sand material, Carling (1999) found that stability fields in such diagrams can be extended to grain-sizes pertaining to coarse gravel. Likewise, Kleinhans et al. (2002) concluded that these diagrams are also valid for supply-limited bedforms in sand-gravel if the plots are used with the bed-load material instead of with the bed material.

Bedform existence fields can be drawn in accordance with stability analysis based on potential flow theory, developed by Anderson (1953), Kennedy (1961) and Reynolds (1965). Potential flow analysis allows for discrimination between 2D and 3D antidunes. In the same manner, the theory outlines the border between UMA and DMA. Nevertheless, a clear delimitation between upper-stage plane bed and DMA is not specified by theory.

1.3 *Bedforms at and close to the transition between lower- and upper-regime*

For fine sediment, transition from lower-stage bedforms to antidunes is characterized by an upper-stage plane bed region. It has been observed that for coarser grain-sizes such a plane bed might not occur, in such a way that the dunes phase can be followed by antidunes.

Carling and Shvidchenko (2002) compiled experimental and field-data belonging to bedforms in the dune-antidune transition in fine gravel and compared them with theory. Descriptions of transitional bedforms reported by different authors showed a variety of morphologies and characteristics that resemble those of dunes or antidunes, or both. Carling and Shvidchenko also contrasted data for DMA with potential flow theory and found an acceptable agreement. They also highlighted the need for more empirical data to delineate the dune-antidune phase transformation in gravel.

Little information exists about bedforms at, and close to, the transition between the lower- and upper flow regimes for sediment mixtures. In this sense, it is worth mentioning the work of Chiew (1991), who studied the effect of sediment gradation on the transition between bedform types. While he found no important effects, he did find a tendency towards the absence of antidunes for higher grain-size standard deviations, which he attributed to the formation of a dynamic armored layer.

In this study we present experimental observations of bed features formed in sand, gravel and two mixtures of these materials for flows with Froude numbers near 1. High-sediment transport rates were required, as the objective was to study bed features that get formed when all the bed material size-fractions are in motion. In a similar fashion to the previous studies described above, data are compared with potential flow theory, and possible reasons for deviations

between theory and experimental evidence are discussed.

2 BEDFORM STABILITY FIELDS OBTAINED FROM POTENTIAL FLOW THEORY

Following the original stability analysis outlined by Anderson (1953) and extended by Kennedy (1961), Kennedy (1963) presented relations for defining bedform stability fields as a function of the Froude number

$$Fr = \frac{V}{\sqrt{gH}} \tag{1}$$

and the wave number $k=2H\pi/L$, where g = gravitational acceleration, H = mean flow depth, L = length of the sediment wave, and V = mean flow velocity. In this manner, the upper-regime occurs when $Fr > Fr_u$, where:

$$Fr_u = \sqrt{\frac{\tanh(k)}{k}} \tag{2}$$

UMA are likely to occur for the range $Fr_u < Fr < Fr_p$, with Fr_p defined by:

$$Fr_p = \sqrt{\frac{1}{k\tanh(k)}} \tag{3}$$

The theory also allows for delimitation between 2D and 3D antidunes, such a border being given by:

$$Fr_d = \sqrt{\frac{1}{k}} \tag{4}$$

Equations 2, 3 and 4 are plotted in Figure 4.

DMA are likely to occur for large wave numbers if $Fr > Fr_p$ and $Fr > Fr_u$. In such a regime the water- and bed- surfaces are in-phase, but in contrast with UMA, the water-depth is greater over the troughs than over the crests, in a similar way to dunes, so that net sediment deposition occurs over the troughs (Carling and Shvidchenko, 2002; Parker, 2004).

Upper-stage plane bed for high Froude numbers cannot be predicted by theory. Nevertheless, for $Fr > Fr_u$ and low wave numbers ($k\rightarrow 0$), i.e., large wave-lengths, antidunes are depressed and upper-stage plane bed is likely to occur (Carling and Shvidchenko, 2002).

According to potential flow theory analysis, the wave-length of antidunes is related to the mean flow velocity by:

$$V = \sqrt{\frac{gL}{2\pi}} \tag{5}$$

This relation does not hold for 3D waves, which are shorter. Such waves on the water surface are formed by the coincidence of stationary waves in the flow direction and cross-waves transversal to the flow; these waves are also known as "rooster-tails". According to Hasegawa and Kanbayashi (1996, after Yokokawa, et al. 2008), short-crested antidunes are formed when the wave-lengths of 2D antidunes and water-surface diagonal-cross waves are the same. From a previous development by Fuchs (1952, in Kennedy, 1961), Kennedy presented the following functional relation between the mean flow velocity and the wave-length of 3D waves in which he considered that the waves celerity and the flow velocity are the same

$$V = \sqrt{\frac{gL}{2\pi}}\sqrt[4]{1+\left(L/L_t\right)^2} \tag{6}$$

where L_t = wave-length normal to the direction of flow, which as a first approximation can be taken as the channel width.

When contrasting equations (5) and (6) with experimental data in sand, Kennedy (1961) found a sound correlation between 2D waves, whereas he found an overestimation trend of the flow velocity for 3D antidunes. Kennedy estimated that the discrepancies for 3D waves could be due to considering the transverse wave-length of the rooster-tails as being equal to the channel width.

3 EXPERIMENTS PERFORMED

The objective of the experiments was to study the flow, sediment transport, and bed features developed at, and close to, the transition between lower- and upper-flow regimes. As a result, high sediment transport rates and flow discharges were required. In order to meet these requirements, a new experimental set-up was used, which was conceived so as to enable the performance of long-lasting runs with a constant feeding of mixed-size material, without requiring a large stock of sediment. This condition was achieved with a system that not only recirculated the sediment collected at the end of the channel, but also separated sand- and gravel-fractions, and fed each size-fraction back into the channel at a constant rate using an automatic feeder. A more detailed description of the feeding and recirculating systems can be found in Núñez-González and Martín-Vide (2009).

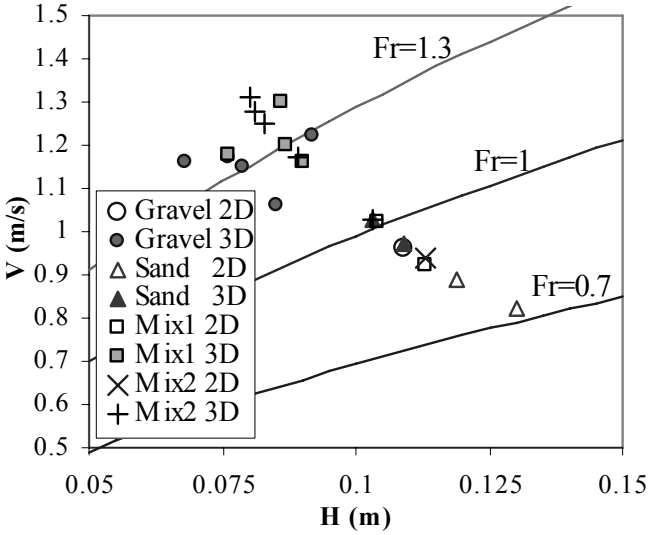

Figure 1. Range of experimental data. 2D and 3D refer to the dominant stationary-wave observed.

Four experimental series were performed, each for a different grain-size material, namely gravel, sand and two sand-gravel mixtures. Geometric mean diameters for the sand and gravel were 1.5 and 3.5 mm, respectively, and geometric standard deviations were 1.3 for the sand and 1.4 for the gravel. The sediment mixtures were obtained by mixing the original sand and gravel with an average proportion of 32% sand content for mixture 1 (Mix1) and 44% for mixture 2 (Mix2). Mix1 was slightly bimodal, while Mix2 was unimodal. Each experimental series consisted of 6 runs, except for the sand series, for which 4 runs were performed.

The experimental flume was rectangular, 30m long (27m effective length), 0.75m wide and 0.60m deep. Water-discharge was controlled with an automatic electronic flow-meter and was fed and recirculated independently from the sediment circuit. Water-depth, and bed- and water-slopes were obtained from measurements of the bed- and water-surface level performed at the channel's glass-paneled walls with rulers that were spaced one meter apart.

Experiments consisted in obtaining mobile-bed equilibrium conditions for a given water-discharge and sediment-feeding rate, mostly by erosion of the original bed profile, i.e., imposing higher flows than those required to transport the sediment fed into the channel. Prescribed unit water discharges and sediment-feeding rates ranged from 78 to 112 l/s/m and 0.081 to 1.07kg/s, respectively. The proof of mobile-bed equilibrium having been attained was the equality of the feeding- and the recirculated-sediment rates, and the persistence of average water-depths, bed- and water-slopes, and bedform dimensions over several hours.

During the equilibrium phase of the experimental runs the bedforms near the channel walls and the water-surface waves were observed, photographed and recorded in video. Some point measurements of some characteristics of the bed and water-surface waves were carried out as well, namely, celerity, amplitude and wave-length. In addition, bedload samples were taken at the downstream end of the channel using a sampler as wide as the channel. The sampler was divided into three parts of equal length, with the aim of proving possible transversal grain-size sorting trends.

At the end of each run, the bed surface was photographed, and surface- and subsurface-bed material samples were taken at different locations along the channel. Bed scour was measured at a section 4.5 meters upstream from the end of the channel by opening a vertical section where original bed-material had previously been replaced by gravel painted with different colors and set at 1cm thick successive horizontal layers.

4 EXPERIMENTAL RESULTS

The range of mean flow velocities, water-depths and Froude numbers measured during the equilibrium phase of the experimental runs is shown in Fig. 1. Equilibrium energy slopes ranged from 0.006 to 0.021, while bed shear stresses, after making modifications which took side-wall effects into account following the Vanoni and Brooks method, ranged from 5.8 to 16.3 Pa. Descriptions of the water- and bed-configurations, scour patterns and grain-sorting are presented as follows.

4.1 *Water surface configuration*

Trains of rooster-tails were observed during most of the runs (see Fig. 2), with varying characteristics of shape, geometry and stability. All the rooster-tails and water waves that were observed showed a net downstream displacement, though a single wave could sometimes, for short periods, remain stationary, migrate upstream or disappear to rebuild again. For most of the runs the rooster-tails were stable in the sense that if they broke they reformed rapidly, while the train of rooster-tails was not markedly affected.

2D waves formed at the upper-part of the channel, some meters downstream from the sediment input, and they then transformed into rooster-tails, normally between 10 to 15 meters downstream from the sediment-input section. For a varying length of 3 to 6 meters the 3D waves kept growing in height and length until they

stabilized at a more or less fixed geometry, which was conserved until the end of the channel downstream.

The criterion for distinguishing between 2D and 3D waves, as plotted in Fig. 1, was mainly related to the dominant wave observed on the surface. Given that most of the runs showed rooster-tails, the criteria used to classify the water-surface as 2D was that the rooster-tail protruded slightly above the surface compared to the other stationary waves – if, that is, such waves were present – or compared to the sediment waves on the bed surface.

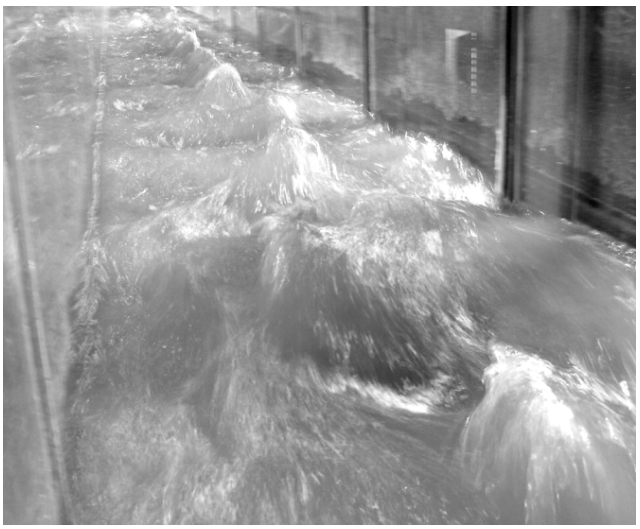

Figure 2. Train of short-crested stationary waves, "rooster-tails", for a sand-gravel sediment mixture with 32% sand content. Run with Fr=1.23. Mean wave-length is 62 cm. Flow from background to foreground.

4.2 *Bed configuration*

Above all in the case of the sediment mixtures run series, bed states observed during the runs consisted of the coexistence of two types of bedforms. On one hand, low amplitude features prevailed next to the channel walls. On the other hand, at the center of the channel 3D-DMA occurred under the rooster-tails. For sand- and gravel-runs, low amplitude bedforms might have been present as well, but could have remained hidden to direct observation because of the higher amplitude and lower wave-length of the dominant bedforms.

As with the rooster-tails, bed features observed next to the flume walls always migrated downstream and evolved along the channel until they reached a stable configuration. Usually, they were first noticeable 3 to 5 meters downstream from the upper-sediment input. From here to where they reached stability – i.e., 10 to 15 meters downstream from the sediment-input section – the features moved faster, and were shorter and lower than their stable counterparts at the last section of the flume downstream. Though we may refer here to a "stable" configuration, this should be considered within a statistical sense, given that for some runs the bedforms near the wall varied their shape and geometry continuously.

The shape of the bedforms near the channel walls and their degree of coupling with the water surface varied with the Froude number and the bed-material. For some conditions, such variation was important even within a single run. In general, unequivocal antidunes (i.e., bedforms which were an in-phase image of the water surface irrespective of their symmetrical or asymmetrical shape, see Fig. 3) appeared with higher Froude numbers for the gravel and mixtures than they did for the sand-run series. A similar trend was observed for transitional bed-states, which are here considered to be those characterized by, firstly, bedforms with a certain degree of coupling between water- and bed-surface and, secondly, those for which the bed configuration alternated between showing dunes and antidunes. Transitional bedforms observed consisted of downstream migrating features, mainly low-relief waves for the mixtures and gravel, and transitional dunes for the sand. Transitional bedforms were rounder the stronger the coupling with the water surface, and the higher the flow Froude number, were. Also, a separation eddy on their leeside was more evident for low Froude numbers, for which the features appeared sharp-crested.

Normally, on account of the turbidity of the water and the local unsteadiness of flow, it was not possible to observe the bedforms at the channel central section. Nevertheless, based on the scarce observations available we can assume that if and when rooster-tails occurred on the surface, then beneath these rooster-tails the bedforms were in-phase with the water wave, and thus can be classed as antidunes. What is more uncertain is the shape and size of these forms. Nonetheless, based on the isolated observations that it was possible to make, and in agreement with observations already made by Kennedy (1961) regarding sand beds, we can infer that the bed under the rooster-tails had the same 3D form as the surface waves, with the difference that the bed waves were neither as high nor as sharp as the surface waves.

Normally, when the water discharge was drawn down at the end of each run (this usually took between 1 and 2 minutes), most of the bedforms were erased. This type of behavior is typical of antidune configurations and is one of the main reasons why antidunes are so rarely preserved (Carling and Breakspear, 2007).

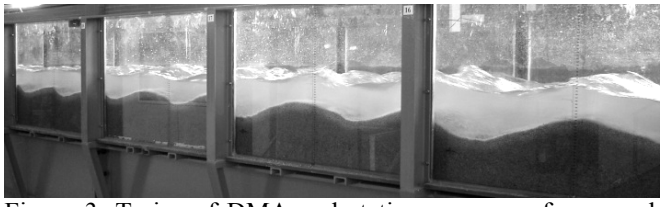

Figure 3. Trains of DMA and stationary waves for a sand run with Fr=1.02. Note that water and bed surfaces appear roughly in-phase, and that water-depth over the troughs is higher than over the crests. Mean wave-length is 53 cm. Flow from left to right. Length of glass panels is 1 meter.

4.3 *Bed scour patterns*

Though antidunes and other steep bedforms were washed away when the water discharge was stopped at the end of the run, the transversal profile of maximum scour that they produced was measured for the sand- and mixtures-run series by identifying the buried colored gravel that remained. For the mixtures, the deepest scour occurred at the center of the channel, except for the runs with the lowest Froude number. A direct qualitative relation was found between the observed strength of the rooster-tail during the run and the depth of scour at the central section. Conversely, scour profiles for the sand-runs were approximately uniform, i.e., the depth of scour was roughly the same all along the transversal section. Such a pattern reflects the tendency for the bedforms in the sand runs to be more two-dimensional than the runs with sediment mixtures, which showed a marked three-dimensionality for most of the runs.

4.4 *Differences between bed materials*

Overall, differences between bedforms for the four bed materials were less important for the gravel compared to the mixtures than they were for the sand compared with gravel and mixtures. For example, similar to the findings made by Kuhnle (1993) with regards to lower-regime bedforms in sand, gravel, and sand-gravel mixtures, we found that bedform amplitudes were higher the higher the sand content in the mixture was. In this manner, amplitudes of sand bedforms were 3 to 5 times higher than in mixtures and in gravel.

With respect to the sediment grain-size sorting for the mixtures-runs, a slight bias towards a finer bed-surface was noticed with increasing Froude numbers. On the other hand, bedload samples showed a subtle trend for coarser material to travel preferentially at the center of the channel. This tendency concurred with visual inspection of the sections opened to measure scour depths in the sense that open-framework gravels were often noticed at the central section.

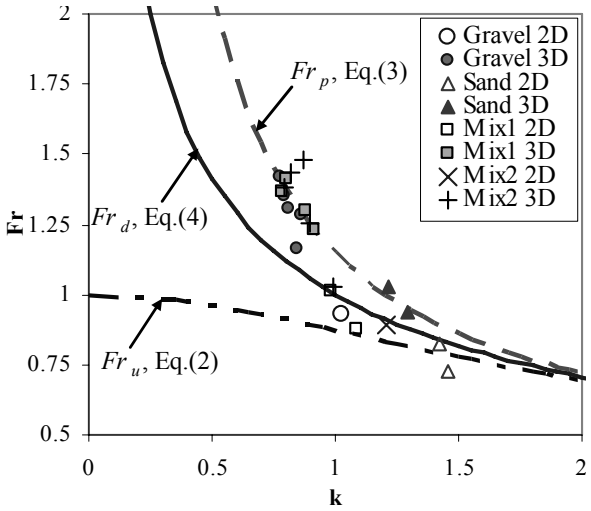

Figure 4. Comparison between experimental data for sand, gravel and sand-gravel mixtures, and bedform occurrence fields delimited with the potential flow theory.

4.5 *Comparison with potential flow theory*

Figs. 4 and 5 show plots of the experimental results compared with potential flow theory as outlined by Eqs. (1) to (6). As can be seen in Fig. 4, most of the data for 3D waves appear close to the curve used to, theoretically, delineate the upper limit for 3D antidunes as well as the lower limit for DMA (Eq. 3). As a result, we may say that theory corresponded adequately to observations for 3D-DMA, except for one gravel data-point and one mix1 data-point, which unequivocally appear inside the region for UMA. The same occurs for most of the rest of the data-points corresponding to 2D waves. For all of these runs the waves moved downstream, so that even when theory accurately predicts the bidimensionality of the majority, it fails to define the direction of their movement correctly.

Fig. 5 depicts the relation between mean flow velocity and wave-length as given by Eqs. (5) and (6), and shows the experimental data for comparison. For most of the 3D waves, Eq.(6) underestimates the experimental mean flow velocities. Conversely, Eq.(5) overestimates flow velocities for most of the 2D waves.

Experimental wave-lengths used for drawing Figs. 4 and 5 were obtained from measurements of rooster-tails and performed by two different methods. The first consisted in a direct measurement of the distance between crests of different waves during the runs using a tape-measure. For the second method the number of crests over a known distance was counted using photos of the last 10 meters of the channel. Standard deviations of the measurements were, on average, 10% of the mean wave-lengths. The procedures for obtaining an average wave-length were not *absolutely* accurate; firstly, because not many waves could be counted owing to the

limited length (10m) of the section observed, which, in turn, limited the number of measurements that could be made of the distance between the wave-crests, and, finally, because the distance between these crests varied significantly from one moment to another.

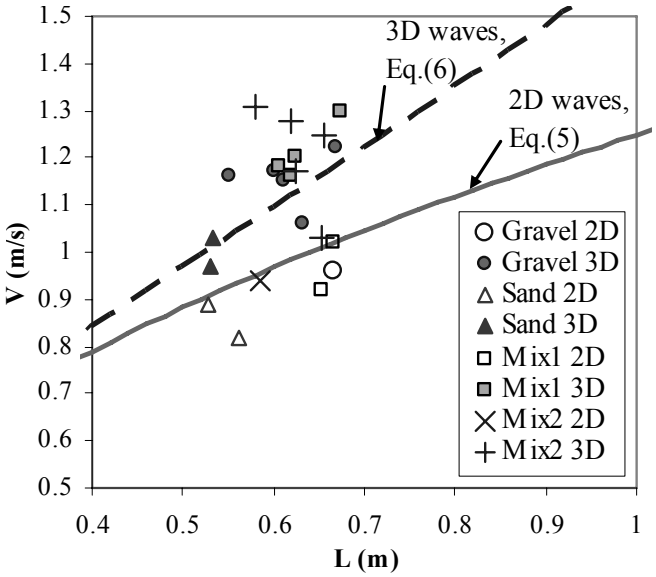

Figure 5. Comparison of measured flow velocities and wave-lengths with potential flow theory, Eqs. (5) and (6), for 2D and 3D waves, respectively.

5 DISSCUSSION

Wave-lengths used for plotting Figs. 4 and 5 were obtained from measurements of the rooster-tails observed in all of the experimental runs. However, based on the experimental observations it was clear that for some runs the dominant bed- and water-configurations were not necessarily 3D, although the water surface did show short-crested 3D waves. For this reason, these bed states were classed as 2D. On the other hand, if the dominant bed- and water-configurations were 2D, then it would follow that short-crested waves may not be necessarily linked to the bulk flow properties. Conversely, local-flow properties at the central section of the channel would be related to the formation of the rooster-tails, as opposed to the mean flow conditions. This would signify that an inconsistency exists in using the measured wave-lengths of the rooster-tails, which are a 3D feature, when applying potential flow theory to a predominantly 2D flow.

As a consequence, for flows with dominant 2D bed- and water-configurations, a different flow velocity than the section mean value should be used in order to coherently test the rooster-tails' existence with potential theory. Such a flow velocity would have to represent the conditions at the channel central section where the rooster-tails were formed. By proceeding in the reverse order, if we consider that Eq.(3) represents the stability conditions for 3D-DMA, we can obtain the flow velocities representative of the central section where the short-crested waves occurred. This is achieved by making Eqs.(1) and (3) equal, and using the measured k and H values. For all points originally indicated as 2D as well as for the two 3D outliers, such velocities were computed. Then, flow velocities obtained in this manner were used with Eq.(6) to compute theoretical wave-lengths. These 3D wave-lengths were found to have, on average, a difference of less than 3% when they were compared with the measured values; that is to say, this percentage is of the same order of magnitude as the measurement accuracy. This proves the appropriateness of relating the formation of short-crested waves in a predominantly 2D bed- and water-configuration to local flow conditions, rather than relating it to the section's average flow properties.

The preceding analysis reflects the transitional nature of flow between well established lower-regimes and upper-regimes. It also reflects the failure of potential flow theory to describe the bedform characteristics when applying the bulk flow properties in such a transition. As a consequence, the definition of the limits where the dune-antidune transition occurs is relevant. Carling and Shvidchenko (2002) considered that, due to lag-effects and possible depth-limitations, the range of Froude numbers within which transitional bedforms can persist in fine gravel varies between 0.5 and 1.8. Nevertheless, they found that, for most of the reported studies, transitional bedforms cannot occur for Fr > 1.3. Our results concur with this upper limit in light of the fact that the highest Foude number for the range of transitional bedforms observed was 1.3.

5.1 *Wave-length and occurrence of 3D-DMA*

In Fig. 4, most 3D-DMA plot within the region where potential flow theory predicts their existence. Nevertheless, wave-lengths in Fig. 5 are overestimated. One cause for this discrepancy is related to the transversal length of the short-crested waves since this length might not necessarily be equal to the channel width.

Although rooster-tails are formed by surface diagonal waves, channel-walls might not be a defining factor for their existence. Kennedy (1961) evidenced this assertion by quoting an experimental run performed at the Colorado State University, for which an isolated train of rooster-tails formed at the center of a 2.4m wide channel. For this run it was apparent that the vertical channel walls did not exercise any influence on the formation of the short-crested waves. As such,

the channel width might not necessarily be equal to the rooster-tail wave-length normal to the direction of flow used in Eq.(6). It is possible that the excavated scour-holes by the rooster-tails could, in some cases, set a transversal boundary narrower than the channel width.

The minimum wave-number for which DMA were reported in data collected by Carling and Shvidchenko (2002) was $k \approx 0.6$ (obtained from Fig. 8 in Carling and Shvidchenko, 2002). As shown in Fig. 4, the minimum wave number registered for DMA in the experimental runs of this study was $k=0.78$, which concurs with the former value.

6 CONCLUSIONS

Transitional bedforms and three-dimensional downstream-migrating antidunes were the most frequent bedforms observed in experiments performed in very coarse sand, very fine gravel and two sand-gravel mixtures, with flow conditions at, and close to, the transition between lower- and upper-regimes. Bedform stability-fields drawn after potential flow theory performed well when compared with the experimental observations, except for the transitional bedforms for which the direction of movement cannot be predicted. Functions relating flow velocity with wave-length failed to adequately describe the experimental results. For three-dimensional downstream-migrating antidunes such a disparity can be attributed to the difficulty of defining a proper transversal border condition.

ACKNOWLEDGMENTS

The first author was supported by the Programme Alβan, the European Union Programme of High Level Scholarships for Latin-America, No.(E04D048796MX), and by Conacyt, México (179047). The authors thank Professor Gary Parker for providing them with a digital copy of Kennedy's original study on antidunes.

REFERENCES

Anderson, A.G. 1953. The characteristics of sediment waves formed by flow in open channels. Third Midwest Conference on Fluid Mechanics, University of Minnesota, Minneapolis, Minn.

Carling, P.A., Breakspear, R.M.D. 2007. Gravel dunes and antidunes in fluvial systems. In Dohmen-Janssen, C.m. & Hulscher, S.J.M.H. (eds.), River, Coastal and Estuarine Morphodynamics: RCEM2007, Taylor & Francis: 1015-1020.

Carling, P.A., Shvidchenko, A.B. 2002. A consideration of the dune:antidune transition in fine gravel. Sedimentology, 49, 1269-1282

Carling, P.A. 1999. Subaqueous gravel dunes. J. of Sedimentary Research, 69(3), 534-545

Cheel, R.J. 2005. Introduction to clastic sedimentology. Course Notes. Department of Earth Sciences, Brock University, Ontario, Canada

Chiew, Y.M. 1991. Bed features in nonuniform sediments. J. of Hydraulic Engineering, 117(1), 116-120

Fuchs, R.A. 1952. On the theory of short-crested oscillatory waves. Gravity Waves, National Bureau of Standards Circular 521, 187-200

Hasegawa, K., Kanbayashi, S. 1996. Formation mechanism of step-pool systems in steep rivers and guide lines for the design of construction. J. of Hydroscience and Hydraulic Engineering 40, 893-900. (in Japanese with English abstract)

Kennedy, J.F. 1963. The mechanics of dunes and antidunes in erodible bed channels, J. of Fluid Mechanics, 16, 521-544.

Kennedy, J.F. 1961. Stationary waves and antidunes in alluvial channels. Rep. no. KH-R-2. W.M. Keck Laboratory of Hydraulics and Water Resources, California Institute of Technology, Pasadena, CA, 146 pp.

Kleinhans, M.G., Wilbers, A.W.E., De Swaaf, A., Van Den Berg, J.H. 2002. Sediment supply-limited bedforms in sand-gravel bed rivers. J. of Sedimentary Research, 72(5), 629-640

Kuhnle, R.A. 1993. Fluvial transport of sand and gravel mixtures with bimodal size distributions. Sedimentary Geology, 85, 17-24

Núñez-González, F., Martín-Vide, J.P. 2009. Bed resistance and sediment transport experiments in sand, gravel and sand-gravel antidunes. 33th IAHR Congress, Water Eng. for a Sustainable Environment, Vancouver, Canada

Parker, G. 2004. 1D Sediment transport morphodynamics with applications to rivers and turbidity currents. Chap. 8. Fluvial Bedforms. E-Book: http://cee.uiuc.edu/people/parkerg/morphodynamics_ebook.htm

Reynolds, A.J. 1965. Waves on the erodible bed of an open channel. J. of Fluid Mechanics, 2*2*, 113-133

Southard, J.B., Boguchwal, L.A. 1990. Bed configuration in steady unidirectional water flows; Part 2, Synthesis of flume data. J. of Sedimentary Petrology, 60(5), 658-679

Vanoni, V. 1974. Factors determining bed forms of alluvial streams. J. of Hydraulic Engineering, 100(3), 363-367

Yokokawa, M., Hasegawa, K., Kanbayashi, S., Endo, N. 2008. 3D antidunes preserved on fine-grained sand bed in an experimental flume: Genetic conditions and their sedimentary structures. Marine and River Dune Dynamics. Leeds, U.K., 345-351